

W. Eric Wong
Editor

Proceedings of the 4th International Conference on Computer Engineering and Networks

CENet2014

W. Eric Wong

Editor

Proceedings of the 4th International Conference on Computer Engineering and Networks

CENet2014

 Springer

Editor

W. Eric Wong
University of Texas at Dallas
Plano, TX, USA

ISSN 1876-1100 ISSN 1876-1119 (electronic)
Lecture Notes in Electrical Engineering
ISBN 978-3-319-11103-2 ISBN 978-3-319-11104-9 (eBook)
DOI 10.1007/978-3-319-11104-9

Library of Congress Control Number: 2014957309

Springer Cham Heidelberg New York Dordrecht London
© Springer International Publishing Switzerland 2015

This work is subject to copyright. All rights are reserved by the Publisher, whether the whole or part of the material is concerned, specifically the rights of translation, reprinting, reuse of illustrations, recitation, broadcasting, reproduction on microfilms or in any other physical way, and transmission or information storage and retrieval, electronic adaptation, computer software, or by similar or dissimilar methodology now known or hereafter developed.

The use of general descriptive names, registered names, trademarks, service marks, etc. in this publication does not imply, even in the absence of a specific statement, that such names are exempt from the relevant protective laws and regulations and therefore free for general use.

The publisher, the authors and the editors are safe to assume that the advice and information in this book are believed to be true and accurate at the date of publication. Neither the publisher nor the authors or the editors give a warranty, express or implied, with respect to the material contained herein or for any errors or omissions that may have been made.

Printed on acid-free paper

Springer International Publishing AG Switzerland is part of Springer Science+Business Media
(www.springer.com)

Contents

Volume I

Part I Algorithm Design

1	A Spatiotemporal Cluster Method for Trajectory Data	3
	Yunbo Chen, Hongchu Yu, and Lei Chen	
2	Use Case Points Method of Software Size Measurement Based on Fuzzy Inference	11
	Yue Xie, Jilian Guo, and Anwei Shen	
3	ATPG Algorithm for Crosstalk Delay Faults of High-Speed Interconnection Circuits	19
	Yuling Shang and Pei Zhang	
4	Application of a Fuzzy-PID Control Method to Synchronized Control of a Multisteping Motor	27
	Wenhao Shi, Lu Shi, Fang An, Zhouchang Wu, Zhongxiu Weng, and Lianqing Zhao	
5	The Improved Bayesian Algorithm to Spam Filtering	37
	Hongling Wang, Gang Zheng, and Yueshun He	
6	Evolution of Community Structure in Complex Networks	45
	Lei Zhang, Jianyu Li, Shuangwen Chen, and Xin Jin	
7	Construction of a Thermal Power Enterprise Environmental Performance Evaluation Model	55
	Xiaofei Liao, Huayue Li, Weisha Yan, and Lin Liu	
8	A Mobile Localization Algorithm Based on SPSO Algorithm	65
	Maoheng Sun and Azhi Tan	

9	A Fast and Accurate Algorithm of Subspace Spectrum Peak Search Based on Bisection Method	73
	Yu Wang, Hong Jiang, and Donghai Li	
10	A CRF-Based Method for DDoS Attack Detection	81
	Yu Wang, Hong Jiang, Zonghai Liu, and Shiwen Chen	
11	Advanced SOM Algorithm Based on Extension Distance and Its Application	89
	Haitao Zhang, Binjun Wang, and Guangxuan Chen	
12	A Trilateral Centroid Localization and Modification Algorithm for Wireless Sensor Network	97
	Yujun Liu and Meng Cai	
13	Simulation Study on Trajectory Tracking in Manipulator Based on the Iterative Learning Control Algorithm	107
	Yanfen Luo	
14	An Improved Gaussian Mixture Model and Its Application	115
	Guang Han	
15	GPU Acceleration for the Gaussian Elimination in Magnetotelluric Occam Inversion Algorithm	123
	Yi Xiao and Yu Liu	
16	Artificial Neural Networks in Biomedicine Applications	133
	Jiri Krenek, Kamil Kuca, Aneta Bartuskova, Ondrej Krejcar, Petra Maresova, and Vladimir Sobeslav	
17	SOC Prediction Method of a New Lithium Battery Based on GA-BP Neural Network	141
	Kai Guan, Zhiqiang Wei, and Bo Yin	
18	Compressed Sensing for Channel State Information (CSI) Feedback in MIMO Broadcast Channels	155
	Yuan Liu and Kuixi Chen	
19	Implementation and Performance Evaluation of the Fully Enclosed Region Upper Confidence Bound Applied to Trees Algorithm	163
	Lin Wu, Ying Li, Chao Deng, Lei Chen, Meiyu Yuan, and Hong Jiang	
20	A New Linear Feature Item Weighting Algorithm	171
	Shiyuan Tian, Hui Zhao, Guochun Wang, and Kuan Dai	

21	Trust Value of the Role Access Control Model Based on Trust	179
	Xiaohui Cheng and Tong Wang	
22	Universal Approximation by Generalized Mellin Approximate Identity Neural Networks	187
	Saeed Panahian Fard and Zarita Zainuddin	
23	Research and Application of Function Optimization Based on Artificial Fish Swarm Algorithm	195
	Meiling Shen, Li Li, and Dan Liu	
24	Robust Hand Tracker Using Joint Temporal Weighted Histogram Features	201
	Zhiqin Zhang, Fei Huang, and Linli Tan	
25	Combination of User’s Judging Power and Similarity for Collaborative Recommendation Algorithm	209
	Li Zhang, Yuqing Xue, and Shuyan Cao	
26	An Improved Naïve Bayes Classifier Method in Public Opinion Analysis	219
	Yun Lin, Jie Wang, and Rong Zou	
27	Overseas Risk Intelligence Monitoring Based on Computer Modeling	227
	Peipei Su	
28	Quality of Service-Based Particle Swarm Optimization Scheduling in Cloud Computing	235
	Shuang Zhao, Xianli Lu, and Xuejun Li	
 Part II Data Processing		
29	Improving Database Retrieval Efficiency	245
	Shaomin Yue, Wanlong Li, Dong Han, Hui Zhao, and Jinhui Cheng	
30	Improving TCP Performance in Satcom Links by Packet-Loss Detection	253
	Yuan He, Minli Yao, and Xiong Xiong	
31	Key Management Scheme in Cluster for WSNs	263
	Xiaoming Liu and Qisheng Zhao	
32	An Energy-Saving Method for Erasure-Coded Distributed Storage System	271
	Lei Yang and Shi Liu	

33 LF: A Caching Strategy for Named Data Mobile Ad Hoc Networks	279
Li Zhang, Jiayan Zhao, and Zhenlian Shi	
34 Topological Characteristics of Class Collaborations	291
Dong Yan and Keyong Wang	
35 Cluster Key Scheme Based on Bilinear Pairing for Wireless Sensor Networks	299
Xiaoming Liu and Qisheng Zhao	
36 The LDP Protocol Formal Description and Verification Based on CPN Model	305
Rengaowa Sa, Baolier Xilin, Yulan Zhao, and Neimule Menke	
37 Self-Adaptive Anomaly Detection Method for Hydropower Unit Vibration Based on Radial Basis Function (RBF) Neural Network	315
Xueli An	
38 A Fast Distribution-Based Clustering Algorithm for Massive Data	323
Xin Xu, Guilin Zhang, and Wei Wu	
39 Design and Implementation of Virtual Experiment System Based on Universal Design	331
Yun Liu, Guoan Zhao, Dayong Gao, and Zengxia Ren	
40 Effects of Information Services on Economic Growth in Jilin Province	341
Fang Xia, Bingbing Zhao, and Xiaochun Du	
41 Day-Ahead Electricity Demand Forecasting Using a Hybrid Method	349
Zirong Li, Xiaohe Zhang, Yan Li, and Chun Liu	
42 Membrane System for Decision-Making Problems	357
Lisha Han, Laisheng Xiang, and Xiyu Liu	
43 Operational Model Management C/S System Based on RUP	365
Rui Guo	
44 Decision Analysis Method Based on Improved Bayesian Rough Set and Evidence Theory Under Incomplete Decision System	371
Zhihai Yang, Weihong Yu, Yan Chen, and Taoying Li	
45 An Enhanced Entropy-K-Nearest Neighbor Algorithm Based on Attribute Reduction	381
Lingyun Wei, Xiaoli Zhao, and Xiaoguang Zhou	

46 Synthetic Safety Analysis: A Systematic Approach in Combination of Fault Tree Analysis and Fuzzy Failure Modes and Effect Analysis 389
 Guannan Su, Linpeng Huang, and Xiaoyu Fu

47 Evaluation Model of Internet Service Provider Attraction Based on Gravity Model 399
 Lihua Heng, Gang Chen, and Zongmin Wang

48 An Application of Ecological Adaptation Evaluation of Orthoptera in Daqinggou Nature Reserve Using SPSS 407
 Chunming Liu, Tao Meng, and Bingzhong Ren

49 Intelligent Diagnostics Applied Technology of Specialized Vehicle Based on Knowledge Reasoning 415
 Licai Bi, Yujie Cheng, Dong Hu, and Weimin Lv

50 On the Evaluation of Influence of Golf Websites in China 425
 Fangzhi Liu

51 An Ensemble Learning Approach for Improving Drug-Target Interactions Prediction 433
 Ru Zhang

52 A Complementary Predictor for Collaborative Filtering 443
 Min Chen, Wenxin Hu, and Jun Zheng

53 Knowledge Discovery from Knowledge Bases with Higher-Order Logic 451
 Guangyuan Li

54 Numerical Analysis on High-Altitude Airdrop Impact Processing of Water Bag 459
 Hong Wang, Tao Xu, and Yahong Zhou

55 Heterogeneous Data Sources Synchronization Based on Man-in-the-Middle Attack 467
 Yunze Wang and Yinying Li

56 Direct Forecast Method Based on ANN in Network Traffic Prediction 477
 Congcong Wang, Gaozu Wang, Xiaoxiao Zhang, and Shuai Zhang

Part III Pattern Recognition

57 Visual Simulation of Three-Point Method Guidance Trajectory for Antitank Missile 487
 Mengchun Zhong, Cheng Li, and Hua Li

58	A Fast and Accurate Pupil Localization Method Using Gray Gradient Differential and Curve Fitting	495
	Yuhui Lin, Zhiyi Qu, Yu Zhang, and Huiyi Han	
59	A Method for the Chinese-Tibetan Machine Translation System's Syntactic Analysis	505
	Zangtai Cai	
60	Analysis of Micro-Doppler Features of an Armored Vehicle Based on EMD	513
	Wanjun Zhang, Minjie Niu, and Xiaoying Wu	
61	Kinect-Based 3D Color Reconstruction	521
	Li Yao, Guosheng Dong, and Guilan Hu	
62	Application of Image Retrieval Based on the Improved Local Binary Pattern	531
	Zhen Sun, Xichang Wang, and Jiang Liu	
63	Intelligent Detection of Complex Gaps in Live Working Based on Video Analysis	539
	Yu Fan, Kangxiong Yu, Xiaoqing Tang, Heping Zheng, Li Yu, and Ge Zhang	
64	Face Detection Based on Landmark Localization	547
	Peng Liu, Songbin Li, Qiongxing Dai, and Haojiang Deng	
65	Image Enhancement Using a Fractional-Order Differential	555
	Guo Huang, Li Xu, Qingli Chen, and Tao Men	
66	An Improved Fractional Differential Method for Image Enhancement	565
	Qingli Chen and Guo Huang	
67	On Qualitative Analysis of High-Contrast Patches in Range Images	573
	Qingli Yin	
68	An Improved Method of Tracking and Counting Moving Objects Using Graph Cuts	583
	Mingjie Zhang and Baosheng Kang	
69	Automatic Detection of Pharyngeal Fricatives in Cleft Palate Speech	591
	Yan Xiao and Mangui Liang	
70	Improved Chinese Word Segmentation Disambiguation Model Based on Conditional Random Fields	599
	Fanjin Mai, Shitong Wu, and Taoshi Cui	

71	Mobile Real-Time Monitoring System Based On Human Action Recognition	607
	Lin Chai, Zhiqiang Wei, and Zhen Li	
72	A Kind of Image Classification Method Study	615
	Guoqing Wu, Bingheng Yang, and Liang Lv	
73	Weld Pool Image Processing and Feature Extraction Based on the Vision of the CO₂ Welding	625
	Xiaogang Liu and Xiaowei Ji	
74	On Energy Distribution Characteristics of Froth Images	635
	Yanpeng Wu, Xiaoqi Peng, Yanpo Song, and Qian Jiang	
75	Classification Performances of Extreme Learning Machine with Choquet Integral	643
	Aixia Chen, Zhiyong Liang, and Zhen Guo	
76	Facial Expression Recognition Using Color-Depth Cameras	649
	Kezhen Xie, Zhen Li, and Zhiqiang Wei	
77	Parallel Pipeline Implementation for Moving Objects Detection in Traffic Video Analysis on a Heterogeneous Platform	659
	Teng Li, Yong Dou, Jingfei Jiang, and Peng Qiao	
78	A Novel Optical Flow Algorithm Based on Bionic Features for Robust Tracing	669
	Weiwu Ren, Xiao Chen, Xiaoming Wang, and Mingyang Liu	
79	An Obstacle Detection System for a Mobile Robot Based on Radar-Vision Fusion	677
	Xiao Chen, Weiwu Ren, Mingyang Liu, Lisheng Jin, and Yue Bai	
80	De-noising Method for Echocardiographic Images Based on the Second-Generation Curvelet Transform	687
	Haihong Xue, Binjin Chen, Kun Sun, and Jianguo Yu	
81	A Novel Method for Image Segmentation Using Pulse-Coupled Neural Network Based on Root Mean Square of Gray Scale	695
	Hongliang Shi, Jian Rong, and Xinmin Zhou	
82	Combined Similarity-Based Spectral Clustering Ensemble for PolSAR Land Cover Classification	705
	Lu Liu, Dong Sun, and Junfei Shi	

83	An Algorithm for Human Face Detection in Color Images Based on Skin Color Segmentation	713
	Chunqiang Zhu	
84	A Social Network Service-Based Environment Monitoring System in Home	719
	Jiajin Zhang, Lichang Chen, Quan Gao, Zhaobo Huang, Lin Guo, and Yanxin Yang	

Volume II

Part IV Cloud Computing

85	Cloud Computing Security Issues and Countermeasures	731
	Ziqian Xiao and Jingyou Chen	
86	A Time-Aware QoS Prediction Approach to Web Service Recommendation	739
	Xuejie Zhang, Zhijian Wang, Weijian Zhang, and Fang Yang	
87	Design Issue and Performance Analysis of Data Migration Tool in a Cloud-Based Environment	749
	Shin-Jer Yang, Chung-Chih Tu, and Jyhjong Lin	
88	Fuzzy Time Series Forecasting Algorithm Based on Maximum Interval Value	761
	Che Liu, Yunfei Zhang, Fang Yang, Wenhuan Zhou, and Xin Lv	
89	Assessing the Effectiveness of Cloud Computing in European Countries	769
	Petra Marešová and Kamil Kuča	
90	Coordination Strategies in a Cloud Computing Service Supply Chain Under the Duopoly Market	777
	Lingyun Wei, Xiaohan Yang, and Xiaoguang Zhou	
91	A Novel Approach to Trust-Aware Service Recommendation	787
	Guoqiang Li, Lejian Liao, Dandan Song, Zhenling Zhang, and Jingang Wang	
92	A Web Service Discovery Method Based on Data Segmentation and WordNet	797
	Tingna Liu and Ling Jiang	
93	OpenSource Automation in Cloud Computing	805
	Vladimir Sobeslav and Ales Komarek	

94 Utilization of Cloud Computing in Education with Focus on Open-Source Technologies 813
 Vladimir Sobeslav, Josef Horalek, and Jakub Pavlik

95 A Survey of Extended Role-Based Access Control in Cloud Computing 821
 Hongjiao Li, Shan Wang, Xiuxia Tian, Weimin Wei, and Chaochao Sun

96 Coordination Strategy in an SaaS Supply Chain with Asymmetric Information About the Market 833
 Lingyun Wei, Jiafei Ling, and Xiaoguang Zhou

97 One More Efficient Parallel Initialization Algorithm of K-Means with MapReduce 845
 Bingliang Lu and Shuchao Wei

98 Equipment Information Management System Based on Web Services 853
 Gangguo Li, Wu Qin, Tingyi Zhou, Yang wang, and Xiaofeng Zhu

99 Maximal Service Profit in MAS-Based Cloud Computing Considering Service Security 861
 Shengji Yu, Hongyu Chen, and Yanping Xiang

Part V Embedded Systems

100 Protection Circuit Design of Lithium-Ion Battery Pack Based on STM32 Processor 871
 Hongtao Zhang, Fen Wu, Hang Zhou, Xiaoli Peng, Chunhua Xiao, and Hui Xu

101 Analysis of an Intelligent 1553B-Bus Communication Module Design Based on ARM Platform 879
 Chunlei Song

102 Design of Multichannel Data Real-Time Processing System Based on Serial Port Communication 889
 Peigang Jia and Sirui He

103 ZigBee-Based Online Dust-Concentration Monitoring System 897
 Hui Chao and Wang Zhou

104 The Application of WeChat to the University Laboratory Management Information System 907
 Jiangsheng Zhao and Xi Huang

105	A Short Loop Queue Design for Reduction of Power Consumption of Instruction-Fetching Based on the Dynamic Branch Folding Technique	917
	Wei Li and Jianqing Xiao	
106	Chip Design of a Continuous-Time 5-MHz Low-Pass Sigma-Delta Modulator	925
	Jhin-Fang Huang, Jiun-Yu Wen, and Wei-Chih Chen	
107	A Fine-Grained Power Gating Technique for Reducing the Power Consumption of Embedded Processor	935
	Wei Li and Jianqing Xiao	
108	Kinematic Simulation for Series-Parallel Combination Laser Machine Tool	943
	Zhiqin Qian, Jiawen Wang, Lizong Lin, and Qun Cao	
109	Implementation of a Fine-Grained Parallel Full Pipeline Schnorr–Euchner Sphere Decoder Algorithm Accelerator on Field-Programmable Gate Array	953
	Shijie Li, Lei Guo, Yong Dou, and Jingfei Jiang	
110	The Bandpass Sigma-Delta Modulator with Converter Chip Design for Positron Emission Tomography Front-End Application	963
	Wen-Cheng Lai, Jhin-Fang Huang, Kun-Jie Huang, and Pi-Gi Yang	
111	Simulation Testing Apparatus and Method for Embedded System Based on Universal Serial Bus Host	971
	Xin Li, Lingping Chen, Rentai Chen, and Shengwen Jiang	
112	Simple Simulation of Abandoned Farmland Based on Multiagent Modeling Approach	979
	Xuehong Bai, Lihu Pan, Huimin Yan, and Heqing Huang	
113	Parallel Parity Scheme for Reliable Solid-State Disks	987
	Jianbin Liu, Hui Xu, Hongshan Nie, Hongqi Yu, and Zhiwei Li	
114	Design of Tibetan Latin Transliteration System in Unicode	995
	Xiaoying Chen, Jinyong Ai, and Xiaodan Guo	
115	Graphical User Interface Reliability Prediction Based on Architecture and Event Handler Interaction	1003
	Zhifang Yang, Sanxing Yang, Zhongxing Yu, Beibei Yin, and Chenggang Bai	

116 An Energy-Efficient Dual-Level Cache Architecture for Chip Multiprocessors 1011
 Mian Lou, Longsheng Wu, Senmao Shi, and Pengwei Lu

117 The Performance Optimization of Component-Based System 1019
 Daisen Wei, Xueqing Li, and Longye Tang

118 Microblog Data Parallel Monitoring Algorithm on Compute Unified Device Architecture 1027
 Yunpeng Cao and Haifeng Wang

119 Universal Central Control of Home Appliances as an Expanding Element of Smart Home Concepts 1035
 Jan Dvorak, Ondrej Berger, and Ondrej Krejcar

120 Lightweight Optimization of Android Permission Model 1043
 Peixin Que, Xiao Guo, and Zhen Wang

121 Modeling of Virtual Electrical Experiment 1051
 Yinling Zhang, Deti Ji, and Renyou Zhang

122 Human Intervention Intelligent Flight Path Planning on Unexpected Threats 1059
 Peng Ren, Xiaoguang Gao, and Jun Chen

Part VI Network Optimization

123 Effectiveness Analysis of Communications Jamming to Battlefield Ad Hoc Network 1071
 Sijia Lou, Jun He, and Wei Song

124 Research and Outlook on Wireless Channel Models 1079
 Yuqing Wang, Cuijie Du, Xiujuan Han, Yuxin Qin, and Hongqi Wang

125 Defending Against Whitewashing Attacks in Peer-to-Peer File-Sharing Networks 1087
 Weimin Luo, Jingbo Liu, Jiang Xiong, and Ling Wang

126 A New Type of Metropolitan Area Network 1095
 Chuansheng Wu, Yunqiu Shi, and Shicheng Zhao

127 Improved Hierarchical Routing Scheme Based on Game Theory in Wireless Sensor Networks 1103
 Wan Qiang Han, Hai Bin Wu, and Zhi Jia Lu

128 An Item-Based Collaborative Filtering Framework Based on Preferences of Global Users 1113
Chengchao Li, Pengpeng Zhao, Jian Wu, Jiumei Mao, and Zhiming Cui

129 Disassortativity of Class Collaboration Networks 1121
Dong Yan, Keyong Wang, and Maolin Yang

130 Online Social Networks Based on Complex Network Theory and Simulation Analysis 1129
Xin Jin, Jianyu Li, and Lei Zhang

131 Analysis of Network Accessibility 1139
Shuijian Zhang and Ying Zhang

132 Mobile Botnet Propagation Modeling in Wi-Fi Networks 1147
Na Li, Yanhui Du, and Guangxuan Chen

133 Dynamic Evaluation of Suppliers for Industrial Value Chain Value-Added Service Platform 1155
Hua Pan and Linfu Sun

134 Energy-Saving Mechanisms for Delay- and Disruption-Tolerant Networks 1165
Yankun Feng and Xiangyu Bai

135 Improved Sensor-MAC Protocol for Wireless Sensor Networks 1177
Jian Di and Zhijun Ma

136 An Approach of Analyzing Transmission Capacity of Multi-hop Wireless Sensor Networks 1185
Shaoqing Wang, Kai Cui, and Ning Zhou

137 A Rapid Payload-Based Approach for Social Network Traffic Identification 1195
Yanping Li and Yabin Xu

138 Performance Prediction of WSNs’ Mobile Nodes Based on GM-Markov Method 1207
Xiaohui Cheng, Jinzhou He, and Qiliang Liang

139 Virtual Network Mapping Algorithm Based on Bi-level Programming Research 1215
Mingchun Zheng, Xinxin Ren, Xiao Li, Panpan Zhang, and Xuan Liu

140 Kalman Filter-Based Bandwidth and Round Trip Time Estimation for Concurrent Multipath Transfer Performance Optimization in SCTP 1225
 Wen Li, Wenbo Wang, Xiaojun Jing, and Wen Liu

141 Common-Knowledge and Cooperation Management I 1235
 Takashi Matsuhisa

142 Detection of Topic Communities in Social Networks Based on Tri-LDA Model 1245
 Wei Ou, Zanfu Xie, Xiping Jia, and Binbin Xie

143 Communications and Quality Aspects of Smart Grid Network Design 1255
 Vladimir Sobeslav and Josef Horalek

144 An Adaptive Greedy Geographical Routing Protocol for Mobile Multihop Wireless Network 1263
 Feng Liu, Jianli Li, Gong Qin, and Fanhua Kong

145 A Coverage-Enhancing Algorithm Based on Local Virtual Force Equilibrium for Wireless Sensor Networks 1273
 Yujian Wang and Kaiguo Qian

146 Network Node Importance Measurement Method Based on Vulnerability Analysis 1281
 Yahui Li, Hongwa Yang, and Kai Xie

147 Modeling for Information Transmission of Consumer Products Quality and Safety Based on the Social Network 1291
 Yingcheng Xu, Xiaohong Gao, Ming Lei, Huali Cai, and Yong Su

148 A Multi-classifier-Based Multi-agent Model for Wi-Fi Positioning System 1299
 Shiping Zhu, Kewen Sun, and Yuanfeng Du

Part I
Algorithm Design

Chapter 1

A Spatiotemporal Cluster Method for Trajectory Data

Yunbo Chen, Hongchu Yu, and Lei Chen

Abstract As positioning and communication technologies become more widespread, the production of large amounts of different types of trajectory data and the extraction of useful information from mass trajectory data have emerged as hot issues in data mining. This paper presents a trajectory data processing method featuring simple operation, high precision, and strong practicability. For low-precision trajectory data that are discrete but contain time information, a clustering algorithm is proposed to extract information from such data. The algorithm can detect a point of interest (POI) in trajectory data by setting space and time thresholds. Trajectory data collected from a taxi using a global positioning system in Kunming, China, are used as experimental data. We conduct an experiment to detect a POI in the collected trajectory data and carry out a visual analysis of these special positions. The experimental results show the effectiveness of the algorithm, which can in addition compress trajectory data.

Keywords Trajectory data • Data mining • Spatiotemporal cluster

1.1 Introduction

Orientation technology and information communication technology have reached the stage in their development where they allow for the tracking, in real time, of dynamic objects, resulting in a huge amount of trajectory data. For example, taxi companies, bus companies, and government agencies have installed global positioning systems (GPS) on vehicles to monitor and manage them. To track vehicles continuously, the systems send location information by GPS for continuous acquisition to a vehicle management control center. When a person's mobile phone communicates with the mobile communication base station, the mobile

Y. Chen

Kunming Urban Planning and Information Center, 650500 Kunming, China

H. Yu (✉) • L. Chen

Faculty of Land and Resource Engineering, Kunming University of Science and Technology,
650500 Kunming, China

e-mail: 1063716089@qq.com

© Springer International Publishing Switzerland 2015

W.E. Wong (ed.), *Proceedings of the 4th International Conference on Computer Engineering and Networks*, Lecture Notes in Electrical Engineering 355,
DOI 10.1007/978-3-319-11104-9_1

3

communication services will collect data on the user's location and reconstruct her trajectory based on the data. In this article, time-continuous position data are called *trajectory data* and may be used to record the trajectories of people or objects. Vehicle management centers and mobile communication service providers generally delete data regularly or irregularly, and large amounts of trajectory data contain a wealth of information.

At present, with the increasing application of positioning technology, the accumulation of large amounts of trajectory data provides opportunities for mining useful information from the data, but the mining of such information presents a challenge. On the basis of an in-depth analysis of the characteristics of trajectory data, this paper proposes and implements a processing algorithm for GPS trajectory data that only requires setting time and space thresholds to detect special positions in trajectories; in addition, the algorithm can compress raw trajectory data.

Some academics called, for example, trajectory data for location history data [1], time-stamped position data, and GPS traces [2, 3]. Studies on such data approach the topic mainly from the following three viewpoints. (1) Data expression: Hangerstrand first introduced the concept of *time trajectory* and *space-time prism* to analyze a human migration model [4]. With time as the variable axis, people's space as the dependent variable axis, using migration records by government statistics or artificial records, he was able to visualize human migration on a three-dimensional coordinate axis. Usually, the trajectory is simply expressed as a series of coordinate pairs: $[(x_1, y_1, t_1), \dots, (x_n, y_n, t_n)]$, $(x_i, y_i) \in \text{space plane}$, $t_1 < t_2 < \dots < t_i < \dots < t_n$, $i \in 1 \dots n$. (2) Data compression: because of the continuously changing spatial position of a moving object, simply recording and transmitting all the positioning data will reduce the performance of the system, so researchers have studied trajectory data compression algorithms with the aim of effectively updating the location of moving objects. (3) Data application: these are primarily applied in mobile communication network optimization and location-based services (LBSs) to provide services in connection with mobile communication in moving users when a user's location needs to be tracked and even to predict the location of users to optimize service and reduce the network load. The premise of the LBS is to know the locations of users, so it needs to track them. In 2010, at the Asian Microsoft Research Institute, Dr. Xie Xin and coworkers launched a research project called GeoLife [5, 6]. This project initially carries GPS data collected daily to conduct research from the following three points of view: to understand a user's life trajectory by deducing travel modes; to obtain an in-depth understanding of users by estimating their travel experiences; to understand the location environment by predicting the user's points of interest (POIs). The results can be applied to the following areas: life experience sharing based on GPS trajectories; common regional travel recommendations, such as, for example, interesting places and travel experts; personalized locations or recommendations of friends.

Based on the foregoing discussion, on the one hand, most current studies focus on specific applications to solve specific problems; on the other hand, less research is being conducted on trajectory data processing methods and existing processing methods because current multilevel segmentation algorithms have certain

limitations with respect to accuracy and practicability. The application analysis of trajectory data is inseparable from the extraction of POIs. Because the coordinates of POIs produced by user access to the same location change frequently, direct analysis of such POIs is infeasible; thus, an algorithm needs to cluster POIs extracted from trajectory data that distribute the adjacent POIs to the same cluster, which (the cluster) is carried out to replace the POI for analysis. In view of this, this paper attempts to provide a spatio-temporal clustering processing method for trajectory data. First, the method makes it possible to extract meaningful positions or temporal events related to the object of study and to compress vast amounts of data.

The chapter is organized as follows. Section 2 presents related concepts and algorithms, Sect. 3 uses the proposed algorithm in an experiment and in the visualization analysis of GPS vehicle trajectory data, and the last section presents conclusions and future prospects.

1.2 Principle Explanation

The moving of objects in space is usually considered an function (generally for a two-dimensional location) which reflects the changes of objects' spatial position over time. In a particular plane coordinate system, the spatial location of an object is represented as a coordinate pair (x, y) , and the trajectory of the object can be expressed as a function $f(t) = (x, y)$, where f is a continuous function and t is time. In real life, we usually take samples from the coordinates of moving objects in spatiotemporal coordinates to express the approximate trajectory [7]. The general sampling methods are as follows:

Time-based sampling: by setting a sampling time interval (e.g., 30 s) in the motion process, the spatial location of objects are recorded once every 30 s. In vehicle monitoring, this is the majority of the sampling mode, typically using a GPS for the position.

Change-based sampling: in motion processing, when changes take place, the position is recorded, such as the position of an object when the object movement direction changes.

Location-based sampling: when an object is close to the sensors which were placed beforehand, the sensors will record the object's position, such as, for example, when scanning objects in a specific location and the delivery and transfer of goods in logistics.

Event-based sampling: the establishment of a position triggered by some event, such as a phone call, or answering when a mobile communication company locates a customer in order to establish a communication link.

The experimental data in this paper are GPS vehicle trajectory data. A taxi sends data to a monitoring center every 15 s to monitor and manage the vehicle. This type of data acquisition is based on the first method of data sampling, which uses short

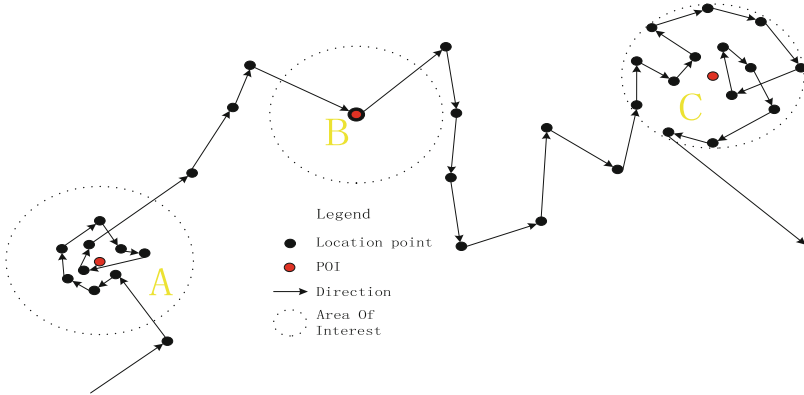


Fig. 1.1 Trajectory sampling of something, points of interest, and interest region sample

sampling intervals, features complete data, is not subject to accidental factors, and makes it easy to analyze people's patterns of travel in traffic. Regardless of the sampling method used, it is necessary to obtain a set of discrete points. For the sake of convenience, discrete points are represented as three-dimensional coordinates (t, x, y) : the spatiotemporal location of the object, which we call the anchor point, and (x, y) , which refer to the location and time. Thus, the trajectory of object A can be represented as a collection of $c = \{(t_i, x_i, y_i) | i \in \mathbb{N}^+\}$, where i represents discrete points sorted by time sequence number and (t_i, x_i, y_i) are the location of the i th point of the trajectory. It is worth noting that the location of the anchor point is generally subject to error because the size is related to the method used to determine the position.

This paper proposes a method of space–time clustering to extract vehicle POIs, defined as a moving person or object, at a location for more than a limited time, to satisfy $\sqrt{(x_j - x_i)^2 + (y_j - y_i)^2} \leq \Delta D$, $t_j - t_i \geq \Delta t$, where ΔD refers to the free space distance threshold and Δt refers to the time interval threshold. Because of the multiscale nature of human activities, different spatial distance and time thresholds are set to detect activity on different scales. In the extraction of residential travel POIs, the spatial distance threshold is generally 400 or 500 m, while the time threshold is generally 30 min [8]. Considering the accuracy of GPS positioning and cluster rationality, this paper adopts time thresholds of 5, 10, and 30 min and spatial distance thresholds of 200, 400, and 800 m for testing and comparison and, ultimately, we selected a distance threshold value of 800 m and a time threshold of 30 min. Figure 1.1 shows the sampling of a trajectory generated from a person or an object moving in space. The arrows indicate the direction of movement, and the black points denote sampling trajectory points based on people or objects in the process of moving in an uneven distribution of the location of the space. We believe that the POI has a special meaning for the object, the red spots in the map are POIs,

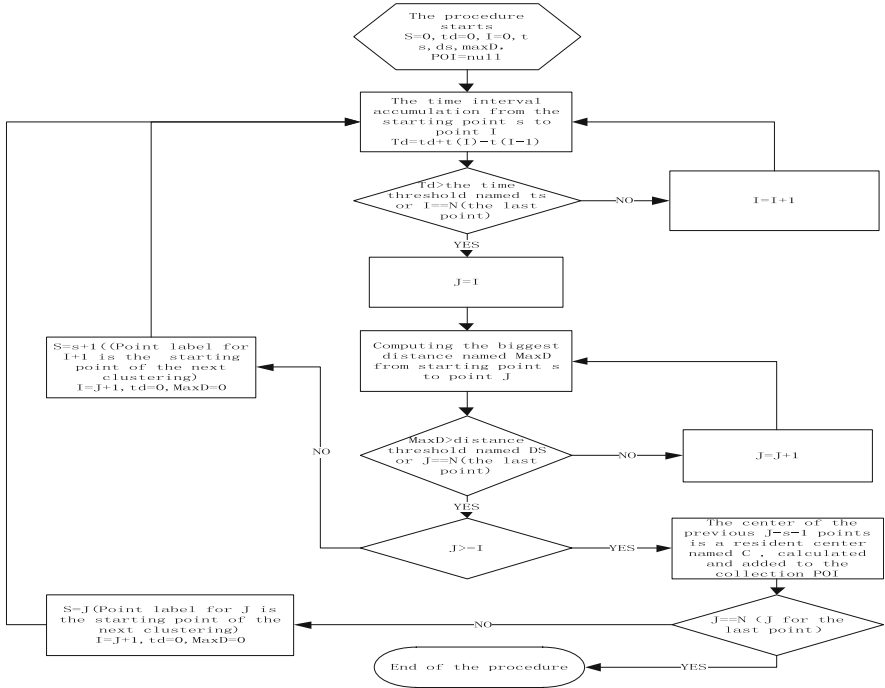


Fig. 1.2 Flow chart of POI extraction

With further considering the geographical region around the POIs in a certain range, draw the dotted line circle as a region of interest.

For the POIs having a special meaning for the object, we designed an algorithm to extract POIs from trajectory data. The objective is to cluster the spatiotemporal data. Here, I is the anchor point number, t_i the time attribute of anchor points labeled I , t_d the total time difference, s the starting point of clustering, J the clustering endpoint, and $MaxD$ the maximum distance between the starting point and the endpoint. T_s is the time threshold, DS the space threshold, N the final anchor point, and POI the collection of POIs. The algorithm procedure is shown in Fig. 1.2.

1.3 Experiments

In this paper, the proposed algorithm was implemented in Visual Studio 2010, with the results visually displayed and analyzed. First, the experimental data are presented, followed by data preprocessing; then the proposed clustering algorithm

Table 1.1 Taxi tracking data example

Stime	Latitude	Longitude	Speed	Orientation	State
2 February 2011 00:00:09	25040101	102732921	51	89	263
2 February 2011 00:00:24	25037901	102732930	58	90	263
2 February 2011 00:00:39	25035863	102732900	48	90	263
2 February 2011 00:00:54	25034553	102732860	10	91	775
2 February 2011 00:01:10	25033483	102732403	46	114	65,799

is used to analyze and process the data; finally, the results obtained by the proposed clustering algorithm are subject to visual analysis in the ArcGIS platform.

1.3.1 Introduction of Data

The data in our study were provided by a taxi company in the city of Kunming, China. The company installed a GPS on a vehicle with the vehicle position data transmitted to the monitoring center every 15 s. The data included the time, longitude, latitude, vehicle running speed and angle, and passenger capacity. Table 1.1 displays the GPS taxi daily travel trajectory data fragments. Of these, *stime* is the acquisition of the anchor point time, here Beijing time, accurate to the second; the format is years–month–day–points–seconds; *latitude* means latitude, and *longitude* means longitude, and latitude and longitude expanded one million times in the original data; *speed* is the instantaneous velocity, in kilometers per hour, of the taxi in operation; *orientation* is the direction of the taxi runtime in degrees; and *state* is the carrying capacity. The GPS positioning precision is 3–10 m, but the vehicle running speed and angle only have a reference value because in most of the time, they are not accurate. Experiments were carried out on a total of 9,579 data points during the week of the study.

1.3.2 Preprocessing

Prior to analysis, the preprocessing made original data satisfy the following processing requirements. (1) Abnormal data elimination: typical noise may shift positioning data, that is, the positioning data change a great deal in the inner space in a short period of time. This kind of noise, caused by unstable GPS signals, is removed as abnormal data prior to analysis. (2) Coordinate conversion: the location of the original data is expressed in the geographical coordinates of latitude and longitude, which is not conducive for calculation of the distance or for integration with the geographic base map, so the analysis should be carried out after the unified coordinate transformation of the data. (3) Data visualization: a GPS track record is



Fig. 1.3 Visualization of GPS track record and GPS trajectory reconstruction

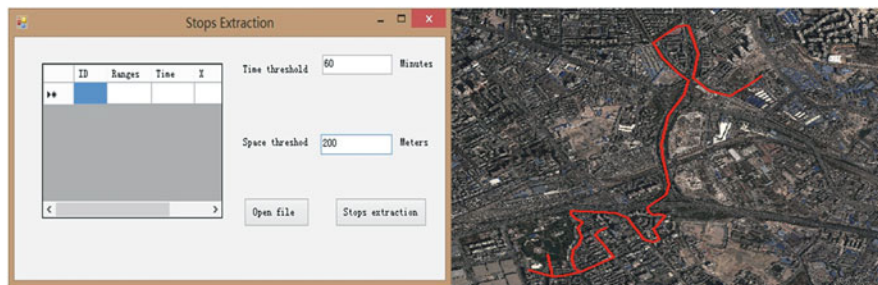


Fig. 1.4 Extraction interface and visualization of POIs

Table 1.2 Statistics for a Taxi, 21–27 February 2011, POIs in 1 Week

Time threshold (min)	Space threshold (m)	Points of interest
5	200	20
10	200	6
10	400	8
10	800	28
30	200	3

not appropriate for intuitive analysis and needs to be visualized; for this reason, it is necessary to connect the track points based on the time sequence so as to reconstruct the vehicle trajectory, as shown in Fig. 1.3.

1.3.3 Analysis of POI Extraction and Visualization

After data preprocessing, the proposed algorithm can be used to cluster and visualize the results. As shown in Fig. 1.4 (top), POI extraction, time threshold, and space threshold should be set before clustering. Obviously, Table 1.2 shows the

characteristics that if the time threshold is set higher and the space threshold lower, there will be fewer POIs, and vice versa. The red points in Fig. 1.4 show the taxi running POI from the map, including the train station, airport, gas station, and other common locations. Further exploration is required to determine whether there is a reference value for the source of taxis transporting passengers.

Conclusion and Prospects

This paper explored a method of clustering trajectory data using an algorithm. Experiments were carried out using real trajectory data, with the results showing that this algorithm could be used effectively to cluster trajectory data and detect the position of research objects in a meaningful manner while effectively compressing the trajectory data. Along with the use of China's Beidou satellite, real-time dynamic object tracking will make it easier to produce more trajectory data. Thus, the trajectory data processing method, the data mining algorithm, and the application research are necessary for LBSs. Nevertheless, further research is still required to mine more data, create more processing algorithms, and develop application models; at the same time, efforts will be made to acquire different object trajectory data for analysis and mining.

References

1. Hariharan R, Toyama K. Project Lachesis: parsing and modeling location histories. *Geogr Inf Sci.* 2004;18(5):106–24.
2. Bamis M, et al. Lightweight extraction of frequent spatio-temporal activities from GPS traces. *Real Time Syst Symp.* 2010;275(31):281–91.
3. Kami N, et al. Algorithm for detecting significant locations from raw GPS data. *Discov Sci.* 2010;321(18):221–35.
4. Hägerstrand T. What about people in regional science? *Pap Reg Sci.* 1970;24(9):7–24.
5. Zheng Y, et al. GeoLife2.0: a location-based social networking service. *Proceedings of the MDM'09*; Beijing, China; 2009. pp. 357–58.
6. Xie X, et al. Understanding user behavior geospatially, contextual and social media understanding and usage. *J ACM.* 2009;214(3):233–41.
7. Zheng Y, et al. Learning transportation mode from raw GPS data for geographic applications on the web. Submitted to WWW 2008; *Journal of the Association for Computing Machinery (JACM)*; 2008.185(2):247–56.
8. Wolfson O, et al. Updating and querying databases that track mobile units. *Distributed Parallel Database.* 1999;7(3):257–387.

Chapter 2

Use Case Points Method of Software Size Measurement Based on Fuzzy Inference

Yue Xie, Jilian Guo, and Anwei Shen

Abstract Size measurement is the key element in software development costs and schedule estimation, and the success of a software project directly relates to measurement accuracy. This paper addresses the problem of use case complexity weight hierarchies of discontinuity in the traditional use case points (UCP) method and proposes an improved complexity weight calculation method that utilizes fuzzy theory to analyze the complexity of use cases. First, with use case transactions as input and complexity weight as output, this paper is based on a fuzzy inference system. Then fuzzy rules are established based on the relationship between complexity weights and transactions in use cases. These fuzzy rules can be used to compute the complexity weight. Studies have shown that the proposed method can eliminate discontinuity grades of use case complexity and enhance the accuracy of UCP estimation as well.

Keywords Software size measurement • UCP • Fuzzy inference • Complexity weight

2.1 Introduction

With the rapid development of computer technology, software has become an important symbol of modern information processes. The increasing complexity and scale of modern software has led to a dramatic rise in costs of software and caused software development to fall far behind schedule [1]. The most important task in the development of software programs is to estimate the labor, cost, and release schedule of software, which are key factors in estimating and ascertaining the scope of software projects. As the key factor in software engineering, the size estimate directly relates to the success of the entire software development project [2].

Y. Xie (✉) • J. Guo • A. Shen
Aeronautics and Astronautics Engineering College, Air Force Engineering University,
710038 Xi'an, China
e-mail: xpy2012@foxmail.com

The use case points (UCP) method is a method for estimating a software project's scope and effort based on use case in the object-oriented development method, which was proposed by Gustav Karner in 1993. It uses cases and actors that have been identified and classified according to their complexity to calculate UCPs and then uses the relation of UCPs to effort to obtain the developmental effort of software projects required in man-hours as the main feature of the method; nevertheless, because a use case is based on usage and places the user at the center of the software rather than the system or design, it shows greater robustness and stability than the Function Point method or the Lines of Code method. A large number of research papers suggest that UCP is a very effective method [3].

UCP has attracted wide research attention since its invention. Some issues related to UCP have been addressed in previous efforts. Anda focuses on adjustment factors, while others highlight the discrepancies in designing use case models [4, 5]. Robiolo and Ochodek propose different size metrics such as transactions, TT points, and paths [6, 7]. In addition, researchers have analyzed the discontinuity problem of use case complexity grades [8, 9]. In this paper we propose an improved UCP method based on fuzzy inference that uses fuzzy theory to analyze the complexity weight of use cases so as to eliminate the division between different complexities of discontinuity problems. In this sense, it makes estimating the scope of software projects much more realistic using UCP.

2.2 Disadvantage of Traditional UCP

In the course of calculating the unadjusted use case weight using the traditional UCP method, the complexity of a use case is determined by use case transactions. However, the complexity hierarchy in the traditional UCP method is discontinuous, which can sometimes result in complexity weight measurements that are inaccurate. Table 2.1 shows three use cases.

Several typical cases are given in the table, as follows:

1. According to the traditional rules for determining use case complexity weights, Use Case_2 and Use Case_3, both with the same weight of 10, are classified as *medium*, but Use Case_3 has two more transactions than Use Case_2. Thus, clearly, Use Case_3 is more complex.
2. Use Case_1, which contains three transactions, is classified as *low* with a weight of 5. But if another transaction is added to Use Case_1, it will become like Use Case_2 and be classified as *medium* according to the complexity rules.

Table 2.1 Determined complexity weight by traditional UCP method

	Use Case_1	Use Case_2	Use Case_3
Transaction	3	4	6
Complexity	Low	Medium	Medium
Weight	5	10	10

Analysis shows that complexity hierarchies are discontinuous in the traditional UCP method and have a certain arbitrariness. If these situations occur in the same software project, the measurements will not conform to the real-world situation, which will lead to serious errors, especially if the number of use cases is very high. To resolve this problem, we use a fuzzy inference method to analyze the complexity weight of use cases so as to eliminate division of the discontinuity effects.

2.3 Improved UCP Based on Fuzzy Inference

2.3.1 Establishing a Fuzzy Inference System

Fuzzy inference is a calculation process that obtains new fuzzy propositions as a conclusion under the condition of a given fuzzy proposition by the fuzzy logic method, also known as fuzzy logic inference. It simulates the human ability to make reasonable decisions in an uncertain and imprecise environment. It can map a given input space to a specific output space. Fuzzy inference has a unique advantage in solving fuzzy and uncertainty problems whose inference process is similar to the thinking process of humans. It can perform nonlinear mapping from input to output and has a strong inference explanation function.

Fuzzy inference can be divided into fuzzification, fuzzy logic inference, and defuzzification [10]. The fuzzy variety is the basis for establishing a fuzzy system, which analyzes problems using the complexity weight of use cases. As shown in the case that follows, considering the transactions of a use case as the input variable and the complexity weight of the use case as the output variable, a fuzzy inference system was constructed, as shown in Fig. 2.1.

This fuzzy inference system uses the Mamdani Controller and defines the input variable as small, medium, large, or extra large and defines the output variable as low, average, high, or extra high. For example, if only one transaction is in the use case, the transaction of the use case is considered to be low. With Gaussian Function as the membership function for the input and output variables, the mathematical description form of the Gaussian membership function is shown in Eq. (2.1):

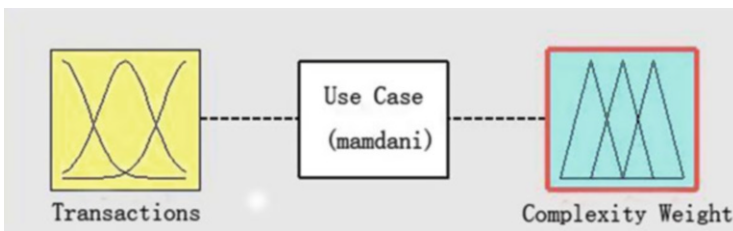


Fig. 2.1 Fuzzy inference system of use case complexity weight

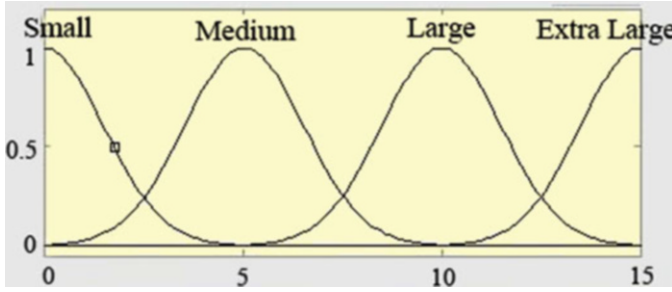


Fig. 2.2 Membership function of transaction

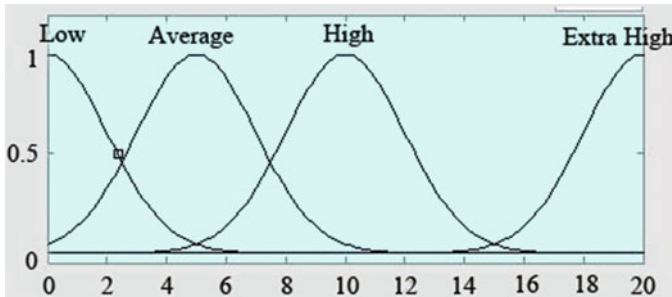


Fig. 2.3 Membership function of complexity weight

$$f(x, \sigma, c) = \exp\left(-\frac{(x-c)^2}{2\sigma^2}\right). \quad (2.1)$$

To determine the parameters in membership functions in real-world situations, there is a kind of description form of use case transaction with an input membership function (transactions) (Fig. 2.2) and output membership function (complexity weight) (Fig. 2.3).

2.3.2 Fuzzy Rules for Analyzing Complexity

As the core of a fuzzy system, fuzzy rules reflect the causality of input and output, similar to the conditional expression in common human language use: *if...then*. Fuzzy systems with a single input and a single output have fuzzy rules such as: IF x is A Then y is B, where x is input, y is output, and A and B comprise a fuzzy collection of input and output. In general, the more fuzzy subsets there are, the higher the output precision will be, but the corresponding calculation costs will increase. In practice, we select the appropriate size of fuzzy rule based on the

Table 2.2 Fuzzy rules

Rule	Transaction (input)	Complexity weight (output)
1	Small	Low
2	Medium	Average
3	Large	High
4	Extra large	Extra high

Table 2.3 Comparison of complexity weight determined using the two methods

	Use Case_1	Use Case_2	Use Case_3
Transaction	3	4	6
Complexity	Low	Medium	Medium
Weight (traditional)	5	10	10
Weight (improved)	5.21	5.96	9.12

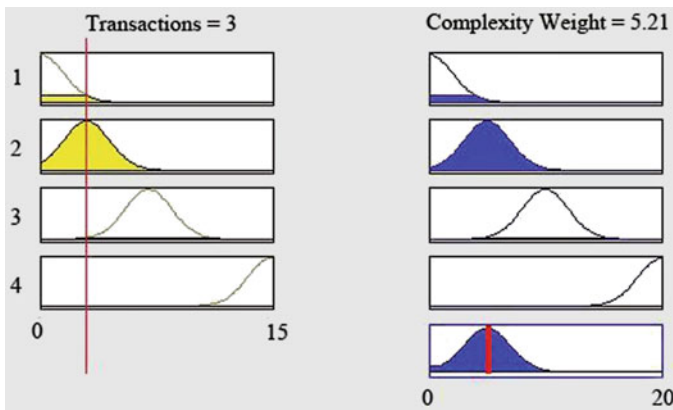


Fig. 2.4 Fuzzy rules observer of use case

requirements for precision. Based on the relation of complexity weight to use case transactions in the traditional UCP method, fuzzy rules are set for the purpose of analyzing the complexity weight, as shown in Table 2.2.

Using the fuzzy rules in Table 2.3, we can obtain fuzzy rules for the complexity weight, as shown in Fig. 2.4, which displays a typical case (the number of input transactions is 3, and the output complexity weight is 5.21). The curve graph of the fuzzy system is shown in Fig. 2.5.

2.3.3 Performance Comparison of Improved UCP

With the fuzzy system constructed here, we analyze the special circumstances in Table 2.1 and obtain the adjusted complexity weight (Table 2.3).

Fig. 2.5 Complexity weight fuzzy curve

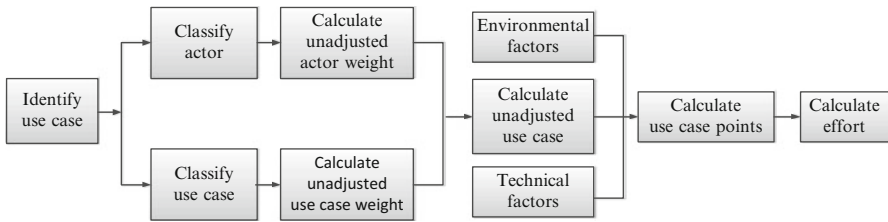
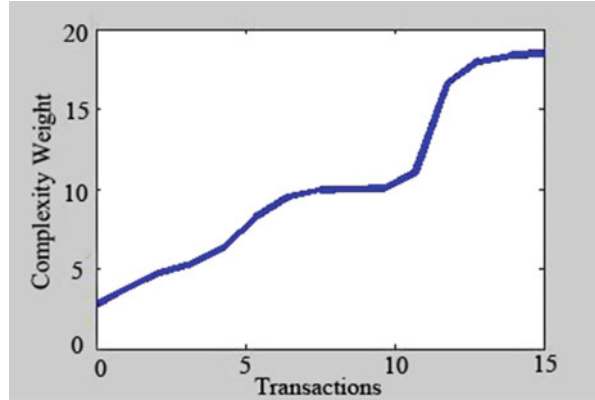


Fig. 2.6 Algorithm flow of UCP

As we can see in Table 2.3, using the improved UCP the adjusted weight of Use Case_1 is 5.21, the adjusted weight of Use Case_2 is 5.96, and the adjusted weight of Use Case_3 is 9.12. Compared with the traditional UCP method, the improved UCP method is more reasonable for determining the complexity weight. As a result, the problem of discontinuous division has been effectively solved, and the estimation of software size is much closer to the actual situation using the improved UCP method. Because the fuzzy inference structure can compute the unadjusted weight of a use case, the adjusted use case point of software projects can be computed.

2.3.4 Improved UCP Application

To reflect the effectiveness of the proposed method, the following specific software programs are shown as an example. We apply the improved UCP method established on the basis of fuzzy inference to estimate the scale of actual software. The algorithm flow is shown in Fig. 2.6 (see [3] for detailed calculation steps); the analysis results are shown in Table 2.4.

We can see from the data in the table that, in general, the UCP method is an effective method of estimation. It has an accuracy similar to that of the Expert

Table 2.4 Comparison estimation of software projects

Software project	Actual (man-hours)	Expert method (man-hours)/error	Traditional UCP (man-hours)/error	Improved UCP (man-hours)/error
Office automation	6,688	8,088/20.81 %	6,240/6.7 %	6,452/3.53 %
Lucky ERP system	10,336	8,816/14.7 %	8,642/16.39 %	9,178/11.2 %
Realty transfer system	2,972	3,800/27.86	4,428/49 %	3,418/15.01 %
Enxel accounting system	4,702	3,496/25.65 %	3,280/30.24 %	3,194/32.07 %

method and can be used in combination with that method. If the estimation error in these two methods is large, recalculation is possible.

The estimation is very similar using the improved UCP and the traditional UCP methods because the improved UCP method stems from the traditional UCP. Three out of four projects have smaller errors using the improved UCP method compared with the traditional UCP method. As is clear from the four projects, the improved UCP method has a higher accuracy than the traditional UCP method; therefore, we can use the improved UCP method, which is based on fuzzy inference, to determine the complexity weight of use cases in situations where UCP can be used so as to obtain greater accuracy.

Conclusion

Because UCP is a novel method for measuring size in software costs and release schedule estimation, especially with respect to object-oriented design in software engineering, it offers some great advantages. Nowadays, with more and more software using object-oriented design, the use and study of UCP will show a rising trend. In this paper, to solve the problems of complexity dividing discontinuous complexity in the traditional UCP method, an improved method was proposed for calculating the complexity weight using fuzzy theory. First, a fuzzy inference system was constructed with use case transaction as the input and complexity weight as the output. Then fuzzy inference rules were established based on the relation of complexity to the number of transactions in order to analyze the complexity weight applying the rules. The research results show that the improved method can effectively overcome the deficiency of the traditional UCP method with respect to analyzing the complexity weight and avoid faulty classification; in addition, its estimation results are much closer to real-world situations.

References

1. Al-Hajri MA, Ghani AA, Sulaiman MN, et al. Modification of standard function point complexity weights system. *J Syst Softw.* 2005;74(2):195–206.
2. Anda B. Improving estimation practices by applying use case models. Proceedings of the 4th International Conference, PROFES; Rovaniemi, Finland; 2002. pp. 383–97.
3. Ashman R. Project estimation: a simple use-case-based model. *IEEE Comput Soc IT PRO.* 2004;4(6):40–4.
4. Anda B, Dreiem H, Sjoberg DIK, et al. Estimating software development effort based on use cases experiences from industry. Proceedings of the 4th International Conference on the Unified Modeling Language, Modeling Languages, Concepts, and Tools; Springer, Toronto, Canada; 2001. pp. 487–502.
5. Arnold M, Pedross P. Software size measurement and productivity rating in a large-scale software development department. Proceedings of the 20th International Conference on Software Engineering; IEEE Computer Society, Los Alamitos; 1998. pp. 490–93.
6. Robiolo G, Orosco R. Employing use cases to early estimate effort with simpler metrics. *Innov Syst Softw Eng.* 2008;4(1):31–43.
7. Robiolo G, Badano C, Orosco R. Transactions and paths: two use case based metrics which improve the early effort estimation. Proceedings of the International Symposium on Empirical Software Engineering and Measurement; IEEE, NJ, USA; 2009. pp. 422–25.
8. Ochodek M, Nawrocki J. Automatic transactions identification in use case. *Balancing Agility Formalism Softw Eng.* 2008;5082(1):55–68.
9. Moataz A, Moshood O, Jarallah A. Adaptive fuzzy logic-based framework for software development effort prediction. *Inf Softw Technol.* 2005;47(1):31–48.
10. Zhou Y. Method of progress metrics in software development based on use case. Shanghai: Shanghai Normal University; 2006 (in Chinese).

Chapter 3

ATPG Algorithm for Crosstalk Delay Faults of High-Speed Interconnection Circuits

Yuling Shang and Pei Zhang

Abstract With the use of ultra-deep submicron technologies, crosstalk has become one of the major causes of failure of signal integrity (SI) in high-speed circuits. Logic faults and time delays in high-speed circuits happen when crosstalk becomes severe, which leads to serious problems during the design verification and test phases in high-speed circuits. In this paper, a vector generation fault test algorithm for crosstalk delay based on the maximum aggressor model and waveform sensitization is proposed for analyzing the four types of crosstalk delay fault in high-speed interconnection circuits; in addition, by improving the traditional FAN algorithm, the proposed algorithm designates a victim line and maximally activates the corresponding aggressive line so as to generate the maximum access delay in a high-speed interconnection circuit induced in a worst-case scenario. In this algorithm, both the gate delay and the line delay are taken into consideration in high-speed interconnection circuits, and two strategies, including static priority and dynamic priority, are examined to achieve a more efficient delay test. The tests were verified in a standard C17 circuit, and the results show that the test vectors for crosstalk delay faults in high-speed circuits can be detected by the proposed algorithm.

Keywords Signal Integrity (SI) • Crosstalk • Delay faults • FAN algorithm

3.1 Introduction

With the fast development of design technology and the craft of integrated circuits (ICs), circuits have become more and more integrated at higher working frequencies. Crosstalk between adjacent lines resulting from the coupling effect is much more likely to happen with the use of ultra-deep submicron technology. Logic faults and time delays occur when the crosstalk becomes severe, which has already become a main reason for function faults in high-speed circuits that use ultra-deep submicron technologies.

Y. Shang (✉) • P. Zhang
CAT7504 Laboratory School of Electronic Engineering and Automation, Guilin University of Electronic Technology, 541004 Guangxi, China
e-mail: shang_yuling@qq.com; 312161945@qq.com

The negative effects of crosstalk can be divided into two categories: glitch fault and delay fault. The crosstalk delay fault is summarized by Chen et al. in which, considering the signal arrival time and the ascend/descend time, the delay model is built using 11 variable values to obtain the crosstalk delay ATPG algorithm [1]. A method of generating a delay test generation taking into consideration the crosstalk effect is studied to seek the maximum delay of circuits on the basis of a genetic algorithm and delay simulation [2]. Nonsturdy test circuit sensitization was applied in the aforementioned study only to discover that the delay faults caused by crosstalk are actually more related to the time delay distribution information of the circuit under test (CUT). Min Yinghua et al. proposed the concept of waveform sensitization and indicated that nonsturdy unpredictable circuits could also be waveform-sensitized upon the theory analysis [3]. The adoption of waveform sensitization and the introduction of delay information under circuit sensitization may not only be much closer to the actual fact of circuit sensitization, but it may also reflect the delay faults caused by crosstalk. Zhang Yue et al. combine 9-value logic with time parameters to test the delay faults in a critical circuit on the basis of a test generation algorithm of waveform-sensitized crosstalk delay faults [4]. The algorithm only considers line delay, not gate delay. In the paper, waveform sensitization technology is adopted considering line and gate delays and is not limited to delay fault testing in critical circuits. With the improved Automatic test vector generation algorithm (FAN) and its advantages, such as sole sensitization, instant inclusion, and multiple pushbacks, the maximum aggressive time can be obtained on the basis of a Maximal Aggressor Fault model (MAF) that designates the aggressive line [5]. The four types of delay fault generated by the interconnection line crosstalk in a circuit are analyzed. Replacing the D/\overline{D} variables with RI, RD, FI, FD, G1, GO, the paper comes up with a mixture of 11-value logic and a time parameter. Then two strategies, such as static priority and dynamic priority, are analyzed to propose a new efficient generation algorithm with respect to test vectors.

3.2 Delay Faults Induced by Crosstalk

The negative effects of crosstalk can be divided into two categories: glitch faults and delay faults, the latter of which is the focus of this paper. The delay fault happens when the neighbor lines jumps simultaneously. If the direction is opposite, then the jump time will obviously increase, as the called crosstalk deceleration; if the two lines jump in the same direction, the jump time will obviously decrease, as the called crosstalk acceleration. Delay faults are classified into four types [6]:

1. In an *ascending delay acceleration fault*, both the victim line and the aggressive line jump forward at some point so that the jump time of the victim line in the forward direction decreases considerably RI.

2. In an *ascending delay deceleration fault*, the victim line jumps in the forward direction, the aggressive line jumps in the backward direction, and the jump time of the victim line in the forward direction increases considerably RD.
3. A *descending delay acceleration fault* occurs when both the victim line and the aggressive line jump in the backward direction and the jump time of the victim line in the backward direction decreases considerably FI.
4. A *descending delay deceleration fault* occurs when the victim line jumps in the backward direction and the aggressive line in the forward direction, and the jump time of the victim line in the backward direction increases considerably. The delay fault caused by crosstalk could lead to as severe as delay errors of the circuit FD.

3.3 ATPG Algorithm for Crosstalk Delay Faults

3.3.1 Basic Idea of Algorithm

In dealing with high-speed interconnection circuits, the algorithm proposed in this paper, which represents an improvement over the traditional FAN algorithm [7], analyzes the four classes of crosstalk delay fault in high-speed interconnection circuits with the maximum aggressive model and waveform sensitization technology. In consideration of gate delay information and line delay information, two strategies, static priority and dynamic priority, are studied in search of an ATPG algorithm of test vectors with the time parameter for the test fault.

3.3.2 Generation Process of Test Vector of Algorithm

After a fault target is selected, the aggressive line is activated by the largest delay. In the generation of a test vector, this paper discusses two test vector generation strategies and makes certain improvements over the FAN algorithm according to the characteristics of the crosstalk fault. Figure 3.1 shows a flow chart of the test vector generation algorithm. The full process of test vector generation mainly includes three phases: sensitization of the victim line, determination of circuit timing information, and the course of test vector generation with the time parameter.

The steps of the flow chart for the test vector generation algorithm are as follows.

3.3.2.1 Sensitization of Victim Line

First, in the course of analyzing a test circuit, a random line is chosen from the test circuit as the fault line with the corresponding maximum aggressive assembly

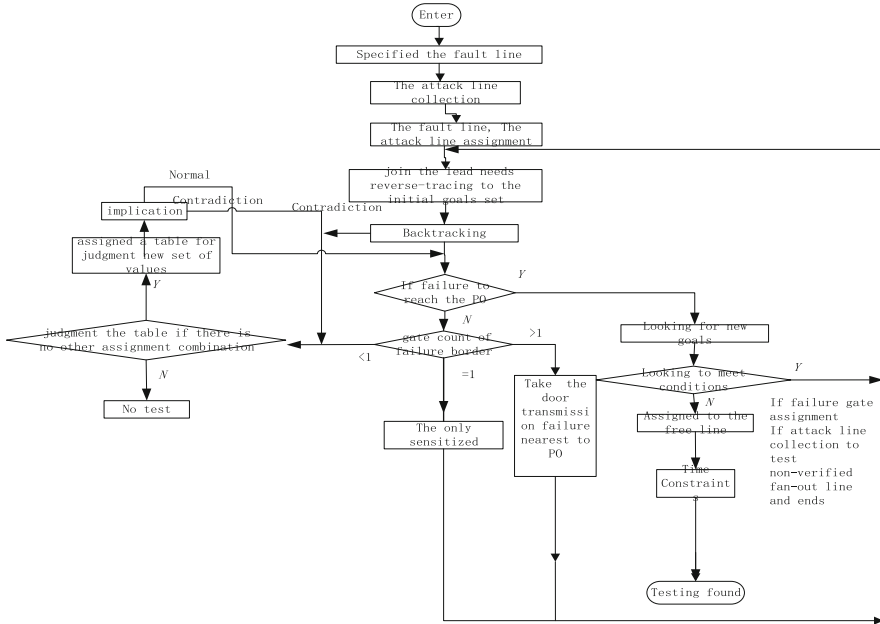


Fig. 3.1 Flow chart of test vector generation algorithm

found as well; then the fault border of the fault line is determined from the test circuit to form a fault border assembly; finally, the specified fault for the fault line is chosen from the four fault types: rising delay accelerated failure RI, rising delay reduction failure RD, falling delay accelerated failure FI, and falling delay slow fault FD.

3.3.2.2 Determination the Circuit Timing Information

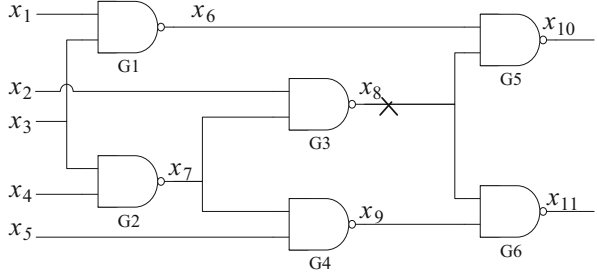
Then, when the delay information of the test circuit has been obtained, the delay information is added to the circuit being tested. First, a static timing analysis of the gate-level net table generated from the test circuit is conducted, which yields information about the circuit line delay and gate delay. Then, both the fault line time and the aggressive line signal time are assumed to be T .

3.3.2.3 Test Vector Generation Process with Time

After the victim line is sensitized and the circuit timing information obtained, the process of generating a test vector with time is conducted, and the steps are as follows:

1. Depending on the fault type of the fault line, first, obtain the jump information on the aggressive line to determine the assignment of the aggressive line; then determine the assignment of all other input lines, in addition to the fault line on the fault border closest to the original output; finally, insert the assignment line directly into the goal assembly using a dynamic priority strategy.
2. Check whether the current target set is empty; if so, go to step (3); if not, to remove a line in the set, delete it from the set and check whether the selected line is the fan outlet. If so, add it to the fan outlet target set; if not, then check whether the line is the original input line. If it is, put it in the backcourt target assembly; if neither, then you are dealing with a pushback process, that is, immediately push back a gate and subtract the gate delay of the logic gate and the line delay passing the lines in case of the current time value T . Repeat step (2) for the pushed-back line. If it still does not satisfy the requirements of the fan outlet line and the input line, keep passing the next gate and push back in the next line until it satisfies step (3).
3. Check whether the fan-out target set is empty; if so, go to step (4); if not, take the fan-out line closest to the original outlet as a target and delete it from the fan outlet target. First, check whether the chosen fan-out line has two or more assignment requirements, if it has only one assignment requirement, the line shall be pushed back following step (2); if there are two or more assignment requirements, make a judgment for each assignment of the fan-out line; take a value and make the validation according to the forward and reverse direction-containing process. If the fault boundary does not change, disappear, or come into the state which contains contradiction, then the value is feasible and thus taken as the value of the outlet; then, continue pushing back with step (2). If the fault boundary does change, disappear, or come into the contain contradiction, the value is not feasible.
4. Finally, check whether the fault line is the original output line; if so, that means the fault has spread to the original output and the fault signal can be sampled after the sampling time t is determined. With the identified assignments of each line, obtain the remaining nonverified lines through the backward and forward contain in the test circuit using the static priority strategy to obtain the test vector with a time coefficient; if the fault line is not the original output line, then spread the fault forward to the next logic gate through the current one, and add the gate delay of the logic gate and line delay of the passed line to the current time value T . The fault boundary will change at the time, while there is no need to determine the jump information of the aggressive line. Repeat the entire test vector generation process starting with step (1). Spread the fault forward to the original output line step by step, and then determine the remaining nonverified lines in the test circuit; finally, a test vector with time can be obtained.

Fig. 3.2 Fault test generation based on algorithm



3.4 Example Verification

For the process described earlier, for the circuit shown in Fig. 3.2, suppose a failure occurs in location x_8 , and then four kinds of fault RI, RD, FI, and FD on it. Follow the steps in the process as mentioned earlier to obtain the corresponding test vector for each fault with the time parameter.

Suppose that a fault, the fault type of which is RI, occurs at x_8 ; the aggressive lines are x_6 and x_9 ; the signal sample is taken in x_{10} with a unit sampling time of $t = 15$. For easy analysis, assume that the gate delay time of the NAND door denoted by g_i is the 2 unit time.

Each line's information is expressed in the following form:

$$\{S, (n_{cr}(S) T_r), (n_{cf}(S) T_f), n_0(S), n_1(S)\}.$$

Each signal represents respectively the target line, number and time of increasing jump required by the target line, number and time of decreasing jump required by the target line, number of logic value 0 required by the target line, and number of logic value 1 required by the target line.

Activate the faults: $x_8 = \text{RI}$, $x_6 = \text{CR}$, $x_9 = \text{CR}$, and set the time T , namely, $(x_8, (1, T), 0, 0, 0)$, $(x_6, (1, T), 0, 0, 0)$, $(x_9, (1, T), 0, 0, 0)$. The fault boundaries are $\{G5, G6\}$ (the fault boundary is the gate directly attached to the fault line); select the fault boundary closest to the original output as the fault propagation path; randomly select $G5$ as the fault propagation path since the distances of $G5, G6$ from the outlet are same. Next, take $(x_8, (1, T), 0, 0, 0)$, $(x_6, (1, T), 0, 0, 0)$, $(x_9, (1, T), 0, 0, 0)$ as the current targets to push them back.

First, take out line x_6 , $(1, T), 0, 0, 0)$, and delete it from the current target set. Considering that the line x_6 is neither the fan outlet nor the input line, push back through the NAND gate $G1$ using the dynamic priority strategy and subtract the gate delay when passing the NAND gate $G1$ to obtain $(x_1, 0, (1, T-G1), 0, 0)$, $(x_3, 0, (1, T-G1), 0, 0)$. Considering that x_1 is the original input, insert $(x_1, 0, (1, T-G1), 0, 0)$ into the endpoint set, and x_3 is the fan-out point; insert $(x_3, 0, (1, T-G1), 0, 0)$ into the fan-out point target set at; then the pushback of line x_6 has been temporarily finished. Then take $(x_8, (1, T), 0, 0, 0)$ out of the current target set, and delete it from the set. Judge out line x_8 is a fan-out line, so insert $(x_8, 0, (1, T), 0, 0)$ into the

fan-out point target set. Now the pushback of line x_8 has been temporarily finished. Then, take line $(x_9, (1, T), 0, 0, 0)$ out of the current target set, and delete it from the set. Push back through the NAND gate G4 using the dynamic priority strategy and subtract the gate delay when passing the NAND gate G4 to $(x_5, 0, (1, T-G4), 0)$, $(x_7, 0, (1, T-G4), 0, 0)$. Determine that x_5 is the original input, insert $(x_5, 0, (1, T-G4), 0, 0)$ into the endpoint set; judge out that x_7 is the fan-out point, insert $(x_7, 0, (1, T-G4), 0, 0)$ into the fan-out point target set. Now the pushback of line x_9 has been temporarily finished.

At this point, all lines of the current set have been taken out; then take out the fan-out points respectively from the fan-out line target in near-to-far order depending on their distance to the original output. First, take out fan-out point x_8 while determining that x_8 has only one assignment requirement with no contradiction. Push back through the NAND gate G3 using the dynamic priority strategy and subtract the gate delay when passing the NAND gate G3 to obtain $(x_2, 0, (1, T-G3), 0, 0)$, $(x_7, 0, (1, T-G3), 0, 0)$. Because x_2 is determined to be the original input, insert $(x_2, 0, (1, T-G3), 0, 0)$ into the endpoint set; x_7 is a fan-out point, so insert $(x_7, 0, (1, T-G3), 0, 0)$ into the fan-out point target set. Now the pushback of line x_8 has been temporarily finished. Take out the fan-out point x_7 , that is $(x_7, 0, (2, T-G3), 0, 0)$. There is no contradiction as with the assignment in x_7 ; continue to push back x_7 using the dynamic priority strategy through the NAND gate G2. Subtract the line delay of fan-out line x_7 and the gate delay passing NAND gate G2 to obtain $(x_4, (2, T-G3-G2-17), 0, 0, 0)$ $(x_3, (2, T-G3-G2-17), 0, 0, 0)$. Then since x_4 is determined to be the original input, insert $(x_4, (2, T-G3-G2-17), 0, 0, 0)$ into the endpoint set; x_3 is a fan-out point, so insert $(x_3, (2, T-G3-G2-17), 0, 0, 0)$ into the fan-out point target set. Now the pushback of line x_7 has been temporarily finished.

Take the fan-out line x_3 out of the fan-out point target set, that is $(x_3, (2, T-G3-G2-17), (1, T-G1), 0, 0)$. Because there is a contradiction in x_3 , the assignment judgment should be conducted next. First, verify this condition that the x_3 assignment is $(x_3, (2, T-G3-G2-17), 0, 0, 0)$. Continuing forward through NAND gate G1, obtain line x_6 's value equivalent to $(x_6, 0, 0, 0, 1)$, which contradicts the original aggressive line $(x_6, (1, T), 0, 0)$ and is thus discarded. Next, validate the other assignment of x_3 $(x_3, 0, (1, T-G1), 0, 0)$, continue forward through NAND gate G2, obtain line x_7 's value $(x_7, 0, 0, 0, 1)$, then continue forward through NAND gate G3, obtain line $(x_8, (1, T), 0, 0, 0)$, which is compatible with the previously defined x_8 value, in the same way continue through NAND gate G4, obtain $(x_9, (1, T), 0, 0, 0)$, which is compatible with the previously defined x_9 value, and the validation finishes. While fanning out point x_3 , the line x_3 value is a negative jump. Take the minimum time according to the time inequality requirement, that is $x_3, 0, (1, T-G3-G2-17), 0, 0)$, and there is no contradiction; if x_3 is the original input, insert $(x_3, 0, (1, T-G3-G2-17), 0, 0)$ into the endpoint set.

When all lines in the initial target set and the fan-out point set have been taken out, spread the fault forward to the next gate through the fault border G5, but after passing G5, it has reached the original output. The delay spreading to the output x_{10} is $T + 18 + G5$ due to the line delay of x_8 and the gate delay of NAND gate G5. The original fault type is RI, which changes to $x_{10} = \text{FI}$ after passing through the NAND gate, that is, the fault signal is collected through the output. With the acquisition

time of output t , the relation between t and T , $t = T + 18 + G5$, can be established. Afterwards, validate all the remaining unverified lines using the static priority strategy. It is proved that line x_{11} is determined by the values of x_8 and x_9 . All the lines have been verified when $x_{11} = FI$ is obtained and there is no contradiction.

From the expression $t = T + 18 + G5$, $T = 11$ can be obtained. According to the T value, all the values of T 's expression will be obtained.

The test vector generation of the fault and the fault types of other lines is the same as that given earlier.

The fault type is RI, and the obtained test vector is

$$\{x_1, x_2, x_3, x_4, x_5\} = \{(1,0,8)(1,0,8)(1,0,3)(0,1,4)(1,0,8)\}.$$

Conclusion

In high-speed circuits, crosstalk can be serious enough to cause errors in the delay of high-speed circuit signals. To ensure the correctness of high-speed circuits, it is necessary to consider the delay growth and delay reduction failure caused by crosstalk in the circuit test phase. The proposed algorithm, on the basis of the FAN algorithm, introduces aggressive set constraints. Aiming at the maximum aggressive time, the paper studies crosstalk fault propagation and the reverse pushback process under two kinds of test vector generation strategies—static priority and dynamic priority—on the basis of 11-value logic and waveform sensitization technology. In consideration of the timing information such as gate delay and line delay, the paper proposes an method for automatically generating test vectors of high-speed interconnection channel crosstalk faults with timing information, and carried out an example verification. The test generation of a crosstalk delay fault was conducted on a certain scale of circuit.

References

1. Chen WY, Gupta SK, Breuer MA. Test generation for crosstalk-induced delay in integrated circuit. Proceedings of the IEEE International Test Conference; Atlantic; 1999. pp. 191–200.
2. Krstic A, et al. Delay testing considering crosstalk-induced effects. Proceedings of IEEE International Test Conference; Baltimore; 2001. pp. 558–67.
3. Min YH, Li ZC, Zhao ZX. Boolean process. *Sci China (Ser E)*. 1996;26(6):542–8.
4. Zhang Y, Li HW, Gong YZ. The test generation aimed at the delay faults caused by the crosstalk. *J Comput Aided Des Graph*. 2004;16(10):1448–53.
5. Yan XL, Liang XL, Shang YL. Test vector generation of the crosstalk delay fault based on MAF model. *Comput Eng Appl*. 2009;45(19):62–5.
6. Shang YL. Research on high-speed interconnection crosstalk fault generation. Xi'an: University of Xi'an Electronic Science and Technology; 2009.
7. Zeng ZD. Digital system test and measurability. Changsha: National Defense Science and Technology University Press; 1992. p. 50–5.

Chapter 4

Application of a Fuzzy-PID Control Method to Synchronized Control of a Multisteping Motor

Wenhao Shi, Lu Shi, Fang An, Zhouchang Wu, Zhongxiu Weng,
and Lianqing Zhao

Abstract The synchronized operating system of multisteping motors is widely applied in industry. In this paper, a method of Fuzzy-PID control based on fuzzy control deduced from the conventional PID control method is introduced. The stability of synchronized operation of multisteping motors can be improved with this method. The simulation analysis based on practical stepping motor parameters shows that this method is simpler and not only has less overshoot but also a shorter setting time than the conventional PID controller. At the same time, its steady-state characteristics and robustness are preferable. This method is easy to implement and has good performance making it possible to apply Fuzzy-PID control in many practical situations.

Keywords Synchronized control • Multi-stepping motor • PID control • Fuzzy control

4.1 Introduction

The PID (Proportional-Integral-Derivative) method is widely applied in industry. Although the conventional PID method with fixed parameters cannot guarantee the results of control in complicated nonlinear systems with significant time lag [1], the Fuzzy-PID method, combining fuzzy control theories with the conventional PID method, obtains excellent results in practical applications [2]. There have been several attempts at applying fuzzy logic to control in various electrical drives [3]. A novel heuristic search algorithm, named ICA, has been employed to contribute to the optimal design of the intelligent Fuzzy-PID controller [4]. A PID-type fuzzy logic controller has been used to achieve improved performance with nonlinear processes [5]. Integration of a robust Fuzzy-PID controller with a classical PID

W. Shi (✉) • L. Shi • F. An • Z. Wu • Z. Weng • L. Zhao
Department of Electric and Electronic Engineering, North China Electric Power University,
Beijing 102206, China
e-mail: shiwenhao@ncepu.edu.cn

controller was described in [6] for a global control scheme. A technique for control of DC motor speed using fractional Fuzzy-PID has also been developed, as described in [7]. The Fuzzy-PID control method possesses great practical significance for the control of multiple stepping motors.

4.2 Overview of the Fuzzy-PID Controller

PID controllers have been used in industrial control systems for several decades and it is a well-developed method [8]. The time-domain expression of a standard PID controller is given by Eq. (4.1):

$$u(t) = K_P e(t) + K_I \int e(t) + K_D \frac{d}{dt} e(t) \quad (4.1)$$

where K_P is the proportional gain, K_I is the integral gain, and K_D is the derivative gain. K_P , K_I , and K_D are all artificially determined constants.

The transfer function is given by Eq. (4.2):

$$U(s) = K_P + K_I \frac{1}{s} + K_D s \quad (4.2)$$

The Fuzzy-PID controller is supposed to obtain good results through realized real-time optimization of K_P , K_I , and K_D using the Fuzzy Logic algorithm according to fuzzy reasoning rules.

The principle of Fuzzy-PID is shown in Fig. 4.1, where e is the error and ec is the rate of change of the error.

As for the Fuzzy-PID controller, its time-domain expression is given by Eq. (4.3):

$$u_{\text{fuzzy}}(t) = (K'_P + \Delta K_P) e(t) + (K'_I + \Delta K_I) \int e(t) + (K'_D + \Delta K_D) \frac{d}{dt} e(t) \quad (4.3)$$

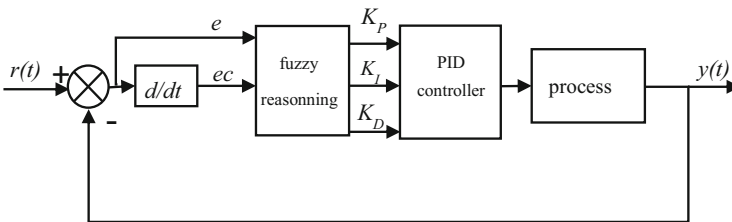


Fig. 4.1 The principle of a Fuzzy-PID control system

And its transfer function is given by Eq. (4.4):

$$u_{\text{fuzzy}}(s) = \left(K'_p + \Delta K_p\right) + \left(K'_i + \Delta K_i\right)s + \left(K'_d + \Delta K_d\right)\frac{1}{s} \quad (4.4)$$

where K'_p, K'_i, K'_d are fixed constants, and $\Delta K_p, \Delta K_i, \Delta K_d$ vary with different e and ec instantly.

The implementation of Fuzzy-PID is given by the following procedures:

1. Obtain e and ec : Measure the difference between a measured process variable and a desired setpoint, and then obtain e and ec .
2. Fuzzification: e and ec are input variables for the fuzzy controller. The “fuzzification” process converts e and ec into fuzzy value sets of membership functions. The fuzzy sets of e and ec are [NB, NM, NS, ZO, PS, PM, PB] ranging from small to large.
3. Fuzzy reasoning: Fuzzy reasoning determines the output variables by IF-THEN rules for example “IF $e=A$ AND $ec=B$ THEN $\Delta K_p=C$ AND $\Delta K_i=D$ AND $\Delta K_d=E$.” The output variables are also fuzzy values defined by the fuzzy set. In Fuzzy-PID controllers, IF-THEN rules satisfy the conventional PID constant setting rule.
4. Defuzzification: The output variables of fuzzy reasoning are fuzzy values. Defuzzification converts fuzzy output variables from fuzzy sets into quantifiable values so that real systems can make use of them. After defuzzification $\Delta K_p, \Delta K_i,$ and ΔK_d are determined.
5. Obtain the final real PID controller: The real-time PID parameters are given by Eq. (4.5) [9]:

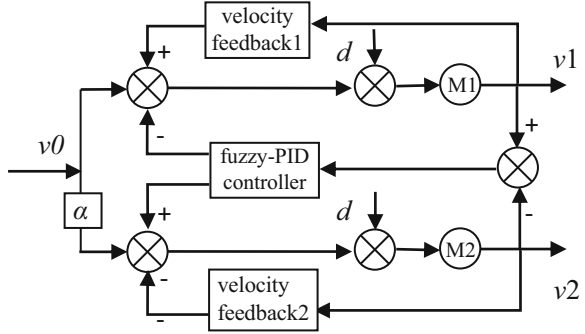
$$\begin{cases} K_p = K'_p + \Delta K_p \\ K_i = K'_i + \Delta K_i \\ K_d = K'_d + \Delta K_d \end{cases} \quad (4.5)$$

4.3 Control Strategy for Multisteping Motors

At present, the control of multisteping motors mostly focuses on a method based on the compensation principle [10]. As shown in Fig. 4.2, the controller of each axle takes the same velocity instruction v_0 as its reference. The coordinated relation of axle velocity is determined by the synchronization coefficient α . This compensation-principle-based control method has a simple circuit that is easily realized. Also, it places an emphasis on the performance of the system trace, showing no lag problems during start-up.

On the basis of the control structure mentioned above, this paper introduces a synchronization control method that combines Fuzzy-PID control with the compensation principle.

Fig. 4.2 A synchronous Fuzzy-PID model for the synchronized multistepping motor model based on the compensation principle



In this method, each motor takes the previous one’s speed output as its given speed. On this basis, after comparing the speed outputs of motors $M1$ and $M2$, the difference is sent to the control terminal of the driven motor or driving motor via the compensator. The coordinated relation between motor velocity $v1$ and $v2$ is determined by α , assuming α to be 1, as illustrated in Fig. 4.2.

This controller possesses the ability to self-learn and self-adapt, while it also has improved tolerance and robustness. As this control scheme is so simple, there is no need to produce a complex algorithm. The rapid controller operation meets the requirements set by the rapidity of the controlled object.

4.4 Mathematics Models for the Stepping Motor

A three-phase hybrid stepping motor can be commonly modeled by a differential equation as shown in Eq. (4.6) [11]:

$$\begin{aligned}
 \begin{bmatrix} u_a \\ u_b \\ u_c \end{bmatrix} &= \begin{bmatrix} R_a & 0 & 0 \\ 0 & R_b & 0 \\ 0 & 0 & R_c \end{bmatrix} \begin{bmatrix} i_a \\ i_b \\ i_c \end{bmatrix} + \begin{bmatrix} L_{aa} & L_{ab} & L_{ac} \\ L_{ba} & L_{bb} & L_{bc} \\ L_{ca} & L_{cb} & L_{cc} \end{bmatrix} \begin{bmatrix} \frac{di_a}{dt} \\ \frac{di_b}{dt} \\ \frac{di_c}{dt} \end{bmatrix} \\
 &+ \frac{\partial}{\partial \theta} \begin{bmatrix} L_{aa} & L_{ab} & L_{ac} \\ L_{ba} & L_{bb} & L_{bc} \\ L_{ca} & L_{cb} & L_{cc} \end{bmatrix} \begin{bmatrix} i_a \\ i_b \\ i_c \end{bmatrix} \frac{d\theta}{dt} \tag{4.6}
 \end{aligned}$$

Rotor torque equilibrium equations are

$$J \frac{d^2\theta}{dt^2} = T - D \frac{d\theta}{dt} - T_l \tag{4.7}$$

$$T = \frac{1}{2} \sum \frac{\partial L_{jj}}{\partial \theta} i_j^2 + \frac{1}{2} \sum \frac{\partial L_{jk}}{\partial \theta} i_j i_k \quad (j = a, b, c; k = a, b, c; j \neq k) \quad (4.8)$$

where u_a , i_a , and R_a , are voltage, current, and resistance in phase A respectively, J is the inertial torque of the load, D is the viscous friction coefficient, T is the electromagnetic torque, T_1 is the load torque, and L_{jj} and L_{jk} are self-inductance and mutual inductance (where higher harmonics can be ignored, they consist of an average component and a fundamental component).

According to the mathematical model of a stepping motor formulated as the differential equations shown above, its transfer function needs to be modeled considering the input of the stepping motor as a step pulse. It is known that with regard to a stepping motor, whilst the rotor theoretically rotates one standard stepping angle θ_1 , it actually rotates θ_2 (the output) and oscillates around the new stationary point. Thus, the stepping motor's transfer function can be deduced as

$$G(s) = \frac{\theta_2(s)}{\theta_1(s)}$$

In order to obtain this function, factors such as the average component and the fundamental component are supposed to be ignored. Taking phase A as the reference, the voltage equilibrium equations of winding for phases A, B, and C can be formulated as

$$\begin{cases} u_A = Ri_A + L \frac{di_A}{dt} - K_m w \sin(Z_r \theta) \\ u_B = Ri_B + L \frac{di_B}{dt} - K_m w \sin(Z_r \theta - 120^\circ) \\ u_C = Ri_C + L \frac{di_C}{dt} - K_m w \sin(Z_r \theta + 120^\circ) \end{cases}$$

The rotor torque equilibrium equation is:

$$\begin{aligned} J \frac{d^2 \theta}{dt^2} + D \frac{d\theta}{dt} + K_m i_A \sin(Z_r \theta) + K_m i_B \sin(Z_r \theta - 120^\circ) \\ + K_m i_C \sin(Z_r \theta + 120^\circ) + T_1 \\ = 0 \end{aligned} \quad (4.9)$$

In Eq. (4.9), i_A , i_B , i_C , u_A , u_B , and u_C are current and voltage in phases A, B, and C respectively. L and R are the self-inductance and resistance of the winding. θ , w , J , and Z_r are the angle position output, the angular velocity, the inertial torque, and the number of teeth of the rotor, respectively. K_m , D , and T_1 are the torque constant, viscous damping, and load torque of the motor, respectively.

In order to obtain the transfer function, we suppose that the motor is energized by the order a-b-c-a. From the equilibrium equation above, the equation of motion of the motor is

$$J \frac{d^2\theta}{dt^2} + D \frac{d\theta}{dt} - \frac{Z_r L i_A^2}{2} \sin(Z_r \theta) = 0 \quad (4.10)$$

Assuming that the rotor reaches the equilibrium position at $t=0$ and $\frac{d\theta}{dt} = 0$ at this time. Since only one phase is being energized then, through further operation, the mathematical model of a stepping motor's transfer function can be concluded to be

$$G(s) = \frac{\theta_2(s)}{\theta_1(s)} = \frac{Z_r L i_A^2 / 2J}{s^2 + \frac{D}{J}s + Z_r L i_A^2 / 2J} \quad (4.11)$$

Taking the parameters of a type of 57-mm stepping motor [12], scilicet $Z_r = 40$, $L = 0.42$ mH, $J = 0.48$ kg cm², $D = 0.07$, and $i_A = 5.8$ A, the stepping motor's transfer function can be concluded to be:

$$G(s) = \frac{235.48}{s^2 + 0.1458s + 235.48} \quad (4.12)$$

4.5 Experimental Results

Our experiment compared the performance difference between a Fuzzy-PID controller and a conventional PID controller. The transfer function in this experiment is given by Eq. (4.12) in Sect. 4.4, and was derived from a 57-mm stepping motor. The parameters of conventional PID controller are already setting to get a good performance.

$$G(s) = \frac{235.48}{s^2 + 0.1458s + 235.48}$$

For the Fuzzy-PID controller, the fuzzy domain of e is $[-6.6]$, the fuzzy domain of ec is $[-3.3]$, the fuzzy domain of ΔK_P is $[-6.6]$, and the fuzzy domain of ΔK_I and ΔK_D are $[-3.3]$. The step function response in the simulation is shown in Fig. 4.3. We determined that the percentage overshoot for Fuzzy-PID control is 2.7 %, while the value for conventional PID control is 12.0 %; the setting time for Fuzzy-PID control is 8.34 ms, 14 % less than the conventional value, which is 9.75 ms.

The change curves for ΔK_P , ΔK_I , and ΔK_D are shown in Figs. 4.4, 4.5, and 4.6, respectively. The fuzzy parameters vary appropriately for current system state.

Fig. 4.3 Output response for the two kinds of PID controllers

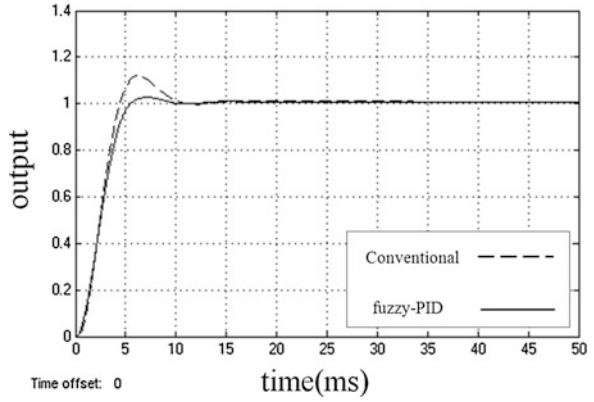


Fig. 4.4 Chang curve for ΔK_p

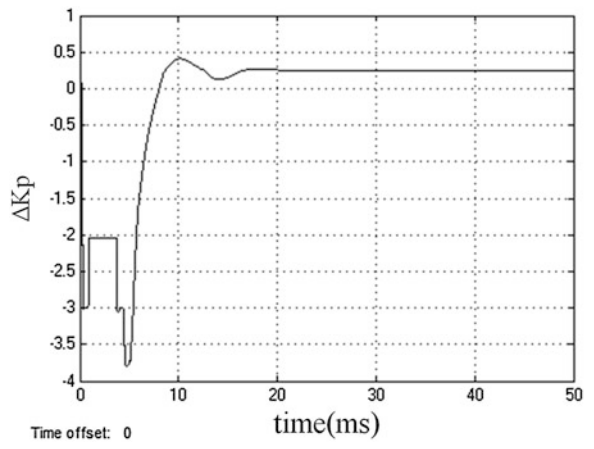


Fig. 4.5 Chang curve for ΔK_i

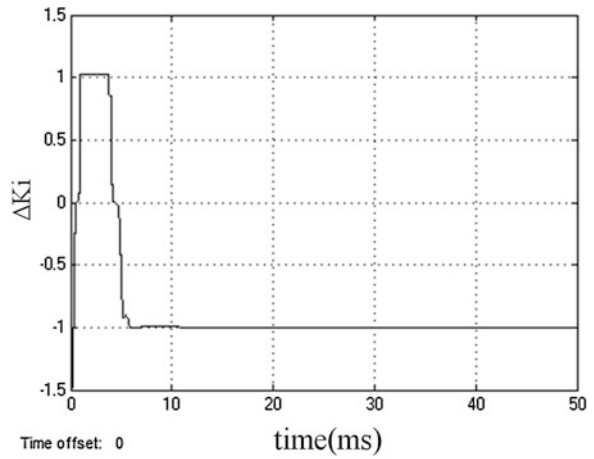
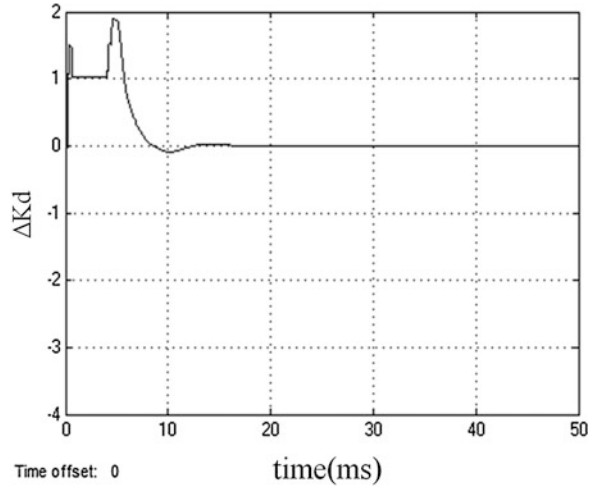


Fig. 4.6 Chang curve for ΔK_D



Conclusion

A Fuzzy-PID control method generated by combining both fuzzy and PID control is employed. We validate the results of this control method using a synchronous model with equal state control structure. It is shown that this synchronous control method is simply formed and easily realized. In addition, it can effectively increase the velocity of reaction of a synchronized multiple stepping motor system and enhance its stability and robustness. This motor control strategy is flexible and easy to implement; it can therefore be applied in cost-sensitive situations where complex approaches cannot be used.

References

1. Tang KS, Man KF, Chen G, et al. An optimal fuzzy PID controller. *IEEE Trans Ind Electron.* 2001;48(4):757–65.
2. Kumar A, FebinDaya JL. A novel self-tuning fuzzy based PID controller for speed control of induction motor drive. *Technology.* 2013;1(1):79.
3. Betin F, Pinchon D, Capolino GA. Fuzzy logic applied to speed control of a stepping motor drive. *IEEE Trans Ind Electron.* 2000;47(3):610–22.
4. Ahmadi A, Sedehi MT, Yazdani AM, et al. Designing an optimal fuzzy-PID controller for speed tracking of stepper motor. In: *IEEE Symposium on Industrial Electronics and Applications (ISIEA);* 2012. p. 193–8.
5. Ghafari AS, Alasty A. Design and real-time experimental implementation of gain scheduling PID fuzzy controller for hybrid stepper motor in micro-step operation. In: *Proceedings of the IEEE International Conference on Mechatronics, 2004, ICM'04;* 2004. p. 421–6.
6. Rubaai A, Castro-Sitiriche MJ, Ofoli AR. Design and implementation of parallel fuzzy PID controller for high-performance brushless motor drives: an integrated environment for rapid control prototyping. *IEEE Trans Ind Appl.* 2008;44(4):1090–8.

7. Gupta SK, Varshney P. Fractional fuzzy PID controller for speed control of DC motor. In: IEEE Third International Conference on Advances in Computing and Communications (ICACC); 2013. p. 1–4.
8. Ang KH, Chong G, Li Y. PID control system analysis, design, and technology. *IEEE Trans Control Syst Technol.* 2005;13(4):559–76.
9. Wang G. *Multimotor in synchronous control strategies based on fuzzy PID compensator.* Shenyang: Northeastern University; 2006.
10. Wan P, Wang L. The research of multi-motor synchronization control based on fuzzy-PID control. *Electron Instrum Cust.* 2009;16(1):21–3.
11. Hou Z. *Research and implementation of the design theory of stepping motor drive system.* Heibei: North China Electric Power University; 2011 (Unpublished).
12. Xiao Y. *Research on the stepping motor control technology based on the fuzzy PID.* Zhejiang: Zhejiang University of Technology, Institute of Mechanical Engineering; 2008.

Chapter 5

The Improved Bayesian Algorithm to Spam Filtering

Hongling Wang, Gang Zheng, and Yueshun He

Abstract Though electronic mail is one of the most popular forms of communication in modern society, spam brings considerable inconvenience to our lives while also very negatively affecting network security; thus resolving this issue has become a rather urgent task. The existing Bayesian algorithm uses a Bernoulli model to process text features in application to spam filtering, but it always misjudges normal mail because it does not distinguish the differing degrees of importance of various features. In this paper, a new and improved Bayesian algorithm is proposed that weights feature words with minimum risk. Experimental results show that this algorithm can reduce the risk of misjudging normal mail and improve the accuracy of mail filtering.

Keywords Spam filtering • Bayesian algorithm • Weighting feature word • Minimum risk

5.1 Introduction

An investigative report on antispam conditions in China in the fourth quarter of 2013 was released recently, according to the Chinese Internet Association, and shows that 92.4 % of users use normal personal e-mail, 5.1 % of users use enterprise e-mail, and only 4.2 % of people do not use e-mail. The report also shows that successful receipt of messages, security, privacy, and antispam functions are the most important features of e-mail. Figures show that Chinese e-mail users receive about 14.6 pieces of spam every week. The percentage of spam is 37.3 % of the total, rising at an annual rate of 4% in the fourth quarter of 2013 [1]. Spam ties up more network resources, reduces the operating efficiency of networks, and consumes a considerable amount of time, money, and energy of receivers; sometimes spam contains malicious content such as fraud and sexually explicit images, which have a harmful effect on society [2]; therefore, antispam technologies must be developed. Antispam methods commonly include black- or white-list technology,

H. Wang (✉) • G. Zheng • Y. He
East China Institute of Technology, 330000 Nanchang, Jiangxi, China
e-mail: whl9win@163.com

keyword filtering technology, Decision Tree, boosting technology, and naive Bayesian algorithms [3]. Bayesian algorithms are the most popular method because of their convenience of design, decision features, and low storage requirements [4]. However, they also present some problems; for instance, they cannot differentiate the importance of feature words and may misidentify normal e-mail as spam. To solve these problems and improve their filtering capabilities, a new Bayesian spam filtering algorithm that carries minimum risk and is based on the weighting of feature words is proposed in this paper.

5.2 Principle of Bayesian Algorithms

A Bayesian algorithm is a classification technology used to predict the possibility of a new event according to past events, as proposed by the famous mathematician Thomas Bayes [5]. By computing the probability of every category in a given text, it classifies the text into the category that is most likely to be the correct category when the algorithm is applied to solve text classification problems. As its basic principle, the algorithm analyzes common keywords in a collection of spam and obtains a distribution statistics model and calculates the probability that a particular e-mail is of spam [6]: d is the text set, $P(c_i|d)$ is the probability that text d belongs to category c_i , $P(c_i)$ is the prior probability of class c_i , $P(d|c_i)$ is the class-conditional probability of the text, $P(d)$ is the appearance probability of the text. $P(c_i|d)$ can be calculated as follows:

$$P(c_i|d) = \frac{P(c_i)P(d|c_i)}{P(d)}, \quad i = 1, 2, 3, \dots, |C|. \quad (5.1)$$

The probability of text $P(d)$ can be calculated as follows:

$$P(d) = \sum_{i=1}^{|C|} P(c_i)P(d|c_i). \quad (5.2)$$

$P(c_i)$ can be estimated according to the historical experience of the training set. Suppose N_k represents the number of texts of class c_i in the training set, and N represents the number of texts in the training set. $P(c_i)$ can be calculated as follows:

$$P(c_i) = \frac{N_k}{N}. \quad (5.3)$$

Then we obtain the class-conditional probability of text $P(d|c_i)$ according to the class-conditional probability of feature words in the texts. This can be calculated as follows:

$$P(d|c_i) = \prod_{t=1}^n (BP(w_t|c_i) + (1 - B)(1 - P(w_t|c_i))), \quad (5.4)$$

where B indicates whether or not the feature word Wt appears, and $P(w_t|c_i)$ is the probability that the feature word w_t will appear in the condition of class c_i . the number of texts in class c_i in which the feature word w_i appears, and N_c is the number of texts in class c_i , N_c is the texts number in class c_i . $P(w_t|c_i)$ can be calculated as follows:

$$P(w_t|c_i) = \frac{N_w}{N_c}. \quad (5.5)$$

Based on the preceding description, we can see the traditional Bayesian filtering approach does not take into consideration the differences between normal text classification and e-mail filtering; in addition, it does not consider the various features in normal e-mail and spam. Therefore, some improvements with regard to feature word detection are made in this paper by studying the Bayesian filtering process.

5.3 Filtering Algorithm Based on Feature Word Weighting

5.3.1 Filtering Process Using Bayesian Algorithm

Spam filtering is a two-class classification problem, and the final result is that e-mails are divided into two groups, normal e-mail (ham) and spam (spam). When the e-mail system receives a new e-mail, it classifies this e-mail by calculating the probability of $P(c_i|d), i \in \{\text{spam}, \text{ham}\}$. The whole process includes two steps: training and classification.

Training process:

1. Build spam and ham sets by collecting many e-mails.
2. Extract individual token strings as feature words such as discount, receipt from every -email title, and the contents in the spam and ham sets. Then calculate the appearance time of the token and build the feature set $f = \{w_1, w_2, \dots, w_n\}$.
3. Build individual hash tables for both normal e-mail and spam. Hash ham is for normal e-mail and hash spam is for spam, where the mapping relation of a feature word token string to word frequency is stored.
4. Calculate the class-conditional probability $P(w_t|c_i)$ for feature word w_t according to Eq. (5.4).
5. Count the prior probability $P(c_i)$ of the class based on Eq. (5.3).

Classification process:

1. Extract feature words from new e-mails.
2. Calculate the probability $P(c_{\text{ham}}|d)$ of normal e-mail and $P(c_{\text{spam}}|d)$ of spam when it satisfies the extracted feature words d .
3. Classify this e-mail based on the results. When the value of $P(c_{\text{spam}}|d)$ is greater than $P(c_{\text{ham}}|d)$ or the threshold λ , this e-mail is tagged as spam.

Spam filtering faces two practical problems in its application: what is the result if spam is identified as normal e-mail? And what is the consequence if normal e-mail is considered spam. Treating spam as normal e-mail will waste a user's precious time and energy; however, treating normal e-mail as spam could delay important events in a user's day, such as meetings.

5.3.2 Improved Algorithm Based on Minimum Risk and Feature Words

Based on the foregoing description, it is evident that the consequences of misidentifying normal e-mail as spam are more serious; therefore, to reduce the risks associated with incorrect spam filtering, some improvements to the filtering model and a new Bayesian spam filtering algorithm based on a minimum risk strategy are proposed in this paper.

5.3.2.1 Analysis and Improvement of Probability Evaluation Model

In the Bayesian filtering model shown in Eq. (5.1), when c_i equals class spam, the probability that text d belongs to the category *spam* can be calculated as follows:

$$P(\text{spam}|d) = \frac{P(\text{spam}) \times P(d|\text{spam})}{\sum_{c \in C} P(c) \times P(d/c)}. \quad (5.6)$$

This means that if $P(\text{spam}|d)/P(\text{ham}|d)$ is greater than the threshold λ , the e-mail is spam, where λ is the risk factor.

The class-conditional probability of e-mail can be calculated according to Eq. (5.7) in the traditional Bayesian method:

$$P(\text{spam}|d) = \frac{P(\text{spam}) \cdot \prod_{i=1}^n w_i P(d_x|\text{spam})}{\sum_{c \in C} P(c) \cdot \prod_{i=1}^n w_i P(d_x|c)}. \quad (5.7)$$

The new model introduces feature weighting to emphasize features with a strong discrimination capability and to suppress features without a discrimination capability or with a weak such capability. If a feature word has a strong discrimination capability in the process of classification, its function should be increased; otherwise, it should be decreased; therefore, the classification ability can be considerably improved. To describe the differentiation capability of feature words, a new weighting function is constructed:

$$\text{Weight}(d) = T(d) \times \text{ECE}(d), \quad (5.8)$$

where $T(d)$ is the number of times the feature word d occurs in e-mail, $\text{ECE}(d)$ is the expected cross entropy improved by feature words. Eq. (5.8) shows that the weighting function takes into account not only the number of times the feature word occurs in e-mail but also the relation between feature word and class. In this way, some feature words with large $\text{ECE}(d)$ can be selected by calculating $\text{ECE}(d)$ in the training process.

In the classification process, the weighting function $\text{Weight}(d)$ will play a role in calculating $P(\text{spam}|d)$. As a result, the role of the feature will be enhanced, in particular, the number of feature words will increase. The form of Eq. (5.7) is changed as follows:

$$P(\text{spam}|d) = \frac{P(\text{spam}) \cdot \prod_{i=1}^n w_i (P(d_x|\text{spam}))^{\text{Weight}(d)}}{\sum_{c \in C} P(c) \cdot \prod_{i=1}^n w_i (P(d_x|c))^{\text{Weight}(d)}}. \quad (5.9)$$

5.3.2.2 Improved Bayesian Filtering Algorithm with Minimum Risk

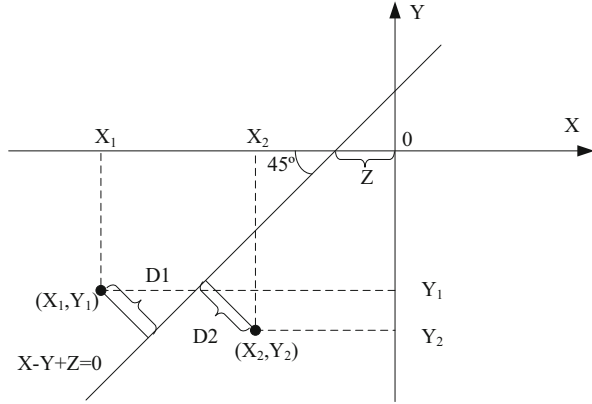
To compare $P(\text{ham}|d)$ and $P(\text{spam}|d)$, some analysis of Eq. (5.10) needs to be performed:

$$f(d) = \log \frac{P(\text{ham}|d)}{P(\text{spam}|d)}. \quad (5.10)$$

The equation shows that $f(d)$ is greater than zero if $P(\text{ham}|d) < P(\text{spam}|d)$; otherwise, $f(d)$ is less than zero. Thus, Eq. (5.6) can reflect the distance between $P(\text{ham}|d)$ and $P(\text{spam}|d)$. Some results can be obtained by analyzing Eqs. (5.4) and (5.6):

$$\begin{aligned} f(d) &= \log \frac{P(\text{ham}|d)}{P(\text{spam}|d)} = \log \frac{P(d|\text{ham})P(\text{ham})}{P(d|\text{spam})P(\text{spam})} \\ &= \sum_{i=1}^n \log P(d|\text{spam}) - \sum_{i=1}^n \log P(d|\text{ham}) + \log \frac{P(\text{ham})}{P(\text{spam})}. \end{aligned} \quad (5.11)$$

Fig. 5.1 Relationship between text dot of unknown e-mail and the classifier line



$$\text{Let } x = \sum_{i=1}^n \log P(d|\text{ham}), y = \sum_{i=1}^n \log P(d|\text{spam}), z = \log \frac{P(\text{ham})}{P(\text{spam})}.$$

Thus, Eq. (5.11) is changed as follows:

$$f(d) = x + y - z \tag{5.12}$$

By analyzing x , y , and z , the results show that x is the sum of the logarithm of probabilities for all feature words in new e-mail occurring in the class *spam*, which reflects the possibility that this new e-mail is spam; y is the sum of logarithm probabilities for all feature words in new e-mail occurring in the class *ham*, which shows the possibility that this new e-mail is ham; z reflects the a priori probability difference between ham and spam. For an unknown e-mail d , x is defined as the measure of belonging to spam and y is the measure of being ham. In the course of classification of new e-mail, the algorithm will get (x,y) that corresponds to a point in two dimensions. Setting $f(d)$ equal to zero, the classifier corresponds to a line in two dimensions; therefore, the classification problem for undefined e-mail can be decided by the distance between the dot corresponding to e-mail text and the classification line.

Figure 5.1 shows the relationship between the text dot of unknown e-mail and the classifier line, where $D1$ is the distance between the dots above the line and the line, and $D2$ is the distance between the dots below the line and the line. It is obvious that $D1$ and $D2$ can be calculated as follows:

$$D1 = D2 = \frac{(X - Y + Z)}{\sqrt{2}}. \tag{5.13}$$

With respect to new e-mail, d , we define RS as risk factors that are determined by the classifier that treats the e-mail d as spam and RH as the risk factor treating this e-mail as ham; therefore, with unknown e-mail, the distance d between its

corresponding dot (x, y) and classification line must be calculated. If $d > RH$ and $x + z < y$, then it classifies the e-mail as ham; if $d > RS$ and $x + z > y$, then it classifies the e-mail as spam. Based on the line geometry division, the improved model has better expansibility. As the number of feature words increases or as e-mails with high decision risk are processed, we can perform a secondary classification so that the classification effect can be improved further. In this sense, two risk factors, RS and RH, are proposed in this paper to describe the decision risk in smaller granularity.

5.4 Analysis of Experimental Results

Some experiments for spam filtering based on minimum Bayesian risk were performed. We tested 3,000 e-mails collected in various ways, which include 2,017 spam and 983 normal e-mails. With 500 pieces of spam and normal e-mail as the training sample and the others as testing data, we tested these e-mails using a traditional Bayesian algorithm and the improved Bayesian algorithm and then compared the results. Refer to Tables 5.1 and 5.2 for the filtering results from the traditional and improved algorithms. Generally speaking, accuracy, precision, and recall are used to evaluate the filtering effect [7]. The evaluation result appears in Table 5.3.

The experimental results show that the improved Bayesian algorithm has better filtering performance and lower misjudgment rate compared with the traditional method using feature word weighing and two risk factors.

Table 5.1 Classification result based on traditional Bayesian algorithm

Classification	Spam	Normal e-mail	Feature words
Spam	1,768	88	1,800
Normal e-mail	249	895	1,800

Table 5.2 Classification result based on improved Bayesian algorithm

Classification	Spam	Normal e-mail	Feature words
Spam	1,812	72	1,800
Normal e-mail	205	911	1,800

Table 5.3 Evaluation of filtering results

Algorithm	Accuracy (%)	Precision (%)	Recall (%)
Traditional algorithm	89	95	88
Improved algorithm	91	94	90

Conclusion

To solve problems that arise in the application of spam filtering using a Bayesian algorithm, some improvements to Bayesian algorithms are presented in this paper. On the one hand, the weighting of feature words is proposed and applied to spam filtering to enhance the role of feature words in the classification process; on the other hand, two risk factors are defined in the process of calculating probabilities. The experimental results showed that the new filtering algorithm has a high accuracy rate and is a better method for solving the spam-filtering problem.

Acknowledgements This work was supported by the National Natural Science Foundation (51364001).

References

1. Chinese Internet Association. The statistical report of the thirty-first Chinese internet development. 2013. http://www.cnnic.net.cn/hlwfzyj/hlwzxbg/hlwtjbg/201301/t20130115_38508.html. Accessed 15 Jan 2013.
2. Graham P. Will filters kill spam? 2013. <http://www.paulgraham.com/wfks.html>. Accessed 27 Nov 2002.
3. Thiago SS, Walmir MC. A review of machine learning approaches to spam filtering. *Expert Syst Appl.* 2009;36(7):10206–22.
4. Zhang X, Dai W, Gui-Rong Xue. Adaptive email spam filtering based on information theory. Berlin: Springer; 2007. pp. 159–70.
5. Cooper GF, Herskovits E. A Bayesian method for the induction of probabilistic networks from data. *Mach Learn.* 1992;9(6):309–47.
6. Androutsopoulos I, Palioursas G, Michelakis E. Learning to filter unsolicited commercial email. Technical report. 2004;2(5):120–29.
7. Dey S, Stori JA. A Bayesian network approach to root cause diagnosis of process variation. *Int J Mach Tools Manufact.* 2005;8(45):75–91.

Chapter 6

Evolution of Community Structure in Complex Networks

Lei Zhang, Jianyu Li, Shuangwen Chen, and Xin Jin

Abstract Community structure has always been considered one of the most significant features in complex networks, and it plays an important role in the topology and function of networks. In this paper, we choose five data sets from various areas to detect the community structure and present two interesting results. We cut all the nodes in the networks from low degree to high degree and then obtain many networks with different scales. First, the relationship between the number of nodes of the maximal communities and the number of communities in the corresponding networks is studied and is shown to be linear. Second, when the number of nodes in the maximal communities increases, the increasing tendency of the number of its edges slows down, which reveals the sparsity of networks.

Keywords Community structure • Linear • Sparsity

6.1 Introduction

In recent years, complex networks have had a profound effect on many research disciplines [1–3], such as, for example, systems science, statistical physics, social sciences, and biology [4–6]. Network structure theory may help us to understand the properties, function, and evolutionary mechanism of complex networks [2, 7]. One of the most crucial research areas in complex networks is community structure [8–13]. Community structure means that, among different groups, the links of nodes between them are of low density, but the links of nodes within a

L. Zhang (✉) • X. Jin
School of Computer Science, Communication University of China, 100024 Beijing, China
e-mail: zhanglei2012@cuc.edu.cn; jinxin0923@cuc.edu.cn

J. Li
Engineering Center of Digital Audio and Video, Communication University of China,
100024 Beijing, China
e-mail: lijianyu@cuc.edu.cn

S. Chen
Information Engineering School, Communication University of China, 100024 Beijing, China
e-mail: csw@cuc.edu.cn

group are of high density. We can provide insight into how network function and topology affect each other to identify these substructures within a network.

Community structure analysis has a wide range of applications in biology, physics, computer graphics, and sociology [14, 15]. For example, in social groups, people with the same hobbies or beliefs often appeal to each other. In molecular response networks, it is possible to distinguish roles or features of molecular from aggregated functional module nodes.

Previous investigations on community structure analysis revealed astonishing conclusions about network function [10, 13, 16]. There are three reasons for exploring network communities [17]. First, it may help to formulate realistic mechanisms for a community's genesis and evolution by revealing the network organization at a coarse level. Second, it may be affected by the modular structure of the graph to better understand the change in dynamic processes in a network. Third, we cannot uncover the relationship between nodes of a graph by simply inspecting it as a whole; the function of the system should be investigated as well.

This paper focuses on the following aspects. First, modularity is used to analyze community structure. Second, the relationship between the number of nodes of the maximal communities and the number of communities in the corresponding network is studied. Third, the relationship between the number of nodes of the maximal communities and the number of their corresponding edges is examined.

6.2 Source Data and Networks Detect Method

To study the features of community structure in complex networks, we need to choose data sets from various areas. Table 6.1 lists the data sets we have used.

1. MATLAB help document: the nodes are key terms in the MATLAB help document. If two nodes have a hyperlink relationship, they are connected.
2. Chinese characters: the nodes are radicals in Chinese characters, and a relation exists between two radicals if they can co-occur in a word.
3. Yeast: the nodes are proteins in yeast, and a relation exists between two proteins if they chemically react with each other [18].
4. Electronic collaboration networks: the nodes are authors who research general relativity and quantum cosmology. A relation exists between two authors if they collaborate on a paper [19].
5. Peer-to-peer file-sharing networks: the nodes are hosts in peer-to-peer file-sharing network topology, and a relation exists between two hosts if they connect to each other [20].

To study community structure, we divide the networks to obtain communities, which help us understand how a real network is constructed. We may also discover how they relate to each other and how they affect the whole network [21]. The main problem is detecting communities in the first place. Most importantly, researchers have provided and designed many methods and techniques to improve it, but few of

Table 6.1 Five data sets, with all nodes in each data set and the existing edges

Source data	Node	Number of nodes	Number of edges
MATLAB help document	Key terms	2,385	10,091
Chinese characters	Radicals	1,174	4,000
Yeast	Proteins	2,361	7,182
Electronic collaboration networks	Authors	5,242	28,980
Peer-to-peer file-sharing networks	Hosts	6,301	20,777

these techniques and methods have been adopted by the scientific community as the most reliable [17].

In this paper, the algorithm we propose for identifying communities is as follows:

1. Calculate the degree of each node in the network, including the out-degree and in-degree.
2. Remove nodes with degree k (the initial value of k is 1) from the network.
3. Remove nodes with degree $k + 1$.
4. Repeat step 3 until no community is left.

6.3 Analysis of Community Structure

6.3.1 Modularity

Modularity Q [22] is a property proposed by Clauset et al. to measure when the division of networks is a good one. The formula is as follows:

$$Q = \frac{1}{2m} \sum_{ij} \left(A_{ij} - \frac{k_i k_j}{2m} \right) \delta(C_i, C_j). \quad (6.1)$$

The quantity will be zero when the fraction of within-community edges is no different from what we could expect for a randomized network. The quantities A_{ij} are the elements of the so-called adjacency matrix. At the same time, the expected number of edges between vertices i and j if edges are placed at random is $\frac{k_i k_j}{2m}$, where k_i and k_j are the degrees of the vertices and m is the total number of edges in the network; if $m=0$, then there is no connection between any two nodes in the network. Vertices i and j respectively belong to communities C_i and C_j . If $C_i = C_j$, then $\delta(C_i, C_j) = 1$. Otherwise, $\delta(C_i, C_j) = 0$. The value of Q ranges between 0 and 1; the greater the value of Q , the more closely it represents the community structure, with $Q=0.3$ generally serving as the lower bound of a network with an obvious community structure. Based on formula (6.1), we calculated the modularity for each data set, as shown in Table 6.2.

Table 6.2 Modularity for each data set

Source data	Number of nodes	Number of edges	Modularity
MATLAB help document	2,385	10,091	0.890
Chinese characters	1,174	4,000	0.302
Yeast	2,361	7,182	0.582
Electronic collaboration networks	5,242	28,980	0.858
Peer-to-peer file-sharing networks	6,301	20,777	0.445

Table 6.2 displays the modularity of the five data sets. The modularity value can indicate the density of the community structure in networks. The greater the modularity value, the greater the density, which means the network has a more obvious community structure and dense connections inside the network. For example, the data from MATLAB may have more obvious community features than the others because it has the largest modularity value (0.890), while a smaller modularity value reveals a lower density, which means the network has a less obvious community structure and sparse connections within. The data from Chinese characters may have a less obvious community feature since it has the smallest modularity value (0.302).

6.3.2 Relationship Between Number of Nodes of Maximal Community and the Number of Communities in the Corresponding Network

In this section, we explore the relationship between the number of nodes of the maximal communities and the number of communities in the corresponding networks to investigate the character of community structure (Fig. 6.1).

Figure 6.1 displays the relationship chart of the five data sets and allows us to draw the conclusion that there exists a linear correlation between the number of nodes of the maximal and the number of communities in the corresponding networks. To study this linear correlation, we quantified five data sets and compared them. From Fig. 6.2 we can observe that the number of communities gradually declines as the number of nodes increases. However, the rate trends vary, and we find that different trends reflect the structure of different complex networks. For example, the linear correlation of the MATLAB help document is steep, which reveals that dense connections inside and sparsely connected outside. Meanwhile, the linear correlation of yeast is relatively smooth, which means sparse connections inside, dense connections outside. Depending on the linear correlation between the number of communities in the whole network, we are better able to study the character of the community structure of complex networks.

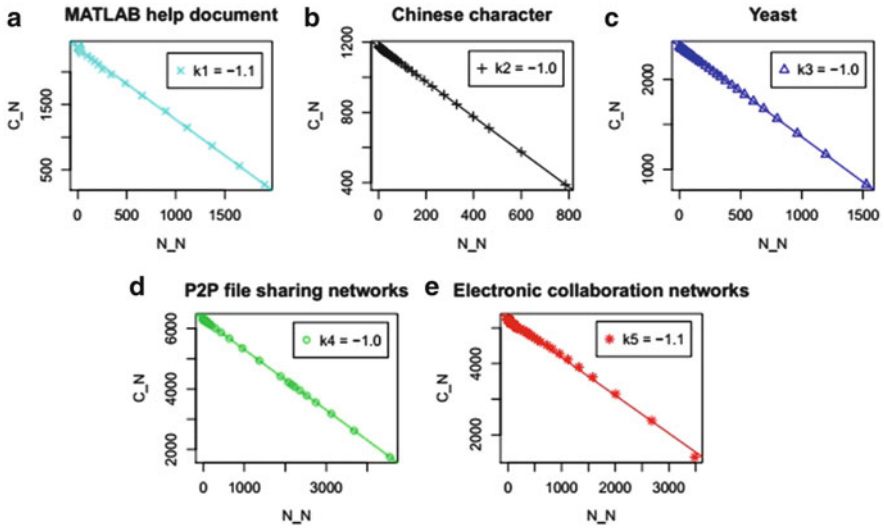


Fig. 6.1 Description of relationship of five data sets. (a) MATLAB help document. (b) Chinese characters. (c) Yeast. (d) P2P file-sharing networks. (e) Electronic collaboration networks. N_N number of nodes of maximal communities, C_N number of communities in corresponding networks

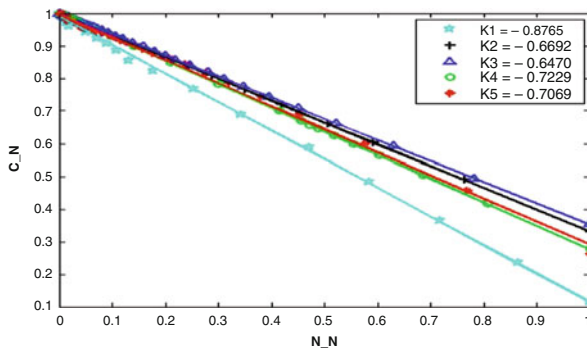


Fig. 6.2 The relationship between the number of nodes of maximal communities and the number of communities is linear, but the slopes of the lines from the five data sets are different, where K_1 , K_2 , K_3 , K_4 and K_5 represent the slopes of five linear fittings of the MATLAB help document, Chinese characters, yeast, electronic collaboration networks, and peer-to-peer file-sharing networks, respectively

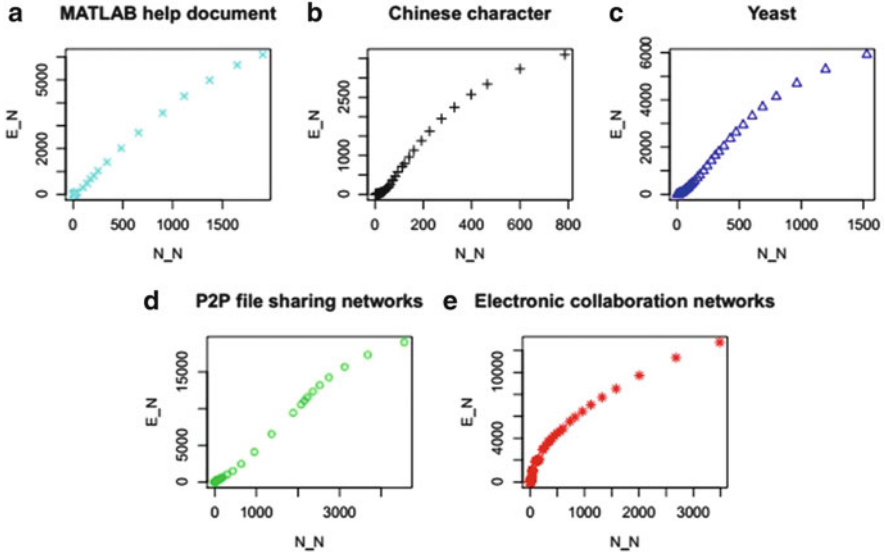


Fig. 6.3 Visualization of relationship of five data sets. (a) MATLAB help document. (b) Chinese characters. (c) Yeast. (d) P2P file-sharing networks. (e) Electronic collaboration networks. N_N number of nodes of maximal communities, E_N number of edges in corresponding maximal communities

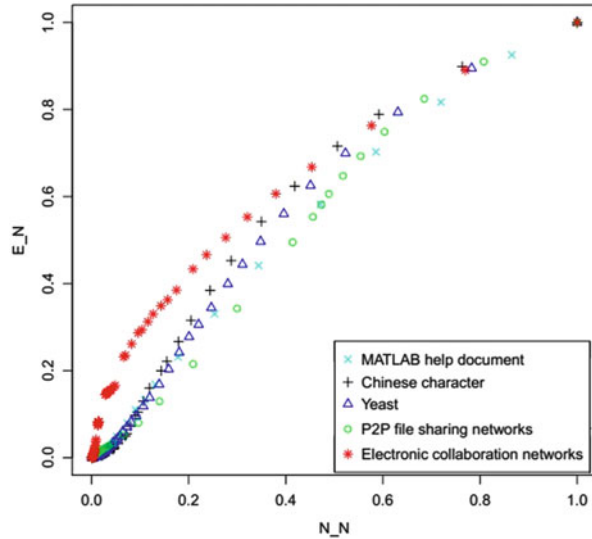
6.3.3 Relationship Between Number of Nodes in Maximal Communities and Number of Their Corresponding Edges

We explore the relationship between the number of nodes in the maximal communities and the number of their corresponding edges using a relationship chart to investigate the character of community structure (Fig. 6.3).

According to the study of the relationship between the number of nodes in maximal communities and the number of communities in the corresponding networks, we find that there exists a linear correlation between them.

We now explore the relationship between the number of nodes of the maximal communities and the number of edges in the corresponding maximal communities. Figure 6.3 displays a chart showing the relationship between the five data sets. The figure shows that the number of edges rapidly increases while the number of nodes initially increases. When the number of nodes reaches a certain level, the increase in the number of edges tends to smooth out while the number of nodes increases. To examine this property, we quantified the five data sets and compared them. Figure 6.4 demonstrates that there are differences in the five data sets; the trend changes in some data sets, such as electronic collaboration networks, are steep,

Fig. 6.4 Quantification of five data sets and their relationships. N_N number of nodes of maximal communities, E_N number of edges in corresponding maximal communities



whereas other data sets, such as peer-to-peer file-sharing networks, change slowly. When the increase in the number of nodes reaches a certain level, the number of edges does not increase but achieves a flat state. Based on the preceding analysis, we may conclude that complex networks have a sparsity feature.

Discussion and Conclusion

Community structure detection plays a significant role in studying the structural properties, functions, and evolutionary mechanisms of complex networks by breaking down the nodes, which is helpful for properly disclosing network construction principles and topology functions.

This paper focused on several data sets from various areas to explore the features of community structure. To begin with, we calculated the modularity of five complex networks, proposing the conclusion that the modularity and density of the communities in the whole networks are positively related. Then, after fitting the number of nodes in the maximum communities to the number of communities in the corresponding networks, we observed a linear correlation between them. We could extend this linear correlation to other kinds of networks and predict their scale. Finally, examination of the relationships between the number of nodes of maximal communities and the number of edges in the corresponding maximal communities revealed the sparse character of the community structure in networks and which revealed the generality feature of complex networks.

(continued)

(continued)

However, a few problems remain. First, there is no common definition of community, which is justified by the nature of the problem itself. What's more, real-world networks are dynamic. An increasing number of studies on complex networks are focusing on excavating the hidden relations and features in real networks such as social networks. Therefore, improving the methods of researching ever-changing dynamic networks represents an innovative and challenging avenue for future work.

Acknowledgements The author would like to thank Prof. Li for helpful suggestions and comments. This research work was supported by Key Research Institute in the University of China, National Center for Radio and Television Studies 2013GDYB07, and National Key Technology R&D Program 2013BAH66F02-02.

References

1. Newman M. *Networks: an introduction*. New York: Oxford University Press; 2010.
2. Barrat A, Barthelemy M, Vespignani V. *Dynamical process on complex networks*. Cambridge: Cambridge University Press; 2008.
3. Vespignani A. Modelling dynamical process in complex socio-technical systems. *Nat Phys*. 2012;8(1):32–9.
4. Leicht EA, Newman MEJ. Community structure in directed networks. *Phys Rev Lett*. 2008;100(11):118703.
5. De Meo P, Nocera A, Terracina G, et al. Recommendation of similar users, resources and social networks in a social internet working scenario. *Inf Sci*. 2011;181(7):1285–305.
6. Durugbo C, Hutabarat W, Tiwari A, et al. Modelling collaboration using complex networks. *Inf Sci*. 2011;181(15):3143–61.
7. Hein DIO, Schwind DWIM, Konig W. Scale-free networks. *Wirtschaftsinformatik*. 2006;48(4):267–75.
8. Caldarelli G, Vespignani A, editors. *Large scale structure and dynamics of complex networks: from information technology to finance and natural science*. New Jersey: Word Scientific; 2007.
9. Fortunato S. Community detection in graphs. *Phys Rep*. 2010;486(3):75–174.
10. Porter MA, Onnela JP, Mucha PJ. Communities in networks. *Not Am Math Soc*. 2009;56(9):1082–97.
11. Arenas A, Fernandez A, Gomez S. Analysis of the structure of complex networks at different resolution levels. *New J Phys*. 2008;10(5):053039.
12. Fortunato S, Barthelemy M. Resolution limit in community dection. *Proc Natl Acad Sci*. 2007;104(1):36–41.
13. Fortunato S, Castellano C. *Community structure in graphs*. New York: Springer; 2012. p. 490–512.
14. Liu J, Deng G. A collaborative recommendation method based on user network community with weighted spectral analysis. *J Dalian Univ Technol*. 2010;50(3):438–42.
15. Cun R, Duan X, Liu X, Li Z. A physical community discovery algorithm. *J Microelectronics Comput*. 2010;27(9):33–6.

16. Traud AL, Kelsic ED, Mucha PJ, et al. Comparing community structure to characteristics in online collegiate social networks. *SIAM Rev.* 2011;53(3):526–43.
17. Lancichinetti A, Kivela M, Saramaki J, et al. Characterizing the community structure of complex networks. *PLoS One.* 2010;5(8):e11976.
18. Bu D, Zhao Y, Cai L, et al. Topological structure analysis of the protein–protein interaction network in budding yeast. *Nucleic Acids Res.* 2003;31(9):2443–50.
19. Leskovec J, Kleinberg J, Faloutsos C. Graph evolution: densification and shrinking diameters. *ACM Trans Knowl Discov Data.* 2007;1(1):0603229.
20. Ripeanu M, Foster I, Lamnitchi A. Mapping the gnutella network: Properties of large-scale peer-to-peer systems and implications for system design [J]. 2002. arXiv preprint cs/0209028
21. De Meo P, Ferrara E, Fiumara G, et al. Enhancing community detection using a network weighting strategy. *Inf Sci.* 2013;222(1):648–68.
22. Clauset A, Newman MEJ, Moore C. Finding community structure in very large networks. *Phys Rev E.* 2004;70(6):066111.

Chapter 7

Construction of a Thermal Power Enterprise Environmental Performance Evaluation Model

Xiaofei Liao, Huayue Li, Weisha Yan, and Lin Liu

Abstract This paper establishes a thermal power enterprise environmental performance evaluation model based on the fuzzy analytic hierarchy process utilizing a listed Chinese thermal power company as an example to verify the model's operability and scientific validity. Our model provides an operational and quantifiable method for evaluation of the environmental performance of Chinese thermal power enterprises.

Keywords Environmental performance evaluation • Fuzzy analytic hierarchy process (FAHP) • Stakeholder theory • Thermal power enterprise

7.1 Introduction

The thermal power industry is one of large scale with strong profitability but serious environmental pollution issues. Setting up a scientifically valid environmental performance evaluation model is a key factor in solving this contradiction.

“Environmental Performance Evaluation” is a relatively new term. David Pierce et al., proposes making environmental resources a part of physical accounting, and making environmental factors significant corporate finance decisions [1, 2]. In 1994, The Canadian Institute of Chartered Accountants listed many examples of the environmental performance of different fields. In August 2000, the World Business Council for Sustainable Development (WBCSD) put forward the world's first set of ecological evaluation criteria, creating an important communication tool between an enterprise and other internal or external stakeholders [3]. Bolet and other scholars studied the changes in power company's environmental and business performance in relation to the U.S. Clean Air Act and then proclaimed the DEA method [4]. The study of environmental performance evaluation in China does not

X. Liao • H. Li (✉) • W. Yan • L. Liu
Changsha University of Science and Technology, Changsha 410004, China
e-mail: xfliao1645@126.com; 234890846r@qq.com; 756878173@qq.com;
764204899@qq.com

have a long history. Tang et al. [5] created 15 indicators in five major categories, also conducting a comprehensive evaluation of environmental performance using the BP artificial neural network method [6].

Because of the diversity of environmental performance evaluation indices, there is no current unified conclusion as to the evaluation of environmental performance. The fuzzy analytic hierarchy process (FAHP) method presented herein can convert qualitative evaluation into quantitative evaluation.

7.2 The Establishment of the Thermal Power Enterprise Environmental Performance Evaluation Index System

7.2.1 The Selection of Level Indicators for the Thermal Power Enterprise Environmental Performance Evaluation Index System

Environmental conditions mainly refer to economic value whereas environmental benefit refers to the measures and gains that contribute to the enterprise's sustainable and ecological environmental protection. Economic benefit represents a comparison of labor costs and labor outcomes of economic activity in a socialist economy. Social benefit refers to the positive and negative effects on society when an enterprise conducts its own environmental management. The three together form the "triple bottom line" of disclosure in the international environmental performance index system [7]. Environmental conditions affect an enterprises' economic development, and the contributions to the economic, social, and environmental benefits, as all four are complementary to each other. The system established in this paper has as the main evaluation levels: environmental states, environmental benefit, economic benefit, and social benefit indicators, and each main evaluation level is further divided into several secondary indices.

7.2.2 The Selection of Secondary Indices for the Thermal Power Enterprise Environmental Performance Evaluation Index System

On the basis of previous studies and China's special environment we selected the first ten pieces of literature cited in our county, 30 articles mainly on coal, paper making, power and other heavy pollution industries from the last 5 years in CSSCI (Chinese Social Sciences Citation Index), and 20 references related to the environmental performance evaluation index system of heavily polluting industries from foreign literature of the past 3 years. We used EXCEL statistics on these 60 articles, and selected the top 30 environmental performance evaluation

Table 7.1 Environmental performance evaluation index system including the secondary indices

Target layer	Level indicators	Secondary indicators
Performance evaluation system environment A	Environmental status indicators B ₁	The annual pollution direct loss proportion C ₁₁
		The attainment rate of afforestation in enterprise C ₁₂
		Standard rate of corporate greening C ₁₃
		Environmental agencies involved in the extent of its product development process C ₁₄
		The type of eco-friendly C ₁₅
		Environmental contribution of green products C ₁₆
	Environmental benefits index B ₂	Unit energy consumption profitability C ₂₁
		Rate of return for utilization of the “Three wastes” C ₂₂
		Environmental agencies involved in the extent of its product development process C ₂₃
		Environmental contribution of green products C ₂₄
		The size and extent of the use of environment-friendly technology C ₂₅
	Economic indicators B ₃	Annual growth rate of energy efficiency C ₃₁
		Energy conservation yields C ₃₂
		Frequency of excessive sewage C ₃₃
		Environmental subsidies and income growth C ₃₄
		Capital expenditures relating to the environment C ₃₅
		Proportion of R&D assigned to green products C ₃₆
	Social indicators B ₄	Hazardous solid waste disposal rate C ₄₁
		The proportion of funds to finance social environment C ₄₂
		Number of environmental pollution disputes C ₄₃
Number of occurrences of employee occupational diseases C ₄₄		
Environmental education training hours C ₄₅		

indicators. We developed the secondary indices shown in Table 7.1 based on our research on the electric power industry.

7.3 The Construction of a Thermal Power Enterprise Environmental Performance Evaluation Model for China Based on FAHP

7.3.1 The Analytic Hierarchy Process (AHP) to Determine Weight

Firstly, design appropriate questionnaires, and using these survey an expert group to determine the mutual importance of the different level indicators. Then, construct a judgment matrix. Put the overall judgment of the environmental performance of multiple elements' weight on these elements into "compared to each other," and convert the thus-compared results into quantitative data to form A . Use a Judgment matrix to calculate the maximum eigenvalue eigenvector.

Calculate M_i , which is the product of the i th row of A ,

$$M_i = \prod_{j=1}^n a_{ij}, \quad i = 1, 2, \dots, n \quad (7.1)$$

Calculate W_i which is the n th power of M_i ,

$$W_i = \sqrt[n]{M_i} \quad (7.2)$$

$W_i = (w_1, w_2, \dots, w_n)$ is normalized to give

$$w_i = \frac{w_i}{\sum_{j=1}^n w_j} \quad (7.3)$$

$W_i = (W_1, W_2, \dots, W_n)$ is the eigenvector of A . If the corresponding of each order matrix's consistency ratio satisfies

$$CR = \frac{CI}{RI} < 0.1 \quad (7.4)$$

$$CI = \frac{\lambda_{\max} - n}{n - 1} \quad (7.5)$$

where RI is the average random consistency index. If $CR < 0.1$, we can judge that the matrix consistency meets the requirements. According to the characteristic equation

$$AW = \lambda_{\max} w \quad (7.6)$$

$$\lambda_{\max} = \sum_{i=1}^n \frac{(AW)_i}{nW_i} \tag{7.7}$$

where $(AW)_i$ means the judgment matrix that is constructed by the element of i of the vector AW using the ‘‘compared to each other’’ method. $A_i = (a_{i1}, a_{i2}, \dots, a_{im})$ means the weighting coefficient matrix of i evaluation, a_{ij} is the weight of each factor of the i th indicators evaluation aspects, which satisfies,

$$0 < a_{ij} \leq 1, \quad \sum_{j=1}^m a_{ij} = 1 (j = 1, 2, \dots, m) \tag{7.8}$$

7.3.2 Establish an Indicator Evaluation Matrix

On the basis of ambiguity in numbers, each expert assigns a value to each of the secondary indices. We use $S_i = (s_{i1}, s_{i2}, \dots, s_{ik})$ giving the evaluation vector where s_{ik} represents the membership of i evaluation factors to rank k . According to the weight matrices A_i and evaluation matrices S_i we obtain the i level evaluation index evaluation vector B_i .

$$B_i = A_i \times R_i = (A_{i1}, A_{i2}, \dots, A_{im}) \times \begin{bmatrix} s_{11} & s_{12} & \dots & s_{1k} \\ s_{21} & s_{22} & \dots & s_{2k} \\ \vdots & \vdots & \vdots & \vdots \\ s_{j1} & s_{j2} & \dots & s_{jk} \end{bmatrix} \tag{7.9}$$

7.3.3 Fuzzy Comprehensive Evaluation

To integrate the single factor fuzzy evaluation result $B_j (j = 1, 2, \dots, n)$, constituted a higher evaluation matrix R , and get the comprehensive evaluation results, namely:

$$B = A * R = (a_1, a_2, \dots, a_m) * (B_1, B_2, \dots, B_n)^T \tag{7.10}$$

Through the FAHP, we set the evaluation of the collection by:

$$U = (u_1, u_2, \dots, u_m) \tag{7.11}$$

With m as the number of evaluations we determine $U = \{\text{excellent, better, good, qualified, unqualified}\}$; the i th evaluation indicator is represented by a vector $C_i = (C_{i1}, C_{i2}, \dots, C_{i5})$, where each indicator is represented on a five rating scale.

7.4 Application of the Thermal Power Enterprise Environmental Performance Evaluation Model to a Chinese Thermal Power Company

We applied the Thermal Power Enterprise Environmental Performance Evaluation Model to listed Chinese thermal power company. To do this we prepared a questionnaire survey for experts, corporate executives, and business users and obtained the results shown in Table 7.2.

Set the fuzzy matrix of the fuzzy matrix's primary index evaluation factors as $R_i (i = 1, 2, 3, 4)$, weight parameters as $A_i (i = 1, 2, 3, 4)$. First, calculate the value of the first level as shown in Table 7.3.

$\lambda_{\max} = 4.096$, $CI = 0.048$, $RI = 0.9$, $CR = 0.053 < 0.1$, the results show that the data meets the consistency.

Using the same method, we can get a comprehensive evaluation matrix,

$$\begin{aligned} A_1 &= (0.33, 0.27, 0.07, 0.20, 0.13) \\ A_2 &= (0.29, 0.24, 0.14, 0.19, 0.10, 0.05) \\ A_3 &= (0.05, 0.29, 0.14, 0.10, 0.19, 0.24) \\ A_4 &= (0.29, 0.25, 0.21, 0.15, 0.10) \end{aligned}$$

According to $B_i = A_i \times R_i (i = 1, 2, 3, 4)$, we can get,

$$\begin{aligned} B_1 &= (0.013, 0.173, 0.287, 0.294, 0.193) \\ B_2 &= (0, 0.197, 0.371, 0.307, 0.135) \\ B_3 &= (0.025, 0.115, 0.207, 0.357, 0.216) \\ B_4 &= (0.045, 0.225, 0.287, 0.288, 0.155) \end{aligned}$$

According to maximum membership principles, the environmental status and environmental efficiency indices are both "good" and the indices of economic indicators and social indicators are both "qualified."

The evaluation results B_1, B_2, B_3, B_4, B_5 shown above constitute a higher level fuzzy matrix R . The comprehensive evaluation factor is A . We therefore have $B = A \times R = (0.1944, 0.17028, 0.27788, 0.30972, 0.18548)$.

According to maximum membership principles of (0.35472), the environmental performance of the company is "qualified." Make the evaluation system of the evaluation level $U = \{\text{excellent, better, good, qualified, unqualified}\}$, for the corresponding score,

$$C = \{100, 80, 60, 40, 20\},$$

Table 7.2 Fuzzy evaluation matrix of a listed Chinese thermal power company

Evaluation	Evaluation factors	Rank				
		Excellent	Better	Good	Qualified	Unqualified
Environmental status indicators	Direct proportion loss pollution	0	0.2	0.5	0.2	0.1
	The proportion of indirect losses pollution	0	0.1	0.3	0.4	0.2
	Standard rate of corporate greening	0	0.2	0.3	0.3	0.2
	Environmental agencies involved in the extent of its product development process	0	0.2	0.4	0.2	0.2
	Environmental contribution of green products	0	0.2	0.3	0.3	0.2
	Unit energy consumption profitability	0	0.2	0.4	0.2	0.2
	Environmental Benefits Index	Rate of return for utilization of the "Three wastes"	0	0.2	0.2	0.3
Environmental agencies involved in the extent of its product development process		0	0.1	0.5	0.4	0.2
Environmental contribution of green products		0	0.1	0.2	0.4	0.3
Size and extent of the use of environment-friendly technology		0.1	0.2	0.2	0.3	0.2
Annual growth rate of energy efficiency		0	0.2	0.4	0.2	0.2
Economic indicators		Energy conservation yields	0	0	0.2	0.6
	Frequency of excessive sewage	0	0.1	0.3	0.3	0.3
	Environmental subsidies and income growth	0.1	0.5	0.1	0.2	0.1
	Capital expenditures relating to the environment	0	0.2	0.2	0.3	0.3
	Proportion of R&D assigned to green products	0.1	0.2	0.2	0.3	0.2
	Hazardous solid waste disposal rate	0	0.2	0.2	0.4	0.2

(continued)

Table 7.2 (continued)

Evaluation	Evaluation factors	Rank				
		Excellent	Better	Good	Qualified	Unqualified
Social indicators	The proportion of funds to finance social environment	0.1	0.2	0.3	0.3	0.1
	Number of environmental pollution disputes	0	0.2	0.4	0.2	0.2
	Number of occurrences of employee occupational diseases	0	0.3	0.2	0.3	0.2
	Environmental education training hours	0.2	0.3	0.4	0.1	0

Table 7.3 The first level judgment matrix

Calculating weights							
A	B1	B2	B3	B4	Geometric mean	Weights	Weighted sum
B1	1	2/3	2/3	1	0.8165	0.2020	0.8141
B2	3/2	1	1	3/4	1.0299	0.2548	1.0409
B3	3/2	1	1	3/2	1.2247	0.3030	1.2211
B4	1	4/3	2/3	1	0.9710	0.2402	0.9839

$$\begin{aligned}
 W &= B \times C^T \\
 &= 0.1944 \times 100 + 0.17028 \times 80 + 0.2788 \times 60 + 0.30972 \times 40 + 0.18548 \\
 &\quad \times 20 \\
 &= 48.3374
 \end{aligned}$$

None of the level indicators are very good. The situation is basically consistent with the results from the electric power industry.

Conclusion

From a theoretical perspective of benefit, and with environmental performance measurement targets as a guide, this paper selected the top 30 environmental performance evaluation indicators from previous studies. With the background research of our work on electric power enterprises this paper established a thermal power enterprise environmental performance evaluation model based on the FAHP method for Chinese companies. We use the thermal power industry of China as an example to verify the model’s operability and scientific validity. Our model provides an operational and quantifiable method for evaluation of the environmental performance of Chinese thermal power enterprises.

Acknowledgments Foundation item: Project (13YBA003) was supported by the Social Science Foundation of Hunan Province, China; Project (13QGB5) was supported by the Modern Enterprise Management Research Center Foundation of Hunan province, China; Project (12JDYB09) was supported by the Enterprise Strategic Management And Investment Decision-Making Research Foundation of Hunan province, China.

References

1. Pearce DW. Green economy blueprint. Beijing: Beijing Normal University Press; 1996. p. 76–81.
2. International Standard Organization, Environmental Performance Evaluation, ISO/DIS 14031, ANSI; 1997.
3. Figge F, Hahn T. Sustainable value added—measuring corporate contributions to sustainability beyond eco-efficiency. *J Ecol Econ*. 2004;48:173–87.
4. Meng F. Environmental accounting information disclosure and theoretical issues related to accounting research. *Account Res*. 1994;4:16–25 (in Chinese).
5. Tang J, Xuan C. BP artificial neural network based on corporate environmental performance evaluation. *Stat Decis*. 2006;11:161–2.
6. Ge J, Li R. A new ideological trend of Western accounting theory of the green accounting theory of the in the ninety's. *Account Res*. 1992;1:1–6 (in Chinese).
7. “Corporate environment and development,” the research group, the Chinese enterprise environment survey[J]. *Manage World*. 1992;2:177–83 (in Chinese).

Chapter 8

A Mobile Localization Algorithm Based on SPSO Algorithm

Maoheng Sun and Azhi Tan

Abstract Localization is important for the wireless sensor network because we need sensor nodes to tell the central monitor the specific location where the event is happening. In this paper, in view of the low positioning accuracy of the mobile node localization in WSN, we propose an improved algorithm called SPSOMCB to improve the localization accuracy. We use the simplified particle swarm optimization algorithm in the Monte Carlo localization boxed algorithm to improve the localization accuracy of the mobile node while not significantly increasing the computational complexity. The SPSOMCB algorithm utilizes the MCB algorithm to predict the position of the mobile node, build the fitness function according to the position error, and then take the SPSO to rapidly optimize the position error function and decrease the localization error as much as possible. In comparison with the MCB algorithm, experimental results show that the proposed SPSOMCB algorithm can reduce the mobile node location error.

Keywords WSN • Mobile node localization • MCB • PSO

8.1 Introduction

Wireless sensor network consists of many sensor nodes which are deployed in monitored areas and capable of detecting information around these areas [1]. As we need the sensor nodes to tell the central monitor the specific location where the event is happening, the localization is important for WSN.

More and more applications take the mobility of the sensor node into account in WSN, for example, the war application scenarios. Researchers pay much attention to the location in the mobile node. Hu and Evans [2] presented a localization algorithm for the mobile sensor sequential Monte Carlo method by taking advantage of the mobility of the sensor node to improve the localization accuracy. Yi and Yang presented an improved algorithm for MCL by using the average distance of

M. Sun • A. Tan (✉)

College of Electronic and Information Engineering, Tongji University,
Shanghai 201804, China

e-mail: sun_mh@tongji.edu.cn; taz19880712@163.com

© Springer International Publishing Switzerland 2015

W.E. Wong (ed.), *Proceedings of the 4th International Conference on Computer Engineering and Networks*, Lecture Notes in Electrical Engineering 355,
DOI 10.1007/978-3-319-11104-9_8

65

hop count between the sensor node and the anchor node to improve the location accuracy [3]. Baggio and Langendoen presented an MCB algorithm [4]. They introduced an anchor box and a sampling box to improve the efficiency of sampling.

In this article, we propose a SPSOMCB algorithm. Based on the MCB and RSSI, it combines the static node localization algorithm with the mobile node localization algorithm to construct the minimum error function, builds the fitness function according to the position error, and then takes the simplified particle swarm optimization algorithm to rapidly optimize the position error function and decrease the localization error as much as possible.

8.2 Related Works

8.2.1 MCB Algorithm

The MCB algorithm contains two steps, the sampling and the filtering. The sampling area is the dashed area shown in Fig. 8.1. P presents the position in $t-1$ time, and s_1 and s_2 , respectively, present the position of one-hop and two-hop anchor node. For the convenience of count, we take the smaller rectangle as the sampling box as shown in Fig. 8.1, but actually the sampling area for the node is the shaded area shown in Fig. 8.1; therefore, we filter those samples to get the efficient samples. l means the sample; we can use formula (Eq. 8.1) to determine the efficient samples.

$$O(l) = \{\forall l \in R_1, d(s_1, l) \leq R\} \wedge \{\forall l \in R_2, R \leq d(s_2, l) \leq 2R\}. \quad (8.1)$$

R_1 represents the set of one-hop and two-hop anchor nodes. $d(s_1, l)$ represents the Euclidean distance between l and the one-hop node when in t time.

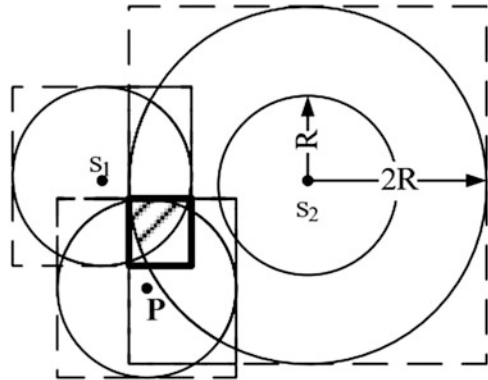


Fig. 8.1 Sampling area (dashed area)

8.2.2 Particle Swarm Optimization

The particle swarm optimization (PSO) algorithm is an optimization algorithm easy for implementation and with high efficiency, and Kennedy and Eberhart proposed the original PSO formula [5]. It has never been used in the mobile node localization algorithm before.

Hu and Li have testified that the processing of optimization has nothing to do with the speed of the particles [6]. The optimization function is shown in formula (Eq. 8.2).

$$x_{id}^{t+1} = wx_{id}^t + c_1r_1(p_{id} - x_{id}^t) + c_2r_2(P_{gd} - x_{id}^t). \quad (8.2)$$

x_{id} represents the current position of particle i , and $i = 1, 2, \dots, m$, $d = 1, 2, \dots, D$, and r_1 and r_2 are random satisfied $U(0,1)$ distributions. c_1 and c_2 are learning factors, usually $c_1 = c_2 = 2$. Compared with the optimization function which Kennedy and Eberhart proposed, formula (Eq. 8.2) deducts the speed information, which we call the simplified particle swarm optimization (SPSO), and it can improve the algorithm's efficiency.

8.3 SPSOMCB Algorithm

Based on the MCB algorithm, we introduce the simplified particle swarm optimization algorithm. We use the particle to represent the estimated location for the mobile node and take average of the final N node's location which is accounted with the MCB algorithm as the initiation particle. If the position of anchor node j is (x_j, y_j) and the position of the i particle is (x_i, y_i) , the distance D_{ij} between i particle and anchor node j can be described as formula (Eq. 8.3).

$$D_{ij} = \sqrt{(x_i - x_j)^2 - (y_i - y_j)^2}. \quad (8.3)$$

At the same time, the mobile node can use the information received from the anchor nodes and the RSSI [7] algorithm to count the distance between itself and the anchor node j at the time of t . The distance of a mobile node and an anchor node j is R_{ij} , and the subtrahend distance of R_{ij} and D_{ij} is e_{ij} , so e_{ij} can be expressed as formula (Eq. 8.4):

$$e_{ij} = \left(R_{ij} - \sqrt{(x_i - x_j)^2 - (y_i - y_j)^2} \right)^2. \quad (8.4)$$

If we assume the mobile node can receive the n node's information at the time of t , the total error function can be expressed as formula (Eq. 8.5).

$$\sum_{j=1}^n e_{ij} = \sum_{j=1}^n \left(R_{ij} - \sqrt{(x_i - x_j)^2 - (y_i - y_j)^2} \right)^2. \quad (8.5)$$

But while taking the error of estimated distance into account, we can take formula (Eq. 8.6) as the error function to decrease the error.

$$F(x) = \frac{\sum_{j=1}^n \left(R_{ij} - \sqrt{(x_i - x_j)^2 - (y_i - y_j)^2} \right)^2}{R_{ij}}. \quad (8.6)$$

So we call formula (Eq. 8.6) as the fitness function for SPSOMCB algorithm. In formula (Eq. 8.6), n is the number of anchor nodes, and R_{ij} is the distance of particle i and anchor node j .

In the process of optimization with the SPSO algorithm, we take the average of N node's location gotten from the end of MCB algorithm as the initial global optimum value, as shown in formula (Eq. 8.7):

$$p_{gd} = \frac{\sum_{i=1}^N l_t^i}{N}. \quad (8.7)$$

Algorithm divides the time into different time segments, and the mobile node estimates its location at the time of t with the algorithm process shown as follows:

- Step 1: the anchor nodes send the position information to the mobile node which determines the sampling box according to one-hop and two-hop anchor node's information. Then we use N samples which random sampled in the sampling box as its initial samples. We can use the set $L_0 = \{l_0^0, l_0^1, \dots, l_0^{N-1}\}$ to describe.
- Step 2: Use formula (Eq. 8.1) to filter and filter out invalid samples.
- Step 3: Judge whether the sampling points meet the requirements with the total number of samples as N ; otherwise return to step 2.
- Step 4: Take the filtered N samples as N particles of the particle swarm and initialize p_{id} as those filtered sample values. Use formula (Eq. 8.7) to calculate the global optimal solution p_{gd} .
- Step 5: Calculate the value of the error function for each particle according to formula (Eq. 8.6). Let the minimum error value of the particle's location information as the local optimal solution p_{id} .
- Step 6: Compare the value of p_{gd} and p_{id} , and then assign the smaller value as p_{gd} .
- Step 7: Update each particle's position according to formula (Eq. 8.2).
- Step 8: Repeat steps 5 and 6. Upon completion of each search, we compare the local optimum value gotten in this time with the global optimum value gotten in the last time, and $p_{gd} = \min(p_{gd}, p_{id})$.

Step 9: Judge whether the maximum number of iterations has been satisfied or not; if not satisfied, repeat steps 5–8; if satisfied, end the iteration. Finally, if the p_{id} gotten in the end is believed to be the mobile node coordinate, end the algorithm.

8.4 Performance Evaluation

This paper uses the Matlab and mcl-simulator [2] to simulate and compare with the MCB algorithm. The simulation area is set to a rectangular region of 100×100 m. The number of nodes is 50 including the anchor nodes and the unknown nodes. Node communication radius R is defined to 20 m. The simulation V is changed from 0 to V_{\max} , and $|V_{\max}| = R$. We use RWP movement model to simulate, $w = 0.2$, $C_1 = C_2 = 2$, sampling point N is 100, the largest number of iterations is set to 30.

8.4.1 Anchor Node Proportion and Average Positioning Error

In this paper, the positioning error of the node is defined as the ratio of the difference between the calculated position and the actual one and the communication radius R .

Figure 8.2 is the simulation result of the anchor node proportion and average node positioning error when the rate of movement of the mobile node is 15 m/s and the communication radius is 20 m. We can see that the average node positioning error is decreasing with the increase of the anchor node proportion when the

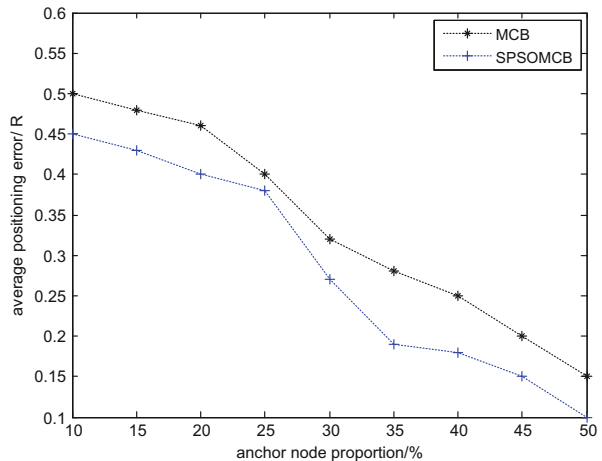
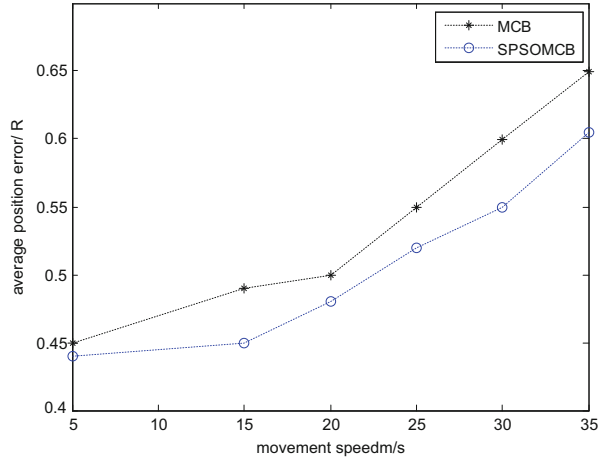


Fig. 8.2 Anchor node proportion relationship with the average node positioning error

Fig. 8.3 Node movement speed and the average position error

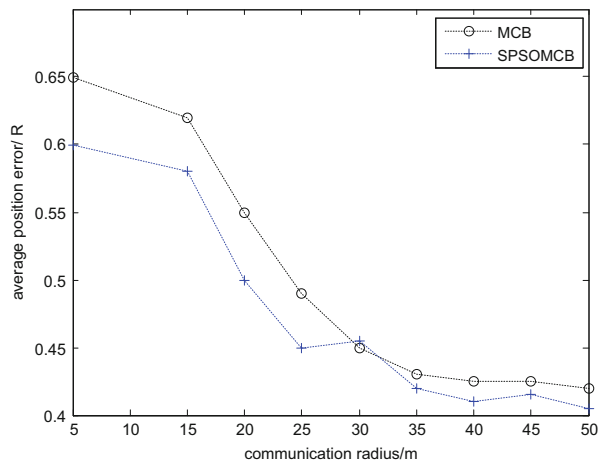


SPSOMCB algorithm is adopted. It is because the mobile nodes will receive more information which can make the sampling box smaller in unit time from more anchor nodes when the anchor node proportion is increasing, and the mobile nodes will have good effect in the process of calculating the fitness function when having more information from the anchor nodes. Such two points will decrease the node positioning error. We can know the positioning error is significantly reduced when the anchor node proportion is 25 % from Fig. 8.2 and the positioning error is 0.11R when the anchor node proportion is 50 %. In the same anchor node proportion, the mobile node's positioning error is smaller when the SPSOMCB algorithm is adopted than the node positioning error when the MCB algorithm is adopted.

8.4.2 Node's Movement Speed and the Average Positioning Error

Figure 8.3 displays the simulation result of the relationship with the mobile node's movement speed and the average positioning error when the anchor proportion is 15 % and the node communication radius is 35 m. As can be seen from the simulation results, when the speed of mobile nodes increases, its positioning error will increase accordingly. It is because when the mobile nodes' speed increases, less information that the mobile nodes receive from the anchor node will lead to higher error when the sampling box is determined. And less information the mobile node receives from the anchor node will lead to less information used by the process of particle swarm optimization; then it will bring a bigger positioning error. Nevertheless, generally, the SPSOMCB algorithm still achieves better location performance under the condition of the increase of the movement speed than that archived by the MCB algorithm.

Fig. 8.4 Node communication radius and average position error



8.4.3 Communication Radius and Average Positioning Error

Figure 8.4 shows the relationship of the node communication radius and average positioning error when the anchor node proportion is 15 % and the speed of mobile node is 20 m/s. We can see in the figure that when the communication radius increased, then the average positioning error will decrease. That is because when the mobile nodes receive more information from the anchor node, then the position error will be reduced. It can be seen from Fig. 8.4 that the SPSOMCB localization algorithm has a smaller positioning error than the MCB algorithm in the same conditions.

Conclusion

Localization is important for the wireless sensor network, especially when we have to take the mobile nodes into account. Because of the mobility of the node, the localization accuracy is a big problem when only the static node localization algorithm is used.

In this paper, we introduce the particle swarm optimization to the mobile localization algorithm. In order to decrease the positioning error, we improve the mobile node algorithm called SPSOMCB. In comparison with the MCB algorithm, experimental results show that the proposed SPSOMCB algorithm can reduce the mobile node positioning error. In the same situation, the mobile node's positioning error is smaller when the SPSOMCB algorithm is used than the node positioning error when the MCB algorithm is used; however, we have just only certified the feasibility and effectiveness of the SPSOMCB algorithm with the simulator. As to our future work, we have to study the behavior of the SPSOMCB algorithm in a real-life setting in the mobile wireless sensor network.

Acknowledgments This study is supported by the Kwang-Hua Fund for the College of Civil Engineering, Tongji University.

References

1. Sun LM, Li JZ, Chen Y. Wireless sensor network. Beijing: Tsinghua University Press; 2005. p. 11–4. In Chinese.
2. Hu L, Evans D. Localization for mobile sensor networks. Proceedings of the 10th Annual International Conference on Mobile Computing and Networking. USA: ACM; 2004. p. 45–57.
3. Yi J, Yang S, Cha H. Multi-hop-based monte carlo localization for mobile sensor networks. Sensor, Mesh and Ad Hoc Communications and Networks. USA: IEEE Press; 2007. p. 162–171.
4. Baggio A, Langendoen K. Monte Carlo localization for mobile wireless sensor networks. Ad Hoc Networks. 2008;6(5):718–33.
5. Kennedy J, Eberhart R. Particle swarm optimization. Proceedings of IEEE International Conference on Neural Networks. Piscataway: IEEE Press; 1995. p. 1942–8.
6. Hu W, Li ZS. A simpler and more effective particle swarm optimization algorithm. Journal of Software. 2007;18(4):861–8. In Chinese.
7. Bahl P, Padmanabhan VN. RADAR: an in-building RF-based user location and tracking system. INFOCOM 2000. Nineteenth Annual Joint Conference of the IEEE Computer and Communications Societies, vol 2. USA: IEEE Press; 2000. p. 775–84.

Chapter 9

A Fast and Accurate Algorithm of Subspace Spectrum Peak Search Based on Bisection Method

Yu Wang, Hong Jiang, and Donghai Li

Abstract The orthogonality of signal subspace and noise subspace could be exploited to achieve a super-resolution direction of arrival (DOA) estimation. In the implementation processing, the computation complexity of peak searching is considerably large, which affects processing in real time. In this paper, we utilize the bisection method to search the spatial spectrum peak. The proposed algorithm can attain fast process speed, high precision, and strong adaptability. Firstly, we use equal interval to compute space spectrum coarsely. Then we apply the continuous bisection method to search the real peak finely. It can quickly and infinitely approach the position of the true peak. Finally, we introduce the principles and steps of the new algorithm and analyze the performance.

Keywords DOA • Space spectrum • Bisection method • Peak search

9.1 Introduction

The methods of subspace-based DOA estimation, for example, multiple signal classification (MUSIC) [1], can provide high resolution. But there exists a large computation complexity in the search peak of spatial spectrum. With Metropolis-Hastings sampler, a fast MUSIC spectrum peak search approach is devised [2]. Although the computation is reasonable, the adaptability of the method is still the restriction [3].

A method with a generalized ratio theory was introduced [4, 5]. It is a useful method for a one-source scenario, while it gets many false peaks in the case of multisources. A new MUSIC spectrum peak search method is proposed, and the computation cost is more than the Metropolis-Hastings sampler [3].

Y. Wang • H. Jiang (✉)

National Digital Switching System Engineering and Technological R&D Center,
Zhengzhou 450002, China
e-mail: jh_1012@126.com

D. Li

Huanghe Science and Technology Institute, Zhengzhou 450063, China

© Springer International Publishing Switzerland 2015

W.E. Wong (ed.), *Proceedings of the 4th International Conference on Computer Engineering and Networks*, Lecture Notes in Electrical Engineering 355,
DOI 10.1007/978-3-319-11104-9_9

This paper discusses the new spectral peak search algorithm, which is based on the bisection method and can attain fast speed, high precision, and strong adaptability. It can quickly and infinitely approach the true peak. The principles and steps of the new algorithm are introduced, and algorithm performance is analyzed.

9.2 Data Model

9.2.1 DOA Data Model

Consider an array that consists of M elements and P signals impinging on it. The received data, which is the M element space vectors, could be represented as an array of the waveforms and noise (linear combination).

Suppose $\mathbf{x}(t)$ is the vector of the received signal, $s(t)$ is the source signal, and $\mathbf{w}(t)$ is the noise vector, where t represents the sampling instant. Take the reference array element as the initial element; thus, the k th element of $\mathbf{x}(t)$ can be written as

$$x_k(t) = \sum_{i=1}^P s_i(t) \mathbf{a}_k(\theta_i) + w_k(t) \quad (9.1)$$

where $k = 1, 2, \dots, M$, i represents the i th signal, θ_i represents the DOA of the i th signal, and $\mathbf{a}(\theta_i)$ represents the steering vector of the i th signal, and the vector form is then

$$\mathbf{x}(t) = \mathbf{A}\mathbf{s}(t) + \mathbf{w}(t) \quad (9.2)$$

where $\mathbf{x}(t) = [x_1(t), x_2(t), \dots, x_M(t)]_{M \times 1}^T$.

\mathbf{A} is the steering vector matrix, $\mathbf{s}(t) = [s_1(t), s_2(t), \dots, s_P(t)]_{P \times 1}^T$ is the signal vector, and $\mathbf{w}(t) = [w_1(t), w_2(t), \dots, w_M(t)]_{M \times 1}^T$ is the noise vector.

$$\mathbf{A} = [\mathbf{a}(\theta_1), \mathbf{a}(\theta_2), \dots, \mathbf{a}(\theta_P)]_{M \times P} \quad (9.3)$$

where M represents the number of elements and P represents the number of signals.

9.2.2 MUSIC Algorithm

The covariance matrix of a received signal is

$$\mathbf{R}_{xx} = E[\mathbf{x}\mathbf{x}^H] = \mathbf{A}\mathbf{R}_{ss}\mathbf{A}^H + \sigma_n^2\mathbf{I} \quad (9.4)$$

where \mathbf{R}_{ss} is the correlation matrix of source signals, \mathbf{I} is the identity appropriate dimension matrix, and H means the conjugate transpose.

The Eigen decomposition of \mathbf{R}_{xx} is as follows:

$$\mathbf{R}_{xx} = \sum_{i=1}^P \lambda_i \mathbf{e}_i \mathbf{e}_i^H + \sigma_n^2 \sum_{i=p+1}^M \mathbf{e}_i \mathbf{e}_i^H \quad (9.5)$$

where λ_i is the eigenvalue according to the eigenvector \mathbf{e}_i , for all $i = 1, 2, \dots, M$.

The eigenvectors of \mathbf{R}_{xx} belong to one of the two subspaces, which are orthogonal to each other, namely, the signal subspace, in other words, the principal eigen subspace (PES), and the noise subspace, which means the minor eigen subspace (MES).

The dimension of the PES is P , and the dimension of the minor eigen subspace is $M - P$. The smallest eigenvalue of \mathbf{R}_{xx} , spanning the noise subspace, is σ_n^2 . The steering vectors, which make up \mathbf{A} , located in the PES, thus, are orthogonal to the MES. The DOAs can be determined by searching all the possible array steering vectors, finding the signal subspace orthogonal to the noise subspace.

In forming the noise subspace, we define the matrix \mathbf{V}_n , which contains the \mathbf{e}_i . And $\mathbf{a}^H(\theta)\mathbf{V}_n\mathbf{V}_n^H\mathbf{a}(\theta) \approx 0$, for θ corresponding to the DOA of a multiple-component.

And the DOAs of the multisources could be calculated by the location of the peaks of a spatial spectrum. Even in low signal-to-noise ratio (SNR), the resolution is still high enough.

$$P(\theta) = \frac{1}{\mathbf{a}^H(\theta)\mathbf{V}_n\mathbf{V}_n^H\mathbf{a}(\theta)} \quad (9.6)$$

9.3 Spectrum Peak Search

9.3.1 Coarse Search

It can be seen from (Eq. 9.6) that DOA estimation is to search the peak of $|P(\theta)|$ and the computation complexity is very large. In general, one sided to develop an algorithm is using a two-step search routine. The first step is calculating $|P(\theta)|$ for a set of θ values between -90 and $+90$ and identifying the θ , which peaks $|P(\theta)|$ over the set of θ values. The second step is locating the local peak, which is closest to the θ value picked out by the first step. And we name the first step as the coarse search and the second step as the fine search.

In general, θ is a set of equal interval θ values between -90 and $+90$ in coarse search, and equal interval value is taken not to affect resolution.

9.3.2 Fine Search

In fine search, θ is a set of equal interval θ values closest to the value of θ picked out by coarse search.

9.4 Fast Peak Search Algorithm

9.4.1 Bisection Method

In the equal interval method, both coarse search and fine search intervals are performed by equal interval, so the speed of search is slow. The coarse search method is performed by the equal interval method, whereas the fine search method is by the bisection method.

For new fast search algorithm, equal interval computing space spectrum is done firstly. And then, in the peak neighborhood, the continuous bisection method is used to search finely and find out the real peak finally. Next, some simulations are performed to verify the effectiveness of the proposed algorithm.

There are three signals impinging on the array that consists of nine elements, and their DOAs are 10.125° , 15.125° , and 20.125° , respectively. The SNR is 10 dB. The MUSIC spatial spectrum is shown in Fig. 9.1, and the search peak position process is shown in Figs. 9.2 and 9.3.

As can be seen from the spatial spectrum, the peak point is 10° , and the spatial spectrum of 11° is bigger than that of 9° . To determine the peak point between 10° and 11° , the calculation $|P(\theta)|$ of the intermediate position and the comparison are performed. Because the value of the middle point is bigger than that of 11° , the peak point is located between 10° and 10.5° . With the calculation and comparison

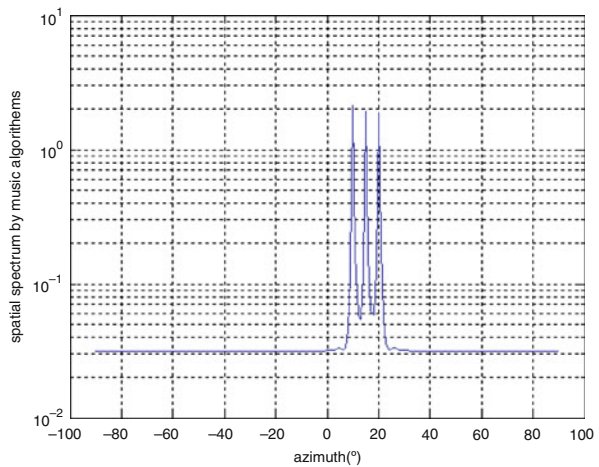


Fig. 9.1 The spatial spectrum of MUSIC

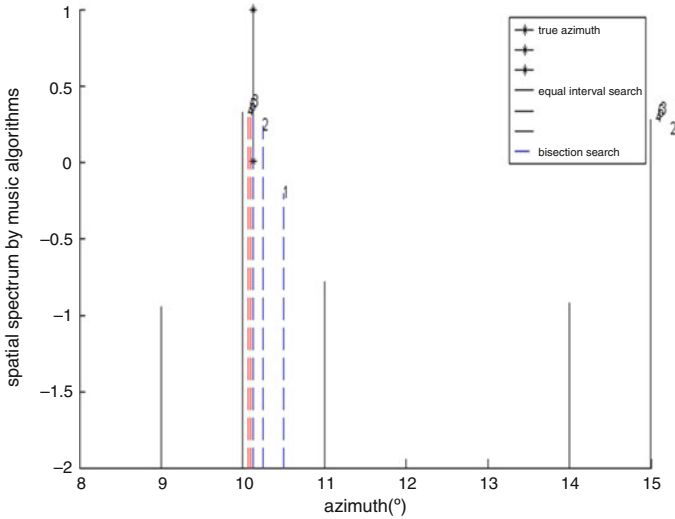


Fig. 9.2 The bisection search spatial spectrum peak detail diagram

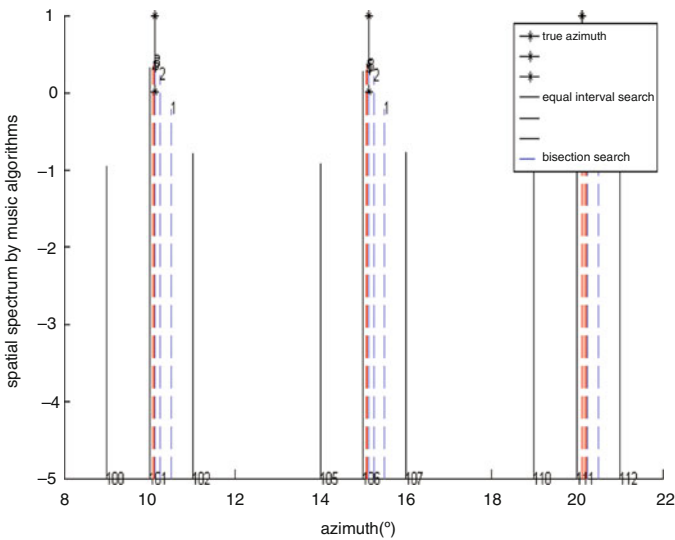


Fig. 9.3 The bisection search spatial spectrum peak diagram

performed repeatedly, we can get a very high estimation precision. Using the bisection method to calculate the five-point $|P(\theta)|$, approximation results are given by Fig. 9.2. From the figure above we can see that the search peak is quickly close to the true value with the search times increasing.

9.4.2 The Speed of the Search

The search speed of the bisection method is fast. This is because in each calculation, the peak point precision is increased by two times, and we perform the calculation p times; the precision is increased by 2^p times. Therefore, with the bisection method accomplished 10 times, precision can be increased by 1,024 times. The relationship between precision and times of search is shown in Fig. 9.4. Search peak error is decreased by two exponential times with the search times increasing.

9.4.3 Precision and Adaptability of the Search

In the bisection method, because of taking the midpoint constantly, the interval is constantly shrunk, and the interval midpoint gradually approaches the true peak. Therefore, the bisection method reflects the limit thinking of infinite approximation. In essence, the bisection method is a numerical algorithm of interval iterative. It can be infinitely close to the true peak; thus, the precision is very high.

The data model of this search algorithm is simple and general. There are not many assumptions, so the adaptability is strong.

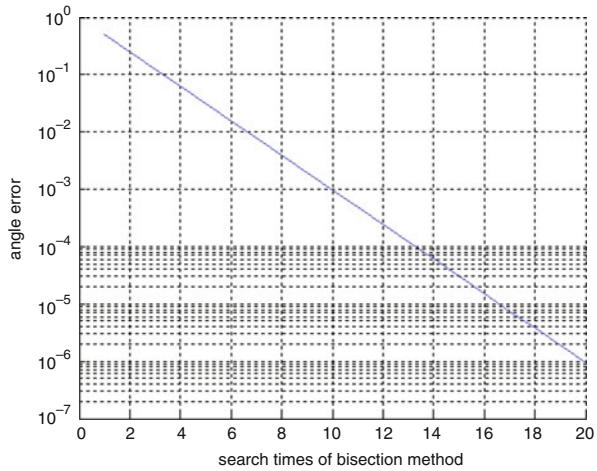


Fig. 9.4 The search speed of bisection method

Conclusion

In this paper, we introduced the bisection method which was used to search the spatial spectrum peak. The method had fast speed, high precision, and strong adaptability. We used the continuous bisection method to search finely and find out the real peak. From the diagram we can see that it can quickly and infinitely approach the true peak, and we analyzed the algorithm performance finally.

References

1. Schmidt R. Multiple emitter location and signal parameter estimations. *IEEE Trans Antennas Propagat.* 1986;34(3):276–80.
2. Guo QH, Liao GS. Fast MUSIC spectrum peak search via Metropolis-Hastings sampler. *J Electronics.* 2005;22(6):599–604. In Chinese.
3. Chen JF, Ma H. An accurate real-time algorithm for spectrum peaks search in 2D MUSIC. *ICMT.* IEEE, Hangzhou, China; 2011. p. 3385–8.
4. Hou YS, Jin Y, Zhang LJ. Low cost algorithm for azimuth-elevation joint estimation. *ICSP.* IEEE, Beijing, China; 2008. p. 92–5.
5. Ferréol A, Boyer E, Larzabal P. Low-cost algorithm for some bearing estimation methods in presence of separable nuisance parameters. *Electronics Lett.* 2004;40(15):966–7.

Chapter 10

A CRF-Based Method for DDoS Attack Detection

Yu Wang, Hong Jiang, Zonghai Liu, and Shiwen Chen

Abstract For the low accuracy of detection and high false-positive rate (FPR) problems in the traditional DDoS attack detection methods, the method based on conditional random fields (CRF) is introduced. The CRF-based model could make full use of the multi-feature fusion together, while it does not demand the characteristics that are independent strictly. The IP flow quintuple entropy conception is put forward as the detection multi-feature vector, which is named as the IPE including the quintuple entropy of the header part of the packets. Our experiments revealed that the multi-feature vector IPE runs well and the CRF-based model detecting method outperforms the other machine learning (ML) methods such as k-nearest neighbor (KNN), support vector machine (SVM), etc. The value of IPE leaps obviously when the DDoS attacks happened under the DARPA 2000 dataset. Simultaneously, the CRF-based method has a better detection performance (more than 90 %) and lower FPR (less than 3 %), as well as a strong ability of anti-background-noise and good robustness under TFN2K attacking dataset.

Keywords Conditional random fields • Distributed denial of service attacks detection • Machine learning • Quintuple entropy

10.1 Introduction

Network anomaly detection is an important part of network management. As DDoS attacks are a major threat to network security, the operation of the network has been impacted seriously [1]. The accuracy and real-time performance of DDoS attack detection are the focus in the research area of network anomaly detection.

The ML-based method is a rising and significant detection method because of the development of machine learning algorithms [2]. By building the normal profile and the attack profile with flow features, DDoS attack detection can be translated into binary classification. The existing research results include naïve Bayes

Y. Wang • H. Jiang (✉) • Z. Liu • S. Chen
National Digital Switching System Engineering and Technological R&D Center,
Zhengzhou 450002, China
e-mail: jh_1012@126.com

(NB) [3], decision tree (DT) [4], RBF network [5], support vector machine (SVM) [6], etc. The common characteristics of these approaches are based on the traffic burst, the dispersion of source IP address caused by the attacks, and the flow asymmetry and other attributes of a particular feature of the attack. However, the context of the traffic is ignored. Considering the specific feature, the universality of these detection approaches is insufficient. The accuracy and false alarm rate have yet to be improved.

This paper discusses a CRF-based method for the detection of DDoS attacks, which is based on CRF [7]. With the capability of combining multi-features and context of the traffic, the CRF-based detection method is introduced. Detecting under the method, the precision is high and adaptability is strong. The principles and steps of the method are introduced, and detection performance is analyzed.

10.2 CRF-Based Model

10.2.1 CRF and Linear Chain CRF

Suppose $P(Y|X)$ is the conditional probability distribution of the random variable Y under the random variable X . If Y could constitute $G = (V, E)$, which is an undirected graph represented by a Markov random field, it can be written as

$$P(Y_v|X, Y_w, w \neq v) = P(Y_v|X, Y_w, w \sim v) \quad (10.1)$$

For any node v holds, then it is called $P(Y|X)$ CRF, where $w \neq v$ means the nodes in the $G = (V, E)$, except v , and $w \sim v$ represents all the nodes, which are connected with the node v by edges. Corresponding to the nodes v and w , the random variables are Y_v and Y_w .

Suppose $X = (X_1, X_2, \dots, X_n)$ and $Y = (Y_1, Y_2, \dots, Y_n)$ are the linear chain sequences of random variables. And the conditional probability distribution, $P(Y|X)$, constitutes the CRF with the Markov property, and $P(Y|X)$ is called the linear chain CRF. That is,

$$P(Y_i|X, Y_1, \dots, Y_{i-1}, Y_{i+1}, \dots, Y_n) = P(Y_i|X, Y_{i-1}, Y_{i+1}) \quad (10.2)$$

10.2.2 Probability Calculation of the CRF Model

Suppose X is the observation sequence and Y is the symbol sequence. Based on the observation sequence, the conditional probability distribution of the symbol sequence, $P(Y|X)$, can be calculated [8]. By the recursive calculation of the forward-backward algorithm, the conditional probability distribution is solved:

$$P(Y_i = y_i | x) = \frac{\alpha_i^T(y_i | x) \beta_i(y_i | x)}{Z(x)} \quad (10.3)$$

$$P(Y_{i-1} = y_{i-1}, Y_i = y_i | x) = \frac{\alpha_{i-1}^T(y_{i-1} | x) M_i(y_{i-1}, y_i | x) \beta_i(y_i | x)}{Z(x)} \quad (10.4)$$

where the forward vector $\alpha_i(x)$ and the forward vector $\beta_i(x)$ are given by

$$\alpha_0(y | x) = \begin{cases} 1, & \text{if } y = \text{start} \\ 0, & \text{otherwise} \end{cases} \quad (10.5)$$

$$\alpha_i^T(x) = \alpha_{i-1}^T(x) M_i(x) \quad (10.6)$$

$$\beta_{n+1}(y_{n+1} | x) = \begin{cases} 1, & \text{if } y = \text{stop} \\ 0, & \text{otherwise} \end{cases} \quad (10.7)$$

$$\beta_i(x) = M_{i+1}(x) \beta_{i+1}(x) \quad (10.8)$$

10.2.3 The Prediction Algorithm

The prediction algorithm of the CRF-based model is as follows:

By giving $P(Y|X)$ and the observation sequence, X, y^* , the symbol sequence with the biggest conditional probability, is solved in the Viterbi algorithm, for tagging the observation sequence [8]. Thus, for the given feature vector $F(y, x)$, the weighted vector w , and the observation sequence, $x = (x_1, x_2, \dots, x_n)$, the goal of the model is to solve $y^* = (y_1^*, y_2^*, \dots, y_n^*)$, the optimal path [9].

10.3 DDoS Attack Detection

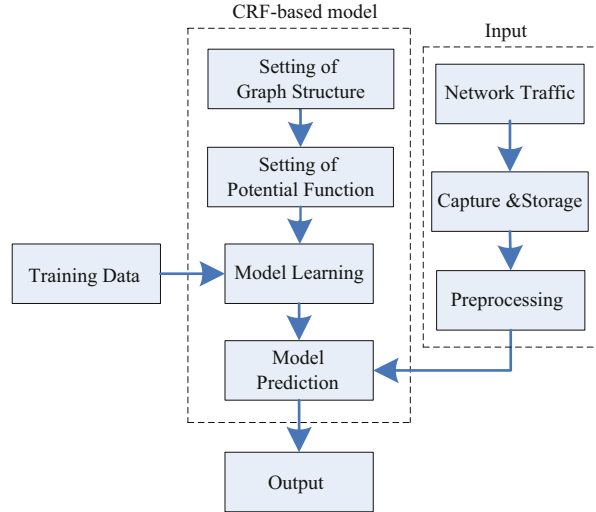
10.3.1 Feature Selection

The feature is closely related with the detection accuracy and computation complexity in the network intrusion detection [10]. And the entropy is a useful tool in the description of network anomaly detection [11–13]. In this paper, the quintuple IP packet entropy (IPE) is used for its advantages in reflecting the multidimensional features of DDoS, as the burst of abnormal traffic, concentration of the destination IP, and source IP.

10.3.2 CRF-Based Detection

The architecture of CRF-based detection is given in Fig. 10.1. And the training data is the DARPA 2000 dataset [14]. By capturing and storage, the network traffic is

Fig. 10.1 The CRF-based DDoS attack detection



taken as input after preprocessing. The preprocessing consists of packet information extraction (sampling the header part of the packets), segmentation in sliding windows with different time granularity of IPE calculation, and the calculation of IPE. After preprocessing, the data goes into the model prediction.

The CRF-based model operates as follows:

1. Setting of graph structure: Choose the undirected graph, G , as a first-order linear chain, with the first-order Markov property in the adjoining label.
2. Setting of graph structure: For a first-order linear chain undirected graph, $G = (V, E)$, the potential function $\psi_{Y_c}(y_c)$ includes the potential functions of the single nodes and the adjacent nodes.
3. Model learning: Use the L-BFGS algorithm [9] for converting parameter estimation to the optimization without constraints.
4. Model prediction: The CRF-based DDoS attack detection is effective for the given feature vector, the weighted vector, and the observation sequence, solving the optimal path, $y^* = (y_1^*, y_2^*, \dots, y_n^*)$. Finally, the output is the sequence with labels. And the output sequence with labels is the detection result of traffic.

10.4 Experimental Results and Analyses

Take LLDoS 2.0.2 inside the dataset of DARPA 2000 dataset [14] as the training dataset, Dataset 1. And Dataset 2 is the abnormal traffic of TFN2K [15], captured by WinDump [16]. Dataset 3 is the MAWI [17]. The evaluation measures are the precision, F -value, TPR, and FPR [18]. All the experiments as follows were

performed under a Windows XP platform with configurations Intel[®] i3-2120 processor, 3 GB RAM.

10.4.1 Validity of Feature Selection

The normalization IPE of Dataset 1 is shown in Fig. 10.1. The sampling interval is set as 1 s, and srcIP represents the normalization entropy of the source IP as well as the dstIP, srcPort, dstPort, and tranPort for the normalization entropy of the destination IP, source port, and destination port, respectively.

When the DDoS attacks happen (as shown in the red box), the IPE is jumping obviously, and IPE is the effective feature of DDoS attacks (Fig. 10.2).

10.4.2 Detection Performance

With Dataset 2, the detection capability of the different methods is depicted in Table 10.1. It is obvious that the CRF-based model has a better capability than the other machine learning methods. And the accuracy of the CRF-based model is higher than 90 %, and FPR is less than 3 %.

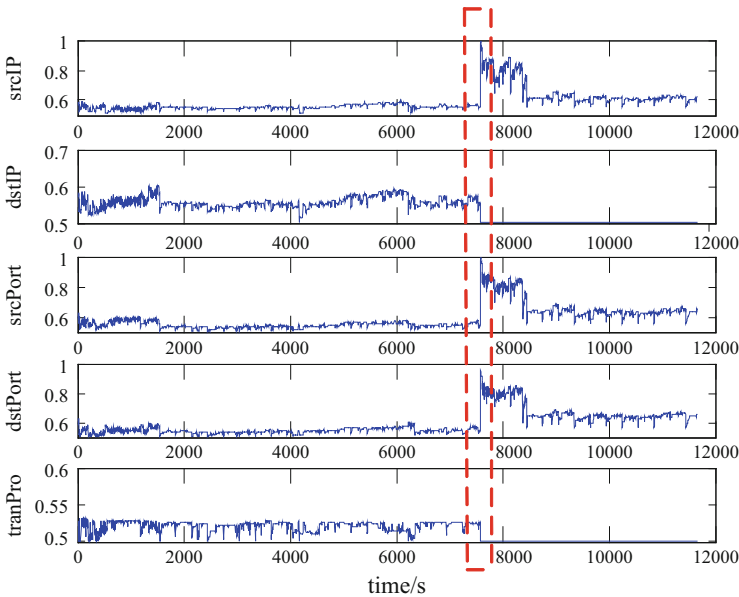
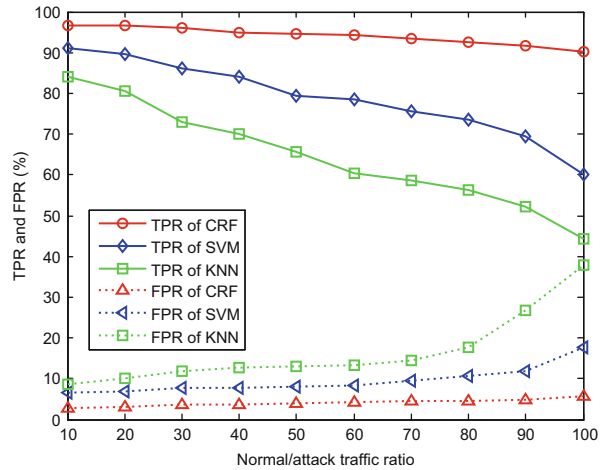


Fig. 10.2 The normalization IPE of LLDoS 2.0.2 inside dataset

Table 10.1 The detection results in the different methods

	Precision	TPR	F-Value	FPR
Naïve Bayes	80.35	85.54	82.86	24.13
KNN	86.60	89.25	87.90	19.81
C4.5 (decision trees)	78.50	82.15	80.28	27.35
SVM	88.32	91.07	89.67	7.26
CRF-based	91.20	92.53	91.86	1.53

Fig. 10.3 The robustness of CRF-based detection



10.4.3 Robustness

In Fig. 10.3, we consider the influence of background traffic. The attack traffic is made of Dataset 2 (TFN2K), and Dataset 3 is the background traffic in varying proportions, ranging from 10 to 100 % (the ratio between normal background traffic and attack traffic). As is shown in Fig. 10.3, the TPR and FPR of CRF-based model are slowly changing, thus, with a better adaptability of anti-background-noise.

Conclusion

In this paper, we introduced the CRF-based method for DDoS detection. Using the CRF-based model to find out the attacks, it has high precision, as well as strong adaptability. And we analyzed the performance. In our future research, we would focus on the improvement of the real-time detection of the CRF-based method and the actual deployment.

References

1. Hakem B, Geert D. Analyzing well-known countermeasures against distributed denial of service attacks. *Comput Commun.* 2012;35(11):1312–32.
2. Bhuyan MH, Kashyap HJ, Bhattacharyya DK, et al. Detecting distributed denial of service attacks: methods, tools and future directions. *Comput J.* 2014;57(4):537–56.
3. Benferhat S, Kenaza T, Mokhtari A. A Naive Bayes approach for detecting coordinated attacks. *IEEE COMPSAC*, Turku, Finland; 2008. p. 704–9.
4. Wu YC, Tseng HR, Yang W, Jan RH. DDoS detection and traceback with decision tree and grey relational analysis. MUE, Qingdao, China; 2009. p. 306–14.
5. Gavrillis D, Dermatas E. Real-time detection of distributed denial-of-service attacks using RBF networks and statistical features. *Computer Networks.* 2005;48(2):235–45.
6. Khan L, Awad M, Thuraisingham B. A new intrusion detection system using support vector machines and hierarchical clustering. *Int J VLDB.* 2007;16(4):507–21.
7. Lafferty JD, McCallum A, Pereira FCN. Conditional random fields: probabilistic models for segmenting and labeling sequence data. Williamstown: *ICML*; 2001. p. 282–9.
8. Li H. *Statistical learning methods*. Beijing, China: Tsinghua University Press; 2012. p. 191–210. In Chinese.
9. Liu DC, Nocedal J. On the limited memory BFGS method for large scale optimization. *Math Prog.* 1989;45(1–3):503–28.
10. Ganapathy S, Kulothungan K, Muthurajkumar S, et al. Intelligent feature selection and classification techniques for intrusion detection in networks: a survey. *EURASIP J Wirel Comm.* 2013;1:1–16.
11. Yu S, Zhou W, Doss R, et al. Traceback of DDoS attacks using entropy variations. *IEEE Trans Parallel Distrib Syst.* 2011;22(3):412–25.
12. Rahmani H, Sahli N, Kammoun F. Joint entropy analysis model for DDoS attack detection. *IAS'09*, Xi'an, China; 2009. p. 267–71.
13. Jeyanthi N, Iyengar NCSN. An entropy based approach to detect and distinguish DDoS attacks from flash crowds in VoIP networks. *Int J Netw Secur.* 2012;14(5):257–69.
14. MIT Lincoln Laboratory. DARPA 2000 intrusion detection scenario-specific data sets. <http://www.ll.mit.edu/mission/communications/ist/corpora/ideval/data/index.html>.
15. GOITWORLD. DDoS tools TFN2K usage. <http://www.goitworld.com/?s=TFN2K>.
16. CACE Technologies. WinDump. <http://www.winpcap.org/windump/>.
17. MAWI Working Group. Packet traces from WIDE backbone. <http://mawi.wide.ad.jp/mawi/>.
18. Bhuyan M, Bhattacharyya D, Kalita J. Network anomaly detection: methods, systems and tools. *IEEE Commun Survveys Tuts.* 2014;16(1):303–36.

Chapter 11

Advanced SOM Algorithm Based on Extension Distance and Its Application

Haitao Zhang, Binjun Wang, and Guangxuan Chen

Abstract In order to solve the low efficiency problem of traditional SOM, a novel model is proposed based on the self-organized map neural network by using the extension theory. A novel extension distance is introduced and aimed to calculate the similarity of data points from the class domain. A proposed extension distance with a distance parameter is used to make the procedure of clustering controlled. It is shown that the proposed advanced SOM based on extension distance has a faster learning speed when compared with SOM neural networks; moreover, the new model is proved to have higher accuracy and lower cost of memory. It is an improvement of the traditional SOM. The new model is testified in respect of its effectiveness and feasibility in experiment on two different datasets.

Keywords Extension theory • Extension distance • SOM • Distance parameter

11.1 Introduction

Kohonen's SOM network is usually used to map a higher dimension of input pattern to reduce the dimension and maintain the same structure of topology [1]. The traditional SOM has been widely used in the application of classification problems, but there are also some shortcomings, e.g., it is difficult to obtain an optimal value and easily falls into a local optimal value. It has a lower learning speed due to the pendulum effect in the convergence process. It is not suitable to process the data points with the interval values.

In practice, objects with interval value features are widely used in application classification [2]. As to objects with characteristics of interval values, it is difficult to process these problems directly by the current neural networks or other methods [3]. Thus, a novel modified SOM with similar topology is proposed to solve these problems as mentioned above; moreover, the advanced SOM could process

H. Zhang (✉) • B. Wang
People's Public Security University of China, 100038 Beijing, China
e-mail: okhaitao@126.com

G. Chen
Zhejiang Police College, 311100 Hangzhou, China

classification problems with interval value features and continue the input patterns following an unsupervised learning procedure. The advantage over the traditional SOM is that the proposed advanced SOM utilizes a novel extension distance (ED) based on the extension theory to do the measurement job of similarity among the data points; it gives shorter training time and a more satisfied accuracy in practice.

11.2 Extenics and Proposed Extension Distance

In extension, the matter-element M is represented as O , and the features of O are defined as P which has a responsive value of v . The description of M in extenics can be defined below:

$$M = (O, p, v) \tag{11.1}$$

wherein O, p, v are the three elements in the extenics set. In practice, there are many interval value problems to solve, e.g., the detailed value v belonging to an interval range and variation form of M can be defined below:

$$M = (O, p, v) = (O, p, \langle d, u \rangle) \tag{11.2}$$

wherein d and u are terminative bounds in a classical domain, respectively.

If $M = (O, P, V)$ is defined as an n -dimensional matter-element, a characteristic vector $P = [p_1, p_2, \dots, p_n]$, and a responsive value $V = [v_1, v_2, \dots, v_n]$, a multidimensional matter-element can be described below:

$$M = (O, P, V) = \begin{bmatrix} O, p_1, v_1 \\ p_2, v_2 \\ \dots, \dots \\ p_n, v_n \end{bmatrix} \tag{11.3}$$

wherein $M_i = (O, p_i, v_i)$. To calculate the degree of a point belonging to an element, a definition of extension distance is proposed to describe the degree of quality. The original extension distance represented by ρ is described below:

$$\rho(t, I_0) = \left| t - \frac{u + d}{2} \right| - \frac{u - d}{2} \tag{11.4}$$

To solve practical problems, a location function is founded to calculate the degree of relation between a point and two different intervals, e.g., $I_p = (d_p, u_p)$, $I_0 = (d_0, u_0)$, and the location function $D(t, I_0, I_p)$ can be defined below:

$$D(t, I_0, I_p) = \begin{cases} \rho(t, I_p) - \rho(t, I_0), & t \notin I_0 \\ -\frac{u_0 - d_0}{2}, & t \in I_0 \end{cases} \quad (11.5)$$

It is defined that $I_0 = (d_0, u_0)$ and $I_p = (d_p, u_p)$ are two intervals, and $I_p \supset I_0$ and the correlation function $K(t)$ can be described below:

$$K(t) = \frac{\rho(t, I_0)}{D(t, I_0, I_p)} \quad (11.6)$$

Formula (11.6) may indicate the degree of relation between a point t and intervals I_0, I_p ; the denominator can be obtained from formula (11.5) [4, 5].

In practice, the foundation of location function is very difficult, and we need not two but three or more different intervals to describe the degree of quality. Thus, a simplified formula of ED is proposed to process the problem of matter-element data tuples.

The new form of measurement method is varied based on the original ED which is represented by ρ . It is designed to describe different correlation degrees between the data point t and an interval $\langle d, u \rangle$; it can be seen that the different positions of t belonging to domains can produce variations of sensitivity. Based on the definition of ED, the membership degree between a data point t and a range can be calculated in the form of quantity. It is evidently different from other methods in the classification application. The novel extension distance (ED) formula is described as follows:

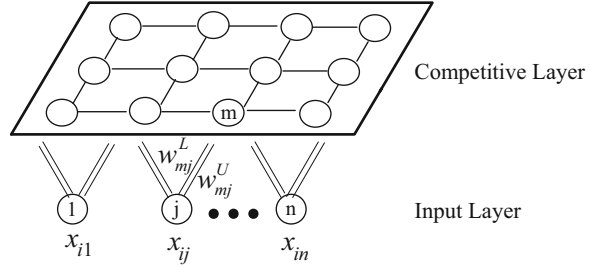
$$\text{ED} = \frac{|2t - (d + u)|}{u - d} \quad (11.7)$$

As described in the above formula, the ED among data point t with other interval $\langle d, u \rangle$ can be calculated. When a point lies in the interval, the distance is not considered as zero due to the different positions of the point in the interval and can be described with the distance value by the proposed extension distance [6].

11.3 Advanced SOM Algorithm

The proposed advanced SOM algorithm is a combination of the traditional SOM and extenics. An ED calculation method is proposed; like the typical SOM, the proposed model is also trained through an unsupervised procedure, and an activity function of neighbor range is used to limit the topological area in the input pattern [7–9]. As stated above in the introduction, the advanced SOM is to accomplish the matter-element datasets with simultaneous stability and high learning speed characteristics. The architecture of the proposed model is depicted in Fig. 11.1.

Fig. 11.1 Architecture of advanced SOM



The model contains two layers, and the nodes are arranged in a two-dimensional lattice. Each input pattern is compared to all nodes, and the closest nodes are then used as the basis to learn. An image is generated by an input pattern received in the input layer and a set of double weight parameters. Unlike the traditional SOM, in the new model, double weights are set with artificial values on each layer; the two weights represent the lower bound and the upper bound, respectively. For example, two weights between j th node and m th node are w_{mj}^l and w_{mj}^u , respectively. A mapping between input pattern and output pattern would be further enhanced in the characterized process. A classification of input pattern would be indicated by one active node in the output layer. The learning algorithm is described in the next section. An activity function of neighbor range is utilized to maintain the original structure relations of the input pattern in the advanced SOM. A distance parameter (DP) is adopted as the threshold value in the proposed method, and the novel ED function is designed and utilized in the procedure of clustering. The artificial parameter λ as a threshold value would be utilized to calculate ED between the cluster centers and responsive boundaries.

The detailed unsupervised learning algorithm is described as below:

- Step 1: initialization: choose the initial series of random weight values in pairs between two layers. Such as $\langle w_{kj}^l, w_{kj}^u \rangle$, the input feature n is set by the given input patterns. The number of output patterns m is determined by the designer. At last, the initial winning spatial domain $N_{j^*}(0)$ and the learning rate α should be built. λ is a measurement of space used as the threshold value. It should be determined as an engineering parameter from an engineering knowledge of practical systems. And $w_{kj}^l = x_{kj} - \lambda$, $w_{kj}^u = x_{kj} + \lambda$ wherein $j = 1, 2, \dots, n$.
- Step 2: the input pattern vectors are read from the training dataset, such as I^p ($p = 1, 2, \dots, n$).
- Step 3: competing phase: the triumph node through calculation of ED would be calculated by using Eq. (11.8). Z_{mj} means the center of the cluster m_j ; the node with the weight interval vector and minimal ED value is the triumph node. Where $m = 1, 2, \dots, k$.

$$ED = \sum_{j=1}^n \left[\frac{2|x_{ij} - Z_{mj}|}{w_{mj}^u - w_{mj}^l} \right], \quad Z_{mj} = \frac{w_{mj}^u + w_{mj}^l}{2} \quad (11.8)$$

Step 4: the winning neighborhood domain should be built. The training procedure should be made in iterations. In every iteration, a given parameter r affects nodes in the activity range.

Step 5: updating of weights. The weights of the triumph nodes with the neighborhood domain are defined to decrease with time τ .

$$\begin{cases} w_{mj}^l(\tau + 1) = w_{mj}^l(\tau) + \alpha(\tau)h_{mj}(\tau)[x_{ij} - Z_{mj}(\tau)] \\ w_{mj}^u(\tau + 1) = w_{mj}^u(\tau) + \alpha(\tau)h_{mj}(\tau)[x_{ij} - Z_{mj}(\tau)] \\ Z_{mj}(\tau + 1) = w_{mj}^u(\tau + 1)/2 + w_{mj}^l(\tau + 1)/2 \end{cases} \quad (11.9)$$

wherein $\alpha(\tau)$ is the learning rate and $h_{mj}(\tau)$ is called the neighborhood function, as a bell curve kernel function. Since the SOM only updates neurons near the winner, the function $h_{mj}(\tau)$ depends on the dimensionality of the neuron lattice. ED_{mj} denotes the extension distance between the coordinates of the triumph nodes m and nodes to be updated.

Step 6: if the learning rate $\alpha(\tau) \leq \alpha_{\min}$, it indicates that the clustering process has been converged; otherwise, return to Step 2.

Obviously, the learning process becomes easy because it only needs to adjust the weights of different clusters. Thus, the proposed method has a faster speed of clustering than other unsupervised learning approaches.

11.4 Experiment Studying

11.4.1 Iris on Experiment

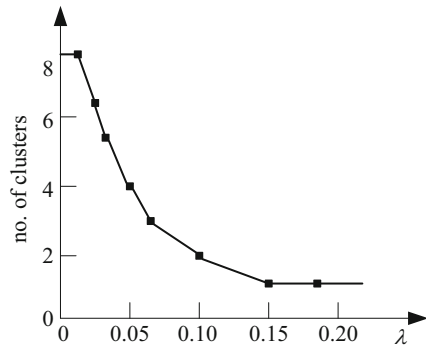
As a benchmark dataset, Iris contains 150 instances, and it can be divided into three classes of 50 instances each with evidently different variables, e.g., length and width of sepal and petal [10]. The structure of the new model based on previous experience contains three and four nodes in input and output layers, respectively. In this case, a half of total instances would be randomly chosen as the training dataset with the remaining used as the testing dataset. The comparison result is shown in Table 11.1. Obviously, the new SOM has a rather simpler structure with 7 nodes and 24 double weights. It is noted that our new model is faster than other models in the clustering process because of the simple adjustment of double weights of the excited connections in the learning of advanced SOM. It shows our model takes shorter time in the learning phase than other models in Table 11.1. Figure 11.2 shows different clustering granularities with different λ . The minimum number of produced clusters is one when the distance parameter λ is the largest. The maximum number of produced

Table 11.1 Classification performance of different neural networks

Model	Structure	Connection number	Learning times	Training error	Testing error
MLP	4-5-4-3	52	45	0.027	0.040
PNN	4-45-3	315	10	0.0	0.054
LVQ	4-10-3	70	30	0.65	0.062
CPN	4-25-3	175	50	0.18	0.172
Proposed	4-3	24	4	0.0	0.030

MLP multilayer perceptron, *PNN* probabilistic neural network, *LVQ* learning vector quantization, *CPN* counter propagation network, *Proposed* advanced SOM

Fig. 11.2 Number of clusters with different distance parameter λ



clusters is eight when the distance parameter λ is the smallest; moreover, the training error rate and the testing error rate of clustering using the new method are low with 0 and 3 %, respectively, in this experiment. The proposed method utilizes the expert’s experience before learning and makes output at a fast speed because the optimal feature boundary has been determined. There are 75 data points contained in the training set with the remaining dataset subject to the testing set.

11.4.2 Zoo Dataset on Experiment

A simple database containing 18 Boolean-valued attributes includes 7 classes of 101 animals. The performances of several clustering methods are listed in Table 11.2 as below. K-means shows almost perfect performance in the clustering of the classes of birds, amphibian, and fish, while K-means partitions the class of mammals into three clusters by mistake. The insect and miscellaneous are not partitioned correctly. Thus we may conclude that K-means is not fit to classes with inequality of size. The hierarchical clustering method shows a good performance in the clustering of classes of mammals, birds, amphibian, and fish. But the insect and miscellaneous are merged into one cluster at the same time, while the reptile is partitioned into three clusters by mistake. The experiment shows that

Table 11.2 Comparison of different methods

Method	Average learning epochs	Average classification accuracy rate (%)
ART	13.9	67
K-means	15.7	69
Fuzzy-C-means	12.7	70
Hierarchical clustering	15.2	84
SOM	11.5	92
Proposed method	3.6	98

hierarchical cluster and Fuzzy-C methods are not good at partitioning overlapping classes. It is shown that our model is fast with less resource than other methods listed in Table 11.2 above. Moreover, the accuracy rate of the new model is quite high, about 98 % in the clustering process.

Conclusion

A novel advanced SOM model is presented based on the extension theory. It shows significant speed advantage over other neural networks and adaptation ability for new dataset, as well as a shorter learning time in terms of the classification application. The proposed method is founded to solve special classification problems with features defined in a range. A matter-element model of the clustering problem can be easily built based on the extension theory; besides, it could obtain different membership degrees in a range of characteristic domain by using a novel ED function. In conclusion, the proposed model has been proved to have a shorter learning time, less computation cost, and higher accuracy. Future studies can be continued to develop the algorithm of the proposed advanced SOM so as to improve the classification performance and adaptation to a new discrete dataset.

References

1. Kiang MY. Extending the Kohonen self-organizing map networks for clustering analysis. *Comput Stat Data Anal.* 2001;38(2):161–79.
2. Cai W. The extension set and incompatibility problem. *J Sci Explor.* 1983;3(1):81–93.
3. Li QX, Liu SF. The method to construct interval elementary dependent function based on the interval distance and side-distance. *J Harbin Inst Tech.* 2006;38(7):1097–100.
4. Wang MH. Extension neural network-type2 and its applications. *IEEE Trans Neural Netw.* 2005;16(6):1352–60.
5. Raghu TS, Kannan PK, Rao HR, Whinston AB. Dynamic profiling of consumers for customized offerings over the Internet: a model and analysis. *Decis Support Syst.* 2001;32(2):117–34.
6. Liu CH. Extending extension theory for classifying data with numerical values. *Neural Comput Appl.* 2013;23:161–7.

7. Lai YH, Che HC. Integrated evaluator extracted from infringement lawsuits using extension neural network accommodated to patent assessment. *Int J Comput Appl Tech.* 2009;35(2):84–95.
8. Wang MH, Chao KH, Sung WT. Using ENN-1 for fault recognition of automotive engine. *Exp Syst Appl.* 2010;37(4):2943–7.
9. Cai W, Shi Y. Extenics: its significance in science and prospects in application. *J Harbin Inst Tech.* 2006;38(7):1079–86.
10. Machine Learning Repository, Center for Machine Learning and Intelligent System. 1993. <http://archive.ics.uci.edu/ml/machine-learning-databases/iris>

Chapter 12

A Trilateral Centroid Localization and Modification Algorithm for Wireless Sensor Network

Yujun Liu and Meng Cai

Abstract A localization and modification algorithm based on received signal strength indicator was studied to solve the key problem of sensor localization. To reduce the error due to the signal attenuation in complex electromagnetic environments, we come up with a trilateral centroid localization and modification algorithm for a wireless sensor network. The algorithm is based on the fact that an unknown sensor node's initial location can be determined with a weighted centroid algorithm for a triangle. The final location information was modified by the modification algorithm.

Keywords Received signal strength indicator • Localization • Weighted centroid • Modification

12.1 Introduction

A wireless sensor network consists of microsensor nodes that are deployed in the monitoring area and possess functions like physical signal acquisition, computing, and wireless communication capabilities [1]. There is a broad space in military applications of wireless sensor networks that support data collection, transmission, and analysis. Sensor network node localization is the first task in the application process [2, 3]. Sensor node positioning technology is a significant area of research [4].

Localization algorithms for wireless sensor networks are generally divided into distance-based location algorithms and localization algorithms unrelated to distance. This research is based on distance. In distance-based positioning algorithms, there are some useful parameters for measuring the distance or orientation between nodes, such as, for example, time of arrival (TOA), time difference of arrival (TDOA), angle of arrival (AOA), and received signal strength indicator (RSSI)

Y. Liu • M. Cai (✉)

Department of Information Engineering, Academy of Engineering Armored Forces,
Beijing 100072, China
e-mail: cm86129192@126.com

[5–7]. RSSI technology is mainly based on RF signal strength, which can use the signals of the sensor nodes themselves without any additional hardware.

However, the attenuation of signals caused by obstacles during transmission will lead to large errors in observed RSSI values. The main RSSI localization algorithm research contents are as follows: designing more suitable transmission models in line with the actual environmental and researching new localization algorithms to improve the positioning accuracy. To obtain a more accurate localization, the paper proposes a trilateral centroid localization and modification algorithm for wireless sensor networks on the basis of a RSSI-based trilateral localization algorithm. The notion of weighting is used to revise the initial positioning result.

12.2 RSSI-Based Trilateral Centroid Localization and Modification Algorithm for Wireless Sensor Network

The positioning process can be divided into three stages: (1) distance measurement: obtaining the distance between the unknown node and neighboring beacon nodes by measuring the RSSI value; (2) calculations: obtaining the locations of unknown nodes in the use of the weighted triangle centroid algorithm on the basis of the calculation of the distances the unknown node and three or more beacon nodes; (3) correction: recalculation of the coordinates, taking the advantage of weighted triangle centroid algorithm, to obtain a more precise result.

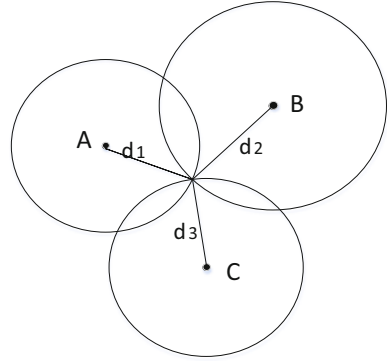
12.2.1 Ranging Based on RSSI Value

Since the radio propagation process has varying degrees of wear and tear, the following approximate loss models are used: a free-space propagation model, a logarithmic-normal distribution model, a logarithmic-distance path loss model, and HATA models [8, 9]. For an open outdoor environment, we chose the logarithmic-normal distribution model to obtain a range of RSSI values. The signal propagation attenuation model [10, 11] is as follows:

$$\text{RSSI}(d) = \text{RSSI}_0 - 10a \cdot \lg(d) + \delta \quad (12.1)$$

in which $\text{RSSI}(d)$ is the RSSI value received at a distance d from the unknown node, RSSI_0 is the value obtained at a distance of 1 m from the unknown node, a is an attenuation factor closely associated with the environment and surrounding barrier and a value of between 2 and 5, δ is randomly distributed Gaussian noise with zero mean and standard deviation of 4–10.

Fig. 12.1 Ideal distance model of RSSI location



According to Eq. (12.1), we can obtain the unknown d -distance between the two nodes, which can be regarded as the distance between the beacon node and the unknown node. We should obtain at least three distances for three beacon nodes, such as d_1 , d_2 , and d_3 (Fig. 12.1).

In an ideal wireless sensor network, we can calculate the coordinates of the unknown node's position information by trilateration according to the model of the distance between the beacons and the unknown node, shown in Fig. 12.1. However, environmental interference and random attenuation of the electromagnetic signal cause the distance that we obtain from the RSSI value to be greater than the actual distance. We construct a new improved distance model like that in Fig. 12.2. The unknown node is located at the area of intersection of the three circles with radii of d_1 , d_2 , and d_3 .

12.2.2 Trilateral Localization Algorithm

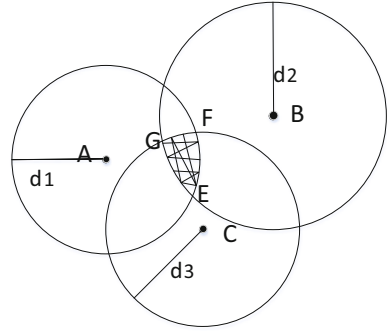
First, we choose a suitable origin of coordinates and build the reference frame. We indicate the beacons' coordinates as $A(x_1, y_1)$, $B(x_2, y_2)$, and $C(x_3, y_3)$ and the unknown node's coordinate as $M(x, y)$.

$$\begin{cases} \text{Circle_A} & (x - x_1)^2 + (y - y_1)^2 = d_1^2 \\ \text{Circle_B} & (x - x_2)^2 + (y - y_2)^2 = d_2^2 \\ \text{Circle_C} & (x - x_3)^2 + (y - y_3)^2 = d_3^2 \end{cases} \quad (12.2)$$

Equation (12.2) is composed of nonlinear equations of the unknown node's coordinate $M(x, y)$ based on the two-dimensional spatial distance calculation formula. However, as shown in Fig. 12.2, Circles A, B, and C intersect with each other. The equals sign = in Eq. (12.2) should be revised as the less than or equal to sign: \leq .

We obtain the crossover point coordinates, which are respectively expressed as $\left\{ \begin{matrix} (a_1, b_1) \\ (a_2, b_2) \end{matrix} \right\}$, $\left\{ \begin{matrix} (a_3, b_3) \\ (a_4, b_4) \end{matrix} \right\}$, $\left\{ \begin{matrix} (a_5, b_5) \\ (a_6, b_6) \end{matrix} \right\}$. Based on the axiom that the distance between any

Fig. 12.2 Actual distance model between beacons and unknown node



point in the three circles' intersecting region and the center of a circle is less than that circle's radius, we can obtain the vertex of the triangle region, where the unknown node is located. We supposed that the three vertices' coordinates are $E(a_1, b_1)$, $F(a_3, b_3)$, $G(a_5, b_5)$, as shown in Fig. 12.2.

12.2.3 RSSI-Based Trilateral Localization Algorithm

The original weighted triangle centroid algorithm calculates the centroid coordinates of $\triangle EFG$ as $(\frac{a_1+a_3+a_5}{3}, \frac{b_1+b_3+b_5}{3})$ based on geometric principles [12]. On the basis of the original triangle centroid localization algorithm, this paper introduces a weighting idea and a iterative amended triangle weighted centroid localization algorithm. In the weighted positioning algorithm, selecting suitable weights is key to improving the positioning accuracy. The values of RSSI measured by the unknown node have a significant effect on the positioning accuracy. The higher the value of RSSI, the greater its effect. The smaller the distance between the beacon and the unknown node is, the higher the RSSI value is. Thus, we take the reciprocal of the distances between the beacons and the unknown node as the weighted value. We use a weighting factor to express the beacons' effect on the target location. Because point E is the crossover point of circles B and C, whose radii are d_2 and d_3 , we use $\frac{1}{d_2} + \frac{1}{d_3}$ to express the factor of a_1 and b_1 . The unknown node's coordinates $M(x, y)$ can be expressed as

$$\begin{cases} x = \frac{a_1 \cdot \left(\frac{1}{d_2} + \frac{1}{d_3}\right) + a_3 \cdot \left(\frac{1}{d_3} + \frac{1}{d_1}\right) + a_5 \cdot \left(\frac{1}{d_1} + \frac{1}{d_2}\right)}{2 \cdot \left(\frac{1}{d_1} + \frac{1}{d_2} + \frac{1}{d_3}\right)} \\ y = \frac{b_1 \cdot \left(\frac{1}{d_2} + \frac{1}{d_3}\right) + b_3 \cdot \left(\frac{1}{d_3} + \frac{1}{d_1}\right) + b_5 \cdot \left(\frac{1}{d_1} + \frac{1}{d_2}\right)}{2 \cdot \left(\frac{1}{d_1} + \frac{1}{d_2} + \frac{1}{d_3}\right)} \end{cases} \quad (12.3)$$

12.2.4 Modification Algorithm

To accurately position, a double localization algorithm is proposed. We added several beacons in combination with a primary beacon group. Thus, the unknown node obtains four groups of RSSI values and then obtains d_1, d_2, d_3, d_4 , the distances between the four beacons and the unknown node. We divide the four parameters into four random combinations, and each combination will be substituted into Eq. (12.3) to obtain one center-of-mass coordinate. We obtain the four coordinate parameters as $M_1(X_1, Y_1), M_2(X_2, Y_2), M_3(X_3, Y_3), M_4(X_4, Y_4)$ from the four random combinations. The final coordinate $P(X, Y)$ can be expressed as follows:

$$\begin{cases} X = \frac{X_1 + X_2 + X_3 + X_4}{4} \\ Y = \frac{Y_1 + Y_2 + Y_3 + Y_4}{4} \end{cases} \quad (12.4)$$

When the number of beacons increases to n , we obtain C_n^3 four coordinate parameters. The final coordinate will change to Eq. (12.5) and be more accurate than before:

$$\begin{cases} X = \frac{X_1 + X_2 + X_3 + L + X_{C_n^3}}{C_n^3} \\ Y = \frac{Y_1 + Y_2 + Y_3 + L + Y_{C_n^3}}{C_n^3} \end{cases} \quad (12.5)$$

However, the complexity and instantaneity of the algorithms must be taken into consideration. Thus, we take the value of n as 4.

12.3 Simulation Verification

The location algorithm was simulated and verified by MATLAB simulation software to verify the modified localization algorithm's advantages. First, we assumed that all nodes in the simulation conditions in the region were able to normally communicate with each other and were in a stationary state. Second, the simulation parameter was set as follows: (1) the wireless sensor network was distributed in a 50×50 m area, and the communication radius of the WSN node was 50 m; (2) signal transmission attenuation factor was 3.3; (3) the entire simulation environment took into consideration Gaussian random noise whose mean was zero and standard deviation was 5; (4) We did 500 Monte Carlo Simulations and took the average of the 500 simulation results as the final position.

The error analysis is as follows:

$$\text{error} = \sqrt{(x - x')^2 + (y - y')^2} \quad (12.6)$$

In Eq. (12.6), x and y are the actual coordinates of the unknown nodes, and x' and y' are the estimated coordinates of the unknown nodes.

In this paper, the trilateral centroid localization and modification algorithm is highly affected by the density of the beacon node, so the simulation mainly targets the efficiency of the modified localization algorithm and the extent to which the number of beacon nodes affects the positioning precision.

Figure 12.3 shows that the error of a ordinary RSSI-based triangle centroid localization algorithm's simulation is 8.83 m, while it is 2.98 m in a RSSI-based weighted iterative modification algorithm, ignoring the beacons' distribution. The two simulation results give us a first thought that the distances measured from RSSI are affected largely by the process of transmission (Fig. 12.4). To prove the modification algorithm's effectiveness, we designed the simulation as earlier in order to prove the algorithm's efficiency for greater numbers of beacon nodes.

Figure 12.5 shows that since the weighted iterative modification algorithm was introduced in the original triangle centroid localization algorithm, the positional accuracy has increased 13.8 % more than the ordinary RSSI-based triangle centroid localization algorithm and 4.3 % more than the weighted centroid localization algorithm under the same simulation conditions. This shows the important role played by weighted iterative modification in the location algorithm. In addition, when the number of beacon nodes increases, the location error of all three of these location algorithms decreases, which indicates that the number of beacon nodes does have an important effect on positional accuracy, proving the iterative location algorithm's accuracy.

Fig. 12.3 RSSI-based trilateral localization algorithm

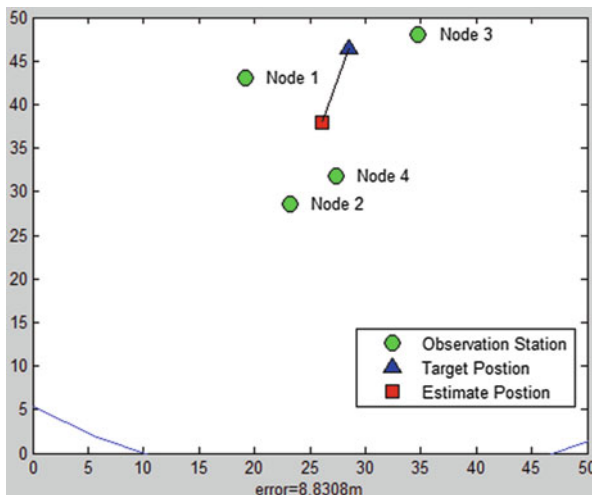
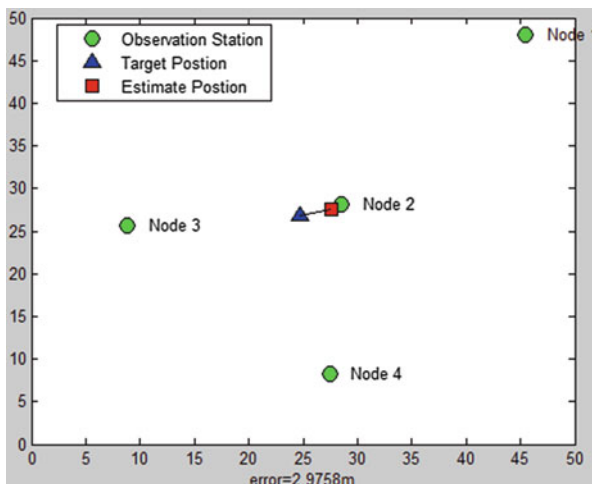


Fig. 12.4 RSSI-based multibeacon weighted centroid localization and modification algorithm

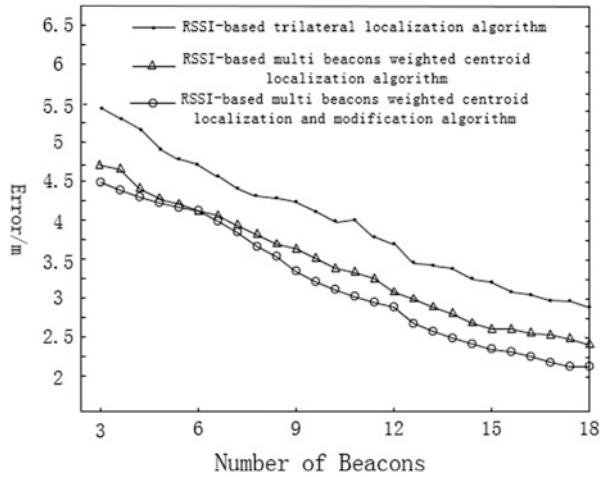


Conclusion

This paper proposed a trilateral centroid localization and modification algorithm based on RSSI for wireless sensor networks and introduced a weighting idea and iterative computation idea. Because measured distances between beacons and unknown nodes are not exact, circles centered on the beacons of radius d will cross, forming a triangle. The unknown node's position coordinates can be determined using the weighted triangle centroid localization algorithm and recalculated based on the notion of iterative modification.

(continued)

Fig. 12.5 Efficacy comparison of centroid localization algorithm modification



(continued)

Based on simulations, the multibeacon weighted triangle centroid iterative localization modification algorithm was clearly proved to be efficient in improving localization accuracy. However, this modified algorithm has increased computing complexity, which could be a topic for future research.

References

1. Fei H, Gao X. *Wireless sensor networks: principles and practice*. Boston: Auerbach Publications; 2010. p. 8–13 (in Chinese).
2. Saute M. *From GSM to LTE: an introduction to mobile networks and mobile broadband*. New York: Wiley; 2011. p. 160–6.
3. Patil MM, Shaha U, Desai UB, Merchant SN. Localization in wireless sensor network using three masters. In: *Personal Wireless Communications, ICPWC 2005*. New Delhi: IEEE; 2005. p. 384–8.
4. Cui X. The origin of WSN as well as it's research and development abroad. *Radio Freq Identif Technol Appl*. 2009;5:45–8.
5. Zhan H. Study on node localization algorithm based on mobile beacon in wireless sensor network. *Guangzhou South China Technol Univ*. 2012:9–11. (in Chinese).
6. Karthick N, Prashanth K, Venkatraman K, et al. Location estimation using RSSI and application of extended Kalman filter in wireless sensor networks. In: *Proceedings of the International Conference on Advanced Computer Control*; 2009, p. 337–41.
7. Peng Y, Dan W. A review: wireless sensor networks localization. *J Electron Meas Instrum*. 2011;25(5):389–99 (in Chinese).
8. Liu Y, Jin M, Cui C. Modified weighted centroid localization algorithm based on RSSI for WSN. *Chin J Sens Actuators*. 2010;23(5):717–21 (in Chinese).
9. Oka A, Lampe L. Distributed target tracking using signal strength measurements by a wireless sensor network. *IEEE J Sel Areas Commun*. 2010;28(7):1006–15.

10. Chen W, Li W, Shou H. Weighted centroid localization algorithm based on RSSI for wireless sensor networks. *J Wuhan Univ Technol.* 2006;30(2):255–68 (in Chinese).
11. Blumenthal J, Grossmann R, Golatowski F, et al. Weighted centroid localization in Zigbee-based sensor networks. *IEEE Int Symp Intell Signal Process.* 2007;10:1–6.
12. Lin W, Chen C. RSSI based triangle and centroid location in wireless network. *Mod Electron Tech.* 2009;2:180–2 (in Chinese).

Chapter 13

Simulation Study on Trajectory Tracking in Manipulator Based on the Iterative Learning Control Algorithm

Yanfen Luo

Abstract There is a kind of problem about trajectory tracking in the actual control; its main task is to find the control law $u(t)$, by which the output $y(t)$ of the controlled plant can track the desired trajectory during the limited time interval $[0, T]$ with zero error. Aiming at this kind of problem, the iterative learning control algorithm is proposed. In this algorithm, the control law $u(t)$ is amended by the previous error information so that the repeated task can be done better in the next operation. Through this interaction, the output in the whole time interval can track the desired trajectory. In this paper, the iterative learning control algorithm is applied in the trajectory tracking system of manipulator, and the tracking results are simulated.

Keywords Iterative learning control • Trajectory track • Convergence

13.1 Introduction

The iterative learning control (ILC) algorithm is fit for the plants whose movements are repeated and the control objective can be better met by iterative amending [1]. This control algorithm is not dependent on the precise arithmetic model of the system. It can control those nonlinear tight coupling dynamic systems with very simple algorithm; although the uncertainty of those systems is high, the desired trajectory is met with high-precision; in this sense, the iterative learning control algorithm is applied widely in movement control areas [2].

Y. Luo (✉)

College of information engineering Nanchang Hangkong University,
330063 Nanchang, China
e-mail: lyf_810318@163.com

13.1.1 Algorithm Principle

Suppose the dynamic equation of the plant is:

$$\dot{x}(t) = f(x(t), u(t), t), y(t) = g(x(t), u(t), t) \quad (13.1)$$

In Eq. (13.1): $x \in R^n$, $y \in R^m$, $u \in R^r$

which, respectively, refer to the state, the output, and the input of the system. $f(\bullet)$ and $g(\bullet)$ are vector functions with proper dimensions, whose structures and parameters are unknown. If the desired control signal $u_d(t)$ exists and the desired output is $y_d(t)$, then the goal of the iterative learning control is to make the control input $u_k(t) \rightarrow u_d(t)$ and make the output of the system $y_k(t) \rightarrow y_d(t)$ in the given time $t \in [0, T]$ through the multiple rerunning of the learning control algorithm. After the k th rerunning, Eq. (13.1) can be expressed in the following form:

$$\dot{x}_k(t) = f(x_k(t), u_k(t), t), y_k(t) = g(x_k(t), u_k(t), t) \quad (13.2)$$

The tracking error is

$$e_k(t) = y_d(t) - y_k(t) \quad (13.3)$$

The iterative learning control can be classified in open-loop learning and closed-loop learning [3]. In the open-loop learning algorithm, the $(k+1)$ th control equals to the correction term of the k th control and the k th output error.

$$u_{k+1}(t) = L(u_k(t), e_k(t)) \quad (13.4)$$

In the closed-loop learning algorithm, the $(k+1)$ th output error is adopted in the correction term.

$$u_{k+1}(t) = L(u_k(t), e_{k+1}(t)) \quad (13.5)$$

In Eqs. (13.4) and (13.5), L is a linear or nonlinear operator [4].

13.1.2 Basic Iterative Learning Control Algorithm

The D law of the iterative learning control algorithm is expressed in the following form [5]:

$$u_{k+1}(t) = u_k(t) + \Gamma e_k^*(t) \quad (13.6)$$

In this equation, Γ is the matrix of the constant gain. Based on the D law algorithm, P law, PI law, and PD law iterative learning algorithms are designed in succession; the special form of PID law iterative learning algorithm as expressed is below:

$$u_{k+1}(t) = u_k(t) + \Gamma e_k^*(t) + \Phi e_k(t) + \Psi \int_0^t e_k(\tau) d\tau \quad (13.7)$$

In this equation, Γ , Φ , Ψ are the matrices of the learning gains. In the open-loop iterative learning algorithm, the error formations $e_k(t)$ and $e_{k+1}(t)$ are adopted in the closed-loop iterative learning algorithm. Both $e_k(t)$ and $e_{k+1}(t)$ are used at the same time in the open-plus-closed-loop iterative learning control algorithm.

The D law algorithm is proposed firstly in which the derivative of the errors is adopted as a correction term. In P law, $\Gamma = 0$, $\Psi = 0$, it can be realized easily. The PD law is the combination of P law and D law. In D law, the gain is adjustable so that the tracking performance and the convergence of the algorithm can be improved, as mentioned in the exponential gain D law iterative learning.

13.2 Key Technology in ILC

1. Stability and convergence

The problem of stability and convergence is to discuss the conditions of learning law and the plant when the ILC is stable and convergent. The stability of the algorithm guarantees the system not to be diverging when the learning times are more. But the stability is meaningless to the learning control system without convergence. The object of optimal control is to make the learning process be convergent to the real value.

2. Initial value

In the course of designing the iterative learning controller, it is necessary to get the plant errors or derivatives of plant errors through the repetitive operation. In this control technology, the iterative learning needs to start from an initial value, such as the initial state or the initial output. In the present iterative learning control algorithm, the initial state of the plant is required to start at the initial state of the expected trajectory with the initial condition shown as: $x_k(0) = x_d(0)$, $k = 0, 1, 2, \dots$

3. Learning rate

In the research of iterative learning algorithm, the condition of convergence is proposed when the times of learning $k \rightarrow \infty$; but as a matter of fact, it is meaningless when $k \rightarrow \infty$. As a result, it is an important problem to make the learning process convergent to the expected value in a shorter time.

The iterative learning control is a feed-forward control technology in essence. The convergence speeds of most learning laws are very slow, and the learning speed can be improved by the knowledge from multiple learning processes.

4. Robustness

As the iterative learning control theory is proposed in the engineering backgrounds, the problem of convergence must be discussed under all kinds of

disturbances. The system of ILC needs to be robust when disturbances exist so that the iterative track can be convergent to the neighborhood of the expected trajectory. When the disturbances disappear, the iterative trajectory can be convergent to the expected trajectory.

13.3 Simulation of the Trajectory Tracking in Manipulator Based on ILC

13.3.1 Design of the Controller

Suppose the dynamic equation of a robot with N joints can be expressed as below:

$$D(q)\ddot{q} + C(q, \dot{q})\dot{q} + G(q) = \tau - \tau_d \quad (13.8)$$

In this equation, $q \in R^n$ is the angular rotation of the N joints, $D(q) \in R^{m \times n}$ is the inertial matrix of the robot, $C(q, \dot{q}) \in R^n$ is the centrifugal force, $G(q) \in R^n$ is the gravity, $\tau \in R^n$ is the control moment, and $\tau_d \in R^n$ is all kinds of errors and disturbances. Suppose that the expected trajectory of the system is $y_d(t)$, $t \in [0, T]$, the k th real output of the system is $y_k(t)$, $e_k(t) = y_d(t) - y_k(t)$. The initial state of learning is $x_0(0)$; the control object is to design $u_{k+1}(t)$ to make the error $e_{k+1}(t)$ decrease.

Three kinds of learning laws are adopted:

1. Closed-loop D law
2. Closed-loop PD law
3. Closed-loop D law with gain scheduling

$$u_{k+1}(t) = u_k(t) + K_d(\dot{q}_d(t) - \dot{q}_{k+1}(t)) \quad (13.9)$$

$$u_{k+1}(t) = u_k(t) + K_p(q_d(t) - q_{k+1}(t)) + K_d(\dot{q}_d(t) - \dot{q}_{k+1}(t)) \quad (13.10)$$

$$u_{k+1}(t) = u_k(t) + K_d(\dot{q}_d(t) - \dot{q}_{k+1}(t)) \quad (13.11)$$

in which K_d is changing in exponential form.

13.3.2 Simulation Example

The PD law iterative learning control algorithm is simulated in the joint manipulator of a robot with the parameters in Eq. (13.8) set as below [6]:

$$D = [d_{ij}]_{2 \times 2} \quad (13.12)$$

$$d_{11} = d_1 l_{c1}^2 + d_2 (l_1^2 + l_{c2}^2 + 2l_1 l_{c2} \cos q_2) + I_1 + I_2 \quad (13.13)$$

$$d_{12} = d_{21} = d_2 (l_{c2}^2 + l_1 l_{c2} \cos q_2) + I_2 \quad (13.14)$$

$$d_{22} = d_2 l_{c2}^2 + I_2 \quad (13.15)$$

$$C = [c_{ij}]_{2 \times 2} \quad (13.16)$$

$$c_{11} = h\dot{q}_2, c_{12} = h\dot{q}_1 + h\dot{q}_2, c_{21} = -h\dot{q}_1 c_{22} = 0, h = m_2 l_1 l_{c2} \sin q_2 \quad (13.17)$$

$$G = [G_1 \quad G_2]^T \quad (13.18)$$

$$\begin{aligned} G_1 &= (d_1 l_{c1} + d_2 l_1) g \cos q_1 + d_2 l_{c2} + g \cos (q_1 + q_2), G_2 \\ &= d_2 l_{c2} + g \cos (q_1 + q_2) \end{aligned} \quad (13.19)$$

$$\tau_d = [0.3 \sin t \quad 0.1(1 - e^{-t})]^T \quad (13.20)$$

$$d_1 = d_2 = 1 \text{ kg} \quad (13.21)$$

$$l_1 = l_2 = 0.5 \text{ m} \quad (13.22)$$

$$l_{c1} = l_{c2} = 0.25 \text{ m} \quad (13.23)$$

$$I_1 = I_2 = 0.1 \text{ kg m}^2 \quad (13.24)$$

$$g = 9.81 \text{ m/s}^2 \quad (13.25)$$

From Eqs. (13.21)–(13.25), these parameters are set by empirical values.

Suppose that the expected positions of the two joints are $\sin(3t)$ and $\cos(3t)$. The initial state of the controlled plant is $x(0) = [0, 3, 1, 0]^T$. In our programs, we use three types of iterative learning algorithm such as the closed-loop D law, the closed-loop PD law, and the closed-loop D law with exponential gain scheduling.

The results of simulation are shown as below (Figs. 13.1, 13.2, and 13.3):

From the results of simulation, the desired positions of the two joints are tracked best by the exponential gain D law iterative learning control. In the exponential gain D law, K_d is changing in an exponential form with the gain scheduling, while the errors between the real values and desired values can be convergent to zero quickly.

Conclusion

This paper describes the principles of the iterative learning algorithm. This algorithm is applied in the trajectory tracking system of manipulator by simulation. From the simulation of three types of iterative learning algorithm, we can find the good performance of this algorithm in respect of trajectory tracking. The expected positions are tracked well, and the errors between the real values and the expected values can be convergent to zero quickly.

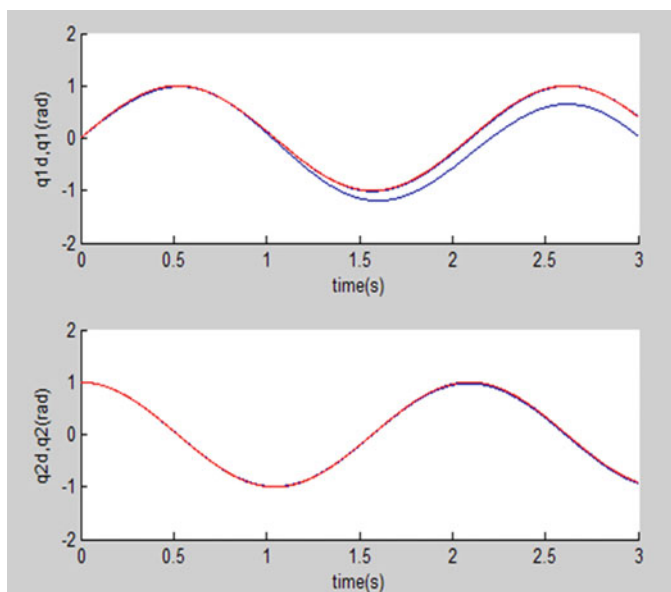


Fig. 13.1 Position tracking during 20 times of D law iterative learning

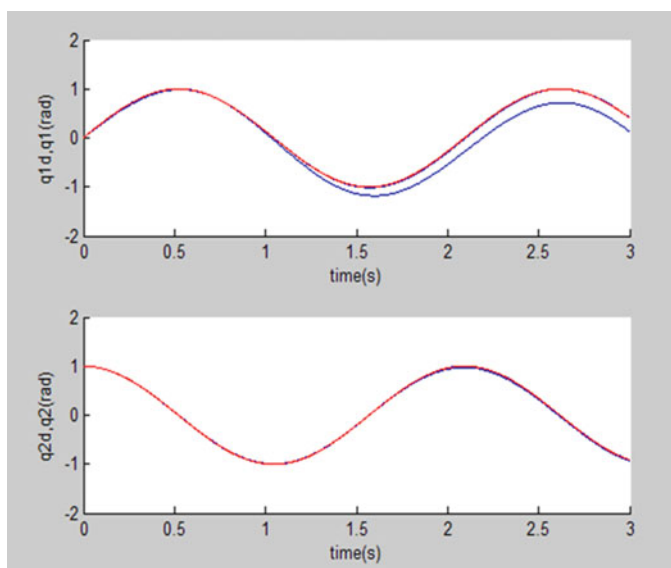


Fig. 13.2 Position tracking during 20 times of PD law iterative learning

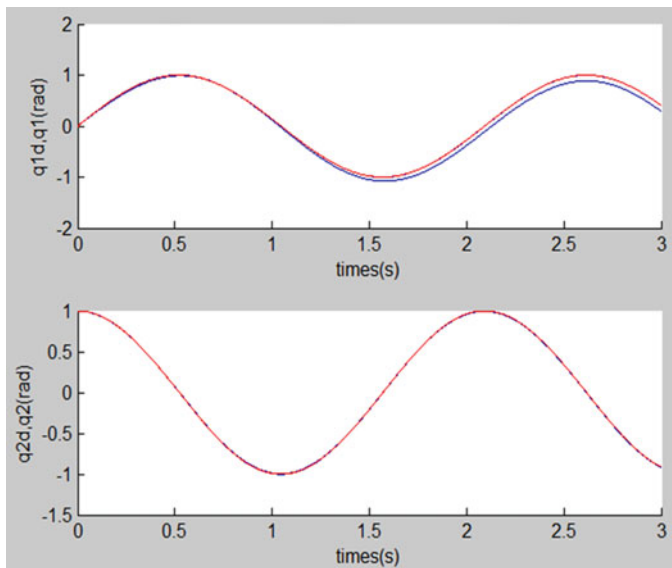


Fig. 13.3 Position tracking during 20 times of exponential gain D law iterative learning

Acknowledgments This work is supported by the Doctor Startup Foundation of Nanchang Hangkong University, Jiangxi Province, China (No. EA201204390).

References

1. Uchiyama M. Formation of high speed motion pattern of mechanical arm by trial. *Trans Soc Instrument Cont Eng.* 1978;19:706–12.
2. Li R-j, Han Z-z. Survey of iterative learning control. *Cont Deci.* 2005;09:961–6 (In Chinese).
3. Arimoto S, Kawamura S, Miyazaki F. Battering operation of robotics by learning. *J Robot Syst.* 1984;1(2):123–40.
4. Kang MK, Lee JS, Han KL. Kinematic path-tracking of mobile robot using iterative learning control. *J Robot Syst.* 2005;22(2):111–21.
5. Jian-Xin X. Recent advances in iterative learning control. *Acta Automatica Sinica.* 2005;01:132–42.
6. Hui L-c, Lin H. Arranging transient process used in iterative learning control system. *Acad J Xi'an Jiaotong Univ.* 2009;01:42–5.

Chapter 14

An Improved Gaussian Mixture Model and Its Application

Guang Han

Abstract This paper proposes an improved Gaussian mixture model (GMM) for outdoor scene classification. The GMM is usually solved by the expectation-maximization (EM) algorithm, but the EM algorithm may easily lead to local optima with the convergence speed of this method unstable and different initial values also leading to fluctuations in the algorithm's performance. As a result, a hybrid particle swarm optimization (PSO) algorithm is introduced to replace the EM algorithm for solving the aforementioned problems with a series of improvements also proposed when the hybrid PSO algorithm is used to solve the GMM. Experimental results with outdoor scene classification show that the proposed algorithm, compared to other algorithms, can enhance global search capabilities and convergence speed; in addition, the accuracy of parameter estimation is high, and classification performance is excellent.

Keywords Intelligent ground robot • Scene classification • Gaussian mixture model • Hybrid particle swarm optimization

14.1 Introduction

Scene classification is an important part of the perception system for intelligent ground robots; it aims to use vision sensors to automatically distinguish grass, land, sand, and other different terrains; this information is then used to help intelligent robots make proper planning and decisions in connection with their actions [1–3]. The Gaussian mixture model (GMM) is a good statistical model and has attracted much attention. In recent years, GMM has been widely used in the field of image classification [4]. Research results show that GMM has better classification performance than other statistical models [5]. GMM has a natural advantage in the scene classification of outdoor environments. Because the same terrain under different lighting conditions will appear different, for example, the same terrain in the sun,

G. Han (✉)

Engineering Research Center of Wideband Wireless Communication Technique, Ministry of Education, Nanjing University of Posts and Telecommunications, Nanjing 210003, China
e-mail: hanguang8848@163.com

shadows, and cloudy conditions will look different. The GMM can well fit features with a variety of appearances. The expectation-maximization (EM) algorithm is usually used to solve GMM parameters; in addition, as a local optimization algorithm, it has poor features, such as an unstable convergence rate and high sensitivity to initial values; therefore, we introduce and improve a hybrid particle swarm optimization (PSO) algorithm to replace the EM algorithm for solving GMM parameters.

An improved GMM for outdoor scene classification is proposed in this paper, whose contributions stem primarily from the following three aspects. First, a hybrid PSO algorithm is introduced and improved to solve GMM parameters for scene classification. Second, the improvement measures on the hybrid PSO include an effective change strategy based on the Butterworth curve instead of a linear strategy, the adoption of position information of particles of the $t - 1$ step to pull back the position of current particles or particles with an improved poor fitness value, for example; finally, the proposed algorithm is used for actual outdoor scene classification. The experimental results show that the precision of parameter estimation can be effectively improved, and the performance of the proposed algorithm is also very excellent when the improved hybrid PSO is adopted to solve GMM parameters.

14.2 Gaussian Mixture Modeling for Scene Classification

There is a group of features (x_k, j_k) , $k = 1, 2, \dots, N$, in which j_k is the integer between $[1, J]$. It shows that x_k comes from the j_k th mixture parts. The distribution of x_k conforms to Eq. (14.1):

$$P(x_k, j_k; \Theta_{j_k}) = p(x_k | j_k; \theta_{j_k}) P_{j_k} \quad (14.1)$$

Assuming that the feature samples are independent, the log-likelihood function is shown in Eq. (14.2):

$$L(\Theta) = \sum_{k=1}^N \ln(p(x_k | j_k; \theta_{j_k}) P_{j_k}) \quad (14.2)$$

$$\begin{aligned} Q(\Theta; \Theta(t)) &= E \left[\sum_{k=1}^N \ln(p(x_k | j_k; \theta) P_{j_k}) \right] = \sum_{k=1}^N E [\ln(p(x_k | j_k; \theta) P_{j_k})] \\ &= \sum_{k=1}^N \sum_{j_k=1}^J P(j_k | x_k; \Theta(t)) \ln(p(x_k | j_k; \theta) P_{j_k}) \end{aligned} \quad (14.3)$$

E-step: In the current framework, the unknown parameter vector is $\Theta^T = [\theta^T, P^T]^T$. Taking the expectation over the unobserved data, conditioned on the training samples and the current estimates, $\Theta[t]$, of the unknown parameters, we can obtain Eq. (14.3).

The serial number k of j_k is removed, and we obtain Eq. (14.4) because, for each k , we sum up over all possible J values of j_k and these are the same for all k .

$$p(x_k|j; \theta) = \frac{1}{(2\pi\sigma_j^2)^{1/2}} \exp\left(-\frac{\|x_k - \mu_j\|^2}{2\sigma_j^2}\right) \quad (14.4)$$

Equations (14.3) and (14.4) are combined into Eq. (14.5) as follows:

$$Q(\theta; \theta(t)) = \sum_{k=1}^N \sum_{j=1}^J P(j|x_k; \theta(t)) \left(-\frac{1}{2} \ln \sigma_j^2 - \frac{1}{2\sigma_j^2} \|x_k - \mu_j\|^2 + \ln P_j \right) \quad (14.5)$$

M-step: Eq. (14.5) is solved using the gradient descent method, and then the estimated value of θ in the $t+1$ step is obtained. Equation (14.5) is differentiated on μ_j , σ_j^2 , and P_j , respectively, to obtain the maximum value [5].

The GMM is trained by constant repetition of E-Step and M-Step, which use the feature data sets; then GMM parameters can be obtained, and GMM is also established. We see from the process described earlier that the convergence speed is unstable by the gradient descent method, and sometimes in the calculation process algorithm may produce a singular matrix, which easily leads to the convergence failure. Meanwhile, only the local extreme is guaranteed to be obtained by the EM algorithm. This algorithm has a strong dependence on the initial value of each class. Once the deviation of the initial estimate from the true value becomes very large, the EM algorithm easily produces the local optimum value, then the quality of the model parameter estimation is affected, and the classification accuracy decreases. This paper introduces a hybrid PSO algorithm to replace the EM algorithm for optimizing GMM parameter estimation and improving the estimation accuracy [5, 6].

14.3 Improved Hybrid PSO Algorithm

14.3.1 Conventional PSO Algorithm

Assume that R is the solution space, D is the dimension of the search space, and the particle swarm contains N particles. To distinguish the preceding feature samples, the position of each particle is expressed by x'_i , and $x'_i = (x'_{i1}, x'_{i2}, \dots, x'_{iD})$ and $V_i = (V_{i1}, V_{i2}, \dots, V_{iD})$ respectively represent the position and velocity of each particle. f_i represents the fitness value of the i th particle, $i = 1, \dots, N$. $\text{pbest}_i = (\text{pbest}_{i1}, \text{pbest}_{i2}, \dots, \text{pbest}_{iD})$ represents the position of the optimal solution of the i th particle, $\text{gbest}_i = (\text{gbest}_1, \text{gbest}_2, \dots, \text{gbest}_D)$ represents the position of the

optimal solution of the whole particle swarm, and the velocity and position of each particle are updated using Eqs. (14.6) and (14.7):

$$V_i(t+1) = c_0 V_i(t) + c_1(\text{pbest}_i - x_i(t)) + c_2(\text{gbest} - x_i(t)) \quad (14.6)$$

$$x'_i(t+1) = x'_i(t) + V_i(t+1) \quad (14.7)$$

For a global search, good search capabilities are required in the early iterative process to obtain the right seeds; while in the late stage of the iterative process, an ability to speed up convergence is required. Eberhart and Shi once proposed an inertia weight algorithm [7] using Eq. (14.6) modified as follows:

$$V_i(t+1) = \omega(t) \times V_i(t) + \phi_1 \mu_1(\text{pbest}_i - x_i(t)) + \phi_2 \mu_2(\text{gbest} - x_i(t)) \quad (14.8)$$

where μ_1, μ_2 are two random numbers uniformly distributed in $[0,1]$, ϕ_1, ϕ_2 are acceleration factors, and $\omega(t)$ is the weight expressed as

$$\omega(t+1) = \omega(t) + d\omega, \quad d\omega = \frac{\omega_{\min} - \omega_{\max}}{T} \quad (14.9)$$

14.3.2 Improved Hybrid PSO Algorithm

As for the problem caused by optimizing Eq. (14.5) using the conventional PSO algorithm, the three improvement measures on the conventional PSO algorithm are as follows.

1. A linear strategy using Eq. (14.8) is not the best choice. In the early stages of the algorithm's operation, to effectively avoid the local optimum, $\omega(t)$ must have a large value for a long period of time, but the value of $\omega(t)$ decreases rapidly with the linear strategy, which is not conducive to avoiding the local optimum for the algorithm; therefore, an effective change strategy is proposed in this paper based on the Butterworth curve with the following specific formula:

$$\omega(t) = \frac{\omega_{\max} - \omega_{\min}}{1 + \lceil t/t_0 \rceil^{2 \times n}} + \omega_{\min}, \quad 1 < t < T \quad (14.10)$$

$$n = R\left(2 + \text{sgn}\left(\frac{\|V_i(t)\|}{\|V_i(t-1)\|} - 1\right)\right) \quad (14.11)$$

where T is the maximum iteration number, t_0 is the cutoff iteration number of the n -order Butterworth curve, $\omega_{\max} = 0.9$, $\omega_{\min} = 0.1$, and $R()$ is a rounding function. Meanwhile, to reduce the computational complexity of $\omega(t)$, we stipulate that if $n < 1$, then $n = 1$; if $n > 4$, then $n = 4$, so $1 \leq n \leq 4$, $n \in \mathbb{Z}$.

Using Eq. (14.10) we can see that $\omega(t)$ will decrease nonlinearly as the iteration number increases. In the early stages of the algorithm's operation, $\omega(t)$ can have a large value for a long period of time, which is very conducive

to having particles jump out of local optima and can cause the algorithm to find the solution within a broad scope; in the late stages of the algorithm, $\omega(t)$ can have a small value for a long period of time until the algorithm stops, which can facilitate the convergence of the algorithm. When $\omega(t)$ has a small value, it can make particles carefully search in the local space around them; while in the intermediate stages of the algorithm's operation, the order number n of the Butterworth curve can effect an adaptive change using Eq. (14.11), and the principle behind this adaptive adjustment is that the real-time adaptive adjustment of order number n can be implemented before and after the two steps of the iteration operation. By Eq. (14.11) we see that if $\|V_i(t)\| > \|V_i(t-1)\|$, then the value of n will become large, the decreasing amplitude of $\omega(t)$ also increases, and then the local search capability of the particles will be strengthened; conversely, if $\|V_i(t)\| < \|V_i(t-1)\|$, then n will become small, the decreasing amplitude of $\omega(t)$ will also decrease, and then the global search capability of the particles will be strengthened. By adaptively adjusting order number n to control the decreasing amplitude of $\omega(t)$, automatic variation in $\omega(t)$ can be achieved with the local and global search capability of the balanced particles, thereby improving the algorithm's performance.

2. Because gbest is used in Eq. (14.8), the problems of large velocity and skipping real solutions easily arise with the iteration of the algorithm. To solve these problems, when particles are close to gbest, they are pulled back using the position information of the particles with the $t-1$ step in this paper; thus, whole particle groups are likely to obtain a global optimal solution with the following specific formula:

$$V_i(t+1) = \omega(t) \times V_i(t) + \varphi_1 \mu_1 (\text{pbest}_i - x'_i(t)) + \varphi_2 \mu_2 (\text{gbest} - x'_i(t)) + \varphi_3 \mu_3 (x'_i(t-1) - x'_i(t)) \quad (14.12)$$

where $\varphi_3 = \exp\left(-\frac{1}{\|V_i(t)\|}\right)$.

3. The general PSO algorithm is simple and can be implemented easily, but it also easily produces the local optimum value. To solve this problem, a hybrid PSO algorithm is adopted [8]. $c_0 V_i(t)$ in Eq. (14.6) is regarded as the variation of the genetic algorithm, $c_1(\text{pbest}_i - x'_i(t)) + c_2(\text{gbest} - x'_i(t))$ in Eq. (14.6) is regarded as the crossover of the genetic algorithm. Firstly the current solution and the individual extremes are crossed, and then the current solution and the global extremes are crossed, and the solution produced is the new location. The variation and crossover in the hybrid PSO algorithm are used; thus, the performance of the global optimal solution is improved, but the speed of the algorithm convergence slows down because all the particles are subject to variation and crossover. In this paper, the preceding hybrid PSO algorithm is used for 30 % of all the particles in each iteration. Here, the 30 % of particles have the minimum fitness value and the previously mentioned hybrid PSO algorithm is improved in terms of the specific problems resulting from the application. The global search capability and the convergence rate of the proposed algorithm are also improved.

The crossover strategy in this paper is to randomly select a crossover region in path 2; the crossover region randomly selected in path 2 is added to a random location in path 1, and the location in path 1 will be deleted. These locations appeared in a crossover region in path 2; the variation strategy in this paper is to randomly select five positions (if the position number of the path is less than 5, then the locations can be selected repeatedly) and then exchange these five positions and the last position in the path, with the remaining unchanged. Thus five different paths can ultimately be produced.

Assume that C_i is the path of the i th particle passing through, C_{pbest} is the path of $pbest_i$ passing through, and C_{gbest} is the path of $gbest$ passing through. The improved hybrid PSO algorithm proposed in this paper is as follows:

1. Randomly generate in the search space the initial value N and the initial speed, and record their initial path.
2. Calculate the fitness value f_i , $i = 1, \dots, N$ of the current position x'_i of each particle.
3. Compare f_i and f_{pbest} , $i = 1, \dots, N$; if $f_i > f_{pbest}$, then $f_{pbest} = f_i$, $pbest_i = x'_i$, and record C_{pbest} .
4. When the optimal value f_{max} and its position x' of the current particle swarm are obtained, compare f_{max} and f_{gbest} ; if $f_{max} > f_{gbest}$, then $f_{gbest} = f_{max}$, $gbest = x'$, and record C_{gbest} .
5. Update the velocity and position of each particle according to Eqs. (14.12) and (14.7), and record C_i .
6. Select 30 % of all the particles. Here the 30 % of particles have the minimum fitness value, the path C_i and C_{gbest} of each selected particle are crossed, and C'_i is obtained.
7. The path of C'_i and C_{pbest} passing through are crossed, and then C''_i is obtained.
8. The variation of C''_i can produce five paths.
9. Obtain the position of the current particle according to the preceding five paths, and calculate their respective fitness values.
10. Select the largest of the five fitness values, denoted by f'_i , with its path denoted by C'''_i .
11. If $f'_i > f_i$, then accept the new value; if rejected, the path C'''_i of the i th particle is still C_i .
12. If the maximum number of iterations T is obtained, stop the calculation; otherwise go to step 2.

14.4 Experimental Results and Analysis

The Natural Scene test suites in the Outex data set are used to evaluate the performance of the above proposed algorithm in this experiment. The child test set (ID is Outex_NS_00001) from the Natural Scene test suites is selected for the

experiment. The child test set contains 22 test images with the an image size of $2,272 \times 1,704$. Half of these images are used for training with the other half for testing. The training images from the 22 images are alternately selected. Four terrain classes are defined in this experiment: grass, road, sky, and trees. Here three terrain classes (the grass, road, and trees) contain two different illumination conditions, such as in the sun and in the shadeo. The existing feature extraction method in this experiment can be used [5]. To accelerate the training speed and reduce the computation cost resulting from too many parameters, the principal component analysis method is used to reduce the dimensions of the extracted feature. A single real terrain region is manually labeled using the method proposed by Castano et al. [9].

Figure 14.1 shows the trend of the fitness value with the iteration step increasing. Five different algorithms are used to solve the GMM, namely, the EM algorithm, the inertia weight PSO algorithm, the PSO + EM algorithm [10], Chen's algorithm [6], and the algorithm proposed in this paper. EM is the conventional algorithm for solving the GMM, while the other four algorithms are based on PSO. Each algorithm has its own advantages and innovations. The GMM is trained by the feature data of four terrains. Equation (14.5) is selected as the fitness function. The fitness value of each terrain is obtained, and then the fitness values of the four terrains are averaged (Fig. 14.1). The proposed algorithm can obtain the global optimal solution much faster than Chen's algorithm [6] and the PSO + EM algorithm [10], with the performance improvement better than with the conventional EM algorithm and the inertia weight PSO algorithm.

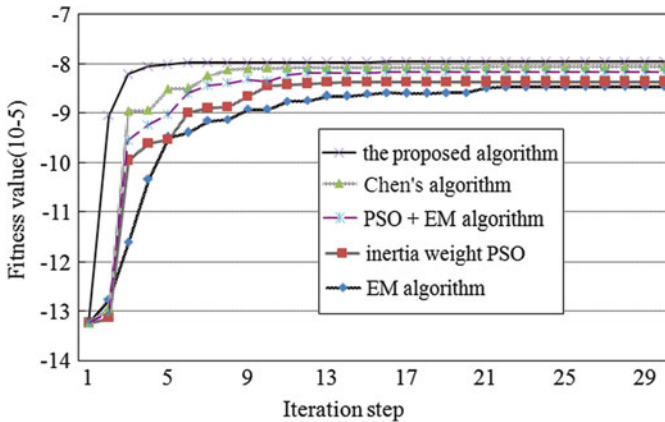


Fig. 14.1 Trend of fitness value with iteration step increasing

Conclusion

An improved GMM is proposed in this paper. Because the EM algorithm easily produces the local optimum value with an unstable convergence rate and is sensitive to initial value, a hybrid PSO algorithm is introduced to replace the EM algorithm for GMM parameter estimation. The algorithm was optimized in terms of the specific problems in the scene classification application, and the proposed algorithm can be applied to outdoor scene classification. Experimental results show that the improved hybrid PSO algorithm, which features a strong global search capability, can escape local optima and speed up convergence. In a scene classification experiment, its results were superior to those of the existing algorithms, which indicates that the proposed method for outdoor scenes are reliable and effective, and the optimized performance of the improved hybrid PSO is better than that of the existing algorithms in terms of GMM parameter estimation.

Acknowledgments This work is supported by China National Natural Science Foundation (61302156) and the University Natural Science Research Project of Jiangsu Province (13KJB510021).

References

1. Christopher AB, Karl I. Self-supervised terrain classification for planetary surface exploration rovers. *J Field Rob.* 2012;29(3):445–68.
2. Marcel H, et al. Probabilistic terrain classification in unstructured environments. *Robot Auton Syst.* 2013;61(10):1051–9.
3. Thomas JP, et al. An improved simple morphological filter for the terrain classification of airborne LIDAR data. *ISPRS J Photogramm Remote Sens.* 2013;77(3):21–30.
4. Li W, Prasad S, Fowler JE. Hyperspectral image classification using Gaussian mixture models and Markov random fields. *IEEE Geosci Remote Sens Lett.* 2014;11(1):153–7.
5. Han G. Algorithmic research for unstructured scene image interpretation. Nanjing: Nanjing University of Science and Technology; 2010 (in Chinese).
6. Chen YJ, et al. Brain MRIS segmentation using the active contours based on Gaussian mixture. *J Comput Res Dev.* 2007;44(9):1595–603 (in Chinese).
7. Eberhart RC, Shi Y. Particle swarm optimization: developments, applications and resources. In: *The 2001 Congress on Evolutionary Computation*, vol. 1. Seoul, Korea: IEEE Press; 2001. p. 81–6.
8. Gao S, et al. Solving traveling salesman problem by hybrid particle swarm optimization algorithm. *Control Decis.* 2004;19(11):1286–9 (in Chinese).
9. Castano R, Manduchi R, Fox J. Classification experiments on real-world texture. In: *Proceedings of the Third Workshop on Empirical Evaluation Methods in Computer Vision*. Pasadena: Jet Propulsion Laboratory; 2001. p. 3–20.
10. Fan SK, Lin Y. A multi-level thresholding approach using a hybrid optimal estimation algorithm. *Pattern Recogn Lett.* 2007;28(5):662–9.

Chapter 15

GPU Acceleration for the Gaussian Elimination in Magnetotelluric Occam Inversion Algorithm

Yi Xiao and Yu Liu

Abstract In order to improve the efficiency of magnetotelluric Occam inversion algorithm, a parallel Gaussian elimination algorithm based on two-dimensional constant bandwidth storage is developed, which is implemented on graphic processing units (GPUs) by using CUDA Fortran. Detailed descriptions of the programming are presented. The parallel algorithm can simultaneously and rapidly calculate multiple large matrices. To make full use of the GPU computational power and memory bandwidth, the data access patterns have been analyzed and optimized in depth for parallel access. The experimental results show that with the increase of the number of matrices, higher speedup can be obtained. The high efficiency of the parallel strategy makes it easier for other algorithms based on two-dimensional constant bandwidth storage.

Keywords Parallel computing • Gaussian elimination • Occam inversion

15.1 Introduction

A system of linear equations is an important basis of many scientific and engineering computing problems. Gaussian elimination is an effective method for linear system. The basic idea of this algorithm is to transform the coefficient matrix into upper triangular matrix by line transformation and then back substitution to solve it. In magnetotelluric Occam inversion algorithm (MT Occam), the finite element method was used to solve the forward module response and obtain the model misfit. The Gaussian elimination method is the principal method of the calculation for the model misfit and the Jacobian matrix [1]. However, the sequential algorithm for Gauss elimination takes a long time to solve the banded matrix equations and unavoidably results in low convergence of the MT Occam when solving a

Y. Xiao • Y. Liu (✉)
College of Information Science and Engineering, Guilin University of Technology,
541004 Guilin, China
e-mail: louisxcode@yahoo.com; lewis_5709@163.com

large-scale inversion model. Therefore, the parallel Gaussian algorithm transfers the coefficient matrix into many compute nodes through the way of “shutter,” thus enhancing the computing speed by multiple computers [2] and multiple CPU cores [3]. But the data transfer and synchronization between different nodes also require a lot of time. The efficiency is not very ideal. As the development of graphic processing units (GPUs), massively parallel computing can be applied [4]. Parallel Gaussian algorithm reduces the computing time greatly by using the GPU massively computational power and high-speed memory bandwidth [5, 6]. The coefficient matrix is usually sparse and symmetrical in the MT Occam. A structure for 2-D band sparse matrix is used to store the coefficient matrix, which greatly reduces the storage space [7]. In this paper, we develop and implement a parallel Gaussian algorithm based on the GPU to solve the banded matrix equations, by combining the two-dimensional constant bandwidth method and basic principle of parallel Gaussian algorithm. We also optimize the algorithm for special storage structure to improve the computing speed of the MT Occam.

15.2 Related Works

15.2.1 *CUDA*

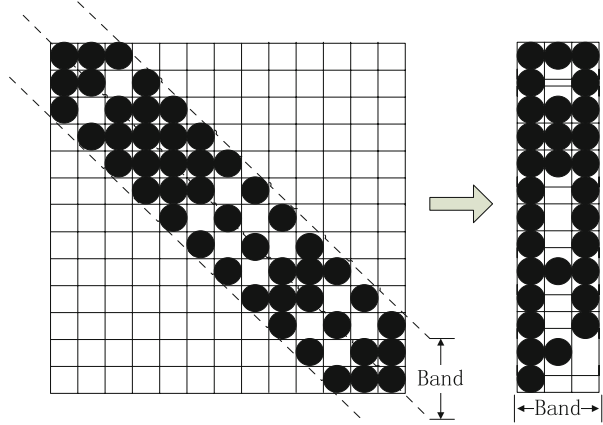
In November 2007, NVIDIA introduced CUDA, a general-purpose parallel computing architecture. In this parallel programming model, the CPU is responsible for carrying out the logic transaction processing and serial computing; the GPU is responsible for the implementation of highly threaded parallel processing tasks. The CPU has the memory of the host side called host memory, and the GPU has the memory of the equipment side called device memory [8].

CUDA Fortran was developed in 2009 by Portland Group (PGI). It is based on CUDA runtime API, but using Fortran 90 constructions and a set of language extension. Thus it is more useful for Fortran programmers in parallel computing [9].

15.2.2 *Two-Dimensional Constant Bandwidth Storage*

In the MT Occam, the geological structure stiffness matrix which is composed of element unit stiffness matrixes has the characters of symmetry and sparsity. All the nonzero coefficients in the stiffness matrix are confined within a band. Thus only the upper half of the band in the stiffness matrix needs to be stored. The transformation of the stiffness matrix storage format is shown in Fig. 15.1. The MT Occam directly uses the Gaussian elimination algorithm in compressed coefficient matrix. It greatly reduces the storage space, but is more complicated.

Fig. 15.1 The transformation of stiffness matrix storage format



15.3 Algorithm Parallelization Solving

15.3.1 Gaussian Elimination Programming with CUDA Fortran

The Gaussian elimination algorithm in the MT Occam is divided into three steps: the coefficient matrix elimination, response solving, and the auxiliary field Jacobian matrix calculation. Assume the n -order coefficient matrix $S(n, n)$, response matrix $RM(n)$, and auxiliary field calculation matrix $RJ(n, nrc)$, in which the nrc is the number of measurement points.

In the S elimination process of the coefficient matrix based on band storage method, select the row m ($1 \leq m \leq n$) of S as the main element row. Then eliminate the row $m+1$ to $m+D-1$ according to Eq. (15.1), where D is the bandwidth. When the coefficient matrix S finishes elimination, calculate the response matrix RM according to Eq. (15.2).

$$S_{m+L, j}^{(m)} = S_{m+L, j}^{(m-1)} - \frac{S_{m, L+1}^{(m-1)}}{S_{m, 1}^{(m-1)}} S_{m, j+L}^{(m-1)} \quad (1 \leq L \leq D-1, 1 \leq j \leq D-L) \quad (15.1)$$

$$RM_{m+L}^{(m)} = RM_{m+L}^{(m-1)} - \frac{S_{m, L-1}^{(m-1)}}{S_{m, 1}^{(m-1)}} RM_m^{(m-1)} \quad (1 \leq L \leq D-1, 1 \leq j \leq D-L) \quad (15.2)$$

Then back substitution to calculate the response according to (15.3) and (15.4). When $n-m+1 > 1$, $NBLIM = D$. Otherwise $NBLIM = n-m+1$.

$$RM_n = \frac{RM_n}{S_{n, 1}} \quad (15.3)$$

$$RM_m = \frac{RM_m - \sum_{j=2}^{NBLIM} S_{m,j} RM_{m+j-1}}{S_{m,1}} \quad (2 \leq j \leq D) \quad (15.4)$$

The general structure of a Fortran program that utilizes GPU computing for Gaussian elimination can have the following simple form:

```

module gpu
  contains:
    attributes(global) subroutine gauss(...)
    ...
  end subroutine gauss
end module gpu

program occam
  use cudafor
  complex, allocatable, dimension(:), device :: d_S, d_RM
  ...
  call gauss<<<num,numthreads,...>>>(d_S, d_RM...)
  ...
end program occam

```

According to Eq. (15.1), the element number needs to be calculated in which each loop is $(NBAND-1)*NBAND/2$, where $NBAND = D$. To make the GPU threads correspond with these elements, we create $numthreads = (NBAND-1)*NBAND/2$ GPU threads. Kernel calculate num coefficient matrixes at the same time which are consecutively stored. Each GPU block calculates a coefficient matrix. The primary line coefficient matrix's deviation value that corresponds to each thread calculation is $offset = (blockIdx \% x-1)*n*NBAND$.

For the back substitution stage, only one block calculates the response. All RM matrixes are stored together. Each thread calculates the corresponding elements based on the row and column value. ROW and COL are defined as follows:

```

col = (threadIdx \% x-1) / (NBAND-1)
row = threadIdx \% x - ((threadIdx \% x-1) / (NBAND-1)) * (NBAND-1)

```

15.3.2 CUDA Fortran Optimization

Shared memory is GPU on-chip memory. It has a very high speed and bandwidth. According to Eq. (15.1), in the elimination process with row m as the pivot element, all the elements to be calculated depend only on the elements of row m and their own, keeping the value of row m unchanged. Therefore, the elements of primary row can be placed in shared memory. The code is shown below:

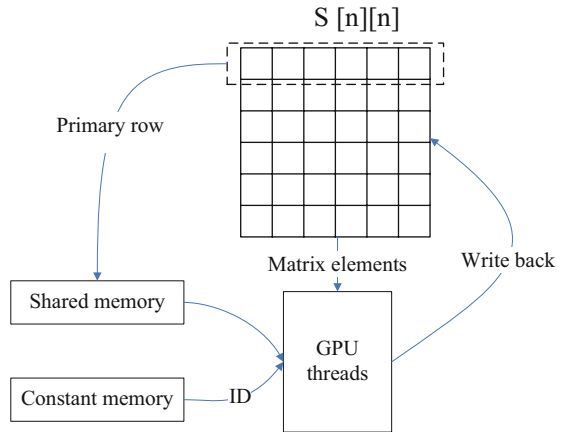
```
complex, shared :: pivot(NBAND*8)
if(threadIdx%x <= NBAND) then
  pivot(threadIdx%x) = S(offset+threadIdx%x)
endif
```

According to Eq. (15.4), each element depends on the elements on following row. On the other hand, every element is used to calculate the elements above it from row n to row 1. Therefore the elements of the required row can be placed in shared memory. The first loop offset of RM in each thread is the last row of the corresponding matrix. The code is shown below:

```
offset = (col-1)*n*nband + (n-nband + row-1)*nband + nband-row + 1
RM(idx) = RM(idx) - pivot(col)*S(offset)
offset = offset-NBAND
```

Constant memory is a high-speed GPU memory. It uses a special cache to improve the access speed, without changing the value in the kernel. We can put the read-only data into constant memory by the host. In the parallel Gaussian algorithm, each thread corresponds to the determined storage position of the element which needs to be eliminated in the elimination process. According to Eq. (15.1), the position of each element that corresponds to the thread is fixed relatively to the primary line's deviation value, without exceeding the boundaries of the matrix. So we only need to change the primary line's location information in each elimination process. Then each thread calculates the storage location of the corresponding element according to the location information and the fixed offset value. The offset value is calculated by the host and transferred to the GPU.

Fig. 15.2 The result of algorithm with different model scale



The coefficient matrix elimination process is shown in Fig. 15.2. Kernel realizes constant memory through the “const” keyword. The specific codes are as follows:

```
integer, allocatable, dimension(:), device:: ID
I=1
do N=1,NBAND-1
  do J=1,NBAND-N
    ID(I)=N*NBAND+J+N*10
    I=I+1
  enddo
enddo
```

To use the coefficient row 1 to row n as the primary line, an elimination process code of each thread is as follows:

```
idx = ID(threadIdx%x)
temp = S(offset+idx)
temp = temp -
pivot((idx/width)+1)/pivot(1)*pivot(idx/width+MOD(idx,width))
S(offset+idx) = temp
if(threadIdx%x <= NBAND .and. threadIdx%x /= 1) then
  S(offset+threadIdx%x) = pivot(threadIdx%x)/pivot(1)
endif
offset = offset+NBAND
```

15.4 Experimental Results

The experiments are performed on a PC with CentOS 6.3 operating system, equipped with an Intel Core i5 3.2 GHz processor, 8 gigabytes main memory, and a NVIDIA GTX680 graphic card. The MT Occam version 3.0 program is provided by Steve Constable at <http://marineemlab.ucsd.edu/Projects/Occam/index.html>. The serial Gaussian elimination algorithm program we used is part of the MT Occam v3.0. We execute the serial algorithm and parallel algorithm under two different inversion model scales. Table 15.1 shows the details of 889-model and 1549-model. 889 and 1549 are the size of the magnetotelluric model (model parameters used), DLY and DLZ represent the width and thickness of each column in meters. NRC is the number of receiver sites.

We substitute the coefficient matrix which is generated by multiple frequency data information under different inversion models into the algorithm to find a solution. The serial algorithm calculates each coefficient matrix successively, and the parallel algorithm calculates all the matrix data in parallel. The experiment's result is shown in Fig. 15.3. It is obvious that the parallel algorithm can greatly reduce the growth of time. Speedup refers to the ratio of the time required by the serial algorithm running on the CPU and the parallel algorithm running on the GPU. The speedup of 889-model is shown in Fig. 15.4. 1549-model has similar trends and values with 889-model. With the increasing number of matrices, the execute time of serial MT Occam is much larger than the parallel.

Table 15.1 The proportion of each part of the serial algorithm running time

Model	DLY	DLZ	NRC	Air layers
889-model	103	35	21	10
1549-model	193	35	41	10

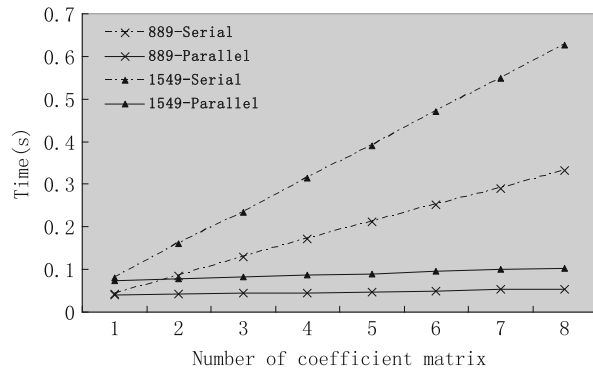
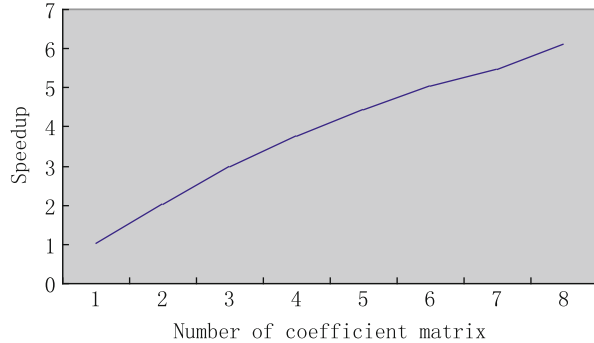


Fig. 15.3 The computing time of algorithm with different model scale

Fig. 15.4 The speedup of algorithm with 889-model scale



Conclusion

A detailed CUDA Fortran implementation of the parallel Gaussian elimination algorithm in the MT Occam based on the GPU was presented. CUDA Fortran can help programmers to parallelize numerical computation on the GPU. By analyzing the characteristics of the algorithm, hardware caching is used to reduce memory access. Optimization for parallel accessing further improves the efficiency of the algorithm. The results show that the parallel algorithm is correct and efficient. The speedup we have achieved is up to 6.1. This greatly reduced the linear equation solving time. As linear equation solving takes a great part of the calculation time of the MT Occam inversion, the total speed of the MT Occam inversion will surely be increased by this parallel algorithm.

Acknowledgments This work has been supported by the National Natural Science Foundation of China under research project 41264005 and also supported by the Guangxi department of education under the research project 201102ZD018.

References

1. DeGroot-Hedlin C, Constable S. Occam's inversion to generate smooth, two-dimensional models from magnetotelluric data. *Geophysics*. 1990;55(12):1613–24.
2. Cosnard M, Marrakchi M, Robert Y, Trystram D. Parallel Gaussian elimination on a MIMD computer. *Parallel Comput*. 1988;6(3):275–96.
3. McGinn SF, Shaw RE. Parallel Gaussian elimination using OpenMP and MPI. *High performance computing systems and applications*. Washington, DC: IEEE; 2002. p. 169.
4. Sanders J, Kandrot E. *CUDA by example: an introduction to general-purpose GPU programming*. Upper Saddle Rive, NJ: Addison-Wesley Professional; 2010. p. 2–4.

5. Buluç A, Gilbert JR, Budak C. Gaussian elimination based algorithms on the GPU. Under review for the Special Issue of Parallel computing on parallel matrix algorithms and applications. 2008; pp. 200–300.
6. Che S, Li J, Sheaffer JW, Skadron K, Lach J. Accelerating compute-intensive applications with GPUs and FPGAs. In Application Specific Processors. Washington, DC: IEEE; 2008. p. 101–7.
7. Zhu J, Taylor ZRL, Zienkiewicz OC. The finite element method: its basis and fundamentals. 6th ed. Burlington, VT: Butterworth-Heinemann; 2005. p. 9–10.
8. NVIDIA Corporation. CUDA C programming guide version 5.5. 2013, pp. 1–6. <http://www.nvidia.com/cuda>
9. Kirk DB, Hwu WW. Programming massively parallel processors: a hands-on approach. 2nd ed. Burlington, VT: Morgan Kaufmann; 2012. p. 359–82.

Chapter 16

Artificial Neural Networks in Biomedicine Applications

Jiri Krenek, Kamil Kuca, Aneta Bartuskova, Ondrej Krejcar, Petra Maresova, and Vladimir Sobeslav

Abstract This paper reviews artificial neural networks (ANN) and their use in various disciplines, especially medicine and biomedicine. As they are progressively evolving, fields of knowledge and modern methods such as ANN help to process information in order to make positive contribution to the development of human knowledge. The article illuminates this information processing in terms of artificial neurons and presents the learning algorithms for ANN. Finally, its current use is reviewed, especially its impact on drug design and development and application in biomedicine.

Keywords Artificial neural networks • Biomedicine • Simulations

16.1 Introduction

The massive expansion of information technologies gives new opportunities for the application of computers in processing of numerous information. In this context, it becomes very important to develop tools and software to handle such a huge volume of information and data as collected. Firstly, we have to archive and sort the data, which can be done by the database systems; secondly, it involves the information processing from the data collection to positive contribution to the development of human knowledge. As to the processing of high volume data, the data mining tools are available and capable of grabbing useful information from the large data sets. Modern style of life, fast business, and extensive research also require an option to predict unknown data with the required attributes. Predictions are widely adopted in economics and industry. In the last years, it becomes very important to improve diagnostics in medicine and increase the medical treatment efficiency. Modern methods such as artificial neural networks (ANN) give a chance to achieve these targets.

J. Krenek • K. Kuca (✉) • A. Bartuskova • O. Krejcar • P. Maresova • V. Sobeslav
Center for Basic and Applied Research, Faculty of Informatics and Management,
University of Hradec Kralove, 50003 Hradec Kralove, Czech Republic
e-mail: jiri.krenek@uhk.cz; kamil.kuca@uhk.cz; aneta.bartuskova@uhk.cz;
ondrej.krejcar@uhk.cz; petra.maresova@uhk.cz; vladimir.sobeslav@uhk.cz

This paper is to give an overview of the artificial neural networks and their possible applications in drug design, medicine, and biomedicine. It serves a short overview in the area of diagnosis of diseases in early stages, image analysis, and an idea of philosophy of ANN usage in the development of new potential drugs.

16.2 Using of ANN for Prediction

The artificial neural networks are intelligent computational methods as inspired by the specific biological structure—a kind of human brain. It consists of billions of neuron cells where every single cell is connected with numerous thousands of others [1]. The number of connections and variability of their networking structure make the cross-linking of cells very complex and strong as an intelligent system. The biological neuron consists of soma (cell body), dendrites, and axons. The dendrites transfer the input signals to the soma where they are processed with the output signal to be transferred by the axons. Connections between such biological neurons (dendrites and axons) are called synapses and the biological neural network consists of tens to hundreds of thousands of these synaptic connections.

16.2.1 Artificial Neuron Characteristics

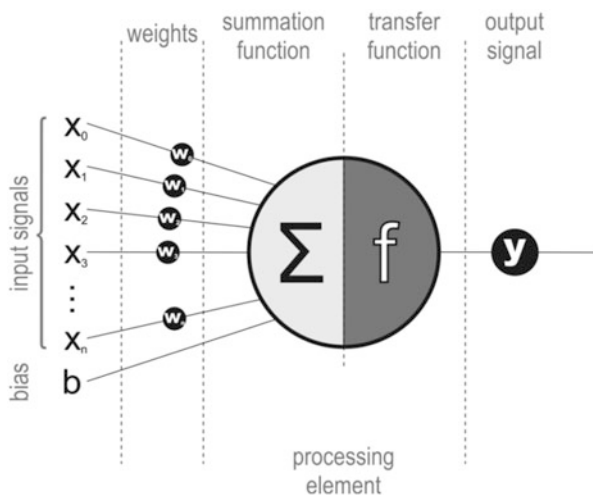
Analogue to the biological neuron is the artificial neuron which is a mathematical processing unit. It consists of the body, the so-called processing element [2], inputs and outputs. Any neuron can have more than one input signal x_i , and each of these signals is multiplied by the synaptic weight w_i . The multiplication of the input signal is done by the appropriate weights, and it sets the priority and a significance of each signal comparing to the other signals of the neuron's input. The weighted signals are then summed in the neuron together with bias b in the processing unit and propagated as the output by the transfer function f .

The mathematical description of artificial neuron can be written as

$$y = f\left(\sum_{i=0}^n w_i x_i + b\right) \quad (16.1)$$

where y is the output value of the neuron, x_i is the input value, w_i is the weight value, b is the bias, and f is the transfer function. The transfer function is mostly a linear or nonlinear function, for example, a sigmoidal or step function. Based on the fact, the artificial neural networks are used for solving complex nonlinear problems and the transfer functions are mainly nonlinear (Fig. 16.1).

Fig. 16.1 Artificial neuron as a mathematical processing unit



16.3 Using of ANN for Drug Design and Development

The development of new drugs is very expensive and time consuming; therefore, the use of advanced computational methods is a big challenge for pharmaceutical industry and the medical treatment. There are approximately only 10 compounds from originally 10,000 substances tested in animal studies processed for further testing on safety in use by human. Finally, it is from the original set with just one compound that passes successfully all tests and is distributed on the market [3]. The development of new drugs is mainly based on *in vivo* and *in vitro* methods. On one side, the *in vivo* methods are perfect for testing new drugs because of drug effect verification and distribution on organisms in their normal state, but these methods are connected with ethical problems and very expensive and subject to quite long lead times in early stages; on the other side, there are the *in vitro* methods that perform testing on biological structures isolated from organisms; it is not possible to describe and cover the distribution of drugs in the metabolism of the living organism, etc., with these methods.

The abovementioned problems lead to the massive development of *in silico* methods, i.e., computational methods. These methods are much cheaper than *in vivo* and *in vitro* methods and they start to play an important role in the drug design. Artificial neural networks do not have to strictly follow the structured experimental designs, but they can also cover the incomplete data or can use some historical data [4] with their characteristic flexibility. As to the description of the compounds, special techniques are adopted such as the quantitative structure–activity relationship (QSAR), quantitative structure–property relationship (QSPR), or quantitative structure–pharmacokinetic relationship (QSPKR). The above described methods derive quantitative models that are confirmed by biological tests and are nowadays deemed as an essential part of drug discovery as

well as toxicity prediction [3]. These techniques use specific theoretical descriptors of chemical, physical, or topological properties of compounds and biological activities.

Besides the experimental data mining, one of the important methods used in drug design is the virtual screening (VS) [5]. It is another computational method used to identify new potential structures within the molecular databases that are most likely to interact with a drug target. It can be used as an example of an enzyme.

The known and effective compounds from experimental data including the newly found potential drug compounds must be constructed in the environment of computer. For this purpose, different SWs are available to draw the molecular structure of chemical compounds. Some representatives of such SWs include ChemSketch (Advanced Chemistry Development), ChemOffice (PerkinElmer Informatics), HyperChem (Hypercube, Inc.), and ISIS draw (Accelrys) [3]. The files representing the molecules are processed in another special SW to calculate the molecular descriptors, for example, Dragon (Taletе s.r.l.), CODESSA (Semichem, Inc.), and PaDEL (National University of Singapore) [3, 6]. Among these molecular descriptor SWs, the most detailed is the Dragon with almost 4,900 descriptors available such as constitutional descriptors, topological and connectivity indices, 2D and 3D autocorrelations, atom pairs, drug-like indices, functional group counts, physical and thermodynamic descriptors, etc.

The number of molecular descriptors must be optimized because too high a number of descriptors makes the neural network very complicated and the calculations very slow. The number of descriptors, i.e., variables, increases linearly the number of calculations in matrixes behind raises exponentially. In order to reduce dimensionality of the network and keep the independent descriptors in the dataset, the correlation analysis of descriptors should be done [6]. In order to protect the descriptors of chance correlation with outputs, the y-randomization shall be made by repeatedly permuting activity values and comparing alternative results with results of the original model.

Finally, the QSAR model data are processed in SW capable to work with artificial neural networks, such as NeuroSolutions (NeuroDimension, Inc.), IBM SPSS Modeler, NeuroIntelligence (Alyuda Research, LLC.), STATISTICA Automated Neural Networks, MATLAB Neural Network Toolbox, Mathematica Neural Networks package (Wolfram), etc. The numerical models of the compounds (drugs) are used for further processing in ANN to predict compounds of newly defined attributes. Artificial neural networks are used for modeling complex pharmacodynamic and pharmacokinetic relationships based on physicochemical and structural information between drug and physiological systems [3]. In the end, outputs of the neural networks are statistically evaluated. In case of successive results, the formal experimental tests will be carried out to confirm the theoretically designed compounds.

QSAR models play an important role in drug development today together with ANN. There are many studies discovering novel, potent, versatile, and safe drugs and agents. These methods have been used for the discovery of safe antibacterial

drugs [7], cholinergic transmission enhancement drugs for patients with Alzheimer's disease [8], and medical treatment in cardiology and oncology [7, 9].

16.4 Other Medicine Discipline Implementation of ANN

ANNs have found a wide range of usages in the medicine over the last two decades. Several thousands of papers have been published about this range of utilization with main fields of applications in medicine covering diagnostics, prognostics, prediction, signal processing, and modeling [2], which are usable almost within any medicinal discipline. ANNs have been used, for example, to generalize in vitro–in vivo relationship to aid pharmaceutical drug development in early stages [10]. The feedforward neural networks have been proven as successful method for determining physicochemical properties such as octanol–water partition coefficient, water solubility, boiling point, vapor pressure, viscosity, surface tension, etc., from molecular structure of the compounds [11].

The image processing ability of ANN is used in radiology and CT colonography, such as the lung nodule detection in chest radiography [12], the classification of lung nodules into benign or malignant in chest radiography [13], or the polyp detection in CT colonography [9, 14]. In these cases, self-organizing maps are the most efficient computational method. The usage of artificial neural networks during evaluation of CT images is to differ nodules from size and shape and can be covered by internal or external inhomogeneities. This can also be covered by the well-designed and trained artificial network.

Artificial neural networks are used for the analysis of electroencephalogram (EEG) signals and classifying those signals according to distribution of energy features into healthy subjects and patients with epilepsy [15–21].

In biomedicine, the ANNs are used for modeling and predicting drug release profiles. There are also successfully developed pharmacokinetic models to predict plasma drug concentration and optimization of drug delivery. Several models are used to estimate concentration of heparin for patients undergoing hemodialysis treatment [8]. The feedforward network is adopted for predicting warfarin doses for patients to include pharmacokinetics and pharmacodynamics depending on factors like age, gender, BMI, genetic variability, etc. [22].

The diagnostics of diseases in the early stages has become very important in medicinal treatment. Supervised ANNs is feasible in the diagnosis of Alzheimer's disease (AD) in the early stages to detect AD biomarkers [23]; ANNs have been used in cancer diagnostics and treatment [24, 25] and in cardiology for prediction of cardiovascular dysfunctions [3].

Conclusion

The computational methods, especially the artificial neural networks present in a variety of designs, show strong potential of pharmaceutical and medicinal application. The wide range of their possible application attributes to their high capability of solving nonlinear complex problems. The ANNs are widely applied to the drug development more like a requisite to achieve business growth and economic profit with cost reduction and faster development of new high-efficiency drugs.

Acknowledgments The paper has been supported by the research project “SP/2014—Economic and Managerial Aspects of Processes in Biomedicine” from FIM, University of Hradec Kralove, Czech Republic.

References

1. Yegnanarayana B. Artificial neural networks. New Delhi: Prentice-Hall of India Pvt Ltd; 2004.
2. Papik K, Molnar B, Schaefer R, Dombovari Z, Tulassay Z, Feher J. Application of neural networks in medicine - a review. *Med Sci Monit.* 1998;4(3):538–46.
3. Luan F, Cordeiro MNDS. Overview of QSAR modelling in rational drug design. Recent trends on QSAR in the pharmaceutical perceptions. Sharjah: Bentham Science Publishers; 2012. p. 194–241.
4. Cheng F, Sutariya V. Application of artificial neural network modeling in drug discovery. *Clin Exp Pharmacol.* 2012;2(3):1–2.
5. Maltarollo VG, Honório KM, da Silva ABF. Application of artificial neural networks in chemical problems. In: Suzuki K, editor. Artificial neural networks - architectures and applications. Rijeka: InTech; 2013. p. 203–23.
6. Speck-Planche A, Klenadrova VV, Cordeiro MNDS. Chemoinformatics for rational discovery of safe antibacterial drugs: simultaneous predictions of biological activity against streptococci and toxicological profiles in laboratory animals. *Bioorg Med Chem.* 2013;15(21):2727–32.
7. Speck-Planche A, Kleandrova VV, Luan F, Cordeiro MNDS. Rational drug design for anti-cancer chemotherapy: multi-target QSAR models for the in silico discovery of anti-colorectal cancer agents. *Bioorg Med Chem.* 2012;20(15):4848–55.
8. Fernandez M, Caballero J, Fernandez L, Sarai A. Genetic algorithm optimization in drug design QSAR: Bayesian-regularized genetic neural networks (BRGNN) and genetic algorithm-optimized support vector machines (GA-SVM). *Mol Divers.* 2011;15:269–89.
9. Munteanu CR, Fernández-Blanco E, Seoane JA, Izquierdo-Novo P, Rodríguez-Fernández JA, Prieto-González JM, Rabunal JR, Pazos A. Drug discovery and design for complex diseases through QSAR computational methods. *Curr Pharm Des.* 2010;16:2640–55.
10. Mendyk A, Tuszyński PK, Polak S, Jachowicz R. Generalized in vitro-in vivo relationship (IVIVR) model based on artificial neural networks. *Drug Des Devel Ther.* 2013;7:223–32.
11. Taskinen J, Yliruusi J. Prediction of physicochemical properties based on neural network modelling. *Adv Drug Deliv Rev.* 2003;55:1163–83.
12. Shiraishi J, Li Q, Suzuki K, Engelmann R, Doi K. Computer-aided diagnostic scheme for the detection of lung nodules on chest radiographs: localized search method based on anatomical classification. *Med Phys.* 2006;33(7):2642–53.

13. Aoyama M, Li Q, Katsuragawa S, MacMahon H, Doi K. Automated computerized scheme for distinction between benign and malignant solitary pulmonary nodules on chest images. *Med Phys.* 2002;29(5):701–8.
14. Paraname V, Admuthe L, Sutar V. Brain tumor detection using method of segmentation based on soft computing. *Brain.* 2013;2(8):3687–95.
15. Krejcar O, Jirka J, Janckulik D. Use of mobile phone as intelligent sensor for sound input analysis and sleep state detection. *Sensors.* 2011;11(6):6037–55.
16. Krejcar O, Penhaker M, Janckulik D, Motalova L. Performance test of multiplatform real time processing of biomedical signals. In *Proceedings of 8th IEEE International Conference on Industrial Informatics, INDIN 2010*; 2010 Jul 13–16; Osaka, Japan; 2010. p. 825–39.
17. Cerny M, Penhaker M. Wireless body sensor network in health maintenance system. *J Electr Electron Eng.* 2013;115(9):113–6.
18. Krawiec J, Penhaker M, Krejcar O, Novak V, Bridzik R. Web system for electrophysiological data management. In *Proceedings of 2010 Second International Conference on Computer Engineering and Applications, ICCEA 2010*; 19. – 21.; Bali Island, Indonesia, Vol. 1; 2010. p. 404–7.
19. Cerny M, Penhaker M. The circadian rhythm monitoring. In *Proceedings of the 5th International Workshop on Wearable and Implantable Body Sensor Network (BSN 2008) IEEE EMBS*; 1–3 Jun 2008; Hong Kong, Hong Kong, s.79–81.; 2008. p. 41–3.
20. Cerny M, Penhaker M. The homecare and circadian rhythm. In *5th Int Conference on Information Technol and Applications in Biomedicine in Conjunction with the 2nd Int Symposium and Summer School on Biomedical and Health Engineering*; 30–31 May 2008; Shenzhen, China; 2008. p. 110–3.
21. Omerhodzic I, Avdakovic S, Nuhanovic A, Dizdarevic K. Energy distribution of EEG signals: EEG signal wavelet-neural network classifier. *World Acad Sci Eng Technol.* 2010;61(1):1190–5.
22. Saleh MI, Alzubiedi S. Dose individualization of warfarin using artificial neural networks. *Mol Diagn Ther.* 2014;18(3):371–9.
23. Di Luca M, et al. Artificial neural networks allow the use of simultaneous measurements of Alzheimer Disease markers for early detection of the disease. *J Transl Med.* 2005;3(30):1–7.
24. Motalleb G. Artificial neural network analysis in preclinical breast cancer. *Cell J.* 2014;15(4):324–31.
25. Nakajima K, Nakajima Y, Horikoshi H, Ueno M, Wakabayashi H, Shiga T, Yoshimura M, Ohtake E, Sugawara Y, Matsuyama H, Ebenbrandt L. Enhanced diagnostic accuracy for quantitative bone scan using an artificial neural network system: a Japanese multi-center database project. *EJNMMI Res.* 2013;3(1):83.

Chapter 17

SOC Prediction Method of a New Lithium Battery Based on GA-BP Neural Network

Kai Guan, Zhiqiang Wei, and Bo Yin

Abstract The prediction of a battery's state of charge (SOC) is one of the key tasks of battery management. Lithium battery internal chemical reactions are complex and have many factors; its SOC prediction has strong nonlinear characteristics. This paper discussed a SOC prediction model which is based on hybrid genetic algorithm and BP neural network. Set BP neural network's training error as genetic algorithm fitness value, and then iterate to find the optimal individual as the neural network initialization thresholds and weights. Simulation results show that this method can accurately predict the new kind of a lithium battery's SOC and have higher accuracy compared with BP neural network.

Keywords State of charge • Genetic algorithm • BP neural networks • Prediction method

17.1 Introduction

A battery's state of charge is an important parameter characterizing the state of the battery. It cannot be directly measured during the charging and discharging of the battery. SOC prediction has a strong nonlinear characteristic and is difficult to describe accurately and mathematically [1]. Artificial neural networks can imitate multiple input and output functions and have some good characteristics, such as high nonlinearity, fault tolerance, and robustness. It can give the corresponding output for external excitation and is very suitable for a battery's SOC prediction [2]. BP neural network's optimization is based on the steepest descent method which has slow convergence speed and is easy to fall into local minimum point [3].

This paper is focused on hybrid genetic algorithm and BP neural network to predict lithium battery SOC. Using genetic algorithm to optimize the initial parameters of BP neural network can enhance the generalization ability of BP neural network [4]. Some simulations and experiments have been done.

K. Guan (✉) • Z. Wei • B. Yin
College of Information Science and Engineering, Ocean University of China,
266100 Qingdao, Shandong, China
e-mail: oucguankai@126.com

17.2 Related Work

The widely recognized definition of SOC is defined by the US Advanced Battery Association (USABC); SOC is the acronym for state of charge; it refers to a certain discharge rate, the ratio of the remaining charge and the rated capacity [5]. SOC is considered 100 % when battery energy reaches saturation at a certain temperature and 0 % when battery energy can no longer be released [6]. SOC is calculated as

$$\text{SOC} = \frac{\text{Remaining charge}}{\text{Maximum discharge capacity}} = \frac{Q(I_m) - Q(I_n)}{Q(I_m)} \quad (17.1)$$

$$Q(I_n) = t \int I_n dt \quad (17.2)$$

where Q_m refers to the maximum discharge capacity of battery when discharged with a constant current I and $Q(I_n)$ refers to the released battery power when discharged with a constant current I .

The discharge test method is the most reliable battery state-of-charge estimation method. It takes a long time and is not on line [7].

AH Metrology: The current flowing into the battery is integrated by time to calculate the inflow and outflow of the total battery charge [8]; it is calculated as

$$\text{SOC} = \text{SOC}_0 - \frac{1}{C_E} \int_0^t idt \quad (17.3)$$

where SOC_0 is the initial SOC value and C_E is the battery rated capacity.

Open-Circuit Voltage Method: When the battery is unused for a long time, the voltage and the battery SOC form a relatively stable linear function. The Kalman filtering method uses linear minimum mean square error criterion, treats the internal state of the battery SOC as a management system variable, and uses estimates of the last moment plus the value of real-time measurements to recursively approach real-time estimation [9].

Neural Network Method: Neural networks have nonlinear characteristics and have a good ability to learn. Using the neural network for SOC prediction, the model is generally constituted by an input layer, an intermediate layer, and an output layer. The accuracy of the training data samples, sample size, and training methods will have a significant impact on the network's accuracy [10].

17.3 SOC Prediction Method Based on GA-BP Neural Network

The neural network is a function approximation method; the most widely used neural network is a BP (error back propagation) neural network; it is a three-layer feed forward network; the output of the previous layer is the input of next layer; each input node has a weight value. A three-layer network model is shown in Fig. 17.1. According to the Kolmogorov theorem, three-layer neural networks can approximate a continuous function with arbitrary precision [11]. A three-layer BP neural network is used to predict the battery SOC. The model is shown in Fig. 17.2.

Genetic algorithm is a randomized iterative probabilistic search algorithm. This algorithm is a kind of imitation of the law of biological evolution. Genetic algorithms do not include the form of the problem; it changes the gene configuration to achieve overall optimization of the problem, and it has inherent parallelism and better global optimization capability.

Use genetic algorithm to optimize the BP neural network. The length of an individual is determined by the structure of the BP neural network. Each individual in the population consists of a set of network weights and thresholds. Genetic

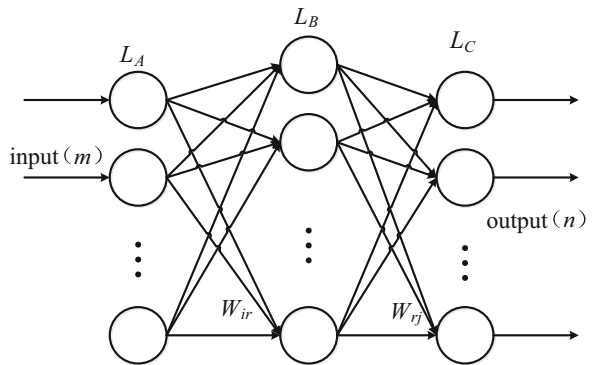


Fig. 17.1 Three-layer BP neural network

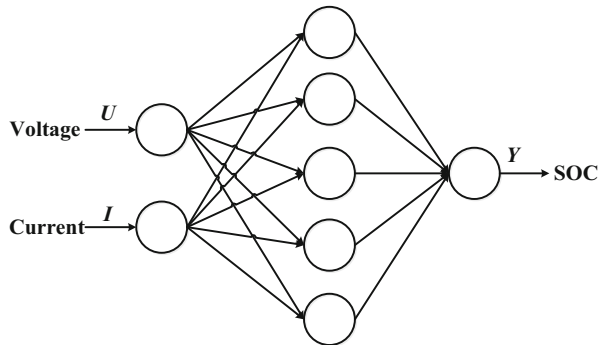


Fig. 17.2 BP neural network SOC prediction model

```

define BP neural network structure
load input data
for i ← 1 to sizepop //sizepop is the population size
    individuals.Code(i)=Code(lenchrom) //code randomly
    individuals.fitness(i)=BP neural network training error //calculate fitness value
end
bestchrom = min(individuals.fitness) //find the best chromosome
for i ← 1 to mangan //maxgen is the maximum evolution generation
    Select() //do select operation
    Cross() //do cross operation
    Mutation() //do mutation operation
    for j ← 1 to sizepop
        individuals.fitness(j)=BP neural network training error //calculate fitness value
    end
    bestchrom = min(individuals.fitness) //update best chrom
    trace the bestfitness value and best individuals //trace best individual in gen j
end
Initialize network weight and threshold = best individual x
net = new GA-BP neural network
set train.epochs and train.goal
net = train(net,inputn,outputn) //GA-BP neural network training
return simulation results

```

Fig. 17.3 Genetic algorithm to optimize BP neural network

algorithm uses selection, crossover, and mutation operations to find the best fitness value and the best individual. The BP neural network takes the best individual as the initialization weights and thresholds, and then the network was trained to predict the function output. The process step pseudo-code is shown in Fig. 17.3.

The network structure model has 15 weights and 6 thresholds, so the genetic algorithm individual code length is 21. Each individual is a real number string.

Individual fitness function is like

$$F = k \left(\sum_{i=1}^n \text{abs}(y_i - o_i) \right) \quad (17.4)$$

where n is the network output nodes, y_i is the expected output value of the i node, o_i is the predicted output value of the i node, and k is the coefficient.

The selection probability of each individual P_i can be calculated as (17.5)

$$P_i = \frac{k}{F_i \sum_{j=1}^N f_j} \quad (17.5)$$

F_i is the fitness value of individual i and k is the coefficient. N is the number of individuals of the population.

Cross operation is calculated as

$$a_{kj} = a_{kj}(1 - b) + a_{lj}b \tag{17.6}$$

$$a_{lj} = a_{lj}(1 - b) + a_{kj}b \tag{17.7}$$

Mutation operation is calculated as

$$a_{ij} = \begin{cases} a_{ij} + (a_{ij} - a_{\max}) \times r_2(1 - g/G_{\max})^2 & r > 0.5 \\ a_{ij} + (a_{\min} - a_{ij}) \times r_2(1 - g/G_{\max})^2 & r \leq 0.5 \end{cases} \tag{17.8}$$

a_{\max} is the upper bound of gene a_{ij} , a_{\min} is the lower bound of gene, r_2 is a random number, g is the current number of iterations, and G_{\max} is the maximum number of evolution.

17.4 Application Instance

Lithium-ion battery data was collected from a new lithium-ion battery of soft carbon negative materials. The carbon anode material is micron and spherical. And it is made up of multiparticles with secondary granulation technology. The charging and discharging properties of materials were improved by shortening the lithium migration path in anode material particles. The charging and discharging curve is shown in Fig. 17.4.



Fig. 17.4 Battery charging and discharging curve

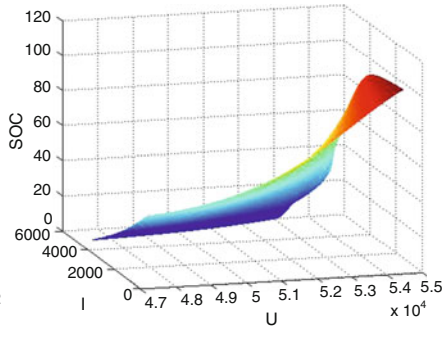
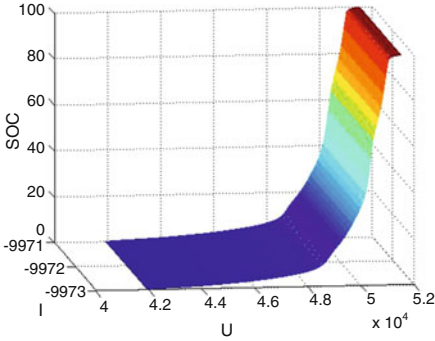
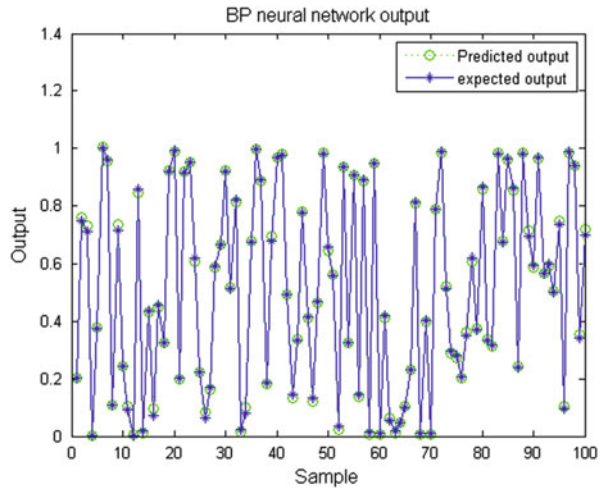


Fig. 17.5 Experimental data

Fig. 17.6 BP neural network predicting output



With the sample data, we carried out a median filter to remove noises and used the difference method to meet the shortage of samples. The results of data processing are shown in Fig. 17.5.

17.4.1 Simulation Results Based on BP Neural Network Model

Through repeatedly testing the parameters of the BP neural networks, we set the number of training iterations as `net.trainParam.epochs = 100`, the learning rate as `net.trainParam.lr = 0.1`, and the training goal as `net.trainParam.goal = 0.00004`. The BP neural network model was built to train and test samples according to the network structure settings. The prediction result of the output with the trained BP neural network using the test data is shown in Fig. 17.6. And errors of prediction output and expected output are like that shown in Fig. 17.7.

Fig. 17.7 BP neural network predicting error

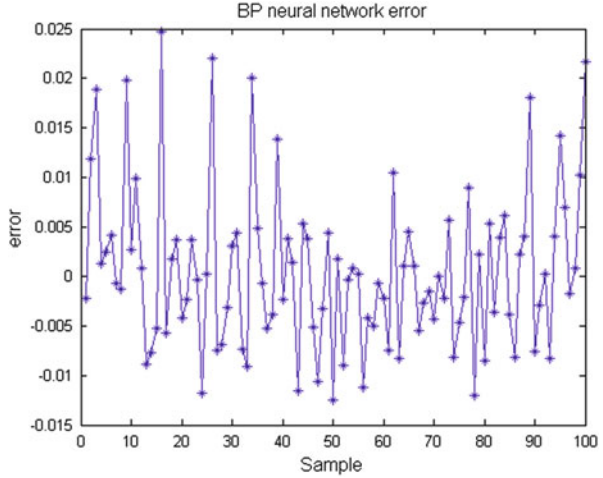
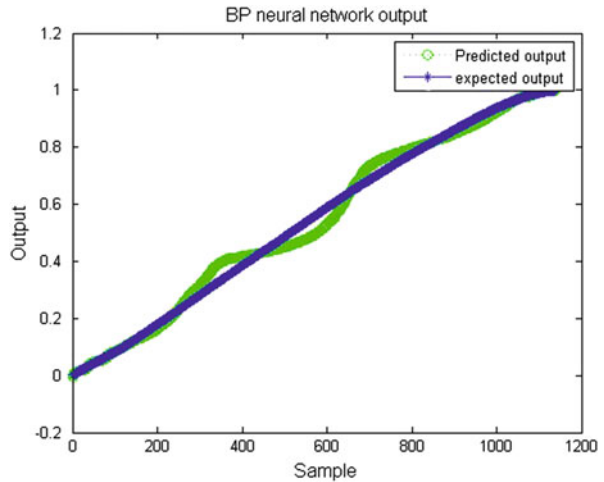


Fig. 17.8 BP network sample predicting output



As shown in Figs. 17.8 and 17.9, the BP neural network trained with the actual training data has good effectiveness on the prediction output. With the parameters of the error feedback network revising, the prediction errors decrease gradually. The maximum error is ± 0.06 , and the average error is 0.02.

The BP neural network has a high fitting capacity for nonlinear functions, but there are still some errors of prediction results. The predicting error of some samples is large.

Fig. 17.9 BP network sample predicting error

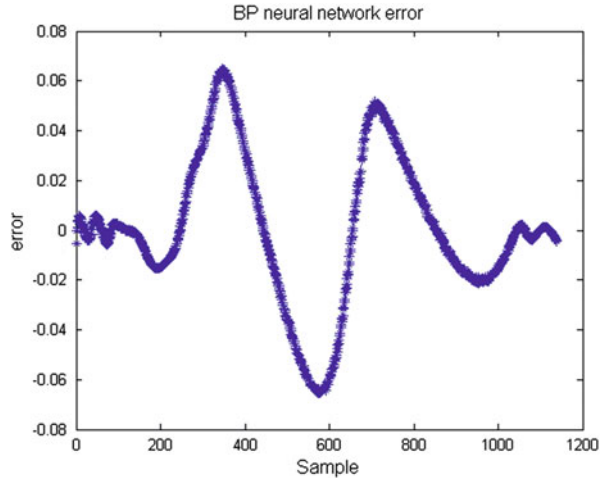
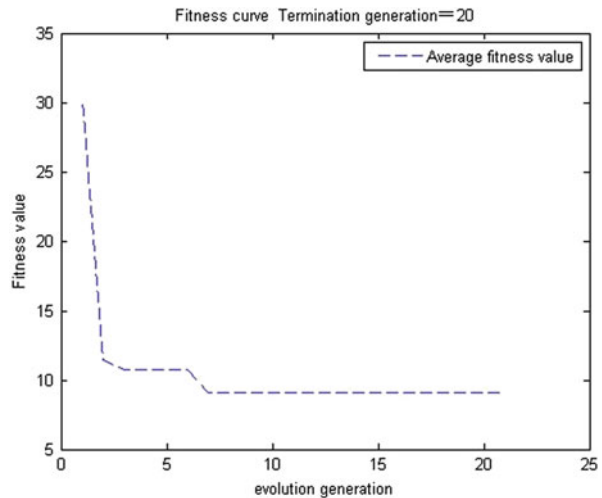


Fig. 17.10 Genetic algorithm fitness curve



17.4.2 Optimization of Simulation Results with Genetic Algorithm

Set the individual length of genetic algorithm as 21 bits. Randomly generate the initial population, and code it as 21 bits real vector. The individual fitness value is the total predicting error of the BP neural network. Perform selection, crossover, and mutation cyclically according to the evolutionary generation. Changes of the best individual fitness value in the genetic algorithm optimization process are shown in Fig. 17.10.

The optimal initial weights and thresholds of the BP neural network optimized by genetic algorithm are shown in Table 17.1.

Fig. 17.11 GA-BP network predicting output

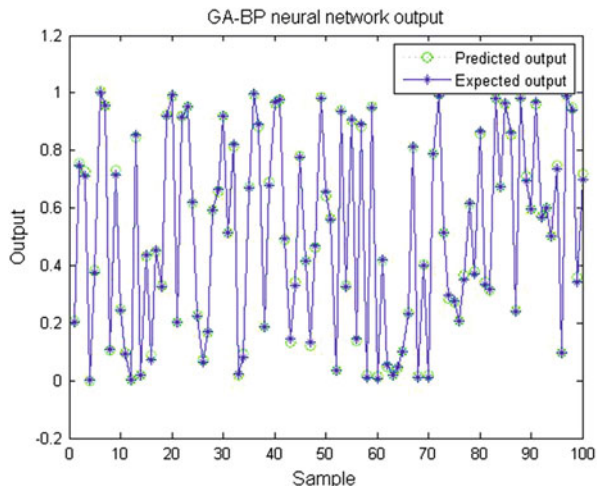
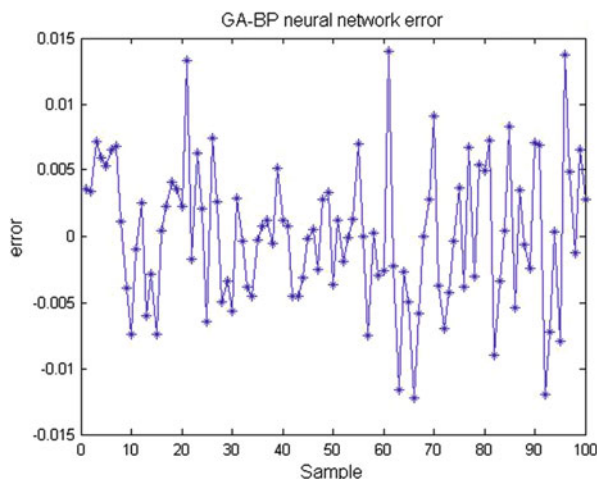


Fig. 17.12 GA-BP network predicting error



Assign the optimal initial weight and the threshold value to the neural network. The trained network optimized by genetic algorithm is denoted as the GA-BP neural network. The prediction result is shown in Fig. 17.11. And errors of prediction are like that shown in Fig. 17.12.

As shown in Figs. 17.13 and 17.14, the GA-BP neural network trained with the actual training data has good effectiveness on the prediction output. The maximum error is ± 0.025 , and the average error is 0.012.

Fig. 17.13 GA-BP sample predicting output

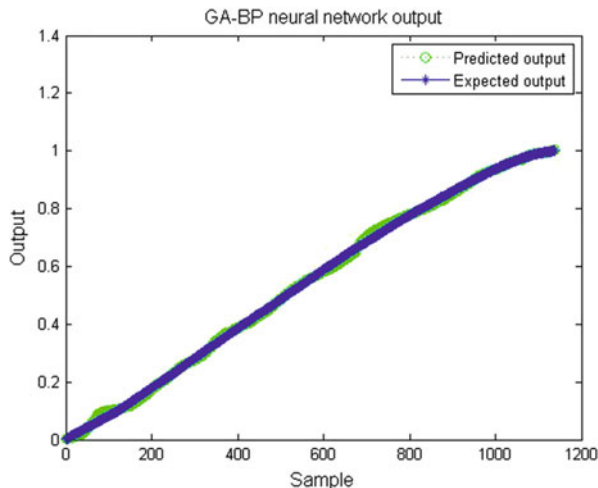
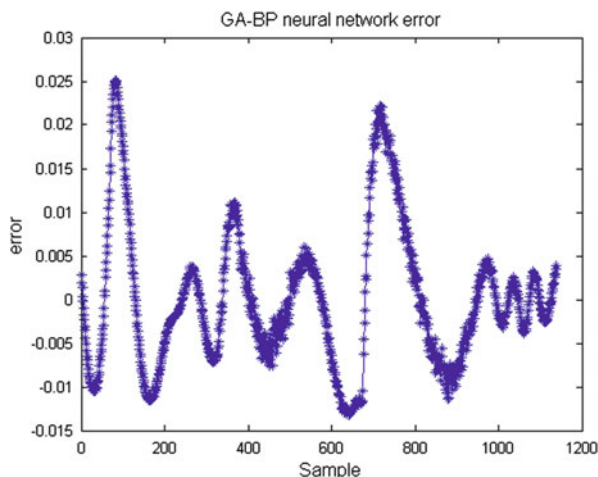


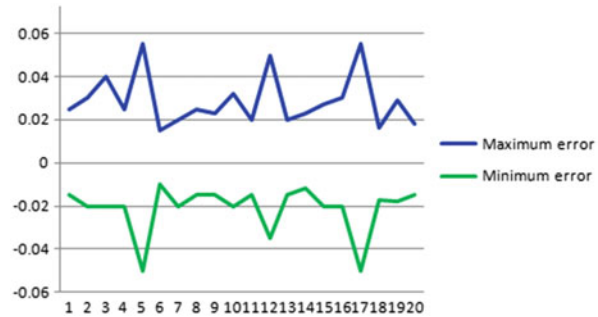
Fig. 17.14 GA-BP sample predicting error



We tested this GA-BP neural network 20 times based on the 1,038 samples. Every training error is shown in Fig. 17.15. The maximum error was always smaller than the error trained by the BP neural network.

The GA-BP neural network has a high fitting capacity for nonlinear functions. The prediction accuracy of the BP neural network optimized by genetic algorithm is higher than the BP neural network. And the mean squared error is significantly improved.

Fig. 17.15 20 training errors of GA-BP neural network



Conclusion

This paper establishes a SOC prediction model which is based on hybrid genetic algorithm and BP neural network to predict a lithium battery's SOC. And the initial weights and thresholds of neural network optimized with the genetic algorithm are applied to SOC prediction of a new sort of lithium battery. Experimental results show that the SOC prediction method based on the GA-BP neural network is feasible. For selected samples, the maximum error of the improved algorithms decreases from 6 to 2.5 % compared with the BP neural network prediction method. And the average error is reduced from 2 to 1.2 %. The GA-BP neural network prediction method has higher accuracy and stability. The prediction precision can meet the practical requirement and is of important practical value.

Acknowledgments This work was financially supported by National 863 Plan Project (2014AA052303-5).

References

1. Kumar P, Kolar AK. Effect of cathode design on the performance of an air-breathing PEM fuel cell. *Int J Hydrogen Energy*. 2010;35(2):671–81.
2. Wu C, Wang F. The research an application on neural network. Harbin: Northeast Agricultural University; 2007 (In Chinese).
3. Li Y. Analysis and improvement applications of BP neural network. Huainan: Anhui University of Science and Technology; 2012 (In Chinese).
4. Wang J, Zhou S, Ye S. Weather threat modeling and assessment based on genetic algorithm and BP neural networks. *Institute of Meteorology. PLA Univ Sci Technol*. 2012;19(03):74–7 (In Chinese).
5. Li H. Research on battery management system of electric vehicle. Zibo: Shandong University of Technology; 2008 (In Chinese).

6. Ma Y, Chen Q, Qi Z. Research on the SOC definition and measurement method of batteries used in Evs. *J Tsinghua Univ (Sci&Tech)*. 2001;41(11):95–7 (In Chinese).
7. Lin C, Wang J, Chen Q. Methods for state of charge estimation of EV batteries and their application. *J Battery Bimonthly*. 2004;34(05):376–8 (In Chinese).
8. Ma A. Design of smart management system of Li-ion battery. Beijing: Beijing Jiaotong University; 2008 (In Chinese).
9. Pan W, Liu X. Research on estimating SOC of lithium-ion battery based on improved Kalman filter. *Comput Simul*. 2014;31(03):148–50 (In Chinese).
10. Huang Y, Tang H. Prediction of lithium-ion battery SOC in EV based on genetic neural network. *J Mech Electr Eng*. 2013;30(10):1255–8 (In Chinese).
11. Shi P, Bu C, Zhao Y. The ANN models for SOC/BRC estimation of Li-ion battery//2005 I.E. International Conference on Information Acquisition. IEEE; 2005. p. 560–4 (In Chinese).

Chapter 18

Compressed Sensing for Channel State Information (CSI) Feedback in MIMO Broadcast Channels

Yuan Liu and Kuixi Chen

Abstract In this paper, we proposed a new method to compress the CSI feedback. When the channel matrix is correlated, the DCT matrix works as a sparsifying basis to transform the channel matrix into a sparse form; the sparse signal is a feedback to the transmitter and reconstructed via the subspace pursuit (SP) recovery algorithm. Both theoretical analyses and simulation results show that the new method can introduce a huge computation cost reduction compared with the OMP algorithm and the codebook-based feedback scheme.

Keywords MIMO • Compressed sensing • CSI feedback • Codebook • Orthogonal match pursuit (OMP) • Subspace pursuit (SP)

18.1 Introduction

Compressed sensing (CS) is also called as compressive sampling or sparse sampling [1]. It emerges as a new sampling theory in sparse signal processing. It is a theory about signal recovery from incomplete and inaccurate measurements [2]. CS has been widely applied in mathematics and image processing [3–5]. In the field of CQI feedback compression, much work has also been done in recent years. Currently, the utilization of Compressed sensing for channel state information (CSI) feedback in MIMO broadcast channels can be divided into two groups.

Most of the methods are based on user selection. Section 18.1.2 discusses applications based on user selection.

There is another kind of methods whose guiding ideology is to create sparse signals via a proper transform, such as DCT, DFT, or wavelet transform, just like in Sect. 18.1.2.

Y. Liu (✉)

School of Information and Electronics, Beijing Institute of Technology, 100081 Beijing, China
e-mail: liuyuan@bit.edu.cn

K. Chen

Beijing NARI Smartchip Microelectronics Technology Company Limited,
100081 Beijing, China

18.2 New Work and Theory

Based on some paper works, I proposed that we can utilize the subspace pursuit (SP) signal recovery algorithm in the massive MIMO system, where the transmitter antenna array and receiver antenna array are spatially correlated [6–8]. I compared the CQI feedback overhead between the codebook-based scheme and CS-based scheme, and I also compared their computation complexity both in theory and in simulation.

18.2.1 System Model

Transmitter

4-QAM and zero-forcing beam forming are adopted.

Channel

Channel matrix is spatially correlated and changes every frame.

Receiver

- *Codebook-based scheme*
Search the most similar channel matrix in a RVQ codebook.
- *CS-based scheme*
The DCT matrix is taken as the sparsifying basis to transform the channel matrix into a sparse signal. OMP and SP signal recovery algorithms are adopted respectively (Fig. 18.1).

18.2.2 Comparison of Complexity

18.2.2.1 Complexity of Codebook-Based CQI Feedback

According to the conclusion in a paper, the rate gap between ideal value and practical value will converge to zero if the feedback bits B is scaled with SNR at a rate of greater than $(M - 1)\log_2 P$ [4].

We assume that the number of transmitter antennas and receiver antennas is both equal to M . P is the SNR.

For convenience, we write the formula $(M - 1)\log_2 P$ as

$$\frac{M \times \text{SNR}_{\text{dB}}}{10} \times \log_2 10 \quad (18.1)$$

and the length of codebook as

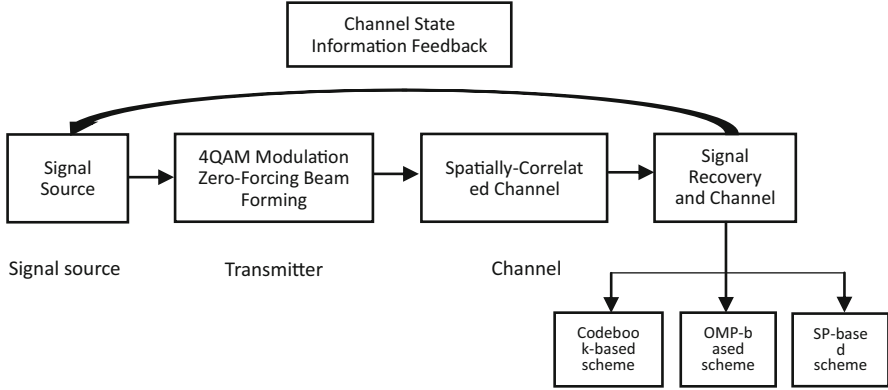


Fig. 18.1 System model

$$L = 2^B = 2^{\frac{M \times \text{SNR}_{\text{dB}}}{10} \times \log_2 10} \tag{18.2}$$

For each receiver, it needs L iterations to find out the most similar channel matrix in the codebook. So the total number of iterations is ML .

In each iteration, the complexity is proportional to M^2 , because the size of both the real channel matrix and the channel matrix stored in the codebook will change with M . Finally, the complexity of the codebook-based CQI feedback scheme can be represented as

$$O\left(M^3 \times 2^{\frac{M \times \text{SNR}_{\text{dB}}}{10} \times \log_2 10}\right) \tag{18.3}$$

18.2.2.2 Complexity of the SP Algorithm

Assume that x is a K -sparse signal, with its element

$$|x_1| \geq |x_2| \geq |x_3| \geq \dots |x_K| \geq 0 \tag{18.4}$$

And $x_j = 0$ for any other $j > K$.

We define

$$\rho_{\min} \frac{|x_K|}{\|x\|_2} = \frac{\min_{1 \leq i \leq K} x_i}{\sqrt{\sum_{i=1}^K x_i^2}} \tag{18.5}$$

Let n_{it} denote the number of iteration that we need to reconstruct x .

Then we have

$$n_{it} \leq \min\left(\frac{-\log\rho_{\min}}{-\log C_K} + 1, \frac{1.5K}{-\log C_k}\right) \quad (18.6)$$

in which

$$C_K = \frac{2\delta_{3K}(1 + \delta_{3K})}{(1 - \delta_{3K})^3} \quad (18.7)$$

δ_{3K} is the requirement of the RIP constraint.

$$K = M^2 \quad (18.8)$$

There are many methods to reduce the computation cost in the CM and projection process. But if we just consider most general framework, the complexity of the SP algorithm in each iteration can be represented as $O(mN + mK^2)$. So the total complexity is given by $O(m(N + K^2) \log K)$ for compressible sparse signals and $O(m(N + K^2)K)$ for arbitrary sparse signals.

When the signal is very sparse, the upper bound of complexity can be written as $O(mN \log K)$ for compressible sparse signals and $O(mNK)$ for arbitrary sparse signals. Finally, the complexity of the SP algorithm can be represented as

$$O(mN \log K = O(2mN \log M)) \quad (18.9)$$

18.2.2.3 Complexity of the OMP Algorithm

OMP always needs K iterations to exactly reconstruct a sparse signal. For a very sparse signal, the complexity of each CM operation is $O(mN)$, and the complexity of projection process is so marginal that we can take the total complexity of the OMP algorithm as $O(mKN)$

$$O(mKN) = O(mM^2N) \quad (18.10)$$

18.3 Results and Findings

Figure 18.2 is plotted via theoretical values in Eqs. (18.8) and (18.9). It demonstrates that to reach the maximum throughput, the complexity of the OMP algorithm should be much larger than that of the SP algorithm.

Figure 18.3 is plotted via model trial values. It demonstrates that to reach the maximum throughput, the complexity of the OMP algorithm should be much larger than that of the SP algorithm. Complexity is reflected via calculating running time in Matlab.

Figure 18.4 is plotted via model trial values. It demonstrates that to reach the maximum throughput, the complexity of the codebook-based feedback algorithm should be much larger than that of the CS-based feedback algorithm. The SNR is

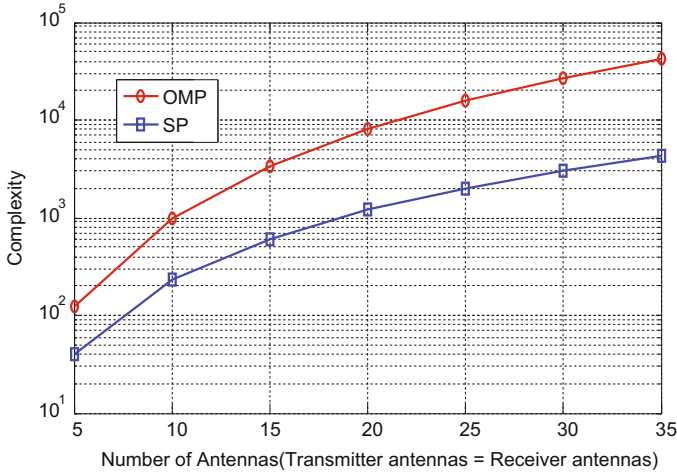
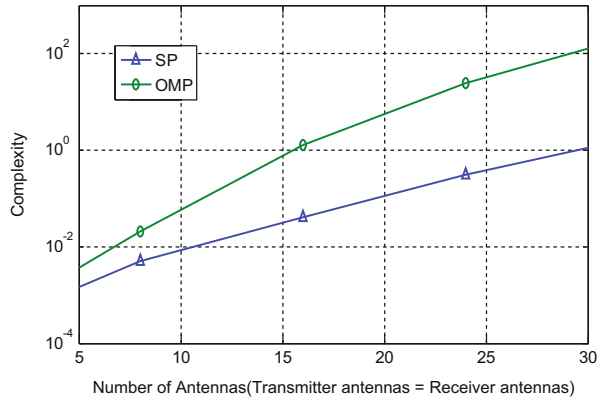


Fig. 18.2 Number of antennas (transmitter antennas = receiver antennas)

Fig. 18.3 Number of antennas (transmitter antennas = receiver antennas)



larger; the difference is more obvious. Complexity is reflected via calculating running time in Matlab.

Figure 18.5 shows there is an intersection of two surfaces, which means that under the condition that the number of antennas is very large and the SNR is very small, the performance of the codebook-based feedback scheme can slightly surpass that of the SP algorithm. For most occasions, complexity of the SP algorithm is much lower than that of the codebook-based feedback scheme. Especially at high SNR, this advantage is more obvious.

Fig. 18.4 SNR(dB)

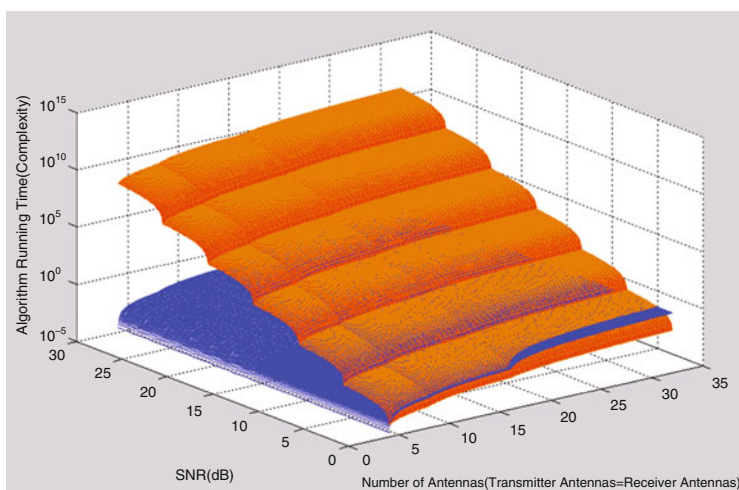
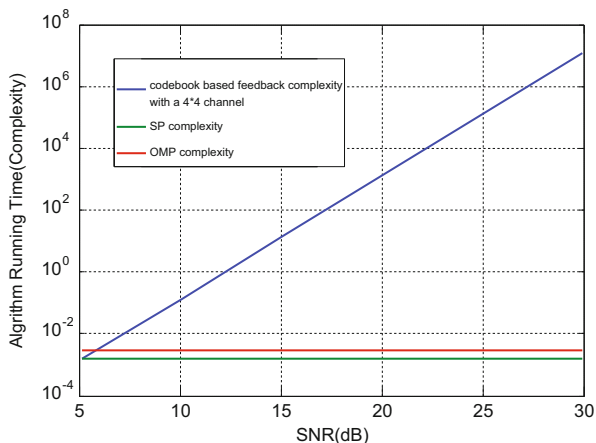


Fig. 18.5 SNR(dB)

Conclusion

My project conducted an in-depth research on the application of the CS technique in the CQI feedback. By both theoretical calculation and experimental simulation, we can get a conclusion that when the transmitter and receiver have a spatially correlated antenna array, the calculation complexity of the CS algorithm is much lower than that of the codebook-based feedback scheme. Furthermore, the SP algorithm has a lower computation complexity than the OMP algorithm.

References

1. Baraniuk RG. Compressive sensing. *IEEE Signal Process Mag.* 2007;24(4):118–24.
2. Candes E, Romberg J, Tao T. Stable signal recovery from incomplete and inaccurate measurements. *Commun Pure Appl Math.* 2006;59(8):1207–23.
3. Tomic I, Frossard P. Dictionary learning. *IEEE Signal Process Mag.* 2011;28(2):27–38.
4. Candès EJ, Romberg J, Tao T. Robust uncertainty principles: exact signal reconstruction from highly incomplete frequency information. *IEEE Trans Inform Theory.* 2006;52(1):489–509.
5. Donoho DL. Compressed sensing. *IEEE Trans Inform Theory.* 2006;52(4):1289–306.
6. Luo P-H, Kung HT, Ting P-A. Compressive sensing based channel feedback protocols for spatially-correlated massive antenna arrays. In *WCNC, 2012 IEEE*; 2012. p. 492-497.
7. Jindal N. MIMO broadcast channels with finite-rate feedback. *IEEE Trans Inform Theory.* 2006;52:5045–60.
8. Dai W, Milenkovic O. Subspace pursuit for compressive sensing signal reconstruction. *IEEE Trans Inform Theory.* 2009;55(5):2230–49.

Chapter 19

Implementation and Performance Evaluation of the Fully Enclosed Region Upper Confidence Bound Applied to Trees Algorithm

Lin Wu, Ying Li, Chao Deng, Lei Chen, Meiyu Yuan, and Hong Jiang

Abstract While the playing performance of UCT (upper confidence bound applied to trees) algorithm is nearly the same as that of top professionals on a 9×9 Go board, its performance on a 19×19 board still needs great improvements. One possible way is to use multiple local UCT searches in parallel by the same computing resources to reach deeper depth. This paper tries to do some tentative work in this regard. After modifying Fuego's implementation of global UCT search algorithm, we have implemented a fully enclosed region UCT local search algorithm and tested it by 64 standard tsume go problems. Present results show that the fully enclosed region UCT can reduce original branching factors from 5–16 to 2.3 without using any domain knowledge on Go. According to the accuracy of testing results and computing speed, it is promising to do further research on running multiple local UCT searches in parallel.

Keywords Search algorithm • Computer Go • Fully enclosed tsume go • Minimum number of simulation

L. Wu (✉) • M. Yuan • H. Jiang
School of Information Engineering and Automation, Kunming University of Science & Technology, 650051 Kunming, China

Computer Application Key Laboratory of Yunan Province, Kunming University of Science & Technology, 650051 Kunming, China
e-mail: wulin5050@gmail.com

Y. Li • C. Deng • L. Chen
School of Information Engineering and Automation, Kunming University of Science & Technology, 650051 Kunming, China

19.1 Introduction

Computer Go features 40 years of history in the field undergoing approximately three development stages: the pattern matching, the machine learning, and the UCT algorithm. Before 2006, the performances of computer Go programs were pretty weak until a French research team introduced the UCT algorithm. While the performance of the UCT algorithm is approaching top professionals on 9×9 , there is a long way to go for the UCT algorithm to beat professionals on 19×19 . In 2010, Junxun Zhou (professional 9 dan) rated Many Faces of Go as amateur 1 dan whose performance was the best on 19×19 at that time [1].

Why does the performance decline so much when changing board from 9×9 to 19×19 ? Based on the analysis of high-quality games between professionals and top UCT-based programs, we've found that the UCT algorithm performs poorly when multiple active local battles appear at the same time [1, 2]. In order to address this issue, many algorithms are proposed. Some researchers use dynamic simulation [3, 4]. Some propose to combine the UCT algorithm with the proof number search or the alpha-beta search. Our paper follows the second one and simplifies it by using the same type of search algorithm: global UCT search and local UCT search algorithm. Our approach is tested by a standard tsume go test set [5] because tsume go is the most basic and important Go local tactical problem [6].

The fully enclosed region UCT algorithm is implemented upon modifying the Fuego source code and tested against GoTools by a standard test set published in 2000. GoTools is a computer Go program specialized to solve tsume problems. It is based on alpha-beta search and uses a lot of domain knowledge to reduce the search scope [5]. It is shown that the fully enclosed region UCT algorithm is comparable to GoTools in accuracy and computing speed; however, it reduces effective branching factors from 5–16 to 2.3 without using any domain knowledge.

Section 19.2.1 explains the UCT algorithm. Section 19.2.2 introduces the fully enclosed region UCT algorithm and its implementation in Fuego. Section 19.2.3 defines the minimum number of iterations. Section 19.3 gives the test results. And Section 19.4 makes a conclusion.

19.2 The Fully Enclosed Resign UCT Algorithm

19.2.1 UCT Algorithm

Traditional search techniques have not been able to achieve meaningful results in the field of computer Go as it has a lot of branching factors [7, 8]. The UCT algorithm has changed this situation. It is a special Monte Carlo search algorithm including the in-tree selection policy, the default play-out policy, and the backup.

The tree policy selects actions by using UCB1 algorithm, which maximizes an upper confidence bound on the value of actions [9]. Specifically, the action value is

augmented by an exploration bonus that is highest for rarely visited state-action pairs, and the tree policy selects the action that maximizes the augmented value.

$$r_i = v_i \pm C \sqrt{\frac{2 \ln \left(\sum_i T_i \right)}{T_i}} \quad (19.1)$$

$$a = \max r_i \quad (19.2)$$

where v_i is the average value of all the simulation of i . T_i is the simulation numbers. C is a constant. The role of C is to use the balance exploitation and the exploration of the UCT algorithm [10].

When the UCT algorithm reaches a leaf node, it will use the default play-out policy to continue the search until the end of the game. The value of the leaf node is 1 when black wins or 0 otherwise. The simplest method is to choose the next step randomly, but most programs tend to use a more complex play-out policy [11]. What is more, it will obtain new v and T values; the UCT algorithm will update the T value and v value of all internal nodes of the path. The formula is

$$v = \frac{\sum_i v_i T_i}{T} \quad (19.3)$$

$$T = \sum_i T_i \quad (19.4)$$

where v is the weighted average of all child nodes' observations backup value v_i and weight is T_i/T . T is visit times of a parent node.

19.2.2 The Fully Enclosed UCT Algorithm and Its Implementation in Fuego

In order to make the UCT algorithm solve fully enclosed tsume problem, we make some modifications of the UCT algorithm:

1. Limit the expansion: these new leaf nodes add not all legitimate nodes, but in a fully enclosed domain of legitimate nodes.
2. Limit the search scope: the next step is not the optional step in all legitimate nodes, but in a fully enclosed domain of legitimate nodes.
3. Modify the evaluation method: the result evaluation is $A_{\text{black}} / (A_{\text{black}} + A_{\text{white}})$. A_{black} is the number of black; A_{white} is the number of white.

We call the modified UCT algorithm as the fully enclosed UCT algorithm.

We modify the Fuego code to achieve the closed domain UCT algorithm. Fuego is the best one in the open-source UCT Go program [1].

19.2.2.1 Implementation of Limit Expansion

Fuego encapsulates board information in Board class and accesses each legitimate point by a variety of Iterator class in Board class. In order to limit the expansion of the scope, we introduce a new class called RestrictedIterator to access those legitimate points in the enclosed domain. Then we produce GoUctRestrictedSearch imitate GoBoard class. Correspondingly, we construct GoUctRestrictedSearchState and GoUctRestrictedSearchStateFactory. A limited extended range is achieved by calling the RestrictedIterator class instead of modifying the Iterator class.

19.2.2.2 Implementation of Limiting the Search Scope

Fuego uses GoUctBoard class in simulation phase. In simulation phase, Fuego uses GoUctBoard class to improve the simulation efficiency. In order to limit the search scope, we construct GoUctRestrictedBoard class to imitate it and rewrite Iterator class. The Iterator class only visits a candidate point in the enclosed domain without considering the points outside the region. The default play-out policy of Fuego is implemented in GoUctPlayoutPolicy <BOARD>. In default play-out policy, we use the GoUctRestrictedBoard class to limit the search scope in GoUctBoard class.

19.2.2.3 Implementation of Modifying the Assessment Methods

We structure GoUctRestrictedSearchState template class by imitating the template class GoUctGlobalSearchState. We change the functions of evaluate and use the evaluation method of the enclosed domain UCT algorithm.

19.2.3 Minimum Number of Iteration

In order to measure the time complexity of the enclosed region UCT algorithm, we propose a new concept: the minimum number of iterations.

Definition 1 we call the simulation number T sufficient for a given UCT algorithm A , and for any given problem Q , if the $T' > T$, when running T' times, the solutions are always the optimal one.

Definition 2 If T is the smallest one of all simulation algorithms for Q in algorithm A , we call the simulation number T the smallest simulation number $T_{\min}(A, Q)$ for the given UCT algorithm A and the given problem Q .

$T_{\min}(A, Q)$ reflects the difficulty by using the UCT algorithm A for solving a given problem Q . The true solution is unknown, so we cannot directly calculate the minimum simulation number $T_{\min}(A, Q)$. In order to simulate the actual use of the enclosed region UCT algorithm, we use the following methods to obtain $\hat{T}_{\min}(A, Q)$. It is approximate to $T_{\min}(A, Q)$. When the search depth is K , it will check the former K steps of the UCT search branches for every T seconds. If it never changes for N times, we consider the UCT search reaching a steady state. We call the simulation times as K -order stable simulation times. And the simulation number at the first time is the k -order actual minimum simulation number, which is denoted as $\hat{T}_{\min}(A, Q)$. In the test, we use the parameters: $k = 3$, $TI = 0.25$, and $N = 6$.

19.3 Test Results of Fully Enclosed UCT Algorithm

19.3.1 Comparison with GoTools

In this paper we use these 64 enclosed tsume Go problems to test our fully enclosed region UCT algorithm [5]. The results are shown in Table 19.1.

In UCT- $\{4, 8, 12, 16\}$ test mode, the UCT algorithm spends $\{0.0625 \text{ s}, 0.125 \text{ s}, 0.1875 \text{ s}, 0.25 \text{ s}\}$ to record results. We may find that the running time has a positive influence on the correct rate. In comparison with UCT- $\{12, 16\}$ and GoTools, the correct rate of the domain UCT algorithm is 78.1 % and 71.9 % as to GoTools. UCT-MinIteration uses 140 s to solve 64 problems in which 88 s accounted for 62.8 % to verify whether the result is stable. The fully enclosed region UCT algorithm actually used only 52 s to solve 64 problems with the average time of 0.81 s/problem. So the fully enclosed region UCT algorithm can solve 88.2 % of problems, higher than the best results of 79.7 % (SC1) of professional players. And the time it used is only half than professional players (JB).

Table 19.1 Comparison of fully enclosed region UCT, GoTool, and human professional players

Player	Time(s)	Failure numbers	Rating
JB	300	30	4 dan
SC1	927	13	5 dan
GoTools	15	18	None
UCT-4 s	4	25	None
UCT-8 s	8	19	None
UCT-12 s	12	1	None
UCT-16 s	16	14	None
UCT-MinIteration	52	11	None
UCT-StableIteration	140	11	None

19.3.2 Analysis of the Minimum Number of Iterations $T_{min}(A, Q)$

There is a practical question: which factor of a tsume go problem is related to the time complexity? In Sect. 19.3.1, more than 62.8 % of the time is used to examine the stability of the simulation results in UCT-StableIteration. If we can accurately predict $\hat{T}_{min}(A, Q)$, this time can be saved. Furthermore, we can better plan and use those computing resources.

In Fig. 19.1, we find $\log(\hat{T}_{min}(A, Q))$ do not have a simple linear relationship with the initial blank point. The slope of the lower bound curve fitting on the figure is 0.2266. And in Fig. 19.2, there is a good corresponding relationship between them. Among these 64 problems, the range of initial blank points is 5–16, so their initial branch coefficient is 5–16. The domain UCT algorithm can drop the branch coefficient below 2.3 without using any domain knowledge. This proves the validity of the UCT algorithm with different depths.

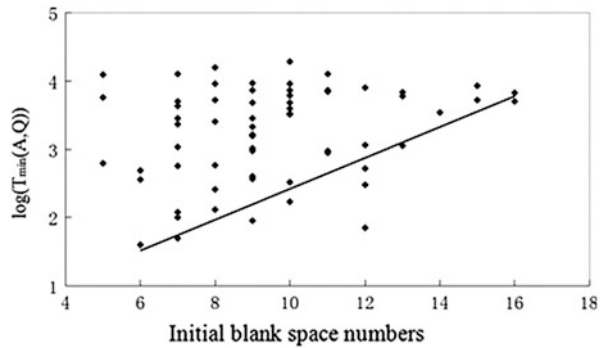


Fig. 19.1 The relationship between $\log(T_{min}(A, Q))$ and initial blank space numbers

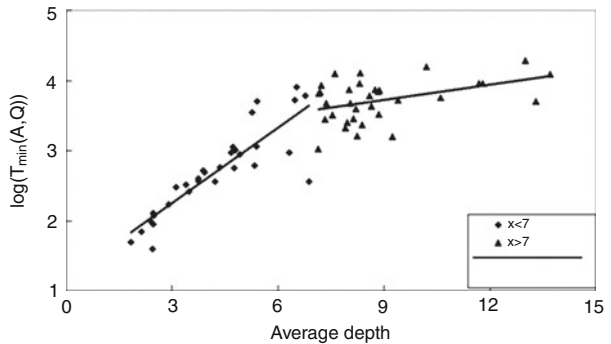


Fig. 19.2 The relationship between $\log(T_{min}(A, Q))$ and the average depth of UCT search

Conclusion

This paper investigates the fully enclosed region UCT algorithm and implementation in Fuego. From the preliminary results, the fully enclosed region UCT algorithm can solve the fully enclosed tsume problems on a rational scale within a reasonable time; therefore, it may be feasible to break the global UCT search into several multiple local UCT searches. In the future, we would like to apply this framework to do some works.

Acknowledgments This work is supported by the National Natural Science Foundation of China (No.61163004) and Natural Science Foundation of Yunnan Province (No.2010CD027).

References

1. Martin M. Fuego-GB Prototype at the Hum- an machine competition in Barcelona 2010.a Tournament Report and Analysis. <http://era.library.ualberta.ca/public/view/item/uuid:9e921da9-5176-4327-be53-43b8dec5d1ac>. (2012)
2. Sylvain G, Yizao W, Remi M, Olivier T. Modification of UCT with Patterns in Monte-Carlo Go. <http://hal.inria.fr/inria-00117266/fr/>.(2006-12-21)
3. David S, Gerald T. Monte-Carlo Simulation Balancing[C]. Proceedings of the 26th International Conference on Machine Learning. Omni press, Montreal, Canada, 945–952 (2009)
4. Arpad Rimmel, Fabien Teytaud and Olivier Teytaud. Biasing Monte-Carlo Simulations through RAVE Values[C]. Proceeding CG'10 Proceedings of the 7th international conference on Computers and games. Berlin, Germany, Springer, 59–68(2011)
5. Wolf T. Forward pruning and other heuristic search techniques in tsume go. Special Issue Informat Sci. 2000;122:59–76.
6. Li L. Solving life and death problems in Go. Comput Appl. 2005;11:2720–2 (in Chinese).
7. Lin W, Pierre B. A Scalable Machine Learning Approach to Go [C] Advances in Neural Information Processing Systems 19. British Columbia: MIT Press; 2007. p. 1521–8.
8. Lin W, Baldi P. Learning to play Go using recursive neural networks. Neural Netw. 2008;21:1392–400.
9. Auer P, Cesa-Bianchi N, Fischer P. Finite-time analysis of the multi-armed bandit problem. Mach Learn. 2002;47:235–56.
10. Gelley S, Wang Y. Exploration Exploitation in Go: UCT for Monte-Carlo Go[C]. In: Twentieth Annual Conference on Neural Information Processing Systems (NIPS 2006): On-line Trading of Exploration and Exploitation, British Columbia: MIT Press, (2006). p. 1121–1128
11. Coulom R. Efficient selectivity and backup operators in Monte-Carlo tree Search[C]. 5th International conference, CG2006, Springer, p. 72–83(2007)

Chapter 20

A New Linear Feature Item Weighting Algorithm

Shiyuan Tian, Hui Zhao, Guochun Wang, and Kuan Dai

Abstract The feature weighting algorithm is a key step in the feature extraction. In this paper, according to two classification situations of web page theme, we've improved the traditional feature item weighting method of TF-IDF. On the basis, We propose a new linear feature weighting algorithm based on the feature's position information and the mutual information as it contains. Experimental results show that this algorithm has higher the theme web page recall rate and precision rate than the traditional method TF-IDF in terms of the theme web page filtering.

Keywords TF-IDF VSM • Feature extraction • Weight calculation • Topic filtering

20.1 Introduction

With the development of network, the topic web crawler has become one of the key technologies to acquire the web information. The topic web crawler is a program that only crawls within relevant area of a web page by adding a topic filtering function to the general web crawler [1]. The topic filtering is used to judge whether a web page document and a set of predetermined topics are related or not, which shall be implemented according to the relevance calculation. At present, there have been many kinds of web page relevancy algorithms with those commonly used including neural network, Naive Bayes, vector space model, instance mapping model, etc. [2]. Because the vector space model can be materialized in the form of unstructured content to vector, thereby the computability and the operability of the document have been increased; thus the vector space model (VSM) is widely used in recent years [3]. The accuracy of web page correlation calculation based on the vector space model has a great relationship with the web page content extraction related topics, that is to say, the themes feature extraction is essential.

This paper analyzes the commonly used text features items weight calculation method (TF-IDF) according to two classification requirements on the topic crawler

S. Tian • H. Zhao (✉) • G. Wang • K. Dai
School of Computer Science and Engineering, Changchun University of Technology,
130012 Changchun, Jilin, China
e-mail: zhaohui@mail.ccut.edu.cn

on the web page text (whether or not related to the theme), and the method is improved. On this basis, in consideration of the vocabulary's location information and the vocabulary's mutual information presents a new linear feature item weighting algorithm. Experiments prove that this new method highlights better theme page recall rate and topic filter accuracy than that of TF-IDF.

20.2 Algorithm of Theme Feature Extraction

After web page pretreatment, we get a series of candidate feature set. Web page is formalized as $\text{doc}_i = \langle t_{i1}, t_{i2}, \dots, t_{in} \rangle$, where doc_i denotes the i document, t_{ik} means the k candidate feature of the i document, its weight vector as $w_i = \langle w_{i1}, w_{i2}, \dots, w_{in} \rangle$, and w_{ik} denotes the weight of t_{ik} . In the weight vector, the weight of candidate feature reflects its own contribution degree of the web page theme. In order to obtain high-quality topic feature vector, the candidate feature must be weighted. In this paper, we analyze TF-IDF and find it does not consider the effect of distribution of the feature in different classes on the weight; therefore, we improve it with the two classification of theme web page and then give the effect of the information on the weight by the previous research results. Finally, we give the effect of the mutual information on the weight. In this paper, we propose a new linear method for computing the weight based on the above three factors.

20.2.1 TF-IDF-Based Two Classifications

TF-IDF is a commonly used method to calculate the weights. It is based on a statistical method used to evaluate the degree of important of a word to a text in a corpus. The calculation formula is shown as below:

$$w_{ij} = tf \times idf = tf_{ij} \times \log\left(\frac{N}{n_i} + 0.01\right) \quad (20.1)$$

w_{ij} denotes the weight of the word i in the text j , TF denotes the term frequency, IDF denotes the inverse document frequency, tf_{ij} means the frequency of word i appears in text j , N is the total number of documents in the corpus, and n_i is the number of documents, while the word i appears in the corpus. The main idea of TF-IDF is if a word appears frequently in a certain document but is rarely seen in other texts, it is useful for distinguishing categories and suitable for a web page theme.

In practice, the vector needs to be normalized. The normalized TF-IDF formula is shown as below:

$$w_{ij} = \frac{tf_{ij} \times \log\left(\frac{N}{n_i} + 0.01\right)}{\sqrt{\sum_{i=1}^n \left[(tf_{ij}) \times \log\left(\frac{N}{n_i} + 0.01\right) \right]^2}} \quad (20.2)$$

As we can see, TF-IDF treats the set of documents as a whole, and in the calculation of IDF, the vocabulary class distribution has not been taken into consideration. IDF's deficiency is that it considers the set of documents as a whole without considering the distribution of words in each category in the corpus and the accuracy of IDF is not so high, so we divide the documents into two categories: related to the theme of the document and unrelated [4]. Suppose that the number of documents in the corpus which is associated with the theme and contains the word $/i/$ is $/v/$, and the number of documents in the corpus which is not associated with the theme and contains the word $/i/$ is $/u/$; the improved TF-IDF formula is shown as below:

$$w_{ij} = \frac{tf_{ij} \times \log\left(\frac{v}{u+v} \times N\right)}{\sqrt{\sum_{i=1}^n \left[(tf_{ij}) \times \log\left(\frac{v}{u+v} \times N\right) \right]^2}} \quad (20.3)$$

Formula (20.3) is an increasing function of the variable v and a decreasing function of the variable u . The more related documents that contain the words $/i/$, the fewer unrelated documents that contain words $/i/$ and the more chance that the vocabulary can serve as the document topic feature item.

20.2.2 Calibration of Candidate Feature Location

In order to obtain the contribution degree of each candidate feature, we need to determine the location information of each candidate feature. During the software scan the web page, digital tags are used to mark the feature locations. Based on the results of previous study [5], the most meaningful values of the labels are the anchor text, title (TITLE), title (H), and label text (META). Let $f(n)$ be a position weight function, and when $/n = 1/$, the candidate feature item is in the anchor text. When $/n = 2/$, the candidate feature item is in the title(TITLE). When $/n = 3/$, the candidate feature item is in the title(H). When $/n = 4/$, the candidate feature item is in the label text (META). The formula is as follows.

$$f(n) = \begin{cases} 0.5, n = 1 \\ 0.4, n = 2 \\ 0.2, n = 3 \\ 0.15, n = 4 \end{cases} \quad (20.4)$$

If a candidate feature shows in more than two locations, select the maximum value of $f(n)$ as the standard position of the candidate feature.

20.2.3 Mutual Information Weight Calculation of Candidate Feature

As to the mutual information based on the probability of candidate features and class co-occurrence, measure the relevance of features with class. As to a certain feature of t , the mutual information of class x_i is bigger, which indicates greater the probability of feature co-occurrence with the class. The mutual information value can be calculated as below:

$$\text{MI}(x_i, t) = \log \frac{p(x_i|t)}{p(x_i)} \quad (20.5)$$

$p(x_i|t)$ means the probability of the word t which appears in the x_i class. $p(x_i)$ to express the probability of category x_i in the corpus. Sorting the candidate features according to the frequency and then calculating the features mutual information with the class x_i . If the mutual information is less than the threshold, the value of the mutual information is zero and the threshold is 0.40. If the mutual information value is greater than 1, it is equal to 1.

On the basis of analyzing such three factors as frequency, location, and the mutual information, as well as using the linear weighted method, we find a new linear weighted method. The formula is shown as below.

$$w_i = aw_{il} + bf(n) + r\text{MI}(x_i, i) \quad (20.6)$$

$|w_i|$ denotes the weight of the word $|i|$. $|a|$, $|b|$, and $|r|$ are regulatory factors. In order to ensure the balance, we set $|a + b + r| = 1$. The normalized formula is shown as below:

$$w_i = \frac{\alpha f_{\text{new}} + bf(n) + r\text{MI}(x_i, i)}{f_{\text{new}} + f(n) + \text{MI}(x_i, i)} \quad (20.7)$$

According to Formula (20.7), we calculate the weight of each candidate feature, sort them descending by weight, and select an appropriate candidate feature.

20.3 Calculation of Web Page Correlation

The algorithm flow is shown as below:

1. According to the training document, we obtain the predetermined topic vector by artificial. The theme vector is as $s = (t_1, w_1; t_2, w_2; \dots t_n, w_n)$, t_i denotes the feature, w_i as the weight of t_i .
2. The web page text is expressed in the form of vector space model; the vector is $d = (t_1', w_1'; t_2', w_2'; \dots t_n', w_n')$, t_i' denotes the feature, and w_i' is the weight of t_i' .
3. According to the vector of "s" to determine the dimension of vector d, if $t_i' \in s$, keep its weight the same; otherwise, change corresponding weight to 0.
4. The formula for calculating the similarity between a given web page text vector and a given topic vector is shown as below:

$$\text{sim}(s, d) = \frac{s \times d}{|s| \times |d|} \quad (20.8)$$

5. Comparing the similarity value with a predetermined threshold value to determine whether the web page text is associated with the theme.

20.4 Experimental Results and Analysis

20.4.1 Experimental Data

Based on the previous literature, the dimension of the topic feature vector web page should not be too high, and the number of feature items is not higher than 20. In this paper, the economic class is adopted in the corpus of Fudan University as the training sample set, and 20 characteristics are selected as the theme vector by manual work. We've also downloaded 1000 documents from Sina, of which 600 are related to the economics with the remaining being irrelevant.

20.4.2 Method of Evaluation

We use the recall rate, the accuracy rate, and the F -measure to compare the performance of such three methods in the case, in which the threshold has different values [1]. The recall rate is defined as the proportion of correct theme web page quantity in the total topic relevant web page quantity under the given threshold c . The accuracy is defined as under the given threshold c the proportion of correct theme web page quantity, and all theme similarity value is greater than c of the number of pages. The formula is shown as below:

$$\text{Recall} = \frac{k_{\text{correct}}}{n_{\text{total}}} \quad (20.9)$$

$$\text{precision} = \frac{k_{\text{correct}}}{m} \quad (20.10)$$

k_{correct} refers to the correct number of theme web page, m is the quantity of web page whose value is greater than the threshold, and n_{total} is the quantity of all the theme web page.

Generally speaking, the precision rate decreases as the recall rate increases, and vice versa. Thus, it is necessary to take them into account. This is the F -measure value. The formula is shown as below:

$$F\text{-measure} = \frac{2 \times \text{precision} \times \text{Recall}}{\text{precision} + \text{Recall}} \quad (20.11)$$

The range of the F -measure is 0 to 1. We can use the F -measure to measure the performance of different feature weighting methods under the same threshold value and then determine the optimal $/c/$ value.

20.4.3 Results and Analysis

In the weight calculation of candidate features, the balance adjustment factor $/a/$, $/b/$, and $/r/$ should be set up according to the web page form. If the form of a web page is fixed, the theme features generally appear in the title and anchor text, so the value of $/b/$ should be greater. For topic class of “economic,” the experimental sustained debug the value of $/a/$, $/b/$, and $/r/$ to obtain the best theme features. The finally selected value is shown as below (Table 20.1).

In the case of the same similarity calculation formula, we use different methods of calculating feature item weighting to compare the value of recall rate, accuracy, and F -measure. This paper compares the traditional TF-IDF method with the improved TF-IDF method firstly, when the values of c were 0.35, 0.50, 0.65, and 0.80; the comparative result of these two methods is shown as below:

The results can be seen in Table 20.2. The improved TF-IDF method has achieved certain results in web page filtering, but the effect is not dramatic because they are based on the statistical method, without considering the semi-structure nature of web documents. The comparative results of the traditional TF-IDF method and the new method is shown in Table 20.3:

The results can be seen in Table 20.3. It shows that the linear weighting method is more effective than the traditional TF-IDF method.

From Tables 20.2 and 20.3, we can see that the three methods get the maximize value of F -measure around 0.50. In order to obtain the optimal threshold, we set

Table 20.1 Parameter list

Balance adjustment factor	a	b	r
Value	0.3	0.4	0.3

Table 20.2 Comparative results of the traditional TF-IDF method and the improved TF-IDF

The value of c	The improved TF-IDF			Traditional TF-IDF		
	Recall	Precision	F	Recall	Precision	F
0.35	0.851	0.440	0.580	0.832	0.412	0.556
0.50	0.659	0.523	0.583	0.628	0.498	0.557
0.65	0.476	0.660	0.553	0.416	0.613	0.495
0.80	0.280	0.780	0.412	0.263	0.756	0.391

Table 20.3 Comparative results of the traditional TF-IDF method and the new method

The value of c	The new method			Traditional TF-IDF		
	Recall	Precision	F	Recall	Precision	F
0.35	0.966	0.561	0.728	0.832	0.412	0.556
0.50	0.793	0.679	0.731	0.628	0.498	0.555
0.65	0.530	0.721	0.610	0.416	0.613	0.495
0.80	0.361	0.826	0.502	0.263	0.756	0.391

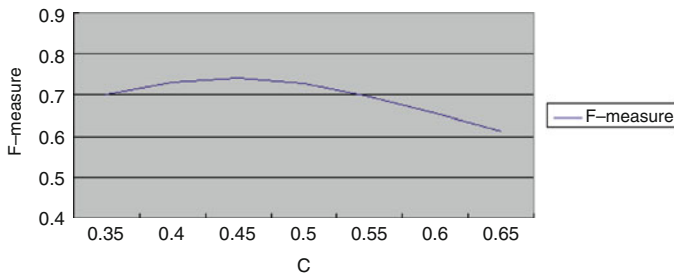


Fig. 20.1 The changes of F -measure value

0.50 as the center and 0.05 of the scale of the segmentation. The changes of F -measure value is as follow (Fig. 20.1):

When the threshold equals to 0.45, the F -measure value obtains the maximum value, which means that the best filtering effect is at this point. In this experiment, the threshold value is determined as 0.45 to compare the filtering effect of the three methods under this threshold value with the results shown as below:

As indicated in Table 20.4, the new liner feature extraction method improves the topic filtering recall and precision rates dramatically below this threshold value,

Table 20.4 Comparison of the three methods at the value of 0.45

The name of method	The number of processed web page	The actual number of relevant web page	Meet the threshold number of pages	The collection number of theme web page	Recall	Precision
New method	1,000	600	869	523	0.870	0.601
Improved TF-IDF	1,000	600	890	425	0.711	0.479
Traditional TF-IDF	1,000	600	893	418	0.697	0.468

Conclusion

In this paper, the new method of combining the improved TF-IDF and considering the location and the mutual information of feature items has better results than the traditional TF-IDF. Experiments show that it is a feasible feature item weighting method.

References

1. Johnson J, Tsiuotsuoliklis K, Giles CL. Evolving strategies for focused Web crawling. // Proceedings of the 20th International Conference (ICML 2003), Menlo Park, CA: AAAI press, 2003. p. 298–305
2. Zheng GL, Ye FY, Lin GJ. Subject information acquisition method based on domain ontology. *Comput Appl.* 2008;28(12):3275–6. In Chinese.
3. Salton G, Wong A, Yang GA. Vector space model for automatic indexing. *Commun ACM.* 1975;18(11):613–20.
4. Li Z, Yang S. Improvement of calculation web page feature weight based on vector space model. *Comput Modern.* 2010;178(6):137–9 (In Chinese).
5. Lin BX. Research and implementation of topic crawler based on domain ontology. Cheng Du: Southwest Jiaotong University, 2010. (In Chinese)

Chapter 21

Trust Value of the Role Access Control Model Based on Trust

Xiaohui Cheng and Tong Wang

Abstract In order to solve the current situation that the trust computation of access control model based on trust is insufficient to conduct a fine-grained and dynamic access control, the access control (role model RACT access control model based on trust) which is a fine-grained and integrated with the context is built. The trust value and the threshold of activation and decision tree algorithm are added into RACT to improve the single trust value algorithm for multiple algorithms and realize dynamic access control which is combined with the session history. Experiments show that RACT has higher security than the existing trust model.

Keywords Access control • Trust • Role access control

21.1 Introduction of the Access Control Model

Because the service is provided by third parties, researchers should focus on how to realize intelligent control through access control technology and avoid to be controlled by third parties [1–3]. Access control technology, as the core technology of operating systems security and a solution to the system security, can effectively prevent the illegal users from entering the system and legitimate users illegal use system resources, and access control is a key technology to ensure the confidentiality and integrity of data; therefore, the research of access control has become one of the highlights in computer science [4]. Current access control model is primarily divided into three categories: the discretionary access control, the mandatory access control, and the role-based access control.

The discretionary access control model is characterized by the transitivity of chain structure of grant permissions, and we can't guarantee the subject not subject to indirect permissions [5]. The subject has administrative authority of the object, which is granted by it. But the subject can't manage the objects of the next level. Authority management is too complex to ensure safety.

X. Cheng (✉) • T. Wang
College of Information Science and Engineering, Guilin University of Technology,
541000 Guilin, China
e-mail: wangtongxx@163.com

The disadvantage of MAC is that every subject and object is attached with the attribute labels by managers. MAC determines whether or not the subject has permissions strictly according to the attribute labels, which may easily cause the statue of the legitimate subject not to have the permission for operation [6].

The disadvantage of the traditional RBAC model ignores the security details [7–9]. When the subject applies for the access objects, the system only assigns roles according to the subject's duties instead of checking the operation behavior of the previous, which can cause long-term object destructions. If attackers get different permissions with different roles, he/she can easily seriously destruct the system [10].

21.2 Role Access Control Model Based on Trust

RBACB96 model consists of three parts: the users, the roles, and the permission. Every user has the role and obtains all permissions of the roles directly. When RBAC is combined with trust, add more constraints to the permission granting to increase the data safety and security [11].

21.2.1 Description of RACT Model

Definition 1 Subject users: $SU = \{su_1, su_2, su_3, \dots, su_n\}$. The subject can be a system or an independent program. In this study for the convenience of description, the subject is a natural person.

Definition 2 Object resources: $OB = \{ob_1, ob_2, ob_3, \dots, ob_n\}$. The object can be data resources or system resources, and the subjects are assigned roles and then given operating permissions. One object can be operated by roles, so the relationship between the subject and object is $1:N$.

Definition 3 Permission: each role has different operating permissions.

$$P = \{(p_1, at_1), (p_2, at_2), (p_3, at_3), \dots, (p_n, at_n)\}, n \in N^+ \sum_{i=1}^n (X_i - \bar{X})^2. \quad \text{When}$$

the user's trust value reaches the access threshold, the subjects can use the permissions. The mapping relationship is available between roles and permissions.

Definition 4 Role: $R = \{r_1, r_2, r_3, \dots, r_n\}$. The role is the set of different permissions which are determined by different duties and levels; so the permissions of users and roles have corresponding relationship.

Definition 5 Trust value: $TV = \{tv_i | tv_i \in [-1, 1], i \in N^+\}$. It is an attribute value of a subject. The trust value TV is calculated with the trust value algorithm and the session history. When the trust value is higher than trust threshold, the permissions are activated.

Definition 6 Operation: It is the set of subjects that can operate on the objects.

$O = \{o_i | o_i \in \{\text{read, write, execute, } \dots\}, i \in N^+\} \sum_{i=1}^n (X_i - \bar{X})^2$. It usually contains reading, writing, and execution.

Definition 7 Context: The context contains the session history of subjects and the environment, etc. The server calculates the subjects' trust value by using appropriate algorithm according to the context.

Definition 8 Session history: The database of trust value records the subjects' trust value and the previous session's behaviors. The server calculates subjects' trust value based on the current session history.

Definition 9 Constraint: There are multiple attributes in this research model. The constraints have been established to make the connection between each attribute. The constraints of each contact are not identical and the constraint can guarantee the model normal running.

Definition 10 Session time: The session time records the time of the subject operated the object.

Definition 11 Group: The objects are divided into groups because of the high degree of similarity of functions and contents. The subjects are divided into groups because of the high degree of similarity of duties and identities.

The relationships between two or more attributes have been described in standardized language, as shown by the following definition:

Definition 1 SRA $\subseteq S \times R = \{(s, r) | s \in S \wedge r \in R\}$, according to the duties, the subjects are assigned different roles.

Definition 2 RPA $\subseteq R \times P = \{(r, p) | r \in R \wedge p \in P\}$, according to the duties of roles which are assigned with different permissions.

Definition 3 TAA $\subseteq TV \times AT = \{(tv, at) | tv \in TV \wedge at \in AT\}$, when the trust value of subject is higher than the threshold of the object, the permissions of subjects are activated.

RACT model improves the security mechanism of the traditional RBAC model and adds access activation threshold and user trust value computation process with models shown in Fig. 21.1.

21.3 RACT Trust Value Algorithm

The trust value of the subject mainly comes from two aspects, the subject's identity and the trust value which is formed during the subject interacts with the object. When there isn't session history of the subject and the object, then the server calculates the recommended trust value according to the session history of the other objects.

Decision tree algorithm is established with the height of the tree of 4. The root node is the subject. The nodes of the second layer are the session history of the

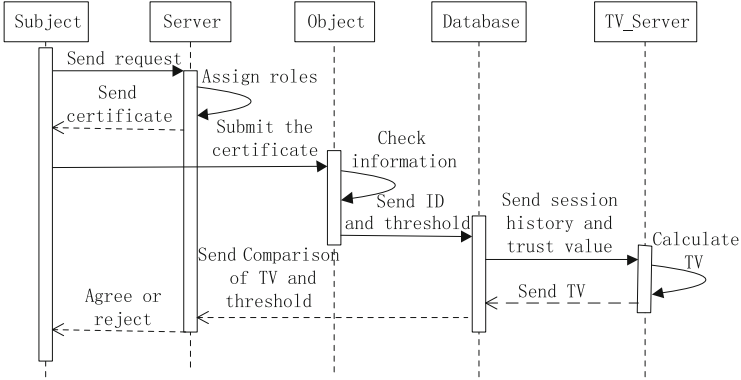


Fig. 21.1 Sequence Diagram of RACT

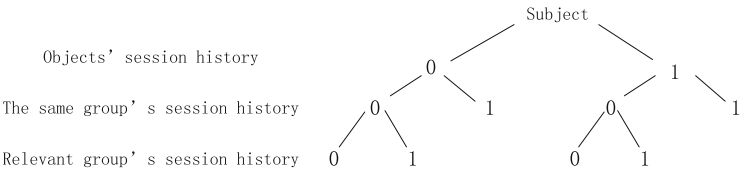


Fig. 21.2 Decision tree algorithm

subject and the object. The nodes of the third layer are the session history of the subject and the other’s objects in the group of the object, and the nodes of the fourth layer are the session history of the subject and the objects in relevant group of the object. In the decision tree algorithm, use 1 and 0 to indicate whether or not there is session history.

When there is a session history of the subject and objects of the same group, the recommended trust value of objects of the same group is more important than the relevant group. According to the above rule, the decision tree algorithm is shown in Fig. 21.2.

1. The subject doesn’t have any session history.
2. The subject doesn’t have session history with the object or the others objects of the same group; it only has session history with the objects of relevant group.
3. The subject only has session history with the objects of the same group.
4. The subject only has session history with the object which is being applied.
5. The subject has session history with the object which is being applied and the objects of the relevant group.
6. The subject has session history with the object which is being applied and the other objects of the same group.

As to the first path, in view of the subject’s duties and identity, the managers assign the lowest trust value as the default value, thereby gradually accumulate the

trust value in the later session so that they can activate the corresponding permissions of its role.

As to the second path and the fifth path, the NICE trust model is used. The core idea is to assign objects' cookie values according to the session. The positive trust value is credible and the negative trust value is not credibly.

As to the third path and the sixth path, the EigenTrust trust model is used with the subject u_i first to find the objects ob_k which has the session history with the subject ob_j ; in the same group with the object, calculate the trust value tv_k according to the recommend trust value of the group, Normalize the recommended values of trust

$v_{u-ob} = \frac{\max(tv_k, 0)}{\sum_u \max(tv_k, 0)}$ and build the trust based on the normalized data matrix V_{u-ob} , superposition integrated computation recommendation trust value $t_{ij} = \sum_k v_{ik}v_{kj}$.

As to the fourth path, the regret trust mode is used. It empathizes the occurrence time. When the subject only has session history with the object, add the importance of time to enhance the reliability of trust value. $T_{D_{p-r}}(\phi)$ is the trust degree of the type ϕ of the subject's su_i action, $ODB_{\phi}^{p,r}$ is the set result of operation, trust decay with time, $p(t, t_i)$ is the decay degree with time, t is the current time, t_i is the occurrence time of events, $IMP(o_i, \phi) \frac{1}{n}$ is the assessment of the event, $L(o_i, \phi)$ is the weight function of loyalty in the event i , and the function of trust value is

$$T_{D_{p-r}}(\phi) = \sum_{o_i \in ODB_{\phi}^{p,r}} \rho(t, t_i) \times IMP(o_i, \phi) \times L(o_i, \phi)$$

21.4 Validation of RACT Security

RACT has been established with JAVA in the Windows operation system. It was integrated with eclipse and SQL Server database. In RACT model, 20 subjects were created; 20 subjects are divided into 4 groups, respectively, high, middle, low, and guest, and each role has different permissions. 20 objects were created and are divided into 4 groups. The names of group are A, B, C, and D, and the name of objects are A1, A2, A3, A4, etc.

Every subject applies the same objects with RACT and a trust access model algorithm. After the subject has obtained permissions, the object operates maliciously. The successful rate of application of every application is shown in Fig. 21.3.

In Fig. 21.3, the square line is the result of single trust value algorithm and the circle line is the result of RACT. After every malicious operation, the rate of successful application of RACT decreases faster than the single trust value algorithm. Until the twentieth malicious operation, the successful rate of the single trust value algorithm is 40%. The high rate indicates that the algorithm can't calculate trust value accurately.

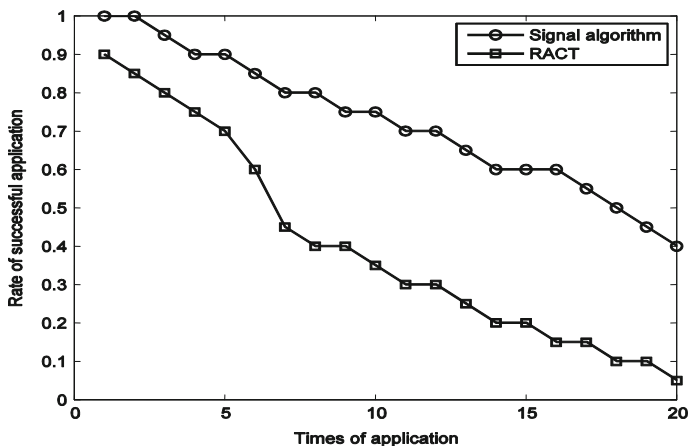


Fig. 21.3 Successful rate of application

Conclusion

RACT uses multiple trust value algorithms. It is closely combined with the subjects' context and session history to realize dynamic access control. As proved by experiments, RACT trust value is calculated according to the session history. It highlights credibility and high degree of safety.

Acknowledgments As the research of the thesis is sponsored by National Natural Science Foundation of China (No: 61262075) and major scientific research project of Guangxi Higher Education (No: 201201ZD012), we would like to extend our sincere gratitude to them.

References

1. Bleckmann DM, Starnes WW, Andersen BD. Method to control access between network endpoints based on trust scores calculated from information system component analysis: U.S. Patent 8,429,412. 2013-4-23.
2. Li Q, Zhang X, Xu M, et al. Towards secure dynamic collaborations with group-based RBAC model. *Comput Security*. 2009;28(5):260–75.
3. Duan J, Gao D, Foh CH, et al. TC-BAC: a trust and centrality degree based access control model in wireless sensor networks. *Ad Hoc Netw*. 2013;11(8):2675–92.
4. Le XH, Doll T, Barbosu M, et al. An enhancement of the role-based access control model to facilitate information access management in context of team collaboration and workflow. *J Biomed Inform*. 2012;45(6):1084–107.
5. Ma X, Li R, Lu Z, et al. Mining constraints in role-based access control. *Math Comput Model*. 2012;55(1):87–96.
6. Zhong R, Sumalee A, Maruyama T. Dynamic marginal cost, access control, and pollution charge: a comparison of bottleneck and whole link models. *J Adv Transp*. 2012;46(3):191–221.

7. Joshi JB, Bertino E, Latif U, et al. A generalized temporal role-based access control model. *Knowl Eng IEEE Trans.* 2005;17(1):4–23.
8. Goyal V, Pandey O, Sahai A et al. Attribute-based encryption for fine-grained access control of encrypted data. *Proceedings of the 13th ACM conference on Computer and communications security.* ACM, 2006: 89–98.
9. Roesner F, Kohno T, Moshchuk A et al. User-driven access control: rethinking permission granting in modern operating systems. *Security and Privacy (SP), 2012 I.E. Symposium on.* IEEE, 2012: 224–238.
10. Park J, Sandhu R, Cheng Y. A user-activity-centric framework for access control in online social networks. *Internet Comput IEEE.* 2011;15(5):62–5.
11. Ferraiolo DF, Sandhu R, Gavrila S, et al. Proposed NIST standard for role-based access control. *ACM Trans Inform Syst Security (TISSEC).* 2001;4(3):224–74.

Chapter 22

Universal Approximation by Generalized Mellin Approximate Identity Neural Networks

Saeed Panahian Fard and Zarita Zainuddin

Abstract This study considers sufficient and also necessary conditions for the universal approximation capability of three-layer feedforward generalized Mellin approximate identity neural networks. Our approach consists of three steps. In the first step, we introduce a notion of generalized Mellin approximate identity. In the second step, we prove a theorem by using this notion to show convolution linear operators of generalized Mellin approximate identity with a continuous function f on \mathbb{R}^+ with a compact support converges uniformly to f . In the third step, we establish a main theorem by using those previous steps. The theorem shows universal approximation by generalized Mellin approximate identity neural networks.

Keywords Universal approximation • Generalized Mellin approximate identity • Generalized lognormal distribution • Electromyographic signals analysis • Uniform convergence

22.1 Introduction

Universal approximation by three-layer feedforward neural networks can be regarded as an important theoretical research in approximation theory of neural networks. Over the past three decades, many researches concerning this problem have been done [1–3]. Lately, Arteaga and Marrero surveyed this topic [4]. Universal approximation by feedforward neural networks states that every function of a certain set of functions can be approximated by feedforward neural networks with arbitrary accuracy [5, 6]. As a related area of research, the universal approximation capability of three-layer feedforward approximate identity neural networks was proved by Turchetti et al. [7].

S. Panahian Fard (✉) • Z. Zainuddin
School of Mathematical Sciences, Universiti Sains Malaysia, 11800, USM, Pulau Penang, Malaysia
e-mail: saeedpanahian@yahoo.com; zarita@cs.usm.my

Approximate identity neural networks use approximate identity as activation functions. The restriction on approximate identity neural networks were weakened by introducing different types of approximate identity. The notions of double approximate identity [8], flexible approximate identity [9, 10], double flexible approximate identity [11], 2π -periodic approximate identity [12], and double 2π -periodic approximate identity [16] can be considered as extensions of approximate identity.

Choosing non-linear activation functions is a challenging task to the development of theory of feedforward neural networks. In this study, we are motivated to consider the conditions for choosing non-linear activation functions from the perspective of approximate identity. In fact, we are interested to propose a notion of generalized Mellin approximate identity. The notion is an extension of generalized Mellin approximate identity [13]. Our next motivation is to investigate universal approximation by three-layer feedforward generalized Mellin approximate identity neural networks. Our networks are constructed based on generalized Mellin approximate identity as neurons.

Our main objective in the study is to investigate sufficient and also necessary conditions for the universal approximation capability of three-layer feedforward generalized Mellin approximate identity neural networks. We solve the problem in the linear space of all continuous functions on \mathbb{R}^+ which is denoted by $C(\mathbb{R}^+)$. The notion of generalized Mellin approximate identity can be considered as one of the main novelties of this study.

The methodology of the study consists of three steps. In the first step, we will formalize a notion of generalized Mellin approximate identity. In the second step, we will prove a theorem to show that convolution linear operators of generalized Mellin approximate identity with a continuous function f in $C(\mathbb{R}^+)$ with a compact support converge uniformly to f . In the third step, we will establish a main theorem by using the results of the previous steps. The proof of the main theorem follows Wu et al.'s Theorem 1 [14]. The main theorem shows sufficient and also necessary conditions for the universal approximation capability of three-layer feedforward generalized Mellin approximate identity neural networks. Our theorems are the other novelties of the study.

The contributions of the study are organized as follows: in Sect. 22.2, we will formalize a notion of generalized Mellin approximate identity. We will also present an example of generalized Mellin approximate identity. In Sect. 22.3, we will obtain some theoretical results in order to show universal approximation capability by three-layer feedforward generalized Mellin approximate identity neural networks in $C(\mathbb{R}^+)$. Finally, we will conclude the study with some remarks in Sect. 22.4.

22.2 Basics

We first propose a notion of generalized Mellin approximate identity functions in the following. The notion will be used in the next section.

Definition 1. Let $k \in \mathbb{R}$ be a constant; let $(\phi_{n,k}(x))_{n \in \mathbb{N}}, \phi_{n,k} : \mathbb{R}^+ :=]0, \infty[\rightarrow]0, \infty[$ be a sequence. We say that the sequence is generalized Mellin approximate identity if it has the following properties:

1. $\int_{\mathbb{R}^+} \phi_{n,k}(x) \frac{dx}{x} = 1.$
2. Given $\epsilon > 0$ and $1 < \delta < +\infty$, there exists N such that if $n \geq N$, then $\int_{\mathbb{R}^+ \setminus [\frac{1}{\delta}, \delta]} \phi_{n,k}(x) \frac{dx}{x} \leq \epsilon.$

We here illustrate the effectiveness of generalized Mellin approximate identity functions by giving an example.

Example 1 ([15]). A sequence of a generalized lognormal distribution is defined as follows:

$$\phi_{n,k}(x) = k \exp\left\{-\frac{1}{2} \left| \frac{\log nx - \mu}{\sigma} \right|^s\right\}; n \in \mathbb{N}, x > 0, -\infty < \mu < \infty, \sigma > 0, s > 0,$$

where $k = \frac{s}{2^{(s+1)s} \sigma \Gamma(\frac{s}{2})}.$

The above sequence of a generalized lognormal distribution can be considered as an example of generalized Mellin approximate identity.

In the next section, we will obtain some theoretical results.

22.3 Theoretical Results for Generalized Mellin Approximate Identity Neural Networks

In this section, we first prove Theorem 1. Theorem 1 shows convolution linear operators of generalized Mellin approximate identity with a continuous function f in $C(\mathbb{R}^+)$ with a compact support converge uniformly to f .

Theorem 1. Let $k \in \mathbb{R}$ be a constant; let $(\phi_{n,k}(x))_{n \in \mathbb{N}}, \phi_{n,k} : \mathbb{R}^+ :=]0, \infty[\rightarrow]0, \infty[$, be a generalized Mellin approximate identity. Let f be a continuous function on \mathbb{R}^+ with a compact support. Then, $\phi_{n,k} * f$ converges uniformly to f on $C(\mathbb{R}^+)$.

Proof. Let $x \in [\frac{1}{\delta}, \delta], \epsilon > 0$, and $1 < \delta < +\infty$. Then, there exists a $\eta > 0$ such that $|f(xy) - f(x)| < \frac{\epsilon}{2kn \|\phi\|_{L^1(\mathbb{R}^+)}}$ for all $y \in \mathbb{R}^+, |xy - x| < \eta$. We define $(\phi_{n,k})_{n \in \mathbb{N}}$ by $\phi_{n,k}(x) = kn\phi(nx)$. Then,

$$\begin{aligned}
\phi_{n,k} * f(x) - f(x) &= \int_{\mathbb{R}^+} kn\phi(ny)\{f(xy) - f(x)\} \frac{dy}{y} \\
&= \left(\int_{\left[\frac{1}{\delta}, \delta\right]} + \int_{\mathbb{R}^+ \setminus \left[\frac{1}{\delta}, \delta\right]} \right) kn\phi(ny)\{f(xy) - f(x)\} \frac{dy}{y} \\
&= I_1 + I_2,
\end{aligned}$$

where I_1 and I_2 are as follows:

$$\begin{aligned}
|I_1| &\leq \int_{\left[\frac{1}{\delta}, \delta\right]} kn\phi(ny)(f(xy) - f(x)) \frac{dy}{y} \\
&< \frac{\epsilon}{2kn \|\phi\|_{L^1(\mathbb{R}^+)}} \int_{\left[\frac{1}{\delta}, \delta\right]} kn\phi(ny) \frac{dy}{y} \\
&= \frac{\epsilon}{2kn \|\phi\|_{L^1(\mathbb{R}^+)}} \int_{\left[\frac{n}{\delta}, n\delta\right]} kn\phi(t) \frac{dt}{t} \\
&\leq \frac{\epsilon}{2kn \|\phi\|_{L^1(\mathbb{R}^+)}} \int_{\mathbb{R}^+} kn\phi(t) \frac{dt}{t} = \frac{\epsilon}{2}.
\end{aligned}$$

For I_2 , we have

$$\begin{aligned}
|I_2| &\leq 2 \|f\|_{C(\mathbb{R}^+)} \int_{\mathbb{R}^+ \setminus \left[\frac{1}{\delta}, \delta\right]} kn\phi(ny) \frac{dy}{y} \\
&= 2 \|f\|_{C(\mathbb{R}^+)} \int_{\mathbb{R}^+ \setminus \left[\frac{n}{\delta}, n\delta\right]} kn\phi(t) \frac{dt}{t}.
\end{aligned}$$

Since

$$\lim_{n \rightarrow \infty} \int_{\mathbb{R}^+ \setminus \left[\frac{n}{\delta}, n\delta \right]} \phi(t) \frac{dt}{t} = 0,$$

we can find an $n_0 \in \mathbb{N}$ such that for all $n \geq n_0$,

$$\int_{\mathbb{R}^+ \setminus \left[\frac{n}{\delta}, n\delta \right]} \phi(t) \frac{dt}{t} < \frac{\epsilon}{4kn \|f\|_{C(\mathbb{R}^+)}}.$$

Combining I_1 and I_2 for $n \geq n_0$, we have

$$\| \phi_{n,k} * f(x) - f(x) \|_{C(\mathbb{R}^+)} < \epsilon.$$

□

Using Theorem 1, we prove Theorem 2. Theorem 2 presents sufficient and also necessary conditions for universal approximation by our feedforward neural networks.

Theorem 2. *Let $C(\mathbb{R}^+)$ be the linear space of all continuous functions on \mathbb{R}^+ with a compact support and $V \subset C(\mathbb{R}^+)$ a compact set. Let $k \in \mathbb{R}$ be a constant; let $\{ \phi_{n,k}(x) \}_{n \in \mathbb{N}}$, $\phi_{n,k} : \mathbb{R}^+ :=]0, \infty[\rightarrow]0, \infty[$, be a generalized Mellin approximate identity functions. Let the family of functions $\left\{ \sum_{j=1}^M \lambda_j \frac{\phi_{j,k}(x)}{x} \mid \lambda_j \in \mathbb{R}, x \in \mathbb{R}^+, M \in \mathbb{N} \right\}$, be dense in $C(\mathbb{R}^+)$ and given $\epsilon > 0$. Then there exists $N \in \mathbb{N}$ which depends on V and ϵ but not on f , such that for any $f \in V$, there exist weights $c_n = c_n(f, V, \epsilon)$ satisfying*

$$\left\| f(x) - \sum_{n=1}^N c_n \frac{\phi_{n,k}(x)}{x} \right\|_{C(\mathbb{R}^+)} < \epsilon.$$

Moreover, every c_n is a continuous function of $f \in V$.

Proof. We follow the proof of Theorem 1 in [14]. Since V is a compact set, for every $\epsilon > 0$, there is a finite $\frac{\epsilon}{2}$ -net $\{f^1, \dots, f^M\}$ for V . It follows that for every $f \in V$, there is an f^j , such that $\|f - f^j\|_{C(\mathbb{R}^+)} < \frac{\epsilon}{2}$. For any f^j , under the assumption of our theorem, there are $\lambda_i^j \in \mathbb{R}, N_j \in \mathbb{N}$, and $\frac{\phi_{i,k}^j(x)}{x}$, so that

$$\left\| f^j(x) - \sum_{i=1}^{N_j} \lambda_i^j \frac{\phi_{i,k}^j(x)}{x} \right\|_{C(\mathbb{R}^+)} < \frac{\epsilon}{2}. \tag{22.1}$$

For every $f \in V$, we define

$$\begin{aligned} F_-(f) &= \left\{ j \mid \|f - f^j\|_{C(\mathbb{R}^+)} < \frac{\epsilon}{2} \right\}, \\ F_0(f) &= \left\{ j \mid \|f - f^j\|_{C(\mathbb{R}^+)} = \frac{\epsilon}{2} \right\}, \\ F_+(f) &= \left\{ j \mid \|f - f^j\|_{C(\mathbb{R}^+)} > \frac{\epsilon}{2} \right\}. \end{aligned}$$

It is obvious that $F_-(f)$ is not empty according to the definition of $\frac{\epsilon}{2}$ -net. If $\tilde{f} \in V$ approximates f such that $\|\tilde{f} - f\|_{C(\mathbb{R}^+)}$ is small enough, then we get $F_-(f) \subset F_-(\tilde{f})$ and $F_+(f) \subset F_+(\tilde{f})$. So $F_-(\tilde{f}) \cap F_+(\tilde{f}) \subset F_-(f) \cap F_+(f) = \emptyset$, which implies that $F_-(\tilde{f}) \subset F_-(f) \cup F_0(f)$. Let us finish with the following:

$$F_-(f) \subset F_-(\tilde{f}) \subset F_-(f) \cup F_0(f). \quad (22.2)$$

Define

$$d(f) = \left[\sum_{j \in F_-(f)} \left(\frac{\epsilon}{2} - \|f - f^j\|_{C(\mathbb{R}^+)} \right) \right]^{-1}$$

and

$$f_h = \sum_{j \in F_-(f)} \sum_{i=1}^{N_j} d(f) \left(\frac{\epsilon}{2} - \|f - f^j\|_{C(\mathbb{R}^+)} \right) \lambda_i^j \frac{\phi_{i,k}^j(x)}{x} \quad (22.3)$$

then $f_h \in \left\{ \sum_{j=1}^M \lambda_j \frac{\phi_{i,k}(x)}{x} \right\}$ approximates f with accuracy ϵ :

$$\begin{aligned} &\|f - f_h\|_{C(\mathbb{R}^+)} \\ &= \left\| \sum_{j \in F_-(f)} d(f) \left(\frac{\epsilon}{2} - \|f - f^j\|_{C(\mathbb{R}^+)} \right) \times \left(f - \sum_{i=1}^{N_j} \lambda_i^j \frac{\phi_{i,k}^j(x)}{x} \right) \right\|_{C(\mathbb{R}^+)} \\ &= \left\| \sum_{j \in F_-(f)} d(f) \left(\frac{\epsilon}{2} - \|f - f^j\|_{C(\mathbb{R}^+)} \right) \times \left(f - f^j + f^j - \sum_{i=1}^{N_j} \lambda_i^j \frac{\phi_{i,k}^j(x)}{x} \right) \right\|_{C(\mathbb{R}^+)} \\ &\leq \sum_{j \in F_-(f)} d(f) \left(\frac{\epsilon}{2} - \|f - f^j\|_{C(\mathbb{R}^+)} \right) \\ &\quad \times \left(\|f - f^j\|_{C(\mathbb{R}^+)} + \left\| f^j - \sum_{i=1}^{N_j} \lambda_i^j \frac{\phi_{i,k}^j(x)}{x} \right\|_{C(\mathbb{R}^+)} \right) \\ &\leq \sum_{j \in F_-(f)} d(f) \left(\frac{\epsilon}{2} - \|f - f^j\|_{C(\mathbb{R}^+)} \right) \left(\frac{\epsilon}{2} + \frac{\epsilon}{2} \right) = \epsilon. \end{aligned}$$

(22.4)

Now, we prove the continuity of c_k for the next step. Due to Eq. (22.2), we obtain that

$$\begin{aligned} & \sum_{j \in F_-(f)} \left(\frac{\epsilon}{2} - \|\tilde{f} - f^j\|_{C(\mathbb{R}^+)} \right) \\ & \leq \sum_{j \in F_-(\tilde{f})} \left(\frac{\epsilon}{2} - \|\tilde{f} - f^j\|_{C(\mathbb{R}^+)} \right) \\ & \leq \sum_{j \in F_-(f)} \left(\frac{\epsilon}{2} - \|\tilde{f} - f\|_{C(\mathbb{R}^+)} \right) + \sum_{j \in F_0(f)} \left(\frac{\epsilon}{2} - \|\tilde{f} - f^j\|_{C(\mathbb{R}^+)} \right). \end{aligned} \tag{22.5}$$

Let $\tilde{f} \rightarrow f$ in Eq. (22.5); we arrive at

$$\sum_{j \in F_-(\tilde{f})} \left(\frac{\epsilon}{2} - \|\tilde{f} - f^j\|_{C(\mathbb{R}^+)} \right) \rightarrow \sum_{j \in F_-(f)} \left(\frac{\epsilon}{2} - \|f - f^j\|_{C(\mathbb{R}^+)} \right). \tag{22.6}$$

By Eq. (22.6), we conclude that $d(\tilde{f}) \rightarrow d(f)$. Thus, $\tilde{f} \rightarrow f$ results

$$d(\tilde{f}) \left(\frac{\epsilon}{2} - \|\tilde{f} - f^j\|_{C(\mathbb{R}^+)} \right) \lambda_i^j \rightarrow d(f) \left(\frac{\epsilon}{2} - \|f - f^j\|_{C(\mathbb{R}^+)} \right) \lambda_i^j. \tag{22.7}$$

Let $N = \sum_{j \in F_-(f)} N_j$ and let us define c_k in terms of

$$\begin{aligned} f_h &= \sum_{j \in F_-(f)} \sum_{i=1}^{N_j} d(f) \left(\frac{\epsilon}{2} - \|f - f^j\|_{C(\mathbb{R}^+)} \right) \lambda_i^j \frac{\phi_{i,k}^j(x)}{x} \\ &\equiv \sum_{n=1}^N c_n \frac{\phi_{n,k}(x)}{x}. \end{aligned}$$

From Eq. (22.7), it is easy to check that c_k is a continuous functional according to f . \square

22.4 Conclusion

In this study, we have formalized the notion of generalized Mellin approximate identity. Using this notion, we have proved Theorem 1. Theorem 1 shows that convolution linear operators of generalized Mellin approximate identity with a continuous function f on \mathbb{R}^+ with a compact support converge uniformly to f on

$C(\mathbb{R}^+)$. Using Theorem 1, we have established Theorem 2. Theorem 2 presents sufficient and also necessary conditions for universal approximation by three-layer feedforward generalized Mellin approximate identity neural networks. Our networks use generalized Mellin approximate identity as neurons. The obtained results generalize the existing results in approximation theory of artificial neural networks. We remark that it is important to clarify the lower bound for the approximation error, which is an interesting topic for future research. We also remark that some numerical examples with simulations are needed to show the effectiveness of the established results.

References

1. Huang GB, Chen L, Siew CK. Universal approximation using incremental constructive feedforward networks with random hidden nodes. *IEEE Trans Neural Netw.* 2006;17(4):879–99.
2. Ismailov VE. Approximation by neural networks with weights varying on a finite set of directions. *J Math Anal Appl.* 2012;389(1):72–83.
3. Costarelli D. Interpolation by neural network operators activated by ramp functions. *J Math Anal Appl.* 2014;419(1):574–82.
4. Arteaga C, Marrero M. Universal approximation by radial basis function networks of Delsarte translates. *Neural Netw.* 2013;46(10):299–305.
5. Yu DS. Approximation by neural networks with sigmoidal functions. *Acta Math Sin Engl Ser.* 2013;29(10):2013–26.
6. Ismailov VE. On the approximation by neural networks with bounded number of neurons in hidden layers. *J Math Anal Appl.* 2014;417(2):963–69.
7. Turchetti C, Conti M, Crippa P, Orcioni S. On the approximation of stochastic processes by approximate identity neural networks. *IEEE Trans Neural Netw.* 1998;9(6):1069–85.
8. Panahian Fard S, Zainuddin Z. Analyses for $L^p[a, b]$ -norm approximation capability of flexible approximate identity neural networks. *Neural Comput Appl.* 2013;24(1):45–50.
9. Panahian Fard S, Zainuddin Z. On the universal approximation capability of flexible approximate identity neural networks. *Lect Notes Electrical Eng I.* 2013;236:201–7.
10. Zainuddin Z, Panahian Fard S. Double approximate identity neural networks universal approximation in real Lebesgue spaces. *Lect Notes Comput Sci I.* 2012;7663:409–15.
11. Panahian Fard S, Zainuddin Z. The universal approximation capability of double flexible approximate identity neural networks. *Lect Notes Electrical Eng.* 2014;277:125–33.
12. Panahian Fard S, Zainuddin Z. The universal approximation capabilities of 2π -periodic approximate identity neural networks. *The International Conference on Information Science and Cloud Computing*; 2013 Dec 7–8; Guangzhou, China; IEEE; 2013.
13. Panahian Fard S, Zainuddin Z. The universal approximation capabilities of Mellin approximate identity neural networks. *Lect Notes Comput Sci I.* 2013;7951:205–13.
14. Wu W, Nan D, Li Z, Long J. Approximation to compact set of functions by feedforward neural networks. In *20th International Joint Conference on Neural Networks*; Orlando, FL; 2007. pp. 1222–5.
15. Singh B, Sharma K, Rathi S, Singh G. A generalized log-normal distribution and its goodness of fit to censored data. *Comput Stat.* 2012;27(1):51–67.
16. Panahian Fard S, Zainuddin Z. The universal approximation capabilities of double 2π -periodic approximate identity neural networks. *Soft Comput.* 2014; DOI [10.1007/s00500-014-1449-8](https://doi.org/10.1007/s00500-014-1449-8)

Chapter 23

Research and Application of Function Optimization Based on Artificial Fish Swarm Algorithm

Meiling Shen, Li Li, and Dan Liu

Abstract The software reliability modeling is an important field in software reliability engineering. As the existing software reliability models are nonlinear, the parameters of these models are difficult to estimate. The artificial fish swarm algorithm is simple and can quickly jump out of local extremum. Now it has been applied to the parameter estimation. On the basis of the basic artificial fish swarm algorithm, this paper improves the algorithm to improve the speed of convergence and gain a strong ability to overcome the local extreme value because the improved algorithm ignores the crowded degree factor; moreover, we make the artificial fishes only to execute the preying behavior and moving behavior in the later stage of algorithm to reduce the visual field of artificial fishes through the introduction of the attenuation factor and thus to improve the precision. The results of simulation experiments verify the improved algorithm has the ideal rate of convergence and precision of optimization.

Keywords Artificial fish swarm algorithm • Crowded degree factor • Attenuation factor • Software reliability engineering

23.1 Introduction

The artificial fish swarm algorithm is a new kind of swarm intelligence optimization algorithm which is proposed upon the in-depth study of artificial fishes' foraging behavior [1]. Each of the artificial fish firstly tries to execute swarming behavior and following behavior respectively; choose the behavior which makes fitness value of this artificial fish improved larger. If the fitness value has not been improved after the artificial fish has executed these two behaviors, we are going to execute the preying behavior; if the fitness of the artificial fish still fails to get improved upon the preying behavior, we'll execute the moving behavior [2]. There are five basic

M. Shen • L. Li (✉) • D. Liu
Changchun University of Science and Technology, Changchun 130012, China
e-mail: ll@cust.edu.cn

parameters of artificial fish swarm algorithm [3]. The selection of the each parameter directly affects the convergence performance of the algorithm. The selection of appropriate parameters can ensure the algorithm convergence speed and the optimization accuracy [4]. Artificial fish swarm algorithm has stronger ability to jump out of local optimum, and it has strong robustness [5]. Now it has been used in many fields such as parameter estimation [6], pattern recognition, and neural network; in spite of the sound performance of the artificial fish swarm algorithm, there are still many aspects need to be improved.

23.2 Improved Artificial Fish Swarm Algorithm

23.2.1 *Improvement Ideas*

The crowded degree factor is used to limit the scale of artificial fish; however, after repeating theoretical analysis and experimental verification, people find that the effect of crowded degree factor is very limited in optimization problems. The results of the complex optimization experiments show that the convergence of algorithm has not been substantially improved upon the introduction of the crowded degree factor. In some cases, it will cause a decline in convergence on the contrary [7]; therefore, this paper ignores the crowded degree factor, which thus reduces the computational complexity of the algorithm, guarantees rapid and stable convergence at the same time, and enables the algorithm to obtain ideal optimization precision and the ability to overcome the local extremum. The artificial fish swarm algorithm features fast convergence speed, and the fishes can quickly reach the vicinity of the global extreme value point in the early stage; however, in the later stage of the algorithm (namely, when the artificial fishes in the area near the global extreme value point), the optimization accuracy is not high and convergence speed is slow [8, 9]. As a result, this article only makes artificial fishes to execute preying behavior and moving behavior in the later stage of algorithm thus to make the algorithm to find the global extreme value point rapidly and accurately. The visual field in artificial fish swarm algorithm has great influence on each behavior. When the visual field is larger, the artificial fishes can find the global extreme value point easily and converge; when the visual field is smaller, the preying behavior and moving behavior of artificial fishes are more outstanding, and the algorithm has better local search ability. As the improved algorithm only executes the preying behavior and the moving behavior in the later stage of algorithm, therefore, this article also introduces the attenuation factor [10]. With the execution of the algorithm, the improved algorithm may reduce the visual field of artificial fishes to strengthen the search ability of them in the nearby neighbor domain and obtain ideal optimization precision.

23.2.2 Steps of the Improved Algorithm

- Step 1: Initialize the population, including population size N , visual, step, try-number, and maximum number of iterations.
- Step 2: Calculate the fitness value of each artificial fish according to the objective function, and use a bulletin board to record the state of the artificial fish which has the biggest fitness value.
- Step 3: When the algorithm executes the first n iterations, evaluate each of the artificial fish in case that the crowded degree factor is ignored, and select a behavior which can make the fitness value of this artificial fish to acquire a bigger improvement to execute (among the preying behavior, swarming behavior, following behavior, and moving behavior). After n iterations, let them only execute the preying behavior and moving behavior by the time when the artificial fishes are going to find the global extreme value. Upon the completion of each iteration, use $\text{Visual} = \alpha \cdot \text{Visual}$ to reduce the visual field of artificial fishes to enhance the local search ability of artificial fishes. Each of the artificial fish would compare its own state and the state of the bulletin board in every action. If its own state is superior to the state of bulletin board, change the state of the bulletin board to its own state.
- Step 4: Judge whether the end conditions are met, if the maximum number of iterations are already achieved, end the cycle; otherwise, return to Step 3, and continue the cycle.

23.3 Simulation Experiment

Under the environment of MATLAB 7.1; we conduct the simulation experiments for the original and the improved artificial fish swarm algorithm with two nonlinear functions selected:

Function F1:

$$\begin{aligned} \max f(x, y) &= \frac{\sin(x)}{x} \cdot \frac{\sin(y)}{y} & (23.1) \\ \text{s.t. } x &\in [-10, 10] \\ y &\in [-10, 10] \end{aligned}$$

Figure 23.1 illustrates the three-dimensional network diagram of F1 function. Figure 23.2a shows the optimized curve of original algorithm as to F1 function in contrast to the one of improved algorithm shown in Fig. 23.2b.

As to function F1, there is a maximum of 1 at the coordinates of (0,0) based on Fig. 23.1. The paper studies the global optimal value of function F1 drawing on the original algorithm and the improved one, and it compares the results and the

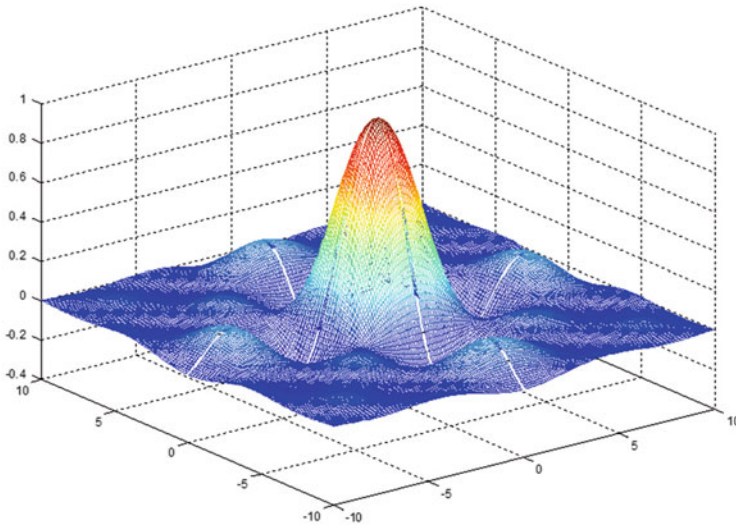


Fig. 23.1 Three-dimensional network diagram of function F1

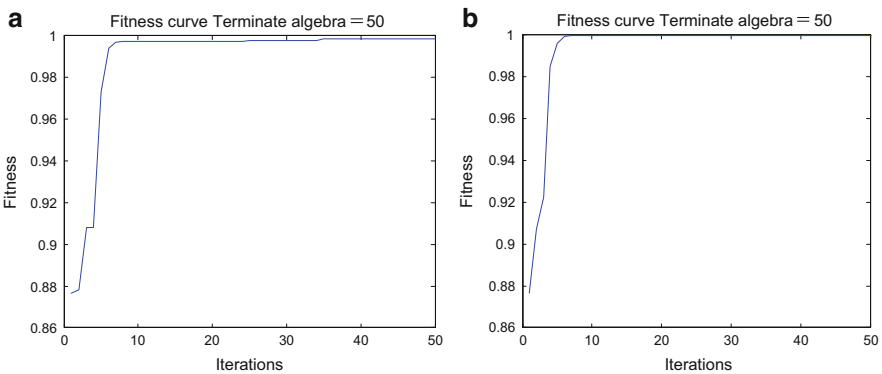


Fig. 23.2 Optimized curve of original and improved algorithms (F1 function)

running time of the two algorithms. It can be concluded that the precision of the latter is higher based on the comparative results of Table 23.1.

Function F2:

$$\begin{aligned} \max f(x, y) &= \left(\frac{3}{0.05 + (x^2 + y^2)} \right)^2 + (x^2 + y^2)^2 & (23.2) \\ \text{s.t. } x &\in [-5.12, 5.12] \\ y &\in [-5.12, 5.12] \end{aligned}$$

Table 23.1 Optimized comparison of original and improved algorithms (F1 function)

	The optimal value	The running time/s
The original algorithm	0.99845102937585	4.145932
The improved algorithm	0.99998089990914	1.312120

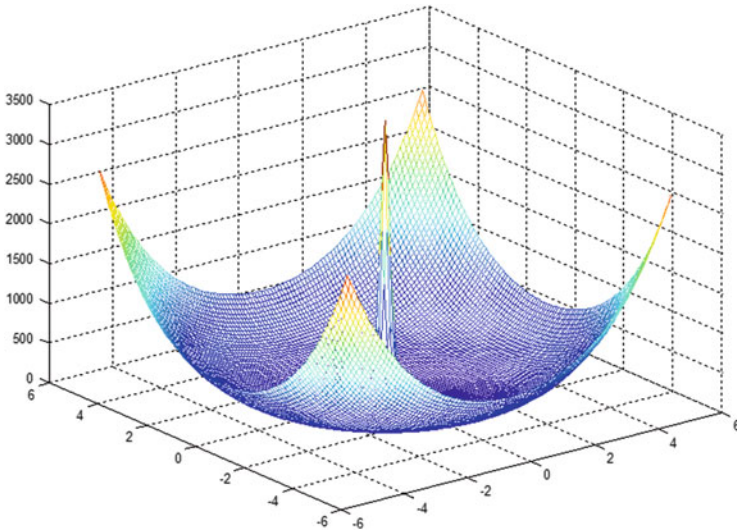


Fig. 23.3 Three-dimensional network diagram of function F2

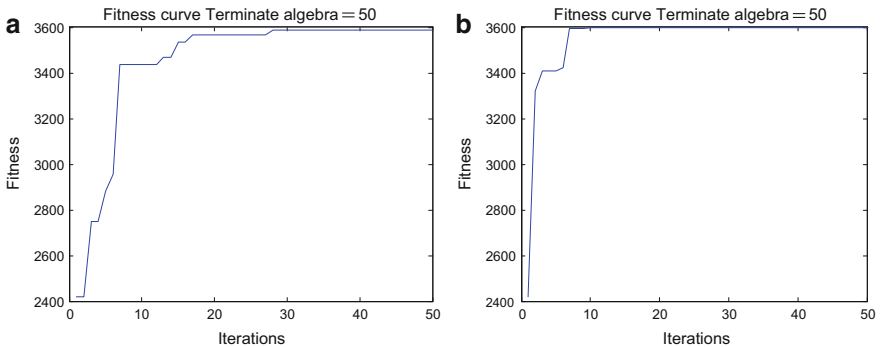


Fig. 23.4 Optimized curve of original and improved algorithms (F2 function)

Figure 23.3 demonstrates three-dimensional network diagram of function F2. Figure 23.4a shows the optimized curve of original algorithm as to function F2 in comparison with the one of improved algorithm shown in Fig. 23.4b.

As to function F2, there is a maximum of 3,600 at the coordinates of (0,0) based on Fig. 23.3. The paper studies the global optimal value of function F2, utilizes the original algorithm and the improved one, and compares the results and the running

Table 23.2 Optimized comparison of original and improved algorithms (F2 function)

	The optimal value	The running time/s
Original algorithm	3.589245463241951e + 003	6.944870
Improved algorithm	3.599158718382575e + 003	1.644836

time of the two algorithms. It is concluded that the precision of the latter is higher based on the comparative results of Table 23.2.

Conclusion

In the two simulation experiments, population size, visual, step, try-number, and maximum number of iterations of two kinds of algorithms are the same. In Figs. 23.2 and 23.4, we can see that relative to the basic artificial fish swarm algorithm, the convergence speed of the improved algorithm is faster, and the convergence process is more smooth and steady primarily because the improved algorithm ignored the crowded degree factor. Tables 23.1 and 23.2 show that the running time of improved algorithm is shorter and optimization precision of it is also ideal because the improved algorithm only makes the artificial fishes to execute the preying behavior and moving behavior when they reach the area around of global extreme value point, and it reduces the visual field of artificial fishes in the process of iteration to gain a higher precision.

References

1. Wang C. The analysis and improvement of artificial fish swarm algorithm. Dalian: Dalian Maritime University; 2008 (In Chinese).
2. Farzi S. Efficient job scheduling in grid computing with modified artificial fish swarm algorithm. *Int J Comput Theory Eng.* 2009;1(1):1793–8201.
3. Yang S, Zhang H. Swarm intelligence and evolutionary computation-Matlab Technology. Beijing: Publishing House of Electronics Industry; 2012. p. 210–3 (In Chinese).
4. Wang G, Shi Q. The parameters of the artificial fish algorithm analysis. *Comput Eng.* 2010;36(24):169–71 (In Chinese).
5. Wang X. Research of artificial fish swarm algorithm improvement. Xian: Xian University of Science and Technology Building; 2007 (In Chinese).
6. Li X, Xue Y, Fei L, Tian G. Parameter estimation method based on artificial fish algorithm. *J Shan Dong University (Eng Sci).* 2004;34(3):84–7 (In Chinese).
7. Jiang Y, Yuan D. Artificial fish algorithm and its application. Beijing: Science Press; 2012. p. 54–9 (In Chinese).
8. Wang G. The research of artificial fish swarm algorithm and its application. Lanzhou: Lanzhou University of Technology; 2009 (In Chinese).
9. Li X. A new type of intelligent optimization method, the artificial fish algorithm. Zhejiang: Zhejiang University; 2003 (In Chinese).
10. Jiang M, Mastorakis NE, Yuan D, Laguans MA. Multi-threshold image segmentation with improved artificial fish swarm algorithm. *Proceedings of the European Computing Conference (ECC 2007)*. Berlin: Springer; 2007. p. 117–20.

Chapter 24

Robust Hand Tracker Using Joint Temporal Weighted Histogram Features

Zhiqin Zhang, Fei Huang, and Linli Tan

Abstract Herein, a novel automatic hand-tracking approach based on temporal histogram features is proposed. Our method utilizes the joint temporal weighted histogram (JTWH) to track the hand robustly. When tracking begins, the hand model is initialized using a hand detector. During the tracking process, the hand model is updated using the most recent frame data and the hand tracker uses the weighted temporal model to track the hand persistently and robustly. The weights are calculated using the temporal and spatial similarity between the hand model and the current tracked hand. Because hand movement can be fast and may produce deformation, a weighted histogram was selected for the single hand model. Experiments demonstrate the proposed algorithm's ability to track the moving hand robustly in comparison with several traditional hand-tracking algorithms. The proposed approach is robust in the complex background, and it can track the hand quickly and effectively.

Keywords Hand tracking • Joint temporal weighted histogram • Spatial similarity • Temporal similarity

24.1 Introduction

The main motivation behind gesture recognition is to recognize specific hand gestures and make human-computer interaction more flexible. Efficient human-computer interfaces (HCI) have to be developed to allow computers to visually recognize hand gestures in real time. Presently, gesture recognition approaches can be mainly divided into a 3D model-based approach and a 2D appearance-based approach. The 3D model-based approach requires a 3D spatial description of the hand whilst the appearance-based approach only needs 2D visual images of the hands [1]. Generally, the 2D approaches must conquer several challenging

Z. Zhang (✉) • L. Tan
School of Computer Science, Wuhan Donghu University, 430000 Wuhan, China
e-mail: zzq9908@sohu.com

F. Huang
Multimedia Research Center, Wuxi YSTEN Technology Co., Ltd., 430000 Wuhan, China

problems such as a complex background, lighting variations, different camera devices, etc.

Generally, the gesture recognition involves both hand tracking and hand detection. Hand tracking is used to track the hand during the human–computer interaction procedure whilst hand detection is used to recognize whether the target is the hand or not. The stability and accuracy of human–computer interaction procedures are mainly dependent on hand-tracking stability. Motion blur and serious hand deformation mean some of the traditional tracking algorithms do not fit hand tracking, for example block matching and key point feature extraction. To track the hand reliably, we must solve several core problems: (1) motion blur, (2) hand deformation, (3) the complex background and light variation, and (4) scale variation.

For this work, we selected the joint temporal weighted histogram (JTWH) to track the hand. JTWH is used to achieve fully real-time performance and can track the hand accurately and reliably. The tracking system also shows reasonable robustness against scale, rotation, different illuminations, and cluttered backgrounds. Generally speaking, the system can work in various complex environments.

This paper is organized as follows. We begin by reviewing existing works on hand tracking in Sect. 2. In Sect. 3, we present the main algorithm module and analyze the reason why it can track the hand robustly. In Sect. 4, we present the experiment results and compare them with alternative methods. In the last section, we summarize our approach and discuss its limitations.

24.2 Related Work

2D vision-based approaches require only a 2D camera, thus realizing the natural interaction between humans and computers without the use of any extra devices. The 2D camera extracts image features to model the visual appearance of the hand and to allow comparison of these features with the extracted features from previous video frames. Real-time performance is ensured because of the easier 2D image features that are used. A simple method described by Stenger [2] utilizes skin color features in the image for tracking. However, this method has some shortcomings. Firstly, it is very sensitive to lighting conditions. Secondly, it is a requirement that there are no other skin-like objects in the image.

Scale-space color features are used to track and detect hand gestures, which are based on feature detection in [3]. The authors of [4] obtained a clear-cut hand contour and integrated the extracted hand contour to track and detect hand gestures and then computed the curvature of each point on the contour. Because of noise and unstable illumination in the cluttered background, segmentation of the integrated hand contour is very difficult and the segmentation results are not reliable.

Tracking parameterized deformable templates of the hand or fingers [5] is a more elaborate and precise method that can handle complex backgrounds. In

particular, particle filter-based tracking [6] has been shown to be a robust approach. Depending on the algorithm and the users clothing (e.g., sleeves rolled up), hand–arm segmentation may also be necessary as an extra processing step [7, 8] in hand tracking or localization. However, various assumptions are made, such as the hand being the only skin-colored object, uniform ambient lighting, or a stationary background, which may not match practical environments.

24.3 JTWH Hand Tracker

Generally, the hand-tracking procedure consists of three main stages: (1) Constructing the hand model. (2) Computing the similarity of the current candidate hand target and model and finding the target location of peak similarity. (3) Updating the model. Tracking reliability and accuracy are mainly dependent on the extracted features for tracking, similarity measurement, and model updating.

24.3.1 Tracker Theory Overview

A block diagram of a generic model-based tracking system [5] is shown in Fig. 24.1. At each frame of the image sequence, a search is executed in the configuration space to find the best parameter that minimizes the matching error, which is a measure of similarity between groups of model features and groups of features extracted from the input images. The search is initiated by a prediction mechanism, based on a model of the system dynamics. In the first frame, a prediction is not available, therefore, a separate initialization procedure is needed,

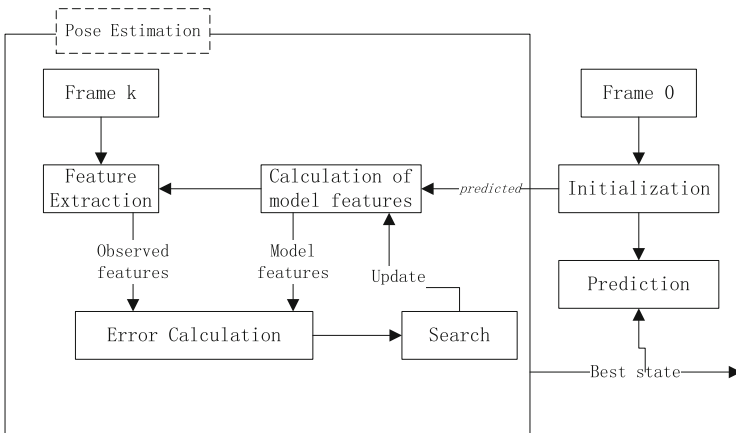


Fig. 24.1 Model-based tracker

and we initialized the model using the hand detector. In the search phase the basic operation is the calculation of the matching error between the features extracted from the input and the features generated by the model. The synthesis of features using the model also enables a selective analysis that focuses on regions or a subset of features instead of the whole input. In the most common implementation, 2D features in the image plane are used.

Considering hand deformation and motion blur, the extraction of point-based features is not a good choice, local or global statistical features can be used which are better for hand tracking. Tracking and Detection is also a good method for solving hand-tracking problems, for example TLD (tracking-learning-detection) [9, 10] algorithm, but the extracted features should be changed, because it is not stable in the hand-tracking system.

24.3.2 Our Approach

24.3.2.1 JTWH Feature

Traditional model-based tracking algorithms are not reliable in complicated environments and it's easy to produce track offset errors due to motion blur and hand deformation. When using skin color detection to track the hand it is also easy to track the wrong target when local luminance and backgrounds are similar to skin color, thus it is necessary to determine statistical features that contain target temporal and spatial information to improve target identification. To improve target identification, use of JTWH features is proposed in this paper. HSV (Hue Saturation Value) is a good color space that can efficiently distinguish hand color from background color [11], so we extract our JTWH features in HSV. The proposed JTWH feature is a kind of JTWH feature group that consists of a temporal weighted histogram and spatial kernel weighted histogram. JTWH is calculated jointly using the target histograms of several of the latest frames such that

$$H_t^{\text{JTWH}} = \frac{\sum_{i=t-n}^n W_i H_i^{\text{SW}}}{U}, \quad (24.1)$$

where H_i^{SW} is the i th frame spatial weighted histogram, U is used for normalization and $U = \sum_{i=t-n}^t W_i$, W_i is the weight function, and $n = 3$ in our experiments. To reduce the background disturbance, H_i^{SW} is weighted using spatial information such that

$$H_i^{\text{SW}}[j] = \sum_x^\Omega K(x) \delta(f(x) - j), \quad (24.2)$$

where j represents for the index of the histogram bin, x is the coordinate of image f and $f(x)$ is the x coordinate pixel value in image f . δ is the delta function and $K(x) = \left\| \frac{x-x_0}{h} \right\|^2$ is a kernel function which is used for calculating the histogram of image patch, x_0 is the center coordinate of the image patch and h is the radius.

The hand color and shape in the current frame are mostly like those of the previous frame, so the temporal weighting function is designed as a Gaussian function such that

$$w_i = e^{-\frac{(t_i - t_0)^2}{b}}, \quad (24.3)$$

where t_0 is the current frame count and t_i is the previous i th frame count.

When the JTWH feature is constructed and extracted, various histogram measurements can be used to calculate the similarity between the model and the candidate hand target; in our experiments we used the Bhattacharyya distance [12, 13] to measure histogram similarity.

24.3.2.2 Tracker System

Model initialization is very important. In our experiment, the model was initialized using hand detection. Firstly, a statistical model was loaded to detect the hand. Then an XML file classifier for frontal gestures was used for detection. The detection and testing stages were then completed using the open source vision library OpenCV. After the hand model was initialized, the tracker system could track a hand robustly and quickly. A brief hand-tracking diagram is shown in Fig. 24.2.

Model updating is another key point for reliable tracking. An adaptive model updating method is proposed in this paper. The proposed model updating method is such that:

$$M_{i-t} = S^2 * T_i + (1 - S^2) * M_{i-t}, \quad (24.4)$$

where T_i is the tracked hand histogram at the i th frame, the temporal interval between T_i and M_{i-t} is the t frame interval, and s is the similarity between histogram T_i and M_{i-t} . In our experiments t was set to 3.

Upon integrating the JTWH feature, model updating and similarity measurement, the proposed tracker system can track the hand robustly and accurately.

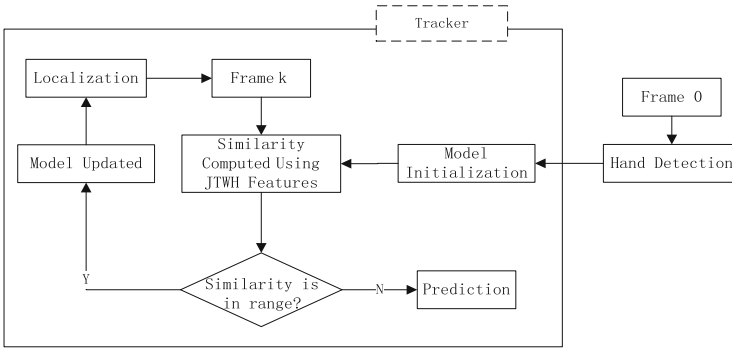


Fig. 24.2 A brief diagram of the tracking system

24.4 Experimental Results and Analysis

To evaluate the performance of the proposed algorithm, we tested the algorithm using some hand gesture data including the palm gesture and the fist gesture. The camera provides video capture with a resolution of 640×480 , at 30 frames per second using a Pentium 4 CPU 2.5 GHz computer.

Hand movement video data were recorded at different scales, rotations, and illumination conditions, along with a cluttered background. The test was run on different video files to evaluate the performance of the JTWH tracker system for different hand motion states and speeds. The results showed an excellent degree of robustness against scale, rotation, illumination, and for a cluttered background.

In Fig. 24.3 some results are presented for the hand tracker system with testing of robustness against scale, rotation, illumination, and for a cluttered background.

We compared the proposed approach with various other approaches, and these detection results are shown in Fig. 24.4. In Fig. 24.4, three different algorithms were compared to test tracking reliability and accuracy. The three different algorithms were camshift, TLD, and the JTWH tracker.

From Fig. 24.4, we can see that the tracking result for camshift is sensitive to the skin color-like background, meanwhile the TLD algorithm is not reliable when tracking a fast deforming hand and it is easy to lose the hand because the hand texture is fuzzy and it is not easy to extract the key point in every frame. On the contrary, the tracking result for our proposed approach has a higher tracking accuracy, and can track the hand more robustly.

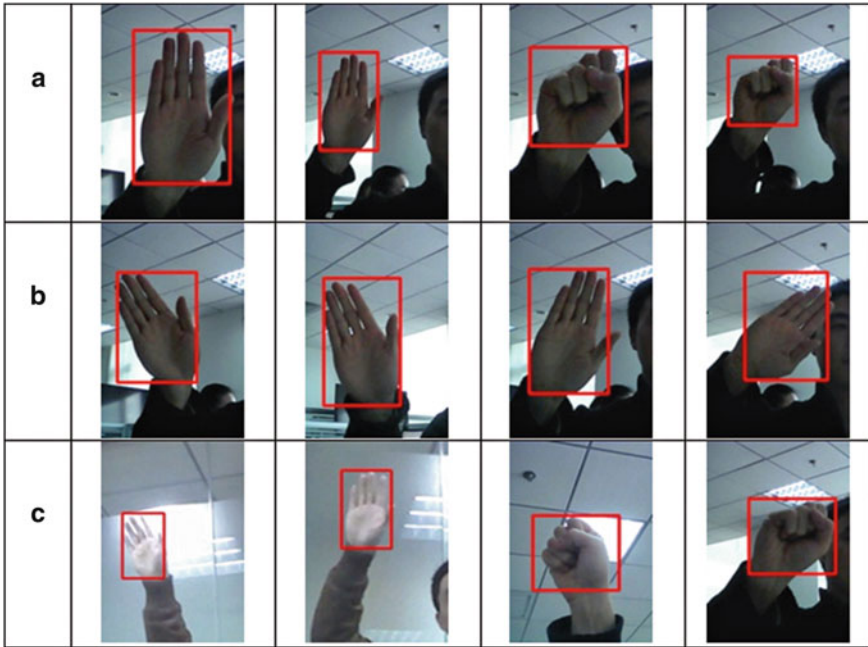


Fig. 24.3 Hand-tracking results using the proposed approach with a cluttered background against: (a) Scale; (b) rotation; (c) illumination

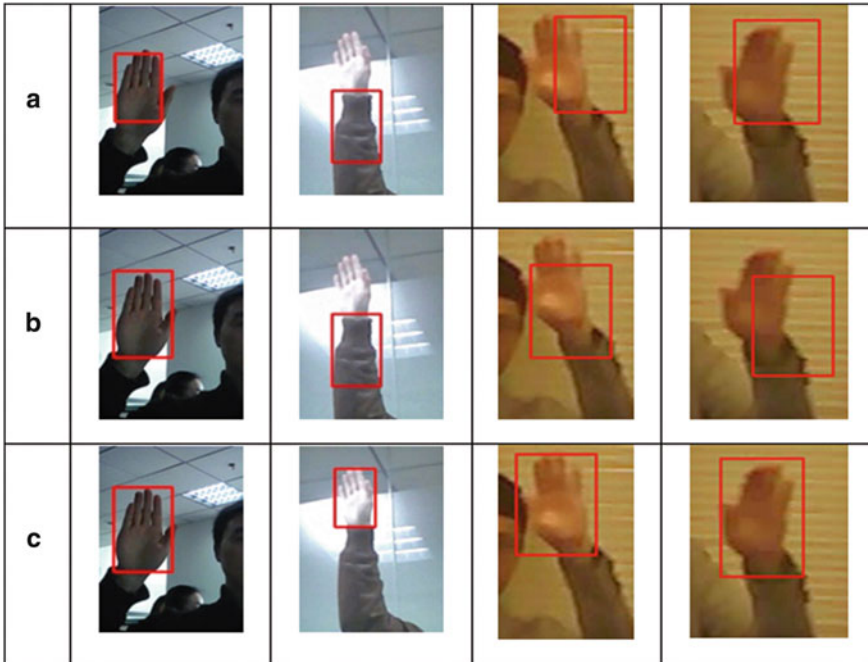


Fig. 24.4 Comparison of tracking results. (a) The tracking result for camshift; (b) the tracking result for TLD; (c) the tracking result for the proposed algorithm

Conclusion

In this paper, we presented a novel hand-tracking approach based on JTWH features. JTWH features are not sensitive to deformation and motion blur, integrating both the similarity measurement and the adaptive model updating method; the proposed algorithm can track the hand reliably and accurately. Future work will aim to test the algorithm in different color spaces to improve skin color discrimination.

References

1. Chang C, Chen I, Huang Y. Hand pose recognition using curvature scale space pattern recognition. In: Proceedings of the 16th International Conference on Pattern Recognition; IEEE Conference Publications, New Jersey; 2002. vol. 2, p. 386–89.
2. Stenger B. Template-based hand pose recognition using multiple cues. In: Proceedings of the 7th Asian Conference on Computer Vision, ACCV2006; Springer, Berlin, Germany; 2006. p. 551–60.
3. Ong E, Bowden R. A boosted classifier tree for hand shape detection. In: Proceedings of the 6th International Conference on Automatic Face and Gesture Recognition; IEEE Conference Publications, New Jersey; 2004. p. 889–94.
4. Hadid A. The local binary pattern approach and its applications to face analysis. In: International Conference on Image Processing Theory, Tools and Applications; IEEE Conference Publications, New Jersey; 2008. p. 1–9.
5. Erol A, Bebis G, Nicolescu M, Boyle RD, Twombly X. Vision-based hand pose estimation: a review. In: Proceedings of the Computer Vision and Image Understanding; IEEE Conference Publications, New Jersey; 2007. p. 52–73.
6. Bazzani L, Cristani M, Murino V. Decentralized particle filter for joint individual-group tracking. In: Proceedings of the CVPR2012; IEEE Conference Publications, New Jersey; 2012. p. 1886–93.
7. Zhang D, Javed O, Shah M. Video object segmentation through spatially accurate and temporally dense extraction of primary object regions. In: Proceedings of the CVPR2013; IEEE Conference Publications, New Jersey; 2013. p. 628–35.
8. Angelova A, Zhu S. Efficient object detection and segmentation for fine-grained recognition. In: Proceedings of the CVPR2013; IEEE Conference Publications, New Jersey; 2013. p. 811–18.
9. Kalal Z, Mikolajczyk K, Matas J. Face-TLD: tracking-learning-detection applied to faces. In: International Conference on Image Processing; IEEE Conference Publications, New Jersey; 2010. p. 3789–92.
10. Chen Q, Georganas N, Petriu E. Real-time vision-based hand gesture recognition using haar-like features. In: IEEE Instrumentation and Measurement Technology Conference Proceedings; IEEE Conference Publications, New Jersey; 2007. p. 1–6.
11. Li Z, Guo J, Cheong L-F, Zhou SZ. Perspective motion segmentation via collaborative clustering. In: Proceedings of the ICCV2013; IEEE Conference Publications, New Jersey; 2013. p. 1369–76.
12. Zuo W, Zhang L, Song C, Zhang D. Texture-preserved image denoising via gradient histogram estimation and matching. In: Proceedings of the CVPR2013; IEEE Conference Publications, New Jersey; 2013. p. 1203–10.
13. Weinzaepfel P, Revaud J, Harchaoui Z, Schmid C. DeepFlow: large displacement optical flow with deep matching. In: Proceedings of the ICCV2013; IEEE Conference Publications, New Jersey; 2013. p. 1385–92.

Chapter 25

Combination of User's Judging Power and Similarity for Collaborative Recommendation Algorithm

Li Zhang, Yuqing Xue, and Shuyan Cao

Abstract As an effective way to solve information overload, the collaborative filtering (CF) algorithm has been widely used in the personalized recommendation. In order to improve the accuracy of recommendation, an improved collaborative recommendation algorithm is proposed. Firstly, evaluate the user's judging power based on historical scoring; then, combine the user's judging power and similarity to improve the traditional user-based CF algorithm. Experimental results show that the judging power is positively correlated with the recommendation abilities of users and also verify that the judging power extracts the depth information from historical scoring and factors to influence a user on adopting the recommendation results.

Keywords Collaborative filtering • Judging power • Similarity • Information diffusion

25.1 Introduction

With the maturity of Web 2.0, the personalized recommendation has been greatly developed, which brings about a large amount of commercial profits and benefits with its accuracy, efficiency, and individuation. Under the efforts from different research fields, the recommendation technologies are becoming more and more mature. Although, along with the increase of users and items, sparse and real-time greatly challenges the performance of the CF algorithm; it is still the most popular recommendation algorithm in the personalized information service. Researchers have carried out a lot of work to improve its performance, such as item-based CF, probability-based CF, matrix reduction-based CF, clustering-based CF, etc. [1]. Some model-based CF algorithms show extraordinary talents, such as the probability model, maximum entropy model, linear regression model, and *Gibbs*

L. Zhang (✉) • Y. Xue • S. Cao
School of Information Technology & Management Engineering, University of International Business and Economics, Beijing 100020, China
e-mail: tasummer@sina.com

abstract and *Bays* model [2]. On the basis of these studies, the user's judging power is combined with the similarity between users to improve the CF algorithm in the paper, which is calculated based on rating data.

25.2 Related Work

The CF algorithm is based on the assumption that similar users always have some common views on interests and hobbies; as to the user-based CF, the main process is trying to find out who can collaborate with the target users. It tries to find N neighbors who have the highest similarity with the target user. In order to improve the performance of the recommendation algorithms and reduce the computational complexity, researchers have done a lot on the similarity calculation and neighbor selecting with related works divided into three branches. One branch is adding time, item attributes, user interest, and other factors into the similarity estimation. The time factor was integrated with user similarity to improve the performance of the recommendation algorithm [3]. On the basis of the amount of co-rated items and the variance of rating to evaluate the similarity between users, Zhang et al. improved the performance by users' dynamic reordering in the nearest neighbor set [4]. Sun et al. do the same work [5]. Some researchers (Cheng et al. and Zitouni et al.) combined item attributes with user rating to calculate the similarity between users and also enhance the algorithms [6, 7]. Zhang et al. calculated users' similarity based on their interests as described by the item similarity, and the algorithm also achieved good results [8]. The second branch is using social network information to enhance similarity. Some scholars (Yuan et al. and Lee et al.) integrated users' rating data with friendship or membership in a social network or social network tag data to calculate the similarity between users [9, 10]. On the other hand, Chen and Fong introduced trust into the calculation of similarity and considered that users with a higher trust degree would have greater similarity [11]. The third branch is to improve the similarity calculation method based on the structure of social network. Zheng et al. calculated the distance between users based on social network graph and adjusted similarity calculation with the distance. They considered that the closer the users were, the greater similarity they would have [12]. Nonetheless, the computational complexity of distance calculation became higher with the increase of users and items. Some researchers introduced the diffusion theory and heat conduction into personalized recommendation and proposed a batch of improved algorithms. Tao Zhou et al. put forward the resource allocation model in the user-item bipartite network. In the CF algorithm, user resources can be viewed as his/her recommendation capability used as weights to calculate similarity [13]. Xing-Yao et al. fused singular values and the above resource allocation model to improve the similarity calculating method [14], which thus enhanced the performance of the recommendation algorithms and alleviated cold-start problems for a certain extent; what is more important is that it brought about a new perspective for related researchers.

The above studies have improved the performance of the CF algorithm to some extent, but they have not taken the impact of professional judgment on recommendation results into consideration. The similarity threshold or limitation may cause users with better judging power cannot be used for recommendation. It has been proved that the professional ability and judging power of information dispersers are important factors which may affect the adoption of recipients in the process of word-of-mouth [15]. We improve the performance of user-based CF algorithm by making use of the user's judging power in this paper, which can reflect the influence of users in the social network and describe user similarity more truly.

25.3 Traditional User-Based CF Algorithm

The paper adopts traditional user-based CF algorithm as the baseline algorithm, which is also called neighbor-based CF algorithm and noted as *SCF* in the paper. Firstly, *SCF* constructs the nearest neighbor sets as the target users by user similarity and then predicts the rating of target users for each item that has been rated by users collectively in the selected neighbor set. Finally, the top-*m* items reordered by the predicted rating are recommended to the target users.

25.3.1 User Similarity

Here, the *Pearson* coefficient is used to estimate the similarity between users. Suppose $I(u)$ and $I(v)$ are item sets that have been rated by user u and v , respectively; thus, $I(u) \cap I(v)$ can mean item intersection rated by user u and v [8]. Then the similarity between user u and v ($\text{sim}(u, v)$) is indicated by Formula (25.1):

$$\text{sim}(u, v) = \frac{\sum_{i \in I(u) \cap I(v)} (R_{u,i} - \bar{R}_u)(R_{v,i} - \bar{R}_v)}{\sqrt{\sum_{i \in I(u) \cap I(v)} (R_{u,i} - \bar{R}_u)^2} \sqrt{\sum_{i \in I(u) \cap I(v)} (R_{v,i} - \bar{R}_v)^2}} \quad (25.1)$$

where $R_{u,i}$ and $R_{v,i}$ denote the scoring on the item $i (i \in I(u) \cap I(v))$ for user u and v , respectively, while \bar{R}_u and \bar{R}_v are their means. All the rating data of users used in this paper is normalized into [0, 1].

25.3.2 Predicted Rating

The weighted mean method is adopted to predict the score for target users [8], as shown in Formula (25.2):

$$p_{u,t} = \bar{R}_u + \frac{\sum_{v \in N_u} \text{sim}(u, v) (R_{v,t} - \bar{R}_v)}{\sum_{v \in N_u} \text{sim}(u, v)} \quad (25.2)$$

where N_u denotes the nearest neighbor set for target user u and $p_{u,t}$ means the predicted score on item $t(t \in I(N_u))$, which is the item intersection rated by users in N_u for user u .

25.4 Improved CF Algorithm Based on User's Judging Power

The traditional user-based CF is to find the nearest neighbors of target users for recommendation. As a result, the recommendation capacity of the neighbor set affects the performance of the algorithm directly, whereas the traditional algorithm has not distinguished the user's judging power while choosing neighbors. Due to the similarity threshold or the limitation on the amount of neighbors, users with better recommendation capacity may not be added into the nearest neighbor set. In order to get a better neighbor set, we make an overall consideration of the similarity between users and recommendation capacity. In this paper, the recommendation capacity is indicated by the user's judging power.

25.4.1 User's Judging Power

Suppose there are N users $\{u_1, u_2, \dots, u_N\}$ and M items $\{I_1, I_2, \dots, I_M\}$. Each user has a different judging power, and each item has a different quality. The judgment of a user and the quality of item are implied from the existing rating information. The mean score is often used as a representation of the inherent quality of items; however, it is affected greatly by noisy data; besides, it supposes each user has the same judging power, which does not comply with the previous assumption. Thus, this paper calculates the user's judging power by the variance score and item's quality [16]. The main steps are shown as below:

1. Calculate quality q_j for item j in the dataset by Formula (25.3):

$$q_j = \sum_{u=1}^N \alpha_{u,j} \times w_u \times R_{u,j} \quad (25.3)$$

where w_u is the judging power of user u and its initial value is $1/N$; $\alpha_{u,j}$ indicates whether user u rated item j ; if he/her rates the item, let $\alpha_{u,j} = 0$; on the contrary, $\alpha_{u,j} = 1$ and $R_{u,j}$ denote user u scoring on item j .

2. Calculate the user's rating variance by Formula (25.4):

$$v_u = \frac{1}{\sum_{j=1}^M \alpha_{u,j}} \sum_{j=1}^M \alpha_{u,j} (R_{u,j} - q_j)^2 \quad (25.4)$$

3. Reckon w_u by Formula (25.5):

$$w_u = \frac{v_u^{-1}}{\sum_{i=1}^N v_i^{-1}} \quad (25.5)$$

4. Repeat 1–3 until the quality difference between two rounds reaches the threshold, and then we can get the final judging power w_u for user u .

25.4.2 Improved CF Algorithm

The improved algorithm in the paper mainly improves the nearest neighbor set selection. The other steps are the same as the *SCF* algorithm. In order to explore the impact of the user's judgment on CF performance, the neighbor set for target users is constructed in two ways, distinguishing *UPCF1* from *UPCF2*.

The main idea of the *UPCF1* algorithm is shown as below:

Input: user rating for items

Output: top- m items

Step 1: calculate the judging power w_u for user u based on the algorithm described in Sect. 25.4.1.

Step 2: combine the user's judgment as a kind of weight with the similarity calculation in Formula (25.1), shown in Formula (25.6), and select k nearest neighbors to generate the neighbor set N_u for user u based on this:

$$\text{sim}'(u, v) = w_v \times \text{sim}(u, v) \quad (25.6)$$

Step 3: generate item set $I(N_u)$ rated by the users collectively in N_u .

Step 4: compute $p_{u,t}(t \in I(N_u))$ by Formula (25.2) and reorder them in descending order based on $p_{u,t}$.

Step 5: select the top- m items and recommend them to user u .

Same as the above UPCF1 algorithm, the main idea of the UPCF2 algorithm can be described as below:

Input: user rating for items

Output: top- m items

Step 1: calculate the judging power w_u for user u based on the algorithm described in Sect. 25.4.1.

Step 2: compute the similarity between user u and another user v by Formula (25.1), and then select N_1 nearest neighbors to build up the candidate neighbor set.

Step 3: reorder the users in the candidate neighbor set according to the user's judging power, and pick out the top- k users in the list to compose the neighbor set N_u .

Step 4: generate item set $I(N_u)$ rated by users collectively in N_u .

Step 5: compute $p_{u,t}(t \in I(N_u))$ by Formula (25.2) and reorder them in descending order based on $p_{u,t}$.

Step 6: select the top- m items and recommend them to user u .

25.5 Experiments

We used *MovieLens* dataset in our experiments, which is provided by *GroupLens Laboratory*. This set includes 100,000 scores rated by 943 users on 1,682 movies; scores vary from 1 to 5; we normalize the rating data into $[0, 1]$ in the algorithm.

25.5.1 Evaluation Metrics

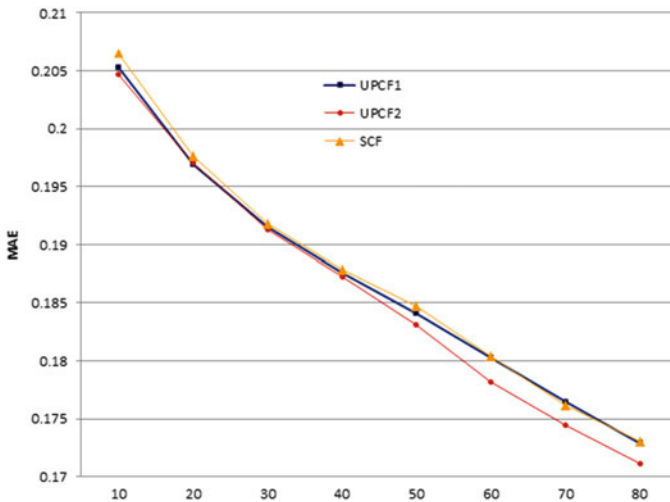
The mean absolute error (MAE) is adopted to measure the recommendation accuracy of the algorithm in the paper. As an absolute value, MAE represents the difference between the predicted score and the real score for user u [8], which will calculate the overall ratings available in the evaluation subset by Formula (25.7):

$$\text{MAE} = \frac{\sum_{t=1}^m |p_{u,t} - R_{u,t}|}{m_u} \quad (25.7)$$

where $m_u(m_u \leq M)$ indicates the number of items rated by user u , $p_{u,t}(t = 1, 2, \dots, m_u)$ is the predicted score for user u on item t , and $R_{u,t}(t = 1, 2, \dots, m_u)$ is his/her real rating. The MAE could offer accuracy performance of the algorithm through computing the deviation between the predicted score and the actual score. That is to say, the smaller the value of the MAE, the higher the quality of recommendation will be.

Table 25.1 Summaries of MAE

Number of neighbors k	10	20	30	40	50	60	70	80
<i>SCF</i>	0.2065	0.1976	0.1918	0.1879	0.1847	0.1804	0.1762	0.173
<i>UPCF1</i>	0.2053	0.1969	0.1915	0.1876	0.1841	0.1803	0.1765	0.1729
<i>UPCF2</i>	0.2047	0.197	0.1913	0.1873	0.1831	0.1782	0.1745	0.1711

**Fig. 25.1** MAE of three algorithms

25.5.2 Experimental Results

In order to measure the performance of the algorithm proposed in the paper, we launched three experiments under the conditions of *SCF*, *UPCF1*, and *UPCF2*, respectively. Table 25.1 and Fig. 25.1 show the experimental results of the three algorithms.

In experiments, the volume k of the neighbor set is set to 10, 20, 30, 40, 50, 60, 70, and 80, respectively, and makes recommendation with the top 20 items. In *UPCF2*, the first step selects N_1 similar users as candidates of neighbors according to Formula (25.1) and $N_1 = 3k/2$. Figure 25.1 shows us that the user's judgment as a weight in combination with the traditional CF algorithm just improves the performance a little; however, the viewing judgment as a screening index and changing the order of the nearest users may enhance the performance a lot (*UPCF2*), particularly when the candidate neighbor set is bigger. This means that the user's judging power plays a critical role in the accuracy of recommendation results. It indicates that the user's judgment will affect his or her capability upon recommendation, and it also has an impact on results adopted by other users for decision making.

From Fig. 25.1, we can see the accuracy of the above three methods has no obvious difference, while $k \in [10, 40]$. As k increases, the *UPCF2* algorithm shows good performance, but *UPCF1* approaches the *SCF* algorithm more and more. This shows us that the user's judging power and its similarity with others have the same trend and also indicates that the more similar the users, the greater the impact on user recommendations will be; but the users still have different judgments. As we are living in a network age, the e-business merchants always choose neighbors of relative great amount to provide us with all kinds of items and services. Some suggestions from neighbors with relative higher judging power may help us select neighbors giving us the best advice.

Conclusion

In the process of information diffusion, the professional capability and judgment of information senders affect the willingness of recipients. In this paper, we integrate the user's natural attribute judging power with the user-based CF algorithm to reflect the influencing factor on the performance of recommendation in a more accurate manner. The result shows positive influence of judgment on the accuracy of algorithm; but as we calculate the judging power without taking into account the subject of items, the improvement is not obvious. As each user has a quite different influence on different domains, the future work is to estimate the user's judging power in the subject-oriented situation.

Acknowledgments This work has been supported by the National Social Science Foundation of P. R. China (no. 13BTQ027).

References

1. Cacheda F, Carneiro V, Fernández D, et al. Comparison of collaborative filtering algorithms: limitations of current techniques and proposals for scalable, high-performance recommender systems. *ACM Trans Web*. 2011;5(1):2–33.
2. Zhang L, Teng P-Q, Qin T. Using key users of social network to solve cold start problem in collaborative recommendation systems. *Inf Technol J*. 2013;12(22):7004–8.
3. Liu NN, Zhao M, Xiang E, et al. Online evolutionary collaborative filtering. Fourth ACM Conf. on Recommender Systems, *ACM*, New York; 2010. p. 95–102.
4. Zhang Y-F, Chen C, Yu. N-H. Dynamic reordering within the nearest neighbor-based algorithm for collaborative filtering. *J Chin Comput Syst*. 2011;32(8):1581–6 (In Chinese).
5. Sun S-H, Kong G-S, Zhao C-W. Collaborative filtering methods based on user relevance degree and weights of recommend-items. 2011 International Conference on Multimedia Technology, *IEEE*; 2011. p. 5322–5.
6. Cheng Z, Zhao X-F, Wang J-W. An item-targeted user similarity method for data service recommendation. 2012 I.E. 16th International Enterprise Distributed Object Computing Conference Workshops, *IEEE*; 2012. p. 172–8.

7. Zitouni H, Berkani L, Nouali O. Recommendation of learning resources and users using an aggregation-based approach. 2012 Second International Workshop on Advanced Information Systems for Enterprises, IEEE; 2012. p. 57–63.
8. Zhang L, Teng P-Q, Qin T. An improved collaborative filtering algorithm based on user interest. *J Softw.* 2014;9(4):999–1006.
9. Yuan Q, Zhao S, Chen L, et al. Augmenting collaborative recommender by fusing explicit social relationships. In *ACM RecSys'09 Workshop on Recommender Systems and the Social Web*, ACM New York; 2009. p. 49–56.
10. Lee DH, Brusilovsky P, Schleyer T. Recommending collaborators using social features and mesh terms. *Proc Am Soc Inf Sci Technol.* 2011;48(1):1–10.
11. Chen W, Fong S. Social network collaborative filtering framework and online trust factors: a case study on Facebook. 2010 Fifth International Conference on Digital Information Management (ICDIM), IEEE; 2010. p. 266–73.
12. Zheng R, Provost F, Ghose A. Social network collaborative filtering: preliminary results. *Proceedings of the Sixth Workshop on eBusiness (WEB2007)*, Montreal; 2007. p. 47–55.
13. Zhou T, Ren J, Medo M, et al. Bipartite network projection and personal recommendation. *Phys Rev E.* 2007;76(4):046115.
14. Yang X-Y, Jiong Y, Ibeahim T, et al. Collaborative filtering model fusing singularity and diffusion process. *J Softw.* 2013;24(8):1868–84 (In Chinese).
15. Bansal HS, Voyer PA. Word-of-mouth processes within a services purchase decision context. *J Serv Res.* 2000;3(2):166–77.
16. Yu Y-K, Zhang Y-C, Laureti P, et al. Decoding information from noisy, redundant, and intentionally distorted sources. *Physica A.* 2006;371(2):732–44.

Chapter 26

An Improved Naïve Bayes Classifier Method in Public Opinion Analysis

Yun Lin, Jie Wang, and Rong Zou

Abstract An improved naïve Bayes classifier is proposed. The method includes aspects of improvement: to get a reduced text feature word set by filtering the synonym, to iterate two different feature selection methods, and to effectively improve the representative feature set. The experimental results show that this method can effectively improve the performance of naïve Bayes classifier.

Keywords Feature selection • Text classification • Synonyms • Naïve Bayes

26.1 Introduction

The text classification module is an important component of the Internet public opinion monitoring system. Text classification result directly affects the accuracy and sensitivity of the Internet public opinion monitoring system. In an Internet public opinion detection system, it is very necessary to have a suitable text classification method. There are many ways to construct the text classification module. The commonly used text classification methods are the Bayes networks, decision methods, instance-based learning method, method of artificial neural network, support vector machine method, genetic algorithm, rough set method, fuzzy set method, etc. [1].

The naïve Bayes classifier is a kind of Bayes classifier which is now recognized as a simple and effective classification method based on the probability theory. Its performance can be comparable with the decision tree and neural network algorithms, even better in some areas. However, the model often encounters problems in practice: One is that to reduce the computational scale, the naïve Bayes classifier is based on conditional independence assumption, but since the restrictions are too strict, it is often difficult to meet them in practice. The other is that the attribute set in preprocessing requires simplifying and that attribute reduction which is good or not will directly affect the classification results.

Y. Lin (✉) • J. Wang • R. Zou
School of Management, Capital Normal University, Beijing 100089, China
e-mail: linyun@cnu.edu.cn

This paper shows two aspects of research. One is how to get a simplified text feature word set by filtering the synonym. The other is how to iterate two different feature selection methods, to effectively improve the representative feature set.

26.2 Related Knowledge

26.2.1 Text Classification

Text classification is the process of classifying the text into predefined categories based on the text content, according to a certain algorithm of automatic classification. From a mathematical point of view, text classification is a process of mapping: A text which does not indicate the categories is mapping to the existing text category. A mathematical formula can be expressed as follows: $f: A \rightarrow B$, where A is a collection of text to be classified and B is the category set. Text classification system establishes the mapping rules and the discriminate rules which summed up the law of classification according to the known samples. The system would classify a new text to the relevant category according to the discriminated rules.

26.2.2 Synonyms

In the field of information retrieval, synonyms do not equal to the synonymous notions in the linguistics and in daily life, which do not consider the feelings of color and tone, and mainly refer to the ability to replace each other and express the same or similar concept vocabulary [2]. The synonyms of information retrieval are divided into the following categories: (1) synonyms and synonyms in phrases, meaning exactly the same words; (2) quasi synonym and near synonym phrases, meaning the same basic words and phrases; (3) some specific hyponyms; and (4) individual antonyms, which are words that describe the same theme but are incompatible. The research is based on “Tongyici Cilin (Extended Edition)” of the Information Retrieval Lab of Harbin Engineering University.

26.2.3 Naïve Bayes Classifier in Public Opinion

A naïve Bayes classifier is a simple probabilistic classifier based on applying Bayes’ theorem with strong (naïve) independence assumptions. Despite their naïve design and apparently oversimplified assumptions, the naïve Bayes classifiers have worked quite well in many complex real-world situations. Despite the fact that the far-reaching independence assumptions are often inaccurate, the naïve Bayes

classifier has several properties that make it surprisingly useful in practice [3]. The main classification steps are as follows:

- Unnumbered training process: to calculate the probability $p(w_i/c_j)$ of feature words w_i belonging to each category c_j .
- Testing process: to calculate the probability $p(c_i/d)$ of test text d belonging to the class c_i ; text d will be classified into the categories of maximum probability.

26.3 Improved Naïve Bayes Classifier

The text classification system is composed of the training process and the testing process. The training process has four steps: (1) public opinion preprocessing, including synonym filter; (2) feature selection, two iterative methods; (3) weight calculation; and (4) construction of the classifier. The testing process has five steps: (1) preprocessing, including synonym filter, (2) feature extraction, (3) weighted calculation, (4) classification, and (5) the classification result evaluation. The main improvement is synonym filtering and the two iterative methods.

26.3.1 Public Opinion Text Preprocessing

- Word segmentation and preliminary preprocessing. Word segmentation is the main task of preprocessing; the effectiveness of segmentation will directly affect the other process. We use the maximum matching segmentation method. After a set of words are obtained, word frequency will be calculated. At the same time, the vocabulary that is not very important like stop words and function words will be removed, and the lower frequency words will be also removed.
- Synonyms processing. The set of feature words filter synonyms based on “Tongyici Cilin (extended version).” After the synonym filtering, the set of feature words no longer contain synonyms, reducing the number of feature words.

26.3.2 Improved Method of Feature Selection

Feature selection is a key problem in text classification. It has simplified calculation and prevents over fitting, reducing the role of vector space dimension. The commonly used feature selection methods mainly include document frequency, mutual information, information gain, expected cross entropy, etc. [4, 5].

In text classification, when the set of feature words change, there will be a lot of differences between the VSM vectors of each sample document. Therefore, even if

the training set is still the original samples, in fact the samples themselves have undergone great changes. The trained naïve Bayes classifier will have very big differences. Feature extraction method calculates the evaluation score for each word in the set. A word is chosen as “the feature word” when its evaluation score is greater than a certain threshold. The experiment shows that different feature extraction methods will produce different feature sets and the minimum coincidence rate of each set of feature words is less than 10 %. Therefore, even in the same learning system and in the same training sample set, performance will also be different. Therefore, a combination might have better effects.

According to the facts above, we try to combine two different feature extraction methods to extract feature word set, in order to obtain better classification effects. Mutual information is widely used in statistical language models, and it is better than other algorithms [6]. The mutual information method extracts different features from the characteristics of different categories, and the expected cross entropy is considered as the distribution of each feature in each category. So we select the mutual information and the expected cross entropy of two kinds of iterative methods. The following is the standard form of the two methods (w is feature; c_i is category).

The mutual information function is defined as follows:

$$MI(w) = p(c_i) \lg \frac{p(w/c_i)}{p(w)} \quad (26.1)$$

$p(w/c_i)$ is the probability of feature w appearing in the class c_i . $p(c_i)$ is the probability of category c_i , and $p(w)$ is the frequency of feature w in the training corpus. For each category, the greater the mutual information of the word w is, the greater the co-occurrence probability of the word and the category is. Normally the maximum w in all kinds of value is the MI.

The expected cross entropy is defined as follows:

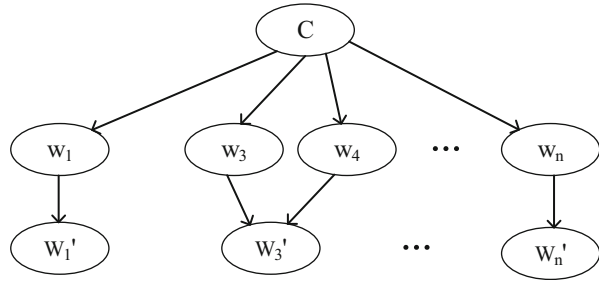
$$\text{CrossEntr}(w) = p(w) \sum_i p(c_i/w) \lg \frac{p(c_i/w)}{p(c_i)} \quad (26.2)$$

$p(c_i/w)$ represents the probability of text belonging to c_i when the text has term w . If terms and categories are strongly correlated, when $p(c_i/w)$ is big, and the corresponding class probability is small, it shows that the effect of term is large on the classification, the corresponding function value is large, and the term is likely to be chosen as the feature item.

26.3.3 The Improved Feature Extraction Process

1. Calculate mutual information and the expected cross entropy of all features.
2. Order features according to the score value.

Fig. 26.1 The improved naïve Bayes classifier



3. Extract feature item according to a certain proportion, and combine the feature to get the subset.
4. Calculate the performance evaluation index.
5. Adjust the proportions; repeat 3 and 4 to obtain the optimal feature subset.

26.3.4 Improved Naïve Bayes Classifier Model

The naïve Bayes classifier is a kind of Bayes classifier which is now recognized as a simple and effective classification method based on the probability theory. In this model, the assumption is that all attributes of w_i ($i = 1, 2, \dots, n$) are independent of the class variable c and that every attribute variable is a class variable as the parent node only. The improved model plus a layer based on the attribute level synonym filtering, such as the properties of w_3 and w_4 as synonyms, is merged into w_3' . Synonyms no longer contain the attribute layer after filtration, and the assumption of feature independence of naïve Bayes was weakening while reducing the feature dimension (Fig. 26.1).

26.4 Experimental Results and Analysis

26.4.1 The Test Set

In order to verify the feasibility and effectiveness of this method, we use the text categorization data of Sogou laboratory (lite version) as the test corpus. Five categories—sports, travel, education, culture, and automobile—were chosen, each of which contained 1990 news releases, a total of 9,950 documents. In the experiment, 1,300 news releases were randomly selected from each category as the training data and 690 as the validation data.

26.4.2 Evaluation Method

The classification performance evaluation of text categorization is often used for precision ratio, recall ratio, and F1. Precision is the ratio of the correct text number by classification and the actual number of classification. Recall is the ratio of the correct text number of classification and the number of all the texts. The F1 test value combines the precision ratio with recall ratio. F1 is the harmonious value of precision and recall.

Precision ratio = distinguishing the text c_j class number/the actual discrimination for text c_j class number

Recall ratio = distinguishing the text c_j class number/the number of texts actually participating in the test in class c_j

F1 = precision ratio \times recall ratio \times 2/(precision ratio + recall ratio)

26.4.3 The Experimental Results

Several comparative experiments using the mutual information method and the improvement method have been done. The results are shown in Tables 26.1 and 26.2. Naïve Bayes-MI shows the mutual information feature selection method. Naïve Bayes-MC shows the two iterative feature selection methods. Improved naïve Bayes-MI shows the mutual information feature selection method for word processing. Improved naïve Bayes-MC shows the iterative synonyms processed by a variety of feature selection methods.

From the table data we can get the conclusion that it is effective to improve the classification by data processing with synonym and the iterative feature selection method.

Table 26.1 The classification result 1

Category	Naïve Bayes-MI			Naïve Bayes-MC		
	Precision	Recall	F1	Precision	Recall	F1
Sports	80.1	95.8	87.2	98.2	93.5	95.8
Travel	88.9	86.6	87.7	99.1	64.6	78.2
Education	70.3	51.1	59.2	90.1	68.2	77.6
Culture	61.5	60.1	60.8	86.7	75.2	80.5
Automobile	66.9	70.5	68.7	56.7	94.9	71.0

Table 26.2 The classification result 2

Category	Improved naïve Bayes-MI			Improved naïve Bayes-MC		
	Precision	Recall	F1	Precision	Recall	F1
Sports	99.4	93.2	97.6	94.1	97.1	95.6
Travel	99.4	60.9	87.5	94.8	86.1	90.2
Education	91.5	66.2	84.0	89.8	75.2	81.9
Culture	86.3	72.2	83.3	67.4	78.9	72.7
Automobile	51.6	94.3	59.8	75.8	80.1	77.9

Conclusion

With the increasing demand for network information processing, the text classification module is an important component of the monitoring system of the Internet public opinion. The paper discusses some key steps in the implementation of the text classification system and proposes an improved naïve Bayes classifier. The method includes aspects of improvement: to get a reduced text feature word set by filtering the synonym, to iterate two different feature selection methods, and to effectively improve the representative feature set. The experimental data shows that the above method reduces the dimension of the feature space and the amount of calculation. The method can effectively improve the performance of the naïve Bayes classifier system.

Acknowledgments This work was supported by the Science and Technology Program of Beijing Municipal Commission of Education (no. KM201410028020 and no. KM201310028020) and the 2014 Youth Talent Development Plan of Beijing City-Owned University (no. CIT&TCD201404155).

References

1. Shi ZZ. Knowledge discovery. Beijing: Tsinghua University press; 2002. p. 352–5 (In Chinese).
2. Tian JL, Zhao W. Words similarity algorithm based on Tongyici Cilin in semantic web adaptive learning system. *J Jilin University*. 2010;28(6):602–7 (In Chinese).
3. Rabiner LR, Juang BH. An introduction to hidden Markov models. *IEEE ASSP Mag*. 1986;3(1):4–16.
4. Riloff E, Lehnert W. Information extraction as a basis for high-precision text classification. *ACM Trans Inf Syst*. 1994;12(3):296–333.
5. Yang YM, Pedersen JO. A comparative study on feature selection in text categorization. *The 14th International Conference on Machine Learning*, Morgan Kaufmann, San Francisco; 1997. p. 412–20.
6. Lewis DD. Feature selection and feature extraction for text categorization. *Proceeding of Speech and Natural language Workshop*, Morgan Kaufmann, San Mateo; 1992. p. 212–7.

Chapter 27

Overseas Risk Intelligence Monitoring Based on Computer Modeling

Peipei Su

Abstract Research on overseas risk intelligence monitoring makes the international companies avoid overseas risk. Computer modeling of overseas risk intelligence monitoring is done on the basis of database management systems, including systems for gathering, cleaning up, researching, and using knowledge. Then the article estimate the model of overseas risk intelligence monitoring using estimation algorithms, including method of algorithms, effectiveness algorithms, and resource quantity algorithms. The whole computer model of overseas risk intelligence monitoring will supply international enterprises with theory and technology.

Keywords Computer model • Database management systems • Overseas risk intelligence • Intelligence monitoring

27.1 Introduction

With global economic development and the deepening of reforms and greater openness, the number of international businesses is increasing. And at the same time, international business faces all kinds of risk. The development of information technology and networks provides international enterprises with a convenient tool for gathering risk signals, which are converted into risk intelligence, and then this risk intelligence is used by international enterprises [1]. However, this process from risk signals to risk intelligence is completed by risk intelligence monitoring. There is an inherent link between intelligence and knowledge. Intelligence is the stationary state of knowledge, and knowledge is the activation of knowledge [2]. These characteristics bring overseas venture problems related to monitoring overseas risk intelligence [3]. This article uses a computer model to monitor overseas risk intelligence. Thus, the article builds a computer model of overseas risk intelligence.

Many scholars conduct research on overseas risks from different aspects. Some scholars examine environmental risks, including political risks and exchange rate risks [4]. Other scholars research inner risks, including moral risks, contract risks, and

P. Su (✉)
Business School of Ho Hai University, 211100 Nanjing, China
e-mail: peipei01_001@hotmail.com

business risks [5]. Still others research how to construct risk indicators and divide these risk indicators into three parts: liquidity indicators, macroeconomic indicators of environmental risks, and capital risk indicators [6]. They believe that computer systems can enhance modern management of enterprises, identify overseas risks, and provide international enterprises with convenience [7]. Computer systems greatly affect economics, informatics, and management. At the same time, computer technology has a great influence on information gathering and system processing [8].

27.2 Theoretical Basis

27.2.1 Concept of Overseas Risk Intelligence Monitoring

Intelligence monitoring includes the gathering and processing of intelligence, analysis and research, and reporting and dissemination [9]. This article divides overseas risks into three parts: external environmental overseas risks, internal overseas risks, and risk from competitor. Overseas risk signals need to be converted into overseas risk intelligence so that overseas risk intelligence can be used by international enterprises. The process requires the use of intelligence monitoring. Overseas risk intelligence monitoring is the process of converting overseas risk signals into overseas risk intelligence by gathering, arranging, researching, and using. Finally, international enterprises obtain the overseas risk using intelligence. By the process of gathering, arranging, researching, and analyzing the intelligence, international enterprises obtain the overseas risk intelligence, but because overseas risk intelligence has the characteristic of knowledge, such as concealment, using overseas risk intelligence is difficult. Thus, according to the SECI model of Nonaka, overseas risk intelligence of concealment is a starting point, and then undergoes socialization, externalization, combination, and internalization, and finally the overseas risk intelligence of concealment can be widely shared throughout the international enterprises [10].

27.2.2 Use of Computer Modeling in Overseas Risk Intelligence Monitoring

27.2.2.1 Use of Computer Modeling in Outside Overseas Risk Intelligence Monitoring

The construction of computer models of international enterprises helps to provide an understanding of the depth of external environmental overseas risk intelligence. External environmental overseas risk includes political risks, legal risks, exchange risks, and economic risks. The establishment of a computer model expands the channels of signal gathering. When international enterprises gathering these risk

signals, they can obtain more overseas risk signals using a computer model based on database management.

27.2.2.2 Use of Computer Modeling in Internal Overseas Risk Intelligence Monitoring

The construction of a computer model by international enterprises helps manage information related to internal overseas risk intelligence monitoring. Internal overseas risks include moral risks and risks related to commercial secrets. When international enterprises face these risks, they cannot identify these risks. Moral risks stem from the fact that international enterprises protect their own interests. The establishment of a computer model encourages workers to share information and assemble database of management. Thus, such a model can contribute to information management. However, knowledge of concealment can be shared by SECI model in the role of bar [11].

27.2.2.3 Use of Computer Modeling in Competitor Overseas Risk Intelligence Monitoring

The construction of a computer model by international enterprises helps in recognizing overseas risk intelligence. Rival overseas risk includes trade barriers to the strategy. A computer model may supply accurate information about risk related to one's competitors. Thus, international enterprises can determine the price of their products in international markets.

27.3 Database Management Model of Overseas Risk Intelligence

27.3.1 Database Management Model of Overseas Risk Intelligence Gathering

When international enterprises gather intelligence on overseas risks, complete information on overseas risks is impossible because of the dependence of overseas risk intelligence. Overseas risk intelligence from different regions relates to areas such as policy, law, and local customs. Thus, the dependence of overseas risk intelligence is described by entity attribute. The entity attributes of overseas risk intelligence are shown in Table 27.1.

Table 27.1 Indicators of overseas risk intelligence monitoring

Attribute	Type
Overseas risk number	Number
Overseas risk area name	Chart
Overseas risk type	Chart
Overseas risk quantity	Chart
Overseas risk start time	Time
Overseas ending time	Time

27.3.2 Database Management Model of Overseas Risk Intelligence Clean-Up

Database management modeling of overseas risk intelligence clean-up involves processing a database management model of overseas risk intelligence gathering. Thus, the description of this entity attribute is the same as the database management model of overseas risk intelligence gathering.

27.3.3 Database Management Model of Overseas Risk Intelligence Research

Database management modeling for researching overseas risk intelligence involves processing the database management model of overseas risk intelligence gathering and clean-up. Thus, the description of this entity attribute is the same as the database management model of overseas risk intelligence gathering and clean-up.

27.3.4 Database Management Model of Overseas Risk Intelligence Use

Database management modeling of overseas risk intelligence use is accomplished on the basis of the three database management models. Following the gathering, clean-up, and researching of the database management model, international enterprises obtain overseas risk intelligence. But overseas risk intelligence has a concealment attribute, so the concealment attribute is in a one-to-one relation to overseas risk intelligence. Thus, this article combines a bivariate table of overseas risk intelligence gathering with a bivariate table of overseas risk intelligence use. The entity attribute of overseas risk intelligence use is divided into two forms: types of overseas risk intelligence and conversion of overseas risk intelligence. The latter form can be described as “the number of knowledge reserve of overseas risk intelligence.”

Table 27.2 Scale reliability analysis

Variable	Cronbach's alpha	Entry number
External environmental overseas risk monitoring	0.709	4
Internal overseas risk monitoring	0.8	3
Competitor overseas risk monitoring	0.72	2

α coefficient of each of the above factors is more than 0.7, which shows that the choice of the sample data is reasonable, so it passes the reliability test

Table 27.3 KMO and Bartlett test

KMO		0.721
Bartlett	χ^2	160.421
	df	50
	Sig.	0.000

The results of the KMO and Bartlett test of sphericity values show that the selected data are appropriate

27.3.5 Empirical Analysis

This study uses a questionnaire format to obtain data; 100 questionnaires were distributed, and 50 valid samples were collected. The article uses SPSS data analysis (Tables 27.2 and 27.3).

27.4 Algorithm Model of Overseas Risk Intelligence Monitoring

27.4.1 Cost Algorithm Model of Overseas Intelligence Monitoring

Overseas intelligence monitoring requires expenditures on manpower and material resources. The cost of overseas risk intelligence monitoring = \sum invested cost of computer systems + \sum time cost of manpower + \sum cost of human resources.

27.4.2 Availability Algorithm Model of Overseas Intelligence Monitoring

The attribute of overseas risk intelligence monitoring is used to explain whether the information of overseas risk intelligence monitoring can be used in the database management model. The algorithm of availability is divided into three numerical numbers:

Now: this means that the risk intelligence needs to be recorded in the database management model.

History: this means that the risk intelligence need not be recorded in the database management model, but it is recorded in the entity attribute of the quantity of overseas risk intelligence.

27.4.3 *Resource Algorithm Model of Overseas Intelligence Monitoring*

The resource algorithm of overseas risk intelligence monitoring can be calculated using the knowledge reserve of overseas risk intelligence monitoring, and overseas risk intelligence is at the core of enterprise resources [12]. Thus, international enterprises need to calculate overseas risk intelligence. The method for calculating overseas risk intelligence is as follows:

$$\begin{aligned}
 & \text{Amount of resources of overseas risk intelligence} \\
 &= \sum \text{amount of knowledge reserve at present} \\
 &+ \sum \text{amount of knowledge reserve in the past} \\
 &- \sum \text{conceal knowledge reserve at present.}
 \end{aligned}$$

27.4.4 *Empirical Analysis*

To reduce costs, a company establishes a model of computer algorithm systems. The systems are based on a database management model. The systems include three parts: external environmental overseas risk monitoring, internal overseas risk monitoring, and competitor overseas risk monitoring. Then the costs are assessed using algorithmic systems (Fig. 27.1).

Conclusion

The establishment of computer management system models contributes to the conducting of overseas risk intelligence monitoring. Moreover, the article assesses computer management system models using algorithm models. The approach presented in this paper has several advantages: first, in the face of overseas risk intelligence, international enterprises update the contents of their management database. Societies and global markets are changing, so it adds the new overseas risk intelligence to management databases in order to share the risk model throughout a company. Second, international companies encourage the sharing of overseas risk intelligence. It can enlarge new knowledge into management database. Last but not least, as for the hardware and software of database management systems, international enterprises update computer hardware and software.

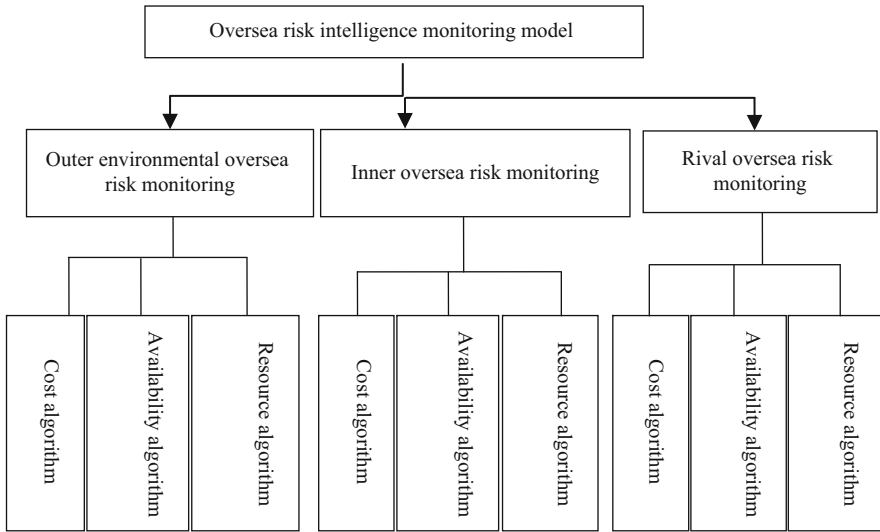


Fig. 27.1 A company of computer algorithm systems

References

1. Hu A. On competitive focus and competitive intelligence activities about intellectual property competitive intelligence of company. *Library Work Study*. 1999;1(04):2-7 (In Chinese).
2. Qian X. *Science and technology of national defense science and technology intelligence work*. Shanghai: Shanghai People's Education Press; 1986. p. 67 (In Chinese).
3. Li J. On problems and solving methods at present enterprises competitive intelligence work. *Library Inf Serv*. 2003;1(01):101-4 (In Chinese).
4. Hu J. State-owned foreign trade corporation facing challenges and development countermeasures. *Theor Exploration*. 2005;6(25):25 (In Chinese).
5. Wang M. Harsh assessment to reduce business risk of overseas. *China Dly*. 2012;5(G02):2-5 (In Chinese).
6. Wang H. Bank's risk monitoring index system discussed in this paper. *Seeking Truth*. 2003;7(54):22-3 (In Chinese).
7. Wang X. Using computer technology to strengthen modern enterprise management. *Liaoning Econ*. 2003;4(9):76 (In Chinese).
8. Zhao J. The application of the computer technology in enterprise information construction. *Comput CD Softw Appl*. 2013;6(31):250 (In Chinese).
9. Wang B, et al. Theory of enterprise competitive intelligence system construction and operation in our country. *J Information*. 1999;8(1):31-4 (In Chinese).
10. Nonaka I. Creating new knowledge the Japanese way. *Harv Bus Rev*. 2003;05(31):160-2.
11. Nonaka I. The knowledge-creating company. *Harv Bus Rev*. 1991;6(44):322-3.
12. Teece DJ. Dynamic capabilities and strategic management. *Strateg Manag J*. 1994;3(3):537-56.

Chapter 28

Quality of Service-Based Particle Swarm Optimization Scheduling in Cloud Computing

Shuang Zhao, Xianli Lu, and Xuejun Li

Abstract Scheduling is important in cloud computing system. In this paper, an adaptive particle swarm optimization (PSO) algorithm is proposed to optimize quality of service (Qos)-guided task scheduling in cloud computing. This scheduling targets a trade-off between completion time and cost. The proposed algorithm adaptively changes PSO parameters according to the evolution state evaluation. This adaptation can avoid premature convergence and explore the search space more efficiently. When swarms are trapped into premature convergence, mutation is introduced to the velocity and position updating strategy to improve the ability of global search. Simulation results reveal that the algorithm can achieve significant optimization of completion time and cost.

Keywords Scheduling • PSO • Time-varying parameters • Qos • Cloud computing

28.1 Introduction

Cloud computing is a popular trend which involves virtualization, networking, parallel and distributed computing, web services and software, etc. Scheduling is vital in cloud computing. Effective and efficient task scheduling algorithm can improve resource utilization. Many scheduling strategies and algorithms have been proposed to solve the scheduling problem more efficiently in the cloud.

S. Zhao (✉)

Beijing Institute of Tracking and Telecommunication Technology, Beijing 100094, China

The College of Postgraduate, Academy of Equipment, Beijing 101416, China

e-mail: zhsh2002@163.com

X. Lu

Beijing Institute of Tracking and Telecommunication Technology, Beijing 100094, China

X. Li

Department of Information Equipment, Academy of Equipment, Beijing 101416, China

28.2 PSO and Scheduling with PSO

In 1995 Kennedy and Eberhart introduced PSO [1]. The algorithm proposed by Shi Y and Eberhart with inertia weight is regarded as the standard algorithm [2]. Many modified PSO algorithms are proposed to get better optimization by an adaptive change of parameters and combination with additional mutation operation.

Due to its simplicity, fast convergence, ease of implementation, and effectiveness, PSO has drawn much attention from various fields and has become popular in a wide range of application. A substantial number of PSO-based algorithms have been proposed to solve scheduling problem and task allocation [3–6].

28.3 Proposed PSO

28.3.1 Particle Encoding Method

To apply PSO successfully to scheduling problems, mapping the particle position to the problem solution must be considered first. In this paper, a particle is expressed as an N (N is the number of tasks) dimension vector and each dimension represents a task. The value of the particle in each dimension represents the resource number that a task is assigned to. The solution of each dimension of particles keeps changing in the search process. The particle position represents a potential scheduling; the position can be decoded to obtain a feasible solution [7].

One of the particles is constructed as shown in Table 28.1. The particle has six dimensions, representing six tasks, and the value of the particle in each dimension represents the number of resource which the task is assigned to. The particle is coded as shown in Table 28.2.

28.3.2 Fitness Function

Fitness function is used to measure the quality of the particles in the population according to the given optimization objective. In this paper the scheduling target focuses on minimizing the Qos parameter, that is, completion time and cost.

Table 28.1 Task-resource allocation

Task	T_1	T_2	T_3	T_4	T_5	T_6
Resource	3	1	2	3	2	0

Table 28.2 Particle encoding

Particle	3	1	2	3	2	0
----------	---	---	---	---	---	---

The execution time ET_{ij} of task t_i on resource r_j is defined as the time taken by r_j to execute t_i . The completion time CT_{ij} is defined as the sum of ET_{ij} and the beginning time bt_{ij} of task t_i on resource r_j .

The time fitness functions of an individual task t_i are defined as

$$f_{\text{time}}(i) = CT_{ij}/\text{avg}T_i \quad (28.1)$$

where $\text{avg}T_i$ is the average execution time of the task assigned to all the resources supposing that the resource has no load.

The cost fitness function of an individual task t_i is defined as

$$f_{\text{cost}}(i) = C_{ij}/\text{avg}C_i \quad (28.2)$$

where C_{ij} is the total cost of task t_i on resource r_j and $\text{avg}C_i$ is the average cost of the task t_i assigned to all the resources.

The objective function $f(x)$ is mathematically stated as to minimizing the completion time and cost of all tasks:

$$f(x) = \min \left(\sum_{i=1}^m w_1 \times f_{\text{time}}(i) + w_2 \times f_{\text{cost}}(i) \right) \quad (28.3)$$

where w_1 is the weight value of time and w_2 is the weight value of cost, $w_1 + w_2 = 1$.

28.3.3 Proposed PSO Algorithm

The PSO is simple in concept and effective, but at the same time it falls into the premature convergence and local optima easily. Many strategies on performance improvement have been applied, including improved parameters, topological structures, and combination with auxiliary operations. This paper presents time-varying parameters of inertia weight and acceleration coefficient to modify the learning strategies of particles. When swarms are trapped into premature convergence, introduce "mutation" to the position and velocity updating strategy to enhance the ability of global search. The algorithm is shown in Fig. 28.1, whose structure is similar to the original PSO.

AccFactor denotes convergence speed and *AssFactor* denotes the aggregation degree of swarm. In the evolution process the best fitness of this iteration is better than that of the last iteration; the quotient of these two values (*AccFactor*) can reflect the convergence speed. *AccFactor* is in the range (0, 1), when *AccFactor* is 1; the evolution is in the state of convergence. The quotient of the best fitness and average fitness (*AssFactor*) of the swarm can reflect the population distribution state. *AssFactor* is also in the range (0, 1). At the early stage, *AssFactor* value is small,

1) swarm initialization	11) end for
2) while (k < MaxIteration)	12) Calculate average fitness value
3) for i=1 to number of particles	13) adjust parameters(w,c1,c2, AccFator, AssFactor)
4) calculate fitness value f(xi)	14) updating new velocity and the position
5) if f(xi) < f(pi)	15) k++
6) pi= xi	16) end while
7) end if	17) output the scheduling scheme and its fitness value
8) if f(pi) < f(gi)	
9) gi= pi	
10) end if	

Fig. 28.1 The general adaptive algorithm

and the distribution is dispersive. When particles flock together and converge to the locally or globally optimal region, the *AssFactor* value is 1.

$$AccFactor = f(gbest_t)/f(gbest_{t-1}) \quad (28.4)$$

$$AssFactor = f(gbest_t)/avgf(x_t) \quad (28.5)$$

$f(gbest_t)$ is the best fitness of this iteration t . $f(gbest_{t-1})$ is the best fitness of the last iteration and $avgf(x_t)$ is the average fitness of this iteration.

28.3.3.1 Inertia Weight

The inertia weight controls the effect of the last velocity on the current iterations. In linearly decreasing mode, its value is usually initialized around 0.9 and decreasing gradually toward the value around 0.4 as the evolution progresses [8]. Meanwhile, a better strategy is to apply adaptive approaches in which w is adaptively modified according to the evolution state of the particles. For the sake of improving the convergence of PSO, a time variant w is used in this paper as shown in Eq. (28.8). The w value is allowed to change with the convergence speed and evolution state of particles [9]:

$$w = w_{ini} - AccFactor \times w_{acc} + AssFactor \times w_{ass} \quad (28.6)$$

where *AccFator* and *AssFactor* are as shown in Eqs. (28.4) and (28.5). w_{ini} is the initial value set to 1 and w_{acc} is set to 0.5 and w_{ass} to 0.2.

28.3.3.2 Acceleration Coefficients

Acceleration coefficients are also important for PSO. In this paper time variants $c1$ and $c2$ are presented as shown in Eqs. (28.7) and (28.8):

Fig. 28.2 Updating velocity and position

1)	for each particle $i(i=1.2\dots m)$
2)	Velocity updating according to standard PSO
3)	Position updating according to standard PSO
4)	if (convergence condition is met)
5)	Velocity updating according to Eq. (9)
6)	Position updating according to Eq. (10)
7)	end if
8)	end for

$$c1 = c1_{ini} - AccFactor \times c_{Acc} - AssFactor \times c_{Ass} \quad (28.7)$$

$$c2 = c2_{ini} - AccFactor \times c_{Acc} + AssFactor \times c_{Ass} \quad (28.8)$$

where $c1_{ini}$ is 2.5, $c2_{ini}$ is 1.5, and c_{Acc} and c_{Ass} are 0.5 (range from 0.4 to 0.6). $AccFactor$ and $AssFactor$ are shown in Eqs. (28.4) and (28.5).

28.3.4 Velocity and Position Updating

Velocity represents the moving direction and trends of a particle. In this paper, when swarms are trapped into convergence, an adaptive mutation operator is added to the velocity and position updating strategy of the particles to enhance the global search capability and avoid premature convergence. The velocity and position updating rules are as follows:

$$v_{ij}(t+1) = wv_{ij}(t+1) + c_1r_1(t)(p_{ij}(t) - x_{ij}(t)) + c_2r_2(t)(p_{gi}(t) - x_{ij}(t)) - c_3\left(\left(p_{ij}(t) + p_{gi}(t)\right)/2\right) \quad (28.9)$$

$$x_{ij}(t+1) = x_{ij}(t+1) + r_3p_{max}/3 \quad (28.10)$$

where $p_{ij}(t)$ is the best particle position, $p_{gi}(t)$ is the best global position, p_{max} is the maximum position of the particles, c_3 is the mutation factor, and r_3 are the random number in the interval of [0, 1] (Fig. 28.2).

28.4 Experiment and Result

Simulations are carried out on CloudSim [10] to observe the quality of the optimum solution and the rate of convergence of the new methods. In order to compare the performance of the algorithms, greedy time (GT) scheduling algorithm, PSO, time-varying parameter PSO, and time-varying parameter PSO with mutation are tested.

The number of iterations is 100 and the particle number is 50. The task length is generated randomly ranging in the interval [1,000, 8,000] MIPS (million instructions per second). The resource number is 10 and 20, computing power ranging from

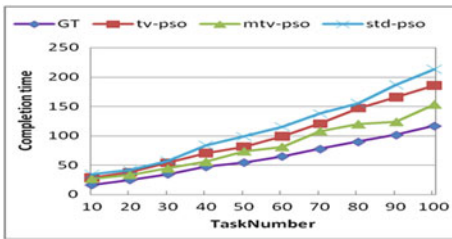
100 to 800 MIPS. Test results are averaged over 10 runs in order to maintain the reliability of the results. Experimental parameter settings are shown in Table 28.3.

28.4.1 Performance Comparison

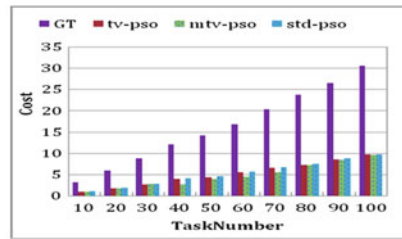
Figures 28.3 and 28.4 show the average completion time and cost values. From the results it is evident that the completion time produced by the greedy time algorithm

Table 28.3 Parameter settings of the algorithm

Algorithm	Inertia weight	c1	c2	Mutation
std_pso	Linear decreasing	2	2	None
tv_pso	As proposed in Eq. (28.6)	As proposed in Eq. (28.7)	As proposed in Eq. (28.8)	None
mtv_pso	As proposed in Eq. (28.6)	As proposed in Eq. (28.7)	As proposed in Eq. (28.8)	As proposed in Eqs. (28.9) and (28.10)

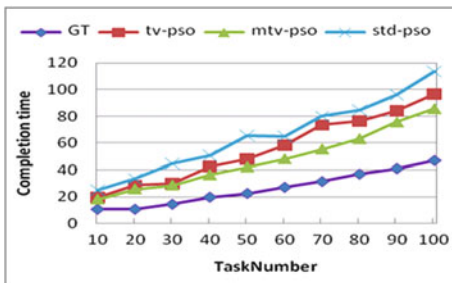


(a) Completion time of 10 resources

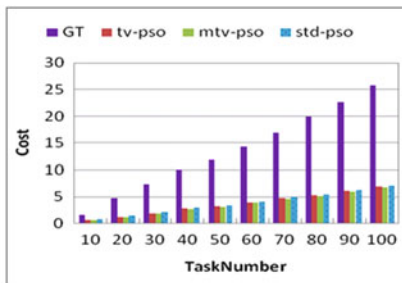


(b) Execution Cost of 10 resources

Fig. 28.3 Execution time and cost of 10 resources



(a) Completion time of 20 resources



(b) Execution Cost of 20 resources

Fig. 28.4 Completion time and cost of 20 resources. (a) Completion time of 20 resources. (b) Execution cost of 20 resources

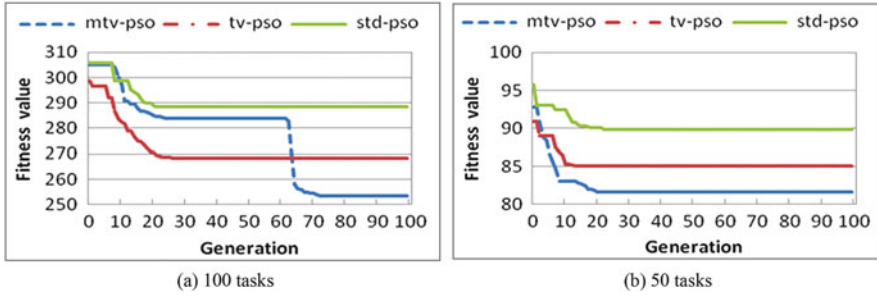


Fig. 28.5 The trend of convergence of PSO. (a) 100 tasks. (b) 50 tasks

is the least in comparison with other approaches, but its cost is large. This is because the greedy time algorithm only considers optimization completion time without considering the cost. Of all the three PSO-based algorithms, the performance of MTV_PSO is the best, which can gain both optimization completion time and cost. The performance of TV_PSO algorithm and standard PSO is similar and TV_PSO is a little better than the standard PSO.

28.4.2 Comparisons on the Convergence Speed

Figure 28.5 plots the convergence of the fitness value over the iteration number produced by PSO. The standard PSO finds a global minimum very fast, and the convergence is rapid, but it traps premature convergence and cannot jump out. The number of iterations needed for the convergence is about ten. The TV-PSO convergence is similar to the standard PSO. MTV_PSO convergence is slow, but when it traps premature convergence, it can jump out by mutation to the velocity and position and get better optimization.

Conclusion

This paper presents a modified PSO to achieve the scheduling goals of minimizing the completion time and cost of applications on cloud computing environments. To overcome the premature convergence and explore the search space more efficiently, dynamic changing inertia weight and acceleration coefficients are applied. At the same time, when a search traps local optimums, the introduced mutation is more effective for particles jumping out. The results obtained by our heuristic are compared with PSO and heuristic that provided by clouds. We find that modified PSO-based task-resource scheduling performs better than the other algorithms in this paper.

References

1. Kennedy J, Eberhart R. Particle swarm optimization(C). In: Proceedings of IEEE international conference on neural networks, vol 4(2), IEEE; 1995. p. 1942–48.
2. Shi Y, Eberhart R. A modified particle swarm optimizer. Evolutionary computation proceedings, 1998. IEEE world congress on computational intelligence. The 1998 I.E. international conference on IEEE. 1998. p. 69–73.
3. Liu H, Abraham A, Hassanien AE. Scheduling jobs on computational grids using a fuzzy particle swarm optimization algorithm. *Future Generat Comput Syst.* 2010;26(8):1336–43.
4. Xue SJ, Wu W. Scheduling workflow in cloud computing based on hybrid particle swarm algorithm. *TELKOMNIKA Indonesian J Electr Eng.* 2012;10(7):1560–6.
5. Zhan S, Huo H. Improved PSO-based task scheduling algorithm in cloud computing. *J Inform Comput Sci.* 2012;9(13):3821–9.
6. Pandey S, Wu L, Guru SM, Buyya R. A particle swarm optimization-based heuristic for scheduling workflow applications in cloud computing environments. In: *Advanced information networking and applications (AINA).* IEEE; 2010. p. 400–7.
7. Ratnaweera A, Halgamuge S, Watson HC. Self-organizing hierarchical particle swarm optimizer with time-varying acceleration coefficients. *Evol Comput IEEE Trans.* 2004;8(3):240–55.
8. Shi Y, Eberhart RC. Fuzzy adaptive particle swarm optimization. *Evol Comput* 2001. Proceedings of the 2001 congress on IEEE; 2001. p. 101–6.
9. Xuanping Z, Du Yuping QG, Zheng Q. Adaptive particle swarm algorithm with dynamically changing inertia weight. *J Xi'an jiaotong Univ.* 2005;39(10):1039–42 (In Chinese).
10. Calheiros RN, Ranjan R, Beloglazov A, et al. CloudSim: a toolkit for modeling and simulation of cloud computing environments and evaluation of resource provisioning algorithms. *Software Pract Ex.* 2011;41(1):23–50.

Part II

Data Processing

Chapter 29

Improving Database Retrieval Efficiency

Shaomin Yue, Wanlong Li, Dong Han, Hui Zhao, and Jinhui Cheng

Abstract To solve the problem in traditional databases of unordered retrieval results and low efficiency of retrieval, on the basis of research on Lucene, a full-text search engine, this paper designs and develops a database full-text retrieval system based on the Lucene index that performs searches by keyword based on the Lucene index database and greatly improves retrieval efficiency. In addition, the paper presents a word frequency location weighted (WFLW) sorting algorithm used for sorting retrieval results. Experimental results show well-organized retrieval results better reflect user query intentions, which can improve users' search experience.

Keywords Lucene • Index structure • Word frequency location • Weighted sorting

29.1 Introduction

With the continuous advance of informatization, as well as the rapid development of the Internet, more and more data need to be stored [1]. The amount of information on large websites keeps growing. E-commerce sites [2], for example, contain vast amounts of data. The traditional database retrieval technology aimed at websites has encountered many problems [3]. For instance, retrieval efficiency is lower and response time is too long, retrieval results are not quite in conformity with users' query intentions, information on retrieval results is incomplete, and search results cannot sort according to user query intentions, which fails to enhance users' search experience.

The point of information retrieval is to query an information collection and obtain information in accordance with user requirements. Among various kinds of information retrieval technology, full-text retrieval is versatile and very practical. Full-text search compares the user's query request with every word in the text. Compared with the field matching of database retrieval, the advantages of full-text

S. Yue • W. Li • D. Han • H. Zhao • J. Cheng (✉)
College of Computer Science and Engineering, Changchun University of Technology,
Changchun 130012, China
e-mail: lwl@mail.ccut.edu.cn

search is that its query is comprehensive, which provides users the most comprehensive and extensive search results. What’s more, full-text search matches the user’s keywords with associated words in the index library. Compared with the sequential search of database retrieval, it represents a considerable improvement in terms of efficiency.

Learning from the index structure of Lucene, a full-text search tool, this paper builds a database full-text retrieval system (DFRS) based on Lucene and proposes a word frequency location weighted (WFLW) sorting algorithm that is used for sorting retrieval results. Experimental results show that the DFRS can improve the efficiency of database retrieval and recall. Based on the relevance of a user’s query intention, the WFLW algorithm can sort results, which gives users a better search experience.

29.2 Lucene-Based Database Full-Text Retrieval System

29.2.1 Structure of DFRS

With open-source code, Lucene is a toolkit of a full-text search engine [4]. It provides an intact index engine and a query engine, along with some text analysis engines [5]. The DFRS based on Lucene is divided into two parts: index creation and index query. The indexing module periodically gathers information from a database, analyzes the lexicon and syntax of the information, establishes an index, and adds the index to the index library. Based on user input, the DFRS obtains the user’s query terms, analyzes the terms, searches the index library, and shows related results to the user. The structure of the DFRS is shown in Fig. 29.1.

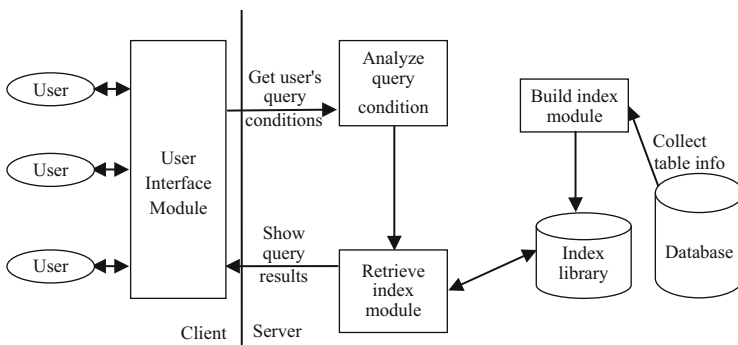


Fig. 29.1 Structure chart of database full-text retrieval system based on Lucene

29.2.2 Structure of Database Index

The structure of the Lucene index is divided into four levels: index, segment, document, and field layers. Like the Lucene index structure, the database index structure is also divided into four layers: index, segment, record, and field layers. Nevertheless, what is stored in the second floor of the database index is the record information of the database. The database index consists of certain segments, each segment consists of records, each record consists of a number of fields, and each field consists of a few terms.

When indexing, not each record is added to the same index file immediately but written to a different small file. Each small file is a segment. Then these small files are merged into one big file. The data source the user provides is a record in a database table. After the database record is indexed, it is stored in the index file in the form of a record.

A record can contain multiple fields, for instance, one record of a database table may contain “Title,” “Abstract,” and other fields, which are stored in the form of a field.

A term is the smallest unit of search, and the content of a field can be decomposed into terms. For instance, field content is “The DFRS can improve the user’s search experience.” Following decomposition, some terms can be obtained, such as “DFRS,” “improve,” “search,” “experience,” and so on. The structure of the Lucene-based database index is shown Fig. 29.2.

29.2.3 Word Frequency Location Weighted Sorting Method

The WFLW algorithm is a common sorting algorithm [6]. It sorts by considering only two factors: the number and location of occurrences of keywords in the table records [7]. It is the most basic sorting algorithm in the field of information retrieval.

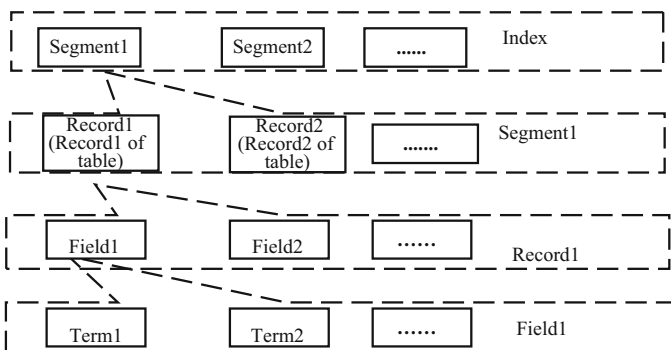


Fig. 29.2 Structure chart of Lucene-based database index

When a user performs a search, if the search results could be sorted based on the user's query intention automatically, this would undoubtedly be very convenient for users [8]. When users want to search by keyword K , if word K can be weighted by a certain strategy and its weight within the records can be obtained, then the retrieval results can be sorted according to the size of the weights, which can improve the retrieval efficiency. The weight calculation method is as follows:

1. Inverse record frequency weighting of word K

The sorting standard of the WFLW algorithm is the size of relevancy of a keyword and record. By the record frequency (RF) and location of keywords in a record, the relevance of the record can be ultimately determined. Moreover, the correlation of keywords in a record is proportional to the weight value of the word in the record. The frequency of a word in the record determines its correlation in the record. The idea derives from an automatic indexing method proposed by Luhn. After filtering out a word without searching for its meaning, Luhn believes that the higher the frequency of a word in a record is, the greater is its importance for the record. That is the theoretical basis of current research on automatic indexing. Word frequency weighting closely resembles it.

A word's record can be roughly divided into two groups: feature words and words without characteristic. Feature words are those that reflect the theme of the record. Words without characteristic do not reflect the topic of the record; they simply result from the requirements of grammar or writing style. RF represents the number of records containing the word K in the record set. If a word's RF is lower, the word is a feature word. If the frequency of a word is higher in a specific record, then using the word reflects well the theme of the record.

A formula to calculate the inverse RF weighting of word K is as follows:

$$W_{rk} = \frac{F_{rk}}{RF_k}, \quad (29.1)$$

where W_{rk} is the inverse RF weighting of word K , F_{rk} its frequency of occurrence in record r , and RF_k its RF.

2. Location weighting of word K

Where a word occurs also affects its relevance. For example, consider a table of student thesis research achievements for example. Depending on whether a word appears in the title, abstract, or other fields of the table, its relevance in the record will be different. Retrieval objects of the DFRS system are recorded in the table. For a record, it shows user the results of different fields. These contents of disparate fields have differing abilities when it comes to expressing the theme of a record. Assume Word1 and Word2 is a record of the two keywords, Word1 in the field Title and Word2 in the field Reference. From the point of view of the paper, words in the Title field can highlight the theme of the record better than words in the Reference field. Suppose the table of student thesis research achievements has the following fields: Title, Keyword, Abstract, Introduction, Article, and Reference. At the same time, through a large number of experiments

Table 29.1 Field weight of keyword

Location of keyword	Weight of field
Title	2
Keywords	1.8
Abstract	1.6
Introduction	1.3
Article	0.7
Reference	1.0

and past experience, and with reference to the research results of others, when word k appears in various fields, its field weight can be set as shown in Table 29.1:

A formula for calculating the location weighting of word K is

$$W_{pk} = \text{Max}(W_{ik})(i = 1, \dots, 6), \tag{29.2}$$

where W_{ik} represents different weights on word k and the aforementioned six corresponding fields, and W_{pk} is the location weighting of word K and is the maximum in the aforementioned fields.

To sum up, the weight calculation formula for word k is as follows:

$$\begin{aligned} W_k &= W_{rk} + W_{pk} \\ &= \frac{F_{rk}}{RF_k} + \text{Max}(W_{ik})(i = 1, \dots, 6). \end{aligned} \tag{29.3}$$

By studying the weighting of the two parts mentioned earlier, we can obtain the weight value of the word in the record. According to the weight size of the word, when retrieving a keyword, the DFRS can sort the records, which can reduce the retrieval time and improve the user’s search experience.

29.3 Experimental Results and Analysis

29.3.1 Experimental Environment

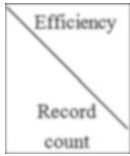
DFRS retrieval and database searches have the same experimental environment: the Web server for Tomcat 7.0, database management system for MySQL, and Lucene API for Lucene version 3.6.

In this paper, the experimental data come from Student, a graduate student management system database. Using DFRS it mainly builds indexes for the data of TermInfo, the table of student thesis research topics. The TermInfo table has a total of 13 fields, and the number of bytes is 3,020. The structure of the table is shown in Table 29.2.

Table 29.2 Structure of TermInfo table

Field name	Field type	Field meaning
Stu_id	varchar(20)	Student ID
Release_date	datetime(20)	Publication date
Release_unit	varchar(60)	Publication unit
Retrieval_rank	varchar(20)	Retrieval rank
Term_title	varchar(30)	Term title
Term_key	varchar(20)	Keywords
Catalogue	varchar(200)	Catalog
Abstract	varchar(500)	Abstract
Foreword	varchar(800)	Foreword
Term_body	Text	Article
Conclusion	varchar(500)	Conclusion
Reference	varchar(800)	Reference
Accessory_path	varchar(50)	Accessory store path

Table 29.3 Comparison of database retrieval and DFRS search

	Database retrieval			DFRS search		
	Result sorted	Search speed of single keyword (ms)	Recall ratio of multiple keywords (%)	Result sorted	Search speed of single keyword (ms)	Recall ratio of multiple keywords (%)
250	No	5–18	0	Yes	4–7	90
2,500	No	71–102	0	Yes	5–27	87
25,000	No	461–774	0	Yes	137–387	91
120,000	No	1,006–1,578	0	Yes	305–712	85

29.3.2 Experimental Analysis

In the first step, inputting a keyword, for different record numbers (250, 2500, 25000 and 120000), database retrieval, and DFRS search will performed in order to seek out the keyword, and take notes on all retrieval results. The above operation will be taken 60 times. In the second step, entering multiple keywords for different numbers of keywords, take the number of keywords for 3, 6, and 9 separately, and conduct a database retrieval and DFRS search to find the keywords, and record all retrieval results. The above operation will be taken 40 times.

After analyzing the experimental results, a comparison of the results of the database retrieval and DFRS search is shown in Table 29.3.

Compared to a traditional database search, the experimental results show that the DFRS retrieval has an advantage with respect to query speed, recall, and sorting the query outcome.

In general, compared with database searches, the search speed of DFRS retrieval represents a significant improvement.

When retrieval conditions include multiple keywords, the DFRS can split all keywords, through the term match records with reversed word order, search out all relevant information, and present results to users. The recall ratio of DFRS retrieval is very high. However, database retrieval does not have the function of the division of the user's query terms, and its recall is 0, that is, it cannot identify related information.

Unlike database retrieval, the DFRS can sort retrieval results according to the user's query intentions and reduce the time the user spends filtering useless information, which can significantly improve the user's search experience and increase user satisfaction, whereas database retrieval results are usually sorted in accordance with the order of the records in the table and do not reflect the user's query intentions. Search results will appear more numerous and more disordered, and there will be much useless information, which will irritate the user and diminish the user's search experience.

To sum up, compared with a traditional database search, database full-text retrieval based on Lucene is more applicable to site data searches and queries.

Conclusion

The traditional database retrieval cannot analyze user query conditions or match records containing opposite word orders; in addition, the recall rate of the retrieved results is generally low. And since there is no similarity calculation, which returns results that have no order and increases the difficulty of retrieval. Database retrieval sequentially looks up records in a table, which prolongs the search time, and generally cannot meet user needs quickly. In contrast to traditional database searches, full-text database retrieval based on Lucene matches records containing opposite word orders and has a high recall rate. In addition, the retrieval results can be sorted in accordance with user preferences, which improves retrieval efficiency. At the same time, such a search is based on an index with a specific format for searching, which may improve the speed of retrieval. The DFRS based on Lucene with quick retrieval speed and high recall ratio is much better than a database search and can better meet the needs of user queries.

Of course, it should be noted that the efficiency of the DFRS can be improved. In terms of the ranking of search results, the DFRS needs to be improved in order to produce results that meet user query demands. At present, the retrieval precision is relatively low and does not satisfy user requirements. Thus, the system should also improve retrieval precision.

References

1. Tang T, Chen L, Zhu W. Research and implementation of full-text search component based on Lucene. *Comput Appl Softw.* 2010;27(2):197–9 (in Chinese).
2. He C, Tan S, Liu J. Design and implementation of web service search engine. *Comput Appl Softw.* 2011;28(1):44–6 (in Chinese).
3. Daiwen W. Full-text retrieval application research based on Lucene. *Micro Comput Appl.* 2011;32(2):63–5 (in Chinese).
4. Li Y, Ding H. The research and application of full text retrieval on Lucene. *Comput Technol Dev.* 2010;20(2):12–5 (in Chinese).
5. Pan Y. The development of full text retrieval system web site based on Lucene. *J Guangxi Inst Educ.* 2007;4(5):63–6 (In Chinese).
6. Zhu W, Zhang Z. Sorting technology based on full-text retrieval toolkit Lucene. *J Chongqing Inst Technol.* 2009;22(12):102–5 (in Chinese).
7. Yang J, Ling P. Improvement on search engine PageRank algorithm. *Comput Eng.* 2009;35(22):35–7 (In Chinese).
8. Chang L, Xia Z. Several kinds of commonly used sorting algorithms of search engine. *Libr Inf Serv.* 2003;8(6):70–3 (in Chinese).

Chapter 30

Improving TCP Performance in Satcom Links by Packet-Loss Detection

Yuan He, Minli Yao, and Xiong Xiong

Abstract In TCP, packet loss is considered to be caused by congestion. In the Satcom on the Move communication system, packet loss is not only caused by channel congestion but is also a characteristic of wireless transmission media. In this case, the TCP transmitter automatically confirms that packet loss is a waste of bandwidth due to congestion and reduction in transmission rate. This problem can be solved by making the TCP source intelligent and able to distinguish the type of loss that occurs and then react appropriately. This paper proposes an improved TCP-D algorithm to achieve that goal.

Keywords Detection of packet loss • Satcom on-the-move (SOTM) • TCP

30.1 Introduction

Communication system in constant motion using GEO as relay satellite, is referred to as Satcom on the Move (SOTM), which features irregular movement of communication carriers at any time that are able to see the satellite so as to ensure the satellite link is connected and able to carry out reliable transmission of data. It is the motion characteristic and the characteristic of high signal frequency range of the SOTM system that makes SOTM links more susceptible to deterioration compared with traditional satellite communication systems. Link interrupts are caused by blockages.

Under the conditions in which SOTM work, the congestion control of transmission control protocol (TCP) is triggered by the packet loss resulting from link deterioration. Regarding the aforementioned problems, TCP works better if it can identify the reason for the packet loss and respond in different ways. Congestion will trigger TCP congestion control, and in case of link deterioration, the transmission state is maintained to achieve higher throughput. The method is to establish a loss signal on a system transmitter (the method means a kind of packet loss detection). The signal may explain the packet loss by monitoring and measuring some source parameters without help from the network. The time of the ACK

Y. He (✉) • M. Yao • X. Xiong

The Second Artillery Engineering University, 710025 Xi'an, China

e-mail: davidheheyuan@126.com

message segment is received for measurement to achieve one-way delay (OWD) and judge the reasons for the packet loss by a simple algorithm (ACK is used to measure OWD and the algorithm uses OWD to judge the reason of packet loss). The system finally realizes the improvement of TCP performance by reacting differently to different types of packet loss.

30.2 Analysis of Existing Methods Differentiating Causes of Packet Loss

There are many methods to differentiate the causes of packet loss at home and abroad. The methods can be divided into two categories, with one adopting the network nodes as medium for data support and the other based on the end-to-end (end-to-end means only need two ends of the link to support the algorithm). The first category, including I-TCP [1] and TCP-Jersey [2], needs the support of mediated network nodes, which is difficult to apply, while the end-to-end method is feasible because it only needs to make some changes at the sender's end. So it is feasible for the SOTM system, which requires miniaturization, to limit the processing capability because the receiving end can differentiate the causes of packet loss, but it needs to send the results to the transmitter for resolution.

The second method includes TCP IAT [3], TCP HMM, MLTCP, and Spike based on the receiving end. As for TCP HMM and MLTCP, the writer gathers different data related to the parameters by simulation and uses them to train a classifier to differentiate the causes of packet loss. In TCP HMM [4], the writer uses a hidden Markov model. In MLTCP [5], the writer uses a decision-tree classification algorithm. The writer finally evaluates the classification by simulation. This is an effective method of adopting a data training classifier to differentiate the causes of packet loss; nevertheless, a rule based on disposable data is difficult to universalize and cannot be implemented under various network environments.

The important advantage of the aforementioned hidden packet-loss detection technique is that there is no need to modify the base stations and other network intermediate nodes, but both of them are only applied to specific network environments. When the topology changes, for example, when the variation range of the bottleneck link bandwidth increases, the decision scheme of a TCP receiver is not ideal.

30.3 Improved Algorithm: TCP-D Algorithm

30.3.1 Algorithm Design

The proposed algorithm is an improved algorithm based on TCP Reno aimed at differentiating between congestion loss and wireless loss with OWD. Because the algorithm operates on a transmitter, only the receiver needs to provide a TCP

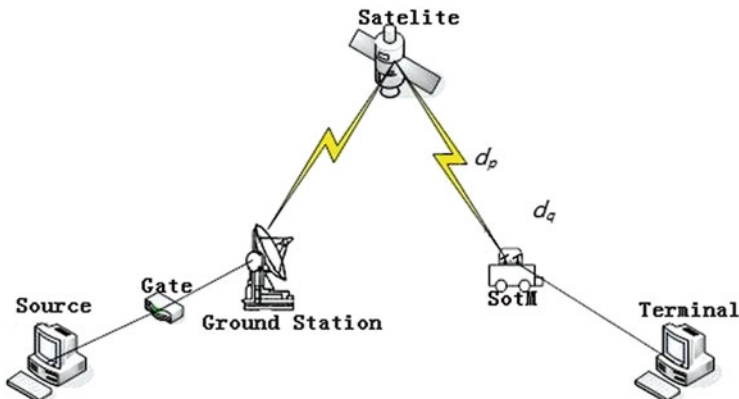


Fig. 30.1 SOTM link

timestamp of Request For Comments (RFC), supported by ISOC, include all design of TCP/IP 1323 [6] so as to compute the anterior delay of the transmitter. The transmitter receives the first repeated ACK message segment, which indicates that the packet loss is entering the TCP-D algorithm. The algorithm is shown in Fig. 30.1.

As shown in Fig. 30.1, d_p means the transmission delay between SOTM and the satellite, and d_q is the queuing delay of the SOTM gateway. If the coding delay is ignored, the OWD can be represented by the following formula:

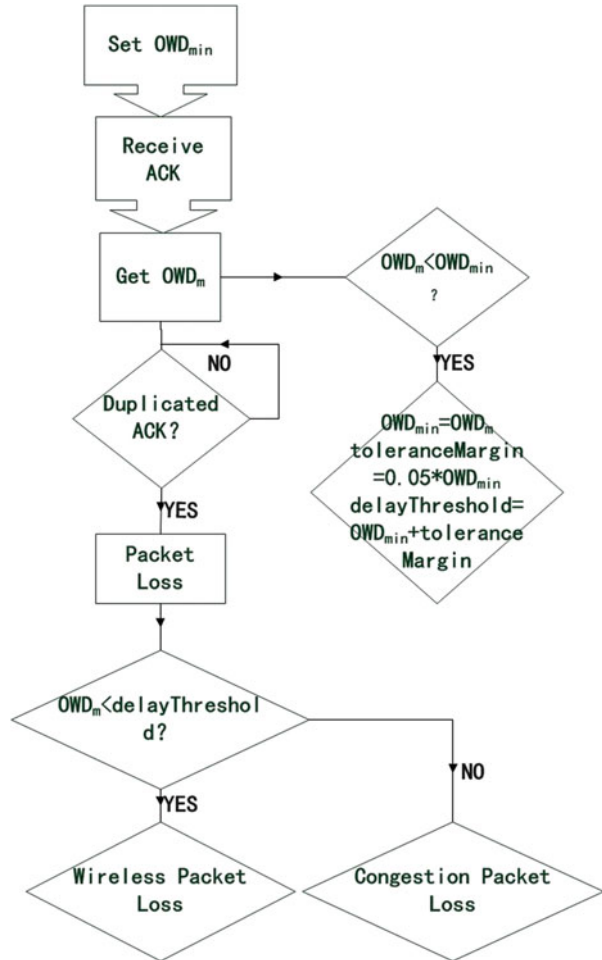
$$\text{OWD} = d_p + d_q. \quad (30.1)$$

In situations without congestion, the queuing delay d_q is 0, $\text{OWD} = d_p$. When the OWD is greater than that value, it indicates a queuing delay and there is congestion. In STOM links, the transmission delay is influenced by channel fading, interrupt, and shadow visibility and, thus, changes continuously, and the change can be processed by adding a small allowance called *toleranceMargin*. In the algorithm, a threshold *delayThreshold* is defined, and it is set at $\text{OWD}_{\min} + \text{toleranceMargin}$. When the transmitter receives an ACK message segment, it must first determine whether it is a repeated ACK. If so, then it indicates that there is packet loss, and then the OWD is measured. When the OWD is greater than the *delayThreshold*, it indicates that there is packet loss due to congestion in the wireless links. The algorithm process is shown in Fig. 30.2.

30.3.2 Influence of Threshold Selection on Algorithm

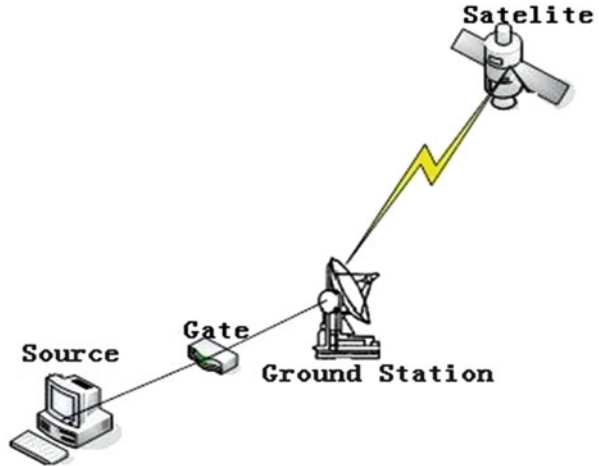
In the TCP-D algorithm, *delayThreshold* influences the performance of the algorithm and is TCP friendly. The smaller *delayThreshold* is, the lower the accuracy of judging wireless packet loss. The more accurate the judgment of the congestion

Fig. 30.2 TCP-D algorithm processes



packet loss is, the higher the TCP fairness is. The more conservative *delayThreshold* is, the error rate of the algorithm is higher. This makes TCP to use standard back-off process to maintain TCP friendly. Conversely, the greater *delayThreshold* is, the more accurate the judgment on the wireless packet loss; and but this may causes judging congestion packet loss to be wireless packet loss. It makes TCP not to take standard back-off process to keep the transmission rate, but influence the transmission efficiency and performance of the TCP source. Thus the setting of *delayThreshold* needs to balance the performance and TCP friendly so as to ensure the fairness of the communication system. It is feasible to set the *delayThreshold* at 5 %.

Fig. 30.3 Model for Simulation



30.3.3 Analog Simulation

This paper uses a network simulator (ns-2 version 2.33) for analog simulation on TCP-D with the applied model shown in Fig. 30.3.

The parameter is set as the transmission error rate r_w , which is used to control the transmission error rate caused by the wireless transmission medium, and its value ranges from 1 % to 20 %. $d1$ and $d2$ are the transmission delay of a wired network and take different values. The queue length of the source host is greater than the queue length of the gateway. In the simulation process, the TCP connection is established from the source host to the gateway of the satellite network. The connection variables use the variables of TCP Reno and TCP-D, and the data flow is provided by FTP.

The performance of the algorithm is measured by the parameters classification accuracy and TCP throughput (TCP Reno and TCP-D).

When there is only wireless packet loss, there is no congestion packet loss.

If the queuing length of the gateway is greater than or equal to the maximum receiving window, then no congestion packet loss will be caused by the queue overflow. The float of r_w between 1 % and 20 % simulates different degrees of wireless loss.

Figure 30.4 shows a simulation of delay. O indicates the OWD that is achieved by the first repeated ACK on a transmitter of wireless links. owd_{min} is the minimum of OWD in the simulation process. $delayThreshold$ is the threshold of TCP-D. The delay corresponding to greatest packet loss is lower than the threshold, which causes the algorithm to recognize it as a wireless packet loss. Other points on the thresholds are caused by a change in the transmission delay of wireless links. Figure 30.5 shows a comparison of throughput of the TCP-D algorithm and the traditional TCP Reno algorithm under the same packet loss rate. It indicates that the throughput of TCP-D is better than that of TCP Reno in a wireless link environment with the same packet loss rate.

Fig. 30.4 Delay time without congestion

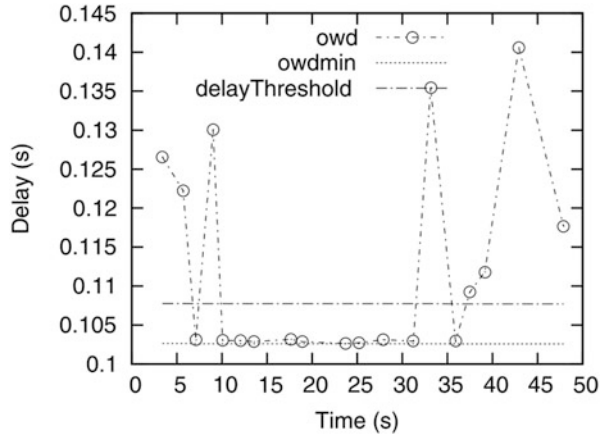
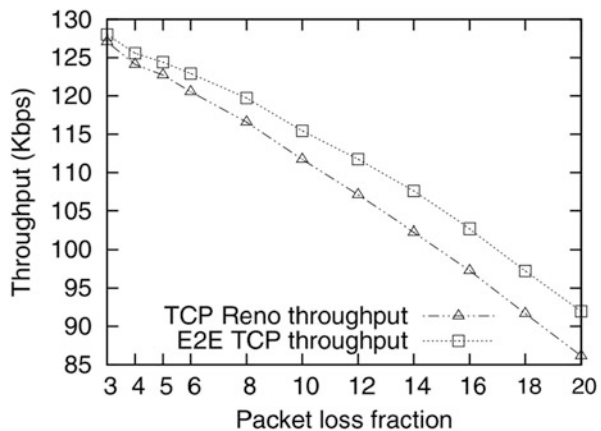


Fig. 30.5 Comparison of throughput



30.3.3.1 Congestion Packet Loss Only, No Wireless Packet Loss

Under this scenario, the queuing length of the route is set at seven packets, and the maximum receiving window is set at ten packets for the simulation to ensure that the queue overflow will lead to congestion packet loss. r_w is set to 0 to ensure there is no wireless packet loss.

Figure 30.6 shows a delay simulation. The asterisk indicates the delay that the transmitter receives with the first repeated ACK. When the queue overflows and congestion packet loss occurs, the end-to-end OWD is greater than the *delayThreshold*, which causes the TCP-D to detect all packet loss as congestion packet loss, which is consistent with the causes of packet loss. Figure 30.7 shows a comparison of throughput of the TCP-D algorithm and the traditional TCP Reno algorithm under the same packet loss rate. Both algorithms process packet loss based on the congestion packet loss, the same to their throughput.

Fig. 30.6 Delay time without wireless packet loss

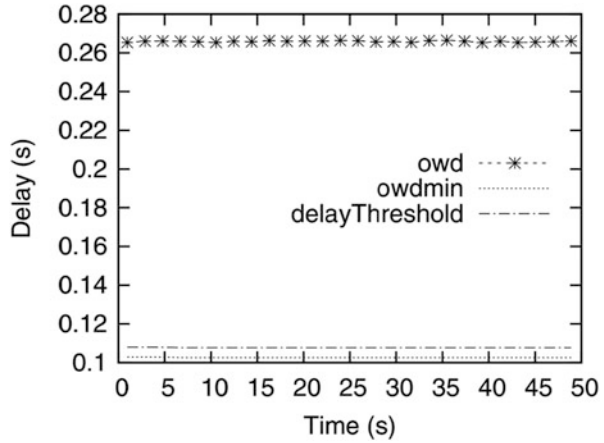
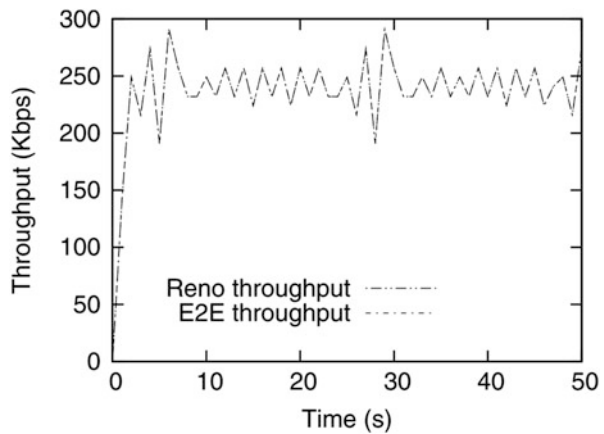


Fig. 30.7 Comparison of throughput



30.3.3.2 Wireless Packet Loss and Congestion Packet Loss

This situation arises by combining the preceding parameters. A float of r_w of 1–20 % is used to simulate different degrees of wireless packet loss. The queuing length of the route is seven packets, and the maximum receiving window is ten packets.

Figure 30.8 shows the delay in packet loss. O indicates the OWD that is achieved by the first repeated ACK on a transmitter of wireless links. In the simulation, all points lower than the threshold value are judged to be wireless packet loss (approximately 10 %). Most points greater than the threshold represent not congestion packet loss but wireless packet loss, which cannot be ascertained by the algorithm. Judging wireless packet loss to be congestion packet loss will cause the TCP to initiate back-off processes to relieve the congestion. Judging congestion packet loss to be wireless packet loss affects TCP fairness. Figure 30.9 shows a comparison of

Fig. 30.8 Delay time in common environment

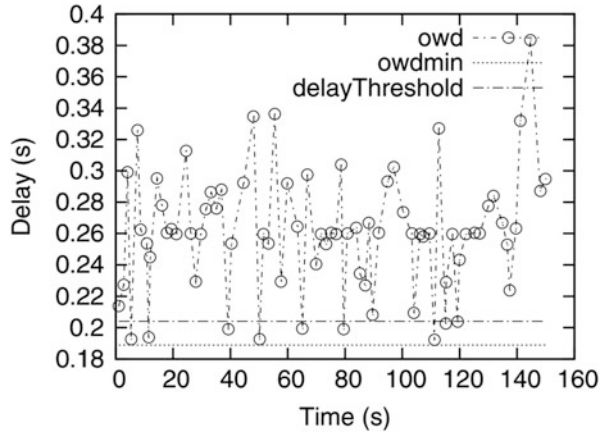
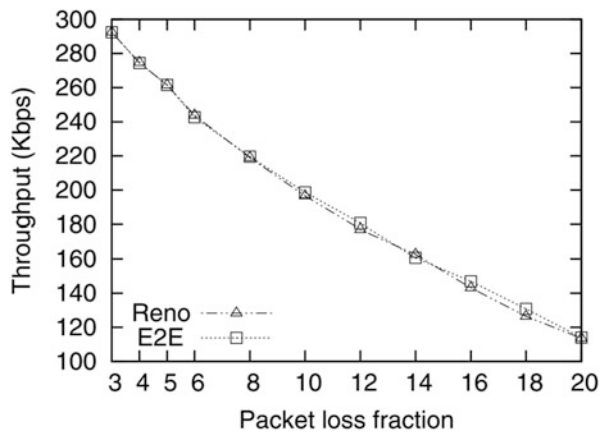


Fig. 30.9 Comparison of throughput



the throughput of the TCP-D algorithm and the traditional TCP Reno algorithm under the same packet loss rate. Because TCP-D detects wireless packet loss accurately, it works better than the traditional TCP Reno.

Conclusion

Using a simulation analog, the performance of the TCP-D algorithm has been improved compared with the traditional TCP Reno algorithm; in addition, the TCP-D algorithm has the following advantages. It is easily applied with low load demands for network management, it only has to modify the transmitter instead of the receiving end, and it neither needs the receiving end to provide extra support nor occupies other bandwidth resources. As for the

(continued)

(continued)

disadvantages of the algorithm, in STOM communication links, the variation in OWD is greater, which reduces the accuracy of the algorithm in differentiating the causes of packet loss and causes it to process packet loss like TCP Reno. To demonstrate the performances of the algorithm, this paper used *toleranceM arg in* to improve the packet-loss detection accuracy of the algorithm based on the surrounding environment, link state, and shadow visibility in STOM communication links.

References

1. Bakre A, Badrinath BR. I-TCP: indirect TCP for mobile hosts. Proceedings of the 15th International Conference on Distributed Computing Systems; IEEE; 1995. p. 136–43.
2. Xu K, Tian Y, Ansari N. TCP-Jersey for wireless IP communications. IEEE J Sel Area Commun. 2004;22(4):747–56.
3. Biaz S, Vaidya NF. Discriminating congestion losses from wireless losses using inter-arrival times at the receiver. Proceedings 1999 I.E. Symposium on Application-Specific Systems and Software Engineering and Technology, ASSET'99; IEEE; 1999. p. 10–7.
4. Liu J, Matta I, Crovella M. End-to-end inference of loss nature in a hybrid wired/wireless environment. Technical report, Boston University Computer Science Department; 2002.
5. Geurts P, El Khayat I, Leduc G. A machine learning approach to improve congestion control over wireless computer networks. Fourth IEEE International Conference on Data Mining, ICDM'04; IEEE; 2004. p. 383–86.
6. Borman D, Braden R, Jacobson V. TCP extensions for high performance," Request for Comments (Proposed Standard) RFC 1323, Internet Engineering Task Force, May 1992[J]. Obsoletes RFC1185

Chapter 31

Key Management Scheme in Cluster for WSNs

Xiaoming Liu and Qisheng Zhao

Abstract The information security of wireless sensor networks is one of the hot issues on the current research; this chapter combines threshold key scheme with the management of security key sharing and group agreement and proposes dynamic key management scheme through clustering level key matrix of authentication mechanism from the cluster to node. The network is divided into different clusters, and the cluster head conducts the key authentication exchange and updates the key management with threshold key schemes, with no need of third authentication center; it reduces computing and communication costs, using the preset public key encrypting the data. The clusters adopt bidirectional authentication to promote communication security.

Keywords Security • Key management • Cluster • Authentication • Matrix • Threshold

31.1 Introduction

The wireless sensor network (WSN) consists of spatially distributed autonomous and battery-powered sensors which are embedded in sensor devices, data processing devices, energy devices, storage devices, and communication devices to monitor physical or environmental conditions, such as temperature, sound, vibration, pressure, motion, or pollutants, and to cooperatively pass their data through the network to a main location (i.e., base station or sink). In recent years, wireless sensor networks have proliferated to a wide range of applications such as battlefield surveillance in military applications, industrial process automation (monitoring and controlling), meteorological areas, home appliances, and health applications [1, 2]. However, wireless sensor nodes have limitations in terms of processing, centralization, limited power capacity, self-sufficiency, multi-hop

X. Liu (✉)

Information Center, Huaihai Institute of Technology, 222005 Lianyungang, Jiangsu, China
e-mail: Liuxm029@gmail.com

Q. Zhao

Computer Engineer College, Huaihai Institute of Technology, 222005 Lianyungang, Jiangsu, China

routing, dynamic topology, and number of nodes. Sensor networks often provide services in hostile environments, which make them targets for malicious attackers. The WSNs face many security issues such as data intrusion and topology destruction via Sinkhole, Sybil, Wormholes, Hello flood intrusion, nodes captured, etc. [2, 3]. It thus makes it very challenging to provide security in WSNs. Currently the main ideas for resisting intrusion are to establish security routing and key management schemes.

31.2 Related Works

There are two types of key management scheme in wireless sensor networks: distributed architecture and clustering architecture. In the distributed architecture, there are no fixed fundamental facilities, the energy and power of network nodes are in the same level, and nodes have the ability of sensing, signal processing, and wireless communication. The nodes communicate with preset keys to establish the security channels. For the distributed architecture, the nodes divide into three categories: base station, cluster heads, and ordinary nodes. The base station is in charge of distributing and updating keys as a distributing center, ordinary nodes just have an ID and some corresponding keys, and others belong to the clusters' mission [4]. As mentioned in the past literatures, μ TESLA adopts sharing keys generating algorithm in full networks unless the key pool and the real keys are stored in the base station; the full networks share the key generating algorithm. It also uses the key chains which are made by one-way hash functions. However, μ TESLA needs a high demand for time synchronization and high memory overhead caused by the delay of publishing keys [3]. Another multi- μ TESLA introduces the multilevel key loop, but it can't tolerate packet loss [5]; MM μ TESLA introduces threshold cryptogram and separates the authentication key into key shadows distributing to multiple base stations. The sensor nodes make use of key shadows to reconstitute authentication keys and broadcast them. However, MM μ TESLA multiple base stations may raise new security issues [6]. Sun proposes an improved key management by taking advantage of a one-way hash function to alleviate the influence of compromised sensors. The function does not affect the connection between neighboring sensor nodes, but it still cannot withstand the Dos attack to the ordinary nodes or even derivative keys conflicts [4, 7]. Si [8] introduces the symmetric key cryptographic algorithms. It is used at the link layer of WSNs, but if one node key is exposed, others will be open and the data of the full network will be vulnerable. The researchers [9–11] propose Q-composite probabilistic plans based on an E-G scheme. These schemes generate less communication traffic and calculated quantity but need increased storage for the keys and have limited network connectivity and security. Wen [12] proposes multi-polynomial functions and a dynamic multicast key management scheme, but this is weak in dealing with multicast unreliability in clusters. Other researchers [13] make use of location-based group key allocation and broadcast-based rekeying by using dynamic composition key schemes. Liu [14]

and Liu [15] propose a novel (q,l) threshold secret sharing scheme in which the key is divided into shadows. This promotes security, but this kind of probabilistic network is low in persistence ration and energy consumption. He et al.’s proposal [16] is different in that the slice keys are put into “virtual cluster head” (VCH) and reconstructed by a “physical cluster head.” However, the proposal does not provide detail about VCH and never discusses the communication during the VCHs. This chapter proposes a security sharing and group dynamic clustering key agreement scheme through (q,l) threshold key authentication mechanism in the cluster management.

31.3 The Clustering Key Scheme

31.3.1 The Model Architecture

In the hierarchical wireless sensor network, the distribution is based on cluster, and one cluster has a cluster head and multi-cluster member, in which the cluster head has special high ability in communication, computing, memory, and power, and cluster members are just ordinary nodes, which allow communication with the cluster head or between them to decrease the energy consumption. Due to the fact that cluster head has more powerful energy so that it could undertake higher cost of computing and communications and interclusters, it’s easier to adopt the public key scheme to make authentication with base station. Another way is that, inside the cluster, the members all communicate with the cluster head and make authentication with it, so we adopt threshold key model (q,l) to carry out the ordinary nodes security and the network architecture model and algorithm as follows (Fig. 31.1):

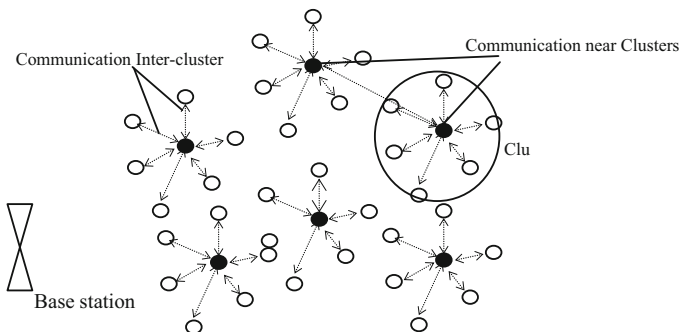


Fig. 31.1 The clustering key model architecture

31.3.2 The Threshold Key Scheme in Cluster Management

Before network nodes deployment, the key management center (KMC) selects a hash function, the elliptic curve and related parameters, and generates the public/private key matrix. It then distributes the above information to the nodes. Each node has its own ID, keys, functions, and other related parameters.

Suppose the open information in the threshold key scheme covers: one big prime number $r > n\beta$ is the primitive element from finite field of $GF(r)$, $m = pq$, and p and q are different prime numbers and are confidential.

Assume that in the cluster member, there are n nodes and like P_1, P_2, \dots, P_n , sharing $k \in GF(r)$ of the key information generated from the cluster head. The key and authentication slices are distributed in the algorithm as follows:

1. At first select $n - 1$ times polynomials function of $f(x) = b_{t-1}x^{t-1} + \dots + b_1x + k \pmod r$ secretly, in which $b_1, b_2, b_3, \dots, b_{t-1}$ and $f(x)$ all belong to $GF(r)$. Randomly select e_1, e_2 as prime as $\varphi(r)$ relatively and expose the e_1, e_2 and $\varphi(r)$ as an Euler function.
2. Calculate:
 $d_1 = (e_1 - 1) \pmod{\varphi(m)}$ and $d_2 = (e_2 - 1) \pmod{\varphi(m)}$
 From $i = 1, 2, \dots, i$, make a progression as follows:
 Compute $S_i = f(\beta^i)$ and $w_i = S_i^{e_2 d_1} \pmod m$ and distribute the S_i and w_i to the clustering members as key and authentication slices.
3. When needed, the sharing key, as long as n participants in the arbitrary, just t cooperators can restore the key k ; assume that there are cluster member P_1, P_2, \dots, P_t cooperators. Using the t key slices, we can get t interpolation points $(\beta^1, S_1), \dots, (\beta^t, S_t)$, and then using Lagrange interpolation, we can refactor the polynomial $f(x)$ of $t - 1$ times and then $S_t = f(\beta^t)$, and we can calculate $k = f(0)$, and the calculating formula of key k is as follows:

$$k = \sum_{i=1}^t s_i \prod_{j=1, j \neq i}^t \frac{-\beta^j}{\beta^i - \beta^j} \pmod r \quad (31.1)$$

31.3.3 The Security of Key Management

To promote the difficulty of cracking keys, put them into the polynomial: for the node i , randomly choose the S_i as the portion of the key S and $a_{i,j} (j \in 1, 2, \dots, n - 1)$ and then construct the threshold polynomial $f_i(x)$ of (t, n) and so

$$f(x) = S + a_1x + a_2x^2 + \dots + a_{n-1}x^{n-1} \pmod r \quad (31.2)$$

$$f_i(x) = S_i + a_{i,1}x + a_{i,2}x^2 + \dots + a_{i,n-1}x^{n-1} \pmod r \quad (31.3)$$

Node i calculates key portions according to the above formulas and sends them to the node j with security channel; node j collects the threshold polynomials from the t nodes from the cluster member, computing $f_i(x)$ to get the main key S :

$$\begin{aligned}
f_1(j) + f_2(j) + \cdots + f_t(j) &= S_1 + a_{1,1}x + a_{1,2}x^2 + \cdots + a_{1,n-1}x^{n-1} \\
&+ \cdots + a_{2,n-1}x^{n-1} + \cdots + S_t + a_{t,1}x + a_{t,2}x^2 + \cdots + a_{t,n-1}x^{n-1} \\
&= (S_1 + S_2 + \cdots + S_t) + (a_{1,1} + a_{2,1} + \cdots + a_{t,1})x \\
&+ \cdots + (a_{1,n-1} + a_{2,n-1} + \cdots + a_{t,n-1})x^{n-1} \\
&= S + a_1x + a_2x^2 + \cdots + a_{n-1}x^{n-1} \pmod{x} = f(x)
\end{aligned} \tag{31.4}$$

31.4 Security Analyses

When needed to recover the sharing key k , there will be some inner deceivers in the t nodes participants from the cluster members. The deceivers use the fault fragment to prevent the regular recovering of sharing key k information, and the outer deceivers would try to join the key recovering as well as getting the information key k . The thresholds keys can take advantage of authentication fragments effectively to detect inner and outer deceivers. Assume that the participants of P_1, P_2, \dots, P_t share the key k information and $P_i (1 \leq i \leq t)$; if $W_i^{e_1} \equiv S_i^{e_2} \pmod{m}$, then P_i is the legal participator bringing forth the real fragments inside the cluster; otherwise, they are deceivers.

To verify, if the P_i is the legal participant with real fragment, they must satisfy the formula

$$W_i^{e_1} \equiv S_i^{e_1 e_2 d_1} \equiv S_i^{e_2} \pmod{m} \tag{31.5}$$

If not, it means that the node shows troubled fragments. If it happens to lose a package in key recovery, then it will not satisfy this formula and can let the node resend the fragment in order to recover the correct key. If some node is attacked by a deceiver and produces troubled fragments, then it must degrade the credit level, change the node, or replace the polynomials.

For the recovery of the sharing keys, if only in n participants, just random t cooperators can restore the key k ; assume that there are cluster member P_1, P_2, \dots, P_t cooperators. Using the kept t key slices, we can get t interpolation points $(\beta^1, S_1), (\beta^2, S_2), \dots, (\beta^t, S_t)$, and then using Lagrange interpolation, we can refactor the polynomial $f(x)$ of $t-1$ times, then $S_t = f(\beta^t)$, and at last, we could calculate $k = f(0)$, and the calculating formula of key k is as follows:

$$k = \sum_{i=1}^t s_i \prod_{j=1, j \neq i}^t \frac{-\beta^j}{\beta^i - \beta^j} \pmod{r} \tag{31.6}$$

When the node are captured, according to the information of the captured node, we can directly or indirectly calculate probability F which means the non-captured nodes; the less F , the stronger the anti-captured node. The resistance to capture for the nodes is the important index to measure the safety of key management schemes. In the key sharing model (q, l) , we discuss the nodes and cluster in terms of anti-captured ability. An ordinary node as the cluster member just have the key sharing

with the cluster and the function to generate the key between the members, so it strongly resists capture and has less value, but with the cluster it has many keys with the base station and distributed functions. The enemy can read the nodes' memory and compute most keys. When there are x nodes which were captured, the enemy can calculate the probability $p(x)$ of the random k_i :

$$p(x) = \begin{cases} 0 & 0 \leq x \leq q \\ 1 - \sum_{i=0}^{q-1} \frac{C_l^i C_{n-l}^{x-i}}{C_n^x} & q \leq x \leq n \end{cases} \quad (31.7)$$

When $x < q$, we consider that k_i is secure in the view of information theory, and when $x \geq q$, k_i will be exposed to capture, but the node owing k_i might not be captured; $F(x)$ stands for the resistance to capture, m is the number of ordinary nodes, and n is the total clusters.

$$F(x) = p(x) \frac{m}{m - \frac{mx}{n}} = p(x) \frac{n}{n - x} \quad (31.8)$$

For the model (q, l) , when q and l are defined and decided, $F(x)$ will increase as x goes up; the more decided x is, the more of $\{l - q\}$; the less $F(x)$ is, the more security of the networking.

Conclusion

This chapter proposes the step-by-step key authentication scheme not under the KMC controlling, combines the scheme of the asymmetrical public key system and threshold key scheme, proposes dynamic key management scheme through the second-level key matrix of authentication mechanism from the cluster to node, and reduces the computing and communication costs, and the clusters adopt bidirectional authentication to promote communication security.

Acknowledgements This research was supported by China National Foundation No. 61103017, Lianyungang Science and Technology Project No. CG1215, and Lianyungang Social Development Project No. SH1212.

References

1. Akyildiz IF, Su W, Sankarasubramaniam Y, Cayirci E. Wireless sensor networks: a survey. *Comput Netw.* 2002;38:393–433.
2. Pamo B, Perrig A, Gligor V. Distributed detection of node replication attacks in sensor networks. In: *Proceedings of the IEEE symposium on security and privacy.* IEEE Computer Society; 2005. p. 49–63.
3. Perrig A, Szewczyk R, Wen V, Culler D, Tygar J.D. SPINS: security protocols for sensor networks. *Wirel Netw.* 2002;8(5):521–34.
4. Chan H, Perrig A, Song D. Key distribution techniques for sensor networks. *Wirel Netw.* 2004;6(2):277–303.
5. Liu DG, Ning P. Multi-level μ TESLA: a broadcast authentication system for distributed sensor networks. *ACM (TECS).* 2004;3(4):800–36.
6. Shen Y-L, Pei Q-Q. MM μ TESLA: broadcast authentication protocol for multiple-base-station sensor networks. *Chin J Comput.* 2007;4:539–47.
7. Qian S. A novel key pre-distribution for wireless sensor networks. *Physics Procedia.* 2012;25:2183–9.
8. Si LL, Ji Z. The application of symmetric key cryptographic algorithms in wireless sensor networks. *Physics Procedia.* 2012;25:552–9.
9. Du WL, Deng J, et al. A key management scheme for wireless sensor networks using deployment knowledge. In: *The 23th IEEE computer and communications proceedings.* IEEE; 2004. p. 586–97.
10. Levi A, Tasc SE, et al. Simple extensible and flexible random key predistribution schemes for wireless sensor networks using reusable key pools. *J Intell Manuf.* 2009;21(5):625–45.
11. Jaworski J, Ren M, Rybarczyk K. Random key redistribution for wireless sensor networks using deployment knowledge. *Computing.* 2009;85(1–2):57–76.
12. Wen T, Zhang Y, Quan G, Li F. Kun. Dynamic group key management scheme for homogeneous wireless sensor networks. *Journal on Communications.* 2012;33(6):164–172.
13. Paek K, Song U, Kim H, Kim J. Energy-efficient key-management (EEKM) protocol for large-scale distributed sensor networks. *J Inf Sci Eng.* 2008;24(6):1837.
14. Wei L, Rong L. A lightweight key establishment protocol for wireless sensor networks. *J Electron Inf Technol.* 2010;32:869–74.
15. Liu YN, Wang J, et al. Threshold key sharing Model in wireless sensor networks. *J Electron Inf Technol.* 2011;33:1913–9.
16. He X, Niedermeier M. Dynamic key management in wireless sensor networks: a survey. *J Netw Comput Appl.* 2013;36:611–22.

Chapter 32

An Energy-Saving Method for Erasure-Coded Distributed Storage System

Lei Yang and Shi Liu

Abstract In replicated distributed storage system (RDSS), most of energy-saving method cannot meet the requirement of the energy efficiency ratio. And other methods for erasure-coded distributed storage system (ECDSS) bring too much computational overhead due to the nature of erasure code. In this chapter, we target at RS code and propose two algorithms to reduce the computational overhead of requesting data while saving energy of ECDSS. The experimental results show that our algorithms can reduce the computational overhead effectively while reducing energy consumption compared with conventional methods. Meanwhile, with the increasing sleep rate and the descending code rate, the reduction effect of the computational overhead will be better.

Keywords Distributed storage system • Erasure code • Energy saving

32.1 Introduction

With the rise of cloud computing, cloud storage system increasingly becomes the underlying infrastructure and data service provider of top-level application. However, high energy consumption becomes one of the major challenges that cloud storage system faces. According to statistics, IT system makes up 1–2 % [1] of the total world energy consumption. Furthermore, storage system accounts for 40 % [2] of the whole system's energy consumption, and the ratio will increase continually with the advent of big data times. Currently, the way to save energy mainly includes sleeping nodes and shutting down nodes. The main strategies adopted are energy-aware data placement and migration algorithm such as MAID [3], Popular Data Concentration (PDC [4]), Hibernator [5], Diverted Access (DIV [6]), Auxiliary Node [7], etc.

For DSS, the general practice is turning part of the nodes that are accessed less into energy-saving method or suspended state through some software strategies while not or less affecting the performance of the data center. In cloud computing environment, the data access frequency of each node is different, such that there is a

L. Yang (✉) • S. Liu

College of Information Science and Engineering, Hunan University, 410000 Hunan, China
e-mail: jt_yl@hnu.edu.cn

lot of optimizing space for energy consumption. According to the periodicity of data accessing, GreenHDFS [8] closes a lot of idle nodes in the cold sector to reduce energy consumption.

From the above, we can see that the existing work on energy saving mainly targets at the replicated distributed storage system (RDSS) while not at the erasure-coded distributed storage system (ECDSS). Considering the energy consumption of the different components in two kinds of energy model [9], coverage-based method is better for DSS because node is regarded as a scheduling unit. Therefore, we propose two algorithms called Redundancy First Sleep (RFS) and Data First Compensation (DFC), respectively, to reduce computational consumption while saving energy of DSS. Moreover, the experiments show that it is capable of reducing energy consumption on the premise that the system's original properties will not be changed when the system is idle.

The remainder of this chapter is organized as follows. Section 32.2 introduces coverage-based energy-saving methods and related theories. Section 32.3 proposes an energy-saving method for ECDSS. Experimental results are presented and discussed in Sect. 32.4. Finally, we discuss future work and conclude in section Conclusion and Future Work.

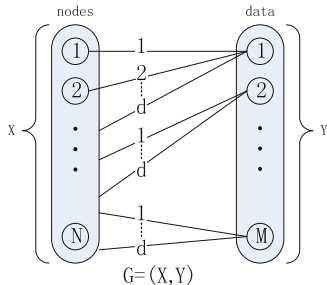
32.2 The Conventional Coverage Method and Related Theories

This section will first introduce a conventional coverage-based energy-saving method (CBESM) in ECDSS. Then based on CBESM, we give the equations of communication and storage overhead in conventional energy-saving method for erasure code, which will be used in subsequent algorithms. And due to limited space, we omit the comparison of communication and storage overhead between erasure code and replication under the energy-saving mode-based CBESM.

32.2.1 *The Conventional CBESM*

Generally, the energy-saving algorithm is to put nodes to sleep as many as possible while ensuring the data availability of the nodes. This energy-saving problem could be described as a bipartite graph $G = (X, Y)$, as shown in Fig. 32.1. X and Y represent M machine nodes and N data items, respectively. Each edge represents a data fragment of the corresponding data unit stored in the corresponding machine node. Our goal is to find a minimal subset of machine nodes covering the data nodes as many as possible, such that the remainder of machine nodes to be in energy-saving method is maximal. If all data items are covered, then we obtain a full coverage.

Fig. 32.1 The bipartite graph of RDSS



To ensure data availability, those uncovered data fragments are migrated to low load active nodes. This solution not only is effective but also has the advantages of low complexity and low overhead. The feasibility analysis for coverage strategy will be illustrated in the following subsection.

32.2.2 Communication Overhead

From [7], we know that any placement algorithm can find a subset covering data items, the proportion of which is $1 - q$ when sleep rate is p , and all covered data items are still available. Moreover, for any size of subset, the proportion of unavailable data items is q , where

$$q = \sum_{i=0}^{k-1} C_d^i \cdot (1 - p)^i \cdot p^{d-i} \tag{32.1}$$

In theory, communication overhead can be regarded as the increment of storage overhead, namely, the load migrated for compensation.

Based on the above, we can see for any placement algorithm of (k, d) code, when sleep rate is p , the ratio of additional fragments to original fragments of the system is $ratio_{ec}$.

$$ratio_{ec} = \frac{frag_{add}}{frag_{origin}} = \frac{\sum_{i=0}^{k-1} (k - i) \cdot C_d^i \cdot (1 - p)^i \cdot p^{d-i}}{d} \tag{32.2}$$

32.2.3 Storage Overhead

Assuming the load rate before sleeping is q_{origin} , then according to Eq. (32.2), the load rate LR_s after sleeping is as in the following equation, where $load_{add}$ is

additional load equaling to $frag_{add}$ due to compensation and $load_{origin}$ is original load rate of the system equaling to $frag_{origin}$.

$$LR_s = q_{origin} \times \left(\frac{load_{add}}{load_{origin} \times (1 - p)} + 1 \right) \quad (32.3)$$

Through Eq. (32.3), we can know load rate by sleep rate p , which is a prerequisite for following energy-saving method.

32.3 Energy-Saving Method for ECDSS

Because of the application of erasure code in energy-saving method, DSS will inevitably bring some computational overhead to itself. Thus, a coverage method for erasure code must be adopted in ECDSS to alleviate the overhead. In this section, we propose this coverage method.

32.3.1 The Algorithms

There are two stages in our general algorithm for energy-saving method, namely, sleep stage which will mark nodes that can be put into sleep mode and compensation stage which compensates data availability caused by some sleeping nodes, respectively. In this subsection, we will present an algorithm called Redundancy First Sleep (RFS) for sleep stage and an algorithm called Data First Compensation (DFC) to compensate availability by using a small amount of storage space in unsleeping nodes, so that any data in the sleeping nodes of the system always remains available. The algorithm of RFS is as follows.

Algorithm 1 Redundancy First Sleep

Input: The queue of candidate sleep and active node, $Queue_{sleep}$ and $Queue_{active}$

Output: Datanode that can be put into sleep, $Queue_{sleep}$

```

1: repeat
2:    $currentData.degree \leftarrow \text{find } Queue_{sleep}.front \text{ in } Matrix_{ds}$ 
3:   if  $currentData.degree \geq k + 1$  then
4:     mark  $Queue_{sleep}.front$  as a determined sleep node
5:      $Matrix_{ds} \leftarrow currentNode.degree - 1$ 
6:   else call  $DataFirstCompensation$ 
7:   end if
8: until  $size[Queue_{sleep}.unmarked] \leq 0$ 
9: Put the nodes in  $Queue_{sleep}$  into sleep mode

```

And when there exists unavailable data, the algorithm of DFC will be called.

Algorithm 2 Data First Compensation

Input: The queue of candidate sleep and active node, $Queue_{sleep}$ and $Queue_{active}$

Output: Targeting nodes of compensation, $Queue_{active}$

```

1:  $currentFragment \leftarrow 0$ 
2: if  $Queue_{sleep}.front.fragmentType_i \in dataFragment$  then
3:    $currentFragment \leftarrow Queue_{sleep}.front.fragment_i$ 
4:   break
5: else
6:   for  $i=0$  to  $d-1$  do
7:     if  $Matrix_{ds}.fragment.fragmentType_i \in dataFragment$  then
8:        $currentFragment \leftarrow Matrix_{ds}.fragment$ 
9:       break
10:    end if
11:  end for
12: end if
13: Migrate  $currentFragment$  to  $Queue_{active}.front$ 

```

Next, we present the general steps of energy-saving method in the following.

1. First, combined with k and d , the algorithm figures out the load rate in each sleep rate as a map table.
2. According to free space, the system chooses the proper sleep rate p by Eq. (32.3) then starts the sleep procedure.
3. The algorithm initiates $Matrix_{ds}$, whose elements present the weight of each data fragment and calculate the weight of every vertices.
4. A queue is constructed to contain all nodes then divided to two priority queues which are $Queue_{sleep}$ where $Queue_{priority} \propto \frac{1}{degree_{data}}$ and $Queue_{active}$ where $Queue_{priority} \propto \frac{1}{degree_{all}}$ (is the degree of nodes represented by data fragments and is the degree of nodes represented by all fragments).
5. The availability of data is checked. If the data in the first node of $Queue_{sleep}$ is available, then the node meets the condition of sleep. Thus, it will be marked as a determined sleep node.
6. If there exists unavailable data, the system will start the compensation procedure that migrates data fragments to the first node in $Queue_{active}$.
7. Repeat step 5 until $Queue_{sleep}$ is empty.
8. After marking every nodes in $Queue_{sleep}$, the system will put the marked nodes to sleep.

32.4 Evaluation

In this section, to evaluate the performances of the algorithms mentioned above and compare with other algorithms, we implement a DSS simulator with 1,000 nodes and 10,000 random text files created by a file generator and validate the effectiveness of our algorithms by analyzing and comparing the experimental results.

32.4.1 Computational Overhead

Targeting at two representative code rates which are (4, 6) and (14, 16), we compare the average speed of decoding 10,000 files with size of 1 MB among the combination of GS and RC, the combination of RFS algorithm and RC, and the combination of RFS algorithm and DFC algorithm.

In this experiment, we target at (4, 6) and (14, 16) codes and compare the decoding rate between combinations of algorithms, as shown in Table 32.1.

As shown in Fig. 32.2, for both code rates, the RFS algorithm improves the decoding speed. For (4, 6) code system whose code rate is high, when the sleep rate is low, the decoding speed of DFC and RC is equal and decreases with the increasing sleep rate. Moreover, when reaching the critical value of 500, the speed of decoding DFC increases with the increasing of sleep rate. While for (14, 16) code system whose code rate is low, DFC is superior to RC when the number of sleep nodes is about 200. Notably, the critical value decreases significantly, which reaches about 300.

Table 32.1 The combination of algorithm in simulation

Algorithms	Sleep stage	Compensation stage
GS-RC	Greedy sleep	Random compensation
RFS-RC	Redundancy first sleep	Random compensation
RFS-DFC	Redundancy first sleep	Data first compensation

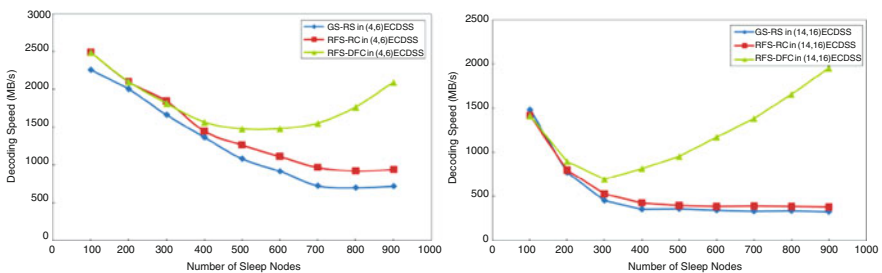


Fig. 32.2 Comparison of decoding rate of (4, 6) and (14, 16) code in GS-RC, RFS-RC, and RFS-DFC algorithms

Therefore, RFS can reduce the computational overhead in all cases. Furthermore, in the case of high code rate and low sleep rate, the improvement of decoding time is not obvious. But in the case of low code rate, DFC is more advantageous and enters the rising area of decoding speed more quickly. In the rising area, with the increasing of sleeping nodes, the computational overhead will decrease gradually, making up for the deficiency of increasing the storage overhead and communication overhead.

Conclusion and Future Work

Based on the coverage-based energy-saving algorithm in replication-based DSS, this chapter deeply studies the performance of using *coverage method* to save energy in ECDSS and proves its feasibility. Then we analyze the defect of classic method and propose an energy-saving algorithm according to the characteristics of erasure code. Experimental results show that the proposed algorithm can effectively reduce the computational overhead of the energy-saving method in ECDSS and improve users' QoS.

However, there are still a few problems which are uncovered or not in-depth study, to be studied in future work. The energy-saving algorithms in this chapter are based on RS or CRS code, ignoring the other non-MDS codes such as LDPC or mixed strategy. Moreover, to save energy and reduce overhead as much as possible for ECDSS, we can consider more performance indexes such as load of different nodes, encoding speed, and fault tolerance and dynamically choose the best data-getting node considering the QoS requirement of users.

Acknowledgement This work is supported by the Fundamental Research Funds for the Central Universities.

References

1. Mingay S. Green IT: the new industry shock wave. Gartner RAS Research Note G 153703. 2007.
2. Brown R, Masanet E, Nordman B. Report to congress on server and data center energy efficiency: Public law 109-431. Lawrence Berkeley National Laboratory. 2008.
3. Colarelli D, Grunwald D. Massive arrays of idle disks for storage archives. In: Proceedings of the 2002 ACM/IEEE conference on supercomputing. Washington, DC: IEEE Computer Society Press; 2002. p. 1–11.
4. Pinheiro E, Bianchini R. Energy conservation techniques for disk array-based servers. In: Proceedings of the 18th annual international conference on supercomputing. New York, NY: ACM; 2004. p. 68–78.
5. Zhu Q, Chen Z, Tan L. Hibernator: helping disk arrays sleep through the winter. In: Proceedings of the 12th ACM symposium on operating systems principles. New York, NY: ACM; 2005. p. 177–90.

6. Pinheiro E, Bianchini R, Dubnicki C. Exploiting redundancy to conserve energy in storage systems. In: Proceedings of the 2006 joint international conference on measurement and modeling of computer systems. New York, NY: ACM; 2006. p. 15–26.
7. Harnik D, Naor D, Segall I. Low power mode in cloud storage systems. In: 2009 I.E. international symposium on parallel and distributed processing. New York, NY: IEEE; 2009. p. 1–8.
8. Kaushik RT, Bhandarkar M. Greenhdfs: towards an energy-conserving, storage-efficient, hybrid hadoop compute cluster. In: Proceedings of the 2010 international conference on power aware computing and systems. Berkeley, CA: USENIX Association; 2010. p. 1–9.
9. Dawson-Haggerty S, Krioukov A, Culler DE. Power optimization-a reality check. Berkeley, CA: Computer Science Division, University of California; 2009.

Chapter 33

LF: A Caching Strategy for Named Data Mobile Ad Hoc Networks

Li Zhang, Jiayan Zhao, and Zhenlian Shi

Abstract Named data networking (NDN) mode has natural advantages in wireless networks but introduces new problems as well. The storage space of nodes in a MANET (mobile ad hoc network) is limited; therefore, the on-path caching strategy of NDN must be modified. A caching strategy, called *less space still faster* (LF), is proposed that chooses nodes to cache data on a packet forwarding path and selects the cached contents based on their popularity. At the same time, the cache distribution of the data and the storage capacity of the nodes are also considered. Simulation results show LF has good performance in terms of response time, network traffic, and cache hit ratio. The design goal of reducing cache redundancy while maintaining a rapid response time is thus realized.

Keywords NDN • MANET • Caching strategy • Popularity

33.1 Introduction and Related Work

The Internet supports communications among processes on different computers, just like communication among different people in different places in the postal delivery system. With increasing numbers of users and applications, the capacity of the Internet is continually being challenged; therefore, researchers are devoting more of their attention to the study of new Internet architectures.

The use of the Internet has changed with the diversity of applications. Currently, the provision of content service is more important than communications. Users only care about the content itself rather than its source or owner. Such applications account for a large proportion of network traffic. Based on the new characteristics of the Internet, researchers have proposed a new Internet architecture called named data networking (NDN) [1]. It is the content name of data, not the IP address of hosts, used by NDN for data inquiry and distribution. In NDN, nodes cache data that

L. Zhang (✉) • J. Zhao • Z. Shi
Beijing University of Technology, 100 Pingleyuan, Chaoyang District,
100124 Beijing, China
e-mail: zl_hlj@126.com

they have forwarded so that later requests can be met using the cached content without having to be routed to the data source.

NDN is more suitable for mobile networks in which users' locations change frequently. When a user moves to another location, the request can be met quickly by surrounding nodes with the content's name [2]. At present, the allocation of IP address to mobile nodes in IP mobile networks is the main challenging confronting mobile applications. The problem has not been sufficiently addressed, although many proposals have been put forward. NDN can avoid this problem because it directly uses content names to forward packets [3] without having to assign an IP address to each node.

The NDN model has its limitations with regard to supporting mobile networks without an infrastructure, such as MANETs (mobile ad hoc networks) [4]. The storage capacity of nodes in a mobile network is limited. It will be difficult to support mobile networks if the cache mechanism of NDN is not changed. Thus, an appropriate caching strategy is needed in named data MANETs (NDMs).

The caching strategy needs to address three main issues: What should be cached? Where should the cache be held? What should be replaced when there is insufficient space? The first two issues are treated in this paper.

Because research on NDN has only recently begun, little has been published on it; however, many research fields have concerns similar to those surrounding NDN, such as content delivery networks (CDNs), and NDN itself is one of the solutions in the field of information-centric networking (ICN) [5, 6]. Some solutions for CDN support caching along the data forwarding path, which is very similar to NDN caching scenarios and could serve as a reference in the study of NDN caching. Therefore, related work will introduce caching research in the fields of CDN, ICN, and NDN.

As for the problem of what should be cached, the popularity of the data is often taken into consideration. The popularity usually is predicted by the count of requests for the data [7–9]. How is that count used? In various ways. For example, WAVE [9] uses the exponential function of the file request count as the number of file subblocks recommended to downstream nodes to cache. The solution results in that data are distributed closer to their source and the redundancy is relatively higher. WAVE counts the number of files but caches the slices of the file, which is not suitable for NDN networks in general. However, using exponential growth to differentiate the cache density of what is popular and what is unpopular is valuable. Li J et al. also use the request count to indicate the data popularity [7]. As for Internet Service Provider (ISP) internal networks, their algorithm requests that each node maintain a tree topology. Each node periodically collects the request count from its subtree. Data with a count less than a threshold are not cached. The algorithm reduces the external traffic by a complex calculation; however, it is only suitable for ISP internal networks, not for NDMs in which the computing ability of nodes is weak and the network topology is irregular and changes quickly. To avoid the one-time use of the caching data, Wang JM et al. cache only the data whose request count exceeds some threshold [8]. They also check the count of the

interfaces from which the requests for the data come. If the interface count exceeds a threshold, the data are cached. Their algorithm is useful and easy to implement.

There are also many different schemes in terms of the choice of nodes to cache data. The basic scheme of NDN is to cache data in nodes along the data forwarding path [1]. The benefit of on-path caching is that it involves the least amount of traffic for caching. The problem is that it occupies too much space, especially in NDMs, where the node space is limited. To reduce the redundant cache in ICN networks, Psaras I et al. have proposed optimizing global caching [10]. The caching decision is based on a probability derived from the sum of the cache space in the data forwarding path and the distance from the node to the user making the request; thus, a greater cache probability is given to nodes closer to the user. The implementation cost of such an algorithm is higher, especially in the wireless network in which nodes move rapidly, so it is not suitable for NDMs.

WAVE [9] also chooses nodes on the data forwarding path to cache data. The caching decision in a node is made by its upstream node based on the number of the requests for the data. It would seem that the data would be distributed in the path. However, in fact, most data are cached around the data source and the nodes closer to the user cache less data. This strategy is more suitable for treelike topology networks in which the edge nodes support fewer terminal users and the intermediate nodes serve more edge nodes. Thus the cache utilization rate can be improved. But for NDMs with irregular topology, it may result in that data are cached closer to the data source and far from the users. A simple strategy has been presented [11] to reduce data redundancy in NDMs. A caching interval field is introduced in the data packet, which is set to an initial value when the data packet is sent out from the node holding the content. The value of the caching interval is reduced by one when the data packet is forwarded by a node. When the caching interval is reduced to zero, the content is cached and the interval is set to the initial value again. The strategy is easy and low cost.

To make the NDN model better support MANETs, a caching strategy called *less space still faster* (LF) has been designed in this paper. In LF, the caching decision falls under the comprehensive consideration of the content distribution in the network and the node's storage capability. LF can ensure that the content is as close as possible to the requesting nodes so as to accelerate the response speed and reduce network traffic; at the same time, the space of mobile nodes is taken into account and the content redundancy in the network can also be reduced.

33.2 LF Caching Strategy

LF involves maintaining a faster response speed with less space. In LF, not all nodes along the data forwarding path cache data. Caching decisions are made by the forwarding nodes based on their situations. The situations include four factors: the distance from the forwarding node to the requesting node, the available space of the forwarding node, whether the data can be requested again, and whether the data

have been cached by the nodes near the forwarding node. The main idea is that the data should be cached in the forwarding node if the forwarding node is far from the requesting node and the data are popular given sufficient space in the forwarding node and that no other nodes nearby are caching the data.

33.2.1 *Factors of LF*

33.2.1.1 Available Space

The available storage space should be considered when a caching decision is made because the forwarding nodes in NDMs are mobile devices which have limited space. The data can be cached only when the space needed for caching is less than a proportion of the available space so as not to affect the applications in the mobile devices.

33.2.1.2 Distance from Forwarding Node to Requesting Node

The distance from a forwarding node to the requesting node is expressed by the hop count of the Interest packet (the request packet is called an *interest packet* in the NDN model). The hop counts the number of nodes that the request packet has passed by.

In NDN, an interest packet is sent to neighbors by the requesting node, and then the receiving node seeks its cache store, a PIT table, and a routing table sequentially. If the requested data are found in the cache, a data packet is sent to the requesting node; otherwise, the receiving node seeks the requested name in the PIT table to see whether it has dealt with other interest packets requesting the same data. If the name is found in the PIT table, then the interface that the interest packet comes from is added to the PIT table in order to forward the response data packet later. A failure of the first two searches indicates that the interest packet for the data is never processed. The interest packet will be forwarded out based on the search result of the routing table, and then a new entry is added to the PIT table.

To obtain the distance from the forwarding node to the requesting node, a hop field is added to the interest packet. The value of the hop field is increased by one each time the packet is forwarded. The hop value is recorded with other information of the interest packet in the PIT table. That is, a hop item, denoted by h , is added to each entry of the PIT table. For the name already in the PIT table, the value of h is changed to the maximum of the original value in the PIT table and that of the new packet (i.e., the number of hops h in the PIT table is used to record the greatest value of the distances from all the requesting nodes to the receiving node). If there is no entry for the requested name in the PIT table, a new entry is created and the value of h is set to the value of the hop field in the packet.

When a node receives a response data packet, the PIT table is searched to obtain the forwarding interface, and the hop count h is checked. If the hop count is greater, meaning the requesting node is far from the node, then the data should be cached to reduce the response time and the network traffic.

33.2.1.3 Whether Data Can Be Requested Again

This refers to the data popularity mentioned in many papers. The request frequency in a certain time period is considered the popularity value for a name that is recorded by every node. The value is the count of the interest packets received by a node in a certain period time, denoted by p , which increases by one at each interest packet for the data received. The popularity value has an expiration date. Expired records are deleted. The main idea is that the data should be cached if they are believed to be popular; otherwise, they are not worth caching.

33.2.1.4 Whether Data Have Been Cached by Nearby Nodes

To reduce the redundancy of data cached, data are not cached if they have already been cached by a nearby node (the last hop in the forwarding path). In order to indicate whether the data were cached by the last hop node, a caching field is added to the data packet. The value has three possibilities: 0, 1, and 2. How to set it is explained in the later section.

33.2.2 Caching Value Computation

To consider the four factors mentioned earlier comprehensively, the following formula is given to compute the caching value, which indicates whether data should be cached. For a data packet i , the data are not cached when the available storage space m of the node is less than some threshold M and are only forwarded. Otherwise, a caching value V_i is computed using the following formula. Data with V_i greater than some threshold V can be cached:

$$V_i = \gamma(\alpha h + \beta B^p). \quad (33.1)$$

In the formula, h is the hop count of the interest packet for the data and obtained from the PIT table, α is its weight coefficient, p is the popularity, β is its weight coefficient, B is the base (2 is used) argument of the popularity, p is obtained by searching the popular table, γ indicates whether the data were cached by the last hop; its value is obtained from the caching field of the data packet.

The value of the caching field is based on the following rules.

1. The caching field is set to 0 if the data are cached because the caching value computed is more than the threshold V . It results in V_i to be 0 when the caching value is computed by the next hop node; therefore, the data are not cached in the next hop regardless of the popularity and distance. The reason is that the data were cached by a nearby node.
2. The caching field is set to 1 if the data are not cached because they were cached by the last hop node. That is, the γ value does not affect the calculation of the caching value of the next hop node.
3. The caching field is set to 2 if the data are not cached because the available storage space is insufficient. This means that the γ value helps increase the caching value in the next hop node. The reason for this is that the data are not cached because of space limitations but should be cached based on distance and popularity. Therefore, it is hoped that the data will be cached by the next hop node.

As the hop and popularity form the two main parts in the value formula, their factors are both set to 1 in consideration of their effect. Thus, the threshold of V_i is set to 2. That is, only data with a caching value greater than 2 can be cached.

Two weight coefficients are discussed in what follows.

1. Weight coefficient α of the hop: we believe that data should be cached by a node if the distance from the data's source to the node exceeds the radius of the network. Suppose the longest edge of the network is n , then the threshold H of the hop should be $n/2$. Thus, we have $\alpha \times n/2 = 1$; therefore, the weight coefficient α of the hop is set to $2/n$. For example, α is 0.25 in an 8×8 topology network.
2. Weight coefficient β of popularity: we believe that data are popular and should be cached if 10 % of the nodes in the network have requested them. Suppose the number of nodes in a network is N , the basic threshold P of the popularity is set to $B^{N/10}$; then $\beta \times P = 1$. Thus, the weight coefficient of the popularity $\beta = \frac{1}{P} = \frac{1}{B^{N/10}}$. For example, in the 8×8 topology, $\beta = \frac{1}{2^{64/10}} = \frac{1}{2^6}$. Taking $N/10$ as the dividing line can minimize the cache number as well as reduce the redundant data considering the relationship between the number of nodes and requests.

In summary, in LF, the action of a node after receiving an interest packet or a data packet is shown in Fig. 33.1.

33.3 Simulation and Evaluation

To evaluate the effect of the LF strategy, a simulation is conducted under ndnSIM [12], which is an extension module of NS-3 with the NDN communication model implemented.

The simulation is done on an Ubuntu-10.04.4 system with libboost version 1.48. There are 64 nodes in the MANET, and the communication distance is 250 m. The simulation lasts 100 s. The simulation environmental parameters are shown in Table 33.1 in detail.

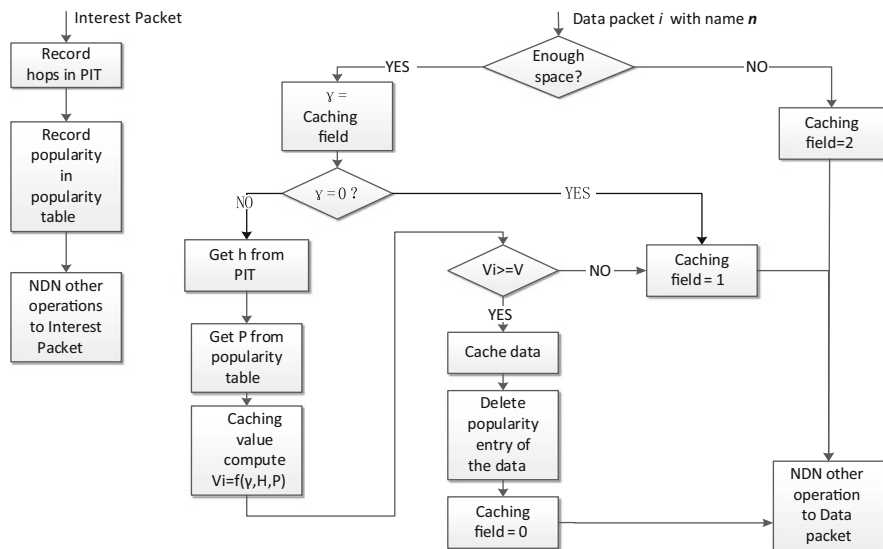


Fig. 33.1 Flow chart of LF strategy

Table 33.1 Simulation environmental parameters

Parameter	Value
Total number of nodes	64
Area size	1,000 × 1,000 m
Data stream type	CBR
Communication distance	250 m
Packet size	512 bytes
Mobility model	Random waypoint
Maximum rate of node movement	30 m/s
Maximum residence time	8 s
MAC type	Ad hocWifiMac
Simulation time	100 s

Sixty-four nodes are randomly distributed in a 1,000 × 1,000 m area. A continuous bit rate (CBR) data stream is chosen as the data source. The node movement model is a random waypoint model. The nodes are stationary initially and move to another position randomly at a speed of 0–30 m/s. The nodes move to the next random position after pausing for some time when they reach a new position. The resident time in a position affects the speed of a node.

A provider–consumer model in ndnSIM is used. A service provider is selected randomly, and the 63 nodes that are left are consumers sending requests. The interest packets arrival process is modeled as Poisson [13]. The average interest packet rate is 20/s. The requested content is under zipf distribution. The CS cache replacement strategy is least recently used (LRU).

The strategy is evaluated in four aspects: response time, network traffic, load of caching node, and cache hit ratio. The on-path caching strategy of NDN [1] and the interval caching strategy [11] are compared.

33.3.1 Response Time

The response time is defined as the period from when an interest packet is sent to when the data packet is received. It is used to evaluate the reduction in response time resulting from the use of caching. The simulation results are shown in Fig. 33.2. The cache used in the on-path strategy has the most extensive coverage, so the average response time of on-path is the lowest of the three strategies. What's more, the delays at the beginning of the three strategies are all higher, but the advantage of the on-path strategy is also outstanding. The response times of both the interval strategy and the LF strategy are long, but the LF strategy is clearly better than the interval strategy. The response times of both the interval strategy and the LF strategy are long, but the LF strategy is clearly better than the interval strategy. The average response time of the interval strategy is longer than that of LF in the middle and late periods. Figure 33.3 shows a comparison of the overall response time of the three caching strategies. It can be seen that the response time of the on-path strategy is the lowest, LF is second, and the interval strategy has the highest response time.

33.3.2 Network Traffic

The sum of the number of interest and data packets is checked to evaluate the network load of the three strategies. Simulation results are shown in Fig. 33.4. It can be seen in Fig. 33.4 that the traffic of the on-path strategy is the lowest, and that of the interval strategy is the highest. LF is in the middle and closer to the on-path strategy because the most caches are used in the on-path strategy that can shorten

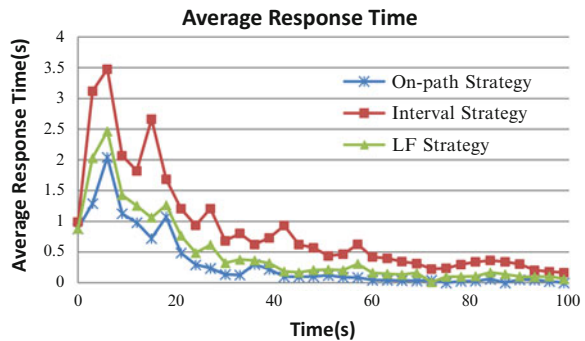


Fig. 33.2 Average response time

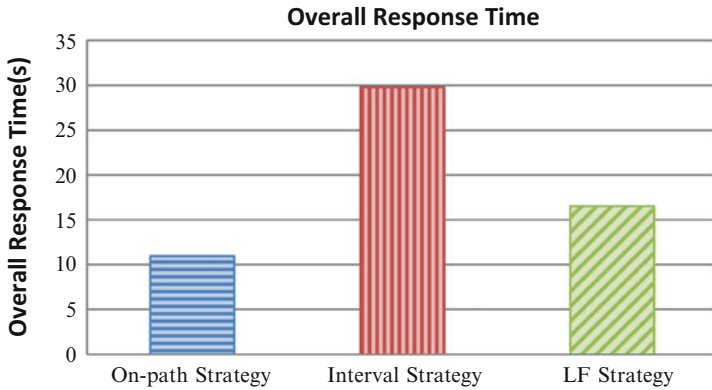


Fig. 33.3 Overall response time

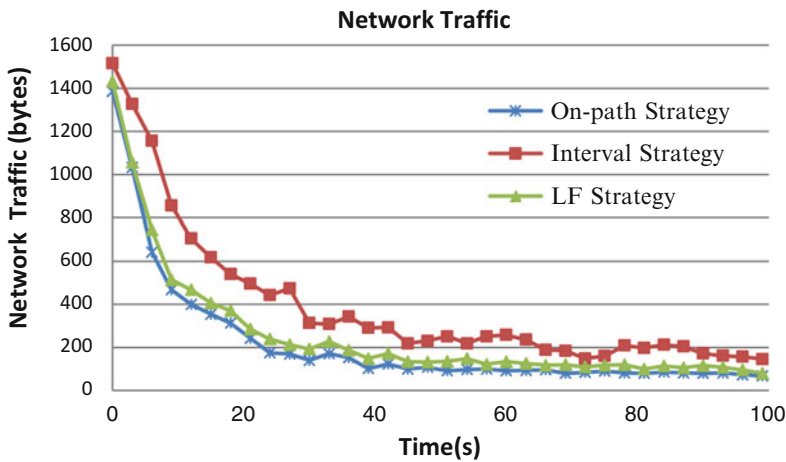


Fig. 33.4 Network traffic

the length of the forwarding path and reduce network traffic. As a result, the traffic of the on-path strategy is the lowest. The caches used by the other two strategies are all less than that of the on-path strategy; however, the interval strategy does not consider the characteristics of the data, whereas the LF strategy considers both the data popularity and the caching situations of the neighbors, and so the traffic of the LF strategy is less than that of the interval strategy. Figure 33.5 shows a comparison of the overall traffic with the three caching strategies.

33.3.3 Load of Caching Nodes

The load of the caching nodes is represented by the amount of cached data. It is used to evaluate the overhead of the three caching strategies. The amounts of cached data

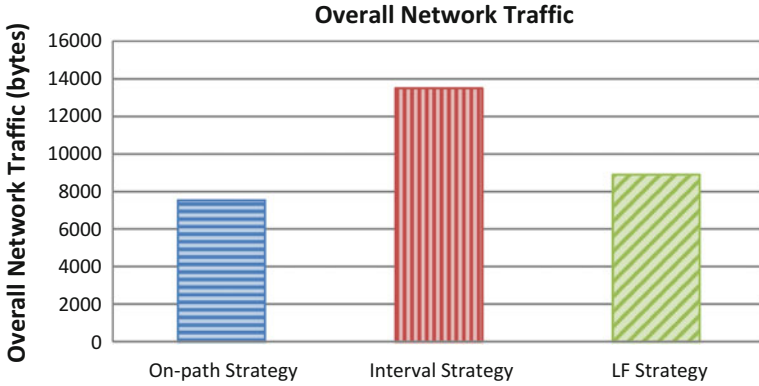


Fig. 33.5 Overall network traffic

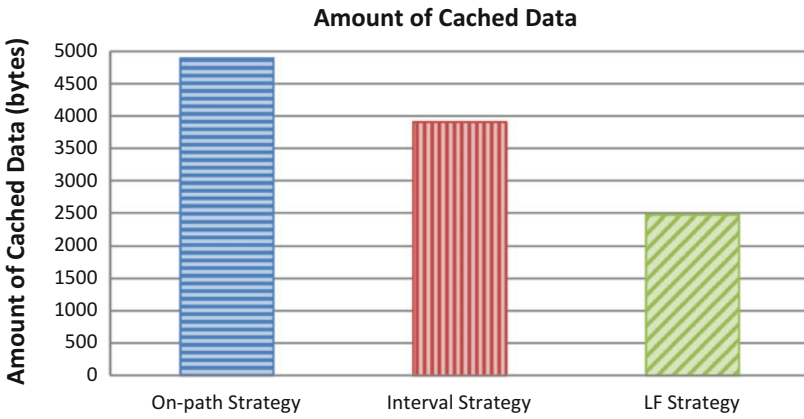


Fig. 33.6 Amount of cached data

are shown in Fig. 33.6. The result shows that the cache used by the on-path strategy is the largest and the overhead is the highest. The interval strategy is in the middle, and the overhead of the LF strategy is the lowest. The storage used by the LF strategy is the lowest and is half that of the on-path strategy.

33.3.4 Cache Hit Ratio

The cache hit ratio is the ratio of the number of requested data found in the cache to the number of total requests. It is used to evaluate the cache efficiency of the three strategies. The cache hit ratio is shown in Fig. 33.7. The hit ratio of the on-path

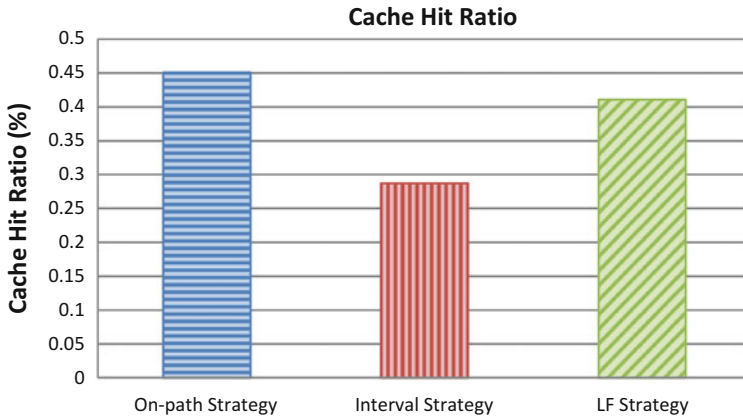


Fig. 33.7 Cache hit ratio

strategy is 0.44, and its cached content is the most effective. The cache hit ratio of the interval strategy is 0.28, which is the lowest of the three strategies. The cache hit ratio of the LF strategy is in the middle and is closer to 0.4, which achieves our design goal.

From the simulation results, it can be concluded that LF strategy can reduce the load of the caching node while maintaining the efficiency of the cache.

Conclusion

To reduce overhead and improve caching efficiency, a caching strategy called LF was designed for NDMs. The caching situation of a node's neighbors and the popularity of the data affect the caching decision in a node in LF. The cache storage capacity of a node was also introduced. Simulation results show that the LF strategy can reduce caching overhead and has good performance in terms of the response time, network traffic, and cache hit ratio.

Acknowledgments This paper is supported by the National Natural Science Foundation of China (61309030) and also supported by project 067100300.

References

1. The NDN Project Team. Named data networking (NDN) project. In PARC Technical report NDN-0001; 2010.
2. Etefia B, Zhang L. Named data networking for military communication systems. In: 2012 I.E. Aerospace Conference; IEEE, Piscataway, N.J. USA; 2012. p. 1–7.
3. Meisel M, Pappas V, Zhang L. Ad hoc networking via named data. In: Proceedings of the Fifth ACM International Workshop on Mobility in the Evolving Internet Architecture; ACM, [MobiArch 10](#); New York, NY, USA; 2010. p. 3–8.

4. Yousefi S, Mousavi MS, Fathy M. Vehicular ad hoc networks (VANETs): challenges and perspectives. In: Proceedings of the International Conference on ITS Telecommunications (ITST); IEEE; Piscataway, N.J. USA; 2006. p. 761–66.
5. Jacobson V, Smetters D, Thornton J, Plass M, Briggs N, Braynard R. Networking named content. In: 5th ACM International Conference on Emerging Networking Experiments and Technologies (CoNEXT 2009); ACM; New York, NY, USA; 2009. p. 1–12.
6. Xylomenos G, Ververidis C, Siris V, Fotiou N, Tsilopoulos C, Vasilakos X, Katsaros K, Polyzos G. A survey of information-centric networking research. *Communications Surveys & Tutorials*, IEEE; Piscataway, N.J. USA; 2014. 16:1024–49.
7. Li J, Wu H, Liu B, Lu JY, Wang Y, Wang X, Zhang YY, Dong LJ. Popularity-driven coordinated caching in named data networking. In: Proceedings of the Eighth ACM/IEEE Symposium on Architectures for Networking and Communications Systems, ANCS'12; ACM; New York, NY, USA; 2012. p. 15–26.
8. Wang JM, Bensaou B. Progressive caching in CCN. In: Proceedings of the Global Communications Conference (GLOBECOM), 2012; IEEE; Piscataway, N.J. USA; 2012. p. 2727–32.
9. Cho K, Lee M, Park K, et al. WAVE: popularity-based and collaborative in-network caching for content-oriented networks. In: 2012 I.E. Conference on Computer Communications Workshops (INFOCOM WKSHPS); IEEE; Piscataway, N.J. USA; 2012. p. 316–21.
10. Psaras I, Chai WK, Pavlou G. Probabilistic in-network caching for information-centric networks. In: Proceedings of the Second Edition of the ICN Workshop on Information-Centric Networking: ICN'12; ACM; New York, NY, USA; 2012. p. 55–60.
11. Zeng YG, Hong XY. A caching strategy in mobile ad hoc named data network. In: 2011 6th International ICST Conference on Communications and Networking in China (CHINACOM); IEEE; Piscataway, N.J. USA; 2011. p. 805–9.
12. Afanasyev A, Moiseenko L, Zhang LX. ndnSIM: NDN simulator for NS-3, Technical Report NDN-0005, 2012. <http://named-data.net/techreports.html>.
13. Chlebus E, Brazier J. Nonstationary poisson modeling of web browsing session arrivals. *Inf Proc Lett.* 2007;102(5):187–90.

Chapter 34

Topological Characteristics of Class Collaborations

Dong Yan and Keyong Wang

Abstract Based on source code reuse, class collaboration diagrams are widely used to glean insight into the interactive relationships among modules in a software system. The relationships seem complex and dazzling but behave in accordance with some potential connectivity laws. Many studies have shown that the evolution theory of complex networks can be a useful approach to the topology analysis of class collaborations. This chapter chooses the prevalent Java Development Kits to study the topological structure, small-world features, and connectivity of actual Java class collaboration networks. The empirical analysis discovers the small-world features of the class collaboration relationships. But the connectivity shows a great distinction between the active behavior and the passive behavior among those relationships, that is, the behavior to import Java classes approximately follows a decaying exponential distribution, while the behavior that Java classes are imported by others obeys a decaying power-law distribution.

Keywords Software topology • Small world • Scale free • Matthew effect

34.1 Introduction

Software architecture is an important field within software engineering aiming at describing both the structure and the behavior of software systems at a high level of abstraction [1]. Network analysis plays an important role in acquiring better comprehension of software systems. Watts and Strogatz firstly found that the connection topology of many real-world networks is neither completely regular nor completely random and then proposed the small-world model in 1998 [2]. Inspired by this discovery, Barabási and Albert studied the dynamic World Wide Web (WWW) based on network analysis and statistics and proposed the famous scale-free model based on preferential mechanism [3]. Subsequently, many information systems are investigated to be scale free [4].

D. Yan • K. Wang (✉)
College of Mechanical Engineering, Shanghai University of Engineering Science,
201620 Shanghai, China
e-mail: [yd_email@aliyun.com](mailto:yid_email@aliyun.com)

In 2003, Myers studied the collaboration networks associated with six different open-source C/C++ software systems and found that their outgoing degree (out-degree), incoming degree (in-degree), and degree distributions reveal the decaying power-law behavior [5]. Šubelj and Bajec investigated the community structure and scale-free connectivity of undirected Java class dependency networks. However, identified communities do not exactly correspond to software packages [6]. Many different large Java software systems were examined to show the scale-free behavior with small-world characteristics [7–9]. Moreover, there exist some local events, such as addition of edges, removal of edges, and rewiring of edges, in the evolution of Java software systems [10]. Li et al. utilized the log information in binary files for Java class complex networks to visualize the software structures and to diagnose software faults and exceptions [11].

Investigating the topology structure of a software system is helpful to discern global collaboration laws of classes. In this chapter, the classical Java Development Kits (JDK) from JDK 1.1.6 to JDK 1.3.0 are chosen to study the topological characteristics of directed Java class collaborations. In Sect. 34.2, the directed Java class collaboration networks (JCCN) are constructed. In Sect. 34.3, the small-world features of the JCCN are examined. In Sect. 34.4, the scale-free behavior of the JCCN is investigated. In Sect. 34.5, conclusions are provided.

34.2 Topology of Java Software Systems

Java as a full object-oriented (OO) programming language can construct many kinds of web application systems independent of platforms. The “import” statements direct the Java compiler to include all of the public classes (interfaces). The relations among classes include “association,” “generalization,” “realization,” and “dependency,” unanimously disposed of by the way of “import” in a Java system.

Class diagrams of a software system with source codes can be abstracted as a complex network by the import relationships among classes according to Unified Modeling Language (UML). Each class can be abstracted as a node, as well as the import relationships among classes can be abstracted as directed edges, as shown in Fig. 34.1, where the nodes marked in the same color possess the same degree value. The directionality of the network is consistent with that of class diagrams defined according to the UML. If a class i imports another class j , then i holds one outgoing edge, namely, an out-degree $k_{out,i}$, and j gets one incoming edge, namely, an in-degree $k_{in,j}$. The degree k_i of i is the sum of its out-degree and in-degree, i.e., $k_i = k_{out,i} + k_{in,i}$.

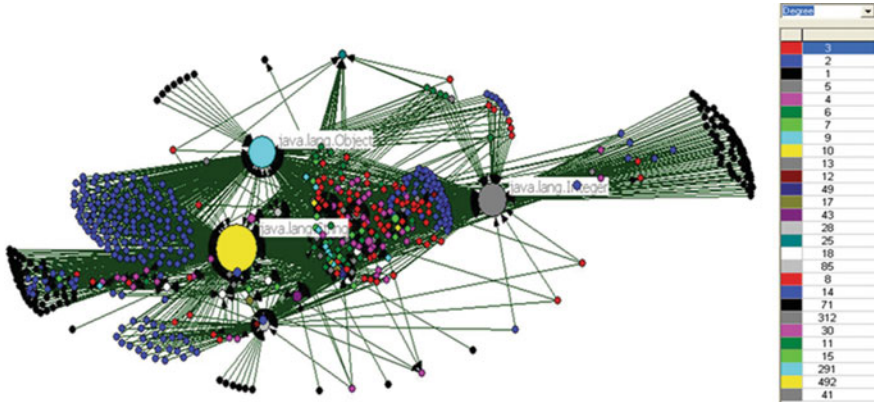


Fig. 34.1 The collaboration network on class diagrams for JDK1.1.6

34.3 Small-World Features

Watts and Strogatz found that many systems can be highly clustered, like regular lattices, yet have small characteristic path lengths, like random graphs. They are called as small-world networks, by analogy with the small-world phenomenon [2]. The small-world features of a system are measured by clustering coefficient and average shortest path length.

In order to investigate the small-world features of Java systems, the clustering coefficients and average shortest path lengths of the JCCN are measured, whereas the directionality of the import relationships among classes is blurred, since the small-world features are typically measured on undirected graphs.

34.3.1 Clustering Coefficients of the JCCN

The clustering coefficient C_i of a Java class i characterizes the import relationships among only its k_i neighbors, defined as the ratio between the actual number and the probably maximal number $k_i(k_i-1)/2$ of pairs of the k_i neighbors, that is,

$$C_i = \frac{E_i}{k_i(k_i - 1)/2} \in [0, 1], \quad (34.1)$$

where E_i is the actual number of edges between the k_i neighbors. If $C_i = 0$, all neighbors of class i do not import each other but hold the import relationships with i , while if $C_i = 1$, they all collaborate with each other to perform the necessary functions.

The clustering coefficient C of a whole network is defined as the average value of clustering coefficients of all nodes, denoted by

Table 34.1 Statistics of clustering coefficients

Ver.	C_{real}	C_{rand}
JDK1.1	0.3	0.008
JDK1.2	0.36	0.007
JDK1.3	0.35	0.006

$$C = N^{-1} \sum_i c_i. \quad (34.2)$$

It implies the global density of triad class collaboration relationships.

Table 34.1 shows the real clustering coefficients C_{real} of the JCCN and the theoretical clustering coefficients C_{rand} of their corresponding random networks with the same numbers of nodes and edges. $C_{\text{rand}} = \langle k \rangle / N$, where $\langle k \rangle$ and N are, respectively, the average degree of an actual network and its scale [12]. Obviously, $C_{\text{real}} \gg C_{\text{rand}}$, so the Java class collaborations exhibit a high clustering, like regular lattices.

34.3.2 Average (Shortest) Path Lengths of the JCCN

Average path length L is defined as the average value of the shortest paths for all possible pairs of nodes in a network, that is,

$$L = \frac{1}{N(N+1)/2} \sum_{i \geq j} d_{ij}, \quad (34.3)$$

where d_{ij} is the shortest path length between a pair of nodes i and j .

The real average path lengths L_{real} of the JCCN are obtained in Table 34.2, where $L_{\text{rand}} = \ln(N)/\ln(\langle k \rangle)$ is the average path length of the corresponding random network with the same numbers of nodes and edges [2, 4]. $L_{\text{real}} \rightarrow L_{\text{rand}}$ means a short average path length for actual Java import relationships, like random graphs. In a class collaboration network, a path length reflects the possible import steps among collaborative classes. The average path length of an information system can evaluate the global efficiency of information transfers. Thus, a short average path length means quick transfers among different classes.

34.3.3 Judgment of Small-World Networks

According to Sects. 34.3.1 and 34.3.2, the JCCN hold a high clustering and a short average path length, so they possess small-world features. When a new Java project is set up, a part of JDK as a black box with necessary fundamental functions should

Table 34.2 Statistics of average path lengths

Ver.	L_{real}	L_{rand}
JDK1.1	4.18	3.98
JDK1.2	3.71	3.05
JDK1.3	3.76	3.1

be packed in the project. The small-world features guarantee high collaborability and quick transfers among classes for programmers and users.

34.4 Connectivity of the JCCN

In a Java class collaboration network, the frequency of a degree is the number of the nodes with the same degree. The probability of the degree is the proportion of its frequency to the number of all nodes. Therefore, the probability distribution of the network can be characterized by probabilities of all degrees.

The degree distribution characterizes the global import tendency in Java systems. In Fig. 34.2, plot (a) shows the out-degree distribution $p(k_{\text{out}})$ on linear-logarithm scales, so $p(k_{\text{out}}) \propto \exp(k_{\text{out}})$. Plots (b) and (c) present the (in-)degree distributions $p(k_{\text{in}})$ and $p(k)$ on log-log scales, so $p(k_{\text{in}}) \propto k_{\text{in}}^{\gamma_{\text{in}}}$ and $p(k) \propto k$. However, all of the actual distribution charts display a fat tail in Fig. 34.2a–c.

In order to eliminate the fat tail and fit data well, one can define the following continuous cumulative degree distribution

$$P_c(k) = \int_k^{+\infty} p(k)dk, \quad (34.4)$$

and then $p(k) \propto k - \gamma$ is written as $P_c(k) \propto k - (\gamma - 1)$. The scaling exponents can be obtained as $\gamma_{\text{in}} \approx 2.25$ and $\gamma \approx 2.43$ by fitting the cumulative distributions in Fig. 34.2e, f.

Both scaling exponents of (in-)degree distributions are larger than 2, and hence, the JCCN possess the scale-free behavior with the Matthew effect. It means the behavior that Java classes are imported by others is dominated by preferential mechanism. Thus, only a minority of classes hold a high reusability, while most others do a low one. In the actual JCCN, only 10 % of classes with maximum in-degrees, respectively, account for about 58 %, 65 %, and 67 % of imported frequencies.

The reusability of source codes reduces redundant program codes, testing, and bug fixing. In addition, efficient class reuse means that many bugs need to be fixed in only one place when problems are discovered. In the light of the above advantages, only a minority of classical and new excellent classes are largely imported, which results in the decaying power-law distributions of in-degrees of the JCCN with the Matthew effect.

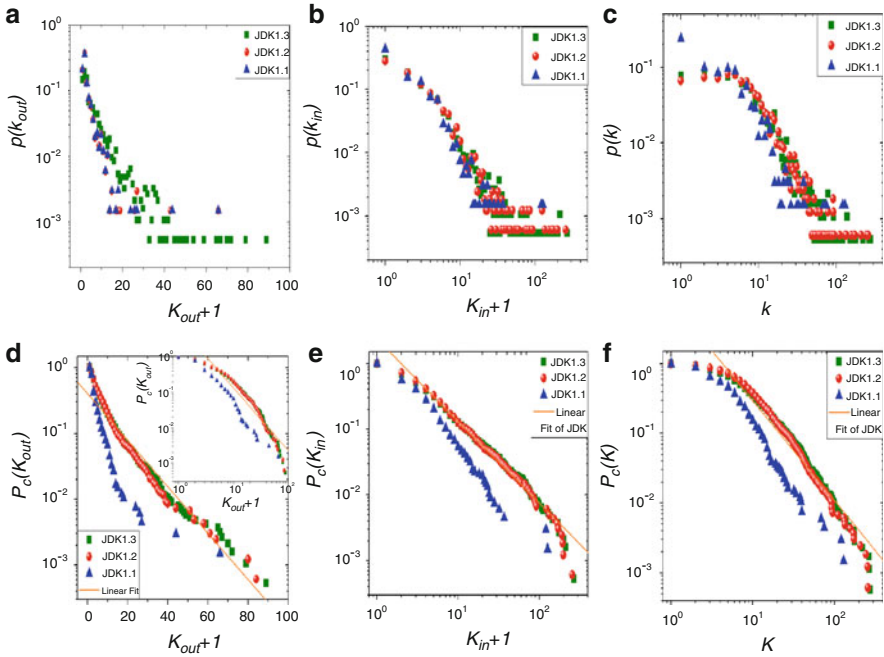


Fig. 34.2 The (out-, in-)degree (cumulative) distributions of actual class collaboration networks

Figure 34.2d shows the approximately exponential relation of k_{out} and $P_c(k_{out})$ on linear-logarithm scales and their far-fetched power-law relation on log-log scales in the right upper corner of this plot. The standard deviation (SD) of the linear fit of the former is less than that of the latter, that is, $0.16095 < 0.24419$. Moreover, the maximal out-degree in plot (d) is less than 100, while the maximal in-degree in plot (e) is close to 400. Thus, $P_c(k_{out}) \propto \exp(k_{out})$. Moura et al. believed that the small-world and scale-free features are generic for large computer programs [12]. Obviously, it is not exactly so.

The decaying exponential out-degree distribution indicates that the behavior to import classes is approximately random. Modular programming is a software design technique that emphasizes separating the functionality of a program into independent, interchangeable modules, such that each contains everything necessary to execute only one aspect of the desired functionality [7]. Conceptually, modules represent a separation of concerns. Thus, properties and behaviors of Java classes as modules are limited in scale and so do their out-degrees in size. It is the reason for the decaying exponential distribution of out-degrees of the JCCN.

Obviously, the JCCN are incomplete scale-free networks. The modularity technique leads the approximately random behavior to import classes, while the reusability one conduces the preferential behavior that a minority of classes are imported largely.

Conclusion

Complex networks present novel perspectives on the study of class collaborations. In this chapter, the JCCN on class diagrams are examined to possess small-world features when their directionality is ignored. Small-world features facilitate better collaborability among classes and higher efficiency of class transfers in software systems. Different from the out-degree distribution of C/C++ class collaborations, that of Java ones approximately follow the decaying exponential distribution. Thus, most classes are prevented from overexpanding in size, as well as the source codes of basic and excellent classes tend to be reused largely. To judge if the architecture of a system is excellent, one aspect is to investigate if its out-degrees obey the decaying exponential distribution due to modularity, while its in-degrees follow the decaying power-law distribution owing to code reuse.

Acknowledgments This work is supported by the National Natural Science Foundation of China (Grant No. 51205220) and the Scientific Research Foundation of Shanghai University of Engineering Science (Grant No. E1-0501-14-0106).

References

1. Shaw M, Garlan D. Software architecture: perspectives on an emerging discipline. Upper Saddle River, NJ: Prentice Hall; 1996. p. 1–9.
2. Watts DJ, Strogatz SH. Collective dynamics of ‘small-world’ networks. *Nature*. 1998;393(4):440–2.
3. Barabási AL, Albert R. Emergence of scaling in random networks. *Science*. 1999;286(15):509–12.
4. Albert R, Barabási AL. Statistical mechanics of complex networks. *Rev Mod Phys*. 2002;74(1):47–97.
5. Myers CR. Software systems as complex networks: structure, function, and evolvability of software collaboration graphs. *Phys Rev E*. 2003;68(4):046116(1–15).
6. Šubelj L, Bajec M. Community structure of complex software systems: analysis and applications. *Phys A Statist Mech Appl*. 2011;390(16):2968–75.
7. Savić M, Lvanoviić M, Radvanović M. Characteristics of class collaboration networks in large java software projects. *Inf Technol Control*. 2011;40(1):48–58.
8. Šubelj L, Bajec M. Software systems through complex networks science: review, analysis and applications. In: *SoftwareMining’12*, Beijing, China. 2012. pp. 9–16.
9. Yan D, Ahmad SZ, Yang D. Matthew effect, ABC analysis and project management of scale-free information systems. *J Syst Softw*. 2013;86(2):247–54.
10. Yan D, Qi G. The scale-free feature and evolving model of large-scale software systems. *Acta Phys Sin*. 2006;55(8):3799–804.
11. Li CF, Liu LZ, Li XY. Software networks of java class and application in fault localization. In: *International conference on intelligent systems design and engineering application*, Sanya, China. 2012. pp. 1117–20.
12. Moura APS, Lai YC, Motter AE. Signatures of small-world and scale-free properties in large computer programs. *Phys Rev E*. 2003;68(1):017102(1–4).

Chapter 35

Cluster Key Scheme Based on Bilinear Pairing for Wireless Sensor Networks

Xiaoming Liu and Qisheng Zhao

Abstract The past security policy about public key management strongly relied on the key matrix which was preset by the base station or generated by the algorithm embedded in the nodes, then to exchange the public key with others to finish the security communications, but a lot of public keys were stored in the nodes, which consumed much energy and might be captured and gained by the attacked nodes. In this chapter, we adopt the bilinear pairing theory to the public key generation and management which does not require the public key in the nodes and applies the node's information to the public keys, which may reduce the cost of managing the public keys and enhances the security of key management; then we propose a cluster key distributed scheme on the basis of clustering by using the bilinear pairing key management in the wireless sensor network and demonstrate its feasibility and security theoretically.

Keywords Security • Key management • Cluster • Authentication • Matrix • Threshold

35.1 Introduction

A wireless sensor network (WSN) consists of spatially distributed autonomous and battery-powered sensors which are facing many security issues, data intrusion and topology destruction via Sinkhole, Sybil, Wormholes, Hello flood intrusion, node capture, etc., which makes it very challenging to provide security in WSNs. Currently, the main idea for resisting intrusion is to establish security routing and key management schemes [1–3].

X. Liu (✉)
Information Center, Huaihai Institute of Technology,
222005 Lianyungang, Jiangsu, China
e-mail: Liuxm029@gmail.com

Q. Zhao
Computer Engineer College, Huaihai Institute of Technology,
222005 Lianyungang, Jiangsu, China

35.2 Related Works

There are two types of key management schemes in terms of wireless sensor network: the distributed architecture and the clustering architecture. In the distributed architecture, there are no fixed fundamental facilities, the energy and power of network nodes are at the same level, and nodes have the ability of sensing, signal process and wireless communication. The nodes communicate with preset keys and establish the security channels. As to the distributed architecture, the nodes are divided into three categories: the base station, the cluster heads and the ordinary nodes. The base station is in charge of distributing and updating keys as distributing centres; the ordinary nodes just have IDs and some corresponding keys and the others belong to the clusters' mission [4]. As mentioned in the past literature, Shamir [5] proposed the concept of identity-based encryption (IBE), which encrypts the message by means of the receiver's identity information as the public key. While compared with the traditional public key management, IBE is not used to manage the certification because it vastly simplifies the security communication operation. Boneh proposed an efficient IBE scheme, which provides complete security under the random oracle model [6, 7]. Another scheme provides complete security under the standard mode [8]; however, the efficiency is very low and the scheme impractical. The first highly efficient security scheme was proposed by Waters [8], which basically needs less modular exponentiation and bilinear pairing computing; but as its main defect, it frequently makes parameters, and it is difficult to implement in the current nodes of wireless sensor networks. Waters also pointed out that it was difficult to determine an efficient identity-based encryption mode of short open parameters under the random oracle model. Zhang proposed to facilitate the secure key establishment between nodes in WSNs by means of an identity-based cryptography technique called pairing [9]. It allows the synchronous execution of multiparty key agreement protocols based on bilinear paring. The number of cluster members will not affect the key agreement and not require interactivity during the key agreement.

35.3 The Clustering Key Scheme

35.3.1 *The Model Architecture*

In the hierarchical wireless sensor network, the distribution is based on clusters. One cluster has a cluster head and multi-cluster members. The cluster head has advanced capability in communication, computing, memory, power, etc. Cluster members are just ordinary nodes, which are only allowed to communicate with the cluster head or between one another to decrease the energy consumption. The network architecture model and the algorithm are shown as below (Fig. 35.1):

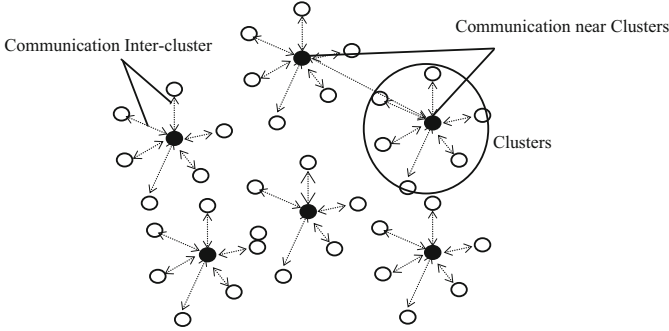


Fig. 35.1 Clustering key model architecture

35.3.2 The Cluster Security Scheme

This scheme includes one private key generator PKG. There are three phrases: the system establishment, the private key generation and the key negotiation.

Assume that l is the safety parameter, G and G_r are cyclical groups of prime number q and $\hat{e}: G \times G \rightarrow G_r$ are bilinear pairings. G^* is the non-identity element in G . Supposing the identity (public key) in the dept $L (G^*)^L (G^*)^L$ constitute the vector quantity, the element of $k + 1$ is the identity of k , $H: \{0, 1\}^* \rightarrow G^*$.

For setup (l), select one random generating element $P \in G$. Every cluster chooses its own key $s_i \in Z_q (i = 1, 2, \dots, L)$, computes the public key $P_{pubi} = s_i P$, according impact factor of the cluster head “weight” confirm the every cluster’s primary key s_i , and then the primary key and public parameters are masterkey = (s_1, s_2, \dots, s_L) , params = $(q, G, G_r, P, \hat{e}, H, s_1 P, s_2 P, \dots, s_L P)$.

The private key generation: if the identity vector quality is $(ID_{0u}^0, ID_{uv}^1, \dots, ID_{ij}^k)$, PKG computes $P_{ij}^k = H(ID_{ij}^k)$ and $d_{ij}^k = s_{k+1} P_{ij}^k (k = 0, 1, \dots, L - 1)$ then transmits in a secret channel to the user U_{ij}^k . As a matter of fact, given the identity vector quality of user U_{ij}^k , the cluster head U_{ki}^{k-1} could calculate its private key by its own private key. The identity vector quality of user U_{ij}^k is $(ID_{0u}^0, ID_{uv}^1, \dots, ID_{ki}^{k-1})$; the private key is $s_{xi}^{k-1} = (s_1 P_{0u}^0, s_2 P_{uv}^1, \dots, s_k P_{xi}^{k-1}, s_{k+1}, s_{k+2}, \dots, s_{L-1})$. The cluster head U_{xi}^{k-1} calculates $P_{ij}^k = H(ID_{ij}^k)$ and $d_{ij}^k = s_{k+1} P_{ij}^k$ then sends $s_{xi}^{k-1} = (s_1 P_{0u}^0, s_2 P_{uv}^1, \dots, s_k P_{xi}^{k-1}, s_{k+1}, s_{k+2}, \dots, s_{L-1})$ to U_{ij}^k in security.

1. Negotiation Communication Between Any Cluster Members

Assume that different user U_{ij}^k needs to establish the sharing partial security key, the identity vector quality of U_{ij}^k is $(ID_{0u}^0, ID_{uv}^1, \dots, ID_{ij}^k)$, and that of U_{pq}^t is $(ID_{0v}^0, ID_{uv}^1, \dots, ID_{pq}^t)$. U_{ij}^k is from $P_{pq}^y = H(ID_{pq}^y) (y = 0, 1, \dots, t)$ and U_{pq}^t is from $P_{pq}^x = H(ID_{ij}^x) (x = 0, 1, \dots, k)$. Respectively compute U_{ij}^k and U_{pq}^t , then get the same sharing keys and the validity could be tested and verified.

$$sk_{kt} = \hat{e}(s_1 P_{0v}^0, P_{0v}^0) \hat{e}(s_2 P_{uv}^1, P_{uv}^1) \dots \hat{e}(s_{t+1} P_{ij}^t, P_{pq}^t) \cdot \hat{e}(s_{t+2} P_{ij}^{t+1}, P_{pq}^t) \hat{e}(s_{t+3} P_{ij}^{t+2}, P_{pq}^t) \dots \hat{e}(s_1 P_{k+1}^k, P_{pq}^t) \quad (35.1)$$

$$sk_{tk} = \hat{e}(P_{0v}^0, s_1 P_{0v}^0) \hat{e}(P_{uv}^1, s_2 P_{uv}^1) \dots \hat{e}(P_{pq}^t, s_{t+1} P_{ij}^t) \cdot \hat{e}(P_{pq}^{t+1}, s_{t+2} P_{ij}^t)^{s_{t+2}} \dots \hat{e}(P_{ij}^k, P_{pq}^t)^{s_{k+1}} \quad (35.2)$$

2. Negotiation Communication Between Inner Clusters

Randomly U_{ij}^k select $\eta_j \in Z_q^*$ ($j = 1, 2, \dots, m$), m is the number of cluster member, and it calculates $r_j = \eta_j P_{ij}^k$. Compute $z_{kj} = s_{k+1} P_{ij}^k \cdot \eta_j$ and broadcast (η_j, z_{kj}) . When receiving the (η_j, z_{kj}) , every member U_{xi}^k of cluster would verify

$$\left(\prod_{j=1, j \neq x}^m \hat{e}(z_{kj}, P) = \prod_{j=1, j \neq x}^m \hat{e}(\tau_j \partial, s_{k+1} P) = \hat{e}\left(\sum_{j=1, j \neq x}^m r_j, s_{k+1} P\right), z_{kj} \right).$$

3. Node Joining and Leaving

One new node of U_{in}^k joins the network. Firstly, send the message ID_{in}^k Join to the cluster head U_{xi}^{k-1} , and then the cluster head U_{xi}^{k-1} broadcasts $AccID_{xi}^k$ Join to the member. Randomly select $\eta_n \in Z_q^*$, and then compute $r_n = \eta_n P_{in}^k$ and $z_{kn} = s_{k+1} P_m^k \cdot \eta_n$. Broadcast (r_n, z_{kn}) and then the cluster and other nodes can verify the validity. If the node is inside the cluster, then network topology does not change; so the cluster computes the sharing keys again. If the node is a cluster member, the cluster topology will change, so the cluster members have to look for a new cluster head, join it and then start to compute the sharing keys of the joining nodes.

35.4 Security Analysis

No matter how many cluster member nodes and clusters are controlled, as long as the attacker does not fully control the nodes and cluster heads, we think this scheme is safe.

Theorem 1 G and G_r are both groups of two orders for prime number q . $\hat{e} : G \times G \rightarrow G_r$ are satisfied with Decisional Bilinear Diffie-Hellman (DBDH). Hash function H is the predicted oracle of this scheme, and this scheme can resist a full controlling attack and sequent attack.

Proof Construct an algorithm B, which has the advantage that it is not ignorant of the probability to resolve DBDH problem. In the cluster key shared negotiation cases, that can break the scheme.

Given $\langle q, \alpha, G, G_r, \hat{e}, P, aP, bP, cP, D, R \rangle$, \hat{e} is the bilinear pairing $\hat{e} : G \times G \rightarrow G_r$, $D = \hat{e}(P, P)^{abc}$, $R = \hat{e}(P, P)^t$. The mission of B is to choose which belongs to the DBDH from $D = \hat{e}(P, P)^{abc}$ and $R = \hat{e}(P, P)^t$.

Simulate the algorithm setup: B chooses the safe public parameters, like the random oracle, function H and the number threshold of the root node; B selects L random number $s_1, s_2, \dots, s_l \in Z_q^*$ and calculates the public key $P_{pubi} = s_i P (i = 1, 2, \dots, L)$; B sends the system parameters $(q, k, G, G_r, P, \hat{e}, H, s_1 P, s_2 P, \dots, s_L P)$ to the attacker A.

$H(\text{ID}_{ij}^k)$ query: If ID_{ij}^k is in the list H^{list} , then B calculates the $H(\text{ID}_{ij}^k) = h_{ij}^k$, randomly selects $\eta_j \in Z_1^*$ and then calculates $r_j = \eta_j P_{ij}^k$, $z_{kj} = s_{k+1} P_{ij}^k \cdot \eta_j$. It gives the $(\text{ID}_{ij}^k, h_{ij}^k, z_{kj}, r_j)$ back to A. If ID_{ij}^k is the neighbour of the cluster, then B stores (ID_{ij}^k, aP) , assigns $H(\text{ID}_{ij}^k) = aP$ and $P_{pubi} = s_{k+1} P = cP$, takes $\eta_j = b$ and $z_{kj} = abcP$ and then returns $(\text{ID}_{ij}^k, aP, abcP, cP)$.

For others, B randomly selects $l_j \in Z_q^*$ and calculates $H(\text{ID}_{ij}^k) = h_{ij}^k = l_j P$. Then B inserts $\hat{e}(z_{k1}, P) \hat{e}(z_{k2}, P) \dots \hat{e}(z_{kj}, P) (H(\text{ID}_{ij}^k), h_{ij}^k)$ into the link list of H^{list} and returns $H(\text{ID}_{ij}^k) = h_{ij}^k$.

Compromise (j) query: Assume j is one of the clusters, and then B terminates or B will return all the security values. Assume the target nodes are cluster heads, and the nodes' identification is $(\text{ID}_{0u}^0, \dots, \text{ID}_{ij}^k)$. B selects random bit $b \in \{0, 1\}$ and executes the following steps:

Query $H(\text{ID}_{ij}^k) = P_{ij}^k, z_{kj}, r_j$:

If $b = 1$, then B calculates

$$\alpha = \hat{e}(z_{k1}, P) \hat{e}(z_{k2}, P) \dots \hat{e}(z_{k(j-1)}, P) \cdot D \cdot \hat{e}(z_{k(j+1)}, P) + \dots + \hat{e}(z_{km}, P).$$

Else B calculates

$$\alpha = \hat{e}(z_{k1}, P) \hat{e}(z_{k2}, P) \dots \hat{e}(z_{k(j-1)}, P) \cdot \hat{e}(z_{k(j+1)}, P) + \dots + \hat{e}(z_{km}, P).$$

Then B gives α to attacker A.

After A finishes querying, it gets the candidate b' . If the output of B is the same as b' , then the question of DBDH is resolved. If the output bit of A is correct, B can give the right guesses for the DBDH issues, so we think this scheme is safe.

Conclusion

This chapter adopts bilinear pairing theory to the sense nodes key generation and management. It uses the node's information as public keys, which may reduce the cost of managing the public keys. In the clustering of wireless sensor networks, we propose the key management scheme based on the bilinear pairing and describe the algorithm in detail; then the chapter theoretically demonstrates the feasibility and security of this approach. In addition to the key distributed efficiency and the energy cost analysis, we still have to make simulation with the clustering key algorithm applied to practical situations so as to verify its efficiency, feasibility and security.

Acknowledgements This research was supported by No. 61103017 China National Foundations, No. CG1215 Lianyungang Science and Technology Project and No. SH1212 Lianyungang Social Development Project.

References

1. Akyildiz IF, Su W, et al. Wireless sensor networks: a survey. *Comput Netw.* 2002;38(4):393–433.
2. Pamo B, Perrig A, Gligor V. Distributed detection of node replication attacks in sensor networks. In: *Proceedings of the IEEE symposium on security and privacy*, vol. 8. IEEE Computer Society; 2005. pp. 49–63.
3. Perrig A, Szewczyk R, et al. SPINS: security protocols for sensor networks. *Wirel Netw.* 2002;8(5):521–34.
4. Chan H, Perrig A, Song D. Key distribution techniques for sensor networks. *Wirel Netw.* 2004;6(2):277–303.
5. Shamir A. Identity-based cryptosystems and signature schemes. In: *Proceedings of the CRYPTO 84 on Advances in Cryptology*; Springer, New York; 1985. p. 47–53.
6. Boneh D, Franklin M. Identity-based encryption from the weil pairing. *SIAM J Comput.* 2003;32(3):586–615.
7. Liu DG, Ning P. Multi-level μ TESLA: a broadcast authentication system for distributed sensor networks. *ACM(TECS)*. 2004;3(4):800–36.
8. Sahai A, Waters B. Fuzzy identity-based encryption. In: *Advances in Cryptology-EUROCRYPT of Lecture Notes in Computer Science*, vol. 3494; Springer, Berlin; 2005. p. 457–73.
9. Zhang F, Safavi Naini R, Susilo W. An efficient signature scheme from bilinear pairings and its applications. In: *Practice and Theory in Public Key Cryptography-PKC, LNCS*, vol. 2947; 2004. p. 277–90.

Chapter 36

The LDP Protocol Formal Description and Verification Based on CPN Model

Rengaowa Sa, Baolier Xilin, Yulan Zhao, and Neimule Menke

Abstract In order to verify the correctness of the label distribution protocol LDP, a function verification model has been constructed for the protocol-integrated analysis in the aspects of safety property, liveness property, and function analysis based on the Colored Petri Nets (CPN). By this integrated analysis method using CPN, it has been confirmed that the protocol can adapt to changes in the network layer routing information and distribute labels effectively. Also, this CPN-based modeling and simulation method, which integrates the protocol property verification and function analysis, contributes a significant methodology to improve the function of a network protocol.

Keywords LDP protocol • Formal description • Colored petri nets • Bounded model checking

36.1 Introduction

MPLS (Multiprotocol Label Switching) is a new technology that uses labels to guide high speed, efficient transfer of data in the new generation IP backbone network. In the MPLS domain, the routers are the label switching routers (LSR), while the routers at the MPLS domain edges are the boundary label switching routers (LER). At the edge of MPLS network domain, the data flows entering the MPLS network will be divided into different forwarding equivalent classes (FEC), and corresponding labels will be requested for these forwarding equivalent classes.

R. Sa (✉)

Computer and Information Engineering College, Inner Mongolia Normal University, 010010 Hohhot, China
e-mail: ciecsrgw@163.com

B. Xilin

Inner Mongolia people's Broadcasting Station, 010010 Hohhot, China

Y. Zhao

College of Computer Science, Inner Mongolia University, 010010 Hohhot, China

N. Menke

Ordos College, Inner Mongolia University, 017000 Ordos, China

© Springer International Publishing Switzerland 2015

W.E. Wong (ed.), *Proceedings of the 4th International Conference on Computer Engineering and Networks*, Lecture Notes in Electrical Engineering 355,
DOI 10.1007/978-3-319-11104-9_36

305

The corresponding relationship between the label and the FEC will be noticed to neighboring routers and maintained by the LDP protocol. The LDP protocol defines a set of procedures to construct the label-switched paths (LSP) which consist of FEC, entering label, outgoing label, and so on.

Relevant research work has been done in the LDP protocol conformance testing based on E-LOTOS [1]. Protocol conformance test is used to verify the consistency of protocol implementation and protocol standards. However, the protocol verification is used to verify the logical correctness of protocol standards which tries to find potential errors or modify performance of the protocol itself, an essential link to guarantee the quality of protocol development. As for the verification of the LDP protocol, no one has done more research except I, having simulated and analyzed the LDP protocol based on its CPN model and then obtained the protocol analysis report in my master degree's thesis at Inner Mongolia University.

Moreover, in this chapter, a model of the LDP protocol for function verification and property analysis has been constructed using CPN Tools. And then through integrated using of CPN occurrence graphs, flow analysis of tokens by simulation tools, description method of protocol properties by the system assertion language ASK-CTL, the label distribution protocol LDP is automatically simulated and verified. Finally, the process to detect and verify protocols is summarized in CPN Tools 2.2.0 environment.

36.2 The Formal Description and Modeling of LDP Protocol

36.2.1 Modeling Constraints

Bounded model checking (BMC) [2] is a method for finding logical errors, or proving their absence, in finite-state transition systems. In this chapter, formal description and protocol model is given using CPN Tools 2.2.0. And the ASK-CTL formula to formalize protocol properties is explained through the state space of the protocol CPN model. In order to avoid the protocol model state space explosion, some complex protocol functions are abstracted and simplified.

The LSR working mode is limited to downstream on-demand label distribution, LSP ordered control, and conservative label retention mode. In the process of establishing the label-switched paths, "Receive Label Request" and "Receive Label Mapping" events are simulated in detail, and "Receive Label Release," "Receive Label Withdraw," and "Detect Change in FEC Next Hop" events are implemented roughly.

36.2.2 Data Description and Modeling

When implementing the LDP protocol model, ingress LER, egress LER, as well as middle LSR in MPLS domain should be distinguished according to LDP protocol-related standards [3, 4]. Thus, the color set `LsrShuXing` has been defined using enumeration color set. In order to express the label switching table that consists of FEC, entering label, outgoing label, and so on, the color set `LspElem` has been defined using record color set. To establish label-switched path (LSP), LDP protocol data packets containing different messages will be transferred between LSRs. Therefore, the data packet color set `PK` and the message type color set `MT` have been defined, `PK` using record color set and `MT` using enumeration color set. When defining the color sets mentioned above, key factors were extracted from data description firstly to form the basic fields and then constructed suitable color sets using a variety of data types (integer, string, product, union, list, record, etc.) of CPN Tools. Thus, data calculation and updates were completed by making full use of operating function of these data types [5, 6]. All the color sets' definition of the LDP protocol model is as shown in Fig. 36.1.

36.2.3 Network Topology Modeling

In the top level of protocol model, the network topology modeling is needed to express the relationship between the different roles of protocol entities.

```

▼ Declarations
  ► Standard declarations
  ▼ colset LdpId=string;
  ▼ colset FEC=string;
  ▼ colset TAG=INT;
  ▼ colset CONTROL=with ORD | INDE;
  ▼ colset LsrShuXing=with INGRESS | EGRESS | B;
  ▼ colset MT=with RQ | MP | WI | RE | NT | AK;
  ▼ colset PK=record SLsr: LdpId*RLsr:LdpId*tp: MT
    *id:INT*fc:FEC*tg:TAG*Rid:INT;
  ▼ colset LspState=with IDLE | ESTAB | UNESTAB;
  ▼ colset LspElem=record Up:LdpId*Down:LdpId
    *RQId:INT*fc:FEC*st:LspState*itag:TAG
    *Otag:TAG*RQ2:INT;
  ▼ colset Ten0=int with 0..10;
  ▼ colset Ten1=int with 1..10;
  ▼ var ti:Ten0;
  ▼ var ri:Ten1;
  ▼ fun Ok(ti:Ten0 , ri:Ten1)=(ri<=ti);
  ▼ var p,q:PK;
  ▼ var r,i: LdpId;
  ▼ var x,y,z,m,t,g,k:INT;
  ▼ var b,bo:BOOL;
  ▼ var sh:LsrShuXing;
  ▼ var f:FEC;
  ▼ var lspE, lspE1, lspE2, lspE3:LspElem;

```

Fig. 36.1 Color sets' definition of the protocol model

When modeling, we assume that for a destination network “X,” there is an ingress LER marked with “a,” there is an egress LER marked with “e,” and there are two middle LSRs marked with “c” and “d”; packets from “a” to “X” may have two paths. In addition, in order to simulate the network layer routing information changes, add a transition “bian” which has the effect of “the route change” function.

A hierarchical method has been used when constructed the protocol model with CPN Tools. When creating a hierarchical net of “top-down,” we start by creating the page that shows the overview of the subpages and how they are connected. The top layer page is as shown in Fig. 36.2, substitution transitions “chulia,” “chulic,” “chulid,” “chulie” express router “a,” “c,” “d,” “e,” respectively. Among them, “a” is modeled on behalf of an ingress label switching router, “e” is an egress label switching router, and “c” and “d” are middle label switching routers. And transition “bian” has the effect of “the route change” function. Among the places around the transition “chulic,” the place “inc” stores all the protocol packets received by the label switching router c, the place “jiegc” stores all the protocol packets that have been processed by the label switching router “c” and will be sent to other label switching routers, the place “TAGc” stores label resources of the label switching router “c,” the place “LSRc” stores the identifier of label switching router “c,” the place “LSPc” stores information about label-switched path on the label switching router “c,” and the place “MIdc” stores the message ID sent by the label switching router “c.” The transition “zhuanc” connected to the place “jiegc” completes the function of forwarding protocol packets by category. The places around the

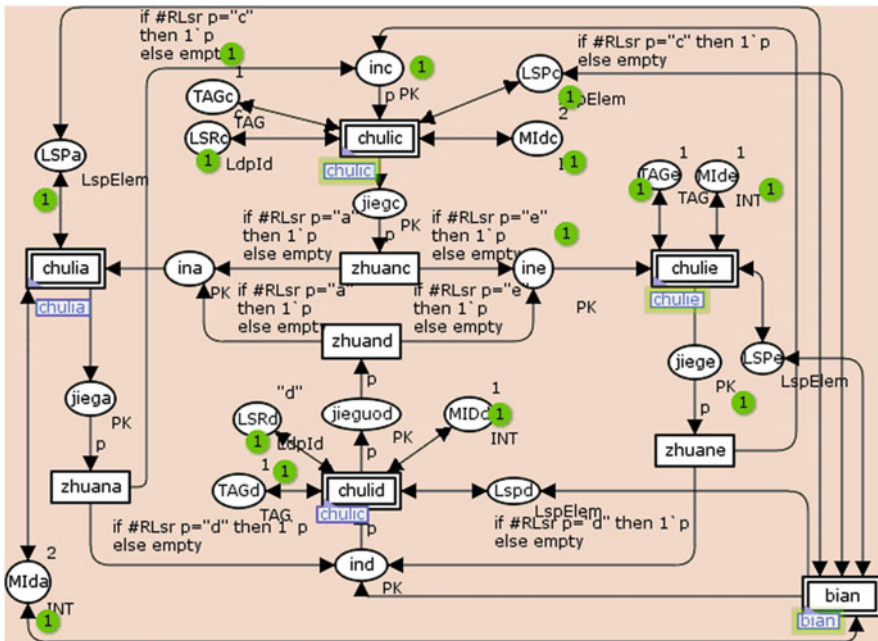


Fig. 36.2 The top page of protocol system model

transition “chulia,” “chulid,” “chulie” have the function similar to the places mentioned above.

36.3 LDP Protocol Safety and Liveness Property Verification

36.3.1 Analysis of the LDP Safety Property and Liveness Property

Property is the inherent characteristic of a system that should be in a particular scenario [7]. The safety property is that some bad things will not occur in the system [8]. And to prove the safety of the system is just one side of system correctness. The other side is to prove the system can do some useful things; this property is liveness property.

The safety properties of LDP protocols in a particular mode selected in this chapter is reflected in the following aspects. Namely, it should be avoided to make repeated label requests to downstream LSR; when intermediate LSR has not gotten label binding messages from its downstream LSR for some FEC, then it must not distribute label binding messages to its upstream LSR.

According to the LDP protocol specification, the LDP protocol liveness property is reflected in the following aspects. After each routing table’s convergency of the network layer, the label-switched path LSP can be established from the ingress LSR to the egress LSR; and if there have been some changes in some of the routing tables, then this will initiate the new label distribution process to establish a new LSP.

36.3.2 Verification of the LDP Safety Property and Liveness Property

When analyzing and simulating based on the protocol CPN model, the following two initial markings have been used. They are shown in Tables 36.1 and 36.2.

According to different initial marking settings, the model can perform different protocol functions. Therefore, to ensure that the model will reflect the protocol safety and liveness property, it is needed to set the initial marking correctly at the key places.

The marking in Table 36.1 means the current router “a” has forwarded a label requesting message to its downstream router “c” for some $FEC = “X”$; but the router “c” has forwarded a label requesting message to its downstream router “e” before it receives the label requesting message from the router “a” mentioned

Table 36.1 The LDP protocol CPN model initial marking 1

Place	Marking
LSPa	{Up="",Down="c",RQId=0,fc="X",Itag=0,Otag=0,st=UNESTAB,RQ2=1}
inc	{SLsr="a",RLsr="c",tp=RQ,id=1,fc="X",tg=0,Rid=0}
LSPc	{Up="a",Down="",RQId=0,fc="X",st=UNESTAB,Itag=0,Otag=0,RQ2=1}
ine	{SLsr="c",RLsr="e",tp=RQ,id=1,fc="X",tg=0,Rid=0}
LSPe	{Up="c",Down="R",RQId=0,fc="X",st=UNESTAB,Itag=0,Otag=0,RQ2=0}

Table 36.2 The LDP protocol CPN model initial marking 2

Place	Marking
LSPa	{Up="",Down="d",RQId=0,fc="X",Itag=0,Otag=0,st=UNESTAB,RQ2=x}
Lspd	{Up="a",Down="e",RQId=0,fc="X",st=UNESTAB,Itag=0,Otag=0,RQ2=0}
LSPe	{Up="d",Down="R",RQId=0,fc="X",st=UNESTAB,Itag=0,Otag=0,RQ2=0}
ind	{SLsr="a",RLsr="d",tp=RQ,id=x,fc="X",tg=0,Rid=0}

above; but at the current time, the router "e" has not received a label requesting message from the router "c."

The marking in Table 36.2 means the current router "a" has forwarded a label requesting message to its downstream router "d" for some FEC = "X"; but the router "d" has not yet forwarded a label requesting message to its downstream router "e" for the FEC = "X."

According to the LDP protocol specification, if a router has forwarded a label requesting message to its downstream for a specific FEC before it receives a label requesting message from its upstream router, then in this case, the router must not forward a label requesting message to its downstream for the FEC again when it receives a label requesting message from its upstream router later. In the model, the initial marking in Table 36.1 is used to reflect this safety property. In this case, transitions "TagDis'Req_NH 1" and "TagDis'request 1" must not occur. ASK-CTL formulas are used to detect whether the two transitions are to be fired. The verification conclusion is false, that the two transitions must not be fired. The ASK-CTL formulas used and implementation results are shown in Fig. 36.3.

According to the LDP protocol specification, a particular scenario is selected, i.e., a router receives a label requesting message from its upstream LSR for a specific FEC, but it has not yet received the label binding message for this specific FEC at the very time from its downstream LSR. Then, in this case, the router must not distribute label binding messages to its upstream LSR. In the model, the initial marking in Table 36.2 is used to reflect this property. This safety property is reflected by transitions "TagDis'map 2" and "TagDis'map2 2"; the two transitions must not occur. ASK-CTL formulas are used to detect whether the two transitions are to be fired. The verification conclusion is false, that the two transitions must not be fired. The ASK-CTL formulas used and implementation results are shown in Fig. 36.4.

According to the LDP protocol specification, regardless of the routing table's changes, the LDP in a particular mode selected can successfully create a label-

```

fun IsconsideredTs a=(TI.TagDis'Req_NH 1=ArcToTI a);
val myASKCTLformula=
MODAL(POS(AF('Is Dead Transition ', IsconsideredTs)));
eval_node myASKCTLformula InitNode;

```

```

val IsconsideredTs=fn:Arc->bool
val myASKCTLformula=MODAL(EXIST_UNTIL(TT,
AF('Is Dead Transition ',fn))) :A
val it=false:bool

```

```

fun IsconsideredTs a=(TI.TagDis'request 1=ArcToTI a);
val myASKCTLformula=
MODAL(POS(AF('Is Dead Transition ', IsconsideredTs)));
eval_node myASKCTLformula InitNode;

```

```

val IsconsideredTs=fn:Arc->bool
val myASKCTLformula=MODAL(EXIST_UNTIL(TT,
AF('Is Dead Transition ',fn))) :A
val it=false:bool

```

Fig. 36.3 The ASK-CTL formulas used under the initial marking in Table 36.1

```

fun IsconsideredTs a=(TI.TagDis'map 2=ArcToTI a);
val myASKCTLformula=
MODAL(POS(AF('Is Dead Transition ', IsconsideredTs)));
eval_node myASKCTLformula InitNode;

```

```

val IsconsideredTs=fn:Arc->bool
val myASKCTLformula=MODAL(EXIST_UNTIL(TT,
AF('Is Dead Transition ',fn))) :A
val it=false:bool

```

```

fun IsconsideredTs a=(TI.TagDis'map2 2=ArcToTI a);
val myASKCTLformula=
MODAL(POS(AF('Is Dead Transition ', IsconsideredTs)));
eval_node myASKCTLformula InitNode;

```

```

val IsconsideredTs=fn:Arc->bool
val myASKCTLformula=MODAL(EXIST_UNTIL(TT,
AF('Is Dead Transition ',fn))) :A
val it=false:bool

```

Fig. 36.4 The ASK-CTL formulas used under the initial marking in Table 36.2

switched path. In the model, this liveness property is reflected by two terminal state nodes of 1277 and 1602. The 1277 state node means that the label forwarding table has finished in a final state after the convergency of the routing table and then all of the routing tables have maintained its original state, generating no change; the 1602 state node means that the label forwarding table has finished in a final state after the convergency of the routing table and then some of the routing tables have changed to cause forwarding new messages to reestablish a new LSP and then at last


```

1277
4:0
C'jiegc 1: empty
C'LSPc 1: 1'{UP="a",Down="e",RQId=1,fc="X",st=ESTAB,Itag=1,Otag=1,RQ2=1} √
C'TAGc 1: 1'2
C'MIdc 1: 1'4
C'ina 1: empty
C'MIda 1: 1'3
C'LSPa 1: 1'{UP="",Down="c",RQId=0,fc="X",st=ESTAB,Itag=0,Otag=1,RQ2=1} √
C'ine 1: empty
C'MIde 1: 1'2
C'TAGe 1: 1'2
C'LSPe 1: 1'{UP="c",Down="R",RQId=1,fc="X",st=ESTAB,Itag=1,Otag=0,RQ2=0} √
C'TAGd 1: 1'1
C'jiega 1: empty
C'jiece 1: empty
C'ind 1: empty
C'jieguod 1: empty
C'LSRc 1: 1'"c"
C'Lspd 1: empty √
C'MIDd 1: 1'1
C'LSRd 1: 1'"d"

```

Fig. 36.5 The tokens in places in state node 1277

terminate in the state of 1602. The tokens in all places of the states of 1277 and 1602 can be viewed using the state space tool. The tokens of all places at the 1277 node are shown in Fig. 36.5 (all places' tokens can be viewed by scrolling), and the tokens' information required to protocol verification are specially marked with red \checkmark symbols; the "st" field values of places "LSPa," "LSPc," and "LSPe" in model are "ESTAB" which means the label-switched path has been established and it is composed of routers "a," "c," and "e"; then the model automatically executing is finished in the state 1277. 1277 is the normal protocol terminated state. The same can also be analyzed in the 1602 state, but the established label-switched path is composed of routers "a," "d," and "e"; 1602 is also the normal protocol terminated state. In terminating states, there cannot be transitions to be fired, and this is verified by the ASK-CTL formulas shown in Fig. 36.6.

36.4 Verification Process Summary in CPN Tools 2.2.0 Environment

First, you should have entered the state space tool. And you have generated the LDP protocol model full state space and strongly connected component graph (SCC graph). To generate the full state space and SCC graph, you should use the state space tool of CPN Tools 2.2.0. It can be found under the Toolbox menu in CPN Tools 2.2.0. Then you will find the Calculate State Space tool button and the

```

val myASKCTLformula=NOT(MODAL(TT));
eval_node myASKCTLformula 1277;

```

```

val myASKCTLformula=NOT(MODAL TT):A
val it=true:bool

```

```

val myASKCTLformula=NOT(MODAL(TT));
eval_node myASKCTLformula 1602;

```

```

val myASKCTLformula=NOT(MODAL TT):A
val it=true:bool

```

Fig. 36.6 The ASK-CTL formulas used for terminated states' verification

Calculate SCC graph tool button in the state space tool palettes. Next, you need to load ASK-CTL logic library:

1. Create an auxiliary box (invoke box from the Aux menu in CPN Tools 2.2.0).
2. In the box type, use (ogpath^"ASKCTLloader.sml").

Now you are ready to write ASK-CTL formulas and do model checking. The ASK-CTL formulas also can be written in auxiliary boxes. In Sect. 36.3 the ASK-CTL formulas used to express the safety and liveness properties have been given. Finally, process the ASK-CTL formulas of protocol properties' description to judge whether the current state space will meet the protocol properties, namely, return "true" or "false" by using the simulator of CPN Tools 2.2.0.

Conclusion

A function verification model has been constructed for the LDP integrated analysis in the aspects of safety property and liveness property based on the Colored Petri Nets. Then the CPN model is executed automatically and the protocol analysis and simulation is completed. At the same time, it has confirmed correctness and robustness of the LDP protocol label distribution function. And this CPN-based modeling and simulation method, which integrates protocol property verification and function analysis, contributes a significant methodology helping to improve the function of a network protocol.

Acknowledgements This research is supported by the Natural Science Foundations of China (No. 61167004 and 61205127) and construction funds of the technology innovation team of Computer and Information Engineering College of Inner Mongolia Normal University.

References

1. Guo XQ. Research on conformance testing of LDP protocol based on E-LOTOS. Master's degree thesis of Inner Mongolia University, Hohhot, China. 2012, (In Chinese).
2. Biere A, Cimatti A, Clarke EM, Zhu Y. Symbolic model checking without BDDs. In: Proceedings of the workshop on tools and algorithms for the construction and analysis of systems (TACAS' 99). Lecture notes in computer science, vol. 1579. Berlin: Springer; 1999. pp. 193–207.
3. Rosen E. Multiprotocol label switching architecture. 2001. <http://www.ietf.org/rfc/rfc3031.txt>. Accessed January 2001.
4. Andersson L. LDP specification. 2001. <http://www.ietf.org/rfc/rfc3036.txt>. Accessed January 2001.
5. Zhang J, Liu J, Ye XM, Xu ZJ. Modeling and simulation of trusted router discovery protocol using colored Petri nets. *J Syst Sim*. 2012;24(3):701–9 (In Chinese).
6. Liu J, Ye XM, Li J. Towards formal modeling methodology of BitTorrent based on Petri nets. *J Syst Sim*. 2011;23(11):2312–20 (In Chinese).
7. Li H. Research on network protocol modeling and interoperability testing based on property. Doctor dissertation of Inner Mongolia University, Hohhot, China. 2010, (In Chinese).
8. Wang YY. Research on web composition services model verification and testing technique based on timed color Petri nets. Doctor dissertation of Xidian University, Xi'an. 2012, (In Chinese).

Chapter 37

Self-Adaptive Anomaly Detection Method for Hydropower Unit Vibration Based on Radial Basis Function (RBF) Neural Network

Xueli An

Abstract In order to improve the adaptability and effectiveness of anomaly condition recognition for hydropower unit, an adaptive anomaly detection method of hydropower unit vibration is presented based on radial basis function (RBF) neural network. The optimal value of vibration parameters in real-time condition is dynamically computed by using RBF neural network in this method. The relative distance between vibration real data and optimal value is calculated as the anomaly. This index can describe the changes of vibration parameters and identify anomalies of hydropower unit condition. The obtained results of abnormal alarm can meet the actual demands by using the proposed method in vibration monitoring of hydropower unit. This method can well describe the slow process of deterioration for vibration parameters and identify abnormal vibration in a sensitive manner. This method will be practical as to the operation guarantee of hydropower unit.

Keywords RBF neural network • Hydropower unit • Vibration parameter • Self-adaptive anomaly detection

37.1 Introduction

At present, the single alarm line for the abnormal vibration of hydropower units is most commonly used based on relevant national and international standards [1–3]. These alarm criteria are built on the basis of the fixed threshold of test statistics. As it hasn't fully considered the actual operating conditions and field conditions, there will be frequent false alarms and leakage alarms in the field application; therefore, it is needed to build adaptive vibration anomaly detection model which

X. An (✉)

China Institute of Water Resources and Hydropower Research, 100038 Beijing, China
e-mail: an_xueli@163.com

can be adaptable to the changes of hydropower units' conditions so as to meet the needs of the field [1, 2].

Radial basis function (RBF) neural network [4–7] is a feedforward neural network model, which has a simple structure and good nonlinear predictive capability. In theory, it is able to prove that RBF neural network is approximate to any function with any accuracy. It has strong mapping ability of input and output while maintaining high precision characteristics of the nonlinear algorithm. It has been successfully used to handle nonlinear function approximation and data classification problems, mainly used in signal processing, system modeling, control, fault diagnosis, pattern recognition, engineering optimization design, and other fields.

The system condition can be described by using a certain number of performance parameters. In the analysis model, the threshold values of these parameters are usually determined at first. Then the system's condition parameters are detected. When they reach a threshold, it is considered that the system is about to fail. In this chapter, an online algorithm based on RBF neural network is designed. This algorithm is used to dynamically estimate the optimal values of vibration condition monitoring parameters of the unit. The relative distance between the optimal values and the real data is defined as an anomaly index. This can achieve adaptive anomaly detection of vibration parameters for hydropower units.

37.2 RBF Neural Network

RBF neural network [4–7], by using bionics principle, simulates the human brain's neural network structure of local coordination and mutual reception receiving range, its schematic diagram shown Fig. 37.1. The local characteristics of its hidden nodes mainly imitate the function of on-center and off-surround of certain biological neurons. RBF neural network is a feedforward network. The input vectors to the hidden layer are mapped by the radial basis function. A simple linear weighting is available from the hidden layer to the output layer. In theory, RBF neural network can be unlimited approximate to any nonlinear model.

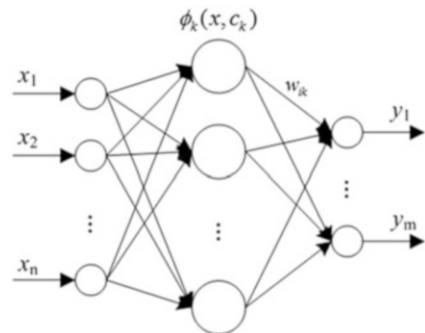


Fig. 37.1 Structure of RBF neural network

The mapping relationship of RBF neural network between input and output is shown below:

$$y_i = f_i(x) = \sum_{k=1}^M w_{ik} \varphi_k(x, c_k) = \sum_{k=1}^M w_{ik} \exp \left[\frac{(x - c_k)^T (x - c_k)}{2\sigma_k^2} \right] \quad (37.1)$$

where x is the input vector, w is the weight coefficient, φ is the basis function, c_k is the center of the k th node, and σ_k is the based width parameter of the k th node. Here the basis function is Gauss-type basis function.

37.3 Self-Adaptive Anomaly Detection Method for Hydropower Unit Vibration

The establishment of a healthy model is pivotal to achieve hydropower units' anomaly detection. According to the complexity of hydropower unit vibrations, RBF neural network is used to establish the health model for vibration parameters. Based on the existing monitoring data, the model is trained. The real-time online monitoring data are substituted into the trained model to analyze the variation trends of vibration parameters in a real-time manner and determine the possibility of abnormalities in various operating conditions. This can achieve the purpose of the early warning of unit abnormalities.

The vibration anomaly detection method of hydropower unit is proposed on the basis of RBF neural network with the specific steps shown as below:

Step 1: Collect the online monitoring data of hydropower unit and determine the health condition of the unit.

Step 2: Analyze the main working parameters which affect the vibration condition of the unit.

A large number of field data analysis shows that active power and working head are main factors affecting the hydropower units' vibration conditions.

Step 3: Train RBF model to obtain the mapping relation between vibration and unit condition parameters.

Based on the RBF neural network, while taking comprehensive consideration of the effect of active power and working head on hydropower unit vibration, the vibration health model $y = f(P, H)$ is built, where P is the unit active power, H is the working head, and y is the vibration parameter.

As to the proposed method, the number of neurons in the input layer is two (P, H) and the number of neurons in the output layer is one (y). In this chapter, the approximate function `newrb` is used to add neurons to the hidden layer of a radial basis network until it meets the specified mean squared error goal.

Step 4: Input real-time data of condition parameters to RBF model and calculate the health standard value of unit vibration parameter in current condition.

Step 5: Calculate the difference between the real values of vibration parameter and its health standard values. If the difference is greater than the alarm threshold, this alarm will be generated.

37.4 Applications Example

In this chapter, the condition monitoring data of a pumped storage unit (rated power: 250 MW, rated speed: 333 rpm) in July 2008–December 2011 are used to verify the proposed method.

The unit's monitoring data (in December 1, 2011–December 15, 2011) of upper bracket horizontal vibration (peak-peak value) in direction X are shown in Fig. 37.2. In this figure, as a result of the variation of working head and frequent conversion of pumping-powering conditions, the changes of vibration parameter are extremely complex. The valid information which can reflect the unit's real condition can't be obtained from the figure; therefore, it is necessary to build a vibration anomaly detection model adaptable to the changes of hydropower unit conditions.

The online monitoring data (in September 22, 2008–September 18, 2009) of unit which has good running condition are selected as health standard data (900 sets data) to establish health model of unit vibration parameters. The active power P and working head H of the data are considered as inputs of the model, while the vibration parameters of the data are considered as the model's outputs. The training samples are input to RBF neural network for training to get the precise mapping relation between input parameters (P , H) and output parameters (c) for unit in sound operating conditions.

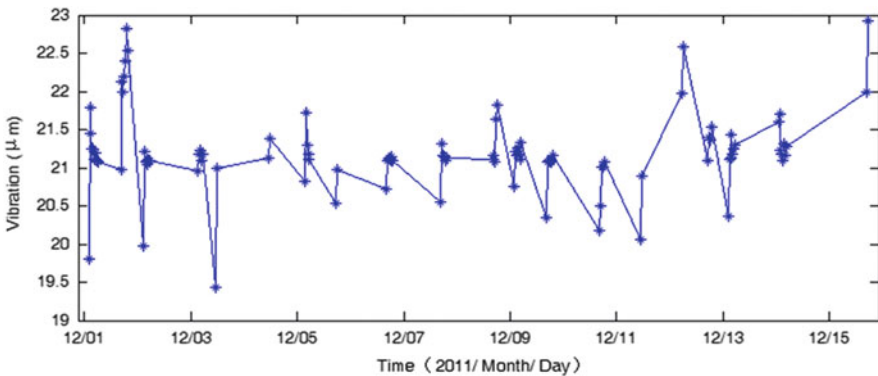


Fig. 37.2 Real condition monitoring data of pumped storage power station unit

Fig. 37.3 The condition monitoring data of pumped storage unit

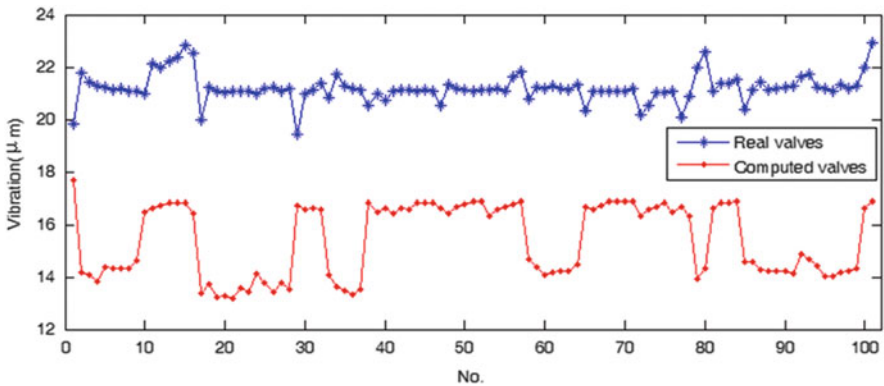
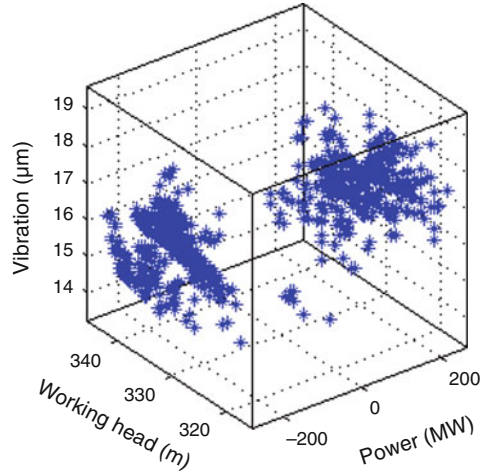


Fig. 37.4 Comparisons between the real valves and the computed values of pumped storage unit

As to the 900 sets of health standard data, 700 sets data (as shown in Fig. 37.3) are used to train the model with the remaining 200 sets data considered as the testing samples to verify the model. In order to make the model a good warning property, the selected health standards data should cover the change intervals of working head and active power. The results show that the model calculated values are generally conforming to the real values. The model's average relative error is 3.13 %, which is of high accuracy.

The unit's online monitoring data from December 1, 2011 to December 15, 2011 are analyzed to adaptively detect the anomaly of vibration parameters. The power and working head of 100 sets monitoring data are substituted into the trained LS-SVM model to calculate the health standard value $c(t)$ of condition parameter under the current operating conditions. The $c(t)$ is compared with the real value $r(t)$ with the results shown in Fig. 37.4. The differences $r(t) - c(t)$ between the health

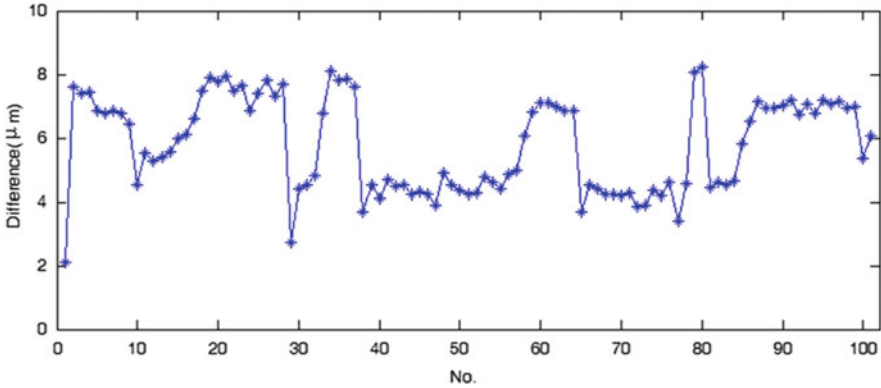


Fig. 37.5 Difference between the real valves and the computed values

standard value and the real value are displayed in Fig. 37.5. From Figs. 37.4 and 37.5, the deterioration of unit's component occurs, and the unit is gradually deviated from the healthy and normal operation after 3 years of unit operation. Although the vibration has started the deviation from the health condition, in most running time, the differences are relatively small and the unit can continue to run.

To sum up, the changing process of unit vibration condition can be dynamically traced by the proposed self-adaptive detection method. It can early detect the continuous change of unit's abnormality or failure; thus, the site operator can deeply check the equipment under abnormal condition, which can effectively avoid the possibility of forced shutdown of the unit.

Conclusion

In order to achieve effective identification of hydropower units' abnormal condition, this chapter presents an adaptive anomaly detection method of vibration parameters for hydropower units based on RBF neural network. The proposed method uses RBF neural network to online continuously calculate the optimal value of vibration parameters in the real-time operating conditions. The relative distances between the real values of vibration data and their optimal values are computed to identify the unit's abnormal conditions and achieve the alarm function of the condition monitoring. The analysis of actual examples shows that this method can adaptively compute the optimal value of vibration parameter in the changing working conditions. It can identify unit's abnormal vibration in a timely and effectively manner, better display the slow deterioration process of unit's vibration performance, and meet the real-time monitoring demand of hydropower units.

Acknowledgements This work was supported by the National Natural Science Foundation of China (grant number 51309258) and the Special Foundation for Excellent Young Scientists of China Institute of Water Re-sources and Hydropower Research (grant number 1421).

References

1. An XL, Pan LP, Zhang F, et al. Condition degradation assessment and nonlinear prediction of hydropower unit. *Power Syst Technol.* 2013;37(5):1378–83. In Chinese.
2. An XL, Pan LP, Zhang F. Early fault warning model of pumped-storage power station unit based on three-dimensional surface. *Water Power.* 2013;39(1):71–5. In Chinese.
3. Liu J, Pan LP, Gui ZH, et al. The current status of on-line state monitoring and fault diagnosis technologies for hydrogenerating unit. *Large Electric Machine and Hydraulic Turbine* 2010; (2):45–9, In Chinese.
4. Chang W. Estimation of the state of charge for a LFP battery using a hybrid method that combines a RBF neural network, an OLS algorithm and AGA. *Int J Electr Power Energy Syst.* 2013;53:603–11.
5. Praga-Alejo RJ, González-González DS, Cantú-Sifuentes M, et al. Statistical inference in a redesigned Radial Basis Function neural network. *Eng Appl Artif Intel.* 2013;26(8):1881–91.
6. Hashemi S, Aghamohammadi M. Wavelet based feature extraction of voltage profile for online voltage stability assessment using RBF neural network. *Int J Electr Power Energy Syst.* 2013;49:86–94.
7. Yin J, Zou Z, Xu F. On-line prediction of ship roll motion during maneuvering using sequential learning RBF neural networks. *Ocean Eng.* 2013;61:139–47.

Chapter 38

A Fast Distribution-Based Clustering Algorithm for Massive Data

Xin Xu, Guilin Zhang, and Wei Wu

Abstract With the rapid development of data collection and storage technologies, the volume of data is getting so enormous for collection and analysis in a reasonable amount of time. Only a small fraction of the original data could be contained in the databases or data warehouses. Traditional clustering approaches are recognized as an indispensable solution to extract useful knowledge from data. However, existing conventional clustering methods all lack of robustness and computation efficiency when applied on massive data. In this work, we have made several efforts to better address the above problems with novel techniques of automatic window initialization, distribution density threshold, and window traversal based on distribution density.

Keywords Distribution-based clustering • Massive data • Data mining

38.1 Introduction

With the rapid development of data collection and storage technologies, it is not uncommon to have massive data in Gs or even Ps, either enterprise specific or private. In the past few years, there has been an exponential growth in the volumes of massive data. Since the data volume is so huge, the databases may contain just a fraction of the original data. For example, in sensor network, due to the transmission failures and variation in the information processing abilities of sensors, the data received at the server node may be incomplete. With no doubt, it is a big challenge to scramble and derive insights from the deluge of data.

It has been recognized that efficient clustering provides an indispensable solution to extract knowledge from such massive data. For this reason, it has already attracted considerable attention of researchers. Even though quite a large number of conventional clustering methods have been proposed, such as k-means [1, 2],

X. Xu (✉) • G. Zhang • W. Wu
Science and Technology on Information System Engineering Laboratory,
NRIEE, 210007 Nanjing, China
e-mail: flora.xin.xu@gmail.com

k-window [3], mixture models [4], OPTICS [5], GDBSCAN [6], and hierarchical clustering [7], the traditional clustering methods all lack of either robustness or computation efficiency, thus difficult to be applied on massive data. Specifically, the conventional clustering algorithms usually fail to meet the following three requirements simultaneously: no prior knowledge of cluster number, ability to discover clusters of arbitrary shapes, computational efficiency, and ease of parallelization.

In this chapter, we have made the following major efforts to better address the above problems. The rest of the chapter is organized as follows. We briefly review related work in data clustering in Sect. 38.2. Our fast distribution-based clustering algorithm for massive data is formally proposed in Sect. 38.3. In Sect. 38.4, we present the experimental results. And we conclude in section Conclusion.

38.2 Related Work

We partition existing clustering methods related to our distribution-based clustering algorithm into three categories, k-mode clustering, variants of k-mode clustering, and the density-based clustering.

The main characteristic of the k-mode clustering methods is the demand of prior knowledge of cluster number. The representative k-mode clustering algorithms include k-means [1, 2] and general mixture model [4]. Another shortcoming of the class of k-mode clustering algorithms is that the shapes of discovered clusters are all convex, rendering it very difficult to capture clusters of arbitrary shapes. As a result, the limitation in flexibility and adaptability of k-mode clustering algorithms has impeded their application in wider domains.

Variants of the k-mode clustering methods have been proposed to address the problem of cluster number specification, such as k-windows [3] and robust multi-view k-means clustering algorithm [2]. These variants of the k-mode clustering algorithms manage to achieve a less time complexity and a better clustering result. Tasoulis proposed a generalization framework of k-windows clustering which explored the roles of different distance functions over the data sets of various structures [3]. In this way, the k-windows clustering algorithm would be scalable for data sets of unstructured nature, i.e., multimedia, time series, or genome sequence.

The final category refers to the density-based clustering, i.e., OPTICS [5] and GDBSCAN [6]. The density-based clustering method has been considered as the most robust one in terms of capturing clusters of arbitrary shapes. We ascribe the hierarchical clustering algorithms [7], as the class of density-based clustering as well. Single link, as one representative density-based clustering algorithm, iteratively merges the closest data pairs according to a certain distance function.

38.3 Method

Suppose there are n number of samples from a m -dimensional data set and the maximum and minimum data values of samples in each dimension are \min_i and \max_i , $1 \leq i \leq m$ respectively. Our fast distribution-based clustering algorithm proceeds in three major steps to identify the clusters of the original massive data, distribution density threshold specification, random window initialization, and distribution-based window traversal. A coverage threshold k is applied to ensure each sample is covered by at least k random windows. And, a granularity threshold g is specified in order to control the sizes of random windows. The windows iteratively merge into clusters until a distribution density threshold δ is reached. The final clusters would then be identified and output.

38.3.1 Distribution Density Threshold Specification

The traditional density-based clustering algorithms adopt a spatial density threshold calculated as the number of samples in one area unit. However, the traditional density-based clustering algorithms take in no account of the variation in the sample size. In a case that the underlying unknown data distribution of the original massive data is fixed, while the number of samples from the original data set varies significantly, i.e., from hundreds to millions, it is almost impossible to predetermine a single one density threshold to accommodate the different sample sizes. As can be seen, the density threshold for the sample set with millions of samples probably could have been 10,000 times as much as that for the sample set with hundreds of samples.

For this reason, a distribution density threshold δ is adopted instead of the traditional spatial density threshold as a more robust correlation measurement for data sets with unknown distributions. Mathematically, the distribution density threshold δ is computed as the proportion of samples covered by the existing random windows. In other words, the distribution density threshold δ is calculated as the proportion of samples that belong to the traversed random windows in our fast distribution-based clustering algorithm.

$$\delta = \frac{\text{num. of samples in random windows}}{\text{sample size}} \quad (38.1)$$

In this way, the underlying distribution of original data could be identified with a single 1 threshold even when the sample size varies. As for the above example, a distribution density threshold δ of 80 % could produce similar clustering results for sample sets whose sizes vary from hundreds to millions.

38.3.2 *Random Window Initialization*

At the second step, a large number of m -dimensional windows are generated randomly, each with width w_i for each dimension i , as calculated below:

$$w_i = (\max_i - \min_i) \times g \quad (38.2)$$

A sample s is assumed to be covered by window c if and only if the distance between sample s and the center of window c is within $w_i/2$ in each dimension i .

$$\text{Relation}(s, c) = \begin{cases} \text{covered,} & \text{if } \forall i |s_i - c_i| \leq w_i/2 \\ \text{uncovered,} & \text{otherwise} \end{cases} \quad (38.3)$$

Random windows would be generated continuously until each sample has been covered k times. During this procedure, we would record and update the coverage count of each sample correspondingly. The generated random windows can be either disjointed or overlapping with each other.

The experimental results indicate that the choice of the coverage threshold k would not influence the final clustering result that much. Usually, a coverage threshold k of 2 or 3 is applied in our fast distribution-based clustering algorithm.

38.3.3 *Distribution-Based Window Traversal*

The third step is distribution-based window traversal. The criterion is quite straightforward. The windows that cover more samples are considered more important and thus would be traversed before the ones covering fewer samples. In the window traversal order, the adjacent traversed windows sharing any sample would merge with each other into a cluster. The proportion of covered samples of each cluster would be updated continuously. The window traversal procedure proceeds iteratively until the proportion of the sum of covered samples in all the traversed windows has reached a predefined distribution threshold δ . The remaining clusters would be output as the final ones.

Figure 38.1 illustrates the outline of our fast distribution-based clustering algorithm for massive data.

As can be seen, our fast distribution-based clustering algorithm scales much better on massive data than the previous k -mode clustering algorithms, the variants, and the density-based clustering algorithms.

Fig. 38.1 A fast distribution-based clustering algorithm for massive data

Parameters:

- D : a m -dimensional sample set;
- n : number of samples in D ;
- g : granularity threshold;
- k : coverage threshold;
- δ : distribution threshold.

Output: clusters w.r.t. g , k and δ .

compute window width $w_i = (max_i - min_i) \times g$

set window size as $w_1 \times w_2 \times \dots \times w_m$

For each sample s

While (sample s has not been covered k times)

generate a new random window c' that covers s

update the coverage count for all samples in c

calculate v_c as the set of samples covered by each window c .

rank the windows in descending order of $|v_c|$: *ORD*.

$V = 0$.

Repeat visit window c in *ORD* order **Do**

$V = V \cup v_c$;

if c covers any sample shared by previous windows or clusters

merge them into one cluster;

Until $|V|/n \geq \delta$.

output the final clusters after window traversal.

38.4 Results

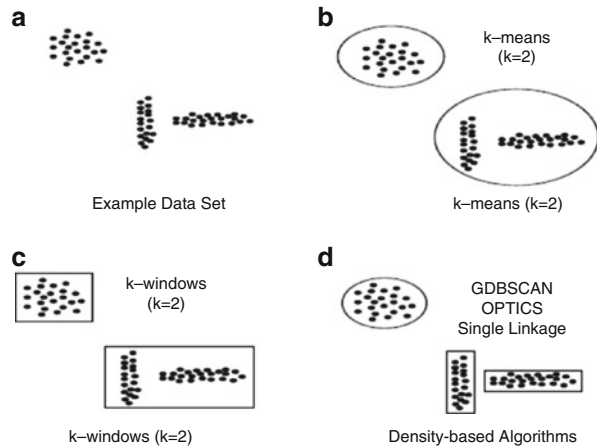
In experiments, we evaluate our distribution-based clustering algorithm for massive data on multivariate normal distributed simulation data. Experimental results suggest that our distribution-based clustering algorithm is both effective and scalable for massive data.

38.4.1 Evaluation of Arbitrary-Shaped Cluster Identification

We compared k-means, k-windows, OPTICS, GDBSCAN, and single linkage algorithms against our method with a simulated data set in Fig. 38.2. The 2D data set is composed of a circle-shaped cluster and two bar-shaped clusters.

As can be seen, k-means and k-windows rely heavily on the prespecified cluster number k which is actually unlikely to be known in advance. Furthermore, these two algorithms recognize convex clusters only and may probably fail to detect clusters of arbitrary shapes. The density-based algorithms OPTICS, GDBSCAN, and hierarchical clustering are much more robust in dealing with arbitrary clusters. However, their computation cost is significantly higher than our algorithm.

Fig. 38.2 Comparison against existing methods



38.4.2 Evaluation of Robustness

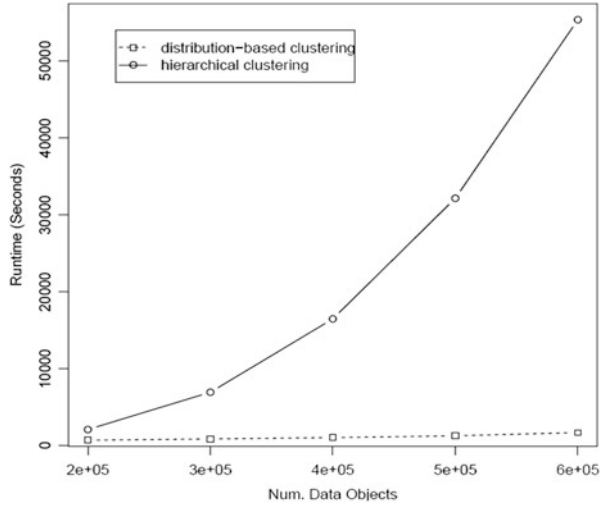
The experimental results indicate that the clustering results would not be affected much when the input parameters vary significantly. For instance, similar clustering results could be obtained when the distribution threshold δ varies between 70 and 95 %, the granularity threshold g fluctuates within range $[1/8, 1/30]$, and the coverage threshold k changes between 1 and 4. It turns out that our distribution-based clustering algorithm is more robust for clustering massive data than the k-mode and its variants. When the initial cluster seeds or k-windows are not selected reasonably across the whole data space, the clustering results of the k-mode and its variants may have been degraded.

In addition, when the sample size varies between 2,000 and 10,000, the final clustering results remain similar under the same parameter setting. On the contrary, the final clustering results of the k-mode clustering, its variants, and the density-based clustering algorithms would be quite different.

38.4.3 Evaluation of Computational Efficiency

We compared the efficiency of our distribution-based clustering algorithm against hierarchical clustering and density-based clustering algorithms with varying sample sizes. Since the runtime of hierarchical clustering and density-based clustering are similar, we only report the comparison with hierarchical clustering here. We used the above initial parameter setting for our distribution-based clustering algorithm and vary the data set sizes between 200,000 and 600,000. Experiments on simulation data sets of various sizes show that our method is significantly more efficient than the hierarchical clustering algorithm. As can be seen from Fig. 38.3, our distribution-based clustering is orders of magnitude faster than the hierarchical

Fig. 38.3 Efficiency comparison



clustering algorithm. In addition, our distribution-based clustering algorithm is easy to parallelize for distributed data and scale well on massive data of enormous size.

Conclusion

In this work, we have proposed a novel distribution-based clustering method for massive data. With this method, we no longer need to specify the number of clusters, as required by the k-mode clustering algorithms. Instead, with our proposed coverage constraint, sufficient number of random windows will be generated automatically. And, by adopting a distribution threshold, we are able to avoid specifying different spatial density threshold due to the variation in sample sizes. Experimental results also indicate that our algorithm is both robust and efficient compared with the k-mode and density-based clustering algorithms.

References

1. Oyana TJ. A new-fangled FES-k-means clustering algorithm for disease discovery and visual analytics. *EURASIP J Bioinformatics Syst Biol.* 2010;2010:981–7.
2. Cai X, Nie F, Huang H. Multi-view K-means clustering on big data. In: *Proceedings of the 23rd international joint conference on artificial intelligence.* Beijing, China: AAAI press; 2013. pp. 2598–604
3. Tasoulis DK, Vrahatis MN. Generalizing the k-Windows clustering algorithm in metric spaces. *Math Comput Model.* 2007;46:268–77.
4. Kannan R, Salmasian H, Vempala S. The spectral method for general mixture models. *SIAM J Comput.* 2008;38(3):1141–56.

5. Ankerst M, Breunig MM, Kriegel H-P, Sander J. Optics: ordering points to identify the clustering structure. In: 1999 ACM SIGMOD international conference on management of data. Philadelphia, PA: ACM Press; 1999. pp. 49–60.
6. Sander J, Ester M, Kriegel H-P, Xu X. Density-based clustering in spatial databases: the algorithm gbscan and its applications. *Data Mining Knowl Discov.* 1998;2(2):169–94.
7. Krishnamurthy A, Balakrishnan S, Xu M, Singh A. Efficient active algorithms for hierarchical clustering. In: Proceedings of the 29th international conference on machine learning. icml.cc/. Edinburgh, Scotland: Omnipress; 2012. pp. 887–94.

Chapter 39

Design and Implementation of Virtual Experiment System Based on Universal Design

Yun Liu, Guoan Zhao, Dayong Gao, and Zengxia Ren

Abstract This paper explores a kind of virtual-experiment system based on a universal design concept aimed at achieving the fast development of virtual experiments. This system provides a reference base for the design and development of the Internet and information products and services, which deserves further research and application.

Keywords Universal design • Virtual-experiment system • User

39.1 Introduction

Since William Wolf proposed *virtual experiments*, virtual experimental systems have developed rapidly [1]. The author searches for “virtual-experiment system” in the China National Knowledge Infrastructure (CNKI project is to achieve full social knowledge sharing and dissemination of value-added utilization of resources for the goal of information, which is launched by Tsinghua University and Tsinghua Tongfang in June 1999.) and then finds that most virtual experimental systems are based on VRML, Flash, Active, Java, QuickTime VR, and others. These systems have the following issues: they are for specific users; they offer low simulation of real tests; their method of application is complex; they are difficult to modify.

Faced with these problems, this paper describes a virtual-experiment system based on universal design that is intended for distance learning by a network education institute, Beijing University of Posts and Telecommunications. How does one create an operation that is easy, flexible, and realistic and provides an adjustable environment that can be changed and extended to meet the varied needs of different users? Universal principles are needed to solve these problems.

Y. Liu (✉) • G. Zhao • D. Gao • Z. Ren
Computer Simulation Technology Laboratory, Network Education Institute, Beijing
University of Posts and Telecommunications, 100876 Beijing, China
e-mail: liuyy0816@163.com

39.2 Universal Design

In 1987, the US designer Ronald Mace defined *universal design* as follows: The design of products and environments to be usable by all people, to the greatest extent possible, without the need for adaptation or specialized design. [2].

Later, a group of architects, product designers, engineers, and researchers of environmental design led by Ronald Mace formulated the following seven principles for universal design: equitable use, flexibility in use, simple and intuitive use, perceptible information, tolerance for error, low physical effort, sufficient size and space for approach and use [3]. These principles are applied to the design and development of virtual-experiment systems, which address the aforementioned problems.

39.3 Design of Virtual-Experiment System

A virtual-experiment system is designed for three types of users: a teacher creating experimental courses, a programmer converting experimental courses and data recorded that created by teachers into code to realize courses virtualization. Figure 39.1 shows the process of the virtual-experiment system.

39.3.1 Selection of Experimental Courses

The virtual-experiment system chooses hardware operation and software operation on communications industry to learn, and the universal design idea emphasizes that more people use the virtual-experiment system, so fundamental communication courses are selected by teachers. For example, a system might select Router Configuration, CMCC Connection, or some other basic experiment.

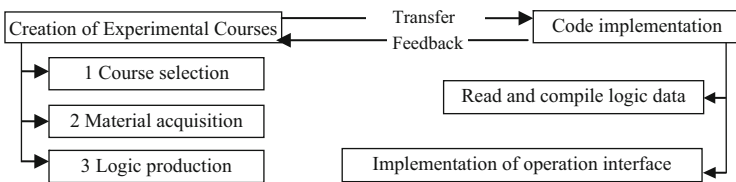


Fig. 39.1 Process of virtual-experiment system. Experimental courses logic compilation

39.3.2 *Acquisition of Experimental Materials*

To ensure the realness of size and space in virtual experiments and reduce development costs, the system uses the idea of a finite-state machine.

Finite-state automaton (FSA) describes state contents and transitions that are widely applied to computer programming [4] and is in the form of a model with a finite number of discrete dynamical systems [5]. Therefore, an event can be broken down into states, input conditions, and transition relationships. Thus, this system regards scenes that are not performed during experiments and scenes after the operation as states, each action as input, and then records the individual state information and transition relations in a database. These records were taken out of the database, and processed through Java handler, and then showed through the front display on a computer and on a network with an operable form. Therefore, teachers acquire as materials photographs and computer screen shots about real-world experimental scenes. At this point, what teachers do ensures the authenticity and fast development of experiments, reflects the importance of universal design on the product to obtain economic benefits, and indicates the development direction that enterprises invest in for useful product development [6].

39.3.3 *Production of Experimental Curriculum Logic*

This module provides a clear and concise basis of communication between teachers and technical personnel. With this module, developers can obtain experimental course material, status, and logical relationships and then convert them into experiments that can be conducted on the Internet; teachers can produce the experimental course logic and modify experimental course materials and the design based on developer feedback.

If teachers manually fill out MS Excel templates, it would be a time-consuming effort. Templates include state templates and state transition templates. Table 39.1 is a state template, whereas Table 39.2 is a state transition template.

1. State template: a state table comprises a state ID, all hardware operations, all software operations, and prompt areas.
 - (a) Hardware and software views
 - Picture ID: number of images required sequentially.
 - Picture name: consistent with the name of the images in the folder.
 - Picture thumbnail: requires a preview of the picture of the state.
 - Picture processing instructions: include the following seven parts.
 - Operating area: Region that need to be operated on the image.
 - Action required: refer to operating area, for example, insert network cable into router cable interfaces.
 - When to send an action: complete the operation on the image.

Table 39.2 State transition template

State ID	Transition condition	Transition condition number	End state ID

- When to send the action number: number of actions sent.
- Data needs to be input: input data are necessary to complete state transformation.
- Each shift direction: when performing different operations, one state will jump toward different states that need to be numbered, which is easy to find and modify later.

(b) Prompt area

- Prompt ID: number of prompts on the state.
- Prompt type: the types of prompt content, such as guided type, encourage type, etc.

2. State transition table

- State ID: number the state under the experimental operation required, or respond with the state ID of the state table.
- Transition conditions: correspond to when to send the action of the state table.
- Transition condition number: corresponds to when to send the action number of the state table.
- End state ID: the next state number of each shift direction of the state table.

We know that teachers will do a considerable amount of work using the aforementioned templates. First, teachers need to learn how to use these templates; second, a lot of data that filled out MS Excel templates are repetitive; again, the completion process is complex and transition relations are easily confused. These all lead to longer development cycles, which does not fit the idea of system development and universal design. A graphical mode of operation was proposed for users to compile experimental course logic.

39.3.4 *Fast Development Tool*

Visio officially supports the secondary development of software, whose way of drawing and environment are wide, which complies with the seven principles of universal design. Figure 39.2 shows the design of the logic tool.

The tool includes a menu bar (file and database (DB) connection), tool library, and drawing area.

- File: file comprises new, insert, open, save, and exit.
- New: create a new Visio file.
- Insert: insert a picture in the drawing area.

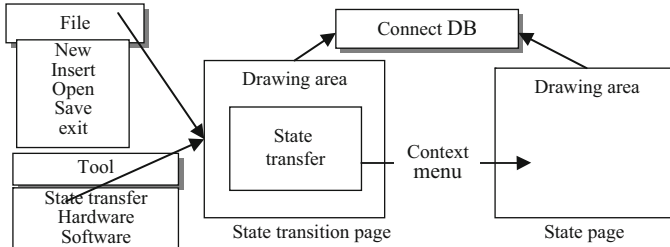


Fig. 39.2 Design of logic tool

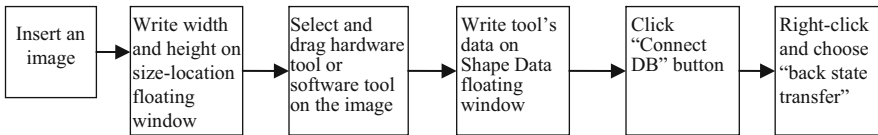


Fig. 39.3 Graphical operation process of states

- **Open:** open an existing file. Teachers can create a new drawing area to produce the course logic, or open a Visio file produced using Visio software. This way reflects the flexibility of universal design.
- **Save:** save as Visio files or images. Teachers save the drawing content as these two types according to what they need.
- **DB connection:** the logic data are stored in a DB. Teachers can click a button to complete the function that stores the logic data in a DB.

1. Completing state transitions

The state transition table contains the transformed state, transfer tool, and drawing area. The tool comprises a hotspot and arrows. The hotspot represents the present state and the end state. The arrows represent the state transition relation. These tools are dragged over drawing area. The state ID is numbered automatically by the Value of Action in the Shape Sheet, which will not be filled out by teachers, and the next state ID is not considered because the transition relationship between states is automatically determined by codes. Thus, teachers only express the relationship using dragging tools.

2. Completion of states

Teachers right-click on the hotspot after they drag a hotspot to the drawing areas, then choose "State Edit" in the context menu and click it to produce states on a new drawing page. Operations should be carried out according to Fig. 39.3.

The size–location floating window and the shape–data floating window are provided by the Visio system. Now teachers only need to write two pieces: when to send an action and prompt content because all IDs are numbered automatically, and this image belongs to the state through right-click entry.

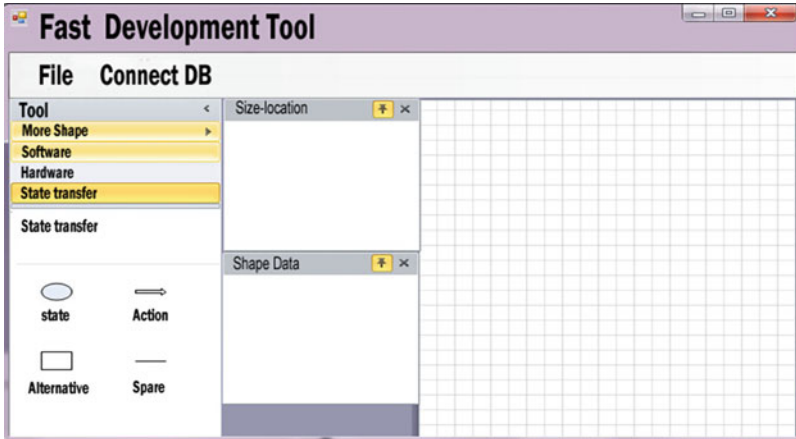


Fig. 39.4 Fast development tool interface

By contrast, the fast development tool greatly reduces the workload of teachers; they do not need to fill in a lot of data. In addition, the tool is clear and easy to understand. Figure 39.4 illustrates the fast development tool interface.

39.4 Implementation

The system uses a hierarchical structure, which enables different users to find and modify their own modules. Figure 39.5 shows the hierarchical relationship of the system.

The database records all data from the logic layer, which is the logic data produced by teachers using the fast development tool. Now the state table and the state transition table are created in the database layer.

The data processing layer completes the data transmission and processing between the user interface layer and the database layer.

The data processing layer receives user actions and then inquires about the next state ID on the database according to the action number and initial state ID and sends the user interface layer the next state ID. Therefore, the data processing layer completes the data transmission in two directions: one is the user interface layer and the data processing layer, the other is the data processing layer and the database layer.

The user interface layer is the presentation layer. The operation interface that showed to users works using Web pages. The design and implementation of the operation interface require the guidance of universal design theory.

The operation interface is divided into three parts—hardware view, software view, and interactive view—for the following reasons: first, the course content is on

Fig. 39.5 Structure of virtual-experiment system

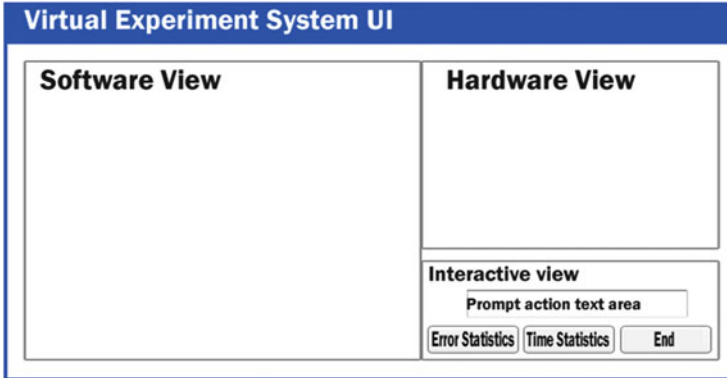
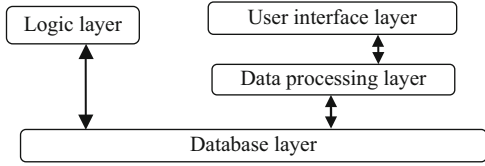


Fig. 39.6 UI design

communication industry including hardware and software operation; second, the learning time of hardware operation is generally less than that of software operation, so the operation area of hardware operation is not equal to that of software operation; third, the operation view can be zoomed to the size of the screen without distortion; in addition, there are error statistics and time statistics functions. Figure 39.6 shows the UI design.

Figure 39.6 uses a flex performance user interface design because the Canvas container of Adobe Flex can achieve view encapsulation. Therefore, the hardware view, software view, and prompt view are encapsulated into three canvas containers using an encapsulation method that is unitary and easily coded and modified. The hardware view canvas is coded as follows:

```

<mx: CanvActionscript>
<mx: Image source="*.jpg" height="400" width="600">
<mx: button x="200" y="200">
</mx: CanvActionscript>
  
```

Conclusion

In this paper, we propose a virtual-experiment system guided by the principle of universal design, which is implemented for three users. The principle of universal design can provide an adjustable environment that can be changed and extended to meet the varied needs of different users. The system provides a reference base for the design and development of the Internet and information products and services, which deserves future research and applications.

References

1. Wang J, Wei X. Virtual experiment of the “hot” and “cold” thinking. *China Educ Technol.* 2011;4:126–9 (In Chinese).
2. Connell BR, Jones M, Mace R, Mueller J, Mullick A, Ostroff E, Sanford J, Steinfeld E, Story M, Vanderheiden G, *The Principles of Universal Design*, 1997. [Online]. Available: http://www.ncsu.edu/www/ncsu/design/sod5/cud/about_ud/udprinciplestext.htm.
3. Cheng J, Zhang W. Universal design changed because of you: the application of universal design principles in product design. *Art Des.* 2007;07:86–8 (In Chinese).
4. Chen WY, Tian L, Cheng W, Liu G. *Finite automata theory*. Beijing: Electronic Industry Press; 2013. p. 58 (In Chinese).
5. Tan F, Wang J, Zhang L, Wang Z. The finite state automata in the application of the complex interface. *Digital Commun.* 2011;05:81–3 (In Chinese).
6. Ma D, Qian H. The application of universal design in product design. *Art Panorama.* 2011;12:143 (In Chinese).

Chapter 40

Effects of Information Services on Economic Growth in Jilin Province

Fang Xia, Bingbing Zhao, and Xiaochun Du

Abstract Information services constitutes an important part of the modern service industry. In consideration of the value-added accounting of information services in Jilin province in this article, the contribution rate and the pull rate of information services to GDP growth are calculated for the period 1993–2012; then the cointegration theory is adopted to carry out a cointegration test and Granger causality test to determine the relationship between the information services industry and the economy in the province, thereby establishing the corresponding error correction model. The research results show that the information services industry in Jilin Province is on a smaller scale with a limited pulling function in economic growth; in addition, a long-run equilibrium relationship with economic growth is available, although its correction capability during periods imbalance is weak. The progress of the information services industry constitutes the Granger cause of economic growth, while economic growth does not constitute the Granger cause of the information industry development.

Keywords Information services • Economic growth • Cointegration test • Granger causality test • Error correction

40.1 Introduction

Information services (INS), as a synthesis of specialized industries, utilizes modern science and technologies, such as computers and network communication, to produce, collect, handle, process, store, transfer, retrieve, and exploit information and provides services for society via information products [1]. With the integration of the global economy and the further advancement of the information process, INS has come to be regarded as the commanding height of participation in global

F. Xia • X. Du (✉)

Jilin University Doctor, Changchun University of Chinese Medicine Teacher,
Changchun University of Chinese Medicine, 130117 Changchun, China
e-mail: duxiaochun215@126.com

B. Zhao

Air Force Aviation University of China, 130022 Changchun, China

© Springer International Publishing Switzerland 2015

W.E. Wong (ed.), *Proceedings of the 4th International Conference on Computer Engineering and Networks*, Lecture Notes in Electrical Engineering 355,
DOI 10.1007/978-3-319-11104-9_40

341

economic competition. In China, nevertheless, the rapid development of modern information technology has gradually become a new growth point and powerful engine of China's economic development, and its development is of great significance to the economy and society. Therefore, this paper will focus on the growth of the INS industry in Jilin province for nearly 20 years to carry out quantitative analysis and study the effects of INS on economic growth.

The concept of INS was first put forward by American scholar Porat [2]. Later, American and other scholars studied the modern INS industry from various perspectives. Braunstein used translog and ECS functions instead of the c-d function to extend the conclusions of Hayes and Erickson to further confirm Hayes and Erickson's analysis [3]. Engelbrecht focused on the emerging industrialized countries and regions as well as the fledgling developing countries only to find that the process of economic transition from a national economy to an information economy greatly depends on the growth of the information sector [4].

Two Chinese economic scholars, Wu and Xie, concluded, from analyzing the effects of information technology on industrial restructuring and research on how information promotes the development of technology, that information technology had promoted industrial restructuring and economic growth [5]. Li and Zhu analyzed the effects of the information industry on economic growth in Hubei province using the two-sector model of economic growth of Frederick. They believed that the information industry should receive support at all levels of government [6].

40.2 Contribution of INS to Economic Growth in Jilin Province

For the purpose of studying how the INS industry promotes economic growth in Jilin province, this paper first explains the added value of Jilin INS from 1993 to 2012 and then analyzes the contribution of the INS industry to economic growth in Jilin province.

40.2.1 Accounting for Added Value of INS Industry in Jilin Province

Given the availability of data and the necessity of empirical research, the sample data used in this article are related to Jilin INS and gross national product (GDP) from 1993 to 2012. The basic data used mainly originate from the Jilin statistical yearbook (1994–2013) with the data selection and processing shown as follows [7]. To avoid heteroscedasticity in time series data, we perform log processing on the sequence.

Table 40.1 Added value of information services industry and its contribution to GDP

Year	Growth of INS (billion)	Growth rate of INS (%)	Contribution rate to GDP (%)	Pulling function to GDP (%)
1993	13.44		–	–
1994	18.94	40.92	2.02	0.62
1995	25.16	32.84	2.21	0.47
1996	31.97	27.07	2.37	0.44
1997	42.2	32	2.88	0.25
1998	43.19	2.35	2.74	0.21
1999	44.38	2.76	2.64	0.18
2000	38.87	–12.42	1.99	0.32
2001	42.13	8.39	1.99	0.17
2002	45.34	7.62	1.93	0.21
2003	58.43	28.87	2.19	0.29
2004	71.52	22.4	2.29	0.4
2005	84.84	18.62	2.34	0.37
2006	108.45	27.83	2.54	0.46
2007	130.29	20.14	2.47	0.58
2008	136.62	4.86	2.13	0.46
2009	172.88	26.54	2.38	0.32
2010	193.58	11.97	2.23	0.43
2011	235.16	21.48	2.23	0.49
2012	250.25	6.42	2.1	0.27

40.2.2 Direct Contribution of INS to Economic Growth

According to the statistical definition, the direct contribution of INS to economic growth can be expressed as the percentage of the added value of the INS industry to that of GDP. The formula is

$$\omega_i = \frac{INS_i - INS_{i-1}}{GDP_i - GDP_{i-1}}, \quad (40.1)$$

where INS_i is the added value of INS in year 1, and GDP_i is the GDP of year 1. The contribution rate is shown in Table 40.1.

We can see that as an independent industry classification, INS makes statistically significant differences and leads to a brief fluctuation in the growth of information services. Taking on the other hand, the contribution rate of Jilin INS industry to GDP growth has always been maintained around 2 %, compared with the Chinese average rate (7–10 %) for the same period, there is still a large difference. After 2000, digital quantity is relatively lower, slightly less than 2 %.

40.2.3 Pull Rate Analysis of Effect of INS Industry on Economic Growth

The contribution rate may reflect the functional degree of INS factors in economic growth; in addition, there is another dynamic index that can reflect the pulling effect on GDP growth, that is, the pull of the INS industry to GDP growth. The calculation method is as follows: $\theta_i = \omega_i * \eta_i$ θ_i is the pull rate of the information service industry to GDP growth, and η_i is the growth rate of GDP. From Table 40.1 we know that, since 1996, the pull function has shown a slow upward trend in volatility, up to a maximum of 0.58 % by 1997. After this year, it shows volatility in the process of slowing down, with an average pull rate of INS to GDP growth of 0.37 %. The change illustrates that the Jilin province INS experienced a period of short transition to maturity.

40.3 Empirical Analysis of INS Industry and Economic Growth in Jilin Province

40.3.1 Variable Selection and Sample Data Determination

To avoid heteroscedasticity in time series data, we carry out log processing on the sequence of data from 1993 to 2012. We use LnGDP and LnINS to represent the natural log values of GDP and INS, respectively.

Twenty samples of processed data are drawn into the time series of the scatter charts (Fig. 40.1). It can be seen that each variable has a growing tendency and there is a strong correlation between the two series, with a correlation coefficient of 0.9805.

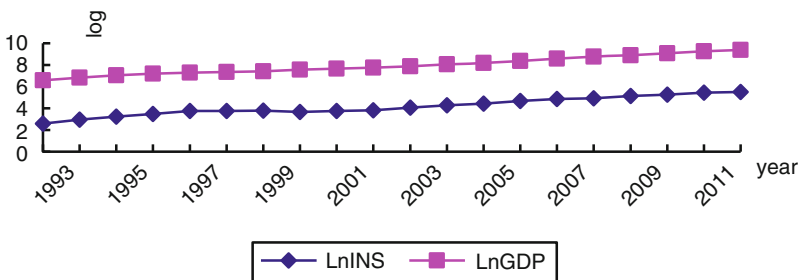


Fig. 40.1 Scatter chart of LnINS and LnGDP time series

Table 40.2 Augmented Dickey–Fuller unit root test of LnGDP and LnINS in Jilin province

Null Hypothesis		<i>D</i> (LnGDP-2) has a unit root		<i>D</i> (LnINS-2) has a unit root	
		<i>t</i> -Statistic	Probability*	<i>t</i> -Statistic	Probability*
Augmented Dickey–Fuller test statistic		−3.1073	0.0463	−5.8781	0.0002
Test critical values	1 % level	−3.9203		−3.8867	
	5 % level	−3.0655		−3.0521	
	10 % level	−2.6734		−2.6665	

40.3.2 Unit Root Test of Time Series Variables

Before we perform a cointegration analysis of the data, we must carry out stationary tests on the variables; otherwise, spurious regression problems may occur. We used the Augmented Dickey–Fuller (ADF) test law on variable LNGDP and LNINS for unit root tests in this paper; After test, the first-level difference of LnGDP and LnINS are nonstationary time series, because the two series are refused zero assumed under the validation 5% of significantly refused level; the results also show that LNGDP, LNINS, and their first-level difference are a nonstationary time sequence; from Table 40.2 we conclude that as a result of the second-level difference of LNGDP and LNINS unit root tests, the null hypothesis is rejected. Then we refuse to unit root hypothesis; so the second-level difference of the LnGDP and LnINS are the stationary sequences [8].

40.3.3 Cointegration Tests on Time Series

The objective of the cointegration test is to determine whether there is a stable equilibrium between the set of linear combination of nonstationary sequences precisely because cointegration establishes a long-run equilibrium relationship. If we can find a dependable link between several variables that seems to have a separate random trend, then by adjusting the model we can exclude the unit root that leads to randomness of trends brought about by the unit root, the so-called error-correction model. Using the E-G two-step testing method, the cointegrated regression model for INS industry development and economic growth in Jilin province are as follows (Table 40.3):

$$\text{LNGDP} = 3.9002 + 0.9734\text{LNINS} \quad R^2 = 0.98 \quad \text{DW} = 0.773 \quad \text{SSE} = 0.118.$$

Then we should do the unit root test to the residuals by Eviews 6.0 with the results shown in Table 40.4

Table 40.3 Cointegrated regression model of LNGDP and LNINS

Variable	Coefficient	Standard error	<i>t</i> -Statistic	Probability
<i>C</i>	3.90027	0.13757	28.3508	0.0000
LNINS	0.97335	0.03236	30.0704	0.0000

Table 40.4 ADF test series residuals

		<i>t</i> -Statistic	Probability*
Augmented Dickey–Fuller test statistic		−7.411652	0.0000
Test critical values	1 % level	−3.886751	
	5 % level	−3.052169	
	10 % level	−2.666593	

Table 40.5 Granger causality test result

	Null hypothesis: Lags: 1		Null hypothesis: Lags: 2	
	<i>F</i> -Statistic	Probability	<i>F</i> -Statistic	Probability
LNINS does not Granger-cause LNGDP	7.44832	0.0149	5.82712	0.0156
LNINS does not Granger-cause LNGDP	1.53316	0.2335	1.12692	0.3537

The test results in Table 40.4 shows that under the significant level of 10 %, the ADF value is less than the threshold of 10 %; series residuals are smooth sequences of residuals. This means that a cointegration relationship existed between LNINS and LNGDP. From this we can see that the INS industry has a long-run positive equilibrium relationship with GNP in Jilin province. If the INS industry increases by 1 unit, the economy will increase by 0.9734 units, which indicates that progress in the INS industry plays a positive a role in boosting economic growth.

40.3.4 Granger Causality Test

The cointegration test results show that the long-run equilibrium relationship between LNINS and LNGDP has been established; but whether the relationship can be identified as a causal link must be tested further using credible Granger-causality analysis.

From Table 40.5 it can be concluded that the development of the INS industry has always been the Granger cause of economic growth, but economic growth is not the Granger cause of services [9]. In addition, economic growth lacks internal demand for INS in Jilin province; economic growth mainly relies on factors, such as the substantial input of resources, other than the development of information technology or related science and technology.

40.3.5 Error-Correction Model

By cointegration analysis, we have discovered a long-run equilibrium relationship between GDP and INS industry, but short-run deviation from the state cannot be learned from cointegration analysis, and the error-correction model is needed to effectively address this problem [10]. By Eviews 6.0, error correction is treated as an explanatory variable model to study models of short-run dynamics and long-run adjustment. The model reflects the short-run dynamic balance of the relationship between the LNINS and LNGDP error-correction model with the following outcomes:

$$D(\text{LNGDP}) = 0.067 + 0.244D(\text{LNINS}) + 0.101D(\text{LNINS}(-1)) \\ + 0.139D(\text{LNGDP}(-1)) - 0.197\text{ECM}(-1) \\ R^2 = 0.646, \text{DW} = 1.685, \text{SSE} = 0.016.$$

Based on these equations, economic growth in short-run movements can be broken down into two parts: the impact of short-run fluctuations in the INS industry and the effect of a partial deviation from the long-run equilibrium on GNP. Short-run fluctuations in INS will give rise to increases in economic growth and transformation. Changing one unit of the INS industry in the short term will cause GDP growth to change by 0.224 units. The error-correction coefficient indicates that changes to the long-run equilibrium of the GDP adjustment speed is 19.68 %, which means that the long-run imbalance has little impact on GDP.

40.3.6 Result

The results indicate that there is a long-run stable relationship between INS development and economic growth in Jilin province. In the short-run, the effect of INS on economic growth is significant; the long-run balanced relationship between INS and economic growth has a weak self-correcting effect on nonbalanced error adjustment in this period.

Conclusion

Using an analysis of the contribution of the Jilin province's INS industry to the region's economic growth, a common conclusion has been reached in this paper: in Jilin province, the INS sector does not play a positive role in promoting economic growth; the emergence of a mutually reinforcing virtuous development model between informatization and economic growth also needs time and support of government. In the era of big data, efforts should be

(continued)

(continued)

made to focus on economic growth and cointegration between progress in the INS industry and progress in the INS industry in development policy; timely raise the informatization level of economic growth in Jilin province; promote the overall development of the INS industry; and ultimately promote the INS industry and economy interaction in Jilin province.

References

1. Ren G. Econometric analysis of service capacity of china's information service industry. *Sci Technol Manag Res.* 2013;33(15):52–4 (In Chinese).
2. Porat MU. *The information economy.* Hunan: Hunan People's Publishing House; 1987. p. 132–43.
3. Braunstein YM. Information as a factor of production: substitutability and productivity. *Inf Soc.* 1985;3(3):166–71.
4. Engelbrecht H-J. Are purchased information services underused in manufacturing evidence from Japan; Korea and Taiwan. *Appl Econ.* 1990;22(2):201–9.
5. Wu J, Xie K. Information technology industry and economic growth. *China's Ind Econ.* 1999;13(1):37–41 (In Chinese).
6. Zhu X, Li P. Quantitative analysis on the contribution of the information industry to economic growth. *Stat Inf Forum.* 2005;20(6):59–62 (In Chinese).
7. Xu Y, Zhao Y. The regional difference and convergence analysis of Changes in China's information service sector total factor productivity. *J Quant Tech Econ.* 2009;26(10):49–60 (In Chinese).
8. Porat G. *Basic econometrics.* Jianping Fei translation. Beijing: Renmin University Press; 2010. p. 235–67.
9. Engle RF, Granger CWJ. Co-integration and error correction: representation; estimation and testing. *Econometrics.* 1987;55(2):251–76.
10. Fan X. The empirical analysis on the contribution of software and information service industry to economic growth in Dalian, China. In: 2010 International Conference on Management and Service Science (MASS) 2010; Wuhan: IEEE; 2010. p. 1–4.

Chapter 41

Day-Ahead Electricity Demand Forecasting Using a Hybrid Method

Zirong Li, Xiaohe Zhang, Yan Li, and Chun Liu

Abstract Nowadays, artificial intelligence is commonly used in many fields including medicine, chemistry, and forecasting. In this paper, artificial intelligence is applied to electricity demand forecasting due to the demand for this from both providers and consumers at this time. In order to seek accurate demand forecasting methods, this article proposes a new combined electric load forecasting method (SPLSSVM), which is based on seasonal adjustment (SA) and least square support vector machine (LSSVM) optimized by the particle swarm optimization (PSO) algorithm, to forecast electricity demand. The effectiveness of SPLSSVM is tested with a dataset from New South Wales (NSW) in Australia. Experimental results demonstrate that the SPLSSVM model can offer more precise results than other methods mentioned in the literature.

Keywords Electricity demand forecasting • Particle swarm optimization • Least square support vector machine

41.1 Introduction

Data mining technology is usually divided into two categories. The first category is represented by the statistical models, the most commonly used being probability analysis, relevance, clustering analysis, and discriminant analysis; the other category is machine learning in artificial intelligence. In this paper, we use an artificial intelligence model to forecast electricity demand. The purpose of short-term power load forecasting is to obtain accurate load forecasting results, because under the premise of meeting power supply quality requirements such data guarantees that

Z. Li (✉)

School of Information and Engineering, Gansu University of Traditional Chinese Medicine, 730000 Gansu, China

School of Information Science and Engineering, Lanzhou University, 730000 Lanzhou, China
e-mail: lizr13@lzu.edu.cn

X. Zhang • Y. Li • C. Liu

School of Information and Engineering, Gansu University of Traditional Chinese Medicine, 730000 Gansu, China

© Springer International Publishing Switzerland 2015

W.E. Wong (ed.), *Proceedings of the 4th International Conference on Computer Engineering and Networks*, Lecture Notes in Electrical Engineering 355,
DOI 10.1007/978-3-319-11104-9_41

349

power providers achieve optimal use of power supply system construction funds, so as to achieve maximum social and economic benefits.

Recently, researchers have put forward a range of models for electricity demand forecasting based on time series technologies, such as artificial neural network models [1, 2], and fuzzy logic grey-based approaches [3, 4]. However, none of these models can obtain the expected forecasting accuracy for all electricity demand forecasting issues [5]. There is no single best method that under every condition can achieve the best forecasting results. Of course, the hybrid or combining model appeared to solve this problem.

The combining model combines the advantages of one, two, or more models. Bates and Granger [6] proposed the hybrid model. Later, Dickinson [7] testified that the hybrid model can obtain higher accuracy than that of an individual model. So, in this article, we propose a new combined model named SPLSSVM that combines seasonal adjustment, particle swarm optimization (PSO), and the least square support vector machine (LSSVM). Firstly, SPLSSVM applied seasonal adjustment (SA) to eliminate the seasonal component. Then, SPLSSVM used the LSSVM for model training and fitting, and for this, LSSVM parameters were optimized by the PSO algorithm. Through comparison of the proposed model with other models, we show that the SPLSSVM model indeed improves accuracy.

The layout of this paper is as follows. We demonstrate the theory of SA, PSO, and the LSSVM model in Sect. 2, and a case study of forecasting electric load is presented in Sect. 3. We conclude this paper in the last section.

41.2 The Hybrid Model

41.2.1 A Review of Seasonal Adjustment

The data series x_1, x_2, \dots, x_T ($T = ml$) is entered as $x_{11}, x_{12}, \dots, x_{1l}; x_{21}, x_{22}, \dots, x_{2l}; \dots; x_{m1}, x_{m2}, \dots, x_{ml}$ in turn, then we calculate the average value of the time series according to $\bar{x}_k = (x_{k1} + x_{k2} + \dots + x_{kl})/l$ ($k = 1, 2, \dots, m$).

Then we get the following result:

$$I_{ks} = \frac{x_{ks}}{\bar{x}_k} (k = 1, 2, \dots, m; \quad s = 1, 2, \dots, l). \tag{41.1}$$

The average value of I_{ks} at the same time in every period is seen as the seasonal index number

$$I_j = \frac{I_{1j} + I_{2j} + \dots + I_{mj}}{m} (j = 1, 2, \dots, l). \tag{41.2}$$

Then the sequence without the seasonal effects is obtained:

$$y_{ks} = \frac{x_{ks}}{I_s} (k = 1, 2, \dots, m; \quad s = 1, 2, \dots, l). \quad (41.3)$$

41.2.2 A Review of Particle Swarm Optimization

In an m -dimensional search space, we define each particle as a possible potential solution to a problem. Here $X_i = (x_{i1}, x_{i2}, \dots, x_{im})$ is considered as the current position of particle i , $V_i = (v_{i1}, v_{i2}, \dots, v_{im})$ is considered as the current velocity, $P_i = (p_{i1}, p_{i2}, \dots, p_{im})$ is considered as the previous position, and $P_g = (p_{g1}, p_{g2}, \dots, p_{gm})$ is the optimal position in all particles. Then the optimal position of particle i can be calculated according to Eqs. (41.4) and (41.5) [8].

$$v_i^{k+1} = w \cdot v_i^k + c_1 \cdot r_1 \cdot (p_i^k - x_i^k) + c_2 \cdot r_2 \cdot (p_g^k - x_i^k), \quad (41.4)$$

$$x_i^{k+1} = x_i^k + \alpha \cdot v_i^k, \quad (41.5)$$

where v_i^k and x_i^k respectively represent the current velocity and position of particle i , c_1 and c_2 are two constants greater than zero, r_1 and r_2 are two independently distributed random variables between $[0, 1]$, and w is the inertia weight.

41.2.3 Least Square Support Vector Machine Model

The LSSVM model was proposed by Suykens and Vandewalle [9]. Given a training dataset of N points $\{x_i, y_i\}_{i=1}^N$ with input data $x_i \in R^n$ and output data $y_i \in R$, then we define the decision function [10]:

$$y(x) = w^T \varphi(x) + b. \quad (41.6)$$

To solve the function estimation problem, this paper introduces structural risk minimization to realize function optimization:

$$\text{Minimize : } \frac{1}{2} \|w\|^2 + \frac{1}{2} c \sum_{i=1}^n \varepsilon_i^2. \quad (41.7)$$

Subject to: $y_i = w^T \varphi(x_i) + b + \varepsilon_i, \quad i = 1, \dots, N.$

To derive the solutions w and ε , the Lagrange multipliers are introduced as follows:

$$L(w, b, \varepsilon, a) = \frac{1}{2}\|w\|^2 + \frac{1}{2}c \sum_{i=1}^n \varepsilon_i^2 - \sum_{i=1}^n a_i [w^T \varphi(x_i) + b + \varepsilon_i - y_i]. \quad (41.8)$$

According to the Karush–Khun–Tucker conditions, the finally result into the LSSVM model for function estimation can be described as:

$$f(x) = \sum_{i=1}^n a_i K(x, x_i) + b, \quad (41.9)$$

where the dot product $K(x, x_i)$ is the kernel function; the radial basis function is applied in this paper; and we defined radial basis function (RBF) with a width of σ as follows:

$$K(x, x_i) = \exp\left(-0.5\|x - x_i\|^2/\sigma^2\right). \quad (41.10)$$

41.3 Simulation Results

For this paper, an electric load dataset from New South Wales in Australia was used; data was collected 48 times per day. The original data series we used for training and fitting the model represents electricity demand data for 35 days, with 1,680 values as shown in Fig. 41.1. Using the original 1440 values, we forecast the following 240 values.

Figure 41.1 shows that the shape of data series in the same day of different weeks is more similar compared with the shape of data series in different days of one week. Considering this cyclic behavior, this study divides the original data series into five groups based on the day of the week, i.e. Monday group, Tuesday group, and so on. This study then analyzes each of these day groups, and forecasts the corresponding day of the week, i.e. using Monday group to forecast following Monday.

From Fig. 41.1, it can be seen that these five data series show strong seasonality. There is no doubt that the forecasting accuracy could be improved if we eliminate the seasonal component before electricity demand forecasting. The Monday group

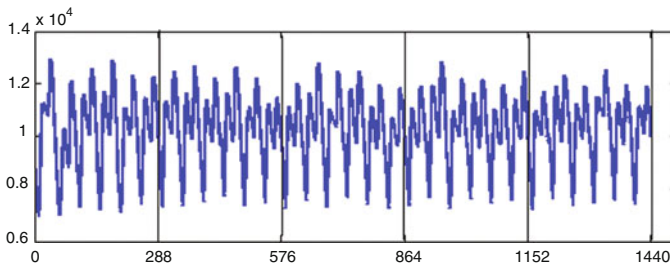


Fig. 41.1 The electricity demand data for model fitting and training

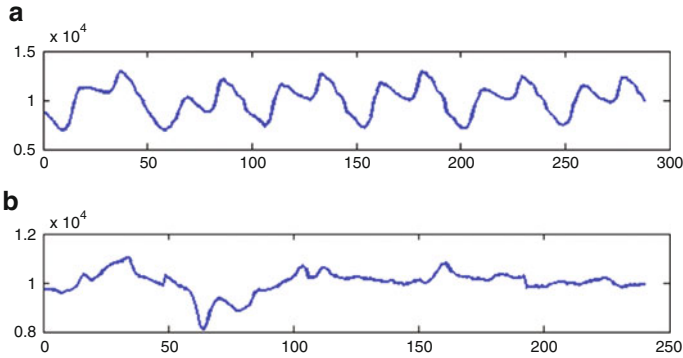


Fig. 41.2 The Monday group electricity demand before and after seasonal adjustment

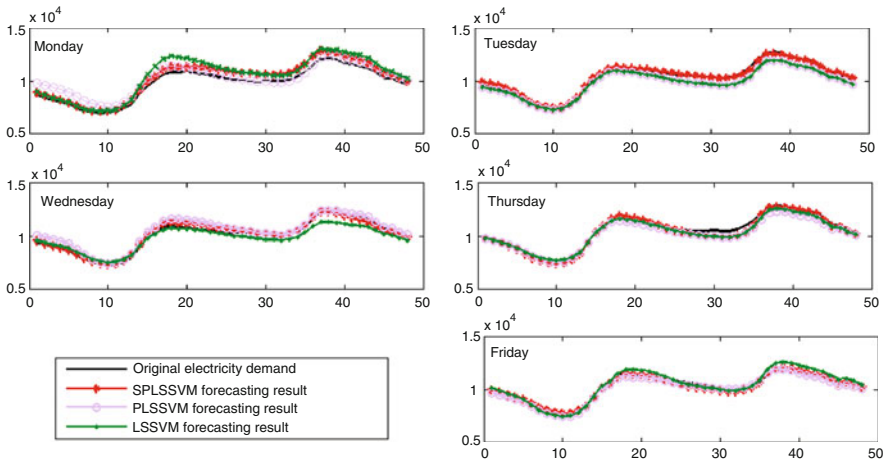


Fig. 41.3 Forecasting results of the three models

data after elimination of the seasonal component is shown in Fig. 41.2. Figure 41.2a shows the original Monday group electricity demand, while Fig. 41.2b shows the seasonally adjusted Monday group electricity demand.

After eliminating the seasonal component, we used the resultant five group datasets to forecast the next five days electricity demand. Here, the LSSVM model was applied to model training and fitting, and the LSSVM parameters were optimized by PSO. In order to verify that the proposed model (SPLSSVM) indeed improved forecasting accuracy, we carried out a comparison between it and the other two models, i.e., LSSVM and LSSVM which has been optimized by PSO (named PLSSVM). The forecasting results for all three models (LSSVM, PLSSVM, and SPLSSVM) for each day are shown in Fig. 41.3.

Table 41.1 lists three performance measures of the three forecasting models, and it reveals many details that are discussed below.

Table 41.1 Three performance measures of the three models

Date	RMSE of			MAE of			MAPE (%) of		
	LSSVM	PLSSVM	SPLSSVM	LSSVM	PLSSVM	SPLSSVM	LSSVM	PLSSVM	SPLSSVM
Monday	829.134	990.900	545.328	728.939	817.925	500.441	7.11	7.52	4.96
Tuesday	479.0918	429.826	217.463	389.771	357.796	181.176	3.74	3.68	1.79
Wednesday	490.726	354.246	169.732	411.620	292.857	136.047	3.79	2.66	1.38
Thursday	284.520	385.538	269.768	226.342	267.756	196.379	2.13	2.41	1.87
Friday	310.800	262.015	150.865	252.275	186.219	116.966	2.37	1.84	1.16
Average value	478.854	484.505	270.631	401.789	384.510	226.202	3.83	3.62	2.23

On comparing PLSSVM and LSSVM, we obtained the following result. Considering the three parameters mentioned in Table 41.1, PLSSVM shows the expected lower values compared to LSSVM for three days: Tuesday, Wednesday, and Friday. In terms of average values for the entire week, the root mean square error (RMSE) of PLSSVM shows a slightly larger value than that of LSSVM. However, the mean absolute error (MAE) and mean absolute percentage error (MAPE) of PLSSVM have decreased by 4.3 % and 5.4 %, respectively. For Monday and Thursday: on the basis of the three parameters, PLSSVM shows slightly higher values compared to LSSVM. However, generally speaking, PLSSVM performs better than LSSVM.

When we compare SPLSSVM and PLSSVM, we obtained the following result. In terms of the three significant parameters RMSE, MAE, and MAPE, PLSSVM has, as desired, lower values than LSSVM for every day of the week. Considering the average values for the whole week, PLSSVM has reduced RMSE, MAE, and MAPE by 44.1 %, 41.1 %, and 38.3 %, respectively.

To sum up, among the three models (LSSVM, PLSSVM, and SPLSSVM), SPLSSVM has the best performance for every day of the week. In terms of average values for the whole week, the RMSE of SPLSSVM is decreased by 44.1 and 43.4 %, MAE is decreased by 41.1 and 43.7 %, and MAPE is decreased by 38.3 and 41.7 % when compared to PLSSVM and LSSVM.

Conclusion

A new electricity demand forecasting model named SPLSSVM is proposed in this paper. SPLSSVM first uses seasonal adjustment to remove seasonal factors from the original data series. Next, SPLSSVM employs LSSVM to model the intermediate series, and PSO is used to optimize the parameters of LSSVM. From the perspective of different evaluation criteria that included RMSE, MAE, and MAPE, we can see that SPLSSVM increases the precision of electricity demand forecasting, and the proposed model could help power utilities in the control and dispatch of electricity.

References

1. Li DC, Chang CJ, Chen CC, Chen WC. Forecasting short-term electricity consumption using the adaptive grey-based approach: an Asian case. *Omega*. 2012;40(6):767–73.
2. Hsu LC. Using improved grey forecasting models to forecast the output of opto-electronics industry. *Expert Syst Appl*. 2011;38(11):13879–85.
3. Kheirkhah A, Azadeh A, Saberi M, Azaron A, Shakouri H. Improved estimation of electricity demand function by using of artificial neural network, principal component analysis and data envelopment analysis. *Comput Ind Eng*. 2013;64(1):425–41.
4. Chang PC, Fan CY, Lin JJ. Monthly electricity demand forecasting based on a weighted evolving fuzzy neural network approach. *Int J Electr Power Energy Syst*. 2011;33(1):17–27.
5. Moghram IS, Rahman S. Analysis and evaluation of five short-term load forecasting techniques. *IEEE Trans Power Syst*. 1989;4(4):1484–91.

6. Bates JM, Granger CW. The combination of forecasts. *Oper Res Q.* 1969;20(4):451–68.
7. Dickinson JP. Some comments on the combination of forecasts. *Oper Res Q.* 1975;26(1):205–10.
8. Eberhart R, Kennedy J. New optimizer using particle swarm theory. In: *Proceeding of the Sixth International Symposium on Micro Machine and Human Science*; IEEE, Piscataway; 1995. p. 39–43.
9. Suykens JAK, Vandewalle J. Least squares support vector machine classifiers. *Neural Process Lett.* 1999;9(3):293–300.
10. Iplikci S. Dynamic reconstruction of chaotic systems from inter-spike intervals using least squares support vector machines. *Physica D.* 2006;216(2):282–93.

Chapter 42

Membrane System for Decision-Making Problems

Lisha Han, Laisheng Xiang, and Xiyu Liu

Abstract A membrane system for decision-making problems is proposed in this paper to provide new ideas for parallel solutions in today's big data environment. Because a membrane system has great parallelism, it could reduce the calculation time complexity and is suitable for solving some complex problems such as decision-making problems. First, the possibility of such a problem's parallelism is analyzed, and then the membrane system is established with all its rules to solve the problem. Finally, an example is given to prove its feasibility. This represents another attempt in the application of a membrane system.

Keywords Membrane system • Membrane computing • P system • Risk-based decision making • Parallel computing

42.1 Introduction

Decision making is a process of choosing the best solution for current or future problems using such techniques as expectations or the decision tree method [1]. Faced with the massive data in today's big data environment, the manner of decision making that we choose greatly affects decision-making efficiency.

Membrane computing is a new computing model initially proposed by Romanian scientist Gheorghe Păun, hence the name P system. It has been applied in many fields such as biological modeling, NPC problems and combinatorial problems because of its vast parallelism [2, 4].

This paper solves the decision-making problem based on the P system's great parallelism. First, the possibility is analyzed, then a P system with all its rules is established, and finally the paper demonstrates its feasibility on a simple test.

L. Han (✉) • L. Xiang • X. Liu
School of Management Science and Engineering, Shandong Normal University,
250014 Jinan, China
e-mail: hlsandzt@163.com

42.2 Preliminary

42.2.1 P System

The P system is a distributed and parallel computing model. It abstracts computing models from the function and structure of living cells [3, 4]. In a cell-like P system, there is a layered structure with basic elements including the membrane structure, objects, and rules. The membranes divide the entire system into different regions. The outermost layer of the membrane structure is called the skin membrane. If there are no other membranes in the interior of a membrane, we call it a basic membrane [5, 6] (Fig. 42.1).

Generally, a P system of degree $m(m \geq 1)$ is constructed as

$$\Pi = (V, T, C, H, \mu, w_1, w_2, \dots, w_m, R_1, R_2, \dots, R_m, \rho_i, i_0).$$

The basic evolution rule is a pair (u, v) in the form $(u \rightarrow v)$. Here, u is a string over V and $v = v'$ or $v = v'\delta$, where v' is a string over $\{a_{\text{here}}, a_{\text{out}}, a_{\text{in}}, |a \in V, 1 \leq j \leq m\}$ and δ is a special symbol not in v . When a rule contains δ , the membrane will be dissolved after performing the rule [6].

The rules perform in a manner of uncertainty and maximal parallelism to guide the transformation and formation of strings [6, 7]. After a number of steps, the P system halts if no rules can be performed or the state of the P system is stable, and the objects in the output membrane are the final result [6].

42.2.2 Decision-Making Problem

Decision making is a core activity. In this paper, the risk type [1] is the focus: policymakers must know not only the corresponding gain values of actions under different states but also the probability distribution of these states.

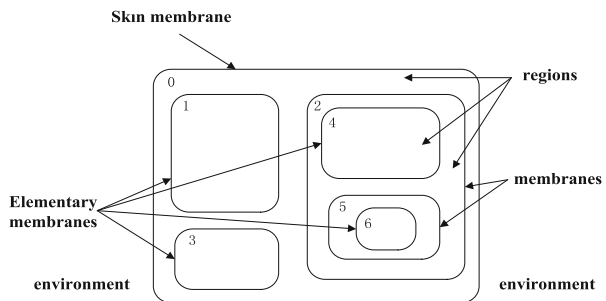


Fig. 42.1 Basic membrane structure

Table 42.1 Computation process of problem under expectation criteria

states	N_1	N_2	...	N_m	$E(S_i)$
weights					
gain values					
action programs	Q_1	Q_2	...	Q_m	-
S_1	a_{11}	a_{12}	...	a_{1m}	$E(S_1)$
S_2	a_{21}	a_{22}	...	a_{2m}	$E(S_2)$
...
S_n	a_{n1}	a_{n2}	...	a_{nm}	$E(S_n)$

By expectation criteria, the gain values in states are seen as discrete random variables. We select the maximum one for the optimal action from mathematical expectations. The computation process is shown in Table 42.1.

In this table, S_i is the action program, N_j the natural state, Q_j the weight of the natural state, a_{ij} the gain value, and $E(S_i)$ the gain expectation of each action, where the gain matrix is denoted by D_{ij} :

$$D_{ij} = \begin{bmatrix} a_{11} & a_{12} & \dots & a_{1m} \\ a_{21} & a_{22} & \dots & a_{2m} \\ \dots & \dots & \dots & \dots \\ a_{n1} & a_{n2} & \dots & a_{nm} \end{bmatrix}. \tag{42.1}$$

42.3 Risk-Based Decision Making by a P System

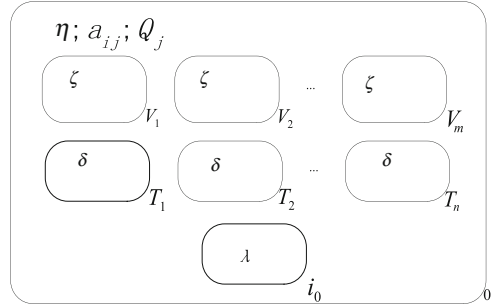
We must now state two assumptions due to some restrictions: the objects in this paper are nonnegative integer variables because the resources required in a P system are polynomial. In addition, the objects to be processed have been transported to membrane 0.

42.3.1 Design of a P System

In this section, a P system for decision making is proposed. In this P system, the structural relationship of membranes is hierarchical; the objects to be processed have been transported to membrane 0, and they are polynomial in the number of individuals. Now we consider the P system as follows:

- $\Pi = (V, C, \mu, S_0, S_{V_j}, S_{T_i}, S_{i_0}, R_0, R_{V_j}, R_{T_i}, \rho);$
- $V = \{\eta, \zeta, \delta, a_{ij}, Q_j\}$ is the collection of objects in the P system;
- $C = \{\eta, \zeta, \delta\}$ is the collection of catalysts in the P system;

Fig. 42.2 Specific P system for the problem



$\mu = [0[v_1]_{V_1}[v_2]_{V_2} \cdots [v_m]_{V_m}[t_1]_{T_1}[t_2]_{T_2} \cdots [t_n]_{T_n}[i_0]_{i_0}]_0$ specifies the membrane structure; $S_0, S_{V_j}, S_{T_i}, S_{i_0}$ indicate the initial states of the membranes; $\rho = \{r_1 > r_2 > r_3 > r_4\}$ is the priority of the rules.

Rules in membrane 0:

$$r_1 = \left\{ \eta Q_j a_{ij} \rightarrow (c_{ij}^{Q_j})_{in_{V_j}} \mid 1 \leq i \leq n; 1 \leq j \leq m \right\}. \tag{42.2}$$

$$r_4 = \{B^{E_1} B^{E_2} \dots B^{E_n} \rightarrow B^{E_1} B^{E_2} \dots B^{E_n} B^{E_{n-1}} B^{E_{n-2}} \dots B^{E_{n-1}}\} \cup \{B^{E'_1} B^{E'_2} \dots B^{E'_n} \rightarrow M_{S_i, in_{i_0}} \mid 1 \leq i \leq n\}_{-E'_i=0}. \tag{42.3}$$

Rules in membrane V_j :

$$r_2 = \left\{ \zeta c_{ij} \rightarrow (b_{ij}^{a_{ij}})_{in_{T_i}} \mid 1 \leq i \leq n; 1 \leq j \leq m \right\}. \tag{42.4}$$

Rules in membrane T_i :

$$r_3 = \{ \delta b_{ij} \rightarrow (B_i, out) \mid 1 \leq i \leq n; 1 \leq j \leq m \}. \tag{42.5}$$

To visualize this specific P system for the problem, Fig. 42.2 shows its architecture.

42.3.2 Calculation Instructions

We now focus on how the rules as designed earlier guide the process of computing in this P system.

Rule r_1 is executed first. Under the catalyst of object η , the objects c_{ij} are generated and successively sent to membrane V_j for the action of rule r_2 . Activated

by catalyst ζ , it generates $a_{ij} \times Q_j$ number of objects b_{ij} , and the objects in the same row are transported to membrane T_i for the next evolution. It should be noted that $a_{ij} \times Q_j$ number of objects b_{ij} are generated because each object c_{ij} can produce a_{ij} number of objects b_{ij} , and there are Q_j number of objects c_{ij} . Then through rule r_3 , the objects b_{ij} in membrane T_i are summed and sent out to generate $E_i = (a_{i1} \times Q_1 + a_{i2} \times Q_2 + \dots + a_{im} \times Q_m)$ number of objects B_i . Finally, when $E'_i = 0$ appears by subtracting each object E_i simultaneously, rule r_4 calculates the maximum expectation M_{S_i} and sends it to the output membrane i_0 . By now, the best decision has been found, and the whole computation is over.

42.4 Test and Analysis

To illustrate how the designed P system runs specifically, a simple example is considered. Suppose a company is required to make a decision on a new production batch. Three alternatives and two states may occur. The company must make a reasonable decision based on the expectation criteria (Table 42.2).

42.4.1 Computing Stages in P System

Here, we analyze the executive rules. The initial state is shown in Fig. 42.3.

In the first step, calculate the gain values under different weights: rules r_1 and r_2 produce the gain values of these three actions to be adopted under scenarios of high demand and low demand, respectively. The state following the calculation in the first step is shown in Fig. 42.4.

In the second step, obtain the expectations of actions: under the catalyst δ , rule r_3 calculates the expectations and sends them out. The state is shown in Fig. 42.5.

In the last step, determine the maximum expectation: rule r_4 determines the maximum expectation. The state following calculation, also the final state, is shown in Fig. 42.6.

Table 42.2 Gain value table in given test

Weights	States	N_1	N_2
	Gain Values	(big demand)	(little demand)
Action Programs		3	7
S_1 (big batch)		8	3
S_2 (middle batch)		4	1
S_n (small batch)		2	1

Fig. 42.3 Initial state for problem in test

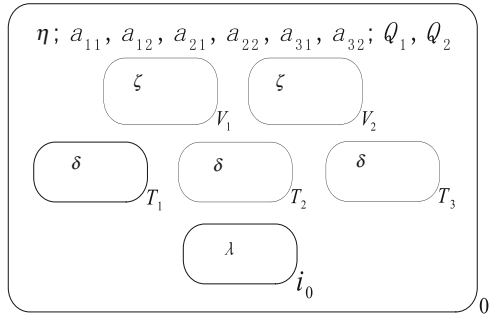


Fig. 42.4 State following calculation in first step

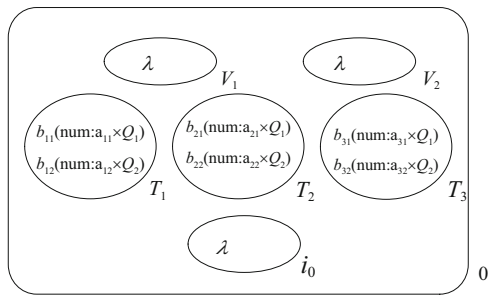


Fig. 42.5 State following calculation in second step

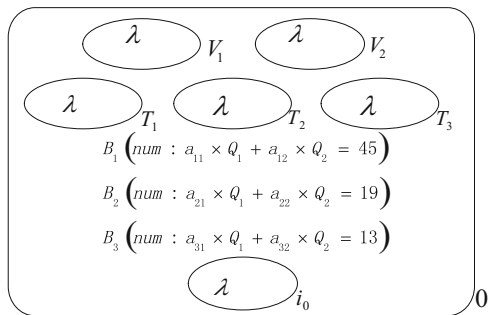


Fig. 42.6 State following calculation in last step

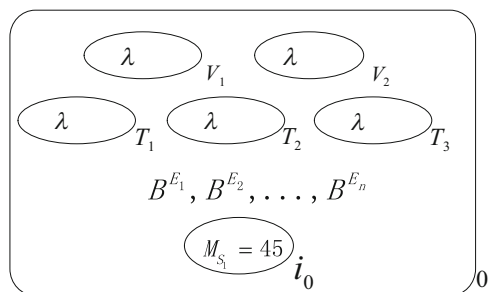


Table 42.3 Detailed computing process of example in serial computing

States Weights Gain Values	N_1	N_2	$E(S_i)$	Calculation times
Action Programs	3	7	-	-
S_1 (big batch)	8	3	$8 \times 3 + 3 \times 7 = 45$	3
S_2 (middle batch)	4	1	$4 \times 3 + 1 \times 7 = 19$	3
S_n (small batch)	2	1	$2 \times 3 + 1 \times 7 = 13$	3

42.4.2 Simple Comparative Analysis

Theoretically, the time complexity is relatively high in accordance with the serial computing. And there are nine times of calculation just to obtain all the gain expectations (Table 42.3).

However, in this designed P system, only three times of parallel computing are required for the whole process. And the P system designed for the problem not only can reduce the time complexity but also has fairly good scalability: the calculation time in the P system designed for this problem will not become longer with an increasing number of actions or states because of the maximal parallelism and distributed nature of the system.

Conclusion

In this paper, we designed a specific P system for a risk-based decision-making problem with expectation criteria. Using a simple test, the proposed P system successfully performed calculations with less computation time because of its maximal parallelism and distributed nature; nevertheless, future work will mainly focus on the following points:

1. The computation time in the proposed P system will be greatly reduced theoretically, and the computational complexity in the P system will be linear, which we will be glad to see.
2. Efforts will be made to apply P systems to more complex calculation problems because of its great parallelism and very good scalability.

References

1. Han BT. Management operations research. Beijing: Higher Education Press; 2010. p. 75–124 (In Chinese).
2. Chen HZ. Application research on membrane computing. Chongqing: Chongqing University; 2011 (In Chinese).

3. Pan LQ, Chen J. Arithmetic operation in membrane system. In: International Conference on Biomedical Engineering and Informatics. Hong Kong, China; 2008. p. 231–34.
4. Luan J, Liu XY. A variant of of P system with a chain structure. *Inf Comput Sci.* 2012;1:1–8.
5. Pan LQ. Solving HPP and SAT by P systems with active membranes and separation rules. *Acta Inf.* 2006;43:131–45.
6. Paun G, Rozenberg G, Salomaa A. *Membrane computing.* New York: Oxford University Press; 2010. p. 56–271.
7. Paun G, Rozenberg G. A guide to membrane computing. *Theor Comput Sci.* 2002;287:73–100.

Chapter 43

Operational Model Management C/S System Based on RUP

Rui Guo

Abstract Rational uniform process (RUP) is a quite popular software development method that has applications in various fields. A client/server (C/S) system is a software model that is widely used in many projects, such as simulation model management systems. To research the use of RUP in controlling the whole framework and process of a system, an operational model management C/S system is used as an example, and the method of applying RUP in C/S systems is discussed in depth.

Keywords RUP • C/S • Operational model management system

43.1 Introduction

Published in 1998 [1], rational uniform process (RUP) is a method that is used to direct software development. It was created by several US technicians, including Jacobson, Booch, and Rumbaugh, and others. Most importantly, RUP is a software development process, meaning a series of actions taken during a period when software is being developed in response to user requirements. However, RUP is not just process; it is a universal process framework that can be used to deal with many kinds of software systems in diverse application fields, organization types, function levels, and project scales.

Uniform modeling language (UML) [2] is always used in RUP in preparation for designing the software blueprints. In fact, UML is an organic part of RUP and was developed synchronously with it. There are three distinctive aspects of RUP: Use Case-driven development; central focus on fundamental frameworks; iteration-guided software development.

Nowadays, client/server (C/S) systems are primary systems with a new structure used to process signals [3] whose evolution is combined deeply with progress in advanced desktop calculation, new store technology, improved network communication, and enhanced database technology. Although a C/S system can be analyzed, designed, structured, and tested using the traditional method, it seems better to use a

R. Guo (✉)

Science and Research Department, Dalian Naval Academy, 116018 Dalian, China
e-mail: msegr@163.com

software engineering method developed on the basis of an event-motivated or object-oriented approach [4].

C/S systems are one of the focuses of software development at present; Browser/server (B/S) systems represent another international mature design method. Both types of system have their pros and cons [5]. In general, C/S systems are suitable for relatively fixed user groups that are capable of controlling information security and are more suitable for information security [6]. In addition, C/S systems are more concerned with processes and checking permissions hierarchies and less concerned with operating speed. Based on the preceding two considerations, we selected a C/S system.

One particular C/S system, i.e., an operational model management system within some simulation software systems, is taken as an example to explore how RUP is used to develop software and how it is applied in C/S systems. This paper is organized as follows. An operational model management C/S system is first briefly introduced. Then some basic ideas and methods are analyzed, and the actual process of developing an operational model management C/S system with RUP is given at the end.

43.2 Operational Model Management C/S Systems

Along with the development of high technology, the number and types of weapons in modern warfare are gradually increasing, and the relations between different weapons are becoming more complex. It is difficult for military commanders or technologists to analyze the operational process and weapons' effect using traditional methods such as sand tables, map maneuvers, and military exercises. A new method based on operational simulation is considered an effective means of qualitative study on war. An operational simulation system can be used to simulate operation plans, test operational tactics, forecast operational effects, and evaluate new operational ideas. Clearly, operational simulation systems will take on increasing importance in the future.

Operational models are a central part of operational simulation systems, and there are many different types operational models. Advanced information systems are required for effective administration of operational models. As a whole, the construction of operational model systems should be directed within an informatization framework, followed by a general program such as model description, VV&A process verification, model architecture design, normalization of model resources, and creating a model with high performance.

The aforementioned features of an operational model system make the C/S structure the preferred design. On the other hand, the operational model system design and management method is consistent with RUP development method. Therefore, it is effective to incorporate RUP into the design of C/S operational model management systems.

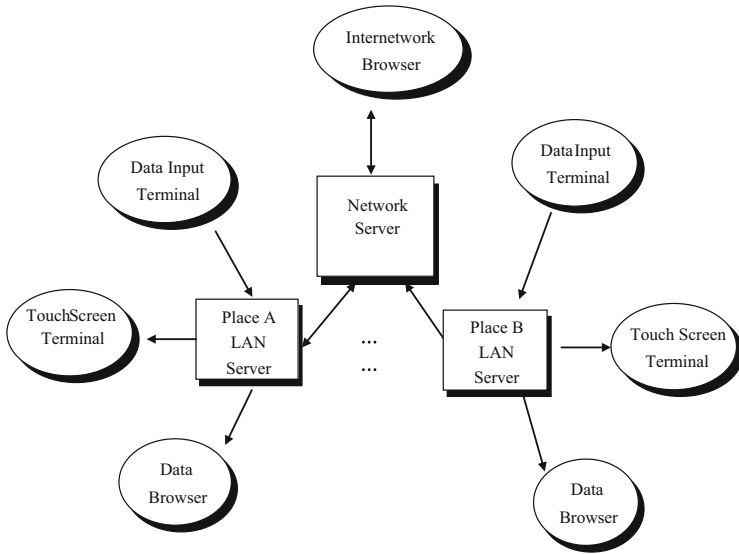


Fig. 43.1 Structure and function of operational model systems

The primary aims of operational model management C/S systems include (1) building a uniform operational model network distributed all over the country, providing services of model management and transfer between different places; (2) helping administrative departments to understand models' application conditions; and (3) searching for, inquiring about, and applying operational models between different locations using information management. The system structure is shown in Fig. 43.1.

As shown in Fig. 43.1, operational model systems have the primary functions of a C/S system, such as clients requesting services and servers offering services. Several questions must be addressed before developing a system.

1. Unifying the data structure, which is the chief part of the design process;
2. Unifying the formal/informal description of the operational model at different institutions;
3. Establishing the priority of different level clients;
4. Designing the graphical user interface (GUI), which should have all the functions of a C/S server.

43.3 Using RUP

RUP can be described by a planar process. The time axis has four development stages, including initialization, detailing, construction, and transfer. The vertical axis has five workflows at every stage, including requirements, analysis, design,

realization, and testing. In RUP, developers should focus most on giving clients what they value most. The first step is to establish use case models and verify client requirements. The second step is to build frameworks that ensure that systems are continually evolving. The last step is to reuse software as much as possible; the final system can be obtained after integrating reusable resources.

1. Driving the development process by use case

The purpose of developing software systems is to provide services to users. The term *user* refers to someone or something that interacts with the system developed by RUP, and the interaction is called a *use case*. Integration of all use cases forms use-case models, which describes all functions of the entire system. Meanwhile, a use case is not only a tool that is used to define system requirement; it also drives many system development processes, including design, realization, and testing. In other words, the whole development process is driven by use cases.

2. Focus on fundamental frameworks

The architecture of a system describes the current system from different perspectives, including the most important static and dynamic characteristics in the system. The architecture describes the overall design of the system. It removes the details and highlights the important features of the system. Because “what is important” partly depends on human, the value of the architecture is dependent on the quality of the people performing the tasks.

3. Iteration-guided software development

Iterative refers to workflow steps, but the increment represents an increase in some products. A software product that is decomposed into parts or a number of smaller mini projects is practical. Each mini project is an iterative process for producing a development increment. To obtain the best effect, the iterative process must be controlled, that is to say, it must be in accordance with the planned steps to be performed selectively.

The preceding three concepts are equally important. The framework provides a structure to guide the iterative process of the work and use cases, set goals, and drive the work per iteration. Removing any of the three concepts would seriously compromise the value of the uniform process.

43.4 Development of Operational Model C/S Systems

The reason RUP is chosen to guide system development is not only that RUP is object-oriented. RUP can also help one to create an explicit system framework under which many tasks at different stages are shown clearly, such as how to do something, what to do, and the consequences.

RUP can be described as a two-dimensional process: the time axis includes four development stages, and the vertical axis includes five workflow tasks occurring at all stages. Because of the *use-case-driven process*, the analysis of requirements plays a key function in the software development process because it identifies

Table 43.1 RUP development stages

Central workflow	Stage			
	Initialization	Detailing	Construction	Transfer
Requirement	(1) Users retrieve models-via internetwork-via LAN (2) Users transfer models-via internetwork-via LAN	“Retrieving via internetwork”: (1) Users log in on web site (2) Choose type of operational models to retrieve (3) Choose names of operational models (4) System provides basic condition of model	“Choose the query model” use case: (1) Search by choosing model types (2) Search by model functions (3) Search by model input/output parameters	Use-case models
Analysis	Target analysis	Index analysis	Hierarchy process analysis map	Analysis models
Design	Preliminary design	Detailed design	Mathematical models	Design models implement models
Realization	Basic functions	Improvement based on feedback information	Reuse	Realization models
Test	System wide test	All subsystem tests	Test cases	Test models
	First iteration	Second iteration	$n - 1$ time iteration	N time iteration

whether the direction in which a project is moving is the right one. If the requirement analysis fails, the software is very likely to become one that “correctly realizes the error function.” What follows is an analysis of the requirement workflow occurring at all stages (Table 43.1).

Each workflow must pass through four stages, such as initialization, detailing, construction, and transfer, and gradually improve in several iterations. There is no exception for “requirement” workflow, and the “retrieving” and “transferring” use cases are confirmed in the initial stage. In the detailing stage, the “retrieving via internetwork” use case in the “retrieving” workflow can be analyzed using tables. In the construction stage, the design of a concrete operation should be considered as the realization of the use case.

For example, A GUI textbox with the database query is used to realize “search by choosing models’ types” use case, and the data display may take the table format, text, graphics, and or something else. Graphics can be further subdivided into, for example, a graph, pie chart, or ladder diagram. These are the workflow tasks of analysis, design, and realization.

It is thus obvious that the requirement workflow will improve in a process of iteration and increment, and its functions will gradually be refined until each user’s

requirement is met. The analysis, design, realization, and testing workflow will take the same method of iteration and increment and be refined and constructed step by step. Finally, all the workflows will form a complete operational model management system.

We began a research project in 2010 whose goal was to effectively manage the operational model between the cities of Dalian in Liaoning Province and Qingdao in Shandong Province to carry out a joint operation simulation. We adopted the design method described earlier and developed a corresponding C/S system. In the last 2 years, the system has been shown to be reasonable and effective.

Conclusion

C/S systems are presently one of the focuses of the software development industry, and B/S systems represent another international mature design method. Both of them have their pros and cons. In general, C/S systems are favored relatively fixed user groups that are capable of controlling information security and are more suitable for information security. In addition, C/S systems focus more on processes and verify permissions hierarchies and less on operating speed. Based on the preceding two considerations, we selected a C/S system.

Under the guidance of RUP ideas, the development process of an operational model management C/S system is designed in four stages, including initialization, detailing, construction, and transfer. Then, further refinements are made in each stage's workflow. The operational model management system developed by using RUP ideas proved to be robust and reliable in practice. Therefore, RUP ideas and C/S architectures can be applied to other similar information management systems.

References

1. Jacobson I, Booch G, Rumbaugh J. The unified process. Rational Software. 2000. <http://www.globalempower.com>.
2. Rational Software Corporation. Summary of UML. 1998. <http://aka.org.cn/aka2/uml.htm>.
3. Jacobson I, Booch G, Rumbaugh J. Rational uniform process of software. Beijing: China Machine Press; 2002. p. 10.
4. Pressman RS. Software engineering. Beijing: Tsinghua University Press; 2002. p. 25.
5. Wang B. Design and implementation of the system of housing sales management based on C/S. Master thesis, Jilin University; 2013.
6. Rong G. Analysis of advantages and disadvantages of B/S\C/S structure. 2012. <http://www.xzbu.com/8/view-3800503.htm>.

Chapter 44

Decision Analysis Method Based on Improved Bayesian Rough Set and Evidence Theory Under Incomplete Decision System

Zhihai Yang, Weihong Yu, Yan Chen, and Taoying Li

Abstract According to the theory of Bayesian rough set and evidence theory, a method of decision information fusion under incomplete decision information system is proposed. Under incomplete decision information system, the evidences are obtained based on the limited tolerance relation and the support degree. Firstly, by using the method of limited tolerance relation and Bayesian rough set, the lower distribution sets of the decision classes are obtained, the classified quality is calculated, and the support degrees of condition attributes to decision classes are obtained on the basis of the above. Finally, the evidences are fused by the improved combination rule, and the new object is classified based on the fusion result. The proposed method is applied to the diagnosis of problems of the equipment fault in order to ultimately prove the effectiveness of this method.

Keywords Bayesian rough set • Evidence theory • Incomplete decision information system

44.1 Introduction

It is a very important issue to classify and make decision on the decision-making properties of the unknown new object with the existing knowledge of information system. Most existing researches are focusing on the decision rules of complete and

Z. Yang (✉)

School of Transportation Management College, Dalian Maritime University, 116026, Liaoning, China

Shanghai Marine Electronic, Shanghai, China

e-mail: yangzhilai302@163.com

W. Yu • Y. Chen • T. Li

School of Transportation Management College, Dalian Maritime University, 116026, Liaoning, China

incomplete information system and use the rules to classify new objects; but the rules are not comprehensive when the information system knowledge is small. Thus, we can not to make decisions in all kinds of situations; on the contrary, we will get a lot of decision rules when the knowledge is big.

Zara [1] used a rough set approach to analyze the subset of preference relations. Liu [2] put forward many new concepts, such as rough space, rough variables, rough operation, reliability measure, and expectations operator concept; constructed the expected value model, the chance-constrained model, and the opportunity-related planning model; and then set up reliability theory [3] with methods in researches on rough problem provided. Wei [4] presented a new approach to selection of attributes for construction of decision tree based on rough set theory and gave an algorithm in a recursive form for construction of decision tree. Jia [5] provided a new definition of attribute reduce for decision-theoretic rough set models. Katz [6] presented a generalization called the variable precision rough sets model with asymmetric bounds to model the decision situations characterized by uncertain information expressed in terms of probability distributions estimated from the frequency distributions in empirical data.

In this chapter, improvements in terms of some relative theorems regarding Bayesian rough set and evidence theory have been made based on the previous literature. The traditional Bayesian rough set theory is improved and extended to multiple decision classes. The attribute reduction method is provided by using the lower distribution reduction. In the incomplete decision information system, evidences are obtained based on the limited tolerance relation and the support degree. The classified quality is calculated and the support degrees of condition attributes to decision classes are obtained on the basis of the above. Then, the basic probability assignment is obtained after normalization. Finally, the evidences are fused by the improved combination rule, and the new object is classified based on the fusion result.

44.2 Improved Bayesian Rough Set and Evidence Theory

Bayesian rough set is a modified variable precision rough set model [7]. Its basic idea is using the priori probability of the event before it replaces the variable precision rough set of precision parameters. By comparing the conditional probability after adding conditional probability of occurrence with the relationship before adding that stuff, we can analyze the influence of decision-making.

Definition 1 gives an information system $S = (U, C \cup D, V, f)$, in which C is a finite nonempty set of condition attributes and D is a finite nonempty set of decision attributes. With equivalence relation C , universe U can be partitioned into a collection of equivalence classes $E = U/R_C = \{E_i | i = 1, 2, \dots, n\}$; similarly, universe U can be partitioned into another collection of equivalence classes $U/R_D = \{d_j | j = 1, 2, \dots, m\}$ with equivalence relation D . Based on belief gain function Bayesian rough set, the positive region $POS_C^M(d)$ of the decision classes $d \in U/R_D$ is

$$\text{POS}_C^M(d) = \cup\{E_i | g(d|E_i) = \max((g(d_1|E_i), \dots, g(d_m|E_i))) > 0, E_i \in E\} \quad (44.1)$$

$$\text{NEG}_C^M(d) = \cup\{E_i | g(d|E_i) = \min((g(d_1|E_i), \dots, g(d_m|E_i))) < 0, E_i \in E\} \quad (44.2)$$

$$\text{BND}_C^M(d) = \cup\{E_i | g(d|E_i) = 0, E_i \in E\}. \quad (44.3)$$

The improved Bayesian rough set can be well applied to multi-value decisions. Positive region $\text{POS}_A^M(d)$ can be regarded as the Bayesian approximation of d on A . Relative to the priori probabilities $P(d)$ of event d , positive region elements set can represent the largest collection of the probability of d occur. Negative region $\text{NEG}_A^M(d)$ represents the largest set of the reduction of d occur. Border region $\text{BND}_A^M(d)$ represents event d , and E is independent with each other.

Definition 2 A basic probability assignment is a function $m: 2^\theta \rightarrow [0, 1]$ which satisfies the following conditions: $m(\emptyset) = 0 \sum_{\theta \subseteq \Theta} m(\theta) = 1$, in which $m(\theta)$ represents the proportion of all relevant and available evidence that supports the claim; a particular element of θ belongs to the set A . In engine diagnostics, $m(\theta)$ can be considered as a degree of belief held by an observer regarding a certain fault.

44.3 Decision-Making Based on Improved Bayesian Rough Set and Evidence Theory Under Incomplete Information System

44.3.1 Obtain Evidence

Definition 3 gives an information system $S = (U, A, V, f)$, in which $U = \{x_1, x_2, \dots, x_m\}$, $C = \{c_1, c_2, \dots, c_n\}$, the decision attribute D is a single property, namely, $\text{card}(D) = 1$, and the range of D is limited, $V_D = \{d_1, d_2, \dots, d_k\}$; thus, the support $\xi_{c_i}^{d_l}$ of $d = U|(D = d_l)$ ($l = 1, 2, \dots, k$) under $c_i(i = 1, 2, \dots, n)$ is

$$\xi_{c_i}^{d_l} = \frac{|\text{POS}_{c_i}^M \cap d|}{|d|} \quad (44.4)$$

1. Evidence Acquisition Based on Support Degree

Give an information table $S = (U, C \cup D, V, f)$. If the condition attribute values of new object x_{m+1} are $C_{m+1} = \{x_{m+1}^1, x_{m+1}^2, \dots, x_{m+1}^n\}$ and the decision attribute

values are unknown, the method of obtaining basic probability assignment of the new object x_{m+1} is as follows:

Assume the decision attribute value of x_{m+1} is $d_{m+1} = d_1$ and the expansion of the universe U' . Firstly, we calculate Bayesian positive region of $U'/(D = d_1)$ under the guidelines for each conditions and get the support degree $\xi_{c_i}^{d_1}$ when the conditional attributes $d_{m+1} = d_1$ are true. Similarly, we can get the support $\xi_{c_i}^{d_l}$ of the condition attributes c_i to $d_{m+1} = d_l (l = 2, \dots, k)$. In order to obtain the basic probability assignment, we need to normalize the approximate classification quality under each condition. We give the normalized method here.

$$m_i(d_l) = \frac{\xi_{c_i}^{d_l}}{2 \sum_{l=1}^k \xi_{c_i}^{d_l} - 1}, \quad m_i(\Theta) = \frac{\sum_{l=1}^k \xi_{c_i}^{d_l} - 1}{2 \sum_{l=1}^k \xi_{c_i}^{d_l} - 1}, \quad l = 1, 2, \dots, k \quad (44.5)$$

Thus, we can get the basic probability assignment based on support degree as $m^{(1)}$.

2. Evidence Acquisition Based on the Greatest Certainty Gain Function

Assume the condition attribute value of x_{m+1} is $d_{m+1} = d_l (l = 2, \dots, k)$ and the expansion of the universe U' . If the greatest certainty gain function of condition attribute c_i to U'/d_l is

$$\max g_{c_i}(d_l) = g(x|E^*) \quad (44.6)$$

we can get the greatest certainty gain function $\max g_{c_i}(d_l)$ of each condition guideline value of each attribute. Because $\sum_{l=1}^k \max g_{c_i}(d_l) \geq 1$ or $\sum_{l=1}^k \max g_{c_i}(d_l) \leq 1$, when $\sum_{l=1}^k \max g_{c_i}(d_l) \leq 1$, we use the following method:

$$m_i(d_l) = \max g_{c_i}(d_l), \quad m_i(\Theta) = 1 - \sum_{l=1}^k \max g_{c_i}(d_l) \quad l = 1, 2, \dots, k \quad (44.7)$$

Thus, we can get the basic probability assignment based on certainty gain function, as $m^{(2)}$. In order to obtain the final evidence probability assignment, we fuse the evidences by using $m^{(1)}$ and $m^{(2)}$, and we use the arithmetic average method to make and have the same weight; thus, the evidence basic probability assignment is

$$m = \frac{m^{(1)} + m^{(2)}}{2}. \tag{44.8}$$

44.3.2 Acquisition Method Based on Limited Tolerance Relation and Support Evidence

In order to process incomplete information systems, the classical rough set theory needs to be extended.

Definition 4 gives an incomplete information system $S = (U, A, V, f)$, in which a limited tolerance relation L is defined in the universe U and $\forall x, y \in U, B \subseteq A, (x, y) \in L_B$, only $P_B(x) = \{a \in A | a(x) \neq *\}$

$$L_B(x, y) = \{(x, y) \in U \times U | \forall a \in B (a(x) = a(y) = *) \vee ((P_B(x) \cap P_B(y) \neq \emptyset) \wedge \forall a \in A ((a(x) \neq *) \wedge a(y) \neq *) \rightarrow a(x) = a(y)))\} \tag{44.9}$$

The lower approximation (X_B^L) and upper approximation (X_B^U) of an object set X with reference to an attribute set $B \subseteq A$ in an incomplete information system can be defined as

$$X_B^L = \{x | x \in U \wedge L_B(x) \subseteq X\}; \quad X_B^U = \{x | x \in U \wedge L_B(x) \cap X \neq \emptyset\} \tag{44.10}$$

Definition 5 gives an information system $S = (U, C \cup D, V, f)$, in which C is a finite nonempty set of condition attributes, D is a finite nonempty set of decision attributes, and $E = U/R_C = \{E_i | i = 1, 2, \dots, n\}$, and universe U can be partitioned into another collection of equivalence classes $U/R_D = \{d_j | j = 1, 2, \dots, m\}$ with equivalence relation D . Based on improved Bayesian rough set, the positive region $POS_C^L(X)$ of the decision classes $X, X \in U/R_D$ is

$$\begin{aligned} POS_C^L(X) &= \cup \{L_C(E_i) | g(X | L_C(E_i)) \\ &= \max((g(X_1 | L_C(E_i)), \dots, g(X_m | L_C(E_i))) > 0, E_i \in E\} \end{aligned} \tag{44.11}$$

The negative region $NEG_C^L(X)$ and the boundary region $BND_C^L(X)$ are

$$\begin{aligned} NEG_C^L(X) &= \cup \{L_C(E_i) | g(X | L_C(E_i)) = \min((g(X_1 | L_C(E_i)), \dots, g(X_m | E_i)) \\ &< 0, E_i \in E\} \end{aligned} \tag{44.12}$$

$$BND_C^L(X) = \cup \{L_C(E_i) | g(X | L_C(E_i)) = 0, E_i \in E\} \tag{44.13}$$

Theorem 1 gives an information system, $X \in U/R_D, B \subseteq A, E_u, E_v \in U/R_B (u \neq v), F \in U/R_B$, and $F = E_u \cup E_v$, then

1. If $E_u \subseteq \text{POS}_B^L(X)$ and $E_v \subseteq \text{POS}_B^L(X)$, then $F \subseteq \text{POS}_B^L(X)$.
2. If $E_u \subseteq \text{NEG}_B^L(X)$ and $E_v \subseteq \text{NEG}_B^L(X)$, then $F \subseteq \text{NEG}_B^L(X)$.
3. If $E_u \subseteq \text{BND}_B^L(X)$ and $E_v \subseteq \text{BND}_B^L(X)$, then $F \subseteq \text{BND}_B^L(X)$.

The approximate classification quality $\gamma_{c_i}^{d_1}$ represents the percentage that reflects the true level of the support of d_1 which is divided under equivalence relation c_i . $\gamma_{C-c_j}^{d_1}$ represents the percentage that reflects the true level of the support of d_1 which is divided under equivalence relation C after deleting the attribute c_j . By the sorting quality of after deleting other attributes, we can measure the supporting degree of the division d_1 on the attribute c_i , which means expressing that by $\gamma_{C-c_j}^{d_1}$ ($j \neq i$).

Definition 6 gives an incomplete information system $S = (U, C \cup D, V, f)$ and $U = \{x_1, x_2, \dots, x_m\}$, $C = \{c_1, c_2, \dots, c_n\}$, in which the decision attribute D is a single property, namely, $\text{card}(D) = 1$, and the range of D is limited, $V_D = \{d_1, d_2, \dots, d_k\}$; then, the support degree $\zeta_{c_i}^{d_l}$ of the division d_l ($l = 1, 2, \dots, k$) under the attribute c_i ($i = 1, 2, \dots, n$) is

$$\zeta_{c_i}^{d_l} = \frac{\sum_{j \neq i} \zeta_{C-c_j}^{d_l}}{n - 1} \tag{44.14}$$

If the condition attribute values of the new object x_{m+1} is $C_{m+1} = \{x_{m+1}^1, x_{m+1}^2, \dots, x_{m+1}^n\}$ and the decision attribute $d_{m+1} \in V_D$ is unknown, suppose the decision attribute values of x_{m+1} is $d_{m+1} = d_1$ and obtain the expanded universe U' . Firstly, calculate the support degree $\zeta_{c_i}^{d_1}$ of $U'/(D = d_1)$ under each criteria condition and obtain the support degree of the attribute condition c_i to $d_{m+1} = d_1$.

The trust function on the Θ : $\text{Bel}(A) = \sum_{B \subseteq A} m(B)$, ($\forall A \subseteq \Theta$). In the D-S evidence combination theory, there is n probability distribution function called m_1, m_2, \dots, m_n . Its orthogonal sum is called m . $m = m_1 \oplus m_2 \oplus \dots \oplus m_n$, which is also called total probability distribution function of completed integration. And

$$m(A) = \frac{1}{1 - K} \sum_{A_1 \cap A_2 \cap \dots \cap A_n = A} m_1(A_1)m_2(A_2) \cdot \dots \cdot m_n(A_n) \tag{44.15}$$

$$K = \sum_{A_1 \cap A_2 \cap \dots \cap A_n = \emptyset} m_1(A_1)m_2(A_2) \cdot \dots \cdot m_n(A_n) \tag{44.16}$$

44.3.3 Algorithm Analysis

The fault information of system is shown in the following incomplete information table. The fault of the system is fed back by four sensors, namely, c_1, c_2, c_3, c_4 . c_1 feedback four kinds of signals, as the distribution of c_1 is $V_{c_1} = \{1, 2, 3\}$, the distribution of c_2 is $V_{c_2} = \{1, 2\}$, the distribution of c_3 is $V_{c_3} = \{1, 2, 3\}$, and the distribution of c_4 is $V_{c_4} = \{1, 2, 3\}$. The fault D of the control system has three

Table 44.1 Incomplete information of the equipment fault

U	C_1	C_2	C_3	C_4	D
x_1	2	3	1	2	1
x_2	3	2	2	2	3
x_3	2	*	*	1	1
x_4	3	2	2	1	2
x_5	*	3	*	3	3
x_6	1	*	3	*	2
x_7	2	3	1	3	2
x_8	*	1	*	1	1
x_9	2	*	3	*	2
x_{10}	2	3	1	*	1

states, namely, $V_D = \{1, 2, 3\}$. The known history of decision table is shown in Table 44.1 which gives the new fault information $x = \{2, 2, *, 2\}$ based on the decision table to determine the fault status.

Step 1: as to the incomplete information decision-making system, we get the limited tolerance class of each object after removed the different condition attributes in the condition attribute sets.

$$\begin{aligned}
 LC_{-c_1}(x_1) &= \{x_{10}\}, LC_{-c_1}(x_2) = \{x\}, LC_{-c_1}(x_3) = \{x_4, x_8\}, LC_{-c_1}(x_4) \\
 &= \{x_3\}, LC_{-c_1}(x_5) = \{x_7, x_{10}\}, \\
 LC_{-c_1}(x_6) &= \{x_9\}, LC_{-c_1}(x_7) = \{x_5, x_{10}\}, LC_{-c_1}(x_8) = \{x_3, x_4\}, LC_{-c_1}(x_9) \\
 &= \{x_3, x\}, LC_{-c_1}(x_{10}) = \{x_1, x_5, x_7\}, \\
 LC_{-c_1}(x) &= \{x_2\} \quad LC_{-c_2}(x_1) = \{x_{10}, x\}, LC_{-c_2}(x_2) = \{\emptyset\}, LC_{-c_2}(x_3) \\
 &= \{x_8, x_{10}\}, LC_{-c_2}(x_4) = \{x_8\}, LC_{-c_2}(x_5) = \{x_7\}, \\
 LC_{-c_2}(x_6) &= \{\emptyset\}, LC_{-c_2}(x_7) = \{x_5, x_{10}\}, LC_{-c_2}(x_8) = \{x_3, x_4\}, LC_{-c_2}(x_9) \\
 &= \{x_3, x\}, LC_{-c_2}(x_{10}) = \{x_1, x_3, x_7, x\}, \\
 LC_{-c_2}(x) &= \{x_1, x_9, x_{10}\} \quad LC_{-c_3}(x_1) = \{x_9, x_{10}\}, LC_{-c_3}(x_2) = \{\emptyset\}, LC_{-c_3}(x_3) \\
 &= \{x_8, x_9, x_{10}\}, LC_{-c_3}(x_4) = \{\emptyset\}, \\
 LC_{-c_3}(x_5) &= \{x_7, x_{10}\}, LC_{-c_3}(x_6) = \{\emptyset\}, LC_{-c_3}(x_7) = \{x_5, x_9, x_{10}\}, LC_{-c_3}(x_8) \\
 &= \{x_3\}, LC_{-c_3}(x_9) = \{x_7\}, \\
 LC_{-c_2}(x_{10}) &= \{x_1, x_3, x_5, x_7, x_9\}, LC_{-c_3}(x) = \{x_9\} \quad LC_{-c_4}(x_1) \\
 &= \{x_3, x_5, x_7, x_{10}\}, LC_{-c_4}(x_2) = \{x_4\}, \\
 LC_{-c_4}(x_3) &= \{x_4, x_9\}, LC_{-c_4}(x_4) = \{x_1, x_7, x_9, x_{10}, x\}, LC_{-c_4}(x_5) \\
 &= \{x_1, x_7, x_{10}\}, LC_{-c_4}(x_6) = \{\emptyset\}, \\
 LC_{-c_4}(x_7) &= \{x_1, x_3, x_5, x_{10}\}, LC_{-c_4}(x_8) = \{\emptyset\}, LC_{-c_3}(x_9) \\
 &= \{x_3, x\}, LC_{-c_4}(x_{10}) = \{x_1, x_3, x_5, x_7\}, LC_{-c_4}(x) = \{x_3, x_9\}
 \end{aligned}
 \tag{44.17}$$

Step 2: we get the expansion decision information table by incorporating the new object, and suppose the value of decision attribute of the new object x is $Dx = 1$ and the expanded universe is U' , $U'/D = \{d_1, d_2, d_3\}$, then

$$\begin{aligned}
 d_1 &= \{x_1, x_3, x_8, x_{10}, x\}, d_2 = \{x_4, x_6, x_7, x_9\}, d_3 = \{x_2, x_5\} \\
 \text{POS}_{C-c_1}(d_1) &= \{x_3, x_{10}, x\}, \xi_{C-c_1}^{d_1} = \frac{3}{5}, \text{POS}_{C-c_2}(d_1) \\
 &= \{x_3, x_8, x_{10}, x\}, \xi_{C-c_2}^{d_1} = \frac{4}{5}
 \end{aligned} \tag{44.18}$$

$$\text{POS}_{C-c_3}(d_1) = \{x_3\}, \xi_{C-c_3}^{d_1} = \frac{1}{5}, \text{POS}_{C-c_4}(d_1) = \{x_3, x\}, \xi_{C-c_4}^{d_1} = \frac{2}{5} \tag{44.19}$$

Suppose the value of decision attribute of the new object x is $Dx=2$ and the expanded universe is U' , and $U'/D = \{d_1, d_2, d_3\}$ among $d_1 = \{x_1, x_3, x_8, x_{10}\}$, $d_2 = \{x_4, x_6, x_7, x_9, x\}$, $d_3 = \{x_2, x_5\}$, then

$$\begin{aligned}
 \text{POS}_{C-c_1}(d_2) &= \{x_6, x_9\}, \xi_{C-c_1}^{d_2} = \frac{2}{5}, \text{POS}_{C-c_2}(d_2) = \{x_7\}, \xi_{C-c_2}^{d_2} = \frac{1}{5} \\
 \text{POS}_{C-c_3}(d_2) &= \{x_9\}, \xi_{C-c_3}^{d_2} = \frac{1}{5}, \text{POS}_{C-c_4}(d_2) = \{x_4\}, \xi_{C-c_4}^{d_2} = \frac{1}{5}.
 \end{aligned}$$

Suppose the value of decision attribute of the new object x is $Dx=3$ and the expanded universe is U' . $U'/D = \{d_1, d_2, d_3\}$, then

$$\begin{aligned}
 \text{POS}_{C-c_1}(d_3) &= \{x_2, x\}, \xi_{C-c_1}^{d_3} = \frac{2}{3}, \text{POS}_{C-c_2}(d_3) = \{x_1, x_3, x_5, x_{10}, x\}, \xi_{C-c_2}^{d_3} = \frac{2}{3} \\
 \text{POS}_{C-c_3}(d_3) &= \{x_5, x_9, x_{10}\}, \xi_{C-c_3}^{d_3} = \frac{1}{3}, \text{POS}_{C-c_4}(d_3) = \{x_2\}, \xi_{C-c_4}^{d_3} = \frac{1}{3}.
 \end{aligned}$$

And the support degrees of condition attributing to decision classes are obtained based on Eq. (44.14), $\zeta_{c_1}^{d_1} = \frac{1}{3}(\frac{4}{5} + \frac{1}{5} + \frac{2}{5}) = \frac{7}{15}$, $\zeta_{c_2}^{d_1} = \frac{1}{3}(\frac{3}{5} + \frac{1}{5} + \frac{2}{5}) = \frac{6}{15}$, $\zeta_{c_3}^{d_1} = \frac{1}{3}(\frac{3}{5} + \frac{4}{5} + \frac{2}{5}) = \frac{9}{15}$, $\zeta_{c_4}^{d_1} = \frac{1}{3}(\frac{3}{5} + \frac{4}{5} + \frac{1}{5}) = \frac{8}{15}$.

Similarly, $\zeta_{c_1}^{d_2} = \frac{3}{15}$, $\zeta_{c_2}^{d_2} = \frac{4}{15}$, $\zeta_{c_3}^{d_2} = \frac{4}{15}$, $\zeta_{c_4}^{d_2} = \frac{4}{15}$, $\zeta_{c_1}^{d_3} = \frac{4}{9}$, $\zeta_{c_2}^{d_3} = \frac{4}{9}$, $\zeta_{c_3}^{d_3} = \frac{5}{9}$, $\zeta_{c_4}^{d_3} = \frac{5}{9}$.

Step 3: the basic probability assignment is obtained upon normalization based on Eqs. (44.5) and (44.7):

$$\begin{aligned}
 m_1(d_1) &= 0.3818, m_1(d_2) = 0.1636, m_1(d_3) = 0.3636, m_1(\theta) = 0.0909 \\
 m_2(d_1) &= 0.3273, m_2(d_2) = 0.2182, m_2(d_3) = 0.3636, m_2(\theta) = 0.0909 \\
 m_3(d_1) &= 0.3253, m_3(d_2) = 0.1446, m_3(d_3) = 0.3012, m_3(\theta) = 0.2289 \\
 m_4(d_1) &= 0.3117, m_4(d_2) = 0.1558, m_4(d_3) = 0.3247, m_4(\theta) = 0.2078.
 \end{aligned}$$

Step 4: the evidences are fused by Formula (44.15) with the result of $m(d_1) = 0.4517$, $m(d_2) = 0.0823$, $m(d_3) = 0.4629$, $m(\theta) = 0.0031$.

Step 5: according to the credibility of degree maximum principle, we can get the decision is d_3 , namely, the fault status of x is 3.

Conclusion

Under the condition of incomplete decision information system, the evidences are obtained based on the limited tolerance relation and the support degree and then the evidences are fused by using the improved combination rule with the decision to be made by the fusion result. By means of the limited tolerance relation and the Bayesian rough set, the lower distribution sets of the decision classes can be obtained when each of the condition attributes is deleted. When the classified quality is calculated, the support degrees of condition attributes to decision classes are obtained on the basis of the above. Then, the basic probability assignment is obtained upon normalization. Finally, the evidences are fused by the improved combination rule, and the new object is classified based on the fusion result. The outcome of the example demonstrates that method mentioned above is more suitable to the decision under the condition of incomplete decision information system.

Acknowledgments This research has been supported by the National Natural Science Foundation of China (Grant No. 71271034), the Fundamental Research Funds for the Central Universities (Grant No. 3132014307, Grant No. 3132014080), the General Project of Liaoning Provincial Education Department (Grant No. L2012173), and the Liaoning Academy of Social Science Fund Project (Grant No. L13DGL060).

References

1. Zaras K. Rough approximation of a preference relation by a multi-attribute stochastic dominance for determinist and stochastic evaluation problems. *Eur J Oper Res.* 2001;130(2):305–14.
2. Liu B. Theory and practice of uncertain programming. Heidelberg: Physica; 2002. p. 195.
3. Alam SS, Ghosh S. Rank by AHP: a rough approach. *ISCF.* 2002;1:185–90.
4. Wei J, Huang D, et al. Rough set based decision tree. In: *Proceedings of the 4th world congress on intelligent control and automation, 2002*;1:426–31.
5. Jia X, Liao W, Tang Z. Minimum cost attribute reduction in decision-theoretic rough set models. *Inform Sci.* 2013;219(1):151–67.
6. Katzberg J, Ziarko W. Variable precision extension of rough sets. *Fundamental.* 1996;27(2–3):155–68.
7. Slezak D, Ziarko W. Attribute reduction in the Bayesian version of variable precision rough set model. *Electron Notes Theor Comput Sci.* 2003;82(4):263–73.

Chapter 45

An Enhanced Entropy-K-Nearest Neighbor Algorithm Based on Attribute Reduction

Lingyun Wei, Xiaoli Zhao, and Xiaoguang Zhou

Abstract Dimension disaster will directly impact on the efficiency and accuracy of K-nearest neighbor (KNN) classification algorithm. In order to reduce the effect, this chapter proposes an improved Entropy-KNN algorithm based on attribute reduction. It combines KNN algorithm with information entropy theory to reduce the attribute, and the test sample is classified by the average distance and the numbers on the respective class. The experimental results show that compared with traditional KNN algorithm, the proposed algorithm enormously raises the classification accuracy rate; meanwhile it also maintains the efficiency of category.

Keywords KNN • Information entropy • Correlation degree • Attribute reduction

45.1 Introduction

The classic data mining classification algorithm (KNN) [1], proposed by Cover and Hart, has been widely used in many fields with its simplicity and higher classification accuracy. KNN algorithm calculates the distance of all condition attributes on samples; however, the influence of different attributes on classification is actually not the same: some attributes are strongly correlated with classification, while some are weakly correlated, and even a few are irrelevant. Thus, the distance between neighbors will be dominated by a large number of irrelevant condition attributes, which is called the dimension disaster [2]. Dimension disaster will directly impact on the efficiency and the rate of accuracy of KNN. When the number of training samples is fixed, classification accuracy will decrease with the increase of dimension, which is called the Hughes phenomenon [3]. Information entropy is used to measure the importance of attributes for category. The smaller the entropy is, the more important the attribute is [4]. Attribute reduction based on the entropy does well in extracting important attributes and removing irrelevant ones, thus greatly reducing the computation of KNN algorithm to improve the classification rate. When the data retains a small amount of attributes only, the combination of

L. Wei • X. Zhao (✉) • X. Zhou
Being University of Post and Telecommunication, 102209, Beijing, China
e-mail: weilingyun2010@sina.com; zhaoxiaoli_bupt@163.co; mzxcg@bupt.edu.cn

important attribute values are extracted as well as the important single-valued ones, which will guarantee the correctness of the classification results. So, this chapter proposes an improved Entropy-KNN algorithm based on attribute reduction in order to reduce the computation of KNN, meanwhile maintaining better classification accuracy.

For traditional KNN, a category is judged by the number of neighbors on the respective category. Failure will easily occur when neighbors of different categories get an equal number [5]. When Entropy-KNN method is used, a category is classified by both the average distance and the number of neighbors on the respective class, thus further improving the classification accuracy [6–8]. Finally, with large numbers of experiments on data sets, the experimental results indicate that compared with traditional KNN algorithm and Entropy-KNN algorithm, the proposed algorithm can ensure the validity of classification and effectively improve the classification efficiency and accuracy at the same time.

45.2 Attribute Reduction

In this chapter, we use attribute reduction to deal with training sets, maintain important attributes, and remove irrelevant attributes. In this way, we greatly reduce computational overhead and improve the classification efficiency.

45.2.1 Definitions

Information entropy and correlation degree are defined as follows.

Definition 1 Given a set of labeled data sample S , let $|S|$ be the number of samples and C_1, C_2, \dots, C_n be the class labels. $V = \{v_1, v_2, \dots, v_i\}$ is the domain of attribute values, and let $|v_i|$ be the number of v_i shown in S and $|v_{ij}|$ be the number of v_i that belongs to C_j ; the entropy of v_i is defined as

$$I(v_i) = -\sum_{j=1}^n p_{ij} \ln(p_{ij}) \quad (45.1)$$

where $p_{ij} = \frac{|v_{ij}|}{|v_i|}$ is the probability that attribute with value v_i belongs to C_j in V .

The entropy of attribute V is defined as

$$E(V) = \sum_{i=1}^n \frac{|V_i|}{S} I(v_i). \quad (45.2)$$

Definition 2 Attribute set V is divided into decision attribute set D and condition attribute set A ; the correlation degree between D and A is defined as

$$\text{Corr}(A) = I(D) - E(A). \quad (45.3)$$

The correlation degree of condition attributes can be divided into three categories, namely, strong-related attributes, weak-related attributes, and irrelevant attributes, where $\text{Corr}(A) = 0$ is expressed as irrelevant attributes [9]. Strong-related attributes are to be selected; otherwise they will seriously affect the classification performance; weak-related attributes are selected depending on the situation; and irrelevant attributes are completely unnecessarily reserved.

45.2.2 Attribute Reduction Based on Correlation Degree

The main steps of attribute reduction based on correlation degree are as follows:

1. Calculate the correlation degree of condition attributes respectively via Eq. (45.3).
2. Determine the threshold of correlation degree. In this test, the threshold with the highest classification accuracy is considered as the correlation threshold value.
3. Attribute reduction. Select the condition attribute with a correlation degree greater than or equal to the threshold and delete the others.

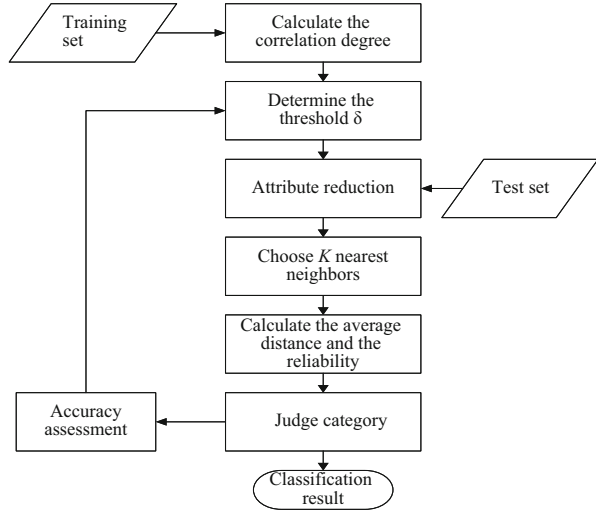
Attribute reduction can be done according to the above three steps [10].

45.3 The Enhanced Entropy-KNN Algorithm Based on Attribute Reduction

After attribute reduction, the selected attributes still have different impacts on classification. The proposed algorithm in this chapter applies information entropy to determine the importance of attribute values. The average entropy between two samples of the same attribute value is defined as distance, thus the neighbor samples are more effectively found. Meanwhile, we use class reliability to comprehensively consider the number of neighbors on respective class and the average distance. Even if the credibility of test sets on respective class is very close, we can get the correct category.

The description of the proposed algorithm is shown in Fig. 45.1.

Fig. 45.1 The description of the proposed algorithm



45.3.1 Definitions

Definition 3 Given any two samples X and Y , let v_1, v_2, \dots, v_n be the same attribute values between X and Y , and then the distance between X and Y is defined as

$$d(Y, X) = \frac{1}{n} \sum_{i=1}^n I(v_i). \tag{45.4}$$

Definition 4 Let C_i be the category and Y be the test sample. N is the total number of nearest neighbor samples, X_i is the nearest neighbor sample that belongs to C_i , and N_i is the number of X_i . $T(C_i, Y)$ is called the reliability with the equation as follows:

$$T(C_i, Y) = \frac{N - N_i}{N} \times \frac{1}{N_i} \sum_{i=1}^{N_i} d(Y, X_i) \tag{45.5}$$

where $\frac{1}{N_i} \sum_{i=1}^{N_i} d(Y, X_i)$ is the average distance of Y of class C_i . The reliability increases with the decrease of $T(C_i, Y)$. Equation (45.5) on the judgment of Y is based on the number of nearest neighbors belonging to C_i and the average distance.

Table 45.1 Raw data

	A1	A2	A3	A4	A5	A6	A7	A8	A9	D
X1	1	9	19	30	55	60	72	79	82	1
X2	5	9	11	32	55	59	76	80	88	2
X3	3	7	14	35	53	60	73	81	88	1
X4	3	10	17	32	55	59	76	80	83	2
X5	3	9	11	35	55	58	72	81	88	1
X6	3	9	14	33	52	57	75	80	85	2
X7	4	9	11	36	54	59	73	80	88	1
X8	4	9	19	33	52	56	75	80	85	2
X9	3	9	11	37	54	60	73	81	88	1
X10	3	10	14	33	55	60	75	79	82	2
X11	1	10	18	34	55	60	72	79	82	1
X12	3	7	19	34	54	57	75	81	88	2
X13	3	10	18	34	55	60	76	77	82	1
X14	4	10	11	32	54	59	76	80	85	2

45.3.2 Example Analysis

The following example illustrates the realization of the proposed algorithm. And in this example, we set the K value to 5.

Table 45.1 is a part of data set mushroom. There are 15 samples with 9 numeric condition attributes $A1, A2, \dots, A9$ and a decision attribute D with values 1 and 2, where training sets are from $X1$ to $X13$ and test set is $X14$.

1. *Attribute reduction.* Equation (45.3) is used to calculate the correlation degree of condition attributes from $A1$ to $A9$: 0.077, 0.003, 0.370, 0.543, 0.176, 0.335, 0.543, 0.178, and 0.223. Let the threshold be 0.35, namely, $\delta = 0.35$. Select the condition attribute with a correlation degree greater than or equal to 0.35 and then delete the others. The selected attributes are $A3, A4$, and $A7$.
2. *Classification.* The same attribute values between $X14$ and $X1-X13$ should be (no) (11, 32, 76) (no) (32, 76) (11) (no) (11) (no) (11) (no) (no) (76). Equation (45.4) is used to calculate the distance between $X14$ and training sets respectively: 1, 0, 1, 0.3189, 0.5623, 1, 0.5623, 1, 0.5623, 1, 1, 1, and 0.63651. Choose five nearest neighbors $X2, X4, X5, X7$, and $X9$, where the class labels of $X5, X7, X9$, are 1, and the others are 2.

We get $N = 5, N1 = 3, N2 = 2$ above. Definition 4 is used to calculate the reliability of $X14$ and judge the category.

$$\begin{aligned}
 T(1, X14) &= \frac{(5-3)}{5} \times \frac{1}{3}(0.5623 + 0.5623 + 0.5623) = 0.2249T(2, X14) \\
 &= \frac{(5-2)}{5} \times \frac{1}{2}(0 + 0.3183) = 0.0995
 \end{aligned}$$

$T(1, X14) > T(2, X14)$, therefore, $X14$ is judged to be class 2 correctly.

In step (1), we get that the nearest neighbors of class 1 are $X5$, $X7$, $X9$, and class 2 are $X2$ and $X4$. Then $X14$ is judged to be the wrong class 1 due to the greater number of neighbors via traditional KNN algorithm.

45.4 Experimental Analysis

In this chapter, in order to verify the effectiveness and correctness of the proposed algorithm, we download three data sets from UCI repository of machine learning databases. The data sets are described in Table 45.2.

The proposed method is used in mushroom data sets on the experiment, and the samples are divided into training sets and test sets. The experimental data in Table 45.3 show the **tendency** of classification accuracy with the variation on K and the threshold value δ . N is the number of selected attributes after reduction.

From Table 45.3, we can find when the threshold value is between 0.175 and 0.205, the classification accuracy is higher. The main reason is that when the threshold value is less than 0.175, the proposed method is unable to effectively reduce the impact of dimension disaster. And when the threshold value is greater than 0.205, it increases the chances of **overfitting**. In order to make the experiment possible, we took 0.190 as the average threshold of 0.175–0.205 to analyze the effect of selected attributes to the performance of classification. Experimental results are shown in Fig. 45.2.

From Fig. 45.1, we can find the accuracy of the proposed algorithm consistently higher than traditional KNN algorithm and Entropy-KNN algorithm as well, even if values of K are different. The accuracy gap increases with the increase of K values, and the larger the data is, the more obvious the effect is. Experimental analysis shows that attribute reduction can select a small amount of features and keep or even improve the classification accuracy, which verifies the effectiveness of the proposed algorithm.

Table 45.2 Data description

	Data set	Samples	Features	Classes
1	Zoo	101	17	7
2	Mushroom	8,124	12	2
3	Adult	32,561	15	2

Table 45.3 Accuracies of selected attributes varying with the number of neighbors K and the threshold δ

δ	K						Average	N
	4	7	10	13	16	19		
0.145	0.9712	0.9716	0.9730	0.9734	0.9775	0.9730	0.9733	12
0.150	0.9716	0.9745	0.9782	0.9778	0.9790	0.9775	0.9764	10
0.155	0.9715	0.9796	0.9790	0.9797	0.9800	0.9808	0.9784	10
0.160	0.9723	0.9804	0.9797	0.9806	0.9808	0.9812	0.9792	10
0.165	0.9730	0.9808	0.9808	0.9810	0.9814	0.9819	0.9798	9
0.170	0.9726	0.9804	0.9812	0.9815	0.9819	0.9819	0.9799	8
0.175	0.9834	0.9826	0.9863	0.9865	0.9874	0.9878	0.9857	7
0.180	0.9867	0.9882	0.9886	0.9882	0.9886	0.9878	0.9880	6
0.185	0.9886	0.9889	0.9893	0.9911	0.9922	0.9952	0.9909	5
0.190	0.9911	0.9926	0.9937	0.9952	0.9978	0.9985	0.9948	5
0.195	0.9882	0.9886	0.9904	0.9886	0.9889	0.9908	0.9892	5
0.200	0.9889	0.9893	0.9893	0.9922	0.9870	0.9886	0.9892	4
0.205	0.9819	0.9882	0.9867	0.9874	0.9845	0.9845	0.9855	4
0.210	0.9749	0.9771	0.9730	0.9730	0.9734	0.9753	0.9744	3
0.215	0.9476	0.9564	0.9598	0.9583	0.9597	0.9612	0.9572	3
0.220	0.9095	0.9135	0.9165	0.9343	0.9231	0.9435	0.9234	2

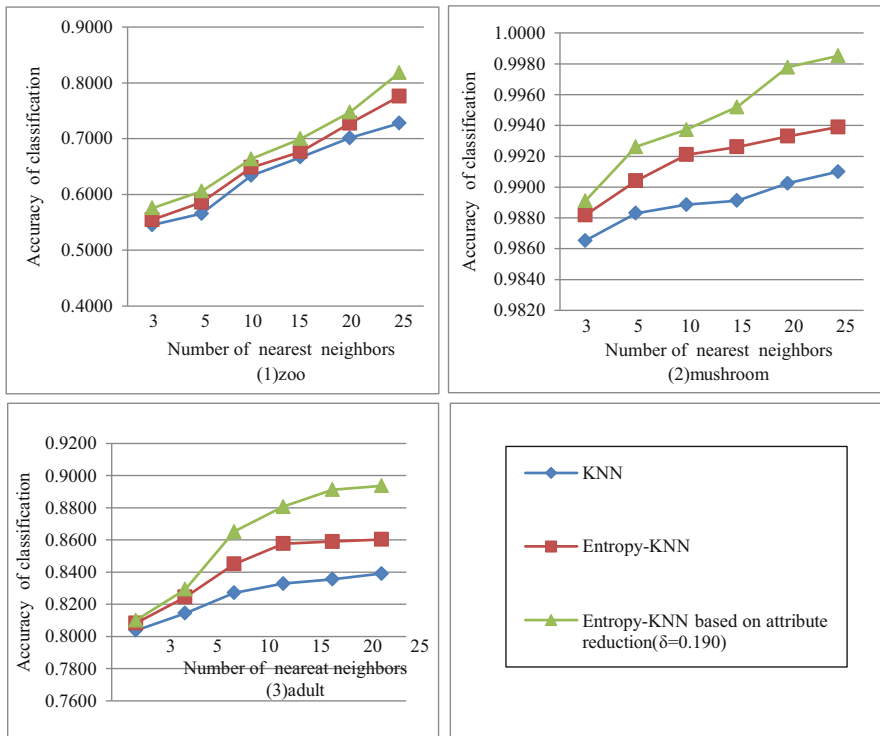


Fig. 45.2 Trends of accuracies with traditional KNN, Entropy-KNN, and proposed algorithm

Conclusion

In this chapter, we proposed an improved algorithm to overcome the dimension disaster impact on classification. Attribute reduction is carried out on training sets before test sets are classified, and we remove redundant attributes that have less or no impact on classifier performance. What's more, the reliability is used to balance the number of neighbors on respective class and average distance. Thus, it makes classification results more accurately. Results indicate that the improved algorithm maintains the integrity of the original data information at the same time effectively decreases the dimension disaster effect on the classification performance.

Acknowledgments This work was supported by National Key Technology R&D Program of the Ministry of Science and Technology of China (No. 2014BAH24F02) and Engineering Research Center of Information Networks, Ministry of Education. It was partly supported by National public industry (food) special funds for scientific research (No. 201313009-08).

References

1. Cover TM, Hart PE. Nearest neighbor pattern classification. *IEEE Trans Inform Theory*. 1967;13(1):21–7.
2. Zhang R, Ooi BC, Tan KL. Making the pyramid technique robust to query types and workloads. In: *Proceedings of the 20th international conference on data engineering*, Boston, MA, USA, vol. 20, pp. 313–24. 2004.
3. Hughes GF. On the mean accuracy of statistical pattern recognizers. *IEEE Trans Inform Theory*. 1968;14(1):55–63.
4. Wang GY, Yu H, Yang DC. Decision table reduction based on conditional information entropy. *Chin J Comput*. 2002;25(7):759–66.
5. Anil KG. On optimum choice of k in nearest neighbor classification. *Comput Stat Data Anal*. 2006;50(11):3113–23.
6. Lindenbaum M, Markovitch S, Rusakov D, Lindenbaum M, Markovitch S, Rusakov D. Selective sampling for nearest neighbor classifiers. *Mach Learn*. 2004;54(2):125–52.
7. Swiniarski RW, Skowron A. Rough set methods in feature selection and recognition. *Pattern Recogn Lett*. 2003;24(2):833–49.
8. Zhou C, Yan Y, Chen Q, Zhou C, Yan Y, Chen Q. Improving nearest neighbor classification with cam weighted distance. *Pattern Recogn*. 2006;39(4):635–45.
9. Kohavi R, John GH. Wrappers for feature subset selection. *Artif Intell*. 1997;97(1–2):273–324.
10. Wang ZM, Wang KJ. Improve KNN algorithm based on entropy method. *Comput Eng Appl*. 2009;45(30):129–31. In Chinese.

Chapter 46

Synthetic Safety Analysis: A Systematic Approach in Combination of Fault Tree Analysis and Fuzzy Failure Modes and Effect Analysis

Guannan Su, Linpeng Huang, and Xiaoyu Fu

Abstract Two classical methods in safety analysis, FTA and FMEA, are generally used separately in operating analysis orientations. But this one-direction systematic technique becomes more difficult in facing today's software architecture with increasingly higher complexity; moreover, the simple risk priority number (RPN) in original FMEA can no longer meet the urgent request of higher accuracy in the development of efficient safety analysis. Thus, a new synthetic approach is put forward with the combination of FTA and FMEA. In addition, a system-level fuzzy-RPN and top-fRPN are provided to show the effect of events on their systems to help people make decisions based on a three-dimensional risk ranking instead of failure probability. The case study has demonstrated the methodology thus developed. Our method tends to improve the range of technical adaptability of safety analysis.

Keywords Safety analysis • FTA • Fuzzy FMEA • AHP

46.1 Introduction

Safety can be described as a characteristic of the system of not endangering or causing harm to human lives or the environment in which the equipment or plant operates [1]. The two fault modeling techniques commonly adopted refer to Failure Mode and Effects Analysis (FMEA) and fault tree analysis (FTA).

The quantitative safety analysis process often has much trouble in getting the exact failure rate/probability of components and specific data value in reliability and safety analysis areas. With more complexity of software systems, the single way of analysis can no longer meet the requirements. In order to solve the

G. Su (✉) • L. Huang • X. Fu
Department of Computer Science and Engineering, Shanghai Jiao Tong University,
200240 Shanghai, China
e-mail: suguannan@sjtu.edu.cn

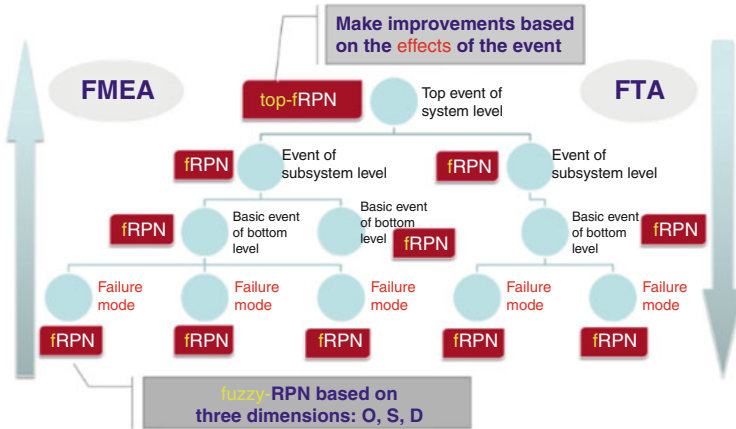


Fig. 46.1 Structure diagram of our synthetic safety analysis approach

uncertainty, the fuzzy theory and technical principles of probabilistic method can effectively compensate for the lack of reliability of complex systems analysis and assessment.

Furthermore, in diverse systems, it seems too absolute to make decisions of events or components only based on the occurrence of failures. In many situations, the effect is more significant than the probability of the failures probability. Thus, with the ideas of FMEA, we try to calculate a new risk priority number of top events and top-fRPN to deal with those failures based on the effect ranking.

Our synthetic safety analysis method can be described in Fig. 46.1.

The main contributions of this chapter include:

- A synthetic method combining FTA and FMEA to analyze the system-level safety in a two-direction way: top-down and bottom-up.
- The top-risk priority number (top-fRPN) is calculated instead of the failure rate/probability, which is the system-level effect of both the basic event (basic failure mode) and either layer of events so as to help people decide the most influential event for treatment.
- Combine the fuzzy method with analytic hierarchy process (AHP). In this way, we can make the calculation suitable to both the increasingly complicated systems and the extended multi-attribute computing dimensions.

As to the remaining part of this chapter, Sect. 46.2 summarizes related works, and Sect. 46.3 provides our synthetic safety analysis approach. A case study in Sect. 46.4 demonstrates the benefits of our method. Finally, Sect. 46.5 gives an outlook on future work and concludes this chapter.

46.2 Related Work

FTA, a systematic and stylized process, is a deductive and top-down method of analyzing the system's design and performance qualitatively and quantitatively. The quantitative FTA often has much trouble in getting the exact failure rate/probability of components and specific data value [2]. Moreover, complex systems analysis may produce thousands of combinations of events (cut-sets) which may cause system failure. The determination of the exact top event probability requires lengthy calculations if the fault tree has a great number of cut-sets.

FMEA, however, is an inductive and bottom-up qualitative analysis method. The criticality assessment module of failure modes uses the following two methods: the fuzzy inference method [3] and the conventional method of risk priority number (RPN) which was initially developed by Bowles et al. [4]. FMEA uses rules based on the expert's knowledge to give the relationship among the O, S, D and risk on a numeric scale from 1 to 10. The well-known "conversion" tables and traditional FMEA evaluation criteria [5] report the typical basis for the linguistic judgment scales to estimate the three quantities for calculating the RPN value in the following equation $RPN = O \times S \times D$. However, the FMEA have been extensively criticized for various reasons [6], one of which is about the limitation of only utilizing three factors in terms of safety with other important factors such as economic aspects being ignored. Besides, the three factors are difficult to determine precisely.

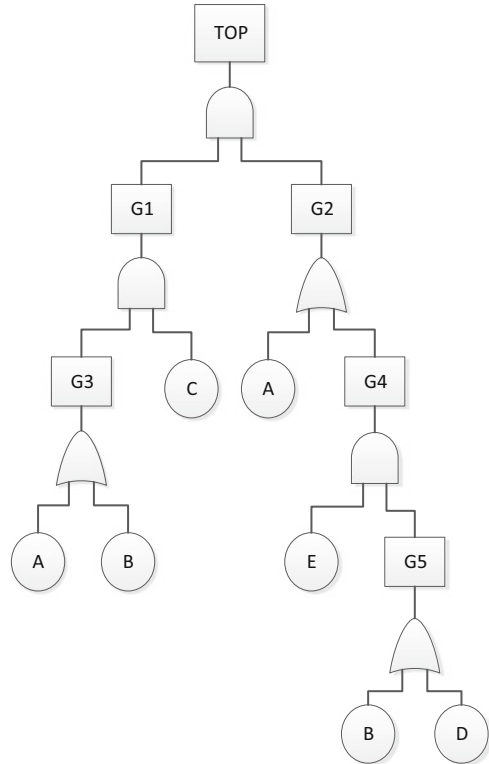
The traditional FTA and FMEA synthetic analysis methods use the FMEA technology to analyze and identify those critical basic events in FTA diagrams in order to show the priority which helps professionals deal with the problem. Another comprehensive application of FTA and FMEA is in the avionic system [7], which focuses more on the hardware level.

In order to formulate an efficient and effective priority ranking of the possible causes of failure, researchers adopt the analytic hierarchy process (AHP), with which the factors and alternative causes of failure are arranged in a hierarchic structure and evaluated by means of a series of pairwise judgments [8].

46.3 Synthetic Safety Analysis

Considering the current situations and difficulties as discussed above, we put forward our synthetic safety analysis approach. Firstly, we use the FTA to analyze the top event; secondly, based on the fault tree as developed, all the basic events are put in FMEA method to give out the final new RPN in basic level. Besides, we adopt the AHP to calculate the importance of each attribute. Thirdly, we use the classical method and transfer the fault tree into one equation, which shows the relation only between the top event and the basic events. With the same principle of fuzzy FMEA with AHP and based on the equation from FTA, the RPN of top event can be computed to show the effect of this top event on its system. Finally, the final

Fig. 46.2 A model of traditional FTA



result, top-fRPN, will help us decide whether the influence of the top event is big enough for treatment.

To generalize our approach, we describe our method in a common mathematical example to focus on the analysis process.

46.3.1 Fault Tree Analysis

Firstly, we use the classic safety analysis method FTA to produce the fault tree of a top event “Top,” which is shown in Fig. 46.2 in the case study. This fault tree has two multiple occurring events, B and C, which occur more than one place in the FTA.

Before beginning the analysis process, the first thing is to identify the root (“top event”) of the tree of logic, which, however, can be diverse. Here we choose the Functional Hazard Analysis (FHA) based on Aerospace Recommended Practice. We leave out this part because it is not the main part of this chapter.

The general fault tree's construction process can be divided into two categories: the deductive method and the computer-aided synthesis or achievements of the decision table method. As to the deductive method, transfer both the top events which are already identified and their direct causes into the appropriate event symbols of the second row. Then based on the logic relations of actual systems, bind the top event and the direct causes with logic gates and symbols. Thirdly, follow the rules of construction in a step-by-step manner to develop the tree down to the basic-level events until all the "leaves" of the tree are the cause events.

46.3.2 Fuzzy FMEA with AHP

The analytic hierarchy process is a structured technique for organizing and analyzing complex decisions on the basis of mathematics and psychology. It is a combination of qualitative and quantitative, systematic, hierarchical analysis.

Our hierarchic fuzzy FMEA process is shown as below:

46.3.2.1 Definition of Attribute Sets

Define the attribute sets of elements and factors. Clearly, there are always three layers in our extended fuzzy FMEA: the first layer of top event, the second layer of basic events, and the third layer of three-dimensional factors. We still use the example that we discussed above. There are $m(m=5)$ basic events in a fault tree. We define them as:

$$\begin{aligned} \text{Top event : } & U = \{U_1, U_2, \dots, U_i\} \\ \text{Basic event : } & U_i = \{O, S, D\}, \quad i = 1, 2, \dots, m \end{aligned} \quad (46.1)$$

46.3.2.2 Definition of Attribute Sets

Directly adopt the evaluation criteria already established above, in which we define the standard evaluation set as $V = \{v_1, v_2, \dots, v_n\}$, where n is the number of evaluation dimension of each basic element in FMEA, here $n = 3$ based on the three basic dimensions O, S, and D.

46.3.2.3 Determine the Evaluation Index Weight

Use analytic hierarchy process (AHP) to determine the weight of each index.

Firstly, construct judgment matrix. The judgment matrix element values for each index reflect a risk assessment of the importance of people's understanding of the safety system. Secondly, let experts make pairwise comparison in terms of the importance of each indicator and then determine ratings layer by layer. Thirdly,

calculate the feature vector of the judgment matrix to determine the contribution of the lower layer to the upper index indicator to achieve the ranking results of the importance of each variable indicator on the target layer ones. Later when the judgment matrix is put into the AHP calculation software, we can get the weight u_i of the superior indicators.

46.3.2.4 Determination the Degree of Indicators' Membership

Use the fuzzy theory and technique to identify the degree of each attribute's membership. We calculate the frequency n_{ijq} of how many times each attribute belongs to our evaluation sets. Then the degree of membership is

$$u_{ij}^q = \frac{n_{ijq}}{n} \tag{46.2}$$

The positive index membership is

$$u_{ij}^q = \begin{cases} 0 & u_{ij} < v_q \\ \frac{u_{ij} - v_q}{u_{q+1} - v_q} & v_{q+1} > u_{ij} \geq v_q \\ 1 & u_{ij} \geq v_{q+1} \end{cases} \tag{46.3}$$

The moderate index membership is

$$u_{ij}^q = \begin{cases} 0 & u_{ij} > v_{q+1}, u_{ij} > v_q \\ \frac{2(u_{ij} - v_q)}{u_{q+1} - v_q} & v_q + (v_{q+1} - v_q)/2 > u_{ij} \geq v_q \\ \frac{2(u_{q+1} - u_{ij})}{u_{q+1} - v_q} & v_{q+1} \geq u_{ij} \geq v_q + (v_{q+1} - v_q)/2 \end{cases} \tag{46.4}$$

The negative index membership is

$$u_{ij}^q = \begin{cases} 1 & u_{ij} \leq v_q (v_{q+1} - u_{ij}) / (v_{q+1} - v_q) \\ 0 & u_{ij} > v_{q+1} \end{cases} \tag{46.5}$$

46.3.2.5 Fuzzy Synthetic Assessment

Based on our experience and experts' identification, combine the equations from (46.2) to (46.5) so that the fuzzy evaluation matrix R_i can be gotten as

$$R_i = \begin{cases} r_{11} & r_{12} & \dots & r_{15} \\ r_{21} & r_{22} & \dots & r_{25} \\ & & \dots & \\ r_{m1} & r_{m2} & \dots & r_{m5} \end{cases} \quad (46.6)$$

Then we get the first-layer synthetic evaluation model Y as

$$Y = u_i R_i \quad (46.7)$$

46.3.3 Top-fRPN

From FTA diagram shown in Fig. 46.2, the probability of the top event, Q , can be obtained as below:

$$Q = q_C q_A + q_C (1 - q_A) q_B q_E q_D \quad (46.8)$$

In our approach, when the judgments on the second layer attributes of the top level (top event) is made, we get the synthetic fuzzy assessment equation as

$$Z = uY = [b_1, b_2, \dots, b_m] \quad (46.9)$$

Final top-fRPN can be obtained in Eq. (46.9) with the results of Eq. (46.9).

46.4 Case Study

In order to illustrate the validity of our synthetic method, we introduce a general case which consists of the normal elements in safety analysis. This example shows the main purpose of our method, i.e., the effect of a basic event on a system is not necessarily relevant to its failure probability, and it is better to make the meaningful improvement based on the failure effect and not simply on the failure rate. In the end of this section, the significance can be reflected through a comparison between our method and the traditional one with only the failure rate computed. In this case, we assume the FTA has been done with a fault tree shown in Fig. 46.2. Since the number of the events and experts is not the determinant of our methodology, we assume they are both five to make the calculation easier.

The index weights of different layers are

$$\begin{aligned}
 \mathbf{u} &= (0.44, 0.25, 0.09, 0.17, 0.05) \\
 u_1 &= (0.32, 0.46, 0.22) \\
 u_2 &= (0.32, 0.41, 0.27) \\
 u_3 &= (0.50, 0.29, 0.21) \\
 u_4 &= (0.27, 0.24, 0.49) \\
 u_5 &= (0.14, 0.34, 0.52)
 \end{aligned}$$

The fuzzy evaluation matrix R_i of the five basic events are

$$\begin{aligned}
 R_1 &= \begin{bmatrix} 0.18 & 0.58 & 0.12 & 0.12 & 0.00 \\ 0.19 & 0.37 & 0.26 & 0.11 & 0.07 \\ 0.17 & 0.25 & 0.27 & 0.11 & 0.20 \end{bmatrix} \\
 R_2 &= \begin{bmatrix} 0.21 & 0.34 & 0.12 & 0.22 & 0.11 \\ 0.23 & 0.37 & 0.13 & 0.07 & 0.20 \\ 0.14 & 0.27 & 0.31 & 0.28 & 0.00 \end{bmatrix} \\
 R_3 &= \begin{bmatrix} 0.13 & 0.37 & 0.13 & 0.17 & 0.20 \\ 0.23 & 0.64 & 0.13 & 0.00 & 0.07 \\ 0.07 & 0.39 & 0.22 & 0.17 & 0.15 \end{bmatrix} \\
 R_4 &= \begin{bmatrix} 0.12 & 0.28 & 0.35 & 0.16 & 0.09 \\ 0.16 & 0.38 & 0.13 & 0.16 & 0.17 \\ 0.19 & 0.35 & 0.18 & 0.15 & 0.13 \end{bmatrix} \\
 R_5 &= \begin{bmatrix} 0.13 & 0.29 & 0.32 & 0.15 & 0.11 \\ 0.09 & 0.30 & 0.38 & 0.16 & 0.07 \\ 0.23 & 0.36 & 0.13 & 0.24 & 0.04 \end{bmatrix}
 \end{aligned}$$

The first-layer synthetic evaluation model Y to second layer basic events:

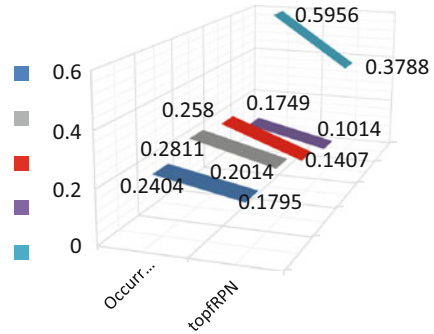
$$\begin{aligned}
 Y_1 &= u_1 R_1 = (0.1824 \quad 0.4108 \quad 0.2174 \quad 0.1132 \quad 0.0762) \\
 Y_2 &= u_2 R_2 = (0.1993 \quad 0.3334 \quad 0.1754 \quad 0.1747 \quad 0.1172) \\
 Y_3 &= u_3 R_3 = (0.1464 \quad 0.4525 \quad 0.1489 \quad 0.1207 \quad 0.1518) \\
 Y_4 &= u_4 R_4 = (0.1639 \quad 0.3383 \quad 0.2139 \quad 0.1551 \quad 0.1288) \\
 Y_5 &= u_5 R_5 = (0.1684 \quad 0.3298 \quad 0.2416 \quad 0.2002 \quad 0.0600)
 \end{aligned}$$

Finally, we get the synthetic fuzzy assessment results:

$$Z = \mathbf{u}Y = (0.1795 \quad 0.3788 \quad 0.2014 \quad 0.1407 \quad 0.1014)$$

Upon comparison, we also give out the outcome O of single failure probability which is the dimension of occurrence here. The comparison diagram is shown in Fig. 46.3:

Fig. 46.3 Comparison between our synthetic method with the traditional failure rate



$$O = \left(u_i \sum_1^5 R_{i1} \right) \Big|_1^5 = (0.2404 \quad 0.5956 \quad 0.2811 \quad 0.2580 \quad 0.1749)$$

The top-fRPN of this simple case is $top-fRPN = 0.0370$.

Based on the result, we can see the basic event B plays a key role on the system; besides, more attentions should be put on event D rather than A because of D's higher influence but not A's big occurrence.

Conclusion and Future Work

In this chapter, we put forward our approach by means of both classic safety analysis approach, FTA and FMEA, in a two-direction way. In addition, a system-level fuzzy-RPN, top-fRPN, is provided instead of traditional failure probability to show the effect of events on their systems to help people make decisions based on a three-dimensional risk ranking instead of failure probability. The case study shows the main purpose of our method, i.e., the effect of a basic event on a system is not necessarily relevant to its failure probability, and it is better to make the meaningful improvement based on the failure effect and not simply on the failure rate. Our method has improved the range of technical adaptability of safety analysis. In the future, we will focus more on effects of social aspects on the systematic safety analysis.

Acknowledgments The work described in this chapter has been supported by the Innovation Program of Shanghai Municipal Education Commission (no. 13ZZ023) and the National Natural Science Foundation of China under grant no. 61232007, 91118004.

References

1. Bozzano M, Villafiorita A. Design and safety assessment of critical systems. Unite States: Auerbach Publishers Inc; 2010. p. 5–121.
2. Stamatelatos M, NASA HQ, et al. Fault tree handbook with aerospace applications, version 1.1. Washington: NASA Publication; 2002. p. 4–6.

3. Wang YM, Chin KS, Poon GKK, Yang JB. Risk evaluation in failure mode and effects analysis using fuzzy weighted geometric mean. *Expert Syst Appl.* 2009;36:1195–207.
4. Yang ZL, Bonsall S, Wang J. Fuzzy rule-based Bayesian reasoning approach for prioritization of failures in FMEA. *IEEE Trans Reliab.* 2008;57(3):517–28.
5. Rausand M, Hoyland A. *System reliability theory: models, statistical methods, and applications*, vol. 2. New Jersey: Wiley Series in Probability and Statistics; 2004. p. 88–9.
6. Liu H, Liu L, et al. Failure mode and effect analysis using fuzzy evidential reasoning approach and grey theory. *Expert Syst Appl.* 2011;38:4403–15.
7. Zhou JL, Sun Q. Reliability analysis based on binary decision diagrams. *J Qual Maint Eng.* 1998;4(2):150–61.
8. Esparza J, Schwoon S. A BDD-based model checker for recursive programs[J]. *Lect Notes Comput Sci.* 2001;2102:324–36.

Chapter 47

Evaluation Model of Internet Service Provider Attraction Based on Gravity Model

Lihua Heng, Gang Chen, and Zongmin Wang

Abstract Internet service providers (ISPs) have committed to coming up with different strategies to improve their competitiveness. This paper uses the gravity model and finally presents a precise evaluation model of ISPs' appeal. By analyzing various aspects of ISPs and using a multiple linear regression model to analyze the collected data, the model accurately determines the impact of ISP attraction factors from specific parameter values. At the same time, it also collects data of other ISPs to verify the model only to find that this model demonstrates a reliable ability to evaluate ISPs' attraction.

Keywords ISP evaluation • Gravity model • Factors • Multiple linear regression model

47.1 Introduction

Today, thousands of ISPs around the world provide services such as access to the Internet and network distribution. To enhance their own competitiveness and attract more users, ISPs such as China Telecom have been working to establish a better and faster network environment. They consider various factors that affect themselves comprehensively, and they propose different strategies, for example, increasing the bandwidth, interconnecting with other ISPs [1], and so on.

Current researches on ISP focus on the evaluation of ISP architecture [2] and network performance, but few studies involve ISPs' appeal. As the appeal of an ISP is an important basis for attracting more users and increasing business traffic, this paper aims to use an economic gravity model to model ISPs' attraction. This paper represents the first time a gravity model is being used to assess ISPs' attraction on

L. Heng • Z. Wang

Henan Provincial Key Lab on Information Networking, Zhengzhou University,
450052 Zhengzhou, China

School of Information Engineering, Zhengzhou University, 450052 Zhengzhou, China

G. Chen (✉)

Henan Provincial Key Lab on Information Networking, Zhengzhou University,
450052 Zhengzhou, China

e-mail: chengang@zzu.edu.cn

the basis of analyzing various factors of ISP and using a multiple linear regression model to achieve a correct evaluation model of ISPs' attraction.

47.2 Related Research

47.2.1 Study on Evaluation of ISPs

Today, work on the evaluation of ISPs can be divided into three aspects: ISP selection and evaluation, evaluation of ISP architecture, and analysis of ISP performance.

ISP selection and evaluation is about considering every factor before choosing the most desirable one upon comprehensive evaluation. There are many methods of evaluating an ISP, such as a sampling survey method, fuzzy set theory [3], and expert systems [4].

The evaluation of ISP architecture has as its goal mainly to evaluate the Internet architecture. The present author has summarized the evaluation mechanism, models, and methods of the current Internet architecture, including, for example, theoretical, game theory, and biological analysis methods [5]. Zhu et al. analyzed and modeled the architecture on the basis of three aspects to examine different application ratios and the effect of economic factors on the sustainable development of the architecture and various schemes [6].

The analysis of ISP performance entails measuring an index, including, for example, throughput and bandwidth. This paper comprehensively obtains the network performances of ISPs by analyzing the performance matrix based on an Autonomous System [7]. Researchers studied the quality of service and implemented a system of network performance based on the experience of users [8].

These studies mostly analyzed the problems of ISPs encountered in networks rather than analyze the factors affecting ISPs. As ISPs improve their competitiveness for attracting more users, ISPs, trading areas [9], and tourist attractions are mostly similar. In this sense, this study analyzes the related influential factors of ISPs based on general research on the gravity model to present an evaluation model of ISP attraction.

47.2.2 Research on Gravity Model and Its Common Applications

The gravity model is based on Newton's law of universal gravitation. Researchers extended it to the field of economics and put forward a relatively complete and

Table 47.1 Common application of gravity model

Model	Researchers	Formula	Parametric representation
Tourism attraction model	Jigang Bao	$T_{ij} = \frac{gP_i^\theta P_j^\phi}{d_{ij}^\delta}$	T_{ij} : number of tourists from i to j in a certain period of time P_i, P_j : population in area of i and j d_{ij} : range from i to j g : gravitational coefficients
Harvard business model	DL Huff	$P_{ij} = \frac{S_j^\mu}{T_{ij}^\lambda} \cdot \frac{S_j^\mu}{\sum_{j=1}^n T_{ij}^\lambda}$	P_{ij} : probability that consumers shop from area i to market j S_j : attraction of market j T_{ij} : resistance caused by distance n : number of competitors
City gravitation model	PD Converse	$I_{ij} = K \frac{w_i P_i \cdot w_j P_j}{d_{ij}}$	I_{ij} : mutual attraction between two cities P_i, P_j : population of cities i and j W_i, W_j : value of P_i and P_j d_{ij} : distance between cities i and j

simple economics model, that is, the gravity model of trade. It was mainly used to predict the interaction between two space and expanded and applied to the other fields, such as tourism and migration. Although it has been applied to various fields, its basic form remains the same. Usually, the simple gravity model is

$$M_{ij} = K \cdot Y_i Y_j / D_{ij}. \tag{47.1}$$

Table 47.1 summarizes common applications of the gravity model [10].

47.3 Analysis of Main Factors of ISPs’ Attraction

Various factors influence ISPs’ attraction, such as user incomes and communication quality. Researchers believe that the selection index of ISPs includes, for example, system security, customer demand, network services, professional services, and technical support [11]. Based on the selection indexes of ISPs and the application characteristics of the gravity model, this paper defines ISP attraction factors as ISP quality, regional quality, and the distance between ISPs and the areas they serve.

ISP quality can be represented by the number of its users and resource scale. The number of users can represent user preferences; resource scale indicates the support of capital of an ISP. This paper defines M_{ISP} , N_{ISP} , and S_{ISP} as ISP quality, number of ISP users, and ISP resource scale. Thus the quality of an ISP can be expressed as

$$M_{ISP} = N_{ISP}^{\alpha_1} \cdot S_{ISP}^{\alpha_2}. \tag{47.2}$$

Similarly, regional quality can be represented by the regional population and the level of economic development of the area. A regional population can indicate the

number of potential users in the area, and the level of economic development can directly determine whether or not people use an ISP. Thus, regional quality, regional population, and regional per-capita income are defined as M_A , P_A , and I_A :

$$M_A = P_A^{\beta_1} \cdot P_A^{\beta_2}. \quad (47.3)$$

In the traditional gravity model, the distance between two objects represents the interaction force. For example, in the Harvard business model, the distance between users and a market is represented by the time it takes users to get to the market; in the tourism attraction model, distance is represented by the specific physical distance; therefore, we define the distance of this model as cost to users to access the Internet and the average response time it takes users to access the cyber source. In this paper, C_{ISP} is the price that users pay to access the Internet, and T_{ISP} is the average response time. The distance between an ISP and the area it serves can be expressed as

$$D = C_{ISP}^{\gamma_1} \cdot T_{ISP}^{\gamma_2}. \quad (47.4)$$

According to the gravity model and regarding ISP quality, regional quality, and distance, this paper takes G as the correction index; thus, an ISP's attraction can be defined as

$$F_{ISP} = G \cdot \frac{M_{ISP} \cdot M_A}{D} = G \frac{(N_{ISP}^{\alpha_1} \cdot S_{ISP}^{\alpha_2}) \cdot (P_A^{\beta_1} \cdot P_A^{\beta_2})}{C_{ISP}^{\gamma_1} \cdot T_{ISP}^{\gamma_2}}, \quad (47.5)$$

where F_{ISP} is the value of the ISP's attraction, N_{ISP} is the number of users, S_{ISP} is the ISP's resource scale, P_A is the regional population, I_A is the per-capita income of the area, C_{ISP} is the price that users pay to access the network through the ISP, T_{ISP} is the average response time that users take to access the network through the ISP, and G is the correction index.

47.4 Study and Verification

47.4.1 Collection of Average ISP Response Time

Based on the previous section, we must collect the average response time of ISPs, which can be represented by the average response time of Web sites. Since the number of Web sites is too large, we just choose those that have lots of traffic. Thus, our work includes three steps: choose the Web sites, design and implement a simple performance test system, and test the average response time.

Table 47.2 Data of China unicom in Henan province

City	Number of users	Resource scale (billion ¥)	Population (million)	Per capita income (¥)	Access price (¥)	Average response time (s)
Zhengzhou	783,200	6.93	8.857	62,628.43	778	0.996
Luoyang	507,600	4.02	6.5671	45,699.01	720	1.081
Nanyang	519,880	4.5	10.263	23,064.38	600	1.327
Xuchang	338,400	1.8	4.296	40,479.52	550	1.168
Xinxiang	416,300	3.54	5.6594	28,605.51	600	1.296
Anyang	319,050	2.5	5.083	31,337.79	658	1.324
Zhoukou	492,160	4.0	8.952	17,788.2	600	1.567
Jiaozuo	236,510	1.643	3.527	44,692.37	600	1.532
Pingdingshan	375,200	3.0	4.904	30,628.06	660	1.609
Shangqiu	40,321	3.2	7.364	19,259.91	600	1.341
Xinyang	33,656	2.5	6.1077	23,064.33	600	1.258
Zhumadian	419,400	3.2	7.0848	19,576.56	600	1.489
Kaifeng	348,790	2.6	4.676	25,921.73	688	1.124
Sanmenxia	214,780	1.402	2.241	51,262.83	680	1.356
Puyang	255,400	2.3	356	27,935.39	538	1.654
Luohe	174,280	1.5	255	31,858.82	570	1.735
Hebi	141,650	1.095	1.5799	35,027.53	480	1.694
Jiyuan	78,930	0.8	0.6789	64,810.72	608	1.324

The data are Domain Name Systems from the related ISPs. After dealing with domain names with large amounts of data, we select the top 30 according to average daily traffic, with the visits to those Web sites accounting for 60 % of the total visits.

Next is the design of the simple performance test system which is based on Pylot. The basic framework is as follows:

The system can run using the command line or GUI. After accessing the Web sites in *testcases* and setting up the related parameters, we can run the system for the average response time. The results are given in Table 47.2, which is not reproduced here.

47.4.2 Purpose and Method of Experiment

One goal of our experiment is to establish the values of the relevant parameters. This paper regards the relevant data of China Unicom in every city of Henan province as the training set. Another goal is to verify the model by collecting data of China Telecom from cities in Henan. This paper inserts the data into a formula and compares the predicted with the actual results.

To obtain the parameter values, we use multivariate regression mathematical methods and make the ISPs' attraction value correspond to the number of ISP users in the area:

$$F_{\text{ISP}} = G \cdot Y_{\text{ISP}}. \quad (47.6)$$

To make the model application in mathematics, we integrate Formulas (47.5) and (47.6), then take the log on both sides of the formula to obtain Formula (47.7):

$$\lg Y_{\text{ISP}} = C + \alpha_1 \lg N_{\text{ISP}} + \alpha_2 \lg S_{\text{ISP}} + \beta_1 \lg P_A + \beta_2 \lg I_A - \gamma_1 \lg C_{\text{ISP}} - \gamma_2 \lg T_{\text{ISP}}. \quad (47.7)$$

Based on a regression analysis of data in Table 47.2, the result shows that the degree of fit is 99.229 %, and we obtain relative parameters such as $C = -1.92277$, $\alpha_1 = 0$, $\alpha_2 = 0.337816$, $\beta_1 = 0.568722$, $\beta_2 = 0.193897$, $\gamma_1 = 0.16743$, $\gamma_2 = 0.26544$.

To make the value of F_{ISP} close to a commonly used numerical value that we can understand, we define the comprehensive correction constant G as $G = 10^{-7.82277}$. Thus, we can finally express the model of ISP attraction as follows:

$$F_{\text{ISP}} = 10^{-7.82277} \frac{(S_{\text{ISP}}^{0.337816}) \cdot (I_A^{0.193897})}{C_{\text{ISP}}^{0.16743} \cdot T_{\text{ISP}}^{0.26544}}. \quad (47.8)$$

From the preceding equation, it can be seen that the model of ISP attraction correlates well with factors including resource scale, population, per-capita income, price, and average response time.

47.4.3 Verification of Model

To verify the validity and accuracy of the ISP attraction model, this paper collects data of China Telecom in cities in Henan Province from Henan Communications Administration and inputs the data into the model to obtain the value of F_{ISP} . In Fig. 47.1, the horizontal axis represents the cities and the vertical axis represents the number of users.

According to Fig. 47.2, compared with the actual results, the predicted number from ISP attraction model is consistent and deviates only slightly from the actual results, which indicates the validity and accuracy of this model.

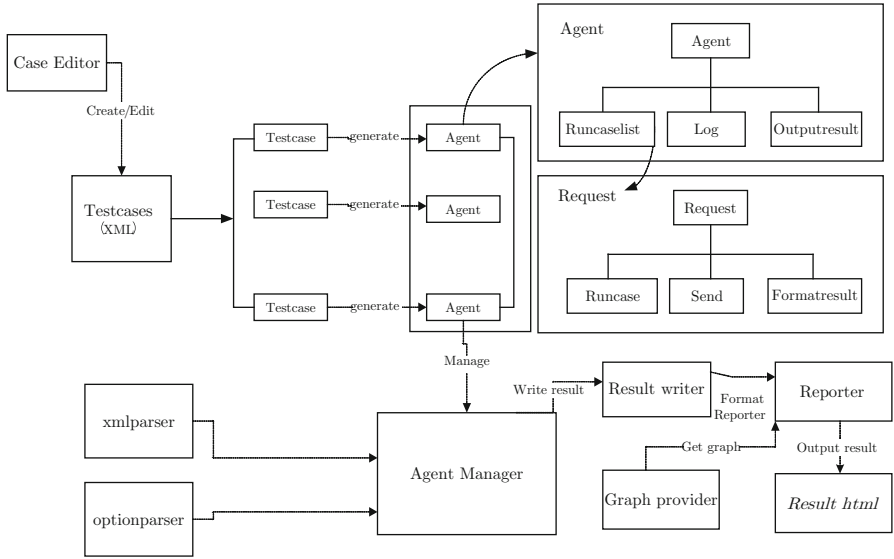


Fig. 47.1 Framework of web performance test system

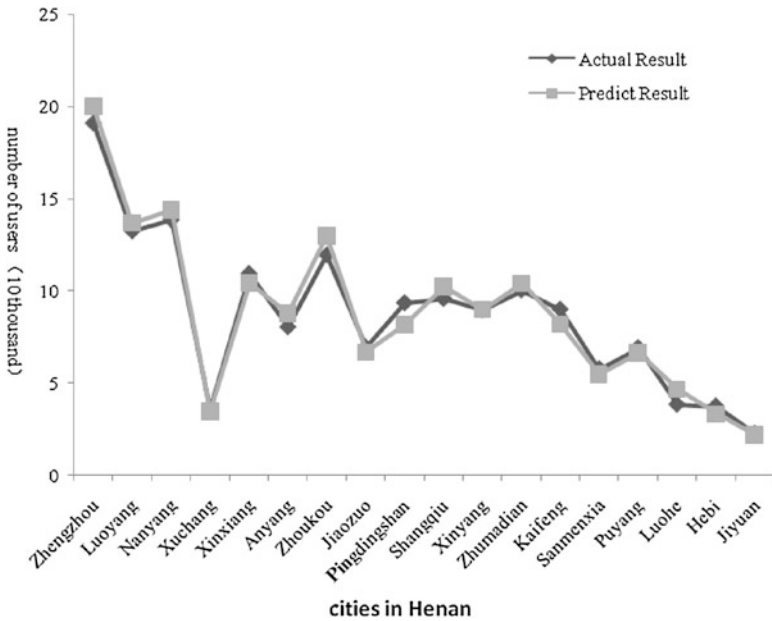


Fig. 47.2 Comparison of predicted and actual results

Conclusion

This paper describes an effective method for evaluating ISP attraction. On the basis of a study of the gravity model in economics, we improve it and apply it to ISP attraction. Based on the analysis of aspects of an ISPs, the paper establishes a model for ISP attraction. Using relevant collected data and a multiple linear regression model, we obtain the parameters of correlation factors. Then we collect data from other ISPs to verify the model with the results showing that the proposed model features high accuracy and effectiveness.

This model can be used to assess ISPs' attraction; therefore, according to the parameters of the model, ISPs can increase their investment, optimize the average response time, or combine different methods to pull in more traffic.

This is the first time the gravity model has been used to predict and evaluate ISPs' attraction, and so the accuracy of the model can still be improved using more factors and data.

References

1. Zhang B. Domestic broadband interoperability problem analysis. Beijing: Beijing University of Posts and Telecommunications; 2013.
2. Wu J et al. Advances in evolvable new generation internet architecture. *Chin J Comput.* 2012;35(6):1094–107.
3. Amin SH, Razmi J. An integrated fuzzy model for supplier management: a case study of ISP selection and evaluation. *Expert Syst Appl.* 2009;36(4):8639–48.
4. Chantarasathaporn K, Kimpan C. Enhancing ADSL customer satisfaction with fuzzy expert system case study: Chiang-Rai, Thailand. *Int Conf Intell Syst Des Appl.* 2012;54(12):998–1005.
5. Xu K et al. Internet architecture evaluation models, mechanisms and methods. *Chin J Comput.* 2012;35(10):1985–2007.
6. Zhu M et al. The evaluation method towards the application adaptability of Internet architecture. *Chin J Comput.* 2013;36(9):1785–97.
7. Qian Y, Ming C. A matrix-based method for evaluating ISP network performance. *IEEE Comput Soc.* 2009;569(34):193–7.
8. Sun H, et al. User-perceived network performance measurement system. *Computer Engineering.* 2007;33(4):115–17.
9. Liu S et al. City circle theory. Beijing: Renmin University of China Press; 2012. p. 54–68.
10. Zhu D et al. Application review of gravity model in economic researches. *J Yunnan Univ Financ Econ.* 2008;133(5):19–24.
11. Kuang Y et al. Dynamical selection of information service providers in outsourcing based on multiple attributes decision making. *Syst Eng Theory Pract.* 2009;29(7):77–85.

Chapter 48

An Application of Ecological Adaptation Evaluation of Orthoptera in Daqinggou Nature Reserve Using SPSS

Chunming Liu, Tao Meng, and Bingzhong Ren

Abstract SPSS is used for the comprehensive ecological adaptation evaluation of orthoptera in Daqinggou Nature Reserve. In this chapter, different habitats are subjected to PCA analysis on the basis of the species and quantity distribution of orthoptera in Daqinggou, and hierarchical clustering analysis is made upon the species distribution of orthoptera. The findings of both analysis methods are quite similar, and they divide the seven different habitats in Daqinggou into three types, which, according to the analysis results and in combination with actual findings, are represented by hygrophyte community at the bottom of the ravine, arid plant community on top of the ravine and unitary plant community. The three types of insects perch respectively at the three different habitats analyzed above, which reflect insects' selection for habitats. The results indicate that SPSS is reasonable and feasible and also SPSS has high accuracy.

Keywords SPSS software • Principal component analysis • Cluster analysis • Ecological adaptation

48.1 Introduction

Daqinggou Nature Reserve in Inner Mongolia is situated in the Horqin Sandy Land known as “800 miles big desert.” Previous studies in this area mainly focused on forest community stability, forest community succession, the prediction of species diversity of plant communities in forests, the origin of plant communities,

C. Liu (✉)

School of Life Science, Jilin Normal University, 136000 Siping, China
e-mail: jlsdlcm@163.com

T. Meng

Guangxi Forestry Survey and Design Institute, 130000 Changchun, China

School of Life Science, Northeast Normal University, 530000 Nanning, China

B. Ren

School of Life Science, Northeast Normal University, 530000 Nanning, China

© Springer International Publishing Switzerland 2015

W.E. Wong (ed.), *Proceedings of the 4th International Conference on Computer Engineering and Networks*, Lecture Notes in Electrical Engineering 355,
DOI 10.1007/978-3-319-11104-9_48

407

landscape diversity, as well as vegetation degradation and recovery in the surrounding areas [1], while studies on the distribution differences in insect species and quantity in different environments in this area have not been reported yet. For the time being, the ecological adaptation of insects is usually analyzed by principal component analysis (PCA), fuzzy clustering analysis, hierarchical weight grade method, the common probabilistic method, etc. [2,3] in SPSS.

Principal component analysis, or PCA, is a multivariate statistical method changing multiple indicators into several aggregative indicators with dimensionality reduction method under the premise of very little information loss [4]. In this chapter, the distribution differences in insect species and diversity in different environments are examined by principal component analysis, and the ecological adaptations of insects are evaluated to probe into the diversity of insect community of different groups in Daqinggou Nature Reserve.

48.2 Natural Survey

Daqinggou Nature Reserve is located at Horqin Left Back Banner, Tongliao City, Inner Mongolia. The geographic location of Daqinggou Nature Reserve is longitude $122^{\circ}13' - 122^{\circ}15'$, latitude $42^{\circ}45' - 42^{\circ}48'$, 168–285 m above sea level and covering an area around 8,183 km². In it, mingled forest of the nature of virgin forest is developed and abundant plant resources are held in store. Therefore, under the effects of composite factors such as terrain, landform, and soil, zonality is significant in plant distribution, and different natural landscapes such as sandy grasslands, open forest, and grassland, and precious mingled forest of broad-leaved species are developed.

48.3 Research Method

According to the different plant communities, the environment in Daqinggou Nature Reserve was divided into seven habitats, respectively, namely, the *Fraxinus mandshurica* plant community (A), Mongolian oak plant community (B), bigfruit elm plant community (C), coniferous forest plant community (D), lakeside plant community (E), paddy field plant community (F), and sandy grassland plant community (G). The orthoptera community in Daqinggou has been investigated for 5 times from July to August 2010 and from June to August 2011, respectively. See the specific documentation [5].

48.3.1 Similarity Analysis of Different Habitats

The seven different habitats in Daqinggou Nature Reserve were sequenced through principal component analysis. The raw data matrix taking the species and quantity of orthoptera as the line and taking the seven different habitats as the row was subject to standardized processing; its inner product matrix was computed; the eigenvalue, eigenvector, loading capacity, and accumulative contribution rate of each principal component were determined; and the sequence coordinate graph of habitats was worked out. Then, hierarchical clustering analysis was made to verify the said PCA sequence [6].

48.3.2 Habitat Clustering Analysis Based on Orthoptera Distribution

Orthoptera data was translated into binary data based on the presence or absence of orthoptera in different habitats. Presence was represented by 1 and absence by 0. Thus, the 48×7 matrix of binary data was obtained. Then, Q-mode analysis was made with this matrix. That is, hierarchical clustering of the seven different habitats was performed by taking the presence or absence of orthoptera in different habitats as properties. The binary orthoptera data was used to calculate Jaccard coefficient, which was in turn used to compare the similarities among different habitats [7].

Calculate formula of Jaccard coefficient, $C_J = j / (a + b - j)$ where j is the common insect species number of habitats A and B, a is the insect species number of habitat A, and b is the insect species number of habitat B.

48.4 Experimental Results

48.4.1 PCA Gradient Analysis of the Seven Habitat Types Based on the Species and Quantity Distribution of Orthoptera

PCA analysis of the seven habitats was made on the basis of the species and quantity distribution of orthoptera in Daqinggou Nature Reserve, and the results are shown as follows (Tables 48.1 and 48.2):

According to the results of principal component analysis, the accumulative contribution rate of the first three principal components lived up to more than 80 %. Namely, the first three principal components accounted for 80 % of the original data information and perfectly reflected the profile of original data.

Table 48.1 Eigenvalues and information amount proportion of seven principal components

Principal component	1	2	3	4	5	6	7
Eigenvalue	3.088	1.665	0.850	0.640	0.376	0.238	0.144
Percentage of information amount (%)	44.117	23.786	12.139	9.139	5.370	3.397	2.052
Accumulative information amount (%)	44.117	67.903	80.042	89.181	94.551	97.948	100.00

Table 48.2 Factor loading matrix of the first three principal components

	Principal component		
	1	2	3
A	0.554	0.628	-0.360
B	0.865	-0.092	-0.294
C	0.818	-0.382	0.190
D	0.899	-0.013	-0.202
E	0.361	0.667	0.237
F	0.084	0.726	0.443
G	0.646	-0.381	0.552

The accumulative contribution rate of the first two principal components also reached 67.9 % and basically maintained the original data information.

The contribution rate of the first principal component was as high as 44 %, and the greatest contributors included Mongolian oak community, bigfruit elm community, and coniferous forest community, indicating that the distributions of insects in the three habitats have much in common. The contribution rate of the second principal component was 23 %, also at a relatively high level, and the major contributors included lakeside, paddy field, and *Fraxinus mandshurica* communities, indicating that insects in the three habitats are species preferring to live in humid environment. Instead, the contribution rate of the third principal component was merely 12 %, which must be a less important analysis target. Nevertheless, the factor loading value of desert grassland was greater than any other habitat. It may suggest that the third principal component also reflects a distribution direction of insects, i.e., the species tending to live in arid environment, namely, the deserts.

48.4.2 *Habitat Clustering Analysis Based on Orthoptera Distributions*

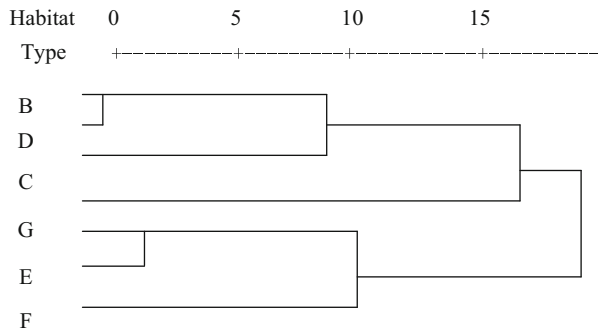
The binary orthoptera data was used to calculate Jaccard coefficient, which was in turn used to compare the similarities among different habitats. The similarity coefficient table (Table 48.3) was obtained via calculation.

The table shows that the similarity coefficient between Mongolian oak and coniferous forest plant communities is the greatest, i.e., 0.706, at the moderately

Table 48.3 Species similarity index of orthoptera in different habitats (Jaccard index)

	A	B	C	D	E	F	G
A	1.000	0.250	0.270	0.286	0.455	0.517	0.226
B		1.000	0.481	0.706	0.323	0.233	0.292
C			1.000	0.519	0.359	0.289	0.344
D				1.000	0.273	0.267	0.391
E					1.000	0.667	0.158
F						1.000	0.212
G							1.000

Fig. 48.1 Daqinggou seven different habitats of clustering analysis



similar level, indicating that the orthoptera species of the two are very similar and they have more species in common. Thus, we can draw the conclusion that the environmental conditions of the two are rather similar, leading to the relatively similar insect distributions. Besides, the similarity coefficient between lakeside and paddy field plant communities and that between coniferous forest and bigfruit elm plant community also live up to moderately similar level, supported by the figures of 0.667 and 0.519, respectively. The smallest similarity coefficient 0.158 was generated between sandy grassland and lakeside plant communities, drawing the ready conclusion that the similarity in insect species of the two habitats results from the extremely different environmental conditions of the two.

The similarities among different taxonomic units were measured, and hierarchical clustering of different habitats was performed by between-group method and with Jaccard coefficient, and the tree diagram (Fig. 48.1) was worked out. The similarities among different habitats reflected in the diagram was identical to those reflected by similarity coefficients.

According to the differences in the intrinsic environmental conditions of the seven habitats, the different habitats allow reasonable explanation of ecological significance regarding the clustering analysis results. Thus, the seven habitats in Daqinggou Nature Reserve can be divided into three major types in general:

The first type involves bigfruit elm community, Mongolian oak community, and artificial coniferous forest community located at the upper stream of the ravine. All of them are communities with poor forest coverage and similar habitat conditions.

The second type involves lakeside, paddy field environment, and *Fraxinus mandshurica* communities at the bottom of the ravine, serving as a common point of the three. Besides, the ambient humidity is commonly higher than that in other environments, especially that in lakeside and paddy field environments. As *Fraxinus mandshurica* community is located at the bottom of the ravine with brook passing through and high forest coverage, the humidity is higher.

The third type involves sandy grassland community. It is quite special and independent of other habitats to be a separate one in the clustering tree diagram. Nevertheless, it is comprehensible, as the most special factor of desert grassland environment is the drought. Besides, the poor vegetation condition is another major cause for its difference with other habitats.

48.5 Discussion

All living beings live in a certain ecological environment, and the biological characteristics they manifest are closely bound up with the surrounding living environment. Different insect compositions are distributed in different environments, and such differences in species distributions are insects' adaptation to different environments and the latter's accommodation of insects [8]. According to the analysis results of the two types of data above and in combination with the environmental conditions and insect species distributions in various habitats found out in actual investigation, the seven habitat types in Daqinggou were divided into three types:

Type I: hygrophite community at the bottom of the ravine, including *Fraxinus mandshurica* plant community, lakeside wetland plant community, and paddy field plant community. This habitat type is the representative of the one with higher humidity and vegetation coverage among various habitats in Daqinggou and is conducive to insect survival compared with other habitats. As a result, a large number of insect species are found thereof [9, 10].

Type II: arid plant community on top of the ravine, including sandy grassland and bigfruit elm plant communities. This type of habitat is the representative of arid environment with poor vegetation coverage. Arid as it might be, it also features typical grassland and complex plant composition. Thus, insects thereof are diversified as well.

Type III: unitary plant community, including artificial coniferous forest plant community and Mongolian oak plant community. The common point of the two is that the vegetation composition features low heterogeneity and almost unitary species composition. Thus, the insect communities thereof are less diversified.

In brief, different insects develop or distribute in different environments, develop their own adaptation to a given living environment [11]. Such adaptation is reflected by insect distributions and dependent on both the impact of vegetation composition on insects in the environment and insects' selection of habitats.

Conclusion

Daqinggou Nature Reserve is a national-level nature reserve and the fact that the special plant communities make various studies on it is quite important. According to the studies on orthoptera community in Daqinggou area, hidden trouble exists as well. Artificial coniferous forest habitat features few species number and low homogeneity, and the habitat condition available for insects under unitary vegetation condition is unitary. As a result, only a few species adapt to such environment and keep on top in the struggles for existence. Subsequently, dominant groups will be developed and population outbreaks will be triggered, which may seriously impair vegetations and cause disasters. It follows that working well on the scientific investigation and monitoring of insects, especially the common pest species, i.e., locusts in Daqinggou area, is very important for the construction of Daqinggou Nature Reserve.

Acknowledgments This study was funded by the program for scientific and technological project (no. 2011-24) of Environmental Protection Department of Jilin Province, China, and the National Natural Science Foundation of China (no. 30471400).

References

1. Nan-nan Z, Ming-tao Y. Spatio-temporal gradients of soil moisture in Daqinggou Nature Reserve, Inner Mongolia. *J Beijing Forestry Univ.* 2008;30(4):95–102.
2. De Roos AM, Persson L, McCauley E. The influence of size-dependent life-history traits on the structure and dynamics of populations and communities. *Ecol Lett.* 2003;6(5):473–87.
3. Caldarelli G, Higgs PG, McKane AJ. Modelling coevolution in multispecies communities. *J Theor Biol.* 1998;193(2):345–58.
4. Jiang Y, Wang Z. Study on the application of the fundamental statistic methods of SPSS in efficacy analysis of Quercetin and Resveratrol mixture. *Adv Inf Sci Serv Sci.* 2012;4(17):380–7.
5. Chunming Liu Yue Z. Study on the insect diversity in Momoge National Nature Reserve. *J Northeast Normal Univ (Natural Science Edition).* 2011;43(3):112–6. In Chinese.
6. Schmidt AKD, Römer H, Riede K. Spectral niche segregation and community organization in a tropical cricket assemblage. *Behav Ecol.* 2013;24(2):470–80.
7. Liu W, Zhou B. Residential environment evaluation and strategy research of city planning and construction of Xi'an city. *JCIT.* 2012;7(18):240–8.
8. Guo C, Liu F. Dynamics study of insect community in Heilihe National Nature Reserve. *J Jilin Agric Univ.* 2011;33(3):287–92. In Chinese.
9. Gu W, Ma L. Insect diversity of different habitat types in Zhalong Wetland, Northeast China, Chinese. *J Appl Ecol.* 2011;22(9):2405–12.
10. Whiles MR, Goldowitz B. Hydrologic influences on insect emergence production from central Platte River wetlands. *Ecol Appl.* 2011;11(6):1829–42.
11. Aoki K, Kato M. Phylogeography of phytophagous weevils and plant species in broadleaved evergreen forests: a congruent genetic gap between western and eastern parts of Japan. *Insects.* 2011;2(2):128–50.

Chapter 49

Intelligent Diagnostics Applied Technology of Specialized Vehicle Based on Knowledge Reasoning

Licai Bi, Yujie Cheng, Dong Hu, and Weimin Lv

Abstract According to the rules on knowledge base, maintenance personnel can use a variety of diagnostics information when one failure occurs in complex system, in order to determine the failure mode of the system by reasoning and implement the fault location and troubleshooting quickly and accurately. Firstly, the framework of intelligent diagnostics based on knowledge reasoning is built, then creation, structure, and updating of knowledge base are analyzed, and then the diagnostics model and reasoning mechanisms are analyzed, and the diagnostics reasoning process is given. Finally, the demonstration of intelligent diagnostics is carried out by one typical failure case in specialized vehicle.

Keywords Intelligent diagnostics • Specialized vehicle • Reasoning • Knowledge base

49.1 Introduction

With the development and application of artificial intelligence technology, intelligent fault diagnostics of vehicle has been kept the focus on in research of the embedded diagnostics, prognostics, and health management. It is possible to simulate human experts effectively for diagnosing complex system through the course of acquisition, transmission, processing, regeneration, and utilization of diagnostics information. Human experts, meanwhile, will play an important role on diagnostics and allow computers and networks to exchange, collect, copy, convey, and preserve

L. Bi (✉) • D. Hu • W. Lv
Seventh Department, Navy Aeronautical Engineering Institute, 264001 Shandong, China
e-mail: 960174092@qq.com

Y. Cheng
School of Reliability and Systems Engineering, Beijing University of Aeronautics and Astronautics, 100191 Beijing, China

their knowledge and experience in long term. Xiao Bao analyzed the structure of intelligent diagnostics system based on neural networks [1]. Tianhong Luo et al. constructed the expert system by integrating fault tree with fuzzy neural network, and the construction of knowledge base and the realization of reasoning engine with expert rule representation and fuzzy representation were completed by taking the example of a common fault of the automobile crane [2]. Yun Shi presented a fuzzy tree for qualitative and quantitative analyses of the common fault of automobile engine by the smallest cut set and the structure function of the fault tree [3]. According to the characteristics of the failures of specialized vehicles, the module of intelligent diagnostics based on knowledge reasoning in vehicle health management system is built, and the applied case of engine in the specialized vehicle is demonstrated.

49.2 Technical Framework

The intelligent diagnostics based on knowledge reasoning is composed by the knowledge base, inference machine, integrated database, and human–computer interface. Its main function is that when one failure occurs, maintenance personnel can use a variety of diagnostics information in the knowledge base to determine the failure mode of the system by reasoning and implement the fault location and troubleshooting quickly and accurately. The framework is shown in Fig. 49.1.

The function of each component is introduced as follows:

Diagnostics knowledge base stores knowledge in format of fault tree, fault reason, and fault elimination solution that come from experts and experienced maintenance personnel.

Integrated database stores information about users' input, the original facts, and diagnostics process.

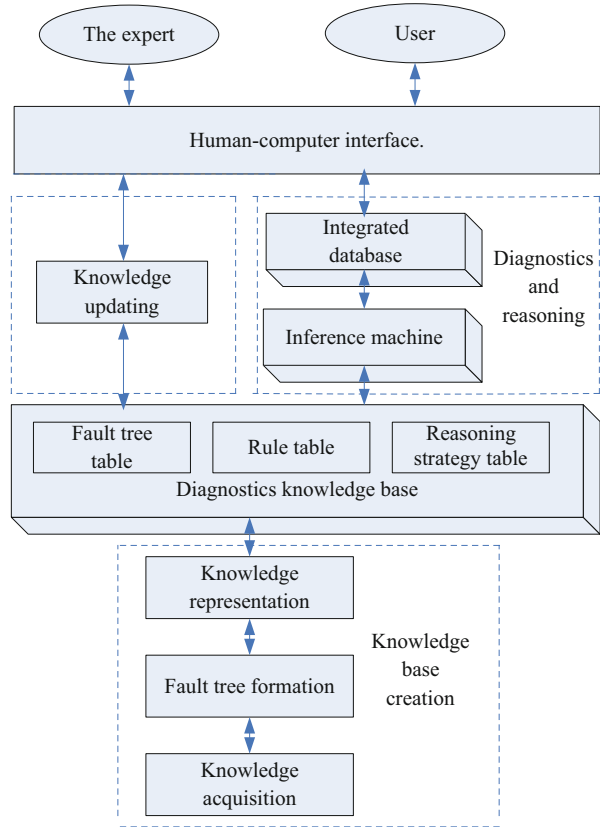
Inference machine conducts the control of solving process for problem and to implement appropriate control strategies to acquire the conclusion.

Human–computer interface is that to make communication friendly.

49.3 Diagnostics Knowledge Base

Knowledge base is one core component of intelligent decision support system. It makes possible for a well-architected structure of knowledge base to reduce the complexity of reasoning effectively and improve efficiency of reasoning. The knowledge base is utilized to store the diagnostics knowledge in the fault tree and provide the basic knowledge to inference machine.

Fig. 49.1 Framework of intelligent diagnostics



49.3.1 Knowledge Base Creation

The creation of knowledge base includes: knowledge acquisition, fault tree formation, and knowledge representation.

49.3.1.1 Knowledge Acquisition

Knowledge is acquired from original resources, which consist of expert knowledge, technical documents, databases, and other human experience. And then knowledge is converted into data in order to enter knowledge base through identification, classification, screening, and induction. The way to acquire knowledge is combining with methods, nonautomatic, and semiautomatic. The method of nonautomatic is completely done by hand, as shown in Fig. 49.2. The method of semiautomatic is completed primarily by knowledge engineer and the acquisition agency of expert system. Knowledge engineers acquire knowledge from the experts in the field and

Fig. 49.2 Nonautomatic

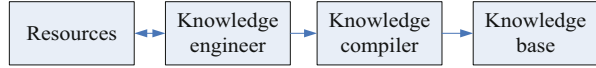
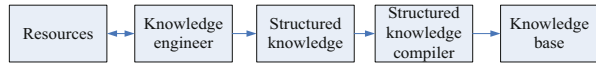


Fig. 49.3 Semiautomatic



then represent them by appropriate models. And the acquisition agency transforms them into accepted forms for storage in the computer and then stores them in the knowledge base, as shown in Fig. 49.3 [4, 5].

49.3.1.2 Fault Tree Formation

Fault tree is logic diagram which is used to describe the symptoms or results of failure. It can clearly reflect logical relationship of failure, give directed logical analysis process, and reasonably describe the level and causation of fault knowledge [6]. The accuracy of qualitative and quantitative analyses lies directly to the perfection of fault tree formation.

49.3.1.3 Knowledge Representation

Knowledge representation, named as knowledge representation model, is such an acceptable description mode in computer that the concise representation of knowledge can improve the accuracy, efficiency, and success of diagnostics [7]. Both of the production rule and frame representation are used for knowledge description.

Production Rule Production, known as rule or production rule, generally is made to represent the knowledge of causation. Its basic form is that: IF condition THEN conclusion. Condition, known as the premise or antecedent, means the condition whether or not is available for production rule. Conclusion, called consequent or action, refers to the conclusion or conduction when conditions are met. The conclusion of one production rule can also supply another production rules as one antecedent. The production rule of knowledge representation is shown as follows:

- [Rule]
- Antecedent = “Parent node Rule NO.”
- Consequent = ... # Measuring point
- Failure solution = ...
- Number of child nodes = Number of conditions
- Child node 1 = Rule NO. # Prerequisite
- Child node 2 = Rule NO. # Prerequisite
- ...

Table 49.1 Form of frame representation

Frame name		
Slot name 1:	Side name 1	Value 1, ...,value k
	
	Side name n	Value 1, ...,value k
Slot name 2:	Side name 1	Value 1, ..., value k
.....	
	Side name n	Value 1, ...,value k
Rule:	Rule 1	
	
	Rule m	

Among them, Rule NO.: “Rule” Rule serial number, rule serial number is the corresponding Rule NO. of each child node in fault tree. Antecedent: the former rule serial number to one rule. Consequent: the questions and its corresponding measuring point which are separated by the “#”. Measuring point: described by the predefined string. If the answer of question for one rule is default without detection data, the measuring point is indicated by character “0”. Failure solution is troubleshooting method. Number of child nodes is the number of follow rules. Child node contents are including rule number and prerequisite. Prerequisite is a special character logo, including “Y”—which means the current rule is established—or “N” which means not.

Frame Representation Frame representation is a structured representation based on frame theory. In frame theory, the understanding of things is stored in people’s memory in the frame form. The frame is composed of slots which are used to describe every aspect and its concept. The level of each slot is defined as side, and each side includes a number of individual values. The form of frame representation is shown in Table 49.1.

49.3.2 Knowledge Base Structure

Three associated data tables which include fault tree table, rule table, and reasoning strategy table are designed as back-end database resources for knowledge management. The structure and relationship of three tables are shown in Fig. 49.4.

Fault tree table is the basic table, which is achieved by establishment of the fault tree. Diagnostics rule comes from the conversion based on the fault tree, resulting in the rule table. Reasoning strategy table is the combination of two tables mentioned above. Among the three tables, the fault tree is an associated entrance, the symptom is keyword to knowledge query, and the appropriate troubleshooting method is determined by rules.

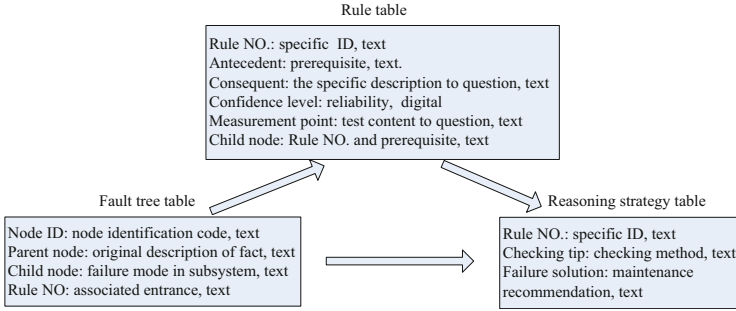
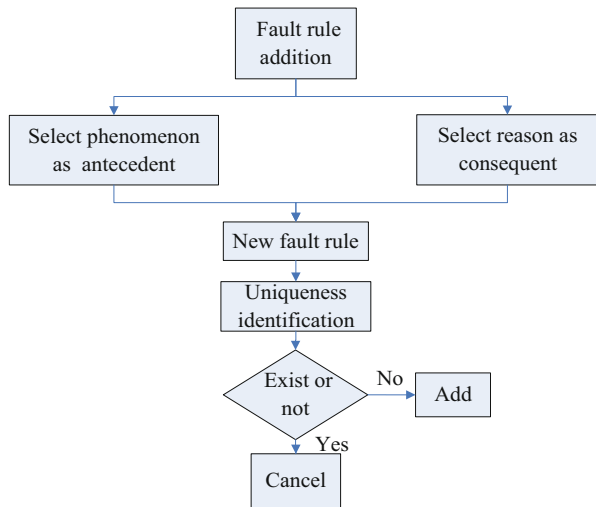


Fig. 49.4 Structure and relationship of three tables

Fig. 49.5 Fault rule addition



49.3.3 Knowledge Base Updating

Knowledge base updating is that to meet users' acquiresments, the experts in the light of field maintenance experience of specialized vehicle keep revising, expanding, and improving knowledge base, making diagnostics results more practical and more perfect. Knowledge base updating includes addition, modification, and removal of knowledge. Here explained in this chapter is only the process of addition, which is related to the fault phenomenon, fault reason, and fault rule [8]. Firstly, it is necessary to decide whether the event is on top and intermediate or bottom of fault tree that is relevant to the phenomenon, reason, or rule. Secondly, the uniqueness of the event needs to be identified. Thirdly, if the event is unique, do add the phenomenon, reason or rule, and vice versa. For example, the fault rule addition is shown in Fig. 49.5.

49.4 Diagnostics Reasoning

Inference machine, another core of intelligent fault diagnostics system, accomplishes knowledge reasoning in computers, including reasoning and control, which is an indispensable component in expert systems [9]. The perfection of this system is largely determined by the efficiency and level of the intelligence of diagnostics reasoning.

49.4.1 Fault Tree Model

Fault tree model can be used for not only presentation of knowledge but also implementation of diagnostics, which is a causal model to describe the structure, function, and relationship of objects and to reflect the hierarchy of fault propagation and causation between parent node and child node. With diagnostics knowledge base built by frame representation, taking into account the factors such as processing ability of inference machine usability of system, promotion of maintenance efficiency, and reduction of support costs, fault tree model is an option for construction of inference machine here.

49.4.2 Reasoning Mechanism

It is important to take into consideration the methods and direction of reasoning. According to the certainty of knowledge, the methods of reasoning are divided into two parts, certain reasoning and uncertain reasoning. The direction of reasoning includes forward, backward, and hybrid [10].

Considering the simple causation of specialized vehicle faults and both with certainty and uncertainty factors, the combination of certain and uncertain reasoning and forward direction is chosen to reason, so the requirements to information exchanging rapidly and the speed and accuracy of intelligent diagnostics may be met.

49.4.3 Control Strategy

Control strategies mainly refer to search strategy and conflict resolution strategy [11]. The causation of specialized vehicle faults does not have many levels, but it is very wide. It is suitable to use first-depth search strategy, which can quickly search

into deep level, and avoid unnecessary lateral search and prevent inconvenience due to long search time. Block ordering is applied in conflict resolution strategy, owing to frame representation [12]. The sequencing of confidence level is used in each frame, and high confidence level is corresponding to front row. The rule in the top of fault tree is searched and matched at first and so on, until the result is inferred.

49.5 Application

Take the abnormal phenomenon of engine, for example, which is the most common and typical failure or condition warning in process of specialized vehicle diagnostics.

When one anomaly of engine oil pressure is monitored, intelligent diagnostics is triggered, as shown in Fig. 49.6. And we click into the intelligent diagnostics interface and then acquire four possible options for the anomaly through screening and matching, as shown in Fig. 49.7. Check by tips until the final diagnostics result is received. The result report is sent and saved, as shown in Fig. 49.8. Moreover, the mission planning function in the vehicle health management system is put forward to notice maintenance task related to the result, as shown in Fig. 49.9.

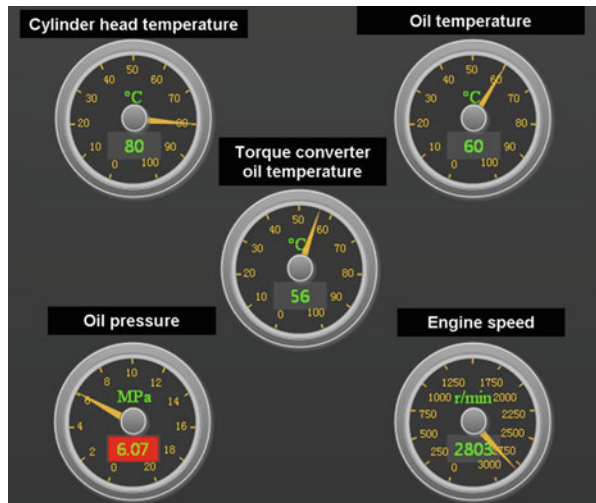


Fig. 49.6 Status monitoring

Fig. 49.7 Diagnostics

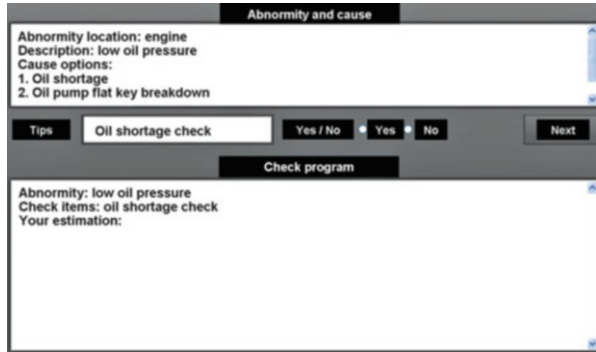
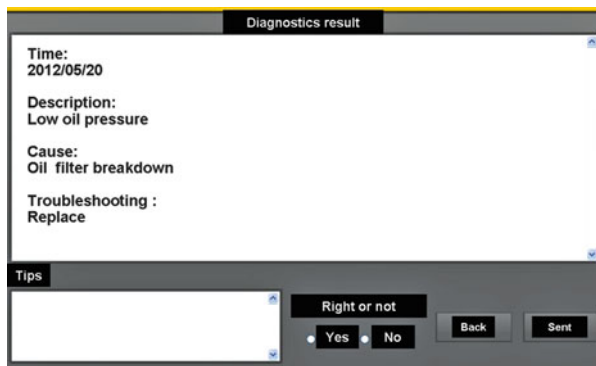


Fig. 49.8 Result report



Maintenance task list								
ID	System	Equip.	Part	Item	Deadline	Prior.	Level	Type
2012104	HPS	FD&C	--	Replace	2012-5-29	3	Opera.	CBM
2012105	CS	Engine	Oil filter	Replace	2012-5-28	4	Opera.	CBM

Spare parts list					Repair program	
ID	Part	Number	Location	Version		
20120301	FD&C	1	SB	FLF4071	1. Demount FD&C from Vehicle by tool E 2. Check for leaks or block up in FD&C 3. If FD&C is in fault condition, replace it by tool A	
20120302	Tool E	1	SV	GJ002		
20120303	Tool F	1	SV	GJ001		

Staff ID: Confirm

Fig. 49.9 Mission planning

Conclusion

On the basis of the characteristics of faults in specialized vehicle, the establishment of intelligent diagnostics module in vehicle health management system based on knowledge base and inference machine can contribute to assist maintenance personnel to determine the fault location quickly and accurately, infer the fault reason, and produce troubleshooting strategies and maintenance recommendations. Furthermore, prognostics module will be developed by our team, in which trend analysis about abnormal phenomenon, thus anomaly, may be provided, and the predictive maintenance (or condition-based maintenance) can be achieved step by step.

References

1. Xiao B. Study on intelligent fault diagnosis expert system of automobile engine. *Technol Dev Enterprise*. 2013;32(6):6–7. In Chinese.
2. Tianhong L, et al. An expert system for diagnosing hydraulic fault of automobile crane using fault tree. *Mech Sci Technol Aerospace Eng*. 2013;32(4):538–44. In Chinese.
3. Yun S. Application of fuzzy fault tree in automobile engine failure diagnosis. *J Guilin Univ Electr Technol*. 2008;28(3):222–4. In Chinese.
4. Meihui L, et al. Research of knowledge acquisition. *Comput Knowl Technol*. 2008;3(9):2056–7. In Chinese.
5. Jun Y, et al. *Intelligent fault diagnosis technology for equipments*. Beijing: National Defense Industry Press; 2004. p. 27–8. In Chinese.
6. Jiazhan Z. Security in the process of certain type of missile fault diagnosis expert system for shallow layer. *Aerospace Control*. 2012;30(6):78–82. In Chinese.
7. Zhi'an Z. Note-knowledge-representation method of definite-fault-diagnosis knowledge. *J Chang'an Univ (Natural Science Edition)*. 2003;23(1):80–3. In Chinese.
8. Rusheng Z, et al. Fault diagnosis expert system for hydraulic system of missile launcher. *Acta Aeronautica ET Astronautica Sinica*. 2008;29(1):197–203. In Chinese.
9. Dawei L, et al. Design for integrated diagnosis inference engine for PHM of aircraft electro-mechanical system. *J Nanjing Univ Aeronaut Astronaut*. 2011;43(S):114–8. In Chinese.
10. Hongfeng J. Develop on inference engine of the EFI engine fault diagnosis expert system [J]. *Highways Automotive Appl*. 2011;4:28–31. In Chinese.
11. Chuanfeng W, et al. Design on inference engine of the spacecraft thermal fault diagnosis expert system. *J Beijing Univ Aeronaut Astronaut*. 2005;31(1):60–2. In Chinese.
12. Zuqiang M, Feng L. Study fault detect expert system of flight simulator base on fault tree analysis. *Sci Technol Eng*. 2012;12(19):4853–6. In Chinese.

Chapter 50

On the Evaluation of Influence of Golf Websites in China

Fangzhi Liu

Abstract The evaluation index system of influence of Chinese golf websites includes website scale, inbound link, website traffic, website utilization rate, etc. Choosing 17 Chinese golf websites as the object of the research, this chapter evaluates their influence on the basis of grey relational analysis and finds that the influence of golf vertical portals is comparatively high, but the impact of most of the Chinese golf websites is low, which are badly in need of reinforcement and promotion.

Keywords China • Golf websites • Influence • Grey relational analysis

50.1 Introduction

With its immediate, massive, global, interactive, and multimedia features, Internet, as the “fourth largest” media, has grown rapidly in China, and the number of Chinese citizens is also making a spurt of progress. According to the thirty-second Chinese Internet development statistics report released by China Internet Network Information Center (CNNIC) in July 17, 2013, Chinese users amounted to 591,000,000 at the end of June in 2013, an increase of 26,560,000 compared to the end of 2012; the Internet penetration rate was 44.1 %, increased by 2 % compared to the end of 2012; at the same time, the number of Chinese mobile phone users was up to 464,000,000, increased by 43,790,000 users compared to the end of 2012. The popularization of 3G, development of wireless network, and innovation of mobile phone applications contribute to the rapid increase of mobile phone users. Thus, the Internet has become an essential communicative tool for 42.2 % of the Chinese people. It has such a great effect on modern citizens that they cannot do without the Internet.

F. Liu (✉)

Physical Education College, Hunan University of International Economics,
410205 Changsha, China
e-mail: 67604219@qq.com

© Springer International Publishing Switzerland 2015

W.E. Wong (ed.), *Proceedings of the 4th International Conference on Computer Engineering and Networks*, Lecture Notes in Electrical Engineering 355,
DOI 10.1007/978-3-319-11104-9_50

425

As a foreign sports, golf has witnessed a history of nearly 30 years in China marked by the establishment of the Guangdong Zhongshan Golf Club in 1984. The history of the development of golf in China was full of twists and turns, but it is also a process to understand golf for the Chinese people. At the beginning of its introduction, golf was regarded as “the Western game,” “official corruptive game,” “a sport for the noble,” “a rich man’s game,” “green opium,” “desert in city,” and so on. However, with the enlargement of China’s reform and opening policy, some people altered their views on golf and regarded golf as a “gentleman’s game,” “an ideal way of leisure,” with an increasing number of people enjoying the game. According to the Forward White Paper in 2012, golf facilities in China were 477 in 2012, a total of 10,570 holes, equivalent to about 581 eighteen-hole golf courses; the national golf facilities produced about 11,500,000 rounds of golf balls; the golf core population was up to 386,000 [1]. This also shows the development of China’s golf industry for 30 years, which is closely linked with the propaganda of the media. Admittedly, the Internet plays an irreplaceable role in golf’s development in China and the Chinese attitudes to golf. How are Chinese golf website influences evaluated? Which are more influential? Thus, it is really significant to solve these problems and is also of important realistic significance for the optimization of golf website resources to attract more readers.

50.2 Designing of Evaluation Scheme

50.2.1 Evaluation Methods of Influence of Website

At present, researches on website influence are fruitful. After a thorough study on such concepts as the Internet public opinion, web information source, and impact of information source, Y Guo, CY Liu, and ZH Yu et al. established an evaluation index system for the study of impact of web information source on public opinion [2]. WY Liu and TB Zhou constructed an evaluation index system on the basis of library web impact such as the website scale, website traffic, inbound link, network user attention meter, and website utilization rate [3]. Taking the number of inlinks and web impact factors (Web-IF) as the indexes to evaluate the influence of the website, YF Duan makes a comparative study of the influence of the websites of Sino-American business schools [4]. YZ Sha and X Oukyng evaluate the influence of the Chinese provincial government websites by link analysis method and the measure of web impact factor of evaluation [5].

From the above research results, scholars have focused on the evaluation of influence of library websites, network public opinions, and government websites. But there is little evaluation on golf websites. This chapter will present the index system of evaluation based on previous researches by investigation and verification and evaluate the influence of golf websites in China.

Table 50.1 Evaluation index system of the influence of golf websites

Index name	Index connotation
Website scale	This is the number of webpages being collected by a search engine. The higher the utilization of websites used by the public is, the more influential they are
Inbound link	This is the number of webpages of the inbound link from other sites. Generally speaking, the inbound link is larger, and the influence is greater
Website traffic	The number of website visits can directly reflect the influence of the websites
Website utilization rate	Website utilization rate = total links/total time of website launch. This index can reflect the utilization efficiency of websites and make up for the defects caused by simply relying on the link statistics. To some extent, it can reflect the influence of the websites

50.2.2 Construction of the Index System of Evaluation

Drawing lessons from the research results above, combining the expert argument and link analysis theory, this chapter fosters the evaluation index system of the influence of golf websites, including website scale, website traffic, inbound link, and website utilization rate as shown in Table 50.1.

50.2.3 Data Acquisition Modes

Website scale: Comparing Baidu, Google, Yahoo, and other search engines, this article selects the Baidu search engine (the fastest search engine in China) [6]. The data of website scale is acquired by inputting “site: website domain name” command on the Baidu page.

Inbound link: The data of inbound link is acquired by inputting “linkdomain: website domain name” command on the Baidu page.

Website traffic: The data of website traffic is acquired by inputting the name of the golf website on the “tool.chinaz.com” page.

Website utilization rate: The data of website utilization rate is acquired by inquiring the CNZZ “whois query.” CNZZ is the most influential free service provider of Internet traffic statistical techniques in China, specializing in Internet data monitoring, statistical analysis technology research, and product development and application.

50.3 An Empirical Evaluation of Golf Website Influence

50.3.1 Sample Choice

This article chooses professional golf websites as the objects of study, not including the branch golf website from Sina, 163, Sohu et al. comprehensive website, and golf club website. Because golf sports in China has a short development time and it requires a strong profession, plus the number of golf websites in China is relatively small, this article chooses only 17 relatively larger websites as the objects of study.

50.3.2 Website Influence Index Data Analysis

The collected data of Chinese golf site influence the evaluation index presented in Table 50.2. The data of index website scale, inbound link quantity, and website utilization rate is counted on December 29, 2013, and website traffic on December 30, 2013.

Table 50.2 Influence index data of Chinese golf websites

	Website	Website scale (pages)	Inbound links (pages)	Website traffic (visits/day)	Website utilization rate (pages/month)
1	http://www.funfungolf.com	42,800	36,500	20,425.0	474.0
2	http://www.21golf.com	1,460	38,700	190.0	276.4
3	http://www.igolfyou.cn	6,040	16,100	33.0	263.9
4	http://www.ugolf.com.cn	29,900	9,980	47.0	76.2
5	http://www.golf998.com	50,600	14,600	80.0	132.7
6	http://www.golftour.cn	67	10,100	33.0	112.2
7	http://www.forwardgolf.com.cn	1,090	10,600	142.0	79.1
8	http://www.golftong.com	5,860	3,990	42.0	117.4
9	http://www.golf.org.cn	3,170	16,200	52.0	137.3
10	http://www.5ugolf.com	2,030	12,600	42.0	206.6
11	http://www.jrgolf.cn	2,230	2,850	4.0	24.4
12	http://www.golf72.cn	535	5,460	1,045.0	60.7
13	http://www.golfonlife.com	12,200	1,080	142.0	10.3
14	http://www.huagolf.com	11,100	9,530	522.0	148.9
15	http://www.golfpunk.com.cn	6,320	1,670	237.0	92.8
16	http://www.92golf.com	6,030	11,300	142.0	152.7
17	http://www.golfme.cn	16,300	16,600	9.0	286.2

50.3.2.1 Website Scale

Through the statistics of 17 golf sites, we got the website scale distribution as presented in Table 50.2. From Table 50.2 we can see there are three website pages exceeding 16,000; they are golf998, funfungolf, and ugolf. There are 11 website pages lower than 8,000; so it reveals that the development of Chinese golf websites is unbalanced, wherein the overwhelming majority are small and only a few are large. Two of the seventeen websites are the smallest, and they are golf72 and golftour.

50.3.2.2 Inbound Link Quantity

The inbound link quantity of 17 golf websites is presented in Table 50.2. From Table 50.2 we can see obviously that 21golf and funfungolf are far ahead. The author thinks that the reason for the high links of 21golf is that it provides distinctive service, opens golf course Teentime searching information, and issues favorable price information of every golf course and golf practice field, and there is a rich golf training knowledge for each stage. Funfungolf, as a golf vertical portal, issues information concerning nearly every aspect of golf sports and provides a one-stop service for golfers, and as it links with many large portal websites, its inbound link quantity is greatly increased.

50.3.2.3 Website Traffic

Website traffic is the visitor volume by the network users, often used as the index of website influence evaluation. Table 50.2 suggests that FunFunFolf is at the top of the list with visits of 20,425 times every day, standing in marked contrast to other websites hundreds of times. The main reason is it provides abundant golf-related information, so it attracts a lot of attention from golfers, golf pros, media, enterprises, etc. This suggests the distinctive advantage of vertical portal.

50.3.3 Correlation Degree Sorting

From Table 50.2 we can see that, according to different indexes, the sorting of Chinese golf websites has a relatively big difference. It is difficult to say which one is more reasonable, so this article chooses the grey relationship analysis (GRA) method to comprehensively evaluate the influence of Chinese golf websites. The GRA method is a multivariate statistical analysis method, describing the strength, size, and sequence of the relationship among different factors based on the sample data of factors. This article chooses a specific time period, according to

Table 50.3 Influence sorting of Chinese golf websites

	Website	Scale	Inbound link	Website traffic	Utilization rate	Correlation degree
0	Standard	1.0000	1.0000	1.0000	1.0000	1.0000
1	www.funfungolf.com	0.7641	0.8953	1.0000	1.0000	0.9148
2	www.21golf.com	0.3396	1.0000	0.3354	0.5399	0.5537
3	www.golf998.com	1.0000	0.4384	0.3342	0.4045	0.5443
4	www.golfme.cn	0.4242	0.4598	0.3334	0.5525	0.4425
5	www.igolfyou.cn	0.3618	0.4542	0.3336	0.5246	0.4186
6	www.ugolf.com.cn	0.5497	0.3958	0.3338	0.3682	0.4119
7	www.5ugolf.com	0.3422	0.4188	0.3337	0.4644	0.3898
8	www.golf.org.cn	0.3476	0.4553	0.3339	0.4078	0.3861
9	www.huagolf.com	0.3901	0.3920	0.3391	0.4163	0.3844
10	www.92golf.com	0.3618	0.4071	0.3348	0.4191	0.3807
11	www.golftour.cn	0.3333	0.3968	0.3336	0.3906	0.3636
12	www.forwardgolf.com.cn	0.3379	0.4010	0.3348	0.3699	0.3609
13	www.golftong.com	0.3609	0.3515	0.3337	0.3940	0.3600
14	www.golfpunk.com.cn	0.3633	0.3369	0.3359	0.3782	0.3536
15	www.golf72.cn	0.3354	0.3614	0.3451	0.3594	0.3503
16	www.golfonlife.com	0.3969	0.3333	0.3348	0.3333	0.3496
17	www.jrgolf.cn	0.3431	0.3441	0.3333	0.3402	0.3402

the development of a situation of similar degree of each evaluation index data of influence of the golf site to measure the complexity of the spatial correlation among the factors, which demonstrates the characteristics of dynamic association among the various indexes and degree of correlation. Then, the results have been sorted according to the correlation degree.

Because of the big difference in the data of different indexes, the article uses the range transformation method to standardize the data of every index in the first place. The standardized data of every index all meet $0 \leq y_{ij} \leq 1$; the optimum is 1 and the worst is 0. Putting the data of 4 indexes in Table 50.2 into the standardized formula (1) and normalizing them, we get the resulting data presented in Table 50.3. The standardized formula is

$$y_{ij} = \frac{x_{ij} - \min_j x_{ij}}{\max_j x_{ij} - \min_j x_{ij}} \quad (1 \leq i \leq 29, 1 \leq j \leq 5) \quad (50.1)$$

The GRA method formula is:

- (1) The calculation formula for the aggregation coefficient of correlation $V(X_0(k), X_i(k))$ at $k = 1, 2, \dots, n$ is

$$\begin{aligned}
 V(X_0(k), X_i(k)) &= \frac{\min_i \min_k |X_0(k) - X_i(k)| + \rho \max_i \max_k |X_0(k) - X_i(k)|}{|X_0(k) - X_i(k)| + \rho \max_i \max_k |X_0(k) - X_i(k)|} \\
 &= \frac{0.5}{|X_0(k) - X_i(k)| + 0.5}
 \end{aligned}
 \tag{50.2}$$

In the equation above, $\min_i \min_k |X_0(k) - X_i(k)|$ is the minimum difference value, and $\max_i \max_k |X_0(k) - X_i(k)|$ is maximum difference value. $\rho \in [0, 1]$ is the resolution ratio. Generally speaking, the bigger the ρ , the higher the resolution is. Normally, we set $\rho = 0.5$ according to the minimum information principle.

(2) The calculation formula for correlation degree is

$$V_{0i} = V(X_0, X_i) = \frac{1}{n} \sum_{i=1}^n V(X_0(k), X_i(k))
 \tag{50.3}$$

(3) Putting the standardized data into the GRA method formula (2) and (3), we get the correlation degree of 17 golf websites. Through sorting the correlation degree, we get the outcome presented in Table 50.3.

Through Table 50.3, we can see that the three most influential golf websites, which have the biggest correlation degrees, are FunFunGolf, 21golf, and golf998; the three least influential golf websites are golf72, golfonline, and jrgolf, with jrgolf being the last one.

Conclusion

Golf Vertical Portals Have Unique Advantages

As a golf vertical portal, FunFunGolf is on the top of the list in website traffic and inbound link quantity.

Golf Websites Should Strengthen Publicity and Promotion

We can see that 14 golf websites' correlation degrees are less than 0.5 in Table 50.3. This suggests that the development of Chinese golf websites is imbalanced and their overall influence is low.

Influence Evaluations of Golf Websites Need Further Study and Investigation

The data acquisition modes of this article need further improvement, so we need further studies and investigations in tools and methods to obtain data of golf websites.

References

1. FORWARD GROUP. China Golf Industry Report, 2012 edition[R/OL]. <http://www.forwardgolf.com.cn/newsshow.asp?id=1608> (In Chinese).
2. Guo Y, Liu CY, Yu ZH, et al. Research on the impact evaluation of web information sources of public opinion [J]. J Chinese Inform Process. 2011;25(3):64–71. In Chinese.
3. Liu WY, Zhou TB. Research on the evaluation of web impact of provincial public libraries in China[J]. Library Construct. 2011;3:85–9. In Chinese.
4. Duan YF. Quantitative analysis of the site characteristics (II) – research on the impact of university website[J]. ITA. 2005;28(2):191–4. In Chinese.
5. Sha YZ, Oukyang X. Research on the evaluation of impact of Chinese provincial government websites[J]. Documentation. 2004;6:17–22.
6. China Internet Network Information Center. Internet users search behavior report in 2013[R/OL]. http://www.cnnic.net.cn/hlwfzyj/hlwzbg/ssbg/201308/t20130820_41306.htm (In Chinese).

Chapter 51

An Ensemble Learning Approach for Improving Drug–Target Interactions Prediction

Ru Zhang

Abstract Prediction of drug–target interactions (DTIs) plays an important role in the drug discovery process. Unfortunately, experimental determination of interactions between drug compounds and target proteins remains a challenging task. Current available heterogeneous data motivate us to develop an effective data integration approach to exploit intrinsic correlations of known interactions between drugs and targets and to predict new interactions. We propose an ensemble learning approach to integrate previously developed methods and to improve the prediction performance. In particular, our algorithm employs a stacking framework, which uses a support vector machine (SVM) classifier as the meta learner to achieve better prediction results.

Keywords Machine learning • Ensemble learning • Interaction prediction

51.1 Introduction

Prediction of drug–target interactions (DTIs) plays an important role in drug discovery and repositioning (i.e., finding new uses of old and abandoned drugs). Currently experimental determination of interactions between small-molecule compounds and proteins remains a laborious, time-consuming, and expensive process [1]. In silico prediction provides a practically useful tool to alleviate this problem, as it can significantly save both experimental time and cost for identifying a new DTI. Computational techniques for predicting unknown DTIs can be basically classified into three categories, including molecular docking [2, 3], ligand-based [4, 5], and network-based approaches [6–9].

R. Zhang (✉)

Changzhou Textile Garment Institute, 213164 Changzhou, Jiangsu, China
e-mail: cztgizr@163.com

In this chapter, we propose a novel machine learning approach, called *ensemble learning* [10], which integrates all the three categories of previously developed methods and significantly improves the prediction results.

Our ensemble learning approach employs a stacking framework, with a two-level learning process. The first level of learning incorporates the previous DTI prediction algorithms, while the second level applies a meta learner to integrate the prediction results of the previous methods and performs the final prediction. Note that similar ensemble learning frameworks have also been developed to address other problems in the field of computational biology, such as disordered protein region prediction [11] and protein tertiary structure prediction [12, 13].

We have tested our ensemble learning approach on four benchmark datasets involving different classes of targets, including enzymes, ion channels, G-protein-coupled receptors (GPCRs), and nuclear receptors. Our cross-validation tests show that our stacking-based framework can significantly improve the prediction performance, in terms of both AUC (area under the ROC curve) and AUPR (area under the precision-recall curve) measures.

51.2 Methods

51.2.1 Overview

We present an ensemble learning approach to boost prediction performance of the previous methods. In machine learning, ensemble methods, such as stacking [14], boosting [15], and random forest [16], incorporate multiple learning models to achieve higher prediction accuracy than the original prediction methods [10]. These original learning models incorporated in an ensemble learning framework are also called the *base learners*. In our DTI prediction problem, we apply the *stacking* technique [14] to combine the previous learning models and achieve better predictive performance. This stacking method trains a second-level learning algorithm to combine the DTI prediction results of the previous learning models (i.e., base learners). This second-level learning algorithm is often called the *meta learner* or *combiner*. Our stacking-based ensemble learning approach consists of two steps: In the first step, we run multiple base learners on the same input DTI data, including the weighted profile method [6], the Gaussian kernel method [9], the Laplacian regularized least squares (LapRLS) method [17], and the network-based inference method [7]. In the second step, we use the support vector machine (SVM) classifier [18] as the meta learner to combine the prediction results produced by the aforementioned base learners. The flow chart of our ensemble learning approach is shown in Fig. 51.1.

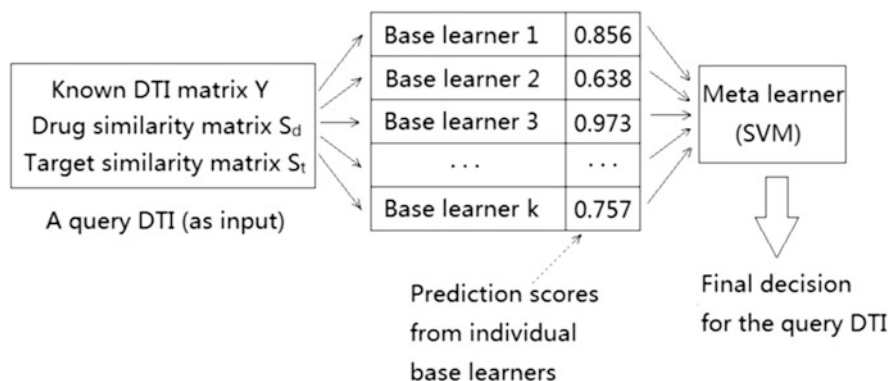


Fig. 51.1 Flow chart of our stacking-based ensemble learning approach

51.2.2 Base Learners

We firstly introduce some notations. Let m and n be the numbers of drugs and targets (proteins) in a given benchmark dataset, respectively. Let $D = \{d_1, d_2, \dots, d_m\}$ be the set of all drugs, and let $T = \{t_1, t_2, \dots, t_n\}$ be the set of all targets in the benchmark dataset. We use an $m \times n$ matrix \mathbf{S}_d to represent the *drug similarity matrix*, in which each element $S_d(i, j)$ stands for the similarity score between drugs d_i and d_j . Similarly, we define the *target similarity matrix* \mathbf{S}_t as an $n \times n$ matrix, in which each element $S_t(i, j)$ represents the similarity score between targets t_i and t_j . We use an $m \times n$ binary matrix \mathbf{Y} to represent the *drug–target interaction matrix*, where each element $Y_{ij} = 1$ if there is a known interaction between drug d_i and target t_j and $Y_{ij} = 0$ otherwise.

We use four previous DTI prediction algorithms [6, 7, 9, 17] as the base learners in our ensemble learning framework. All these base learners take the same input data, including the drug–target interaction matrix \mathbf{Y} , the drug similarity matrix \mathbf{S}_d and the target similarity matrix \mathbf{S}_t . We use an $m \times n$ matrix \mathbf{F} , which is called the *prediction matrix*, to store the prediction scores of missing drug–target interactions, where each element $0 \leq F_{ij} \leq 1$ represents the prediction score between drug d_i and target t_j . A higher prediction score for a drug–target pair means that they are more likely to interact with each other. In the following subsections, we will briefly describe individual prediction algorithms which are used as the base learners in our stacking model.

51.2.2.1 The Weighted Profile Method

The *weighted profile* method exploits the drug–target interaction profiles and uses the drug or target pairwise similarity scores to weigh these interaction profiles [6]. In particular, the target interaction profile of drug d_i is defined as a binary vector derived from the i th row of the drug–target interaction matrix \mathbf{Y} . Then, the profile of drug d_i is

reconstructed by taking the weighted average of all drugs using the drug similarity scores. Likewise, the profile of a target is reconstructed using the weighted average of the target similarity scores. The final prediction matrix \mathbf{F} is then computed based on these reconstructed interaction profiles of individual drugs and targets:

$$F_{ij} = \frac{1}{2} \left(\frac{\sum_{k=1}^m S_d(i, k) \cdot Y_{kj}}{\sum_{k=1}^m S_d(i, k)} + \frac{\sum_{k=1}^n S_t(j, k) \cdot Y_{ik}}{\sum_{k=1}^n S_t(j, k)} \right) \quad (51.1)$$

51.2.2.2 The Gaussian Kernel Method

In *Gaussian kernel* method for predicting DTIs, the known drug–target interaction profiles together with chemical and genomic information are first encoded in a kernel, called the *Gaussian interaction profile* (GIP) kernel. Then, a *regularized least squares* (RLS) approach is applied to perform the kernel-based classification and predict unknown DTIs [9]. More specifically, for a pair of drugs d_i and d_j , the following Gaussian kernel is used to encode their interaction profiles,

$$K_{\text{GIP},d}(d_i, d_j) = e^{-\gamma_d \left\| y_{d_i} - y_{d_j} \right\|^2}, \quad (51.2)$$

where y_{d_i} is the interaction profile of drug d_i , and $\gamma_d = \frac{m}{\sum_{i=1}^m |y_{d_i}|^2}$, in which m is the total number of drugs.

Hence, $\mathbf{K}_{\text{GIP},d}$ is an $m \times m$ matrix representing the similarities of the interaction profiles for all drug pairs. Likewise, a similar kernel $\mathbf{K}_{\text{GIP},t}$ of size $n \times n$ can be constructed to represent the similarities of the interaction profiles for all target pairs. After combining the interaction profiles with chemical and genomic information, we have the following weighted averages:

$$\mathbf{K}_d = \frac{1}{2} \mathbf{K}_{\text{chemical},d} + \frac{1}{2} \mathbf{K}_{\text{GIP},d}, \quad \mathbf{K}_t = \frac{1}{2} \mathbf{K}_{\text{chemical},t} + \frac{1}{2} \mathbf{K}_{\text{GIP},t}, \quad (51.3)$$

where $\mathbf{K}_{\text{chemical},d}$ is the kernel representing the drug pairwise similarity scores and constructed from chemical information, and $\mathbf{K}_{\text{chemical},t}$ is the kernel representing the target pairwise similarity scores and constructed from genomic information.

Using the RLS classifier, the final prediction matrix \mathbf{F} can be computed in closed form:

$$\mathbf{F} = \frac{1}{2} \left[\mathbf{K}_d (\mathbf{K}_d + \mathbf{I})^{-1} \mathbf{Y} \right] + \frac{1}{2} \left[\mathbf{K}_t (\mathbf{K}_t + \mathbf{I})^{-1} \mathbf{Y}^T \right]^T. \quad (51.4)$$

51.2.2.3 The Laplacian Regularized Least Squares Method

The *Laplacian regularized least squares* (LapRLS) method for drug–target interaction computes an analytical solution of the prediction matrix \mathbf{F} in closed form by minimizing the squared loss function with a regularized term between the drug–target interaction matrix \mathbf{Y} and the drug similarity matrix \mathbf{S}_d (or the target similarity matrix \mathbf{S}_t) [17]. More specifically, let \mathbf{K}_d be an $m \times m$ matrix representing the similarity scores of the interaction profiles for all drug pairs, where each element $K_d(i, j)$ represents the number of shared target proteins for a pair of drugs d_i and d_j . Likewise, an $n \times n$ matrix \mathbf{K}_t is defined to represent the similarity scores of the interaction profiles for all target pairs. After that, two weighted similarity matrices \mathbf{W}_d and \mathbf{W}_t are defined as follows:

$$\mathbf{W}_d = \frac{\gamma_{d1}\mathbf{S}_d + \gamma_{d2}\mathbf{K}_d}{\gamma_{d1} + \gamma_{d2}}, \quad \mathbf{W}_t = \frac{\gamma_{t1}\mathbf{S}_t + \gamma_{t2}\mathbf{K}_t}{\gamma_{t1} + \gamma_{t2}}, \quad (51.5)$$

where γ_{d1} , γ_{d2} , γ_{t1} , and γ_{t2} are the weighting parameters.

In addition, we define the following new diagonal matrices \mathbf{D}_d and \mathbf{D}_t by

$$D_d(k, k) = \sum_{i=1}^m W_d(k, i), \quad D_t(k, k) = \sum_{i=1}^n W_t(k, i). \quad (51.6)$$

After solving the regularized regression problem, we can derive the following prediction matrices \mathbf{F}_d and \mathbf{F}_t for the drug and target domains, respectively:

$$\mathbf{F}_d = \mathbf{W}_d \left[\mathbf{W}_d + \beta_d \left(\mathbf{I} - \mathbf{D}_d^{-\frac{1}{2}} \mathbf{W}_d \mathbf{D}_d^{-\frac{1}{2}} \right) \right]^{-1} \mathbf{Y}, \quad (51.7)$$

$$\mathbf{F}_t = \mathbf{W}_t \left[\mathbf{W}_t + \beta_t \left(\mathbf{I} - \mathbf{D}_t^{-\frac{1}{2}} \mathbf{W}_t \mathbf{D}_t^{-\frac{1}{2}} \right) \right]^{-1} \mathbf{Y}^T, \quad (51.8)$$

where β_d and β_t are the weighting parameters. Then, the final prediction matrix is defined by $\mathbf{F} = \frac{\mathbf{F}_d + \mathbf{F}_t^T}{2}$.

51.2.2.4 The Network-Based Inference Method

The *network-based inference* (NBI) method employs a two-step diffusion process to infer unknown drug–target interactions in a bipartite drug–target interaction network [7]. In particular, the prediction matrix is defined as follows:

$$F_{ij} = \sum_{p=1}^n \frac{Y_{ip}}{k(t_p)} \sum_{q=1}^m \frac{Y_{qp} Y_{qj}}{k(d_q)}, \quad (51.9)$$

where $k(d_q) = \sum_{s=1}^n Y_{qs}$ and $k(t_p) = \sum_{s=1}^m Y_{sp}$.

51.2.3 *Meta Learners*

In the second-level learning process of our stacking framework, we employ a support vector machine (SVM) method [18] as the meta learner to integrate the prediction results of individual base learners and make the final prediction. For a query DTI, input data to the meta learner is a vector storing the prediction scores of this DTI computed by all base learners. Thus, the dimension of the input vector to the meta learner is equal to the total number of the base learners incorporated in our stacking model. Given a query DTI, we use the distance between the input vector to the meta learner and the separating hyperplane to measure the likelihood of this query DTI. For all unknown DTIs, their distances resulting from the SVM are normalized and rescaled from 0 to 1. The normalized values are then outputted as the final prediction scores.

In principle, for the meta learner, we could also apply other learning algorithms, such as voting or averaging the prediction results of the base learners. However, as different prediction algorithms employed in our framework choose distinct scaling schemes to report the final prediction decisions, the simple voting or averaging strategy is not suitable for solving this prediction problem. A similar issue has also appeared in other computational biology problems [11–13].

51.2.4 *Implementation*

Our stacking-based ensemble learning framework, including both base learners (i.e., the previously described DTI prediction algorithms) and meta learner (i.e., SVM), has been implemented in Java. For each base learner, we choose the default parameters reported in the original paper. We use the LibSVM library [19] to perform the SVM classification task in our ensemble learning framework. We also choose the default parameters and kernel setting for LibSVM in our experiment.

51.3 Results

51.3.1 *Datasets*

We tested our ensemble learning approach on four benchmark datasets involving four different target classes, including enzymes, ion channels, G-protein-coupled receptors (GPCRs), and nuclear receptors. These four benchmark datasets have been already analyzed¹ [6]. Statistics about these datasets is given in Table 51.1. In these benchmark datasets, DTI information was obtained from KEGG

¹ The dataset can be downloaded from <http://web.kuicr.kyoto-u.ac.jp/supp/yoshi/drugtarget/>.

Table 51.1 Statistics of the four benchmark datasets

Statistics	Enzyme	Ion channel	GPCR	Nuclear receptor
Drugs	445	210	223	54
Targets	664	204	95	26
Interaction	2,926	1,476	635	90

BRITE [20], BRENDA [21], Super Target [22], and DrugBank [23]. Chemical structure information was derived from KEGG LIGAND [20], and the chemical structure similarity scores between drugs were computed using SIMCOMP [24]. Genomic information of target proteins was obtained from KEGG GENES [14], and the sequence similarity scores between targets were computed using a normalized version of the Smith-Waterman algorithm [25].

51.3.2 Performance Evaluation

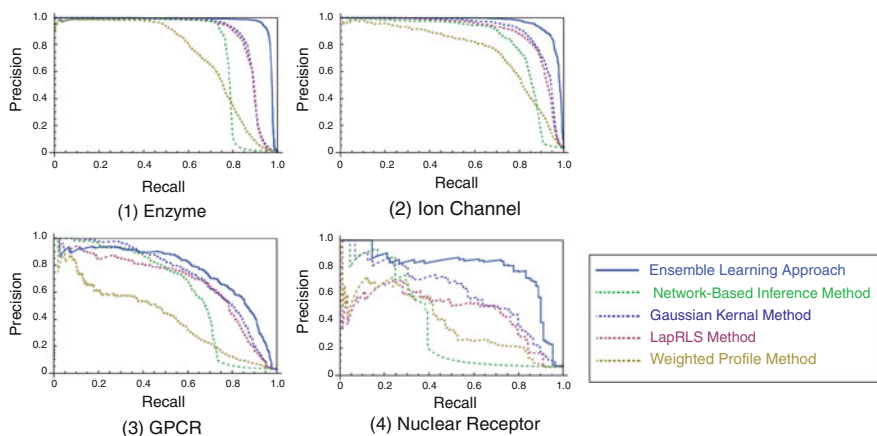
To examine whether our ensemble learning approach can improve the previous DTI prediction methods, we performed 100 trials of 10-fold cross-validation on each benchmark dataset for all methods, including our ensemble learning approach, and compared their prediction results. The average scores of AUC (area under the ROC curve) and AUPR (area under the precision-recall curve) were reported and used as evaluation measures. For drug–target interaction data which are highly unbalanced, AUPR provides a better measure to evaluate different prediction algorithms, although it is often positively correlated to AUC [8, 9]. Thus, our performance evaluation mainly focused on AUPR, though we also reported AUC in our tests. During cross-validation tests, a predicted DTI is said to be *true positive* if it is present in the benchmark test data and is said to be *false positive* otherwise. The terms *true negative* and *false negative* are defined similarly.

Table 51.2 summarizes the comparison results between our ensemble learning approach (EL) and the previous prediction algorithms which were used as the base learners in our stacking framework, including the weighted profile method (WP), the Gaussian kernel method (GK), the network-based inference (NBI) method, and the Laplacian regularized least squares (LapRLS) method. The corresponding AUPR curves are shown in Fig. 51.2, where, for each dataset, the solid line represents the PR curve of our ensemble learning approach, while the dashed lines represent the PR curves for other four methods. Most of the AUC and AUPR scores reported here for the previous prediction approaches agreed with those reported in the original papers [6, 7, 9, 17] or recent review paper [1].

As shown in Table 51.2 and Fig. 51.2, for all four benchmark datasets, our ensemble learning approach outperformed four previous prediction approaches. In particular, our approach improved the AUPR score of the Gaussian kernel method, which achieved the best performance among all four previous methods, by more than 8.5, 5.5, 0.9, and 11.7 for enzymes, ion channels, GPCRs, and nuclear

Table 51.2 Comparison results between our approach and previous ones

Dataset	Method	AUC		AUPR	
		Mean	95 % CI	Mean	95 % CI
Enzyme	WP	95.032	[95.015, 95.048]	72.485	[72.452, 72.518]
	GK	97.333*	[97.313, 97.353]	88.060*	[88.015, 88.105]
	NBI	89.320	[89.283, 89.358]	77.159	[77.095, 77.222]
	LapRLS	96.414	[96.394, 96.435]	87.027	[86.990, 87.064]
	EL	99.012*	[98.927, 99.095]	93.507*	[91.391, 95.623]
Ion channel	WP	96.055	[96.033, 96.078]	74.979	[74.900, 75.059]
	GK	97.728*	[97.686, 97.770]	90.991*	[90.920, 91.062]
	NBI	92.725	[92.665, 92.786]	82.763	[82.681, 82.845]
	LapRLS	97.645	[97.620, 97.670]	89.458	[89.398, 89.518]
	EL	99.47*	[99.454, 99.490]	96.513*	[96.475, 96.551]
GPCR	WP	88.656	[88.604, 88.708]	42.480	[42.375, 42.585]
	GK	94.142	[94.088, 94.195]	72.755*	[72.606, 72.904]
	NBI	83.355	[83.265, 83.444]	61.036	[60.862, 61.209]
	LapRLS	94.231*	[94.166, 94.296]	68.199	[68.051, 68.346]
	EL	96.891*	[96.660, 97.122]	75.892*	[73.101, 78.684]
Nuclear receptor	WP	80.932	[80.812, 81.053]	38.352	[37.887, 38.817]
	GK	89.947*	[89.712, 90.181]	61.722*	[61.275, 62.169]
	NBI	67.596	[67.316, 67.875]	39.047	[38.560, 39.534]
	LapRLS	85.493	[85.287, 85.699]	51.501	[51.069, 51.932]
	EL	93.206*	[92.825, 93.586]	72.116*	[69.201, 75.030]

**Fig. 51.2** Precision-recall (PR) curves of different approaches for four benchmark datasets

receptors, respectively. For the nuclear receptor targets, the NBI method achieved relatively low prediction accuracy. Probably this was not only due to the small scale of training data (Table 51.1) but also caused by the fact that NBI used only DTI data and did not consider the drug or protein similarity scores into prediction. These comparison results indicate that our ensemble learning approach can achieve better predictive performance by effectively integrating multiple prediction models into a unified framework.

Conclusion

In this chapter, we presented a stacking-based ensemble learning approach to boost performance of previous DTI prediction methods. Our approach employs an SVM method as the meta learner to integrate the prediction results of previous methods. Tests on four benchmark datasets involving different types of target proteins show that our ensemble learning approach can achieve high prediction accuracy and thus have practical applications in the fields of drug discovery and repositioning.

In our current prediction problem, we only predict interactions between drugs and individual targets. It would be more useful to extend our approach to identify a drug that can simultaneously act on a set of targets which play essential roles in a specific disease. In addition, it would be interesting to extend our algorithm to address other related problems, such as prediction of drug side effects, which can be essentially formulated into a similar network link prediction problem.

References

1. Yamanishi Y, Kotera M, Kanehisa M, Goto S. Similarity-based machine learning methods for predicting drug–target interactions: a brief review. *Brief Bioinform.* 2013. doi:10.1093/bib/bbt056, URL: <http://bib.oxfordjournals.org/content/early/2013/08/10/bib.bbt056.abstract>.
2. Cheng AC, Coleman RG, Smyth KT, Cao Q, Soulard P, Caffrey DR, et al. Structure-based maximal affinity model predicts small-molecule druggability. *Nat Biotechnol.* 2007;25(1):71–5.
3. Morris GM, Huey R, Lindstrom W, Sanner MF, Belew RK, Goodsell DS, et al. AutoDock4 and AutoDockTools4: automated docking with selective receptor flexibility. *J Comput Chem.* 2009;30(16):2785–91.
4. Keiser MJ, Roth BL, Armbruster BN, Ernsberger P, Irwin JJ, Shoichet BK. Relating protein pharmacology by ligand chemistry. *Nat Biotechnol.* 2007;25(2):197–206.
5. Keiser MJ, Setola V, Irwin JJ, Laggner C, Abbas A I, Hufeisen S J, et al. Predicting new molecular targets for known drugs. *Nature.* 2009;462(7270):175–81.
6. Yamanishi Y, Araki M, Gutteridge A, Honda W, Kanehisa M. Prediction of drug–target interaction networks from the integration of chemical and genomic spaces. *Bioinformatics.* 2008;24(13):i232–40.
7. Cheng F, Liu C, Jiang J, Lu W, Li W, Liu G, et al. Prediction of drug–target interactions and drug repositioning via network-based inference. *PLoS Comput Biol.* 2012;8(5):e1002503.
8. Bleakley K, Yamanishi Y. Supervised prediction of drug–target interactions using bipartite local models. *Bioinformatics.* 2009;25(18):2397–403.

9. van Laarhoven T, Nabuurs SB, Marchiori E. Gaussian interaction profile kernels for predicting drug–target interaction. *Bioinformatics*. 2011;27(21):3036–43.
10. Zhou ZH. Ensemble methods: foundations and algorithms. Boca Raton, FL: Chapman & Hall/CRC; 2012.
11. Ishida T, Kinoshita K. Prediction of disordered regions in proteins based on the meta approach. *Bioinformatics*. 2008;24(11):1344–8.
12. Bujnicki JM, Elofsson A, Fischer D, Rychlewski L. Structure prediction meta server. *Bioinformatics*. 2001;17(8):750–1.
13. Ginalski K, Elofsson A, Fischer D, Rychlewski L. 3D-Jury: a simple approach to improve protein structure predictions. *Bioinformatics*. 2003;19(8):1015–8.
14. Wolpert DH. Stacked generalization. *Neural Netw*. 1992;5(2):241–59.
15. Freund Y, Schapire RE. A decision-theoretic generalization of on-line learning and an application to boosting. Berlin: Springer; 1995. p. 23–37.
16. Breiman L. Random forests. *Mach Learn*. 2001;45(1):5–32.
17. Xia Z, Wu LY, Zhou X, Wong ST. Semi-supervised drug-protein interaction prediction from heterogeneous biological spaces. *BMC Syst Biol*. 2010;4 Suppl 2:S6.
18. Cortes C, Vapnik V. Support-vector networks. *Mach Learn*. 1995;20(3):273–97.
19. Chang CC, Lin CJ. LIBSVM: a library for support vector machines. *ACM Trans Intell Syst Technol*. 2011;2(3):27.
20. Kanehisa M, Goto S, Hattori M, Aoki-Kinoshita KF, Itoh M, Kawashima S, et al. From genomics to chemical genomics: new developments in KEGG. *Nucleic Acids Res*. 2006;34 Suppl 1:D354–7.
21. Schomburg I, Chang A, Ebeling C, Gremse M, Heldt C, Huhn G, et al. BRENDA, the enzyme database: updates and major new developments. *Nucleic Acids Res*. 2004;32 Suppl 1:D431–3.
22. Günther S, Kuhn M, Dunkel M, Campillos M, Senger C, Petsalaki E, et al. SuperTarget and matador: resources for exploring drug–target relationships. *Nucleic Acids Res*. 2008;36 Suppl 1:D919–22.
23. Knox C, Law V, Jewison T, Liu P, Ly S, Frolkis A, et al. DrugBank 3.0: a comprehensive resource for ‘omics’ research on drugs. *Nucleic Acids Res*. 2011;39 Suppl 1:D1035–41.
24. Hattori M, Tanaka N, Kanehisa M, Goto S. SIMCOMP/SUBCOMP: chemical structure search servers for network analyses. *Nucleic Acids Res*. 2010;38:W652–6. doi:[10.1093/nar/gkq367](https://doi.org/10.1093/nar/gkq367). Web Server issue.
25. Smith TF, Waterman MS. Identification of common molecular subsequences. *J Mol Biol*. 1981;147(1):195–7.

Chapter 52

A Complementary Predictor for Collaborative Filtering

Min Chen, Wenxin Hu, and Jun Zheng

Abstract Recommender systems provide users with personalized suggestions for products or services. Collaborative Filtering (CF) is a method commonly used in recommender systems to establish a connection between users and products by analyzing past transactions. There are two successful approaches to CF, one is the Slope One scheme, which is efficient to query and easy to implement, and the other is the latent factor models, which directly profile both users and products. In order to obtain better accuracy and efficiency, a new combined approach is proposed by taking advantages of both Slope One and SVD models. The method is tested on the MovieLens dataset with the experimental results showing that the proposed final solution may achieve great improvement in prediction accuracy when compared to using the Slope One or SVD models alone.

Keywords Collaborative filtering • Slope One • SVD

52.1 Introduction

The development of information technology allows people to enjoy the convenience of the Internet but they also encounter problems because electronic retailers offer such a huge selection of products and modern consumers are inundated with choices. Recommender systems [1, 2] are widely used with great success because they can recommend personalized items to users on the basis of their preferences. Many technologies are found in recommender systems, such as content-based recommendation [3], collaborative filtering [4], and the ensemble methods [5]. In past Netflix prize [6] and KDD-Cup [7] competitions, many teams have used the ensemble methods and achieved good results.

Collaborative filtering is the most famous algorithm in recommender systems. Slope One [8] can simply and easily implement the collaborative filtering algorithm based on memory and it is efficient, updatable, and quick. However, the Slope One algorithm also has its drawbacks because the accuracy is not good and for reasons

M. Chen (✉) • W. Hu • J. Zheng
Computer Center, East China Normal University, 200062 Shanghai, China
e-mail: abcdcamey@qq.com

of recommendation, especially in the case of sparse data. Sparse data can generally be processed using the matrix dimension reduction method SVD (singular value decomposition) [9], which belongs to the latent factor model and is commonly used.

In this paper, a new idea is proposed: the SVD technique is used to reduce the dimension of data, and then the similarity between items is calculated based on the thus-processed data. Finally, as Slope One is based on item similarity, the recommendation will be based to a greater extent on local data, while the SVD scheme considers global characteristics to a greater extent. The movie rating prediction system has a high real-time demand, and as the SVD model is constructed using all data if the amount of user and movie data is large, the construction needs more time. As Slope One is simple, fast, and efficient, it is more suitable to such real-time prediction. The final proposed method combines both SVD and Slope One based on item similarity to be applicable in a real-time system.

Section 2 describes the preliminaries, while Sect. 3 discusses the proposed algorithm. Section 4 presents the experiments, including details of our dataset, evaluation metrics, and experimental procedure as well as discussing the various experimental results. A conclusion is presented in the last section.

52.2 Preliminary

52.2.1 Notations

In our notation, users u, v , and items i, j are the special indexing letters reserved for users and items. The rating from user u for item i is represented as r_{ui} , and the predicted rating is denoted as \hat{r}_{ui} . The subset of items which are rated in u is $S(u)$, the average ratings for user u is denoted \bar{u} , the (u, i) pairs for which r_{ui} is known are stored in the training set $\tau = \{(u, i) | r_{ui} \text{ is known}\}$, and τ' is the testing set. The set $S_i(\tau)$ is the set of all evaluations $u \in \tau$ such that they contain item $i (i \in S(\tau))$.

52.2.2 Slope One Algorithm

52.2.2.1 The Slope One Scheme

The principle of Slope One is to apply a simple linear regression $f(x) = x + b$ to generate a prediction $f(x)$, where x denotes another known item's rating, and b is the average deviation between two item's ratings. Given a training set τ , and any two items i and j with ratings r_{ui} and r_{uj} respectively in some user evaluation u (annotated as $u \in S_{i,j}(\tau)$), we consider the average deviation of item i with respect to item j as:

$$\text{dev}_{i,j} = \sum_{u \in S_{i,j}(\tau)} \frac{u_i - u_j}{|S_{i,j}(\tau)|}. \quad (52.1)$$

Given the known rating r_{uj} , $\text{dev}_{i,j} + r_{uj}$ is a prediction for r_{ui} , and a reasonable predictor might be the average of all such predictions:

$$\hat{r}_{ui}^{so} = \frac{\sum_{j \in R_i} \text{dev}_{i,j} + r_{uj}}{|R_i|}, \quad (52.2)$$

where $R_i = \{j | j \in S(u), j \neq i\}$. is the set of all relevant items.

52.2.2.2 The Weighted Slope One Scheme

One of the drawbacks of Slope One is that the number of ratings is not taken into consideration. For a given user u and known ratings r_{uj} and r_{uk} , If the size of $S_{i,j}(\tau)$ is greater than the size of $S_{i,k}(\tau)$, \hat{r}_{ui} is likely to get more contributions from r_{uj} . Thus, we define the weighted Slope One prediction (WSO) as follows:

$$\hat{r}_{ui}^{wso} = \frac{\sum_{j \in R_i} (\text{dev}_{i,j} + r_{uj}) \cdot |S_{i,j}(\tau)|}{\sum_{j \in R_i} |S_{i,j}(\tau)|}. \quad (52.3)$$

52.2.3 SVD Model

SVD assumes that a known rating r_{ui} can be calculated from the user's feature vector p_u and the item's feature vector q_i ; the vector p_u and q_i should be learned automatically by minimizing the following cost function:

$$C(\tau) = \sum_{(u,i) \in \tau} (r_{ui} - p_u^T q_i)^2 + \lambda(\|p_u\|^2 + \|q_i\|^2). \quad (52.4)$$

Here, τ is the training set, $(r_{ui} - p_u^T q_i)^2$, which represents the regularized squared error between the predicted rating and actual rating, $\lambda(\|p_u\|^2 + \|q_i\|^2)$, used to avoid the over-fitting problem. This equation can be optimized by simple gradient descent. Firstly, we derivative p_u and q_i as follows:

$$\frac{\partial C}{\partial p_u} = -2 \cdot q_i e_{ui} + 2\lambda p_u \quad \frac{\partial C}{\partial q_i} = -2 \cdot p_u e_{ui} + 2\lambda q_i. \quad (52.5)$$

Here, $e_{ui} = r_{ui} - p_u^T q_i$, and all known ratings should be looped in training set τ ; for a given rating r_{ui} , p_u and q_i are updated in each iteration of the simple gradient descent:

$$p_u \leftarrow p_u + \alpha(e_{ui} q_i - \lambda \cdot p_u) \quad q_i \leftarrow q_i + \alpha(e_{ui} p_u - \lambda \cdot q_i). \quad (52.6)$$

The parameters α (step size) and λ (regularization factor) are determined by cross-validation. Finally, the predictive expression of SVD is:

$$\hat{r}_{\text{svd}}^{ui} = p_u^T \cdot q_i. \quad (52.7)$$

52.3 Complementary Predictor

52.3.1 Weighted Slope One Based on Cosine Similarity

The weighted Slope One scheme uses the number of user both rate item i and j as the relationship between item i and j . Actually, we can calculate the similarity more accurately by use the rating data. For each item, each user's ratings for an item can be seen as a vector; so the similarity can be calculated with the following expression:

$$\text{Sim}_{i,j}^{cs} = \cos(\vec{r}_i, \vec{r}_j) = \frac{\vec{r}_i \cdot \vec{r}_j}{|\vec{r}_i| \cdot |\vec{r}_j|}. \quad (52.8)$$

\vec{r}_i is a vector that contains all user ratings for item i , and the weighted Slope One based on cosine similarity (WSOCS) is defined as:

$$\hat{r}_{ui}^{\text{wsocs}} = \frac{\sum_{j \in R_i} (\text{dev}_{i,j} + r_{uj}) \cdot |\text{Sim}_{i,j}^{cs}|}{\sum_{j \in R_i} |\text{Sim}_{i,j}^{cs}|}. \quad (52.9)$$

52.3.2 Weighted Slope One Based on SVD Cosine Similarity

We can see above that the obvious disadvantage in calculating the similarity in this way is that the dimension of ratings data is relatively large, requiring high computational cost. Therefore, we explore use of the feature vector produced by the SVD scheme, while at the same time some of the noise data can be effectively removed by dimensionality reduction. The similarity between items i and j is described by:

$$\text{Sim}_{i,j}^{scs} = \cos(\vec{q}_i, \vec{q}_j) = \frac{\vec{q}_i \cdot \vec{q}_j}{|\vec{q}_i| \cdot |\vec{q}_j|}. \quad (52.10)$$

\vec{q}_i is the feature vector produced by the SVD scheme, and the final weighted Slope One based on the SVD cosine similarity (WSOSCS) predictor is given by:

$$\hat{r}_{ui}^{\text{wsoscs}} = \frac{\sum_{j \in R_i} (\text{dev}_{i,j} + r_{uj}) \cdot |\text{Sim}_{i,j}^{scs}|}{\sum_{j \in R_i} |\text{Sim}_{i,j}^{scs}|}. \quad (52.11)$$

52.3.3 SVD Combined With Weighted Slope One Based on SVD Cosine Similarity

Slope One based on the item similarity recommendation takes into account local data more than the SVD scheme which considers global characteristics to a greater extent. At the same time, the SVD scheme is generally calculated off-line while Slope One is suitable for online computation because it is simple, fast, and efficient. Therefore, we try to utilize the SVD predictor: $\hat{r}_{ui}^{\text{svd}} = p_u^T \cdot q_i$. Making full use of the advantages of both algorithms, the complementary predictor combining SVD and the weighted Slope One based on SVD cosine similarity (SVDWSO) is as follows:

$$\hat{r}_{ui}^{\text{svdwsos}} = \varepsilon * \hat{r}_{ui}^{\text{svd}} + (1 - \varepsilon) * \hat{r}_{ui}^{\text{wsoscs}}. \quad (52.12)$$

ε is the parameter which controls the weight of the two predictors.

52.4 Experimental Analysis

52.4.1 Evaluation Metrics

These experiments are based on the MovieLens 1 M dataset. The dataset consists of 1000209 ratings from 6,040 users for 3,952 movies, the values of which range from 1 to 5.

The effectiveness of a given recommend algorithm can be measured precisely. In order to do so, the root mean squared error (RMSE) metric is employed to measure prediction accuracy. RMSE is defined as:

$$\text{RMSE} = \sqrt{\frac{\sum_{(u,i) \in \tau'} (r_{ui} - \hat{r}_{ui})^2}{|\tau'|}}. \quad (52.13)$$

Here, the lower the value of RMSE the better, and τ' refers to the testing set.

52.4.2 Experimental Procedure

In the experiments, the dataset was randomly divided into a training set τ (80 % of total data) and a testing set τ' (additional data). In order to reduce the over-fitting problem, fivefold cross validation technology was used in each experiment.

For comparison of the proposed algorithm in terms of accuracy and efficiency, the Slope One and SVD schemes are employed as the benchmark algorithms. Figure 52.1 shows the experimental results, with the y-axis showing RMSE

Fig. 52.1 The SVD predictor with different loops and the Slope One predictor

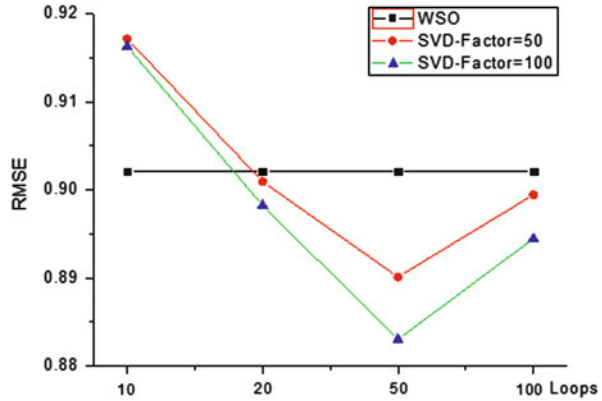
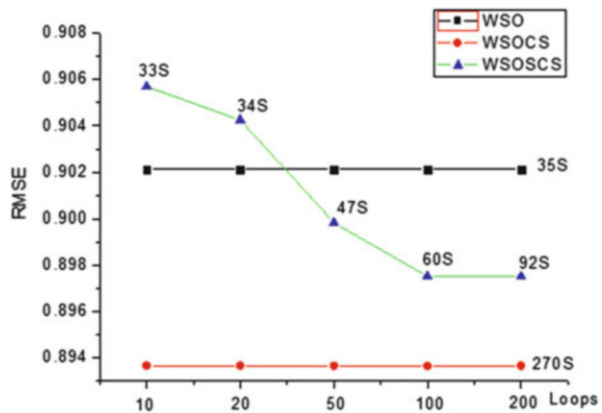


Fig. 52.2 Adoption of item similarity to improve the Slope One scheme



which is defined in Eq. (52.13), while the x -axis shows the number of iterations in the SVD model. The three curves correspond to the following three experiments: SVD-Factor=50 and SVD-Factor=100 represent the factor numbers 50 and 100 in the SVD Model, while WSO shows the weighted Slope One scheme discussed in Sect. 2.2.

Figure 52.2 shows the experimental results that calculate item similarity to improve Slope One. WSOCS is the weighted Slope One based on cosine similarity method that uses the user’s rating data to calculate item similarity and improve Slope One. WSOSCS uses the item’s feature vector to calculate item similarity to improve Slope One with the operating time marked near each data point in the experiment. It can be seen that WSOCS has the greatest effect, but it requires great cost in terms of time. In comparison with the WSO algorithm, the WSOSCS algorithm (factor = 50) increases the iteration number, but it can improve accuracy to a certain extent while not increasing the time cost too much.

SVD considers global features to a greater extent than the Slope One scheme based on item similarity which predominantly uses local characteristics.

Fig. 52.3 SVD combined with the weighted Slope One based on SVD cosine similarity

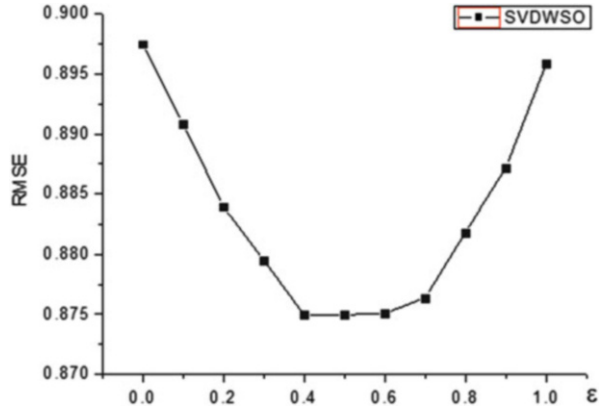


Table 52.1 Comparison of all algorithms based on RMSE and time

Algorithms	RMSE	Time (s)
SVD	0.8940	53
WSO	0.9021	35
WSOSCS	0.8975	60
WSOCS	0.8937	271
SVDWSO	0.8750	64

Therefore, herein, SVD combined with weighted Slope One based on SVD cosine similarity (SVDWSO) is proposed with the experiment result shown in Fig. 52.3.

52.4.3 Experimental Results

Table 52.1 presents the experimental results when using the algorithm mentioned above. Firstly, SVD and the weighted Slope One (WSO) schemes are the benchmark algorithms. The RMSE value is 0.89 in the SVD model, almost the same as determined in two excellent papers [9, 10]. WSO has an accuracy that is relatively speaking somewhat lower when compared to the SVD model, but the operation time is much shorter. Compared with the WSO algorithm, the weighted Slope One based on cosine similarity (WSOCS) algorithm improves RMSE by about 0.93 %, but the time cost is increased ca. 8 times. The weighted Slope One based on SVD cosine similarity (WSOSCS) algorithm can improve RMSE slightly (by about 0.51 %) without too much of a time cost increase. In addition, the table shows that the performance of Slope One can be improved by considering the similarity between items which is calculated by the SVD feature vector, but using the similarity one cannot reach the performance obtained when calculating using the ratings data, although the computing time is much shorter. SVD uses global data in each iteration of the process. Slope One uses the local ratings data to make

predictions, especially item similarity. Finally, the experimental results for SVD combined with weighted Slope One based on SVD cosine similarity (SVDWSO) show that the complementary predictor can improve accuracy (by about 2.1 %) and the time cost is acceptable.

Conclusion

In this paper, the weighted Slope One scheme based on item similarity is analyzed and we found that the item similarity calculation can be optimized using the result of SVD. The advantages of SVD and Slope One based on item similarity are made full use of in our proposal of a complementary predictor for collaborative filtering that combines both global and local characteristics. Compared with the benchmark algorithms, it can improve prediction accuracy by ca. 2.1 %.

Acknowledgements This study was funded by the Science and Technology Commission of Shanghai Municipality (12DZ2274300).

References

1. Ben Schafer J et al. Collaborative filtering recommender systems. *Adapt Web Lect Notes Comput Sci.* 2007;4321:291–324.
2. Adomavicius G, Tuzhilin A. Toward the next generation of recommender systems: a survey of the state-of-the-art and possible extensions. *IEEE Trans Knowl Data Eng.* 2005;17(6):734–49.
3. Balabanovic M, Shoham Y. Content-based recommendation systems. *Adapt Web Lect Notes Comput Sci.* 2007;4321:325–41.
4. Su X, Khoshgoftaar TM. A survey of collaborative filtering techniques. *Adv Artif Intell.* 2009;2009:1–19.
5. Breiman L. Random forests. *Mach Learn.* 2001;45(1):5–32.
6. Netflix prize 2009. <http://www.netflixprize.com/>.
7. ACM KDD CUP 2012. <http://sigkdd.org/kddcup/>.
8. Lemire D, Maclachlan A. Slope one predictors for online rating-based collaborative filtering. In: *Proceedings of the SIAM Data Mining Conference*; SIAM Press, California; 21–23 Apr 2005.
9. Koren Y. Factorization meets the neighborhood: a multifaceted collaborative filtering model. In: *Proceedings of the 14th ACM SIGKDD International Conference Knowledge Discovery and Data Mining*; ACM, ACM Press, New York; 2008. p. 426–34.
10. Koren Y, Bell R, Volinsky C. Matrix factorization techniques for recommender systems. *IEEE Comput.* 2009;42(8):42–9.

Chapter 53

Knowledge Discovery from Knowledge Bases with Higher-Order Logic

Guangyuan Li

Abstract Knowledge discovery from knowledge bases is an important problem in the field of data mining because it can solve the problem of a lack of knowledge, which is a bottleneck in intelligent systems based on knowledge bases. With the expansion of knowledge bases and structured data becoming more complex, first-order logic is no longer capable of knowledge representation and induction, so higher-order logic is naturally used in this case. In this paper, the process by which knowledge representation is adopted from first-order logic to higher-order logic is discussed, and a decision-tree algorithm learned with higher-order logic is also presented. Experimental results show that the proposed algorithm is efficient.

Keywords Knowledge discovery • Higher-order logic • Knowledge base

53.1 Introduction

In the past two decades, more and more good results have been obtained in studies of knowledge discovery in databases (KDD). KDD mainly focuses on mining structured data. Compared with invariable data, knowledge is stable and reflects the high level of data is a representation of data abstraction, so studying the relationship between knowledge and knowledge is an important target in data mining, but very little attention has been paid to how to discover more and higher levels of knowledge from large knowledge bases. Finding rules in knowledge bases in the areas of knowledge engineering and machine learning is a very important problem because successful results can be applied to knowledge acquisition and the construction of large knowledge bases. Techniques of knowledge discovery in knowledge bases (KDK) are presented to discuss such problems [1].

G. Li (✉)

School of Computer and Information Engineering, Guangxi Teachers Education University, 530001 Nanning, China

Guangxi Key Laboratory of Hybrid Computation and IC design Analysis, 530006 Nanning, China

e-mail: guangyuanli2004@163.com

53.2 Related Work

Although the techniques on data mining in databases have been investigated for a long time and successful results have been obtained, very little attention has been paid to the research of knowledge discovery in knowledge bases. In [2], the author outline a framework for inductive learning with knowledge and address the problem of discovering regularities in large knowledge bases that contain many assertions in different domains. Experimental results show that such an approach can reveal useful regularities and is a helpful tool for expanding knowledge bases [2]. The authors present some of the directions of KDK and proposes using machine learning and induction techniques to mine regularities and high-level knowledge in knowledge bases [3–5]. A novel approach is presented for the discovery of two kinds of implicit knowledge based on machine learning techniques: one is a general and pertinent rule and the other comprises taxonomies of domain concepts [6]. The author introduces the possible benefits of mining knowledge and describes a technique for reorganizing knowledge and discovering higher-level concepts in a knowledge base. The rules input may have been acquired manually or automatically using an existing data mining technique. In either case, once the knowledge exists in propositional form, a formal concept analysis is applied to the rules to develop an abstraction hierarchy from which multilevel rules can be extracted. The user is able to explore the knowledge at and across any of the levels of abstraction to provide a much richer picture of the knowledge and understanding of the domain [7]. The authors describe techniques for combining two types of knowledge systems: expert and machine learning. Both the expert system and the machine learning system represent information by logical decision rules or trees. Unlike the classical views of knowledge-base evaluation or refinement, the author's view accepts the contents of the knowledge base as completely correct. The knowledge base and the results of its stored cases will provide direction for the discovery of new relationships in the form of newly induced decision rules [8].

53.3 KDK with Higher-Order Logic

Logic is called higher order if it allows for quantification over higher-order objects, such as, for example, functions of individuals, relations between individuals, functions of functions, and relations between functions. Higher-order logic was also called *type theory* in the previous century, while classical type theory has long since been overshadowed by set theory as a foundation of mathematics, and recent decades have shown a remarkable comeback in the fields of mechanized reasoning. In computer science, higher-order logic is used in, for example, program correctness and hardware verification.

53.3.1 *Knowledge Representation with Higher-Order Logic*

To discover knowledge from a knowledge base using higher-order logic, first of all, the representation of knowledge from first-order logic to higher-order logic is extended, and then we apply some techniques of higher-order logic to investigate the process of KDK.

Traditional machine learning systems adopt attribute values as the method of knowledge representation, and every example is described by a constant tuple. Each dimension of the tuple is a certain feature value. It is easy to understand knowledge that is represented by an attribute value, and representing knowledge in this way has the advantage that, using such a representation, the algorithm is more efficient, but using an attribute value to describe a complex knowledge structure has some drawbacks, as follows.

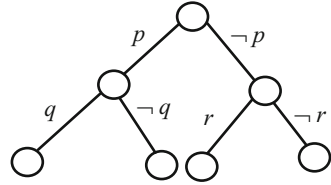
First, when describing knowledge using a complex structure, the attribute value will become too long. Second, because knowledge usually has many features, it is very difficult to select the best features and to determine the criteria for selecting the features that are suitable for all fields. Third, attribute-value representation captures no information about the structure of knowledge. Finally, it is limited when using the background to reasoning. Given such a background, some researchers propose that knowledge representation should be described using first-order logic, which promotes the development of the induction logic, and it is successfully applied to many practical systems, such as, for example, FOIL and LINUS. These systems adopt the first-order logic language Prolog for knowledge representation and reasoning, and it can solve some of the problems mentioned earlier to a certain degree, but there still exist two problems: one problem is that it loses the type concept, which is the key component of the attribute-value language, while the other problem is that it cannot provide higher-order constructions as well as flexible meta-programming description.

Studies show that under certain conditions, it is necessary to use new predicates for successful inductive learning, but the predicates of design and usage are problems in Prolog because it is a concept belonging to higher-order content, so it is only under the higher-order condition that the problem can be solved fully. Giraud-Carrier and Lloyd present knowledge representation based on the higher-order logic language Escher.

Escher is a general-purpose, declarative programming language that integrates the best features of both functional and logic programming languages. It has types and modules, higher-order and metaprogramming facilities, concurrency, and declarative input/output.

Compared with traditional propositional logic and first-order logic, Escher has some of the following features; using them we can design learning algorithms to deal with complex structured data. Escher supports all kinds of data types, such as set, multiset, graphs, and other complex data types, and it can describe examples with complex structured data. In addition, knowledge obtained can be expressed in a unified way, so it is easy to understand the natural features of data. Each example

Fig. 53.1 Decision tree with predicate pruning mechanism



in a set is described by a close item, which puts all the information of the example in a place that makes it convenient to use the information in the learning process.

53.3.2 Decision-Tree Learning with Higher-Order Logic

Decision-tree learning is a common machine learning method that is widely used in many applications. A decision tree is a flowchartlike tree structure where each internal node denotes a test on an attribute. Each branch represents an outcome of the test, and each leaf node holds a class label; thus, the choice of which node to split is very important because it affects the performance of the learning algorithm. Usually, the problem faced is one of attribute selection, and an attribute selection measure is a heuristic for selecting the splitting criterion that “best” separates a given data partition. Attribute selection measures are also known as *splitting rules* because they determine how the tuples at a given node are to be split. The appeal of decision trees lies in their relative power, ease of use, robustness with a variety of data and levels of measurement, and ease of interpretability. In KDK, the mining of complex structured data requires efficient tools, and higher-order logic is suitable for complex data mining compared to traditional decision-tree learning with higher-order logic, such as Escher. The nodes can be split using a predicate pruning mechanism. Figure 53.1 is a model of a decision tree with higher-order logic.

In Fig. 53.1, p , q , and r are predicates. A learning algorithm based on the model of the decision tree in Fig. 53.1 takes three inputs: a set of training examples, some background knowledge, and a collection of predicates. The algorithm functions in a top-down manner that makes binary splits at each node in the tree; if ϵ is the set of examples at the current node, then a predicate p induces a partition $P = (\epsilon_1, \epsilon_2)$, where $\epsilon = \epsilon_1 \cup \epsilon_2$, $\epsilon_1 \subseteq \epsilon$ is the set of examples that satisfies p , and $\epsilon_2 \subseteq \epsilon$ is the set of examples that do not satisfy p . The quality of the partition P is determined by a real-valued predicate selection function $f(P)$. Given a set of examples, we seek a predicate p such that $f(P^*)$, where P^* is the partition of ϵ induced by p , is optimized.

Now, suppose there are c classes in all. Let ϵ be a set of examples, N the number of examples in ϵ , n_i the number of examples in ϵ in the i th class, and $p_i = n_i/N$. First, some definitions are given in what follows [9].

Definition 1 The majority class of ϵ is defined as the class to which the greatest number of examples in ϵ belongs.

Definition 2 The accuracy, A_ε , of a set ε of examples is defined by $A_\varepsilon = P_M$, where M is the index of the majority class of ε .

Definition 3 Let $P = \{\varepsilon_1, \varepsilon_2, \dots, \varepsilon_n\}$ be a partition of a set ε of examples, where the number of examples in ε_i is N_i , the total number of examples in P is N , and we define the accuracy, A_P , of the partition P by

$$A_P = \sum_{i=1}^n \frac{N_i}{N} A_{\varepsilon_i}. \quad (53.1)$$

Definition 4 Let ε be a set of examples and $(\varepsilon_1, \varepsilon_2)$ a partition of ε . We say a partition $(\varepsilon'_1, \varepsilon'_2)$ of ε is a refinement of $(\varepsilon_1, \varepsilon_2)$ if $\varepsilon'_1 \subseteq \varepsilon_1$.

Definition 5 Let $P = (\varepsilon_1, \varepsilon_2)$ be a partition of a set ε of N examples, where n_i is the number of examples in ε in the i th class and $n_{j,i}$ is the number of examples in ε_j in the i th class, for $j = 1, 2$ and $i = 1, \dots, c$. We define the classification refinement bound, B_P , of the partition P by

$$B_P = \frac{1}{N} \left(\max \left\{ n_i + \max_{k \neq i} n_{1,k} \right\} \right). \quad (53.2)$$

Proposition 1 Let ε be a set of examples and P a partition of ε . If P' is a refinement of P , then $A_{P'} \leq B_P$, in particular, $A_P \leq B_P$.

Proposition 1 can be used to prune the search space when searching for a predicate to split a node. During this search, we record the best partition P found so far and its associated accuracy A_P . When investigating a new partition S , the quantity B_S is calculated. According to the proposition, if $B_S < A_P$, then the partition S and all its refinements can be safely pruned.

Now, an algorithm of decision-tree learning based on higher-order logic is presented as follows.

Input: ε //set of examples,
 S // bound of nodes in decision tree
Output: decision tree

1. Tree has only one node initialized;
2. *finished* := *false*;
3. *whilenotfinisheddo*
4. n := *node*;
5. F := ε // ε is the set of examples related to n
6. Search the predicate p that can partition the n with the highest accuracy
7. P is the result with the predicate p to partition F
8. *if*($A_P > A_F$)
9. Then the node n is split into two branches, one branch satisfies p , denoted by n_1 , the other does not;

Table 53.1 Efficiency of predicate pruning mechanism

Data set	lsl	Searched
Int Trees	396	98
Mutagenesis	535	82
East West	2,073	625
Headline	2,850	786
Protein	9,262	3,210

10. $S := S - 1$;
11. *if*($S = 0$)
12. *finished* := *false*;
13. *node* := n_1 ;
14. *else*
15. *finished* := *true*;
16. *endwhile*;
17. Output tree;

53.4 Experimental Study

To evaluate the performance of the proposed decision-tree learning algorithm with higher-order logic, we adopt the same data sets and the same experiment as in [9] to test the efficiency of the algorithm. Five data sets are used to test the effectiveness of the pruning mechanism in the decision tree, and for each data set, we give (1) the size of the predicate search space $|S|$ and (2) the number of predicates actually tested in a complete search of the predicate space aided by pruning. The results are shown in Table 53.1.

From the experimental results we can see that a significant reduction in search can be achieved. It has been shown that the effectiveness of the pruning mechanism is not a function of the size of the search space but a function of the structure of the search space and the way the training examples are actually labeled [9].

Conclusion

In this paper, we present some issues related to KDK with higher-order logic, including knowledge representation with higher-order logic and an algorithm of decision-tree learning with a predicate. Knowledge discovery with higher-order logic can overcome some drawbacks of traditional KDD, and it can be expected to spur developments in knowledge discovery. In the future, we plan to investigate the theory of KDD and efficient algorithms for KDD.

Acknowledgements In this paper, the research was sponsored by open fund of Guangxi Key laboratory of hybrid computation and IC design analysis and the fund of the Department of Education of Guangxi Province in China.

References

1. Yang B, et al. Research on the structure model and mining algorithm for knowledge discovery based on knowledge base. *Chin Eng Sci.* 2003;5(6):49–54 (In Chinese).
2. Shen W. Discovering regularities from knowledge base. *Int J Intell Syst.* 1992;7(7):623–35.
3. Yang B. Knowledge discovery theory based on inner cognitive mechanism. Beijing: National Defense Industry Press; 2009. p. 72–6 (In Chinese).
4. Yang B, et al. Kdk based double-basis fusion mechanism and its structural model. *Int J Artif Intell Tools.* 2005;14(3):399–423.
5. Yang B, et al. Kd(d&k): a new knowledge discovery process model for complex systems. *Acta Autom Sin.* 2007;33(2):151–5 (In Chinese).
6. Breidenstein T, et al. Knowledge discovery in rule bases. In: *Proceedings of the 10th European Workshop on Knowledge Acquisition, Modeling and Management*; Catalonia, Spain; 1997. p. 78–90.
7. Richards D, et al. Multi-level rule discovery from propositional knowledge bases. *International Workshop on Knowledge Discovery in Multimedia and Complex Data*; Taipei; 2002. pp. 11–9.
8. Weiss SM, et al. Knowledge-based data mining. In: *Proceedings of the SIGKDD*; Washington; 2003. p. 1–6.
9. Ng KS, et al. Predicate selection for structured decision. In: *Proceedings of the 15th International Conference on Inductive Logic Programming*; Bonn, Germany; 2005. p. 33–47.

Chapter 54

Numerical Analysis on High-Altitude Airdrop Impact Processing of Water Bag

Hong Wang, Tao Xu, and Yahong Zhou

Abstract The impact process of water bag that was air-dropped from 200 m high altitude is discussed by using the method of numerical simulation; microscopic changes of the main mechanical parameters are obtained in the process of water bag airdropping. Judging from the changing process of parameters such as the changing form, the nodal displacement, the nodal speed, and so on, the main reason which leads to the destruction of water bag is that the liquid spreads rapidly and sharply at the landing moment; moreover, the side face of the water bag may be the most easily damaged part.

Keywords Free drop • Airdrop water bag • Dropping impact • Numerical simulation

54.1 Introduction

Following the rapid development of hardware and numerical simulation theory and the software platform becoming mature, numerical simulation has been a dispensable method of studying and analyzing in many fields, which not only the circle of development is shortened but also massive developing funds are saved. ANSYS/LS-DYNA is a kind of numerical simulation software platform being widely used [1], the kind of explicit nonlinear dynamic analysis of general finite element program, which can solve various 2D and 3D nonlinear structures of large deformation dynamic responses such as high-speed collision, explosion and mould pressing, and so on. Lagrangian is used as the main arithmetic to describe the incremental method, and control equations are also used such as conservation of momentum, conservation of energy, conservation of quality and boundary conditions, and so on. Nearly a hundred material models of metal and nonmetal are provided for selection, and properties are considered such as material failure, damage, anisotropy, stickiness, creep, strain rate, correlation temperature and correlation strain rate, and so on. The ANSYS/LS-DYNA program has a powerful

H. Wang (✉) • T. Xu • Y. Zhou
Air Force Airborne Academy, 541003 Guilin, China
e-mail: spwqsp@163.com

functional pre- and post-processing program [2], by which the grid division and results calculation can be very conveniently processed and 3D motion picture of the calculation results is also showed.

The study object in this chapter is the free drop of liquid materials; double hyperelastic materials are used as packaging solution to liquid materials, and based on ANSYS/LS-DYNA numerical simulation and analysis system, by theoretical calculation analysis and computer simulation, numerical simulation analysis is done on its high-altitude airdrop impact process [3]. Dynamic simulations of the landing impact and landing process are made; in the study, changes on the volume and form of the package when landing and impacting, production of impact force, changes of nodal speed, ways of damage to the package, etc. [4] are all focused on, which can provide a basis to the free drop cushioning packaging design of liquid materials.

54.2 Example and Simulation Condition

Landing of airdropped materials is a process with multiple condition limitations and multiple outputs in addition to the limitation of airdrop altitude, which makes the experiment very difficult, and there are no experimental indoor conditions nowadays. Therefore, by numerical simulation method to simulate and analyze the whole process of airdrop landing and to predict the general range of a few key cushioning performance parameters [5], which is very helpful to the decision of choosing cushioning packaging materials and the design of packaging way.

54.2.1 Simulation Object

According to the study object of free drop of liquid materials, 5 kg of drinking water is chosen as the airdrop material; double-layer hyperelastic materials are used as the simulation water bag with structure size of 400×350 mm to simulate the landing impacting process of free drop from an altitude of 200 m above the ground with water in it. By simulation calculation, deformation mode of the water bag in the impacting process is found; change rules of a series of parameters are got by calculating the material pressure, speed, deflection, and the received impact load.

According to certain packaging solution when using hyperelastic materials, plastics similar to nitrile rubber are used as simulation packaging material, the intensity limit and modulus is 25 MPa, the density is $1,500 \text{ kg/m}^3$, and the elasticity modulus is 0.04 MPa. In the process of numerical simulation analysis, hyperelastic material model is used as the packaging material; hydro-model is used as water and air; Gruneisen equation is used as the state equation; concrete dynamic elastic-plastic material is used as the ground material.

Fig. 54.1 Calculating structure model of airdrop landing impact of double-layer water bag

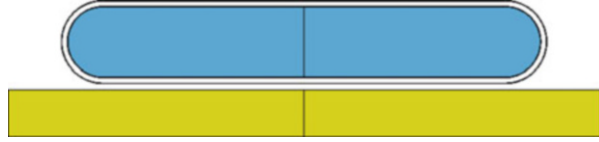
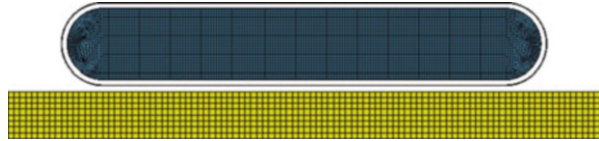


Fig. 54.2 Calculating finite element grid division of airdrop landing impact of double-layer water bag



54.2.2 Boundary Condition and Solving Control Condition

Before calculating, the boundary condition and solving control condition on the model are as follows:

1. Boundary constraint condition: the ground is rigid; all degrees of freedom are bounded.
2. Impact velocity is 50 m/s.
3. Impact simulation time is 1,800 μ s.
4. Newton, centimeter, microseconds, and gram are used as calculate units.
5. Calculating method: ALE.

54.2.3 Structure Model

According to the structure of the water bag with water in it, calculating the model of airdrop landing impact of double-layer water bag is determined as Fig. 54.1 shows.

And on this basis, finite element grid division is done as Fig. 54.2 shows.

54.3 Results and Analysis

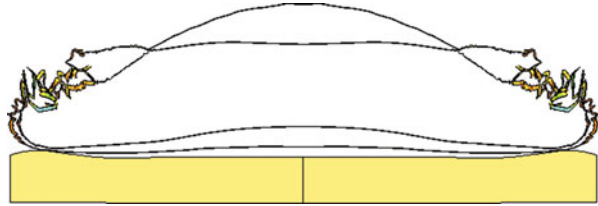
54.3.1 Deformations of Water Bag in the Landing Impact Process

At the landing moment, air between the inner bag and the outer one is squeezed, expansion occurred, and expansion and deformation occurred in the outer bag; being under the combined action of the air pressure in the middle and the inner water pressure, there is a basic balance state between the two, and not much deformation occurred in the inner bag, as shown in Fig. 54.3.

Fig. 54.3 State of the landing moment



Fig. 54.4 State of 47.2 μs after landing



After landing at 3 μs , the two-layer water bag is fit at the landing place, the air between the two layers of water bag is flown up and around, and comparatively large expansion and deformation occurred in the outer bag, while not much deformation occurred in the inner one.

After landing at 10 μs , the two-layer water bag is fit at the landing place, the down movement of the water in the water bag is interrupted and it flows around, the water bag is impacted by the flowing water to expand around, at the same time bounce occurred in the middle part of it, and depressed deformation also occurred on the ground surface.

As time passes by, continuous impact is made by the flowing water, and the deformation around is on the rise.

From 47 μs after landing, damage is produced around the water bag till it is completely broken, as shown in Fig. 54.4.

54.3.2 *Changes of Mechanical Parameters Around the Water Bag*

1. Changes of mechanical parameters of the side node of the water bag

The side unit nodes of the inner and outer water bags are chosen to analyze.

From the displacement curves showed in Fig. 54.5, slowly changes begin in the displacement of unit node; when at 53 μs , the side of the water bag is strongly impacted by the liquid, the displacement suddenly increases, and the water bag breaks soon.

Figure 54.6 is the speed curves of the side unit node of the water bag moving out horizontally; within 50 μs at the beginning of landing, the node is doing fore and aft motion; at 52 μs when being impacted strongly by water, the node moves out rapidly; the peak value of speed amounts to 5,500 m/s.

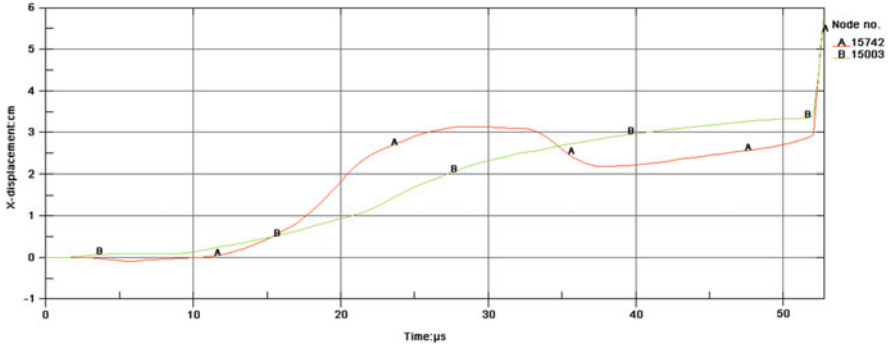


Fig. 54.5 Horizontal displacement curves of nodes (A is the outer bag, B is the inner one)

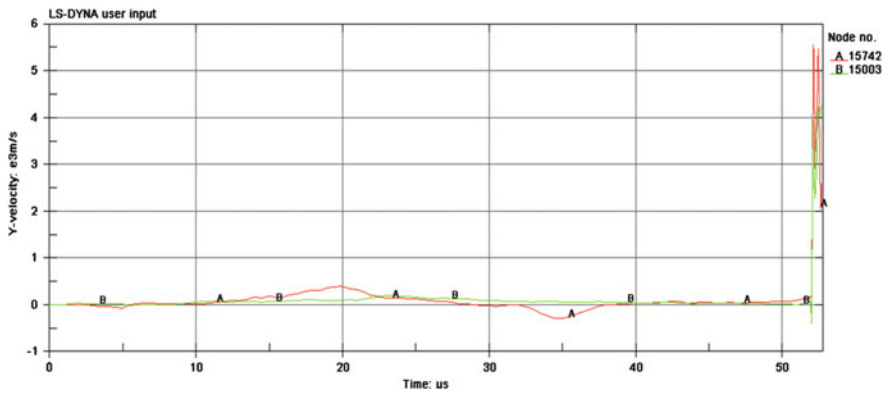


Fig. 54.6 Speed curves of node X (horizontal direction). (A is the outer bag, B is the inner one)

2. Changes of mechanical parameters of the intermediate node of the under part of the water bag

The intermediate unit node of the under part of the inner water bag and the outer one is chosen to analyze.

Figure 54.7 is the speed change curves of the node. At the landing moment, the node bounces upward rapidly; the node moves downward at first and then changes to upward, and its speed peak value of moving upward is above 100 m/s and then falls slowly.

3. Changes of mechanical parameters of the intermediate node of the upper part of the water bag

The intermediate unit nodes of the upper part of the inner water bag and the outer one are chosen to analyze.

Figure 54.8 is the speed change curves of the node. At the landing moment, the node of the outer water bag bounces upward rapidly at first; the node moves

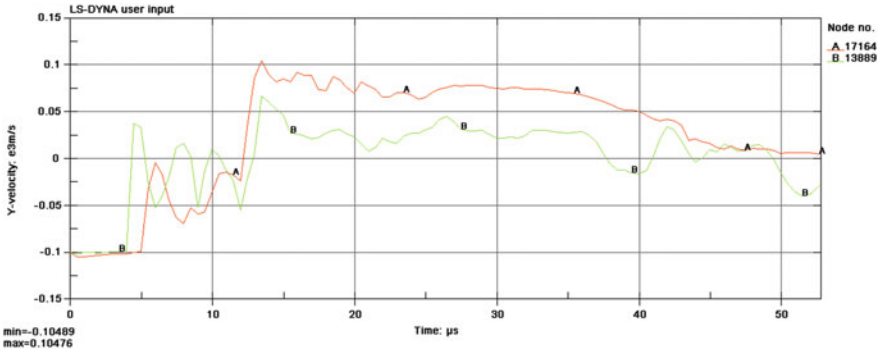


Fig. 54.7 Speed curves of node Y (vertical direction). (A is the inner bag, B is the outer one)

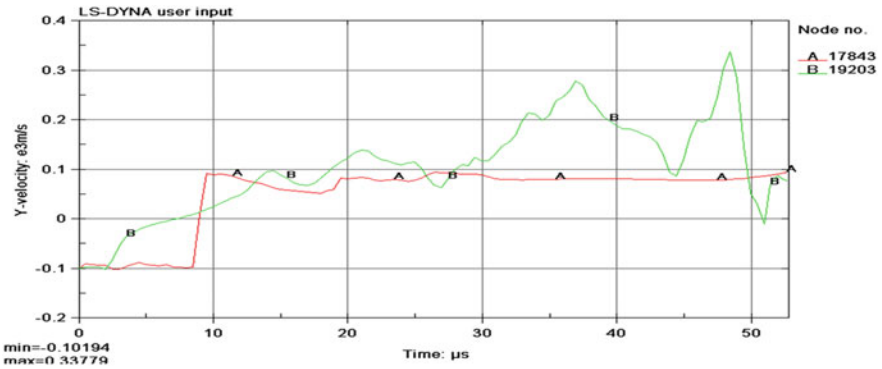


Fig. 54.8 Speed curves of node Y (vertical direction). (A is the inner bag, B is the outer one)

downward and then changes to upward, and its speed peak value of moving upward is above 330 m/s and then falls rapidly.

Conclusion

Shown from the results of numerical analysis, the packaging method of using double-layer hyperelastic materials cannot meet the packaging needs of that liquid material free dropping from 200 m high altitude; the inner and outer water bag are all broken. On the other hand, judging from the results of numerical simulation, the damage to the airdropped water bag is mainly because the water spreads around rapidly at the landing moment. Firstly, seen from the deformation process and node displacement of the water bag, maximum deformation is found in the surrounding edge of the water bag; sudden change of displacement occurred at one moment, which is the most easily damaged part. Seen from the simulation results of speed, great changes

(continued)

(continued)

occurred in the speed of the side node at one moment (within 2 μ s). All this amounts to explain why the water bag is damaged, the main reason is that liquid spreads around rapidly after landing, and the most easily damaged part is the side part, which are all key issues that should be considered in packaging scheme.

Aiming at problem of airdropping drinking water, hard materials are usually used in packaging at before with high costs and often takes space. In this chapter, double-layer hyperelastic materials are used as soft packaging solution for the first time. By numerical simulation analysis of its impact process of airdropping from high attitude, the water bag's changing process of mechanical parameter and damage mechanism are gotten, which provides technical references to the airdrop of soft water bag. The soft materials of the airdropped water bag may be used in many succor actions to airdrop directly below 200 m altitude.

References

1. Li L-C, Huang G, Li W-S, Wang Z-S. Simulation analysis of new type landing cushion airbag based on ANSYS/LS-DYNA. *Packag Eng.* 2012;33(15):16–20.
2. Zhang G-M, Wu J-H, Guo F-B. Drop analysis of pop can based on ANSYS/LS-DYNA. *Packag Eng.* 2011;32(5):4–6.
3. Tan J, Xu H, Liu X. Numerical analysis and improvement of airdrop landing process of special vehicles. *Packag Eng.* 2010;31(1):57–61.
4. Dong H-D, Ge Z-H. Drop-impact simulation of product based on ANSYS/LS-DYNA. *J Luoyang Inst Sci Technol (Natural Science Edition).* 2010;20(3):35–9.
5. Hu M-X, Chen Y, Du Z-J, Zhang Y-J. Simulate of packaging drop based on ANSYS/LS-DYNA. *Packag Eng.* 2007;28(11):53–4.

Chapter 55

Heterogeneous Data Sources Synchronization Based on Man-in-the-Middle Attack

Yunze Wang and Yinying Li

Abstract With the help of the idea of Man-in-the-Middle Attack and the introduction of synchronization agent having a Man-in-the-Middle role, this chapter comes up with synchronization system architecture of heterogeneous data sources on the top of SyncML (Synchronization Markup Language) protocol. The synchronization process achieves the two prototypes of client in the synchronization agent completing respectively the data synchronization with the corresponding SyncML server. The data synchronization system of this chapter could better solve synchronization problems of heterogeneous data sources in the distributed computing environment.

Keywords SyncML • Heterogeneous data sources • Data synchronization • Sync agent

55.1 Introduction

As there is a wide demand of database application for geographically dispersed companies, groups, and organizations and a rapid development of computer network communication technology, the distributed database system on the basis of a centralized database system could appear and develop. However, in the process of building a distributed database system, due to some objective reasons, it forms a distributed heterogeneous database system with a centralized database using a different data model or a different database product [1]. In order to maintain their data consistency, some technology of data synchronization may be inevitable.

Y. Wang (✉) • Y. Li
The School of Information Technology, Hebei Institute of Communications,
050071 Shijiazhuang, China
e-mail: 32720811@qq.com

55.2 The Shortcomings of Existing Technology for Synchronization

55.2.1 The Data Synchronization Between db4o and Relation Database

The dRS (db4o (Open Source Object-Oriented Database) Replication System) can achieve the two-way synchronization (replication) between db4o and a variety of relational databases to ensure data consistency [2]. However, the dRS system has some limitations: it only executes the two-way synchronization between relational database and object-oriented database, lacking a general model.

55.2.2 The Data Synchronization for SyncML

The solution strategy of heterogeneous database replication based on SyncML is also put forward, in which JDBC (Java Data Base Connectivity) and SyncML are adopted to complete a common data replication [3], implementing two-way data record replication between two heterogeneous databases. The architecture of the solution strategy is shown in Fig. 55.1.

Furthermore, the solution strategy has also some disadvantages: it is still based on standard data synchronization prototype system for SyncML, while SyncML server is the center and different SyncML clients carry on synchronization operations with SyncML server. SyncML server as the master node may become a bottleneck for system performance, while SyncML clients need asymmetric data replication to work with it. So this solution may popularize difficultly in distributed applications.

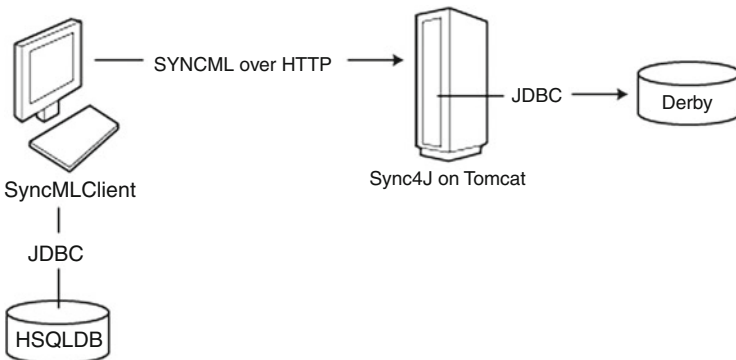


Fig. 55.1 Implementation of data synchronization based on SyncML

55.3 Design of Synchronous Prototype System

In view of the limitations and shortcomings of data synchronization solution strategy of heterogeneous data sources for db4o and SyncML protocol, the chapter builds synchronization agent as an intermediary role to data synchronization between the SyncML server by means of Man-in-the-Middle Attack and SyncML client, which can guarantee the data consistency of two peer entities (SyncML server). The designed synchronization prototype system is shown in Fig. 55.2.

In the prototype system, data synchronization is carried out between the SyncML Server1 and SyncML Server2 through synchronization agent. However, for the two SyncML servers, the other server is transparent, because the two SyncML servers do not interact directly and synchronization agent takes charge of receiving, processing, and forwarding message in the synchronization process between the two SyncML servers.

55.3.1 The Idea of Man-in-the-Middle Attack

The so-called Man-in-the-Middle Attack (abbreviated MITM attack) is an indirect intrusion. It means the attacker will insert their host into the gap between two target nodes of communication path, allowing it to become a trunking so as to monitor the communication between the target hosts [4].

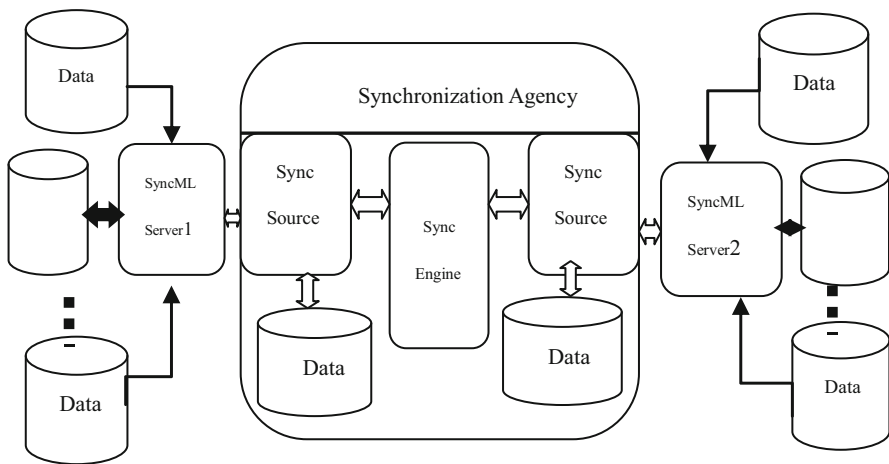
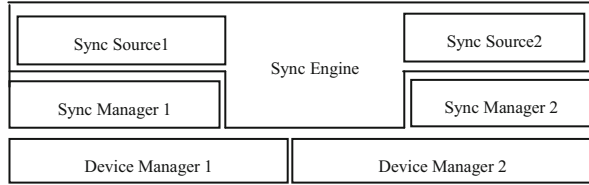


Fig. 55.2 Synchronization prototype system

Fig. 55.3 The structure of synchronization agent



55.3.2 Synchronization Agent Design

Based on the Sync4j (SyncML for Java) client architecture, synchronization prototype system, as well as synchronization agent structures, this chapter gives the ultimate level of division and module design shown in Fig. 55.3 [5].

There are two Sync Source interfaces corresponding with Sync Source1 and Sync Source2 in Fig. 55.3. They need to be implemented in order to execute the synchronization process with the two SyncML servers. These two Sync Sources carry on synchronization session in charge of sending and receiving SyncML messages with corresponding SyncML server. Therefore, during the course of two SyncML servers synchronization, two relatively independent and linked synchronization sessions exist simultaneously.

In addition, in the light of synchronization agent prototype of SyncML client, two Sync Managers (Sync Manager1 and Sync Manager2) and Device Managers (Device Manager1 and Device Manager2) need to be created, which complete their respective functions and tasks in the synchronization process.

55.4 The Definition and Design of the Synchronization Process

55.4.1 The Data Synchronization Process of SyncML

The synchronization process for SyncML can be divided into three stages: the synchronization initialization [6], data updates, and data ID mapping as shown in Fig. 55.4.

55.4.2 The Design of the Synchronization Process

In view of the preamble design of the synchronization prototype system and the data synchronization process of SyncML, the synchronization process in this chapter is divided into five stages shown in Fig. 55.5.

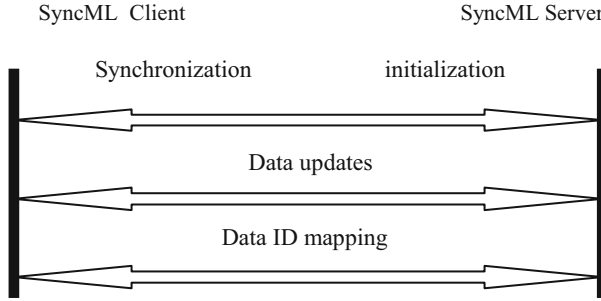


Fig. 55.4 The synchronization process of SyncML

1. Obtain data updates of Sync Server1.

This is the initial stage of the synchronization process, and the Sync Engine in synchronization agent initializes synchronization. At this stage, the synchronization process is completed by Sync Source1 and corresponding Sync Server1 and then eventually gets data updates of Sync Server1. This stage can be divided into two steps again: First, SyncML is initialized with synchronization initialization interaction between Sync Source1 and Sync Server1; second, data update interaction for SyncML is carried out.
2. Obtain data updates of Sync Server2.

The synchronization session is initiated by the Sync Engine in this phase and gets data updates for Sync Server2. The synchronization process of this phase may be performed simultaneously with data updates of the Sync Server1 that the synchronization is concurrent at this stage. Synchronous interaction based on SyncML could take place between synchronization agent in Sync Source2 and corresponding Sync Server2 and ultimately obtain data updates of Sync Server2. As the same as the above phase, this phase can be divided into two steps: first, the SyncML synchronization initialization is completed; second, the two sides exchange data updates.
3. Data conflict resolution and data mapping.

Learning from the first two stages, the synchronization agent could interact with sync server concurrently to get access to both data updates. In this stage, the Sync Engine may resolve data conflict and map data between the sync servers, which create conditions for the following two-stage data update execution.
4. Execute data updates for Sync Server2.

The Sync Engine in synchronization agent could implement data analysis and conflict resolution according to the data update of each Sync server. After the completion of the previous phase, in this phase, the synchronization agent is responsible for transferring data updates from Sync Server2 to Sync Server1 finishing appropriate data updates. In this stage, synchronous interaction is also based on the SyncML protocol, namely, at first, the second synchronization initialization happens between Sync Source1 and Sync Server1 and then data update interaction is achieved.

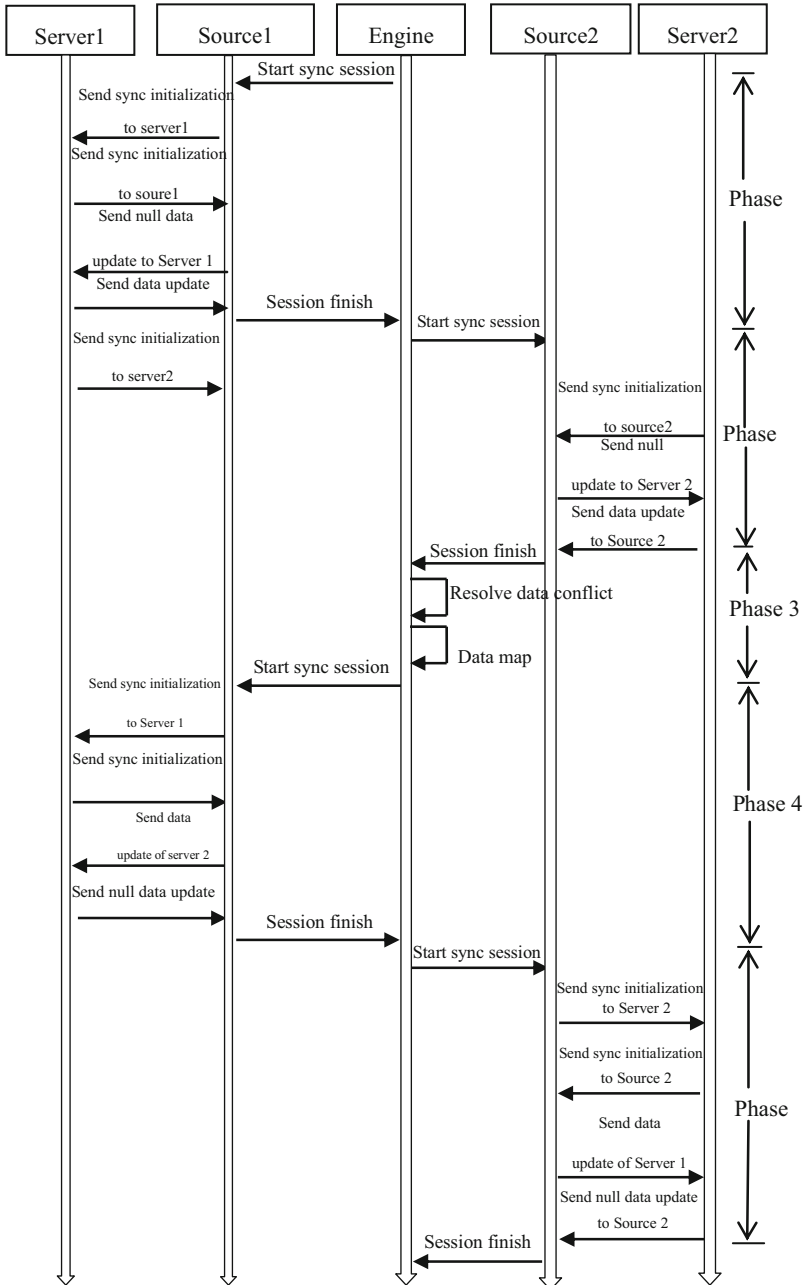


Fig. 55.5 Five-phase synchronous process definition

5. Execute data updates for Sync Server1.

It is quite different between the abovementioned five stages of the synchronization process and the SyncML synchronization protocol definition, but each stage is completed on the basis of the provisions of the agreement, according to the synchronization initialization sequence data updates and data mapping for synchronous interaction. The data mapping phase gives the necessary adjustments and modifications, due to the special design of the prototype system.

55.5 Implementation of Synchronization Process

With the idea of data synchronization in the third segment, this chapter takes shape in the implementation of data synchronization design. The two-stage data synchronization process implementation is shown in Fig. 55.6.

1. Synchronization initialization

Firstly, Sync Engine calls sync () function of Sync Manager to start the synchronization process. After that, Sync Manger will send SyncML message containing the information of synchronization initialization and synchronization

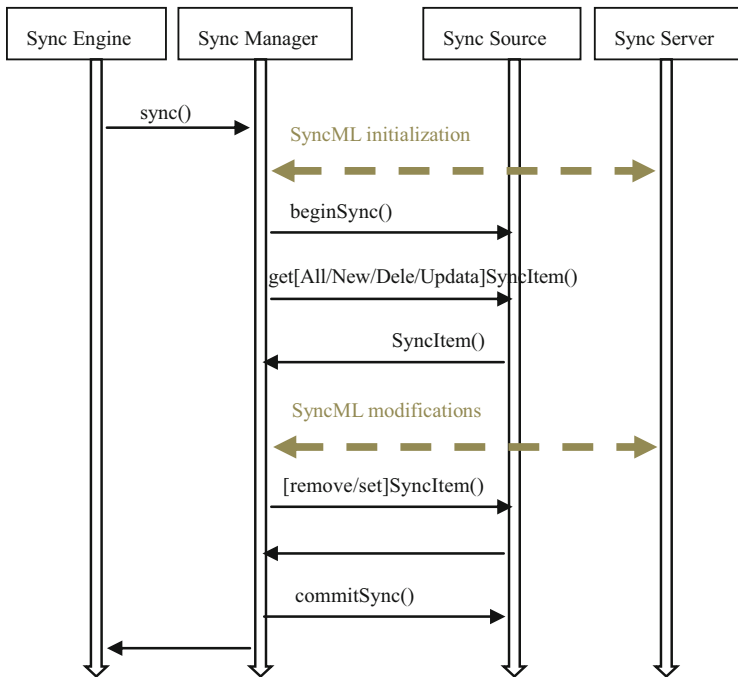


Fig. 55.6 The first two phases of the synchronization flow chart

request to the sync server. Then the sync server should deal with messages and reply to them containing the state to accept or reject messages to the Sync Manger.

2. Access to data updates of synchronization server

In this stage, Sync Manager calls the function of Sync Source getting information of local and server data source from the Device Manager. Then, Sync Manger calls beginsync() function in Sync Source to complete local data detection. Soon afterwards, Sync Manger will send SyncML message of no data update to Sync server. After receiving the data update message, synchronization agent handles updated data items one by one. If it needs adding or modifying, the synchronization agent will call setSyncItem() function of Sync Source; if it needs deleting, it may call removeSyncItem() function. The process is transparent for the Sync Engine.

55.6 Experiment Results

When SyncML client asks for data synchronization, synchronization system may complete data synchronization for two heterogeneous databases of object database and relationship database with the purpose of keeping the data consistency. The result of the experiment is shown in Fig. 55.7 which displays status after synchronization for db4o and Access.

Compared with the standard synchronization system for SyncML, the synchronization system prototype in this chapter utilizes synchronization agent to achieve synchronization process instead of the server, which could reduce the workload of the server and overcome system bottleneck. In addition, compared to non-peer data synchronization prototype system of SyncML, the system can implement synchronization of two heterogeneous data sources for SyncML server, namely, synchronization of two peer entities.

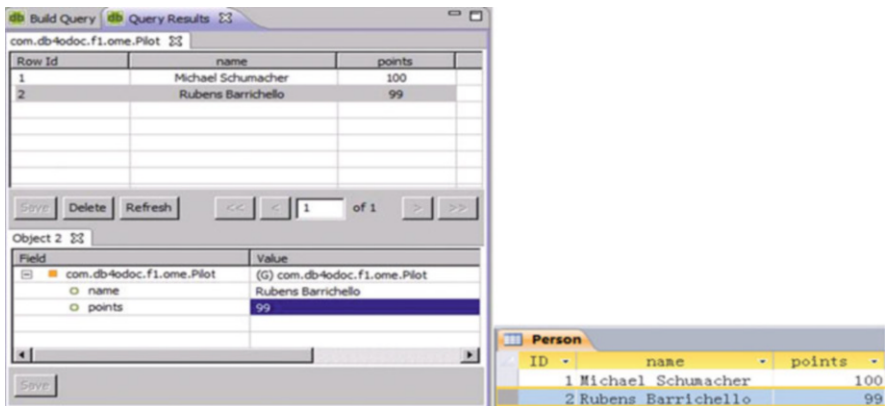


Fig. 55.7 The experiment result of data synchronization

By means of experiments of process and result, the scheme to resolve data conflict is extremely novel in this chapter. Generally speaking, the SyncML protocol rules of Sync Engine in SyncML server may resolve data conflict, but it is possible that SyncML client has possessed the function of Sync Engine. If data conflict is resolved by Sync Engine in one of the Sync servers, it is improper because of destroying parity between two Sync servers to some extent. In order to resolve data conflict between two real Sync servers, the synchronization system prototype puts Sync Engine in synchronization agent as a middleman role and gives a necessary strategy to resolve data conflict.

Conclusion

Analyzing advantages and disadvantages of synchronization solution of the existing heterogeneous data source and considering the various synchronization schemes, this chapter comes up with synchronize data from heterogeneous data sources between two peer entities based on SyncML protocol standard as well as by means of the idea of MITM attack. This chapter gives these achievements as follows:

1. This chapter chooses SyncML protocol as synchronization standard, which not only can play its advantages in the field of data synchronization of the mobile terminal but also lead into creatively non-mobile terminal data synchronization stage, which may embody its superiority better.
2. This chapter pulls into creative synchronization agent playing a middleman role, which may open the way of achieving data synchronization problems between peer entities.
3. This chapter proposes the main component—synchronization agent in data synchronization prototype system. This synchronization agent is designed based on SyncML client, but its position is different from SyncML client in data synchronization prototype system. It is a middleman role instead of an independent entity in data synchronization as well as an important communication bridge of two peer-to-peer entities in the process of heterogeneous data sources synchronization. It could receive, handle, and send SyncML messages which ultimately ensure consistency on a variety of data of both SyncML servers.

References

1. Zeng G, Fu X, Lv Z. Design and realization for heterogeneous database integration middleware. *Comput Technol Dev.* 2011;21(3):151–3. In Chinese.
2. Wang X, Zhou T. Integration of heterogeneous data source in academic information resources. *China J Med Lib Inf Sci.* 2012;21(2):15–8. In Chinese.
3. Cui J, Chen G. The research on object-oriented database Db4o. *Comput Knowl Technol.* 2011;7(1):140–1. In Chinese.

4. Guotian Xu. The Research of “Man in the Middle” Attack on ICMP Redirection. [J]. NetInfo Security. 2012;2:30–33. In Chinese.
5. Wang Y, Li Y, Guo L. Research of mobile endpoint user interface framework. Comput Eng Des. 2012;33(4):1670–5. In Chinese.
6. Yuan Tian. The Design and Implement of Mobile Multi-terminal Data Synchronization System Based on the SyncML Protocol [D] Chengdu: University of Electronic Science and Technology of China. 2013. In Chinese.

Chapter 56

Direct Forecast Method Based on ANN in Network Traffic Prediction

Congcong Wang, Gaozu Wang, Xiaoxiao Zhang, and Shuai Zhang

Abstract In this chapter, ARIMA (autoregressive integrated moving average) model and direct and iterative forecast methods based on ANN (artificial neural network) are adopted to fit and forecast the network traffic sequences. Different methods for predictive modeling are adopted to deal with the actual network traffic flow at different time intervals. With the GRA (gray relational analysis) method, the comparison and analysis of performance of the model show that the prediction error will be less if we use direct method for predictive modeling.

Keywords Traffic prediction • ANN • Direct forecast method • GRA

56.1 Introduction

The network traffic prediction plays an important role in traffic management, risk warning, network planning, and performance analysis. Rational allocation of network resources based on traffic prediction value can effectively improve the network performance. Essentially, the network traffic is a kind of time series. We can use the time series forecasting model for network traffic prediction.

Models commonly used in time series forecasting include the AR (autoregressive), ARMA (autoregressive moving average), ARIMA, and ANN. In addition, the FARIMA (fractional autoregressive integrated moving average) and the WT (wavelet transform) are also applied to the network traffic prediction [1, 2]. All kinds of methods have their own characteristics. AR and ARMA model is suitable to the network traffic characterized by short-related characteristics of and high accuracy in short-term prediction. The ARIMA and FARIMA improved from ARMA model can capture both of the long- and short-relevant characteristics of network traffic [3]. Several kinds of prediction models described earlier can be used for the smooth processing of network traffic. The WT and ANN can handle nonstationary network traffic. Especially, the ANN attracts attentions of the

C. Wang (✉) • G. Wang • X. Zhang • S. Zhang
Information Security Laboratory, Northwestern Polytechnical University,
710072 Xi'an, China
e-mail: wang_congcong@foxmail.com

researchers because it is suitable to describe the instability of flow rate with high precision and high flexibility.

Time series analysis can be adopted in forecasting both single and multiple periods. The direct and iterative forecasting methods can also be adopted to predict multiple periods. Weigend, Huberman, and Rumelhart showed that the iterative method was superior to the direct method in their sunspot data analysis [4]. Kline got the opposite conclusion by using three methods (iterative, direct, and joint law) for multistep forecasting. The results showed that the direct method was superior to the iterative method, but the training sample size and baseline forecast would affect the outcome [5].

The above studies show that there is no optimal solution presently. It is thought that the direct method is superior to the iterative method generally. In this chapter, we compare the application performances of ARIMA and direct and iterative methods based on ANN, which are used in nonstationary network traffic prediction. We also analyze the relationship between the latter two methods and ANN. Section 56.2 describes the ARIMA model; Sect. 56.3 presents the important parameters of ANN; and Sect. 56.4 discusses an example application with the GRA to evaluate and compare the application performance. Finally, the main conclusions are made.

56.2 ARIMA Model

The ARIMA model, as a kind of Box-Jenkins approach, is used to predict network traffic. After the d th ($d = 0, 1, 2$) difference disposal is applied to previous sequence Y_t , we can get new stationary series X_t . Then X_t fits ARMA (p, q) models. Furthermore, we get the forecast data of Y_t by restoring the original differential d times. The general ARMA (p, q) model can be expressed as

$$x_t = \phi_1 x_{t-1} + \phi_2 x_{t-2} + \cdots + \phi_p x_{t-p} + u_t + \theta_1 u_{t-1} + \theta_2 u_{t-2} + \cdots + \theta_q u_{t-q} \quad (56.1)$$

where the first half of Formula (56.1) is the autoregressive part, nonnegative integer p denotes the orders of the AR model, and ϕ_1, \dots, ϕ_p denotes the regression coefficients. The latter part is the MA part. Nonnegative integer q denotes the orders of the MA model, and $\theta_1, \dots, \theta_q$ denotes the moving average coefficients. X_t is the related sequence for network traffic. u_t is the white noise and its variance is equal to σ_2 .

When $q = 0$, the model becomes AR (p) model: $x_t = \phi_1 x_{t-1} + \phi_2 x_{t-2} + \cdots + \phi_p x_{t-p} + u_t$.

When $p = 0$, the model becomes MR (q) model: $x_t = \theta_1 u_{t-1} + \theta_2 u_{t-2} + \cdots + \theta_q u_{t-q}$.

The ARIMA (p, d, q) model of collective modeling process can be divided into the following six steps:

Step 1: test the stationary of data.

Step 2: carry out stationary disposal for the nonstationary signals.

Step 3: determine the order of ARMA (p, q) model after the difference disposal is applied to the nonstationary signals.

Step 4: estimate the parameters of the model.

Step 5: test the validity of the model and select the optimization model.

Step 6: when the model passes the white noise test, it can be used for prediction and simulation.

We adopt the ARIMA model as established in the literature written by Xue, K., Li, Z.Z., and Li, L. [6].

56.3 Artificial Neural Network

ANN was presented as a kind of mathematical model in the 1940s. It was designed to mimic the structure and function of information processing system of the human brain [7]. A typical ANN is usually comprised by three layers of units, namely, the input layer, hidden layer, and output layer.

The parameters of the hidden layer will affect the efficiency of ANN. Research shows that neural networks with one hidden layer are approximate to any nonlinear function by an arbitrary accuracy [8]. Kaastra and Boyd (1996) suggested that all MLPs should firstly run with two-hidden-layer structure at most [9]. The number of neurons in the hidden layer is also important. If you consider the generalization, you should use less number of neurons in one MLP. The more the number of hidden-layer neurons, the more accurate the result will be; moreover, it will increase the training time and cause a decline in the network fault tolerance. In order to solve the problem, we determine the number by trial and error [9]. Studies have shown that limiting the number of hidden-layer neurons may get better results. The number of neurons in the output layer is another factor that may affect the performance of the MLP. In the timing analysis, the number of neurons in the output layer is determined by the cycle length. If the analysis is only a baseline period, the number is 1. If it is a multi-cycle, the number of output neurons is determined by the preselection methods. If an iterative method is adopted, the number of output neurons is 1. If the direct method is used, the total number of forecast periods can be used as the number of output neurons. The iterative method is mainly used for single-cycle timing analysis. The predicted value is regarded as an input to forecast the value of the next period. When the number of forecasting periods is large enough, it will decrease the forecast accuracy. The direct method only utilizes the previous data to forecast trends.

56.4 Application Methods

In this study, we work on two different series (A and B) and predict them by using ARIMA and direct and iterative methods based on ANN. Samples are obtained by the monitoring center of campus network router port export flow. The sequence for A is a set of real network traffic data with a time span of 2 days with a sampling interval of 5 min (total of 576 sample values). The other is a set of real network traffic data with a time span of 1 h with a sampling interval of 1 min (total of 60 sample values). These data are divided into two parts, respectively: the first part as the known historical data prior to the start of the algorithm, used to build the algorithm model, and the second part as the test data to be compared with the predicted values of the algorithm, test error, and analysis algorithm performance, which is shown in Fig. 56.1.

Take the L-M (Levenberg-Marquardt) method as the learning algorithm in this ANN, and train it for 1,000 times. As listed in Table 56.1, a sequence of A and B of the MLP model is built. We use direct method to predict the test set of all values at the same time. Figures 56.2 and 56.3 indicate the possible network structure used for iteration and direct methods.

Mathematical output expressions of the MLPs shown in Figs. 56.2 and 56.3 are given below:

$$F_{t+l} = \alpha_l + \sum_{j=1}^m v_{jl} f \left(\sum_{i=1}^k w_{ij} Y_{t-i} + \theta_j \right) \tag{56.2}$$

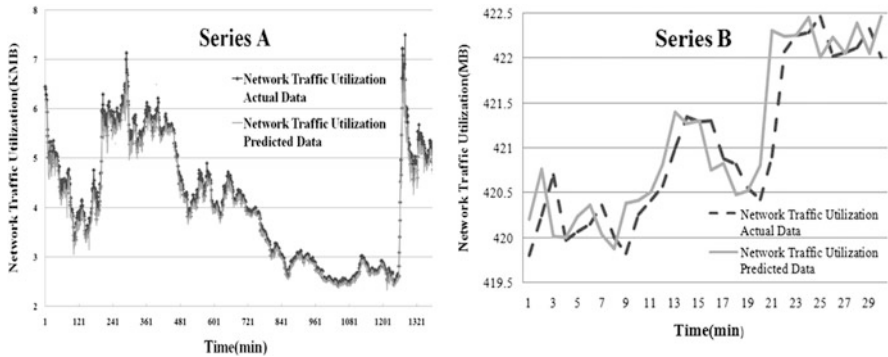


Fig. 56.1 Comparison of actual and forecasting data utilized by server network traffic

Table 56.1 MLP model set up to forecast with direct approach

Series	# of neurons			Activation function	
	Input	Hidden	Output	Hidden layer	Output layer
A	11	2	10	tanh	Linear
B	10	2	10	tanh	Linear

Fig. 56.2 Iterative forecast

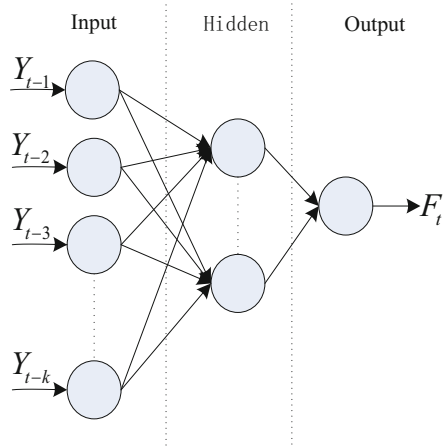
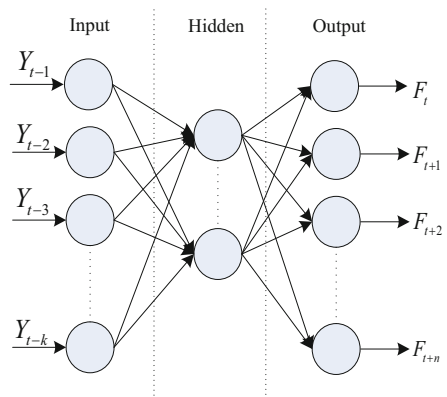


Fig. 56.3 Direct forecast



Here, Y_{t-i} ($i = 1, 2, \dots, k$) is the value of past k periods. F_{t+l} ($l = 0, 1, 2, \dots, n$) is used for forecasting this period and future n periods. W_{ij} ($i = 1, 2, \dots, k; j = 1, 2, \dots, m$) are weights that connect the input-layer and hidden-layer neurons. α_l ($l = 0, 1, 2, \dots, n$) and θ_j ($j = 1, 2, \dots, m$) are the bias connection weights. v_j ($j = 1, 2, \dots, m; l = 0, 1, 2, \dots, n$) are weights between the hidden-layer neurons and output-layer neurons. f is the activation function.

Forecasting with the direct approach, MLPs of each series should run and record the corresponding results. Choose it as the best MLP, which can get the best results for the corresponding series. Tables 56.1 and 56.2 present the best MLP structure corresponding to the test set and the best results, respectively.

The direct method is adopted to predict the results, which are shown in Table 56.2. Tables 56.3 and 56.4 show the comparison of the results for the test set generated by the direct method, iterative method, and ARIMA.

Values of the performance standards SSE and SAE are shown in Tables 56.3 and 56.4. In this stage, the GRA was used in the performance evaluation of all

Table 56.2 Performance criteria regarding the results obtained by direct forecast

Series	SAE training	SAE validation	SAE test	SAE training	SAE validation	SAE test
A	326.761	1.672	2.4136	129.152	0.576	1.029
B	382.608	1.781	3.4976	188.088	0.484	2.101

Table 56.3 Comparison of sum of squared errors

	Series A	Series B
Direct	1.022	2.1022
Iterative	1.683	5.1304
ARIMA	1.964	13.501

Table 56.4 Comparison of sum of absolute errors

	Series A	Series B
Direct	2.413	3.497
Iterative	2.964	5.347
ARIMA	3.204	8.997

methods mentioned while taking both of the two standards into account. The GRA is a statistical analysis method provided in the GT (gray theory) [10, 11]. All sources of randomness are regarded as the source of the gray in GT so that GT can be used for those situations if statistical assumptions are unsatisfactory [12]. This is the reason why the GRA performed well in Tables 56.3 and 56.4.

The GRA is used to describe the degree of influence between the given comparison sequence and the reference sequences in the measuring system. The degree of influence is defined as GRD (gray related degree). The GRA model is shown below [13]:

Step 1: let the reference sequence be $x_0 = (x_0(1), x_0(2), x_0(3), \dots, x_0(n))$. The results of comparisons for m sequences and x_0 sequences are defined as $x_i = (x_i(1), x_i(2), x_i(3), \dots, x_i(n))$, $i = 1, 2, \dots, m$.

Step 2: sequence must be normalized if the units of measurement are different. Data can be trained by one of the following three normalized methods:

Larger is the better	Smaller is the better	Ideal is the better
$x_i(k) = \frac{x_i^0(k) - \min x_i^0(k)}{\max x_i^0(k) - \min x_i^0(k)}$	$x_i(k) = \frac{\max x_i^0(k) - x_i^0(k)}{\max x_i^0(k) - \min x_i^0(k)}$	$x_i(k) = 1 - \frac{ x_i^0(k) - x^0 }{\max x_i^0(k) - x^0}$

$x_i^0(k)$ are the original value in k th of i sequence. $x_i(k)$ are values that have been normalized. $\min x_i^0(k)$ is the minimum of i sequence. $\max x_i^0(k)$ is the maximum. x^0 represent the expected values.

Step 3: gray relational coefficient is taken as $\varepsilon(x_0(k), x_i(k))$, and its calculation formula is shown below:

Table 56.5 GRD for series A

SSE	Series A		
	SAE	GRD	
Reference	1.022	2.413	1
Direct	1.022	2.413	1
Iterative	1.683	2.964	0.336
ARIMA	1.964	3.204	0.268

Table 56.6 GRDs of the three methods

	Series A	Series B
Reference	1	1
Direct	1	1
Iterative	0.336	0.484
ARIMA	0.268	0.266

$$\varepsilon(x_0(p), x_i(p)) = \frac{\min_{\forall j} \min_{\forall k} |x_0(k) - x_j(k)| + \zeta \max_{\forall j} \max_{\forall k} |x_0(k) - x_j(k)|}{|x_0(p) - x_j(p)| + \zeta \max_{\forall j} \max_{\forall k} |x_0(k) - x_j(k)|} \quad (56.3)$$

Here, $\zeta \in (0,1)$ (usually $\zeta = 0.5$) are the distinguishing coefficient. $i = j = 1, 2, \dots, m$ and $k = p = 1, 2, \dots, n$.

Step 4: finally, GRD, $\gamma(x_0, x_i)$, approximates Function (56.4):

$$\gamma(x_0, x_i) = \frac{1}{n} \sum_{k=1}^n \varepsilon(x_0, x_i) \quad (56.4)$$

Here, $\gamma(x_0, x_i)$ is a kind of geometric similarity measure between x_0 and x_i sequences in gray system. The degree of the GRD can prove the strong interaction between x_0 and x_i .

Based on the above four steps and Tables 56.3 and 56.4, the values of the SSE and SAE are combined into a single response value, which is named as GRD. For example, the results of series A have been shown in Table 56.5. Then the minimum value of SSE and SAE is selected to generate the reference sequence (1.022, 2.413). n is taken as 0.5 by using the “smaller is better” normalized method. The greater the value of GRD is, the more approximate the comparison sequence is to the reference sequence. Deal with the remaining series in the same way.

Table 56.6 shows the GRDs of both series. Here, the data range from 0 to 1 without normalization. ζ is taken as 0.5. GRDs correspond to the three methods that are listed in Table 56.7.

In Table 56.7, we have direct < iteration < ARIMA in descending order based on GRDs. As it also can be seen that the direct method is the best, the ARIMA is the worst. The direct method has obvious advantages than other methods.

Table 56.7 GRDs of the three methods

	GRD
Direct	0.989
Iterative	0.4
ARIMA	0.268

Conclusion

We study on the application of ARIMA and direct and iterative methods based on ANN in terms of the nonstationary network traffic prediction. The GRA is adopted to compare the performance of different time sequences. Meanwhile, point out that the direct method is in the superiority of iterative method. In addition, the comparison shows that the forecast effect with ANN is better.

This study supports the superiority of research before the declaration of the direct method. In order to promote the conclusions presented in this study, it is necessary to use a more stable and nonstationary network traffic sequence to carry out further study.

References

1. Zhang K, Chai Y, Fu X. A network traffic prediction model based on recurrent wavelet neural network. In: 2nd international conference on computer science and network technology (ICCSNT), 2012. IEEE, China; 2012. pp. 1630–3.
2. M.K. Dong, C. Chen, M.H. Huang, Jin, Y. Joint network traffic forecast with ARIMA models and chaotic models based on wavelet analysis. *Appl Mech Mater.* 2011;55:743–6.
3. Deth CG, Wakde DG. On the prediction of packet process in network traffic using FARIMA time-series model. *J Indian Inst Sci.* 2013;84(1 and 2):31–7.
4. Weigend AS, Huberman BA, Rumelhart DE. Predicting sunspots and exchange rates with connectionist networks. In: Santa Fe institute studies in the sciences of complexity, vol. 12. Addison-Wesley, USA; 1992. pp. 395.
5. Forecasting T S. Methods for multi-step time series forecasting with neural networks[J]. *Neural networks in business forecasting*, 2004: 226.
6. Xue K, Li ZZ, Li L. Network traffic prediction based on ARIMA model. *Microelectron Comput.* 2004;21(7):84–7.
7. Yegnanarayana B, Reddy KS, Kishore SP. Source and system features for speaker recognition using AANN models. In: Proceedings of the IEEE international conference on acoustics, speech and signal processing, Salt Lake City, UT, May 2001. pp. 409–12.
8. Hornik K. Approximation capabilities of multilayer feedforward networks. *Neural Netw.* 1991;4(2):251–7.
9. Kaastra I, Boyd M. Designing a neural network for forecasting financial and economic time series. *Neurocomputing.* 1996;10(3):215–36.
10. Lin Y, Lin S. A historical introduction to grey system theory. In: IEEE SMC 2004 international conference on systems, man and cybernetics, Hague, The Netherlands. 2004. pp. 2403–8.
11. Lin Y, Chen MY, Liu S. Theory of grey systems: capturing uncertainties of grey information. *Kybernetes.* 2004;33(2):196–218.
12. Liu SF, Lin Y. *Grey information: theory and practical applications*, vol. 2. London: Springer; 2006. pp. 25–47.
13. Wen KL. The grey system analysis and its application in gas breakdown and var compensator finding. *Int J Comput Cogn.* 2004;2(1):21–44.

Part III
Pattern Recognition

Chapter 57

Visual Simulation of Three-Point Method Guidance Trajectory for Antitank Missile

Mengchun Zhong, Cheng Li, and Hua Li

Abstract To solve problems of trajectory simulation in the training system for antitank missile of infantry fighting vehicle, three-point method guidance trajectory equations have been developed, and numerical simulation is performed in MATLAB software. It is difficult to keep balance between the fidelity and real-time simulation in large scale of terrain, but we managed to solve this problem by applying MultiGen Creator to construct the infantry fighting vehicles, antitank missiles and 3D entity model, and multi-resolution LOD terrain segmentation algorithm to optimize the battlefield environment. The virtual reality software Vega was used as the core graphics engine to realize the visual simulation of antitank missile, while the corresponding specific settings joined in the system, such as missile tail flame and explosion, so that training personnel can directly observe the missile flight state and damage effect. This study might provide a feasible method to improve the fidelity of the training system and the quality of training effect as well.

Keywords Antitank missile • Three-point method • Visual simulation

57.1 Introduction

With the development of science and technology in weapon system, the process of operating equipment has become increasingly complicated, which puts up higher requirements for the person who operates the new equipment. Countries around the world have taken measures in order to improve the training approaches and the environment for training activities so as to strengthen the operators' skills and their operations. At present, the army of China mainly uses AFT07 all-digital simulation of infantry antitank missile training simulator to carry out simulation training, but the system focuses on the operation method and operation steps. In trajectory simulation, it uses the projectile points (red light) to replace the missile, so the

M. Zhong (✉) • C. Li • H. Li
Department of Weapon Engineering, Academy of Armored Force Engineering,
100072 Beijing, China
e-mail: 1017548181@qq.com

simulation result is not realistic, and the trajectory simulation fidelity is directly related to the Sagittarius whether he can learn the characteristic of flight control live from training or not. Therefore, study on the antitank missile attacking process visual simulation technology is essential to improve the training effect of the system.

This chapter developed the three-point method of antitank missile guidance trajectory equation and the infantry antitank missile trajectory visual simulation calculated by software MATLAB and the virtual reality software Vega, so the weapon system can adopt professional analysis methods and perception means to get the simulation data of 3D scene graphs, and other forms of output, which is quite efficient.

57.2 Development of Three-Point Method Guidance Trajectory Equations

57.2.1 Reference Coordinate System

Coordinate system is selected as reference and describes the missile position and movement. Coordinate system can be determined based on the habit and the convenience of studying the problem [1]. Research on the guidance law of the three-point method is generally used in radar coordinate system $OX_R Y_R Z_R$, as is shown in Fig. 57.1: the origin O is the guidance station location, usually installed in infantry chariots; OX_R connects shaft in the infantry and target. The OY_R axis in the vertical plane is perpendicular to the OX_R axis. OZ_R shaft, OX_R shaft, and OY_R shaft united a right-handed Cartesian coordinate.

Angle ε is the elevation angle between the OX_R axis and the horizontal plane. Angle β is the azimuth angle—the angle of OX_R axis in the horizontal plane projection and the ground coordinate axis.

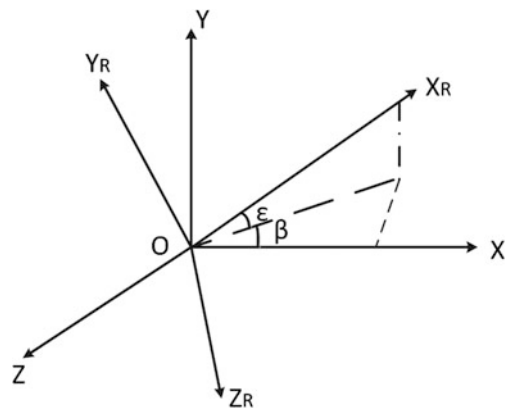
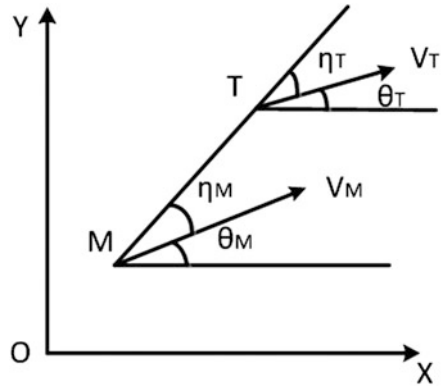


Fig. 57.1 Schematic diagram of the radar coordinate system and ground coordinate system

Fig. 57.2 Diagram of the relative movement



In order to determine the relative movement between the missile and target, it still needs to refer to the relative coordinates [2], as is shown in Fig. 57.2:

The missile position is M , the target position is T , and MT , called the line of sight angle, is the line between the missile and target. η_T is the lead angle of the target between the velocity vector and MT . In the same way, η_m is the lead angle of target, and θ_m is the angle between the missile velocity vector and the ground coordinates OX called the trajectory inclination of the missile. In the same way, θ_T is the trajectory inclination of the target. By combining with the radar coordinate system, missile elevation angle ϵ_m is the sum of the lead angle η_m and the trajectory inclination angle θ_m . That is,

$$\epsilon_m = \eta_m + \theta_m \tag{57.1}$$

In the same way, target elevation angle ϵ_T is the sum of the lead angle η_T and the trajectory inclination angle θ_T :

$$\epsilon_T = \eta_T + \theta_T \tag{57.2}$$

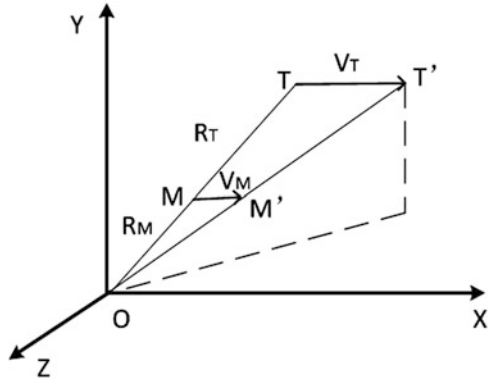
57.2.2 Establishment of Motion Equations

The three-point guidance law refers to the process in the target missile, missile guidance station, and always in a straight line [3]; the missile and guidance station line azimuth angle ϵ_m and the objectives and guiding station line azimuth angle ϵ_T must be equal.

That is,

$$\epsilon_m = \epsilon_T \tag{57.3}$$

Fig. 57.3 Diagram of the three-point guidance



Therefore, guiding relations between the three-point method are shown in Fig. 57.3:

The distance of the missile M to the origin O is called R_m , and R_T is the distance from the target T to the origin O . Using the reference coordinate system and the three-point method guidance law geometry, we can obtain relative motion equations of the three-point method for guidance:

$$\left. \begin{aligned}
 \frac{dR_m}{dt} &= V_m \cos \eta_m \\
 R_m \frac{d\epsilon_m}{dt} &= -V_m \sin \eta_m \\
 \frac{dR_T}{dt} &= V_T \cos \eta_T \\
 R_T \frac{d\epsilon_T}{dt} &= -V_T \sin \eta_T \\
 \epsilon_m &= \theta_m + \eta_m \\
 \epsilon_T &= \theta_T + \eta_T \\
 \epsilon_m &= \epsilon_T
 \end{aligned} \right\} \tag{57.4}$$

From Type (4), we can see that it is difficult to solve the trajectory equation directly. But when we get the initial condition $R_{T0}, R_{m0}, \eta_{T0}, \epsilon_{T0}, \epsilon_{m0}$, we can solve the equation by numerical solution.

57.3 Calculation of Ballistic Numerical Simulation

For discussion, we assume that the target does the rectilinear motion at a uniform velocity on the horizontal plane $V_T = 10$ m/s, infantry fighting vehicle is in static state, and the antitank missile intercepts the target by the three-point method and at a constant velocity, $V_m = 120$ m/s.

The initial condition of the guide to the missile is $R_{T0} = 500$ m, $R_{m0} = 10$ m, $\eta_{T0} = \epsilon_{T0} = \epsilon_{m0} = 60^\circ$, $\eta_{m0} = 30^\circ$. Applying the four-order Runge-Kutta method in

Fig. 57.4 Three-point method trajectory curves

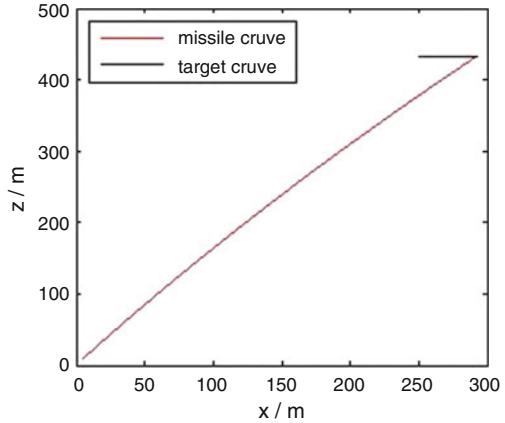
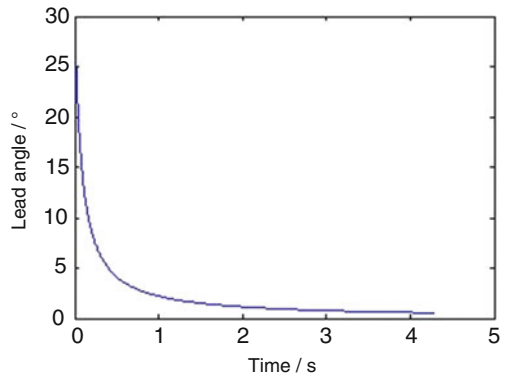


Fig. 57.5 Lead angle $\eta_m - T$ curve



MATLAB software to numerical solution Type (4), the missile trajectory is shown in Figs. 57.4 and 57.5.

In Fig. 57.4, the black curve stands for the trajectory of the target, and the red curve stands for the trajectory of the missile. The result shows that the meeting point of the missile and target is (290,433). Figure 57.5 is the curve that the lead angle of missile changes over time in the course of flying. According to the meeting point, $R_m = R_T$, so it can be obtained after 4.28 s the missile hit the target.

57.4 Antitank Missile Trajectory Visual Simulation

Visual simulation is an important form of virtual reality technology, which is based on information technology, multimedia technology, virtual reality technology, and its application in the field of related technology, a comprehensive technology study of the system by using the system model of the actual or assumed [4]. Traditional

simulations are usually based on Vega, while this study introduces the virtual reality software trajectory data to realize the visual simulation of the antitank missile attack process, by which a more intuitive result can be generated.

57.4.1 Construction of 3D Virtual Battlefield

The construction of 3D virtual battlefield includes 3D solid modeling and 3D terrain modeling. This article uses the current mainstream modeling tool MultiGen Creator to build infantry fighting vehicles, antitank missile, target tank 3D solid model, and the 3D terrain battlefield based on digital elevation model DEM terrain reconstruction methods [5, 6].

Level of detail (LOD) node technology is a fast rendering technology in the premise without affecting the visual effect to simplify the complex scene. In the past, LOD was simplified on grid entities in frame structure and did not pay attention to the terrain texture simplification of the corresponding. With the development of scene simulation, the fidelity of the scene puts up higher requirements, usually using high-resolution satellite images to construct terrain texture. Due to the large amount of image data, in order to improve the fidelity and the speed of simulation program, this chapter adopts four binary tree LOD terrain texture segmentation algorithms based on terrain rendering. According to the distance between view point and the ground, LOD, the terrain is divided into three levels (3LOD)—low, medium, and high resolution—as is shown in Table 57.1:

In medium resolution, each “tile” corresponds to a $1,024 \times 1,024$ RGB format texture map, while in high resolution, it needs four 256×256 RGB format texture maps combined into the $1,024 \times 1,024$ texture map. So we can make the terrain changes effect at different distances in a certain view range and reduce the rendering load so as to improve the real-time performance of the system. In the method, the virtual battlefield construction of Creator is shown in Fig. 57.6:

57.4.2 Visual Simulation of Missile Attack Process

The Creator software is adopted to build the three-dimensional model. In order to realize the model object driven in a 3D scene, it still needs to import the model of virtual reality software Vega for the corresponding initialization. Any visualization system will require much parameter setting in order to run; in Vega, such

Table 57.1 Details of hierarchy level

LOD level	Block	Tiles	Block status
High	1, 024 m	16	4×4
Medium	2,048 m	4	2×2
Low	4,096 m	1	1×1

Fig. 57.6 Battlefield simulation effect diagram



Fig. 57.7 Antitank missile and its plume effects

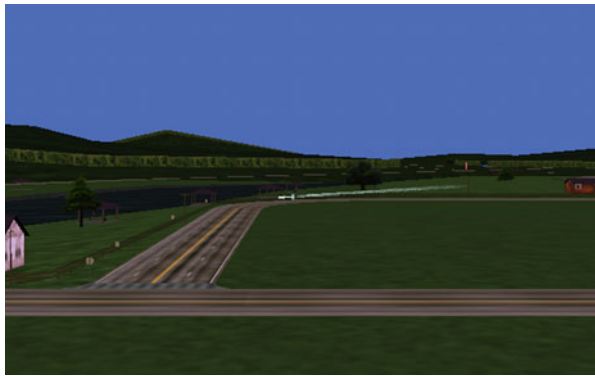


Fig. 57.8 Effects of the explosion



parameters are saved in the ADF file. In order to make the simulation looks more real, the corresponding specific settings are in the scene. The particle system generation is applied to make missile tail flame, target debris, and smoke effects. The flight process of the missile and the effects of the explosion are shown in Figs. 57.7 and 57.8.

Conclusion

This chapter studied the antitank missile motion by adopting the three-point method, where it is applied to MATLAB to solve the trajectory equations of the missile. The battlefield environment was optimized based on LOD terrain segmentation algorithm. It certainly solved the problem of balance between the fidelity and real-time simulation in large scale of terrain. By achieving the visual simulation of the missile attack process, this study provided a feasible method to improve the fidelity of the training system, and it might be of great significance to improve the effect of training simulator.

References

1. Li Y-Q. Study of surface to air missile operational command system and flight attack process simulation. Harbin: Harbin Engineering University; 2007.
2. Zhao Y-S, Wu B. The missile introduction. Xi An: Northwestern Polytechnical University Press; 2009. p. 60–3.
3. Zhang D-Y, Zhao Y-Q. The ground to air missile three point method for three dimensional kinematic trajectory modeling and simulation. *Flight Mech.* 2012;30(1):58–61.
4. Wan C, Meng X-F, Wan L. Visible target movement simulator based on MFC/Vega. *Comput Simul.* 2007;24(9):218–40.
5. Du J, Liang Q, Yao F-F. Virtual Battlefield environment program terrain generation method. *The Journal of Academy of Armored Force Engineering.* 2013;27(4):80–5.
6. Boubekeur T, Schlick C. A flexible kernel for adaptive mesh refinement on GPU. *Comput Graphics Forum.* 2008;27(1):102–13.

Chapter 58

A Fast and Accurate Pupil Localization Method Using Gray Gradient Differential and Curve Fitting

Yuhui Lin, Zhiyi Qu, Yu Zhang, and Huiyi Han

Abstract Pupil localization plays a key role in recognizing the biological characteristics of iris that is self-evident. In recent years, the most common procedures to localize the pupil have been based on the edge detector and circle finder, such as integro-differential operator and Hough transform. However, the circle finder over-emphasizes geometric characteristics, which reduces the accuracy and real-time performance under complex conditions. In this chapter, a new threshold method using discrete gray gradient differentials based on the unique features of gaps in the gray gradients of pupil boundaries is proposed to binarization first. We then highlight the geometric characteristics of the pupil by adopting the strategy of combining outline filling with curve fitting to locate pupil boundaries. Compared to the Wildes system, the proposed method is feasible, fast, accurate, and stable.

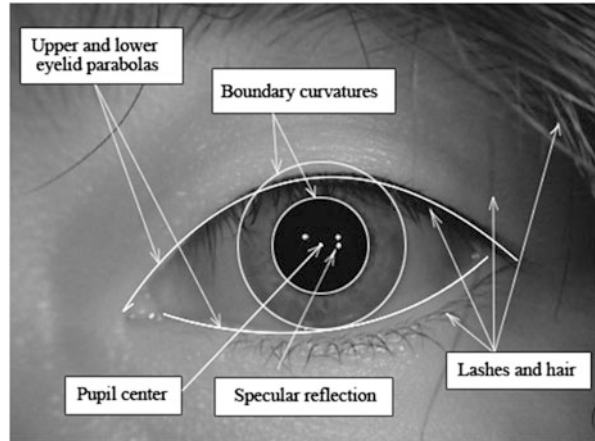
Keywords Pupil localization • Biometrics • Curve fitting • Hough transform • Gray gradient

58.1 Introduction

In the modern complex social environment, public safety is gaining significant attention from both governments and citizens. Traditional security systems for public safety mainly rely on simple identification technologies such as passwords, IC, and ID cards, which can be easily copied and stolen. For instance, a pair of twins could use the other's identity card to board an airplane, which may be hardly detected by current airport security systems; a hacker can take money using a copy of the credit card after stealing the passwords. Hence, the biometric technology, which relies on physiological and physical characteristics (e.g., fingerprints, palm prints, voice recognition, iris patterns, and DNA) which are hardly stolen and

Y. Lin (✉) • Z. Qu • Y. Zhang • H. Han
Institute of Applied Computer Technologies, School of Information & Engineering,
Lanzhou University, Lanzhou 730000, China
e-mail: linyih12@lzu.edu.cn

Fig. 58.1 Four-function eye model



duplicated, has been used to verify and identify individuals [1]. As an iris pattern is easily detected in public places and difficult to counterfeit [2], the iris recognition has recently gained attention in research communities.

A typical iris recognition system comprises four basic procedures: near-eye infrared image acquisition, iris localization and segmentation, feature extraction, and matching and recognition [3]. Iris segmentation plays key roles in the entire system. Generally, an eye model is described by four functions (shown in Fig. 58.1) consisting of the upper and lower eyelid parabolas, the boundary curvatures of the iris and the whites of the eyes, and the boundary curvatures of the pupil and iris; these functions are widely used in iris segmentation [4, 5]. The large gap between the pupil and iris boundary curvatures was used in the new image thresholding method. Pupil boundary extraction and center localization represent the first step in iris segmentation. Previous work [6] has revealed that a fast and accurate pupil localization method will make the iris segmentation procedure simpler and faster.

A pupil localization method includes image de-noising, thresholding, pupil boundary detection, and pupil center localization. Image de-noising is primarily used to dilute noise and blocks of hair in image acquisition. The general thresholding procedure typically uses a fixed threshold, and when an image of an eye is subjected to thresholding, the appropriate threshold plays a decisive role in the detection and localization of its boundaries. However, fixed thresholds are not typically used for various images. There are some common procedures, such as the bimodal method [7] or Otsu method [8], that are mainly based on the properties of the entire image instead of the low gray value area containing the pupil. Traditional methods for pupil boundary detection and pupil center localization are mainly based on the Canny operator and Hough transform [9]. The purpose of the Hough transform is to find imperfect instances of objects within a certain class of shapes by a voting procedure, and it is only efficient if a high number of votes fall to the correct object [3]. If the object is too small or the edges are too complex, some votes will fall to a neighboring object, which reduces the visibility of the main object.

Therefore, the Hough transform overemphasizes the boundary geometric characteristics of the image and ignores the properties of the external outline, which reduces the localization accuracy of the method under complex conditions.

58.1.1 The Related Works

Researchers have used diverse methods to detect the pupil boundary and localize the pupil center. Daugman used an integro-differential operator to localize the pupil [5], but this technique could fail for images containing objects with low brightness or specular reflection pollution. Wildes designed a classical method to detect the pupil boundary using the Hough transform and Canny operator [8]. Similarly, the Wildes system may not perform efficiently and may fail to obtain an appropriate threshold under high pollution caused by low-intensity regions, because other binary objects (e.g., eyebrows, lashes, hairs, and the black frames of glasses) contain areas with similar gray scale, and will strongly mislead the detection algorithm. Recently, Farmanullah designed a bi-valued adaptive threshold and two-dimensional (2D) properties to localize the pupil boundary [10]. He ignored the upper gray level range and focused only on the low gray value region, specifically the bottom 1 % of all gray values. However, this method will fail for an image in which the region with the lowest gray value does not exist in the pupil. Likewise, the use of the Hough transform increases time complexity, and he did not propose a method to handle specular reflection within the pupil boundary.

The major problems that exist in traditional and recently improved detection and localization methods include difficulty in obtaining an appropriate threshold for image thresholding, the handling of specular reflections within the pupil boundary, and reducing complexity. In this study, to localize the pupil quickly and accurately, eye images are processed using de-noising technology, which reduces the disruptive factors of an image significantly. Then, a novel threshold method using discrete gray gradient differentials is proposed to separate key pixels used for pupil localization. Finally, traditional pupil localization methods are analyzed based on the Canny operator and Hough transform, and we adopt a method of combining outline filling with curve fitting which is proposed to localize the pupil.

58.2 The Principle of Proposed Method

In the following subsections, image de-noising is introduced briefly. Then, a proposed discrete gray gradient differential method is applied to the processing of image thresholding. Finally, the relevant localization principle is introduced in detail, and the traditional localization method is compared with the new method.

58.2.1 *Image De-noising*

Image de-noising is primarily used to dilute noise and blocks of hair in image acquisition. During the exposure period, the distribution of bad light particles in camera sensors is random. We consider noise to be described as a chance variable in a probability density function [11]. Therefore, noise is a sample of the Gaussian random field and can be modeled using a Gaussian distribution function. Human hairs and wrinkles have tiny-pixel characteristics, and these pixels may be completely covered using Gaussian template in the convolution operation. To reduce Gaussian noise and fine lines within the image, the Gaussian blur method, which utilizes a two-dimensional Gaussian function to generate the Gaussian blur template, is used [12]. Using the characteristics of the Gaussian blur, this method can play a certain role in diluting hairs, wrinkles, and light points.

58.2.2 *Discrete Gray Gradient Differential Thresholding Method*

During thresholding, individual pixels in an image are marked as “object” pixels if their value is greater than a threshold value and as “background” pixels otherwise [13]. Therefore, an appropriate threshold plays a key role and is still an issue in scientific research [7]. Several traditional methods have been proposed that are mainly based on the properties of an entire image instead of the low gray value area containing the pupil, such as the bimodal method and the Otsu method.

A discrete gray gradient differential thresholding method is established in this chapter. The method is a non-universal algorithm that is used to calculate an image threshold based on the specific characteristics of a gray histogram that is statistically generated at a close distance. The principle of the algorithm is that in an eye image, there is a large gap in the gray values between the pupil and the other parts of the image (shown in Fig. 58.2). This feature is characterized by a large gap in the gray histogram. Therefore, we generate a discrete differential of the gray histogram and analyze the gap degree of the gray gradient to obtain an appropriate image threshold. To illustrate the process in more detail, each step of the algorithm is explained below.

- Step 1: Go through all points of pixel set C in eye image $P1$. Analyze the gray distribution to obtain a mapping set $A\{(z,p(z))\}$ and average the gray value $\text{avg}(z)$, where z is the gray value and $p(z)$ is the number of points in this gray value.
- Step 2: Go through mapping set A and perform a calculation to obtain a differential mapping set $B\{(z,w(z))\}$, where “step” is the differential length and $w(z) = (p(z + \text{step}) - p(z))/\text{step}$.

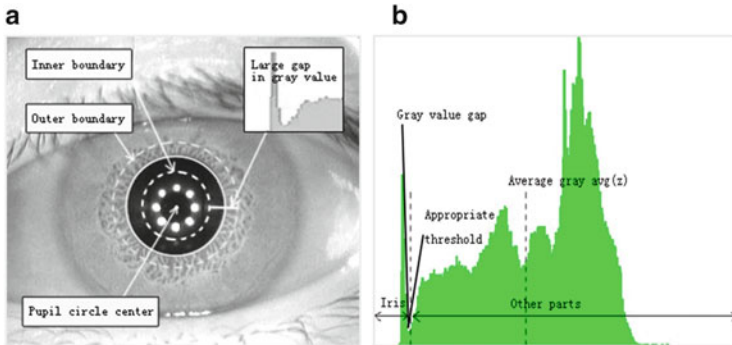


Fig. 58.2 Gray gradient statistics in an eye image. (a) Gray value gap in an eye image, (b) Histogram statistics of the gray gradient

Step 3: Go through mapping set B to determine the position $(z', w(z'))$ that has the minimum value of $w(z)$, where $0 < z < \text{avg}(z)$.

Step 4: Calculate $\alpha' = z' - p(z')/w(z')$ based on the previously described results.

Step 5: Round up α' to obtain the appropriate threshold α .

58.2.3 Outline Filling and Curve Fitting Localization

The Canny operator was proposed by John F. Canny in 1986 for multilevel boundary detection in images [14]. The main idea behind the Canny operator is to use a lagging threshold to limit the intensity gradient boundaries and use the finite difference of the first partial derivative to calculate the amplitude and orientation of the gradient in the image. Wildes proposed a method using Canny detection and the Hough transform to localize the pupil in 1997. This method first detects the boundaries within the image and processes them using the Hough transform to find the circle with the longest radius, setting its boundary as the pupil boundary and its center as the pupil center [8]. However, when light reflective interference of its boundaries exists within the image, the Hough transform over-emphasizes the boundary geometric characteristics and ignores the properties of the external outline, which ultimately leads to error.

To circumvent the errors produced by the Wildes system as a result of light reflection and the Hough transform, this work proposes an alternative method of active circle fitting to determine the actual position and diameter of circles within the image. In addition, the proposed system uses an outline filling method to eliminate light reflective errors and curve fitting to detect circles in the image, in contrast to the Hough transform. The specific method is as follows:

Step 1: Detect boundaries by using the Canny operator in the threshold image $P1$. Connect the detected boundaries to obtain an outline set C .

- Step 2: Go through outline set C to determine the outline X with the largest connected area.
- Step 3: Fill the outline X with white and the inside and outside areas with black to create image $P2$.
- Step 4: Apply the ellipse curve fitting method to outline X in image $P2$ to obtain an ellipse O .
- Step 5: Calculate the eccentricity e of ellipse O . Set c as the determination threshold of accuracy. If $1 - c < e < 1 + c$, set the ellipse O 's boundary as the pupil boundary and the geometric center as the pupil center; otherwise, the threshold image $P1$ is not within the limits.

58.3 Experiment Result

Programs in this experiment were written in Visual C 2010 and OpenCV2.3 and run on a Windows 7 64-bit platform. The hardware environment was a 2.27 GHz i3 350 processor, and the memory consisted of 4 GB DDR3. The internationally popular iris database CASIA Ver4.0 was employed in the experiments. Three hundred eye images were randomly chosen and tested with the Wildes system and the proposed method. The original image is shown in Fig. 58.3a, and the processed image using the traditional fixed threshold method is shown in Fig. 58.3b. The fixed threshold is not common for various images, and large areas of noise appear in the resulting image.

Next, a threshold method using the discrete gray gradient differential method was used. The differential step is set based on the accuracy of the iris and pupil's gray values in the eye image. Given the major gray gradient between the pupil and iris and the minor difference in the adjacent pixels in the experiments, we set the length of the differential step to 2. The calculated results were $z' = 19$, $p(z') = 2,959$, and $w(z') = -1,052$, and the appropriate image threshold was $\alpha = 22$. The results processed by the proposed threshold method are shown in Fig. 58.3b. By using the appropriate threshold as calculated by the proposed method, we were able to extract the low gray value pupil area accurately and eliminate related noise in the eye image.

Next, the Canny operator was used to detect the boundaries in Fig. 58.3b and to obtain Fig. 58.4a. Outline filling produces Fig. 58.4b.

Finally, the Wildes system based on the Hough transform was compared to the proposed method for pupil localization. The result is shown in Fig. 58.5 and indicates that the new proposed method can localize the pupil more accurately than the Wildes system.

A comparison of the Wildes system and the proposed method is shown in Table 58.1. The analysis indicated that the average running speed and accuracy of the new method represent a 28.70 % and 90.90 % improvement over the Wildes system, respectively.

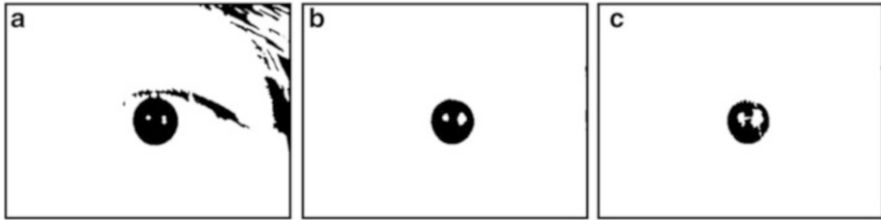


Fig. 58.3 Results using different thresholding methods. (a) Image processed using the traditional fixed threshold method. (b) Processing result by the proposed method with threshold $\alpha = 22$. (c) Compared processing result with threshold $\alpha = 20$

Fig. 58.4 Results before and after outline filling. (a) Detected result using the Canny operator. (b) Outline filling result

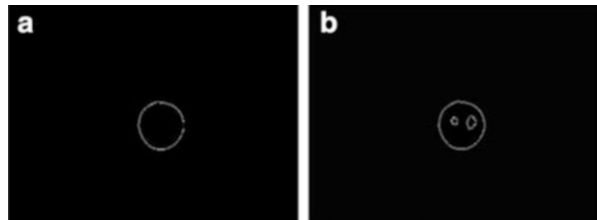


Fig. 58.5 Pupil localization results using the Wildes system (left) and the proposed method (right)



Table 58.1 Efficiency and accuracy analysis

Method	Average running time (ms)	Accuracy (%)
Wildes system	56.72	47.67
New method	40.44	91

The accuracy of the traditional method is relatively poor (47.67 %, see Table 58.1), and under complex conditions, the pupil cannot be localized. The new method can localize the pupil more accurately under complex conditions using the improved threshold extraction technology, which combines outline filling and curve fitting. Examples of accurate pupil localization are shown in Fig. 58.6.

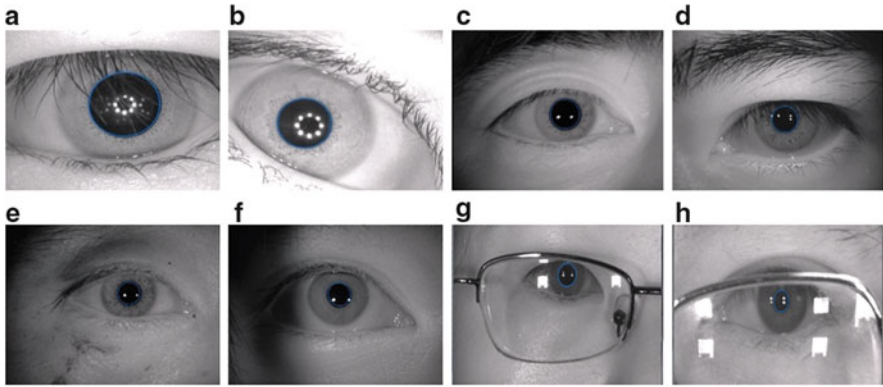


Fig. 58.6 Accurate pupil localization results on challenging eye images. Eye images with (a, b) specular reflections, (c, d) eyebrows and eyelids, (e, f) speckles and shadows, (g, h) glasses and occlusion

Discussion and Conclusion

In this study, a novel method for quick and accurate pupil localization was proposed. In the proposed method, localization is performed by diluting noise and blocks of hair during the image preprocessing stage using the Gaussian blur method. A threshold image is then obtained using the proposed discrete gray gradient differential thresholding method. Finally, the pupil is localized using the curve fitting and outline filling method.

The experimental results demonstrated that the new proposed method is more accurate, more robust, and quicker than the traditional Wildes method, particularly under complex conditions. The results demonstrated that during performance, good verification of the iris database CASIA Ver4.0 can be obtained. After analysis, the average running speed of the new method decreased to 40 ms, while the accuracy improved by over 90 % compared to the traditional method.

Using this method, we were able to quantitatively obtain the pupil size and center based on the localized boundary between the pupil and iris. Based on its high accuracy and speed, this method can be used in many fields to develop automatic recognition and quantification tools. In medicine, the proposed method is viable for measuring pupil size to diagnose mental illness. For example, changes in pupil size resulting from different physical conditions and outside stimuli can be detected. For safe driving applications, pupil observation, and blink detection in particular, can be applied as part of a safety monitoring system to reduce the risks from driving under fatigued conditions. In addition, the proposed method can be used for iris recognition in biological feature identification applications.

(continued)

(continued)

The proposed method achieved excellent results when applied for the localization of fully exposed pupils. However, there are also limitations to the proposed method. When the pupil is fully or partly blocked in the original image, it may result in major errors. Additionally, this method cannot localize the pupil accurately when the original image is captured from a long distance or if the image has low sharpness. Furthermore, it is not reasonable to discard the detected ellipse when its eccentricity does not meet the determination threshold for accuracy.

Our future work will focus on the following issues. First, we are working to extract the key pixel area from images captured at long distances and then apply the proposed method to the key pixel area. Second, we would like to improve the process of finding a reasonable approach to process the discarded ellipse. Finally, we are working on localizing the pupil more accurately at the pixel level, marking different pixels within the pupil, and detecting eye movements.

References

1. Ibrahim MT, Khan TM, Khan SA, Khan MA, Guan L. Iris localization using local histogram and other image statistics. *Opt Lasers Eng.* 2012;50:645–54.
2. Daugman JG. How iris recognition works. *IEEE Trans Circuits Syst.* 2004;14:21–30.
3. Daugman JG. High confidence visual recognition of persons by a test of statistical independence. *IEEE Trans Pattern Anal Mach Intell.* 1993;15:1148–61.
4. Bowyer KW, Hollingsworth K, Flynn PJ. Image understanding for iris biometrics: a survey. *Comput Vis Image Understand.* 2008;110:281–307.
5. Prewitt JMS, Mendelsohn ML. The analysis of cell images. *Ann NY Acad Sci.* 1966;128:1035–53.
6. Cui J, Wang Y, Tan T, Ma L, Sun Z. A fast and robust iris localization method based on texture segmentation. *SPIE Def Secur Symp.* 2004;5404:401–8.
7. Otsu N. A threshold selection method from gray-level histograms. *IEEE Trans Syst Man Cybern.* 1979;1:62–6.
8. Wildes R. Iris recognition: an emerging biometric technology. *Proc IEEE.* 1997;85:1348–63.
9. Jan F, Usman I, Agha S. Reliable iris localization using Hough transform, histogram-bisection, and eccentricity. *Signal Process.* 2013;93:230–41.
10. Shah S, Ross A. Iris segmentation using geodesic active contours. *IEEE Trans Inf Forensics Security.* 2009;4:824–36.
11. Portilla J. Image denoising using scale mixtures of Gaussian in the wavelet domain. *IEEE Trans Image Process.* 2003;12:1338–51.
12. Gudbjartsson H, Patz S. The Rician distribution of noisy MRI data. *Magn Reson Med.* 1995;34:910–4.
13. Sauvola J, Pietikainen M. Adaptive document image binarization. *Pattern Recogn.* 2000;33:225–36.
14. Kakarala R. On achievable accuracy in edge localization. *Proc IEEE Int Conf Acoust Speech Signal Process.* 1991;4:2545–8.

Chapter 59

A Method for the Chinese-Tibetan Machine Translation System's Syntactic Analysis

Zangtai Cai

Abstract Machine translation system (MTS) is a typical nature language processing system with the language technique as the main technique. The applied MTS commonly adopts the translation with restrained languages on the basis of certain rules as the main measure. In combination of the research practice based on the 973 project—Research of Chinese—Tibetan machine translation key technology, this chapter discusses the principle which combines both the word information and the syntax rules. It also advances the dichotomy of syntax analysis that focuses on verbs. Accordingly, as to the range of restrained languages, this chapter affords a useful method to create a machine translation rule highlighting high adaptability so as to effectively advance the efficiency of MTS' syntax analysis.

Keywords Machine translation • Dichotomy • Sentence structure • Syntax analysis

59.1 Introduction

With the growing popularity of computer technology, how to translate a large number of Chinese and English technology information, textbooks, references, and popular science readings into Tibetan in time has led the services of science and technology, education, and culture to constrain the socioeconomic development in most Tibetan areas. In face of dire shortage of Chinese-Tibetan translators in these days, the development and promotion of the application of Chinese-Tibetan machine translation system will definitely contribute to the resolution of such problem. Language technology is the key skill in the machine translation system. The discussion of syntax analysis of machine translation system is thus an important issue [1]. Machine translation has many methods based on the statistical machine translation, the example-based machine translation, and the rule-based machine translation. The rule-based machine translation is a system we adopt for our 973 project, Chinese-Tibetan Machine Translation System. What the machine translation does is the conversion between two languages of an infinite set of

Z. Cai (✉)

Department of Computer, Qinghai Normal University, Qinghai 810000, China
e-mail: tsezung@aliyun.com

sentences. At the existing scientific level, computer science cannot theoretically prove the possibility of conversion between the source language and the target language of an infinite set of sentences by a limited rule-based machine translation system; therefore, what is more applicable in practice is to apply restricted natural languages. The Chinese-Tibetan translation machine system on which we conduct our research is exactly the kind of restricted language machine translation system.

59.2 Combination of Lexical Items and Grammatical Rules

As stated in the introduction, the language technology is the key technology in the machine translation system. The following is the discussion of some problems of syntax analysis of Chinese-Tibetan machine translation system.

With the development of technology, the position of dictionary has become more and more important in the natural language processing system and the electronic dictionary has already become the basis of development of natural language processing application system [2]. As far as the dictionary is concerned, as an integral part of translation system, the adjunctive information of every lexical item in the dictionary need to integrate grammatical rules in the system application so that the driving rules of lexical items could be achieved. It is because one of the core technologies of machine translation is the completion of internal structural conversion between two different languages. In order to achieve the goal, it is necessary to understand the characteristics of the sentence structures of the two languages. At the macro-level, the sentence structures between contemporary Chinese and Tibetan are distinct primarily from the following three aspects.

59.2.1 Different Word Order

Chinese order is usually SVO (S is subject, V is predicate, and O is object). Tibetan is SOV. For example:

Table 59.1 Different word order

Chinese sentence	Chinese structure	Tibetan sentence	Tibetan structure.
我是教师	S+V+O	ང་དགོ་ཚན་ཡིན།	S+O+V
我看了书	S+V+O	ང་ཡིས་དཔེ་ཆ་ལ་བཟུང།	S+auxiliary+O+auxiliary+V
学生在教室里	S+V+O	སློབ་མ་སློབ་ཁང་དུ་ཡོད།	S+O+auxiliary+V

Meaning of Tibetan or Chinese sentences in English in Table 59.1: ① I am a teacher. ② I read the book. ③ Students in the classroom

Another expression of different word orders is that adjectives, numerals, and pronouns used as attributes precede the central words in Chinese language, but they come after the central words in Tibetan language. For example:

Table 59.2 Different word order (Another)

Chinese sentence	Chinese structure	Tibetan sentence	Tibetan structure
新兵	adj+Center word	དམག་མི་གསར་བ།	Center word+adj
三国	No.+Center word	རྒྱལ་ཁབ་གསུམ།	Center word+No.
那个人	pron+Center word	མི་གཞན།	Center word+pron

Meaning of Tibetan or Chinese sentences in English in Table 59.2: ① New soldiers. ② Three countries. ③ That person

59.2.2 Different Morphological Changes

Chinese language lacks morphological change whereas Tibetan language has morphological changes. The form of verb tense is an obvious difference [3]. Tibetan verbs have tense forms. For example, the Tibetan word “eat” has three tense forms, ཟླ་བ (continuous), བཟུགས་བ (past), and བཟུང་བ (future), but Chinese verbs do not have tense forms. For example, “吃” is the only form. Tense is expressed by such particular words as “了” for the past and “将” for the future.

59.2.3 Different Ways of Expression

The expression of Chinese sentences mainly depends on word order while Tibetan sentences rely on auxiliaries. Addition and connection of auxiliaries in Tibetan sentences have direct impact on the accuracy of Tibetan expressions. The following is a further comparison between Chinese verbs and Tibetan verbs.

Both Chinese and Tibetan have transitive and intransitive verbs, but there is an obvious difference. In Chinese, there is only one form of relationship between a transitive verb, subject, and object, which is SVO. In Tibetan, there are many types of relationships between a transitive verb, subject, and object requiring the addition of auxiliaries [4]. In addition, Chinese transitive verbs don’t have dependent and independent verbs while Tibetan transitive verbs do (the action of independent verbs can be decided subjectively whereas the action of dependent verbs cannot) and the collocation of dependent transitive verbs and intransitive verbs with subject and object has different structures. Thus, the adjunctive information of verbs in dictionary needs to reflect the characteristics of Tibetan verbs enabling combinations to abide by the grammatical rules. For example, T and I, respectively, represents transitive and intransitive with z, t, and l represents Tibetan independent transitive verbs, intransitive verbs and possessive relationship, x, l and k represent

the relationship of three forms of Tibetan transitive verbs, subject and object. X represents agents, L represents predicate, and object in Tibetan represents the target of the verb, the place of the action, the result of the action, and the tools of the action as well. L also represents the auxiliaries of possessor-subject. The information of lexical items of part-of-speech tagging of verbs could be related to the information of Tibetan grammatical structure as shown in the following example.

Table 59.3 Different ways of expression

Verbs	Item	C-sentence	C-structure	T-sentence	T-structure
来到	vttl.	我·来到·北京	S+V+O	ང་ལ་ཅིན་དུ་སྐྱེབས།	S+O-L+V
保持	vtx.	我们·保持·联系	S+V+O.	ང་ཚོས་འབྲེལ་བ་རྒྱན་འགྲུབས་ཟེད།	S+X+O+V
研究	vttk	我·研究·问题	S+V+O	ངས་གནད་དོན་ལ་ཞིབ་འཇུག་ཟེད།	S+X+O+L+V
有	vtl	我·有·书	S+V+O	ང་ལ་དཔེ་ཆ་ཡོད།	S+L+O+V
来自	vtz	我·来自·青海	S+V+O	ང་མཚོ་རྫོན་ནས་འོང།	S+O+L+V
得出	vitl	我·得出·结论	S+V	ང་ལ་རྫོམ་ཚོག་ཐོབ།	S+L+V
讲课	vitx	老师·讲课	S+V	དག་ནན་གྱིས་སྐབ་ཐོབ་ཟེད།	S+X+V

Meaning of Tibetan or Chinese sentences in English in Table 59.3: ① I came to Beijing. ② We keep in touch. ③ I have studied the problem. ④ I have a book. ⑤ I come from Qinghai. ⑥ I concluded. ⑦ Teaching

As shown by the above-said example, the combination of the information of lexical items and grammatical rules allows a rule-based system of a larger adaptive machine translation within a range of restricted language.

59.3 Syntactic Analysis Dichotomy

Any machine translation system is only possible upon testing and improvement for a long time because an addition of a commonly used word is likely to add new rules or modify the original rules. Consequently, new rules often lead to recombination and readjustment of rules of the whole system; therefore, minimizing the adjustment workload or shortening the adjustment time is important to the development of machine translation system [5]. The combination of BZD Chinese-Tibetan document machine translation system introduces a form of generating method of sentence analysis. It can effectively reduce the number of rules so that the time of reorganization of rules and adjustment could be reduced.

The existing machine translation systems consider a sentence as a unit to do the translation and the grammatical analysis algorithm is also a result of the analysis of sentences. As both Chinese and Tibetan have subject, predicate, and object, the trichotomy is applied and the sentences are combined and converted according to subject, predicate, and object [6]. We apply syntax analysis dichotomy during the

development of BZD Chinese-Tibetan machine translation system and it is as effective as trichotomy. But the number of grammar rules is greatly reduced, which can be explained from the following two aspects.

59.3.1 *Basic Way of Syntax Analysis Dichotomy*

As we can see from the discussion of combination between the information of lexical items and grammatical rules, the basic structure of Chinese sentences is SVO and it is basically a structure of word order; nevertheless, Tibetan is different. Although the basic structure is SOV, the structure has many forms, for example, SOLV, SXOV, SXOLV, SOV, SLOV. The generations of predicate-object and subject-predicate phrases facilitate the general collocation of subject, predicate, and object in Tibetan language. It is also applicable to Chinese language even if the synthesis of SVO is completed through synthesis of predicate-object and subject-predicate phrases. Two points are highlighted upon synthesis: firstly, the verb is based on the understanding of the pivot and the axis of sentence structure which sets the integrated word of verb-object and subject-predicate phrases as verb [7]. Secondly, the generation of verb-object phrases should be prioritized over that of subject-predicate phrases. By so doing, SVO in a sentence can be presented by a subject-predicate phrase. This is because a complete sentence with only one subject and one predicate is enough. For example, the Chinese structure of “我是学生 (I am a student)” is SVO. No matter it is $SVO \rightarrow S+VO$, or $V+O \rightarrow V$, SV includes SVO. In the case of Tibetan, the sentence structure is SOV. No matter it is $SOV \rightarrow S+OV$, or $O+V \rightarrow V$, SV includes SOV as well. The Chinese structure of “我有书 (I have a book)” is SVO which can be presented by verb-object phrase $V+O \rightarrow V$ and subject-predicate phrase $S+V$. In the case of Tibetan, the structure of the sentence is SLOV which can be presented by verb-object phrase $O+V \rightarrow V$ and subject-predicate phrase SLV: $SLOV-S+L+V-S+L+O+V$.

59.3.2 *Advantages of Applying Syntax Analysis Dichotomy*

As stated above, the addition of new rules often leads to recombination and readjustment of the rules of the whole system; therefore, the reduction of number of new rules is in favor of the adjustment of machine translation system while using syntax analysis dichotomy with the verb as the center also contributes to the general reduction of the rules. As shown by the following example, the trichotomy uses one grammatical rule for “我学习物理学 (I studied physics)” whereas the dichotomy uses two grammatical rules; but the rules that dichotomy needs for the rest of sentences are greatly reduced. The lexical item information for the word “学习 (Learning)” is $vvttk$; therefore, the structure of $S+X+O+L+V$ is applied into Tibetan SOV relationship.

The sentences in Table 59.4 usually need ten grammatical rules. With the application of the syntax analysis dichotomy, V+O, U+V, D+V, and S+V rules alone can achieve the function of ten generating and converting rules.

We know that scientific language is more standard and the grammatical phenomenon for document corpus is more sophisticated. Chinese-Tibetan machine translation system applies trichotomy, and document translation system uses dichotomy. The testing results show that the sustainability of scientific translation system and that of document translation system are almost the same for a non-enclosed corpus, but the document translation system has relatively less grammatical rules than scientific translation system which shows the advantage of dichotomy.

Table 59.4 Examples of dichotomy

C-sentence	C-sentence-structure	T-sentence	T-sentence structure
我学习物理学	S+V+O	ངས་དངོས་ལུགས་ལ་སློབ་རྗེས་ལྷན་ཅིང་།	S+X+O+L+V
我学习	S+V	ངས་སློབ་རྗེས་ལྷན་ཅིང་།	S+X+V
学习物理学	V+O	དངོས་ལུགས་ལ་སློབ་རྗེས་ལྷན་ཅིང་།	O+L+V
要学习物理学	U+V+O	དངོས་ལུགས་ལ་སློབ་རྗེས་ལྷན་ཅིང་དགོས།	O+L+V+U
一定要学习物理学	D+U+V+O	ངེས་པར་དུ་དངོས་ལུགས་ལ་སློབ་རྗེས་ལྷན་ཅིང་དགོས།	D+O+L+V+U
我要学习物理学	S+U+V+O	ངས་དངོས་ལུགས་ལ་སློབ་རྗེས་ལྷན་ཅིང་དགོས།	S+X+O+L+V+U
我一定要学习物理学	S+D+U+V+O	ངས་ངེས་པར་དུ་དངོས་ལུགས་ལ་སློབ་རྗེས་ལྷན་ཅིང་དགོས།	S+X+D+O+L+V+U
要学习	U+V+	སློབ་རྗེས་ལྷན་ཅིང་དགོས།	V+U
我要学习	S+U+V	ངས་སློབ་རྗེས་ལྷན་ཅིང་དགོས།	S+X+V+U
我一定要学习	S+D+U+V	ངས་ངེས་པར་དུ་སློབ་རྗེས་ལྷན་ཅིང་དགོས།	S+X+D+V+U

Meaning of Tibetan or Chinese sentences in English in Table 59.4: ① I studied physics. ② I am learning. ③ Learning physics. ④ To learn physics. ⑤ Be sure to learn physics. ⑥ I want to learn physics. ⑦ I have to learn physics. ⑧ To learn. ⑨ I want to learn. ⑩ I must learn

Conclusion

The application of machine translation is not only very promising in the field of language information processing, but a challenging research topic as well. This article introduces the structure of Chinese-Tibetan machine translation system. After being tested and tried by some experts and users, it has been shown that the system has already reached the level of practicality. The analysis of verbs is the key to sentence structure in Chinese-Tibetan machine translation system. With verb-predicate as the axis, the integration of grammatical analysis and semantic analysis can be achieved by means of combination of the lexical item information with the grammatical rules and integration of the grammatical analysis and the semantic analysis; besides, the application of syntax analysis dichotomy can greatly improve the efficiency of grammatical analysis by machine translation.

References

1. Degai C, Li Y. Brief analysis on Chinese-Tibetan scientific machine translation system. In: Progress in the Interface and Application of Intelligent Compute. Beijing: Electronic Industry Press. 1997; 175–179. (In Chinese).
2. Yu S. The detailed information of contemporary Chinese grammar information. Beijing: Tsinghua University Press. 53–54; 1998. (In Chinese).
3. Jiang D. The classification of Tibetan Verbs and relative patterns based on semantics and syntax. *J Chinese Inform Process*. 2006; 20(1): 37–43. (In Chinese).
4. Dougai C. Brief analysis on the classification of Tibetan terms with the focus on phrases in Chinese-Tibetan machine translation system. In: Progress in the Interface and Application of Intelligent Computer. Beijing: Tsinghua University Press; 1995. p. 233–237. (In Chinese)
5. Feng Z. The new theory of natural language machine translation. Beijing: Yuwen Press. 87–88; 1994. (In Chinese).
6. Xiang B. A discussion on the translation of Chinese Names in Chinese-Tibetan machine-translation. *J Qinghai Normal Univ. Xining*. 2011; 4: 88–90. (In Chinese).
7. Cai R. Research on large-scale Sino-Tibetan Bilingual Corpus Construction for Natural Language Processing. *J Chinese Inform Process*. Beijing. 2011; 25(6): 157–161. (In Chinese).

Chapter 60

Analysis of Micro-Doppler Features of an Armored Vehicle Based on EMD

Wanjun Zhang, Minjie Niu, and Xiaoying Wu

Abstract The micro-Doppler (m-D) caused by micromotions of an armored vehicle including both movement and geometry information is an important feature for target identification and classification. A mathematical model for the m-D echo signal of both wheel and track is established in this paper. The signal analysis of the line target is derived, and for the nonstationary and nonlinear echo signal, the m-D instantaneous frequency could be extracted by empirical mode decomposition (EMD). Simulation results show that instantaneous frequency (IF) imagery has higher time-frequency resolution compared to traditional analysis; wheeled and tracked vehicles can be classified and motion features can be identified with this method.

Keywords Empirical mode decomposition • Line target • Micro-Doppler • Armored vehicle

60.1 Introduction

The widespread use of camouflage and stealth technology makes target recognition more difficult on the modern battlefield. V.C. Chen, professor at the U.S. Naval Research Laboratory, once suggested use of the micro-Doppler effect to resolve the characteristics of the micromotion echo signal [1], including vehicle vibration, radar rotation, and body movements [2–4] to identify a target. Micro-Doppler can be seen as extra modulation on the echo spectrum due to rotation or vibration of the target or its components when the target has relative radar motion [5], for example, the rotation of the wheels and tracks of armored vehicles is a typical micromotion. High frequency radar can detect details of an armored vehicle; the key is how to extract the useful component from the complex nonstationary and nonlinear echo signal [6].

W. Zhang • M. Niu (✉) • X. Wu
Department of Arms Engineering, Academy of Armored Forces Engineering,
Beijing 100072, China
e-mail: minjieniu@139.com

Empirical mode decomposition (EMD) has unique advantages in dealing with a nonstationary and nonlinear signal because it has overcome the dependence on the Fourier transform (FT) of traditional time-frequency analysis [7]. In this paper, a mathematical model for the echo signal of wheel and track micromotion is established and the signal by line target integral method is simulated to calculate the instantaneous m-D frequency by EMD; then efforts are made to analyze the features of the micromotions.

60.2 Echo Signal Model

The frequency shift of an echo signal caused by the relative motion between radar and a vehicle is the Doppler Effect [8]. The echo signal should contain the translation component and the micromotion component with useful information on micromotion extractable through analysis of the Doppler sideband. As to high frequency radar, the incident wave can be approximately regarded as the plane wave under the far field condition and the vehicle can be seen as an electrically large target. As the line of sight (LOS) of radar is constant, in this sense, the radar coordinate system of wheel and track echo signals is established as shown in Fig. 60.1.

As shown in Fig. 60.1, the coordinate origin of the radar is $Q(X, Y, Z)$ and the reference coordinate is $O(x, y, z)$. On the centroid of the wheel, which is parallel to the radar coordinate, the direction of axis Ox and axis QX are the same. R_0 is the initial distance from point O to point Q , \mathbf{V} is the relative velocity between the vehicle and radar. Supposing use of the continuous wave $S(t)$ as the transmitted radar signal, $S(t) = \exp(j2\pi f_0 t)$, where f_0 is the carrier frequency.

Figure 60.1a shows the scattering echo signal model of a wheel; here the LOS direction vector is $\mathbf{n} = [\cos \beta \cos \alpha, \cos \beta \sin \alpha, \sin \beta]^T$, l is the semidiameter of the wheel, scatter point P is at the circumference, and the angle between the vehicle and Ox is γ . At the moment t , the P coordinate in the reference coordinate is $(\cos \theta_t \cos \gamma, -l \cos \theta_t \sin \gamma, l \sin \theta_t)$, where $\theta_t = \theta + \omega t$; here θ is the initial angle, ω is the rotational speed, the distance between the reference coordinate and the

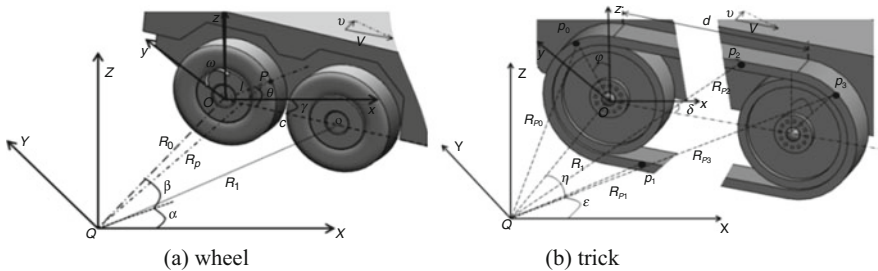


Fig. 60.1 Echo signal model for (a) Wheel and (b) Track

vehicle is $R_t = R_0 + vt$, the radial velocity relative to the radar is $v = \cos(\alpha + \gamma)|\mathbf{V}|$, and the distance between two wheels is c . Supposing there are six wheels, R_1 and R_2 are the initial distance of the other two wheels: $R_1 = [R_0^2 + c^2 - 2R_0c \cos(\pi - \alpha - \gamma)]^{1/2}$, $R_2 = [R_0^2 + 4c^2 - 4R_0c \cos(\pi - \alpha - \gamma)]^{1/2}$. Thus, the immediate distance from P to the radar in time t is:

$$\begin{aligned} R_p(t) &= \|\mathbf{R}_t + \mathbf{OP}\| \\ &= \left[\begin{aligned} &(R_t \cos \beta \cos \alpha + l \cos \theta_t \cos \gamma)^2 + (R_t \cos \beta \sin \alpha - l \cos \theta_t \sin \gamma)^2 + \\ &(-R_t \sin \beta + l \sin \theta_t)^2 \end{aligned} \right]^{1/2} \end{aligned} \quad (60.1)$$

Then, the echo signal of the scattering point P is:

$$\begin{aligned} s_p(t) &= \rho(x, y, z) \exp \left[j2\pi f_0 \left(t + \frac{2R_p(t)}{c} \right) \right] \\ &= \rho(x, y, z) \exp[j\varphi(t)] \exp(j2\pi f_0 t) \end{aligned} \quad (60.2)$$

where c is the electromagnetic wave propagation velocity, $c = 3 \times 10^8$ (m/s), set the scattering coefficient $\rho(x, y, z) = 1$, $\varphi(t)$ of the instantaneous phase. Regard the wheel echo signal is simulated by N scattering points integral along the circumferential direction, thus, the line target echo signal is:

$$s_{l1}(t) = \exp(j2\pi f_0 t) \int_0^{2\pi} \exp[j\varphi(t)] d\theta = \sum_{n=0}^N \exp[j\varphi_n(t)] \exp(j2\pi f_0 t) \quad (60.3)$$

Supposing there are six wheels, the echo signal of the other two wheels $s_{l2}(t)$, $s_{l3}(t)$ can be calculated in the same way, and then the total signal is $S_l = s_{l1} + s_{l2} + s_{l3}$.

The scattering echo signal model of a track is shown in Fig. 60.1b; here the angle between the vehicle and Ox is δ , the track is composed of two planes whose length is d and two semicirculars whose radius is r_0 , and the LOS vector is $\mathbf{n} = [\cos \varepsilon \cos \eta, \cos \varepsilon \sin \eta, \sin \varepsilon]$. Take four characteristic points p_0, p_1, p_2 , and p_3 on the track. There is no micromotion echo signal for P_0 because it has no relative velocity. At the moment t , the initial angle of p_0, p_3 is φ and the initial position of p_2 is y_0 , so the immediate distance from each point to the radar is:

$$R_{p0}(t) = \left[\begin{aligned} &(R_t \cos \eta \cos \varepsilon + r_0 \cos \varepsilon_t \cos \delta)^2 + (R_t \cos \eta \sin \varepsilon - r_0 \cos \varepsilon_t \sin \delta)^2 + \\ &(-R_t \sin \eta + r_0 \sin \varepsilon_t)^2 \end{aligned} \right]^{1/2} \quad (60.4)$$

$$R_{p2}(t) = \left[\begin{aligned} &(R_t \cos \eta \cos \varepsilon + (y_0 + vt) \cos \delta)^2 + (R_t \cos \eta \sin \varepsilon - (y_0 + vt) \sin \delta)^2 + \\ &(-R_t \sin \eta + r_0)^2 \end{aligned} \right]^{1/2} \quad (60.5)$$

$$R_{p3}(t) = \left[\begin{aligned} &(R_t \cos \eta \cos \varepsilon + r_0 \cos \varepsilon_t \cos \delta + b \cos \delta)^2 + \\ &(R_t \cos \eta \sin \varepsilon - r_0 \cos \varepsilon_t \sin \delta - b \sin \delta)^2 + (-R_t \sin \eta + r_0 \sin \varepsilon_t)^2 \end{aligned} \right]^{1/2} \quad (60.6)$$

Then, the echo signal of the scattering points is:

$$s_{pk}(t) = \rho(x, y, z) \exp \left[j2\pi f_0 \left(t + \frac{2R_{pk}(t)}{c} \right) \right] \quad k = 0, 2, 3 \quad (60.7)$$

Integral along the track, then the total echo signal of the track is:

$$S_b(t) = \int_{\pi/2}^{3\pi/2} s_{p0}(t) d\varepsilon + \int_0^d s_{p2}(t) dy_0 + \int_{-\pi/2}^{\pi/2} s_{p3}(t) d\varepsilon \quad (60.8)$$

Obviously, the echo signal of both the wheel and the track is a nonlinear and nonstationary type, the Fourier transform is the core of traditional time-frequency joint analysis but constrained by the Uncertainty Principle.

60.3 Analysis of m-D

60.3.1 EMD

EMD was put forward by Huang NE [7]. A complex signal can be decomposed into a set of intrinsic mode functions (imf) by this method. The micromotion echo signal $s(t)$ can be adaptively decomposed into a set of narrow-band signal components.

$$s(t) = \sum_k \text{imf}_k(t) + r(t) \quad (60.9)$$

where $\text{imf}_k(t)$ represents the k th intrinsic mode function, while $r(t)$ is the residue component that signifies the average trend of a signal. Essentially, the imf calculation process is a screening process of the frequency band. Different micromotion parts are not consistent with frequency, which makes it possible to calculate the instantaneous frequency (IF) characteristic of the micromotion. Then, the imaginary component $H[\text{imf}_k(t)]$ can be obtained through a one-dimensional Hilbert transform about imfs. The analytic signal of the echo signal is

$$D(t) = \text{imf}_k(t) + iH[\text{imf}_k(t)] \tag{60.10}$$

Equation (60.10) ignores the residue component; the instantaneous frequency $\vartheta_k(t)$ can be obtained from the analytic signal:

$$\vartheta_k(t) = \frac{d}{dt} \arctan\left(\frac{H[\text{imf}_k(t)]}{\text{imf}_k(t)}\right) \tag{60.11}$$

60.3.2 Simulation

The echo signal of a wheel and track is simulated here. We adopt the following parameters: the carrier frequency of CW $f_0 = 2$ GHz, initial distance $R_0 = 2$ km, $|\mathbf{V}| = 15 + 0.2t$, $l = 1$ m, $r_0 = 0.5$ m, $d = 6$ m, $\alpha = \pi/4$, $\beta = \pi/4$, with a sampling frequency of 100 Hz while the simulation results use the normalized frequency. As shown in Fig. 60.2, by using EMD, the echo signal of a wheel is decomposed into five imfs and one residual while the track is decomposed into six imfs and one residual. The component frequency decreases as the mode increases. A three-dimensional time-frequency image of the instantaneous frequency of imfs is shown in Fig. 60.3.

The features of the translational component and the m-D component are not obvious in Fig. 60.3; the translational component disturbs the image, which makes it hard to extract m-D. Sum the prime four imfs whose wave seems more obvious, namely, $\text{imf}(t) = \text{imf}_1(t) + \text{imf}_2(t) + \text{imf}_3(t) + \text{imf}_4(t)$, then, according to Eq. (60.11), we get the time-frequency imagery of the instantaneous frequency, as shown in Fig. 60.4.

Contrasting the instantaneous m-D frequency of the echo signal for the wheel and track in Fig. 60.4, you see the m-D component move up and down around the translational component, and the frequency gradually increasing with time. In addition, the time-frequency imagery of the wheel has significant periodicity

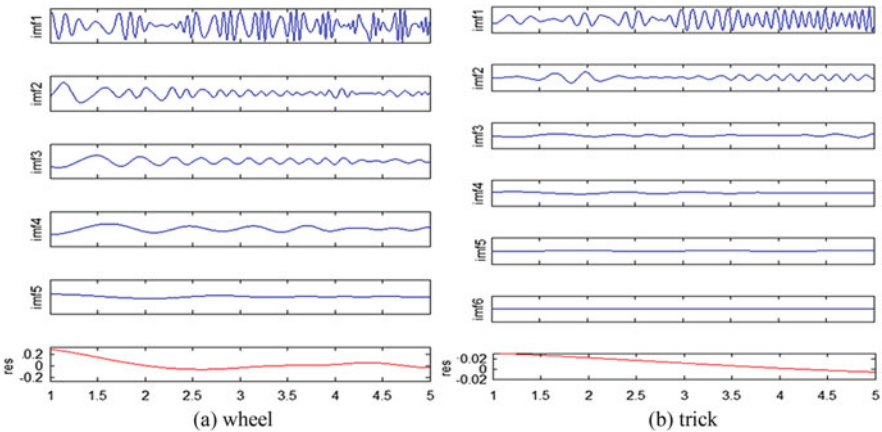


Fig. 60.2 imfs of the echo signal of a wheel (a) and track (b)

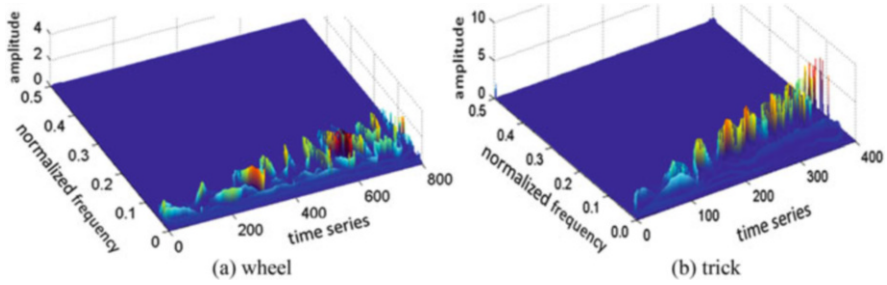


Fig. 60.3 Instantaneous frequency of imfs of the (a) wheel and (b) track

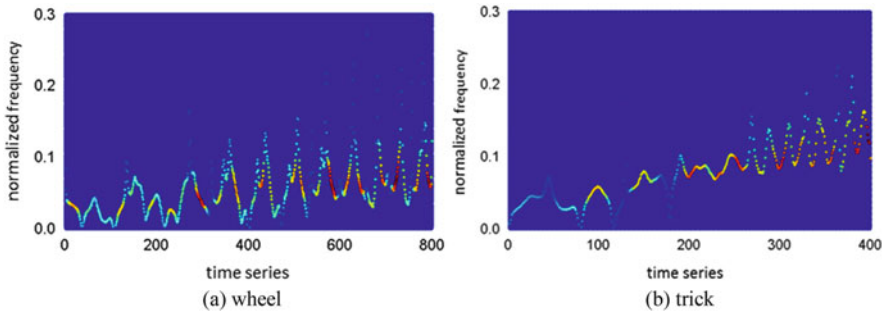


Fig. 60.4 Time-Frequency imagery of the echo signal (a) Wheel (b) Track

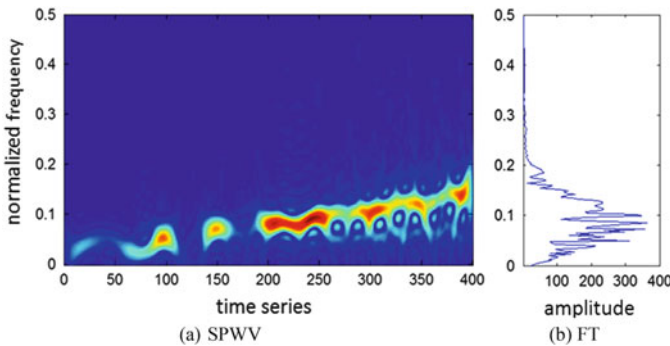


Fig. 60.5 Time-Frequency imagery of the track echo signal (a) SPWV (b) FT

whereas the track doesn't, which can be used to detect the difference between a tracked and wheeled vehicle. The Smoothed Pseudo-Wigner Distribution (SPWV) and Fourier Transform (FT) of the track echo signal are illustrated in Fig. 60.5. SPWV can respond to the main trend of the signal frequency, but the m-D is obscure because it is limited by a window function and the uncertainty principle [9]; FT only represents the distribution state in each frequency.

60.3.3 Analysis of *m*-D

The instantaneous frequency of the echo signal contains the Doppler component and the *m*-D component, among which, the Doppler component is produced by the translation of the armored vehicle and the *m*-D component is produced by the track, wheel, etc. Take the Doppler features of track as an example, in order to simplify the calculation, set $\delta = 0$, the translational Doppler frequency of scattering point is $f_d = 2f_0/c[v \cos \eta \cos \varepsilon]$. Figure 60.6a shows the SPWV peak value test. As translation is a predominant component, the peak test results show that the translational Doppler is a linear function, inconsistent with the calculation results. Figure 60.6b shows a binomial linear fitting of the *m*-D sideband peaks, and the fitting results and peak test results are basically consistent, namely, it is desirable to obtain the translation trend from the *m*-D sideband.

Take the echo signal of the wheel for example by changing the speed parameter to $V/2$. The instantaneous frequency imagery is shown in Fig. 60.7. Because EMD endpoint leak may cause serious signal distortion [10], we take the peak point coordinates of the *m*-D sideband over the time series 300–700 as presented in Table 60.1. Within this interval, the average peak frequency at speed V is 0.13, and it is 0.06 at $V/2$. The simulation results show that the faster the speed is, the greater the *m*-D and it maintains this linear relationship.

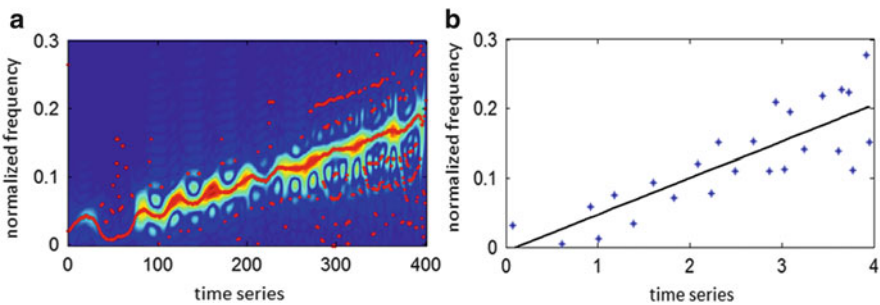


Fig. 60.6 Peak test of SPWV and binomial linear fitting of *m*-D sideband peaks. (a) Estimated translational Doppler with peak test. (b) Binomial linear fitting of *m*-D sideband peak

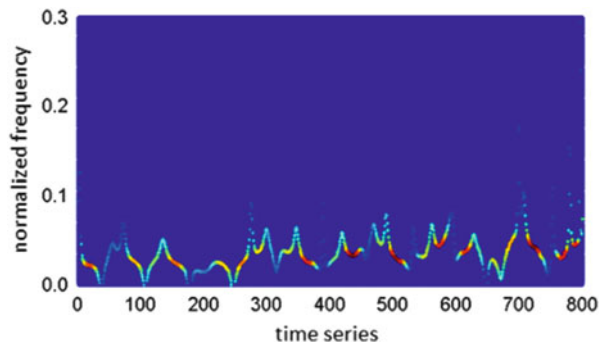


Fig. 60.7 IF imagery at a speed of $V/2$

Table 60.1 Peak point coordinates of the m-D sideband

V	<i>T</i>	3.61	4.37	5.12	5.75	6.32	6.87
	<i>F</i>	0.12	0.13	0.14	0.13	0.13	0.12
V/2	<i>T</i>	3.02	3.51	4.23	4.93	5.95	7.13
	<i>F</i>	0.06	0.06	0.05	0.07	0.07	0.03

Conclusion

For a complex target such as an armored vehicle, the phase modulation of the radar echo signal contains abundant information; the m-D features not only respond to movement information, but also contain geometry information. This paper, by taking advantage of the m-D of micromotions of a wheel and a track, proposes a new method based on EMD to analyze the echo signal with the instantaneous m-D frequency of the vehicle model extracted. It reflects micromotion features and can be used to distinguish the echo signal of a wheel and a track. When compared to SPWV and FT, it has a better time-frequency concentration. We went on to discuss the impact of translational velocity on m-D. The simulation results validate the theoretical analysis and propose a foundation for further study to identify a target using m-D.

Acknowledgments The paper was supported by the National Natural Science Foundation of China (61174219).

References

1. Chen VC. Micro-Doppler effect in radar phenomenon, model and simulation study. *IEEE Trans Aerosp Electron Syst.* 2006;42(1):2–21.
2. Zhou XH, Ai XF, et al. Bistatic micro-Doppler feature of the precessing cone-shaped warhead. *J Electron Inf Technol.* 2012;34(3):609–15 (in Chinese).
3. Guo KY, Sheng XQ, et al. Precise recognition of warhead and decoy based on components of micro-Doppler frequency curves. *Sci China.* 2012;55(4):850–6 (in Chinese).
4. Zhan Y, et al. Human motion identification based on micro-Doppler feature. *J Southwest Univ.* 2010;32(3):156–61 (in Chinese).
5. Chen VC. Doppler signatures of radar backscattering from objects with micro-motions. *IET Signal Proc.* 2008;2(3):291–300.
6. Chen VC. *The micro-Doppler effect in radar.* Boston: Artech House; 2011. p. 17–20.
7. Huang NE, et al. The empirical mode decomposition and Hilbert spectrum for nonlinear and non-stationary time series analysis. *Proc Roy Soc Lond A.* 1998;454(1971):903–95.
8. Gill TP. *The Doppler effect, an introduction to the theory of effect.* Moscow: Logos Press; 1965. p. 2–5.
9. Zhang XD. *Modern signal processing.* Beijing: Tsinghua University Press; 2002. p. 447–8 (in Chinese).
10. Huang NE, Wu ML, Long SR, et al. A confidence limit for the empirical mode decomposition and Hilbert spectral analysis. *Proc Roy Soc Lond A.* 2003;459(1123):2317–45.

Chapter 61

Kinect-Based 3D Color Reconstruction

Li Yao, Guosheng Dong, and Guilan Hu

Abstract As the artificial burn area assessment causes high error and traditional three-dimensional scanning system is of high cost, and the operation is complex, this chapter presents a three-dimensional color reconstruction of human body scanning from a Kinect. The system combines open-source OpenNI to firstly obtain color information, color calibration information, and the depth. Then two-dimensional color space information overlay technology is adopted to get 3D point cloud data with color information. With KinectFusion registration algorithm, the surface can be reconstructed from the point cloud data as obtained. The Poisson optimization algorithm is introduced to patch voids so as to make the model smooth and fine. Experiments in this chapter show that the proposed method can be used to reconstruct 3D color body model with the Kinect in a fast and accurate manner, and this will be of great value in the clinical evaluation.

Keywords Color reconstruction • KinectFusion registration • Poisson optimization • Voids patching

61.1 Introduction

Accurate estimation of the burned area plays a crucial role in the clinical diagnosis and treatment. In the twentieth century, Rule of Nines [1] and the Rule of Palms [2], as the main burn area assessment methods, were applied worldwide. However, these methods are rough 2D estimation methods and suffered from subjective factors. In the last decade, scholars have developed a series of computer-aided 3D body surface area estimation methods. Taiwan National Tsinghua University has developed a 3D body scanning system [3], but it is not suitable for extensive burns or some special parts or burns because of the fixed-site and high-cost facilities and large deviation results caused by the body moving. The two systems, Burncase 3D

L. Yao • G. Dong (✉) • G. Hu
Department of Computer Science and Technology, Donghua University,
201620 Shanghai, China
e-mail: dongguosheng2008@126.com

[4] developed in Austria and EPRI 3D Burn Vision [5] developed in the United States, both estimate the burn area by the system where the human models are pre-stored. Their main drawback is ignoring some factors such as the obese physique and the physical deformities. And BAI system [6] was developed by scholars at the University of Seville in Spain to solve the problem above. However, all of these systems only use the limited 3D models with different features and sizes. Although it restricts the fixed storage space, there are still many limitations, the lack of specific feature model and actual accurate 3D model, for example.

With the emergence of Kinect [7], 3D scanning technology gets a further development. In recent years, researches are mainly based on the following two methods: one is the reconstruction by fixed multiple Kinects [8, 9]; another one is a no-color reconstruction by one Kinect [10]. In this chapter, a novel 3D scanning system is proposed. By using one 3D camera Kinect, the system uses data of 3D color point cloud that is converted from the depth information and RGB information, which is the input of reconstruction. The 3D color model of a real person can be obtained by our method as described below. The effectiveness of the method has been tested.

61.2 Overview of 3D Color Body Reconstruction System

The 3D color body reconstruction system proposed gets the model in real time by the two scanning manners. One is by fixing the body posture while moving Kinect around the object to be tested. Another one is by fixing Kinect while the test person rotates for one circle. In this chapter, the latter is applied because the former is not much sensitive to the noise.

The presented system contains three main steps: obtaining the point cloud in the color space, reconstructing, and refining model, as shown in Fig. 61.1.

61.3 Color Reconstruction

In order to reconstruct a model with the color information, firstly, 3D point clouds data with color information must be obtained, and then the reconstruction algorithm as we propose is used to reconstruct the 3D model.

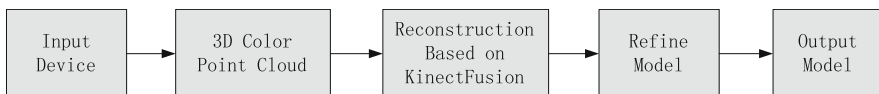


Fig. 61.1 Flowchart of the 3D color body reconstruction system

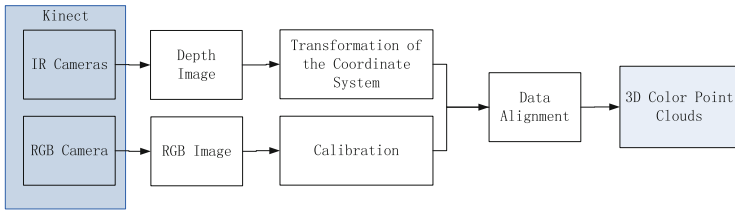
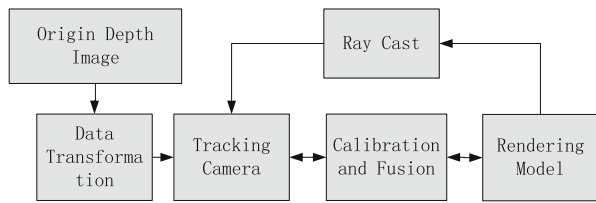


Fig. 61.2 Flowchart of obtaining 3D color point cloud

Fig. 61.3 Reconstruction based on KinectFusion



61.3.1 3D Color Point Cloud

The Kinect has three cameras: one is the color camera with 2D RGB images and the other two are depth cameras (IR Cameras) by which the depth images can be obtained. Because of different locations of the depth cameras and the RGB camera, different parameters of different lens, the RGB image obtained from one frame is not correspondent to the depth image from the frame. OpenNI [11] has the alternative view function, which can quickly amend the differences of the perspectives. The 3D point clouds with color information are obtained by superimposing the depth information and the color information. The detailed process is shown in Fig. 61.2.

61.3.2 KinectFusion-Based Reconstruction

The KinectFusion algorithm is to reconstruct a single frame of the smooth surface of the object by fusing the depth image data obtained from the continuous views [10]. The concrete process is shown in Fig. 61.3.

Firstly, transform the original depth image. The job is to convert the original depth frame captured from Kinect to the floating data in meters.

Then, track the camera to compute the global position and posture of the camera. When Kinect is moving, its camera’s posture information is recorded in time by iterative registration algorithm. It ensures the system to know well the current camera posture relative to that of the initial frame.

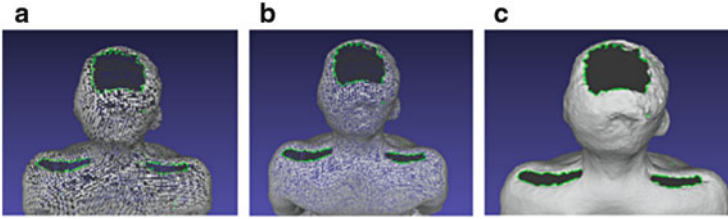


Fig. 61.4 Voids of a body model: (a) point cloud data of the body model, (b) meshed data of the body model, and (c) surface model of the body model

After that, the processed depth data will be integrated into the cubic space which is the scene around the camera. And the object surface will be reconstructed by processes of smoothing and denoising in real time; at the same time, the surface is continuously optimized to patch voids where some feature points are missing.

Finally, conduct ray casting from a global space of the scene where the current camera orients. And then the reconstructed model will be rendered.

61.4 Patching Voids

The measurement principle and human factors, for example, the low reflection coefficient of the device, improper scanning way, or much complex conformation, lead to the presence of voids [12] on the surface of 3D model. These voids will affect the result model of one reconstruction. The voids of a body model without color are shown in Fig. 61.4.

61.4.1 The Voids

A triangular mesh is defined by a set of vertices and triangles connecting these vertices. If there are two triangles sharing the same edge, the two triangles are called adjacent triangles, and one edge can be shared by at most two triangles. The edge is called critical edge when it is owned by only one triangle, and the vertices on the critical edge are called critical points; in this sense, a critical triangle is defined by a triangle that contains the critical edges and the critical points. Thus, a void in the triangular meshes is defined by a closed loop composed of critical edges, as shown in Fig. 61.5.

Fig. 61.5 Void of the meshed model

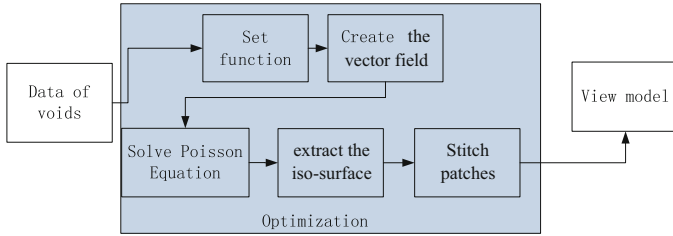
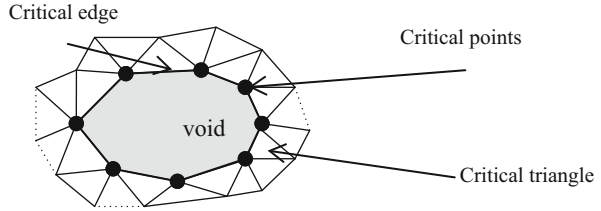


Fig. 61.6 Procedure of Poisson optimization

61.4.2 Poisson Optimization

Using Poisson optimization [13] method by which the indicator function is estimated and the iso-surface of the model is extracted, the void can be patched by reconstructing an approximation surface with new triangles. The Poisson optimization procedure is shown in Fig. 61.6.

An octree [14] is firstly established with the point cloud data optimized. And the point cloud data with voids are added to the octree. Each node on the tree is defined by a function, with the center node p , as shown in Eq. (61.1):

$$F_p = F\left(\frac{p - p_c}{p_w}\right) \frac{1}{p_w^3}, \quad p_c = \frac{1}{k} \sum_{j=1}^k p_j \tag{61.1}$$

Here, p_c denotes the center node p , p_j denotes the j th node, and p_w denotes the width of the node. We transform the reconstruction of directed vertices set into the spatial Poisson problem, defining a function space that can be translated and scaled in the space. The function space has a higher resolution at a closer distance from the surface of the model. Here, we mark F as the primary function of the function space and use the n -order convolution box-filter. Thus the primary function is defined by Eq. (61.2), where $B(t)$ denotes the filter function and n denotes the order of the filter. We can find that the function F that more approaches to the Gaussian filter and its support scope becomes larger when n is increasing. And we use piecewise quadratic approximation making $n = 3$:

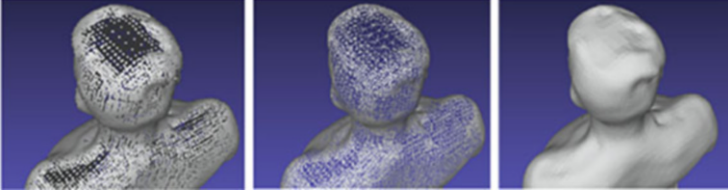


Fig. 61.7 Results of hollow optimization of the model. *Left*: point cloud data; *middle*: the meshed data; *right*: surface reconstruction data

$$F(x, y, z) = (B(x)B(y)B(z))^{*n}, \quad B(t) = \begin{cases} 1 & |t| < 0.5 \\ 0 & \text{other} \end{cases} \quad (61.2)$$

Under the well-distributed sampling, the model surface can be evaluated by approximating the gradient of the indicator function in the vector field. In order to avoid sample point position fixed to the center of the leaf node that contains the sampling point, the sample points have to be allocated to the eight neighboring nodes by using the three linear interpolation methods. According to the function F_p of each node, the approximation of the gradient of the indicator function is below:

$$V(p) = \sum_{s \in S_p \in Nb_D(S)} \sum \partial F_p \mathbf{N}_p \quad (61.3)$$

wherein S is the point set of the point cloud data, s denotes the nearest neighbor of the point p , $Nb_D(S)$ denotes the eight nodes whose depth is D in the nearest-neighbor region of the point p , ∂ is the linear coefficient, and \mathbf{N}_p is a normal vector of the fixed point p .

After obtaining the vector field \mathbf{V} , the Poisson equation $\Delta \tilde{x} = \nabla \cdot \vec{V}$ can be solved by Laplace matrix iterative method. In order to get the reconstructed surface, an appropriate threshold is required. By using MC (moving cube) algorithm [15] to extract the iso-surface and finally stitching the extracted triangle patches, the 3D reconstructed surface model is obtained. The result of the hollow optimization for the model without color is shown in Fig. 61.7 to demonstrate the effect of filling voids.

61.5 Results

In this chapter, the experiment has been conducted. The results of color reconstruction are shown in Fig. 61.8. After the color reconstruction of the human upper body model by using this system, the total number of points is 82,777, and the one of patches is 165,554, taking time of 35 s, as shown in Fig. 61.9. It is clear to see that

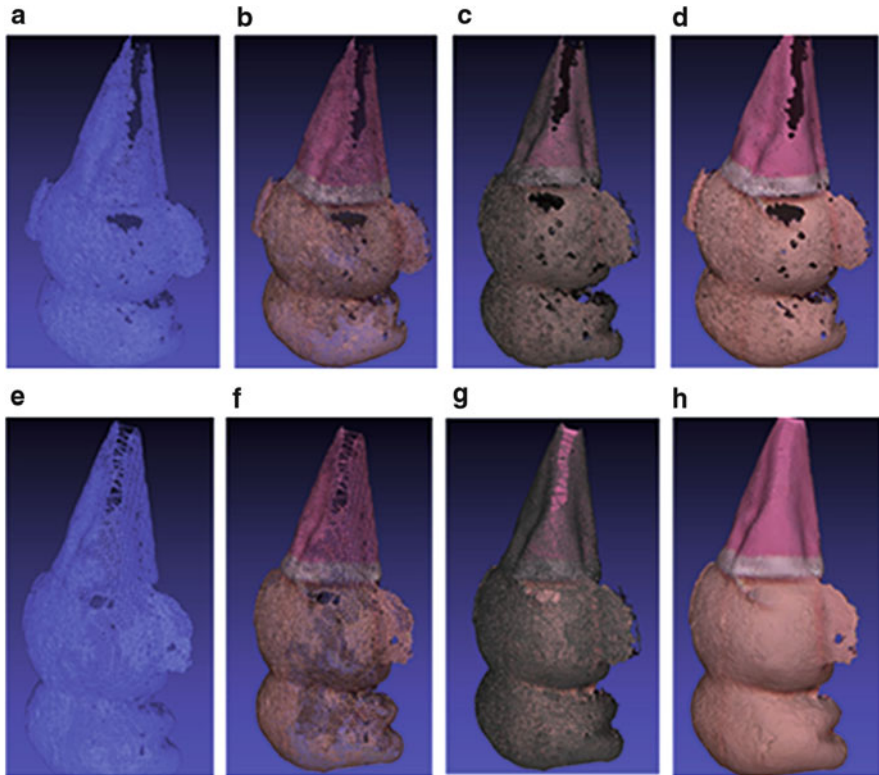


Fig. 61.8 Reconstruction renderings of the toy Winnie model (a) the meshed model with no color information before optimization, (b) the meshed model with color information before optimization, (c) the highlight meshed model with color information before optimization, (d) the reconstructed model with color information before optimization, (e) the meshed model with no color information after optimization, (f) the meshed model with color information after optimization, (g) the highlight meshed model with color information after optimization, and (h) the reconstructed model with color information after optimization

the 3D color model is more accurate to represent the characteristics of the object than that with no color information. The system proposed can be used to create 3D models of individual patients with color information, but also to describe and compute the burn area and its percentage.

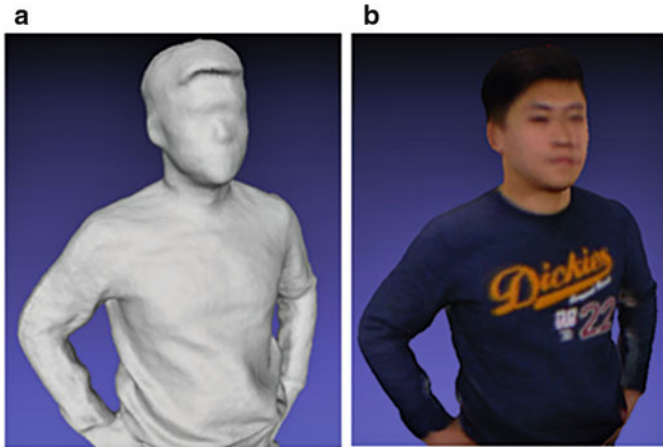


Fig. 61.9 Reconstruction of person's upper body model: (a) model without color and (b) model with color

Conclusion

This chapter describes a 3D color scanning system for burn area assessment. With a portable device Kinect, the depth information of individual surface is obtained fast. The color reconstruction method we proposed can rebuild a complete model with patching voids on the initial model. Results have represented a better performance in a real person.

References

1. Wallace AB. The exposure treatment of burns [J]. *Lancet*. 1951;257(6653):501–4.
2. Wachtel TL, Berry CC, Wachtel EE, et al. The inter-rater reliability of estimating the size of burns from various burn area chart drawings. *Burns*. 2000;26(2):156–70.
3. Yu CY, Lo YH, Chiou WK. The 3D scanner for measuring body surface area: a simplified calculation in the Chinese adult. *Appl Ergon*. 2003;34(3):273–8.
4. Haller HL, Dirnberger J, Giretzlehner M, et al. “Understanding burns”: Research project BurnCase 3D: overcome the limits of existing methods in burns documentation. *Burns*. 2009;35(3):311–7.
5. Neuwalder JM, Sampson C, Breuing KH, et al. A review of computer-aided body surface area determination: SAGE II and EPRI's 3D Burn Vision. *J Burn Care Res*. 2002;23(1):55–9.
6. Prieto MF, Acha B, Gómez-Cía T, et al. A system for 3D representation of burns and calculation of burnt skin area. *Burns*. 2011;37(7):1233–40.
7. Smisek J, Jancosek M, Pajdla T. 3D with Kinect. In: *Consumer Depth Cameras for Computer Vision*. London: Springer; 2013. p. 3–25.
8. Alexiadis DS, Zarpalas D, Daras P. Real-time, realistic full-body 3D reconstruction and texture mapping from multiple Kinects. In: *IVMSP Workshop, IEEE 11th, 2013*. [10.1109/IVMSPW.2013.1-4](https://doi.org/10.1109/IVMSPW.2013.1-4).

9. Tong J, Zhou J, Liu L, et al. Scanning 3D full human bodies using kinects. *IEEE Trans Vis Comput Graph*. 2012;18(4):643–50.
10. Izadi S, Kim D, Hilliges O, et al. KinectFusion: real-time 3D reconstruction and interaction using a moving depth camera. In: *ACM Symposium on User Interface Software and Technology*. New York, NY: ACM. 2011; 559–568.
11. The OpenNI Organization, “Introducing OpenNI”, Open Natural Interaction Library, <http://www.openni.org>. Accessed 28 Mar 2014.
12. Zhao W, Gao S, Lin H. A robust hole-filling algorithm for triangular mesh. *Vis Comput*. 2007; 23(12): 987–997.
13. Kazhdan M, Bolitho M, Hoppe H. Poisson surface reconstruction. In: *Eurographics Symposium on Geometry Processing*. The Eurographics Association; 2006. p. 61–70.
14. Poppinga J, Pfingsthorn M, Schwertfeger S, et al. Optimized octree data structure and access methods for 3D mapping. In: *Safety, Security and Rescue Robotics, 2007. SSRR 2007*. IEEE International Workshop on. IEEE. 2007; 1–6.
15. Lorensen WE, Cline HE. Marching cubes: a high resolution 3D surface construction algorithm. In: *ACM Siggraph Computer Graphics*. ACM. 1987; 21(4): 163–169.

Chapter 62

Application of Image Retrieval Based on the Improved Local Binary Pattern

Zhen Sun, Xichang Wang, and Jiang Liu

Abstract The local binary pattern (LBP) is a kind of effective texture description operator of an image. As the traditional method is getting LBP operator in local 8-neighborhood, the traditional LBP operator is too simple to result in loss of texture information. As the improved method of extracting the LBP operator, the circular neighborhood is adopted. Nevertheless, each method is easily influenced by the center pixel gray level. This chapter puts forward a new method of determining the LBP operator according to the pixel 8-neighborhood average gray level and variance so as to describe the local texture feature more effectively. The experimental results show that while compared with other algorithms, the improved algorithm can effectively extract the texture features of image and improve the accuracy of image retrieval.

Keywords Image retrieval • Improved local binary pattern • Texture feature

62.1 Introduction

With the rapid development of computer technology and network technology, the popularization and application of multimedia, there are thousands of images generated from the image library every day. How to find the image satisfying the user quickly and accurately from such a mass of image database has become the urgent problem to be solved [1]; therefore, people put forward the image retrieval technology based on the content. This technology includes visual features extraction of images: color, texture, shape, position, and mutual relations to match the image in

Z. Sun (✉)

School of Management Science and Engineering, Shandong Normal University,
Jinan 250014, China

e-mail: sunzhen1988126@126.com

X. Wang

The Education Department of Shandong Province, Jinan 250014, China

J. Liu

Image Research Center of ShanDong Oumasoft Company, Jinan 250014, China

© Springer International Publishing Switzerland 2015

W.E. Wong (ed.), *Proceedings of the 4th International Conference on Computer Engineering and Networks*, Lecture Notes in Electrical Engineering 355,

DOI 10.1007/978-3-319-11104-9_62

the database and the sample image in the feature space and retrieve images from the database similar to the sample [2].

Texture characteristics may reflect the visual characteristics of homogeneous phenomena in the image. The main texture feature extraction methods are gray co-occurrence matrix [3] and Markov random field model [4] of Gabor filters group [5]. In recent years, texture analysis methods based on the local binary pattern have been widely studied. Gray level co-occurrence matrix is a matrix function of pixel distance and angle, wide range of parameter selection, and large amount of calculation. In Markov random field model, it is difficult to estimate the model parameters with large amount of calculation as well. As Gabor filters have a lot of scale parameters and orientation parameters, large amount of calculation will be carried out. Compared with the three methods, the local binary pattern is relatively simpler with smaller amount of calculation.

Local binary pattern is a kind of texture description operator which Ojala put forward in 1996 [6]. In recent years, the LBP has been subject to constant development and evolution and widely used in the field of image processing and pattern recognition. Its basic principle is to define the LBP operator of center pixel by the relationship between the center pixel gray value and local neighborhood; nevertheless it is too simple and easily leads to loss of neighborhood texture information [7].

With the extensive application and in-depth study, a variety of extended LBP operators emerge to extract the local texture information. For example, multi-resolution texture description with LBP [8]; rotation invariant texture description with LBP variance [9]; Tan X puts forward LTP (local ternary patterns) [10] stating that the LBP is extended to ternary; Mäenpää puts forward a uniform binary pattern texture [11] to reduce the dimension of texture description. This chapter presents an improved method. With the circular LBP and the local average gray level information, the LBP operator is applied to larger areas while in full consideration of local information. Tests have been carried out to compare the image database and evaluation criteria, the improved algorithm shows better results than the traditional in terms of the image retrieval.

62.2 The Principle of LBP

62.2.1 *The Principle of Traditional LBP*

The basic principle of LBP value compares the center pixel gray level with its 8-neighborhood pixel gray level in the image. If the neighborhood pixel gray level is not less than the center pixel gray, the point value is set to 1; otherwise, the point value is set to 0. Then the result and a weighted template correspond to multiplication summation. As shown in Fig. 62.1, the method can get LBP value of the center pixel.

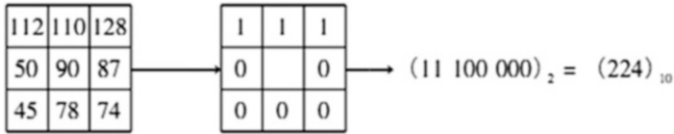


Fig. 62.1 LBP value of the center pixel calculation method

Fig. 62.2 A picture of horse



$$\text{LBP}(x, y) = \sum_{i=0}^7 S(G_i - G_0) \times 2^i \tag{62.1}$$

$$S(x) \begin{cases} 1, & x \geq 0 \\ 0, & \text{other} \end{cases} \tag{62.2}$$

where G_0 is the center pixel gray level and G_i is the 8-neighborhood pixel gray level. LBP value of center pixel is thus obtained according to Eqs. (62.1) and (62.2):

$$H(k) = \sum_{i=0}^N \sum_{j=0}^M f(\text{LBP}(x, y), k) \tag{62.3}$$

$$f(\text{LBP}(x, y), k) \begin{cases} 1, & \text{LBP}(x, y) = k \\ 0, & \text{other} \end{cases} \tag{62.4}$$

where M and N represent the image matrix and k represents the LBP value. Through the histogram of LBP value, get the texture feature description according to Eqs. (62.3) and (62.4). Figure 62.2 presents a picture of horse; its gray level histogram and LBP value histogram are shown in the Fig. 62.3.

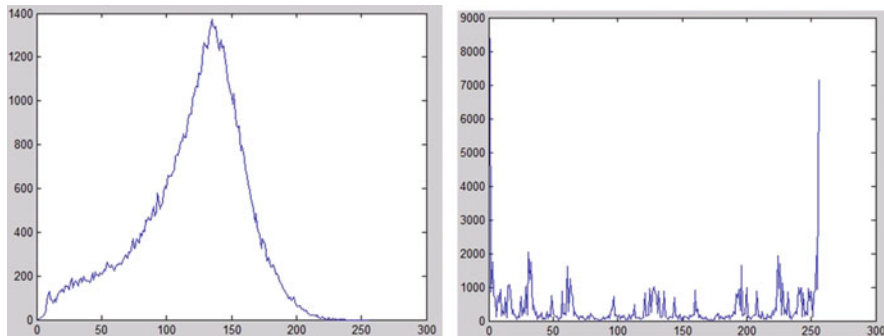


Fig. 62.3 The gray level histogram and LBP value histogram of the picture of horse

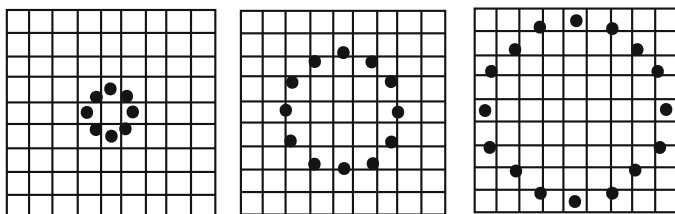


Fig. 62.4 The circular neighborhood of center pixel with different scales

62.2.2 The Principle of Extended LBP

Because of the maximum LBP value of 8-neighborhood is 255, the scale of texture features the description range of 1–255. In order to describe the texture feature in different scales, Ojala puts forward the extended LBP to describe the image texture features through the circular local binary pattern ($LBP_{P,R}$) value.

As shown in Fig. 62.4, the neighborhood pixels have larger scale than the 8-neighborhood. The first circular neighborhoods have 8 pixels, the second have 12 pixels, and the third have 16 pixels.

$$G_i \begin{cases} x_i = x_0 + R \cos \left(\frac{2\pi p}{P} \right) \\ y_i = y_0 + R \sin \left(\frac{2\pi p}{P} \right) \end{cases} \quad (62.5)$$

where P is the number of circular neighborhood pixels, R ($R > 0$) is the radius of the circle, G_0 is the center pixel gray level, and G_i is the neighborhood pixel gray level in the circle. If the G_0 coordinate is (x_0, y_0) , get the G_i coordinate (x_i, y_i) according to Eq. (62.5). Then estimate the gray level of G_i through bilinear interpolation:

$$\text{LBP}_{P,R}(x,y) = \sum_{i=0}^{P-1} s(G_i - G_0) \times 2^i \quad (62.6)$$

Then the $\text{LBP}_{P,R}$ value of the center pixel can be obtained according to Eq. (62.6). In the actual calculation, the calculation result is $[1, 2^i - 1]$, and the texture feature description scale is in the range from 1 to $2^i - 1$. Then the texture feature description can be obtained according to Eqs. (62.3) and (62.4).

62.3 The Average Model LBP

Circular form of the LBP operator can be used to extract texture features of image, but the algorithm is to find the pixel which gray level which is less than the center pixel gray level in local neighborhood. When the value is set at 0 or at 1, it will lose some useful information; in addition, when the gray level of neighborhood pixels is compared with the center pixel only, the stability is bad. This chapter puts forward a kind of improved LBP, called the average LBP.

$$G_\mu = \frac{1}{P} \sum_{i=0}^{P-1} G_i \quad (62.7)$$

$$G_\sigma = \frac{1}{P} \sum_{i=0}^{P-1} (G_i - G_\mu)^2 \quad (62.8)$$

where P is the number of circular neighborhood pixels, G_i is the neighborhood pixel gray level, G_μ is the local average gray level, and G_σ is the local variance.

$$\text{LBP}_{P,R}(x,y) = \sum_{i=0}^{P-1} S(G_i - G_\mu) \times 2^i \quad (62.9)$$

$$S(x) \begin{cases} 1, & x \geq 0 \text{ or } G_i - G_\mu \geq -G_\sigma \\ 0, & \text{other} \end{cases} \quad (62.10)$$

Using the neighborhood pixel average gray level instead of the center pixel gray level, the average-LBP value according to Eqs. (62.9) and (62.10) can be obtained.

62.4 Experimental Results and Analysis

The experimental environment is shown as below: CPU, 2.66G; memory, 4G; system, Win7; software, Matlab7.0.

The test data from three image databases. Image database 1 is Corel Image Gallery, which has 1,000 images and is divided into ten categories. Each category contains 100 images. Image database 2 includes 109 categories of Brodatz texture images with each category image (640×640) divided into 16 nonoverlapping images (160×160) which have 1,744 images. Image database 3 is the texture feature database and divided into 25 categories with each category containing 40 images. The creation of this database is partially supported by the National Science Foundation under grant IIS-0308087, the European project LAVA, the UIUC-CNRS Research Collaboration Agreement, the UIUC Campus Research Board, and the Beckman Institute.

In order to test the results, a few concepts are provided; precision (P) is the signal to noise ratio of image retrieval, namely, the positive samples image retrieved and all image retrieved percentage, which is expressed as below:

$$P = \frac{Q}{N} \times 100\% \quad (62.11)$$

where:

1. Q is the positive samples image retrieved number to meet the requirement,
2. N is the total number of the positive samples image retrieved.

In Fig. 62.5, “*” represents the precision ratio of texture description by traditional LBP operator; “ Δ ” represents the precision ratio of texture description by

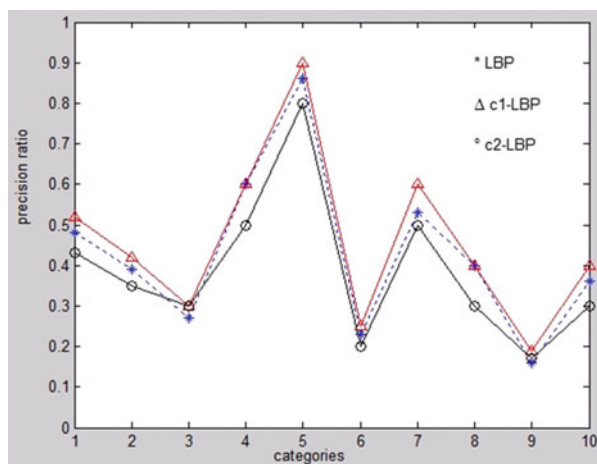


Fig. 62.5 The precision ratio of image retrieval

Fig. 62.6 The precision ratio of image retrieval

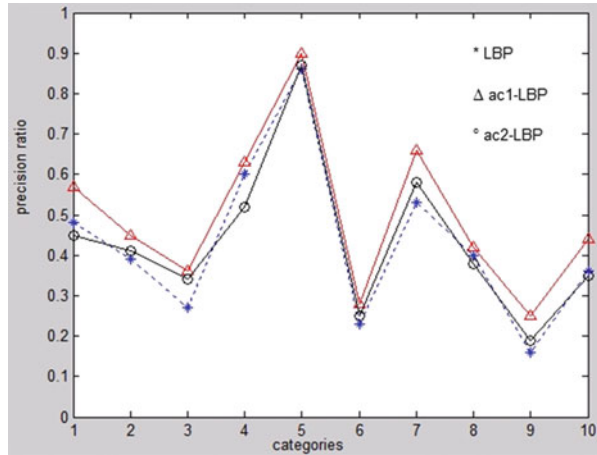


Table 62.1 The precision of each database with traditional method and improved method

Image database	Precision (%)			
	Database 1	Database 2	Database 3	Average
Traditional method	42.1	56.4	52.4	50.3
Improved method	61.4	65.2	68.8	65.1

extended LBP operator, where P is 8 and R is 1; and “○” represents the precision ratio, where P is 8 and R is 1. The extended LBP can improve the precision ratio of image retrieval, but when the circular local neighborhood is expanded, the precision ratio decreases.

In Fig. 62.6, “*” represents the precision ratio of texture description by traditional LBP operator; “Δ” and “○” represent the precision ratio of texture description in this chapter. It shows that average-LBP can improve the precision ratio and the radius of circle shall be controlled in a certain range. If the radius of circle is too large, the precision ratio is reduced.

Supposing a retrieved image, the image is retrieved from the image database. The calculation and results are sorted according to the similarity. Get the average precision and average recall of each class. The results are shown in Table 62.1.

Conclusion

Based on the analysis of the texture description operator by the traditional LBP and the extended LBP, this chapter describes a new texture description operator which is more effective to extract image texture feature and can effectively reduce the influence on LBP operator by the center gray level. The experimental results show that the average-LBP can improve the precision ratio of image retrieval and have certain application value.

References

1. Li L, Gang-yao K. Overview of image textural feature extraction methods. *J Image Graph.* 2009;14(4):622–35.
2. Wei W, Feifei H, Jianwei L, et al. Face description and recognition by LBP pyramid. *J Comput Aid Des Comput Graphics.* 2009;21(1):94–101.
3. Haralick RM, Shanmugam K. Textural features for image classification. *IEEE Trans Syst Man Cybern.* 1973;SMC-3(6):610–21.
4. Cross GR, Jain AK. Markov random field texture models. *IEEE Trans Pattern Anal Mach Intell.* 1983;PAMI-5(1):25–39.
5. Manjunath BS, Ma WY. Texture features for browsing and retrieval of image data. *IEEE Trans Pattern Anal Mach Intell.* 1996;18(8):837–42.
6. Ojala T, Pietikainen M, Harwood D. A comparative study of texture measures with classification based on feature distribution. *Pattern Recogn.* 1996;29(1):51–9.
7. Loris N, Alessandra L, Sheryl B. Survey on LBP based texture descriptors for image classification. *Expert Syst Appl.* 2012;39(3):3634–41.
8. Ojala T, Pietikainen M, Maenpaa T. Multiresolution gray scale and rotation invariant texture analysis with local binary patterns. *IEEE Trans Pattern Anal Mach Intell.* 2002;24(7):971–87.
9. Zhen-hua GUO, Lei ZHANG, David Z. Rotation invariant texture classification using LBP variance(LBPV) with global match. *Pattern Recogn.* 2010;43(3):706–19.
10. Tan X, Trigs B. Enhanced local texture feature set for face recognition under difficult lighting conditions. *IEEE Trans Image Process.* 2010;19(6):1635–50.
11. Mäenpää T, Ojala T, Pietikäinen M. Robust texture classification by subsets of local binary patterns. In: *Proc. 15th International Conference on Pattern Recognition, USA, IEEE Computer Society.* 2000; 3947–50.

Chapter 63

Intelligent Detection of Complex Gaps in Live Working Based on Video Analysis

Yu Fan, Kangxiong Yu, Xiaoqing Tang, Heping Zheng, Li Yu,
and Ge Zhang

Abstract To avoid safety accidents, live work operators must maintain a correct posture to ensure their own complex gap within the limits of request body extension size. The traditional measurement of complex gaps of live working operators in training mainly depends on the subjective empirical judgment of the expert on the spot, which features strong subjectivity and safety risks. As for existing problems, this paper proposes a novel intelligent detection algorithm based on video analysis technology that uses multi-Gaussian background modeling, blob detection, and the foreground merged method. Taking a 500 KV tower as an example, the experimental results indicate that the proposed method can measure the real-time complex gap of an operator in a timely and accurate manner; moreover, the proposed method can standardize operations and improve the safety level of live working effectively.

Keywords Live working • Complex gap • Video • Gaussian mixture mode • Blob detection • Pattern recognition

63.1 Introduction

Guaranteeing the personal safety of operators during live work is a top priority; thus, maintaining a safe distance is one of the most frequently encountered problems in live working. The minimum complex gap is an indicator of safe distance. It refers to the sum of two distances: one is the distance between the human body and the grounding body, and the other is the distance between the human body and a charged body.

Y. Fan • K. Yu • X. Tang • H. Zheng
Technical Skills Training Center, State Grid Sichuan Electric Power Company, 611731
Chengdu, China

L. Yu • G. Zhang (✉)
School of Automation Engineering, University of Electronic Science and Technology of
China, 611731 Chengdu, China
e-mail: lyzg_sky@foxmail.com

Currently, the focus of domestic studies on complex gaps involves aspects such as studies on the minimum complex gap in the live working of transmission lines [1], the establishment of a modified Rizk model appropriate to the complex gap discharge of live work on ultra-high-voltage transmission lines [2], and the analysis of complex gap discharge developments in the course of equal potential working and its influencing factors using the electric field calculation method [3]. However, more attention is being paid to the intelligent detection of real-time complex gaps, which is conducive to standardizing operations and reducing risk. To avoid accidents, the complex gap is monitored to guarantee that the operator maintains a correct posture from the ground potential to the equipotential or from the equal potential back to the ground potential.

At present, the measurement of complex gaps of operators in traditional live work training depends primarily on the observations of experts on the spot. Nevertheless, the determination of the complex gap distance is prone to certain errors due to fatigue and missing observations. In this sense, detecting complex gaps intelligently becomes a key issue in the power industry. In response to this issue, this paper presents an innovative approach to intelligent identification of complex gaps in live work based on video image analysis technology, which combines the Gaussian mixture model, blob detection, and the foreground merged method.

63.2 Complex Gap Algorithm Framework

With respect to outdoor light in objective environments, we combine a variety of pattern recognition algorithms such as the Gaussian mixture model, blob detection, the foreground merged method, and relevant knowledge on live work to detect the real-time complex gap and safety information of the operator.

The algorithm flow chart is shown in Fig. 63.1:

Among them, the Gaussian mixture model (GMM) is the core part of the algorithm.

63.3 Complex Gap Algorithm

63.3.1 Determination of Monitoring Bounding Box

Since operators enter an electric field along an insulator string, the insulator string is considered to be the main area of human activity; therefore, we define this area as a major monitoring bounding box to calculate the real-time complex gap of operators.

To extract a frame image from a camera, the monitoring bounding box is defined according to the position of the insulator string with the image of the width W_{image}

Fig. 63.1 Algorithm flow chart

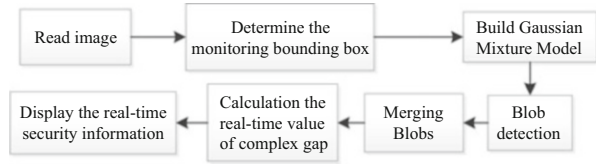
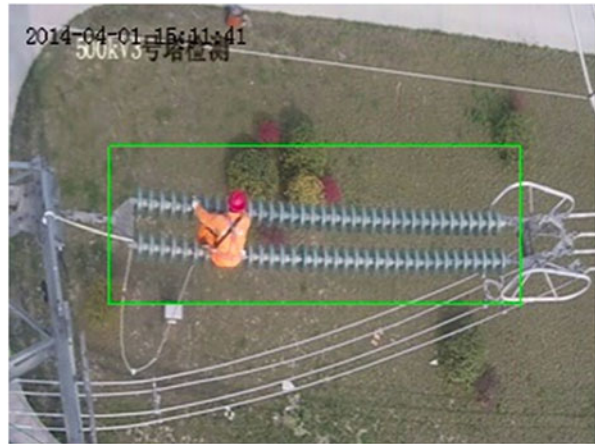


Fig. 63.2 Monitoring of the bounding box



of the corresponding areas and the height $H_{\text{ForeRegion}}$ of the foreground recorded as shown in Fig. 63.2:

The region surrounded by green lines in Fig. 63.2 is the monitoring bounding box.

63.3.2 Gaussian Mixture Model

The GMM began in 1894 as a powerful clustering model. It has been widely used, for example, in voice signal processing, image segmentation, video background modeling, and moving object detection [4]. Most importantly, it is sensitive to noise.

Stauffer proposed an adaptive GMM with each pixel, $\{X_1, \dots, X_t\}$, originating from a Gaussian mixture of K components. The probability of the pixel in the background can be expressed as

$$P(t) = \sum_{i=1}^k \omega_{i,t} N(t, \mu_{i,t}, \sum_{i,t}), \tag{63.1}$$

where K (3–5) is the number of distributions, ω_i is an estimate of the weight (what portion of the data is accounted for by this Gaussian) of the i th Gaussian in the

mixture at time t , $\mu_{i,t}$ is the i th Gaussian mean value in the mixture at time t , $\Sigma_{i,t}$ is the i th covariance matrix value, and η is a Gaussian probability density function [5]:

$$\eta(t, \mu_{k,t}, \Sigma) = \frac{1}{(2\pi)^{\frac{d}{2}} |\Sigma|^{\frac{d}{2}}} e^{-\frac{1}{2}(t-\mu_t)^T \Sigma^{-1} (t-\mu_t)}. \quad (63.2)$$

The covariance matrix can be expressed as

$$\Sigma_{k,t} = \sigma^2 I. \quad (63.3)$$

The parameters of the model are updated using the following formulas:

$$\omega_{k,t+1} = (1 - \alpha)\omega_{k,t-1} + \alpha M_{k,t}, \quad (63.4)$$

$$\mu_t = (1 - \rho)\mu_{t-1} + \rho t, \quad (63.5)$$

$$\sigma_t^2 = (1 - \rho)\sigma_{t-1}^2 + \rho(t - \mu_t)^T (t - \mu_t), \quad (63.6)$$

$$\rho = \alpha \eta(t | \mu_k, \sigma_k). \quad (63.7)$$

Finally, each Gaussian distribution is arranged in descending order according to ω_k / σ_k . A threshold T is applied to the cumulative sum of weights, the first B distributions are considered to be the background model, defined as [6]

$$B = \arg \min_b \left(\sum_{k=1}^b \omega_k > T \right). \quad (63.8)$$

Intuitively, Gaussians with the highest probability of occurrence, ω_k , and the lowest variability in the distribution, measured by σ_k , indicating a representative mode, are the most likely to model the background accurately.

After the monitoring bounding box is determined in Fig. 63.2, we select four samples using the GMM with the results of the foreground mask of the operator based on GMM shown in Fig. 63.3.

63.3.3 Blob Detection

The foreground mask of the current frame is processed to calculate the rectangular region that encloses each blob tightly of the new moving target in the monitoring bounding box.

Blob detection algorithms include the following steps: foreground mask extraction, foreground mask correction, and blob segmentation by connecting the component labeling with the region calculation.



Fig. 63.3 Results of foreground mask based on GMM

First, basic operations of binary morphology, such as dilation, erosion, closing, and opening, are used for the foreground mask correction. The holes are filled up in the closing operation, while juttred pixels or small isolated pixel regions are eliminated by the opening operation in blob detection [7].

Second, the blobs need to be segmented into several blobs of interest, and then the larger blobs (perhaps caused by sudden changes in the lighting) and the blobs overlap with some and those blobs overlapped with blobs that have already been tracked are filtered out. The remaining blobs are sorted in descending order, leaving only a few relatively large blobs.

Finally, in accordance with specific rules, substandard blobs are filtered out, and the new real blobs are saved in the list.

63.3.4 Merging Blobs

We assume that one blob represents one person; however, there are many disturbance factors whose parts are mistaken as multiple targets. One way to avoid this problem is to merge these blobs by assuming that blobs in similar locations belong to one object.

Let us consider two blobs, A and B . The distances between A and B in the horizontal and vertical directions can be expressed as V_{AB} and H_{AB} .

The merger depends on the following criterion, ν and h is a small fixed value.

$$\text{Merge if } V_{AB} \leq \nu H_{AB} \leq h. \quad (9)$$

After the merging process, a rectangular box can be used to tightly enclose each blob of Fig. 63.3, and the width of the box can be calculated. The results are shown in Fig. 63.4.

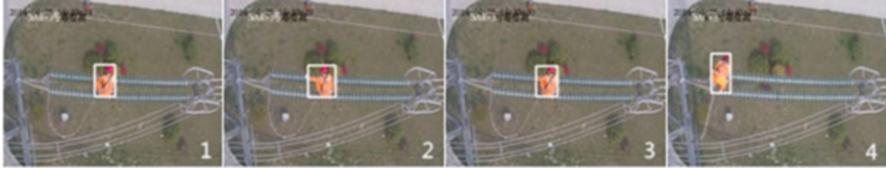


Fig. 63.4 Results of blobs after merging process

63.3.5 Calculate Real-time Value of Complex Gap

To avoid having a complex gap of an operator that is too small, it is recommended that one enter the electric field of 500 KV transmission line towers from the side of the tower that is parallel to the line. At the same time, only one operator should be on the insulator string. The maximum width in the horizontal direction of the operator is no more than the sum of the width of four insulators.

In this sense, the detection of the real-time value of a complex gap is replaced by the detection of the width of the operator.

The visual distortion of the insulator string on the right-hand side is slightly greater than that on the left. To reduce the error caused by visual distortion, this paper uses an appropriate threshold of $k=0.098$ based on the analysis of many frames of video images. X_{core} represents the centroid of the operator.

The minimum width threshold of the operator is as follows:

$$\begin{cases} D_{mini} = 0.098 * W_{image}, & 0 < x_{core} < 0.6 * W_{image} \\ D_{mini} = (0.098 * W_{image}) + 1, & 0.6 * W_{image} < x_{core} < W_{image} \end{cases}, \quad (63.10)$$

where D_{comgap} is the real-time width of the operator in the foreground image.

Compare D_{comgap} with D_{mini} , which is the minimum width D_{mini} of the corresponding voltage level. If D_{comgap} is greater than D_{mini} , then the real-time value of the operator's complex gap is too small, and the operator is in danger.

63.4 Experimental Results

We test our algorithm on a video in which the operator enters the electric field along the insulator string of 500 KV transmission line towers; in addition, sound and light warnings are given in the case of illegal operations.

The size of the captured video image is 240×320 with Visual Studio 2010 and opencv2.3 used for programming and experimenting. Based on intensive experimental analysis, the parameters as selected in this paper of the GMM that obtain the best effect are $K=3, T=0.8, \alpha=0.02$, and $\omega_0=0.33$. The execution time of the proposed algorithm for every frame image is 12 ms.

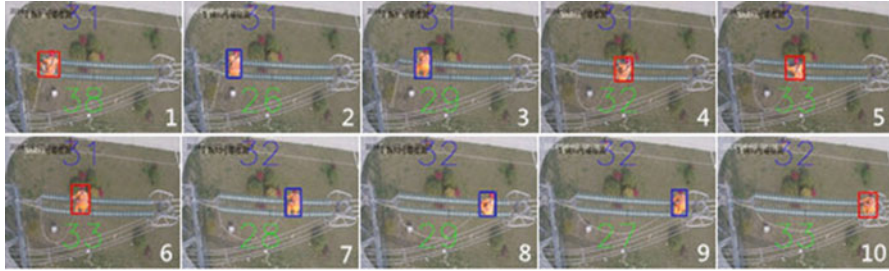


Fig. 63.5 Classification results using proposed algorithm

Table 63.1 Classification results using different methods

Sample number	Body width	Safety information (our method)	Safety information (empirical judgments)
1	38	Dangerous	Dangerous
2	26	Safe	Safe
3	29	Safe	Safe
4	32	Dangerous	Safe
5	33	Dangerous	Dangerous
6	33	Dangerous	Safe
7	28	Safe	Safe
8	29	Safe	Safe
9	27	Safe	Safe
10	33	Dangerous	Dangerous

According to Eq. (63.10), the minimum width threshold of the operator in this experiment can be written as:

$$\begin{cases} D_{\min i} = 31, & 0 < x_{\text{core}} < 0.6 * W_{\text{image}} \\ D_{\min i} = 32, & 0.6 * W_{\text{image}} < x_{\text{core}} < W_{\text{image}} \end{cases} \quad (63.11)$$

Figure 63.5 shows the classification of eight representative images using the proposed algorithm. The blue numbers at the top represent the threshold of minimum width, and the green numbers at the bottom represent the real-time width of the operator. When the operator is safe, the bounding box is blue; by contrast, when the operator is in danger, the bounding box is red. To demonstrate the validity of the proposed method, the results using the complex gap algorithm are compared with the results obtained using the traditional method (Table 63.1).

When the width of the operator’s body is less than the sum of the widths of four insulators, the results obtained using our method are consistent with the results of empirical judgment, such as Samples 2, 3, 7, 8, and 9. However, when the width of the operator’s body is greater than the sum of the width of four insulators, our method’s results are inconsistent with those obtained under the traditional method,

such as Samples 4 and 6. By checking the stored pictures, experts can see immediately that their judgment is wrong.

The proposed algorithm has been tested many times in a live working training center. Experiments have shown that no omission is existing with this algorithm, though false alarms sometimes do occur. Analysis of the results show that the false alarms were caused by shaking of the insulator string and the rope with which the operator was equipped.

Conclusion

This paper focuses on an intelligent detection algorithm for complex gaps based on video image analysis. At present, there is no research in which complex gaps based on the video image analysis technology were detected. Compared with traditional methods and the most advanced complex gap detection algorithms, such as the analysis of complex gaps using the electric field calculation method [3], the proposed method measures the width of the operator intelligently and produces results in real time and, thus, not only overcomes the disadvantages of a strong electric field but can also be robustly expanded. The experimental results have verified the algorithm's validity.

Because it does have limitations, such as the need to install cameras or distortions caused by the shaking of insulator strings or ropes, our method will be affected by the accuracy of the results. In future work, we will seek to improve the approach and make it more robust.

References

1. Hu Y, et al. Research on combined gap of live line work for 750 kV power transmission line. *Electr Equip*. 2006;7(1):29–32.
2. Wang L, et al. Complex gap discharge mechanism of live working on ultra high voltage transmission lines. *High Voltage Eng*. 2011;37(5):1224–31.
3. Wang L, et al. Research on complex gap discharge model of live working on EHV and UHV high-voltage transmission lines. *Can J Electr Comput Eng*. 2014;37(1):11–8.
4. Tang Y, et al. Multi-resolution image segmentation based on Gaussian mixture model. *Syst Eng Electron*. 2006;17(4):870–4.
5. Stauffer C, Grimson WEL. Adaptive background mixture models for real-time tracking. In: *Proceedings of the IEEE International Conference on Computer Vision and Pattern Recognition*; 1999 June 23–25; IEEE Computer Society, Fort Collins, Colorado, USA; 1999. vol. 2, p. 246–52.
6. Bouttefroy PLM, et al. On the analysis of background subtraction techniques using Gaussian mixture models. In: *2010 I.E. International Conference on Acoustics Speech and Signal Processing (ICASSP)*; IEEE, Dallas, TX; 2010. p. 4042–45.
7. Nguyen TB, Chung ST. An improved real-time blob detection for visual surveillance. In: *2nd International Congress on Image and Signal Processing, CISP'09*; IEEE, Tianjin; 2009. p. 1–5.

Chapter 64

Face Detection Based on Landmark Localization

Peng Liu, Songbin Li, Qiongxing Dai, and Haojiang Deng

Abstract This chapter proposes a face detection method based on the facial landmark localization. Firstly, it uses AdaBoost-based frontal face detector to yield coarse face detection results; then it uses the facial landmark detector to get the localization result and the quality score. If the quality score is larger than the preset threshold, the candidate image is considered to be a face; however, the quality score may be affected by expression and other factors. When it is not larger than the threshold, in order to prevent mistakes, the nose area is used for validation. That is because the nose area appears least affected by interference factors. The experimental results show that the proposed face detection method can achieve good results, of which the average F_1 -score is 0.988.

Keywords Face detection • Landmark localization • Deformable part model

64.1 Introduction

Face detection is adopted to determine whether or not there are any faces in an arbitrary image and, if present, return the image location and extent of each face [1]. It is an important research subject that is widely adopted in the security, entertainment, financial payment, and other fields. As the key component of face analysis and recognition systems, it is of great commercial value and academic value. Almost all relevant applications of faces, such as the face recognition, the gender recognition, the age estimation, and the video character indexing, are based on the results produced by the face detection. The results of face detection are decisive for the procedure followed.

P. Liu • S. Li (✉) • Q. Dai
Haikou Laboratory, Institute of Acoustics, Chinese Academy of Sciences,
570105 Haikou, China
e-mail: lisongbin_work@126.com

H. Deng
National Network New Media Engineering Research Center, Institute of Acoustics,
Chinese Academy of Sciences, 100000 Beijing, China

In recent years, the face detection has been widely studied because of its great potential in various industries. The current face detection studies can obtain good results under limited conditions; however, it's still a challenge to detect face under unlimited conditions. Because there are too many variables, such as expression, illumination, posture change, shade, decoration, and racial difference, they may have effects on the final results.

The face detection approaches differ in the cues and characteristics used to model a face. The existing approaches can be classified into four categories [2]: the feature-invariant approaches, the template matching methods, the knowledge-based methods, and the appearance-based methods. Thanks to the rapid growing computation ability and the data storage space, the appearance-based methods have showed better performance than others; therefore, we take the appearance-based method in this study.

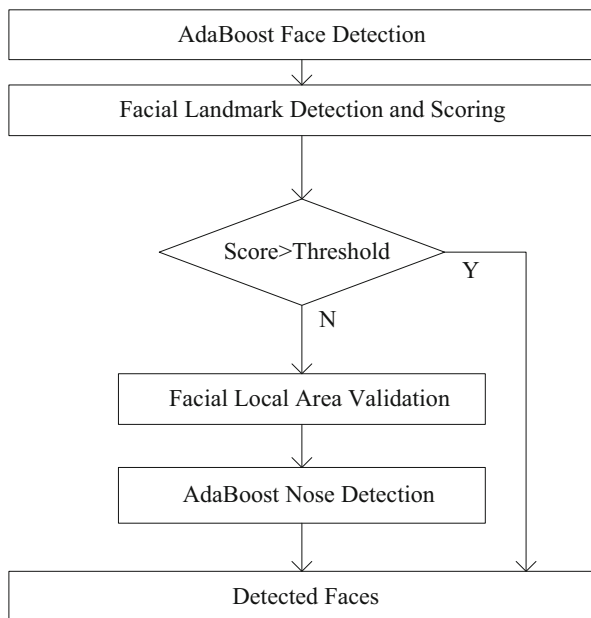
At present, the face detection is dominated by scanning window classifiers [3–6]. They regard the face detection problem as a binary classification problem, namely, to determine whether a correctly framed face instance is contained in the current detector window. A variety of machine learning methods such as the classification trees [7], the neural networks [8], and the convolution neural networks [9] have been used as classifier for face detection; however, one method has received the most ubiquitous attention: the boosting-based cascades [10]. Viola and Jones [10] proposed a simple but effective face detector by using haar-like features to train weak classifiers with AdaBoost algorithm. It could achieve high detection rates that meet the real-time requirements; however, the detection accuracy declines obviously in case of detecting faces against complex background.

Recent studies on common object detection have shown that the incorporating parts during detection help capturing object class spatial layout better, which will effectively improve the detection accuracy [11, 12]. As motivated, this chapter presents a landmark localization based on the face detection method.

64.2 Proposed Method

First of all, we use AdaBoost-based frontal face detector to yield coarse face detection results, namely the candidate images; then we combine the facial landmark detection and the scoring together with the facial local area validation to determine whether the candidate images are human face images. We use the facial landmark detector to get the localization result l^* and the quality score S_{\max} . If S_{\max} is larger than the preset threshold S_{δ} , the candidate image is considered to be a face. After a lot of experiments, we determine the value of threshold S_{δ} to be 115, which leads to the best performance of face detection. Furthermore, we will combine the local area validation of human face for secondary judgment as supplementary detection, that is, when $S_{\max} \leq S_{\delta}$, we will choose the nose area of human face to

Fig. 64.1 Flowchart of the proposed face detection method



conduct the validation. Our method is able of reducing the number of false positives as well as the number of false negatives; therefore, it can improve the final recall ratio and precision ratio. The proposed face detection method is shown in Fig. 64.1.

64.2.1 Facial Landmark Detection and Scoring

Before face detection, the facial landmark detector should be trained firstly. The deformable part model (DPM) is used for the modeling of facial landmark localization problem. Let $I \in R^{M \times N}$ denotes a candidate image with $M \times N$ pixels where R denotes a set of pixel values. Face model can be denoted by a graph $G = (V, E)$. $V = \{v_1, \dots, v_n\}$ denotes n parts of a face, and the edge $(v_i, v_j) \in E$ denotes the connection between two parts. A landmark configuration can be expressed with $I = \{l_1, l_2, \dots, l_n\} \in L$, where l_i represents the location of part v_i and L is the set of all the configurations. As to the image I , $p_i(I, l_i)$ is used to measure the model matching degree of part v_i in l_i position, which can be called the local appearance model; $q_{i,j}(l_i, l_j)$ is used to measure the model deformation degree of part v_i and v_j in position l_i and l_j , which can be called the deformation cost model. The quality of the landmark configuration can be measured by a scoring function:

$$f(I, \mathbf{l}) = \sum_{i=1}^n p_i(I, l_i) + \sum_{(v_i, v_j) \in E} q_{i,j}(l_i, l_j) \quad (64.1)$$

When $f(I, l)$ takes the maximum value S_{\max} , the landmark configuration has a best quality; therefore, the best landmark configuration can be obtained by

$$I^* = \arg \max_L \left(\sum_{i=1}^n p_i(I, l_i) + \sum_{(v_i, v_j) \in E} q_{i,j}(l_i, l_j) \right) \quad (64.2)$$

Seven landmarks are trained with the Labeled Faces in the Wild (LFW) database: the tip of the nose, the corners of the mouth, and the canthi of the left and the right eye. The landmark detector can be achieved by the structured output support vector machine (SVM) method [13].

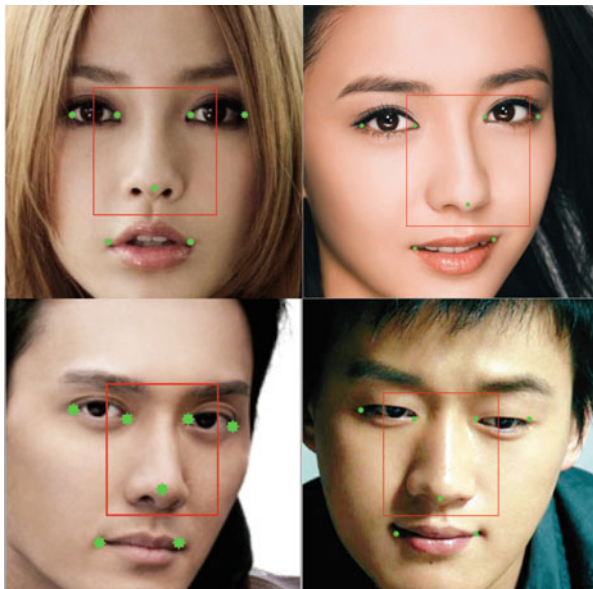
The model is trained based on the vital organs of human face such as eyes, nose, and mouth so as to comprehensively represent the appearances, the texture, and the geometric features of human face. When the model is applied to detect the candidate images, higher quality score indicates more information of human face contained in the candidate image; thus the candidate image is more likely to be human face. When the corresponding match score of the optimal match result is higher than our preset threshold, we determine the candidate image as human face.

64.2.2 Facial Local Area Validation

The core idea of object-detection studies is to reduce false positives and false negatives as much as possible. As described above, the facial landmark detection and scoring mainly aim at addressing false-positive situations. In this sense, the preset threshold S_δ is somewhat large; nevertheless, some candidate image which has a lower quality score than S_δ may still be human face image, which is the false-negative situation. As a result, when $S_{\max} \leq S_\delta$, we will choose the nose area of human face to conduct the validation so as to reduce the number of false negatives. For the nose area is geometrically stable and least sensitive to the influences of the illumination, noises, and expressions among all the organs of human face. We will also use the results of the facial landmark detection and scoring in the secondary judgment.

The coordinates localized by the facial landmark detector can be denoted as $(x_{L-in}^{eye}, y_{L-in}^{eye})$, $(x_{L-out}^{eye}, y_{L-out}^{eye})$, $(x_{R-in}^{eye}, y_{R-in}^{eye})$, $(x_{R-out}^{eye}, y_{R-out}^{eye})$, $(x_L^{mouth}, y_L^{mouth})$, $(x_R^{mouth}, y_R^{mouth})$, and (x^{nose}, y^{nose}) . The upper left coordinate (x_{rect}, y_{rect}) , the width $width_{rect}$, and the height $height_{rect}$ of nose area can be obtained by (64.3). Some samples are shown in Fig. 64.2. The nose area is inside the red rectangle:

Fig. 64.2 Some examples of nose areas obtained by our approach



$$\begin{cases} x_{\text{rect}} = x^{\text{nose}} - \text{width}_{\text{rect}}/2 \\ y_{\text{rect}} = \min(y_{\text{L-out}}^{\text{eye}}, y_{\text{R-out}}^{\text{eye}}) - (\max(y_{\text{L}}^{\text{mouth}}, y_{\text{R}}^{\text{mouth}}) - y^{\text{nose}})/2 \\ \text{width}_{\text{rect}} = (x_{\text{R-in}}^{\text{eye}} + x_{\text{R-out}}^{\text{eye}})/2 - (x_{\text{L-in}}^{\text{eye}} + x_{\text{L-out}}^{\text{eye}})/2 \\ \text{height}_{\text{rect}} = (\max(y_{\text{L}}^{\text{mouth}}, y_{\text{R}}^{\text{mouth}}) - y^{\text{nose}})/2 - y_{\text{rect}} \end{cases} \quad (64.3)$$

When the image of nose area is obtained, AdaBoost-based nose detector is used to detect the nose. If a nose is detected, the candidate image is considered to be a face.

64.3 Experiments

Three datasets are adopted for the performance evaluation: the frontal subset of CAS-PEAL-R1, the Self-Collected High Resolution Images (SCH) dataset, and the Self-Collected Frontal-Face Images (SCF) dataset.

CAS-PEAL-R1 dataset is built by the Institute of Computing Technology, Chinese Academy of Sciences. All images are collected in limited conditions. It contains the head-shoulder images of 1,040 Chinese individuals, of which the frontal subset contains exactly 360 * 480 resolution pictures of the 1,040 individual frontal faces. In consideration of the actual work environment of the system being non-limited, two self-collected datasets are created by gathering and sorting out Web pictures to assess the performance more precisely. The Self-Collected High Resolution Images dataset contains 207 pictures, of which the resolutions are

Table 64.1 Face detection result

Methods	CAS-PEAL-R1		SCH		SCF	
	σ_r (%)	σ_p (%)	σ_r (%)	σ_p (%)	σ_r (%)	σ_p (%)
Proposed method	100	99.9	97.6	96.4	99.1	100
Viola and Jones	100	96.4	98.4	33.1	100	70.3
Zhu and Ramanan	99.8	99.2	96.4	53.8	94.2	96.8



Fig. 64.3 Some examples of the output of the face detectors on images from the two self-collected dataset. The results of the proposed method, the Viola and Jones method, and the Zhu and Ramanan method are set in the first, second, and third line, respectively

between 300 and 2,400 million pixels, and it contains 247 human faces in total. The Self-Collected Frontal-Face Images dataset contains 227 pictures and 223 human faces.

The proposed face detector in this chapter, classical Viola-Jones cascade detector in OpenCV [10], and effective part model-based detector of Zhu and Ramanan [12] are compared, and the results are shown in Table 64.1. The recall ratio σ_r and precision ratio σ_p are used as the measure standard. Some samples are shown in Fig. 64.3.

Conclusion can be drawn from Table 64.1 that three methods can all acquire ideal detection results on the frontal subset of CAS-PEAL-R1, of which the images are collected in limited conditions. The recall ratios and precision ratios of these three methods have slight differences on this dataset; however, three methods perform distinctly differently on the two other non-limited datasets. On the SCH dataset, the precision ratios of Viola and Jones method and Zhu and Ramanan method both have remarkable declines while compared to the proposed method in this chapter. It is because the backgrounds of the pictures in this dataset appear to be more complex, the images vary a lot in quality, and there is a lot of noise. Besides, when the size of the minimum scan window is fixed, the increase in resolution will significantly raise the amount of the windows; thus it will more likely expose the

weakness of low precision ratio of one method. On the SCF dataset, a major drop of precision ratio of the Viola and Jones method turns up. It is because the dataset contains a lot of ties of complex texture, which will lead to many misjudgments.

Between the recall ratio and the precision ratio, there is a trade-off. When one falls, the other rises. In order to measure the experimental result, the average F_1 -scores of the three methods are calculated as the evaluation standard. The mathematical formula of F_1 -score is

$$F_1 = \frac{2 \cdot \sigma_p \cdot \sigma_r}{\sigma_p + \sigma_r} \quad (64.4)$$

The average F_1 -scores of the three methods is 0.988, 0.768, and 0.88, respectively. It can be seen that the proposed method in this chapter has obvious advantage in F_1 -score.

Conclusion

The face detection and the landmark localization have been traditionally considered as two separable problems. Nevertheless, recent studies on common object detection has shown that incorporating parts during detection help better capturing object class spatial layout, which will significantly improve the detection accuracy. As inspired, we present an effective landmark localization-based face detection method.

In this chapter, the frontal subset of CAS-PEAL-R1, the Self-Collected High Resolution Images dataset, and the Self-Collected Frontal-Face Images dataset are adopted for the performance evaluation. The proposed face detector, the classical Viola-Jones cascade detector in OpenCV, and the effective part model-based detector of Zhu and Ramanan are compared. The average F_1 -scores of the three methods are 0.988, 0.768, and 0.88, respectively.

Comparing with the Viola and Jones method and Zhu and Ramanan method, the proposed method has obvious advantage in F_1 -score, which can meet practical requirements on detection accuracy.

Acknowledgements This work is supported partly by Important Science and Technology Project of Hainan Province under grant JDJS2013006 and partly by the Young Talent Frontier Project of Institute of Acoustics, Chinese Academy of Sciences.

References

1. Hjeltnäs E, Low BK. Face detection: a survey. *Comput Vis Image Underst.* 2001;83(3):236–74.
2. Yang MH, Kriegman D, Ahuja N. Detecting faces in images: a survey. *IEEE Trans Pattern Anal Mach Intell.* 2002;24(1):34–58.
3. Wu J, Brubaker SC, Mullin MD, et al. Fast asymmetric learning for cascade face detection. *IEEE Trans Pattern Anal Mach Intell.* 2008;30(3):369–82.

4. Li SZ, Zhang ZQ. FloatBoost learning and statistical face detection. *IEEE Trans Pattern Anal Mach Intell.* 2004;26(9):1112–23.
5. Anvar SMH, Yau WY, Teoh EK. Multiview face detection and registration requiring minimal manual intervention. *IEEE Trans Pattern Anal Mach Intell.* 2013;35(10):2484–97.
6. Ma K, Ben-Arie J. Vector array based multi-view face detection with compound exemplars. In: 2012 I.E. conference on computer vision and pattern recognition (CVPR), Providence, RI; 2012. p. 3186–93.
7. Dantone M, Gall J, Fanelli G, et al. Real-time facial feature detection using conditional regression forests. In: 2012 I.E. conference on computer vision and pattern recognition (CVPR), Providence, RI; 2012. p. 2578–85.
8. Rowley HA, Baluja S, Kanade T. Neural network-based face detection. *IEEE Trans Pattern Anal Mach Intell.* 1998;20(1):23–38.
9. Garcia C, Delakis M. Convolutional face finder: a neural architecture for fast and robust face detection. *IEEE Trans Pattern Anal Mach Intell.* 2004;26(11):1408–23.
10. Viola P, Jones MJ. Robust real-time face detection. *Int J Comput Vis.* 2004;57(2):137–54.
11. Cevikalp H, Triggs B, Franc V. Face and landmark detection by using cascade of classifiers. In: 10th IEEE international conference and workshops on automatic face and gesture recognition (FG), Shanghai, China; 2013. p. 1–7.
12. Zhu X, Ramanan D. Face detection, pose estimation, and landmark localization in the wild. In: IEEE conference on computer vision and pattern recognition (CVPR), Providence, RI, USA; 2012. p. 2879–86.
13. Uříčář M, Franc V, Hlaváč V. Detector of facial landmarks learned by the structured output SVM. In: VISAPP '12: proceedings of the 7th international conference on computer vision theory and application, Rome, Italy; 2012. p. 547–56.

Chapter 65

Image Enhancement Using a Fractional-Order Differential

Guo Huang, Li Xu, Qingli Chen, and Tao Men

Abstract To improve the effect of image enhancement, a kind of filter based on the noninteger step of a fractional-order differential was constructed. This paper describes the mathematical principles of the filter. The core idea of the algorithm is to appropriately adjust two freedom parameters, called *step* and *order*, to change the parameters of the filter within a certain range. The experimental results show that the proposed method, in contrast with the integer differential operator and the traditional fractional-order differential operator in image enhancement, was better in the noise-free case and had a certain amount of noise immunity in the noise case.

Keywords Fractional calculus • Noninteger step • Image enhancement

65.1 Introduction

Image enhancement is an area of fundamental research in image processing, and many algorithms for image enhancement already exist [1–4]. The theory of fractional calculus applications in image processing has become more and more widely applied and led to many important research results [5–10]. The key in fractional-order differential theory as applied to digital image processing is to increase a freedom parameter called *order* on the basis of an integer differential and, following an appropriate adjustment in the size of the order, use it to construct a corresponding mask operator to obtain a better image enhancement effect. However, in the method of fractional-order differentials as applied to digital image enhancement, the following issue arises: during digital image sampling, grids are used to discretize the image to attain a series of small cells and each small grid corresponds to the average brightness value of a simulation image, so the information between neighboring pixels is completely ignored. Because the traditional

G. Huang (✉) • Q. Chen • T. Men

Laboratory of Intelligent Information Processing and Application, Leshan Normal University,
614000 Leshan, China

e-mail: huanguoxuli@163.com

L. Xu

School of Physics and Electronics, Leshan Normal University, 614000 Leshan, China

© Springer International Publishing Switzerland 2015

W.E. Wong (ed.), *Proceedings of the 4th International Conference on Computer Engineering and Networks*, Lecture Notes in Electrical Engineering 355,

DOI 10.1007/978-3-319-11104-9_65

fractional-order differential method applied in image enhancement is usually based on the Grünwald–Letnikov theory in which the step between two variables is unit one, and important information between adjacent pixels is ignored, which results in a certain bias of the precision of the fractional-order differential numerical calculation. There is significant autocorrelation of the gray scale of pixels in a neighborhood, that is, adjacent pixels in an image have a high degree of correlation. The closer a pixel is to the target pixel, the greater the similarity between the two pixels, so a filter based on a noninteger step of a fractional-order differential is constructed, which contradicts the idea that the step in numerical calculations based on the Grünwald–Letnikov definition takes unit one, that is, the new method adds a parameter called a *step* on the basis of the Grünwald–Letnikov theory.

65.2 Related Theories and Analyses

Different fractional calculus definitions could be obtained from different angles to analyze problems. Among the many definitions of fractional calculus, there are four classic definitions, including Grünwald–Letnikov (G–L), Cauchy, Riemann–Liouville, and Capotu. This work mainly introduces the G–L definition; for the other fractional calculus definitions, the interested reader is referred to the relevant documents.

As we know, the n -order derivative of the function $I(x)$ is as follows:

$$I^n(x) = \lim_{h \rightarrow 0} \frac{1}{h^n} \sum_{m=0}^n (-1)^m \binom{n}{m} I(x - mh). \tag{65.1}$$

The order in Eq. (65.1) expands the differential order from integer n to decimal v by a Gamma function, so it can produce Eq. (65.2):

$${}_a^G D_t^v I(x) \triangleq \lim_{\substack{h \rightarrow 0 \\ nh = t - a}} h^{-v} (-1)^m \sum_{r=0}^n \frac{\Gamma(v + 1)}{\Gamma(m + 1)\Gamma(v - m + 1)} I(x - mh). \tag{65.2}$$

The method of polynomial interpolation is divided into four types, including the Lagrange interpolation method, the Newton forward (backward) interpolation method, the low section interpolation method, and the spline interpolation method. The present work makes use of the low section interpolation method to solve the interpolation problem of a noninteger of a fractional-order differential. Therefore, the following discussion briefly introduces the Lagrange interpolation formula as shown in Eq. (65.3):

$$\begin{aligned}
 L_n(x) &= y_0 l_0(x) + y_1 l_1(x) + \cdots + y_2 l_2(x) \\
 &= \sum_{k=0}^n y_k \frac{(x-x_0) \cdots (x-x_{k-1})(x-x_{k+1}) \cdots (x-x_n)}{(x_k-x_0) \cdots (x_k-x_{k-1})(x_k-x_{k+1}) \cdots (x_k-x_n)}. \quad (65.3)
 \end{aligned}$$

65.3 Mathematical Analysis of Filter Based on Noninteger Step of Fractional-Order Differential

Suppose the unit step of the original discrete image is a large window, the unit step is divided by n as a small window, and one large window is made up of n small windows. Thus, we could define two key concepts, a large window offset a and a small window offset b . The large window offset $a = \lfloor \frac{k}{n} \rfloor$, which stands for the integer distance deviating from the target pixel; if the value of parameter a is larger than the value of the target pixel, then the number of adjacent pixels deviating from the target pixel included in a numerical calculation of the G–L definition is greater; otherwise, the opposite is true. The small window offset $b = k - an$, which refers to the noninteger distance deviating from the target pixel; if the value of parameter b is larger than the value of the target pixel, the partition value of the unit step is greater, and the result is more accurate using the numerical calculation of the G–L definition; otherwise, the opposite is true. According to Eq. (65.2), to suppose the parameters $h = 1/n$, $k = an + b$, $a, b \in Z^+$ that could produce Eq. (65.4) as follows:

$$\begin{aligned}
 {}_0^G D_x^v I(x) &= \lim_{h \rightarrow 0} \lim_{nh = t-a} n^v \sum_{k=0}^{Nn-1} \binom{-v}{k} I\left(x - \frac{k}{n}\right) \\
 &\approx n^v \sum_{k=0}^{Nn-1} (-1)^k \binom{v}{k} I\left(x - a - \frac{b}{n}\right) \\
 &= n^v \sum_{k=0}^{Nn-1} (-1)^k \binom{v}{k} I\left(x - a - \frac{b}{n}\right) \\
 &= n^v \sum_{k=0}^{Nn-1} (-1)^k \frac{\Gamma(v+1)}{\Gamma(k+1)\Gamma(v-k+1)} I\left(x - a - \frac{b}{n}\right). \quad (65.4)
 \end{aligned}$$

In Eq. (65.4), because the corresponding grayscale value of the coordinate point $\varepsilon = x - a - b/n$ does not exist, it must make use of Eq. (65.3) to estimate the grayscale value of the coordinate point $\varepsilon = x - a - b/n$. The coordinate point ε is between $x - a - 1$ and $x - a$ ($x - a \in Z^+$), so the grayscale values of the shortest four pixels deviating from the coordinate point $\varepsilon = x - a - b/n$:

$$\begin{aligned}
 I\left(x-a-\frac{b}{n}\right) &= \frac{1}{6}\left[\left(\frac{b}{n}-1\right)\left(\frac{b}{n}\right)\left(\frac{b}{n}+1\right)I(x-a-2)-3\left(\frac{b}{n}-2\right)\left(\frac{b}{n}\right)\right. \\
 &\left.\left(\frac{b}{n}+1\right)I(x-a-1)+\dots+3\left(\frac{b}{n}-2\right)\left(\frac{b}{n}-1\right)\left(\frac{b}{n}+1\right)I(x-a)\right. \\
 &\left.-\left(\frac{b}{n}-2\right)\left(\frac{b}{n}-1\right)\left(\frac{b}{n}\right)I(x-a+1)\right].
 \end{aligned}
 \tag{65.5}$$

To a certain extent, we could eliminate some noise of an image by the weighting function $w(x)$, as in Eq. (65.6), during the course of the interpolation process. The weighting function $w(x)$ makes use of the features of a Gaussian function whereby the closer the target pixel gray value is to the mean gray value of an image within a certain range, the greater the weighting value of the corresponding target pixel is:

$$\begin{cases} m = \frac{1}{4}\sum_{i=-2}^1 I(x-a+i) & i = -2, -1, 0, 1. \\ w(x) = e^{-f(x)-m)^2/2\sigma^2} \end{cases}
 \tag{65.6}$$

Then by Eqs. (65.5) and (65.6), we could attain Eq. (65.7), which describes the process for partially eliminating image noise as follows:

$$\begin{aligned}
 I\left(x-a-\frac{b}{n}\right) &= \frac{\left(\frac{b}{n}-1\right)\left(\frac{b}{n}\right)\left(\frac{b}{n}+1\right)}{6}I(x-a-2)w(x-a-2) \\
 &- \frac{\left(\frac{b}{n}-2\right)\left(\frac{b}{n}\right)\left(\frac{b}{n}+1\right)}{2}I(x-a-1)w(x-a-1)+\dots \\
 &\frac{\left(\frac{b}{n}-2\right)\left(\frac{b}{n}-1\right)\left(\frac{b}{n}+1\right)}{2}I(x-a)w(x-a) \\
 &- \frac{\left(\frac{b}{n}-2\right)\left(\frac{b}{n}-1\right)\left(\frac{b}{n}\right)}{6}I(x-a+1)w(x-a+1).
 \end{aligned}
 \tag{65.7}$$

Finally, by Eqs. (65.4) and (65.7), we could attain the numerical expression of a noninteger step of a fractional-order differential of a one-dimensional signal as shown in Eq. (65.8):

$$\begin{aligned}
{}_0^G D_x^\nu I(x) &\equiv n^\nu \sum_{k=0}^{Nn-1} (-1)^k \binom{\nu}{k} I\left(x - a - \frac{b}{n}\right) \\
&\quad (-1)^k \frac{1}{\Gamma(k+1)\Gamma(\nu-k+1)} \left[\left(\frac{b}{n}-1\right) \left(\frac{b}{n}\right) \left(\frac{b}{n}+1\right) I(x-a-2) \right. \\
&\quad \quad \quad w(x-a-2) - 3 \left(\frac{b}{n}-2\right) \left(\frac{b}{n}\right) \left(\frac{b}{n}+1\right) I(x-a-1) \\
&= \frac{n^\nu \Gamma(\nu+1)}{6} \sum_{k=0}^{Nn-1} w(x-a-1) + 3 \left(\frac{b}{n}-2\right) \left(\frac{b}{n}-1\right) \left(\frac{b}{n}+1\right) I(x-a) \\
&\quad \quad \quad \left. w(x-a) - \left(\frac{b}{n}-2\right) \left(\frac{b}{n}-1\right) \left(\frac{b}{n}\right) I(x-a+1) w(x-a+1) \right].
\end{aligned} \tag{65.8}$$

65.4 Numerical Implement on Two-Dimensional Noninteger Step of Fractional-Order Differential Filter

As is known from the properties of a high-dimensional fractional Fourier transform, The theory of fractional-order differential application to two-dimensional image is separable in certain conditions. And it could obtain the Eqs. (65.9) and (65.10):

$$\begin{aligned}
\frac{\partial^\nu I(x,y)}{\partial x} &\equiv n^\nu \sum_{k=0}^{Nn-1} (-1)^k \binom{\nu}{k} I\left(x - a - \frac{b}{n}, y\right) \\
&\quad (-1)^k \frac{1}{\Gamma(k+1)\Gamma(\nu-k+1)} \left[\left(\frac{b}{n}-1\right) \left(\frac{b}{n}\right) \left(\frac{b}{n}+1\right) I(x-a-2, y) \right. \\
&\quad \quad \quad w(x-a-2, y) - 3 \left(\frac{b}{n}-2\right) \left(\frac{b}{n}\right) \left(\frac{b}{n}+1\right) I(x-a-1, y) \\
&= \frac{n^\nu \Gamma(\nu+1)}{6} \sum_{k=0}^{Nn-1} w(x-a-1, y) + 3 \left(\frac{b}{n}-2\right) \left(\frac{b}{n}-1\right) \left(\frac{b}{n}+1\right) I(x-a, y) \\
&\quad \quad \quad w(x-a, y) - \left(\frac{b}{n}-2\right) \left(\frac{b}{n}-1\right) \left(\frac{b}{n}\right) \\
&\quad \quad \quad \left. I(x-a+1, y) w(x-a+1, y) \right],
\end{aligned} \tag{65.9}$$

$$\begin{aligned}
 \frac{\partial^v I(x,y)}{\partial y} &\equiv n^v \sum_{k=0}^{Nn-1} (-1)^k \binom{v}{k} I\left(x, y - a - \frac{b}{n}\right) \\
 &\quad (-1)^k \frac{1}{\Gamma(k+1)\Gamma(v-k+1)} \left[\left(\frac{b}{n}-1\right) \left(\frac{b}{n}\right) \left(\frac{b}{n}+1\right) I(x, y - a - 2) \right. \\
 &= \frac{n^v \Gamma(v+1)}{6} \sum_{k=0}^{Nn-1} w(x, y - a - 2) - 3 \left(\frac{b}{n}-2\right) \left(\frac{b}{n}\right) \left(\frac{b}{n}+1\right) I(x, y - a - 1) \\
 &\quad w(x, y - a - 1) + 3 \left(\frac{b}{n}-2\right) \left(\frac{b}{n}-1\right) \left(\frac{b}{n}+1\right) I(x, y - a) \\
 &\quad \left. w(x, y - a) - \left(\frac{b}{n}-2\right) \left(\frac{b}{n}-1\right) \left(\frac{b}{n}\right) I(x, y - a + 1) w(x, y - a + 1) \right].
 \end{aligned}
 \tag{65.10}$$

Finally, it performs linear filtering operations with a size of $M \times N$ image $I(x,y)$, namely, implements the spatial convolution operation as the Eq. (65.11). Then, in accordance with the ratio column of the results after implementation of the convolution operation in eight directions, the final expression of the image enhancement operator based on a noninteger step of the fractional-order differential is combined using a linear weight, as shown in Eq. (65.12):

$$\left\{ \begin{aligned}
 g(x, y)_x^+ &= I(x, y) * w_x^+ \\
 g(x, y)_x^- &= I(x, y) * w_x^- \\
 g(x, y)_y^+ &= I(x, y) * w_y^+ \\
 g(x, y)_y^- &= I(x, y) * w_y^- \\
 g(x, y)_x^{45} &= I(x, y) * w_x^{45} \\
 g(x, y)_x^{135} &= I(x, y) * w_x^{135} \\
 g(x, y)^{225} &= I(x, y) * w_x^{225} \\
 g(x, y)_x^{315} &= I(x, y) * w_x^{315}
 \end{aligned} \right. , \tag{65.11}$$

$$\begin{aligned}
 g(x, y) &= \frac{g(x, y)_x^+}{\text{sum}(x, y)} g(x, y)_x^+ + \frac{g(x, y)_x^-}{\text{sum}(x, y)} g(x, y)_x^- + \frac{g(x, y)_y^+}{\text{sum}(x, y)} g(x, y)_y^+ + \dots \\
 &\quad \frac{g(x, y)_y^-}{\text{sum}(x, y)} g(x, y)_y^- + \frac{g(x, y)_x^{45}}{\text{sum}(x, y)} g(x, y)_x^{45} + \frac{g(x, y)_x^{135}}{\text{sum}(x, y)} g(x, y)_x^{135} + \dots \\
 &\quad \frac{g(x, y)^{225}}{\text{sum}(x, y)} g(x, y)^{225} + \frac{g(x, y)_x^{315}}{\text{sum}(x, y)} g(x, y)_x^{315}.
 \end{aligned}
 \tag{65.12}$$

65.5 Experiments and Theoretical Analysis

In general, neighboring pixels of a digital image have a high correlation, that is, the closer a pixel is to the target pixel, the greater the similarity between the two, but the distance between the two cannot exceed a certain range; otherwise, the results of the image enhancement obtained may be abnormal. The large window offset a stands for the distance deviating from the target pixel unit. In general, the set $1 < a < 5$, that is, the center pixel associated with distance 1–5 unit step has a high Autocorrelation. Thus, this work sets $k = 11$, $n = 3$, $v = 0.5$ to take into Eq. (65.10), and then we could attain eight directions mask operators whose size is 5×5 .

In Fig. 65.1, panel a is a lena picture that did not include noise, and panels b–e respectively show the results from carrying out image enhancement using a Sobel operator, Laplace operator, traditional fractional-order differential operator, and the operator proposed in this work, and panel f presents the results of image e minus image d. Images g–i respectively shows the effect of image enhancement using a Laplace operator, the traditional fractional-order differential operator, and the noninteger step of a fractional-order differential. Therefore, a comparative analysis can be made as follows. First, from images b and c, one can see that an integer-order differential operator primarily enhances the image edge information. However, it completely ignores regional image-smoothing information. Secondly, from images d and e, one can see that the fractional-order differential operator, compared with the integer-order differential, weakly strengthens the high-frequency information of the image and keeps the image of low-frequency information as much as possible. Finally, it will be seen that the operator proposed in this work compared with the traditional fractional-order differential operator further enhances the edge information of the image and retains the low-frequency regional information of the image.

Conclusion

Fractional calculus as the basis of fractal geometry and fractal dynamics has been widely applied in many subject areas and achieved remarkable success. However, many questions require in-depth study. A new method of image enhancement based on a fractional differential is proposed in this paper. The simulation experimental results show that the new image enhancement method can be used to enhance the edge information of an image while at the same time retaining the contour information of color images.

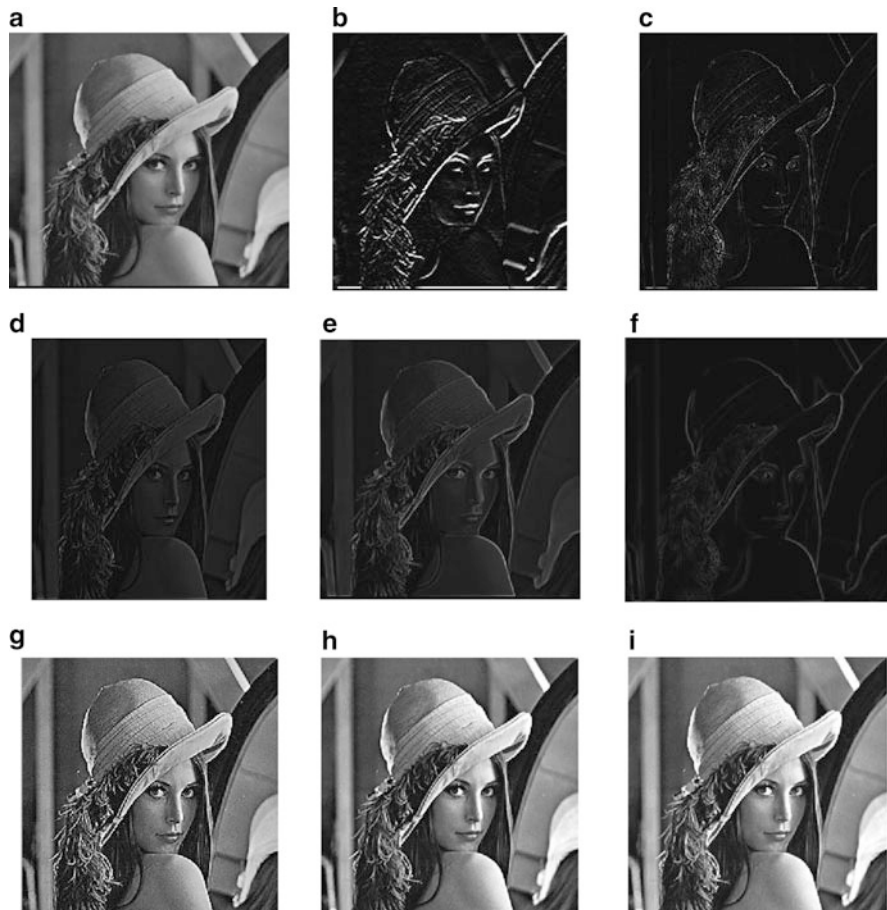


Fig. 65.1 Image enhancement operator and contrast effects of image enhancement (a) Original image (b) Sobel operator (c) Laplacian operator (d) Traditional fractional differential operator (e) Proposed operator in this work (f) The image after image (e) minus image (d) operator (g) Effect image by implementing Laplace operator (h) Effect image by implementing the traditional fractional differential operator (i) Effect image by implementing the proposed operator in this paper

Acknowledgements This work is partially supported by the National Natural Science Foundation of China (61201438), Technology Support Program of Sichuan Province Science (2012ZZ023), Scientific Research Fund of Sichuan Province Education Department (13ZB0104, 12ZA067, 13TD0014, 13ZB0105), Science and Technology Bureau of Leshan Town (12GZD067), Science and Technology Innovation Seed Fund of Sichuan Province (2012ZZ023), and the Scientific Research Fund of Leshan Normal University (Z1272). In addition, the authors would like to thank all the reviewers for their valuable suggestions.

References

1. Chen B, Latifi S, Kanai J. Edge enhancement of remote sensing image data in the DCT domain. *Image Vision Comput.* 1999;17(12):913–21.
2. Yang C-C. Image enhancement by the modified high-pass filtering approach. *Optik.* 2009;120(17):886–9.
3. Pu Y-F, Zhou J-L, Yuan X. Fractional differential mask: a fractional differential-based approach for multiscale texture enhancement. *IEEE Trans Image Process.* 2010;19(2):491–511.
4. Ramponi G. Contrast enhancement in images via the product of linear filters, signal processing. *Signal Process.* 1999;77(3):349–53.
5. Gilboa G, Sochen N, Zeevi YY. Variational denoising of partly textured images by spatially varying constraints. *IEEE Trans Image Process.* 2006;15(8):2281–9.
6. Jun Z, Zhi-hui W. A class of fractional-order multi-scale variational models and alternating projection algorithm for image denoising. *Appl Math Modell.* 2011;35(5):2516–28.
7. Huang G, Pu Y-F, Chen Q-L, Zhou J-L. Research on image denoising based on fractional order integral. *Syst Eng Electron.* 2011;33(4):925–32.
8. Sun X-L, Wang J-P, Song G-X. Anisotropic diffusion filtering method with a fidelity term. *Syst Eng Electron.* 2008;30(8):1421–3.
9. Bai J, Feng X-C. Fractional-order anisotropic diffusion for image denoising. *IEEE Trans Image Process.* 2007;16(10):2492–502.
10. Yuan X, Zhang H-Y, Yu J-B. Fractional-order derivative and design of fractional digital differentiators. *Acta Electron Sin.* 2004;32(10):1658–65.

Chapter 66

An Improved Fractional Differential Method for Image Enhancement

Qingli Chen and Guo Huang

Abstract In order to enhance texture details and edges information, an improved fractional differential (IFD) method for image enhancement is proposed. Firstly, the fractional directional derivative and its numerical method are deduced. In order to efficiently utilize the autocorrelation in the neighborhood, then, the improved fractional differential masks in eight directions are drawn. Experiments show that the proposed method can not only greatly improve the edges and texture information, but also can nonlinearly enhance the smooth area of digital images. And the images enhanced by the proposed method have better quality than before; it is an effectual method for rich textural images.

Keywords Image enhancement • Texture enhancement • Fractional differential

66.1 Introduction

Texture and edge contain important information about structure and content of image. Hence, enhancing these useful information is a very important task in image processing. Different types of algorithms can be employed for this purpose. Due to its simplicity and applicability, histogram equalization (HE) is the most commonly used method [1, 2], and it has been applied to many domains. Homomorphic filtering is another kind of image enhancement method by combining frequency filtering and gray transformation together. It represents an input image as the product of the illumination and reflectance in frequency domain. It can compress gray range and can improve the image contrast [3]. Main defects of homomorphic filtering are that some detail in low-frequency part will be lost, the dynamic range will be compressed, and holistic lightness will be reduced. The unsharp masking is a simple sharpening operator; it achieves image enhancement purpose by subtracting or smoothing original image [4, 5]. The Retinex is an image formation model-based enhancement. In Retinex, one or both of the illumination and the reflectance are first estimated, the estimated terms are next enhanced, and the output

Q. Chen (✉) • G. Huang

School of Computer Science, Leshan Normal University, 614004 Leshan, China

e-mail: cctcop75@163.com; huangguoxuli@yeah.net

© Springer International Publishing Switzerland 2015

W.E. Wong (ed.), *Proceedings of the 4th International Conference on Computer Engineering and Networks*, Lecture Notes in Electrical Engineering 355,

DOI 10.1007/978-3-319-11104-9_66

565

image is finally obtained by combining the enhanced terms [6]. However, the Retinex is empirical and experimental.

In recent years, image enhancement methods based on fractional differential have gotten much interest [7–9]. Many findings show that fractional differentiation is a powerful approach for dealing with texture details [8, 9]. Fractional differential-based methods can not only maintain the maximum low-frequency information, but also nonlinearly enhance the high-frequency information [10].

The chapter attempts to apply an improved R–L fractional differential mask for image texture enhancement. The chapter is organized as follows: the basic mathematical description of the method and its numerical implementation and the fractional differential mask for image enhancement are presented in Sect. 66.2. Experiments and result analysis are given in Sect. 66.3; the conclusion and further work are summarized in Sect. 66.4.

66.2 The Fractional Differential Algorithm

In this section, the definition of fractional derivatives in the Riemann–Liouville sense is briefly presented, and a fractional differential algorithm for texture enhancement is constructed too.

66.2.1 Discrimination of Fractional Differential

Several types of fractional derivative and integral have been proposed [11]. And in the Riemann–Liouville definition, the fractional derivative of a real function $f(x)$ with order ν , denoted by ${}_aD_x^\nu f(x)$, is given by

$${}_aD_x^\nu f(x) = \frac{1}{\Gamma(-\nu)} \int_a^x (x - \tau)^{-\nu-1} f(\tau) d\tau, \quad \nu < 0 \quad (66.1)$$

where $n = [\nu]$ is the function that can give an integer n which is equal to or not greater than ν . The operator $f^{(n)}(x)$ $n \in \mathbb{N}$ is the classical n th-order derivative of $f(x)$, and $\Gamma(x)$ is the Euler's gamma function. By choosing the integer $n = 1$, then, we have

$${}_aD_x^\nu f(x) = \sum_{k=0}^{n-1} \frac{(x-a)^{k-\nu} f^{(k)}(a)}{\Gamma(k-\nu+1)} + \frac{1}{\Gamma(n-\nu)} \int_a^x \frac{f^{(n)}(\tau)}{(x-\tau)^{\nu-n+1}} d\tau \quad (66.2)$$

Consider a grid of N points in the $\tau \in [0, x]$ interval with grid $\{x_j = jh, h = x/N, j = 0, 1, 2, \dots, N\}$; on the grid discretize the integral as

$${}_aD_x^\nu f(x) = \frac{1}{\Gamma(1-\nu)} \left[\frac{f(0)}{x^\nu} + \sum_{k=0}^{N-1} \int_{kx/N}^{(kx+x)/N} \left(\frac{d}{d\tau} f(x-\tau) \frac{d\tau}{\tau^\nu} \right) \right] \tag{66.3}$$

Using a back-difference scheme to compute first-order differential of $f(x)$

$$f'(x_j) = \frac{f_j - f_{j+1}}{x/N} + o(h) \tag{66.4}$$

Taking Eq. (66.4) into Eq. (66.3), we have [10]

$$\begin{aligned} {}_aD_x^\nu f(x) &\approx \frac{1}{(x/N)^\nu \Gamma(2-\nu)} \left\{ \frac{(1-\nu)f_N}{N^\nu} + \sum_{j=0}^{N-1} [(j+1)^{1-\nu} - j^{1-\nu}] [f_j - f_{j+1}] \right\} \\ &\approx \sum_{j=-1}^{N-1} w_j(\nu) f_j \end{aligned} \tag{66.5}$$

Equation (66.6) is a discrete approximation of analytic solutions of fractional differential, and it transforms the integral operation into simple multiplication and addition. In general, the approximation is imperfect, the relative error term generally depends on orders ν and N , and it should tend to zero as N approaches infinity.

66.2.2 The Improved Fractional Differential Mask

In general, image processing with a nonlinear filter is moving the filter mask from point to point in an image. This linear filtering operation is given by Eq. (66.6) [12]:

$$g(x, y) = \sum_{s=-a}^a \sum_{t=-b}^b w(s, t) f(x + s, y + t) \tag{66.6}$$

where $f(x, y)$ is the image to be processed and $w(s, t)$ is the template coefficient. Equation (66.5) can be extended to 2-D; the approximation of fractional partial differentiation on $0\pi/4$ is expressed as [10]

$$\frac{\partial^\nu f(x, y)}{\partial x^\nu} \cong \frac{1}{\Gamma(2-\nu)} \left(\begin{aligned} &f(x, y) + \sum_{k=1}^{n-1} [(k+1)^{1-\nu} - 2k^{1-\nu}] f(x-k, y) \\ &+ [(1-\nu)n^{-\nu} - n^{1-\nu} + (n-1)^{1-\nu}] f(x-n, y) \end{aligned} \right) \tag{66.7}$$

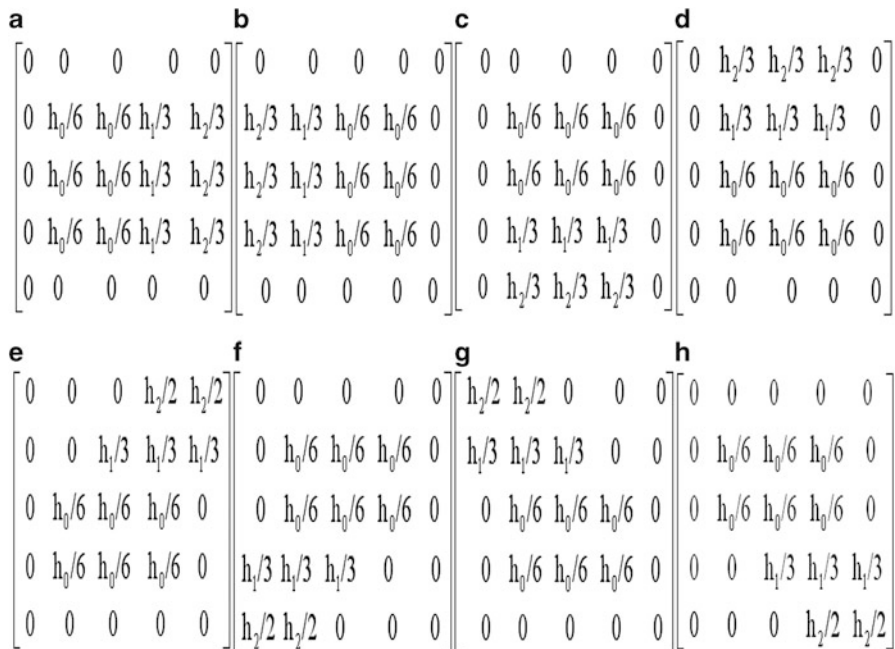


Fig. 66.1 Improved fractional differential masks on eight directions (a) $0\pi/4$, (b) $4\pi/4$, (c) $6\pi/4$, (d) $2\pi/4$, (e) $\pi/4$, (f) $5\pi/4$, (g) $3\pi/4$, (h) $7\pi/4$

There is great autocorrelation among neighborhood pixels in 2-D image, and to efficiently utilize the autocorrelation and make masks having anti-rotation, assume $n = 3$, $h_0 = 1/\Gamma(2 - \nu)$, $h_1 = (2^{1-\nu} - 2)/\Gamma(2 - \nu)$, and $h_2 = ((1 - \nu)n^{-\nu} - n^{1-\nu} + (n - 1)^{1-\nu})/\Gamma(2 - \nu)$; improved 5×5 R-L fractional differential masks on eight directions are shown in Fig. 66.1.

It can be seen from Fig. 66.1, in general, that the sum of coefficients of each mask is not equal to zero, which is a prominent difference between fractional and integral differential. In order to avoid the pixel value being more than 255, it is necessary to normalize the mask. Then, the final expression is

$$g(x, y) = \sum_{k=0\pi}^{7\pi/4} g_k(x, y) / \left[8 * \left(\sum_{i=0}^2 h_i \right) \right] \tag{66.8}$$

where $g(x, y)$ is the enhanced image and $g_k(x, y)$ ($k = 0, 1, \dots, 7$) are the enhanced images on eight directions.

66.3 Experiments and Result Analysis

To measure the performance of the improved fractional differential algorithm, experiments are carried out in this section. All experimental images are real images. The mask is 5×5 in size.

Observing Fig. 66.2 carefully, Fig. 66.2a is a rich-texture image. IFD can obviously enhance the high-frequency edge information. Due to the fact that the fractional differential of constant is not equal to zero, IFD can nonlinearly enhance texture details in those areas that pixel values little changes. Figure 66.2 shows that IFD in $0 < \nu < 1$ is a multi-scale fractional operator; here ν is the scale-controlling parameter. After employing IFD with different fractional orders, the edges are becoming more clear-cut, and the complex textural details are becoming clearer than before. The contrast of the image is increasing with the fractional differential order. We also see from Fig. 66.2 that there is slight texture and edge enhancement



Fig. 66.2 Image enhancement of Goldhill by IFD with different fractional differential orders (a) $\nu = 0.0$, (b) $\nu = 0.1$, (c) $\nu = 0.3$, (d) $\nu = 0.5$, (e) $\nu = 0.7$, (f) $\nu = 0.9$

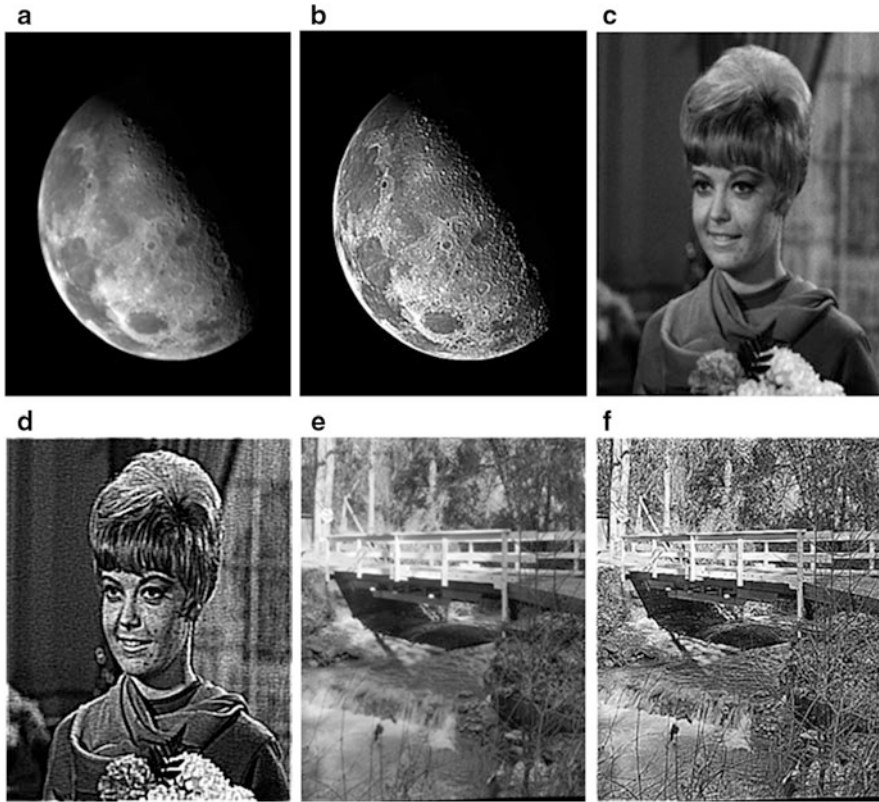


Fig. 66.3 Image enhancement results by the proposed method: (a), (c), and (d) are original images, and (b), (d), and (f) are enhanced images with order $\nu = 0.93$, 0.91 , and 0.92 , respectively

when the order is in the range of $0-0.8$, the texture of the image is increasing evidently when the order is bigger than 0.8 , and subjectively the visual effect is the best when $\nu = 0.92$. Some other results are shown in Fig. 66.3.

In our next experiment, the IFD method compares with HE, the Retinex method [6], G–L fractional differential, and R–L fractional differential [7, 10]. The results of comparison are shown in Fig. 66.4. It can be seen from Fig. 66.4 that all algorithms mentioned above get good enhancement performances. HE has the better result, but the texture enhancement is finite, and has the minimum information entropy. Retinex_mccann99 can greatly increase brightness and enhance the dark area (hair), but ineffectively enhance texture details and edges. The fractional differential methods could nonlinearly enhance the complex texture details, but also can enhance the contrast. By comparing G–L and R–L methods, the IFD has the best visual effect (see Fig. 66.4d–f).



Fig. 66.4 Texture enhancement capability comparison of Lena image (a) original image (b) HE, (c) Retinex mccann99, (d) G-L with $\nu=0.8$, (e) R-L with $\nu=0.8$, (f) IFD with $\nu=0.92$

Conclusion

Fractional differential is becoming an important mathematical tool for image processing, and it has become a hotspot in image processing. In this chapter, an improved method IFD for image texture details and edges enhancement is presented, which has the advantage of enhancing edges, as well as keeping texture details of image. The IFD method can control the degree of enhancement effects by fractional differential order. Comparison with state-of-the-art methods involving fractional differential shows better results in terms of quality.

Acknowledgements This work is partially supported by the National Natural Science Foundation of China (No. 61201438), the Scientific Research Fund of Sichuan Province Education Department (13ZB0104, 13TD0014), the Science and Technology Innovation Seeding Fund of Sichuan Province (2012ZZ023), and the Scientific Research Fund of Leshan Normal University (Z1272); the authors would like to thank all the reviewers for their valuable suggestions.

References

1. Pizer SM, Amburn EP, Austin JD, et al. Adaptive histogram equalization and its variations. *Comput Vis Graph Image Process.* 1987;39:355–68.
2. Stark JA. Adaptive image contrast enhancement using generalizations of histogram equalization. *IEEE Trans Image Process.* 2000;9(5):889–96.
3. Seow MJ, Asari VK. Ratio rule and homomorphic filter for enhancement of digital colour image. In: 13th European symposium on artificial neural networks. New York: IEEE Press; 2006. p. 2507–11.
4. Polesel A, Ramponi G, Mathews VJ. Image enhancement via adaptive unsharp masking. *IEEE Trans Image Process.* 2000;9(3):505–10.
5. Ilk HG, Jane O, Ilk Ö. The effect of Laplacian filter in adaptive unsharp masking for infrared image enhancement. *Infrared Phys Technol.* 2011;54(5):427–38.
6. Funt B, Ciurea F, McCann J. Retinex in Matlab. *J Electron Imaging.* 2004;13(1):48–57.
7. Yang ZZ, Zhou JL, Yan XY, et al. Image enhance based on fractional differentials. *J Comput Aid Des Comput Graph.* 2008;20(3):343–8 [in Chinese].
8. Pu YF, Zhou JL, Yuan X. Fractional differential mask: a fractional differential-based approach for multi-scale texture enhancement. *IEEE Trans Image Process.* 2010;19(2):491–511.
9. Pu YF, Wang WX, Zhou JL. Fractional differential approach to detecting textural features of digital image and its fractional differential filter implementation. *Sci China Ser F Inf Sci.* 2008;51(9):1319–39.
10. Chen QL, Pu YF, Huang G, et al. 0~1 Order Riemann–Liouville fractional differential enhancing mask of digital image. *J Univ Electron Sci Technol China.* 2011;40(5):772–6 [in Chinese].
11. Oldham KB, Spanier J. *The fractional calculus: theory and applications of differentiation and integration to arbitrary order.* New York: Academic Press; 1974. p. 45–60.
12. Gonzalez RC, Woods RE. *Digital image processing.* Upper Saddle River: Prentice-Hall; 2001. p. 152–68.

Chapter 67

On Qualitative Analysis of High-Contrast Patches in Range Images

Qingli Yin

Abstract In “On the Nonlinear Statistics of Range Image Patches,” H. Adams and G. Carlsson use computational topology to the data set of 5×5 and 7×7 range image patches and show that some density subsets have the topology of a circle. In this chapter, we study the space of range images locally by expanding them to 8×8 and 9×9 patches and experimentally prove that the subspaces of the space of all high-contrast patches exist in both cases, topologically equivalent to a circle and the Klein bottle, respectively, which have improved Adams and Carlsson’s results.

Keywords Range image • Persistent homology • Barcode • High-contrast patch • Experiment

67.1 Introduction

A large number of results on statistics of images have been obtained by researchers [1–3]. Most successful works on image statistics concentrate on local region properties, modeled by spaces of $n \times n$ patches of pixels in images with small n , while the whole statistics of pixel values in images has not yet been depicted. One main advantage of analyzing a space of images locally is to reduce the dimensional problem. Because when we believe an image as a vector, its dimension will be very high. In 1992, J. H. van Hateren found that a local statistics may supply a lot of information about the global statistical features of images [3]. In 2003, Lee, Pedersen, and Mumford depicted distributions of 3×3 patches from optical and range images; they show that high-contrast 3×3 range patches are densely gathered around the binary patches [2]. In 2008, Carlsson et al. studied optical patches with topological tools; they show a one high-density subset called the primary circle and a two-dimensional subset having the topology of a Klein bottle [4]. In 2009, Adams et al. discussed 5×5 and 7×7 range patches and proved that they’ve possessed the primary circle behavior [5]. In this chapter, we will continue to

Q. Yin (✉)

Department of Laboratory and Facility Management, Shandong Jianzhu University,
250101 Jinan, China

e-mail: yinq169@163.com

© Springer International Publishing Switzerland 2015

W.E. Wong (ed.), *Proceedings of the 4th International Conference on Computer Engineering and Networks*, Lecture Notes in Electrical Engineering 355,
DOI 10.1007/978-3-319-11104-9_67

573

study spaces of $n \times n$ high-contrast range image patches with small n . We find that how many n is, spaces of $n \times n$ range image patches still have similar properties as $n=3, 4, 5, 6, 7$. With a large amount of calculation, we only take $n=8, 9$ and we get similar results for the spaces of $n \times n$ image patches as the cases $n=3, 4$. Our results will improve the techniques of image compression [6].

67.2 Persistent Homology

Persistent homology is an algebraic method for measuring the underlying space's topological features through only a finite sampling. In order to use the persistent homology, firstly, we construct complexes for a given point set S sampled from an underlying space X . Because both the Čech and VR complexes may produce much higher dimensional simplices, we use lazy witness complexes in practice.

For a given point cloud S , a landmark subset L , let $m(p)$ be the distance $p \in S$ to the closest landmark point. A lazy witness complex $LW_1(S, L, \epsilon)$ is defined as below: (1) the vertex set is L ; (2) for vertices a and b , edge $[ab]$ is in $LW_1(S, L, \epsilon)$ if there exists a witness point $p \in S$ so that

$$\max\{d(a, p), d(b, p)\} \leq \epsilon + m(p)$$

(3) A higher dimensional simplex is in $LW_1(S, L, \epsilon)$ if all of its edges are in $LW_1(S, L, \epsilon)$. We give a simple example. Considering a 20-point set sampled from points on a figure “8” (unknown to us), could we determine the underlying space? We construct a sequence of lazy witness complexes. Here, we choose six landmark points and $\epsilon = 0.05, 0.5, 0.65$, and 0.8 as shown in Fig. 67.1a–d, respectively. From Fig. 67.1, we observe that Fig. 67.1c gives the right answer.

Obviously the values of parameter of ϵ are very important, which we do not know how to choose without priori information of the underlying space; however, by the JAVAPLEX software package developed by Adams and Tausz [7], we can calculate the Betti numbers over a range of ϵ values and illustrate the result by a Betti barcode. The intuition explanation is that long intervals correspond to actual topological characteristics of the underlying space while short ones are explained as noise.

67.3 Range Data Sets

We draw two data sets of high-contrast 8×8 and 9×9 patches from the range images in the Brown database by Huang et al. [8], a set of about 200 range images. The Brown database can be downloaded from the website <http://www.dam.brown.edu/ptg/brid/range/index.html>. Our main spaces X_8 and X_9 are sets of 8×8 and 9×9 patches of high contrast built by seven steps, which are very similar to the

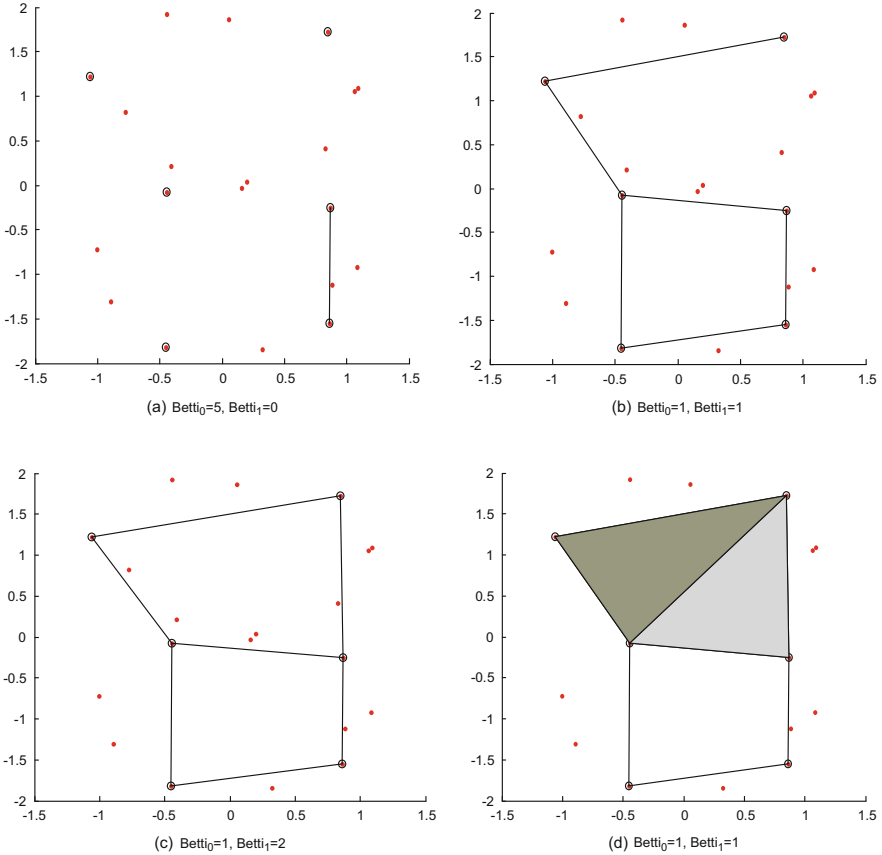


Fig. 67.1 Lazy witness complexes for points sampled from figure “8”

procedures used [4, 5]. Each of range data sets X_8 and X_9 contains 374,500 and 294,605 high-contrast log range patch, respectively. For computational feasibility, we randomly choose 50,000 patches from each X_8 and X_9 , denoted by \bar{X}_8 and \bar{X}_9 , respectively.

67.4 Relation Between Klein Bottle and Space of Binary Polynomials

As well known, the Klein bottle can be constructed by identifying opposite sides of a square as shown in Fig. 67.2.

We consider all binary polynomials \wp in the form of $a_2(a_1x + b_1y)^2 + b_2(a_1x + b_1y)$; here (a_1, b_1) and (a_2, b_2) are points on a planar unit circle S^1 . We define a map $g : S^1 \times S^1 \rightarrow \wp$ by $(a_1, b_1, a_2, b_2) \rightarrow a_2(a_1x + b_1y)^2 + b_2(a_1x + b_1y)$ [4]. Note that

Fig. 67.2 Representation of Klein bottle as an identification space

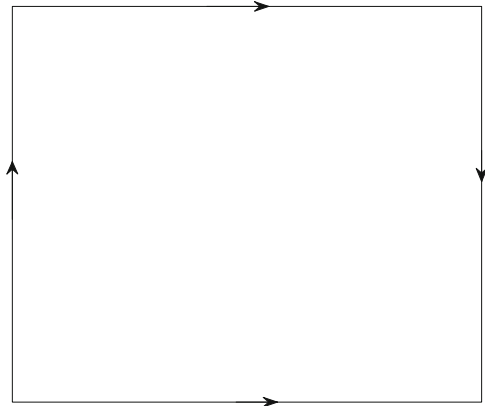
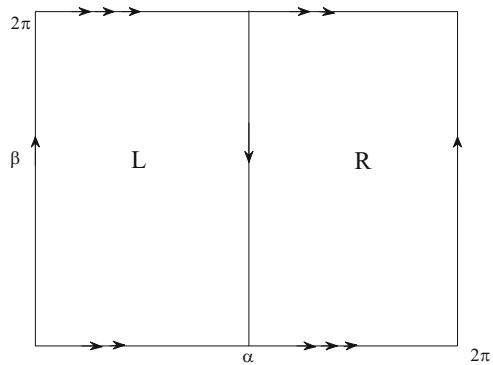


Fig. 67.3 Klein bottle, the image of the map g



the points (a_1, b_1, a_2, b_2) and $(-a_1, -b_1, a_2, -b_2)$ have the same polynomial as their image; hence the relation $(a_1, b_1, a_2, b_2) \sim (-a_1, -b_1, a_2, -b_2)$ is an equivalent relation. Let us present the pairs (a_1, b_1) and (a_2, b_2) by α and β separately; both α and β take value at the interval $[0, 2\pi]$; thus the equivalent relation can be denoted by $(\alpha, \beta) \sim (\pi + \alpha, 2\pi - \beta)$; therefore the space $\mathcal{I} = \text{im}(g)$ is homeomorphic to $S^1 \times S^1 / (\alpha, \beta) \sim (\pi + \alpha, 2\pi - \beta)$.

A torus can be expressed by pasting a square with the opposite edges, similar to the representation of the Klein bottle instead of pasting them with reversal orientation. The result of the map g on the torus is demonstrated in Fig. 67.3. The right half, indicated by R in Fig. 67.3, is identified by g with the left half indicated by L while the identifications on the boundary are as shown. Each half is a standard representation of the Klein bottle; thus the image of g is homeomorphic to the Klein bottle and so is \mathcal{I} [4].

Define a map $h_8 : \mathcal{I} \rightarrow S^{63}$ through a compound by evaluating the polynomial at each point in the grid $H_8 = \{-3, -2, -1, 0, 1, 2, 3, 4\} \times \{-3, -2, -1, 0, 1, 2, 3, 4\}$ subtracting the mean and normalizing. Similarly, we define a map $h_9 : \mathcal{I} \rightarrow S^{80}$ on the grid $H_9 = \{-4, -3, -2, -1, 0, 1, 2, 3, 4\} \times \{-4, -$

3, -2, -1, 0, 1, 2, 3, 4}. As shown by Carlsson et al. [4], the image $\text{im}(h_n)$ ($n = 8, 9$) is homeomorphic to the Klein bottle.

67.5 Experimental Results

In order to obtain our experimental results, firstly we insert the Klein bottle into unit sphere S^{63} and S^{80} , respectively. We uniformly choose n points from the unit circle (indicated by $\{x_1, \dots, x_n\}$ and $\{y_1, \dots, y_n\}$ separately); all possible tuples (x_i, y_j) form a point set of the torus $S^1 \times S^1$. Secondly, we transform each of the n^2 points into S^{63} and S^{80} by maps $h_8 \circ g, h_9 \circ g$, and denote the images as $K_8(n)$ and $K_9(n)$, respectively. Here we take $n = 140$; Figs. 67.4 and 67.5 display the PLEX results for the spaces $K_8(140)$ and $K_9(140)$. Each of the figures indicates $\beta_0 = 1, \beta_1 = 2, \beta_2 = 1$, which are the Betti numbers of the Klein bottle, that is, $K_8(140)$ ($K_9(140)$) is a suitable approach of the Klein bottle in S^{63} (S^{80}).

Given $x \in X$ and $k > 0$, set $\rho_k(x) = |x - x_k|$, where x_k is the k th nearest neighbor of x . Larger k values give more global estimations, whereas small k values produce local density estimates. As to a fixed k , we sort the points of X by descending the density and pick the points denoted by $X(k, p)$ whose densities are in the top p percent. The core subset $X(k, p)$ may supply important topological information, which may be lost for all the points of X . The core subset, which depends on the patch size $n \times n$ and the density parameters k and p , is denoted by $\bar{X}_n(k, p)$. Here we consider core subsets with density parameter $k = 300$ and cut percentage $p = 30\%$.

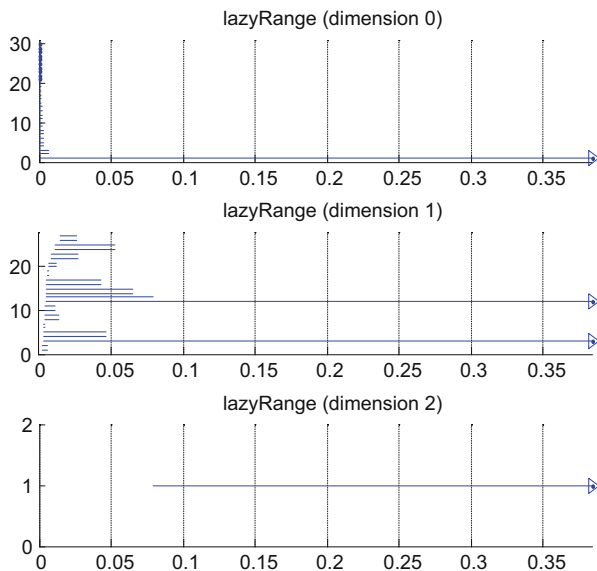


Fig. 67.4 Barcodes for $K_8(140)$

Fig. 67.5 Barcodes for $K_9(140)$

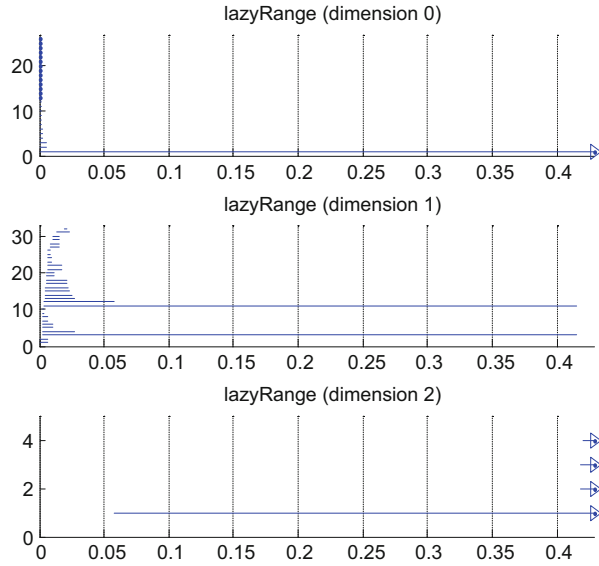
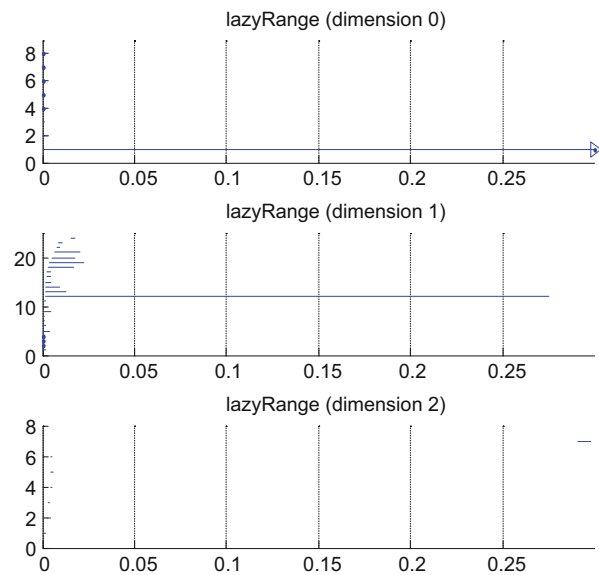


Fig. 67.6 Barcodes for $\bar{X}_8(300, 30)$



We take the core subsets $\bar{X}_8(300, 30)$ and $\bar{X}_9(300, 30)$ for 8×8 and 9×9 patches and compute the barcode by JAVAPLEX software; sample Betti barcode plots for the core subsets are shown in Figs. 67.6 and 67.7. Obviously, they give Betti numbers $\beta_0 = 1$, $\beta_1 = 1$, and $\beta_2 = 0$, which means that they have the topology of a circle, visible in Figs. 67.8 and 67.9. We run many trials on $\bar{X}_8(300, 30)$ and \bar{X}_9

Fig. 67.7 Barcodes for $\bar{X}_9(300, 30)$

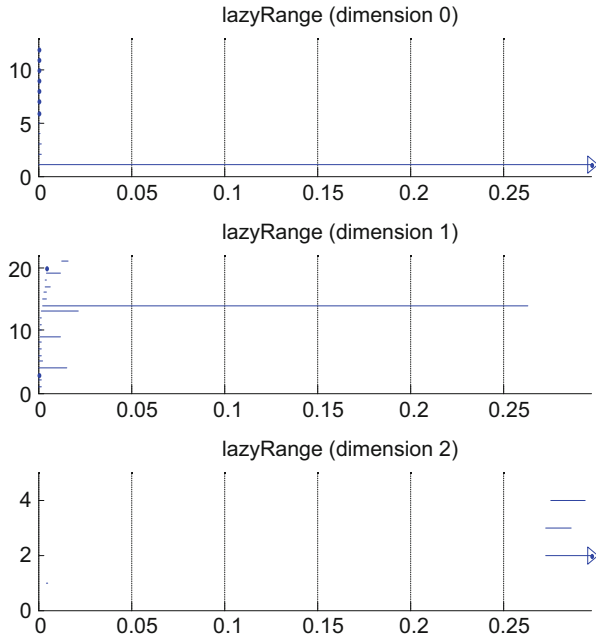
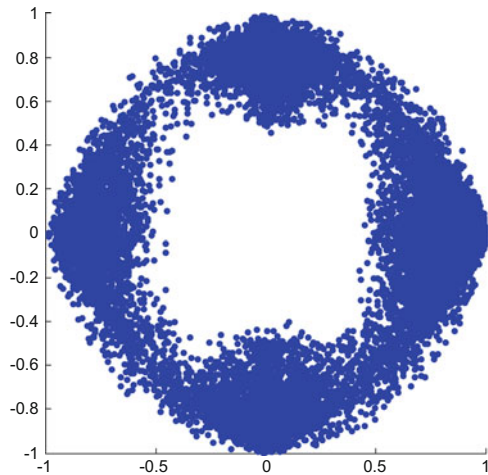


Fig. 67.8 Projection of $\bar{X}_8(300, 30)$



(300, 30) by choosing different landmark points. In each experiment, the PLEX plot gives $\beta_0 = 1, \beta_1 = 1$, and $\beta_2 = 0$ for nearly a whole range of ϵ values, and other Betti plot intervals are very short. Hence the results are very robust.

As shown above, S^{63} and S^{80} have subspaces $K_8(140)$ and $K_9(140)$, respectively, whose homology is that of a Klein bottle. Through $K_8(140)$ and $K_9(140)$, we construct subspaces of X_8 and X_9 so that the subspaces have the topology of the

Fig. 67.9 Projection of $\bar{X}_9(300, 30)$

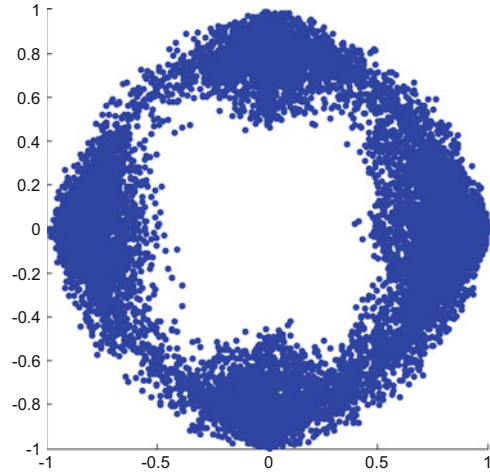
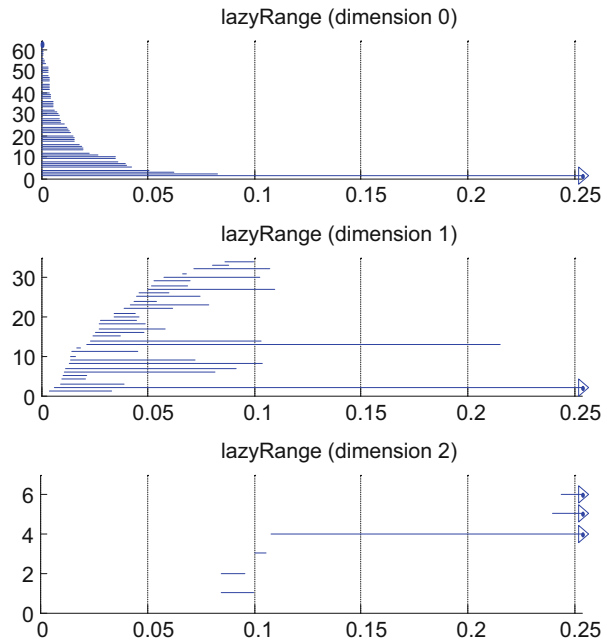


Fig. 67.10 PLEX results for $K_8(140, 9)$



Klein bottle proved by experimentation. We describe how to get subspaces of X_8 and X_9 as below.

For each point $x \in K_8(140)$, we compute the Euclidean distance from x to every point of X_8 , and then we take m closest points of X_8 to the point. We collect all m closest points to any $x \in K_8(140)$ to obtain the subspace of X_8 and denote it as $K_8(140, m)$. Similarly, we can get the subspace $K_9(140, m)$ of X_9 .

Fig. 67.11 PLEX results for $K_9(140, 9)$

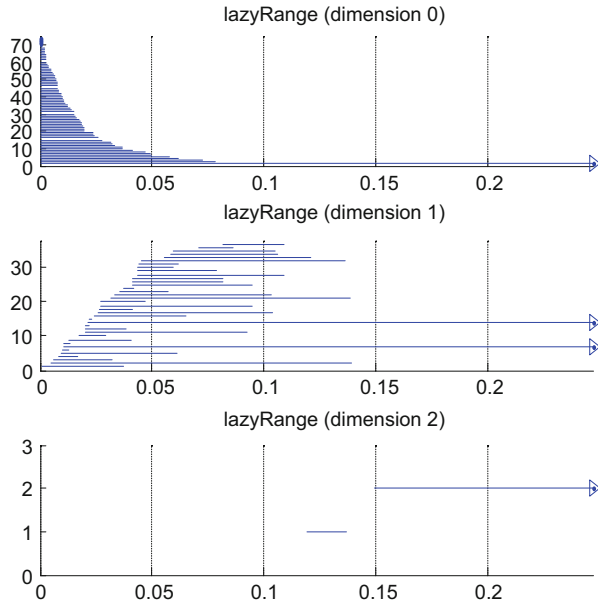


Figure 67.10 shows the PLEX result for the space $K_8(140, 9)$. We observe that the β_0 barcode clearly displays the single component nearly on the whole interval, the β_1 barcode gives two lines at an interval $[0.11, 0.21]$ of parameter ϵ , and finally the β_2 barcode shows a single line on roughly the same interval. It indicates that $K_8(140, 9)$ has the topology of the Klein bottle. Figure 67.11 shows that $K_9(140, 9)$ have the topology of the Klein bottle. We do more than 100 experiments on $K_8(140, 9)$ and $K_9(140, 9)$ by selecting different landmark points 60–80; all PLEX barcodes show that $\beta_0 = 1$, $\beta_1 = 2$, and $\beta_2 = 1$ at a proper interval of ϵ values; hence the results are very stable.

Conclusion

In this chapter, we study qualitative topological analysis of spaces of 8×8 and 9×9 range patches with the persistent homology. As the main merit, it allows us to detect nonlinear structures within the data which would be very hard to find out by statistical techniques. We’ve proved that the spaces of high-contrast 8×8 and 9×9 patches have core subsets modeled as a circle. Through the relation between the spaces of range patches and the space of binary polynomials, we experimentally find that there are subspaces in X_8 and X_9 , which have the homology of the Klein bottle, which generalize the results. We check our discovery by adopting the same method to the distinct size patches.

References

1. Grenander U, Srivastava A. Probability models for clutter in natural images. *IEEE Trans Pattern Anal Mach Intell.* 2001;23(4):424–9.
2. Lee B, Pedersen KS, Mumford D. The non-linear statistics of high-contrast patches in natural images. *Int J Comput Vis.* 2003;54(3):83–103.
3. Hateren JH. Theoretical predictions of spatiotemporal receptive fields of fly LMCs, and experimental validation. *J Comput Physiol A.* 1992;171(2):157–70.
4. Carlsson G, Ishkhanov T, Silva V, Zomorodian A. On the local behavior of spaces of natural images. *Int J Comput Vis.* 2008;76(1):1–12.
5. Adams H, Carlsson G. On the nonlinear statistics of range image patches. *SIAM J Image Sci.* 2009;2(1):110–7.
6. Perea JA, Carlsson G. A Klein-bottle-based dictionary for texture representation. *Int J Comput Vis.* 2014;107(1):75–97.
7. Adams H, Tausz A. Javaplex tutorial. http://javaplex.googlecode.com/svn/trunk/reports/javaplex_tutorial/javaplex_tutorial.pdf.
8. Huang J, Lee A, Mumford D. Statistics of range images. In: *Proceedings of IEEE conference on computer vision and pattern recognition, Hilton Head Island, SC, vol. 1; 2000.* p. 324–31.

Chapter 68

An Improved Method of Tracking and Counting Moving Objects Using Graph Cuts

Mingjie Zhang and Baosheng Kang

Abstract To improve the efficiency of tracking and counting moving objects under occlusion conditions, an improved tracking and counting method is proposed. First, a graph cut method is employed to segment an image from a static scene, and foreground objects are identified by the sizes and positions of foreground areas obtained. Second, to distinguish moving objects, object classification based on shape is applied. In addition, in the object tracking phase, the proposed tracking method is used to calculate the centroid distance of neighboring objects and facilitate object tracking and people counting under occlusion conditions. In the experiments of moving object tracking and people counting in two video clips, compared with traditional methods, the experimental results show that the proposed method can increase the averaged detection ratio by approximately 11 %. Thus, the method can be used to reliably track and count.

Keywords Graph cuts • Object tracking • Image segment • Object classification

68.1 Introduction

Object tracking and counting have been widely used in many public domains [1]. In recent years, a number of elegant algorithms have been developed. In Marcenaro et al.'s study [2], to reduce the influence of occlusion, a linear Kalman filter was used in object tracking by matching shape features. Lien et al. [3] used a multimode method to increase the efficiency and accuracy of object tracking in crowded conditions. Six modes of object tracking were defined using a heuristic approach,

M. Zhang (✉)

School of Information Science and Technology, Northwest University, 710127 Xi'an, China

School of Economics and Management, Xi'an University of Post and Telecommunications, 710061 Xi'an, China

e-mail: 75711650@qq.com

B. Kang

School of Information Science and Technology, Northwest University, 710127 Xi'an, China

and counting was finally performed by template tiling. Chan [4] proposed using a Gaussian process as a characteristic function, which showed textural features from crowded segmentation. To accurately count people, Fehr et al. [5] compared various counting methods, using an extended Kalman filter to implement the segmentation method in different backgrounds.

The aforementioned methods of tracking objects relies on effective object segmentation and are sensitive to changes in illumination. Thus, to improve the accuracy of tracking and counting, an improved tracking and counting method is proposed. The main contributions of this paper consist of (1) using a graph cut method to segment images from a static scene for object tracking and, in the process of tracking, (2) using the proposed algorithm to carefully consider the tracking states of an object's merger and split.

68.2 Overview of Algorithm

The proposed framework of the object tracking and counting algorithm is shown in Fig. 68.1. First, graph cuts are used to segment moving objects from the video frame. Then the moving objects are distinguished using an object classification method based on shape. After acquiring the foreground objects, four states, including new, leaving, merged, and split, are defined based on the presence of an object in the current frame, and the four states are assigned to the detection of moving objects. In particular, to reduce occlusion effects, objects are identified as being in states of merging or splitting through an analysis of the centroid distances between objects in the previous frame, and further tracking is carried out. Finally, to obtain the objects' tracking and counting results, objects are tagged in four states [6].

68.3 Image Segmentation Using Graph Cuts

A foreground object can be obtained using the graph cut method [7]. Using this method, the following energy related to the labeling function λ was minimized:

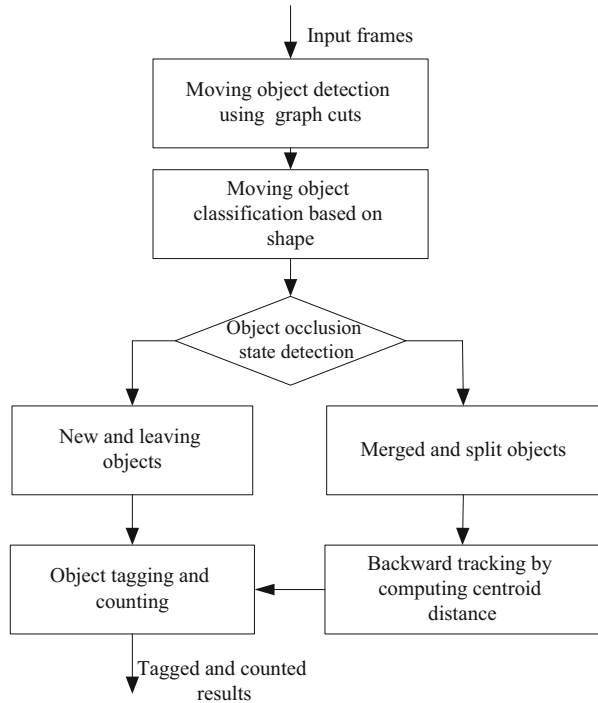
$$J(\lambda) = \varepsilon_D(\lambda) + \varepsilon_R(\lambda), \quad (68.1)$$

where ε_D measures the likelihood P_i that a pixel belongs to an object i :

$$\varepsilon_D(\lambda) = - \sum_{x \in \Omega^i} \sum_{i=0}^N \ln(P_i(x)) \delta(\lambda(x) - i). \quad (68.2)$$

In Eq. (68.2), $\delta(m)$ is the characteristic function. Here, if $m = 0$, then $\delta(m) = 1$, and if $m = 1$, $\delta(m) = 0$. ε_R is

Fig. 68.1 Framework of proposed method



$$\epsilon_R(\lambda) = R_\Omega \sum_{x \in \Omega'} \sum_{x \in N^l(x)}^N F(I(x, t), I(z, t)) [1 - \delta(\lambda(x) - \lambda(z))]. \quad (68.3)$$

In Eq. (68.3), $F: IR \times IR \mapsto IR^+$ is a decreasing function that penalizes the spatial discontinuities of the segmentation according to the image data. $R_\Omega > 0$ is the regularization parameter, and a cost is then incurred when two neighboring pixels x and z have different labels, i.e., $\lambda(x) \neq \lambda(z)$ and $\delta(\lambda(x) - \lambda(z)) = 0$.

This regularization is equivalent to the minimization of the length of the boundaries between objects. Note that the neighborhood of a pixel x involved in Eq. (68.1) is defined as

$$N^l(x) = \{z \in \Omega'0 < |z - x| \leq l\}. \quad (68.4)$$

With such a model, the foreground image is instantaneously obtained.

68.4 Shape-Based Object Classification

In this paper, several shape features of moving objects are defined and support vector machines (SVMs), which are based on small-sample statistical learning theory, are chosen to classify different objects.

Several shape features of moving objects are defined as follows.

Height–width ratio: ratio of the bounding rectangle height and the bounding rectangle width.

Discrete degree: ratio of square of object perimeter (P) and object area (A).

Fill ratio: ratio of size of blob segment area and the total bounding rectangle area.

Hu invariant moments [8]: invariant about scale, translation, and rotation.

Segment area: number of object pixels.

Perimeter: border pixels of blob.

Considering that the tagging of many samples is a complex task, SVM is used to classify different objects.

SVMs [9] have been proposed for classifier learning. The proposed method uses SVM for classification with the selected features and can distinguish moving objects between people and other objects.

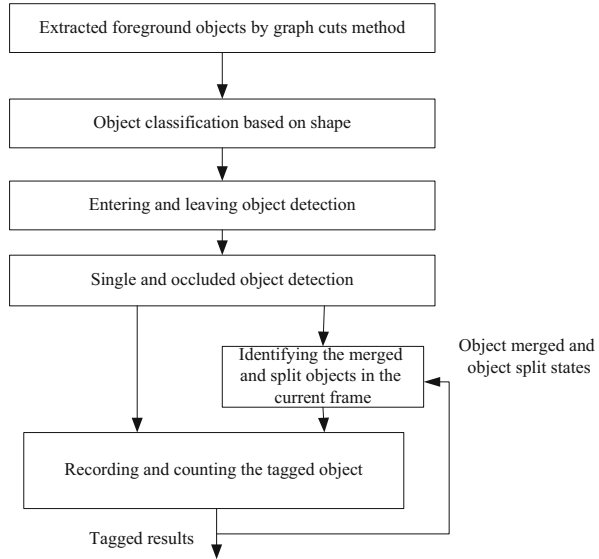
68.5 Method for Tracking and Tagging Objects

After having the segmented results from the graph cut method, based on the completeness of the regional contours, areas of interest are identified from the foreground image. When object regions are detected from the areas of interest, the physical constraints of the human body are considered and the area of the shape and the dynamic range of pixel grayscale values are included. When objects match the constraints, ellipses with minimized areas are constructed using ellipse radii, centroids, distances, and the corresponding position parameters.

Figure 68.2 shows a framework for tracking and tagging objects. In the improved tracking method, four tracking states, including new object, leaving object, merged object, and split object, are set. The method is used to understand the current frame. *New object* indicates that an object is entering the scene; *leaving object* means that an object is leaving the scene. With merged object and split object states, contact with the object is detected in adjacent frames. By backward tracking the objects that appear in the previous frame, the merging and splitting of an object in the current frame can be identified. Finally, relying on the continuity of the location of the tagged characters in the previous frame, tags are assigned to a single object.

Compared with the traditional overlap tracking method, our proposed tracking method performs backward tracking of tagged objects in the previous frame. In the current and previous frames, we analyze the centroid distances between objects in merged and split states. A dynamic radius is obtained by $s = (w + h)/2$, where w and

Fig. 68.2 Framework of tracking and tagging objects



h are the long and short radii of an object ellipse, respectively. An object in a merged state in the current frame is recognized by determining that the two adjacent elliptical centroid distances are less than the sum of their dynamic radii in the previous frame. To determine split objects, it is to conform to that, the sum of dynamic radii in two neighboring ellipses is larger than their centroid distance in the current frame.

After analyzing the object state of the current frame, the algorithm assigns tags to a single object. Moreover, each object’s tag is recorded, and that tag can provide a reference for tracking the object in the next frame. When calculating the number of objects, the state of the object can help in counting people.

68.6 Experimental Results

The proposed method is tested on two video sequences. Figure 68.3 shows segment images from the experimental video sequences. Results from Fig. 68.3 show that the graph cut method can effectively separate objects and obtain reliable results.

Figure 68.4 displays the number of people counted in each frame using the proposed method, the ground truth, and the Kalman filter method [10].

In the first panel of Fig. 68.4, the proposed method obtains good counting results from sequence 1. In particular, the judgment of entering and leaving states is accurate on the 100–200th frames, so the method can be reliably used for tracking and counting. The second panel in Fig. 68.4 displays the people counting results from sequence 2. Although occlusions from merging and splitting objects occur frequently, the proposed method can be used reliably for tracking and counting.



Fig. 68.3 Segmentation results of two video clips

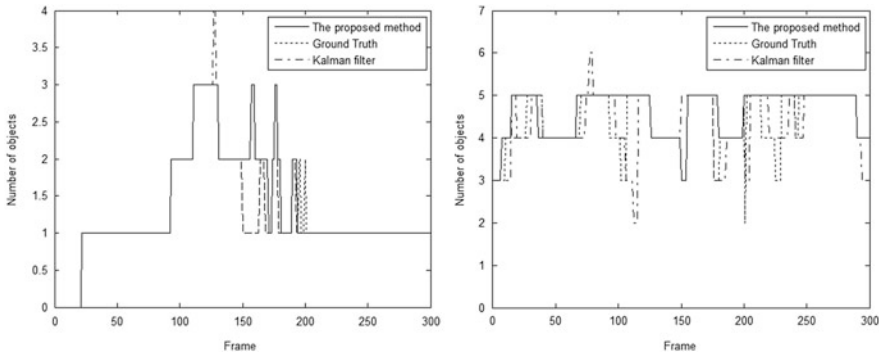


Fig. 68.4 Number of objects in two video clips using proposed method, Kalman filter method, and ground truth

Compared with the Kalman filter method and the ground truth, the proposed method performs better in terms of tracking.

To evaluate the tracking and counting accuracy, the methods are compared by calculating the detection ratio and average root mean-squared error (RMS) in average. E_{rms} shows the averaged RMS error from counting people [6].

The average detection ratios and errors associated with the two video clips are listed in Table 68.1. Table 68.1 shows that the proposed method has higher detection ratios and smaller errors on object counting in two videos than Yilmaz et al.'s method and the ground truth. The experimental results show that the proposed method can increase the average detection ratio by approximately 11 %. Thus, the method can be used to reliably track and count. The execution time associated with these two video clips is listed in Table 68.2. Thus, the execution time is short and its efficiency is higher using the proposed method.

Table 68.1 Comparison of average detection ratios and RMS from two video sequences

Sequence	Detection ratio			E_{rms}		
	Proposed method	Ground truth method	Yilmaz et al.'s scheme	Proposed method	Ground truth method	Yilmaz et al.'s scheme
1	0.87	0.73	0.76	0.57	0.63	0.70
2	0.78	0.68	0.73	0.70	1.02	1.09
Averaged	0.82	0.71	0.75	0.64	0.83	0.90

Table 68.2 Comparison of execution time from two video sequences

Sequence	Frame	Proposed method (s)	Ground truth method (s)	Yilmaz's scheme (s)
1	300	33.78	39.01	40.12
2	300	34.56	40.32	39.56

Conclusion

In this paper, an improved tracking and counting method was proposed. Foreground regions were segmented using the graph cut method. Then, foreground objects were identified by the sizes and positions of the obtained foreground areas. To track objects, an improved tracking method was presented and used to reduce the effects of object occlusion when splitting and merging. Experimental results showed the superiority of the proposed method over the traditional method.

Acknowledgments This work was financially supported by the Ministry of Education in China Project of the Humanities and Social Sciences (13YJCZH251).

References

1. Cristani M, Raghavendra R, et al. Human behavior analysis in video surveillance: a social signal processing perspective. *Neurocomputing*. 2013;100(1):86–97.
2. Marcenaro L. Multiple object tracking under heavy occlusions by using Kalman filters based on shape matching. In: *Proceedings of the IEEE ICIP*; IEEE Press, Piscataway, NJ; 2002. p. 341–44.
3. Lien CC, Huang YL, et al. People counting using multi-mode multi-target tracking scheme. In: *Proceedings of the IEEE IHH-MSP*; IEEE Press, Piscataway, NJ; 2009. p. 1018–21.
4. Chan A, Liang Z, Vasconcelos N. Privacy preserving crowd monitoring: counting people without people models or tracking. *CVPR*; IEEE Press, Piscataway, NJ; 2008. p. 1–7.
5. Fehr D. Counting people in groups. In: *Proceedings of the AVSS*; IEEE Press, Piscataway, NJ; 2009. p. 152–57.
6. Zhang MJ, Kang BS. Modified object tracking and counting method based on gaussian mixture model. *ICMRA*; TTP, Switzerland; 2013. p. 598–602.

7. Boykov Y, Jolly MP. Interactive graph cuts for optimal boundary and region segmentation of objects in n-d images. In: Proceedings of the IEEE International Conference on Computer Vision; IEEE Press, Piscataway, NJ; 2001. p. 105–12.
8. Hu MK. Visual pattern recognition by moment invariants. *IEEE Trans Inf Theory*. 1962;8:179–87.
9. Cristianini N, Shawe-Taylor J. Introduction to support vector machines. Cambridge: Cambridge University Press; 2000. p. 22–6.
10. Yilmaz A, Javed O, et al. Object tracking: a survey. *ACM Comput Surv*. 2006;38(4):22–32.

Chapter 69

Automatic Detection of Pharyngeal Fricatives in Cleft Palate Speech

Yan Xiao and Mangui Liang

Abstract Pharyngeal fricatives are produced as substitutes of normal fricatives by speakers with cleft palate. This chapter introduces a method of extracting acoustic features of pharyngeal fricatives by means of one-third octave analysis. The results show that the pharyngeal fricatives have higher amplitude below 4,000 Hz and lower amplitude above 4,000 Hz than the normal fricatives. Amplitudes of eight one-third octave bands are extracted to represent the acoustic features of pharyngeal fricatives. A pattern classifier based on logistic regression is also proposed here and obtains acceptable classification accuracy (90 %) when these acoustic features are used as the input factors. Detection of the pharyngeal fricatives is also automated in combination of such pattern classifier and an automatic selection of consonant component.

Keywords Cleft palate speech • Pharyngeal fricative • One-third octave • Logistic regression

69.1 Introduction

Cleft palate is a kind of congenital malformation caused by deviant facial development during gestation [1]. This deformity leads to the oral and nasal cavities interlinked and causes many serious dysfunctions especially in articulation [2]. Pathological articulation becomes habitual in the childhood development with cleft palate and it is difficult to correct even if the cleft palate is repaired successfully. In this case, clinicians need to judge a lot of cleft palate speech samples with different errors to assist the treatment. There are many errors in cleft palate speech and compensatory articulations which refer to the sounds replacement with other sounds produced at different places of articulation, the most common errors [2]. The glottal stop and the pharyngeal fricative which represent two types of compensatory articulations exhibited by speakers with cleft palate have attracted the most research attention and substantial therapeutics.

Y. Xiao (✉) • M. Liang

Institute of Information Science, Beijing Jiaotong University, 100044 Beijing, China
e-mail: huakinthos@163.com

Glottal stops are plosive consonants with a closure at glottis, which are observed as substitutes for stop consonants. Pharyngeal fricatives, examined here, as its name implies, are produced by retracting the tongue to the pharyngeal wall and narrowing the pharyngeal airway [3]. In previous studies, clinical studies used medical instruments, such as radiographic [4], to observe the velopharyngeal motion of cleft palate speech and these characteristics of pharyngeal fricatives have been found. Speakers with cleft palate often substitute pharyngeal fricatives for sibilant fricatives which are normally produced in the front of the mouth and sometimes for affricates.

Pharyngeal fricatives are important to cleft palate speech but normally not produced in Mandarin. Very few studies have examined the pharyngeal fricatives by using objective acoustic analysis. Some researchers used spectrogram analysis to observe the acoustic features of pharyngeal fricatives [3]. They found that the spectral characteristics of pharyngeal fricatives were different markedly from normal fricatives produced in the front of the mouth. On the basis, one-third octave analysis is used in this study to represent the acoustic features of pharyngeal fricatives as an auditory spectrum [5]. It seems to be compatible with the concept of spectral analysis as an auditory model.

In this chapter, we investigate the acoustic differences between pharyngeal fricatives and normal fricatives using one-third octave analysis and extract a set of distinctive acoustic features. These features can be used as the input factors of a pattern classifier based on the logistic regression to detect the pharyngeal fricatives objectively. After combining such pattern classifier with an automatic selection of consonant component, we can detect the pharyngeal fricatives in cleft palate speech automatically.

69.2 Materials and Methods

There are 56 native speakers of Mandarin Chinese (34 males and 22 females) involved in the study. All subjects are divided into two groups according to the judgment of experienced clinicians. One group is the cleft palate group including 30 subjects (17 males and 13 females) who are speakers with palatal clefts ranging from 7 to 45 years old ($M = 22$, $SD = 11$). Another group is the control group including 26 subjects who are normal speakers ranging from 9 to 28 years old ($M = 18$, $SD = 5.6$).

69.2.1 Speech Samples and Recording Procedure

Syllables of /sha/ are selected as the target speech samples in this study because the experienced clinicians consider this syllable that usually produces as compensatory pharyngeal fricatives and has the most obvious characteristics of pharyngeal

fricatives in cleft speech. The syllable /sha/ is presented in Chinese scripts that mean “sand” and shown on a card. All subjects are asked to repeat syllable /sha/ three times with 2-s time interval in a quiet environment. Each subject’s speech is recorded by a digital voice recorder (Sony IC Recorder ICD-UX80) at a sampling frequency of 44.1 kHz and saved as a whole file separately. Three times of syllable /sha/ are cut out separately from each file with 50-ms silence before and after each sample. All samples produced by subjects in the cleft palate group are judged by three experienced experts independently of one another. If more than two experts agree that a sample is a pharyngeal fricative, this sample will be included in pharyngeal fricative set. Pharyngeal fricative set includes 83 samples of syllable /sha/ with obvious features of pharyngeal fricatives. Samples produced by subjects in the control group are all included in normal fricative set without pharyngeal fricative errors. There are 78 samples in normal fricative set.

69.2.2 Automatic Selection of Consonant Component

All samples are down-sampled to 16 kHz and the consonant onset and vowel onset of each sample are labeled automatically by short-time zero-crossing number analysis. The short-time zero-crossing number is defined as the number of times the speech signal changes sign within every short time interval. According to the foregoing reports [6], the short-time zero-crossing number for voiceless consonant is 47/10 ms which is significantly different from the one for vowel (14/10 ms). Rectangular window is used to multiply the speech signal and the frame length is 10 ms which is the short time interval. The zero-crossing number is calculated frame by frame with a window shift of 5 ms.

The short-time zero-crossing number is defined as below [7]:

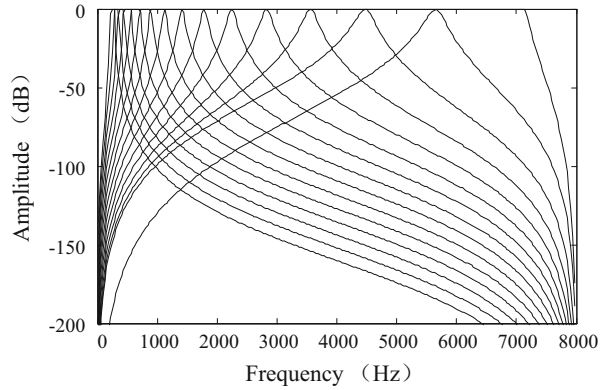
$$Z_n = \frac{1}{2} \sum_{m=0}^{N-1} |\text{sgn}[x_n(m)] - \text{sgn}[x_n(m-1)]| \quad (69.1)$$

$\text{sgn}[\cdot]$ is a sign function:

$$\text{sgn}[x] = \begin{cases} 1, & (x \geq 0) \\ -1, & (x < 0) \end{cases} \quad (69.2)$$

Z_n is the short-time zero-crossing number of x_n , x_n is the n th frame of a speech signal. $N = 0.01 \times f_s$, where f_s is the sampling frequency (16 kHz), so the upper limit of the frequency range is 8 kHz. If Z_n is first more than 47 in one frame, the center of this frame is marked as the consonant onset. After the consonant onset, when Z_n falls to less than 14, the center of the frame would be detected as the vowel onset. The speech component between consonant onset and vowel onset is the consonant component of a speech signal.

Fig. 69.1 Responses of 15 one-third octave digital bandpass filters



69.2.3 Feature Extraction

One-third octave analysis is used in this study to extract acoustic features of pharyngeal fricatives. The consonant component of each speech signal is filtered using 15 one-third octave digital bandpass filters with center frequencies from 250 to 6.3 kHz. The responses of 15 one-third octave filters are shown in Fig. 69.1. Each one-third octave filter uses Chebyshev-type infinite impulse response filter with a passband ripple of ± 0.2 dB [5]. The root mean square (rms) of each one-third octave filter output is calculated for every 1.25 ms and is averaged to indicate the mean amplitude of each one-third octave band. Amplitudes of 15 one-third octave bands form a one-third octave spectrum which indicates the acoustic features of a speech sample. Since the speech samples are produced by different subjects, the intensity levels are variable. So, all spectra are normalized in dB relative to the mean level of these 15 one-third octave bands to make the comparisons possible.

69.2.4 Pattern Classifier

Logistic regression which is a probabilistic classification model is used here to create a pattern classifier. It is commonly used in the clinical fields for predicting whether a patient has a given disease [8]. Logistic regression can evaluate the relationship between independent input factors and a categorical dependent variable. The categorical dependent variable used in this chapter is binary because the available categories are two here. One available category whose variable value is coded as “1” represents that a speech sample is a pharyngeal fricative. Another category whose variable value is coded as “0” represented that a speech sample is a normal fricative. Independent input factors for logistic regression function are the acoustic features of each speech sample and the output is the probability of a speech

sample being a pharyngeal fricative. The logistic regression function is shown as below [9]:

$$y = P(Y = 1 | X_1 = x_1, X_2 = x_2, \dots, X_n = x_n) \\ = 1 / \left\{ 1 + \exp \left[- \left(a + \sum_{i=1}^n b_i X_i \right) \right] \right\} \quad (69.3)$$

y is the probability of a speech sample being a pharyngeal fricative and its values are between zero and one. In contrast, $1 - y$ is the probability of a speech sample being a normal fricative. X_i ($i = 1, \dots, n$) refers to the input factors which indicate the acoustic features in this study. n is the amount of input factors, and a and b_i are the coefficients for this function. A threshold δ is needed to be selected by ensuring that the false-positive rate and false-negative rate are equal [10]. The speech sample is classified as a pharyngeal fricative when $y > \delta$. In the other cases, samples are determined as normal fricatives.

69.3 Results and Discussion

The consonant component of each speech signal is filtered by 15 one-third octave digital bandpass filters and obtains a one-third octave spectrum. Averaged these spectra across samples in pharyngeal fricative set and samples in normal fricative set, two average one-third octave spectra are obtained. As showed in Fig. 69.2, one-third spectrum for pharyngeal /sh/ produced by speakers with cleft palate differs markedly from /sh/ sounds produced in the front of the mouth. For the pharyngeal fricative set, the levels of the bands below 4 kHz except 1.6 kHz are higher and the levels of the bands above 4,000 Hz are lower than those for the normal fricative set. Pharyngeal /sh/ has two spectral maxima in the levels of the band whose center frequencies are 800 Hz and 2.5 kHz. These results are in

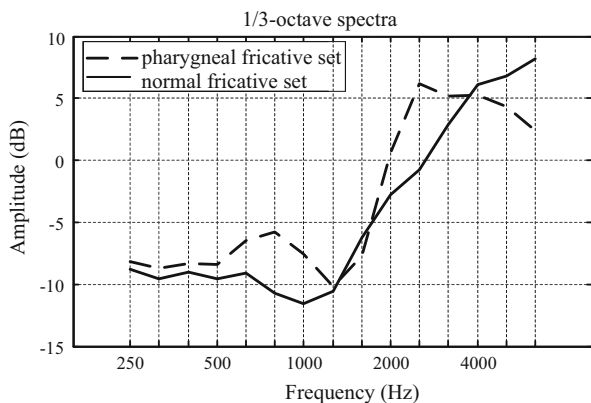


Fig. 69.2 Average 1/3 octave spectra from the two speech sample sets

Table 69.1 Results of analysis of variance (ANOVA) for differences in mean level of each one-third octave band among the two speech sample sets

Band (Hz)	250	320	400	500	630	800	1 k	1.25 k	1.6 k	2 k	2.5 k	3.2 k	4 k	5 k	6.3 k
<i>p</i>	0.5	0.3	0.4	0.1	<0.001	<0.001	<0.001	0.6	0.1	0.001	<0.001	0.001	0.2	<0.001	<0.001

The band in this table means the center frequency of the one-third octave band

Table 69.2 Classification results of the pattern classifier with the threshold $\delta = 0.52$

Observed	Predicted			Overall percentage
	Pharyngeal fricative set	Normal fricative set	Accuracy	
Pharyngeal fricative set	75	8	90.3 %	90.0 %
Normal fricative set	8	70	89.7 %	

agreement with the spectral characteristics of pharyngeal fricative in the foregoing reports [7]. These results are not surprising because the constriction places for pharyngeal fricatives are in the lower pharynx where is more posterior than those for normal fricatives produced in the front of the mouth. It leads to pharyngeal fricatives having a larger anterior cavity than normal fricative; longer anterior cavity results in energy concentrated in the lower frequency range.

An analysis of variance (ANOVA) is used in this study as the statistics analysis for differences in mean amplitude of each one-third octave band among the two speech sample sets. The results are shown in Table 69.1. The statistical significance level is set at 0.05. The significant differences are found in the levels of the bands whose center frequencies are 630 Hz, 800 Hz, 1, 2, 2.5, 3.2, 5, and 6.3 kHz. Amplitudes of these bands are chosen to form an acoustic feature vector as the input factors for the logistic regression function.

The pattern classifier is indicated as the logistic regression Eq. (69.3) using the amplitudes of the eight one-third octave bands (630 Hz, 800 Hz, 1, 2, 2.5, 3.2, 5, and 6.3 kHz) as the input independent variables. The classification accuracy of the pattern classifier is 90 % with the threshold $\delta = 0.52$ (Table 69.2).

The obtained pattern classifier is

$$\left\{ \begin{array}{l} y = 1 / \left\{ 1 + \exp \left[- \left(a + \sum_{i=1}^8 b_i A_i \right) \right] \right\} \\ a = 0.7196 \\ b_i = [-0.0348, 0.1167, 0.0015, -0.0141, 0.0342, 0.0289, 0.0787, -0.1261] \\ \delta = 0.52 \end{array} \right. \tag{69.4}$$

If $y > 0.52$, the speech sample is detected as a pharyngeal fricative, otherwise as a normal fricative.

Conclusion

One-third octave analysis is utilized in this study to extract the acoustic features for pharyngeal fricatives and normal fricatives. The syllable /sha/ is the target speech sample. The results show that pharyngeal fricatives have higher acoustic energy in the low frequency range because the anterior cavity for pharyngeal fricatives is larger than the one for normal fricative produced in the front of the mouth. An automatic detection of consonant onset and vowel onset based on short-time zero-crossing rate analysis is proposed in this study to choose the consonant component of a speech sample. Amplitudes of eight one-third octave bands are selected to indicate the acoustic features which are the input factors for the pattern classifier. Detection of pharyngeal fricatives in cleft palate speech is automated in combination of the pattern classifier with the automatic selection of consonant component with acceptable performance achieved as a result.

References

1. Edwards M, Watson ACH. *Advances in the management of cleft palate*. Edinburgh: Churchill Livingstone; 1980.
2. Kuehn DP, Moller KT. Speech and language issues in the cleft palate population: the state of the art. *Cleft Palate Cran J*. 2000;37:348-1-35.
3. Weinberg B, Horii Y. Acoustic feature of pharyngeal /s/ fricatives produced by speakers with cleft palate. *Cleft Palate J*. 1975;12:5-11.
4. Trost JE. Articulatory additions to the classical description of the speech of persons with cleft palate. *Cleft Palate J*. 1981;18:193-203.
5. Kataoka R, Warren DW, Zajac DJ, et al. The relationship between spectral characteristics and perceived hypernasality in children. *J Acoust Soc Am*. 2001;109:2181-9.
6. Yin HB, Qin B, Zhang F, et al. An endpoint detection algorithm of speech based on MZR. *Prog Comput Technol Appl*. 2006;17:459-63.
7. Wu YH. Analysis and application of short-time magnitude and short-time zero-crossing rate in speech. *Comput Knowl Technol*. 2009;33:9314-5.
8. Boyd CR, Tolson MA, Copes WS. Evaluating trauma care: the TRISS method. Trauma score and the injury severity score. *J Trauma*. 1987;27:370-8.
9. Bishop CM, Nasrabadi NM. *Pattern recognition and machine learning*. Heidelberg: Springer; 2006.
10. Martin A, Doddington G, Kamm T. The DET curve in assessment of detection task performance. In: *Proceedings of Eurospeech'97*; 1997. p. 1895-8.

Chapter 70

Improved Chinese Word Segmentation Disambiguation Model Based on Conditional Random Fields

Fanjin Mai, Shitong Wu, and Taoshi Cui

Abstract This paper proposes an improved model that can eliminate the sense ambiguity of Chinese word segmentation based on conditional random fields (CRFs). First, this model segments words based on a bidirectional maximum matching algorithm and extracts the ambiguous part. Then it resolves ambiguity based on the conditional random field algorithm for segmentation ambiguity and outputs a more accurate result for the segmentation. The test results show that this model can reduce the error rate of segmentation caused by the ambiguity of word segmentation.

Keywords CRF • Chinese word segmentation • Maximum matching • Ambiguity resolution

70.1 Introduction

Chinese word segmentation technology is a fundamental issue in the field of natural language processing, and the problem of ambiguous segmentation represents one of the difficulties in Chinese word segmentation technology. Currently many model algorithms exist that have been applied in word segmentation ambiguity processing, such as the hidden Markov model (HMM), maximum entropy model, simple Bayesian, support vector machines (SVMs), and genetic algorithms. For example, Chao Sun proposed a Chinese word segmentation disambiguation method based on phrase match [1]. Ting Wang proposed a word segmentation

F. Mai (✉)

College of Mechanical and Control Engineering, Guilin University of Technology,
541000 Guilin, China

e-mail: gltide2010@126.com

S. Wu • T. Cui

College of Information Science and Engineering, Guilin University of Technology,
541000 Guilin, China

e-mail: xilanhuago@163.com

© Springer International Publishing Switzerland 2015

W.E. Wong (ed.), *Proceedings of the 4th International Conference on Computer
Engineering and Networks*, Lecture Notes in Electrical Engineering 355,

DOI 10.1007/978-3-319-11104-9_70

disambiguation model based on bidirectional maximum matching and HMM [2]. In view of the mixed ambiguity problem of a statement, Hui Ren conducted classification research on a system and established a maximum entropy model of word segmentation on the basis of enriching word characteristics at the same time [3]. The paper of Hui Ren solves these problems fundamentally. However, every word segmentation method has its own advantages and limitations. Especially in the face of ambiguity problems in Chinese word segmentation, all these methods have many shortcomings. HMM requires a strict independence assumption, and it cannot tab accurately. The maximum entropy model can accommodate any information about dependent characteristics, but, due to local normalization, there are so-called tag prejudice problems in the traditional maximum entropy model.

The CRF model was proposed in 2001. It is an improved condition model. Compared with the maximum entropy model, it can also accommodate any characteristic information and achieve global normalization of all characteristics. It takes advantage of the characteristics of long distance, and there is no tag offset weakness. The CRF model has inherited the advantages of the HMM. But the shortcomings of the HMM don't exist in the CRF model, and the CRF model solves the so-called tag prejudice problems. The essential difference between CRF and HMM is that, based on the representation characteristics of the current relative information, HMM resolves the figure of correlativity of relative information just below in line with the exponential form of the characteristics of all relative information. The CRF method is based on the current text string and represents the correlativity of all relevant information characteristics combined with the exponential form. In practical applications, there exists a certain correlation between many text strings. Information plays an important role in word segmentation. Thus, in Chinese word segmentation, the application effect of conditional random fields (CRFs) has a certain advantage over HMM and the maximum entropy model. Therefore, to improve the disambiguation accuracy of Chinese word segmentation, this paper proposes an improved Chinese word segmentation disambiguation model based on CRFs.

70.2 Bidirectional Maximum Matching Algorithm

The bidirectional maximum matching algorithm contains a positive maximum matching algorithm and a reverse maximum matching algorithm. If two algorithms can obtain the same segmentation result, it is a participial success. Otherwise, it is thought that the ambiguity problems or an out-of-vocabulary problem arises. The drawback of the bidirectional maximum matching algorithm is that it is unable to deal with the ambiguity problem. Although the best way to solve ambiguity is through context [4], we also can analyze the relationship between the contexts of an ambiguous segment, extract the information on syntax or semantic aspects that can indicate the resolution of ambiguity in the context, and integrate them into a statistical model [5]. But with this we face many difficulties in actual practice.

This paper introduces an improved algorithm of CRFs to solve the ambiguity problem.

70.3 Improved Disambiguation Algorithm of Conditional Random Fields

The CRF model is an undirected graph model. It represents a good method for using relevant contextual information and effectively carrying out the statistical calculation of the degree of connection of words. Then it is more reasonable to put the characters together to form words. When dealing with large-scale text strings in practical applications, this method can effectively extract the relevant information about the characteristics of a given observation sequence and meet the needs of the actual situation.

70.3.1 Word Segmentation Ideology of Conditional Random Fields

In Chinese word segmentation, some numerals, temporal words, and alphabetic strings are out-of-vocabulary, so they are easily misidentified. To enhance the accuracy of recognition of these special strings, this paper introduces the idea of *classification and generalization*.

All Arabic numerals, for example, 0, 1, and 2, are replaced by the tag “#N.” Some punctuation marks, for example full stops, exclamation marks, and question marks, are replaced by the tag “#C.” All English letters, for example, a, A, b, B, are replaced by the tag “#L.” All Chinese characters are divided into seven classes, and all numbers are marked “T1,” for example, 1, 2, Chinese character 1, Chinese character 2. Temporal word postfixes are marked “T2”; these include year, month, day, hour, minute, and second. All English letters are marked “T3.” The top n Chinese characters with the highest frequency (c, S) in the training corpus are marked “T4.” The top n Chinese characters with the highest frequency (c, B) in the training corpus are marked “T5.” The top n Chinese characters with the highest frequency (c, E) in the training corpus are marked “T6.” Other Chinese characters are marked “T7.”

Of these, frequency (c, P) refers to the frequency of a Chinese character c in word position P . T4, T5, and T6 mainly help generalize Chinese characters with a representative location. N equals 100 in the experiment.

70.3.2 *Parameter Estimation of Conditional Random Fields*

The CRF model is used to solve feature weights λ . Chinese word segmentation based on CRFs often combines with maximum-likelihood estimation (MLE) to solve certain parameters [6].

If the training set is $T = \{ \langle X^k, Y^k \rangle \}$, then MLE is setting that $P(Y|X, \lambda)$ is the function of λ . Make the logarithm value of $P(Y|X, \lambda)$ achieve the largest estimated value of λ . Equations (70.1) and (70.2) represent respectively the likelihood value and the maximum value:

$$\begin{aligned} L_{\lambda} &= \sum_T \log P(Y^k | X^k, \lambda) \\ &= \sum_T \log \frac{1}{Z(X^k)} \exp \left(\sum_j \lambda_j F_j(Y^k, X^k) \right) \end{aligned} \quad (70.1)$$

$$\begin{aligned} &= \sum_T \left\{ \sum_j \lambda_j F_j(Y^k, X^k) - \log(Z(X^k)) \right\} \\ \lambda^* &= \arg \max_{\lambda} \sum_T \log P(Y^k | X^k, \lambda). \end{aligned} \quad (70.2)$$

70.3.3 *Improved Format of Training and Test Corpus Based on Conditional Random Fields*

Whether an ambiguous segment is separated or grouped, this problem can be converted into a problem of marking an observed sequence through the CRFs. It can be dealt with based on the contextual information of the ambiguous segment [7].

The format of training and test files that is used by CRFs must meet a particular need. The requirements include the following. Usually, the training and test files need to contain multiple tokens. The number of columns in a token is greater than two. We can select the appropriate token based on the actual condition, such as, for example, words, word position, or part of speech. But the end of a line must be comprised of tags that are used by CRFs in training. A token must stand in a line separately, and all columns should use spaces or tabs to demark intervals between them. The token sequence can form sentences and must use a blank line to separate sentences from each other.

First, we define a token, and in the corresponding table are three rows: word, part of speech and markup. The tag column contains other fields besides the ambiguous segments in the sentence and are labeled X . If the ambiguous segments are grouped, then label them 1. If the ambiguous segments are separated, then label them 2. Regardless of whether the ambiguous segments are grouped or separated, label their parts of speech Y .

Table 70.1 Training corpus format

Word	ta	dehua	chang chang	bode	guan zhong	huixin	de	xiao sheng	.
Part of speech	r	Y	d	v	n	d	u	a	w
Markup	X	1	X	X	X	X	X	X	X

Table 70.2 Token instance of two columns

	sw	N
bei	Bns	LOC
jing	Mns	I-LOC
shi	Ens	I-LOC
shou	Bn	N

Here we use Pinyin to represent Chinese sentences. The sentence is “ta/r de/u hua/n changchang/d bode/v guanzhong/n huixin/d de/u xiaosheng/n./w.” Table 70.1 shows the training corpus format.

The format of the test corpus is similar to that of the training corpus except the test corpus does not have a markup row.

70.3.4 Feature Selection and Customized Templates

Because the CRF model is used to sequence tags, feature templates must be determined in advance. A row represents a sub-template of [xxx] in the template. The format of a template is %x[row, column]. It can represent a token in the output data. The default location of a row and column is 0. In the table, a row represents the relative number of rows with the current token, and a column represents the absolute number of columns. Usually, we take the m rows up and down the current row and take $n-1$ columns (no more than the total number of n columns), as in Table 70.2.

If the current row is the third row, then the selection of features is as in Table 70.3.

70.4 Experimental Results and Analysis

The experiment is carried out in a Microsoft Visual Studio 2005 environment, the main program code is written in C++, and the database is Microsoft SQL Server 2005.

We need to train the corpus after coding and testing. In this process, we will construct a word bank, collect a corpus, and train the corpus. There are two methods for building the word bank. One is based on statistics, the other on a dictionary and rules. In the experiment, we adopt the method based on the dictionary and rules. We use a 128,000-word dictionary.

Table 70.3 Selection of features

%x[-2,0]	Row negative 2, column 0	“
x[-1,0]	Row negative 1, column 0	bei
%x[0,0]	Row 0, column 0	jing
%x[1,0]	Row 1, column 0	shi
%x[2,0]	Row 2, column 0	shou
%x[-2,1]	Row negative 2, column 1	Sw
%x[-1,1]	Row negative 1, column 1	Bns
%x[0,1]	Row 0, column 1	Mns
%x[1,1]	Row 1, column 1	Ens
%x[2,1]	Row 2, column 1	Sw
%x[-1,0]/%x[0,0]	Combination of row negative 1, column 0 and row 0, column 0	bei/jing
%x[0,0]/%x[1,0]	Combination of row 0, column 0 and row 1, column 0	jing/shi
%x[-2,1]/%x[-1,1]	Combination of row negative 2, column 1 and row negative 1, column 1	Sw/Bns
%x[-1,1]/%x[0,1]	Combination of row negative 1, column 1 and row 0, column 1	Bns/Mns
%x[0,1]/%x[1,1]	Combination of row 0, column 1 and row 1, column 1	Mns/Ens
%x[1,1]/%x[2,1]	Combination of row 1, column 1 and row 2, column 1	Ens/Sw
%x[-2,1]/%x[-1,1]/%x[0,1]	Combination of row negative 2, column 1, row negative 1, column 1, and row 0, column 1	Sw/Bns/Mns
%x[-1,1]/%x[0,1]/%x[1,1]	Combination of row negative 1, column 1, row 0, column 1, and row 1, column 1	Bns/Mns/Ens
%x[0,1]/%x[1,1]/%x[2,1]	Combination of row 0, column 1, row 1, column 1, and row 2, column 1	Mns/Ens/Sw

Table 70.4 Results comparison of closed test

	<i>R</i> (%)	<i>P</i> (%)	<i>F</i> ($\beta = 1$) (%)
Maximum entropy model	97.92	98.07	97.99
CRFs	98.32	98.15	98.23

Table 70.5 Results comparison of open test

	<i>R</i> (%)	<i>P</i> (%)	<i>F</i> ($\beta = 1$) (%)
Maximum entropy model	96.73	96.51	96.62
CRFs	97.64	97.38	97.51

In the process of training and testing, we use the tagged corpus of the newspaper *People's Daily* as reference. It was developed by Beijing University and Foxconn Company.

Table 70.4 shows the experimental results of the closed test, and Table 70.5 shows the experimental results of the open test. We evaluate the performance of word segmentation from recall, precision, and *f*-measure. Of these, the *f*-measure is the main performance index. Compared with the maximum entropy model, the system's effectiveness is very good under the conditions of the closed test.

This shows that the method can be fully adapted for the training corpus. Under the conditions of the open test, the system to the requirement of corpus is greater. This is mainly because the system can use the context feature. For the correct segmentation of ambiguous segments, the system is very effective, and the time complexity is more appropriate.

Conclusion

In view of the segmentation ambiguity problem in Chinese word segmentation technology, this paper proposes an improved model that eliminates the sense ambiguity of Chinese segmentation based on CRFs. It uses a positive maximum matching and reverse maximum matching algorithm to complete the initial segmentation, and then identifies the ambiguous part. Finally, it resolves the ambiguity based on an improved CRF algorithm. Thus, it obtains more accurate segmentation results. Compared with other model algorithms, the CRF model effectively improves segmentation accuracy. It has more practical value than some basic methods.

References

1. Sun C, Zhang YS. A Chinese word segmentation disambiguation method based on phrase match. *Comput Eng Design*. 2010;(21):4704–8. (in Chinese)
2. Mai FJ, Wang T. The word segmentation disambiguation model based on bidirectional maximum matching and HMM. *Mod Libr Inf Technol*. 2008;(8):37–41. (in Chinese)
3. Ren H, Lin HF, Yang ZH. The resolution of crossing ambiguities based on smooth maximum entropy model of fusion word characteristics. *J Chin Inf*. 2010;24(4):18–24 (in Chinese).
4. Qin Y, Wang XJ, Zhang SX. The research of combinatorial ambiguity in Chinese word segmentation. *J Chin Inf*. 2007;21(1):3–8 (in Chinese).
5. Mai FJ, Li DP, Yue XG. The Chinese word segmentation technology research based on the bidirectional matching method and the feature selection algorithms. *J Kunming Univ Sci Technol (Nat Sci Ed)*. 2011;36(1):47–51 (in Chinese).
6. Yu JD, Fan XZ, Yin JH. Information extraction of Chinese research papers based on conditional random fields. *J South China Univ Technol (Nat Sci Ed)*. 2007;(9):90–4. (in Chinese)
7. Tu MP. The comparative study of semantic disambiguation based on bayesian classifier and conditional random fields model. *Cult Educ Inf*. 2011;48(2):121–3 (in Chinese).

Chapter 71

Mobile Real-Time Monitoring System Based On Human Action Recognition

Lin Chai, Zhiqiang Wei, and Zhen Li

Abstract Mobile real-time monitoring system which is based on the wireless network meets the requirements of users who want to monitor and manage the home in a mobile scene or an emergency scene. This chapter designs and implements a real-time monitoring system based on mobile terminal. At the same time, human action recognition is applied to the system. A method combining the 3D skeleton shape histogram with dynamic time warping (DTW) is proposed to improve the accuracy of recognition.

Keywords Mobile real-time monitoring system • Human action recognition • Shape histogram • DTW

71.1 Introduction

As the development of intelligent analysis technology and network technology, mobile real-time monitoring system is possibly applied to the home. The system can reduce the responsibility of young people to a certain extent. Even if they are far away from home, they can remotely monitor their homes. Especially they are able to receive the real-time status of children or elderly people. Therefore, the monitoring system needs to detect and track the target in the monitored scene and automatically describe the event which is happening. In other words, the system needs to recognize the actions of children or elderly people.

As an important research of computer vision, human action recognition attracts more and more attention. The purpose of human action recognition is to help the computer system to understand individual actions, interaction between individuals, and the environment by analyzing data collected by sensors [1].

Traditional surveillance systems are based on the images or videos. The transmission of large amount of data and the requirements of high bandwidth are great

L. Chai (✉) • Z. Wei • Z. Li
College of Information Science and Engineering, Ocean University of China,
266100 Qingdao, China
e-mail: oucchailin@163.com

challenges for wireless networks. Kinect is a new motion-sensor equipment introduced by Microsoft in November 2010. With the help of infrared camera, Kinect can identify human body and track the skeleton points. Based on the 3D skeleton points, we can easily implement a 3D reconstruction. The amount of transmission data can be greatly reduced, and also the accuracy of action recognition can be improved.

A real-time monitoring system based on mobile terminal is proposed in this chapter. The system uses C/S design patterns. System architecture includes server and client. The server tracks target person and collects skeleton points to recognize actions using Kinect. The server also transmits data through a wireless network to the client. The client is an intelligent terminal running the Android operating system which can send monitoring requests and receive data to create a 3D reconstruction. The system meets the needs of real-time monitoring.

71.2 Related Work

In the last two decades, many action recognition and intelligent video surveillance projects have had some victories. For example, the US Defense Advanced Research Projects Agency set up a major project—VSAM (Visual Surveillance and Monitoring)—in 1997, which was related to intelligent monitoring [2].

Feature extraction is to obtain the action description feature by processing the original data. Wearable sensors were usually used in early studies to get some motion information [3, 4]. At present, representation method based on vision is an in-depth study. This method is easy to implement by using the body shape feature, but its computation complexity is high. The common method is based on motion features now. For example, Zhu et al. studied the batting action in tennis with optical flow method [5].

Human action is a dynamic process, so the recognition method is dynamic too. Much more reliable methods so far are grammar-oriented, probability-based, and template-based methods. Grammar-oriented methods include some context-independent methods such as finite-state machine (FSM). Hong defined gestures as ordered sequence of spatial-temporal space and identified gestures using FSM [6]. But grammar-oriented methods have poor robustness of model and low accuracy. And also it cannot describe the dynamic motion process accurately. The most widely used method based on probability is hidden Markov model (HMM). Zhang et al. researched interactive behaviors between individuals in a meeting using two layers of HMM [7]. Template-based methods mainly include template matching [8], dynamic time warping [9], and dynamic programming [10].

In this chapter, we use the 3D coordinates of the skeleton points collected by Kinect to a computer 3D shape histogram. The histogram is used to represent posture feature. Each action is a series of postures. So we use DTW to match two posture sequences automatically and compute the distance between the two sequences in order to recognize different actions.

71.3 Overall Design of the System

System architecture consists of server and client, presented in Fig. 71.1.

71.3.1 Server

The server is a personal computer connecting to a Kinect. It collects and saves image information by using Kinect to monitor home. At the same time, it also tracks 3D coordinates of the target's skeleton points. In a standing mode, Kinect can track 20 joints including hip center, L/R hip, spine, shoulder center, head, L/R shoulder, L/R elbow, L/R wrist, L/R hand, L/R knee, L/R ankle, and L/R foot. According to these skeleton points, the server extracts features for action recognition. The server transmits positions of skeleton points to the client through wireless network in real time.

71.3.2 Client

The client is an intelligent terminal running the Android operating system. It sends monitoring requests and establishes a connection with the server. Then it receives positions of skeleton points in real time. And a 3D reconstruction using OpenGL is implementing to draw a model, while an action recognition result is shown. Since some joints are close to each other, such as foot and ankle, wrist and hand, spine, and hip center, L/R ankle, L/R wrist, and spine are ignored when reconstructing the human body.

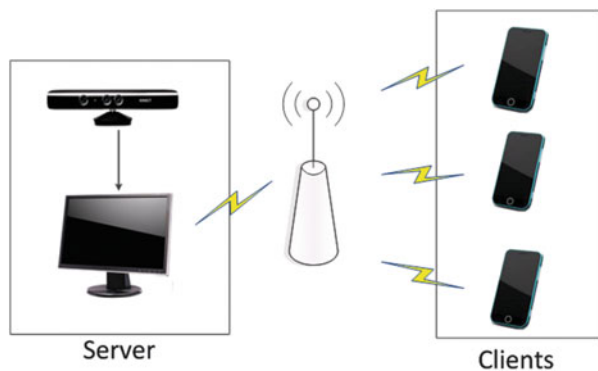
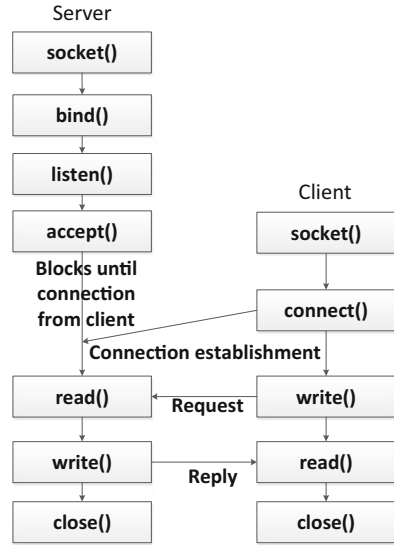


Fig. 71.1 System architecture

Fig. 71.2 The client-server model



71.3.3 Network Connection

Data transmission through network is based on the connection of the server and client. Socket is used to establish network connection and support multiple clients monitoring at the same time. The client-server model of socket programming is shown in Fig. 71.2.

The server has a thread listening to the connection requests continuously. When a client connects to the thread, a new connection is established. The thread puts the new connection into a connection pool to manage, and continues listening to the connection requests. When the service thread finds a new task, it provides service to the client by using the corresponding connection. After the task is finished, the server and the client both close connection. Meanwhile the service thread is idle and waiting for a new task.

71.4 Action Recognition Method

The key to recognize human actions is to detect and track the moving target correctly, extract features of moving target, analyze characteristic parameters of actions, and then recognize the action.

71.4.1 Feature Extraction

Action is a collection of postures because an action at every moment is a static posture. Since different people have different clothes or body shapes, there is a great difference in appearance with the same actions. But the skeleton points are similar. Therefore, using 3D coordinates of skeleton points to extract features can represent postures well. In this chapter, we use the shape histogram to represent 3D skeleton points.

3D shape histogram was proposed by Ankerst et al. [11]. The shape histogram of a point is a distribution of relative positions with its neighboring points. Each axis represents a parameter in a polar coordinate system. Each bin around the point is defined in space. In the radius direction, bins uniformly distribute in log-polar space. So the close point is more important than the distant point. If there are X bins in the radius direction, Y bins for the azimuth, and Z bins for the elevation, in the 3D shape histogram there are $X \times Y \times Z = N$ bins in total.

According to skeleton points collected by Kinect, we can draw a 3D skeleton. Then as shown in Fig. 71.3, the 3D space can be transformed into a spherical coordinate system which the origin is the center of the skeleton. Accumulating the number of points in each bin can get a skeleton histogram. Since the coordinate system origin is the center of the skeleton, this histogram is translation invariant.

For any two 3D skeletons A and B , their shape histograms are denoted as $h_A(n)$ and $h_B(n)$, where $n = 1, 2, 3, \dots, N$. The similarity of two histograms can be computed using χ^2 -distance:

$$d(A, B) = \frac{1}{2} \sum_{n=1}^N \frac{(h_A(n) - h_B(n))^2}{h_A(n) + h_B(n)} \quad (71.1)$$

The distance between two histograms being smaller means that the two skeletons are more similar.

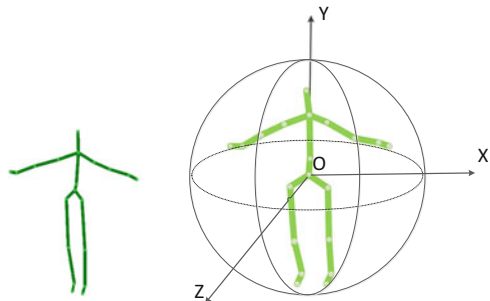


Fig. 71.3 3D skeleton in a spherical coordinate system

71.4.2 Action Recognition Using DTW

We know how to calculate the similarity of two static postures. But the action is a posture sequence. It is different to compare two sequences because the other information about the sequences is unknown, such as the length, the starting position, and the interval time of the sequence. In this chapter, DTW algorithm is utilized to compare two sequences. DTW was successfully applied to speech recognition firstly since it could deal with the inconsistency of the talking speed [12]. And there are similar problems in the action sequence, such as walking speed may be fast or slow.

At first we choose a section of the action as a sample, and then compare it with the samples in our template database. Finally we select the most appropriate sample to mark the action. The sample in the template database is called a reference template, defined as $R = \{R_1, R_2, \dots, R_m, \dots, R_M\}$, where M is the total number of frames in the reference template. The input action sample to be recognized is called as a test template. The test template is $T = \{T_1, T_2, \dots, T_n, \dots, T_N\}$, where N is the total number of frames in the test template. The DTW distance of the test template and the reference template can be calculated as:

$$g(i, j) = \min \begin{cases} g(i-1, j) + d(i, j) \\ g(i-1, j-1) + 2d(i, j) \\ g(i, j-1) + d(i, j) \end{cases} \quad (71.2)$$

where $d(i, j)$ is the χ^2 -distance of two histograms. Dynamic rules are applied to compute the distance. Starting from (M, N) backwards to $(1, 1)$ can get a matching path with the shortest distance, as shown by the dotted line in Fig. 71.4.

The distance calculated by DTW can accurately represent the similarity between two actions. Since the calculation is not exchangeable, we can exchange the two action sequences and compute a new distance. And then calculate the average distance as the distance between the two action sequences.

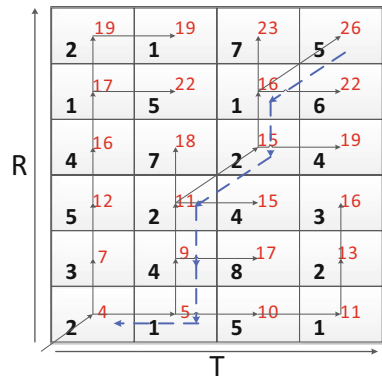


Fig. 71.4 DTW path retrieval

71.5 Results

According to testing results, the server could maintain connections with more than 20 clients stably and simultaneously. The server got 30 frames of joints data per second by Kinect and the average data bandwidth for the client was 20 kB/s. The client ran on an Android mobile phone. The monitoring human model was drawn fluently and the data delay was in 5 s. Running results of the client is shown in Fig. 71.5.

To build a template action database, we collected seven kinds of indoor actions: stand up, sit down, walk, wave, bend, push, and pull. Each action was performed five times by 10 different people: eight males and two females. Therefore, the database contained 350 action samples. We also collected these seven actions from five volunteers to test our algorithm. Each action was tested 20 times, respectively, based on the sample database. Table 71.1 shows the action recognition rate.

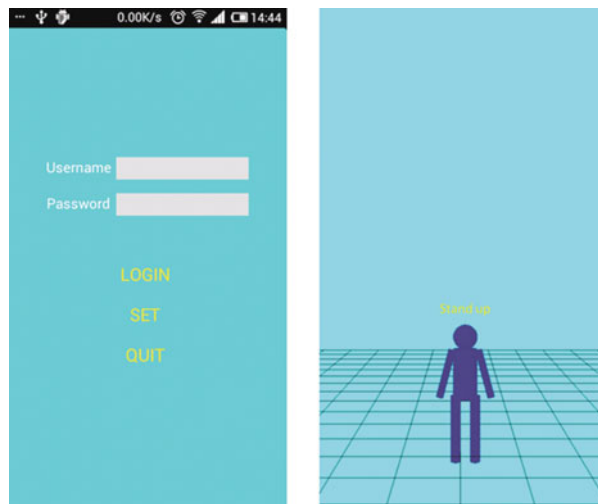


Fig. 71.5 Client running results

Table 71.1 Action recognition rate

Actions	Results						
	Stand up (%)	Sit down (%)	Walk (%)	Wave (%)	Bend (%)	Push (%)	Pull (%)
Stand up	94.5	0.0	1.5	0.0	3.5	0.5	0.0
Sit down	0.0	95.5	0.0	0.0	4.5	0.0	0.0
Walk	2.5	0.0	96.5	0.0	0.0	0.5	0.5
Wave	0.0	0.0	0.0	100	0.0	0.0	0.0
Bend	0.0	2.5	0.0	0.0	97.5	0.0	0.0
Push	1.5	2.0	1.5	0.0	1.0	88.5	5.5
Pull	0.0	2.5	1.5	0.0	0.0	4.0	92.0

Conclusion

A real-time monitoring system based on mobile terminal is designed and implemented in this chapter. The server not only tracked the target and communicated with clients, but also used the 3D skeleton shape histogram and DTW to recognize actions. The client could implement a 3D reconstruction in real time. The testing results show that the system could perform the mobile real-time monitoring, and the action recognition rate is high. In the future, color image information and depth image information could be applied to action recognition to get more details and higher recognition rate. Moreover, in order to make the system more intelligent, the server will send warning message to clients when dangerous action is recognized.

Acknowledgements This work was supported by the National Natural Science Foundation No. 61202208 of China and the Fundamental Research Funds for the Central Universities No. 201413021.

References

1. Moeslund TB, Hilton A, Kruger V. A survey of advances in vision-based human motion capture and analysis. *Comput Vis Image Underst.* 2006;104(2):90–126.
2. Collins R, Lipton A, Kanade T, et al. A system for video surveillance and monitoring. VSAM final report, CMU-RI-TR-00-12. Pittsburgh, PA: Carnegie Mellon University; 2000.
3. Ward JA, Lukowicz P, Troster G, et al. Activity recognition of assembly tasks using body-worn microphones and accelerometers. *IEEE Trans Pattern Anal Mach Intell.* 2006;28(10):1553–67.
4. Yin J, Yang Q, Pan JJ. Sensor-based abnormal human-activity detection. *IEEE Trans Knowl Data Eng.* 2008;20(8):1082–90.
5. Zhu G, Xu C, Huang Q, et al. Action recognition in broadcast tennis video. In: 18th International conference on pattern recognition. IEEE; 2006. p. 251–4.
6. Hong P, Turk M, Huang T. Constructing finite state machines for fast gesture recognition. In: Proceedings of 15th international conference on pattern recognition. IEEE; 2000. p. 691–4.
7. Zhang D, Gatica-Perez D, Bengio S, et al. Modeling individual and group actions in meetings with layered HMMs. *IEEE Trans Multimedia.* 2006;8(3):509–20.
8. Davis JW, Bobick AF. The representation and recognition of action using temporal templates. In: 1997 I.E. Computer Society conference on computer vision and pattern recognition. IEEE; 1997. p. 928–34.
9. Zhu Y, Ren H, Xu G, Lin X. Toward real-time human–computer interaction with continuous dynamic hand gestures. In: Fourth IEEE international conference on automatic face and gesture recognition. IEEE; 2000. p. 544–9.
10. Bobick A, Wilson A. Using configuration states for the representation and recognition of gestures. MIT media lab perceptual computing section technical report no. 308; 1995.
11. Ankerst M, Kastenmüller G, Kriegel HP, et al. 3D shape histograms for similarity search and classification in spatial databases. *Advances in spatial databases.* Berlin: Springer; 1999. p. 207–26.
12. Rabiner LR. Fundamentals of speech recognition. Upper Saddle River: PTR Prentice-Hall; 1993. p. 221–31.

Chapter 72

A Kind of Image Classification Method Study

Guoqing Wu, Bingheng Yang, and Liang Lv

Abstract With the rapid development of information technology, the construction of information thruway, and the broad application of the Internet, people have walked into a society of information. In the information society, the Internet provides a lot of usable resources to people, such as text, picture, video, and audio resources. It also becomes an important source of education; nevertheless, the variety and the complex sequences of information from the Internet bring about some difficulties in the retrieval of information. This article brings forward the method of web images classification, which lays foundation for the retrieval of web images.

Keywords Image classification • Icon and pictures • Photograph and drawing

72.1 Introduction

With the rapid development of the Internet technology, the Internet user can reach a lot of information via network. In order to access the information faster and better, it is necessary to preprocess the information very often. The image classification technique that this article discusses about is the pretreatment technology.

Web image varies, and it can be classified from different angles. This article classifies images into the icon image and the picture image according to its function. The icon image's contents are relatively simple with smaller size, while the picture image is more complex, usually having the performance of content, and the content can manifest the landscape, animals, and people; besides, the picture images can be further classified into photograph and graphic images.

G. Wu (✉) • B. Yang • L. Lv
Naval Aeronautical Engineering, Institute Qingdao Branch, 266042 Qingdao, China
e-mail: wgq_toay@sina.com

72.2 Analysis of Image Characteristics

1. Icon class characteristics

The button icon class includes images, trademarks, logos, and other similar small images. The main function of such images is to give users a simple prompt identification, reference, and fast operation.

2. Image class image features

(a) Photo image

A photo picture usually refers to the texture or the trend of texture process with pictures through real pictures or technical software (such as Photoshop and 3D Max). It features vivid, bright, rich, and gradated color.

(b) Drawing image

A drawing image is drawn by hand or software. The drawing image mainly includes cartoons, paintings, and WordArt. While compared with the photo pictures, the drawing images use fewer colors, but the regional color saturation is usually higher, the color transition is also faster than the photo pictures, and the color gradation is thin.

72.3 Study on Classification

72.3.1 *Classification Method of Icons and Picture Image Category*

The classification algorithm about icon images and picture images is relatively simple. The key issue is how to determine the size of the main parameters. There are many methods of parameters to emulate size, such as image size and diagonal size. By the experimental analysis, the diagonal size of the image is taken as the classification parameter. The reference threshold herein is 100 pixels.

72.3.2 *Reclassification of Picture Image (Photographs and Drawings Class Category)*

According to the content of the picture, it can be classified as photos, images, and drawing images. These two types have different characteristics and can be extracted from the classification parameters and classified based on the parameters.

First of all, it can be simply classified. According to previous discussion about the picture character, the picture image is generally characterized by rich, plump colors, usually involving 256 colors or 24b. As to the picture image, its color is generally simpler and less in quantity. As the 2-color and 16-color feature low

Fig. 72.1 2-Color and 16-color drawing image



Fig. 72.2 Color resolution's picture

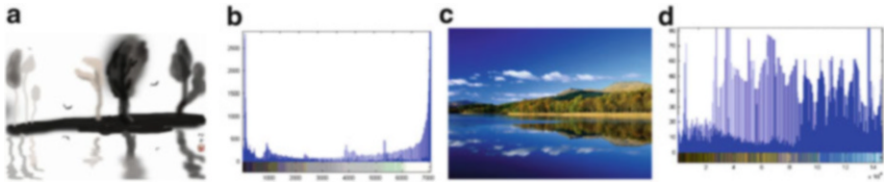
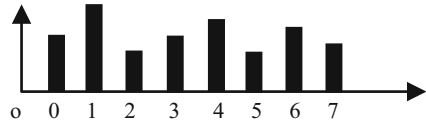


Fig. 72.3 Picture of 24b color resolution. (a) 24b picture, (b) color resolution's picture, (c) 24b photograph, (d) color resolution's picture

resolution, the photo pictures generally do not use the 2-color or 16-color construction. Thus, 2-color and 16-color drawing images can be directly classified as picture image (Fig. 72.1).

The method of using the number of color parameters on image classification only applies to simple pictures. As to the construction of complex images, we use histogram parameters for classification. The image color histogram is referred as the histogram, which is actually a one-dimensional discrete function [1]. Namely,

$$H(k) = n_k \quad k = 0, 1, \dots, L - 1 \tag{72.1}$$

In the formula above, k represents the image feature values and represents certain value of specific color for the color histogram. L is the number of characterized values, namely, the total number of colors, for instance, as to the 256 color images, $L = 256$. n_k is the number of pixels of the image having a characteristic value equal to k . Namely, it is the number of pixels with a specific color value in the picture. As to the diagram shown below, the eight straight side bars correspond to the number of pixels of eight grayscale image (Fig. 72.2).

The following diagrams are 256- and 24b-color resolution histogram. In Fig. 72.3a-d are the 24b picture, color resolution of the picture, 24b photograph, and color resolution of the color histogram, while in Fig. 72.4a-d are the 256 picture, color resolution of the picture, 256 photograph, and color resolution of the color histogram.

Based on comparison and analysis of the above picture, no matter if pictures are of 256 colors or 24b colors, we could find that the distribution of colors of photograph pictures are more even in the color histogram, the number of varieties

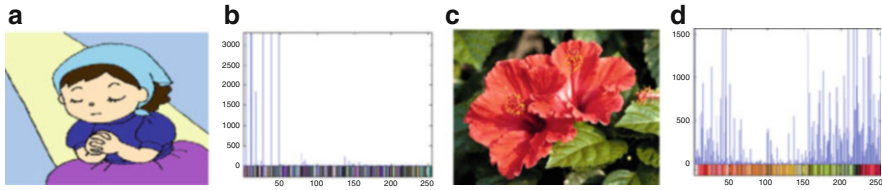


Fig. 72.4 Picture of 256 color resolution. (a) 256 picture, (b) color resolution's picture, (c) 256 photograph, (d) color resolution's picture

of colors are much more, and the total amount of pixels of specific color are generally in low level.

While the distribution of the drawing picture's color is relatively sparse with less colors, the total number of a particular kind of color has large number of pixels [2].

When it comes to classification, images need to be processed, respectively, in two parts, according to the number of colors, number of colors of 24b and number of colors of 256. We know that the total number of 24b-resolution colors image in the palette is $2^{24} = 16 * 10^6$; obviously, it should take a large amount of calculation. If it takes the number of 24b-color image's histogram, it is a very time-consuming matter. Therefore, firstly, you should simplify the color palettes, producing the simplified color histogram of color palettes.

Thus, the calculation will be relatively small. When we simplify the palette of 24b color picture, the method of abandoning parts of color could be used. The 24b colors on the picture, the picture in the construction of the palette, and the R, G, B three-color components use eight binary representations. In order to simplify the color palette, we have to abandon the use of R, G, B color after the four components of the method, that is, only use four-bit binary representation before each of the color components. Thus, the total number of colors, 24b colors, will be reduced to $2^{12} = 4,096$ species. After such processing, the calculation amount of color histogram could be reduced enormously, and the computation time could be shortened greatly. Moreover, the accuracy could be hardly influenced.

During the procedure of algorithm design, the size of the picture should be taken into consideration. If the size of the image is not equal, the number of large size images on more natural color histogram size may be also large; thus, it does not directly use an absolute color histogram as a standard of classification. In the passage, the color histogram will be processed in quantity, that is, the data in color histogram will be normalized, producing relative color histogram. Then, parameters of relative color histogram could be used to classify things.

As to the classification, it is necessary to calculate the frequency of colors. When classifying, it is necessary to calculate high frequency of numbers of color of pictures, that is, the number of columns in color histogram which exceed the threshold. Based on the experimental analysis, the threshold value of the 256 color pictures is set to 0.3, and the 24b image threshold value is set to 0.14. If the number of color histogram exceeds a threshold value, the picture is a photo image; otherwise, the picture is a drawing image.

After the experimental analysis on a huge number of pictures, the appropriate threshold can be selected. Different color resolution images possess different class-based thresholds. Images of 24b color possess a class-based threshold of 250; the class-based threshold of 256 color is 18.

72.3.3 *Reclassification Algorithm of Photo Class Pictures (Man-Made and Natural Scenery Class Category)*

Photos can be further classified into class pictures. The classification from different angles leads to different classes. In this article, the photo image can be classified into natural scenery class pictures and artificial scenery images based on the photo's content.

72.3.3.1 Classification Parameters

Most of the class pictures of natural scenery, animals, plants, and other images often feature brightly color, slow transitions between colors, and no obvious trend in terms of the picture texture. The artificial landscape class pictures generally involve cities with tall buildings, religious temples, and indoor object images with relatively high line drawings and obvious trend texture.

72.3.3.2 Analysis of Classification Algorithm

Firstly, look at line detection methods. There are many line detection methods. We use the Hough transform to detect and extract the line.

Basic Principles of Hough Line Detection Algorithm

The basic principal of Hough transform is the point-line duality. This transformation is a dotted line-like description method. The principle is as below:

Suppose a linear equation

$$y = mx + c \quad (72.2)$$

where x and y represent variables and m and c represent parameters in this equation. If the parameter value is known, the relationship between the coordinates of the point can be determined. If the previous equation is reexpressed:

$$c = y - mx \quad (72.3)$$

In Eq. (72.3), m and c are the variables that we are interested; x and y are constant. The above equation represents the (m, c) , a line in space. Then, a straight line in the space (x, y) corresponds to a point in the (m, c) space. It is noted that the shape of the curve depends on the parameter space for a graph of the original function. Therefore, in practice, often in the form of polar coordinates of a straight line rather than explicit representation, a straight line is to avoid problems posed by the vertical line. Linear polar equation is expressed as below [3]:

$$\rho = x \cos \theta + y \sin \theta \quad (72.4)$$

Hough linear change can be achieved by the following method:

The (x, y) each discrete data point transforms to (ρ, θ) to be divided into many small pieces with each piece of a small unit of ρ and θ that can build a small unit $(\Delta\rho, \Delta\theta)$. Corresponding to each small unit, it can be provided with an accumulator. In the (x, y) , it might be a curve of each point corresponding to the transform domain in a straight line in the domain $\rho = x \cos \theta + y \sin \theta$. The value of $0, \Delta\theta, 2\Delta\theta, 3\Delta\theta$, etc. could be assigned to θ , then the corresponding value of ρ could be figured out. Then we could calculate the number of times of falling in each junior unit, respectively. After the transformation of all data points in (x, y) , we could detect the junior units. In this way, it could be inferred that this point was common points of many curves if there were more points falling in a junior unit, points which are corresponded to those curves could be considered collinear. Detection of (x, y) n points on the plane, the coordinates of the intersection curve (ρ_0, θ_0) substitute $\rho = x \cos \theta + y \sin \theta$. We can get the linear equation [4].

Specific Classification Algorithm

What's mentioned above is the principle of Hough line detection method. In practices, the color images should be converted into grayscale images firstly. Then we could extract the edge of images via a canny operator and conduct binarization processing, obtaining image edge point binary image. Eventually, we should detect straight lines in images through Hough line detection method.

In specific terms, the need for the parameter space (ρ, θ) of the two-dimensional array of the accumulation, the cumulative array, is located (ρ, θ) , as shown in Fig. 72.5:

According to Formula (72.4), ρ value locates in the range $[-L, L]$ (L is diagonal length of the image). The ρ value should be transformed into positive in the process of setting the array. As used herein, ρ values will be converted to positive in the formula $\rho = \rho + L$. Upon conversion, the ρ value should range $[0, 2 * L]$, then $\rho_{\max} = 2 * L$. θ_{\max} is 180. Wherein the quantization of ρ interval = 1, the quantization of θ interval = 10. At first, array A should be set to zero, then edge pixels in picture space should be processed, making $\theta, \Delta\theta, 2\Delta\theta, 3\Delta\theta \dots \theta_{\max}$ equal 0. Finally, according to Formulas (72.3), (72.4), calculate corresponding value of ρ . According to the value ρ and θ (the set are quantized and have been rounded), it is

Fig. 72.5 Schematic diagram of the 2D accumulator array

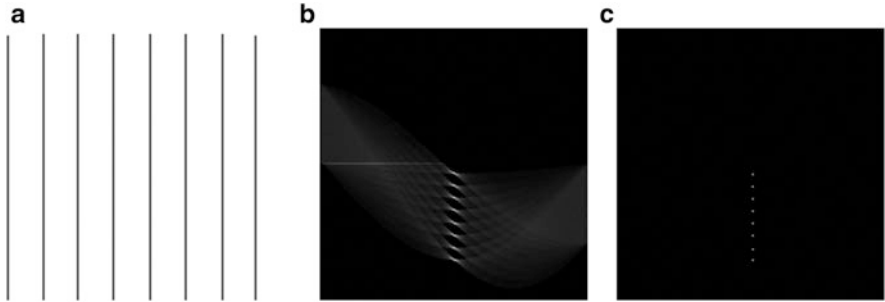
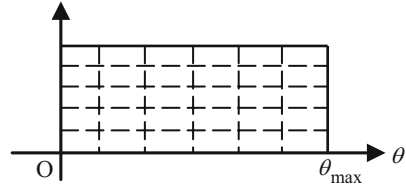


Fig. 72.6 Schematic diagram of detection of Hough line

accumulated: $A(\rho, \theta) = A(\rho, \theta) + 1$. At the end of accumulation, according to $A(\rho, \theta)$ values, it is known as to how many points are collinear, i.e., $A(\rho, \theta)$ value is in the number of the collinear points on $A(\rho, \theta)$. After the experiment, the appropriate threshold is taken to determine the straight line.

```

For(ρ=0, ρ<ρ_max, ρ++)
  For(θ=0, θ<θ_max, θ++)
    If A(ρ, θ) > flag
      threadNum = threadNum + 1
    End
  End
End
    
```

As shown in Fig. 72.6, (a) is the edge of the image, (b) is the expression of histogram of the gray scale about ρ, θ by using the previous algorithm of the picture, and (c) is the result chart that is shown by the detected line. In diagram b and c, x -axis represents the angle of θ , y -axis represents ρ .

The number of edge points in huge size images of natural landscape is still huge after a series of operations, including transferring grayscale images, taking the edge, binaryzation and image refining cause pictures in photo gallery vary a lot in size.

Due to the shortcomings of Hough transformation, the adjacent point is not considered; therefore, it is easy to produce error during the detection. A group of pixels is approximately a straight line or a mistaken straight line. If the absolute

number of linear classification is used as a classification threshold, apparently, the error will be great.

Therefore, we perform the classification by the method of relative linear parameters which refer to the ratio of the number of all edges straight points and the number of pixels in the picture. The line is passed by the Hough transform detection. In other words, the number of detected straight line is obtained by normalizing the value.

Based on the analysis of lots of image experiments, the threshold can be set. If the relative line number parameter value is greater than the threshold value in the picture, the image can be judged as the artificial scenery; otherwise, the image will be classified as natural scene image. After the test, the flag = 0.4.

Result and Conclusion

In order to verify the accuracy of image classification, it is necessary to calculate the proportion of correct images classification in the whole image glossary; the following formula can be adopted to calculate the correct classification rate:

$$\text{Accuracy} = \frac{\text{Number of images which have been correctly classified}}{\text{Number of images which should be correctly classified}} \quad (72.5)$$

1. Results and analysis of classification of icons and pictures

We test 1,100 images (including 500 charts and 600 picture class image) by 12 min; 86.4 % (432/500) icon images and 87.5 % (525/600) picture images can be correctly classified.

2. Results and analysis of reclassification of picture images (photograph and picture type)

1,056 pictures (including 576 pictures and 480 picture images) are tested in the experiment by 16 min; 91.67 % (528/576) photo images and 88.13 % (423/480) picture images can be correctly classified.

3. Results and analysis of reclassification of photographs (man-made and natural scenery class category)

We perform experiment on 876 photo images by 23 min (including 428 natural scenery and 448 artificial scene images); 84.8 % (363/428) natural scene images can be classified correctly with 82.1 % (368/448) artificial scene images classified correctly.

Based on the results of image classification, we can see that the method herein is useful and effective.

References

1. Zhang Y. Content based visual information retrieval. Beijing: Cornell University Press; 2003. p. 64, 84–96 [In Chinese].
2. Hartmann A, Lienhart R. Automatic classification of images on the web. Santa Clara: Intel Corporation; 2001.
3. Meng X, Liu TY. Study on an automatic classification method based on image. J Inform. 2005;9:14–5 [In Chinese].
4. Wang X. Advanced image processing technology. Beijing: China Science and Technology Press; 2001. p. 238–94 [In Chinese].

Chapter 73

Weld Pool Image Processing and Feature Extraction Based on the Vision of the CO₂ Welding

Xiaogang Liu and Xiaowei Ji

Abstract In order to capture a clear image of the weld pool, the experimental system based on the reflection of the arc visual and CCD image acquisition was established in this chapter. As to the molten pool image characteristics of CO₂ arc welding, this chapter introduces a method for welding pool image processing which may access the pool edge information more accurately. Firstly, it is based on the fuzzy entropy filter to remove noise in the multilevel image, modify the image gray value, and enhance the edge of the welding pool image; secondly, it uses the canny operator edges positioning and adopts the mathematical morphology corrosion and expansion comprehensive processing edge of image; thirdly, the edge detection is used for grayscale morphological gradient; and finally, the molten pool characteristic parameters are calculated. Thus it can lay foundation for the real-time control of the welding.

Keywords Visual robotic welding • Welding pool image • Image processing

73.1 Introduction

With the development of social science and technology, the welding quality is increasingly demanded. The shape characteristics and dynamic changes of welding molten pool are important factors which may affect the inner welding quality and the quality of the forming appearance [1, 2]. The real-time detection of weld pool

X. Liu

Guilin University of Aerospace Technology, 541004 Guilin, Guangxi, China

Guangxi University of Science and Technology, 545006 Liuzhou, Guangxi, China

e-mail: 1017834958@qq.com

X. Ji (✉)

Guangxi University of Science and Technology, 545006 Liuzhou, Guangxi, China

e-mail: 5716280@qq.com

shape is one of the key steps to ensure the quality of welding. There are many confounding factors in pooling information transmission and digital quantitative process, such as arc interference. It is difficult to obtain characteristic parameters of the pool; thus it is necessary to get the pool image processing by eliminating the interference factors such as arc image so that we can obtain the correct and clear weld pool image.

Welding pool characteristic parameters usually include the pool half-length, the maximum weld width, and the pool area, in which, the pool image processing is to detect the edge of the pool to get the pool features. In terms of the pool of feature extraction, people have carried out a lot of researches. Based on the weld pool image extraction and analysis, they've successfully extracted the edge of the pool and laser stripe as well as calculated the surface of molten pool 3D shape [3–6]. Cui has established a compound filter system according to the characteristic spectrum of magnesium alloy [7]. Based on the double arc welding molten pool image, the complete pool edge image can be obtained. Chen proposed a new weld pool edge extraction method on the basis of passive light via component tree model [8]. In view of the welding image feature of strong noise and poor stability, a fuzzy detection algorithm of welding image based on wavelet and morphology denoising was presented [9, 10]. Nevertheless, most of these methods used general image processing algorithms without considering the actual situation of the welding process. In this sense, with CO₂ arc welding as the research object, the laboratory's visual acquisition system is adopted to collect the welding pool images by means of fuzzy image processing, thus to extract the welding pool characteristic information, calculate the characteristic parameters of the pool, and to improve the quality of CO₂ arc welding as well.

73.2 Robot Visual Acquisition System

Robot visual image acquisition system consists of the ABBIRB1400 welding robot, the welding control box, the power supply, the computer, the image acquisition card, the CCD camera, the computer lenses, and the workbench. As shown in Fig. 73.1, install a CCD camera on the robot arm. When we were welding, we through nearly infrared composite filter and arc reflection principle to eliminate the interference of arc. The pool image information is put into the image acquisition card then converted into a digital signal and transferred to the computer. Based on the fuzzy entropy filter to remove noise in multilevel image, modify image gray value, and enhance the welding pool image, we can get clear images of the welding pool.



Fig. 73.1 Experiment of the image acquisition system

73.3 Fuzzy Image Processing of Welding Pool

73.3.1 Image-Filtering Process

We collect the pool image to get useful information of weld pool. After the welding pool image processing, we get the edge information of the image; but the acquisition of original welding image is always subject to many interference factors and useless information such as sound, light, electricity, heat, magnetism, and other debris; as a result, we have to preprocess the image to remove the noise interference. Classic methods primarily include the median filtering, the domain average filtering, and the Gaussian filtering. This chapter adopts a fuzzy entropy filter for noise removal in multilevel image. The method is to create a physical model correspondingly according to the characteristics of degradation of multi-value image, construct a class of fuzzy entropy which can reflect the actual image information, and finally restore image to the minimum entropy principle. Assuming four gray values of weld pool image are a , b , c and d , the degradation of the image gray value matrix is shown as below.

$$W_n(i,j) = \begin{bmatrix} \vdots & \vdots & \vdots & \vdots & \vdots \\ \cdots & x(i-1,j-1) & x(i,j-1) & x(i+1,j-1) & \cdots \\ \cdots & x(i-1,j) & x(i,j) & x(i+1,j) & \cdots \\ \cdots & x(i-1,j+1) & x(i,j+1) & x(i+1,j+1) & \cdots \\ \vdots & \vdots & \vdots & \vdots & \vdots \end{bmatrix} \quad (73.1)$$

Four fuzzy sets can be defined as A , B , C , and D with their fuzzy entropy defined as

$$e_a(A) = \frac{1}{(n \times n)} \sum_{k=-(n-1)/2}^{(n-1)/2} \sum_{l=-(n-1)/2}^{(n-1)/2} H_a(u_a(x(i+k, j+l))) \quad (73.2)$$

$$e_b(B) = \frac{1}{(n \times n)} \sum_{k=-(n-1)/2}^{(n-1)/2} \sum_{l=-(n-1)/2}^{(n-1)/2} H_b(u_b(x(i+k, j+l))) \quad (73.3)$$

$$e_c(C) = \frac{1}{(n \times n)} \sum_{k=-(n-1)/2}^{(n-1)/2} \sum_{l=-(n-1)/2}^{(n-1)/2} H_c(u_c(x(i+k, j+l))) \quad (73.4)$$

$$e_d(D) = \frac{1}{(n \times n)} \sum_{k=-(n-1)/2}^{(n-1)/2} \sum_{l=-(n-1)/2}^{(n-1)/2} H_d(u_d(x(i+k, j+l))) \quad (73.5)$$

Calculate the four fuzzy entropy and minimum value, and use the minimum principle for image restoration. Upon the process of image denoising as shown in Fig. 73.2, the original image of welding pool is shown in Fig. 73.3, the pool images upon processing.

Fig. 73.2 The original image of welding pool

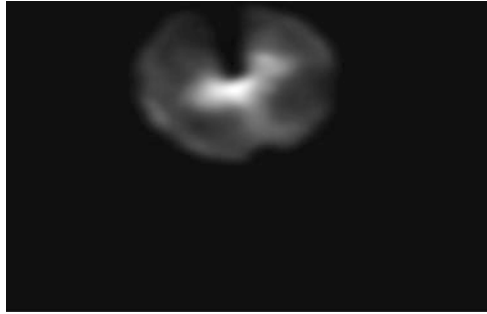
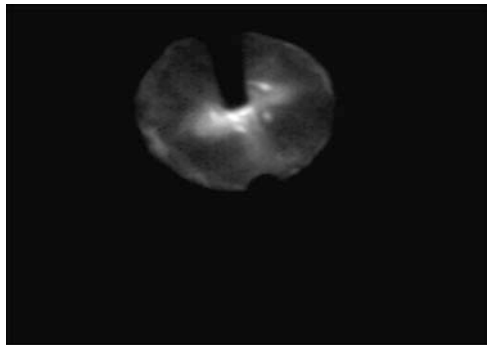


Fig. 73.3 Pool images after processing



73.3.2 Image Edge Enhancement

After filtering, the pool image noise can be greatly inhibited; but the pool edge information is still subject to similar gray, welding pool edge blur and other issues; therefore, the image edge enhancement processing is demanded. This chapter uses the following enhancement operator to enhance the pool images, which is shown as below:

$$EG(i,j) = k + [FG(i + 3,j)] + FG(i + 2,j) + FG(i + 1,j) - FG(i - 1,j) - FG(i - 2,j) - FG(i - 3,j) \quad (73.6)$$

In which, FG refers to the filter with (i,j) for pixel gray value and k for enhancement coefficient. The gradation curve is distinctively different of the images after and before the image edge enhancement. Before the edge enhancement, the gray curve is smooth and many edge information are lost; but after the edge enhancement, a series of peaks and troughs exist at the welding pool edge of gray value. In this sense, we can transform the edge point calculation into the search of extreme value point of gray value calculation. The image has been enhanced as shown in Fig. 73.4 with the weld pool edge image shown in Fig. 73.5, the enhanced weld pool edge image.

Fig. 73.4 The weld pool edge image

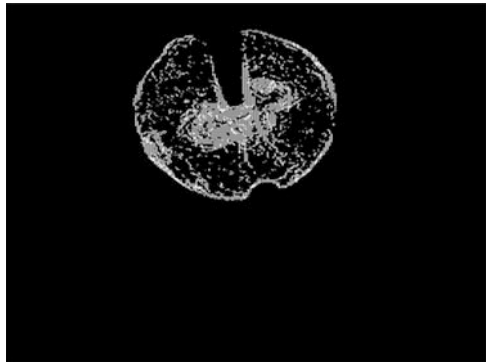


Fig. 73.5 The enhanced weld pool edge image



73.3.3 Pool Edge Detection

The weld pool image upon processing by the filter and image edge enhancement will become relatively clear; however, these projecting pixels are not all the edge point. There are interference noise points and individual points so that we further need to search the weld pool edge to find the real pool edge. In order to obtain the pool feature information, based on the images as enhanced above, the canny operator positioning edge is thus adopted with mathematical morphology erosion and dilation integrated computing adopted afterwards; finally, the gray values of the morphological gradient edge detection pool edge image can be obtained as shown below.

Grayscale morphology corrosion: in order to determine the results which signal A refers to the structure element B (also as a signal) at the point X corrosion. By sliding B , make its X with the origin and push up the elements of its structure. Structure elements that are still below signal A can achieve maximum value which is the result of corrosion. The formula is defined as

$$(A \ominus B)(x) = \max\{y : gx + y \leq A\} \quad (73.7)$$

Grayscale morphological expansion: gray scale expansion is the dual operation of gray corrosion, which takes advantage of the structural elements of the reflection. We can use a reflection structure element, the signal limited in the domain of structural elements, and calculate on the structural elements to make it more than the minimum value at the time signal. The formula is defined as:

$$(A \oplus B)(X) = \min\{y : gx + y \geq A\} \quad (73.8)$$

As shown in Fig. 73.6 indicating the pool edge processing and Fig. 73.7 indicating the pool edge corrosion expansion, we find that the method can better filter out noise while retaining a relatively more abundant pool edge information.

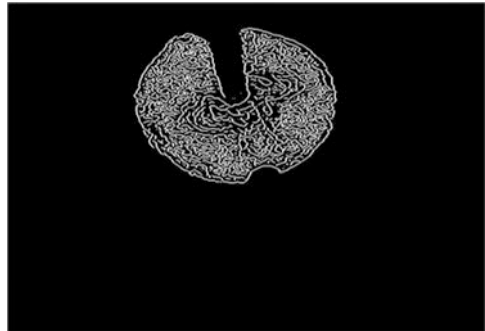
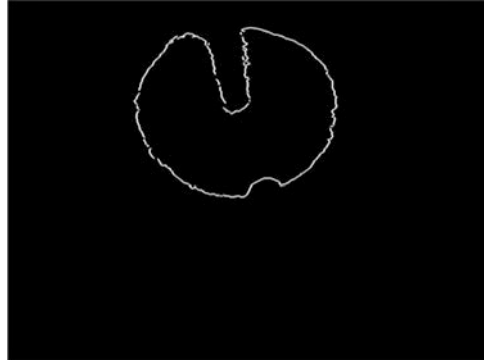


Fig. 73.6 The weld pool edge processing image

Fig. 73.7 The pool edge images after processing



73.4 Characteristic Parameter of Weld Pool Extraction

The pool edge image is obtained by article through image acquisition and processing. Set the width of the weld pool in W , the back of the welding pool length $L/2$, and the angle of the prop α . As shown in Fig. 73.8, we can clearly see the pool edge. We save detection of welding pool edge in array $WL[i]$ and $WR[i]$. We can use the array and formula to calculate the edge characteristics of the weld pool.

The width of the weld pool:

$$W = \max(WR[i] - WL[i]) + 1 \quad (73.9)$$

The back of the welding pool length:

$$L/2 = i_{\max} - i_{\min} + 1 \quad (73.10)$$

The angle of the prop:

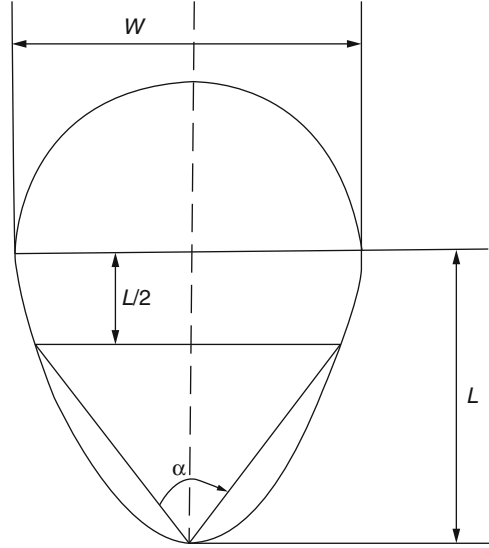
$$\alpha = \arccos \left| \frac{a^2 + b^2 - c^2}{2ab} \right| \quad (73.11)$$

In line with the largest welding pool width i_{\max} and the welding pool tail line with i_{\min} , see formula (11) a , b , c , respectively:

$$a = \sqrt{\left(WR(i_{\max}) - WL\left(\frac{i_{\max} + i_{\min} + 1}{2} + 1\right) \right)^2 + \left(\frac{i_{\max} - i_{\min} + 1}{2}\right)^2} \quad (73.12)$$

$$b = \sqrt{\left(WR\left(\frac{i_{\max} + i_{\min} + 1}{2}\right) - WL(i_{\max}) + 1 \right)^2 + \left(\frac{i_{\max} - i_{\min} + 1}{2}\right)^2} \quad (73.13)$$

Fig. 73.8 Schematic of weld pool



$$c = WR \left(\frac{i_{\max} + i_{\min} + 1}{2} \right) - WL \left(\frac{i_{\max} + i_{\min} + 1}{2} \right) + 1 \quad (73.14)$$

Conclusion

In this chapter, as far as CO₂ visual welding robot is concerned, the experimental system has been established on the basis of the reflection of the arc visual and CCD image acquisition. It is better able to capturing pool image.

According to the characteristics of the weld pool images and the demand of actual welding process control, this chapter proposes a method based on the fuzzy image processing featuring simple algorithm, significant effect and easy parallel processing, smooth edge extraction, and continuous image of the skeleton with less breakpoints; besides, it can extract the main geometric parameters of the pool in a more accurate manner. The experimental results also verify its effectiveness and feasibility.

References

1. Li MX, Wu YX, Cai Y, Sun DW. Research review and developmental trends of image technology in extracting welding pool feature parameters. *Casting Forging Welding*. 2013;39(21):142–5 [in Chinese].
2. Leong KH, Sabo KR, Altshuller B, Wilkinson TL, Albright CE. Laser beam welding of 5182 aluminum alloy sheet. *J Laser Appl*. 2013;11(3):109–18.

3. Zhang YM, Kovacevic R. Real time sensing of sag geometry during GTA welding. *J Manuf Sci Eng.* 2014;119(2):151–60 [in Chinese].
4. Wang YF, Liu NS, Lin HL. Based on structured light projection welding pool image acquisition and processing. *Trans China Weld Inst.* 2012;29(10):81–4 [in Chinese].
5. Matsunawa A, Seto N, Kim J. Observation of keyhole and molten pool behavior in high power laser welding. *Trans Joining Weld Res Inst.* 2014;30(1):14–6.
6. Gallo I, Binaghi E, Raspanti M. Semi-blind image restoration using a local neural approach. *Neurocomputing.* 2012;73(2):389–96.
7. Cui Y, Ma GH, Ma SL. Weld pool image processing in double arc welding. *Hot Working Technol.* 2013;42(23):160–2 [in Chinese].
8. Chen D, Li J, Huang YY, Xu ZL, Zhang T. Weld pool edge extraction method based on passive light via coarse localization and component tree model. *Appl Res Comput.* 2013;30(5):1574–6 [in Chinese].
9. Gao XD, Khalid Hafez M, Katayama SJ. Restoration and characteristic analysis of X-ray images of molten pool during laser deep penetration welding. *Tran China Weld Inst.* 2013;34(2):1–4.
10. Ma HB, Wei SC, Sheng ZX. Robot weld seam tracking method based on passive vision for thin plate closed-gap butt welding. *Int J Adv Manuf Technol.* 2012;48(9–12):945–53.

Chapter 74

On Energy Distribution Characteristics of Froth Images

Yanpeng Wu, Xiaoqi Peng, Yanpo Song, and Qian Jiang

Abstract In this chapter, the model of relationship between flotation process status and its energy distribution character of froth image is proposed. Energy spectrum of froth image is calculated by FFT. The energy distribution of foam images in different frequency domain is analyzed to obtain characteristic decision formula based on energy spectrum distribution of foam image. Using this formula to recognize the flotation conditions, each recognition rate of the working conditions is 90.9 %, 92.9 %, 92.2 %, and 85.2 %, respectively. The average recognition rate reaches 91.4 %. Compared to character decision methods of foam images based on edge segmentation, the proposed method has a faster calculation speed and higher character recognition rate.

Keywords Flotation • Froth image • Fast Fourier Transform • Energy spectrum

74.1 Introduction

Flotation is widely used in complex mineral beneficiation process. In the production process of mineral flotation, status of floating process is closely related to bubbles' geometry [1], RGB components [2], velocity [3], and other information. Works

Y. Wu

School of Energy Science and Engineering, Central South University,
410083 Changsha, China

Provincial Key Laboratory of Informational Service for Rural Area of Southwestern Hunan,
Shaoyang University, 4222000 Shaoyang, China

X. Peng (✉)

School of Energy Science and Engineering, Central South University,
410083 Changsha, China

Department of Information Science and Engineering, Hunan First Normal University,
410000 Changsha, China

e-mail: pengxq126@126.com

Y. Song • Q. Jiang

School of Energy Science and Engineering, Central South University,
410083 Changsha, China

usually regulate and control the flotation process by judging the geometrical structure of the bubbles floating on the tank surface [4].

There are two main froth size distribution analysis methods. One is based on image segmentation method [5, 6]. Such methods enjoy a high recognition rate of image features, but its algorithm is complex with the low real-time performance. The other method is to be determined based on froth characteristics [7, 8].

In this chapter, a Fast Fourier Transform analysis of the energy distribution of different-sized froth is made, and a model of relationship between flotation process status and its energy distribution character of froth image is proposed.

74.2 Definition of the Basic Characteristics of the Flotation Froth Image

At the flotation industrial site, the operators judge the flotation conditions according to the size and number distribution of froth. The froth is divided into four categories: large, medium, small, and others, as shown in Table 74.1. It is generally considered that a large froth has a poor degree of mineralization and carries a small number of concentrate ore; a medium froth has a good mineralization degree, while a small one has high degree of mineralization but low recovery rate.

74.3 The Flotation Froth Image Feature-Determining Algorithm Based on the Amplitude Spectrum's Energy Statistics

Using Fast Fourier Transform to generate the Fourier spectrum is a common method for frequency domain analysis and widely used in such fields as digital image processing.

Table 74.1 Feature definition of froth images

Image class	Feature definition	Description
s	A large number of large froth. Foam inhibitors should be added	Large image occupies more than 50 % area of the total image area
m	A large number of medium froth. Normal condition	Medium image occupies more than 50 % area of the total image area
l	A large number of small froth. Foaming agent should be added	Small image occupies more than 50 % area of the total image area
o	Otherwise, transition state	Large, medium, and small images occupy less than 50 % area of the total image area

Let the image data be $f(x, y)$ ($x = 0, 1, \dots, M-1$; $y = 0, 1, \dots, N-1$), then the discrete Fourier Transform is:

$$F(u, v) = \frac{1}{MN} \sum_{x=0}^{M-1} \sum_{y=0}^{N-1} f(x, y) e^{-i2\pi\left(\frac{ux}{M} + \frac{vy}{N}\right)} \quad (74.1)$$

where $u = 0, 1, \dots, M-1$; $v = 0, 1, \dots, N-1$.

The inverse transformation formula of formula (74.1) is:

$$f(x, y) = \frac{1}{MN} \sum_{u=0}^{M-1} \sum_{v=0}^{N-1} F(u, v) e^{i2\pi\left(\frac{ux}{M} + \frac{vy}{N}\right)} \quad (74.2)$$

where $x = 0, 1, M-1$; $y = 0, 1, \dots, N-1$.

When $M = N$, the discrete Fourier Transform is:

$$\begin{aligned} F(u, v) &= \frac{1}{NN} \sum_{x=0}^{N-1} \sum_{y=0}^{N-1} f(x, y) e^{-i2\pi\frac{ux+vy}{N}} \\ &= \frac{1}{N} \sum_{x=0}^{N-1} f(x, y) e^{-i2\pi\frac{ux}{N}} \cdot \frac{1}{N} \sum_{y=0}^{N-1} f(x, y) e^{-i2\pi\frac{vy}{N}} \end{aligned} \quad (74.3)$$

where $u = 0, 1, \dots, M-1$; $v = 0, 1, \dots, N-1$.

The inverse transformation formula of formula (74.3) is:

$$\begin{aligned} f(x, y) &= \frac{1}{NN} \sum_{u=0}^{N-1} \sum_{v=0}^{N-1} F(u, v) e^{i2\pi\frac{ux+vy}{N}} \\ &= \frac{1}{N} \sum_{u=0}^{N-1} F(u, v) e^{i2\pi\frac{ux}{N}} \cdot \frac{1}{N} \sum_{v=0}^{N-1} F(u, v) e^{i2\pi\frac{vy}{N}} \end{aligned} \quad (74.4)$$

To calculate the two-dimensional Fast Fourier Transform of $f(x, y)$, we first calculate the one-dimensional Fourier Transform along each column and then along each of its rows, i.e., the Fourier amplitude spectrum is:

$$|F(u, v)| = \sqrt{R^2(u, v) + I^2(u, v)} \quad (74.5)$$

The Fourier energy spectrum of the image $f(x, y)$ is:

$$E(u, v) = |F(u, v)|^2 = R^2(u, v) + I^2(u, v) \quad (74.6)$$

The froth image is composed of froth of different sizes and the background. Considering the sharpness of the image and the factor of operation speed, we

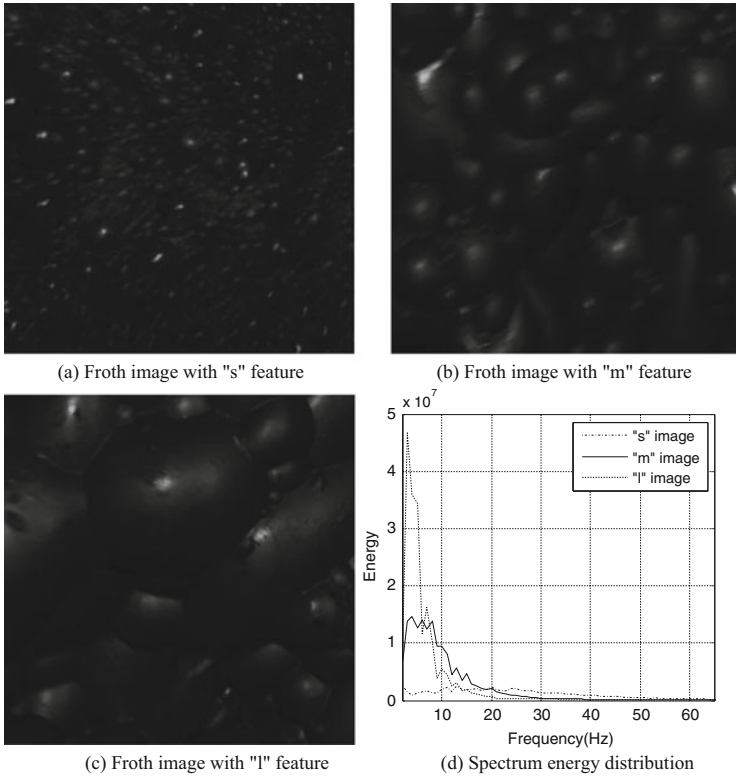


Fig. 74.1 Typical froth images and their spectrum energy distribution. (a) Froth image with “s” feature. (b) Froth image with “m” feature. (c) Froth image with “l” feature. (d) Spectrum energy distribution

choose the middle of the froth image, i.e., area $n * n$ ($n = 22k$). The gray scale is normally calculated, and the linearity of the average gray scale of all froth images is adjusted to 0.20, and we apply the Fast Fourier Transform processing to obtain the spectrum image. Figure 74.1 shows typical froth images and their spectrum energy distribution.

74.4 Experiment Studying

Let low-frequency region be $[1, 100)$, middle-frequency region be $[100, 500)$, and high-frequency region be $[500, 1,000)$. Let e_1 be energy sum of low-frequency components, e_2 be energy sum of middle-frequency components, e_3 be energy sum of high-frequency components, and e_0 be total energy sum of all components. Then,

$$e_0 = e_1 + e_2 + e_3 \tag{74.7}$$

Table 74.2 Statistical analysis of the energy distribution on typical froth images

Froth images	e_1	e_2	e_3	R_1	R_2	R_3
Small feature	13,675,564	54,714,426	7,076,940	0.24	7.73	1.93
Medium feature	107,089,510	50,139,814	1,665,910	2.13	30.09	64.28
Large feature	140,497,303	40,572,071	2,174,475	3.46	18.65	64.61

Also we define the symbols as following:

$$R_1 = \frac{e_1}{e_2} \tag{74.8}$$

$$R_2 = \frac{e_2}{e_3} \tag{74.9}$$

$$R_3 = \frac{e_3}{e_1} \tag{74.10}$$

We make a statistical analysis of the energy distribution of the three typical froth images as shown in Table 74.2.

Then we get a froth image feature-determining formula as follows:

$$H(G) = \begin{cases} s, & 0 < R_2 \leq 11.7 \text{ and } 0 < R_3 \leq 15.1 \\ m, & 0 < R_1 \leq 3.0 \text{ and } R_2 \geq 11.5 \\ 1, & R_1 \geq 3.0 \text{ and } R_3 \geq 32.7 \\ o, & \text{otherwise} \end{cases} \tag{74.11}$$

78 froth image samples taken from flotation industrial site are randomly selected, including 6 small images, 39 medium images, 28 large images, and 5 images without classification, to froth image feature-determining formula. The program runs 75.884 s and the cluster analysis results are shown in Figs. 74.2, 74.3, 74.4.

The calculation results show that:

- (1) Rate of recognition of froth images: “s” type is 90.9 %, “m” type is 92.9 %, “1” type is 92.2 %, and “o” type is 85.2 %. The average recognition rate is 91.4 %.
- (2) Because “o”-type froth image is easy to be confused with other type images in recognizing spectrum energy feature, its recognition rate is the lowest in all froth images.
- (3) The average processing time for each froth image is 0.3852 s, while the average time cost of all other methods based on edge segmentation is over 1 s. Obviously the proposed method is highly efficient with a good real-time performance, thus being practically suitable for real-time production condition criterion.

Fig. 74.2 Cluster analysis on R_1-R_2 to froth images

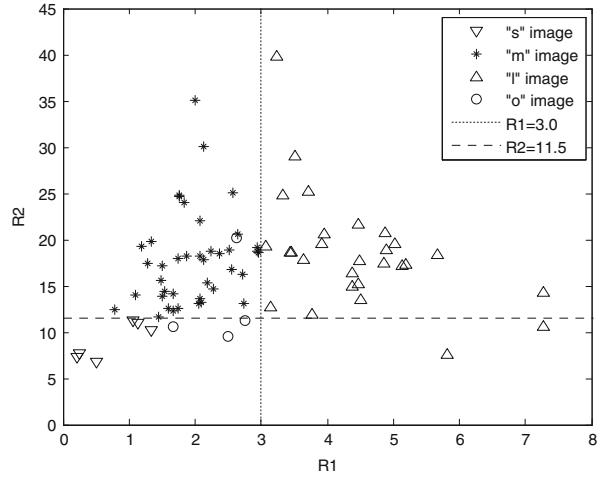


Fig. 74.3 Cluster analysis on R_1-R_3 to froth images

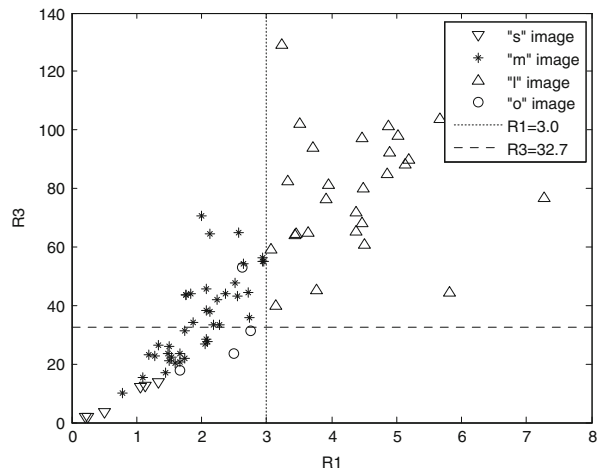
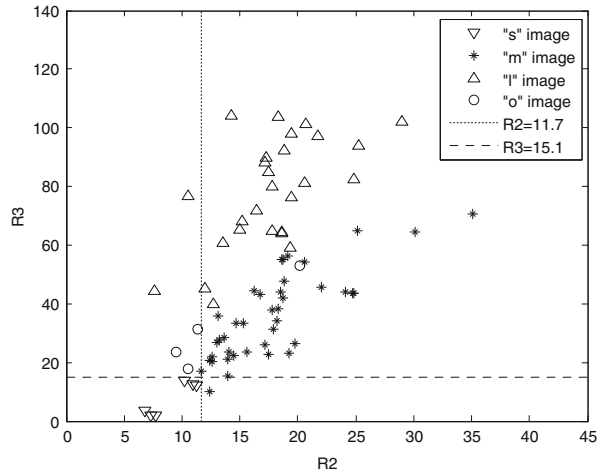


Fig. 74.4 Cluster analysis on R_2 – R_3 to froth images



Conclusion

In the low-energy statistical region, the small froth has the highest energy, the medium froth less high, and the large froth the lowest, respectively, while in the high-energy statistical region, the large froth has the highest energy, the medium froth less high, and the small froth the lowest, respectively. A method of froth image classification and recognition based on analysis of spectral structure characteristics is proposed in this chapter. Simulation results for the froth images obtained from industrial process of alumina flotation show that the average accuracy rate of proposed algorithm is 91.4 % and the average processing time of each frame is 0.3852 s. And it comes to a conclusion that this method achieves a high accuracy rate of recognition and it has good real-time performance, which has a strong popularizing and application value.

Acknowledgements This work was supported by the Natural Science Foundation of China (No. 61134006), Natural Science Foundation of China (No. 61273169), Hunan Province Science Foundation of China (No. 14JJ7077), and Fund of Hunan Provincial Education Department of China (13B107).

References

1. He G, Huang K. Study of the relation between flotation indexes and froth digital images. *Metal Mine*. 2008;386(8):97–101 [in Chinese].
2. Hatonen J, Hyotylliemi H, Miettunen J. Using image information and partial least squares method to estimate mineral concentrations in mineral flotation. In: *Proceedings of the second*

- international conference on intelligent processing and manufacturing of materials, Hawaii, USA; 1999. p. 459–64.
3. Mu X, Liu J, Gui W, et al. Flotation froth motion velocity extraction and analysis based on SIFT features registration. *Inf Control*. 2011;40(4):525–31 [in Chinese].
 4. Ren H-F, Yang C-H, Zhou X, et al. Froth image feature weighted SVM based working condition recognition for flotation process. *J Zhejiang Univ Eng Sci*. 2011;45(12):2115–9 [in Chinese].
 5. Lezoray O, Cardot H. Cooperation of color pixel classification schemes and color watershed: a study for microscopic images. *IEEE Trans Image Process*. 2002;11(7):783–9.
 6. Wang W, Bergholm F, Yang B. Froth delineation based on image classification. *Miner Eng*. 2003;16(3):1183–92.
 7. Bartolacci G, Pelletier P, Tessier J, et al. Application of numerical image analysis to process diagnosis and physical parameter measurement in mineral processes—Part I: Flotation control based on froth textural characteristics. *Miner Eng*. 2006;19(6):734–47.
 8. Moolman DW, Aldrich C, Van Deventer JSJ, et al. Digital image processing as a tool for on-line monitoring of froth in flotation plants. *Miner Eng*. 1994;9(7):1149–64.

Chapter 75

Classification Performances of Extreme Learning Machine with Choquet Integral

Aixia Chen, Zhiyong Liang, and Zhen Guo

Abstract The Choquet integral is a kind of fuzzy integral with respect to fuzzy measure that reflects the interaction of the features. So Choquet integral has been generally applied in classification and multiple classifier fusion, when the interactions exist in the group of features. The difficult step is the learning of the fuzzy measure used in Choquet integral classifier. The ELM technique is used to settle this problem and the ELM Choquet integral classifier is proposed in this chapter. The implementations and performances of ELM Choquet integral classifier and single Choquet integral classifier are compared by a number of experiments on some data sets.

Keywords Choquet fuzzy integral • Possibility distribution • Extreme Learning Machine

75.1 Introduction

Nonadditive set functions have been served as a proper model for describing their interaction mathematically, i.e., the contribution rates. And several types of nonlinear integrals with respect to nonadditive set functions have been defined. In 1974, Sugeno defined the Sugeno fuzzy integral and the fuzzy measure, in which the additivity condition was replaced by the monotonicity, which is weaker than the additivity. And Murofushi and Sugeno presented Choquet fuzzy integral in 1987.

Many researchers have attempted to use nonlinear integral as a fusion operator in multi-attribute classification problems, and the results are very inspiring [1]. In the kind of approaches, the classification results of many classifiers are fused into a final classification result by a fuzzy integral in regard to a fuzzy measure, which shows the weights and the interactions of each classifier for a given class. Sugeno integral and Choquet integral have been used in the nonlinear classification by

A. Chen (✉) • Z. Guo
Hebei University, 071002 Hebei, China
e-mail: aixia_chen@163.com

Z. Liang
Hebei Information and Engineering School, 071000 Hebei, China

many researchers. The upper integral has been used in the nonlinear classification, and the performance of upper integral classifier is competitive [2, 3].

In the chapter, we attempt to introduce ELM into the Choquet integral classifier. Our idea is the following. As is known to all, the decision of nonadditive set function is the difficult problem in fuzzy integral classifiers. Considering the efficiency and performance of Extreme Learning Machine, we will introduce ELM into the Choquet integral classifier. In our ELM Choquet integral classifier, the nonadditive set functions are produced randomly, so the learning complexity of the set functions is reduced hugely. Because the weights β_j are here, we also expect that ELM Choquet integral classifier has better performance than the single Choquet integral classifier.

Following, we briefly present the basic firstly. And then ELM Choquet integral classifier is proposed. In the end, the comparison of ELM Choquet integral classifier and single lower integral classifier are provided by experiments with some data sets.

75.2 Fuzzy Integral

Because the feature spaces that we deal with are generally finite, the following definitions are stated in the finite spaces restrictively. Sugeno has introduced fuzzy measures in 1974. And in 1987, Murofushi and Sugeno presented Choquet integral.

Definition 1 Assume that $X = \{x_1, x_2, \dots, x_n\}$ and Z is the power set of X . A set function $\mu : Z \rightarrow [0, 1]$ where

$$(1) \quad \mu(\Phi) = 0$$

$$(2) \quad A \subseteq B \Rightarrow \mu(A) \leq \mu(B)$$

is named a fuzzy measure, and (X, Z, μ) is named a fuzzy measure space.

Definition 2 Let $X = \{x_1, x_2, \dots, x_n\}$ and (X, Z, μ) be a fuzzy measure space. $f: X \rightarrow [0, 1]$, and f is measurable. Assume that $1 \geq f(x_1) \geq f(x_2) \geq \dots \geq f(x_n) \geq 0$ and $A_i = \{x_n, \dots, x_i\}$. The Choquet integral of f with respect to μ is defined as

$$(C) \int f d\mu = \sum_{i=n}^1 (f(x_i) - f(x_{i+1}))\mu(A_i)$$

where $f(x_{n+1}) = 0$.

Example 1 Let $X = \{x_1, x_2, x_3\}$. The function f is given by $f(x) = \begin{cases} 2 & x = x_1 \\ 9 & x = x_2 \\ 7 & x = x_3 \end{cases}$.

And the set function μ is given in the following Table 75.1. Then the Choquet integral of f with respect to the measure μ is

Table 75.1 The set function μ in Example 1

Set	Φ	$\{x_1\}$	$\{x_2\}$	$\{x_1, x_2\}$	$\{x_3\}$	$\{x_1, x_3\}$	$\{x_2, x_3\}$	$\{x_1, x_2, x_3\}$
μ	0	0.7	0.1	0.9	0.2	0.8	0.3	1

$$\begin{aligned}
 (C) \int f d\mu &= [f(x_1) - 0]\mu(x_1, x_2, x_3) + [f(x_3) - f(x_1)]\mu(x_3, x_2) \\
 &\quad + [f(x_2) - f(x_3)]\mu(x_2) \\
 &= [2 - 0] + [7 - 2] \times 0.3 \vee [9 - 7] \times 0.1 \\
 &= 3.7
 \end{aligned}$$

As the length of the chapter is limited, the properties of fuzzy integral are referred into the literatures.

75.3 Learning Process of the ELM Choquet Integral Classifier

75.3.1 Possibility Distribution

Possibility theory, which generalized the theory of fuzzy logic, was proposed by L.A. Zadeh in 1978 [4]. It is an uncertainty theory and substitution of probability theory, which is used to deal with the incomplete information. Possibility theory has been used in a number of domains, for example, interval analysis and database querying.

Definition 4 X and Z are the same as those in Definition 1. $\Pi : Z \rightarrow [0, 1]$ is called possibility measure, where

- (1) $\Pi(\Phi) = 0, \quad \Pi(X) = 1$
- (2) $\Pi(A \cup B) = \Pi(A) \vee \Pi(B)$

Denote $\pi(x) = \Pi(x)$, and $\pi : X \rightarrow [0, 1]$ be called possibility distribution of X . If there is $x_0 \in X$, such that $\pi(x_0) = 1$, then $\pi : X \rightarrow [0, 1]$ be named normal possibility distribution of X .

Example 2 Assume that a bus is coming every five miniatures. One person has reached the bus station randomly. Let X be the time of waiting a bus at the bus station. In the situation, the possibility distribution of X is the following:

$$\pi(x) = \begin{cases} 1 & x \in [0, 5] \\ 0 & \text{elsewhere} \end{cases}$$

75.3.2 Learning Process

Now we will consider the learning process of ELM Choquet integral classifiers. Assume that there are l_j samples $X_1^j, \dots, X_{l_j}^j$ in class $C_j (j = 1, 2, \dots, m)$. We denote $l = \sum_{j=1}^m l_j$ as the number of all samples and use indices k, i, j to denote a sample, a feature and a class, respectively.

Let X be a sample to be classified. The possibility distribution $\pi(C_j|X)$ is the degree of X belonging to class C_j . In the same manner, the possibility distribution $\pi(C_j|x_i)$ is the partial degree of X with the feature x_i belonging to C_j . Using Cox's axioms, as everyone knows

$$\pi(C_j|x_i) = \pi(x_i|C_j) \quad \forall i, j$$

So, we should assign all $\pi(x_i|C_j)$ at first.

We will learn a known $\pi(x_i|C_j)$ as follows. And we use all the samples in class C_j to construct a "possibilistic histogram". First of all, we will construct a histogram with r boxes p_1, \dots, p_r from the samples, where p_h is the frequency of box h . And the tightest possibility distribution π_1, \dots, π_r will be searched. Assume that $p_1 \geq \dots \geq p_r$; then it is obtained by $\pi_h = \sum_{s=h}^r p_s$. At last, the linear interpolation of the values π_h is used to obtain the continuous $\pi(x_i|C_j)$.

As we know, the determination of the set functions is the hard problem of nonlinear integral classifiers. In our chapter, the Extreme Learning Machine technique is applied in Choquet fuzzy integral classifier to solve the problem [5]. We will describe the scheme of ELM Choquet integral classifier briefly. Denote D as the given training data set and T as the testing data set:

(1) For each feature in class C_j samples, we determine the frequency histogram. With continuous feature i , determine h boxes and their own frequencies p_i . With nominal feature i , consider each value of feature i as a box and their own frequencies p_i .

(2) Rearrange the frequencies p_i , and determine the possibility distribution π_j^i of each feature. The linear interpolation is used to obtain the possibility distribution when the feature is continuous.

(3) For l arbitrary different sample (x_i, t_i) , here $x_i = (x_{i1}, x_{i2}, \dots, x_{im})^T \in R^m$, and $t_i = (t_{i1}, t_{i2}, \dots, t_{in})^T \in R^n$, standard single hidden layer feedforward networks, which have N hidden nodes, are formulated as

$$\sum_{j=1}^N \beta_j g \left((L) \int f(x_i) d\mu_j \right) = o_i$$

where $g(x)$ is the activation function; μ_j is the set function, which connects the input nodes and the j th hidden node; and β_j is the weight vector, which connects the output nodes and the j th hidden node.

It is equivalent to minimize the cost function

$$E = \sum_{i=1}^l \left\| \sum_{j=1}^N \beta_j g \left((L) \int f(x_i) d\mu_j \right) - t_i \right\|$$

In the end, one ELM Choquet fuzzy integral network is produced for each class. In the method, the nonadditive set functions are produced randomly, so the learning complexity of the fuzzy measure is reduced hugely. Because the weights β_j exist, the ELM Choquet integral network could also show itself smoothly and effectively.

(4) Test the ELM Choquet integral classifier on some real data.

75.4 Test on Real Data

We will do some experiments on many real databases which have been widely applied in testing the performances of the classifiers to look into how the ELM Choquet integral classifier works. The information of data sets is listed in Table 75.2.

We use tenfold cross-validation for 20 times worked at each data set in our experiments. Firstly, we construct the possibility histogram for each feature using the samples in class j . If the feature is continuous, it will fall into equal-sized r boxes (it is usually suitable that r is between 7 and 15). Only for continuous attributes, we need the linear interpolation. Then, the ELM Choquet integral classifier will be trained, in which the set functions μ_j are randomly generated and weights β_j are trained to minimize the function E .

The comparison of the accuracy of ELM Choquet integral and single Choquet integral is shown in Table 75.3.

Table 75.2 Data used in experiment

Data set	Number of examples	Number of classes	Number of attributes
Iris	150	3	5
Pima	768	2	9
Wine	178	3	14
Hayes	132	3	6
<i>E. coli</i>	336	8	8
Tic-tac-toe	958	2	9

Table 75.3 Comparison between ELM Choquet integral and Choquet integral

Data set	Choquet integral		ELM Choquet integral	
	Mean	Std dev	Mean	Std dev
Iris	0.9527	0.0088	0.9711	0.0079
Pima	0.7572	0.0122	0.7818	0.0094
Wine	0.9527	0.0095	0.9697	0.0071
Hayes	0.6430	0.0243	0.6681	0.0117
<i>E. coli</i>	0.7499	0.0156	0.7721	0.0110
Tic-tac-toe	0.6511	0.0107	0.6871	0.0079

From Table 75.3, it is known that the ELM Choquet integral classifier works well on both features. And an accuracy comparison between Choquet integral and ELM Choquet integral is present. It is known that the performance of ELM Choquet integral classifier precedes the single Choquet integral classifier. We know the decision of nonadditive set function is the difficult problem in fuzzy integral classifiers. In our ELM Choquet integral classifier, the nonadditive set functions are randomly generated. We can see that the computational complexity will be largely reduced. Because the weights β_j exist, the ELM Choquet integral network could also show itself smoothly and effectively.

Conclusion

To use the information from each feature effectively, motivated by the effectiveness of ELM, this chapter proposed ELM Choquet integral classifier. In this method, the fuzzy measures are produced randomly and the learning complexity of the fuzzy measures is reduced hugely. So the training speed of ELM Choquet integral classifier is very fast. Because ELM Choquet integral classifier takes into account the weights and interactions of individual features, it is able to model the interactions of the features flexibly. From the experimental results on real data sets, we can see that ELM Choquet integral classifier could do effectively the continuous and nominal features. And the performance of ELM Choquet integral classifier is better than the single Choquet integral classifier. This chapter has demonstrated that the effectiveness of the ELM Choquet fuzzy integral classifier, but relationship between the classification performance and the type of fuzzy integral will be under the investigation.

Acknowledgements The chapter was supported by Projects of Hebei Provincial Department of Education (Nos. Z2012101 and QN20131055) and the Youth Foundation of Hebei University (No. 2010Q26).

References

1. Grabisch M. The application of fuzzy integrals in multicriteria decision making. *Eur J Oper Res.* 1995;89(3):445–56.
2. Wang XZ, Chen AX, Feng HM. Upper integral network with extreme learning mechanism. *Neurocomputing.* 2011;74(16):2520–5.
3. Chen AX, Liang ZY, Feng HM. Classification based on upper integral. In: *Proceedings of 2011 international conference on machine learning and cybernetics, vol. 2.* IEEE, Hebei University; 2011. p. 835–40.
4. Zadeh LA. Fuzzy sets as a basis for a theory of possibility. *Fuzzy Set Syst.* 1978;1:3–28.
5. Huang GB, Zhu QY, Siew CK. Extreme learning machine: theory and applications. *Neurocomputing.* 2006;70(1–3):489–501.

Chapter 76

Facial Expression Recognition Using Color-Depth Cameras

Kezhen Xie, Zhen Li, and Zhiqiang Wei

Abstract We present a novel facial expression recognition approach based on both color images and depth images obtained by color-depth sensors in this chapter. Firstly, we estimate the head pose by a scale-invariant projection method proposed by Pamplona Segundo, M. Facial expression images are separated into three categories and we get the corresponding category of the expression according to the head pose. Expression features are extracted through Gabor wavelet and principal component analysis (PCA) method. Finally, the recognition is performed by Hidden Markov Model (HMM). Through the experiments, the recognition rate of the proposed method is 92.4 %.

Keywords Facial expression recognition • Scale-invariant projection • Gabor • HMM

76.1 Introduction

Facial expression is a basic manner for human to deliver emotions in nonverbal communications. The Rule of Mehrabian indicates that speaker's facial expression contributes 55 % to the effect of the whole message [1]. Facial expressions provide important information of one's inner world; thus, facial expression recognition can provide the information to apprehend the emotion activity of a person's interest [2].

As early as in 1970s, Paul Ekman developed the Facial Action Coding System (FACS) to describe facial behaviors by dividing faces into a number of Action Units (AUs) [3]. Before the recognition of expressions, face detection and feature extraction should be performed. For face detection, the algorithm using Haar-like features described by Viola and Jones and Guillaume Gibert has studied a face detection method based on photoplethysmography [4, 5]. Facial feature extraction methods such as principal component analysis (PCA) and linear discriminant analysis (LDA) [6, 7] have been widely studied. For facial expression classification, when

K. Xie (✉) • Z. Li • Z. Wei
Department of Computer Science and Technology, Ocean University of China,
266100 Qingdao, China
e-mail: xiekezhenivy@163.com



Fig. 76.1 Facial expression recognition system

gray information is extracted as features, the classification method based on distance is generally adopted.

Over the past 30 years, most researches focused on 2D facial expression recognition based on color images. However, the recognition rate is generally not high. Motivated by this fact, a color-depth camera is used in this chapter which has 3D depth sensors and a color camera for acquisition. The proposed method uses a 3D detector to locate faces under pose variation and gives an estimation of the head pose using a scale-invariant projection method. Then color images and depth images are normalized to a standard size and Gabor wavelet and PCA are applied to extract facial expression features [6]. Finally, HMM model is used for facial expression recognition. As is shown in Fig. 76.1:

76.2 Facial Expression Recognition

76.2.1 Data Acquisition

A color-depth camera is used to capture color and depth images. Depth images are insensitive to illumination and pose variations, and color images contain more details of facial expressions; thus, we can obtain more information of facial expressions by adopting both color images and depth images for facial expression recognition.

76.2.2 Face Detection

In the face detection stage, a boosted cascade classifier of Harr features is applied to classify image regions as face or non-face in the color-depth sensor. Pamplona Segundo proposed an idea that multiple scale-invariant projection images are created from different viewpoints in order to represent rotated faces as frontal faces [8]. This idea can also be used to detect face expressions under pose variation for the purpose of face expression recognition. In this chapter, only the viewpoint changes around x -axis (pitch rotations) and y -axis (yaw rotations) are considered since there is little pose variation around z -axis in everyday use of computers. α and β are the maximum values for pitch and yaw rotations. In this work, $\alpha = 50$ and $\beta = 30$. Multiple scale-invariant projection images are created for all viewpoints within the range specified by α and β at 5° steps which are more detailed than those

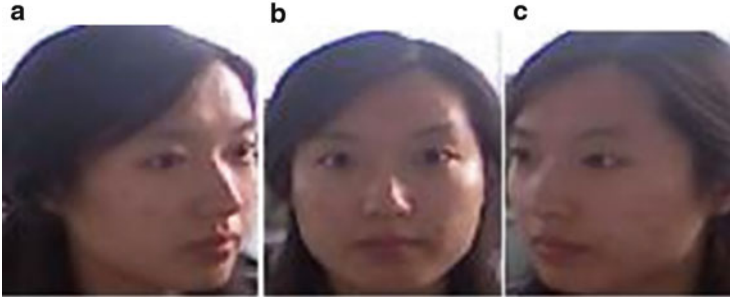


Fig. 76.2 Three categories of images: (a) the left half of the face, (b) the front face, (c) the right half of the face

in Segundo's work to acquire more accurate data. The detection result is used to obtain a rough estimation of the head pose.

Pamplona Segundo [8] divided each image into three different regions of interest (ROIs) in his normalization stage: the left, the right, the nose region. This idea can also be applied in this work. In this chapter, expression images are separated into three different categories: the left half of the face, the front face which contains the whole face and the right half of the face, respectively, shown in Fig. 76.5b–d. According to the estimated head pose, the expression to be detected would be compared with the corresponding images and HMMs, which can save time and improve the recognition rate. The front face is selected for frontal face, the left half of the face is selected when the user is looking to the right, and the right face is selected when the user is looking to the left (Fig. 76.2).

76.2.3 Facial Expression Feature Extraction

Before feature extraction stage, all facial expression images are preprocessed: both color images and depth images are normalized, and then the normalized color images are converted to grayscale images. In facial expression feature extraction stage, Gabor wavelet is used to extract features from preprocessed depth images and color images. PCA method is adopted to reduce feature dimensions.

76.2.3.1 Gabor Wavelet Feature Extraction of Facial Expression

Gabor feature of a person's facial expression image is the result of convolution of the image and the Gabor wavelet $\psi_{u,v}(x, y)$. Assume that $f(x, y)$ represents the gray distribution of an image, then the Gabor feature is expressed as follows:

$$Q_{u,v}(x, y) = f(x, y) * \psi_{u,v}(x, y) \quad (76.1)$$



Fig. 76.3 The Gabor feature extraction process

* is the convolution factor, and $Q_{u,v}(x,y)$ is the convolution result on the corresponding dimension v and direction u . In order to obtain the Gabor wavelet feature values of the coordinates (x,y) , we combine $f(x,y)$ and the corresponding amplitude values of Gabor wavelet for five dimensions and eight directions. To unite the Gabor wavelet feature values of every (x,y) , we get the Gabor feature vector of the whole image.

The Gabor feature A of the preprocessed color image is obtained by the convolution of the corresponding grayscale image and the Gabor wavelet. The Gabor feature B of the preprocessed depth image is obtained by convolution of the normalized depth image and the Gabor wavelet. Then, the Gabor feature of this expression is the combination of A and B . As is shown in Fig. 76.3:

76.2.3.2 Feature Dimension Reduction Using PCA

After two-dimensional Gabor sampling on five scales and eight directions, the Gabor feature dimension of every image is 40 times as large as the gray image’s dimension. Suppose all the facial images are of $64 * 64$ pixels, then the feature dimension of an image turns to 163,840 ($64 * 64 * 40$) after Gabor wavelet transform. Then the Gabor feature dimensionality of this expression is 327,680 ($163,840 * 2$). To avoid excessive computation and improve computing speed, PCA is adopted to reduce dimensions.

Assume m -dimensionality feature vector x_i ($i = 1, 2, \dots, N$) is used to express N sample images of facial expressions; first, every sample image x_i is normalized to x'_i which fits the normal distribution $N(0, 1)$. All the normalized images form the matrix $X = (x'_1, x'_2, \dots, x'_N)$, and the covariance matrix is $Q = XX^T$. The eigenvector E of Q is sorted according to the eigenvalue λ of Q . Then the first n columns of the sorted eigenvector are taken as the linear transformation matrix W_{pca} . After PCA transformation, we get the feature vector as follows:

$$y_i = W_{pca}^T X'_i \quad (i = 1, 2, \dots, N) \tag{76.2}$$

W_{pca}^T is the transposition of W_{pca} and y_i is an n -dimensionality column vector. In this chapter, the number of feature dimension of every image is reduced to 128.

76.3 Facial Expression Training and Classification

Hidden Markov Model (HMM) can be written as $\lambda = (N, M, \pi, A, B)$, shortened as $\lambda = (\pi, A, B)$. HMM is divided into two parts: one part is Markov chain, described as π, A , the output is state sequence; the other one is random process, described as B , the output is observation values sequence. HMM model can be described as the following parameters specifically:

1. N : The number of Markov chain state in the model. The N states are set as S_1, S_2, \dots, S_N and the Markov chain state at time t is $q_t, q_t \in (S_1, S_2, \dots, S_N)$.
2. M : The possible number of observation values corresponds to each state. The M observation values are V_1, V_2, \dots, V_M , and the observation value at time t is $O_t, O_t \in (V_1, V_2, \dots, V_M)$.
3. π : The initial state probability vector, $\pi = (\pi_1, \pi_2, \dots, \pi_N)$.

Among this,

$$\begin{cases} \pi_i = P(q_1 = S_i), & 1 \leq i \leq N \\ \pi_i \geq 0 \\ \sum_{i=1}^N \pi_i = 1 \end{cases} \quad (76.3)$$

4. A is the state transition probability matrix, $A = (a_{ij})_{N \times M}$.

Among this,

$$\begin{cases} a_{ij} = p(q_{t+1} = S_j | q_t = S_i), & 1 \leq i, j \leq N \\ a_{ij} \geq 0 \\ \sum_{i=1}^N a_{ij} = 1 \end{cases} \quad (76.4)$$

5. B is probability matrix of observed values, $B = (b_{jk})_{N \times M}$.

Among this,

$$\begin{cases} b_j(k) = p(O_t = V_k | q_t = S_j) = p(V_k | S_j), & 1 \leq j \leq N, \quad 1 \leq k \leq M \\ b_j(k) \geq 0 \\ \sum_{k=1}^M b_j(k) = 1 \end{cases} \quad (76.5)$$

The training stage is to provide an optimized HMM by training multiple facial expression images for each kind of expression. Seven kinds of facial expression are adopted in this chapter: happiness, sadness, fear, disgust, surprise, anger, and neutral emotion; thus, seven HMMs are trained for each kind, which means 21 ($7 * 3$) models are trained in total.

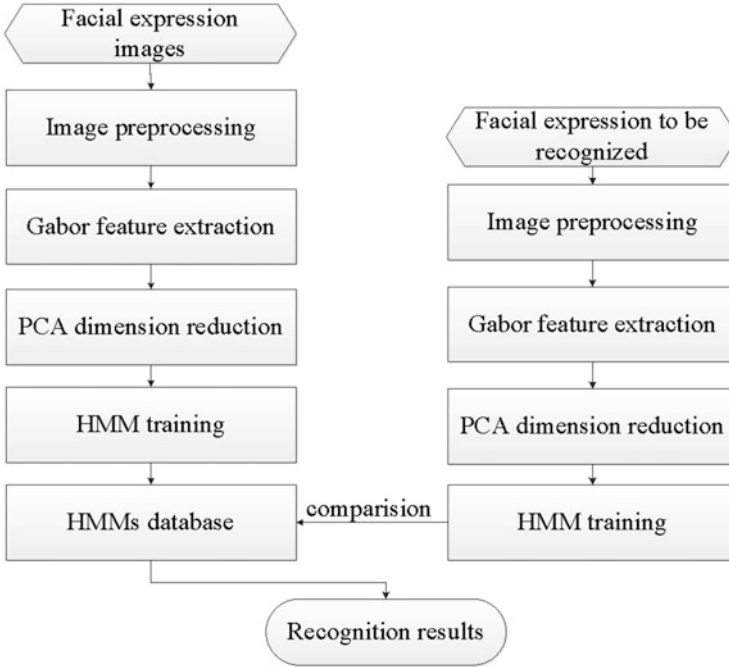


Fig. 76.4 The expression recognition flowchart

The steps of training HMMs are as follows:

1. After the observation sequence $O = O_1, O_2, \dots, O_n$ and the model $\lambda = (\pi, A, B)$ are obtained, the occurred probability $P(O|\lambda)$ of observation sequence under this model is calculated using forward–backward algorithm.
2. The corresponding state sequence $S = q_1, q_2, \dots, q_n$ is selected by Viterbi algorithm which can explain the observation sequence reasonably, that is, to uncover the implicit part of the model and to find the optimal state sequence in the optimization criterion.
3. Baum–Welch algorithm is used to adjust the model parameters $\lambda = (\pi, A, B)$, and it can offer the five parameters in the model which can make $P(O|\lambda)$ the maximum.

In this chapter, observation vectors are constructed using extracted features in 2.3 and each expression corresponds to an HMM. For a facial expression to be recognized, the HMM is obtained using the training steps, then the HMM is compared with the HMMs in database. The expression with the greatest probability is the one to identify. The expression recognition flowchart is shown in Fig. 76.4.

76.4 Experimental Results

The facial expression recognition experiment is performed on our own database. The database contains eight people, each of which has seven kinds of expression for every category (the left half of the face, the right half of the face, and the front face) with both color image and depth image. It contains 336($8 * 7 * 3 * 2$) $64 * 64$ pixel facial images in total. As is shown in Fig. 76.5a–c, these are parts of the database. The expressions are anger, disgust, fear, happiness, neutral emotion, sadness, and surprise from left to right. The 336 images are divided into three groups, one group is of the left half of the face, another is of the right half of the face, and the third one is of the front region. Thus, each group has 112 images ($8 * 7 * 2$). HMM is trained for every expression in each group. The eight people who appeared in the database are employed for the test. The results are shown in Table 76.1:



Fig. 76.5 Part images of the database: (a) color images of front face, (b) depth images of front face, (c) color images of left half of the face, (d) color images of the right half of the face

Table 76.1 The results of facial expression recognition

	Anger	Disgust	Fear	Happiness	Neutral	Sadness	Surprise	Recognition rate (%)
Anger	56	2	0	0	0	1	1	93.3
Disgust	2	55	0	0	1	2	0	91.67
Fear	0	1	55	0	1	1	2	91.67
Happiness	0	0	1	57	1	0	2	95
Neutral	0	1	2	1	54	1	1	90
Sadness	2	2	0	0	0	55	1	91.67
Surprise	1	1	0	0	1	1	56	93.3
Overall recognition rate								92.4

As can be seen from Table 76.1, the proposed method can obtain better recognition rate. But it can also be seen from the table that there always exists misrecognition.

Conclusion

In this chapter, a new method of facial expression recognition is proposed. Head pose is estimated in face detection stage. Then facial expression features are extracted using Gabor wavelet and PCA method and the corresponding HMM is trained. The corresponding HMM is compared with HMMs in the database. It is more accurate in recognition and we have achieved 92.4 % of the overall recognition rate. The method is well used in practice and the program using the method runs smoothly on computers.

Acknowledgement This work was supported by the National Natural Science Foundation No. 61202208 of China.

References

1. Mehrabian A. Communication without words. *Psychol Today*. 1968;2(4):53–6.
2. Shishir B. Recognition of facial expressions using Gabor wavelets and learning vector quantization. *Eng Appl Artif Intell*. 2008;21(7):1056–64.
3. Ryan A. Automated facial expression recognition system. In: *Security technology*. Piscataway: IEEE; 2009. p. 172–7.
4. Viola P, Jones M. Rapid object detection using a boosted cascade of simple features. In: *Computer vision and pattern recognition (CVPR)*. Piscataway: IEEE; 2001. p. 511–8.
5. Gibert G, D’Alessandro D, Lance F. Face detection method based on photoplethysmography. In: *Advanced video and signal based surveillance (AVSS)*. Piscataway: IEEE; 2013. p. 449–53.
6. Chen J, Zhao Z, Sun H. Facial expression recognition based on PCA reconstruction. In: *Computer science and education (ICCSE)*. Piscataway: IEEE; 2010. p. 195 – 8.
7. Dalal N, Triggs B. Histograms of oriented gradients for human detection. In: *Computer vision and pattern recognition (CVPR)*. Piscataway: IEEE; 2005. p. 886–93.
8. Pamplona Segundo M, Sarkar S, Goldgof D, Silva L, Bellon O. Continuous 3D face authentication using RGB-D cameras. In: *Computer vision and pattern recognition workshops (CVPRW)*. Piscataway: IEEE; 2013. p. 64–9.

Chapter 77

Parallel Pipeline Implementation for Moving Objects Detection in Traffic Video Analysis on a Heterogeneous Platform

Teng Li, Yong Dou, Jingfei Jiang, and Peng Qiao

Abstract Moving objects detection is important in traffic video analysis, and many algorithms are being increasingly applied to moving objects detection. Most of these algorithms are time-consuming and cannot satisfy real-time demand in traffic video analysis by using a conventional central processing unit (CPU) sequential method. The emergence of the graphics processing unit (GPU) and multi-core CPU provides a method to accelerate the aforementioned algorithms to meet demand. In this study, we provide a GPU-accelerated implementation of the background subtraction algorithm and the morphological operation algorithm. Then, the connected component labeling algorithm is parallelized on a multi-core CPU with Open Multi-Processing (OpenMP). Furthermore, parallel pipeline implementation on a heterogeneous platform is proposed by integrating the aforementioned algorithms. Experimental results show that the proposed implementation achieves a significant speedup of up to $5\times$, compared with sequential implementation on a CPU.

Keywords Moving objects detection • Parallel • Pipeline • Heterogeneous platform

77.1 Introduction

Moving objects detection in traffic video analysis is a widely studied topic in computer vision, which has become increasingly important with high demands for applications such as security surveillance and intelligent traffic surveillance.

The basic principle of moving objects detection in traffic video analysis is extracting objects area by analyzing video frame in spatial and temporal domain. In the last few decades, a lot of moving objects detection methods have been

T. Li (✉) • Y. Dou • J. Jiang • P. Qiao
Department of Computer Science, National Laboratory for Parallel and Distributed Processing,
National University of Defense Technology, 410073 Changsha, China
e-mail: liteng09@163.com

proposed. And three popular methods are wildly used today. The first one is the optical flow method [1], which detects moving objects by identifying motion flow field. The second one is the frame difference method [2], which detects moving objects by identifying the difference between two adjacent frames at a fixed threshold. The third one is the background subtraction method [3], which detects moving objects by identifying the difference between the captured frame and the background frame. In our study, we proposed a moving objects detection method based on background subtraction.

A moving objects detection method based on background subtraction is described in this chapter. The method consists of three algorithms: the background subtraction algorithm (Step 1), the morphological operation algorithm (Step 2), and the connected component labeling algorithm (Step 3). Steps 1 and 2 are implemented on a CPU via the Open Source Computer Vision (OpenCV) [4]. Step 3 is also implemented on a CPU. The computational efficiency of CPU implementations is low, and such implementations can be parallelized property. Steps 1 and 2 are mapped onto a graphics processing unit (GPU) via the Compute Unified Device Architecture (CUDA) [5], whereas Step 3 is accelerated by using the Open Multi-Processing (OpenMP) application program interface [6]. We further use OpenMP and CUDA to describe pipeline implementation on a heterogeneous platform.

The remainder of this chapter is organized as follows. Section 77.2 provides an overview of the background and related works. Section 77.3 introduces our implementation method. Section 77.4 describes the experimental result.

77.2 Background and Related Works

Figure 77.1 illustrates the moving objects detection method described earlier. In Step 1, a difference image is obtained by using a background image and a frame captured from cameras or video files. In Step 2, the obtained difference image is filtered via a morphological operation (opening and closing). In Step 3, connected components are obtained from the filtered difference image. These connected components are the object in the traffic videos and are highlighted by colored rectangles.

The background subtraction algorithm, which is a common processing algorithm in moving objects detection method, has been successfully accelerated on GPU in

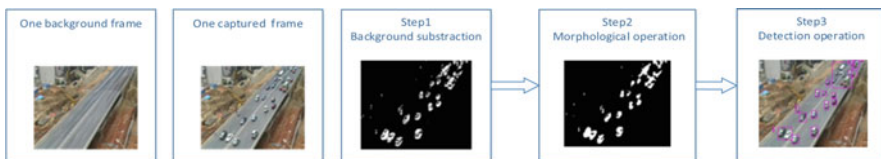


Fig. 77.1 Sequential implement on a CPU

the last few years. Carr [7] and Li et al. [8] provide a parallel optimization by using different method on GPU with performance gains of $5\times$ and $24\times$ speedup, respectively.

The morphological operation algorithm, which is based on pixel matrix computation, is a highly time-consuming algorithm on CPUs. Rane [9] and Adrjanowicz et al. [10] provided parallel optimization on a GPU, in which they achieved speedups of $2\times$ and $3.5\times$, respectively.

These researchers employed a GPU to calculate one frame each time. Such process does not require a GPU to have a massively computing capability. Moreover, frequent data transfer between a CPU and a GPU causes a big performance loss on a GPU.

The connected component labeling algorithm is an important algorithm in computer vision; Suzuki [11] and Suzuki et al. [12] provided different sequential algorithms, which are not fit for GPU implementation. Hawick et al. [13] described a novel parallel algorithm, wherein an image has many multi-connected components. The distances between each connected component vary significantly from one another, and an asymmetrical feature is prominent. By conducting an experimental implementation on a GPU, the parallel algorithm exhibits only a few speedups at the pixel level.

In this study, we proposed an accelerated implementation of the moving objects detection method based on background subtraction. We implement the background subtraction algorithm (Step 1) and the morphological operation algorithm (Step 2) for CUDA on a GPU. Both algorithms are suitable for parallel implementation because of data dependency at the pixel level. Then, we design a multi-core CPU implementation for connected component labeling algorithm (Step 3), which is parallelized at the image level. Furthermore, pipeline implementation on a heterogeneous platform is provided to enable high-performance processing of moving objects detection in traffic video analysis.

77.3 Implementation Method

77.3.1 Implementing CUDA on a GPU

The GPU used in our experiment is the NVIDIA GTX 580, which includes 16 multiprocessors. During implementation, the computed kernel has 16×16 threads per block, and each block computes one frame at the pixel level by using a loop in the kernel function. The blocks are organized into 2-D grids to compute for N frames at the image level.

Step 1: The background subtraction algorithm

In Fig. 77.2, N source images are copied from the CPU to the global memory to the GPU. To satisfy memory alignment requirements, data are loaded as a 1-D array. The source image is an RGB image, wherein each pixel has three channels

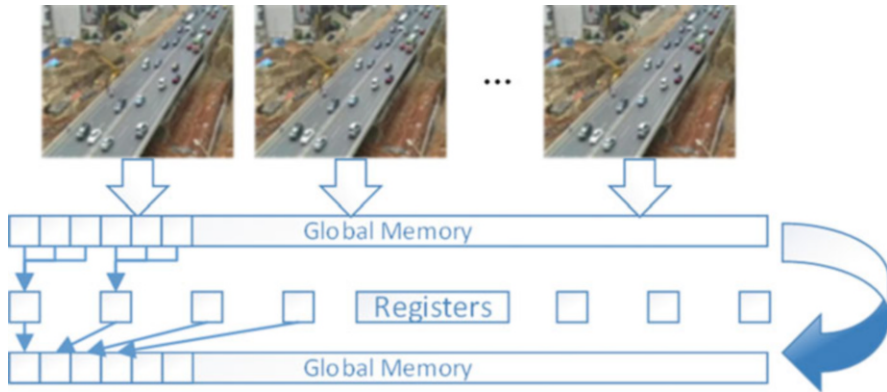


Fig. 77.2 Background subtraction algorithm storage model on a GPU

with an 8-bit width. The resulting image is a binary image, wherein each pixel has one channel with an 8-bit width. To maximize global memory space, the background image is preprocessed on the CPU, and only one binary background image is stored in the GPU because of data reuse.

In the kernel, each source image is initially converted from RGB to grayscale; the intermediate results for the 16×16 threads are stored in the register (the fastest memory of the GPU). Each thread in the block executes the background subtraction algorithm in parallel until the block covers the entire image. Finally, the computed results are reloaded into the global memory for the next step. The results from the implementation of the background subtraction algorithm are shown in Fig. 77.1.

Step 2: The morphological operation algorithm

In our proposed method, the morphological operation algorithm includes an opening and closing operation, which comprises erosion and dilation operations. Notably, the morphological operation algorithm has a high frequency of data reuse.

In Fig. 77.3, the erosion operation is given as an example. The blue pixel searches for the minimum value from its neighborhood by using the specified structuring element (3×3 in our figure).

To increase efficiency in using the GPU memory, the texture memory of the GPU is used to bind N binary pictures (from Step 1). In the kernel, each block has 16×16 threads. These threads have a high frequency of data reuse, and thus, data are loaded from the texture memory to the shared memory to increase memory utilization and reduce execution time. However, Fig. 77.4a presents a problem for the shared memory, that is, some threads are required to solve apron pixels, which cannot load from the texture memory only one time. Moreover, some threads in the block are also needed to solve the nonexistence of data apron pixels in the picture.

In Fig. 77.4b, the shared memory is divided into four parts, and data from the texture memory are copied four times. An apron test is performed for each pixel. If the data exceed image size, then the image will have special data so that the data of each pixel can be computed correctly. Inside the computation loop for searching, a

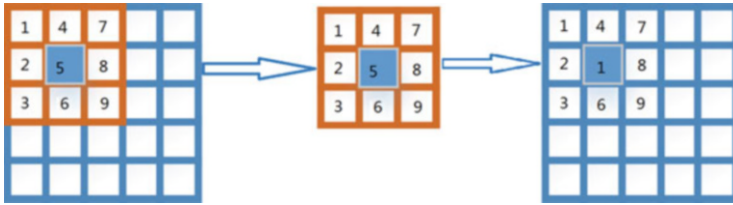


Fig. 77.3 The erosion operation with 3×3 structuring element

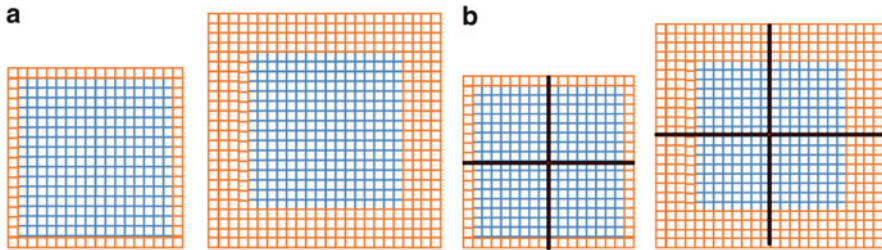


Fig. 77.4 The apron effects of morphological operation. (a) Shared memory without division. (b) Shared memory with division

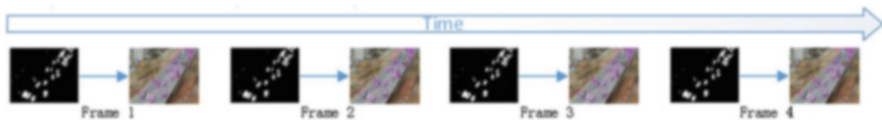


Fig. 77.5 Sequential processing model

bank conflict occurs. Such conflict prevents threads to simultaneously access the shared memory at the same time. Hence, the shared memory is rearranged into a 1-D array to avoid bank conflict. The results from the implementation of the morphological operation algorithm are shown in Fig. 77.1.

77.3.2 Implementing OpenMP on a Multi-core CPU

Step 3: The connected component labeling algorithm

Based on the previous work, the connected component labeling algorithm is applied to detect objects from the source image. In Fig. 77.5, the conventional sequential algorithm is implemented on the CPU, that is, the image is processed in a sequential method. Given the independence for each image, we use multi-core CPU to accelerate independent image in parallel at the coarse-grained level (image level) (Fig. 77.6).

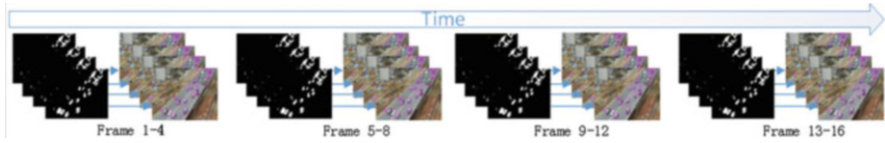


Fig. 77.6 Parallel processing model

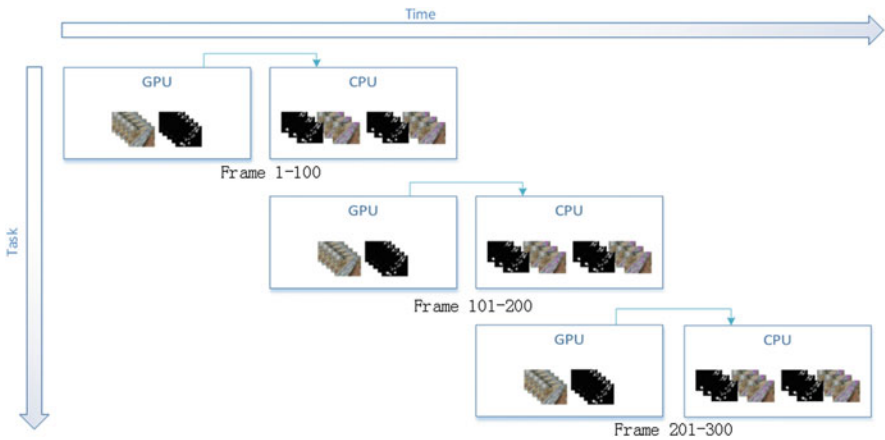


Fig. 77.7 Parallel pipeline processing model

We use OpenMP to parallelize the connected component labeling algorithm in coarse-grained and several special variables to maintain the correct order of the images derived in Step 2.

77.3.3 Parallel Pipeline Implementation on a Heterogeneous Platform

As shown in Fig. 77.7, when the N frames detected from traffic video complete the background subtraction algorithm and the morphological operation algorithm on the GPU, the multi-core CPU continues to execute the connected component labeling algorithm in OpenMP, while the GPU executes another N frames operation because of the independence of the CPU and the GPU.

Based on the feature of the heterogeneous platform, OpenMP is used to control the multi-core CPU and GPU. In our implementation, a thread is assigned to control

the GPU, while other threads are used for CPU computing. When the previous cycles of the CPU and the GPU completed, a synchronize operation occurs to ensure the processing accuracy.

77.4 Experiment Results

We measured the results of the images with dimensions of 704×576 from a traffic video. All the results are run on the following platform:

CPU: Intel[®] Core[™] i3-2100 Quad CPU @3.10 GHz

GPU: NAVIDIA GeForce GTX 550 (4) MP (48) CUDA cores/MP @1.90 GHz

GPU: NAVIDIA GeForce GTX 580 (16) MP (32) CUDA cores/MP @1.54 GHz

To fully utilize GPU resources, 100, 200, and 300 frames are chosen for the test.

Figure 77.8a and b compare the experiment performance of the single CPU and the quad core CPU and GPU for the background subtraction algorithm and the morphological operation algorithm. Parallel GPU implementation obtains speedups of $50 \times / 6 \times$ relative to sequential implementation and $25 \times / 4 \times$ relative to parallel multi-core implementation.

Figure 77.8c compares the experiment performance of the single CPU with that of the quad core CPU implementations for the connected component labeling algorithm, wherein parallel multi-core implementation obtains speedups of $2 \times$ relative to sequential implementation.

In order to compare the performance of the algorithms in this study with that of other GPU-based implementations, we list the performance described by others [7–10]. Table 77.1 shows that our implementations obtain better performance because we fully exploit the parallelism of the algorithms. For a fair comparison of the results, we pick Li et al. [8] and Adrjanowicz et al. [10] as the works that we compared with and run our algorithm on a lower computation power GPU platform, GTX 550. Our methods achieve about 1.42 and 1.28 performance improvement to that of the implementation of Li and Adrjanowicz, respectively. Compared to Li, we obtain more efficient parallel algorithm. We eliminate the extra computation on the CPU and reduce the storage time by using registers. In the morphological operation algorithm, Adrjanowicz only adopts 3×3 structuring element for

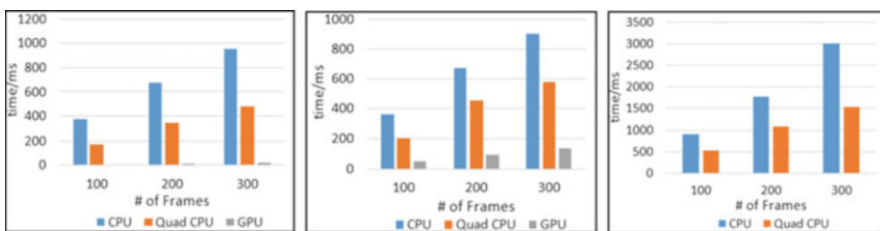
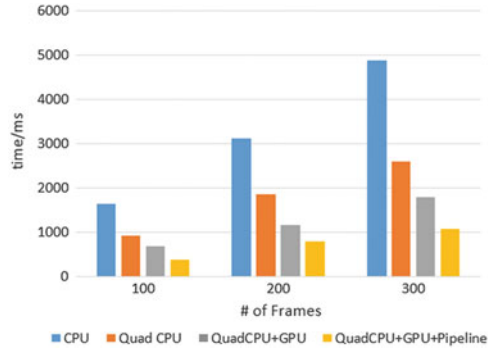


Fig. 77.8 Execution time compared with Step 1, Step 2, and Step 3 (GTX580)

Table 77.1 Performance comparison between different GPU-based implementations

Related works	GPU type	Algorithm	Speedup	Related works	GPU type	Algorithm	Speedup
[7]	8600GT	Background subtraction	5	[9]	GTX480	Morphological operation	2
[8]	GTX480		24	[10]	C1060		3.5
Ours1	GTX550		34	Ours1	GTX550		4.5
Ours2	GTX580		50	Ours2	GTX580		6

Fig. 77.9 Comparison of the different methods (GTX580)



experiment and calculates one frame each time, wherein the degree of parallelism is smaller than our implementation.

In our GPU implementation, we adopt our experiments on a lower computation power GPU platform; the experiment results show that our schemes can also meet demand with less hardware costs and obtain an acceptable speedup when compared with sequential implementation and other implementation schemes.

In Fig. 77.9, parallel pipeline implementation on a heterogeneous platform achieves speedups of up to $5\times$ higher than that of conventional sequential implementation, $2\times$ to $3\times$ higher than that of quad core CPU parallel implementation, and $1.5\times$ to $2\times$ higher than non-pipeline implementation on a heterogeneous platform.

In our implementation, a thread is assigned to control the GPU, while other threads are used for CPU computing, in which the threads affect the performance of the CPU to a certain extent. Moreover, based on previous studies, when the number of threads for CPU computing decreases, execution time increases by up to $2\times$ that of the GPU. Hence, pipeline implementation achieves approximately $1/3$ performance promotion compared with non-pipeline implementation.

Conclusion

Moving objects detection is important in traffic video analysis. We present a GPU implementation for the background subtraction algorithm and the morphological operation algorithm and a multi-core implementation for the connected component labeling algorithm. A novel parallel pipeline implementation on a heterogeneous platform is also provided. Based on the results of our study, we believe that our proposed optimization methods can provide a promising direction for future works on video analysis.

References

1. Horn BKP, et al. Determining optical flow. *Artif Intell.* 1981;17:185–203.

2. Migliore DA, et al. A reevaluation of frame difference in fast and robust motion detection. In: *Proceeding of the 4th ACM international workshop on video surveillance and sensor networks*. Santa Barbara: ACM; 2006. p. 215–8.
3. Elgammal A et al. Non-parametric model for background subtraction. In: *ECCV*. Dublin: Springer; 2000. p. 751–67.
4. Laganiere R. *OpenCV 2 computer vision application programming cookbook*. Birmingham: Packt Publishing; 2011. p. 117–37.
5. NVIDIA Corporation. *CUDA Compute Unified Device Architecture Programming Guide version 5.5*. NVIDIA; 2013.
6. OpenMP.org. *The OpenMP API specification for parallel programming*. OpenMP; 2013.
7. Carr P. GPU accelerated multimodal background subtraction. In: *Digital image computing: techniques and applications*. Canberra: IEEE; 2008. p. 279–86.
8. Li Y et al. Three-level GPU accelerated gaussian mixture model for background subtraction. In: *SPIE-IS&T*, vol. 8295; 2012. p. 829514-1–6.
9. Rane MA. *Fast morphological image processing on GPU using CUDA*. Pune: Department of Computer Engineering and Information Technology, College of Engineering; 2013.
10. Adrjanowicz L et al. GPU accelerated image processing for lip segmentation. In: *PPAM*. Torun: Springer; 2012. p. 357–65.
11. Suzuki S. Topological structural analysis of digitized binary images by border following. In: *CVGIP*, vol. 31. 1985. p. 32–46.
12. Suzuki K, et al. Linear-time connected-component labeling based on sequential local operations. *Comput Vis Image Underst.* 2003;89(1):1–23.
13. Hawick KA, et al. Parallel graph component labelling with GPUs and CUDA. *Parallel Comput.* 2010;36(12):655–78.

Chapter 78

A Novel Optical Flow Algorithm Based on Bionic Features for Robust Tracing

Weiwu Ren, Xiao Chen, Xiaoming Wang, and Mingyang Liu

Abstract The existing optical flow algorithms don't meet the requirements of human visual habits. In this chapter, a novel optical flow algorithm is proposed, in order to enhance the bionic features of optical flow. It is sensitive for new algorithms to extract the visual interesting feature such as color and motion. The robust tracing framework based on new optical flow algorithm can track more corners in the opponent color space which has the optimal bionic effect. Experiments show new framework can find new bionic features and trace more bionic corners.

Keywords Opponent color space • Robust tracing framework • Bionic features • Bionic corners

78.1 Introduction

With the advent of the era of big data, the volume of image information is growing explosively. As a result, it is hard to understand images from the massive image data in manual mode. Computer vision can not only help human eyes to identify images, but also trace motions instead of human eyes, which makes the processing and analysis of huge volume of image information possible.

Nowadays, motion tracing algorithms have been widely used in the field of computer vision. It is still a huge challenge to study a robust, accurate, and real-time

W. Ren

College of Computer Science and Technology, Changchun University of Science and Technology, 130022 Changchun, China

X. Chen (✉)

College of Information and Technology, Jilin Agricultural University, 130022 Changchun, China

e-mail: xiaoxiaocctv5@126.com

X. Wang

Changchun Branch of China Mobile, Changchun, China

M. Liu

College of Instrument Science and Electrical Engineering, Jilin University, 130022 Changchun, China

© Springer International Publishing Switzerland 2015

W.E. Wong (ed.), *Proceedings of the 4th International Conference on Computer Engineering and Networks*, Lecture Notes in Electrical Engineering 355, DOI 10.1007/978-3-319-11104-9_78

669

motion tracing algorithm. There are some kinds of motion tracing algorithms based on different theories: motion tracing algorithm based on contrast; motion tracing algorithm based on region correlation; motion tracing algorithm based on feature corners; and motion tracing algorithm based on optical flow.

Motion tracing algorithm based on optical flow has two subclasses: continuous optical flow and feature optical flow. Feature optical flow algorithm has a small amount of computation. It fits the requirements of tracing fast-moving targets, large targets, or multiple targets. But the corner detection and matching algorithm are easily interfered by noise.

At present researches on motion tracing algorithm based on optical flow can be divided into three classes:

Algorithms in other fields are introduced to improve the existing optical flow algorithm. Pramuk et al. [1] proposed a robust optical flow estimation technique using gradient orientations. Their technique can perform optical flow estimation regardless of irregular lighting by introducing gradient orientations. Tu et al. [2] proposed a novel combined post-filtering method to improve the accuracy of optical flow estimation. Its attractive advantages are that outlier reduction is attained while discontinuities are well preserved, and occlusions are partially handled.

The real-time performance is improved by using hardware asset. Mhamoudi et al. [3] ran both parts of the algorithm (i.e., corner selection and tracking) implemented on GPU. The software is immensely fast, allowing for real-time motion tracking on videos in full HD or even 4K format.

Motion tracing algorithms [4, 5] are introduced to apply in different fields such as autopilot and cell monitoring. Guo et al. [6] proposed an optical flow method to track red blood cells. They utilized it to calculate the displacement of a cell in two adjacent frames. Guzman et al. [7] proposed an overtaking detection system based on visual motion cues that combined feature extraction, optical, solid-objects segmentation, and geometry filtering, working with a low-cost compact architecture based on one focal plane and an on-chip embedded processor. Halfawy et al. [8] proposed a novel approach for automated analysis and tracking of camera motion in sewer inspection closed circuit television videos.

On the basis of summarizing the previous representative work [9, 10], a novel optical flow algorithm based on bionic feature for robust tracing is proposed in this chapter. There are two main contributions in our chapter: (1) opponent color space which is most consistent with human visual habits is introduced into motion tracing algorithm based on optical flow. The existing Lucas Kanade algorithm is improved to meet the biological characteristics of humans. (2) Feature corner description is redefined in the new color space, which improves the bionic features of algorithm under the premise of ensuing accuracy.

The rest of the chapter is organized as follows: in Sect. 78.2, the robust tracing framework based on the improved algorithm OCPRLK is proposed, and the solving process of velocities in opponent color space is illustrated. In Sect. 78.3, comparisons with other representative algorithms are made. In Sect. 78.4, experimental results are exhibited and analyzed. Finally, we summarize our conclusions and future work.

78.2 Robust Tracing Framework Based on Bionic Features

The framework of motion perception is shown in Fig. 78.1 as follows. The first step is selecting two successive frames from a sequence; the second step is describing two frames by color space; the third step is calculating Harris corner in the first frame; the fourth step is calculating descriptions in each color space; the fifth step is calculating the optical flow estimation of two successive frames in different color space; the sixth step is tracing key points by the optical flow field.

The core algorithm of this framework is an optical flow estimation algorithm based on color space. The traditional optical flow algorithm estimates optical flow in the gray space. In the opponent color space, the optical flow estimation should be calculated as follows:

We assumed that color gradation $F_\theta(x)$ is a constant. Based on the definition of color gradation, the new optical flow equation is shown as follows:

$$\frac{\partial F_\theta}{\partial x} \cdot u + \frac{\partial F_\theta}{\partial y} \cdot v + \frac{\partial F_\theta}{\partial t} = 0 \tag{78.1}$$

Color space has three components: red–green components, blue–yellow components, and black–white components. They have their own roles. In the three components, the optical flow gradation constraint equation is deduced as follows:

$$\begin{cases} \frac{\partial RG}{\partial x} \cdot u + \frac{\partial RG}{\partial y} \cdot v + \frac{\partial RG}{\partial t} = 0 \\ \frac{\partial BY}{\partial x} \cdot u + \frac{\partial BY}{\partial y} \cdot v + \frac{\partial BY}{\partial t} = 0 \\ \frac{\partial BW}{\partial x} \cdot u + \frac{\partial BW}{\partial y} \cdot v + \frac{\partial BW}{\partial t} = 0 \end{cases} \tag{78.2}$$

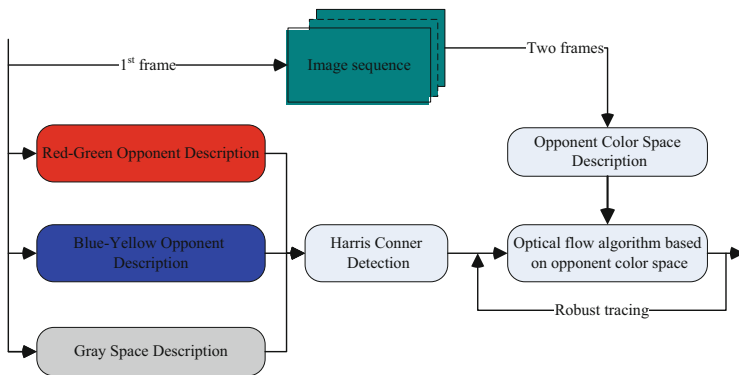


Fig. 78.1 The robust tracing framework based on opponent color space

The above three equations solve two unknowns with the following method:

$$A = \begin{bmatrix} RG_x & RG_y \\ BY_x & BY_y \\ BW_x & BW_y \end{bmatrix}, \quad b = \begin{bmatrix} RG_t \\ BY_t \\ BW_t \end{bmatrix}, \quad U = \begin{bmatrix} u \\ v \end{bmatrix} \tag{78.3}$$

The solved equation:

$$U = (A^T A)^{-1} A^T b \tag{78.4}$$

The speed solutions of optical flow in three components are, respectively, (U_{RG}, V_{RG}) , (U_{BY}, V_{BY}) , and (U_{BW}, V_{BW}) . They are substituted in the equation. The final speed (u, v) is the sum of three speed components.

$$(U,V)=(URG, VRG)+(UBY, VBY)+(UBW, VBW) \tag{78.5}$$

78.3 Comparing OCPRLK with Other Representative LK Algorithms

Some representative LK algorithms are going to be compared to the improved algorithm (OCPRLK) in this part. The original algorithm simulates the velocity field by optical flow field. It only computes velocity of object without considering the factors of colors. So if some objects have the same velocity with background, they can't be found. However, the improved algorithm computes three velocities in three opponent color spaces, and three velocities are accumulated. Some objects which have significant colors are noticed. They are usually bionic features of humans concerned. They are enlarged by the process of accumulating velocities.

In Table 78.1, it can be drawn that the improved algorithm doesn't have obvious advantages on some key indicators. Instead, they have some disadvantages. The reason why the noise increased is that three velocities are accumulated. Compared with the standard image of ground truth, especially, inaccuracy increases significantly. But the improved algorithm of this chapter is designed for sensing the motion of bionic features instead of the accuracy of velocity. So inaccuracy is within the tolerance range.

Table 78.1 Comparisons with other representative LK algorithms

Data	LK		PRLK		RGLK		OCPRLK	
	AAE	AEPE	AAE	AEPE	AAE	AEPE	AAE	AEPE
Rubber whale	7.38	0.23	7.32	0.22	6.38	0.19	6.94	0.25
Hydrangea	3.87	0.37	3.53	0.33	3.32	0.21	3.98	0.27
Urban2	20.68	6.38	18.57	5.38	15.39	4.26	15.68	4.87
Grove2	5.43	0.29	4.95	0.24	4.76	0.25	4.54	0.24

78.4 Experiment Studying

78.4.1 Bionic Features Corner Detection

In Table 78.1, it can be concluded that the improved algorithm doesn't have obvious advantages on some key indicators, but it has some disadvantages. The reason why the noise increased is that three velocities are accumulated. Compared with the standard image of ground truth, inaccuracy increases especially significantly. But the improved algorithm of this chapter is designed for sensing the motion of bionic features instead of the accuracy of velocity. So inaccuracy is within the tolerance range.

In Fig. 78.2, sub-figures (a) and (b) show, respectively, source image and results of detecting corners by sifting. (c) and (d) show, respectively, results of Harris detection corner in RG space and in BY space. (e) shows results in gray space. (f) is the fusion results of (c), (d), and (e). Compared with sifting detection result and detection result in gray space, results in the sub-figure (f) have more detection corners and more comprehensive descriptions. In the process of application, a non-maxima suppression method is used to delete neighbor corners. This can achieve efficient and well-distributed corner descriptions.

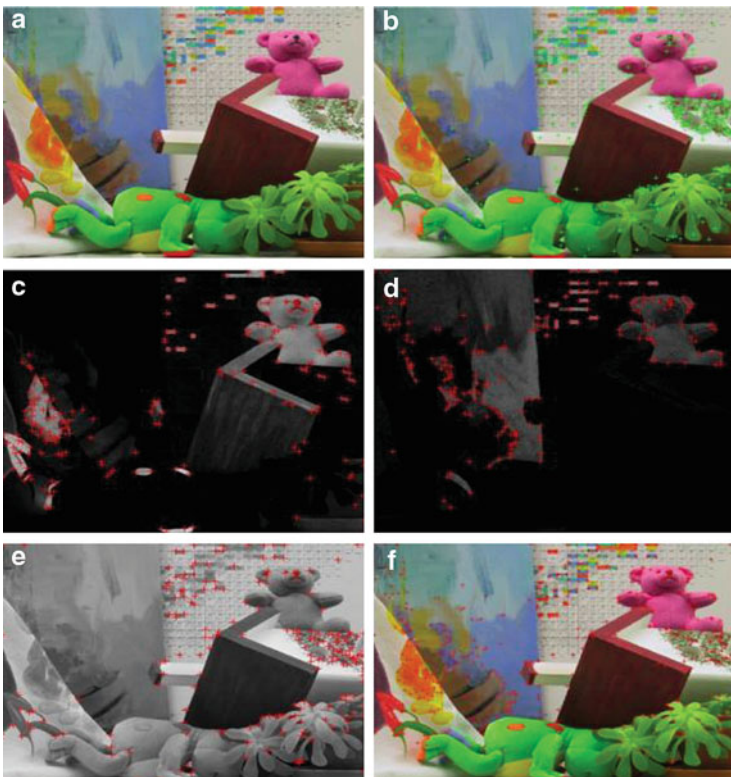


Fig. 78.2 Comparison with sift corner detection

78.4.2 Robust Tracing

Experimental samples are extracted from Middlebury-labeled optical flow image library. The first seven results of Fig. 78.3 show the bionic feature corners being tracked in every sample. The last result (h) of Fig. 78.3 shows trajectories of bionic



Fig. 78.3 Results of tracing children

feature corners. In the sequence of consecutive frames, the significant motion is the action of picking up a child. The last result shows that the trajectory of corners is tracking the motion of picking up a child. Moreover, the number of corners being tracked gradually decreases from sub-figure (a) to (g), and corners are finally stable in the last two frames. Compared with tracing in the gray space, OCPRLK has more stable corners of being tracked.

Conclusion

In this chapter a novel optical flow algorithm based on bionic features is proposed, and its framework based on this algorithm for robust tracing is also proposed and implemented. The framework detects bionic feature corners in the opponent color space and traces them. Compared with tradition optical flow algorithms and their frameworks, new algorithm and framework can not only detect the motion which has bionic features, but also trace them effectively. A series of experiment results on Middlebury-labeled optical flow image library indicate that the improved algorithm and the proposed framework have superior performance in both robustness and stability.

References

1. Pramuk B, Toshiaki K, et al. A robust optical flow estimation technique using gradient orientations. *Scienceasia*. 2014;40(1):73–83.
2. Tu Z, van der Aa N, et al. A combined post-filtering method to improve accuracy of variational optical flow estimation. *Pattern Recogn*. 2014;47(5):1926–40.
3. Mahmoudi SA, Kierzynka M, et al. Real-time motion tracking using optical flow on multiple GPUs. *Bull Pol Acad Sci Tech Sci*. 2014;62(1):139–50.
4. Shindler L, Moroni M, Cenedese A. Using optical flow equation for particle detection and velocity prediction in particle tracking. *Appl Math Comput*. 2012;218(17):8684–94.
5. Fujta K, Hanada T, Kitazawa Y, Kawabe A. A debris image tracking using optical flow algorithm. *Adv Space Res*. 2012;49(5):1007–18.
6. Guo D, van de Ven AL, et al. Red blood cell tracking using optical flow methods. *IEEE J Biomed Health Informat*. 2014;18(3):991–8.
7. Guzman P, Diaz J, et al. Low-cost sensor to detect overtaking based on optical flow. *Mach Vis Appl*. 2014;25(3):699–711.
8. Halfawy MR, Hengmeechai J, et al. Optical flow techniques for estimation of camera motion parameters in sewer closed circuit television inspection videos. *Automat Constr*. 2014;38:39–45.
9. Chen C, Wang Y, Yu J. Tracking pylorus in ultrasonic image sequence with edge-based optical flow. *IEEE Trans Med Imag*. 2012;31(3):843–55.
10. Pan C, Deng H, Yin XF. An optical flow-based integrated navigation system inspired by insect vision. *Biol Cybernet*. 2011;105(3–4):239–52.

Chapter 79

An Obstacle Detection System for a Mobile Robot Based on Radar-Vision Fusion

Xiao Chen, Weiwu Ren, Mingyang Liu, Lisheng Jin, and Yue Bai

Abstract This paper presents a systematic scheme for obstacle detection using infrared radar and a monocular vision sensor. On the basis of the visual attention method we use fusion of infrared radar and vision data to obtain better detection performance. In the vision module, salient detection is invalid when no obstacle is present in an image. But infrared radar is used to detect and pre-locate objects. Then vision module locate objects by salient location method. Lastly, we test our radar-vision system in an indoor simulation environment, and our experiments show that the method is both rapid and feasible.

Keywords Fusion strategy • Obstacle detection • Salient location • Infrared radar • Visual sensor

79.1 Introduction and Prior Work

Itti et al. [1] introduced a biologically inspired visual attention model based on the human visual system (HVS). According to the feature integration theory, a saliency map was constructed using the center-surround mechanism and normalization of a set of low-level contrast features. Considering that salient objects in scene images

X. Chen

College of Information and Technology, Jilin Agriculture University, 130000 Changchun, China

W. Ren (✉)

College of Computer Science and Technology, Changchun University of Science and Technology, 130022 Changchun, China

e-mail: xiaoxiaocctv5@163.com

M. Liu

College of Instrument Science and Electrical Engineering, Jilin University, 130000 Changchun, China

L. Jin

College of Traffic, Jilin University, 130000 Changchun, China

Y. Bai

Northeast Normal University, 130000 Changchun, China

© Springer International Publishing Switzerland 2015

W.E. Wong (ed.), *Proceedings of the 4th International Conference on Computer Engineering and Networks*, Lecture Notes in Electrical Engineering 355,
DOI 10.1007/978-3-319-11104-9_79

677

are generally conspicuous and compact, Gopalakrishnan [2] proposed an unsupervised graph presentation detection method of random walk saliency based on a Markov random walk. Hou and Zhang [3] proposed a quick Fourier spectral residual analysis algorithm based on mathematical statistics. Their model uses the spectral residual of an image and Fourier inversion based on the statistical properties of the Fourier spectrum. All the salient detection methods mentioned above represent bottom-up computational models, and they detect salient intensity without considering whether there is an object in the image.

Traditional approaches in dealing with object detection problems have concentrated on developing more accurate algorithms to improve the robustness of the background model [1–3] and object segmentation methods by extracting more content data (such as color features, edge features, and texture features) [4] using spectral residual analysis only. However, creating the most advanced recognition, tracking, and detection approaches for different environments is more difficult. A better way of improving the quality of input data is the use of multi-image information fusion, which improves overall detection system performance [5]. The integration of radar with a monocular vision sensor for detecting obstacles may improve overall detection system performance, and as a result, using a complementary combination of imagery from an infrared sensor, which captures information from reflected and emitted radiation, is a feasible scheme to consider [6].

To solve the problem noted above, the method that we propose combines a salient detection model for location with a pre-location mask obtained from infrared sensor information on the objects. To extract the integrity feature of an object, we make use of local energy features instead of orientation features, which is helpful for obstacle location. In terms of salient detection, we use infrared sensors to detect whether the object is a barrier. The pre-location mask derived from infrared sensor results is useful for the efficiency of the algorithm. The object location method is based on object segmentation. Radar-vision fusion represents a pre-treatment. Then we design a maximum entropy estimation method for obstacle location. Finally, we test our radar-vision system in an indoor simulation environment.

79.2 The Design of the Obstacle Detection System

A multi-information fusion method is introduced to improve the robustness of obstacle detection. Visual selective attention based on the theory of human visual perception provides a referenced scheme for real-time and significant visual information processing as shown in Fig. 79.1 [5]. A biologically inspired algorithm was used in our obstacle detection project for the construction of real-time detection systems for intelligent mobile robots based on the visual attention model. The visual sensor is a camera used to obtain video information, whilst the infrared radar is used to gather information about the direction and distance of objects. Information is then processed for obstacle detection (see Fig. 79.1). The entire

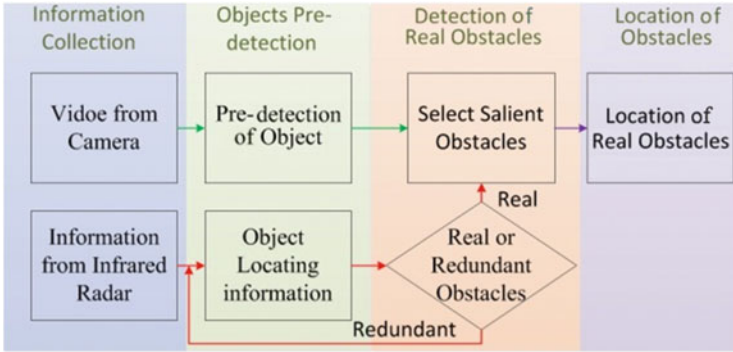


Fig. 79.1 Obstacle detection framework

process we constructed to obtain information on obstacles was inspired by human visual consciousness and behavior.

All pre-detected salient pixels from the visual sensor are regarded as potential obstacles, similar to the human visual glimpse behavior that guides pre-attention in human eyes. The visual module is used to detect the salient region via a visual obstacle detection algorithm. Detected salient pixels from the visual sensor can be thought of as clues to potential obstacles. Then we use infrared radar to analyze potential obstacles that are redundant or real. Through infrared radar, obstacles that are closer and on the route of the mobile robot could provide information for obstacle pre-location. This will be helpful in reducing the influences of complex circumstances, and may also be useful for improving the real-time performance of obstacle detection, more accurately positioning the target with less computational load and less processing time. The information processing noted above may lead to a decrease in false and redundant obstacle detection from radar. Thus, complex and time-consuming visual tasks can be carried out easily and quickly.

79.3 Obstacle Detection Model Based on Radar-Vision Sensors

Our proposed model consists of three parts. First, we obtain the saliency map using biologically inspired structure. This could pre-detect a salient object close-by and in-front of the robot. Next we detect real obstacles via information fusion. Object information concerning direction and distance from the infrared radar is useful for pre-locating real obstacles from object pre-detection data. Lastly, we analyze the salient intensity of images to locate obstacle edges.

79.3.1 *Pre-Detection of Objects Via the Visual Sensor*

Herein, we propose a computational method to more accurately detect objects. Our saliency detection algorithm method is based on Itti's visual attention saliency model [1]. To improve the intensity representation feature of salient objects, we construct a more reliable and useful saliency map, which combines the additional feature channel with the local energy channel instead of the orientation feature channel. Local energy can be used to more accurately extract the contour feature of objects [7]. The primary visual cortex always responds with greater sensitivity to stimuli with the local energy distribution. Thus, local energy relates to the perceptual significance of important features, and could therefore be used in biologically inspired models. The local energy function $E(x)$ is computed from the sum of the squared responses of visual operators with even and odd symmetry receptive fields:

$$E(x) = \sqrt{I^2(x) + H^2(x)}, \quad (79.1)$$

where $I(x)$ and $H(x)$ are respectively the even and odd 2-D Gabor function. We obtain saliency maps using the general Itti architecture, but use local energy feature channels instead of the orientation channel of the original model. In the local energy channel, we use 2-D Gabor functions 0, 45, 90, and 135, combined into one "local energy" channel. We then use image pyramids and center-surrounding differences to construct new feature maps, as in Itti's original model: for each of the three feature channels, center-surrounding scales are obtained from dyadic pyramids with three scales, i.e., from scale 0 (the original image) to scale 2. In Itti's original model only two biological features (color and intensity) were employed, while we introduce the local energy feature here which might be more useful in the description of object contours.

A simple object (round) that is located in a noncentral area of the images is used to evaluate the performance of local energy. We present the Itti model and our method in Fig. 79.2. The orientation channel is constructed by the 2-D Gabor function. The Gabor function can extract more features distributed in the center than the surrounding areas of the image, whereas local energy can respond to features in the whole image. So the saliency model we propose describes the integrity information of objects more accurately.

79.3.2 *Detection of Obstacles Via Infrared Radar*

In our robot platform, six infrared sensors can be used for obstacle detection. We use three sensors on the front of the robot, and the range of detection covers the width of the robot (see Fig. 79.3).

The three infrared sensors are named NO.1, NO.2, and NO.3 from left to right. They work concurrently for obstacle detection. If some of them detect an object, a

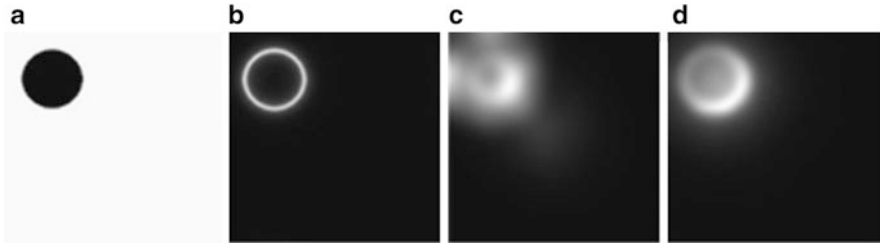
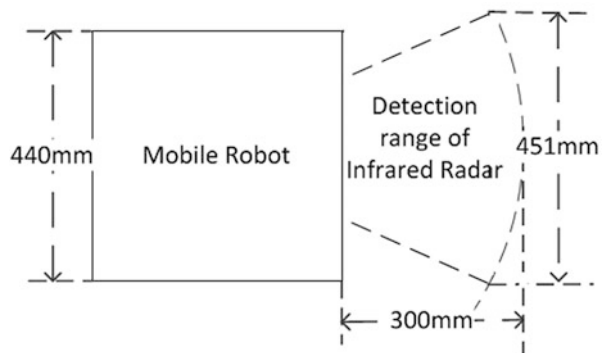


Fig. 79.2 Feature maps from the different methods: (a) original image, (b) local energy, (c) Itti's saliency map, (d) our result

Fig. 79.3 Detection range of infrared radar



pre-location mask is selected from the result from all three sensors; the pre-location mask is a binary image. Then, the pre-location mask blends with the saliency map, so that the normally time-consuming obstacle location can be carried out easily and rapidly; the process of obstacle pre-detection using vision camera and radar fusion can be seen in Fig. 79.4.

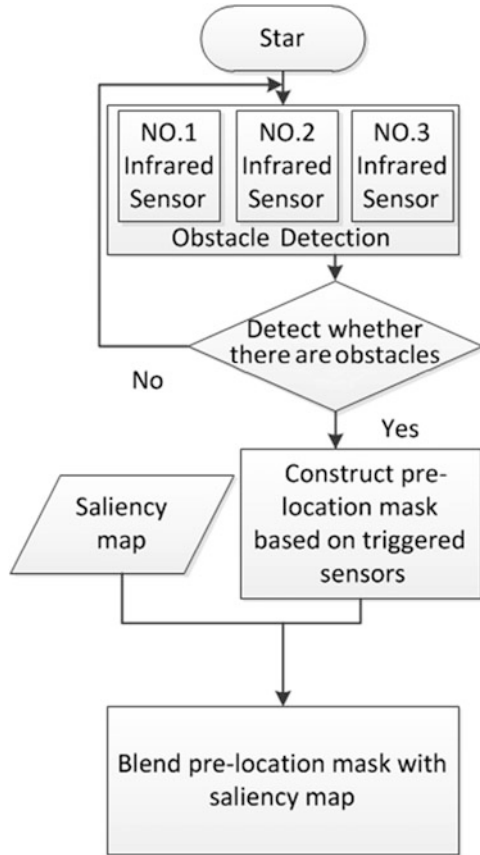
79.3.3 Salient Obstacle Location

Before using the pre-location saliency map to locate obstacles, it is necessary to analyze the composition of the scene image.

In the field of object segmentation, novelty fluctuations are likely to correspond to salient objects and the nonsalient part is the background (redundant information). The purpose of generating a saliency map is to dispose of the redundancies and focus on the salient parts. Salient detection can be achieved by blending the optimal mask with the original image. The proposed method of obstacle detection based on the saliency model has the following steps [8]:

Step 1: Estimate an object's entropy $H_O(t)$ and the nonsalient part $H_B(t)$ using the maximum entropy method. Assuming that two classes are respectively pixels

Fig. 79.4 Fusion processing of obstacle pre-location using radar and a camera



O and B (in our research O denotes the salient object class and B denotes the redundancy class), t is the threshold gray value in the image array, and $H_O(t)$ and $H_B(t)$ are defined as:

$$H_O(t) = \ln \sum_i^t \frac{P_i}{P_O(t)} \tag{79.2}$$

$$H_B(t) = \ln \sum_{i=t+1}^{255} \frac{P_i}{P_B(t)}, \tag{79.3}$$

where p_i represents the probability gray-level value, $p_i = n_i / (M \times N)$, ($i \in G$), where n_i represents the number of pixels with gray value i . There is $M \times N$ pixels in a discrete image, where $P_O = \sum_{i=0}^t p_i$, and $P_O(t) + P_B(t) = 1$. The information of image consists of two part, objects $H_O(t)$ and background $H_B(t)$. The entropy of image is $H(t)$, is defined as $H(t) = H_O(t) + H_B(t)$. Let $H^*(t)$ be the gray level

that maximizes $H_O(t) + H_B(t)$. It is evident that $H^*(t)$ is a function of t , when $t = t^*$, $H^*(t)$ is maximum, and the entropy of objects is

$$H_O(t^*) = \ln \sum_{i=0}^t \frac{P_i}{P_O(t^*)}. \quad (79.4)$$

Step 2: Remove redundant information from the image. Calculate the binary mask of $g_i(x)$ by setting gray value x in the saliency map. Assume novelty fluctuations are the pixels of maximal intensity parts and the other pixels are the redundant information parts. To remove the redundant information, the minimal intensity pixel is set to gray value 0, and the other pixels to 1. The binary image from the original saliency map is used as the binary mask. Then, render mask pixel's bits by blending them with original image pixel's bit using the equation $f_i(M) = (f \cup g_i)(x)$, the images $f_i(M)$ are the results of object location [8].

Step 3: Calculate the entropy values of $f_i(M)$, $H(M)$ approximate to $H_T(t)$ from step1, so that $f_i^*(M)$ is the object detection result.

79.4 Implementation and Results

In our experiment, some relatively simple indoor environments were selected in which to test our obstacle detection method and the velocity of the mobile robot was set to less than 5 m/s. For our experiment, we randomly placed a few obstacles on the road such as a hat, a book, and a stapler. Most of the experimental data had one or two obstacles within visual sensor range for detection. In this case, our mobile platform was used to obtain the radar data and the corresponding image sequences. The field of vision for detection was 0.33 m in length and 0.44 m in width. Within this region, an obstacle detected by infrared radar could be aligned well within the area covered by the camera image, which was used for further vision-based obstacle detection and location of real obstacles. Therefore, our experiment used infrared radar data within a region of less than 0.3 m. The MATLAB code was used for programming within the Windows XP operating system and on a notebook equipped with a 2.4-GHz Core Duo CPU and 2 GB RAM.

We demonstrated the average processing time taken by different video sequence resolutions (see Table 79.1; we have 3,000 frames from the 300-s video) Fig. 79.5 presents some of our obstacle location results. Figure 79.6 shows the false result from the detection method without infrared radar.

Conclusion

Because infrared radar can be used for obstacle detection, integration of vision sensors with infrared radar has made obstacle location more accurate

(continued)

Table 79.1 Execution times and frame rates

Frame resolution	354 × 288	640 × 480	600 × 800
Execution time (s)	0.091	0.109	0.127
Frame rate (fps)	10.99	9.17	7.87

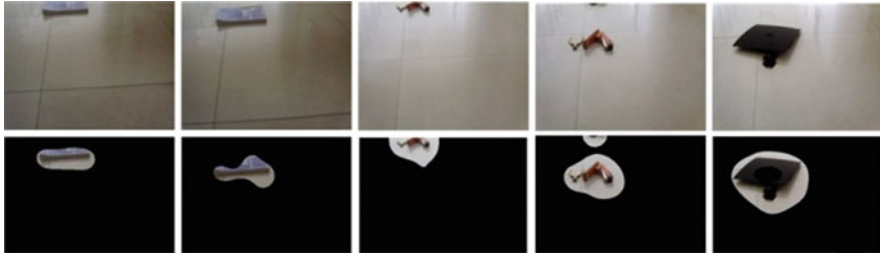
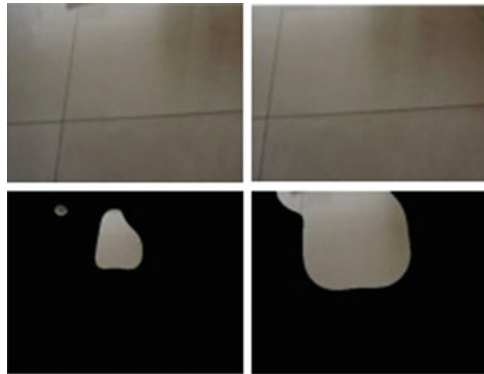


Fig. 79.5 The result of our proposed obstacle location method

Fig. 79.6 The false result of the detection method without infrared radar



(continued)

than when using vision only. The drawback of saliency detection is when no object is present in the image. Infrared radar is the remedy for visual saliency. As a solution we provide a system to detect and locate obstacles. Our obstacle detection system is a real-time system for obstacle location and can be used with indoor mobile robots. This work was supported by the Doctoral Foundation of Jilin Agriculture University.

References

1. Itti L, Koch C, Niebur E. A model of saliency-based visual attention for rapid scene analysis. *IEEE Trans Pattern Anal Mach Intell.* 1998;20(11):1254–9.
2. Gopalakrishnan V, Hu Y, Rajan D. Random walks on graphs for salient object detection in images. *IEEE Trans Image Process.* 2010;19(12):3232–42.

3. Hou X, Zhang L. Saliency detection: a spectral residual approach. In: 2007 I.E. Conference on Computer Vision and Pattern Recognition (CVPR'07). Minneapolis: IEEE; 2007. p. 1–8.
4. Hafez A, Chari V, Jawahar CV. Combine texture and edges based on goodness weights for planar object tracking. In: International Conference on Robotics and Automation (ICRA); 2007; Roma, Italy. p. 4620–5.
5. Cubells-Beltrán MD, Reig C, Martos J, Torres J. Soret limitations of magnetoresistive current sensors in industrial electronics applications. *Int Rev Electr Eng.* 2011;6(1):423–9.
6. Tu Z, Van der Aa N, et al. A combined post-filtering method to improve accuracy of variational optical flow estimation. *Pattern Recogn.* 2014;47(5):1926–40.
7. Henriksson L, Hyvarinen A, Vanni S. Representation of cross-frequency spatial phase relationships in human visual cortex. *J Neurosci.* 2009;29(45):14342–51.
8. Chen X, Zhao H, Liu P, Zhou B, Ren W. Automatic salient object detection via maximum entropy estimation. *Optics Lett.* 2013;38(10):1727–9.

Chapter 80

De-noising Method for Echocardiographic Images Based on the Second-Generation Curvelet Transform

Haihong Xue, Binjin Chen, Kun Sun, and Jianguo Yu

Abstract As a novel multiscale transform, curvelet transform has the ability to give a better sparse representation of images with singularity along curves. After analyzing the second-generation curvelet transform, this work presents a new de-noising technique for echocardiographic images corrupted with speckle noise. We employed this new technique, nonlinear diffusion based on total variation, to suppress artifacts resulting from curvelet transform. The results show that this method gives better performance in noise suppression while preserving the edges of echocardiographic images, compared to existing methods. The application of curvelet transform reveals its great potential in echocardiographic image processing.

Keywords Echocardiographic images • Image de-noising • Speckle noise • Curvelet transform • Nonlinear diffusion

80.1 Introduction

Curvelet transform was established and developed by Candès and Donoho, based on wavelet transform research, in 1999, and has been used in a variety of fields since that time [1]. In the 20 years since its emergence, excellent research and application results have been achieved based on wavelet transform, and this can be attributed to its satisfactory performance in the efficient analysis of 1-dimensional

H. Xue

Department of Pediatrics, Xinhua Hospital, School of Medicine, Shanghai Jiaotong University, Shanghai 200092, China

B. Chen • J. Yu

Department of Electronic Engineering, Fudan University, Shanghai 200433, China

K. Sun (✉)

Department of Pediatric Cardiology, Xinhua Hospital, School of Medicine, Shanghai Jiaotong University, Shanghai 200092, China

e-mail: drsunkun@163.com

(1D) smooth partition signals. However, from a visual point of view, the 2-D wavelet consists of the tensor product of 1-D wavelets, and the base of such 2-D wavelet transform has the character of an isotropic—therefore, not “along the edge”—information, such as direction and continuity. But only “across the edge” information can be expressed by discrete wavelet transform in 2-D images, and this is one of the limitations of traditional wavelet transform in 2-D image processing. To overcome this limitation, Candès and Donoho proposed curvelet transform, which is characterized by anisotropy, while preserving the multiscale and multiresolution functionality of wavelet transform, and is therefore considered to be of special value in the field of image processing.

80.2 Methods

80.2.1 Basic Theory and Digital Realization of Curvelet Transform

The core of the first-generation curvelet transform put forward by Candès and Donoho in 1999 was ridgelet transform theory [2], in which line singularity was mapped to point singularity through radon transform, and wavelet transform was employed to process and capture point singularity in the radon domain. In the digital realization process of Cartesian coordinates conversing to polar coordinates in ridgelet transform, the interpolation algorithm was used, which made the image reconstruction in the first-generation curvelet transform inaccurate, and the high redundancy of the algorithm also limited the application of curvelet transform.

After its development in recent years, the second-generation curvelet transform technique, which is based on unequally spaced fast Fourier transform (USFFT), was used in practice [3]. Its basic algorithm steps include:

1. 2-D FFT transform is used for $f(t_1, t_2)$ of $L^2(R^2)$ to get:

$$F(n_1, n_2), \quad -\frac{n}{2} < n_1, n_2 < \frac{n}{2} \quad (80.1)$$

2. For each scale and direction parameter (j, l) , the interpolation method is used for sampling $F(n_1, n_2)$ and to get:

$$F(n_1, n_2 - n_1 * \tan \theta_1) \quad (80.2)$$

3. Parabolic window function \tilde{U}_j (size of \tilde{U}_j must obey the rule that width = height²) is multiplied by $F(n_1, n_2 - n_1 * \tan \theta_1)$, thus achieving the localization of F :

$$\tilde{F}_{j,l}(n_1, n_2) = F(n_1, n_2 - n_1 * \tan \theta_1) \tilde{U}_j(n_1, n_2) \quad (80.3)$$

4. 2-D discrete IFFT transform is performed for $\tilde{F}_{j,l}(n_1, n_2)$ after localization, after which the curvelet transform coefficient $C(j, l, k)$ is obtained.

It is evident from the above steps that the second-generation curvelet has separated itself completely from ridgelet transform, the definition and localization are directly performed in the frequency domain, and the curvelet transform coefficient is obtained by 2-D discrete IFFT transform after localization.

80.2.2 Application of the Second-Generation Curvelet Transform for Echocardiographic Image De-noising

Basing on the de-noising method in wavelet transform, we employed a de-noising technique for echocardiographic images corrupted with speckle noise based on the second-generation curvelet transform. The specific steps involved are as follows:

1. After curvelet transform of the collected echocardiographic data, the curvelet transform coefficients of different resolution layers (gradually from coarse to fine scale) are obtained.
2. The threshold value of the curvelet transform in each layer is determined, and then the curvelet coefficient of each layer after the transform is screened, classified, and de-noised. The relationship between input and output of de-noising by the hard threshold method is expressed as:

$$y_\lambda = \begin{cases} y & |y| \geq \lambda \\ 0 & \text{others} \end{cases} \quad (80.4)$$

The selection of the de-noising threshold is related to the mean and variance of the transform coefficient. Starck et al. estimated the variance of noise after curvelet transform based on the Monte Carlo algorithm, but it was computationally complex. This chapter employed the method based on generalized cross-validation (GCV) to determine the de-noising threshold. This method only depends on the input and output data and is independent of the energy of the noise signal. The definition of GCV is [4]:

$$\text{GCV}(\lambda) = \frac{\frac{1}{N} \|y_\lambda - y\|^2}{\left[\frac{N}{N_0}\right]^2} \quad (80.5)$$

where N refers to the number of curvelet coefficients, N_0 stands for the number of curvelet coefficients when its value is 0, y stands for the image corrupted with

noise signal, and y_λ stands for the image after de-noising. The de-noising threshold is then determined based on the GCV:

$$\lambda_{OPT} = \text{argminGCV}(\lambda) \tag{80.6}$$

3. After inverse curvelet transform for curvelet coefficients (including high-frequency and low-frequency coefficients) in each layer, the estimated value of the signal, i.e., the image after de-noising, is eventually obtained.
4. Elimination of artifacts. While the de-noising technique based on curvelet transform is different from classical methods, such as the de-noising technique based on wavelet transform, both of these methods have their respective advantages. Curvelet transform is helpful for capturing the detailed information at the edge of an image, but new artifacts, such as rut-like artifacts, which did not exist in the original image before de-noising, may also be introduced at the edge of the image. The nonlinear diffusion technique has been reported to be highly effective for eliminating artifacts [5]; therefore, the nonlinear total variation de-noising technique based on the total variation (TV) principle was adopted to suppress the artifacts [6].

80.3 Results

80.3.1 Simulation Experiment

First, we simulated the image speckle signal of cardiac ultrasonography and contaminated it by artificial Rayleigh distributional noise. Next, we used the hard threshold method of de-noising, combined with generalized cross-validation, for confirming the function criteria to determine the noise threshold. Figure 80.1 shows the results of our noise reduction method compared with other classical noise reduction methods.

We have calculated the edge-preserving quantization parameter α as follows:

$$\alpha = \frac{\Gamma(\Delta s - \overline{\Delta s}, \Delta \hat{s} - \overline{\Delta \hat{s}})}{\sqrt{\Gamma(\Delta s - \overline{\Delta s}, \Delta s - \overline{\Delta s}) \cdot \Gamma(\Delta \hat{s} - \overline{\Delta \hat{s}}, \Delta \hat{s} - \overline{\Delta \hat{s}})}} \tag{80.7}$$

$$\Gamma(s_1, s_2) = \sum_{(i,j \in \text{ROI})} s_1(i,j) \cdot s_2(i,j) \tag{80.8}$$

Table 80.1 shows the comparison of results between the peak signal-to-noise ratio (PSNR) of an image treated with several noise reduction methods and the quantitative parameter (α) of edge preservation.

Based on the data shown in Fig. 80.1 and Table 80.1, we have concluded that the peak signal-to-noise ratio achieved by our de-noising method is higher than those

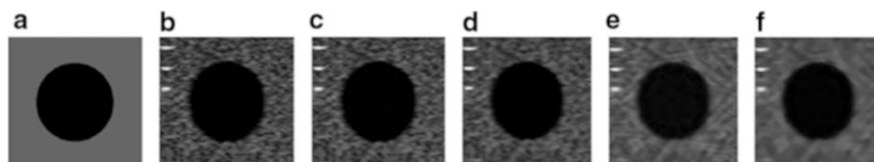


Fig. 80.1 Experimental results of various noise reduction methods applied to the simulated image. (a) Original image. (b) Original image with noise. (c) Results by hard wavelet shrinkage. (d) Results by anisotropic diffusion. (e) Results by curvelet thresholding. (f) Results by the suggested method

Table 80.1 Quantitative results from simulation experiment using quality measures PSNR (dB) and alpha (%)

Method	PSNR	α
Hard wavelet shrinkage	18.1201	0.4271
Anisotropic diffusion	18.4739	0.5756
Curvelet thresholding	18.8192	0.8032
Suggested method	18.9815	0.8146

obtained by the other methods, because the threshold calculated from the function criterion based on generalized cross-validation is the optimal threshold of minimum mean square error. Moreover, by using nonlinear diffusion technology based on the variational principle, the artifacts generated by the wavelet transform were eliminated, and the image was improved by keeping the advantages of the curvelet transform method of de-noising.

80.3.2 Comparison of Gray Graphs for De-noising Performance

The data at line 103, column 45–105, of the original ultrasound image were selected to draw the gray graph. The original image and gray graphs using various de-noising methods are shown in Fig. 80.2.

After comparing the gray graphs for de-noising performance, a relatively strong noise region was found at the valve close to the left atrium, which could not be effectively suppressed by a filtering method based on wavelet transform or nonlinear anisotropic diffusion, and a “double-peak” phenomenon was found on the gray graphs by these two methods. However, the “double-peak” phenomenon could not be found on the gray graph obtained by curvelet transform.

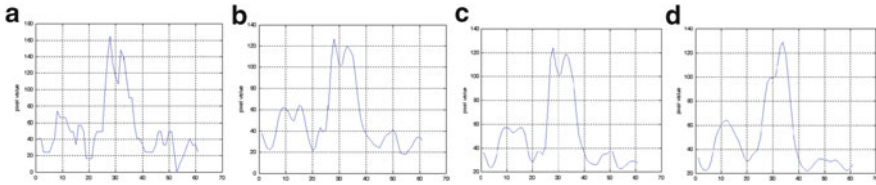


Fig. 80.2 Comparison of gray graphs for de-noising performance in echocardiographic images. (a) The gray graph using the original image. (b) The gray graph using the wavelet transform method. (c) The gray graph using the nonlinear anisotropic diffusion method. (d) The gray graph using the de-noising method described in this chapter

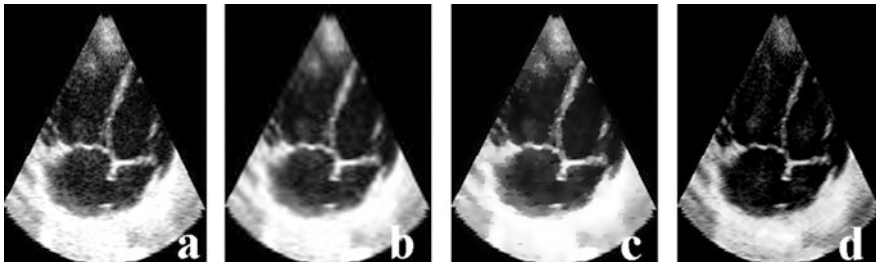


Fig. 80.3 Comparison of de-noising performance for echocardiographic 4-chamber images. (a) The original echocardiographic image. (b) Result of de-noising by wavelet transform. (c) Results of de-noising by nonlinear anisotropic diffusion. (d) Result of de-noising by the method described in this chapter

80.3.3 Comparison of De-noising Performance for Echocardiographic 4-Chamber Images

The comparison of de-noising performance for echocardiographic 4-chamber images by different filtering methods and the results of de-noising are shown in Fig. 80.3.

The results suggest that the speckle noise abundant in certain regions of the echocardiographic image (such as the left and right atrium or the left and right ventricle) could be effectively suppressed by curvelet transform. At the same time, the border pattern of chambers and valves could be well maintained, and the “over-smooth” phenomenon in wavelet domain or the “staircase” effect commonly found in nonlinear anisotropic diffusion could still be avoided.

80.4 Discussion

The de-noising of medical ultrasound images is not only aimed at improving the visual quality of images but also at making preparations for the next image segmentation. The second-generation curvelet transform inherited the excellent local characteristics of the time-space domain and frequency domain of wavelet analysis, and at the same time, it has better sparse signal expression. The characteristics to be analyzed must first be extended to multiple scale components in wavelet transform analysis; however, curvelet transform is capable of characterizing edge signals, such as curvelet transform coefficients, with fewer curves or a larger numerical value. Curvelet transform can produce good energy efficiency, and it is also helpful in reducing the noise in echocardiographic images.

Figure 80.3 shows that the mitral valve is close to the ventricular wall, with a fuzzy boundary between them in the original image, whereas the image obtained by curvelet transform maintained or even enhanced the boundary region between the mitral valve and the ventricular wall after suppressing the strong noise signal inside the four chambers, thus manifesting its effectiveness. Compared to the de-noising method based on wavelet transform, the method described in this chapter has a better suppression of speckle noise. Furthermore, this method has a better preservation of the edges in images. Figure 80.2 shows that the continuous muscular structure of the chamber wall at the right side of the original image is “fractured” after wavelet transform or anisotropic diffusion, while the method described in this chapter preserved the continuity of this structure, which could be helpful for further analysis and diagnosis.

The emphasis in ultrasonic image de-noising is on multiresolution signal processing and multidirectional analysis characterized by anisotropy [7]. As a relatively novel signal analysis method, curvelet transform is capable of multiscale signal transformation and can also accurately capture and express the directional information of the signal [8]. Using this feature, an echocardiographic image de-noising model was established in the curvelet domain. The optimal de-noising threshold against transform coefficients in each scale, each direction, and each location could be calculated using an unbiased risk estimate principle combined with neighborhood information of the curvelet transform coefficient, and the nonlinear anisotropic diffusion method, based on projection transformation, was employed to suppress the artifacts that may occur during the curvelet transform [9].

As a novel multiscale analysis method, curvelet transform has the significant advantages of capturing line singularity in images and expressing it optimally in an efficient manner compared to wavelet transform. But curvelet analysis also has its own shortcomings, such as the Gibbs artifact, which may be produced in the reconstructed images processed with inverse curvelet transform, and the reason for this artifact is that curvelet transform does not have the characteristic of translation invariance. However, Ma et al. effectively eliminated artifacts derived from curvelet transform by using the total variational model based on the projection principle [10].

Conclusion

Conventional image de-noising methods remove noise at the expense of sacrificing some detailed information at the edge of the image and reducing image definition. A better visual effect can be produced by using the de-noising method for echocardiographic images described in this chapter. The results showed that the peak signal-to-noise ratio (SNR) and edge-preserving quantization parameters after the de-noising method based on the second-generation curvelet transform are higher than those obtained after conventional de-noising algorithms. In addition, the ability of de-noising in the regions of interest and preserving the edges is especially improved, thereby demonstrating the great application potential of curvelet transform for the suppression of speckle noise in echocardiographic image processing.

Acknowledgement This work was supported by the basic research project of Shanghai Science and Technology Commission (12JC1406600).

References

1. Bhadauria HS, Dewal ML. Medical image denoising using adaptive fusion of curvelet transform and total variation. *Comput Electr Eng.* 2013;39(5):1451–60.
2. Starck JL, Candes EJ, Donoho DL. The curvelet transform for image denoising. *IEEE Trans Image Process.* 2002;11(6):670–84.
3. Minhas R, Mohammed AA, Wu QM. Shape from focus using fast discrete curvelet transform. *Pattern Recogn.* 2011;44(4):839–53.
4. Josse J, Husson F. Selecting the number of components in principal component analysis using cross-validation approximations. *Comput Stat Data Anal.* 2012;56(6):1869–79.
5. Rahman MM, Kumar MPK, Aziz A, Arefin G, Uddin MS. Adaptive anisotropic diffusion filter for speckle noise reduction for ultrasound images. *Int J Converg Comput.* 2013;1:50–9.
6. Landi G, Piccolomini EL. An efficient method for nonnegatively constrained total variation-based denoising of medical images corrupted by poisson noise. *Comput Med Imaging Graph.* 2012;36(1):38–46.
7. Stoitsis J, Golemati S, Nikita KS. A modular software system to assist interpretation of medical images-application to vascular ultrasound images. *IEEE Trans Instrum Meas.* 2006;55(6):1944–52.
8. Hao X, Gao S, Gao X. A novel multiscale nonlinear thresholding method for ultrasonic speckle suppressing. *IEEE Trans Med Imaging.* 1999;18(9):787–94.
9. Zhang F, Yoo YM, Mong KL, Kim Y. Nonlinear diffusion in laplacian pyramid domain for ultrasound speckle. *IEEE Trans Med Imaging.* 2007;26(2):200–11.
10. Ma J, Plonka G. Combined curvelet shrinkage and nonlinear anisotropic diffusion. *IEEE Trans Image Process.* 2007;16(9):2198–206.

Chapter 81

A Novel Method for Image Segmentation Using Pulse-Coupled Neural Network Based on Root Mean Square of Gray Scale

Hongliang Shi, Jian Rong, and Xinmin Zhou

Abstract PCNN (pulse-coupled neural network) has good properties for image segmentation. A novel method which integrates root mean square of grayscale threshold with PCNN, called root mean square of grayscale threshold PCNN (RMS-PCNN), is proposed. In simplified method there is only one parameter to be determined. Furthermore, the PCNN threshold is computed once so that the image is segmented during an ignition process. Better performance and faster computation are demonstrated. Experimental results validate the effectively simplified method on segmentation.

Keywords PCNN • Image segmentation • RMS-PCNN (root mean square of grayscale threshold PCNN)

81.1 Introduction

An image is separated into parts in that each part represents a meaningful physical object such as the background or the foreground, called image segmentation. Different segmentation methods have been created. But so far there has been no effective method for all image types due to the variety of image types [1].

PCNN is widely used in aspects of image processing for its advantages of information processing system closer to biological characters [2]. However, the traditional PCNN algorithm shows many disadvantages, such as too many parameter selections, iteration times, and so on.

Root mean square of grayscale threshold PCNN (RMS-PCNN) is put forward in this chapter. It integrates root mean square of image grayscale statistics with PCNN. In this chapter, the PCNN is simplified because only one parameter is to be determined. Moreover, the PCNN threshold is computed once. The image is simply segmented during an ignition process. Better performance and faster computation

H. Shi • J. Rong (✉) • X. Zhou

College of Mechanical and Traffic, Southwest Forestry University, 650224 Kunming, China
e-mail: swordrong@163.com

are demonstrated. Experimental results validate the effectively simplified method for segmentation.

81.2 Root Mean Square of Grayscale PCNN Model

81.2.1 Simplified PCNN

The simplified PCNN is shown as follows: $F(i, j)$ is the feeding and $S(i, j)$ is the grayscale level of pixel (i, j) ; $L(i, j)$ is the linking, β is the linking constant; $U(i, j)$ is the internal activity; M is the connection matrix in feedback input domain; θ is constant and related to the grayscale statistics of the image; and $Y(i, j)$ is the pulse output (Fig. 81.1).

The feeding is the image gray scale $S_{i,j}$:

$$F_{i,j} = S_{i,j} \tag{81.1}$$

The linking output is shown as follows:

$$L_{i,j} = \sum_{k \in G} M_k S_k \tag{81.2}$$

G is 3×3 linking field, which is shown in Fig. 81.2.

$U(i, j)$ is formed by biased linking inputs multiplied with the feeding:

$$U_{i,j} = F_{i,j}(1 + \beta L_{i,j}) \tag{81.3}$$

At each ignition step, $Y(i, j)$ is set to 1 if the $U(i, j)$ is greater than the threshold θ or else is set to 0, which is shown in Eq. (81.4):

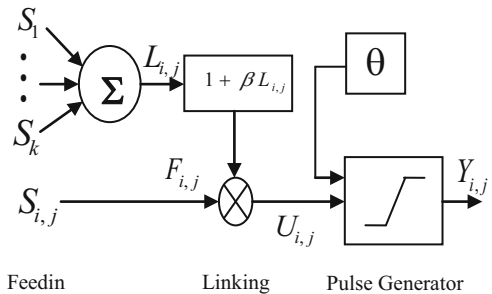


Fig. 81.1 The proposed PCNN model

Fig. 81.2 3 × 3 linking field

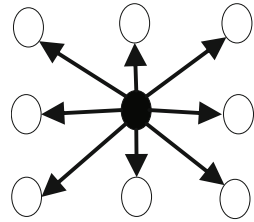
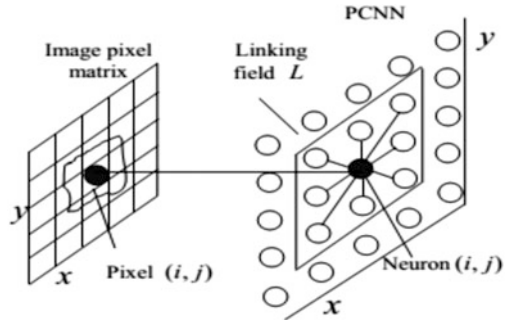


Fig. 81.3 PCNN segmentation model



$$Y_{i,j} = \text{step}[U_{i,j} - \theta] = \begin{cases} 1, & U_{i,j} > \theta \\ 0, & \text{otherwise} \end{cases} \quad (81.4)$$

81.2.2 Root Mean Square of Grayscale Threshold

This chapter defines the root mean square of the grayscale level of each pixel as threshold θ . It is shown in Eq. (81.5):

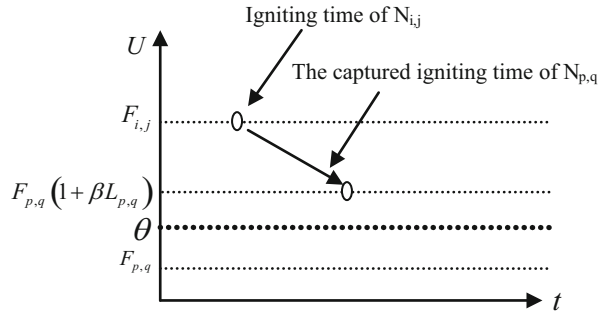
$$\theta = \sqrt{\frac{\sum_{(i,j) \in I} S^2(i,j)}{m \times n}} \quad (81.5)$$

where m, n are the pixel numbers of the image in the rows and columns, respectively, and i is the $m \times n$ grayscale matrix of the image.

81.2.3 RMS-PCNN Image Segmentation

The neuron is one-one onto the image that is a two-dimension network. It is shown in Fig. 81.3 [1].

Fig. 81.4 The captured igniting time of neuron $N_{p,q}$



Assume the initial $Y(i, j) = 0$, and let $U_{i,j} = S_{i,j}$. The neuron will ignite if $S_{i,j} > \theta$, and $Y(i, j) = 1$, or otherwise, the neuron will not ignite, and $Y(i, j) = 0$, according to Eq. (81.4) in the iteration. The neuron $N_{p,q}$ which does not ignite in the iteration can be captured by the neuron $N_{i,j}$ which has ignited in the neighboring field of $N_{p,q}$ according to the coupling effect of PCNN of Eq. (81.2). Thus the internal status of $N_{p,q}$ is converted into $F_{p,q}(1 + \beta L_{p,q})$ from $F_{p,q}$. Assume $F_{p,q} < \theta$ but $F_{p,q}(1 + \beta L_{p,q}) > \theta$, then the unignited neuron $N_{p,q}$ is captured by the ignited neuron $N_{i,j}$, shown as Fig. 81.4.

If the grayscale level of neuron $N_{p,q}$ is lower than that of neuron $N_{i,j}$, which leads to $F_{p,q}(1 + \beta L_{p,q}) < \theta$, then neuron $N_{p,q}$ cannot be captured by neuron $N_{i,j}$. Therefore, this PCNN characteristic determines the spatial connection and grayscale level correlation of neurons. Thus a coherent structure of the image is indicated by each continuous set of synchronous pulse neurons, which makes image segmentation using PCNN theoretically correct.

81.3 Experiment Results

In the experiments, RMS-PCNN is proved significantly.

81.3.1 The Evaluation of RMS-PCNN

Figure 81.5 shows the segmentation results. By using the method based on OSTU and normal PCNN, the unit-linking PCNN, GIT-PCNN, and the RMS-PCNN severally, Lena image is segmented. (b), (d), and (e) are obscured for the facial organs. There are more details in the hair, but it is ill segmented obviously compared with the proposed RMS-PCNN in image (c).

Figure 81.6 shows the results of track image; (b) is over-segmented and (c) is ill segmented especially in the left bottom block. Relatively, the RMS-PCNN provides



Fig. 81.5 (a) The original image, (b) the method based on OSTU, (c) the method based on normal PCNN, (d) the unit-linking PCNN [3], (e) the GIT-PCNN [1], and (f) RMS-PCNN

a clear foreground and segment foreground from background. Of course, the three methods are unsatisfied with segmenting regions affected by illumination like the upper part in the original image.

Figure 81.7 shows the results of cameraman image; (b), (c), and (d) are filled with more noise in the bottom in contrast with the proposed RMS-PCNN. Especially, the proposed RMS-PCNN can segment foreground from background in the upper part or the facial part of the image clearly.

81.3.2 Objective Evaluation to Segmentation Performance

The criterion of cross entropy (CE) [4], uniformity measure (UM) [5], shape measure (SM) [5], and contrast measure (CM) [6] is used for objectively evaluating the algorithm performance, shown as follows:

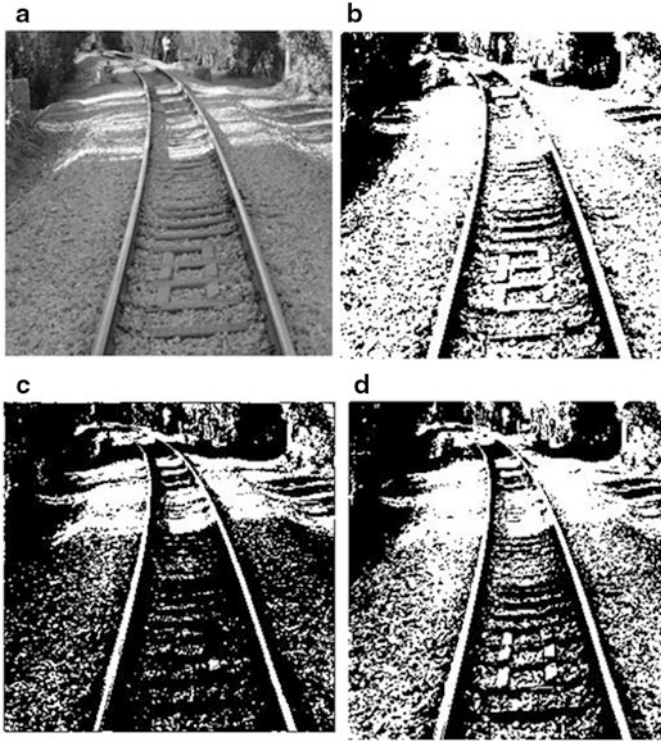


Fig. 81.6 (a) The original track image, (b) the method based on OSTU, (c) the method based on normal PCNN, and (d) RMS-PCNN

$$\begin{aligned}
 CE = & \sum_{f=0}^t \left[f \times h(f) \times \ln \frac{f}{\mu_1} + \mu_1 \times h(f) \times \ln \frac{\mu_1}{f} \right] \\
 & + \sum_{f=t+1}^Z \left[f \times h(f) \times \ln \frac{f}{\mu_2} + \mu_2 \times h(f) \times \ln \frac{\mu_2}{f} \right] \tag{81.6}
 \end{aligned}$$

$$\mu_1 = \frac{1}{\sum_{f=0}^t h(f)} \sum_{f=0}^t f \times h(f) \tag{81.7}$$

$$\mu_2 = \frac{1}{\sum_{f=t+1}^Z h(f)} \sum_{f=t+1}^Z f \times h(f) \tag{81.8}$$

where f is the image gray scale and $h(f)$ is the statistical histogram of image gray scale and t is a hypothetical threshold. Generally, smaller value of CE is better:

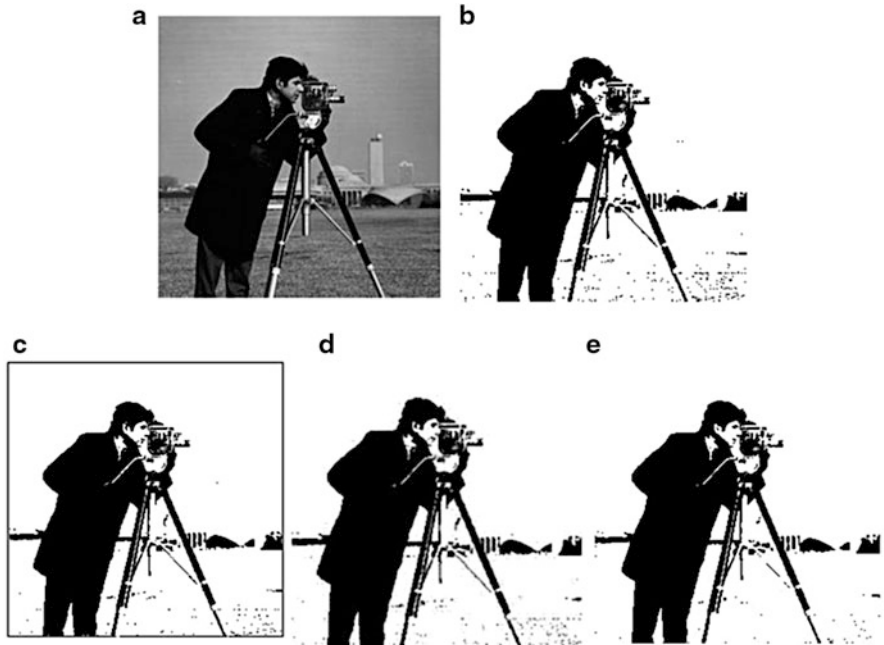


Fig. 81.7 (a) The original cameraman image, (b) the method based on OSTU, (c) the method based on normal PCNN, (d) the GIT-PCNN in [1], and (e) RMS-PCNN

$$UM = 1 - \frac{1}{A} \sum_{i=1}^2 \left\{ \sum_{(x,y) \in R_i} \left[f(x,y) - \frac{1}{A_i} \sum_{(x,y) \in R_i} f(x,y) \right]^2 \right\} \quad (81.9)$$

The original image is divided into two parts: R_1 and R_2 . $f(x, y)$ is the pixel (x, y) grayscale level. A is the image pixel numbers, and A_i is the pixel numbers in region R_i :

$$SM = \frac{1}{C} \sum_{(x,y)} \text{sgn}[f(x, y) - f_N(x, y)] \Delta(x, y) \text{sgn}[f(x, y) - t] \quad (81.10)$$

where C is the normalized factor, $f_N(x, y)$ is the average gray scale of adjacent domain $N(x, y)$, t is the grayscale threshold, and $\Delta(x, y)$ is generalized gradient:

$$CM = \frac{|f_o - f_b|}{f_o + f_b} \quad (81.11)$$

where f_o and f_b are the average gray scale of foreground and background separately. A larger CM shows a better segmentation result. It is the same with UM and SM.

Table 81.1 Three segmentation algorithm performance comparison

	OSTU				PCNN				RMS-PCNN			
	CE	UM	SM	CM	CE	UM	SM	CM	CE	UM	SM	CM
Lena	0.114	0.987	0.841	0.819	0.122	0.962	0.845	0.965	0.109	0.995	0.847	0.959
Cameraman	0.041	0.990	0.891	0.734	0.040	0.988	0.912	0.763	0.038	0.992	0.933	0.766

Table 81.1 indicates the better RMS-PCNN except that the CM of normal PCNN are slightly greater than that of RMS-PCNN, but the parameters of the proposed method are less than the normal PCNN and the structure of RMS-PCNN is simpler.

81.3.3 Time Complexity Analysis

Time complexity analysis is an important factor for evaluating an algorithm. It is given in Table 81.2.

From Table 81.2, we can know that the proposed algorithm is much better than the GIT-PCNN with the increasing iteration times. k is the width of linking matrix. s is the iteration times of GIT-PCNN in threshold calculation and $s \gg 1$. There will be significant differences with the increasing iteration times, shown in Fig. 81.8.

81.3.4 Speed Performance

The four segmentation methods (include proposed method) are executed on PC (Intel Xeon E3-1230 v3 and 8 GB RAM). The results are shown in Table 81.3.

The same image with the size of $256 * 256$ is segmented. Each method is applied to process the image 20 times and get the average run time to make the results more objective. It is obvious that the RMS-PCNN is faster than the other methods

Table 81.2 Time complexity analysis

	Convolution part	Iteration part	Constant
GIT-PCNN	$O(m \times n \times k^2)$	$O(m \times n \times s)$	$O(1)$
RMS-PCNN	$O(m \times n \times k^2)$	$O(m \times n)$	$O(1)$

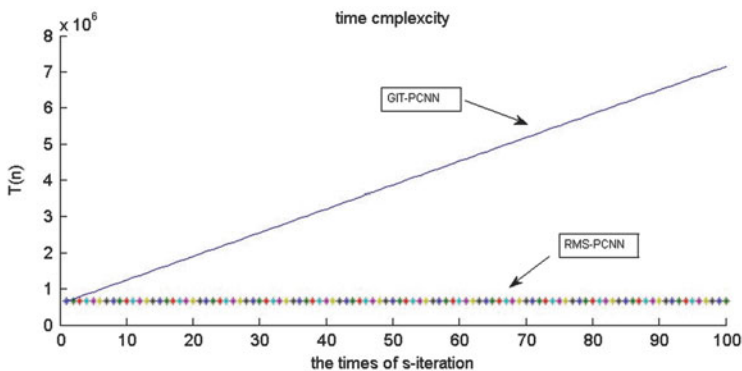


Fig. 81.8 The comparison of time complexity

Table 81.3 Processing time and the iteration time of five methods (unit, s)

OSTU	The GIT-PCNN		The normal PCNN		RMS-PCNN	
Processing time	Iteration time	Processing time	Iteration time	Processing time	Iteration time	Processing time
1.15	1	7.62	8	1.15	1	0.60

because the proposed method uses the root mean square of grayscale threshold which does not require iteration and the whole algorithm is just required once.

Conclusion

In this chapter, compared to traditional segmentation, the root mean square of grayscale threshold PCNN presents many advantages:

- (1) The root mean square of grayscale threshold is better than the threshold of traditional PCNN.
- (2) In RMS-PCNN, only one parameter is determined once. Therefore, the method is simpler and faster.
- (3) The experiment results illustrate that the RMS-PCNN can get satisfied processing results.

Acknowledgements The project is supported by the National Natural Science Foundation of China (61261013) and the Science and Technology Innovation Foundation of Southwest Forestry University (1418).

References

1. Li HY. The pulse coupled neural network and its application in image enhancement and face detection. Kunming: Yunnan University; 2010.
2. Ma YD, Dai RL, et al. A new algorithm of image segmentation based on pulse-coupled neural networks and the entropy of images. In: 8th international conference on neural international processing, computational and information sciences, Chengdu; 2001. p. 71–4.
3. Gu XD, Zhang LM, et al. Automatic image segmentation using unit-linking PCNN without choosing parameters. *J Circuits Syst.* 2007;12(6):54–9 [in Chinese].
4. Solomon K. Information theory and statistics. New York: John Wiley; 1959. p. 67–8.
5. Sahoo PK, Soltani S, et al. A survey of thresholding techniques. *Comput Vis Graph Image Process.* 1988;41(2):233–60.
6. Levine MD, Naxif A. Dynamic measurement of computer generated image segmentation. *IEEE Trans PAMI.* 1985;7(2):155–64.

Chapter 82

Combined Similarity-Based Spectral Clustering Ensemble for PolSAR Land Cover Classification

Lu Liu, Dong Sun, and Junfei Shi

Abstract This chapter proposes a novel spectral clustering ensemble method for unsupervised land cover classification of PolSAR data. This method increases the diversity to overcome the instability results caused by the random sampling during Nyström approximation. Compared with the standard spectral clustering methods, the proposed scheme has the contributions in three aspects: firstly, during the process of spectral clustering, Wishart-derived distance measure and polarimetric similarity are combined to obtain the complementary information from the spatial and polarimetric relations between pairwise pixels. Secondly, a new similar function based on MRF potential function is used to construct the similarity matrix, which improves the robustness of spectral clustering to the scaling parameter. Finally, multiple individual classifications are obtained and integrated by an ensemble strategy. The experimental results demonstrate that the proposed method is superior to the compared methods.

Keywords Spectral clustering ensemble (SCE) • Polarimetric SAR • Wishart distance • MRF

82.1 Introduction

Land cover classification using polarimetric synthetic aperture radar (PolSAR) data is one of the significant applications in remote sensing. With the development of related researches, multiple PolSAR land cover classification approaches have been proposed.

In practice, unsupervised classification has been extensively used due to no need to collect label information. It consists of two parts: scattering- and statistic

L. Liu (✉) • D. Sun • J. Shi
Key Laboratory of Intelligent Perception and Image Understanding of Ministry of Education,
International Research Center for Intelligent Perception and Computation, Xidian University,
Xi'an 710071, Shaanxi, China
e-mail: liulu0613@163.com

characteristics-based methods and clustering analysis. The former are actually based on extracting and selecting the polarimetric features, such as H/a [1], H/a-Wishart [2], and Wishart ML classifier [3] combining Freeman decomposition [4]. The latter are some clustering algorithms such as MRF-based clustering [5], fuzzy clustering [6], and hierarchical clustering [7].

However, traditional clustering methods are based on the spherical sample space. Once the samples fall into the non-convex domain, poor efficiency and local optimum results will arise easily. Thus, the spectral clustering (SC) method is adopted as a remedy. According to the diversity similarity of samples, SC constructs an affinity matrix to explore the internal relation between samples and divide all the samples into a given number of clusters. Therefore, the SC method is superior to traditional clustering algorithms. Some related approaches have been proposed in PolSAR classification, e.g., spectral graph partition [7], Wishart-derived distance measures [8], and polarimetric similarity measures [9].

The SC method is sensitive to the scaling parameter. To overcome this sensitivity, we use spectral clustering ensemble (SCE) [10] strategy and a novel MRF potential function-based similarity matrix [11].

82.2 The Framework of PolSAR SCE

The framework of PolSAR SCE consists of two stages. Firstly, the similarity matrix is constructed by combining Wishart-derived distance and selected polarimetric features. Then, the PolSAR SCE classification is executed.

82.2.1 Wishart-Derived Distance

Originally, the data of each pixel in PolSAR image can be expressed by its coherency matrix T , which is a 3×3 hermit matrix [2]

$$T = k * k^*; k = (1/\sqrt{2}) * [S_{HH} + S_{VV} \quad S_{HH} - S_{VV} \quad 2S_{HV}]^T \quad (82.1)$$

Anfinsen et al. [8] defined a symmetric revised Wishart distance as follows:

$$d_{SRW}(A, B) = \frac{1}{2}(d_{RW}(A, B) + d_{RW}(B, A)) - q \quad (82.2)$$

$$d_{RW}(A, B) = \ln \frac{|B|}{|A|} + \text{tr}(B^{-1}A) - q \quad (82.3)$$

$A \sim W(n, \Sigma A)$ and $B \sim W(n, \Sigma B)$ are sample coherence matrices generated from unknown and potentially different Wishart densities.

82.2.2 Polarimetric Feature Selection

We analyzed the distribution of different polarimetric features in order to select the most distinguished features to construct the similarity matrix. The subimage of Flevoland area is shown in Fig. 82.1. Figure 82.2 shows the selected feature distributions of the six types of terrain from Fig. 82.1.

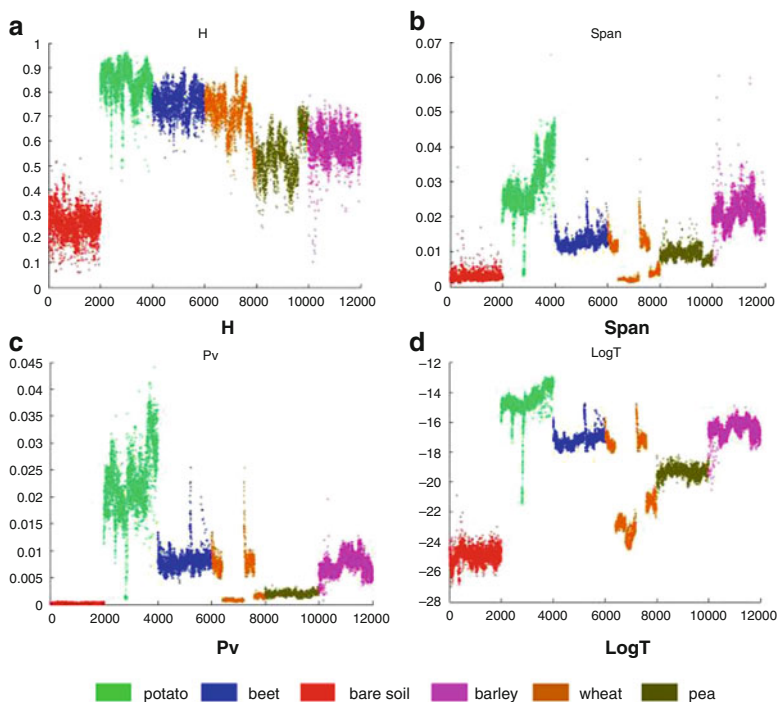
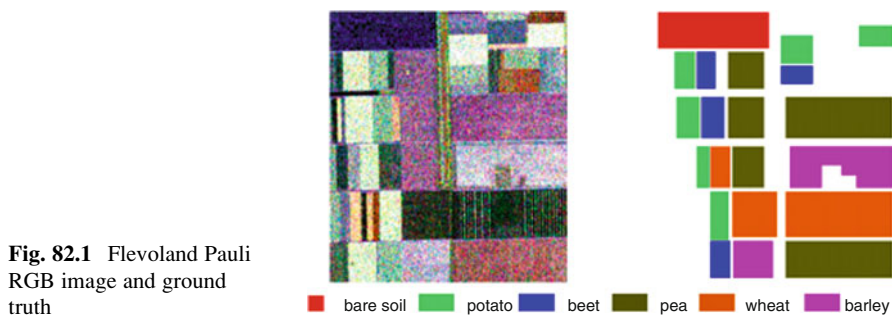


Fig. 82.2 The feature distribution of the six types of terrain in different selected feature spaces. (a) H , (b) $SPAN$, (c) P_V , (d) $\text{Log}T$

After that, these effective features, H (the scattering entropy), $SPAN$ (the total power), Pv (the volume scattering powers based on Freeman decomposition), and $\text{Log } T$ (the logarithm of coherency matrix T), compose polarimetric eigenvector F

$$F = [H, SPAN, Pv, \text{Log } T] \quad (82.4)$$

The scattering entropy H and total power $SPAN$ are defined as follows:

$$H = \sum_{i=1}^3 -P_i \log_3 P_i \quad (82.5)$$

$$P_i = \lambda_i / \sum_{i=1}^3 \lambda_i \quad (82.6)$$

$$SPAN = \lambda_1 + \lambda_2 + \lambda_3 \quad (82.7)$$

where $\lambda_1 \geq \lambda_2 \geq \lambda_3$ are the eigenvalues of coherence matrix T .

82.2.3 Similarity Matrix Construction

To reduce the sensitivity of traditional SC to the scaling parameter and select optimal parameters easily, Hou et al. [11] proposed a novel MRF potential function based on the context information to construct the similarity matrix. The adopted MRF potential function involves intensity Euclidean distance and spatial position information of adjacent pixels.

Potential function is crucial to construct the MRF prior model because it describes the relationships of feature intensities of adjacent pixels. The potential function is defined as follows:

$$V_c(x_i, x_j) = \begin{cases} \beta & x_i = x_j \\ \frac{\sigma_i^2}{\sigma_i^2 + (y_i - y_j)^2} \beta & x_i \neq x_j \end{cases} \quad (82.8)$$

where y_i and y_j are the observation point intensities of x_i and x_j , respectively, d_{ij} is the spatial position information of x_i and x_j , β is a constant, and σ_i is the deviation of the class that pixel x_i belongs to. Thus, the potential function can be used to describe the similarity between pairwise pixels. The similarity matrix is defined as follows:

$$W_{ij} = \begin{cases} 1 & i = j \\ \frac{1}{1 + \Delta_{ij}d_{ij}} & i \neq j \end{cases} \quad (82.9)$$

According to the Huber function [12], Δ_{ij} is defined as follows:

$$\Delta_{ij}^{\text{SRW}} = \begin{cases} d_{\text{SRW}}^2(T_i, T_j) & d_{\text{SRW}}(T_i, T_j) \leq t_1 \\ t^2 + 2t(d_{\text{SRW}}(T_i, T_j) - t) & d_{\text{SRW}}(T_i, T_j) > t_1 \end{cases} \quad (82.10)$$

$$\Delta_{ij}^{\text{F}} = \begin{cases} d_{\text{F}}^2(F_i, F_j) & d_{\text{F}}(F_i, F_j) \leq t_2 \\ t^2 + 2t(d_{\text{F}}(F_i, F_j) - t) & d_{\text{F}}(F_i, F_j) > t_2 \end{cases} \quad (82.11)$$

$$\Delta = \Delta_{ij}^{\text{SRW}} * \Delta_{ij}^{\text{F}} \quad (82.12)$$

We use a similarity function by formulas (82.10)–(82.12). Then, the similarity matrix is constructed by formula (82.9).

82.2.4 Spectral Clustering Ensemble (SCE) Classification

Zhang et al. [10] developed an ensemble approach based on SC to avoid the selection of the scaling parameter for single SC. The SCE includes two parts, the formation of individual clustering and the integration of diversity clustering results. The construction of SCE can be depicted as follows. Firstly, it extracts the selected features previously mentioned at pixel level as the input of each component clustering. Then, SC using Nyström approximation [13] is employed as the basic clustering. Based on the results of the former step, both the hypergraph-based meta-clustering algorithm (MCLA) [14] with lower complexity and the majority voting method are used as the consensus function to combine those clusters.

The consensus function is intended to find a suitable result that shares the most information with the original clusterings. Mutual information provides a sound indication of the shared information between a pair of clusterings [14]. The normalized mutual information between two cluster labelings can be estimated by [10].

$$\phi^{(\text{NMI})}(\lambda^{(a)}, \lambda^{(b)}) = \frac{\sum_{i=1}^k \sum_{j=1}^k n_{ij} \log \left(\frac{n_{ij}n}{n_i^{(a)}n_j^{(b)}} \right)}{\sqrt{\left(\sum_{i=1}^k n_i^{(a)} \log \frac{n_i^{(a)}}{n} \right) \left(\sum_{j=1}^k n_j^{(b)} \log \frac{n_j^{(b)}}{n} \right)}} \quad (82.13)$$

where $n_i^{(a)}$ is the number of objects in cluster i according to $\lambda^{(a)}$, and $n_j^{(b)}$ is the number of objects in cluster j according to $\lambda^{(b)}$. n_{ij} denotes the number of objects that are in cluster i according to $\lambda^{(a)}$ as well as in cluster j according to $\lambda^{(b)}$. Then the average normalized mutual information between the final ensemble clustering result $\hat{\lambda}$ and the cluster label set Λ can be defined as

$$\phi^{(\text{AMNI})}(\Lambda, \hat{\lambda}) = \frac{1}{r} \sum_{j=1}^r \phi^{(\text{NMI})}(\lambda^{(j)}, \hat{\lambda}) \quad (82.14)$$

$$\Lambda = \left\{ \lambda^{(q)} \mid q \in \{1, \dots, r\} \right\} \quad (82.15)$$

After that, combining the selected result of MCLA and majority voting approach, the final decision with larger average mutual information is obtained.

82.3 Proposed Method

Our proposed method for land cover classification is illuminated as follows:

- (1) PolSAR data is processed by performing refined Lee filter.
- (2) Gain the Cloude decomposition of each pixel from its coherency matrix T . And calculate H , $SPAN$, P_v , and logarithm of T . Then, polarimetric eigenvector F is composed. Normalize it to gain the polarimetric characteristic matrix F .
- (3) According to formulas (82.9)–(82.12), calculate the combined similarity matrix.
- (4) Execute the SCE strategy mentioned in Sect. 82.2.4, which combines the selected result of MCLA and majority voting approach.
- (5) Iteratively implement Wishart classifier to improve the classification accuracy. Finally, the classification result of PolSAR data is obtained.

82.4 Experimental Results

The data used in Fig. 82.1 was acquired over Flevoland in the Netherlands by NASA/JPL AIRSAR on August 16, 1989.

For our spectral clustering ensemble of PolSAR data, Nyström approximation method is employed and the sample set is 100. The thresholds t_1 and t_2 are randomly selected in the range of 1–10. The number of Wishart iterations is set to 20.

Three state-of-the-art algorithms, H/a-Wishart (Ref 1 for short), SCE with Wishart-derived distance (Ref 2 for short), and SCE with polarimetric similarity (Ref 3 for short), are used as a comparison to demonstrate the effectiveness of our proposed method. Furthermore, in order to evaluate the ensemble strategy of spectral clustering, single SC is compared, too. Final results are shown in Fig. 82.3. The classification accuracy of five methods is provided in Table 82.1. Table 82.2 shows the confusion matrix of the SCE method.

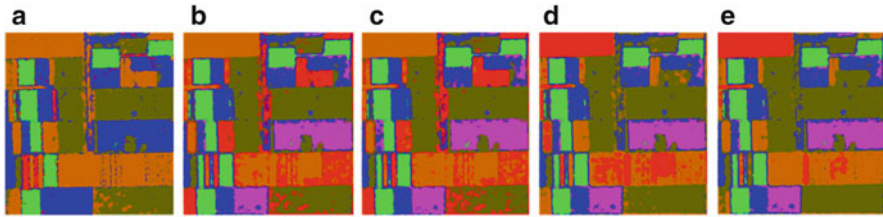


Fig. 82.3 Classification results with different methods. (a) H/a-Wishart. (b) SCE with Wishart-derived distance. (c) SCE with polarimetric similarity. (d) Single SC method. (e) Proposed method

Table 82.1 Classification accuracy comparison

Method Accuracy	Ref 1	Ref 2	Ref 3	Single SC method	Proposed method
Bare soil	0	0	0	0.9551	0.9562
Potato	0.8799	0.9246	0.9236	0.9238	0.9233
Beet	0.8669	0.9337	0.9526	0.9177	0.9172
Barley	0	0.9456	0.9593	0.9468	0.9432
Wheat	0.9334	0.5649	0.6762	0.6136	0.9089
Pea	0.9376	0.9505	0.9136	0.9850	0.9895
Total accuracy	0.6947	0.7636	0.7780	0.8859	0.9484

Table 82.2 Confusion matrix of the proposed method

	Bare soil	Potato	Beet	Barley	Wheat	Pea
Bare soil	0.9562	0.0	0.0154	0.0	0.0284	0.0
Potato	0.0	0.9233	0.0211	0.0556	0.0	0.0
Beet	0.0	0.0396	0.9172	0.0432	0.0	0.0
Barley	0.0	0.0104	0.0464	0.9432	0.0	0.0
Wheat	0.0565	0.0019	0.0071	0.0	0.9089	0.0256
Pea	0.0	0.0	0.0086	0.0011	0.0008	0.9895

Bare soil is allocated to wheat in Fig. 82.3a–c. Barley is allocated to beet in Fig. 82.3a. Partial of pea are mistaken as bare soil or wheat in Fig. 82.3b–d. In addition, the proposed method reduces the classification error of wheat compared with others.

In Table 82.1, the proposed method achieves a total accuracy of 94.84 %, which improves 25.37 %, 18.48 %, 17.04 %, and 6.25 % compared with other methods, respectively. Ref 1, Ref 2, and Ref 3 cannot distinguish bare soil, while our method obtains a significant accuracy of 95.62 %. It can also achieve a better accuracy of 98.95 % in the classification of pea. Furthermore, the proposed method reduces the ratio of error obviously as shown in Table 82.2.

Through the statistic analysis, it is obvious that the SCE method can distinguish diverse categories better and achieve visible improvement in region uniformity and connectivity. Furthermore, the proposed method has the advantage of fine stability.

Conclusion

We have employed ensemble strategy to implement SC for PolSAR data classification. In order to improve the classification performance, the SCE method is modified through constructing similarity matrix based on MRF potential function. By this way, SCE strategy eliminates the effect caused by the sensitivity to scaling parameter. Combining with spatial and polarimetric relations between pairwise pixels, the proposed method shows an ability of capturing more detailed similarity information. Future works will be concentrated on feature selection and ensemble strategy to achieve more effective performance for PolSAR land cover classification.

References

1. Cloude SR, Pottier E. An entropy based classification scheme for land applications of polarimetric SAR. *IEEE Trans Geosci Remote Sens.* 1997;35(1):68–78.
2. Lee JS, Grunes MR, Ainsworth TL, et al. Unsupervised classification using polarimetric decomposition and the complex Wishart classifier. *IEEE Trans Geosci Remote Sens.* 1999;37(5):2249–58.
3. Lee JS, Grunes MR, et al. Unsupervised terrain classification preserving polarimetric scattering characteristics. *IEEE Trans Geosci Remote Sens.* 2004;42(4):722–31.
4. Freeman A, Durden SL. A three-component scattering model for polarimetric SAR data. *IEEE Trans Geosci Remote Sens.* 1998;36(3):963–73.
5. Yu P, Qin AK, Clausi DA. Unsupervised polarimetric SAR image segmentation and classification using region growing with edge penalty. *IEEE Trans Geosci Remote Sens.* 2012;50(4):1302–17.
6. Liu B, et al. Superpixel-based classification with an adaptive number of classes for polarimetric SAR images. *IEEE Trans Geosci Remote Sens.* 2013;51(2):907–24.
7. Ersahin K, et al. Segmentation and classification of polarimetric SAR data using spectral graph partitioning. *IEEE Trans Geosci Remote Sens.* 2010;48(1):164–74.
8. Anfinson SN, Jenssen R, Eltoft T. Spectral clustering of polarimetric SAR data with Wishart-derived distance measures. In: *Proceedings of POLinSAR*, vol. 7, Frascati, Italy; 2007.
9. Li X, Lin W, et al. Spectral classification of polarimetric SAR images based on polarimetric similarity. *J Comput Appl.* 2010;30(5):1415–7 [in Chinese].
10. Zhang XR, Jiao LC, et al. Spectral clustering ensemble applied to SAR image segmentation. *IEEE Trans Geosci Remote Sens.* 2008;46(7):2126–36.
11. Hou YM, Lun XM, Meng W, et al. Unsupervised segmentation method for color image based on MRF. In: *International conference on computational intelligence and natural computing*, vol. 1. Wuhan: IEEE; 2009. p. 174–7.
12. Huber PJ. *Robust statistics*. Berlin: Springer; 2011. p. 1248–51.
13. Fowlkes C, Belongie S, Chung F, Malik J. Spectral grouping using the Nystrom method. *IEEE Trans Pattern Anal Mach Intell.* 2004;26(2):214–25.
14. Strehl A, Ghosh J. Cluster ensembles—a knowledge reuse framework for combining multiple partitions. *J Mach Learn Res.* 2003;3(3):583–617.

Chapter 83

An Algorithm for Human Face Detection in Color Images Based on Skin Color Segmentation

Chunqiang Zhu

Abstract Face detection has attracted increased attention as a hot research topic in the field of pattern recognition and computer vision. Skin color has provided an important basis for human face detection. This paper presents a novel expectation-maximization (EM) algorithm for the face detection of image segmentation in the YUV color space. To separate brightness information from chroma information in the expression of color, the algorithm uses the clustering method for skin color in the color space and improves the velocity performance in the separation of a regional face from a regional nonhuman face. This paper also designs and optimizes the concrete steps. Finally, the segmentation experimental results and experimental analysis in terms of color images are given; in addition, the paper provides the necessary conditions for EM algorithm convergence.

Keywords Face detection • EM algorithm • Skin color segmentation • Template matching • YUV space

83.1 Introduction

Face detection algorithms have been extensively studied since the early 1990s, with many solutions proposed, such as, for example, neural networks, machine learning, template matching (including the deformable template matching), Hough transform, and color analysis. Of these, the neural network method requires large numbers of face and nonface training sets, and they are always used in the detection of positive correct grayscale images [1–4]. The template matching method is commonly used in face detection where the initial position is known. As an important basis for the skin color of human face detection, skin color is one of the important pieces of information with respect to the face. It has relative stability

C. Zhu (✉)

Department of Computer Science, Xi'an Electric Power College, Xi'an 201405, Shaanxi, China

e-mail: 8302526@qq.com

© Springer International Publishing Switzerland 2015

W.E. Wong (ed.), *Proceedings of the 4th International Conference on Computer Engineering and Networks*, Lecture Notes in Electrical Engineering 355,
DOI 10.1007/978-3-319-11104-9_83

713

and can be distinguished with most background object colors; therefore, color images using skin color information for rapid detection are used in the study of faces. In this paper, which uses expectation maximization (EM) to solve the problem of the Gaussian mixture model, a method of segmenting color images based on skin color is used to achieve superior segmentation effects that can be further applied to face detection [5].

83.2 EM Solution of Gaussian Mixture Model

Set a normal distribution with the totality containing the K independent and equal variance, that is, $N_i(\mu_j, \sigma^2), j = 1, 2, \dots, K$, with the value $p_j, 0 \leq p_j \leq 1, \sum_j p_j = 1$. The likelihood function of X_i is shown in Eqs. (83.1) and (83.2) [5]:

$$L = L(X_i; \theta) = L(X; p_j, \mu_j, \sigma^2), \tag{83.1}$$

$$L(X; p_j, \mu_j, \sigma^2) = \prod_{i=1} \prod_{j=1} (p_j \varphi_j)^{z_i}, \tag{83.2}$$

where $p_j \varphi_j$ is the normal distribution of a probability density function, as shown in Eq. (83.3):

$$\varphi_j(X_i) = \frac{p_j}{\sqrt{\sigma^2 2\pi}} \exp \frac{-z_{ij}(X_i - \mu_j)^2}{2\sigma^2}. \tag{83.3}$$

The only difference between a plurality of mixed normal distributions and multiple independent normal distributions is the different degrees of overlap. Thus, some z_{ij} in X_i cannot be determined, meaning we cannot distinguish which X_i belong to which normal distribution [6–8]. In this case, the likelihood function of X_i is as follows:

$$\begin{aligned} L &= L(X_i; \theta) = L(X; p_j, \mu_j, \sigma^2) \\ &= \prod_i^n \left[\sum_j p_j \varphi_j(X_i) \right], \end{aligned} \tag{83.4}$$

$$\ln L = \sum_i \ln \left[\sum_j p_j \varphi_j(X_i) \right] \tag{83.5}$$

Which X_i in the mixed normal distribution of a probability density function is as follows [9–10]:

To satisfy (83.6), the iterative approximation uses the EM algorithm, namely, E (expectation) step: in the given t wheel parameters $\theta^{(t)} = (p_j^{(t)}, \mu_j^{(t)}, \sigma^{2(t)})$, $\omega_{ij}^{(t)}$: calculates the conditional probability of the normal distribution of each X_i that belongs to i :

$$\omega_{ij}^{(t)} = p_j^{(t)} \varphi_j^{(i)} / \sum_j p_j^{(t)} \varphi_j^{(i)}. \tag{83.6}$$

M (maximization) step: based on $\omega_{ij}^{(t)}$ and X_i , which give the maximum-likelihood estimates of $\theta^{(t+1)}$:

$$\begin{aligned} p_j^{(t+1)} &= \omega_j^{(t)} / n, \\ \omega_j^{(t)} &= \sum_i \omega_{ij}^{(t)}, \\ u_j^{(t+1)} &= \sum_i \omega_{ij}^{(t)} X_i / \omega_j^{(t)}, \\ \sigma^{2(t+1)} &= \sum_{i,j} \omega_{ij}^{(t)} (X_i - \mu_j^{(t+1)})^2 / n. \end{aligned} \tag{83.7}$$

Using the results of the first t times and obtaining $\omega_{ij}^{(t+1)}$ and substituting $\omega_{ij}^{(t+1)}$ and X_i into Eq.(7), we arrive at the result $\theta^{(t+2)}, \dots$. Like these E and M loop iterations, both values of the parameter estimation and $\ln L$ gradually converge. When they satisfy a certain set of convergence criteria (such as before and after two rounds of the corresponding numerical difference is not more than 10^{-6} or 10^{-4}), the calculation ends and the result θ is the maximum-likelihood estimates of the relevant parameters. The EM algorithm is shown in Fig. 83.1.

83.3 Image Segmentation Based on EM Algorithm

The commonly used RGB method is not suitable for the skin model. In RGB space, the three primary colors (R, G, b) not only represent color, also said the brightness. Due to changes in environmental lighting, the brightness may make face detection more complex. It is not reliable for skin segmentation. To use the clustering of skin in the color space, the chrominance and luminance information must be separated in the color expression. The R, G, and B conversion for the color expression space with chrominance and luminance separation will achieve this objective. As shown in Fig. 83.2, this paper uses the YUV color space to process image data: $Y = 0.3, 0.59, 0.11$ R, $U = -0.15, -0.29, 0.44$ G, $V = 0.61, -0.52, -0.096$ B uses the UV data to build EM data: $\text{atan2}(V,U)$.

Fig. 83.1 Iterative process diagram of EM algorithm

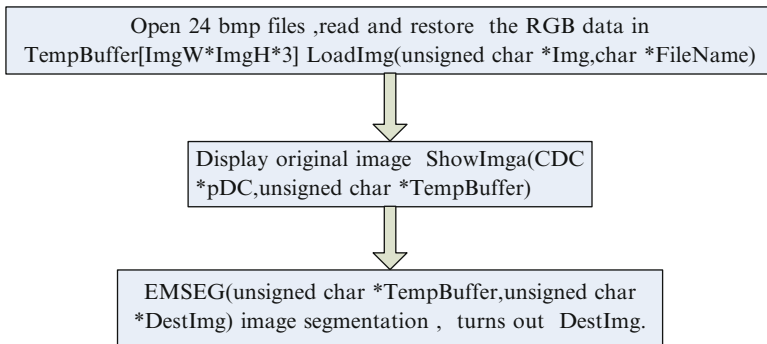
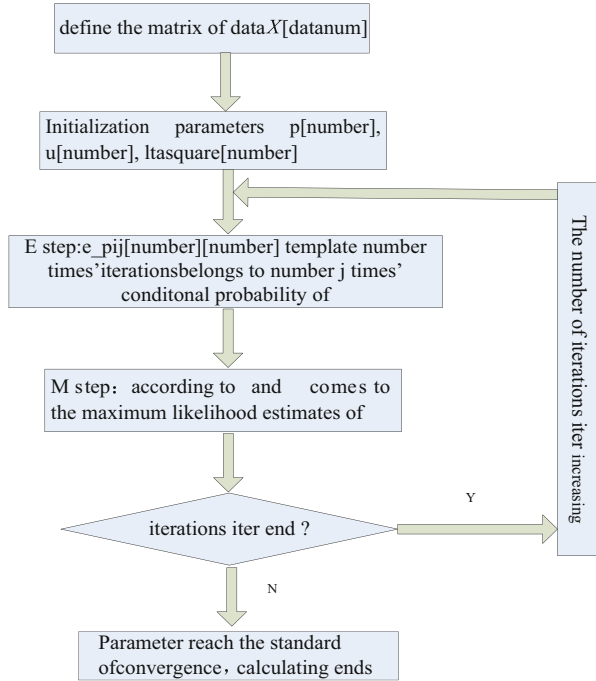


Fig. 83.2 The EM algorithm applied to image segmentation program flow chart

83.4 Experimental Results and Analysis of EM

Image segmentation is based on color difference signals. The program used to segment three colors was used to distinguish gray value 255,125, 0. This is better than simply using brightness value segmentation.

Although the skin color of different people might vary greatly, color differences are far less pronounced than differences in brightness, that is, people of different

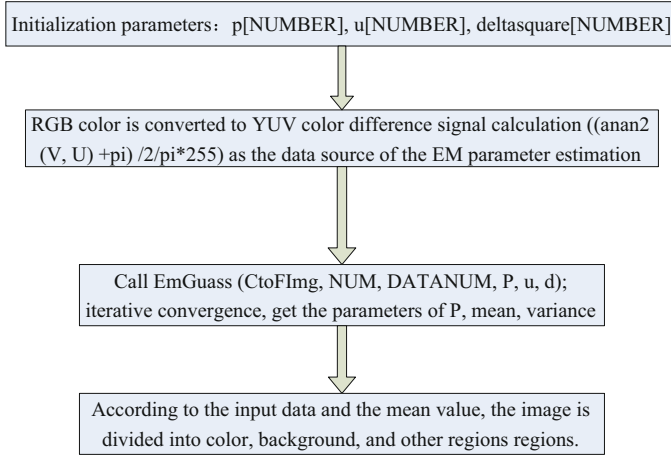


Fig. 83.3 Program flowchart of image segmentation using EM algorithm

colors tend to have very similar chroma and only differ in brightness because different skin colors have the same two-dimensional Gaussian model $G(m, V2)$.

With complicated backgrounds, especially ones that have similar skin colors, an obvious segmentation error, which is only useful in face recognition. The segmentation algorithm does not perform well enough to remove skin regions that are obviously not the face, a challenge that will have to be tackled in the future. The skin color region which obviously not face also has to be eliminated. After skin color segmentation to get connected regions $W1, W2, W3$ series . . . These regions include the region of skin, background region which similar to the skin color. In complex background, there may exist many non face region that similar to face color region, which is segmented out (such as hand and arm etc.). In a complex background, many facial skin colors similar to nonface regions are segmented (e.g., hands and arms).

First, the region where skin segmentation is to be performed has undergone erosion or dilation, remove the noise from the skin color segmentation. Then, based on statistical characteristics of facial skin color regional analysis, the following pretreatment of skin color segmentation can be carried out to obtain the greatest amount of facial region. Because of the input requirements of the EM algorithm (this paper considered that the same kind of data distribution should be more intensive near to mean value, different regions data should be spread out as much as possible) the convergence speed of the EM algorithm. So the EM algorithm's convergence speed and convergence result can be better guaranteed. Program flow chart of image segmentation using EM algorithm has been shown in Fig. 83.3.

83.5 EM Convergence of Algorithm Research

Necessary conditions for convergence: analysis of the M step in the EM algorithm, $Q(\theta^{(r+1)}|\theta^{(r)}) = \max Q(\theta|\theta^{(r)})$. If there is a K -dimensional continuous differentiable function $F(\bullet)$ that can be based on $\theta^{(r+1)} = F(\theta^{(r)})$, through to the $F(\bullet)$ constraint, thus the EM algorithm is convergent. As for the transformation of $F(\bullet)$, if it satisfies the following conditions: (1) $F(\bullet)$ is continuously differentiable in the θ domain; (2) the θ of its domain on the Jacobian matrix, that is $(J(\theta))^T, J(\theta)$, has a characteristic result of less than 1, thus the EM algorithm is convergent.

Conclusion

Theoretical analysis and numerical results show a high correlation between the correct convergence of the Gaussian mixture density of an EM algorithm and the overlap of the mixture density.

Acknowledgments This project is supported by the Research Development Fund of Xi'an University of Science and Technology (201333), the National Science Foundation of China under Grant 90607008, and the Education Department of the Shaanxi Provincial Government Research Project (09JK594).

References

1. Viola P, Jones MJ. Robust real-time face detection. *Int J Comput Vis.* 2004;57(2):137–54.
2. Shan S, Gao W, Cao B, et al. Illumination normalization for robust face recognition against varying lighting conditions. In: *Proceedings of the IEEE workshop on AMFG Signal Processing*, vol 140; 2003. p. 157–64
3. Park YK, Park SL, Kim JK. Retinex method based on adaptive smoothing for illumination invariant face recognition. *Signal Process.* 2008;34(88):1929–45.
4. Yang MH, Kriegman D, Ahuja N. Detecting faces in images: a survey. *IEEE Trans Pattern Anal Mach Intell.* 2002;24(1):34–58.
5. Georghiades A, Belhumeur P, Kriegman D. From few to many: illumination cone models for face recognition under variable lighting and pose. *IEEE Trans Pattern Anal Mach Intell.* 2001;23(6):643–60.
6. Dubuisson M-P, Jain AK. A modified Hausdorff distance for object matching. In: *Proceedings of the 12th International Conference on Pattern Recognition*, vol 50; Jerusalem, Israel. 2004. p. 566–8.
7. Huttenlocher DP, Klanderman GA, Ruchlidge WJ. Comparing images using the Hausdorff distance. *IEEE Trans Pattern Anal Mach Intell.* 2003;15(9):850–63.
8. Wang Y. Robust image matching Hausdorff. *Comput Aided Des Comput Graph.* 2002;14(3):238–41.
9. Zhijia Z, Shabai H, Zelin S. A fast strategy for image matching using Hausdorff distance. In: *Proceedings of the 2003 I.E. Conference on Robotics, Intelligent Systems and Signal Processing*, vol 90; 2003. p. 915–9.
10. Borgefors G. Distance transforms in digital images. *Comput Vis Graph Image Process.* 2006;34(3):344–71.

Chapter 84

A Social Network Service-Based Environment Monitoring System in Home

Jiajin Zhang, Lichang Chen, Quan Gao, Zhaobo Huang,
Lin Guo, and Yanxin Yang

Abstract This chapter proposes an alternative approach that utilizes the existing infrastructures of social network service (SNS) Sina Weibo in China and its open platform resource in order to integrate a wireless sensor network (WSN) into the web, offering social status in WSN. As a case study, a home environment monitoring system employing our proposal method has been developed. Experiment results show that this system can reduce the burden of the implementation and management of WSN and the proposed approach is feasible, cost-effective, and flexible for exploiting a SNS-based WSN quickly.

Keywords Social network service • Wireless sensor network • Sina Weibo • SDK

84.1 Introduction

SNS, such as Twitter, Facebook, MySpace, and LinkedIn, makes it possible for people to communicate and share information easily. And the SNS can be defined as web-based social spaces concentrating on facilitating communication, collaboration, and content sharing among people who would like to publish, share, and discuss short messages on the web [1]. With web-based WSN, the physical world can interact with the Internet more closely. And in general, system developers will do lots of work and it is hard for system administrators to manage WSN. For example, they have not only to master basic knowledge and web programming skills (e.g., HTML, JavaScript, and PHP) to create their web sites but also to build a web server. Furthermore, security and authorization may need to be considered in most cases. A database server also may be needed in order to save sensor data from

J. Zhang • Q. Gao
School of Science and Information Engineering, Yunnan Agricultural University,
Kunming 650201, China

L. Chen (✉) • Z. Huang • L. Guo • Y. Yang
School of Mechanic and Electronic Engineering, Yunnan Agricultural University,
Kunming 650201, China
e-mail: zjjc@163.com

WSNs. Consequently, the system design and network management of WSN have become a critical issue.

In China, Twitter and Facebook are unavailable. Sina Weibo is the most popular microblogging service in China and it has over 300 million users. Additionally, Sina Weibo has a stable open SDK that provides rich possibilities to application developers [2]. This chapter proposes an alternative approach that uses Sina Weibo as a platform for sensor network monitoring systems to solve the issues mentioned above. As a case study, a home environment monitoring system employing our proposal method has been developed.

84.2 Related Works

There are some studies that use SNS as a platform for sensor network systems. However, Twitter or Facebook is generally employed in these researches. Thereinto, a framework to globally share locally measured sensory readings based on Twitter is provided [3]. SoMoS proposed a platform-independent middleware to manage wireless sensor networks by integrating social network services like Twitter and Facebook [4]. Twitter can provide an “open” publish-subscribe infrastructure for sensors and smartphones and also pave the way for ubiquitous crowd-sourced sensing and collaboration applications [5]. The functionality and the Web 2.0 technologies provided by Facebook to transform the interaction with the Smart Home into a shared, social experience have been exploited [6].

Our approach with Sina Weibo is a better choice than the previous researches with Twitter or Facebook which is unavailable in China. This is why we selected Sina Weibo to take advantage of user-friendly functions.

84.3 The Description of a Typical Architecture of WSN Without SNS

A traditional and typical WSN system toward home environment monitoring through the web without SNS is introduced.

Without SNS's support, home environment monitoring system based on a typical and traditional architecture is as shown in Fig. 84.1 [7–9]. Obviously, in order to design and implement the above WSN-based system, we realize that many great efforts have been made by developers, including web programming, maintaining the web server and network security issues of WSN management.

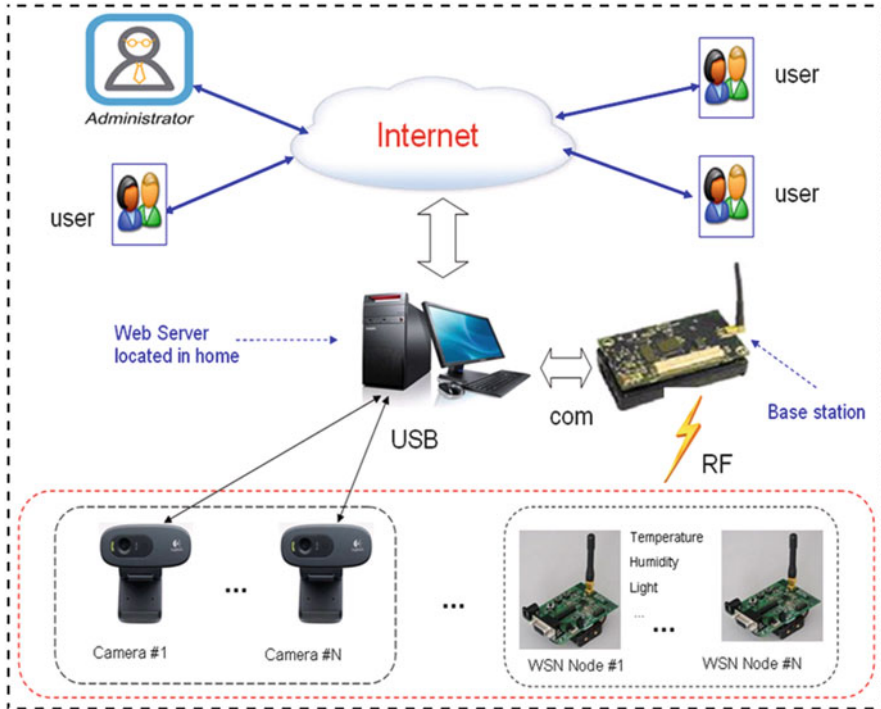


Fig. 84.1 Typical architecture of WSN in home environment monitoring system through web

84.4 The Description of Proposed System

84.4.1 Architecture of Proposed System with SNS

The structure of our proposed home environment monitoring system employing SNS Sina Weibo is viewed in Fig. 84.2. The data from wireless sensor nodes and USB cameras containing captured image, temperature, humidity, and light intensity in real home environment are transferred to a gateway Raspberry Pi, a low-cost and tiny single-board Linux computer which has recently become very popular, through ZigBee base station, respectively. Afterward, Raspberry Pi periodically posts the data on Sina Weibo. Authorized users on Sina Weibo can remotely have access to the sensor data from home-in environment by laptop computer and other mobile devices such as smartphone and tablet PC.

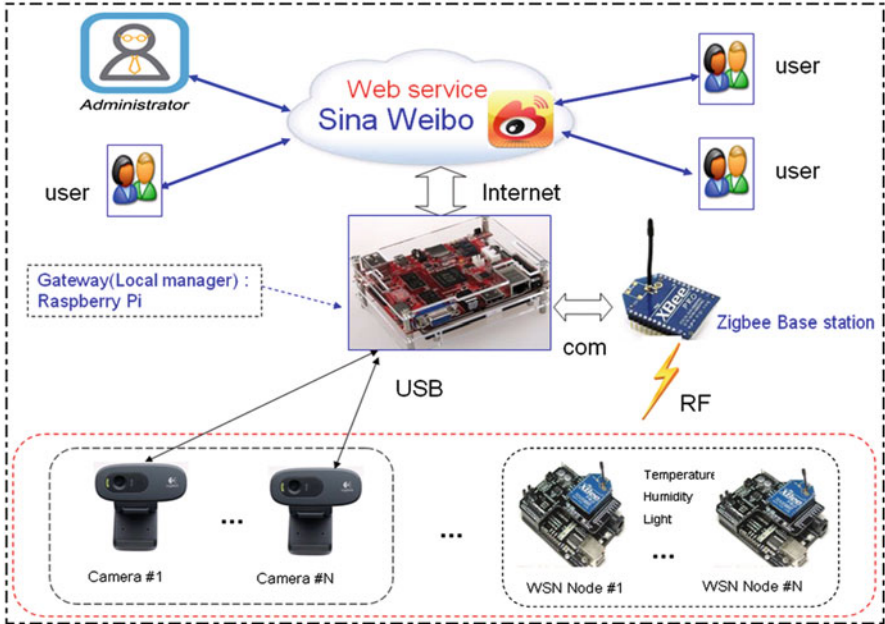


Fig. 84.2 Architecture of our approach

84.4.2 Hardware Specification

In our proposed system, with ease of use, low-cost, rich libraries and standardized components and programming language are cited as reasons for choosing Arduino [10] and Raspberry Pi [11] platforms. In our work, a Raspberry Pi, with an ARM1176JZF-S core CPU at 700 MHz, 256 MB RAM and Debian Wheezy7.5 Linux operating system, is deployed as a gateway or local manager, not only for hosting the Internet proxy but also for the bridging the gap between SNS Sina Weibo and physical devices.

Meanwhile, in our experiment system, USB cameras and wireless sensor nodes equipped with temperature, humidity, and light sensors are used. Also, the wireless sensor node (Fig. 84.3) is mainly composed of an Arduino microcontroller, a DHT11 which is a low-cost digital temperature-humidity sensor, a DFRobot BH1750 light sensor, and an XBee PRO communication module based on the IEEE ZigBee/IEEE 802.15.4 standards [12]. For easy interfacing with DHT11 sensor, light sensor, and XBee PRO module, Arduino Nano board was used.

In addition, our system requires a ZigBee base station to be connected to a gateway, namely, Raspberry Pi, via RS-232 serial port. And for capturing images in a house, a plug-and-play camera module from a Logitech C270 webcam which offer a relatively good flexibility and quality, connecting a Raspberry Pi with USB port, is adopted.

Fig. 84.3 Wireless sensor networks node



84.4.3 ZigBee Wireless Sensor Network

ZigBee is an open specification that enables low power consumption, low cost, and low data rate for short-range wireless connections between various electronic devices. The XBee PRO module is a ZigBee/IEEE 802.15.4 compliant solution for WSNs.

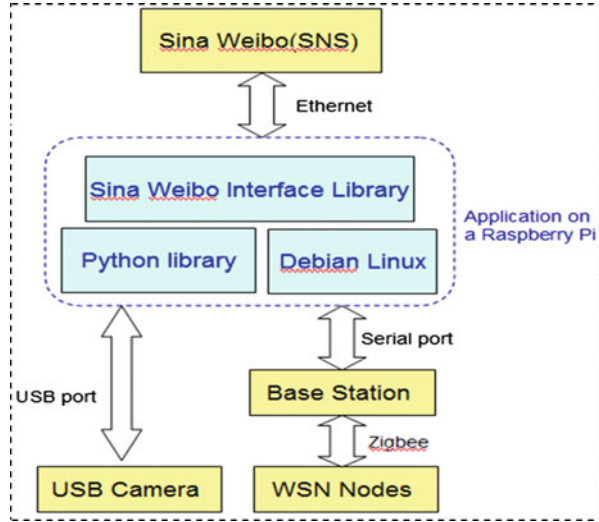
The base station is connected to a gateway Raspberry Pi with a wired serial connection. The gateway runs an application software in Debian Linux, providing web access functionality. This essentially provides Internet access to wireless sensor reading collected via XBee PRO base station. The gateway serves as an application gateway and interconnects the SNS and ZigBee network. The sensor reading periodically sent by wireless sensor nodes to a gateway through a base station is composed of a header, ID of wireless sensor node, values measured, and checksum.

84.4.4 Gateway Side Application

The wireless sensor nodes send their measurements periodically to a gateway Raspberry Pi located at the home. Then the information is transmitted to the Sina Weibo via Raspberry Pi. As a result, a gateway side application is necessary. Figure 84.4 shows the relationship among components in our solution.

As described above, the data from wireless sensor nodes and cameras is transferred to the Raspberry Pi side gateway application. And the data is saved and processed in order to make text and graph images in this application blending with Sina Weibo Python SDK. After that, the application periodically uploads the processed text and graph images to Sina Weibo. Sina Weibo Python SDK is a

Fig. 84.4 Block diagram of our proposed system



key prerequisite for the realization of gateway side application consists of four core features including (1) log in/out, (2) take and renew an access token, (3) post and delete text, and (4) upload images. To use the Python Weibo SDK of Sina Weibo to assist the development, developers have to register as a “developer” in Sina Weibo developer platform and obtain the corresponding app key and app secret to complete the guided registration [3]. Authentication is needed before Sina Weibo SDK works. SDK provides a Weibo class to achieve a new Weibo object and set app key, app secret, and URL. At the same time, web user login and authorization are processed by calling the pages provided by SNS Sina Weibo, but our system doesn’t involve it. We assume that workflow is as illustrated in Fig. 84.5.

84.4.5 Results of the Case Study

To validate the concept of the proposed system, the developed system is tested by installing the environment condition sensing units and setting up ZigBee networks in a house. The wireless sensor nodes are located in the bedroom, living room, kitchen, and toilet respectively in the house. And several cameras are located close to the veranda, gate, and living room. Figures 84.6, 84.7, 84.8, and 84.9 illustrate the graphical representation of type “#1” wireless sensor node information in gateway side application, and this node is deployed in a living room. Measurements related to temperature, humidity, and light intensity are shown in Figs. 84.6, 84.7, and 84.8, respectively. Moreover, Fig. 84.9 displays a captured image from the camera labeled “#1” in living room.

Figure 84.10 depicts periodically posted pictures and texts including sensor readings of temperature, humidity, and light intensity from a remote home which are revealed on Sina Weibo.

Fig. 84.5 Flowchart of the gateway side application

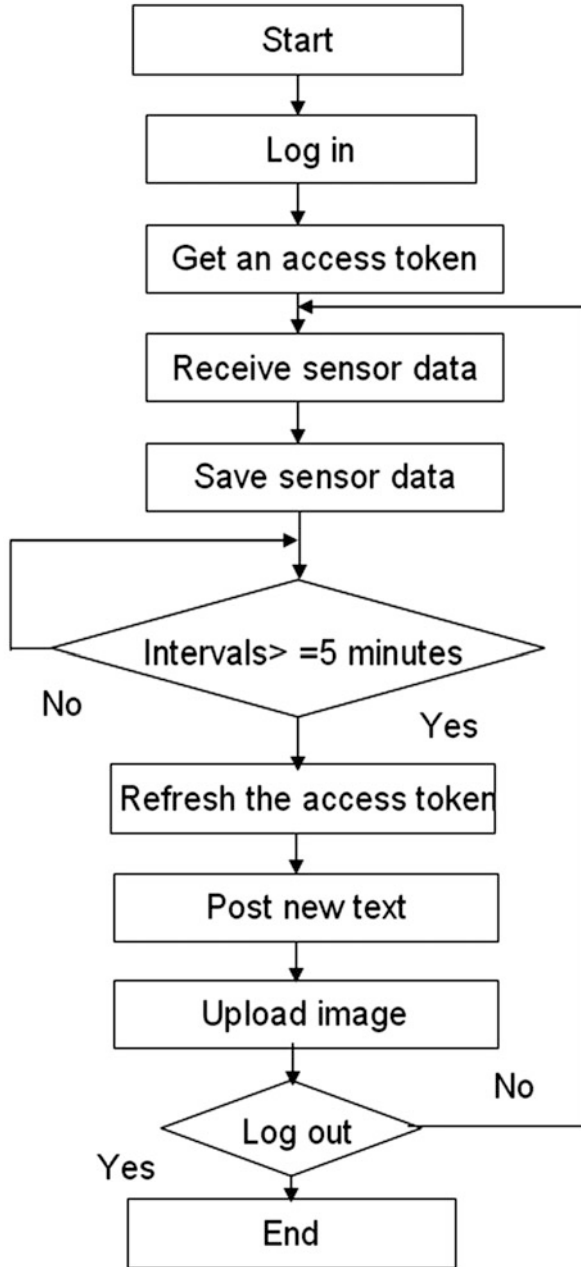


Fig. 84.6 Temperature in a living room

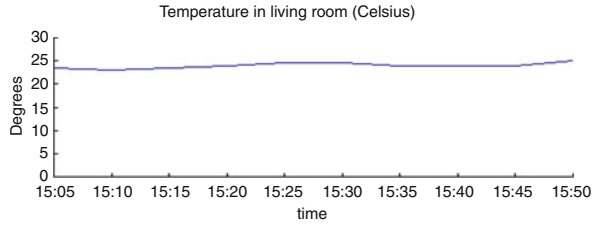


Fig. 84.7 Humidity in a living room

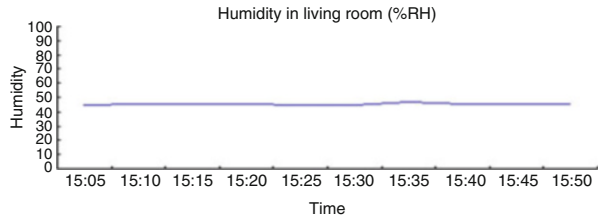


Fig. 84.8 Light intensity in a living room

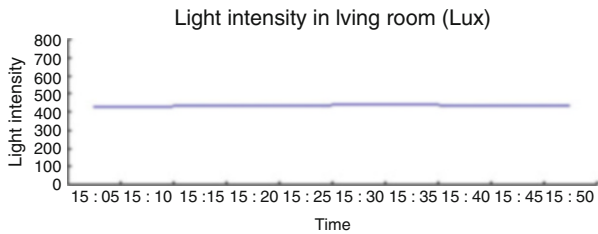
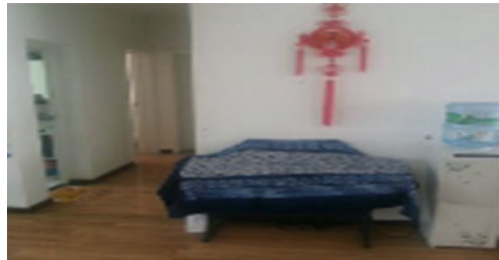


Fig. 84.9 A captured image in a living room



84.4.6 Comparison Between the Traditional and Typical WSN Solution and Our Proposed Approach Based on SNS

As we mentioned earlier, in the traditional and typical WSN solution without SNS, for developers, there are lots of efforts to do in order to build up WSN through the web. Compared with our proposed approach based on SNS, the comparison of two different systems is described as shown in Table 84.1.

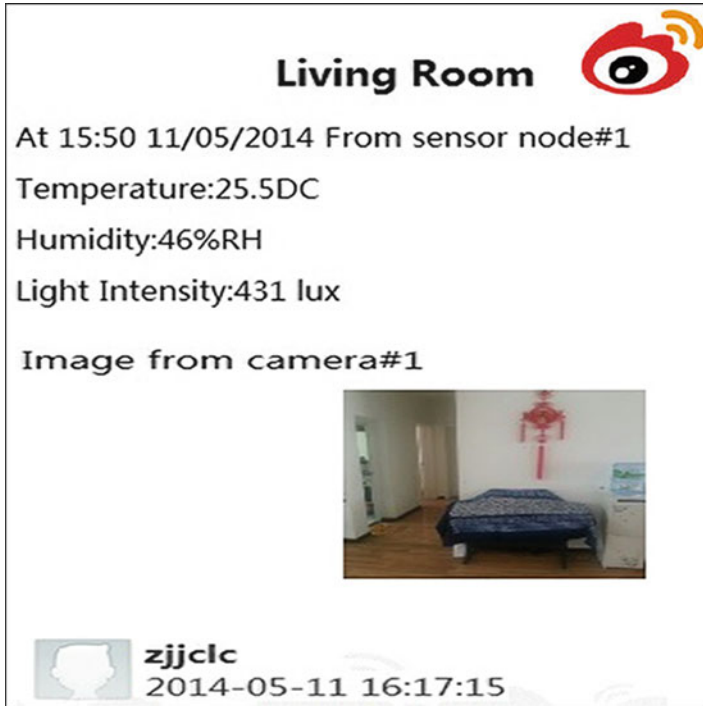


Fig. 84.10 Posted text and image on Sina Weibo

Table 84.1 Comparison of two different systems

Solution	Web server	Database server	Implementation of security and authorization
A traditional and typical solution	Requirement	Requirement	Requirement
Our work	No requirement	No requirement	No requirement Sina Weibo has completed it

From the Table 84.1, apparently our proposed approach can reduce the overall system design complexity.

Conclusion

In this chapter, by utilizing Sina Weibo open platform, we proposed an efficient method to monitor the sensor data and manage a WSN. In our study, a gateway application running in Raspberry Pi for integrating WSN to SNS was developed. In addition, we implemented home environment monitoring system as a case study.

In our proposed system, on the one hand, our method can help us save money and time. On the other hand, our proposed solution can provide an alternative common environment for the interaction between SNS and physical world. Our experimental result indicates the feasibility of integrating a WSN monitoring the house into the existing infrastructures of the SNS Sina Weibo by presuming upon its open, web-based SDKs.

As future work, on the basis of the present study, we will intend to incorporate more advanced technology and develop actuator networks aimed at residential smart meters, information household appliance control, etc., which can strengthen the interactive capability between people and connected devices.

References

1. Boyd DM, Ellison NB. Social network sites: definition, history, and scholarship. *J Comput-Mediat Comm.* 2007;13(1):210–30.
2. Sina. Sina Weibo open platform. [Online]. <http://open.weibo.com/>
3. Baqer M, Kamal A. S-sensors: integrating physical world inputs with social networks using wireless sensor networks. In: Proceedings of the 5th international conference on intelligent sensors, sensor networks and information processing (ISSNIP). Los Alamitos: IEEE; 2009. p. 213–8.
4. He B, Iwai M, Chen J, Chen H, Sezaki K. An interactive social network service-enabled middleware for wireless sensor networks. In: Proceeding of the eighth international conference on networked sensing system (INSS2011), Penghu, Taiwan, June 12–15; 2011. p. 108–23.
5. Demirbas M, Bayir MA, Akcora CG, Yilmaz YS, Ferhatosmanoglu H. Crowd-sourced sensing and collaboration using twitter. In: Proceedings of the IEEE international symposium on “a world of wireless, mobile and multimedia networks” (WoWMoM), Montreal, Canada; 2010. p. 1–9.
6. Kamilaris A, Pitsillides A. Social networking of the smart home. In: Proceedings of the IEEE 21st international symposium on personal indoor and mobile radio communications (PIMRC'10); September, 2010. p. 2632–7.
7. Kansal A, Nath S, Liu J, Zhao F. Senseweb: an infrastructure for shared sensing. *IEEE Multimedia.* 2007;14(4):8–13.
8. Prehofer C, van Gurp J, di Flora C. Towards the web as a platform for ubiquitous applications in smart spaces. In: Second workshop on requirements and solutions for pervasive software infrastructures (RSPSI), at Ubicomp, Innsbruck, Austria; 2007. p. 16–9.
9. Guinard D, Trifa V. Towards the web of things: web mashups for embedded devices. In: WWW'09: Proceedings of the 18th international conference on World Wide Web, Madrid, Spain; 2009. p. 678–83.
10. Arduino. Arduino homepage. [Online]. <http://arduino.cc/>
11. Raspberry Pi. Raspberry Pi homepage. [Online]. www.raspberrypi.org
12. Digi Inc. XBEE:Connect devices to the cloud. [Online]. <http://www.digi.com/xbec>

Part IV
Cloud Computing

Chapter 85

Cloud Computing Security Issues and Countermeasures

Ziqian Xiao and Jingyou Chen

Abstract As a new kind of distributed computing model, cloud computing develops rapidly and becomes the focus of academia and industry. With the growing popularity of cloud computing, the importance of its security issues shows a gradual upward trend and becomes an important factor in its progress. This chapter introduces the importance, advantages, and current development of cloud computing, points out that security risk is a major obstacle to the development of cloud computing, analyzes cloud computing security framework and its research status, emphasizes on the various security threats which the cloud computing is facing, and gives the methods and countermeasures of reducing the risk of cloud computing security.

Keywords Cloud computing • Cloud technology framework • Security policy

85.1 Introduction

Cloud computing is a mode of information processing, which makes use of the network to organize and invoke various ICT information resources flexibly and realize large-scale computing. Cloud computing uses the techniques of distributed computing and virtual resource management, centralizes all the distributed ICT resources through the network to form a shared resource pool, and offers services to users in dynamic on-demand and measurable way. But at present, cloud computing services are facing many security issues. With the growing popularity of cloud computing, the importance of its security issues shows a gradual upward trend and becomes an important factor in its progress. This chapter describes the importance, advantages, and prospects of cloud computing, notes that security risks are a major obstacle to the development of cloud computing, focuses on the analysis of research status of cloud computing security theory, points out that security risk is an important new research direction of cloud computing, and gives a strategy for reducing security risks of cloud computing.

Z. Xiao • J. Chen (✉)

Hainan College of Software Technology, Qinghai 571400, Hainan, China
e-mail: xiaoziqian1234@163.com; jingyou513@163.com

85.2 Cloud Computing Development and Security Status

85.2.1 Cloud Computing Development Status

Although the global cloud computing industry is still in its infancy and its market is small, it will transform the traditional ICT industry to the social services and its future development space will be very broad. In 2011, the global-scale services of cloud computing were approximately \$90 billion. The aggregate size of the cloud computing services market currently accounts for only 1/40 of the world's total ICT market, but with the rapid growth its average annual growth rate will be expected to exceed 20 % in the coming years [1].

85.2.2 Development of Security Technology of Cloud Computing

In the IT industry, various types of cloud computing security products and solutions are emerging. For example, Sun has released open-source cloud security tools which can ensure the safety and security of Amazon's EC2, S3, and virtual private cloud platform [2]. Microsoft's Azure cloud computing platform code-named Sydney's preparations for the security plan to help business users exchange data between servers and Azure cloud to solve virtualization and multi-tenant environment security. EMC, Intel, VMware, and Hadoop have made greater contributions in the field of security of cloud computing security [3].

85.3 Cloud Computing Security Challenges

85.3.1 New Risks Brought by Virtual Technologies

Virtualization brings new risks mainly in the virtual machine being abused, the virtual machine escape, and multi-tenant isolation between the failures of security policy migration of virtual machines [4].

85.3.2 Shared Data Security Environment

Under the cloud service model, users are very worried about whether the data stored in the service provider will be compromised, tampered, or lost. Man-made threats facing the user data mainly come from service providers, hackers, malicious neighboring tenants, and subsequent tenants.

85.3.3 Cloud Platform Application Security

There are some application security problems existing in Cloud Computing Services, no matter Saas, Paas or Iaas, mainly including three categories. The first one is the malicious program review. The second one is the application interface security. The third one is code and test safety.

85.3.4 Authentication and Access Control in the Cloud Service Model

Under the cloud service model, user authentication and access control face new challenges, for example, the authentication and authorization of massive users, the rational division of access rights, and the management of accounts, passwords, and keys. In dealing with massive users' changeable business and their identification, the cloud service providers need to fully automate users' authentication and access management [5].

85.3.5 The Backward Measures of Operation, Maintenance, and Management of Cloud Services

Currently, the operation and maintenance of cloud service security has inefficiencies. Firstly, some negligence made by privileged users like administrators can cause service disruptions and other serious consequences. Secondly, the operation and maintenance level of cloud services has changed. The original physical host-based monitoring is no longer valid, which is unable to effectively monitor if the virtual host has a problem or not.

85.3.6 Compliance Reviews Becomes More Difficult

In the cloud services, it's extremely difficult to position and block the harmful content because of the dynamical binding between the information and its publishing carrier. Meanwhile, the overseas cloud computing services usually provide encrypted channel for shared access node SSL. It cannot detect any other content except the certificate issuer name, IP, and port, which makes traditional content filtering unable to start.

Table 85.1 Definition of actors

Actor	Definition
Cloud consumer	A person or organization that maintains a business relationship with the cloud providers and uses their services
Cloud provider	A person or organization that is responsible for making a service available to interested parties
Cloud auditor	A party that can conduct independent assessment of cloud services, information system operations, performance, and security of the cloud implementation
Cloud broker	An entity that manages the use, performance, and delivery of cloud services and negotiates relationships between cloud providers and cloud consumers
Cloud carrier	An intermediary that provides connectivity and transport of cloud services from cloud providers to cloud consumers

85.4 Cloud Computing Security Technology Framework

85.4.1 *Cloud Computing Framework*

The US National Institute of Standards and Technology (NIST) in the September 2011 release of “NIST Cloud Computing Reference Architecture” [6] proposed Cloud Computing Reference Architecture. The NIST Cloud Computing Reference Architecture defines five major actors: cloud consumer, cloud provider, cloud carrier, cloud auditor, and cloud broker. Table 85.1 briefly lists the definition of each actor in the NIST Cloud Computing Reference Architecture.

85.4.2 *Cloud Computing Security Framework*

NIST in May 2013 released “NIST Cloud Computing Security Reference Architecture,” [7] the proposed cloud security reference architecture shown in Fig. 85.1.

85.5 Methods and Measures to Deal with Cloud Computing Security Threats

85.5.1 *Infrastructure Security*

Cloud computing infrastructure includes some IT-based resources such as the storage, computing, and networking of cloud computing and so on. The main role of infrastructure security is to provide security for cloud computing upper services, including three aspects:

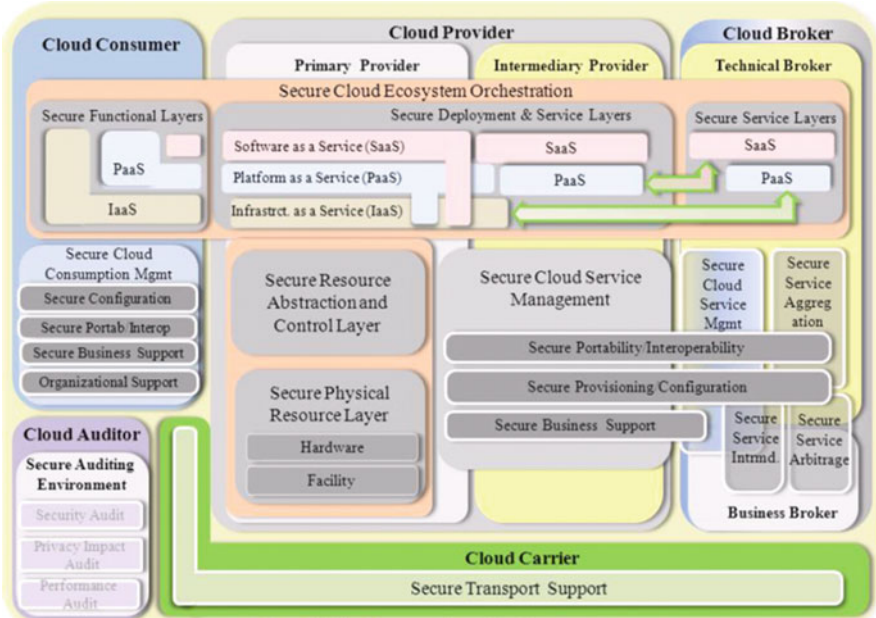


Fig. 85.1 NIST cloud computing security reference architecture

First, the safety of the equipment: the main methods include intrusion tolerance, disaster recovery, backup redundancy, and isolation [8], the isolation of the user’s access as shown in Fig. 85.2.

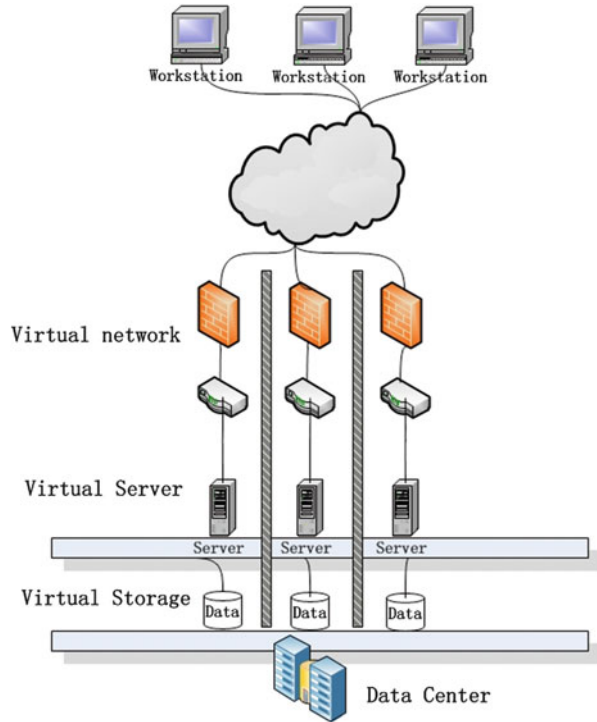
Second, system security: the main security methods include authentication, authorization, and trusted computing. These methods can be carried out by identity management to ensure the safety and reliability of the user’s identity.

Third, network security: the main protection methods include DOS prevention and intrusion detection. DOS defenses are taken in network security, which can effectively filter too many requests and analyze the invasion to prevent malicious attacks.

85.5.2 Virtualization Security

The security measures of virtualization are as follows: virtual firewall, virtual machine security management, virtual machine isolation, virtual machine vulnerabilities, and virtual machine monitor. Through these measures, we can monitor the information between applications to achieve security and control access. And we also prevent information leakage between the virtual machines [9].

Fig. 85.2 Isolation user access



85.5.3 Data Security

Data security mainly provides security guarantee for the data stored in the cloud computing. Because the IaaS platform provides services in the form of infrastructure, data is mainly managed by the user and the public storage data is less. The data security is mainly concentrated in a PaaS and SaaS platform, which mainly involves several aspects: encryption, decryption, key management, transport security, and access control. These mature measures can ensure the security of data.

85.5.4 Service Security

Cloud computing provides resources to users in the form of services. Service security has become the major security issue. As well as data security, service security on the PaaS platform and SaaS platform is more obvious. The main security defense methods are to use a digital signature to ensure the integrity of the service message, set up a trust model for the service to interoperate safely, and use some identity authentication technology to identify the users of cloud computing such as static password, dynamic password, and certificate [10].

Conclusion

As a new kind of distributed computing mode, cloud computing has a broad prospect for development, while the security challenges it's facing are also unprecedented. Based on the existing model of cloud computing security, this chapter analyzes the existing safety problems and provides supports for solving the security of cloud computing from the perspective of management and technology.

References

1. Ministry of Industry and Information Technology of the People's Republic of China. Cloud Computing White Paper. <http://www.miit.gov.cn>
2. Sun Cloud Architecture Introduction White Paper (in Chinese). http://developers.sun.com.cn/blog/functionalca/resource/sun_353cloudcomputing_chinese.pdf
3. Feng G, Zhang M. Cloud computing security research. *J Softw.* 2011;22(1):71–83.
4. Chen Q. China cloud services and supervision of road safety issues. <http://www.catr.cn>
5. Lin Z, Fu X, Wang R, Han Z. Research on the key issues of cloud computing security. *Inf Res.* 2011;37(2):1–4.
6. U.S. National Institute of Standards and Technology. NIST Cloud Computing Reference Architecture. <http://www.nist.gov/>
7. U.S. National Institute of Standards and Technology. NIST Cloud Computing Security Reference Architecture. <http://www.nist.gov/>
8. Okuhara M, Shiozaki T, Suzuki T. Security architectures for cloud computing. *Fujitsu Sci Tech J.* 2010;46(4):397–402.
9. Cloud Security Alliance Security Guidance for Critical Areas of Focus in Cloud Computing. <http://www.cloudsecurityalliance.org/>
10. Raj H, Nathuji R, Singh A, England P. Resource management for isolation enhanced cloud services. In: Sion R, editor. Proceedings of the 2009 ACM workshop on cloud computing security, CCSW 2009, co-located with the 16th ACM computer and communications security conference, CCS 2009. New York: Association for Computing Machinery; 2009. pp. 77–84.

Chapter 86

A Time-Aware QoS Prediction Approach to Web Service Recommendation

Xuejie Zhang, Zhijian Wang, Weijian Zhang, and Fang Yang

Abstract With the increasing number of Web services, recommending and selecting the optimal Web services for consumers has become one of the most important challenges in the field of service computing. The goal of consumers is to discover and use services that lead to their experiencing the highest quality. The quality of service (QoS) performance of Web services is highly related to invocation time since the service status and the network environment change over time. Invoking a huge number of Web services for consumers to predict the quality is time-consuming, resource-consuming, and sometimes even impractical. To address the challenge, this paper proposes a time-aware QoS prediction approach for Web services and designs a prediction framework. In our experiment, we collect QoS information with timestamps from geographically distributed service consumers through the framework. Based on the information, we predict the quality of services; in addition, the relationship between their expectations and the level of the services is considered. As a result, we can obtain a list of recommended services for selection. Finally, the experiment shows that the approach achieves better prediction.

Keywords Web service • QoS prediction • Time-aware

86.1 Introduction

With the increasing number of Web services, recommendation and selection of the optimal Web services has become one of the most important challenges in the service computing field [1]. Quality of service (QoS) is usually employed to

X. Zhang (✉)
Huaian Research Institute of Hohai University, 223001 Huaian, China
e-mail: xuejie_zh@hhu.edu.cn

Z. Wang • F. Yang
College of Computer and Information, Hohai University, 210098 Nanjing, China

W. Zhang
College of Distance Learning and Continuing Education, Hohai University, 210098 Nanjing, China

describe the nonfunctional properties of services in service computing. It is important to evaluate the QoS performance of services to differentiate the qualities of service candidates. Web services are usually deployed in remote servers and accessed by consumers through Internet connections. The QoS performance of Web services is highly related to invocation time since the service status and the network environment change over time. Time-aware QoS prediction approaches provide useful information to assist service consumers in improving the performance of applications [2].

Existing approaches to quality evaluation mostly assume that consumers' primary goal is the optimization of performance, so that consumers are unable to effectively identify services that will best meet their needs. However, this approach is impossible in practice. In addition, it consumes time and resources to invoke all Web services each time a service is requested because there may be a large number of function-equivalent candidate Web services [3, 4].

In addressing the aforementioned challenge, we propose a time-aware QoS prediction framework for Web services. In our framework, we collect QoS information with timestamps from geographically distributed service consumers. Based on this information, we evaluate the QoSs and the relationship between the expectations of the consumers and the level of the services is considered. As a result, we can obtain a list of recommended services for selection.

The remainder of this paper is organized as follows. Section 86.2 presents our Web service prediction framework, quality space description, and quality data collection. Section 86.3 describes the time-aware QoS prediction approaches in detail. Section 86.4 discusses the experiments and results. Finally, the section "Conclusion" concludes the paper.

86.2 Quality Prediction for Web Services

86.2.1 Web Service Prediction Framework

Since most service consumers are not experts in service testing, to reduce the efforts service consumers spend on testing QoS performance, we design a QoS prediction framework for service consumers (Fig. 86.1). The framework mainly contains four entities: *Web service monitor*, *QoS predictor*, *recommender*, and *Quality Database*. In this paper, we will not discuss the monitoring issue.

A Web service monitor is responsible for monitoring the QoS performance of Web services when consumers send invocations. The QoS information is stored in a quality database (QDB) and will be used for prediction. The collected data format will be presented in detail in Sect. 86.2.2. The QoS predictor is responsible for providing time-aware QoS value prediction based on the QoS information collected by the Web service monitor. The recommender is responsible for recommending several services to consumers based on the predicted results and consumer expectation. The detailed prediction process and approach are presented in Sect. 86.3.

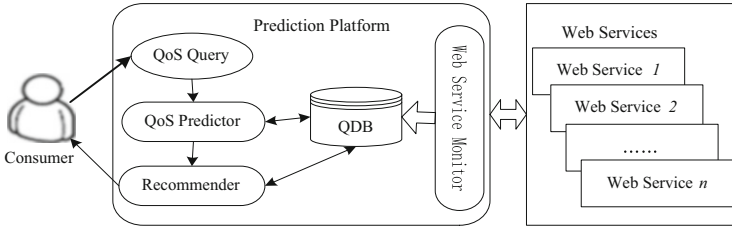


Fig. 86.1 Time-aware QoS prediction framework

86.2.2 Quality Space Description

Consumer use a set of quality data to determine the suitability of a service. To make predictions about the future performance of the service, the decision-making process is concerned with the analysis and aggregation of the quality data [5]. Here we refer to a quality data description notation developed by Gareth Shercliff [6]. In this approach, data are distributed across multiple linked *quality spaces* $[Q = (e, d, r)]$ representing consumer expectations (e), delivered values (d), and ratings (r). All data are recorded in the QDB. A single instance of provision is represented by three points in each of the spaces (86.1). The location of a point within each space is defined by its value, and the lines between points indicate that they refer to the same record. Figure 86.2 illustrates the description approach.

86.2.3 Quality Data Collection

Monitoring information can be used by both the predictor and the recommender. During monitoring, performance information is stored in a QDB. Each time a monitoring result is received by the QDB, a new quality tuple, q_t , is added to the database, $q_t = \{t, s_i, c_m, e_c, d, r_c\}$, where t is a timestamp stating when the recording was made, $s_i \in S$ is the service, $c_m \in C$ is the consumer consuming the service, $e_c \in [0, 1]$ is c_m 's expectation in terms of the QoS attribute, $d \in [0, 1]$ is the level of service delivered in terms of the QoS attribute, and $r_c \in [0, 1]$ is the rating of the service provided by consumers.

For example, given a service (S_3), the information represented by using “Q-spaces” notation is as illustrated in Fig. 86.2. The information is stored in the QDB, whose contents are described in Table 86.1. Here, there are three records of provision indicated by the three points in each of the spaces. The location of a point in each space is defined by its value, and the lines between points indicate that they refer to the same record.

Fig. 86.2 Quality space description S_3

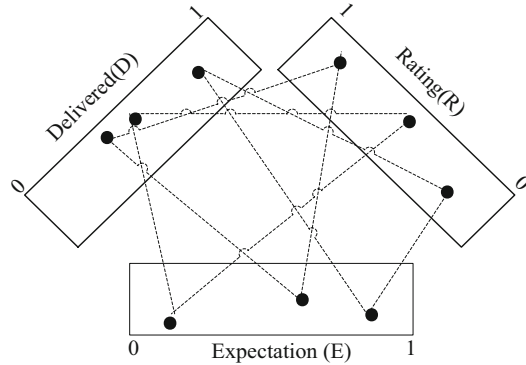


Table 86.1 Service quality information in QDB

ID	T	S	C	E	D	R
1	1	S_1	C_1			
2^a	3	S_3	C_2	0.15	0.5	0.5
...
28	60	S_2	C_3			
29	61	S_3	C_3	0.6	0.4	0.85
30	64	S_3	C_1	0.85	0.8	0.15
...

^aAll records about S_3

86.3 Time-Aware QoS Prediction

86.3.1 Process of QoS Prediction

In this paper, the research is focused on predicting the level of a service based on past-performance information. In terms of the level of services and the consumer’s expectation, a series of satisfied services is recommended. It is a D–E-space pattern that can be described by the quality space notation in Sect. 86.2.2. The overall process is as follows (Fig. 86.3):

- (i) Identify point clusters in D space: D-space points are classified using cluster analysis techniques that are described in detail in the literature [7]. We will not discuss them in this paper.
- (ii) D–E-space mapping: the E-space points for each of the D-space points are identified. We will describe the stage in detail in Sect. 86.3.1.1.
- (iii) Identify service class boundaries in E space: using the clusters identified in the D space, the boundaries of the potential service classes are identified in the E space.
- (iv) All points in the E-space within the same potential service class with E_c are selected. E_c is the expectation of the current consumer.

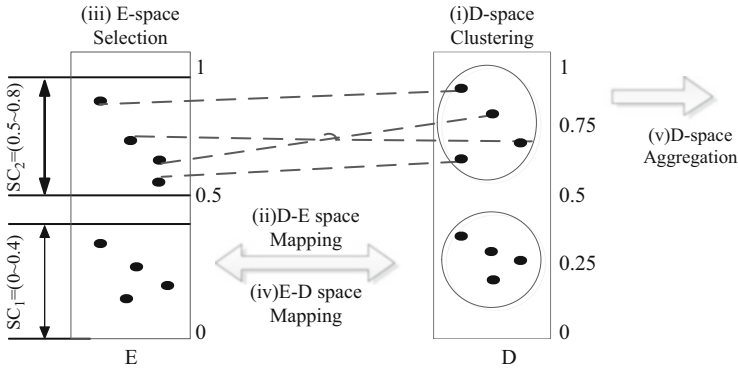


Fig. 86.3 QoS prediction process

- (v) E–D-space mapping: the identified E-space points are mapped to the D space to determine the level of service delivered by the service in each of these cases. This step can be regarded as selecting all D-space points that are paired with the E-space points selected in the previous stage. These points will correspond to one of the clusters identified in Step 1 (Sect. 86.3.1.2).
- (vi) D-space aggregation: the identified D-space points are aggregated using techniques described in Sect. 86.3.2 to predict the likely future behavior of the service for consumers with expectations within this service class.

86.3.1.1 D–E Space Mapping

With the clusters in the D space having been identified, the corresponding points of each cluster are identified in the E space. The purpose of this mapping is to identify the upper and lower expectation limits for each of the service classes. We do this by determining the lowest and highest expectations in each point set. The result of such identification is a set of service class ranges $SC = \{SC_1, \dots, SC_n\}$, where each range $SC_i = (E_{i(low)} \sim E_{i(high)})$. $E_{i(low)}$ and $E_{i(high)}$ are delimited by an upper and lower expectation value. Here, we consider that the ranges identified in E-space should be nonoverlapping.

86.3.1.2 E–D-Space Mapping

The purpose of the stage of prediction in this approach is to determine the level of a service that consumers with an expectation Ec would receive if they were to use the service. As in the D–E-space prediction method, Ec is used to determine the likely service class into which the consumer falls, and all E-space points within the class are identified, mapped to the D space, and finally aggregated. The mapping process is not trivial according to the data in the QDB. We focus on the method of D-space aggregation.

86.3.2 D-Space Aggregation

The set of D-space points were selected. In this section, the goal is to aggregate D-space points to produce a prediction of the likely current behavior of a service. Fundamental to the time-aware method of prediction is the correlation between time (t) and delivered level of service (d). The level of a service may change over time. Therefore, at a particular point in time the relationship between d and t may be in one of three possible states: d is constant, d is increasing, and d is decreasing. The first case can be considered as a special case. In the latter two cases, d is changing. To predict the likely current behavior of the service, it is necessary to determine the ratio of proportionality between d and t . The problem of prediction may be regarded as one of determining the degree of slope of the line through the collected d -space data and then extrapolating the line to the current point in time.

The prediction can be broken down into four stages. First, linear regression is used to determine a line of best fit through the set of D-space points. Second, the equation of the line may be used to extrapolate the current delivered value of the service (d_c) at the current time (t_c). Third, a level of uncertainty in the data is determined to generate the line of best fit. Finally, based on a consideration of the three stages, a projection algorithm may be specified.

86.3.2.1 Linear Regression

Linear regression is used to establish the correlation between a set of variables [8]. In this paper, we focus on predicting the level of service at a certain time based on past information. Given the set of observed data points $P = \{(t_1, d_1), \dots, (t_n, d_n)\}$, we commit to finding the correlation between time (t) and delivered level of service (d). Thus, the goal is to establish a straight line of best fit through data points P . In doing so, the two line parameters a and b must be determined. , in the equation

$$d = at + b, \quad (86.1)$$

where a is the regression coefficient and b is a constant term. We calculate a and b by the least-squares method. When applied to the set of D-space points $D = \{d_1, d_2, \dots, d_n\}$, the parameters of the line will minimize the sum of the squared errors such that $\min \sum_{i=1}^n (d - d_i)^2$. Therefore, a and b should be determined to satisfy

Eq. (86.2) as

$$a = \frac{\sum_{i=1}^n (t_i - \bar{t})(d_i - \bar{d})}{\sum_{i=1}^n (t_i - \bar{t})^2}, \quad b = \bar{d} - at. \quad (86.2)$$

With the line parameters having been identified, the delivered value (d_c) at the time of prediction (t_c) may be extrapolated by substitution of the values into Eq. (86.1). d_c is a prediction of the most likely level of service that consumers would receive if they were to use the service immediately following the prediction.

86.3.2.2 Correlation Coefficient

A correlation coefficient is usually employed to measure the strength and direction of a linear relationship between two variables. The result indicates the quality of the line of best fit. A standard correlation coefficient is provided by Eq. (86.3):

$$r = \frac{\sum (t - \bar{t})(d - \bar{d})}{\sqrt{\sum (t - \bar{t})^2} \sqrt{\sum (d - \bar{d})^2}}. \quad (86.3)$$

The value of r falls into the range (0, 1), where 1 indicates a perfectly positive correlation. A value of 0 indicates that there is no correlation between the variables. The coefficient of determination (r) is also a measure of the proportion of variability in the data that may be explained by the relationship between the two variables. As such, r may be considered a direct indicator of the uncertainty in the line of best fit

Algorithm 1: Projection Algorithm

Input: $D = \{(t_1, d_1), \dots, (t_n, d_n)\}$, the set of D-Space points and associated timestamps relevant to the current service and service class; t_c , the time of prediction.

Output: $0 \leq d_r \leq 1$, a prediction of the likely current level of service provided by the service level; $0 \leq r \leq 1$, the quality of the prediction.

// Calculate sum and sum of squares for d and t

1 **foreach** $(t_i, d_i) \in D$ **do**

2 $sumD = sumD + d_i$;

3 $sumD2 = sumD2 + d_i * d_i$;

4 $sumT = sumT + t_i$;

5 $sumT2 = sumT2 + t_i * t_i$;

6 $sumDT = sumDT + d_i * t_i$;

7 **end**

// Calculate average d and t

8 $avgD = sumD / n$;

9 $avgT = sumT / n$;

// Calculate sum of squared error

10 **foreach** $(t_i, d_i) \in D$ **do**

11 $sumNum = sumNum + (t_i - avgT) * (d_i - avgD)$;

12 $sumTen = sumTen + (t_i - avgT) * (t_i - avgT)$;

13 $sumDen = sumDen + (d_i - avgD) * (d_i - avgD)$;

14 **end**

15 $a = sumNum / sumTen$; // Calculate the parameters of the line

16 $b = avgD - (a * avgT)$;

17 $d_r = a * t_c + b$; // make prediction for time t

18 $r = sumNum / \sqrt{sumTen} * \sqrt{sumDen}$ // Calculate correlation coefficient

86.3.2.3 Projection Algorithm for Prediction

Based on the calculation of the three stages described in this section, a projection algorithm can be derived. It is described as Algorithm 1 and is used by the time-aware QoS prediction approach to perform the final D-space aggregation.

First, the projection algorithm calculates the sums and sums of squares (lines 1–7), which are required to determine the coefficients and projections. This process is completed by iterating through the set of points. The second iteration is to determine the sum of square errors for each of the points (lines 10–14), based on calculated averages for d and t (lines 8 and 9). Finally, the coefficients (lines 15 and 16) and prediction (line 17) using the above calculated values.

86.4 Experimental Study

86.4.1 Data Collection and Experimental Method

We use the prediction error to evaluate our proposed QoS prediction approach. A smaller value means a higher predictive accuracy. When the predictive accuracy is consistently higher, consumers can reliably determine which services are likely to meet their needs.

We collect the data from PlanetLab [9, 10], which is a distributed test bed consisting of hundreds of computers all over the world. The data set contains 150 files, where each file includes Web service invocations on 100 Web services by a service consumer. We calculate the prediction error in cases where the number of service classes is 2, 3, 4, 5, and 6. The number of service classes increases the distinction between the levels of service for each class also decreases.

We employ tenfold Cross Validation to examine our prediction approach. The data set is divided into a training set and a test set. The 90 % original data are in the training set, and the remainder is in the test set. In every experiment, we predict the level of data in the test set based on the data in the corresponding training set. Then the prediction error is obtained by comparing the predicted value with the real value. Finally, the overall prediction error is calculated, which is the average of ten times prediction error.

86.4.2 Experimental Results

The experimental results are illustrated in Table 86.2. All the prediction errors are less than 0.1. The predictive accuracy is greater than 90 %. Moreover, the smaller the number of service classes, the higher the predictive accuracy. The result indicates that the prediction result is in the expectation range. In other words,

Table 86.2 Experiment results

Number of SC	Expectation Prediction Error	0.0-0.1	0.1-0.2	0.2-0.3	0.3-0.4	0.4-0.5	0.5-0.6	0.6-0.7	0.7-0.8	0.8-0.9	0.9-1.0
$N_{sc} = 2$		0.04	0.01	0.02	0.03	0.02	0.01	0.05	0.03	0.02	0.04
$N_{sc} = 3$		0.03	0.01	0.02	0.06	0.02	0.03	0.06	0.05	0.02	0.05
$N_{sc} = 4$		0.03	0.01	0.03	0.01	0.05	0.02	0.02	0.09	0.02	0.05
$N_{sc} = 5$		0.03	0.02	0.05	0.03	0.06	0.07	0.07	0.08	0.07	0.05
$N_{sc} = 6$		0.02	0.03	0.03	0.07	0.04	0.03	0.07	0.03	0.08	0.05

consumers can obtain satisfactory service using our proposed prediction approach. Since our prediction approach remains largely unaffected by the number of service classes and their boundaries, when considered across the range of experiments it is generally preferable. An approach that consistently provides low error predictions is generally preferable to one whose performance is so heavily tied to the characteristics of the underlying data.

Conclusion

This paper describes an effective method for predicting the quality of a service in time. Moreover, we provide a quality space description method on the basis of which the approach can recognize the relationship between points in E space and D space. By selecting, mapping, and aggregating the values in the spaces, we predict the level of a service. As a result, satisfactory services can be recommended to consumers. An experiment demonstrated that the approach is effective. For future work, we will investigate more techniques for improving prediction accuracy.

Acknowledgments This paper is supported by the National Natural Science Foundation of China (61272543), the Central University Basic Scientific Research Project (2013B16114), and the Open Foundation of Huaian Research Institute of Hohai University.

References

1. Zhang LJ, Zhang J, Cai H. Services computing. Beijing: Springer and Tsinghua University Press; 2007. p. 15–8.
2. Zheng ZB. QoS management of web services. Hong Kong: The Chinese University of Hong Kong; 2011.
3. Huhns MN, Singh MP. Service-oriented computing: key concepts and principles. *IEEE Internet Comput.* 2005;9(1):75–81.
4. Shao LS, Zhang J, Wei Y, Feng J, Xie ZB, Mei H. Personalized QoS prediction for web services via collaborative filtering. In: 2007 I.E. International Conference on Web Services (ICWS 2007). Salt Lake City: IEEE Computer Society; 2007. p. 439–46.
5. Zhang XJ, Wang ZJ, Xu F. Reliability evaluation of cloud computing systems using hybrid methods. *Intell Autom Soft Comput.* 2013;19(2):165–74.
6. Shercliff G. Quality assessment of service providers in a conformance-centric service oriented architecture. Cardiff: Cardiff University; 2009.
7. Zhang XJ, Wang ZJ, Lv X, Qi RZ. A clustering-based QoS prediction approach for web service selection. In: The 2013 International Conference on Information Science and Cloud Computing. Salt Lake City: IEEE Computer Society; 2013. p. 193–8.
8. Gross J. Linear regression. Berlin: Springer; 2003.
9. Zheng ZB, Ma H, Lyu MR. Distributed QoS evaluation for real-world web services. In: The Proceedings of the IEEE International Conference on Web Services. Los Alamitos: IEEE Computer Society; 2010. p. 83–90.
10. Zhang YL. Modeling and exploiting QoS prediction in cloud and service computing. Hong Kong: The Chinese University of Hong Kong; 2013.

Chapter 87

Design Issue and Performance Analysis of Data Migration Tool in a Cloud-Based Environment

Shin-Jer Yang, Chung-Chih Tu, and Jyhjong Lin

Abstract With the popularization of Web applications and the emergence of cloud computing technology, database management and storage has evolved from PC to Web-based, even to cloud-based services as well. Also, with big data applications in cloud computing, more many organizations will eventually move their data from Web applications to a cloud-based environment. Except the cloud migration method, the cloud platform must provide an automatic tool in application and data migration for easy implementation. The existing Sqoop data migration tool requires users to be familiar with existing migration commands or move the data manually to a cloud-based database. Hence, the purpose of this paper is to design a new automatic data migration tool named MSCH using the migration of MySQL to HBase as an example to improve on the processing performance of Sqoop. After simulations, the experimental results show that the MSCH migration tool was 33 %, 25 %, and 15 % faster than Sqoop in terms of number of entries. CPU utilization during migration was also reduced by 35 %, 43 %, and 33 %, while memory usage was reduced by 90 %, 72 %, and 74 %, proving that the MSCH data migration tool shortens data migration time and lowers the load on computing resources to enhance the performance in data migration under cloud-based environment. Further studies will be conducted to determine the migration accuracy ratio of MSCH migration tools and Sqoop.

Keywords Cloud computing • Cloud based • MSCH • Relational database • HBase

S.-J. Yang (✉) • C.-C. Tu
Department of Computer Science and Information Management, Soochow University,
100 Taipei, Taiwan
e-mail: sjyang@csim.scu.edu.tw

J. Lin
Department of Information Management, Ming Chuan University, 111 Taipei, Taiwan

87.1 Introduction

The rise of the World Wide Web (WWW) and the emergence of the Web 2.0 concept have seen data change from being stored on personal computers (PC) for personal use to a sharing-oriented setup. Under Web-based architecture, data is stored on remote data centers and provided as a service to users. The service provider must continue to update the architecture to improve service accessibility and stability. Except the cloud migration method, the cloud platform must provide an automatic tool in application and data migration for easy implementation. In order to cope with the massive amounts of data and processing demand, corporate organizations began looking for solutions that offered faster processing speeds. Cloud computing in particular was renowned for its ability to process huge amounts of data. Data has rapidly become more complex and diverse with the rise of cloud computing and big data over the past few years [1]. The demand for management of unstructured and semi-structured data has also continued to increase [2]. However, big data uses relational or non-relational databases as its data storage model. This is why there will inevitably be increasing demand to migrate data from relational databases to cloud-based databases.

Apache Sqoop is a tool that is designed to transfer large amounts of data with high efficiency between the structured data of Apache Hadoop and a relational database [3]. When Sqoop is used to carry out the migration, the user must enter command codes to convert the tables, which may inconvenience the user to some extent. To solve the above problem, this paper designs a migration tool named MSCH (MySQL Convert to HBase) that simplifies the conversion of tables, which does not require the user to memorize commands or syntax. Finally, the simulations are used to compare the relevant key performance indicators of Sqoop and MSCH. The MSCH tool designed in this paper has the following advantages: (1) When the user enters relevant details into the migration tool, all of the tables in the existing relational database are extracted to the local client for temporary storage. The MSCH migration tool proposed in this paper is then used to migrate the data to HBase. The user cannot migrate tables to a cloud-based database without entering complex commands. (2) The proposed MSCH migration tool was evaluated based on the difference in Sqoop's migration time. (3) Finally, KPIs such as CPU utilization and memory usage by MSCH and Sqoop were assessed to prove that MSCH has a lower CPU and memory usage.

In cloud computing, migration can be divided into two types: data migration and application migration. Data migration moves the data from an existing database to a cloud-based database. Application migration is about deploying existing application systems to a cloud environment. As there is a great deal of Web-based data that has not yet been migrated to a cloud environment, this paper focuses on the migration of data to a cloud-based database.

87.2 Related Work

The technology development and rapid increasing of data volume in the WWW have made cloud computing one of the hottest topics in recent years. Unlike the traditional approach where computing tasks were completed by a single computer with high performance, cloud computing links multiple computers with relatively low independent computing capabilities together into a server cluster that acts like a large community in order to complete the computing task. In 2002, Amazon began to offer a new form of cloud computing service [4]. The Web-based Google App Engine as well as the Microsoft Azure Platform based on .NET subsequently appeared. Cloud computing has the following traits: on-demand access, elasticity, pay per use, connectivity, resource pooling, and abstracted infrastructure.

87.2.1 Cloud Computing Platform

In 2004, Google introduced the MapReduce model it used internally but did not publish the source code. The MapReduce model proposed by Google was then used by the Apache Foundation as a guide to develop a distributed open-source software model [5] called Hadoop. Hadoop featured at least eight DSLs (domain-specific languages) and APIs as well as a low-level socket channel for interfacing with MapReduce [6]. A typical MapReduce application model may involve several GB or even TB of data running on tens to tens of thousands of clusters. The goal of Hadoop is to make it easy, even for programmers with no related development experience, to use the resources of large distributed processing systems [7]. The Hadoop Distributed File System contains NameNode and DataNode. As the name suggests, DataNode is where data is stored in the distributed file system. Each Hadoop file system may contain several DataNode clusters. Also, the NameNode is responsible for controlling and recording what data is stored in which DataNode. A NameNode failure would make it impossible to connect to the data.

MapReduce plays a critical role in Hadoop. MapReduce itself can be broken down into map and reduce components. The MapReduce functions responsible for distributing or executing tasks are called the JobTracker and TaskTracker. The JobTracker is mainly responsible for assigning tasks to the TaskTracker, while the TaskTracker is responsible for executing the tasks it receives from JobTracker. Most situations, the user only needs to pay attention to the two points [8]: (1) map function, responsible for converting the entered data into key/value (the converted key/value is then paired with each other) and (2) reduce function, which creates a summary of values in key/value pairs.

The best known function in Hadoop is word count. It basically works by having the map function break down the character strings before the reduce function recombines the strings.

HBase is a distributed open-source database modeled on Google's BigTable. HBase is one of the projects at the Apache Foundation and was developed by Jim Kellerman, Michael Stack, and Bryan Duxbury as a non-relational database for storing structured data [5, 9, 10]. The HBase software uses Hadoop's HDFS format, and its capabilities are similar to Google's BigTable. HBase is designed for use with clusters of servers that contain tens to hundreds of billions of tables and require random access [9]. HBase uses data stored in a distributed file system, and unlike past database systems that make use of structured query language (SQL), HBase uses NoSQL syntax for data queries. The distributed file systems allow the data to be farmed out to each server. By tracking the region servers, data can be accessed when necessary through the headers [10]. The HBase can offer some advantages [11]: elasticity, high write throughput, efficient and low-latency strong consistency semantics, efficient random reads from disk, high availability and disaster recovery, fault isolation, atomic read-modify-write primitives, and range scans.

87.2.2 Migrating for Cloud Computing

Businesses will increasingly migrate their data to a cloud environment, but the migration will face two challenges: (1) business factors (existing investments in IT, cost, data security, regulations, and provisioning) and (2) technical factors (existing infrastructure, security architecture, complexity, network and support, IT skills, and service-level agreements).

For a migration model of cloud computing, Rashim et al. proposed the iterative waterfall model in the software development life cycle. The iterative waterfall model in cloud computing migration involves the following steps: feasibility study, requirement analysis and planning, migration, testing and development, and monitoring and maintenance. Also, easy implementation is an essential factor that cloud migrations must take into account and involves three key areas [12]:

1. A suitable cloud migration method: As relational databases are different from the cloud environment in structure, finding a suitable method to migrate data to a cloud environment is a must.
2. Automatic cloud migration tool: A cloud migration tool capable of automated operation is needed to shorten the migration process and time.
3. Standardized technology and application structure: There is currently no standardized technology and application structure for migration to cloud computing. The handling of special characters and symbols during the migration process is another issue in migration.

Apart from a suitable data migration tool, the data migration tool itself must support automated processing and be easy to set up.

87.2.3 Sqoop

Sqoop is a tool from the Apache Foundation that can migrate tables in a relational database to a cloud-based database. As different data access formats and query commands are used by relational and non-relational databases, Sqoop plays the role of a bridge when migrating data from a relational to a non-relational database [12]. With Sqoop, the user enters the command at the node to migrate data from the specified database to the cloud-based database. The workflow of Sqoop can help the user with migrating data to HBase, but it does contain three weaknesses: (1) The user must manually enter the migration command at the terminal. Therefore, difficulty in understanding command syntax may lead to errors during user connection. (2) There are specific versions of Sqoop for different Hadoop and HBase versions. Mismatched versions will not work. (3) Increased data leads to a significant increase in CPU utilization and memory usage that causes the computer to stop responding.

For this reason, the MSCH, an automated cloud data migration tool, makes it possible for the user to migrate tables from a MySQL database to HBase without having to memorize complicated commands, reducing the time and cost associated with table conversion.

87.3 Operations and Design Issues of MSCH

Sqoop was designed to migrate tables from a relational database to a cloud-based database. The user must, however, work in terminal mode, and the commands have to follow the set syntax. The need for manual intervention means it cannot be considered an automated data migration tool. To overcome this deficiency, this paper designs a new algorithm called the MSCH data migration tool that offers an improvement on the migration procedure of Sqoop. MSCH can extract tables from MySQL and migrate them to the cloud-based HBase. Using the MSCH proposed in this paper, tables can be extracted and migrated to a cloud-based database without any user intervention in the migration operation or memorization of multiple commands.

87.3.1 Operating Procedure and Algorithm Design of MSCH

The operating procedure of the MSCH data migration tool is shown in Fig. 87.1. First, the user enters the account and password for the MySQL database. Once the user has been authenticated by the system, he or she can select the name of the table

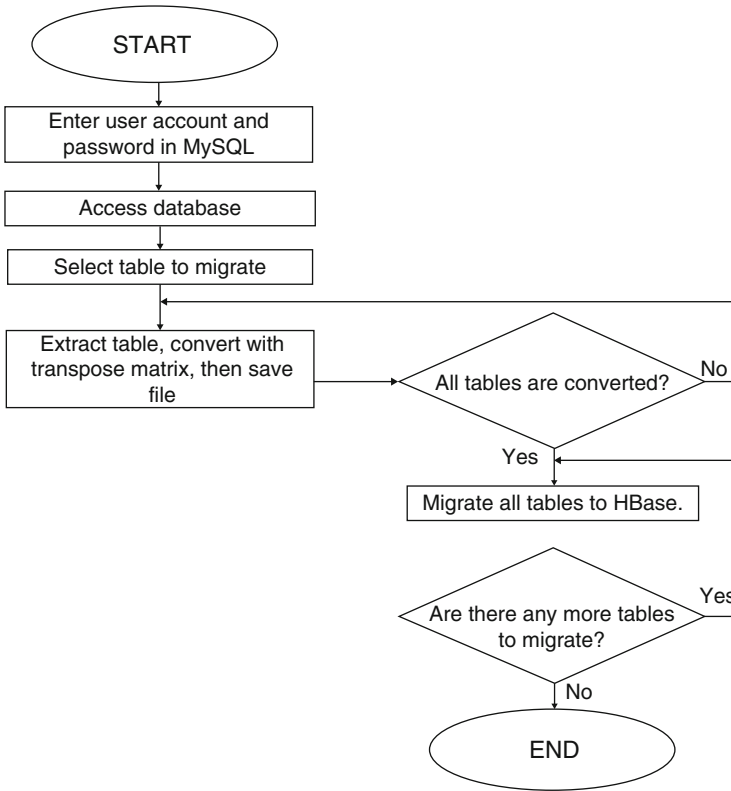


Fig. 87.1 The operating process of MSCH

to migrate. Once the table has been selected, the data migration tool extracts the fields of the table into a CSV file, converts them using a transpose matrix, and then stores the results in the cloud. The MSCH tool then connects to HBase and Zookeeper to complete the migration of data from the CSV file to HBase. Hence, we design the algorithm of MSCH tool based on Fig. 87.1.

Algorithm MSCH()

```

{
Input:
#define HtableDescriptor //To describe the tables attributes in HBase
#define HColumnDescriptor //To add Column Family via "Put" method
#define Configuration //To receive the values of hbase-site.xml
#define HBaseAdmin //To use privilege files in HBase
#define BufferedReader //To read streams data in CSV files using JAVA
Output: To complete Migration process;
Method:
BEGIN {
    New HtableDescriptor;
    New HColumnDescriptor;
    HBase Configuration;
    HBaseAdmin;
    Read CSV File from Route
    To migrate to table name in HBase
    If(admin.tableExists(tablename)
    Output TableExists
    Else
    admin.CreateTable;
    New BufferedReader BR;
    Data = line.split;
    CSVBeanReader(); // To read CSV file
    } End
    Put File to HBase
    while(bufferReader != null) {
    BufferedReader.NextToken
    For ColumnsData do
    TableHead= ColumnsData[0];
    TableData = ColumnsData[i];
    New put;
    Put.add(Bytes.toByte("ColumnFamilyName"),BytestoBytes("RowName"),TableData;
    End For
    } End
    }
End MSCH.

```

87.3.2 Transpose Matrix

The matrix is a type of equation in linear algebra. The transpose matrix swaps the data in the matrix's rows and columns. In this paper, a table is treated as a matrix while extracting data, there is conversion from rows of data to columns and vice versa. When the migration is in progressing, MSCH can read the row of data to

Table 87.1 Experimental computer setup

Software and hardware configuration	Software and hardware specifications
Operation system	Ubuntu 12.04
CPU	2 cores 2.5 GHz
Memory	2 GB
Disk	500 GB
MySQL version	5.5
Hadoop version	Hadoop 1.2.0
HBase version	0.95.1
JDK version	JDK 1.7.0-25

Table 87.2 Key performance indicators

Key performance indicators (KPIs)	Purpose of KPIs' analysis
Migration time	Time taken to complete migration of tables from MySQL to HBase database
CPU utilization	CPU utilization during migration of tables from MySQL to HBase database
Memory usage	Memory usage during migration of tables from MySQL to HBase database

reverse from row to column and column to row. The transpose matrix used for file processing as shown in formula (87.1) performs a row transpose of the data within the matrix to improve the performance of file access:

$$A = \begin{bmatrix} a1 & a2 & a3 \\ a4 & a5 & a6 \\ a7 & a8 & a9 \end{bmatrix} \quad A^t = \begin{bmatrix} a1 & a4 & a7 \\ a2 & a5 & a8 \\ a3 & a6 & a9 \end{bmatrix} \quad (87.1)$$

87.4 Simulation Setup and Result Analysis

87.4.1 Simulations Setup

In this paper, MySQL is installed on the computer of a single node, and MSCH is used to migrate the tables to HBase in order to evaluate related performance indicators. The software and hardware specifications are shown in Table 87.1.

Ganglia performance monitoring software used in this paper can monitor the computing resource usages, allowing the measurement of indicators such as CPU utilization and memory usage when data is being migrated from MySQL to HBase with Sqoop and MSCH. In this paper, three key performance indicators (KPIs) are proposed to analyze the results of the simulation experiments as shown in Table 87.2.

Fig. 87.2 Data migration time for Sqoop and MSCH

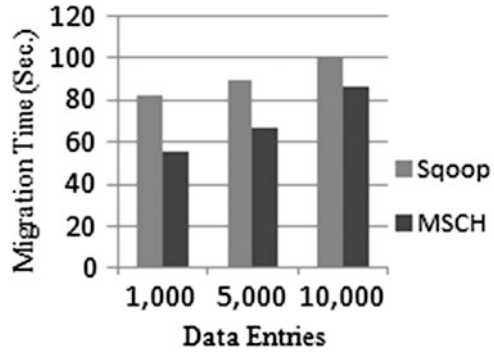
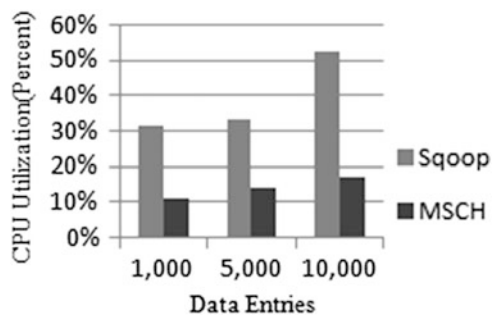


Fig. 87.3 CPU utilization during data migration for Sqoop and MSCH



87.4.2 Results Analysis

The data migration of 1,000, 5,000, and 10,000 entries can be carried out and correspond to the three KPIs of this paper. Each type of migration is carried out 10 times with the mean of the three median values taken as the experimental data. For the migration time of KPI, Sqoop requires the commands to be entered manually, while the ultimate goal of this paper is to design an automated data migration tool for cloud-based databases. Hence, the experimental results are shown in Figs. 87.2, 87.3, and 87.4.

The migration times for Sqoop and MSCH are shown in Fig. 87.2. The data migration of 1,000, 5,000, and 10,000 entries can be carried out, and the migration time for MSCH was 33 % faster than Sqoop for 1,000 entries, 25 % faster for 5,000 entries, and 15 % faster for 10,000 entries. Figure 87.3 shows CPU utilization during data migration for Sqoop and MSCH. CPU utilization for Sqoop increased with the amount of data, while the CPU utilization for MSCH is 11.3 %, 14.3 %, and 17.4 % for 1,000, 5,000, and 10,000 entries, respectively, making it just 35 %, 43 %, and 33 % of Sqoop with relatively little variation. Figure 87.4 shows memory usage. The memory usage of MSCH is 90 %, 72 %, and 74 % less than Sqoop for the above order of data migration. There is no significant increase in the amount of memory used by MSCH between the migration of 5,000 and 10,000 data entries.

Fig. 87.4 Memory usage during data migration for Sqoop and MSCH

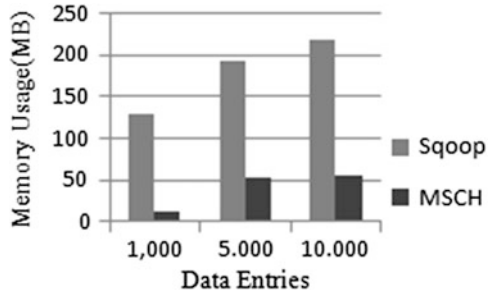


Table 87.3 The summarized simulation results

Performance indicator	Migration tool	Data entries		
		1,000 entries	5,000 entries	10,000 entries
Migration time	Sqoop	82 s	89 s	101 s
	MSCH	55 s	67 s	86 s
CPU utilization	Sqoop	31.4 %	33.1 %	52.5 %
	MSCH	11.3 %	14.3 %	17.4 %
Memory usage	Sqoop	128.7 MB	192.3 MB	218.7 MB
	MSCH	12 MB	53.7 MB	55.3 MB

The above simulations indicate that MSCH can effectively reduce the load on computing resources during data migration. The advantage of MSCH is particularly overwhelming in terms of CPU utilization and memory usage. Hence, the summarized simulation results for Sqoop and MSCH are shown in Table 87.3.

Conclusion

This paper proposes MSCH as a new data migration tool that overcomes the problems faced by Sqoop during data migration. KPIs are used to measure the migration time, CPU utilization, and memory usage of MSCH and Sqoop during data migration. The results showed that MSCH is 33 %, 25 %, and 15 % faster than Sqoop when migrating 1,000, 5,000, and 10,000 entries of data, respectively. CPU usage during migration is also reduced by 35 %, 43 %, and 33 %, while memory usage is reduced by 90 %, 72 %, and 74 %, proving that the MSCH data migration tool shortens data migration time, lowers CPU utilization, and reduces memory usage, enhancing the performance in data under cloud-based environment. There are main objectives as following on this paper. Firstly, users do not need to enter lengthy command when they are applying MSCH tool. Next, MSCH is used to effectively improve the migration time, CPU utilization, and memory usage of Sqoop during cloud migration. Finally, MSCH can provide a suitable cloud migration tool for automatic cloud migration and easy implementation. In the future, research direction will focus on the distributed nodes and examination of data migration accuracy when the data is stored in distributed cloud nodes.

References

1. Oriaku C, Lami IA. Holistic view angles of cloud computing services. In: Provisions, 2012: International conference on cyber-enabled distributed computing and knowledge discovery. IEEE New York, NY, USA. 2012. pp. 97–105.
2. Roitman H, Schenkel R, Grobelnik M. Search and mining entity-relationship data. In: CIKM '11: Proceedings of the 20th ACM international conference on information and knowledge management, ACM New York, NY, USA. 2011. pp. 2639–40.
3. The Apache Software Foundation. Apache Sqoop. <http://sqoop.apache.org>. Accessed 20 Mar 2014.
4. Mokhtar SA, Ali SHS, Al-Sharafi A, Abdulaziz Aborujilah. Cloud computing in academic institutions. In: ICUIMC '13: Proceedings of the 7th international conference on ubiquitous information management and communication, ACM New York, NY, USA. 2013.
5. The Apache Software Foundation. Apache Hadoop. <http://hadoop.apache.org>. Accessed 12 Apr 2014.
6. Nikhil RS. Abstraction in hardware system design. ACM Queue. 2011;9(18):1–15.
7. Brown RA. Hadoop at home: large-scale computing at a small college. In: Proceedings of the 40th ACM technical symposium on computer science education, ACM New York, NY, USA. 2009. pp. 106–10.
8. Chen R, Chen H. Tiled-MapReduce: efficient and flexible MapReduce. In: Proceedings on multicore with tiling, ACM transactions on architecture and code optimization, vol. 10, no. 1, Article 3. ACM New York, NY, USA. 2013. pp. 3:1–30.
9. Gao X, Nachankar V, Qiu J. Experimenting lucene index on HBase in an HPC environment. In: HPCDB '11: Proceedings of the first annual workshop on high performance computing meets databases, ACM New York, NY, USA. 2011. pp. 25–8.
10. The Apache Software Foundation. The apache software foundation blogging in action. https://blogs.apache.org/sqoop/entry/apache_sqoop_highlights_of_sqoo. Accessed 18 Apr 2014.
11. Borthakur D, Gray J, Sarma JS, et al. Apache Hadoop goes realtime at facebook. In: SIGMOD '11: Proceedings of the 2011 ACM SIGMOD international conference on management of data, ACM New York, NY, USA. 2011. pp. 1071–80.
12. Rashmi, Mehfuz S, Sahoo GB. A five-phased approach for the cloud migration. Int J Emerg Technol Adv Eng. 2012;2(4):286–91.

Chapter 88

Fuzzy Time Series Forecasting Algorithm Based on Maximum Interval Value

Che Liu, Yunfei Zhang, Fang Yang, Wenhuan Zhou, and Xin Lv

Abstract To solve problems such as imprecise domain partition and improvement of limitations in establishing fuzzy time series forecasting methods that make it hard to adapt to the emergence of new relationships, a new fuzzy time series forecasting algorithm is proposed. Based on fuzzy theory, the domain partition algorithm is optimized by establishing the connection between the minimum value of historical data and the value of parameter spec; then a second division is divided depending on different numbers in each domain; the third-order fuzzy logic is to establish the fuzzy rules to obtain different sets of trends; finally, the predicted value is obtained by defuzzification. The experiment shows that this method features high feasibility and adaptability.

Keywords Fuzzy time series • Domain partition • Fuzzy logic forecasting • Similarity

88.1 Introduction

Time series are a kind of common high-dimensional data with time dependence and have become an important field in the study of data mining because of its good continuity and extension in the real world.

Box and Jenkins [1] first proposed a time series data model: the autoregressive moving average (ARMA) method. Based on ARMA, ARCH/GARCH [2] has been proposed and is widely used in the natural sciences and social sciences. Along with the in-depth research of data mining, analysis on time series has received more attention. Heikki Mannila [3] first introduced the concept of ideological association rules and inertial ordering rules to the sequence rule model and made frequent discoveries in terms of a time series plot algorithm. Agrawal et al. [4] first proposed a similarity search on time series database research papers; since then, many association rule algorithms have been proposed. Zadeh (LAZadeh) [5] proposed the concept of fuzzy set for handling vagueness and imprecision in ordinary

C. Liu (✉) • Y. Zhang • F. Yang • W. Zhou • X. Lv
College of Computer and Information, Hohai University, 211100 Nanjing, China
e-mail: njliuche@163.com; yunfeizhang@hhu.edu.cn

reasoning, which is now widely used in various fields. Song [6] first proposed the concept of fuzzy time series and improved the original model [7], which has greatly improved prediction accuracy. Chen [8], based on the analysis of Song's algorithm, substituted an arithmetic operation for a maximize-minimize (max-min) operation to improve its applicability and robustness and thereby improved the applicability and robustness of the model. Egrioglu [9] discovered that most of the existing methods have ignored the membership function of fuzzy sets and proposed a membership function based on a new order fuzzy time series forecasting model.

Most of the existing prediction algorithms must consider fuzzy rules to predict future data; however, if a new rule comes out, the fuzzy logic cannot be determined, then the prediction accuracy will be greatly reduced. With this in mind, we propose a fuzzy interval time series prediction algorithm based on improved similarity, then the dependence on history data has been reduced by improving fuzzy relational approach. To sum up, the new algorithm features a higher accuracy of predicted values and a wide range of applications.

88.2 Relevant Knowledge

The fuzzy time series concept is illustrated as follows.

Definition 1. Let T be a time set and x_t a random variable ($t \in T$); if T is a discrete set, such as $T = \{1, 2, \dots\}$, then $\{x_t\}$ is called a *random sequence*. Due to the random sequence $\{x_t\}$, t describes the time increment at equal intervals; thus, it usually relates to a random sequence of time series.

Definition 2. If $Y(t)(t = 1, 2, \dots, n)$ is a subset of R in which the universe of fuzzy sets $f_i(t)(t = 1, 2, \dots, m)$ is defined and $F(t)$ is a collection of $f_i(t)(t = 1, 2, \dots, m)$, then $F(t)$ is called a fuzzy time series on $Y(t)(t = 1, 2, \dots, n)$.

88.3 Fuzzy Time Series Model

In this section, we propose a new fuzzy time series forecasting algorithm, making some improvements in [domain partitioning](#) and the division of fuzzy logic.

The algorithm is made up of the six following steps.

1. Perform first [domain partition](#):

define the universe of discourse U for the historical data. First, we find the minimum data D_{\min} and the maximum data D_{\max} in the historical time series data; then we define the universal discourse U as $[D_{\min}, D_{\max}]$. Here, let $D_{\min} = ab * 10^z$, a and b are between 0 and 9, and z is a nonnegative number.

The formula for calculation is as follows:

$$\text{spec} = a * 10^z + (b - 1) * 10^{(z-1)}.$$

Then expand the space U to obtain a new domain:

$$U' = [D_{\min} - \text{spec}/10, D_{\max} + \text{spec}/10]. \tag{88.1}$$

Based on Eq. (88.2), calculate the two historical data $x(i)$ and $x(i - 1)$ ($i = 1, 2, \dots, n - 1$) of the absolute values of differences, sum these $n - 1$ values, average it, and then divide in half as the cumulative length:

$$\text{Range} = \frac{\sum_{i=1}^{n-1} |x(i + 1) - x(i)|}{2(n - 1)}. \tag{88.2}$$

According to Table 88.1 [10], calculate the range for rounding.

The domain U is partitioned using the average method into m subintervals $U_1 U_2 \dots U_m$ and $U_1 = U_2 = \dots = U_m$. The partition rule is presented as Eq. (88.3)

$$\text{MAX} = D_{\max} + \text{spec}/10, \quad \text{MIN} = D_{\min} - \text{spec}/10,$$

so $U_i = [\text{MIN} + (i - 1) * \text{Range}, \text{MIN} + i * \text{Range}]$, as $i = 1, 2, \dots, m$:

$$m = \left\lceil \frac{\text{MAX} - \text{MIN}}{\text{Range}} \right\rceil. \tag{88.3}$$

2. Perform second domain partition.

Following the first domain division, the domain interval is divided into n regions, $A = \{A_1, A_1, \dots, A_n\}$, where A_i represents the semantic variable fuzzy set A .

Based on the existing method, the secondary domain partition is carried out as follows:

Here, partition the domain according to the different numbers of points of each interval with the specific partition shown as follows:

$$U_{1-1} = [D_{\min} - \text{spec}/10 + \text{range} * 1/n_1^2, D_{\min} - \text{spec}/10 + \text{range} * 2/n_1^2],$$

$$U_{1-2} = [D_{\min} - \text{spec}/10 + \text{range} * 2/n_1^2, D_{\min} - \text{spec}/10 + \text{range} * 3/n_1^2] \vdots ,$$

Table 88.1 Base mapping

Range	Base
[0.1,1)	0.1
[1,10)	1
[10,100)	10
[100,1000)	100

Table 88.2 Distribution of logical relationships

Type	Relation	Fuzzy relation	Name
1	$i < j < k$	$A_i, A_j, A_k \rightarrow A_l$	“up-up” trends fuzzy logic group
2	$i < j = k$	$A_i, A_j, A_k \rightarrow A_l$	“up-equal” trends fuzzy logic group
3	$i = j < k$	$A_i, A_j, A_k \rightarrow A_l$	“equal-up” trends fuzzy logic group
4	$i = j = k$	$A_i, A_j, A_k \rightarrow A_l$	“equal-equal” trends fuzzy logic group
5	$i > j > k$	$A_i, A_j, A_k \rightarrow A_l$	“down-down” trends fuzzy logic group
6	$i > j = k$	$A_i, A_j, A_k \rightarrow A_l$	“down-equal” trends fuzzy logic group
7	$i = j > k$	$A_i, A_j, A_k \rightarrow A_l$	“equal-down” trends fuzzy logic group
8	$i < j > k$	$A_i, A_j, A_k \rightarrow A_l$	“up-down” trends fuzzy logic group
9	$i > j < k$	$A_i, A_j, A_k \rightarrow A_l$	“down-up” trends fuzzy logic group

$$U_{2-1} = [D_{\min} - \text{spec}/10 + \text{range} + \text{range} * 1/n_2^2, D_{\min} - \text{spec}/10 + \text{range} + \text{range} * 2/n_2^2] \dot{:} ,$$

$$U_{2-n_2} = [D_{\min} - \text{spec}/10 + \text{range} + \text{range} * (n_2 - 1)/n_2^2, D_{\min} - \text{spec}/10 + \text{range} + \text{range}/n_2] \dot{:} ,$$

$$U_{m-n_m} = [D_{\min} - \text{spec}/10 + (m - 1)\text{range} + \text{range} * (n_m - 1)/n_m^2, D_{\min} - \text{spec}/10 + (m - 1)\text{range} + \text{range}/n_m].$$

Based on the second division, we are dealing with fuzzy data. For example, when $x(t) \in U_{i_m}$, $x(t)$ is fuzzified into A_{i-1+b} , where $b = m/n_i$, and n_i is the number of historical data in U_i .

3. Establish fuzzy relations

Any third-order fuzzy relationship can be expressed as $A_i, A_j, A_k \rightarrow A_l$.

Based on the fuzzy relations given earlier, it is possible to obtain nine types of distribution, as shown in Table 88.2:

An adaptive effect has been achieved by means of different models in various fuzzy logic groups.

4. Calculate similarity:

Here Liu’s [11] method is adopted: based on Table 88.2, determine the prediction point $x(n+3)$ of the first three points, where $x(n+2), x(n+1), x(n)$ corresponds to the type of fuzzy sets $S(A_i, A_j, A_k)$, and thus calculate the similarity. Assume that $S(A_i, A_j, A_k)$ is the “up-up” trend fuzzy logic; then partition it into the corresponding set according to its type, for example, the “up-up” type is classified into the “up-up” group. If the “up-up” type has the number of elements, namely: $\{S_1, S_2, \dots, S_{num}\}$, then calculate the similarity between these num elements and the S . The methods are as follows.

Suppose $S_a (1 \leq a \leq num)$ the third-order fuzzy logic of three consecutive time points, $x(m-2), x(m-1), x(m)$, which is denoted by (A'_i, A'_j, A'_k) . Fig. 88.1a, b shows the trends of fuzzy sets S and S_a .

Then the similarity between S and S_a is calculated using Eq. (88.4):

$$\text{similar}(S, S_a) = 1 - \text{distance}(S, S_a). \tag{88.4}$$

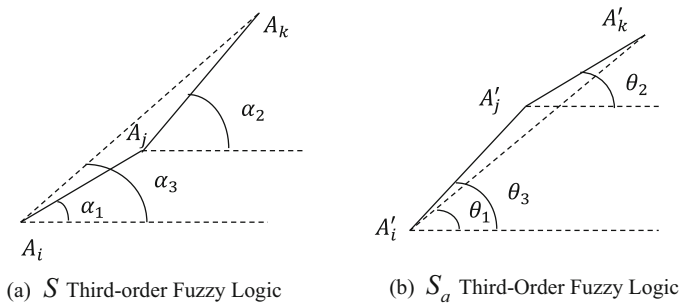


Fig. 88.1 Third-order fuzzy logic. (a) S third-order fuzzy logic. (b) S_a third-order fuzzy logic

Definition 3. Any distance(S, S_a) between two third-order fuzzy logical a and b is represented by Eq. (88.5):

$$\text{distance}(S, S_a) = (|\sin \alpha_1 - \sin \theta_1| + |\sin \alpha_2 - \sin \theta_2| + |\sin \alpha_3 - \sin \theta_3|)/3. \tag{88.5}$$

In summary, the similarities between S and all elements of the logical relationship are shown in Eq. (88.6):

$$\text{similar } P(S, S_a) = \frac{\text{similar}(S, S_a)}{\sum_{\alpha=1}^{\text{num}} \text{similar}(S, S_a)}. \tag{88.6}$$

5. Predict the future value of the expected point:

The elements in the logical relationship $(S_1, S_2, \dots, S_{\text{num}})$'s offset corresponding to the fuzzy prediction are $D_1, D_2, \dots, D_{\text{num}}$.

The fuzzy logic of the predicted point $x(n+1)$ is $S(A_i, A_j, A_k \rightarrow A_{(n+1)})$; then determine the matched logic in S . $D(n+1)$ is the expected value of the fuzzy logic offset value. Calculate it using Eq. (88.7):

$$D(n+1) = \sum_{i=1}^{\text{num}} D_i * \text{similar } P(S, S_a). \tag{88.7}$$

Then the fuzzy value of the predicted point, represented as $A(n+1)$, can be obtained from the following formula:

$$A(n+1) = A_k + D(n+1). \tag{88.8}$$

6. Defuzzify.

With the fuzzy prediction point $A(n+1)$, find $A(n+1)$'s interval U_i and the corresponding fuzzy set A_i ; then the offset value in the interval

fuzzyDif($A(n + 1), A_i$) is calculated using Eq. (88.9):

$$\text{fuzzyDif}(A(n + 1), A_i) = k + D(n + 1) - i. \tag{88.9}$$

Calculate the intermediate value U_i ; then the predicted value $F(n + 1)$ is as follows:

$$F(n + 1) = M[U_i] + \text{fuzzyDif}(A(n + 1), A_i) * \text{length}(U_i), \tag{88.10}$$

where $\text{length}(U_i)$ represents the length of U_i and $M[U_i]$ represents the middle value of U_i .

88.4 Model Verification

The analysis of the model is based on the data used in Zheng’s method [12], that is, 40 elements in the data set are utilized to verify the validity of the proposed model. Using Eq. (88.2), we can obtain a range of 5.87, and then $\text{Base} = 1$ can be determined from Table 88.1, so the range is adjusted to 6. By Eq. (88.3),

$$m = \left\lceil \frac{\text{MAX} - \text{MIN}}{\text{Range}} \right\rceil = \left\lceil 67.5 - 28 + \frac{5}{6} \right\rceil = 7.$$

Now we have seven domains, U_1, U_2, \dots, U_7 . Upon calculation, U_1, U_2, \dots, U_7 in turn contains the number of the data, 2, 10, 8, 7, 9, 2, 2; then a secondary domain partition is carried out, $U_{1-1} = [28, 30.6]$, $U_{1-2} = [30.6, 34]$, and so on. Since the data in the time sequence are progressive, the departure of the point from the predicted point produces a weak effect; then third-order fuzzy logic is used to establish fuzzy rules and obtain the corresponding trends; therefore, third-order fuzzy logic is adopted to establish fuzzy rules to obtain different sets of trends. The final results are predicted as follows (Fig. 88.2):

A comparison between the proposed algorithm and existing ones is given in Table 88.3, with the results obtained from Eqs. (88.11) and (88.12):

$$\text{MAE} = \frac{1}{n} \sum_{t=1}^n |\text{AuctalValue}(t) - \text{ForecaseValue}(t)|, \tag{88.11}$$

$$\text{RMSE} = \sqrt{\sum_{t=1}^n [\text{AuctalValue}(t) - \text{ForecaseValue}(t)]^2 / n}. \tag{88.12}$$

From Table 88.3, it is clear that the proposed algorithm has a better accuracy, that is, it has advantages in terms of indicators (MAE and RMSE) over the algorithms in [10, 13]. Due to the limitations of historical data rules, some existing algorithms are unable to predict future data due to a lack of unlearned rules.

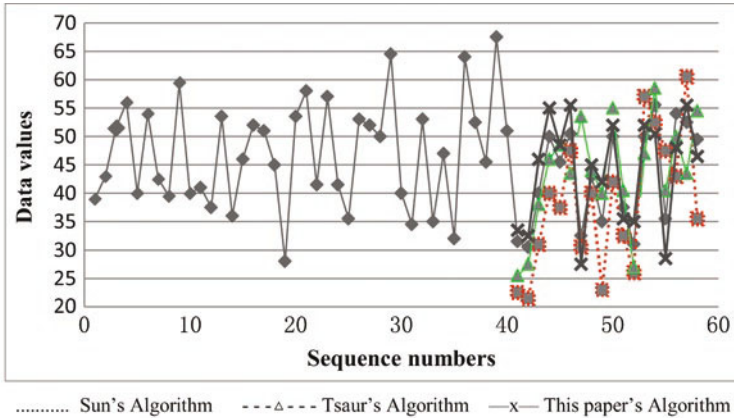


Fig. 88.2 Prediction comparison chart

Table 88.3 Comparison of prediction performances

Algorithm	MAE	RMSE
Sun	7.6667	8.3997
Tsaur	5.1667	6.6875
Proposed	3.9444	4.062

In contrast, our algorithm has greater suitability and accuracy in terms of predicting unknown data.

Conclusion

In this paper, based on similarities in fuzzy time series logic relations, a new fuzzy time series forecasting algorithm is proposed to predict future data values and overcome the limitations of the existing statistics of algorithms based on fuzzy rules by means of the trend prediction of time series. Experiments show that the proposed algorithm, in terms of MAE and RMSE, is better than similar prediction algorithms because of its higher prediction accuracy.

Acknowledgments This paper was supported by the National Natural Science Foundation of China: “Research on Trusted Technologies for The Terminals in The Distributed Network Environment” (Grant 60903018), “Research on the Security Technologies for Cloud Computing Platform” (Grant 61272543), “National Twelfth Five-Year Key Technology Research and Development Program of the Ministry of Science and Technology of China” (Grant 2013BAB06B04), and “Key Technology Project of China Huaneng Group” (Grant HNKJ13-H17-04).

References

1. Lu Y, AbouRizk SM. Automated Box–Jenkins forecasting modelling. *Autom Constr.* 2009;18(5):547–58.
2. Engle R. GARCH 101: the use of ARCH/GARCH models in applied econometrics. *J Econ Perspect.* 2001;15(4):157–68.
3. Agrawal R, Srikant R. Mining sequential patterns. In: *Proceedings of the 11th International Conference on Data Engineering.* New Jersey: IEEE; 1995. p. 3–14.
4. Agrawal R, Faloutsos C, Swami A. Efficient similarity search in sequence databases. In: *Proceedings of the 4th International Conference on Foundations of Data Organization and Algorithms,* Chicago; 1993. p. 69–84.
5. Zadeh LA. Fuzzy sets [J]. *Inf Control.* 1965;8(3):338–53.
6. Song Q, Chissom BS. Fuzzy time series and its models. *Fuzzy Sets Syst.* 1933;54(3):269–77.
7. Song Q, Chissom BS. Forecasting enrollments with fuzzy time series-part II. *Fuzzy Sets Syst.* 1994;62(1):1–8.
8. Chen SM. Forecasting enrollments based on fuzzy time series[J]. *Fuzzy Sets Syst.* 1996;81(3):311–9.
9. Aladag CH, Basaran MA, Egrioglu E, et al. Forecasting in high order fuzzy times series by using neural networks to define fuzzy relations. *Expert Syst Appl.* 2009;36(3):4228–31.
10. Sun XH, Li YM. Average-based fuzzy time series models for forecasting Shanghai compound index. *World Journal of Modelling and Simulation.* 2008;4(2):104–111.
11. Liu F, Guo GD. Interval-similarity based fuzzy time series forecasting algorithm. *J Comput Appl.* 2013;33(11):3052–6 (in Chinese).
12. Zheng GQ, Le YJ, Wang R, et al. Method of long-term IFTS forecasting based on parameter adaptation. *Syst Eng Electron.* 2014;36(1):99–104 (in Chinese).
13. Tsaur RC, Kuo TC. The adaptive fuzzy time series model with an application to Taiwan’s tourism demand. *Expert Syst Appl.* 2011;38(8):9164–71.

Chapter 89

Assessing the Effectiveness of Cloud Computing in European Countries

Petra Marešová and Kamil Kuča

Abstract Cloud computing is a technology which is considered to be very promising and beneficial in the countries of the European Union. However, its implementation in business is not currently that noticeable, and many companies do not manage to assess and voice its contribution. The introduction of cloud computing not only brings significant benefits but also costs and risks. The aim of this contribution is therefore to propose a topical system of criteria for assessing the effectiveness of cloud computing, which is based on the existing experience with this particular technology. Several methods are used in order to achieve this goal, namely, bibliographic search, interviews with cloud computing experts on the implementation and design of cloud computing, and a questionnaire survey among enterprises in the selected country.

Keywords Cloud computing • Evaluation criteria • Benefits • Risk

89.1 Introduction

Cloud computing is a new technology which is acknowledged to be very beneficial in the companies of the countries of the European Union. Cloud computing can be seen as the form of services accessible to customers by means of a communication network as well as all hardware and software tools used by the data centres providing these services [1]. Forrester Research, a global research and advisory firm, has widened the definition mentioned above so that it also covers the standardisation of ICT tools on the supplier's side and self-service principals on the user's side. Cloud computing is in fact a package of standardised ICT capacities (services, software solutions or infrastructure) accessible via the Internet on the basis of self-service principles and the pay-per-use model [2].

P. Marešová (✉) • K. Kuča
Faculty of Informatics and Management, University of Hradec Kralove, 50003 Hradec Kralove, Czech Republic
e-mail: petra.maresova@uhk.cz; kamil.kuca@fnhk.cz

Within the field of cloud computing, two types of service models can be distinguished: public and private. A service model is a way of providing cloud computing services to the end user. Cloud platforms have been categorised into three main groups according to the type of provided services: infrastructure, platform and service.

The decision whether to implement cloud computing in the organisation is related to benefits and risks. By comparing them, it is possible to come to the conclusion whether or not the technology is suitable for the organisation. In practice, however, there is no accessible device, apart from online calculators, which would make the decision-making process easier before addressing a provider. On the other hand, the problem of decision-making related to accepting cloud computing has been tackled by universities as well as the private sector, mostly with respect to the field of application.

A current review of the cloud computing effectiveness evaluation is available in many sources [3–6]. The literature of cloud computing has explored the costs of using cloud with the help of individual case studies [7–12]. The most frequently mentioned criteria for the decision-making process related to accepting cloud computing is security, confidentiality, backup and recovery, efficiency and performance, elasticity and costs [13]. The next area pertains to performance. Companies and organisations worry about not being able to access their data because of the unavailability of cloud services when they need them. Usually there is little if any forewarning of the possibilities of services being unavailable [14, 15]. Some industry leaders argue that it is still an advantage for businesses to keep services and valuable data in their own infrastructure, to ensure that they can gain access to them at any time. The final challenge for utilising cloud services is cost. This is a quickly evolving field, with rapid reductions in cost. Different vendors have different pricing models, and there is encouraging information that cloud is cost competitive when compared with local server solutions for applications that require very large storage. The overall most frequently used criteria are [16–29]:

- Security
- Efficiency and performance
- Adaptability
- Elasticity
- Legal matters laws and treaties covering the storage, access and transmission of data
- Availability and usage restriction
- Backup and recovery
- Response time
- Usability
- Customisation
- Elasticity
- Interoperability
- Scalable storage
- Hardware cost

- Software cost
- Portability
- Reliability
- Compliance with standards
- Client support

89.2 A Case Study: Criteria for Assessing the Effectiveness of Cloud Computing According to Small and Medium Enterprises in the Czech Republic

In August 2013, a questionnaire survey was carried out in the Czech Republic. Its topic was “Utilisation of ICT in Czech companies”. The aim of this survey was to determine current attitudes of companies towards using technologies in order to support financial management, customer relation management (CRM) and cloud computing. Companies from all CZ-NACE categories were addressed, with a focus on SME. A total of 200 questionnaires were collected.

Respondents in the Czech Republic indicated the most significant criteria for successful utilisation of cloud computing: scalability (14 %), elasticity (14 %), scalable storage (12.9 %), availability (12.9 %) and customisation (13.4 %). The problem of data security is dismissed as less significant in cloud computing. It becomes a problem only when respondents are asked about risks linked to the implementation of cloud computing.

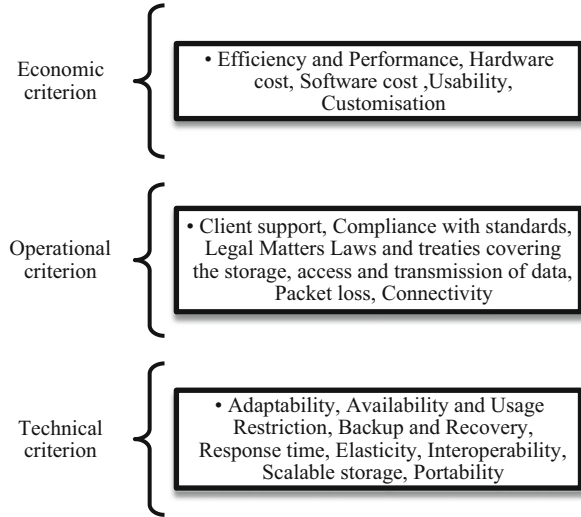
Some managers perceive the following obstacles: data security, dependence of operation on Internet access, insufficient knowledge of cloud computing and its possibilities, low priority of perceiving cloud computing as necessary, the related lack of time for analysing strengths and weaknesses and financial burden.

All in all, the implementation of cloud computing in SME in the Czech Republic is quite low (only 9 % of addressed companies). The main reason for the low utilisation of cloud computing in Czech companies is the fact that companies do not perceive the need to implement this technology (68.5 %) and do not have sufficient knowledge of its possibilities (14.5 %).

89.3 System of Criteria for Assessing the Effectiveness of Cloud Computing

The criteria mentioned above for the utilisation of cloud computing also serves as a starting point to create a cloud computing model. The proposed model has three basic levels (Fig. 89.1) based on the relation of the given criteria to the technical characteristics of the technology and on the relation to customer needs. The proposed levels are:

Fig. 89.1 System of criteria for assessing the effectiveness of cloud computing



- Technical
- Operational
- Economic

The model is based not only on the literature review but also on the opinions of five experts in the field of implementing this technology in the Czech Republic.

Economic criteria are related to the effectiveness of application, costs and the user friendliness of cloud. These criteria include costs of hardware and software. Overall, these are investment costs. These items should be then compared with the qualitative benefits. However, this causes difficulties in numerical formulation of effectiveness of cloud computing. Nevertheless, even for these purposes, there are well-established methods (cost-benefit analysis).

Operational criteria are related to determining the service-level agreement (SLA). SLAs are part of service contracts and are agreements usually between two parties (service provider and customer), which formally define the services. Service contracts use the percentage of service availability as a unit [30]. SLA is a specification of services [31]. The company Cisco Systems, Inc. implements the agreement on the quality of service in its devices under the name Cisco IOS IP [32].

Finally, the last group consists of *technical criteria*. The success of cloud services depends on the required functionality and other characteristics such as availability, respond time, latency, performance, timeliness, scalability and high availability. All of these characteristics can be covered by the term Quality of Cloud Service (QoCS), which comes from general QoS [33]. QoS (Quality of Service) is used in computer science for booking and control of data flows in telecommunication and computer networks. QoS can set, for example, a top or low transfer zone for certain data, prefer some operations or divide the operations into categories

according to the set parameters. Thus, QoS attempts to provide its users with the services which can guarantee quality in advance in order to avoid any delays, loss-making or waste [34].

Conclusion

Currently, a growth is predicted in the area of cloud computing utilisation in Europe in the following years. At the same time, the economic situation in many countries makes companies consider every new investment. Cloud computing is a technology that is related to costs and benefits, many of which are difficult to grasp and express.

The aim of this contribution is to propose a system for assessing the effectiveness of cloud computing. The described system is based on the study of relevant literature and on the opinions of experts. This research suggests that the basic criteria for assessing the effectiveness of cloud computing is a set of technical, operational and economic criteria.

The created model for the time being only specifies the basic levels at which subjects implementing cloud computing could identify their requirements and expectations (using both soft and hard metrics). The model is expected to be further developed with the intention to propose concrete methods for measuring individual levels. The model is expected to be further tested in real practices.

Acknowledgements This paper is published thanks to the support of the internal projects of the University of Hradec Kralove: Economic and Managerial Aspects of Processes in Bio-medicine and specific university research (MSMT no. 2111/2014).

References

1. Armburst M, Fox A, Griffith R, Joseph A.D, Katz RH, Konwinski A et al. Above the clouds: a Berkeley view of cloud computing. 2009. <http://www.eecs.berkeley.edu/Pubs/TechRpts/2009/EECS-2009-28.html>.
2. Forrester, Reichman R, Chi E. File storage costs less in the cloud than in-house. 2011. <http://www.forrester.com/File+Storage+Costs+Less+In+The+Cloud+Than+InHouse/fulltext/-/E-162RES36696?objectid%4RES57696>.
3. Accenture. Accenture cloud computing accelerator. 2009. http://www.accenture.com/SiteCollectionDocuments/PDF/Accenture_Technology_Labs_Cloud_Computing_Accelerator.pdf.
4. Boruff B. Computer sciences corporation. Doing business in the cloud. 2009. <http://assets1.csc.com/dk/downloads/DoingBusinessInTheCloud.pdf>.
5. Hosseini AK, Greenwood D, Sommerville I. Cloud migration: a case study of migrating an enterprise IT system to IaaS. In: 3rd international conference on cloud computing (IEEE CLOUD 2010). Washington, DC: IEEE Computer Society; 2010. pp. 450–7.
6. Sriram I, Hosseini AK. Research agenda in cloud technologies. Technical Report. 2010. <http://arxiv.org/ftp/arxiv/papers/1001/1001.3259.pdf>.

7. Assuncao M, Costanzo A, Buyya R. Evaluating the cost-benefit of using cloud computing to extend the capacity of clusters. In: 18th ACM international symposium on high performance distributed computing (HPDC '09), Munich. 2009. pp. 141–50.
8. Calheiros RN, Ranjan R, Beloglazov A, Rose CAFD, Buyya R. CloudSim: A toolkit for modeling and simulation of cloud computing environments and evaluation of resource provisioning algorithms. *Software Pract Exper*. 2011;41(1):23–50.
9. Deelman E, Singh G, Livny A, Berriman B, Good J. The cost of doing science on the cloud: the Montage example. In: ACM/IEEE conference on supercomputing (SC'08), Oregon, USA. 2008. pp. 1–12.
10. Kondo D, Javadi B, Malecot P, Cappello F, Anderson DP. Cost-benefit analysis of Cloud Computing versus desktop grids. In: IEEE XPLORÉ international symposium on parallel & distributed processing. *IEEE Xplore*; 2009. pp. 1–12.
11. Walker E. The real cost of a CPU hour. *Computer*. 2009;42(4):35–41.
12. Walker E, Brisken W, Romney J. To lease or not to lease from storage clouds. *Computer*. 2010;43:44–50.
13. Pilevari N, Eshlaghy AT, Sanaei M. A framework for evaluating cloud computing user's satisfaction in information technology management. *Int J Manage Bus Res*. 2011;1(4):231–40.
14. Allan R. Cloud and Web 2.0 resources for supporting research. 2012. <http://tyne.dl.ac.uk/NWGrid/Clouds/>.
15. Pepitone J. Amazon EC2 outage downs Reddit, Quora. CNN. 2011. http://money.cnn.com/2011/04/21/technology/amazon_server_outage/index.htm.
16. Alhamad M, Dillon T, Chang E. Trust-evaluation metric for cloud applications. *Int J Mach Learn Comput*. 2011;1(4):416–21.
17. Aumueller D. IT-compliance analysis for cloud computing, M.Sc. dissertation, Faculty of Computer Science, University of Applied Sciences Darmstadt. 2010. <http://germany.emc.com/collateral/about/news/emc-publications/articles/it-compliance-analysis-for-cloud-computing-dirk-aumueller.pdf>.
18. Chen D, Zhao H. Data security and privacy protection issues in cloud computing. In: International conference on computer science and electronics engineering. *IEEE Xplore*; 2012. pp. 647–51.
19. Chowhan S, Saxena R. Customer relationship management from the business strategy perspective with the application of cloud computing. *The Proceedings of DYNAA*. 2011;2(1):28–38.
20. Xue J, Zhang J-J. A brief survey on the security model of cloud computing. In: Ninth international symposium on distributed computing and applications to business, engineering and science. *IEEE*; 2010. pp. 475–8.
21. Khazaei H, Mi J, Mi VB. Performance analysis of cloud computing centers. In: Proceedings of the seventh international ICST conference on heterogeneous networking for quality, reliability, security and robustness (QShine). 2010.
22. Xiong K, Perros H. Service performance and analysis in cloud computing. In: Proceedings of the IEEE world conference services, *IEEE Xplore*. 2009. pp. 693–700.
23. Yang B, Tan F, Dai Y, Guo S. Performance evaluation of cloud service considering fault recovery. In: Proceedings of the first international conference on cloud computing. Berlin: Springer; 2009. pp. 571–6.
24. Abbadi M. Self-managed services conceptual model in trustworthy clouds' infrastructure. workshop on cryptography and security in clouds. 2011. <http://www.zurich.ibm.com/~cca/csc2011/submissions/abbadi.pdf>.
25. Ristola J. Information technology service management for cloud computing. M.Sc. dissertation, Aalto University School of Science and Technology. 2010. <http://lib.tkk.fi/Dipl/2010/urn100243.pdf>.
26. Ness LR. Assessing the relationships among information technology flexibility, strategic alignment, and information technology effectiveness. *J Inf Technol Manage Assoc Manage*. 2005;16(2):1–17.

27. Costa P, Lourenço JC, Silva M. Evaluating cloud services using a multiple criteria decision analysis approach. In: 11th international conference on service-oriented computing, ICSOC 2013, Berlin, Germany. Berlin: Springer; 2013. pp. 456–64.
28. Tallon PP, Kraemer KL, Gurbaxani V. Executives' perceptions of the business value of information technology: a process-oriented approach. *J Manage Inf Syst.* 2000;16(4):145–73.
29. Albrecht JP. Draft Report on the proposal for a regulation of the European Parliament and of the Council on the protection of individual with regard to the processing of personal data and on the free movement of such data (General Data Protection Regulation). J. a. H. A. Committee on Civil Liberties (ed.). 2012. <http://www.europarl.europa.eu/sides/getDoc.do?pubRef=-%2F%2FEP%2F%2FTEXT%2BREPORT%2BA7-2013-0402%2B0%2BDOC%2BXML%2BV0%2F%2FEN&language=EN>.
30. Bauer E, Adams R. Reliability and availability of cloud computing. Hoboken, NJ: Wiley-IEEE Press; 2012. p. 352.
31. Armbrust M, Fox A, Griffith R, Joseph AD, Katz R, Konwinski A, et al. A view of cloud computing. *Communications of the ACM.* 2010;53(4):50–8.
32. Cisco Systems, Inc., Cisco IOS IP SLAs configuration guide. 2008. http://www.cisco.com/en/US/docs/ios/12_4/ip_sla/configuration/guide/hsla_c.html.
33. Chen ChT, Hung WZ, Lin KH, Cheng HL. An evaluation model of service quality by applying linguistic TOPSIS method. In: IEEE/INFORMS international conference on service operations, logistics and informatics. IEEE Xplore; 2009. pp. 335, 340.
34. Service Level Agreement Zone (DT): an outline of the core elements of an SLA. 2014. <http://www.sla-zone.co.uk/>

Chapter 90

Coordination Strategies in a Cloud Computing Service Supply Chain Under the Duopoly Market

Lingyun Wei, Xiaohan Yang, and Xiaoguang Zhou

Abstract Nowadays, cloud computing has become a very hot topic in the IT industry. We study a cloud computing service supply chain consisting of one application infrastructure provider (AIP) and two competing application service providers (ASPs). As a result of longitudinal and transverse competitions, the efficiency of integration is always difficult to achieve in the distributed cloud computing service supply chain. Therefore, how to coordinate the cloud computing service supply chain under the duopoly market to achieve the efficiency of integration is of great importance to the cloud computing industry. We develop and evaluate four situations. We analyze the reasons that the wholesale price contract and revenue-sharing contract can't achieve coordination effectively and propose all-quantity discount contract.

Keywords Cloud computing • Service supply chain • Coordination strategies • Bertrand competition • Duopoly market

90.1 Introduction

Cloud computing has been expanded so rapidly in recent years. According to Rebollo and Mellado [1], cloud computing is a model for enabling convenient, on-demand network access to a shared pool of configurable computing resources that can be rapidly deployed and released with minimal management effort. Based on the above definition, cloud computing can be composed of three service models: Infrastructure as a Service (IaaS), Platform as a Service (PaaS), and Software as a Service (SaaS) [2].

With the information technology developed rapidly in the world, cloud computing has become a very hot topic in the IT industry. Many scholars do a lot of

L. Wei • X. Yang (✉) • X. Zhou

School of Automation, Beijing University of Posts and Telecommunications, 100876 Beijing, China

e-mail: weilingyun2010@sina.com; yangxiaohan2101@163.com; zxg@bupt.edu.cn

© Springer International Publishing Switzerland 2015

W.E. Wong (ed.), *Proceedings of the 4th International Conference on Computer Engineering and Networks*, Lecture Notes in Electrical Engineering 355,
DOI 10.1007/978-3-319-11104-9_90

777

research focusing on this field. Toka, Aivazidou, and Antoniou [3] are the advanced group of scholars who study cloud computing in the supply chain management. They address an overview of cloud-based supply chain management. However, there has been relatively little research conducted that studies the coordination strategies in a cloud computing service supply chain. Demirkan and Cheng [4] are the first group of scholars who study the ASP strategies. They discuss the supply chain coordination strategies and analyze a monopolistic ASP's optimal pricing and capacity policies considering the delay cost of users. Kar and Rakshit [5] evaluate the cloud computing service pricing models and contract terms, and they point out that the per transaction charge is the most common way of charging the cloud computing service in industry. We also charge the ASP services by this method. But neither of them had a discussion about the other actor of the cloud computing service supply chain—AIP. Moreover, previous studies about the supply chain coordination are more based on one AIP and one ASP. Demirkan and Cheng [6] study coordination strategies in an SaaS supply chain consisted of one AIP and one ASP. They propose that it is possible to create the right incentives so that the economically efficient outcome is also the Nash equilibrium. However, their works mentioned above don't involve the horizontal completion between two ASPs. We analyze duopolistic price competition of two ASPs by considering the impact of congestion cost. Our model is more in line with the reality of the cloud market.

In this paper, we design a cloud computing service supply chain consisting of one AIP and two competing ASPs. AIP provide packages the computer capacity as services and supplies them to ASPs, and in turn ASPs sell the same value-added application services to the common market via the Internet. We consider two ASPs who sell their same value-added services to the common market and compete for customers.

90.2 The Model of the Cloud Computing Service Supply Chain

We attempt to research the coordination strategies of the cloud computing service supply chain. We assume that there is full information, and AIP and ASPs are risk neutral. Supply chain contacts in our article are by Cachon [7]. The following sequence of events occurs in the Stackelberg Game: the AIP dominates the cloud computing service supply and plays the leading role. The AIP offers two ASPs the same contact; as a follower, the ASP $_i$, $i = 1, 2$, accepts or rejects the contact; assuming the ASP $_i$ accepts the contract, the ASP $_i$ submits a computer capacity order quantity, μ_i , to the AIP; the AIP must provide computer capacities to the ASP $_i$ on demand; and finally transfer payments are made among the players based on the agreed contract.

At the same time, we assume that there are only two ASPs sharing the market of services provided by two ASPs, and the market can be regard as a duopoly market.

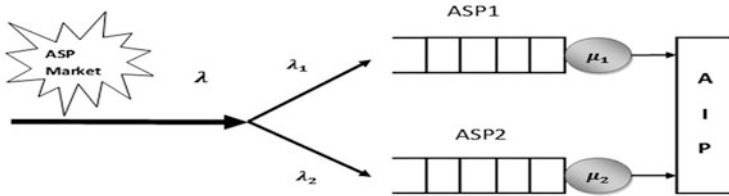


Fig. 90.1 The ASP duopoly market

In this case, the Bertrand competition model [8] is used to characterize the competitive relationship between two ASPs.

The AIP provides the IaaS to two ASPs at wholesale price w per unit of capacity. In turn the ASP $_i$ sells its SaaS to the market at price p_i per transaction of processing. The ASP $_i$ service system is modeled as an M/M/1 queuing system with processing capacities μ_i in transactions per unit of time, and λ_i is a Poisson rate of transactions per unit of time arriving at the ASP $_i$ system. We assume that λ is the market demand and one has

$$\lambda = \lambda_1 + \lambda_2, \quad \mu = \mu_1 + \mu_2 \tag{90.1}$$

$$\lambda_i \geq 0, \quad \mu_i \geq \lambda_i + \varepsilon \tag{90.2}$$

where $\varepsilon > 0$ is fixed and arbitrarily small. Figure 90.1 shows the ASP duopoly.

Two ASPs sell the same value-added application services to customers via the Internet. The Bertrand competition model is used to characterize the competitive relationship between two ASPs. We let $\lambda_i(p_1, p_2)$ be the market demand of ASP $_i$ ($j \neq i$):

$$\lambda_i(p_1, p_2) = \alpha - \beta p_i + m p_j, \quad 0 < m < \beta \tag{90.3}$$

where α , β , and m are constants; α_i is the market scale of ASP $_i$; β is the linear demand distribution parameter; and m is the substitutability coefficient of the services.

As a result of the queuing delay [9], let $T_{si}(\lambda_i, \mu_i)$ denote the expected time each transaction stays in the service system. The marginal cost of a customer is

$$p_i + vT_{si}(\lambda_i, \mu_i) \tag{90.4}$$

The marginal value of cloud computing services is represented by $V'(\lambda_i)$:

$$V'(\lambda_i) = \frac{\alpha}{\beta - m} - \frac{\beta \lambda_i + m \lambda_j}{(\beta - m)(\beta + m)} \tag{90.5}$$

When the market equilibrium is achieved, thus, one has

$$V'(\lambda_i) = \frac{\alpha}{\beta - m} - \frac{\beta\lambda_i + m\lambda_j}{(\beta - m)(\beta + m)} = p_i + vT_{si} \tag{90.6}$$

Hence, we get the market clearing price:

$$p_i = \frac{\alpha}{\beta - m} - \frac{\beta\lambda_i + m\lambda_j}{(\beta - m)(\beta + m)} - \frac{v}{\mu_i - \lambda_i} \tag{90.7}$$

90.3 Coordination Strategies of the Cloud Computing Service Supply Chain

90.3.1 Centralized Control

In this situation, a single firm plays an integrated role of one AIP and two competing ASPs. The supply chain can be coordinated and obtain the maximal profit. The per unit time expected profit of the whole supply chain SP_1 is

$$SP_1 = p_1\lambda_1 + p_2\lambda_2 - c(\mu_1 + \mu_2) - e\mu_1^2 - e\mu_2^2 \tag{90.8}$$

To find the whole optimal profit

$$\max_{\lambda_1, \lambda_2, \mu_1, \mu_2} SP_1 \tag{90.9}$$

The first-order conditions lead to

$$\frac{dSP_i(\lambda_i, \lambda_j, \mu_i, \mu_j)}{d\mu_i} = \frac{v\lambda_i}{(\mu_i - \lambda_i)^2} - c - 2e\mu_i = 0 \tag{90.10}$$

$$\frac{dSP_i(\lambda_i, \lambda_j, \mu_i, \mu_j)}{d\lambda_i} = \frac{\alpha}{\beta - m} - \frac{2\beta\lambda_i + 2m\lambda_j}{(\beta - m)(\beta + m)} - \frac{v\mu_i}{(\mu_i - \lambda_i)^2} = 0 \tag{90.11}$$

We find that $\lambda_1 = \lambda_2 = \frac{\lambda}{2}$, $\mu_1 = \mu_2 = \frac{\mu}{2}$ and $p_1 = p_2 = p_0$. Hence, solutions to the expressions above provide us the optimal arrival rate, λ^* ; the optimal capacity, μ^* ; and the optimal whole profit, SP_1^* .

90.3.2 Wholesale Price Contract

With a wholesale price contract, the AIP, ASP1, and ASP2 independently make decisions to pursue optimal profits. Let $HP_2(w)$, $AP_{2i}(P_i, \lambda_1, \mu_1)$ be the per unit time expected profits of the AIP and ASPi, respectively, and they can be described by

$$HP_2(w) = w(\mu_1 + \mu_2) - c(\mu_1 + \mu_2) - e\mu_1^2 - e\mu_2^2 \quad (90.12)$$

$$AP_{2i}(p_i, \lambda_i, \mu_i) = p_i\lambda_i - w\mu_i \quad (90.13)$$

In this case, the ASPi solves the following problem to find its optimal profit:

$$\max_{p_i, \lambda_i, \mu_i} AP_{2i} \quad (90.14)$$

The first-order conditions lead to

$$\frac{dAP_{2i}(\lambda_i, \mu_i)}{d\lambda_i} = \frac{\alpha}{\beta - m} - \frac{2\beta\lambda_i + m\lambda_j}{(\beta - m)(\beta + m)} - \frac{v\mu_i}{(\mu_i - \lambda_i)^2} = 0 \quad (90.15)$$

$$\frac{dAP_{2i}(\lambda_i, \mu_i)}{d\mu_i} = \frac{v\lambda_i}{(\mu_i - \lambda_i)^2} - w = 0 \quad (90.16)$$

If the wholesale price contract can coordinate the cloud computing service supply chain, under the premise that equations above are satisfied, we should enable Eqs. (90.10) and (90.11) to be valid. However, $\frac{dAP_{2i}(\lambda_i, \mu_i)}{d\lambda_i} = \frac{dAP_{2j}(\lambda_j, \mu_j)}{d\lambda_j} \neq \frac{dSP_i(\lambda, \mu)}{d\lambda}$. Hence, the wholesale price contract cannot coordinate the cloud computing service supply chain.

90.3.3 Revenue-Sharing Contract

In this situation, the ASPi shares to the AIP a percentage $(1 - \delta)$ of his/her revenue, so δ is the fraction of supply chain revenue the ASPi keeps. The profit function of AIP is

$$HP_3(p_1, p_2, \lambda_1, \lambda_2) = w(\mu_1 + \mu_2) - c(\mu_1 + \mu_2) - e\mu_1^2 - e\mu_2^2 + (1 - \delta)p_1\lambda_1 + (1 - \delta)p_2\lambda_2 \quad (90.17)$$

The profit function of ASPi is

$$AP_{3i}(p_i, \lambda_i, \mu_i) = \delta p_i \lambda_i - w \mu_i \quad (90.18)$$

In this case, the ASPi solves the following problem to find its optimal profit:

$$\max_{p_i, \lambda_i, \mu_i} AP_{3i} \quad (90.19)$$

The first-order conditions lead to

$$\frac{dAP_{3i}(\lambda_i, \mu_i)}{d\lambda_i} = \delta \left[\frac{\alpha}{\beta - m} - \frac{2\beta\lambda_i + m\lambda_j}{(\beta - m)(\beta + m)} - \frac{v\mu_i}{(\mu_i - \lambda_i)^2} \right] = 0 \tag{90.20}$$

$$\frac{dAP_{3i}(\lambda_i, \mu_i)}{d\mu_i} = \delta \frac{v\lambda_i}{(\mu_i - \lambda_i)^2} - w = 0 \tag{90.21}$$

If the revenue-sharing contract can coordinate the cloud computing service supply chain, under the premise that equations above are satisfied, we should enable Eqs. (90.10) and (90.11) to be valid. We find that $w = \delta(c + e\mu)$ and $\delta = \left[\frac{\alpha - \lambda}{\beta - m} - \frac{2v\mu}{(\mu - \lambda)^2} \right] / \left[\frac{\alpha}{\beta - m} - \frac{2\beta\lambda + m\lambda}{2(\beta - m)(\beta + m)} - \frac{2v\mu}{(\mu - \lambda)^2} \right]$. However, after illustrating the results by numerical examples, we find that only when δ tends to zero can the supply chain be coordinated. In other words, the ASPi shares so little profit that it refuses this revenue-sharing contract. So the revenue-sharing contract can't coordinate the cloud computing service supply chain.

90.3.4 All-Quantity Discount Contract

We investigate whether an all-quantity discount strategy coordinates a supply chain with one AIP and two competing ASPs. Let $w(\mu_i)$ be the AIP's wholesale price:

$$w(\mu_i) = \begin{cases} w_0, & \mu_i < \mu^* \\ w_4^*, & \mu_i \geq \mu^* \end{cases} \tag{90.22}$$

The profit function of ASPi is

$$AP_{4i}(p_i, \lambda_i, \mu_i) = p_i\lambda_i - w(\mu_i)\mu_i \tag{90.23}$$

The profit function of the whole supply chain is

$$SP_4 = p_1\lambda_1 + p_2\lambda_2 - c(\mu_1 + \mu_2) - e\mu_1^2 - e\mu_2^2 \tag{90.24}$$

Assuming that the revenue of ASPi is a constant proportion of SP_4 , we have

$$AP_{4i} = \eta_i SP_4, \quad 0 < \sum \eta_i < 1 \tag{90.25}$$

We assume $\eta_1 = \eta$ and find that

$$\eta_1 = \eta_2 = \eta \tag{90.26}$$

$$w(\mu_i) = \begin{cases} w, \mu_i < \frac{\mu^*}{2} \\ \frac{[p_0\lambda^* - 2\eta(p_0\lambda^* - c\mu^* - 0.5e\mu^{*2})]}{\mu^*}, \mu_i \geq \frac{\mu^*}{2} \end{cases} \tag{90.27}$$

$$\eta SP_4 \geq AP_{11} = AP_{12} \tag{90.28}$$

As a result of the flexibility in the profit distribution, the all-quantity discount contract ensures that participation constraints of AIP and ASPs can be satisfied when the system performance achieves the optimal. So, the supply chain can be coordinated.

90.4 Numerical Examples

In this part, we select a set of parameters (see Table 90.1) to illustrate whether the contracts can coordinate the cloud computing service supply chain under the duopoly market. After some calculation, we can get the computed results in Table 90.2. We can find that the maximal supply chain expected profit is 3.2447. In other words, when the expected profit can reach 3.2447 with one supply chain contract, we can deem that this contract can coordinate the cloud computing service supply chain. Obviously, the revenue-sharing contract and all-quantity

Table 90.1 Baseline parameters

<i>c</i>	<i>α</i>	<i>v</i>	<i>e</i>	<i>β</i>	<i>m</i>
1.00	3.00	0.025	1.00	1.00	0.50

Table 90.2 Computed results

	Centralized	Wholesale price	Revenue sharing	All-quantity discount
λ_1	0.7557	0.9740	0.7557	0.7557
λ_2	0.7557	0.9740	0.7557	0.7557
λ	1.5114	1.9480	1.5114	1.5114
μ_1	0.8397	1.0727	0.8397	0.8397
μ_2	0.8397	1.0727	0.8397	0.8397
μ	1.6794	2.1454	1.6794	1.6794
P_1	4.1908	3.7987	4.1908	4.1908
P_2	4.1908	3.7987	4.1908	4.1908
P_0	4.1908	3.7987	4.1908	4.1908
δ	—	—	0	—
η	—	—	—	0.32
<i>w</i>	—	2.5	0	2.5352
HP	—	0.9167	3.2447	1.1681
AP ₁	—	1.0182	0	1.0383
AP ₂	—	1.0182	0	1.0383
SP	3.2447	2.9531	3.2447	3.2447

discount contract can satisfy the above conditions. However, we can find that only when δ tends to zero can it make the supply chain be coordinated under revenue-sharing contract. This implies that the ASPi rarely shares the profit, so this revenue-sharing contract can't be accepted. We can draw a conclusion that the revenue-sharing contract can't really coordinate the supply chain. On the other hand, we assume that w is 2.5 with the wholesale price contract, and we can find that the whole supply chain expected profit is 3.2447. It shows that the all-quantity discount contract can coordinate the cloud computing service supply chain. Moreover, the profits of AIP and the two ASPs are not lower than the profits when they don't accept this contract where the parameter η is between 0.3138 and 0.3587. We illustrate the results by numerical examples.

Conclusion

In this article, we aim to coordinate a two-staged cloud computing service supply chain consisting of an AIP and two competing ASPs. We examine four coordination strategies above. After analyzing the reasons that the wholesale price contract and revenue-sharing contract can't achieve coordination effectively, we propose all-quantity discount contract. As a result of the flexibility in the supply chain profit distribution, the all-quantity discount contract ensures that participation constraints of one AIP and two competing ASPs can be satisfied when the system performance achieves the optimal. Ultimately, we reach the conclusion that the all-quantity discount contract can coordinate the cloud computing service supply chain.

Acknowledgements This work is supported by the Natural Key Technology R&D Program of the Ministry of Science and Technology of China (No. 2014BAH24F02). This work is also supported by the Engineering Research Center of Information Networks, Ministry of Education. This work is partly supported by the Natural Public Industry (Food) Special Funds for Scientific Research (No. 201313009-08).

References

1. Rebollo O, Mellado D, Fernández-Medina E. A systematic review of information security governance frameworks in the cloud computing environment. *J UCS*. 2012;18(6):798–815.
2. Latif R, Haider A, Saïd A, Qasim A. Cloud computing risk assessment: a systematic literature review. In: *Future information technology*. Berlin: Springer; 2014. pp. 285–95.
3. Toka A, Eirini A, Antonios A, Konstantinos AD. Cloud computing in supply chain management. In: *E-logistics and e-supply chain management: applications for evolving business*, 2013. pp. 218–309.
4. Demirkan H, Cheng HK. The risk and information sharing of application services supply chain. *Eur J Oper Res*. 2008;187(3):765–84.
5. Kar AK, Rakshit A. Pricing of cloud IaaS based on feature prioritization—a value based approach. In: *Recent advances in intelligent informatics*. Springer; 2014. pp. 321–30.

6. Demirkan H, Cheng HK, Bandyopadhyay S. Coordination strategies in an SaaS supply chain. *J Manage Inform Syst.* 2010;26(4):119–43.
7. Cachon GP. Supply chain coordination with contracts. *Handbooks in Operations Research and Management Science.* 2003;11:227–339.
8. Bertrand J. Review of Walras's "Théorie Mathématique de la richesse sociale" and Cournot's "Recherches sur les principes mathématiques de la théorie des richesses", translated into English by James W. Friedman. Cambridge: Cambridge University Press; 1988.
9. Mendelson H. Pricing computer services: queueing effects. *Commun ACM.* 1985;28(3):312–21.

Chapter 91

A Novel Approach to Trust-Aware Service Recommendation

Guoqiang Li, Lejian Liao, Dandan Song, Zhenling Zhang,
and Jingang Wang

Abstract The cloud computing paradigm has received more and more attention in both industry and academia. Its important premise is to select reliable services to meet user requirements. Following the recommendation technology applied to service selection, a trust relationship between users of social networks is adopted. However, users' similarity is only computed on the basis of ratings by users on services. For this shortcoming, a similarity to the trust ratings among users is proposed in our approach where distrust information is also considered. A novel recommendation algorithm is presented. Finally, the Epinions data set is used to validate our method. Experimental results show the effectiveness of our approach.

Keywords Cloud computing • Service recommendation • Web service • Social network

91.1 Introduction

Cloud computing mainly includes several services levels: infrastructure as a service (IaaS), platform as a service (PaaS), and software as a service (SaaS) [1]. This paradigm has different levels of significance for different users, e.g., a single service may be invoked by a terminal user, and many single services (mashups) may be invoked to achieve a complex task by a developer. Choosing a reliable or trusted service from services that possess the same functions is an important issue.

Collaborative filtering (CF), a well-known technology, is used to recommend movies and services [2]. CF is most effective when users have given enough ratings to have common ratings with other users, but it seems inadequate to cope with the

G. Li
Beijing Institute of Technology, 100081 Beijing, China
School of Informatics, Linyi University, 276000 Linyi, China
L. Liao • D. Song (✉) • Z. Zhang • J. Wang
Beijing Institute of Technology, 100081 Beijing, China
e-mail: sdd@bit.edu.cn

cold-start beginning user and sparse data questions [3]. For these shortcomings, the social network is explored to make recommendations as long as a new user is connected to others in this network. A key question is how to construct the trust network. Another key issue is how to integrate the trust information into the recommender system. To solve these questions, we propose a comprehensive solution based on existing works. The main contributions of this paper include the following: (1) to find more users who are similar to a given user, we first propose to explore the user–user trust rating similarity that is incorporated into CF. It is worth emphasizing that distrust information is considered; (2) a new concept, *trusted degree*, is defined to find a similar set for one user.

91.2 Related Work

To realize a service recommendation, CF has been adopted in many works where QoS prediction is the key issue, for example, [4]. Usually, the value of the QoS factor is objective, which is different from the rating that a user gives to an item or product on some web site. To generalize, we take one item as a service. A trust-aware recommender system (RS) architecture is proposed to show that trust awareness can solve some of the traditional problems of RSs [3]. FilmTrust uses the trust values of people who have rated a film as a recommended rating in semantic Web-based social networks [5]. A trust factor model is proposed to determine a user's trust factor value. Then a harmonic weight is designed to combine with the traditional RS to calculate the trust value [6]. The T-Man algorithm is used to cluster similar users together using a variation of Pearson similarity as a distance metric [7]. Two different trust models are developed: one based on profile-level trust, the other on item-level trust. Then three ways are described to incorporate the trust values into a standard collaborative filtering algorithm [8]. A multi-criteria trust-enhanced CF recommendation is developed where each item is described using a different set of criteria [9]. Even though trust is employed [10], direct neighbors of the target user are only used; nonadjacent users are disregarded.

A trust-network reconstructed algorithm is proposed that removes statements between users where the similarity between the users falls below a set threshold correlation. Three weightage schemes for rating predictions are proposed and compared [11]. The group relationship is given in the trust network. Then two combination methods for formulating trust metric and similarity metric are given [12]. A linear combination model is proposed using an enhanced PCC similarity and raising the product of trust degree on a trust path to compute nonadjacent users' trust value [13]. The network flow theory is used to model a trust graph that considers the trust and confidence levels as two trust factors [14]. A random walk method is used to combine trust-based and item-based recommendations, and the confidence in the predictions is introduced [15]. A distributed algorithm to build a trust network classifies a user's neighbors on the basis of their social distance and

defines neighbors' priority based on their topic-related degree and target-related degree [16].

In their analyses, the aforementioned works do not consider distrust information about users in a social network. Distrust is incorporated first in trust propagation [17]. For a recommendation application, the notion that distrust can play an important role is discussed first [18]. Three new strategies are then described where distrust is taken to have three roles: as an indicator to reverse deviations, as a filter, and as a debugger of a web of trust [19]. A user's distrust relations are interpreted as *dissimilar* relations [20]. Ratings are predicted using both explicit trust and propagated trust using the proposed trust-with-distrust models by setting the maximum propagation distance at two [21]. In this paper, the approach is similar to that in [21], which uses distrust information to enhance the prediction quality, but the distrust information is used in a different way.

91.3 Recommendation Framework

In recommendation systems, there are two basic sets: users $U = \{u_1, u_2, \dots, u_m\}$ and items (services used as synonyms) $S = \{s_1, s_2, \dots, s_n\}$. A rating matrix expresses the ratings on items by users. $R = [r_{u,i}]_{m \times n}$ where $r_{u,i}$ denotes the rating of user u on item i . Usually, the rating value is in the range [1, 5] which denotes different rating levels. After introducing the trust network of users, a trust rating matrix $T = [T_{u,v}]_{m \times m}$ is formed by each user u giving the ratings to his direct neighbors. These two matrixes are important and independent inputs to a recommender system.

91.3.1 Similarity of User–User Trust Rating

The typical collaborative filtering technology first computes the similarity of a pair of users employing the method; for example, the Pearson correlation coefficient (PCC) is shown by Eq. (91.1):

$$S_{a,u} = \frac{\sum_{i=1}^m (r_{a,i} - \bar{r}_a) \times (r_{u,i} - \bar{r}_u)}{\sqrt{\sum_{i=1}^m (r_{a,i} - \bar{r}_a)^2 \sum_{i=1}^m (r_{u,i} - \bar{r}_u)^2}}, \quad (91.1)$$

where m denotes the number of services rated by users a and u , and \bar{r}_a and \bar{r}_u denote the average value of services rated by a and u , respectively. The final prediction equation is Eq. (91.2):

$$p_{a,i} = \bar{r}_a + \frac{\sum_{k=1}^m s_{a,k} \times (r_{k,i} - \bar{r}_k)}{\sum_{k=1}^m s_{a,k}}. \tag{91.2}$$

To our knowledge, we are the first to explore user-user trust rating similarities $TS_{u,v}$. Intuitively speaking, we think that two users' trust ratings are very similar when they have a rating similar to the same user set. That is to say, we pay more attention to the subjective character of trust. Formally, for u_i , $U^i = (u_1^i, u_2^i, \dots, u_k^i)$ is the user set who u^i rated. Then the corresponding rating vector is denoted by $TR^i = (tr_1^i, tr_2^i, \dots, tr_k^i)$. Given two users u_i and u_j , we propose using the PCC to compute the trust similarity:

$$TS_{i,j} = \frac{\sum_{k=1}^m (r_{i,k} - \bar{r}_i) \times (r_{j,k} - \bar{r}_j)}{\sqrt{\sum_{k=1}^m (r_{i,k} - \bar{r}_i)^2 \sum_{k=1}^m (r_{j,k} - \bar{r}_j)^2}}. \tag{91.3}$$

Thus, when $s_{a,u}$ is replaced by $TS_{a,k}$, Eq. (91.2) is transformed into Eq. (91.4):

$$p_{a,i} = \bar{r}_a + \frac{\sum_{k=1}^m TS_{a,k} \times (r_{k,i} - \bar{r}_k)}{\sum_{k=1}^m TS_{a,k}}. \tag{91.4}$$

Finally, based on Eqs. (91.2) and (91.4), a general equation is proposed:

$$p_{a,i} = \bar{r}_a + \frac{\sum_{k=1}^m GS_{a,k} \times (r_{k,i} - \bar{r}_k)}{\sum_{k=1}^m GS_{a,k}}, \tag{91.5}$$

where $GS_{a,k}$ can be $s_{a,u}$ or $TS_{a,k}$ described by the following section:

$$GS_{a,k} = \begin{cases} S_{a,k} & \text{if}(S_{a,k} > TS_{a,k}) \\ TS_{a,k} & \text{if}(TS_{a,k} > S_{a,k}) \end{cases}. \tag{91.6}$$

i.e., their maximum is adopted, or

$$GS_{a,k} = \alpha S_{a,k} + \beta TS_{a,k}, \quad (91.7)$$

i.e., their linear combination, $\alpha + \beta = 1$.

91.3.2 Trust-Aware Recommendation Implementation

We introduce a new quantization factor, trusted degree (TD), which helps to calculate the trust value between two nonadjacent users. The equation used to calculate TD is as follows:

$$TD_u = \frac{\text{Num}_u^+}{\text{Num}_u}, \quad (91.8)$$

where Num_u^+ is the number of all users who trust u , and Num_u is the number of users who give their trust level with respect to u . We choose the maximum trust among all paths between two users.

Input: user-service rating matrix(R), user-user trust matrix(T)

output: MAE, RMSE

1. For each user u_k , ($u_k \in S_u$)
2. For each other user u_s , ($u_s \in S_u$)
3. finding the items set rated by two users, compute the similarity using equation (1)
4. finding the users set rated by two users, compute the trust similarity using (3) or (4)
5. End for
6. End for
7. For each service s_i ,
8. finding the user set S_{ui} rating this service
9. For each user $u_j \in S_{ui}$, $u_k \in S_{ui}$
10. compute the predicted value P_{pcc} using equation (2)
11. compute the predicted value P_{is} using equation (9)
12. End for
13. End for

Two metrics, mean absolute error (MAE) and root-mean-squared error (RMSE), will be used to measure the prediction quality of our proposed approach.

In this algorithm, the data preprocessing part is from lines 1 to 6. The prediction part is in lines 7–14. The time complexity of the first part is $O(m(m+n))$ since most m users will be trusted by one user and most n services invoked by a user. The second one is $O(m \times n)$. In practice, m is much larger than n . So the time complexity of this algorithm is $O(m^2)$.

91.4 Experiment

We use the extended Epinions data set in our experiments. There are 132,000 users, 1,560,144 articles, and 841,372 statements (717,667 trusts and 123,705 distrusts). Considering the run time, we also use only the top 1,000 users that have the largest number of trust and distrust relationships in [21]. These experiments were performed on an Inter Core i5 CPU (3.2 GHz) with 4 GB of RAM running Windows 7. The trust value is 1 or -1 , where negative one means distrust and positive one means full trust.

91.4.1 Performance Comparisons

To measure RS performance, we use the leave-one-out method, which consists in hiding a rating and trying to predict its hidden value. We first compare the recommendation results with those of the following methods:

- CF: the classic collaborative filter used to predict missing values.
- Trust-distrust: our proposed method, which makes use of Eq. (91.7).
- Trust: using the trust value to replace users' similarities [3].

Table 91.1 presents the results. From the results we observe that our methods consistently outperform the CF on the MAE and RMSE using this data set. But the “trust” method performs the best. After analyzing our data, we find that approximately 98 % of the user ratings equal 1. A realistic situation is that each user has two similar users who have both co-users and co-items at the same time. Thus, this test result may not be suitable if one user has many similar users.

91.4.2 Impact of Trusted Numbers of One User

We set the different number of users (TSN) who are trusted by a user from more than 30–120. In Figs. 91.1 and 91.2, the MAE and RMSE have an overall downward trend affected by the number of users. But when the number of trusted users is 90, their values are abnormal. In other words, their values are higher than that of TSN 60. Analyzing the data, we find that 40 % of users' trust similarities is smaller than 0.99 when TSN is 90, while 72 % of users' trust similarities is smaller than 0.99 when TSN is 60.

Table 91.1 Performance comparisons

	CF	Trust-distrust	Trust
MAE	0.1388	0.1323	0.0736
RMSE	0.3028	0.2928	0.1667

Fig. 91.1 MAE impacted by TSN

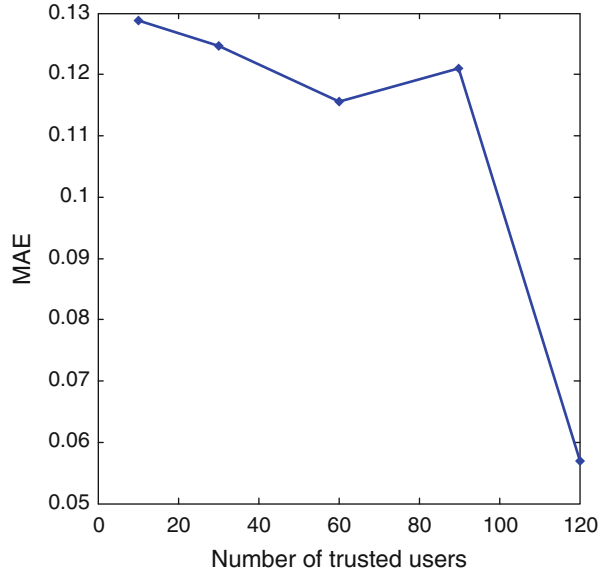
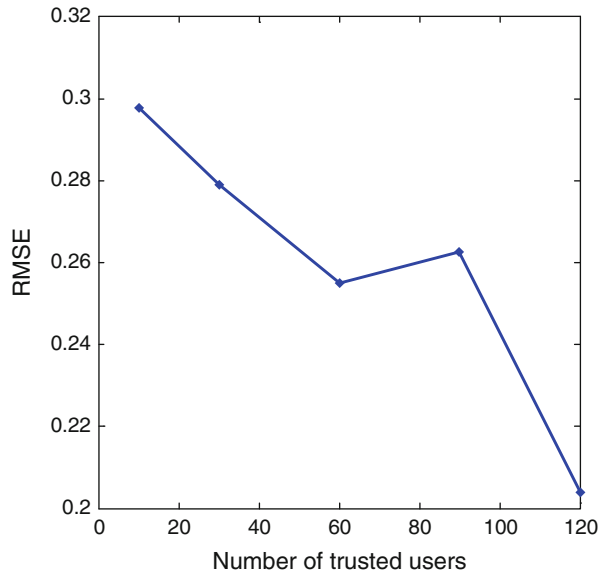


Fig. 91.2 RMSE impacted by TSN



Conclusion and Future Work

In this paper, we proposed to explore user-user rating similarities to enhance the recommendation accuracy. In the trust network construction, we introduced the notion of *trusted degree* to compute the trust value between two nonadjacent users. The experiments were conducted and the results validated our proposed method's effectiveness. Our work may provide some insights to researchers using the same data set.

As an initial research project, we conducted the experiments with a relatively small data set to test the proposed approach. The next task will be to do more tests with more data. Last but not least, we will consider combining matrix factorization with a constructed trust network to enhance recommendation accuracy.

Acknowledgments This work was funded by the National Program on Key Basic Research Project (973 Program, Grant 2013CB329605), National Natural Science Foundation of China Grants 61003168, 61100078, 61100172, the Natural Science Foundation of Shandong Province (ZR2011FL014).

References

1. Vaquero L, Rodero-Merino L. A break in the clouds: towards a cloud definition. *ACM SIGCOMM Comput Commun Rev.* 2008;39(1):50–5.
2. Manikrao US. Dynamic selection of web services with recommendation system. *International Conference on Next Generation Web Services Practices.* Seoul, Korea: IEEE Computer Society; 2005. p. 1–5.
3. Massa P, Avesani P. Trust-aware collaborative filtering for recommender systems. *Federated International Conference on the Move to Meaningful Internet: CoopIS, DOA, ODBASE, Volume 3290, Agia Napa, Cyprus.* New York: Springer; 2004. p. 492–508.
4. Yu Q, Zheng Z, Wang H. Trace norm regularized matrix factorization for service recommendation. In: *International Conference on Web Services.* Santa Clara: IEEE Computer Society; 2013. p. 34–41.
5. Golbeck J, Hendler J, Park C. FilmTrust: movie recommendations using trust in web-based social networks. *Consumer Communications and Networking Conference;* 2006. Las Vegas: IEEE Computer Society; 2006. p. 282–6.
6. Guo Y, Cheng X, Dong D. An improved collaborative filtering algorithm based on trust in E-commerce recommendation systems. *International Conference on Management and Service Science.* Wuhan: IEEE; 2010. p. 1–4.
7. Maguireanu S, Dokoohaki N, Mokarizadeh S, Matskin M. Epidemic trust-based recommender systems. In: *International Conference on Privacy, Security, Risk and Trust and International Conference on Social Computing.* Minneapolis: IEEE Computer Society; 2012. p. 461–70.
8. O'Donovan J, Smyth B. Trust in recommender systems. In: *International Conference on Intelligent User Interfaces.* San Diego: ACM; 2005. p. 167–74.
9. Shambour Q, Lu J. Integrating multi-criteria collaborative filtering and trust filtering for personalized recommender systems. In: *IEEE Symposium on Computational Intelligence in Multicriteria Decision-Making.* Paris: IEEE; 2011. p. 44–51.

10. He J, Chu WW. A social network-based recommender system (SNRS). *Data Min Soc Netw Data Ann Inf Syst.* 2010;12:47–74.
11. Ray S, Mahanti A. Improving prediction accuracy in trust-aware recommender systems. In: *International Conference on System Sciences*. Koloa: IEEE Computer Society; 2010. p. 1–9.
12. Gao Y, Xu B, Cai H. Information recommendation method research based on trust network and collaborative filtering. In: *International Conference on e-Business Engineering*. Beijing: IEEE Computer Society; 2011. p. 386–91.
13. Tang M, Xu Y, Liu J, Zheng Z, Liu XF. Trust-aware service recommendation via exploiting social networks. In: *International Conference on Services Computing*. Santa Clara: IEEE Computer Society; 2013. p. 376–83.
14. Wang G, Wu J. FlowTrust: trust inference with network flows. *Front Comput Sci China.* 2011;5(2):181–94.
15. Jamali M. TrustWalker: a random walk model for combining trust-based and item-based recommendation. In: *International Conference on Knowledge Discovery and Data Mining*. Paris: ACM; 2009. p. 1–9.
16. Jiang W, Wang G. SWTrust: generating trusted graph for trust evaluation in online social networks. In: *International Conference on Trust, Security and Privacy in Computing and Communications*. Changsha: IEEE Computer Society; 2011. p. 320–7.
17. Guha R, Kumar R. Propagation of trust and distrust. In: *International Conference on World Wide Web*. New York: ACM; 2004. p. 403–12.
18. Victor P, Cornelis C, De Cock M, Krijgslaan S, Decock M. Enhanced recommendations through propagation of trust and distrust. In: *International Conference on Web Intelligence and Intelligent Agent Technology*. Hong Kong: IEEE Computer Society; 2006. p. 263–6.
19. Victor P, Cornelis C, Golbeck JA, Massa P, Avesani P, Donovan JO. Trust-and distrust-based recommendations for controversial reviews. *IEEE Intell Syst.* 2011;26(1):48–55.
20. Ma H, Lyu MR, King I. Learning to recommend with trust and distrust relationships. In: *ACM Conference on Recommender Systems*. New York: ACM; 2009. p. 189–96.
21. Victor P. Utility of distrust in online recommender systems. *Technique report*. Tacoma: University of Washington; 2010. p. 1–6.

Chapter 92

A Web Service Discovery Method Based on Data Segmentation and WordNet

Tingna Liu and Ling Jiang

Abstract The Web service infrastructure has been an important software component on the Internet. A critical step in Web service applications is the service discovery method. The structured information in the web services description language (WSDL) of a Web service is unsuitable when using the traditional information retrieval (IR) method. We propose a Web service discovery method that is based on extracting information from WSDL documents. The method employs data segmentation to analyze the information to a meaningful structure where the traditional IR techniques can be applied. Furthermore, WordNet has been exploited in this method to carry out a synonym search. The experiments show that our method represents a significant improvement in the performance of Web service discovery.

Keywords Web service discovery • Search engine • Lucene • WordNet

92.1 Introduction

A Web service is a self-containing and self-describing modular application that can be published, located, and invoked across the Web. The effective discovery technology in a Web service is of vital importance and is a critical issue in the development of Web services. Existing research in Web service discovery focuses on three main fields: text-based matching [1], semantic-based matching [2], and similarity cluster matching [3].

This paper presents a Web service discovery method that makes use of both extracting information from the web services description language (WSDL) by the web services description language for Java toolkit (WSDL4J) and establishing indexes by Lucene. To improve the accuracy of Web service searches, we employ a kind of data segment to parse the structured information of WSDL into human

T. Liu • L. Jiang (✉)

School of Resources and Environment, University of Electronic Science and Technology of China, 611731 Chengdu, China

e-mail: jiangl_sre@uestc.edu.cn

© Springer International Publishing Switzerland 2015

W.E. Wong (ed.), *Proceedings of the 4th International Conference on Computer Engineering and Networks*, Lecture Notes in Electrical Engineering 355,

DOI 10.1007/978-3-319-11104-9_92

797

natural language. In addition to segment processing, WordNet is also used to achieve a functional similarity to Web service discovery.

The paper is organized as follows. In Sect. 92.2, we present a method to extract information from Web services based on WSDL documents and build indexes by Lucene. In Sect. 92.2.4, we discuss how to incorporate the WordNet synonym thesaurus into Web service discovery. In Sect. 92.3, we describe a prototype system of Web service discovery and discuss the experimental results. The last section provides a conclusion.

92.2 Building Indexes for Web Services

92.2.1 *Extracting Information from Web Services*

Currently, the majority of Web services are described by WSDL1.1, which can be parsed by WSDL4J [4], which allows for the creation, representation, and manipulation of WSDL documents. In this paper, we extract the service address, service name, service operations, and I/O parameters from WSDL documents using WSDL4J.

92.2.2 *Segmentation Processing*

When using a Web services search engine, a service requester submits meaningful words, for example the word “weather,” as a keyword. WSDL is an XML-based language that is processed by a computer, in which most of the information is not described in a natural language. For example, take a service operation name—`getWeatherForecast()`—as an example; the service structured information is almost described as a compound word form in WSDL documents. Traditional information retrieval techniques will treat *getWeatherForecast* as a unit, leading to mismatch errors with the keyword “weather” in a Web service search. Apparently, some useful Web services could not be found because of this limitation.

In analyzing WSDL documents, we find that most Web service names accord with CamelCase notation. The CamelCase-format names of Web services can be separated easily into meaningful words, which is helpful to services requester for discovering potential Web services. Let us use again the Web service operation name `getWeatherForecast()` as an example. The CamelCase word *getWeatherForecast* will be segmented into three words—*get*, *weather*, and *forecast*. It seems like we are violating the Web service operation structure, but it actually makes sense in practice [5].

The use of segmentation processing may lead to a lower recall rate. Take the previous example of `getWeatherForecast()`; it is likely to result in redundant search

Table 92.1 Fields in an index document

Field	Store	Analysis
serviceName	Yes	Yes
operationName	Yes	Yes
ioType	Yes	Yes
Documentation	Yes	Yes
url	Yes	No

results because of the separation of weather and the forecast, Web services such as *financial forecast* or *sales forecast* may also be discovered in addition to *weather forecast* when *forecast* is submitted as a keyword. Selective keywords are needed to find a desired Web service in this case.

92.2.3 Building Indexes

Apache Lucene is an open source information retrieval software library, originally created in Java by Doug Cutting [6]. In this paper we build indexes for Web service information by Lucene. As shown in Table 92.1, five fields are created in an index document.

Lucene has a very complicated scoring mechanism. Lucene’s conceptual scoring formula is as follows [6]:

$$\text{score}(q, d) = \text{coord}(q, d) \times \text{queryNorm}(q) \times \sum_{t \text{ in } q} \left(\text{tf}(t \text{ in } d) \times \text{idf}(t)^2 \times t.\text{getBoost}() \times \text{norm}(t, d) \right). \tag{92.1}$$

The factor $\text{coord}(q, d)$, which depends on how many of the query terms are found in a specified document, is affected by the segmentation processing we used in the proposed method. $\text{norm}(t, d)$ encapsulates a few (indexing time) boost and length factors as follows:

$$\text{norm}(t, d) = d.\text{getBoost}() \times \text{lengthNorm}(\text{field}) \times \prod_{\text{field } f \text{ in } d} f.\text{getBoost}(). \tag{92.2}$$

The $\text{lengthNorm}(f)$ factor is of vital importance for our experiments; its formula is as follows:

$$\text{lengthNorm}(f) = \frac{1}{\sqrt{\text{num of terms in field } f}}. \tag{92.3}$$

The service name reflects the Web service’s function to some extent, which

should thus be given much more weight while matching Web service with keywords given by users. A relatively short service name usually contributes less to the score based on the Lucene scoring mechanism. The service operation is the same as the service name. We increase the service and operation names' weights as appropriate to highlight their importance when building an index document for Web service information. The default weights are 1.0 in Lucene, and we increased the weights of the fields *serviceName* and *operationName* by 2.0 and 1.5, respectively.

92.2.4 Introducing WordNet

As discussed in Sect. 92.2.2, the desired Web service is probably missed if a keyword mismatches with WSDL information in a Web services discovery. A refined keyword might be a solution in that case, whereas the Web service discovery has lost its universal significance. Moreover, the same semantic service could be described using synonymous words [7], creating more difficulties in syntactic rule-based Web service matching. For example, say a service name contains the word *car*, which can be matched to a keyword, but the service name contains the word *vehicle*, which cannot be matched with the same keyword [8].

WordNet is an English dictionary developed by researchers at Princeton University that differs from a regular dictionary in that it contains semantic information [9, 10]. In recent years, many researchers have incorporated WordNet into the discovery of Web services and obtained some notable results [11]. We can effectively solve the aforementioned problems, which caused by using synonymous words in Web service descriptions, by incorporating WordNet's synsets of synonyms into Web service discovery. There are 203,147 synonym records in the WordNet2.0 *ws_n.pl* file. We use *Syns2Index.java* to build a Lucene index of synonyms in order to improve search speed [12]. The search accuracy is improved in two ways with respect to retrieval processing—one for synonym retrieval and another for Web service matching.

92.3 Prototype System and Results Analysis

Data used in this paper are from Dr. Yilei Zhang's research results [13], including 3,738 WSDL files [14]. We use the JAVA language to extract Web service features in addition to using WSDL4J and Princeton WordNet.

To verify the performance of the method proposed in this paper, in our experiments, five words that are commonly used in Web services are selected as keywords: *email*, *weather*, *map*, *news*, *fund*.

Table 92.2 Four experiments designed based on whether segmentation or WordNet is used

	Experiment 1	Experiment 2	Experiment 3	Experiment 4
Segmentation	Yes	Yes	No	No
WordNet	Yes	No	Yes	No

92.3.1 Recall

The recall ratio of a Web search is reflected by the total number of search results (we use *hits* instead). We perform four groups of experiments based on whether word segmentation processing or WordNet synsets synonyms are used, as shown in Table 92.2.

The results are shown in Fig. 92.1a–c, where the vertical axis represents the total hits of the search results and the horizontal axis represents the five keywords we selected.

A comparison of the results of Experiments 1 and 2 is shown in Fig. 92.1a, from which we see the total hits of the keywords *map*, *news*, and *fund*, which increased significantly under WordNet. A comparison of Experiments 1 and 3 is shown in Fig. 92.1b, which illustrates that the total hits of all five keywords significantly increased under segmentation processing. A comparison of Experiments 1 and 4 is shown in Fig. 92.1c, which demonstrates a huge difference between incorporating or not incorporating segmentation processing and WordNet into Web service discovery.

Note that the hits of the keywords *email* and *weather* did not increase even when using WordNet. Actually, WordNet contains a limited collection of synonyms. To increase the accuracy and recall ratio, it is necessary to establish professional WordNet synonym libraries.

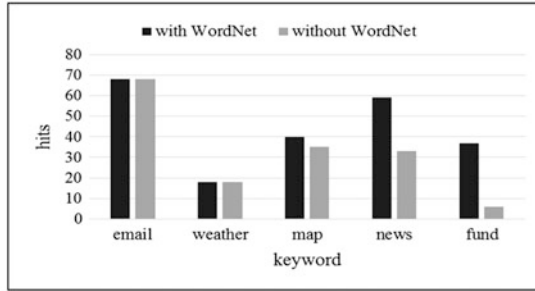
92.3.2 Precision

Precision is another feature of Web service discovery. In this subsection, we perform four sets of experiments depending on whether segmentation processing or WordNet is used, just as in Sect. 92.3.1.

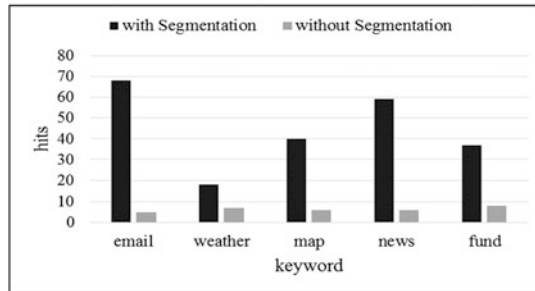
We choose the same five keywords as previously. The experimental results are shown in Fig. 92.2a–d, in which the vertical axis represents the precision reflected by scores of the results and the horizontal axis represents the top five results that best match the keywords.

A comparison of Fig. 92.2b, d shows that segmentation processing brings significantly improved performance with respect to the top five matches. A comparison of Fig. 92.2a, b shows that the scores from matching the keywords *news* and *map* decline with the use of WordNet synsets synonyms. This is because WordNet synsets synonyms turn keywords into a type of synonym set. The accuracy of the

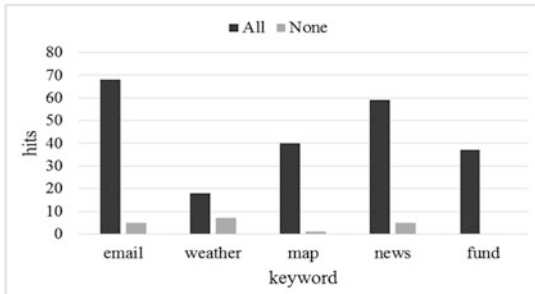
Fig. 92.1 (a) Comparison of hits in results with and without WordNet. (b) Comparison of hits in results with and without segmentation. (c) Comparison of hits in results with and without both WordNet and segmentation



(a) The comparison of hits in results with and without WordNet



(b) The comparison of hits in results with and without segmentation

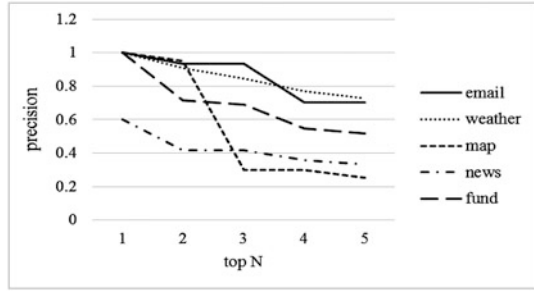


(c) The comparison of hits in results with and without both WordNet and segmentation

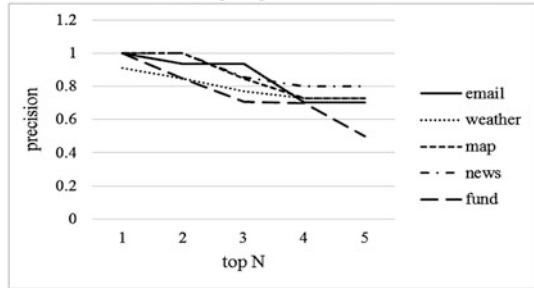
results may be decreased to some extent by using WordNet, but it is worth doing because of the significant increase in the recall ratio [8].

In theory, we know that the score will decline when document d matches few keywords based on the scoring formula factor $coord(q, d)$. Only one expression of the synonym set will be used in a Web service WSDL document, which means the score will decline when the synonym set is used for keywords. However, the score of search results such as *weather* does not decline, which indicates that what we did at the end of Sect. 92.2.3 has come into effect.

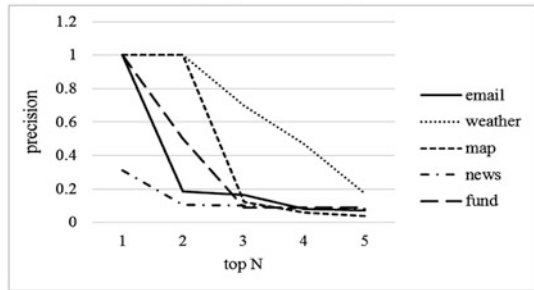
Fig. 92.2 (a) Precision using segmentation and WordNet. (b) Precision using segmentation only. (c) Precision using WordNet only. (d) Precision without using Segmentation or WordNet



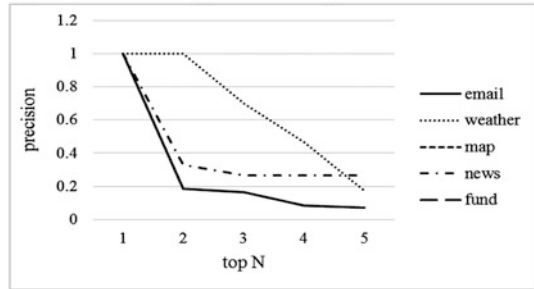
(a) Precision of using Segmentation and WordNet



(b) Precision of using Segmentation only



(c) Precision of using WordNet only



(d) Precision without using Segmentation nor WordNet

Conclusion

By analyzing the WSDL, we built an index document of Web services using data segmentation processing and a WordNet synonym thesaurus in the discovery method. Retrieval was carried out twice in this method to realize discovery for Web services. Experimental results showed that the precision and recall ratio of Web service discovery improved to some extent. Meanwhile, there are also problems with the method, such as no guarantee of the validity of search results; additionally, a specialized thesaurus for WordNet synset synonyms should be created. In future work, we will devote attention to the quality of service and try to establish a professional WordNet thesaurus.

Acknowledgments The work conducted by Ling Jiang is partially supported by the National Natural Science Foundation of China (Grant 41201388), the Open Research Fund of the State Key Laboratory of Information Engineering in Surveying, Mapping, and Remote Sensing, and the Fundamental Research Funds for the Central Universities (Grant ZYGX2012J154).

References

1. Stroulia E, Wang Y. Structural and semantic matching for assessing web-service similarity. *Int J Coop Inf Syst.* 2005;14(04):407–37.
2. Naveen Kumar S, Pabitha P, Mansoor Ahamed AK. Web service discovery based on semantic description. In: *Proceedings of the IEEE International Conference on Cloud & Ubiquitous Computing & Emerging Technologies (CUBE 2013)*. Washington, DC: IEEE Computer Society; 2013. p. 199–203.
3. Mecella M, Pernici B, Craca P. Compatibility of e-services in a cooperative multi-platform environment [M]. In: Casati F, Georgakopoulos D, Shan MC, editors. *Technologies for E-services*. Berlin: Springer; 2001. p. 44–57.
4. WSDL4J [EB/OL]. <http://wsdl4j.sourceforge.net/> (2014).
5. Liu F, Shi Y, Yu J, Wang T, Wu J. Measuring similarity of web services based on wsdl. In: *Proceedings of the IEEE International Conference on Web Services (ICWS 2010)*. Washington, DC: IEEE Computer Society; 2010. p. 155–62.
6. Lucene [EB/OL]. <http://lucene.apache.org/> (2014).
7. Wang M, Chen R, Shi R. Web services discovery based on service description. In: Du W, editor. *Informatics and management science III*. London: Springer; 2013. p. 243–52.
8. Elgazzar K, Hassan AE, Martin P. Clustering wsdl documents to bootstrap the discovery of web services. In: *Proceedings of the IEEE International Conference on Web Services (ICWS 2010)*. Washington, DC: IEEE Computer Society; 2010. p. 147–54.
9. Miller GA. WordNet: a lexical database for English. *Commun ACM.* 1995;38(11):39–41.
10. Fellbaum C. WordNet: an electronic lexical database. Cambridge: MIT; 1998.
11. Birukou A, Blanzieri E, D’Andrea V, et al. Improving web service discovery with usage data. *IEEE Softw.* 2007;24(6):47–54.
12. Syns2Index [EB/OL]. <http://www.chencer.com/techno/java/lucene/wordnet.html> (2014).
13. Zhang Y, Zheng Z, Lyu MR. Wsexpress: a qos-aware search engine for web services. In: *Proceedings of the IEEE International Conference on Web Services (ICWS 2010)*. Washington, DC: IEEE Computer Society; 2010. p. 91–8.
14. WS-DREAM [EB/OL]. <http://www.wsdream.net/dataset.html> (2014).

Chapter 93

OpenSource Automation in Cloud Computing

Vladimir Sobeslav and Ales Komarek

Abstract This chapter covers basic OpenSource automation and configuration management tools that can be used to alleviate common operations tasks and processes in cloud systems. It shows a quick survey of major cloud computing solutions and introduces simple abstraction layer for the management of physical and virtual resources. The last chapter covers some of the common automation scenarios from both cloud computing provider and consumer perspectives and their possible open-source implementations.

Keywords Cloud computing • Infrastructure as a Service (IaaS) • Configuration management • Continuous integration • Automation

93.1 Introduction

Cloud computing can be defined as “computing in an independent or remote location with shared resources available on demand” [1]. Cloud computing is a new delivery and consumption model for IT services. This involves provision of dynamically scalable and often virtualized resources typically over the Internet. This chapter narrows the use of the term cloud computing to supply Infrastructure as a Service. In cloud computing, everything becomes a service. Primary motivation for organizations to move to cloud computing may reduce the cost by dynamic resource allocation [2]. The underlying physical infrastructure of cloud computing solutions is maintained by the cloud providers who configure the physical servers along with variety network and storage devices. The individual devices and physical servers can be usually managed [3, 4] by consoles or SSH which needs to be properly configured.

The cloud computing consumers do not have to worry about hardware layer and work solely with virtualized resources. Many consumers today need [1] more than one cloud computing solution when they solve their final IT infrastructure. This

V. Sobeslav (✉) • A. Komarek
Computer Networks and Operating System Laboratories, Faculty of Informatics and Management, University of Hradec Kralove, Hradec Kralove 50003, Czech Republic
e-mail: vladimir.sobeslav@gmail.com

typically means private or public clouds matched with development and support systems. These multi-cloud deployments are now commonly set up [2]. Individual cloud computing resources can be managed with their native interfaces and consoles. These approaches are hardly scalable [3]. There are too many parts to consider, and the operations without the advantage of automation will not be effective in the long term. Another approach is to remove yourself from these different interfaces or devices by means of an abstraction layer. As a result, both providers and consumers can easily provide and manage [5] heterogeneous systems across many types of cloud computing solutions and hardware components.

This chapter shows how modern OpenSource tools can provide complete application stack for the purpose of automatic management of cloud computing used by cloud consumers as well as providers. At some point, both the consumers and providers use the same deployment and operation patterns and thus face the same problem.

The continuous integration is used to test the development of OpenStack platform core services [6]. The Apache Foundation [7] uses CI tools to test the majority projects that it supports.

93.2 Configuration Management of Models

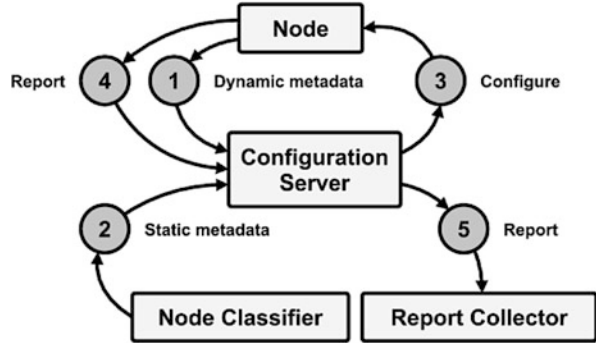
Configuration management usually details the information that describes the enterprise's hardware and software [5]. This information typically includes the versions and updates that have been applied to the installed software packages, the locations and addresses of the hardware network devices and the service interfaces, etc. When a system or a component of a system needs to upgrade a hardware or software, a technician can access the configuration management to see what has been currently installed. The configuration management software is usually available in both the free OpenSource and the paid commercial forms.

93.2.1 Configuration Management Tools

Today there are a lot of configuration management tools, but our focus is narrowed to the most popular configuration management platforms. The user describes the system services [8] and their state by using the platform's declarative language. The configuration server discovers the system information and compiles the resources into a system-specific catalogue. This catalogue contains all resources and dependencies, which are applied to the target system.

CFEngine is the first OpenSource configuration management system written by Mark Burgess in 1993 [9]. It is primarily to provide automated configuration and maintenance of large-scale computer systems. It involves the management of servers and embeds the networked devices or mobile smartphones. Shortly after

Fig. 93.1 Configuration management cycle



its birth, CFEngine inspired a field of research into automated configuration management.

Puppet is a tool designed to manage the declarative configuration of Unix/Linux and Windows systems [10]. It has great community with the configuration management recipes with a lot of software components and unique features.

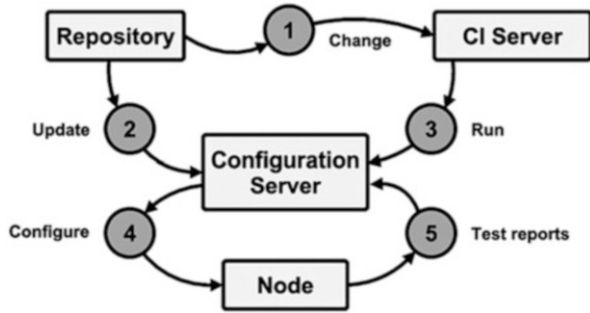
Ansible combines the multi-node deployment [11], the ad hoc task execution, and the configuration management in one tool. Ansible manages nodes over SSH and does not require any additional remote software to be installed on them. Modules work over JSON6 and standard output and can be written in any language. YAML7 is used to express reusable descriptions of systems.

SaltStack takes a new approach to the infrastructure management by developing a software that is easy enough to get running in seconds [12], scalable enough to manage tens of thousands of servers, and fast enough to control and communicate with them in milliseconds. SaltStack delivers a dynamic infrastructure communication bus used for orchestration, remote execution and configuration management, etc.

All changes to the management infrastructure are propagated in the configuration management cycles. This is common to all configuration management systems. If the configuration is managed in a decentralized way, the managed node will become its own configuration server (Fig. 93.1).

The following enumeration explains every step in the configuration management cycle. (1) The node sends normalized data about itself. (2) The external metadata server sends service classification for the given node. (3) The facts and metadata are used to compile final service catalogue that specifies how the node will be configured. (4) The node sends report back to configuration to indicate that the configuration run is complete.

Fig. 93.2 Continuous integration cycle



93.3 Continuous Integration

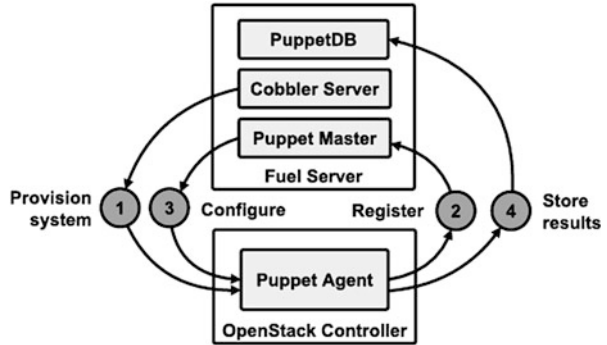
Continuous integration (CI) adds an important value to software configuration management. It ensures that each change is integrated. It provides important information about the health of a project. CI integrates all changes as early as possible. The basic idea [5] is to integrate new code as early as possible and test the modifications in the context of the entire project. In order to be able to use CI for configuration management, a few requirements must be fulfilled.

The changes to the infrastructure through the configuration management tools are handled in continuous integration cycles. A CI service fetches the source code of configuration management definitions after each change and runs tests to check the functionality. If a defect is found in the code, it can be identified and corrected as soon as possible. If the code passes the initial tests, it is built in the test environment and the result is tested (Fig. 93.2).

(1) The CI server detects the code changes in the version control system and starts to auto-test the changed code by basic test suite. (2) After the CI server confirms to code changes (recipes, metadata), they get propagated to the configuration server. (3) After the configuration server is updated, the CI server calls configuration server to commit the new settings. (4) The configuration server uses a new configuration to set up the target systems. (5) The target systems send report about their configuration management runs to the configuration server. The CI server processes data from the configuration server and sets the changes to the code as good or broken.

The continuous integration is important for the rapid software development. It is very helpful for testing changes as to complex software systems because the change in one part of the system may consequently affect other components. By turning the server's provision and configuration into an automated process driven by the service models, the same principles as the software development are applicable. The traditional continuous integration tools can be used to facilitate the test integrity, security, and performance whenever the change to the system models is detected.

Fig. 93.3 Mirantis fuel architecture



93.4 Automated Cloud Computing Scenarios

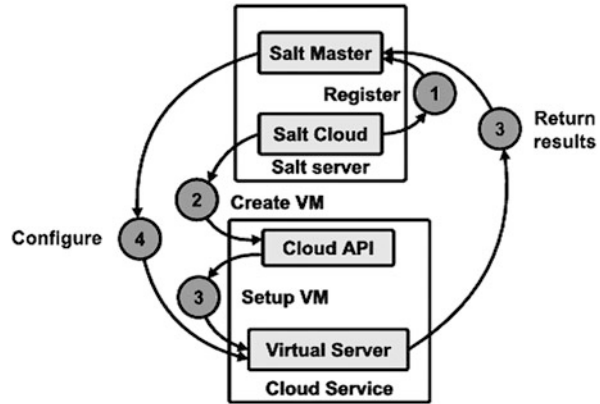
There are many use cases concerning where the automation can be used in cloud computing. The cloud providers have to set up physical infrastructures to monitor its operation and manage hardware failures as quickly as possible. The cloud consumers want to automate the development and operations of their application infrastructures; besides, everyone needs proper backup and recovery policies. The following examples show how the open-source solutions solve most of the common automation scenarios. The scenarios are tested in the CEPSOS laboratory [13] at Hradec Kralove.

Auto Provisioning With well-defined models of architectures, the cloud controller or physical hardware suppliers can set up the desired servers and configuration management service to complete their configuration. Mirantis Fuel [14] is a tool based on the OpenStack Fuel project [15–17] that automates installation of the entire OpenStack infrastructure. The Fuel server provides web interface to set up proper metadata, while the Cobbler service provides physical servers and Puppet Master with detailed configuration of every server. Basic setup starts with three controller servers in high availability setup with two or more compute servers. As Mirantis Fuel is an open-source solution backed up by commercial support, it is put together by Mirantis with the majority coded based on the community (Fig. 93.3).

- (1) Cobbler server installs operating system with Puppet Agent on all servers.
- (2) Servers are auto-registered in Fuel’s integrated Puppet Master.
- (3) State definition from Fuel is used to configure the target systems.
- (4) Servers report status of their configuration runs.

Another tool that automates the installation of OpenStack infrastructure is the DevStack project [18] by Red Hat, which is a set of scripts for quick deployment of an OpenStack cloud infrastructure. These tools provide simple way to provide metadata to hardware suppliers as well as configuration management service. This approach can provide any number or server at once. More examples of automated provision can be found in the chapter Multi-cloud Architectures.

Fig. 93.4 Salt cloud provision architecture



Monitoring and Metering The service monitoring is an important part of the system operations. The monitoring is essential for measuring the quality of services and should be set up along with services that are being measured. The configuration management can ease the deployment of local and remote checks and update them only whenever the infrastructure changes. Sensu [19] is often described as the monitoring router. Sensu takes the results of each check script from across many systems. If certain conditions are met, it passes their information to one or more handlers. Checks are used, for example, to determine whether a service like Apache is up or down. Checks can be used to collect other data, such as PostgreSQL or Redis query statistics or any application metrics. Handlers take actions by using the information from the check results, send an e-mail, send message to a chat room, or add a data point to a graph.

Multi-cloud Architectures Modern enterprise systems require distribution of application infrastructures across availability zones, regions, or even cloud services. Distribution of load across infrastructure components is hosted in one or more cloud services. OpenSource tools combine standard cloud libraries with configuration management services to fully automate the creation process within cloud services. With the standard libraries, there will be no vendor lockin. Foreman [20] is a lifecycle management tool for both physical and virtual servers. Though it's a smart proxy architecture, it can automate repetitive tasks, quickly deploy applications, and manage changes on premise VMs, bare metal, or virtual servers in the cloud. Foreman well integrates Puppet or Chef and provides external classification service for Puppet. It provides nice web interface as well as API for further integrations. Aside from cloud integration, Foreman can provide hardware resources although it's a proxy architecture [21] (Fig. 93.4).

Another example of tool supporting multi-cloud architectures is Salt Cloud [22], which can be configured to provide multiple virtual servers at different cloud computing providers at once [22–24]. (1) The Salt Cloud creates new keys for all

new virtual servers. (2) The Salt Cloud calls the cloud API through standard library to create new virtual servers. (3) The cloud controller launches virtual machines and sets up connection to the Salt Master. (4) The Salt Master enforces configuration on all virtual servers. (5) Salt Minions report the status of their configuration runs to the Salt Master.

Conclusion

The operating enterprise systems without automation are not sustainable in the long term. We can see rapid development of new cloud computing resources coping up with increasing demand to support these complex infrastructures. The open-source world introduces some enterprise level solutions to many common automation scenarios. The ability of automatic operations and transition processes by continuous integration has become crucial in the IT environment that is never still. With the open-source automation, we utilize more efficiently the laboratory hardware resources by turning the system architecture into fully edged IaaS solution that can now support educational as well as research projects. The own cloud computing platform allows us to automate the provision of new virtual servers and thus adopt the last missing step to continuously integrate the process. With this infrastructure, we can continuously test the open-source automation scenarios involving the installation of OpenStack platform on physical servers and the deployment of virtual servers for education and various distributed systems. With the continuous integration, we can keep enhancing the quality of all undergoing projects in CEPPOS laboratory. This work and the contribution have been supported by project “SP/2014/05—Smart Solutions for Ubiquitous Computing Environments” from the University of Hradec Kralove.

References

1. Reese G. Cloud application architectures: building applications and infrastructure in the cloud. Sebastopol, CA: O'Reilly Media; 2009. ISBN 978-0596156367.
2. Wilder B. Cloud architecture patterns. Sebastopol, CA: O'Reilly Media; 2012. ISBN 978-1449319779.
3. Reese G, Scott JA, Nisse D, editors. Guide to the software engineering body of knowledge, 2004 version. Los Alamitos, CA: IEEE Computer Society Press; 2004. ISBN 0-769523307.
4. NIST. The NIST definition of cloud computing. 2011. <http://csrc.nist.gov/publications/nistpubs/800-145/SP800-145.pdf>.
5. Duvall PM. Continuous integration: improving software quality and reducing risk. TODO: Addison-Wesley; 2007. ISBN 978-0321336385.
6. OpenStack. OpenStack project infrastructure. <http://ci.openstack.org/>. Accessed 9 May 2014.
7. Apache foundation: build services. 2014. <http://ci.apache.org/>. Accessed 15 May 2014.
8. Ivanov I, van Sinderen M, Shishkov B, editors. Cloud computing and services science. New York, NY: Springer; 2012. ISBN 978-1461423256.
9. CFEngine. FCEngine 3.5 documentation. <https://cfengine.com/docs/3.5/index.html>. Accessed 2 Mar 2014.

10. Dunn C. Craig Dunn designing puppet: roles and profiles. <http://www.craigdunn.org/2012/05/239/>. Accessed 3 Mar 2014.
11. Ansible Documentation. Ansible documentation. <http://docs.ansible.com/>. Accessed 2 Mar 2014.
12. SaltStack. Salt built-in pillars. <http://docs.saltstack.com/ref/pillar/all/index.html#all-salt-pillars>. Accessed 3 Mar 2014.
13. CEPoSOS. Projekty a veda. <http://www.cepos.cz/cinnost.html>. Accessed 11 May 2014.
14. Mirantis. Mirantis OpenStack v4.1 documentation: reference architectures. <http://docs.mirantis.com/fuel/fuel-4.1/reference-architecture.html>. Accessed 2 May 2014.
15. OpenStack. Fuel wiki. <https://wiki.openstack.org/wiki/Fuel>. Accessed 15 May 2014.
16. OpenStack. Jenkins job builder. <http://ci.openstack.org/jenkins-job-builder/>. Accessed 15 May 2014.
17. OpenSource. Duplicity. <http://duplicity.nongnu.org/index.html>. Accessed 1 Apr 2014.
18. Fedora Project. OpenStack devstack. http://fedoraproject.org/wiki/OpenStack_devstack. Accessed 15 Apr 2014.
19. Senu. Senu documentation. <http://sensuapp.org/docs/0.12/overview>. Accessed 21 Apr 2014.
20. Lang JP. The foreman. The manual: compute resources. <http://theforeman.org/manuals/1.4/index.html#5.2ComputeResources>. Accessed 10 Apr 2014.
21. Lang JP. The foreman. Smart Proxy. <http://projects.theforeman.org/projects/smart-proxy/wiki>. Accessed 10 Apr 2014.
22. SaltStack. Salt cloud. <http://docs.saltstack.com/topics/cloud/index.html>. Accessed 5 Apr 2014.
23. SaltStack. Salt virt. <http://salt.readthedocs.org/en/latest/topics/virt/index.html>. Accessed 5 Apr 2014.
24. Gitlab.com. GitLab community edition. <https://www.gitlab.com/gitlab-ce/>. Accessed 2 Mar 2014.

Chapter 94

Utilization of Cloud Computing in Education with Focus on Open-Source Technologies

Vladimir Sobeslav, Josef Horalek, and Jakub Pavlik

Abstract Cloud Computing uses possibilities of remote and instantly unlimited access to informational system sources. It accesses server systems using data networks like LAN, WAN, and World Wide Web with protocols HTTP, HTTPS, etc. Users, then, can access Cloud and its mediated server services through commonly available technological devices like laptops, desktop computers, smart phones, and tablets. Applications and necessary data are provided and administered in Cloud Computing by Cloud server that becomes remotely available without any physical or time limit. These aspects predetermine Cloud Computing among others for effective application in teaching. This chapter presents the implementation of OpenStack Cloud Computing platform and the results of integration in the educational process.

Keywords Cloud technology • Education • E-learning • OpenStack • Efficient education • Computer networks

94.1 Introduction

Solutions based on Cloud Computing allow the usage and sharing of hardware, infrastructure, and computing platform and applications as a service through Internet technologies [1–5].

Cloud Computing works on the logic and rules of virtualization, distributed composition, and corporate IT administration. However, Cloud allows individualization of its use based on the requirements and possibilities of the user, that is, thanks to its effective employment and cooperation with suitable virtual technologies. The function of Cloud Computing can be standardly divided into three different segments that logically correspond with the requirements that we make. We talk about software as a service (SaaS), which is a model that is used to host applications by the provider of the service. Next, there is platform as a service

V. Sobeslav (✉) • J. Horalek • J. Pavlik
Computer Networks and Operating System Laboratories, Faculty of Informatics and Management, University of Hradec Kralove, 50003 Hradec Kralove, Czech Republic
e-mail: vladimir.sobeslav@gmail.com

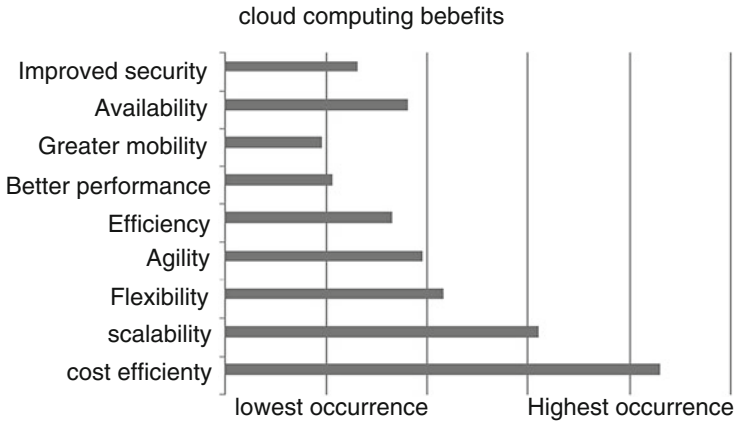


Fig. 94.1 The advantages of implementing cloud computing [4]

(PaaS), a model of the Cloud Computing service that provides a computing platform and a solutions stack as a service. The last model is infrastructure as a service (IaaS) that provides system tools of physical or virtual devices. All of the abovementioned models have then their own specific purposes and they support different products [6, 7, 8]. The main benefits that are brought by Cloud Computing are represented in Fig. 94.1.

A significant contribution of Cloud Computing is its possibility of being used for e-learning support as a service for students in schools, institutes of science, and universities. Cloud systems, as a matter of fact, are able to centralize the administration of the provided system tools and services used in the educational process. That includes the tools for administration and interface. Individual models of Cloud Computing facilitate their users to use compiled infrastructure on the level of the services, system tools, or their combinations [9, 10, 11]. The current research view on the utilization of Cloud Computing in education can be divided into two main areas: First is the development and optimization of specialized e-learning applications. Numerous research projects can be found in this area [12–17]. This use of Cloud Computing appears to be dynamic and is currently adopted. Second is the generalized view of the benefits and utilization of these modern technologies. The economic benefits of Cloud Computing are summarized [18]. The impact of integration and optimization educational process and e-learning is presented [19–21]. The aim of this chapter is not to analyze the whole spectrum of technologies and systems that are usable in the e-learning area but to focus on the specific area of utilization of Cloud Computing services in teaching process.

94.2 Cloud Computing and E-Learning

Making use of the idea of Cloud Computing and related investigation in the area of education is closely connected with the issue of e-learning. E-learning typifies an educational approach with the support of modern technologies, such as LMS (learning management systems), specialized databases, dictionaries, SW testing, and many other gadgets that broaden distance learning possibilities. From the architectonic point of view, what matters is the connection, editing, or migration of classic e-learning systems in Cloud service environment. Cloud Computing services in the area of e-learning can be divided into three basic categories according to the type of Cloud Computing services that are mentioned below [4]. The first layer is IaaS—infrastructure as a service. It represents the fundamental layer separating physical hardware source by virtualization of processors, disk storages, memory, network infrastructure, etc. The next layer is PaaS—platform as a service. It is the middle layer of e-learning systems. Its aim is to define linking on the lower infrastructure layer and to define the standards for running of applications. The task of this layer is not to specify the manipulation of hardware sources. A typical example, in this kind of integration in the most widespread LMS like Blackboard and Moodle, is an interface for other applications or plug-ins for interconnection of video servers, informational systems, databases, or other data sources that allow extending knowledge bases of the whole LMS. The third and the last layer is SaaS—software as a service—that represents the particular services and applications of a given system, or rather users' way of working, and a user interface that significantly influences the way of working with the system and the organization of educational modules, such as item classification module (ICM) or course selection module (CSM). This layer then integrates teaching and educational sources, interactive courses, discussion forums, knowledge bases, grading subsystems, and many other significant elements.

It is obvious that Cloud Computing is by no means another whole new e-learning architecture but rather another possibility of how to distribute teaching material to end users [11]. In some cases, especially concerning Cloud services, which offer only the IaaS level, it is just a very effective solution of the infrastructure for the running systems. One of the main advantages of Cloud Computing is the reduction of the total cost for the infrastructure run that includes solving with high availability, security, the ability to reduce the demands of the administrators of the systems, and help to secure the access from anywhere.

94.3 Requirements and Motivations for Cloud Solution

The main motivation is to develop the accessible solution for students in 24/7 mode and allow them to prepare themselves effectively for classes and improve in this way their competences and skills. Previously, the laboratory team had to challenge

the non-automated management of student infrastructure (virtual servers, networks, monitoring systems, etc.). This kind of student infrastructure is also closed for online education and the integration with e-learning tools is complicated. Therefore, the primary requirement for development and implementation of the presented solution is to make hardware devices accessible for the needs of teaching server operating systems and their configuration. The basic requirement is to make one up to three server instances accessible to every student. That is, it would be Windows Server 2008 and another two client instances implemented by the operating system would be Windows 7. This solution requires sufficient system tools in the form of sufficient operating memory, time processing, and memory space for permanent data saving. The aim of this proposed solution is to consolidate system tools in the form of hardware devices for distribution needs of educational instances of server operating systems. Within the hardware sources, there are 11 IBM servers at disposal, each with processor Intel Xeon x3400 with 8 Hyper-Threading cores, with 2 local HDDs connected in RAID field in striping regime in order to increase the performance to 1 TB, and also with RAM with a capacity of 16 GB and 3 network interface controllers.

One of the possible platforms that meet requirements mentioned above and the parameter from the whole range of available solutions, being taken into consideration with its individualization and price, is OpenStack. OpenStack was designed as a unit for the operation of “scalable Cloud operating system.” Several separated services were created in a way to achieve that. Together they are supposed to create an adequate “infrastructure as a service” (IaaS). The integration of these services runs through public application programming interfaces (API) that provide or use the individual services. These interfaces are usually accessible even to end users of Cloud.

94.4 Proposal for Cloud Architecture with OpenStack

Proposed solution takes into consideration the requirements presented in Chap. 3 and works on the principles of the use of Cloud Computing as IaaS with selected functions of PaaS. The main task of the solution is to facilitate the users (students) to access and to virtualize instances of Windows server 2008 R2, Windows 7, and Linux Red Hat 6 that are used to work on their assignments. The authentication to this environment is connected to the university LDAP in a way that enables the students use their standard log-in details. The student chooses specific preset operation system image that he has to activate with corresponding hardware sources in every class. It is either a clean installation or an installation with predefined services and server roles that student processes further or performs troubleshooting on.

Specific architecture of the solution is presented in the following picture. The basis is a consolidation of ten individual servers with computing sources needed for the run of virtualized servers for end users. These system tools are consolidated

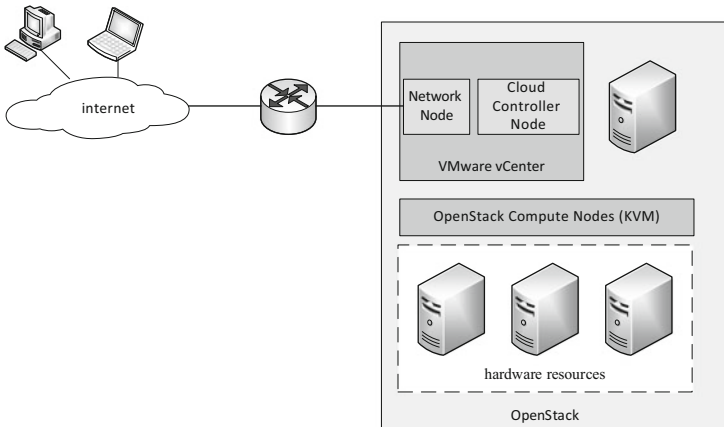


Fig. 94.2 OpenStack platform architecture for e-learning

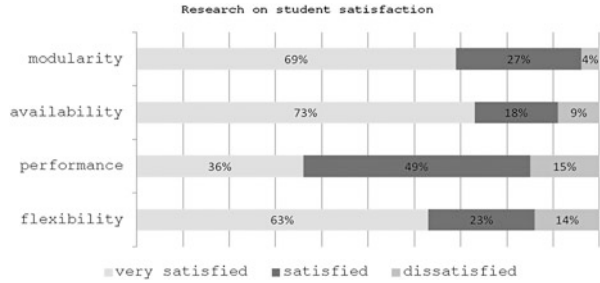
with the help of OpenStack Nova project (Compute) that manages nodes of individual open instances that student approaches through a web browser thanks to the technology noVNC—native implementation of classic VNC console to HTML5. These individual devices are virtualized by means of Kernel-based Virtual Machine (KVM) that runs on Linux distribution Ubuntu 12.04 LTS.

Management, administration, and organization of Cloud solution OpenStack operate on two virtual servers—controller node and network node. Those are placed on HA cluster based on the vCenter Operations Management Suite technology from VMware. This solution enables an optimized automatic access to the management and administration of individual modular parts of OpenStack system. Furthermore, it contains the central database MySQL and the message broker RabbitMQ that communicates through all the OpenStack components.

Network node is a server that implements the whole solution of networking, i.e., access to the Internet, firewall between projects, NAT, etc. On this server, there are L3 agent and DHCP agent running. L3 agent creates virtual routers and in that way secures routing of virtual networks. DHCP agent assigns addresses to student instances. Communication between the student instances themselves and network modem is put into practice using SDN (Software-Defined Networking), more specifically, using protocol VXLAN (Fig. 94.2).

The system was set in pilot operation for teaching so that the actual configuration could be tested. Furthermore, it was set in order to find within the testing the optimal configuration of hardware elements and the Cloud system OpenStack. Up to 50 individual instances of Windows server 2008 R2 were created within the pilot operation. With these, the limit values of the use of system tools available on connected hardware resources were reached. Apart from teaching, the solution was accessible to students in 24/7 mode so that they could prepare themselves effectively for classes and improve in this way their competences and skills. Eight weeks

Fig. 94.3 Research on student satisfaction



after the initiation of this pilot operation, a survey about the connection of OpenStack system and its inclusion to teaching were conducted among the participating students and lecturers (Fig. 94.3).

Conclusion

The presented solution represents one of the possibilities of using Cloud Computing for the effective use of e-learning. Barring the already several times mentioned advantages of the very placement and the use of Cloud Computing not only in teaching, within the use of Cloud-type services for teaching, with the use of open-source solution, which means with minimal expenses for licenses, we get a tool that makes teaching significantly more effective. This introduced solution allows the individualization of teaching according to the needs of individual students and that has a very unique possibility on the level of university education.

The system allows assembling specific assignments that can be put together on different levels of difficulties including the possibilities of searching for errors and repairing the current system. That creates a unique possibility to simulate a real company environment. The possibilities of the system are limited mostly only on the level of accessible system tools that basically are allowed in an easy way to supplement or deprive the system tools in the computing system according to current possibilities and requirements. This can happen if we use the possibility of consolidation of computing power.

From the evaluation of pilot operation, it is obvious that this system represents an effective alternative of using modern Cloud technologies and in that way it enables students to work effectively when solving practical problems. This work and the contribution were supported by the project "SP/2014/05—Smart Solutions for Ubiquitous Computing Environments" from University of Hradec Králové.

References

1. Nagalakshmi B, Archana S. Advanced cloud computing technology for accelerating innovations in e-learning. *Middle-East J Sci Res.* 2014;20(3):343–6.
2. Paul PK, Dangwal KL. Cloud based educational systems and its challenges and opportunities and issues. *Turk Online J Dist Educ.* 2014;15(1):89–98.
3. Veerabhadram P, Conradie P. Mobile cloud framework architecture for education institutions. Paper presented at the proceedings of 2013 science and information conference, SAI 2013, Art. No. 6661851. 2013. p. 924–7.
4. Selviandro N, Hasibuan ZA. Cloud-based e-learning: a proposed model and benefits by using e-learning based on cloud computing for educational institution. *Inform Commun Technol.* 2013;7804(2):192–201.
5. Rashid AI SM. A unified cloud computing model towards developing ‘E-learning as a service’ based education system. *Int J Comput Appl.* 2013;72(7):38–51.
6. Cătălin B, Pocatilu P, Cristian T. The economics of cloud computing on educational services. *Procedia Soc Behav Sci.* 2013;93(7):1050–4.
7. Aruna R, Prakasam S. Enhancing cloud based E- learning using knowledge sharing system. *Int J Comput Appl.* 2013;84(9):26–30.
8. Arora AS, Sharma MK. A proposed architecture of cloud computing based e-learning system. *IntJ Comput Sci Netw Secur.* 2013;13(8):31–4.
9. Wang A, Huang LH. E-learning exploration based on cloud computing. *Appl Mech Mater.* 2013;333–335(3):2226–30.
10. Wang RC, Lin JP, Hu SS. Virtualization technology for multimedia interaction cloud education services. In: *Proceedings of the 2013 international conference on advanced ICT for education*, vol. 33, issue 2. 2013. p. 154–9.
11. Chunwijitra S, Berena AJ, Okada H, Ueno H. Advanced content authoring and viewing tools using aggregated video and slide synchronization by key marking for web-based e-learning system in higher education. *IEICE Transac Inform Syst.* 2013;E96D(8):1754–65.
12. Stein S, Ware J, Laboy J, Schaffer HE. Improving K-12 pedagogy via a Cloud designed for education. *Int J Inform Manage.* 2013;33(1):235–41.
13. Elamir AM, Jailani N, Bakar MA. Framework and architecture for programming education environment as a cloud computing service. *Procedia Technol.* 2013;11(3):1299–308.
14. Zurita G, Baloian N, Frez J. Using the cloud to develop applications supporting geo-collaborative situated learning. *Future Generat Comput Syst.* 2014;34(7):124–37.
15. Ezenwoke A, Omoregbe N, Ayo ChK, Sanjay M. NIGEDU CLOUD: model of a national e-education cloud for developing countries. *IERI Procedia.* 2013;4(3):74–80. ISSN 2212-6678.
16. Sultan N. Making use of cloud computing for healthcare provision: opportunities and challenges. *Int J Inform Manage.* 2014;34(2):177–84.
17. Behan M, Krejcar O. Modern smart device-based concept of sensoric networks. *EURASIP J Wirel Commun Netw.* 2013;1(155):1–13. doi:[10.1186/1687-1499-2013-155](https://doi.org/10.1186/1687-1499-2013-155).
18. Hexiao H, Shiming Z, Haijian Ch. Reengineering from tradition to cloud: a case study. *Procedia Eng.* 2012;29(11):2638–43.
19. Ozdamli F, Huseyin B. Effects of training on cloud computing services on M-learning perceptions and adequacies. *Procedia Soc Behav Sci.* 2014;116(21):5115–9.
20. Sommerville I. Teaching cloud computing: a software engineering perspective. *J Syst Softw.* 2013;86(9):2330–2.
21. Boja C, Pocatilu P, Toma C. The economics of cloud computing on educational services. *Procedia Soc Behav Sci.* 2013;93(6):1050–4.

Chapter 95

A Survey of Extended Role-Based Access Control in Cloud Computing

Hongjiao Li, Shan Wang, Xiuxia Tian, Weimin Wei, and Chaochao Sun

Abstract Access control is one of the key mechanisms for cloud computing security. When it comes to being used in cloud computing environments, RBAC is more scalable and more suitable compared with traditional discretionary and mandatory access control models. A straightforward way is to extend RBAC from traditional fields to cloud computing environments. In this chapter, several extended role-based access control schemes are surveyed from basic extension, A-RBAC, and trust-based RBAC separately. Core techniques of the proposed schemes are detailed. Comparisons around the proposed schemes are analyzed.

Keywords Cloud computing • Access control • RBAC • A-RBAC • Trust

95.1 Introduction

Nowadays, cloud computing is becoming one of the most popular and trendy computing model in the technology world. In cloud computing model, access is performed through network which has the characteristics of ubiquity, convenience, and service-on-demand. The computing resource is a configurable shared pool consisting of networks, servers, storage, applications, and services [1]. There are different slots or sections of a cloud service. Among them, infrastructure as a service (IaaS), platform as a service (PaaS), and software as a service (SaaS) are the three service models. With the cloud computing having more and more deployment, security issues have become important factors restricting its development and application [2].

Access control is the process of limiting access to system resources for only authorized people, programs, processes, or other system components, which plays an important role in the field of information security. Traditionally, there are three kinds of access control models: (1) discretionary, (2) mandatory, and (3) role based [3]. Among the three models, RBAC model is the most scalable, especially in such cases that tracking the users of the services cannot get through a fixed identity.

H. Li (✉) • S. Wang • X. Tian • W. Wei • C. Sun
School of Computer, University of Shanghai Electric Power, 200090 Shanghai, China
e-mail: hjli@shiep.edu.cn

Accordingly, when used in cloud computing environments, RBAC models have the superiority.

In this chapter, from the view of the underlying techniques, we survey several extended RBAC schemes for cloud computing. In Sect. 95.2, basic techniques for using RBAC are analyzed. In Sect. 95.3, the core techniques of the proposed schemes and its application in cloud computing are detailed. In Sect. 95.4, we compare the schemes from attaining goals, and technique aspects and future works are listed. And in section Conclusion our conclusions are given.

95.2 Requirement of Using RBAC for Cloud Computing

In RBAC [4–6], the burden of the server is limited by restricting users from accessing the contents out of their zone. RBAC model is formalized by using the following notations: **U**, **R**, **OBS**, **OPS**, and **S**. In turn, they denote user set, role set, protected objects, operations set, and sessions set, respectively. To employ the RBAC model, identifying corresponding entities is the first task. In the SPI model, the identification among the three services (SaaS, PaaS, and IaaS) needs to be separated because each of them has different nature and scope.

Users/agents In SaaS, users can be individual persons, enterprises, or corporations and those web services wishing to access resources. All users identified in SaaS could be included in PaaS. In most cases, the acknowledgment from a virtual machine is received by an IaaS user, who is responsible for fulfilling the system configuration.

The categorization of **Roles** lies in their job functions. In cloud computing, roles can be consumers, tenants, and service providers. The permissions and functions of roles could inherit from a parent role so that the inheritance characteristic of RBAC can embody it.

The definition of **Permissions** is in accordance with the job functions of roles. To perform secure access in cloud computing, permissions are defined on data access, program access, and service access. Disabled and enabled permissions are done through the use of sessions.

From the view of object, resources with the cloud are **protected objects**. Objects, data, programs, and services are representative groups, corresponding to the permissions mentioned earlier. The granularity of the permission definition is consistent with the identification of project objects.

95.3 Extended RBAC Schemes in Cloud Computing

According to the basic components of RBAC model, several extended RBAC models have been proposed from different angles to accommodate to cloud computing environments.

95.3.1 *Basic RBAC Extension*

95.3.1.1 RBAC Extension Based on PKI and Domain Information

dRBAC (distributed role-based access control) [7] extends standard RBAC by using PKI and domain information in the certificate. If certificates for internal users (role and user in the same domain) and other companies' users (role and user in other domains) are to be authenticated and assigned permissions, the certificate is used to sign and issue. Conditions are written as attributes.

coRBAC (cloud optimized RBAC) [8] model is proposed which aims to achieve services optimization and enhancement of the access control system. Based on coRBAC, the certification process of multilevel cache of establishing secure connection is simplified, and multilevel cache is set up, which greatly improves the user's experience and performance of the access control system. coRBAC extends the dRBACs from two aspects: combing authentication services from different ends and expanding the CAs. Further, the added hierarchical caches make the **coRBAC** more efficient.

95.3.1.2 RBAC Extension Using Restriction Policy

The new advance E-RBAC (efficient RBAC) [9] presents a new extended architecture of RBAC which can resolve the security issues and data loss issues by using restriction policy on the number of roles, users per role, and transaction per day/hour/user. With the help of this new architecture, security level can be enhanced or improved. Another new feature and backup policy helps to reduce the data loss. It means that security level can be enhanced or improved with the help of this new architecture. One new feature is added into this architecture, and that is the backup policy which helps to reduce the data loss. But still there is a point of number of transaction by one ID of one specific role which could be the loop hole of this architecture.

95.3.1.3 RBAC Extension Using Role Ontology

Extended O-RBAC [10] is an extension using role ontology to extend RBAC for multi-tenancy architecture in clouds. For a specific domain, the role hierarchy is built up using ontology. This helps to increase the security by restricting the number of users per role, transaction per user. If the cloud crashes or does not work properly, there is also a concept of backup and restoration to avoid the loss of important data. In this case chances of loss of data are very few. This strategy enhances the security by adding the restraint policy, backup policy, and restore policy.

This extended O-RBAC uses reference ontology to enhance the security and simplify the system design and implementation which is an enhancement in policies in architecture of RBAC. Later, the development of a new back-end database schema for RBAC extension should be taken into account. Another aspect, the scalability of extended RBAC using reference ontology is to be measured.

95.3.1.4 RBAC Incorporating Dynamic Character

In task role-based access control model (task-RBAC) [11], the validation of user access permissions is dynamic because of the assigned roles and its associated task to be performed, which makes it viable for cloud computing environment. TRBAC [12] is a standard RBAC with temporal extension. During running, the role can be enabled and disabled against user requests. It is argued that static roles should always be enabled under some situations, while the assignment of users and permissions is dynamic [12]. The salient feature of this model is that the roles enabled are periodic. But several other important temporal constraints can't be dealt with. Subsequently, James et al. proposed GTRBAC [13]. In this model, the avocation is not role activation but role enabling. In GTRBAC, the constraints can be enabled and disabled. The upper limit of user active duration is within a particular time interval. Also, the number of role activations by a single user is limited. Unfortunately, the problem of trust relation in multi-domains cannot be solved by the model. X-RBAC [14] is a framework which deals with XML-based RBAC policy specification, and it is used to access control enforcement on dynamic XML-based web services. However, trust and context-aware access control is not attained. To solve the above problems, X-GTRBAC [6] is proposed. It combines the X-RBAC with GTRBAC models and the assignment of roles to users is performed by trusted third parties (e.g., any PKI certification authority). The users' trust level (as part of *user profile*) is affected by context information (such as time, location, or environmental state at the time the access requests are made), and it is part of its access control decisions. The users'/roles' access privileges have something to do with the threshold (i.e., the trust level), which is determined by the requestor's access patterns. X-GTRBAC can suit the above real-time requirement.

95.3.2 Attribute Role-Based Access Control

95.3.2.1 Role-Based Encryption

RBE [15] is a new encryption scheme which solves the encrypted data storage in public cloud with an efficient user revocation. In RBE scheme, the encryption is role based. That is, the data encrypted by data owner can only be decrypt and viewed by the users with appropriate roles specified by A-RBAC policy. The role grants permissions to users who qualify the role. Also, the permissions from existing users of the role can be revoked. Role hierarchies can also be coped with by RBE scheme, that is, one role can inherit another role's permissions. If a user joins a role in which its owner has encrypted the data for, after that, the user can access that data and data re-encryption can be omitted. Whenever a user is evoked, it can no longer access any future encrypted data representing the role. That is, the revocation of the user from its role has nothing to do with other users and roles in the system. By using this approach, the RBE scheme achieves an efficient decryption on the client side. RBE scheme is described by broadcast encryption algorithm.

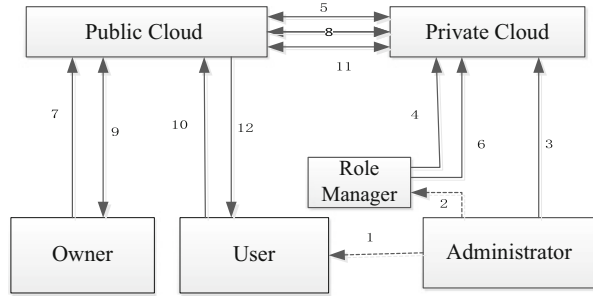
95.3.2.2 Cloud Infrastructure Based on RBE

Based on the proposed RBE scheme, a secure cloud data storage architecture using a hybrid cloud infrastructure is developed [16], which is illustrated in Fig. 95.1. According to this architecture, the users who wish to access the encrypted data and the data owners who wish to encrypt their data only interact with the public cloud. The role hierarchy and user to role mappings related to the organization are maintained in the private cloud which is only accessible to the administrator of the organization. The administrator specifies the role hierarchy and the role managers who manage the user membership relations.

95.3.2.3 Applying A-RBAC in Cloud Computing

The RBE scheme can achieve efficient user revocation. In the RBE-based cloud storage architecture, an organization is allowed to store data securely in a public cloud, while the sensitive information related to the organization's structure is maintained in a private cloud. The characteristics of constant size ciphertext and decryption key are embodied in the proposed architecture. Also, both encryption and decryption computations are efficient on the client side, and decryption time at the cloud can be reduced by having multiple processors. Accordingly, the proposed system has the potential to be useful in commercial situations.

Fig. 95.1 RBE system architecture



95.3.3 Trust-Based RBAC

According to the concepts of trust in social sciences [17, 18], the description of trust in [19] is a mental state. It comprises three aspects: *expectancy*, *belief*, and *willingness to take risk*. In cloud computing environment, the semantics of trust is the same as above; but for cloud entities, the expectancy and the characteristics of cloud entities are still needed to meet competency, integrity, and goodwill.

95.3.3.1 TBDAC Model

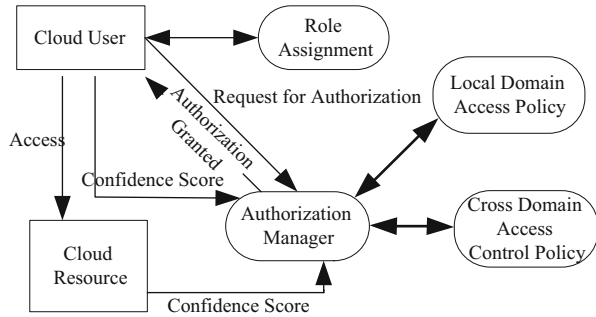
TBDAC model [20] is the extension for RBAC. Based on GTRBAC, dynamic access authorization is done by introducing authorization trust factor; in this way, the users' trust-degree and the conditions about constraints can be determined. Accordingly, the information about role and the trust-degree are used to validate the users' legal identities. Also, the privileges for resource access control can be acquired. In TBDAC, a new ticket is proposed to satisfy the dynamic and real-time characters based on a modified Kerberos protocol. The certificate trust-degree is decided by direct trust-degree (**DT**) and recommendation trust-degree (**RT**). To calculate trust-degree, confidence factor (**CF**) and time factor (**TF**) are introduced.

Security theoretic analysis shows that when exchanging information using TBDAC model, security-hidden trouble can be reduced, and the security of overall organization is enhanced. TBDAC is a framework in accordance with the standard of RBAC. Also, it is a dynamic access control model based on trust and the security of resource is ensured.

95.3.3.2 TOrBAC

In O-RBAC (organization-based access control) [21], the abstract concept of role, purpose, activity group, and structure is for the subjects, objects, and actions. Entities are abstracted by security policy. **TOrBAC** (trust organization-based

Fig. 95.2 Dynamic access control based on trust



access control) [22] is a new model for specifying such security policies, and a confidence index is calculated recursively using a formula. TTP is a third party which ensures that the interactions between two parties are both trustworthy. In TorBAC model, the cloud computing function of TTP and parameters confidence indicators are taken into account for the trust management. When used in cloud computing, it should be extended to a model which has the deeper mechanisms of detection of rape. In another aspect, the consistency and completeness of the security policy are also to be verified. Also, there is a need to develop more realistic use case and the associated mechanisms.

95.3.3.3 TCloud

Based on trust, a new cross-domain framework, TCloud [23], is proposed to meet the requirements of cloud computing. In multiple domains, access control will be based on the conversion of roles. The role assignment and conversion will take place dynamically. The high-level framework of multiple domain access control is depicted in Fig. 95.2.

First, the cloud user obtains an appropriate role by the role of the management center; then, a user ID, password, role, and resources to be accessed are submitted. After that, the user will interact with the authentication and authorization center to apply for authorization to access. If the resources requested for access are in the local domain, the local access control policies are invoked. Otherwise, cross-domain access control policies of permissions and management will be implemented.

Tcloud is a dynamic model for access control across multiple domains based on the traditional model of role-based access and trust. In single domain, the access is based on the traditional mechanism, while in multiple security domains, the roles are dynamically converted according to the domain of interest. This framework can be more intuitive, effectively protecting cloud users and ensuring the security of the cloud computing platform.

95.3.3.4 CTTM

CTTM (cross-tenant trust models) [24] is formalized based on four potential types of cross-tenant trust relations. In the formalization of CTTM, there are three entity components: **users (U)**, **permissions (P)**, and **tenants (T)**. A novel component **T** is introduced to express accesses in multi-tenant environments in which the other components should fit. **PO** is a many-to-one relation from **P** to **T**. **UO** may be a many-to-one relation or a many-to-many relation from **U** to **T** depending on implementation. **RB-CTTM** is a role-based extension of CTTM.

To verify the feasibility in the cloud, a cloud-based platform named multi-tenant authorization as a service (MTAaaS) is used. Each tenant has its own access control policy stored in the cloud service and managed through the MTAaaS platform. Also, attribute-based extensions of CTTM and other possible models which are compatible with MTAaaS platform should be investigated.

95.3.3.5 MT-RBAC

MT-RBAC (multi-tenant role-based access control) [25] family aims to provide fine-grained authorization in collaborative cloud environments by building trust relations among tenants. In MT-RBAC, the cross-tenant trust relation is established by the resource owner rather than by the resource requester. MT-RBAC extends the traditional RBAC model with two new built-in entity components: issuers and tenants. Three MT-RBAC models integrate three different trust relations with increasingly finer-grained constraints, respectively, tenant trust (MT-RBAC0), trustee-independent public roles (MT-RBAC1), and trustee-dependent public roles (MT-RBAC).

MT-RBAC models aim to address multi-tenant authorization for collaborative cloud services and enable fine-grained cross-tenant resource access by building tenant-level granularity of trust relations. Performance and scalability results show that the AaaS platform with MT-RBAC incurs an acceptable overhead and is scalable for the cloud storage service.

95.4 Comparisons and Future Work

95.4.1 Comparisons

As illustrated in Table 95.1, we compare these schemes which we have surveyed. We compare these schemes by the criteria of domain (single or multiple), dynamic (supported or not), multi-tenant (supported or not), goal (performance, security level, data loss, etc.), core techniques, etc.

Table 95.1 Comparisons of extended RBAC models

	Domain	Dynamic	Multi-tenant	Goal	Core technique
Basic RBAC extension	dRBAC			Identify different enterprises and organizations	PKI and domain information contained in the certificate are taken advantage of
	CoRBAC			Improve overall efficiency	Reduce the established secure connection and set up multilevel cache
	E-RBAC			Improve security level and reduce data loss	Restriction policy
A-RBAC	O-RBAC		√	Security level enhanced and data loss reduced	Role ontology
	GTRBAC	√		Advocate for activation of roles	The dependencies relation among roles is temporal, which is enabled periodically
	X-GTRBAC	√		Trust level of a user is affected	Trusted third party provides the certification, the context is consider
	A-RBAC	√		Reduce the attack surface, overcome collusion attacks	Cloud data storage architecture based on RBE
Trust-based RBAC	TBDAC	√		Reduce security-hidden trouble, enhance security of overall organization	Authorization trust factor
	TorBAC			The external connection of users with different accesses are better controlled, the confidence of business operators cloud is strengthened	A confidence index is calculated using a recursive formula
MT-RBAC	TCIoud	√		The degree of trust in single as well as multiple domains are established and calculated	Trust concept
	CTTM	√	√	Bridge authorization domains of each tenant	Cross-tenant trust relations
	MT-RBAC		√	Provide fine-grained authorization	Build trust relations among tenants

Remark: √ denotes that the criteria is supported
Do domain, *Dy* dynamic, *Mt* multi-tenant, *S* single, *M* multiple respectively

95.4.2 Future Work

The extended RBAC model above proposed different mechanisms for accommodating cloud computing environment, but still there are more issues to be resolved for the RABC model to be deployed.

If the users, roles, objects, and attributes of the environment are to be applied, it is necessary to develop property-driven RBAC model. Also, permission assignment for the real-time application needs to be developed to implement access control decisions. Based on the properties of the user to roles, the rules being used in assigning permission for the real-time application need to be developed to implement access control decisions.

Development of position-sensitive role-based access control model incorporated into PEP prevents user identity, role or position in the cloud from leaking to the remote server (may not be fully trusted), and only when the user is in a logical location within the boundaries of space enable/activate characters (calculated from the true position by the particular mapping function).

In cloud computing, there is the need of more formal definitions for different entities in RBAC. Also, more efforts on industrial standards, best practices, and large-scale experiments need to be put into.

At present, there is not much research going on for solving the access control problem involving multi-domain in industry and academia of cloud applications, but this problem cannot be ignored and new solutions are needed. Dynamic access control and multi-tenant architecture support also need further enhanced research efforts.

Conclusion

In this chapter, extended RBAC mechanisms for cloud computing are discussed elaborately. Basic RBAC extension is based on PKI and domain information, using restriction policy, role ontology, or incorporating dynamic characteristic separately. A-RBAC enforces RBAC policies on encrypted data using a hybrid cloud infrastructure. Trust-based RBAC models incorporate the trust concept into RBAC. It can be concluded that as the RBAC model gradually improves and combines with other security mechanism, RABC model will play a more and more important role in cloud computing security. We believe that the more successful on RBAC, the more maturity of the cloud computing platform.

Acknowledgments This paper was funded by the Innovation Program of Shanghai City Board of Education No. 11YZ194 and No. 12YZ146, No. 12YZ147, the founding Program of Shanghai Natural Science No. 11ZR1414300 and 12ZR1411900, and the founding Program of National Natural Science No. 61202020.

References

1. Mell P. The NIST definition of cloud computing. *Int J Eng Technol.* 2009;4(5):284.
2. Feng DG, Zhangetc M. Research on cloud computing security. *J Softw.* 2011;22(1):71–82. In Chinese.
3. Meghanathan N. Review of access control models for cloud computing. In: ICCSEA, SPPR, CSIA, WimoA – Computer Science & Information Technology (CS & IT). 2013. p. 77–85.
4. Ferraiolo D, Kuhn DR. Role-based access control. In: Proceedings of the 15th national computer security conference. 1992. p. 554–63.
5. Ferraiolo DF, Sandhu R, Gavrila S, Kuhn DR, Chadramouli R. Proposed NIST standard for role-based access control. *ACM Trans Inform Syst Secur.* 2001;4(3):224–74.
6. Shin ME, Ahn G. UML-based representation of role-based access control. In: IEEE 9th international workshops on enabling technologies: infrastructure for collaborative enterprises (WET ICE'00). 2010. p. 195–200.
7. Freudenthal E, Pesin T, Port L, Keenan E, Karamcheti V. dRBAC: distributed role-based access control for dynamic coalition environments. In: 22nd IEEE international conference on distributed computing systems (ICDCS'02). 2002. p. 411–20.
8. Zhu TY, Liu WD, Song JX. An efficient role based access control system for cloud computing. In: 11th IEEE international conference on computer and information technology. 2011. p. 97–102.
9. Parminder S, Sarpreet S. A new advanced efficient RBAC to enhance the security in cloud computing. *Int J Adv Res Comput Sci Softw Eng.* 2013;3(6):1136–42.
10. Parminder S, Sarpreet S. Towards novel and efficient architecture for extended-RBAC in cloud computing. *Int J Comput Sci Inform Technol.* 2013;4(3):515–8.
11. Sejong O, Park S. Task-role-based access control model. *J Inform Syst.* 2003;28(6):533–62.
12. Bertino E, Bonatti PA, Ferrari E. TRBAC: a temporal role-based access control model. *ACM Trans Inform Syst Secur.* 2001;4(3):191–233.
13. Joshi JBD, Bertino E, Latif U, Ghafoor A. A generalized temporal role-based access control model. *IEEE Trans Knowl Data Eng.* 2005;17(1):4–23.
14. Bhatti R, Joshi JBD, Bertino E, Ghafoor A. Access control in dynamic XML-based web-services with XRBAC. In: Proceedings of the 1st international conference on web services. 2003. p. 243–9.
15. Zhou L, Varadharajan V, Hitchens M. Enforcing role-based access control for secure data storage in the cloud. *Comput J.* 2011;54(10):1–143.
16. Zhou L, Varadharajan V, Hitchens M. Achieving secure role-based access control on encrypted data in cloud storage. *IEEE Trans Inform Forensic Secur.* 2013;8(12):1947–60.
17. Blomqvist K. The many faces of trust. *Scand J Manage.* 1997;13(3):271–86.
18. Mayer R, Davis J, Schoorman F. An integrative model of organizational trust: past, present and future. *Acad Manage Rev.* 1995;20(3):709–34.
19. Huang J, Nicol D. A formal-semantics-based calculus of trust. *IEEE Internet Comput.* 2010;14(5):38–46.
20. Tan ZJ, Tang Z, Renfa L, Ahmed Sallam, Yang L. Research on trust-based access control model in cloud computing. In: IEEE 6th joint international information technology and artificial intelligence conference (ITAIC). 2011. p. 339–44.
21. Cuppens F, Cuppens-Boulahia N, Mie GE A. Inheritance hierarchies in the Or-BAC model and application in a network environment. In: Second foundations of computer security workshop (FCS'04). 2004. p. 1–10.
22. Saidi MB, Elkalamec AA. TOrBAC: a trust organization based access control model for cloud computing systems. *Int J Soft Comput Eng.* 2012;2(4):122–30.
23. Ullah S, Zheng XF, Zhou F. TCloud: a dynamic framework and policies for access control across multiple domains in cloud computing. *Int J Comput Appl.* 2013;62(2):1–7.
24. Tang B, Sandhu R. Cross-tenant trust models in cloud computing. In: IEEE 14th international conference on information reuse and integration (IRI). 2013. p. 129–36.
25. Tang B, Li Q, Sandhu R. A multi-tenant RBAC model for collaborative cloud services. In: 11th annual international conference on privacy, security and trust (PST). 2013. p. 229–38.

Chapter 96

Coordination Strategy in an SaaS Supply Chain with Asymmetric Information About the Market

Lingyun Wei, Jiafei Ling, and Xiaoguang Zhou

Abstract Cloud computing is a rising type of service system in today's IT world. In this paper we try to design an appropriate contract to coordinate a cloud computing service supply chain with asymmetric information. Our study is based on the SaaS model proposed by Demirkan et al. in 2010, which consists of one application infrastructure provider (AIP) and one application service provider (ASP). However, the assumption of complete information in their model is far from realistic. So we assume that ASP processes private information about its user's delay cost. Through numerical analysis, we find that if restricted only by a simple wholesale-price contract, ASP has an incentive to overstate user's delay cost to obtain a lower rental price from AIP. Therefore, we apply another two contracts—revenue-sharing contract and cost-based pricing policy—to solve the problem and only find that the former is invalid. The latter, on the other hand, works well for AIP to coordinate the supply chain even with incomplete information about terminal market.

Keywords Cloud computing • Service supply chain • SaaS • Coordination • Contract • Information asymmetry

96.1 Introduction

Cloud computing is a type of service system in today's IT world. And it is defined as "... a model for enabling convenient, on-demand network access to a shared pool of configurable computing resources that can be rapidly provisioned and released with minimal management effort or service provider interaction" by the National Institute of Standards and Technology [1]. As one type of service supply chain (SSC), it is unlikely for it to avoid those problems commonly seen in an SSC, such as the issue of coordination and the issue of information asymmetry. In the light of

L. Wei • J. Ling (✉) • X. Zhou
School of Automation, Beijing University of Posts and Telecommunications,
100000 Beijing, China
e-mail: cherrylynn2012@gmail.com

different degrees of resource integration, cloud computing can be divided into three categories: infrastructure as a service (IaaS), platform as a service (PaaS), and software as a service (SaaS). Among them, SaaS is the highest value-added model.

With regard to the problem of coordination in SaaS, Demirkan and Cheng [2] for the first time studied the issue of coordination between an application infrastructure provider (AIP) and an application service provider (ASP) from the perspective of supply chain (SC). By examining the supply chain's performance under different coordination strategies involving risk and information sharing between the AIP and the ASP, they found that a strategy based on competition and cooperation could coordinate the SC. Besides, they found that there was a better outcome when letting the ASP, rather than the AIP, coordinate the SC. Their work offers us a good reference to further studies on interaction among different participating parties in the SC. Then Demirkan, Cheng, and Bandyopadhyay [3] considered the effects of queuing congestion, introduced the concept of "customer's delay cost" [4] into their SaaS model, and proposed a new market equilibrium constraint.

With regard to the problem of information asymmetry in SaaS, Kern, Willcocks, and Lacity [5] thought that information asymmetry was the major cause of risks facing those enterprise customers applying application service outsourcing. Risks included the service provider selection problem due to the asymmetric information of providers' service capability in the initial stage and the supplier incentive problem caused by the asymmetric information of supplier's service cost during the process of outsourcing. Balachandran and Radhakrishnan [6] considered an M/M/1 queue and examined the capacity choice problem when the delay cost per unit of time was not known. They managed to devise a cost allocation scheme that induces truthful reports from the divisions. And then Balachandran and Radhakrishnan [7] expanded their theory to an M/G/1 queue. Overall, cost and demand are two main aspects where information asymmetry lies in the study of traditional SC. Literatures [8–10] are all about the issue of traditional SC coordination under asymmetric information, which offer us multiple methods to solve the problem.

However, in the field of cloud computing service, there are only a few studies taking into account both the issue of coordination and the issue of information asymmetry. Ling Xinming, Liao Xiuwu, and Liu Yang [11] suggested AIP adopting a policy of predetermined service capacity to avoid opportunistic behavior of ASPs with low technical competence. Encouraged by a combined contract of cost and risk sharing, the ASP would enhance both its efforts during the free trial period and its final service capacity order quantity, so that the best effect of free trial for the whole SC was achieved.

Our study belongs to the territory of information economics in IT service supply chain management. We try to design an appropriate contract under which supply chain members will automatically select the behavior of information sharing. Our paper is based on the model proposed by Demirkan et al. in 2011 [3]. We analyze the probability of ASP's opportunistic behavior when users' delay cost is its private knowledge and respectively test the coordination effect of a wholesale-price contract and a revenue-sharing contract under such asymmetric information. Finally,

we propose a simple but practical way—changing the pricing mechanism of AIP’s service capacity—to coordinate the cloud service supply chain with asymmetric information.

96.2 Problem Description

The cloud SSC discussed in this paper consists of one AIP, one ASP, and terminal users. The AIP locating upstream of the SC-rents virtualized computing and storage capacities to the ASP downstream, which in turn provides value-added application developed on these capacities to its clients via Internet.

Assumption 1: The market demand arriving at ASP’s application (measured by tasks/transactions) can be described as an M/M/1 queuing model, which follows Poisson distribution. The number of homogeneous transactions arriving at ASP’s cloud software per unit of time is λ (the Poisson rate), while the processing capacity that ASP leases from AIP is μ , which means ASP’s cloud software can process μ transactions per unit of time.

Assumption 2: ASP charges its clients a price of p for processing one transaction. And we have tasks’ marginal value in the form of $V'(\lambda) = D/\lambda^k$, in which constant $D > 0$ and $1 > k > 0$. Considering their delay cost, the total cost for terminal users to process one transaction in the cloud system is $(p + \nu/(\mu - \lambda))$, in which ν denotes customer’s delay cost per transaction per unit of time and $T(\lambda, \mu) = 1/(\mu - \lambda)$ is the total time a transaction spends in the system. In the long run, queuing system will achieve dynamic equilibrium when users’ added value equals the cost they have to pay for one additional transaction, i.e., the arriving rate of transactions, λ , will be stabilized at a certain level as long as the cloud system is designed. Thus, we have the market equilibrium constraint as

$$V'(\lambda) = \frac{D}{\lambda^k} = p + \nu \cdot \frac{1}{\mu - \lambda} \tag{96.1}$$

Assumption 3: Let $C(\mu)$ represent the total cost that AIP has to pay for providing μ unit service capacity, and it can be denoted as $C(\mu) = c\mu + e\mu^2$ [3].

Assumption 4: Since AIP charges ASP a rental price of ω per unit of virtualized resource, the transfer payment between AIP and ASP per unit of time is $\omega\mu$.

Concerning Eq. (96.2), we have the expected profit function of AIP, ASP, and the whole SC per unit of time as follows:

$$\pi_{AIP} = \omega\mu - (c\mu + e\mu^2) \tag{96.2}$$

$$\pi_{ASP} = p\lambda - \omega\mu = D\lambda^{1-k} - \frac{\nu\lambda}{\mu - \lambda} - \omega\mu \tag{96.3}$$

$$\pi_{SC} = p\lambda - (c\mu + e\mu^2) = D\lambda^{1-k} - \frac{\nu\lambda}{\mu - \lambda} - c\mu - e\mu^2. \tag{96.4}$$

Assumption 5: AIP is the stronger one and it is responsible for designing contracts to coordinate the SC. The cost structure of either AIP or ASP is completely transparent, while the information on market demand is not. Specifically, AIP is aware of the expression of Eq. (96.2), but it does not know the exact value of the three constants, D , k , and ν . To highlight the key points, our paper only picks user’s delay cost, ν , as the asymmetric information, i.e., constants D and k are common knowledge while ν is ASP’s private knowledge. So AIP has to inquire of ASP about the exact value of ν before it designs the contract.

96.3 Problem Analysis

Here is the gaming process between AIP and ASP:

- *Stage One:* ASP reports information related to the market, mainly, $\tilde{\nu}$, to AIP.
- *Stage Two:* AIP develops a contract aiming at maximizing the profit of the whole SC, based on the information it got. When AIP believes that $\tilde{\nu} = \nu$, it gets the equilibrium condition $D/\lambda^k = p + \tilde{\nu}/(\mu - \lambda)$. For the overall optimal solution, the following first-order conditions need to be satisfied:

$$\left\{ \begin{array}{l} \frac{\partial \pi_{SC}(\mu, \lambda)}{\partial \mu} = \tilde{\nu}\lambda - c - 2e\mu = 0 \\ \frac{\partial \pi_{SC}(\mu, \lambda)}{\partial \lambda} = D(1 - k)\lambda^{-k} - \tilde{\nu}\mu \end{array} \right. \frac{1}{(\mu - \lambda)^2} = 0. \tag{96.5}$$

AIP also knows that, for ASP’s optimal solution, the following first-order conditions need to be satisfied:

$$\left\{ \begin{array}{l} \frac{\partial \pi_{ASP}(\mu, \lambda)}{\partial \mu} = \tilde{\nu}\lambda - \omega = 0 \\ \frac{\partial \pi_{ASP}(\mu, \lambda)}{\partial \lambda} = D(1 - k)\lambda^{-k} - \tilde{\nu}\mu \end{array} \right. \frac{1}{(\mu - \lambda)^2} = 0 \tag{96.6}$$

In theory, the SC is coordinated when solutions to Eqs. (96.5) and (96.6) are the same. Therefore, AIP’s unit capacity sale price must satisfy

$$\omega^* = c + 2e\mu^*(\tilde{\nu}). \tag{96.7}$$

Table 96.1 Baseline parameters for numerical explorations

D	k	c	e	v
1	0.5	1	1	0.1

Table 96.2 Key calculating process (a)

	For Table 96.3	For Table 96.4
Objective function	$\text{Max}_{p, \mu, \lambda} \pi_{SC} = p\lambda - (c\mu + e\mu^2)$	$\text{Max}_{p, \mu, \lambda} \pi_{ASP} = p\lambda - \omega\mu$
Market equilibrium	$\frac{D}{\lambda^*} = p + \tilde{\nu} \cdot \frac{1}{\mu - \lambda^*}, \nu = \tilde{\nu}$	$\frac{D}{\lambda^*} = p + \nu \cdot \frac{1}{\mu - \lambda^*}, \nu = 0.1$
Contract parameters	$\omega^* = c + 2e\mu^*$	The same as ω^* in Table 96.3
Other profit functions	Eqs. (96.2) and (96.3)	Eq. (96.2), $\pi_{SC} = \pi_{AIP} + \pi_{ASP}$

Table 96.3 Centralized decision with symmetric information

$\tilde{\nu}$	λ^*	μ^*	ρ^*	p^*	ω^*	π_{AIP}^*	π_{ASP}^*	π_{SC}^*	π_{AIP}^*/π_{SC}^*	π_{ASP}^*/π_{SC}^*
0.04	0.055	0.100	0.562	3.324	1.196	0.010	0.066	0.076	0.127	0.873
0.06	0.040	0.090	0.470	3.664	1.171	0.007	0.047	0.054	0.135	0.866
0.08	0.029	0.075	0.394	4.068	1.149	0.006	0.034	0.039	0.141	0.859
0.10	0.021	0.065	0.328	4.569	1.129	0.004	0.024	0.028	0.148	0.852
0.11	0.018	0.060	0.298	4.871	1.119	0.004	0.020	0.023	0.151	0.849
0.12	0.015	0.055	0.270	5.217	1.110	0.003	0.016	0.019	0.155	0.845
0.13	0.012	0.050	0.244	5.620	1.101	0.003	0.013	0.016	0.158	0.842
0.14	0.010	0.046	0.218	6.095	1.092	0.002	0.011	0.013	0.161	0.839
↑	↓	↓	↓	↑	↓	↓	↓	↓	↑	↓

- *Stage Three:* ASP determines its optimal renting quantity of virtualized hardware resource and the optimal price per transaction, $\{p_{ASP}^*, \mu_{ASP}^*\}$, depending on the contract that AIP provides and the real market demand (mainly, ν).
- *Stage Four:* Market demand is fulfilled according to the real delay cost ν and ASP’s policy of $\{p_{ASP}^*, \mu_{ASP}^*\}$; profit is allocated between AIP and ASP by the contract.

Since the contract is unenforceable, a few questions arise:

- Q1: Can a wholesale-price contract really coordinate this cloud service supply chain?
- Q2: Will ASP give false information about $\tilde{\nu}$ in order to enhance its own profit? If “yes,” will it exaggerate or underplay the user’s delay cost?

We can answer these questions through numerical analysis. Tables 96.3 and 96.4 respectively show the results of centralized decision with symmetric information and of ASP’s opportunistic behavior with asymmetric information. The baseline parameters for computational explorations are summarized in Table 96.1. And key solving processes are listed in Table 96.2. In Table 96.3, ASP reports the real delay cost per transaction per unit of time, i.e., $\tilde{\nu} = \nu$. In Table 96.4, AIP still makes its

Table 96.4 ASP’s opportunistic behavior with asymmetric information

$\tilde{\nu}$	λ_{ASP}^*	μ_{ASP}^*	ρ_{ASP}^*	p_{ASP}^*	$\omega^*(\tilde{\nu})$	π_{AIP}^*	π_{ASP}^*	π_{SC}^*	$\frac{\pi_{AIP}^*}{\pi_{SC}^*}$	$\frac{\pi_{ASP}^*}{\pi_{SC}^*}$
0.04	0.017	0.054	0.308	5.079	1.196	0.008	0.020	0.02753	0.279	0.721
0.06	0.018	0.058	0.316	4.883	1.171	0.007	0.021	0.02779	0.235	0.765
0.08	0.020	0.061	0.322	4.717	1.149	0.005	0.023	0.02794	0.192	0.808
0.10	0.021	0.064	0.328	4.569	1.129	0.004	0.024	0.02798	0.148	0.852
0.11	0.022	0.066	0.331	4.501	1.119	0.004	0.024	0.02797	0.125	0.875
0.12	0.023	0.068	0.334	4.435	1.110	0.003	0.025	0.02794	0.102	0.898
0.13	0.023	0.069	0.337	4.371	1.101	0.002	0.026	0.02788	0.077	0.923
0.14	0.024	0.071	0.339	4.309	1.092	0.001	0.026	0.02781	0.028	0.052
↑	↑	↑	↑	↓	↓	↓	↑	↔	↓	↑

decision of ω , which is optimal for the overall SC, by the way that is elaborated in stage two, because it does not know about ASP’s lie. So ω in Table 96.4 is the same one figured out in Table 96.3. Suppose that the real delay cost in Table 96.4 is 0.1. $\rho = \lambda/\mu$ is the utilization ratio of the system.

Comparing Table 96.4 with Table 96.3, we find that:

- Seen from Table 96.3, the unit capacity sale price, which is made by AIP to maximize the overall profit, decreases with an increasing $\tilde{\nu}$ that ASP reported. Therefore, ASP will exaggerate $\tilde{\nu}$ to obtain a lower rental price of virtualized resource.
- Seen from Table 96.4, in ASP’s decentralized scenario, a higher $\tilde{\nu}$ will bring ASP a higher profit π_{ASP}^* but a lower profit π_{AIP}^* for AIP. It is worth noting that the overall profit, π_{SC}^* , first increases but then decreases as the value of $\tilde{\nu}$ becomes larger and it reaches its maximum when $\tilde{\nu} = \nu$. When ASP exaggerates $\tilde{\nu}$, it can buy more computer capacity ($\mu_{ASP}^* \uparrow$) at a lower rental price ($\omega^*(\tilde{\nu}) \downarrow$) and sell its value-added application service to a larger market ($\lambda_{ASP}^* \uparrow$) at a lower price ($p_{ASP}^* \downarrow$). This opportunistic behavior allows ASP to get a higher profit than that when it reports the real ν . However, at the same time, this behavior harms the interest of AIP. Especially when $\tilde{\nu} > \nu = 0.1$, the decreasing rate of AIP’s profit is faster than the increasing rate of ASP’s profit, which is the reason why the overall profit decreases after $\tilde{\nu} = \nu = 0.1$. So, in order to maximize the overall cake of profit, AIP, as the coordinator of SC, has to set up an effective mechanism to induce ASP to report real information. Either in Table 96.3 or Table 96.4, AIP shares a small proportion of total supply chain profit. As the stronger one in the chain, AIP will never accept this result. So the simple wholesale-price contract cannot satisfy AIP.

In conclusion, the wholesale-price contract can neither coordinate the cloud service supply chain (because AIP will not accept it) nor keep the ASP from doing its opportunistic behavior. Consequently, AIP needs a more powerful contract.

96.4 Contract Design

96.4.1 Revenue-Sharing Contract

Revenue-sharing contract is a popular means of coordination in traditional supply chain, and it is reasonable to apply it to the cloud service supply chain: ASP carries out the whole process of software development, deployment, operation, and maintenance on the infrastructure that AIP provides, so, besides the rental price, it is rational for ASP to pay a certain percentage of its software sales to AIP, to cover AIP's cost of offering ASP extra value-added service besides infrastructure.

Suppose AIP's unit capacity sale price is still ω . Parameter ϕ is the percentage of terminal sales that ASP holds back, and $(1 - \phi)$ is the percentage of terminal sales that AIP receives. Therefore, there are two parameters in revenue-sharing contract that need AIP to decide, i.e., $\{\omega, \phi\}$. Obviously, only when ω and ϕ are both related to $\tilde{\nu}$ can AIP keep itself from ASP's opportunistic behavior by adjusting the two contract parameters. So contract parameters can be further expressed as $\{\omega(\tilde{\nu}), \phi(\tilde{\nu})\}$.

This time, AIP has realized the problem of $\tilde{\nu}$'s realness and that market demand is fulfilled by the real ν . So besides the market equilibrium condition Eq. (96.2), AIP has made some appropriate adjustments to each profit function:

$$\pi_{AIP}(\tilde{\nu}, \mu, \lambda) = \omega(\tilde{\nu}) \cdot \mu - (c\mu + e\mu^2) + (1 - \phi(\tilde{\nu})) \cdot p\lambda \tag{96.8}$$

$$\begin{aligned} \pi_{ASP}(\tilde{\nu}, \mu, \lambda) &= \phi(\tilde{\nu}) \cdot p\lambda - \omega(\tilde{\nu}) \cdot \mu \\ &= \phi(\tilde{\nu}) \cdot \left(D\lambda^{1-k} - \frac{\nu\lambda}{\mu - \lambda} \right) - \omega(\tilde{\nu})\mu \end{aligned} \tag{96.9}$$

$$\pi_{SC}(\mu, \lambda) = p\lambda - (c\mu + e\mu^2) = D\lambda^{1-k} - \frac{\nu\lambda}{\mu - \lambda} - c\mu - e\mu^2. \tag{96.10}$$

On the one hand, with the same thinking in Sect. 96.3, in order to coordinate the supply chain, AIP should design a contract that makes the solutions to the first-order conditions of Eq. (96.9) equal those to the first-order conditions of Eq. (96.10):

$$\begin{cases} \frac{\partial \pi_{SC}(\mu, \lambda)}{\partial \mu} = \frac{\nu\lambda}{(\mu - \lambda)^2} - c - 2e\mu = 0 \\ \frac{\partial \pi_{SC}(\mu, \lambda)}{\partial \lambda} = D(1 - k)\lambda^{-k} - \frac{\nu\mu}{(\mu - \lambda)^2} = 0 \end{cases} \tag{96.11}$$

$$\begin{cases} \frac{\partial \pi_{ASP}(\tilde{\nu}, \mu, \lambda)}{\partial \mu} = \phi(\tilde{\nu}) \cdot \frac{\nu\lambda}{(\mu - \lambda)^2} - \omega(\tilde{\nu}) = 0 \\ \frac{\partial \pi_{ASP}(\tilde{\nu}, \mu, \lambda)}{\partial \lambda} = \phi(\tilde{\nu}) \cdot \left[D(1 - k)\lambda^{-k} - \frac{\nu\mu}{(\mu - \lambda)^2} \right] = 0 \end{cases} \tag{96.12}$$

On the other hand, AIP has to set up an effective mechanism to induce ASP to report its real information. ASP will get its optimal profit only if it tells the truth. That is to say, ASP’s profit function, $\pi_{\text{ASP}}(\tilde{\nu}, \mu, \lambda)$, is strictly concave about $\tilde{\nu}$, and equations following need to be satisfied:

$$\left. \frac{\partial \pi_{\text{ASP}}(\tilde{\nu}, \mu, \lambda)}{\partial \tilde{\nu}} \right|_{\nu=\tilde{\nu}} = \frac{\partial \phi(\tilde{\nu})}{\partial \tilde{\nu}} \cdot \left(\frac{D\lambda^{1-k} - \tilde{\nu}\lambda}{\mu - \lambda} \right) - \mu \cdot \frac{\partial \omega(\tilde{\nu})}{\partial \tilde{\nu}} = 0 \tag{96.13}$$

$$\begin{aligned} \left. \frac{\partial^2 \pi_{\text{ASP}}(\tilde{\nu}, \mu, \lambda)}{\partial \tilde{\nu}^2} \right|_{\nu=\tilde{\nu}} &= \frac{\partial^2 \phi(\tilde{\nu})}{\partial \tilde{\nu}^2} \cdot \left(\frac{D\lambda^{1-k} - \tilde{\nu}\lambda}{\mu - \lambda} \right) - \frac{\lambda}{\mu - \lambda} \cdot \frac{\partial \phi(\tilde{\nu})}{\partial \tilde{\nu}} \\ &\quad - \mu \cdot \frac{\partial^2 \omega(\tilde{\nu})}{\partial \tilde{\nu}^2} < 0. \end{aligned} \tag{96.14}$$

Lemma 1 When Eq. (96.13) is satisfied, we have $\left. \frac{\partial^2 \pi_{\text{ASP}}(\tilde{\nu}, \mu, \lambda)}{\partial \tilde{\nu}^2} \right|_{\nu=\tilde{\nu}} \equiv 0$.

Proof We can derive Eqs. (96.15) and (96.16) from Eq. (96.13):

$$\begin{aligned} \phi(\tilde{\nu}) &= \frac{-\mu(\mu - \lambda)}{\lambda} \\ &\quad \cdot \left\{ \frac{\omega(\tilde{\nu})}{-D\lambda^{-k}(\mu - \lambda) + \tilde{\nu}} + \int \frac{\omega(\tilde{\nu})}{[-D\lambda^{-k}(\mu - \lambda) + \tilde{\nu}]^2} d\tilde{\nu} \right\} + C_1, \end{aligned} \tag{96.15}$$

$$D\lambda^{1-k} - \frac{\tilde{\nu}\lambda}{\mu - \lambda} = \frac{\mu \cdot \frac{\partial \omega(\tilde{\nu})}{\partial \tilde{\nu}}}{\frac{\partial \phi(\tilde{\nu})}{\partial \tilde{\nu}}}. \tag{96.16}$$

Putting Eq. (96.16) in Eq. (96.14), we get

$$\left. \frac{\partial^2 \pi_{\text{ASP}}(\tilde{\nu}, \mu, \lambda)}{\partial \tilde{\nu}^2} \right|_{\nu=\tilde{\nu}} = \frac{\partial^2 \phi(\tilde{\nu})}{\partial \tilde{\nu}^2} \cdot \frac{\mu \cdot \frac{\partial \omega(\tilde{\nu})}{\partial \tilde{\nu}}}{\frac{\partial \phi(\tilde{\nu})}{\partial \tilde{\nu}}} - \frac{\lambda}{\mu - \lambda} \cdot \frac{\partial \phi(\tilde{\nu})}{\partial \tilde{\nu}} - \mu \cdot \frac{\partial^2 \omega(\tilde{\nu})}{\partial \tilde{\nu}^2}. \tag{96.17}$$

The first and second derivatives of Eq. (96.15) about $\tilde{\nu}$ are

$$\left\{ \frac{\partial \phi(\tilde{\nu})}{\partial \tilde{\nu}} = \frac{-\mu(\mu - \lambda)}{\lambda} \cdot \frac{1}{-D\lambda^{-k}(\mu - \lambda) + \tilde{\nu}} \cdot \frac{\partial \omega(\tilde{\nu})}{\partial \tilde{\nu}} \right. \tag{96.18}$$

$$\left. \frac{\partial^2 \phi(\tilde{\nu})}{\partial \tilde{\nu}^2} = \frac{-\mu(\mu - \lambda)}{\lambda} \cdot \left\{ \frac{-1}{[-D\lambda^{-k}(\mu - \lambda) + \tilde{\nu}]^2} \cdot \frac{\partial \omega(\tilde{\nu})}{\partial \tilde{\nu}} + \frac{1}{-D\lambda^{-k}(\mu - \lambda) + \tilde{\nu}} \cdot \frac{\partial^2 \omega(\tilde{\nu})}{\partial \tilde{\nu}^2} \right\} \right\}. \tag{96.19}$$

Equation (96.18) divided by Eq. (96.19) equals Eq. (96.20) as follows:

$$\left(\frac{\partial^2 \varphi(\tilde{\nu})}{\partial \tilde{\nu}^2}\right) / \left(\frac{\partial \phi(\tilde{\nu})}{\partial \tilde{\nu}}\right) = \frac{-1}{-D\lambda^{-k}(\mu - \lambda) + \tilde{\nu}} + \left(\frac{\partial^2 \omega(\tilde{\nu})}{\partial \tilde{\nu}^2}\right) / \left(\frac{\partial \omega(\tilde{\nu})}{\partial \tilde{\nu}}\right). \quad (96.20)$$

Putting Eq. (96.20) in Eq. (96.19), we obtain the result

$$\begin{aligned} \left.\frac{\partial^2 \pi_{\text{ASP}}(\cdot, \tilde{\nu}, \mu, \lambda)}{\partial \tilde{\nu}^2}\right|_{\nu=\tilde{\nu}} &= \mu \cdot \left[\frac{-1}{-D\lambda^{-k}(\mu - \lambda) + \tilde{\nu}} \cdot \frac{\partial \omega(\tilde{\nu})}{\partial \tilde{\nu}} + \frac{\partial^2 \omega(\tilde{\nu})}{\partial \tilde{\nu}^2} \right] \\ &+ \mu \cdot \frac{1}{-D\lambda^{-k}(\mu - \lambda) + \tilde{\nu}} \cdot \frac{\partial \omega(\tilde{\nu})}{\partial \tilde{\nu}} - \mu \cdot \frac{\partial^2 \omega(\tilde{\nu})}{\partial \tilde{\nu}^2} \\ &\equiv 0 \end{aligned} \quad (96.21)$$

Proposition 1 No matter what kind of form that $\{\phi(\tilde{\nu}), \omega(\tilde{\nu})\}$ has, Eqs. (96.13) and (96.14) will never be satisfied at the same time. In other words, revenue-sharing contract cannot curb ASP's opportunistic behavior in the context of asymmetric information. It does not work well in encouraging information sharing.

96.4.2 Cost-Based Pricing Policy

The primary cause of the success of ASP's opportunistic behavior is that the rental price ω is related to $\tilde{\nu}$, while AIP does not have effective incentives or penalties to keep ASP from lying about $\tilde{\nu}$. Therefore, we attempt to solve this problem by changing AIP's fee structure.

The service capacity that ASP rents from AIP can be viewed as machine instances (MIs) at various levels. Variable μ represents different types of MIs. Obviously, there should be a price variance among MIs with different computing and storage capacity. Suppose that AIP charges ASP a price of $\omega(\mu)$ per unit of time. The profit functions become

$$\pi_{\text{AIP}} = \omega(\mu) - (c\mu + e\mu^2) \quad (96.22)$$

$$\pi_{\text{ASP}} = p\lambda - \omega(\mu) \quad (96.23)$$

$$\pi_{\text{SC}} = p\lambda - (c\mu + e\mu^2). \quad (96.24)$$

Repeating the work in Sect. 96.3, we find that when $\omega'(\mu) = c + 2e\mu$, the contract is in accordance with the principle of incentive compatibility and able to coordinate the SC. Now $\omega(\mu)$ takes the form of $\omega(\mu) = f + c\mu + e\mu^2$, in which f is an adjustable constant. Instead of a fixed wholesale price ω , AIP gives a tariff varying with μ here. We can observe that $\omega(\mu)$ is completely based on AIP's cost and the constant f can be used to adjust the profit-sharing ratio between the two parties.

Table 96.5 Key calculating process (b)

	For Table 96.6
Objective function	$\text{Max}_{p, \mu, \lambda} \pi_{\text{ASP}} = p\lambda - \omega(\mu)$
Variables	f, μ, λ
Market equilibrium	$\frac{D}{\lambda^s} = p + \nu \cdot \frac{1}{\mu - \lambda}, \nu = 0.1; \pi_{\text{AIP}}/\pi_{\text{SC}} = 0.5$
Contract parameters	$\omega(\mu) = f + c\mu + e\mu^2$
Other profit functions	Eq. (96.2), $\pi_{\text{SC}} = \pi_{\text{AIP}} + \pi_{\text{ASP}}$

Table 96.6 Coordination results under cost-based pricing policy

$\tilde{\nu}$	f	λ_{ASP}^*	μ_{ASP}^*	ρ_{ASP}^*	p_{ASP}^*	$\omega^*(\mu) = f + c\mu + e\mu^2$	π_{AIP}^*	π_{ASP}^*	π_{SC}^*	$\frac{\pi_{\text{AIP}}^*}{\pi_{\text{SC}}^*}$
0.04 ~0.14	0.014	0.021	0.064	0.328	4.568	0.083	0.014	0.014	0.028	0.500

This cost-based price $\omega(\mu)$ relies on readily available information from cost accounting systems, and it is free from information reported by ASP, such as $\tilde{\nu}$. So this cost-based price per unit of time can eliminate the influence from ASP’s opportunistic behavior resulting from demand information asymmetry downstream. It is one of the benefits of cost-based price.

The expected profit per unit of time of AIP is $\pi_{\text{AIP}} = \omega(\mu) - (c\mu + e\mu^2) = f$. By adjusting the value of f , AIP is able to determine any profit distribution ratio between them. Of course the final profit distribution ratio also depends on the bargaining power of both. Table 96.5 and Table 96.6 respectively show the process of computation and the outcome when profit-sharing ratio is 1:1.

Numerical analysis further shows that regardless of the realness of the information ASP provided, AIP can always set up the right rental price per unit of time, $\omega(\mu)$, to maximize the overall profit and get an ideal profit sharing by pricing based on its cost and ASP’s actual service capacity leasing amount later on.

Conclusion

This paper further explores the SaaS model proposed by Demirkan et al. in 2011. Self-interest and maximization of individual outcomes have been major assumptions of neoclassical microeconomics since about 1870. The assumption of opportunistic behavior, together with bounded rationality, represents the central assumption in the argument of transaction cost economics. In our paper, AIP is the monopolist responsible for coordinating the SC, but it is ASP that processes the private information about market—user’s delay cost per transaction per unit of time, ν . Opportunistic behavior occurs when ASP takes advantage of its superior knowledge about the market, in order to increase its own interests. Numerical analysis in Sect. 96.3 proves that ASP is very likely to exaggerate the value of ν .

(continued)

(continued)

Using contracts is a conventional way to coordinate an SC. An unenforceable contract without enough incentives or penalties, however, will probably fail to achieve a win-win situation. ASP distorts the value of ν and waits until AIP makes the agreement and then benefits from it.

There exist two drawbacks when AIP develops a single fixed service capacity rental price, ω , aiming at obtaining the overall optimal profit: (1) AIP only gets a small proportion of the overall surplus, while ASP occupies the most of it, and (2) AIP cannot prevent ASP from reporting false information about the market, such as ν . Consequently, we try another two types of contracts so that AIP cannot only realize the coordination of the supply chain, but also avoid the negative impact caused by information asymmetry. Here is the result:

- Proved by formula derivation, revenue-sharing contract $\{\omega(\tilde{\nu}), \phi(\tilde{\nu})\}$ fails to satisfy the first and second order conditions simultaneously for truthful reporting to be always optimal for ASP, as a Nash equilibrium.
- Cost-based service capacity pricing policy is free of the false information from ASP, since it only depends on AIP's cost structure and the final type of machine instance ASP rents. The rental price has the form of $\omega(\mu) = f + c\mu + e\mu^2$, in which f is used for profit allocation and the rest for covering AIP's cost.

Acknowledgments This work was supported by Beijing Natural Science Foundation (4122052) and by Engineering Research Center of Information Networks, Ministry of Education.

References

1. Demirkan H, Goul M. Introduction to the cloud service science and systems minitrack. In: Proceedings of the 46th Hawaii international conference on system sciences. IEEE; 2013. p. 1015.
2. Demirkan H, Cheng HK. The risk and information sharing of application services supply chain. *Eur J Oper Res.* 2008;187(3):65–784.
3. Demirkan H, Cheng HK, Subhajyoti B. Coordination strategies in an SaaS supply chain. *J Manage Inform Syst.* 2011;26(4):119–43.
4. Mendelson H. Pricing computer services: queuing effects. *Commun ACM.* 1985;28(3):312–21.
5. Kern T, Willcocks LP, Lacity MC. Application service provision: risk assessment and mitigation. *MIS Quar Exec.* 2002;1(2):113–26.
6. Balachandran KR, Radhakrishnan S. Cost of congestion, operational efficiency and management accounting. *Eur J Oper Res.* 1996;89(2):237–45.

7. Balachandran KR, Radhakrishnan S. Service capacity decision and incentive compatible cost allocation for reporting usage forecasts. *Eur J Oper Res.* 2004;157(1):180–95.
8. Akan M, Lariviere BM. Asymmetric information and economies of scale in service contracting. *Manuf Serv Oper Manage.* 2011;13(1):58–72.
9. Gan X, Sethi SP, Zhou J. Commitment-penalty contracts in drop-shipping supply chains with asymmetric demand information. *Eur J Oper Res.* 2010;204(3):449–62.
10. Babich V, Li H, Ritchken P, Wang Y. Contracting with asymmetric demand information in supply chains. *Eur J Oper Res.* 2012;217(2):333–41.
11. Li X, Liao X, Liu Y. Research on service supply chain coordination based on SaaS model. *Chin J Manage Sci.* 2013;21(2):98–106. In Chinese.

Chapter 97

One More Efficient Parallel Initialization Algorithm of K-Means with MapReduce

Bingliang Lu and Shuchao Wei

Abstract Because the main deficiencies of a k-means++ algorithm is its internal orderliness, which restricts its applicability in the field of big data processing, we propose an initialization algorithm called pk-means++ based oversampling technology. The initial cluster centers that are obtained using the new algorithm are proved to be very close to the desired cluster centers used for iterative algorithms. It is implemented based on MapReduce of Hadoop, and the experimental results demonstrate that the improved MapReduce pk-means++ algorithm is much more efficient than random and k-means++ initialization algorithm used in k-means based MapReduce and can reach a good approximation.

Keywords Cloud computing • Hadoop • MapReduce • Clustering • k-means • pk-means++

97.1 Introduction

Cluster analysis is a very important area of research on data mining [1, 2], and with advances in technology, big data analysis and application represent general trends. Thus, clustering studies face many new problems and challenges, such as massive data analysis and new computing environments. K-means algorithms are good clustering methods in terms of speed and simplicity in the field of data mining. They have been identified as one of the top ten algorithms for data mining [3]. Some researchers have achieved parallelization of k-means algorithms using MapReduce, but the initial part of it that is used is a largely random initialization method, which is easy to fall into local optima and might still not be well parallelized. (The initial value of the inappropriate choice would result in local optimal solution. For example, the distance of selected points randomly is very close. In this case, we have several randomly chosen initial values and then selected the optimal solution.) Thus, the focus of this study is to search for a better parallel initialization algorithm for k-means

B. Lu (✉) • S. Wei
School of Computer, Shenyang Aerospace University, 110136, Shenyang, China
e-mail: bingliang_lu@163.com; scwade@foxmail.com

algorithms to improve the quality and overall performance (we try to find a more perfect and simply realization method of k-means on distributed platforms).

In this area, Arthur and Vassilvitskii proposed an initialization method called k-means++ [4], which obtained excellent theoretical guarantees for clustering performance. Using this method, the convergence time of Lloyd's iteration was reduced by means of a good set of starting centers. But the main deficiencies of the k-means++ algorithm is its internal orderliness, so it is not parallelizable. This fact is more serious in the field of big data processing [5].

Research efforts are being devoted to improving and realizing a k-means++ parallel method based on the MapReduce programming model. One parallel version of the initialization algorithm called pk-means++ is proposed.

97.2 The of K-Means Algorithm

First, some notation is established. Let $X = \{x_1, x_2, \dots, x_n\}$ be a data set in the d -dimensional Euclidean space. Next, let K be a number of clusters of k-means, and the value of K is specified based on experience (this is not the focus of this paper).

Let $C = \{c_1, c_2, \dots, c_n\}$ be a set of points and $\|x_i - x_j\|$ denote the Euclidean distance between x_i and x_j . The k-means method generates k centers by optimizing the criterion of minimum squared error (MSE, the cost of clustering), which is given by $\phi_X(C) = \sum_{x \in X} \min_{c \in C} \|x - c\|^2$.

The ultimate goal of a k-means clustering algorithm is to sample a new set C that includes k centers in order to minimize $\phi_X(C)$. Finally, the data set X is divided into K data sets Y , and $Y = \{Y_1, \dots, Y_k\}$, $\bigcup_{i=1}^k Y_i = X$, $Y_i \cap Y_j = \emptyset$.

One study has proven that finding $\phi_X(C)$ is an NP-hard problem [6]. A variety of options have been researched on providing approximate solutions. Among them, Lloyd's algorithm is widely used in k-means algorithms.

Next, we discuss the algorithm of k-means++ in more detail (Sect. 3). Then, in Sect. 3.1, we give a new initialization algorithm. Finally, a more precise overview of the MapReduce mode is given in Sect. 3.2.

97.3 Parallel Initialization Algorithm Design of PK-Means++

The main idea of k-means++ is that the first centroid is chosen randomly, and then subsequent centers are chosen one by one from the remaining data points [4]. The k-means++ initialization algorithm is presented as follows:

Algorithm 1 : k-means++

1. $C \leftarrow \phi$
 2. Choose one center x as c_1 uniformly at random from X , $C = C \cup \{x\}$.
 3. Repeat
 - Choose $x \in X$ with probability $d^2(x, C) / \phi_X(C)$
 - $C = C \cup \{x\}$
 4. Until k centers are chosen, Output: $C = \{c_1, c_2, \dots, c_k\}$.
-

Formally, k-means++ samples a single point in each pass. It runs very fast in practice, and if the data are clustering well [7], it can guarantee a solution will be found that is an $O(\log k)$ approximation to the optimal k-means [6].

But the major downside of the k-means++ is that it is applicable only to big data: a parallel initialization algorithm is proposed based on the k-means++ algorithm and oversampling technology; we call it pk-means++.

97.3.1 Basic Idea of PK-Means++

The main idea of the new initialization algorithm is that it chooses $O(k)$ points in each pass and obtains a nearly optimal solution after a logarithmic number of passes. Finally, $O(k \log n)$ points will be left, and experimental results show that a constant number of passes suffices in practice.

Then we set $\langle \text{num}[i], c_i \rangle, i = 1, 2, \dots, k$ as the weight of every centroid selected; it represents the number of objects in set X to the centroid point of c_i . Next, we recluster these points using k-means++ initialization. Next, the points are reclustered into k initial centers, and Lloyd's iteration can continue. Finally, we use a standard k-means algorithm to complete the clustering.

97.3.2 MapReduce Implementation of PK-Means++

MapReduce is a programming model for efficient distribution, but also for processing big data sets. A typical MapReduce program consists of three stages: the Mapper stage, Shuffle stage, and Reduce stage. Also, the data set should have the following characteristics [5]: it can be broken into many small data sets, and every small data set can be processed completely in parallel.

In a k-means algorithm, the distance from each element to the centroid is calculated independently, with different elements not being linked to each other in the course of operation. Thus, the parallelized version of Lloyd's iterations based MapReduce modules can be easily realized. The basic idea is that each iteration

starts a MapReduce process. According to the computing needs of MapReduce, the data are stored by row and can be sliced by row, with no correlation between the chip data. However, this is not the focus of the present study, though it has been achieved by some researchers [5, 8], and it will not be discussed any further.

According to the preceding analysis, the MapReduce implementation of the pk-means++ algorithm should be divided into two stages, Mapper and Reduce. First, in the Mapper stage, complete steps 1–7 of the pk-means++ algorithm, including generating a temporary data set and calculating the weight of each element of the set. Reduce the stage to complete the remaining part of the algorithm. To obtain the final set of initial cluster centroids C , we integrate k-means++ algorithm with reduce methods. Please refer to the specific implementation which is described in what follows.

The Mapper of pk-means++ initialization

Input : k , the number of clusters $X = \{x_1, x_2, \dots, x_n\}$, a set of data points.

Output: $\langle num[i], c_i \rangle, i = 1, 2, \dots, k$; $num[i]$ presents that the number of objects in set X to the centroid point of c_i .

1. $C \leftarrow \phi$
 2. Choose one center x as c_1 uniformly at random from X , $C = C \cup \{x\}$
 3. for $i = 1; i \leq O(k \log n); i++$ do
 4. $num[i] = 0$
 5. $\phi \leftarrow \phi_x(C)$
 6. for $O(\log \phi)$ times do
 7. $C' \leftarrow$ each point x is chosen from X with probability $f \cdot d^2(x, C) / \phi_x(C)$ respectively.
 8. $C \leftarrow C \cup C'$
 9. End for
 10. for $i = 1; i \leq O(k \log n); i++$ do
 11. find the nearest center $c_i \in C$ for x_i then $num[i]++$
 12. output $\langle num[i], c_i \rangle$ and $TempC = C$;
-

As described above, several expensive distance computations can be carried out with MapReduce. Step 7 can be performed in the following manner: each Mapper can sample independently and merge the intermediate results. Step 8 will be given a small set C of centers, and we can compute the value as follows: each Mapper job of Hadoop works on an input data split and then merges these intermediate results from all Mappers to obtain an output for Reducer.

The task of the Reducer function is to update, based on the output of the Mapper function, update the cluster centers for the next round of the Mapper function to use.

Meanwhile, calculate the standard measure for the main function to determine whether the iteration is over. The specific description of the Reducer function is as follows:

The Reducer of pk-means++ initialization
Input : k , the number of clusters ;The output of Mapper: < num,c > , <i>TempC</i>
Output: $C = \{c_1, c_2, \dots, c_k\}$

1. $C = \emptyset ; X = TempC$
2. Choose one center x as c_1 uniformly at random from $X , C = C \cup \{x\}$
3. while $|C|$ is lesser than K, do
 - 3.1 Choose x from X with the probability of $d^2(x, C) / \phi_x(C)$
 - 3.2 $C = C \cup \{x\}$
5. Until k centers are chosen ; output: $C = \{c_1, c_2, \dots, c_k\}$

6. Continue the process with the normal k-means clustering algorithm

The preceding MapReduce procedure is called in the main function. Each iteration is applied to a new job until the square error, which is calculated by the old centers before iteration and the new centers obtained after iteration, is less than the given threshold value; then the iteration ends.

97.4 Experimental Results and Analysis

The parallel experiments are performed on a homogeneous Hadoop cluster running the latest stable version of Hadoop 1.2.1. The cluster consists of four machines with one master node and three slave nodes. Each node has one Intel Core i5-2400 3.10 GHz Quad-Core CPU, 4 GB RAM, 500 GB hard disk, Intel 82551 10/100 Mbps ethernet controller. The operating system of each node is CentOS-6.3 server 32 bit and per Hadoop daemon is allocated 1 GB memory. This cluster consists of one TaskTracker and one DataNode daemon running on each slave and a single NameNode and JobTracker daemon on the master. Two map slots and two reduce slots are configured on each node. The experiments are conducted on the KDDCup1999 data set. This is a real data set whose size is 4.8 M; the points of the data set are 42 dimensions in Euclidean space. In the experiments, it is assumed that when the initialization method is finished, Lloyd’s iterations are continued implicitly.

Let us first analyze the run time of different initialization procedures in the tables. Comparing the data in Table 97.1, it is found that when one suitable parameter f is selected for the pk-means++ algorithm, the convergence speed of the clustering algorithm used by pk-means++ is the fastest and the total time using the random k-means++ is at least one-fourth that of the other algorithm. Combined

Table 97.1 Total clustering time (minutes) of k-means

Initialization algorithm	k (number of clusters)	
	200 ^a	500 ^a
Random	320.0	474.8
k-means++	408.5	1,027.2
pk-means++, $f = 0.5 k$	66.5	44.5
pk-means++, $f = 1.0 k$	73.6	87.2
pk-means++, $f = 2.0 k$	64.2	82.5
pk-means++, $f = 4.0 k$	79.5	104.2

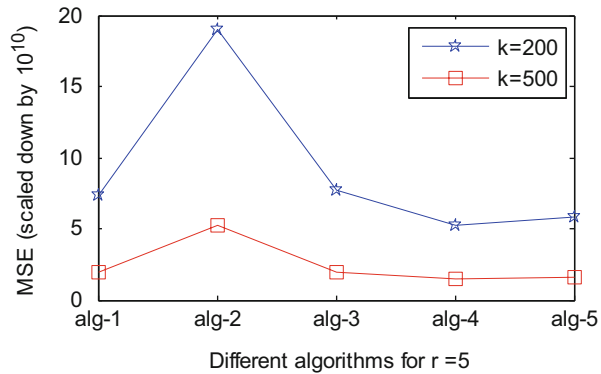
^aThe experimental results can be easily observed and contrasted

Table 97.2 Clustering cost (MSE-scaled down by 10^{10}) of different algorithms for $r = 5$

Initialization algorithm	k (number of clusters)	
	200 ^a	500 ^a
Random	6.7E + 7	6.5E + 7
k-means++ (alg-1)	7.2	2.0
pk-means++, $f = 0.5 k$ (alg-2)	18.5	5.3
pk-means++, $f = 1.0 k$ (alg-3)	7.5	2.2
pk-means++, $f = 2.0 k$ (alg-4)	5.1	1.6
pk-means++, $f = 4.0 k$ (alg-5)	5.75	1.52

^aThe experimental results can be easily observed and contrasted

Fig. 97.1 Clustering cost (MSE) of different algorithms for $r = 5$

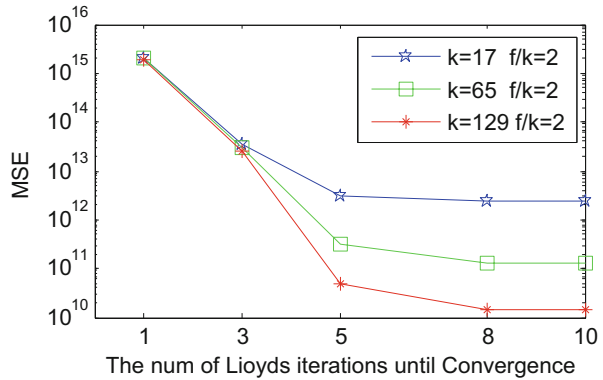


with the final clustering quality analysis we found that, when $f = 2.0 k$, the performance of the pk-means++ clustering algorithm is the best.

As described in Table 97.2 and Fig. 97.1, it is clear that pk-means++ outperforms k-means++ by orders of magnitude. When the coefficient $f = 0.5 k$, the convergence value of the objective function is higher than that of the k-means++ algorithm. But when the coefficient $f > 1 k$, the objective function value of the algorithm exhibits a linear downward trend, suggesting that the effect of clustering with an increasing f value will be significantly improved. By setting the value of k to 200 and 500, we find that the larger the value of k clusters is, the smaller the convergence value is.

To describe the experimental data of Table 97.2 in a more intuitive way, the following description uses a line chart. As described in Fig. 97.1:

Fig. 97.2 Effect of different parameter settings on final cost of algorithm



Next, Let us evaluate the influence of different settings of parameter carefully. The experiment is conducted with a changing value of a k-based data set that represents a 10 % sample of KDDCup1999. The detailed data are as follows:

As described in Fig. 97.2, when $f = 2k$, we find that the MSE shows a downward trend with the increased number of passes. Further, it is found that even a small number of passes is enough to reduce the final convergent cost substantially. The total clustering cost is the cost after the completion of Lloyd’s iteration, and when, after a certain value of r is reached, the r value is changed again, and the change in the clustering cost becomes very negligible.

Conclusion

In this paper, we develop an efficient k-means++ initialization algorithm with MapReduce, and a parallelized version based on MapReduce called pk-means++ is proposed. The standard k-means++ initialization is also applied to the Reducer phase of pk-means++.

For the Reducer of MapReduce projects, the new algorithm saves considerable communication and I/O costs. Extensive experiments on real data were conducted. The results indicate that the proposed MapReduce pk-means++ algorithm is much more efficient and random than k-means++ and demonstrates that the improved MapReduce pk-means++ algorithm is much more efficient and can obtain good approximations.

References

1. Moise D, Shestakov D, Gudmundsson G, Amsaleg L. Indexing and searching 100 m images with map-reduce. In: Proceedings of the 3rd ACM Conference on Multimedia Retrieval; ACM, New York; 2013. p. 17–24.
2. Xu Z, Ke Y, Wang Y, Cheng H, Cheng J. A model-based approach to attributed graph clustering. In: Proceedings of the 2012 ACM SIGMOD International Conference on Management of Data; ACM, New York; 2012. p. 505–16.

3. Wu X, Kumar V, Ross Quinlan J, Ghosh J, Yang Q, Motoda H, McLachlan GJ, Ng A, Liu B, Yu PS, Zhou Z-H, Steinbach M, Hand DJ, Steinberg D. Top 10 algorithms in data mining. *Knowl Inf Syst.* 2008;14(1):1–37.
4. Arthur D, Vassilvitskii S. k-means++: the advantages of careful seeding. In: *Proceeding of the Eighteenth Annual ACM-SIAM Symposium on Discrete Algorithms*; Society for Industrial and Applied Mathematics, Minneapolis,. 2007; p. 1027–35.
5. Zhao W, Ma H, He Q. Parallel k-means clustering based on mapreduce. In: *Proceedings of the 1st International Conference on Cloud Computing*; Springer, Berlin, Heidelberg; 2009. p. 674–79.
6. Aloise D, Deshpande A, Hansen P, Popat P. NP-hardness of Euclidean sum-of-squares clustering. *Mach Learn.* 2009;75(2):245–48.
7. Bahmani B, Moseley B, Vattani A, Kumar R, Vassilvitskii S. Scalable k-means++. *PVLDB.* 2012;5(7):622–33.
8. Lloyd SP. Least squares quantization in PCM. *IEEE Trans Inf Theory.* 1982;28(2):129–36.

Chapter 98

Equipment Information Management System Based on Web Services

Ganguo Li, Wu Qin, Tingyi Zhou, Yang wang, and Xiaofeng Zhu

Abstract Heterogeneous equipment using in range test bring the problem of information management and equipment long-distance control in real time. To solve this problem, an equipment information management system based on Web services is designed that has features of equipment synthesis information management and equipment long-distance control in real time. Experimental results show that the system has a quick browser response speed and short information transmission delay.

Keywords Web service • Middleware • Database • Information management system

98.1 Introduction

More and more information-based weapons systems have been used in the range test along with the high-speed development of information and network techniques. Consequently, some information systems have been built for range tests for certain equipment. However, most of these information systems are heterogeneous and do not have a uniform information interaction mechanism [1]. Heterogeneous equipment of range brings the problem of information management and equipment long-distance control in real time. Therefore, it is necessary to design an equipment information management system using information and network techniques [2]. Currently there are several information management mechanisms such as Simple Network Management Protocol (SNMP) [3], Desktop Management Interface (DMI) [4], and Common Management Information Protocol (CMIP) [5]. These mechanisms adopt middleware architectures for generating the interface between heterogeneous systems. Among the commonly used middleware architectures, PHP, Java servlets, and Enterprise Java Beans (EJB), Java servlets can be located on a separate machine for better load balancing [6]. This paper presents the design

G. Li (✉) • W. Qin • T. Zhou • Y. wang • X. Zhu
91 Sub-Unit, 92941 Unit, Huludao, No.1 HaiBin road,
125001 Huludao city, LiaoNing province, China
e-mail: liganguo1982@126.com

of an equipment information system based on Web services that uses Java servlet middleware architecture. The main design and realization processes are briefly described in what follows.

98.2 Design of an Equipment Information System

98.2.1 System Function

An equipment information system needs to have two main system functions: equipment synthesis information management and real-time equipment long-distance control. Equipment synthesis information management mainly includes the following features: equipment information maintenance, real-time equipment performance index, real-time equipment state monitoring, equipment maintenance process management, real-time equipment information statistics, and equipment disposal state index. Real-time equipment long-range control mainly includes two parts: real-time equipment-running-state long-distance show in real time and real-time equipment running process long-range control.

98.2.2 System Architecture

The system architecture of equipment information systems based on Web services is shown in Fig. 98.1, which consists of equipment, system users, and servers. The servers, equipment, and system users are connected by a test network through a Web service.

Servers includes Web servers, application servers, database servers, and flow media servers. Web servers supply information management functions, such as, for example, requirement analysis, safety checkup, browse control, and database browse function disposal, for system users and equipment. Application servers supply application rules and common function modules for the whole information system, which makes it possible to process all types of equipment information and show it in multiple forms. Database servers save equipment data information, and flow media servers save equipment flow media information.

System users are responsible for their interaction with information systems, which includes functions of user information input and user checkup results feedback. Equipment mainly carries out functions having to do with equipment information such as equipment real-time state upload, daily data input, and running log file saves using middleware methods. Otherwise, both system users and equipment can access, process, and display equipment information being saved in database servers and flow media servers based on their requirements.

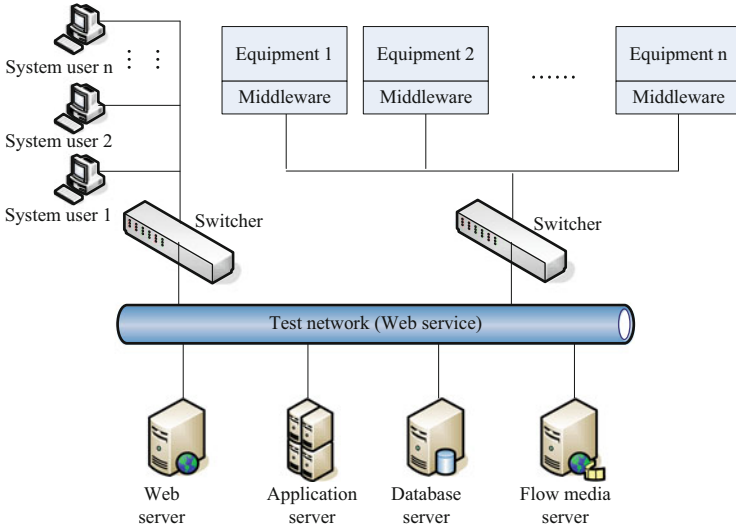


Fig. 98.1 Equipment information system architecture

98.3 Realization of Equipment Information System

98.3.1 Equipment Synthesis Information Management

The layered architecture of an equipment synthesis information management system is illustrated in Fig. 98.2. Equipment synthesis information management is divided into three layers: a resource layer, a service layer, and an application layer.

98.3.1.1 Resource Layer

A resource layer is a database for the storage of equipment information, including data information and flow media information. The database is constructed by Oracle [7], which manages multiple data types, such as, for example, setting parameters, original experiment files, process data, result data, equipment documents, and equipment image, audio, and video data. In addition, the database is mainly composed of five databases: a basic equipment information database, an extended equipment information database, an equipment specification file database, an equipment interface feature database, and a file database for equipment control in long distance.

The basic equipment information database stores basic equipment information, which includes, for example, equipment ID, type, model number, manufacturer, factory name, work state, maintenance record, user, and disposal unit.

The extended equipment information database stores extended equipment information, which includes equipment function description, description of general

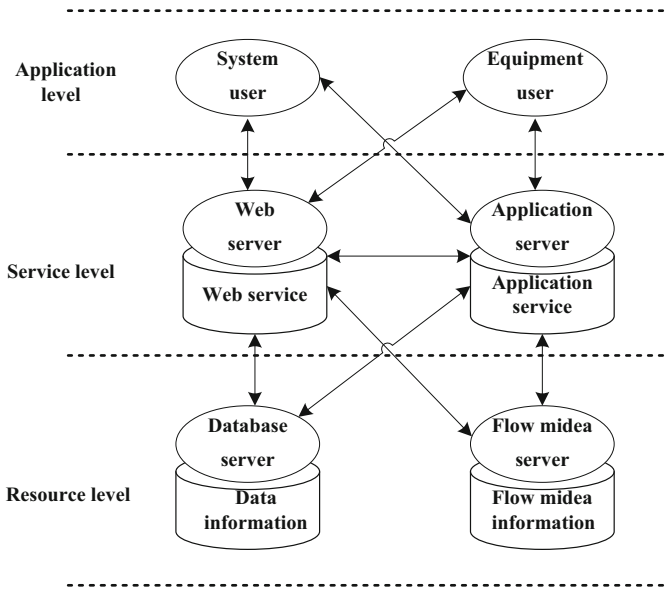


Fig. 98.2 Layer architecture of equipment synthesis information management

condition, position information, configuration information, and environment information (such as air temperature and humidity).

The equipment specification file database stores equipment specification files, which include equipment working theory specification files, equipment usage, and maintenance specification files.

The equipment interface feature database stores equipment interface features, which include equipment software and hardware interface types, communication protocol descriptions, packaging description.

The file database for equipment control in long distance stores files for equipment control in long distance, which includes equipment virtual object models and component models.

98.3.1.2 Service Layer

A service layer is a layer between the resource and application layers that is responsible for the organization and management of a database and provides the interface for application software. The services supported by the service layer are based on the Web service methods and composed of equipment index services, equipment management services, equipment maintenance services, and safety management services. Equipment index services include equipment list index service and equipment detail information index service. Equipment management services include, for example, adding equipment, removing equipment, updating

equipment information, and relocating equipment maintenance services include starting maintenance and stopping maintenance services. Safety management services include user manage service and safety verification.

98.3.1.3 Application Layer

The application layer supplies equipment information input, use, and management functions for equipment and system users, which include an equipment information logging function, an equipment information maintenance function, real-time equipment performance monitoring, real-time equipment information statistics, and an equipment disposal state index. All the software of the application layer is developed in the form of Browser/Server, by which equipment and system user can load application service and use system information through a browser.

98.3.2 Equipment Long-Distance Control in Real Time Based on Middleware

Equipment long-range control in real time based on middleware contains two main parts: connecting way and packaging way of equipment.

98.3.2.1 Connecting Equipment Hardware

The ways in which equipment hardware is connected can be divided into direct and indirect ways. The direct way is suitable for equipment with control computers, on which middleware can be run (Fig. 98.3). The indirect way is suitable for equipment without control computers or computers on which middleware cannot be run (Fig. 98.4). As we see from Fig. 98.3, the middleware is running on the equipment control computer. As the connecting hardware, the equipment control computer directly connects the equipment with the test network, and the equipment control software transmits information with middleware through an object model, which realizes the equipment long-range control in real time.

As we see from Fig. 98.4, the middleware is running on the equipment access computer. The equipment access computer, as the connecting hardware, connects to the test network on one side and to the equipment on the other side by Ethernet or RS422 interface.

Fig. 98.3 Diagram of direct connection

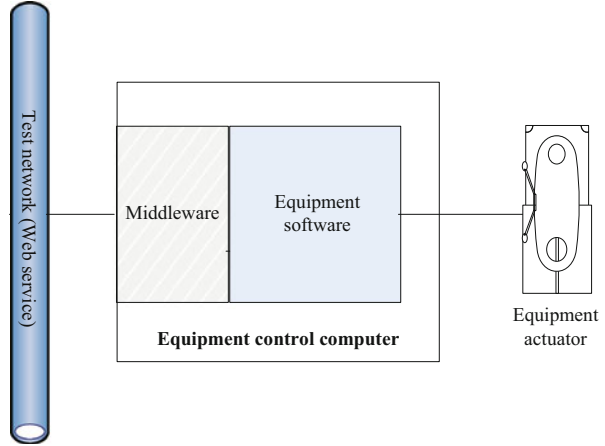
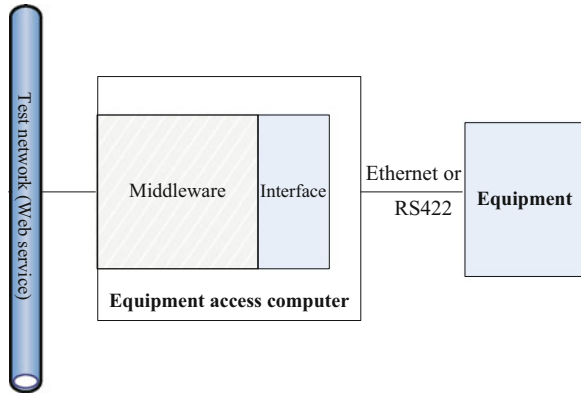


Fig. 98.4 Diagram of indirect connection



98.3.2.2 Packaging Equipment

Equipment is packaged as a resource model. The resource includes an object model and a component model. An object model is the abstract presentation of resources in a test system. A component model is used to operate object model.

The basic packaging steps are as follows.

- Step 1: The resource object model is constructed using PowerDesigner [8] and exported as description XML files of the object model.
- Step 2: The interface window of component model is designed by Qt Designer [9] and exported as UI files.
- Step 3: The protocol is defined by a protocol designer [10] and exported as protocol formatted files.

Step 4: The component model is produced using middleware API and component designer software that loads the XML files, UI files, and protocol formatted files and is exported as DLL files [11, 12].

98.4 Experimental Study

To compare the performance of different middleware architectures, some experiments were conducted, and the results are shown in Table 98.1.

As we see from Table 98.3, Java servlet middleware produces a higher peak interaction throughput per minute at a lower CPU utilization rate because of the reduction in database index.

After the equipment information management system was built, test experiments were conducted. The results are shown in Tables 98.2 and 98.3.

As we see from Table 98.2, when the number of system users increases, the browser response time increases. When there are up to 200 users, the browser response time is less than 2.5 s, which shows that the system database is well organized and the system has a quick response speed.

As we can see from Table 98.3, the average information transmission delay time is basically the same regardless of the amount of equipment connected to the network. And the information transmission delay time is very small, which satisfies the requirement of real-time equipment control.

The experimental results show that the system we built has a quick browser response speed and small information transmission delay, which means it is capable of carrying out the functions of equipment synthesis information management and equipment long-range control in real time.

Table 98.1 Performance of PHP, Java servlets, and EJB

Middleware architecture	Peak interaction throughput per minute	CPU utilization at peak throughput (%)
PHP	520	70
Java servlets	630	70
EJB	370	100

Table 98.2 Browser response time with different numbers of system users at the same time

Number of system users	10	40	60	150	200
Browser response time (s)	1	1.2	1.5	1.8	2.3

Table 98.3 Average information transmission delay time with different amount of equipment

Pieces of equipment	2	3	5	10	30
Information transmission delay (ms)	108	110	112	114	114

Conclusion

In summary, this paper describes an equipment information management system based on Web services that can perform equipment synthesis information management and equipment long-range control in real time. Using the equipment information management system, the automatic level of equipment control is largely improved, and information management is more scientific and convenient.

References

1. Du D, Shao H. The construction analysis of education information resource share network frame. *Softw Guid.* 2013;12(7):120–2 (in Chinese).
2. Hu S, Shen X, et al. Web remote real-time monitoring and control system based on Ajax and SVG. *Comput Eng Des.* 2011;32(2):132–6 (in Chinese).
3. Stallings W, SNMP W. The infrastructure network management. *IEEE Commun Mag.* 1998;36(3):37–43.
4. DMTF. Desktop management interface standards. 2005. <http://www.dmtf.org/standards/dmi>.
5. Modiri N. The common network management information service element interfaces. *IEEE Commun Mag.* 1991;29(7):29–38.
6. Maximilien EM, Ranabahu A, et al. Toward cloud-agnostic middlewares. In: *Proceedings of ACM SIGPLAN International Conference on Object-Oriented Programming, Systems, Languages, and Applications*. Orlando: ACM; 2009. p. 805–6.
7. Lv H, Weng J. Research on performance optimization approaches for web-based large-scale oracle application system. *Comput Appl Softw.* 2012;29(5):184–7 (in Chinese).
8. Cao F. Database system construction based on power designer. *Electron Sci Technol.* 2011;24(3):104–5 (in Chinese).
9. Wang J, Liu H. The design and application of storage analysis system based on QT. *Softw Guid.* 2011;10(7):87–8 (in Chinese).
10. He Y, Shen H. Astochastic Petri net-based performance bottleneck location strategy for web services composition. *Chin J Comput.* 2013;36(1):1953–8 (in Chinese).
11. Wu Q. Network computing middleware. *J Softw.* 2013;24(6):67–76 (in Chinese).
12. Yu J. Frame format conversion based on NDIS. *Commun Technol.* 2013;46(8):73–5 (in Chinese).

Chapter 99

Maximal Service Profit in MAS-Based Cloud Computing Considering Service Security

Shengji Yu, Hongyu Chen, and Yanping Xiang

Abstract In recent years, new computing paradigms have been proposed and adopted such as cloud computing. Service is an important aspect in cloud computing. From service provider's perspective, a major concern is the method to get maximal service profit. The chapter describes a model-based multi-agent for processing user's service. The optimal service task partition and distribution is given in the model for maximizing service profit. In the model, genetic algorithm and universal generating function technique are proposed for solving the optimization problem. Considering user's security demand for the service, the model presents a method using service security level to satisfy the needs of user. Illustrative examples are presented.

Keywords Cloud computing • Multi-agent • Service security • Maximal service profit • GA • Universal generating function

99.1 Introduction

Service is an important aspect in cloud computing. The service can be a software, infrastructure, or platform [1]. One of the most important measures of service performance is the service time [2]. From the service provider's perspective, a major concern is to find a scheduling method to maximize the service profit. There are a large number of resources in cloud computing, and multi-agent system is appropriate for managing plenty of resources. Therefore, multi-agent system is proposed for resource management in cloud computing.

Because of external attacks, the service security should be considered. Security level is adopted for the proposed approach. The proposed approach should find the optimal service partition and distribution considering service security. Genetic algorithm is very efficient in solving optimization problem. Universal generating function is applied to calculate the expected service price.

S. Yu • H. Chen (✉) • Y. Xiang
Department of Computer Science and Engineering, University of Electronic Science and Technology of China, 611731 Chengdu, China
e-mail: 18080944962@163.com

Table 99.1 Notations

m : service security level, for $m = 1, 2, 3$	$E(W)$: the price of service
P : the profit of service	V_r : the cost of resources executing the task
V_c : the cost of communication channels executing the task	λ_j : failure rate of resource j
V_{pr} : the cost of protecting the resources	u -function: universal generating function
V_{pc} : the cost of protecting the communication channels	M : unacceptable service time
B : success probability of resource or communication channel	Θ : random service time
π_j : failure rate of communication channel j	Θ_f : the f th realization of Θ
$P_f(t_{ij})$: probability of EB j be successfully finished	Q_f : probability of realization Θ_f of Θ
F : total number of realizations of Θ	N_i : the number of times scheduling agent i running
M_i : the number of times scheduling agent i be attacked when running	
p_i : the security probability of scheduling agent i , it's equal to $(N_i - M_i)/N_i$	
$u_{i,j}(z)$: the u -function to define PMF of resource j 's execution time for EB i	
$U_i(z)$: the u -function to define PMF of EB i 's execution time	
$U(z)$: the u -function to define PMF of entire service task execution time	
$q_j^{res}(t)$: probability that resource j fails before time t	
$q_j^{com}(t)$: probability that communication channel j fails before time t	
e_m : security probability lower bound according to service security level m	
A : external attacks density (reduction ratio on success probability of each resource and communication channel, $A > 1$)	
D : protection density (rising ratio on success probability of each resource and communication channel, $1 < D \leq A$)	

Maximal profit was considered by optimal service task partition and allocation, without attention to service security and multi-agent [2]. Redundancy distribution approach was considered to minimize service cost in grid computing, without attention to service profit and cloud computing [3]. The service time minimization was considered without attention to service cost [4].

The rest of this chapter is organized as follows Table 99.1. Section 99.2 presents the model for processing service. Section 99.3 describes service security level and scheduling agent selection. Section 99.4 describes the algorithm and technique for maximizing the service profit. In Sect. 99.5, illustrative examples are provided. Section Conclusion gives conclusions.

99.2 The Model

This section presents an agent-based model for processing the user’s service. It includes two kinds of agents, which are global agent and scheduling agent. Each agent consists of four modules, which are monitor module, analyzer module, planner module, and executor module. The structure of model can be described in Fig. 99.1.

When a service request arrives, the monitor module of global agent receives the service task information, which includes service security level, input data blocks, task computational complexity, and other parameters. Then, the analyzer module of global agent sends the collected service task information to all scheduling agents.

Once the monitor module of each scheduling agent receives the service task information, the analyzer module of scheduling agent needs to make a decision whether to add extra protection according to the service security level. The details will be presented in Sect. 99.3.

The analyzer module of scheduling agent guides the intra-scheduling process by the effective optimization tools, such as genetic algorithm and universal generating function. When the analyzer module of scheduling agent obtains the maximal profit and its corresponding policy, it returns a message including the maximal profit to the analyzer module of global agent.

When the analyzer module of global agent receives the messages of all scheduling agents, it will select the scheduling agent according to the largest profit.

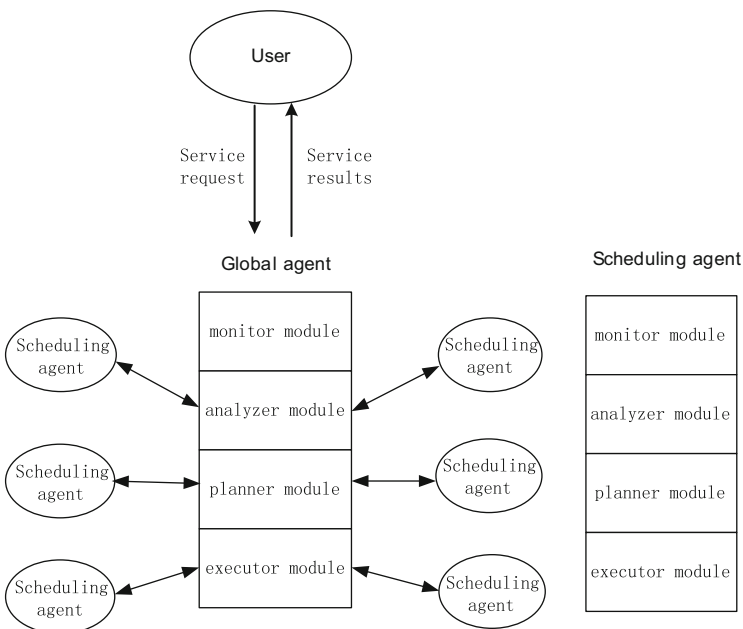


Fig. 99.1 The structure of model

The selected results will be sent to the planner module of global agent. The planner module will send a notification to the selected scheduling agent.

Once the selected scheduling agent receives the notification, it replies a confirmation notification to the global agent and then the planner module of the selected scheduling agent arranges the task partition and distribution for execution according to the policy that provides the maximal profit.

Then the executor module of selected scheduling agent performs the execution plan and returns the final execution results to global agent. Since a completed execution does not necessarily mean that the service is successful, the monitor module of global agent needs to trigger a rescheduling process in case the execution has failed. The final execution results are reported to the executor of the global agent, which outputs the results of the implementation to the customers.

99.3 Service Security Level and Scheduling Agent Selection

99.3.1 Service Security Level

When external attacks occur, the scheduling agent may have a failure. Therefore service time may be delayed. Thus, service security level is provided for customers to choose, which according to the lower bound required for scheduling agent's security probability. The higher the security level is, the higher the lower bound is. Scheduling agent's security probability is the probability of scheduling agent not being attacked. Take scheduling agent i , for example, its security probability is given in Eq. (99.1).

$$p_i = (N_i - M_i)/N_i \quad (99.1)$$

If $p_i \geq e_m$, the scheduling agent doesn't need to consider extra protection because the service security level is satisfied; otherwise the scheduling agent i needs to add protection.

Assume the protection density as D and $D \leq A$.

Proposition D is at least $[A * (e_m - p_i) + 1 - e_m]/(1 - p_i)$.

Proof

$$\therefore p_i \times B + (1 - p_i) \times B \times D/A \geq e_m \times B + (1 - e_m) \times B/A$$

$$\therefore A \geq D \geq [A(e_m - p_i) + 1 - e_m]/(1 - p_i)$$

□

If the scheduling agent needs to add protection, the density of protection is at least $[A * (e_m - p_i) + 1 - e_m]/(1 - p_i)$. Simply, the least density $[A * (e_m - p_i) + 1 - e_m]/(1 - p_i)$ is selected for the following study.

99.3.2 The Scheduling Agent Selection

Different combination of subtasks, resources, and communication channels would cause different service time and profit. Assuming that a combination is given, we need to calculate the scheduling agent's profit.

Firstly, the service price is described in Sect. 99.4. Then, the service cost is considered. The whole cost consists of four aspects: V_r , V_c , V_{pr} , and V_{pc} . V_r and V_c can be computed according to the execution time and execution unit cost. V_{pr} and V_{pc} can be computed according to the execution time, protection density D , and protection unit cost. The service cost is given in Eq. (99.2).

$$V = V_r + V_c + V_{pr} + V_{pc} \quad (99.2)$$

Next, the scheduling agent's profit can be computed in Eq. (99.3).

$$P = E(W) - V_r - V_c - V_{pr} - V_{pc} \quad (99.3)$$

Finally, we need to find the optimal combination in order to get the maximal profit. As we know, GA (genetic algorithm) is very efficient in solving this kind of problem, so we use GA to choose the optimal combination.

When all scheduling agents have calculated the maximal service profit, the global agent would select the scheduling agent, which has the largest profit.

99.4 Maximizing the Service Profit

The GA has been proven to be an effective optimization tool for a large number of complicated problems [5]. GA is proposed for choosing the optimal combination that corresponds to the largest profit. Universal generating function technique is used for calculating the expected service's price.

The u -function (universal generating function) technique was introduced [6]. The u -function representing the PMF (probability mass function) of a discrete random variable Y is defined as a polynomial in Eq. (99.4)

$$u(z) = \sum_{i=1}^N \alpha_i z^{y_i} \quad (99.4)$$

where the random variable Y has N possible values and α_i is the probability that Y equals y_i .

When resource j and corresponding communication channel j completes EB i successfully, we assume that the EB execution time is t_{ij} and the probability is $P_j(t_{ij})$. Considering external attacks and protection, failure rate of resource j changes

to $1 - (1 - \lambda_j)D/A$, and failure rate of communication channel j changes to $1 - (1 - \omega_j)D/A$.

According to Ebeling [7], the probabilities that resource j and communication channel j fail before t are given in Eqs. (99.5) and (99.6).

$$q_j^{\text{res}}(t) = 1 - e^{-[1-(1-\lambda_j)D/A]t} = 1 - e^{-\{1-(1-\lambda_j)[A*(e_m-p_i)+1-e_m]/[A*(1-p_i)]\}t} \tag{99.5}$$

$$\begin{aligned} q_j^{\text{com}}(t) &= 1 - e^{-[1-(1-\omega_j)D/A]t} \\ &= 1 - e^{-\{1-(1-\omega_j)[A*(e_m-p_i)+1-e_m]/[A*(1-p_i)]\}t} \end{aligned} \tag{99.6}$$

When no failures in resource or communication channel occur during the time t_{ij} , we obtain that the EB is successfully finished; the probability is given in Eq. (99.7).

$$\begin{aligned} P_j(t_{ij}) &= [1 - q_j^{\text{res}}(t_{ij})] [1 - q_j^{\text{com}}(t_{ij})] \\ &= e^{-\{2-(2-\lambda_j-\omega_j)[A*(e_m-p_i)+1-e_m]/[A*(1-p_i)]\}t_{ij}} \end{aligned} \tag{99.7}$$

If any failure in resource or communication channel happens during subtask execution, the subtask cannot be finished in acceptable time; we denote the unacceptable service time as M . We can use the u -function to define PMF of resource j computing time for EB i . The u -function is given in Eq. (99.8).

$$u_{i,\{j\}}(z) = P_j(t_{ij})Z^{t_{ij}} + [1 - P_j(t_{ij})]Z^M \tag{99.8}$$

In general, one EB is often executed by several resources parallelly. Therefore, the EB execution time is determined by the shortest resource execution time. Thus, the u -function to define PMF of each EB execution time is expressed in Eq. (99.9).

$$U_i(z) = u_{i,\{j\}} \underset{\min}{\otimes} u_{i,\{m\}} \cdots \underset{\min}{\otimes} u_{i,\{n\}} \tag{99.9}$$

The entire service task consists of several EB; its execution time is determined by the longest EB execution time. Thus, the u -function to define PMF of entire service task execution time is given in Eq. (99.10).

$$U(z) = U_1(z) \underset{\max}{\otimes} U_2(z) \cdots \underset{\max}{\otimes} U_h(z) \tag{99.10}$$

The final u -function $U(z)$ represents the PMF of random service task execution time θ in the form: $U(z) = \sum_{f=1}^F Q_f Z^{\theta_f}$. Combining with the tariff, the expected service price can be determined.

99.5 Numerical Examples

We assume that the model is composed of one global agent and three scheduling agents. The security probability of scheduling 1, 2, and 3 is 0.9, 0.93, and 0.75. Service security level 1, 2, and 3 corresponds to lower bound 0.8, 0.9, and 0.95, respectively. Scheduling agents 1 and 2 satisfy the security level; they don't consider protection. However, scheduling agent 3 needs to consider protection. Assume external attacks density A as 2. The protection density D can be calculated by the equation $[A * (e_m - p_i) + 1 - e_m] / (1 - p_i)$. D is equal to 1.6.

Using the universal generating function and genetic algorithm, we can obtain the maximal profit of each scheduling agent.

We assume the maximal profit of scheduling agents 1, 2, and 3 is 80.54, 83.63, and 85.7. So, we select scheduling agent 3, which has the largest profit.

Single-agent system could manage a small amount of resources. However, there are a large number of resources in cloud computing. Therefore, multi-agent system is more appropriate for managing plenty of resources in cloud computing.

Conclusion

The chapter considers a multi-agent-based model for processing the user's service request in cloud computing. The proposed method considers user's security need. Service security level and security probability are presented and security factors are used as major parameters in universal generating function which is applied to calculate the expected service price. Though some of the assumptions made in this chapter look limited, they can be easily relaxed in further works.

References

1. Bhadra S, Gayen T. A distributed service and business model for providing cloud computing service. *Int J Cloud Comput Serv Sci*. 2013;2(2):148–58.
2. Xiang Y, Fan H, Levitin G. Maximal profit service task partition and distribution in computer grid. *Comput Indus Eng*. 2013;64(1):153–61.
3. Yang B, Huajun H, Guo S. Cost-oriented task allocation and hardware redundancy policies in heterogeneous distributed computing systems considering software reliability. *Comput Indus Eng*. 2009;56(4):1687–96.
4. Levitin G, Dai Y. Optimal service task partition and distribution in grid system with star topology. *Reliab Eng Syst Saf*. 2008;93(1):152–9.
5. Goldberg DE. Genetic algorithms in search, optimization. *Machine Learning*. 1989;2(2–3):95–9.
6. Ushakov IA. A universal generating function. *Sov J Comput Syst Sci*. 1986;24(5):118–29.
7. Ebeling CE. An introduction to reliability and maintainability engineering. New York, NY: Tata McGraw-Hill Education; 2004.

Part V
Embedded Systems

Chapter 100

Protection Circuit Design of Lithium-Ion Battery Pack Based on STM32 Processor

Hongtao Zhang, Fen Wu, Hang Zhou, Xiaoli Peng, Chunhua Xiao, and Hui Xu

Abstract This paper describes a protection circuit based on the STM32F103 processor used for a power lithium battery pack. The protection circuits from overcharge voltage and current and short circuiting of the battery pack are built into the system and include data collection, an equilibrium module, and switching protection. The control strategy regarding battery temperature and voltage equalization between single cell batteries is discussed.

Keywords STM32F103 • Lithium-ion battery • Protection circuit • Balanced circuit

100.1 Introduction

Lithium-ion batteries are small and have a small self-discharge but a long life. With the development of electric bicycles and electric vehicles, they will be the most important type of battery for a very time to come; however, due to strict voltage and current requirements regarding charge and discharge procedures, once the voltage or current exceeds a safe range, the temperature of the battery will rise and lead to

H. Zhang • F. Wu • H. Zhou • X. Peng
Department of Communication Engineering, School of Electric and Electronic Engineering,
Hubei University of Technology, 430068 Wuhan, China

Lab of Nanoelectron Technology and Microsystem, Hubei university of technology,
430068 Wuhan, China

C. Xiao (✉)
Electronic Engineering Institute, Wuhan Vocational College of Software and Engineering,
430205 Wuhan, China
e-mail: xiaochunhua.wh@gmail.com

H. Xu
Lab of Nanoelectron Technology and Microsystem, Hubei university of technology,
430068 Wuhan, China

Experiments Centre, School of Electric & Electronic Engineering, Hubei University
of Technology, 430068 Wuhan, China

permanent damage, which will cause the battery to explode. As a result, the protection circuit design of a lithium battery is a key issue in the use of lithium batteries [1].

This paper presents a lithium-ion battery pack protection circuit design based on the STM32 chip set. With an STM32F103VET6 controller as the core, efforts have been devoted to achieving lithium battery overcharge, overdischarge, overcurrent, and temperature protection, recording the charge–discharge procedure for user queries, and displaying an alarm icon in case there are problems.

100.2 STM32 Microcontrollers

The STM32F103 controller is made by STMicroelectronics and features a high-performance 32-bit ARM Cortex-M3 core, high-speed memory (up to 128 KB of flash memory and 20 KB of SRAM), and three modes, including sleep, shutdown, and standby modes, which may satisfy low power requirements [2]. The device has up to 80 general I/O ports, three general 16-bit timers, and a Pulse Width Modulation timer, nine standard and advanced communication interfaces: two I²C, three USART, two SPI, one USB, and one CAN. In particular, its internal integration 12-bit AD converter with 16 channels and 1 μ s fast conversion time make it unnecessary to add additional A/D chips, which reduces costs.

100.3 Hardware Design

As shown in Fig. 100.1, the design scheme of STM32F103 controlling modules contains data acquisition (including voltage, current, and temperature), equilibrium, display, storage, and communication modules. The circuit monitors the battery status by analyzing the data, which are sent by detection circuits, and then an internal integrated A/D converter processor module is formed, and the processor will accordingly dispose them. By observing the current, we can estimate the battery pack's charge, discharge, overcurrent, or idle time; By observing the voltage, we can estimate a battery's charge, discharge, overcharge, or overdischarge, and we can also determine whether the battery's voltage is balanced and decide whether it is necessary to activate the equilibrium module. By observing the temperature value, we can determine whether the system is in a normal or dangerous state, and thus decide whether it is necessary to stop the battery's modulus operation and to allow it to cool down. In addition, the processors store all information by direct memory access in the FLASH of STM32F103 and show the battery status on the LCD.

Fig. 100.1 Overall design scheme of STM32F103 controlling modules

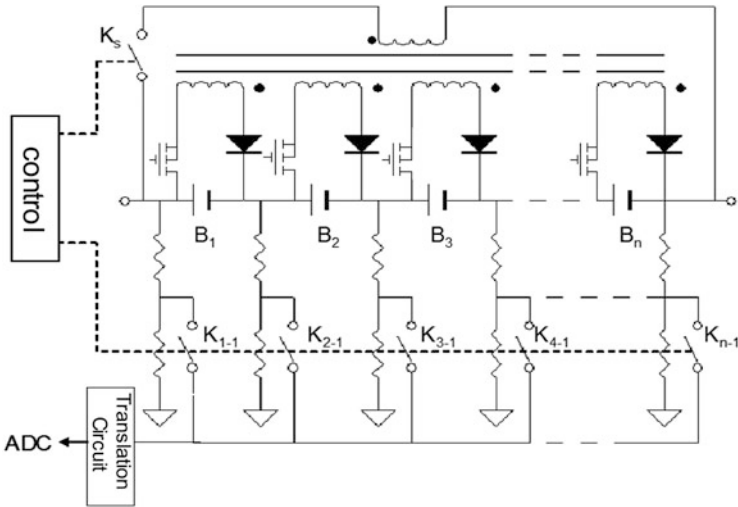
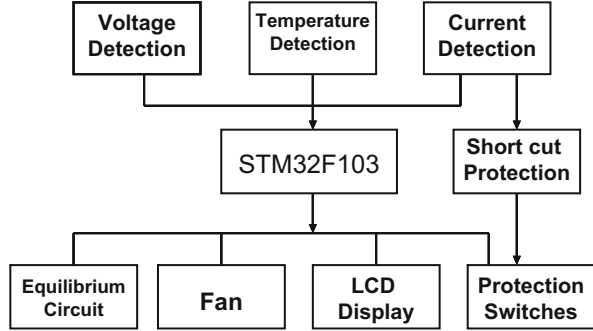


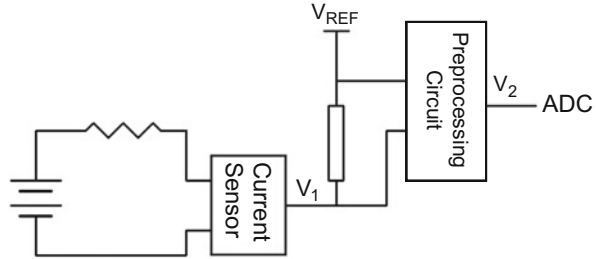
Fig. 100.2 Schematic of voltage detection and equilibrium circuit

100.3.1 Data Collection

As regards the collection of voltage, current, and temperature data of a lithium-ion battery, the values measured by the sensors in real time are discrete and sent to STM32F103 with A/D converter to evaluate the safety risk in accordance with the established conditions.

- Voltage detection
A lithium-ion battery has strict voltage demands in the charge procedure and requires real-time detection of single-cell voltage. The information is sent to the processor to determine the risk of danger, and the processor then responds accordingly. The course of the voltage detection circuit is shown in Fig. 100.2: the two-resistor voltage divider mode is used, and two appropriate value resistors are connected in a series to divide the voltage and send voltage signals to the AD

Fig. 100.3 Schematic of current detection circuit



converter pin of an ATM32F103 processor. Under specific circumstances, the processor sends the control signals to the switches K_{1-1} – K_{n-1} ; only two switches can be closed at a time (measure the voltage of B1, for example, then turn off the K_{1-1} and K_{1-2} switches), and they obtain the voltage of the battery by subtracting the two voltages and then let the voltage pass through an amplifier to match the A/D converter operating range [3]. Here the internally integrated A/D converters of the STM32F103 chip are chosen to reduce the cost of the design. In an actual circuit, a relay or selector can be adopted instead of switches.

- Current detection

In this design, we use the hall closed loop current sensor to obtain the current value using the current detection circuit shown in Fig. 100.3. The current sensor captures the current value converted to the corresponding voltage value V_1 , sends it to a preprocessing circuit to match the A/D converter operating range, obtains the voltage V_2 , and finally sends the signals to the A/D converter. Here we also use the A/D converter of the STM32F103 chip.

- Temperature detection

Lithium batteries require very high temperatures that range from $-20\text{ }^\circ\text{C}$ to $+55\text{ }^\circ\text{C}$, but when the temperature is higher than $45\text{ }^\circ\text{C}$, the self-discharge increases and the capacity decreases, and it is inadvisable to charge quickly. The temperature of the battery pack is measured by the DS18B20 digital temperature sensor of the STM32F103 chip in a range of $-55\text{ }^\circ\text{C}$ to $+125\text{ }^\circ\text{C}$. The temperature of a single-cell lithium-ion battery can be measured using a thermistor with two batteries sharing one thermistor.

100.3.2 Equilibrium Module

In the battery charge and discharge procedure, the voltage of a single-cell battery cannot be consistent in the same pack due to the varying performances of all each individual cell. In a normal charge (discharge) procedure, if one single battery's voltage is charged (discharged) to the upper (lower) limit before other batteries, continuing to charge (discharge) the battery pack will lead to the overcharge (overdischarge) of a single battery. The equilibrium module is an effective solution to this problem. The most commonly used equilibrium circuit can be divided into

energy consumption and energy feedback types. The different equilibrium types include resist equilibrium, capacity equilibrium, and transformer equilibrium. Resistor equilibrium can transfer extra energy out through the shunt resistor. The method is simple and low cost, but it can lead to energy waste and is apparently unsuitable for motive power [4]. Capacitor equilibrium may transfer excess energy through a capacitor to other cells and thus greatly shorten the equilibrium time, but the equilibrium current is generally small and does not apply to motive power.

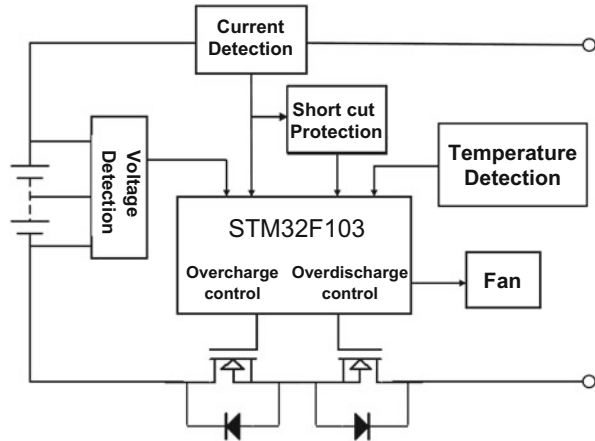
In this design, we achieve a balance in battery pack voltage by using transformers to transfer excess energy from a single cell to other cells based on the schematic shown in Fig. 100.2. Specifically, a work processor sends control signals to the Ks switch by analyzing the received voltage information of single cells. If a single cell has reached the equilibrium point, the Field Effect Transistor (FET) linked to the battery is always in the open state once the Ks switch closes the equilibrium circuit. If there no battery reaches the equilibrium point, the FET linked to the battery is always in a closed state and the equilibrium circuit does not work.

100.3.3 Switching the Protection Circuit

The voltage and temperature signals of each single cell collected by the thermistor-detection circuit will be sent to the A/D port of the STM32F103 chip, the current value of the battery packs can be computed using the previously given detection values, and the temperature value of the battery pack detected by DS18B20 will be sent to the I/O port of the STM32F103 chip and compared with the upper and lower limits that have been already established. Switching the protection circuit can achieve the following main types of protection [5].

- Temperature protection and control
The temperature value measured by DS18B20 is regarded as the environmental temperature [6]. When it is less than $-20\text{ }^{\circ}\text{C}$, the system will shut down; when it is higher than $-20\text{ }^{\circ}\text{C}$ and less than $+75\text{ }^{\circ}\text{C}$, the system will function; when it is higher than $+75\text{ }^{\circ}\text{C}$, the system power will be cut off; when the ambient temperature is $-20\text{ }^{\circ}\text{C}$ to $+10\text{ }^{\circ}\text{C}$, it will not allow high-current charging, when it is higher than $+55\text{ }^{\circ}\text{C}$ and less than $+75\text{ }^{\circ}\text{C}$, high-current charging will not be allowed and a high voltage will be produced to open the cooling fan.
- Overcharging voltage and overdischarging voltage protection
If the cell voltage is between the overvoltage and undervoltage values, the normal battery charge and discharge will process the normal battery charge and discharge. If any one cell voltage is above (below) the overvoltage value (undervoltage value), shut off the overcharge (overdischarge) control to stop the battery pack from charging (discharging), as shown in Fig. 100.4.

Fig. 100.4 Schematic of switch protection circuit



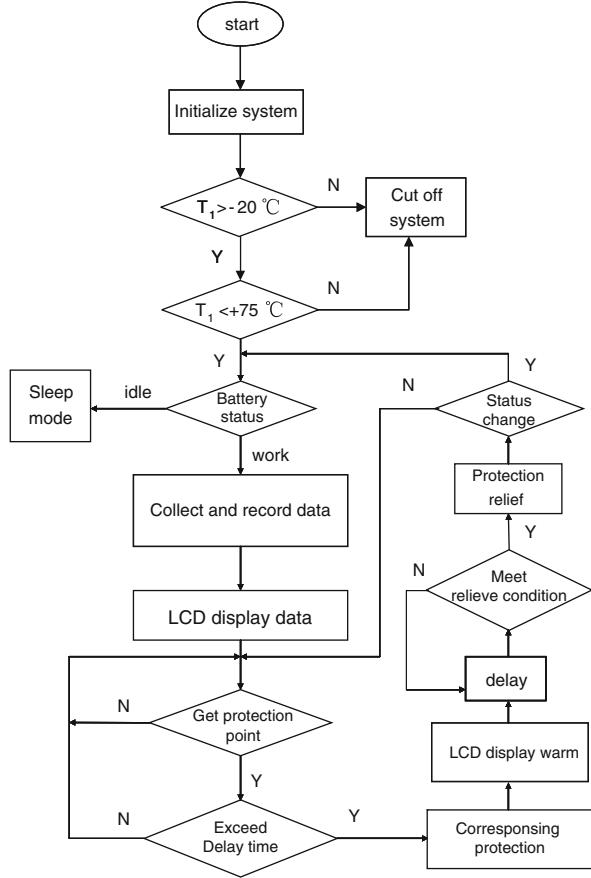
- Overcharging current and overdischarging current protection
If the battery pack's charge (discharge) current value exceeds the upper (lower) current limit, shut off the discharge control terminal and cut off the discharge circuit.
- Short cut protection
Short-circuit protection is connected to the overdischarge control. If the battery pack is short-circuited, the protection circuit will pull down the STM32F103 control to shut off and then cut off the charge and discharge circuit. In an actual circuit, according to the requirements of charge and discharge currents, select the N-channel MOSFET model; if the required power consumption is large, more than two MOS transistors can be used in parallel.

100.4 Software Design

The software design of this circuit is comprised of an embedded system based on the $\mu\text{C}/\text{OS}$ operating system, which contains a single battery voltage measurement procedure, battery current measurement procedure, temperature measurement procedure, protection control program, LCD display program, and several other modules. The main flowchart is shown in Fig. 100.5, with T1 for the ambient temperature and T2 for the single battery temperature.

The voltage and the current value use an A/D converter of the STM32F103 chip for analog–digital conversion. In the cyclic scan mode, the protection point is estimated using a comparison program, and in the charging process, the voltage value is compared to the upper limit voltage value and the current value is compared to the upper limit current value; in the discharging process, the voltage value is compared to the lower limit voltage value and the current value is compared to the lower limit current value. To avoid false judgments of overcharge,

Fig. 100.5 Main flowchart of software design



overdischarge, and overcurrent situations, the processor should record the duration, starting protective action if it exceeds the delay time, which is determined by the interrupt program. When one of the values exceeds the comparison value, the corresponding time variable will add one, otherwise it is cleared. The main program will continue to check the timing variables if a time variable exceeds the set value and return to the corresponding protection operation [7].

The LCD display uses the $\mu\text{C}/\text{GUI}$ general embedded software graphical user interface. The graphic design tasks include a battery status display interface, real-time battery voltage, current, temperature, and other information display interfaces, including a parameter setting interface requiring users to set different protection conditions and a warning icon to notify users of abnormalities in the battery pack when a protection event occurs [5].

Conclusion

In this paper, a lithium-ion battery charge and discharge protection circuit based on STM32F103 was presented using an embedded system to design software and hardware. Both $\mu\text{C}/\text{OS}$ and $\mu\text{C}/\text{GUI}$ are revised and transplanted into the development board. The overcharge voltage, overdischarge voltage, overcharge current, discharge current, short-circuit protection of the battery pack and battery temperature control strategy, and voltage equalization between single-cell batteries were discussed. The circuit could have a wide range of uses, which conforms to the design trends of electronic products currently being released.

References

1. Wu Y, Yin Y. Distributed power battery management system base on CAN bus. *Automot Eng.* 2004;27(5):530–3.
2. Deng S, Wang Y, Li X, Huang H. Lithium battery protection circuit design. *Electron Technol.* 2006;1(10):68–72 (in Chinese).
3. Wang S. MOSFET/IGBT driver ICs and application (in Chinese). Beijing: People's Posts and Telecommunications Press; 2009. p. 153–62.
4. Chen Y, Li J, Song B. Cortex-M3 + $\mu\text{C}/\text{OS-II}$ introduction to embedded system development and application (in Chinese). Beijing: People's Posts and Telecommunications Press; 2010. p. 123–6.
5. Halalay IC, Fuller TJ, Zou L. US20120082893 A1(2010.10.1).
6. Tang J, Sun Q, Xu S, Li X, Luo J. CN102097647 A(2009.12.9) (in Chinese).
7. Halalay IC, Harris SJ, Fuller TJ. US20110151333 A1(2009.12.18).

Chapter 101

Analysis of an Intelligent 1553B-Bus Communication Module Design Based on ARM Platform

Chunlei Song

Abstract The intelligent 1553B-bus communication module based on the ARM platform is mainly applied to extending the 1553B-bus interface of the Compact PCI computer system. In terms of hardware, the module adopts the ARM control unit and dual-port RAM while incorporating the round buffer design with respect to software, which effectively strengthens the stability of data transmission and substantially decreases the possibility of data loss during transmission.

Keywords 1553B • Intelligent • CPCI • ARM

101.1 Introduction

The 1553B data bus is comprised of an active bus controller (BC) and up to 31 active remote terminals (RTs), both of which are connected by a redundancy bus [1]. Each node can function as a BC, RT, or MT bus monitor. However, the network should have only a BC. The 1553B bus in modern weapon systems has received increased attention and become a platform in vehicles, ships, aircraft, and other weapons and constitutes the main pillar of electronic systems.

The maximum data transmission velocity of a 1553B bus is 1 Mbps, which is far slower than that of a PCI bus. If a 1553B bus is continuously sending or receiving data, the connection may be interrupted [2], leading to data loss. In most of the 1553B bus modules, a non-intelligent, single-function, single-channel design method is generally used. Despite the failure of intelligent design to completely eliminate such a phenomenon, it can effectively reduce the possibility of connection interruption. This paper's innovation points are that in hardware design it adopts the ARM platform and dual-port RAM to improve transmission stability and in software design it adopts a circular buffer and lower frame rate.

C. Song (✉)

Jiangsu Automation Research Institute, 222006 Lianyungang, China
e-mail: 121933769@qq.com

101.2 Design Principle

The module primarily achieves the intelligent 1553B function. The CPU (AT91RM9200) is assigned to process the information packets in the 1553B network [3]. The module mainly consists of AT91RM9200, SDRAM, FLASH, IDT70V28L (Dual-port RAM), a 61581 (1553B protocol chip), PCI9052, a buffer, and a level translator. For more details, please refer to Fig. 101.1.

101.3 Implementation Methods: Hardware Design

101.3.1 Design of Buffer

A 16-bit bidirectional data buffer is adopted with the following features: Device compatible with 3.3 V to 5 V input, 1–4 ns input and output delay, and 1–5.5 ns delay between the enable pin and the output.

101.3.2 Design of ARM and 1553B Interface

The read/write time for the 61581, the protocol controller of the 1553B, is comparatively long (up to 3.5 μ s). The processor bus timing therefore fails to directly match it [4]. After the ARM starts access, the matching between bus timing and 61581 becomes possible via a field-programmable gate array (FPGA). The signal connection methods are shown in Fig. 101.2.

The 61581 has 64 KB RAM and a 32-byte control register space, which requires two chip-select signals. The FPGA will use a latched NCS2 and SA address bus [25:17] to complete the decoding select of two space base addresses. The chip-select signals output by decoding are the address strobe, /STRBD (chip-select input), of the 61581 and MEM/REG. The 61581 deems the signals effective if they last for at least 10 ns. The 61581 will output a /IOEN signal after up to another

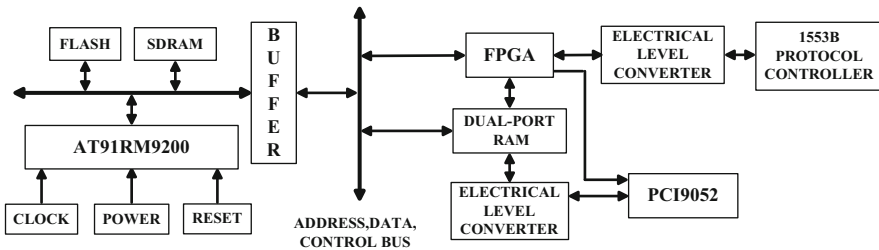
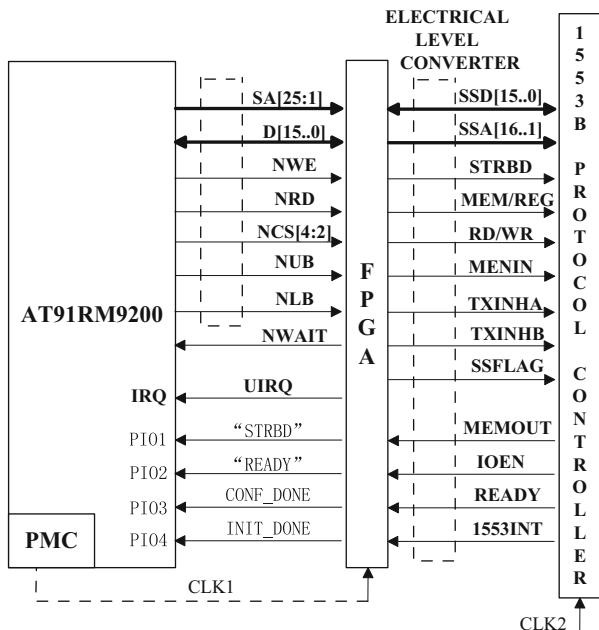


Fig. 101.1 Hardware structure diagram

Fig. 101.2 Signal connections for 1553b protocol controller



2.8 μ s. Then the FPGA used /STRBD, the address strobe, to output MEM/REG (differentiate the register space and RAM space). The FPGA then decodes the RD/WR of the 61581 by latched write enabled (NWE) signals and chip-select signals [5]. If all conditions are consistent with the foregoing, the 61581 will output a /MEMOUT signal while the FPGA assigns the outputted signal directly to MENIN, the output signal. During the time when /STRBD remains valid, the latched address wire and date cable (write operation) will also be valid. TXINHA and TXINHB will be lowered while SSFLAG will be pulled up. Meanwhile, /STRBD will be output to a status on ARM, which PIO will judge as to whether it is a read/write operation. When the 1553B finishes the read/write operation, it will output a READY signal to the accessor, and the FPGA will return this answering signal to the ARM.

101.3.3 Logic Implementation for ARM and Dual-Port RAM

There are two spaces inside the dual-port RAM: the 64 KB storage space and 8-byte SEMPHORE space. The FPGA needs to decode them into two chip-select signals, /CEOR and /SEMR, through high-order chip select and Address A [25:17] of ARM. Other control buses can directly connect to each other inside the FPGA.

The access time for the IDT70V28L (the dual-port RAM) is longer than 20 ns. When the bus speed is 60 MHz, the access time for the processor is approximately

18 ns. The processor allows insertions of up to 128 wait states. Every time a wait state is inserted, the read/write will then be extended to a certain period. Insert three wait states through the FPGA to complete the matching between their timings. This design uses signal lights to avoid conflicts.

101.3.4 Logic Implementation for PCI9052 and Dual-Port RAM

The PCI9052 uses the nonmultiplex and periodic read/write model. The IDT70V28L offers a BUSYL signal in an attempt to avoid any conflict generated when writing in the same address. Such a signal functions as the interrupt source of the PCI9052 [6]. The IDT70V28L provides the INTL signal that can be applied either to communication or as an approach to avoiding any conflict that might arise in connection with writing in the same address. This signal serves as the interrupt source for the PCI9052. The operating mode for the IDT70V28L is SEMPHORE, under which it is entirely possible to avoid conflicts related to simultaneous writing or concurrent read/write.

101.3.5 Clock

The clock input of the ARM core circuit is supplied by external crystals. The 25 MHz crystal oscillators output two clocks to the FPGA and PCI9052 through the CY2305 clock distributor (the PCI9052 is a 5 V component while CY2305 and 9052 satisfy the TTL electrical level). A 16 MHz crystal oscillator functions as the clock input for the 61581 (5 V component).

101.3.6 Power Supply

The same types of voltage converter chips from companies like LINEAR, National Semiconductor, Texas Instruments, Semtech, and Intersil were considered. The final decision was made to select the TPS62202 and TPS54312 from Texas Instruments and the ISL6520 from Intersil respectively as the 1.8, 1.2, and 3.3 voltage converter chips. They all demonstrate a converting efficiency of over 90 % with a ripple voltage of less than 2.5 %.

101.3.7 Design of FPGA

As shown in Fig. 101.3, there are three interrupt sources in the FPGA: the dual-port RAM interrupt, a 1553b interrupt, and a PCI interrupt. Inside the FPGA are five control registers. The exact port addresses for these registers are determined by SA [3:1]. The significance of these registers is as follows:

- Indicator register: controls indicators with read/write.
- Interrupt the enable register: functions as an enable interrupt source with read/write.
- Interrupt register and record the interrupt source states: read only.
- Interrupt the prioritized register and set the priority to enable interrupt source: read only.
- Control registers inside FPGA with read/write.

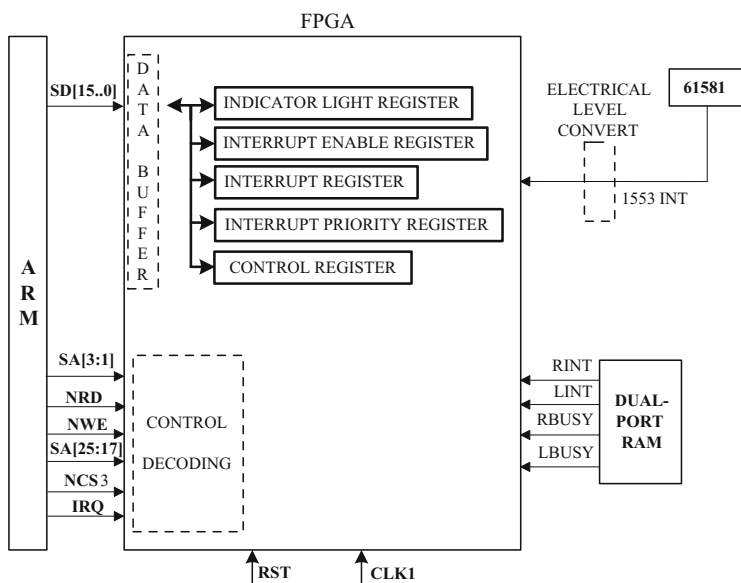


Fig. 101.3 Registers inside FPGA

101.4 Software Design

101.4.1 Initialization of ARM Processor

Mainly responsible for interrupting the exception table allocation, initializing FLASH, setting the clock, initializing SDRAM, initializing the debug serial port, initializing the coprocessors and different modes of stack allocations.

101.4.2 Communication Between ARM Processor and PCI9052

Communication between the ARM and host machine is conducted through dual-port RAM. In dual-port RAM, a 4-byte address will be used (offset address from 0 to 3). Each byte represents the checksum, transaction passwords, data volume pointer, data volume with read/write requests, offset address pointer, read/write data offset indicator, stator word, and return packet confirmation. Based on this information, two buffer areas are explored within the dual-port RAM, the receiving buffer area and the sending buffer area.

During the receiving of data, the input buffer generates a timeout interrupt when there are data in the receiving terminal, leading the input buffer to the flip-flop stage, or when there are bytes remaining in the buffer area for over 4-byte time frames. Two situations need to be taken into account. The first situation is when the receiving buffer area is underfilled, and so data can be directly placed in the area. The second situation is when the receiving buffer area is filled, making it necessary to cover the next data in order to guarantee that the received data are always updated. It is also necessary to inform the host machine every time the receiving buffer area receives data so that the host machine can accept the data. For instance, when FIFO receives abcd character and generates interrupt, it is necessary to first press the data from the input FIFO to the circular receiving buffer area and then change Wp pointer. Data should be first placed in the receiving buffer area, during which time the Wp pointer and the receiving counter will each add one more value every time data are placed there. When the host machine receives data, the Rp pointer will add one more value while the CNT receiving counter will be decreased by one value, until the value of the CNT receiving counter is equivalent to zero. At this time, Rp is equal to Wp. The circular receiving buffer area is shown in Fig. 101.4.

During the sending process, when the host machine is about to send data, the length of those data will be written into the dual-port RAM with the address offset. Subsequently, the data that are ready to be sent will be stored in the sending buffer

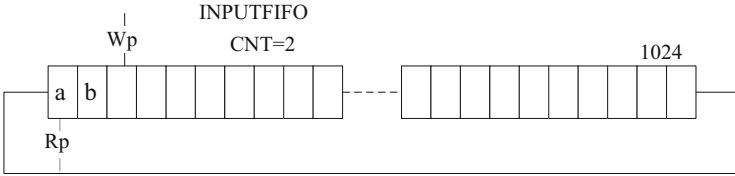


Fig. 101.4 Circular receiving buffer

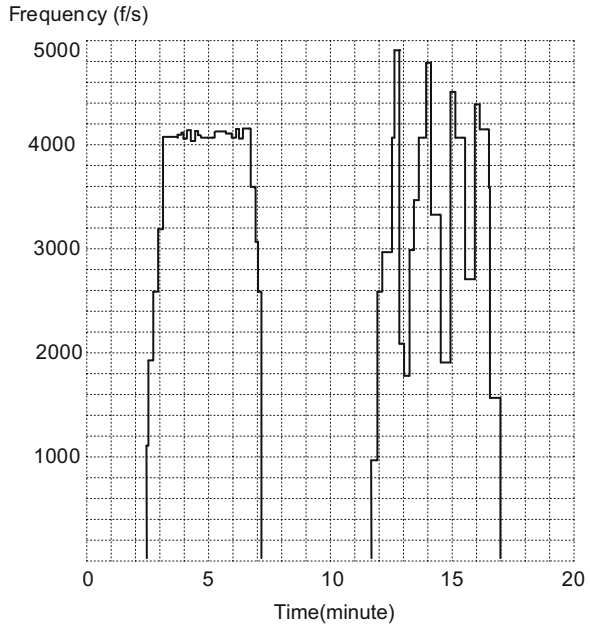


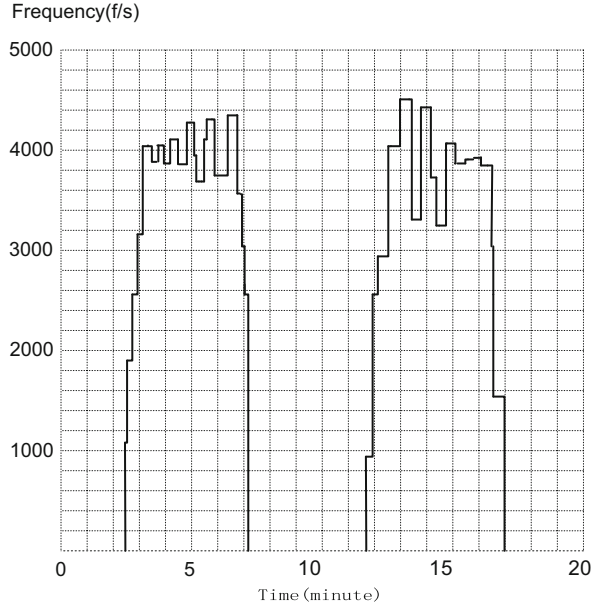
Fig. 101.5 Data transmission rate for ordinary 1553B module

area. When they are sent, a byte of data will be sent first. After a sending interrupt has been generated, the interrupt service subprogram can send the data via output FIFO, until all the data are sent in the sending buffer area.

101.5 Running Results

On the same host machine, a comparison between the intelligent 1553B module and ordinary 1553B module has been launched. A 1553B bus analyzer is adopted to record the frame numbers sent each second. The vertical axis refers to the sending frequency whose unit is frames/second (f/s), while the horizontal axis is the time. In Fig. 101.5, the first wave indicates the status for the ordinary

Fig. 101.6 Data transmission rate for intelligent 1553B module



1553B module of the host machine, which only implements the sending task, and the second wave refers to the status of the same module, but while it operates other tasks. In Fig. 101.6, the first wave is the status for the intelligent 1553B module of the host machine when it is only delivering data, and the second wave is the status of the same module when it is performing other tasks. A comparison shows that the nonintelligent module will be significantly affected by the software environment of the host machine.

Conclusion

The design presented here fully demonstrated the features of the intelligent 1553B communication module. The whole design incorporates a tightly integrated structure and stable performance, along with a strong anti-interference capacity.

References

1. Sun T, Zhang H. Based on the 1553B protocol of the bus controller and remote terminal FPGA implementation. *J Grad Sch Chin Acad Sci.* 2011;(04):523–28.
2. Wu G, Yang J. The 1553B bus remote endpoint data link layer protocol of the FPGA implementation. *Mod Electron Tech.* 2012;(03):163–66.
3. Sun J, Feng P. The FPGA chip application in high speed data acquisition caching system. *New Device Appl.* 2012;(12):25–30.

4. Zhou L. The ARM, microcontroller basis and actual combat. Beijing: Beihang University Press; 2008. p. 20–50.
5. Liu M, Li X. The data acquisition and compression system based on FPGA. *Instrum Tech Sens.* 2012;1(1):36–9.
6. Ling Z, Tan L, Tao K. BU-65170-based 1553B terminal design. *Microcomput Inf.* 2008;2(1):273–77.

Chapter 102

Design of Multichannel Data Real-Time Processing System Based on Serial Port Communication

Peigang Jia and Sirui He

Abstract To improve production efficiency, reduce production costs, and realize automation management under the virtual instrument software LabVIEW graphical programming language environment in industrial production processes, this paper uses weighing machines and a temperature acquisition module to collect data, send the data to a principal computer by multichannel serial port communication, analyze and process the data on the principal computer, and finally realize real-time data display and storage functions. The system effectively implements quality control and management in the production process, and its use in production showed that it works stably and has excellent reliability and scalability.

Keywords LabVIEW • Multi-channel • Data acquisition • VISA

102.1 Introduction

With advances in industrial automation, the collection, analysis, observation, and automatic storage of real-time data have become increasingly important in the production process [1]. And because of its rich function modules and nodes, simple and intuitive graphical programming language, the virtual instrument software LabVIEW, which is based on a computer platform, is now widely used in complicated programming tasks, which greatly reduces the time and cost of application development [2]. Currently, bus technology has been very widely used, but because of its simple interface and convenient usability [3], serial ports are still widely used as common data transmission channels between computers and external serial devices in various kinds of low-speed test systems. And the virtual instrument system that comprises the RS232 or RS485 serial port communication interface and personal computers is the main component of these test systems [4].

P. Jia • S. He (✉)
The College of Mechanical and Electrical Engineering, Xi'an Technological University,
710021 Xi'an, China
e-mail: yilyc@163.com

In this paper, data are gathered and transferred to a personal computer using serial port communication based on the LabVIEW programming environment and information such as, for example, weight, temperature, and quantity, is displayed in real time on an upper computer, the data are gathered and transferred to a personal computer and in real time on the computer, and then the quality of the products is monitored and managed.

102.2 Structural Design of System

102.2.1 System Design Scheme

This system consists of a temperature acquisition module, four weighing machines, and a computer host. Each production line is equipped with a weighing machine and connected to the PC host by an RS232 serial port. When a product from the production line is packaged up and passes the weighing machine on a conveyor belt, the machine then sent the material number, the package weight, and other product information to the PC through its corresponding RS232 serial port. Meanwhile, the temperature acquisition module in turn collects the temperature of the incoming product material from the production line and the current environment. If the distance is so long that data transmission is easily disturbed [5], RS485 serial port communication is selected. A block diagram of the overall system scheme is shown in Fig. 102.1.

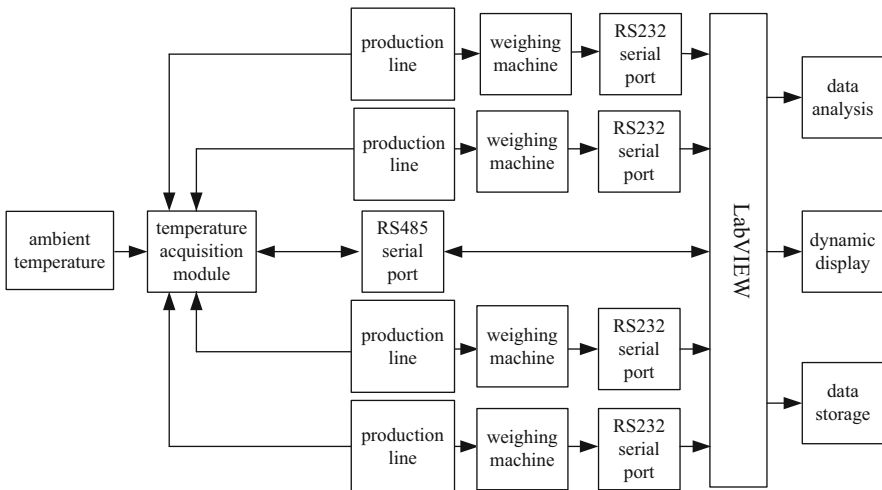


Fig. 102.1 Block diagram of overall system scheme

102.2.2 System Hardware

102.2.2.1 Temperature Acquisition Module

As a quality indicator of qualified product, the performance of the temperature sensor will directly affect system stability and reliability. Temperatures at five locations need to be detected, so the system uses an eight-way PT100 temperature acquisition module, AE102 (Aneasy Technology Co., Beijing, China). The AE102 can simultaneously input data from the PT100 temperature sensor through eight channels and connect to the PLC, DCS, RTU, PC, serial port station, and GPRS radio equipment directly. At the same time, five PT100 platinum thermal resistances with three-wire were used here as the temperature sensors.

102.2.2.2 Weighing Machine

To output the data about the package weight after the product is packaged on the production line, the system uses the latest weight display controller, the IND560 (METTLER TOLEDO Co., Switzerland). The IND560 has a 366 Hz A/D conversion rate and a 50 Hz I/O refresh rate; it can precisely measure an object's weight in the milligram to ton range and can be connected to a commonly used strain foil sensor and high-precision electromagnetic force compensation sensor. It also has many ways of communicating with PLC control and digital I/O ports and provides an RS-232/422/485 and Ethernet TCP/IP network interface.

102.3 System Software Design

LabVIEW provides rich instrument control function, and uses software programming standards such as, for example, VISA, SCIP, and IVI. In terms of serial port communication, VISA is the main function of the serial port operation node. A VISA library resides in the computer system, and its essence is a standard API interface that is used as a virtual instrument system [6]; and by calling the underlying driver to establish a connection between the computer and an instrument [7], the instrument is controlled by a program. Users can connect with the many instrument buses, including, for example, GPIB, USB, serial port, PXI, VXI, and Ethernet, without learning various kinds of communication protocols of instruments using VISA.

This paper mainly uses the node function of VISA Configure, VISA Read, VISA Write, VISA Close, and VISA Bytes at the serial port. Due to the material packages are transferred steady from production line by the conveyor belt to the weighing machine so that data are sent to the machine consecutively, which is a passive data

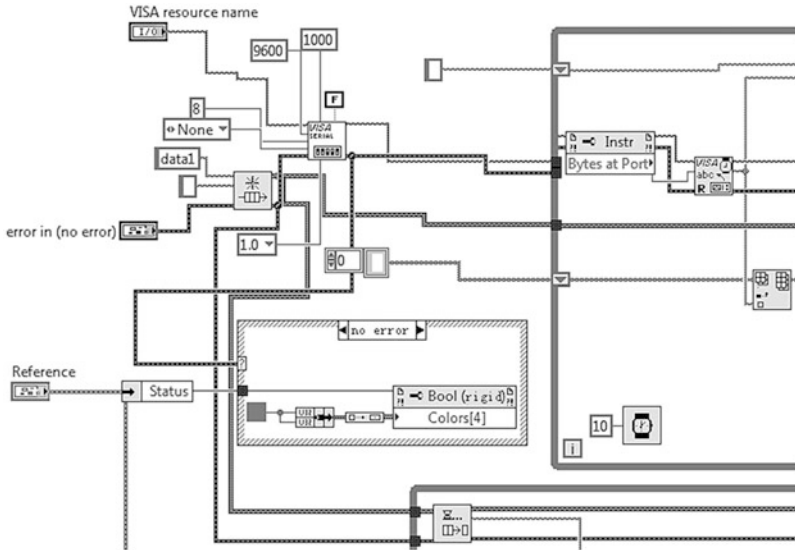


Fig. 102.2 Local diagram of parallel loop serial port communication procedure

type. The producer/consumer model was adopted here to obtain data by creating a queue and using a parallel loop function. This model can solve the problem of data nonuniform acquisition and processing rate and effectively prevent the loss of data. The program local block diagram is shown in Fig. 102.2.

However, the temperature acquisition module collects information circularly by receiving instructions from the principal computer, which is an instrument control type. The instrument needs time to respond to instructions, and the instructions from the computer to the serial port also take time to be sent. Thus, a certain delay between VISA Write and VISA Read needs to be incorporated into the module. The local procedure VI is shown in Fig. 102.3, where a 600 ms wait function node was added.

After the weighing machine sends the data to the buffer, the procedure the data string that contains the material number and the package weight is automatically intercepted by the queue, then the config.ini configuration file, which was prestored in computer, is matched to obtain the weight range. At the same time, the temperature module receives an instruction to ceaselessly query the temperature of the material and the environment. If the package weight is in a given range and the temperature difference of the material and the environment is less than 5 °C, then the system determines that the package is qualified; otherwise, it is unqualified and the reasons for that are given. Meanwhile, relevant information is displayed on the panel. Finally, the information is saved to the folder of the corresponding production line in the form of an Excel spreadsheet. The storage program is shown in Fig. 102.4, and Fig. 102.5 gives the entire program flow diagram.

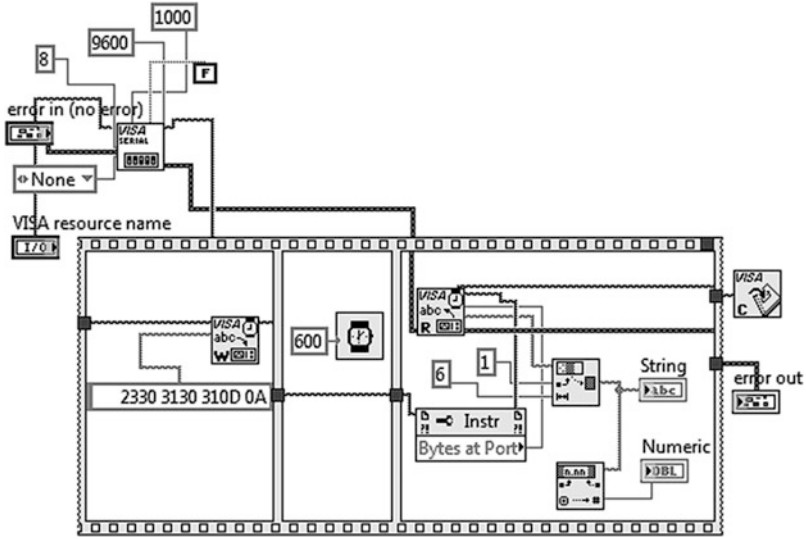


Fig. 102.3 Local diagram of temperature acquisition module procedure

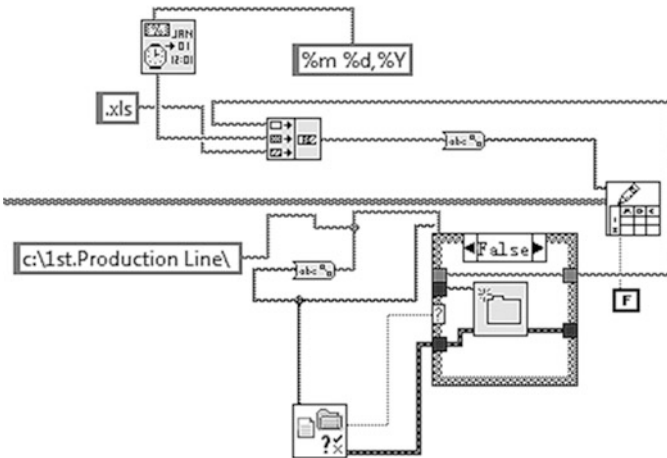
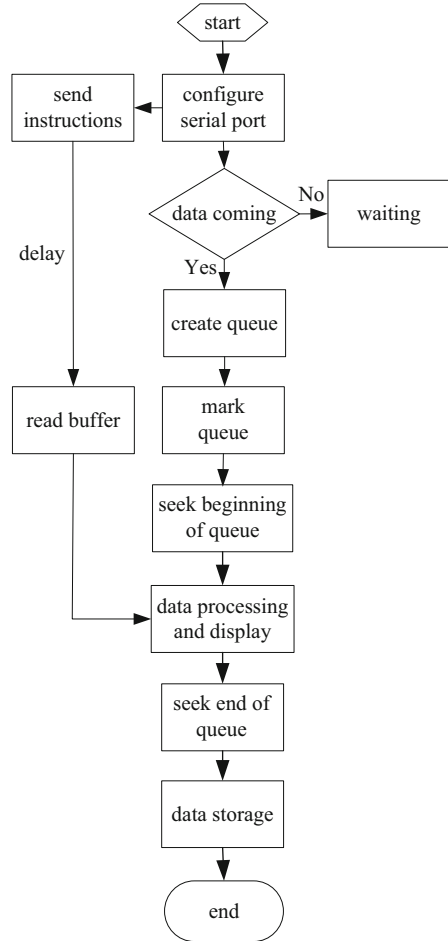


Fig. 102.4 Diagram of data storage program

102.4 Application Results

Because there are not enough serial ports on the principal computer to satisfy system requirements, the AE102 serial port uses a USBTOCOM adapter with a USB interface to communicate with the computer. In addition, the weighing machine sends data passively, so the system only needs to connect the RXD, TXD, and GND pins of the weighing machine serial port to the corresponding

Fig. 102.5 Flow diagram of program



serial port pins of the computer. The serial port must be chosen before the LabVIEW procedure is executed on the computer, and the port is not allowed to reload midway through the process. The status lamp will give the port a signal indicating whether it is properly selected.

The panel is shown in Fig. 102.6. When the system is running, it is intuitive for the user to observe information such as the temperature, weight, quantity, and time of the four production lines in the production process. To easily detect an unqualified package, which is helpful in managing product quality in a timely manner, qualified packages are displayed in green and unqualified packages in red. The test result is shown in the table in real time and in seven rows of data for a display loop to cover the previous content.

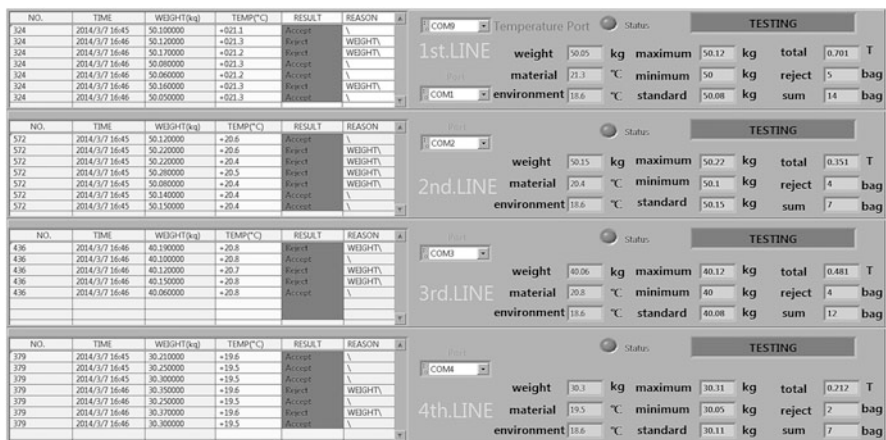


Fig. 102.6 Running diagram of procedure in front panel

Conclusion

As a virtual instrument development platform with good openness, this paper described a practical multichannel data acquisition, analysis, and processing system. Running in an actual industrial environment, the system was shown to operate simply, conveniently supervised the quality of products in the production process, and was able to monitor the overall production process by analyzing a stored spreadsheet. In addition, the system has strong applicability, reliability, and scalability than currently existing systems.

References

1. Liang G, et al. The realization and application of DAQ system based on LabVIEW and serial port. *Mod Machinery*. 2009;10(5):57–9 (in Chinese).
2. Xu M, et al. Multi-channel data acquisition system based on LabVIEW serial port communication. *Machinery Electron*. 2010;7(1):172–4 (in Chinese).
3. Zhao Q, et al. Design of serial data collection system based on LabVIEW. *Comput Technol Dev*. 2011;21(11):224–30 (in Chinese).
4. Dong H, et al. The application of serial communication on LabVIEW in data acquisition. *Netw Commun*. 2011;30(23):63–8 (in Chinese).
5. Huang H, et al. Measurement and control system for gas-tight deep-sea water sampler based on LabVIEW. *Chin J Sci Instrum*. 2011;32(1):40–5 (in Chinese).
6. Nithyaa V, et al. A real time foot pressure measurement for early detection of ulcer formation in diabetics patients using LabVIEW. *Procedia Eng*. 2013;11(64):1302–9.
7. Wu R, et al. A dimension tolerance detector based on LabVIEW. *Manuf Autom*. 2012;34(3):8–10 (in Chinese).

Chapter 103

ZigBee-Based Online Dust-Concentration Monitoring System

Hui Chao and Wang Zhou

Abstract To meet the needs related to detecting dust, this paper describes a system based on ZigBee communication technology, which allows for smart real-time monitoring of the concentrations of dust in system fields. The system is mainly composed of a particulate matter sensor module, data acquisition and processing module, and a ZigBee communication module. ZigBee communication technology replaces traditional monitoring systems that transmit data by wired cable or via a mobile communication base station. The particulate-matter-detecting sensor uses a PD4NS dust sensor based on the principles of photoelectricity and particle counting. It can detect particles whose size is greater than 1 μm . Its maximum detection range is up to 8,000 pcs/283 mL with measured results at Pulse Width Modulation (PWM). Currently, the system obtains signals sampled by the PD4NS dust sensor and handled by a microcontrol unit (MCU) and then data are sent to the monitoring center (PC) via a ZigBee communication network. The system can be applied to similar monitor systems based on the Internet of Things because of its simple structure, low cost, and high movability.

Keywords Particulate matter sensor • Wireless sensor networks • ZigBee • Monitoring system

103.1 Introduction

The International Organization for Standardization (IOS) defines dust as a suspended solid particle whose size is less than 75 μm . Dust contaminates the working environment and can directly threaten human health by causing a variety of occupational lung diseases. Moreover, excessive dust concentration can cause

H. Chao

Institute of modern optical technology of Soochow University, 215006 Suzhou, China
e-mail: 873021438@qq.com

W. Zhou (✉)

Province Key Laboratory of Modern Optical Technology of Jiangsu, Institute of modern optical technology of Soochow University, 215006 Suzhou, China
e-mail: wang58@suda.edu.cn

dust explosions [1, 2]. Traditional dust-monitoring systems usually use a standalone monitoring device and requires that the people doing the monitoring enter the environment carrying equipment to detect dust. This type of system is not only inefficient and constrained by conditions in the field environment, including temperature and chemicals that may be present, but also requires manual data aggregation, which cannot be done in real time.

To acquire real-time data in dust-sensitive areas, it is of practical significance to build a wireless network monitoring system; however, some wireless sensor networks, for example Bluetooth, while they can replace traditional cable detection systems, are expensive and operate under short transmission distances [3, 4].

ZigBee communication technology has more advantages as a monitoring system than other systems. It can directly sequence the spread spectrum on an unlicensed spectrum, namely, the industrial scientific and medical band (ISM) [2.4 GHz (global)]. With ZigBee communication technology, a dust-detection system can be installed without lines, which saves on costs related to building the system; in addition, a network can be built automatically and the number of nodes and measurement positions can be changed as desired. Here, the nodes are low-power. This wireless-network dust-monitoring system has the potential to become a common application on the Internet of Things [5–8].

103.2 System Structure

The online monitoring system is composed of three modules: a particulate matter sensor module, a data collection and processing module, and the ZigBee communication module. The particulate matter sensing structure is designed to detect dust concentrations (the number of particles in a unit volume) in real time. The second module converts electrical signals collected by the dust sensor into data, which can be displayed on the digital display device and transmitted to the monitoring center by the ZigBee module at the same time. Finally, the data are processed and graphically displayed on a computer monitor (Fig. 103.1).

103.2.1 Data Collection and Processing Module

This experiment uses a Micro Control Unit (MCU) (STC12C5A60S2) as the main control chip of the system. Compared with the ARM series, the MCU-51 series

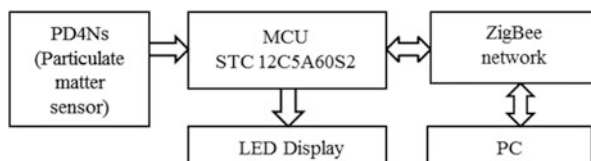


Fig. 103.1 Schematic diagram of system

features a simpler structure and a wider application; therefore, the system is implemented using the MCU-51. The STC12C5A60S2 is treated as the main control chip that mainly processes data from the dust sensors, displays data by LED devices, and communicates data through the ZigBee modules.

103.2.2 Particulate Matter Sensor Module

This experiment uses a PD4NS as the particulate matter sensor (Fig. 103.2). The resistance heater in the sensor can inhale air automatically when heated. Particles whose diameter is more than 1 μm , such as, for example, cigarette smoke, house dust, mold, pollen, and spores, can be detected by the sensor. The sensor has a maximum detection range of 8,000 pcs/283 mL with the measured results at PWM.

The PD4NS dust sensor is reliable for detecting particulate matter based on the principle of detecting and separating particles. The PD4NS dust sensor circuit is mainly composed of an LM324 (quad operational amplifier), an infrared (IR) LED, IR photodiode, slide rheostat (potentiometer), and capacitance (Fig. 103.3). The IR photodiode is a Positive/Negative junction with photosensitive characteristics and unidirectional conductivity; therefore, it needs to add a reverse voltage while operating. Because of the IR LED, the module may avoid the effects of visible light. When the photodiode is not under light, there is only a very small reverse leakage current called a dark current; at this time, the photodiode is cut off. When the photodiode is exposed to light, the reverse leakage current increases and forms a photocurrent that varies with the incident light intensity. The photodiode transfers the dust information into a weak electrical signal. Part 3 (one op-amp of LM324) of the op-amp (operational amplifier) is an amplifier of an AC circuit. Circuit magnification is $1 + R5/R4$ (approximately 79). The VR3 and R2 play a role in creating the partial pressure in the circuit when connected to the photodiode. Part 4 (one op-

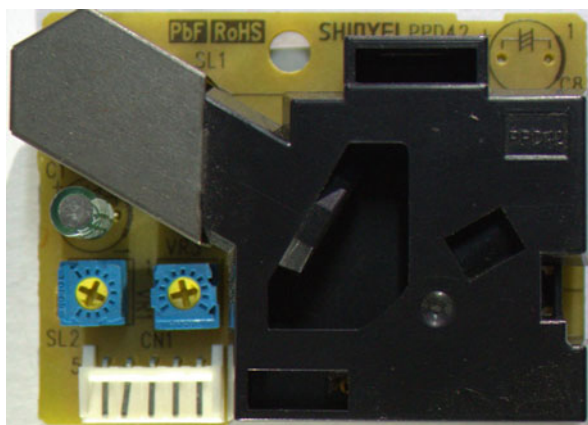


Fig. 103.2 PD4NS particulate matter sensor

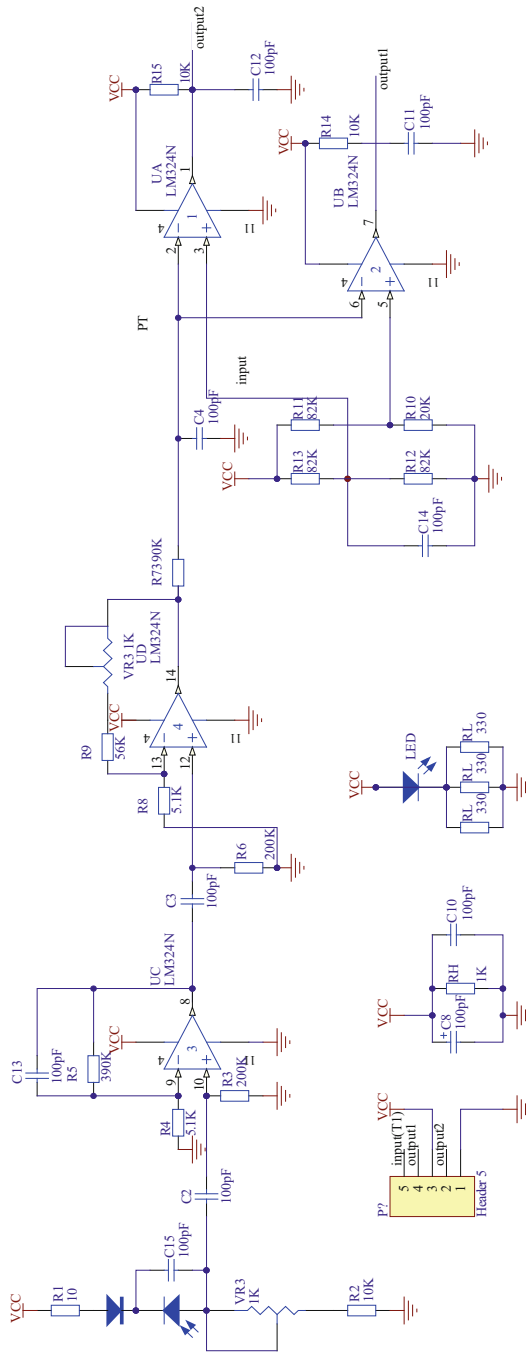


Fig. 103.3 Schematic diagram of PD4NS particulate matter sensor

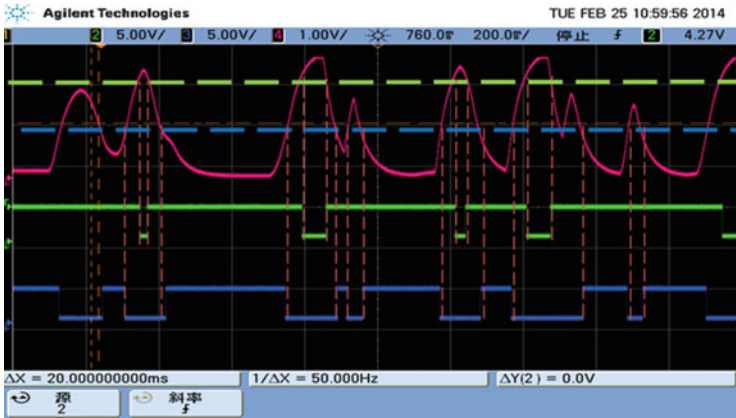


Fig. 103.4 Output1 and Output2

amp of LM324) of the op-amp is an amplifier just like part 3, and the circuit magnification is $1 + (VR3 + R9)/R8$ (approximately 11). C3 and C2 are used in AC coupling, by which only the AC signal can pass and the DC signal is isolated (or power) in order to avoid the effects of the operating point of an amplifier. Both parts 1 and 2 of the op-amp are voltage comparators. Their reference voltages are respectively 2.5 V and 1.0 V. The signal of the dust after amplification accesses the inverting input terminals of parts 1 and 2 of the op-amp. When the input signal voltage is greater than the reference voltage, the sensor inputs a low level of voltage; otherwise, it inputs a high level of voltage. The working chart obtained by Agilent OSC (MS07054A) is shown in Fig. 103.4.

In Fig. 103.4, the pink line represents signal 1, marked TP, after two operating amplifiers and before entering the two voltage comparators. The green line represents signal 2 output by the external pin 2 of the dust sensor. The blue line represents signal 3 output by the external pin 4 of the dust sensor. The green and blue dotted lines in Fig. 103.4 stand for the reference voltages in part 1 (2.5 V) and part 2 (1.0 V), respectively. Signal 1, through inverting the input terminal of parts 1 and 2 respectively, in contrast to the reference voltages of 2.5 V and 1.0 V, turns into signals 2 and 3.

According to the principle of particle counting, the number of measured voltage pulses refers to the number of particles, and the signal intensity of the measured voltage pulses represents the size of the particles. Thus, according to signals 2 and 3, the two corresponding dust concentrations can be analyzed qualitatively. The pulse waveform of signal 2 indicates a larger particle, and the pulse waveform of signal 3 indicates a smaller particle.

As shown in Fig. 103.4, in the experiment, small particles certainly exist when big particles arise. If the reference voltage of the two comparators changes continuously (1.0–4.5 V), more ranges of particle concentration can be obtained with postprocessing because of the relationship of particle size to voltage amplitude.

103.2.3 ZigBee Communication Module

To satisfy the requirements of small and low-cost sensors for use in wireless networks, the ZigBee Alliance, established in 2002, has defined a wireless communication technology. The ZigBee protocol follows the IEEE 802.15.4 standard because wireless sensor networks (WSNs) employs lower data rate requirements but with higher specifications. The ZigBee network features low costs, self-configuration, and a multihop mesh network with security services based on a 128-bit AES algorithm added to the security model. It is provided by IEEE 802.15.4, which encourages its use in the monitoring field.

Although WSNs come in many varieties, the ZigBee has its own unique advantages. Compared with Wi-Fi, the general packet radio service (GPRS), and Bluetooth, ZigBee technology basically has several characteristics as follows: low system power consumption, low cost, safe data transmission, flexible working frequency band, large network capacity, and a flexible network structure. In particular, ZigBee technology has the capability to network automatically upon powering on the modules, for example, when a network module is powered down, the network has the capability to perform self-repair.

This experiment uses the DRF2618-ZUSB and DRF2619A as the coordinator and router nodes, respectively. In the same ZigBee network, all nodes must have the same channel and PAN ID. Data transmission is carried out via transparent transmission and short addresses. By configuring the sending module in a certain way, the sending module will transmit data with a short address of itself attached at the end of such data; then the receiving module receives an additional 2 bytes of data (the short address).

103.3 System Software Design

The software of the online monitoring system includes the main program, a PWM data sampling subroutine, two external interrupt subroutines, a serial port subroutine, a timer subroutine (Timer0 interrupt program), and a LED display program. The main flowchart of the program is shown in Fig. 103.5. The main program starts with the initialization of variables. The system can automatically detect the concentration of dust based on the data displayed on the LED in real time. The MCU sends data to the monitoring center using ZigBee communication technology every 8 s, and the data are stored at the monitoring center of the host to process the dust data later; therefore, we can obtain the concentration of dust particles ($1\ \mu\text{m} < \text{dust} < 2.5\ \mu\text{m}$) and particles ($2.5\ \mu\text{m} < \text{dust}$). Figure 103.6 is a flowchart of a serial port interruption. It can process the data sent to the monitoring center when the MCU receives commands from the host; in this sense, it is a bidirectional communication.

Fig. 103.5 Flowchart of main program

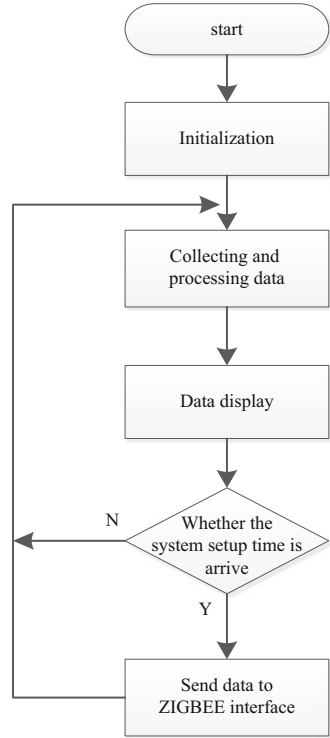
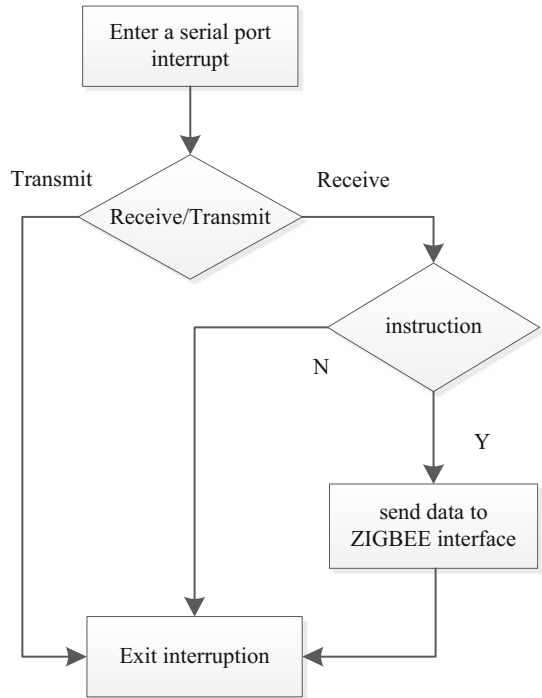


Fig. 103.6 Flowchart of serial port interruption program



103.4 Experimental Results

An experimental dust-monitoring system was built, as shown in Fig. 103.7. The experimental data are shown on LEDs of a department unit of a note, which counts both external pulses from a PD4NS dust sensor for every 8 s of sampling when detection is being performed. Then the MCU sends the results to the monitoring center using the ZigBee communication technology. Figure 103.8a shows a group of the data “00160010” displayed on 8 units LEDs at one of the nodes, while the four digits on the left, 0016, represent the number of pulses of particles ($1\ \mu\text{m} < \text{dust} < 2.5\ \mu\text{m}$) detected in 8 s of sampling and the four digits on the right, 0010, represent the number of pulses of particles ($2.5\ \mu\text{m} < \text{dust}$) collected at the same time as that mentioned earlier. Figure 103.8b shows the results (data list table) of detecting dust from the monitoring center. The two values 14 3E represent the short address of the router. The data 16 and 10 are the first group of data in the list and represent the number of particles ($1\ \mu\text{m} < \text{dust} < 2.5\ \mu\text{m}$ and $2.5\ \mu\text{m} < \text{dust}$, respectively) corresponding to the number displayed on the LEDs. The last column in the data list table represents the time when the data are received. We can see that the monitoring center receives data every 8 s.

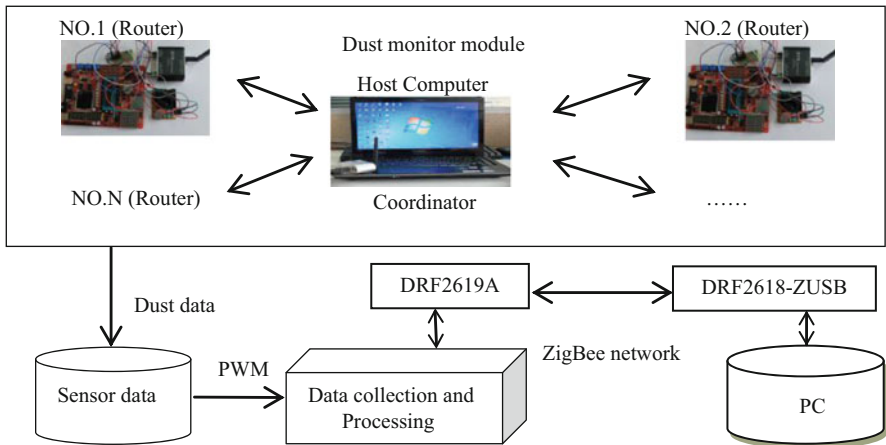


Fig. 103.7 Architecture of dust-monitoring system

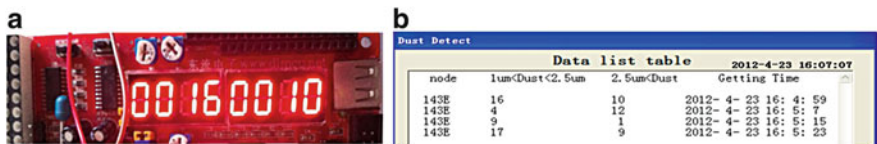


Fig. 103.8 Experimental data

Conclusion

This paper presented the design of an online monitoring system for dust detection using ZigBee communication technology. When the ZigBee module is connected to the MCU (STC12C5A60S2) microprocessor, the monitor system can provide more flexibility and mobility and save money and energy spent on integrated wiring; in addition, the system collects information on dust concentration using the PD4NS sensor and then the information is processed by the MCU (STC12C5A60S2). It measures two dust concentrations in the system field. Moreover, the monitoring system proves the feasibility of ZigBee technology applied in wireless monitor systems featuring sound expansibility and broad application prospects.

References

1. Xuezhen C, et al. Testing and control technologies of coal dust in coal mine. *Min Res Dev*. 2007;27(06):78–85 (in Chinese).
2. Lili D, Limin T, et al. Dust hazard in workshops in Sichuan. *J Occup Health Damage*. 2013;28(3):129–32 (in Chinese).
3. Ren-qing LIU. Design of dust sensor based on Bluetooth technology. *Commun Technol*. 2009;42(03):252–4 (in Chinese).
4. Bisdikian C. An overview of the Bluetooth wireless technology. *IEEE Commun Mag*. 2001;39(12):86–94.
5. Chengbo Y, Yangzhe C, et al. Zigbee wireless sensor network in environmental monitoring applications. *Wireless Communications, Networking and Mobile Computing, WiCom'09*. 5th International Conference on. IEEE; 2009. p. 1–5.
6. Farahani S. ZigBee wireless networks and transceiver. *Newnes*; 2011. p. 25–32.
7. Gomaa R, Adly I, Sharshar K, et al. ZigBee wireless sensor network for radiation monitoring at nuclear facilities. *Wireless and Mobile Networking Conference (WMNC), 2013 6th Joint IFIP*. IEEE; 2013. p. 1–4.
8. Cifuentes C, Braidot A, Rodriguez L, et al. Development of a wearable ZigBee sensor system for upper limb rehabilitation robotics. *Biomedical Robotics and Biomechatronics (BioRob)*, 2012 4th IEEE RAS & EMBS International Conference on. IEEE; 2012. p. 1989–94.

Chapter 104

The Application of WeChat to the University Laboratory Management Information System

Jiangsheng Zhao and Xi Huang

Abstract In the current mobile Internet era, mobile applications to university laboratory management information systems represents a broad trend. This paper states the necessity and feasibility of incorporating WeChat into a management information system by comparing WeChat and mobile apps. At the same time, we analyze some important problems that arise between system design and system realization. In addition, some examples of practical applications are given. The application of WeChat not only injects much fresh energy into the traditional laboratory information system but also provides a new way of managing university laboratories.

Keywords Mobile Internet • University laboratory management information system • WeChat • University laboratory management

104.1 Introduction

104.1.1 Overview of University Laboratory Management Information System

The university laboratory serves as an important base for experimental teaching and scientific research, and the level of its management has a direct effect on the cultivation of talent and scientific research of the university [1]. The university laboratory management information system (abbreviated as “lab information system” in what follows) is an important part of the management of the university lab; therefore, it should have a common platform for students, teachers, and laboratory managers. Through the platform, students and teachers can obtain access to the resources they need conveniently, and laboratory managers can provide better service. The people serving in these three roles not only facilitate access to the

J. Zhao (✉) • X. Huang
Software School of Xiamen University, 361005 Xiamen, China
e-mail: zjs@xmu.edu.cn

latest information about the lab but they can also communicate with each other conveniently using the information system. This kind of information system can greatly improve the quality and level of management and help to bring about the modernization of laboratory management.

104.1.2 Overview of WeChat

On January 15, 2013, the official account of Tencent Weibo announced that the number of WeChat users had broken the 300 million mark [2], which was a landmark of great historic significance. Moreover, this happened just 2 years after the birth of WeChat version 1.0. In 2013, WeChat had become the hottest mobile Internet application [3].

With the rapidly increasing number of WeChat users, the large market that originally belonged to Weibo was divided up. Many of Weibo's users turned to WeChat. Registering a WeChat account is becoming fashionable among university students. Therefore, incorporating WeChat into the laboratory information system to provide a more convenient and faster service for students and teachers is an urgent issue that must be solved.

104.2 Requirement Analysis of System

104.2.1 Necessity and Feasibility of Incorporating WeChat into a Laboratory Information System

This is the era of the mobile Internet. Entering a long URL and accessing the laboratory information system via computer are now outdated practices [4]. A preferred method of accessing the system is by smart phone or tablet. This would allow students and teachers to obtain the latest information on time, and apply for these research equipment, meeting rooms, and labs conveniently. Moreover, the laboratory manager can check the usage states of the labs and equipment. WeChat is a very suitable platform to satisfy the aforementioned requirements for the following reasons:

1. The application of WeChat embodies the idea of the mobile Internet, and it can provide service anytime, anywhere. This breaks through the great limitation of traditional information systems, which require computers. Meanwhile, WeChat already has a wide group of users, including the users of laboratory information systems, namely, the teachers and students at colleges and universities. And this paves the way for the import of WeChat to laboratory information systems.
2. WeChat can bring revolutionary change to information systems. The traditional information system requires users to remember long URLs, domain names, or

arcane long number strings. However, WeChat is more convenient; the user need only scan the QR code and follow the account.

3. WeChat has a message pushing function that traditional information systems do not have. Traditional information systems can only send e-mail or chargeable text messages, which would make the receiver feel inconvenienced or even tired. However, in WeChat, the service account can send a group message every month, and then the other users can click the related menu to retrieve the message. If users think that it is a useful or interesting message, they can share it with their circle of friends.
4. WeChat also introduces a significant change in laboratory management. To obtain basic information and usage information on laboratory equipment, students need only use WeChat to scan the QR code to decide whether to apply for one piece free equipment at once. A laboratory manager also can scan the QR code to obtain statistical information on laboratory equipment use, which is very useful for routine lab inspections or for visitors.

In conclusion, applying WeChat to a traditional laboratory information system can improve the system.

Regarding feasibility, transforming the current system into a B/S-based (Browser/Server) laboratory information system would be very inexpensive. First, the amount work involved in constructing a Web site in WeChat that would be suitable for equipment with small screens, such mobile phones, is limited because no back-end work is involved. And if the front page of the original information system is suitable for mobile equipment, then the cost would be even lower. Second, WeChat's platform features menus and auto response services, which would help in quickly completing the information system.

104.2.2 Comparison of WeChat and App

Through the preceding discussion, based on the current technologies, the manager can select developing the mobile app or creating an official WeChat account to mobilize the information system by the WeChat platform. The reasons for choosing WeChat rather than the mobile app are as follows:

1. Cost of development [5]: It is easily to accomplish the Web site and the mobile Web site on WeChat, with few difficulties and at a low cost.
2. Cost of promotion: the most prominent feature of WeChat is its circle of friends, which makes sharing easy. Moreover, promoting it is very easy, while the app must be developed from scratch, which is difficult.
3. Convenience: WeChat is a widely used application. It is easy to determine whether an information system is added to the WeChat platform. The official WebChat account has its own management system. However, application of the laboratory information system app is unusual, so that many users will have a hard time finding it among those numerous applications.

The app certainly has a better user interface. But an exhaustive comparison between the app and WeChat shows clearly that WeChat is the better choice.

104.2.3 Functions and Principles Suitable for Realizing in the WeChat Public Number

The traditional laboratory information system has many base modules, such as, for example, a press release, equipment application, machine application, meeting room application, message board, and [recruitment advertising](#). Similarly, a WeChat official account must also have these modules. In addition, there exist other optional modules, such as, for example, the management subsystem for a graduation project, a registration system, and a questionnaire survey. These modules usually include some functions that are not suitable for WeChat. For example, the press release includes a press list, press details, and press background management; however, the press background management function is not suitable for WeChat.

To use the mobile equipment, some principles must be considered to determine whether to appear these functions or not.

First, the functions which should be reserved must have little input, such as displayint news, or approving a workflow.

Second, given the size of the screen, some of these Web pages must be redesigned, namely, the mobile Web pages should be redesigned to remove those unnecessary parts and get to be lightweight ones.

104.3 Several Problems in System Design and Implementation

104.3.1 Service Account Versus Subscription Number

In WeChat version 5.0, the official account is classified as the service account and the subscription account. The differences between them are given in [Table 104.1](#).

It is clear from the preceding comparison that the subscription account is mainly used to promote a product or business, while the service account is mainly used to provide a service for users. A feature-rich and fully customizable menu would provide users with a more full-service experience. The subscription account with a push message one time per day would help promote itself quickly.

Our aim here is to show that the laboratory information management system will provide more and better services to students and teachers and not merely demonstrate that such a system exists at the university. Therefore, we should choose the service account rather than the subscription account.

Table 104.1 Differences between service account and subscription number

	Service account	Subscription number
Group-send message	One/month	One/day
Message display	Chatting list	Subscription number folder
Push reminder	Yes	No
Menu	Yes	No

104.3.2 WeChat Menu Design Menu

The menu represents very important content in the service account because the main orientation of the service account is to let users choose the service they need independently. Therefore, a custom menu is very important. Every WeChat account can construct only the three first level menu items, and each first-level menu can create five second-level menu items, which makes the use of menus valuable.

The functions of a laboratory management information system need to be analyzed. The first major function is the online machine application. Students do not need to go find some teacher for a signature; they simply retrieve it online. Therefore, this function should be displayed in the menu.

The second major function is the application of lecture hall, namely, not only teachers but also students can directly apply the appreciating hall online. However, displaying four Chinese characters in the WeChat menu item is the best choice. Therefore, we set it as “classroom application.”

Now, the system has many applications, so the approval of leaders can also be realized in WeChat. Clearly, almost all examining operations only include agreeing, disagreeing, and providing some reasons that would make the approval flow confirm that the mobile is able to display simple and light content.

The third major function is obviously the management of students. This function is more complicated and has and the student information have a few changes. Therefore, this function is not in the design because it is not suitable for WeChat.

In conclusion, the three first-level menu items must display *Machine application*, *Classroom application*, and *More*, and there are two second-level menus, *Pending works* and *About us* in the first-level menu *More*.

104.3.3 Auto Response Design

The WeChat service account lets users actively select the menu. In addition, it also provides auto responses for users to query, that is, users need only send messages with the corresponding content under the developer mode.

After analyzing the main functions of the management system, The query of machine and lecture hall must be responded automatically. Therefore, we use the following keywords for query. The words in quotation marks are the words the user needs to input.

1. Input “Empty machine positions”: these three words sent to the service account allow the user to obtain the available machine positions.
2. Input the machine number directly: in laboratory management, each machine has a unique number. The user inputs the number to obtain the details of the queried number. The details include whether or not the machine is occupied, who occupies the machine, and the specific configuration of the machine.
3. Input laboratory name: the user inputs the laboratory name to find out basic information about the laboratory and about available machines in the lab.
4. Input the name of the lecture hall and “arrangement”: this operation allows users to obtain the arrangement of the appreciating hall during this week.

104.3.4 Micro Nameplate Design

Naturally, WeChat could not exist without the technology of QR code. Use of QR code technology can generate a QR code nameplate for each lab. The students only need to scan the nameplate to obtain details about lab usage and the configuration of the machines in the lab. Then the free machines have many buttons. Users can click button directly to apply for the corresponding machine, which is simple and convenient. Similarly, a visitor at the lab can also scan the nameplate to obtain specific usage information and some simple tables.

104.3.5 Screen Width

When developing applications related to mobile phones, it is necessary to understand the differences in the displays of mobile phones and computers. With mobile phones, the size of the screen is always fixed. However, in some mobile phones, the screen has two orientations: vertical and horizontal. The challenge is to customize the size of the window; the width of the mobile phone is usually defined during the loading phase. At the same time, the size of the screen in mobile phones does not usually exceed 1,000 pixels. Therefore, retina technology is required in display applications.

104.3.6 Size of Web Page

Because a WeChat service account actually represents a combination of WeChat technology and Web technology, the technology of Web pages plays an important role in the program. However, because of mobile phone screen widths, there are many challenges involved in designing Web pages. In this program, we discard the idea of directly defining the width of the screen during the process of loading; instead, we use bootstrap technology to define the width of the screen dynamically.

Loading a Web page using bootstrap technology is a somewhat slow process, but Web sites are more suitable for variety of mobile phone resolutions and more complex situations. Meanwhile, we can develop Web pages that can be correct displayed simultaneously on pc and mobile phone. Browser compatibility is not an issue, which makes development simpler and more convenient.

After the advantages are analyzed, the disadvantages need to be analyzed too. Compared with the traditional technology, there is no doubt that the cost of using a framework is more loading time and more complicated Web pages. However, the program is used mostly around a lab, which has a high probability of finding Wi-Fi. Even if Wi-Fi cannot be found, the size of the bootstrap is only 200 KB, which is completely acceptable. In addition, compiling java scripts can also keep the size of the Web page down to approximately 150 KB with few differences; writing another java script can also keep the size of the Web page down to approximately 150 KB, so it is similar to bootstrap.

104.4 Practical Example

104.4.1 Menu

The setting of a menu is simple. A finished menu is shown in Fig. [104.1](#).

104.4.2 Micro Nameplate

The realization of a micro nameplate is more complicated. First, input the lab and meeting room. Next, generate two-dimensional code using the method given by the system, which is shown in Fig. [104.2](#).

Next, paste the generated QR code at the entrance of each lab. Students, teachers, and managers can query the details of the lab or share details on their mobile phones using the scan function if they want to know the usage state of a machine in the lab.

Fig. 104.1 Final menu

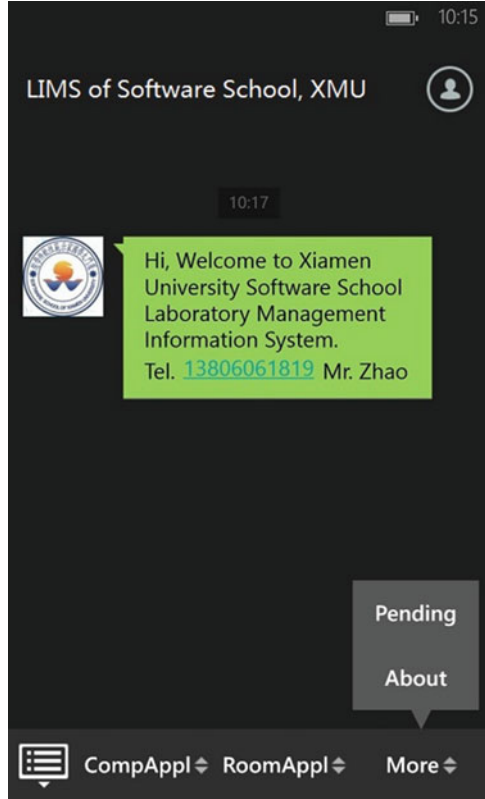
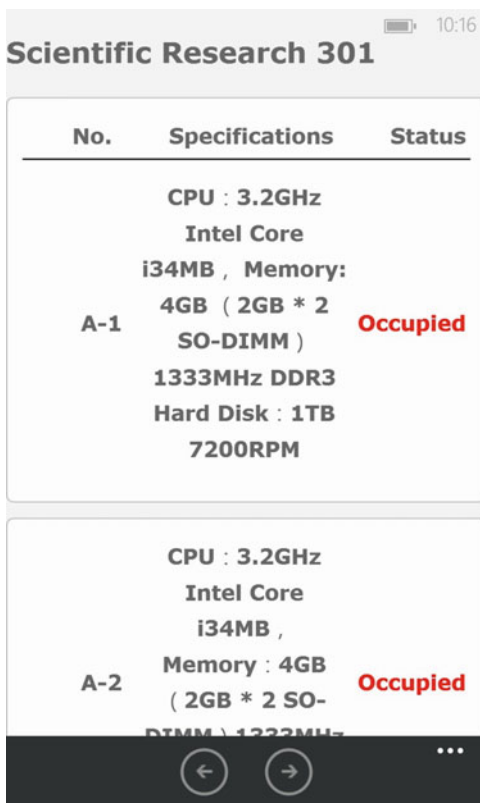


Fig. 104.2 QR code of lab



Fig. 104.3 Laboratory information details



Finally, students can directly apply for the machines using a password obtained by the QR code and the system, which realizes mobile working and telecommuting. The laboratory information details are shown in Fig. 104.3.

Conclusion and Outlook

Several laboratory management information systems based on WeChat have been installed and deployed in some university experimental centers such as the Software School of Xiamen University. With positive feedback given by teachers and students, these systems have become the most common work platform. Thus, not only can new mobile Internet technologies such as WeChat in a traditional information system laboratory allow for the use of multiple platforms to greatly improve the user experience, but this kind of application can also quickly be deployed at low cost. It can be concluded that this technology not only brings new vitality to laboratory information systems but also provides a new method for managing university laboratories.

(continued)

(continued)

Although the system has greatly enhanced the efficiency of management, there is still room for improvement.

First, university labs have many business flow requirements, such as equipment applications and meeting room applications. All these business flows are very popular in the management of university laboratories. Providing more and better services on WeChat is a good way to approach managing a laboratory information system.

Second, following a long period of development and evolution, system data will be more valuable. Such data can also provide decision support for lab and institute managers using data mining technology. For example, it is possible to determine students' interests and personal blueprint by analyzing students' reasons for using machines or the times when students usually use them.

Finally, papers addressing the combination of WeChat and laboratory management systems are few, which shows that its exploration has just begun. WeChat presents tremendous opportunities in connection with the management information system of a university laboratory. Whether WeChat deserves a place in university laboratory management depends on whether the system incorporating WeChat can provide better and more convenient services or a better user experience. However, based on current practices and research, laboratory management systems that incorporate WeChat have broad application prospects.

References

1. Fransen SM, Nyrup A. Implementation of a "standard" LIMS. *Lab Autom Inf Manag.* 1998;33:227–233
2. Longzhong H. WeChat reached 300 million users. <http://www.ifanr.com/235574>. Accessed 16 Jan 2013
3. Sutu Institute. WeChat user behavior analysis report in 2013. ChinaByte. <http://net.chinabyte.com/161/12644161.shtml>. Accessed 20 June 2013
4. Gerst G. A brief history of LIMS. *Lab Autom Inf Manag.* 1996;32:1–5.
5. IT Times. Who will have the last laugh between WeChat and App? [EB/OL]. PUTUI. [2013-05-27]. <http://www.putui.com/shehuihuayingxiao/179.html>.

Chapter 105

A Short Loop Queue Design for Reduction of Power Consumption of Instruction-Fetching Based on the Dynamic Branch Folding Technique

Wei Li and Jianqing Xiao

Abstract On the basis of analyzing the characteristics of short loop instructions in embedded processors, this paper proposes a short loop instruction queue technique for reducing the power consumption of instruction fetching. By means of adding an instruction queue to store the short loop instruction between the fetch stage and the decode stage of the processor pipeline and dynamic detection circuits so as to detect the short loop instruction, this technique can reduce the delay resulting from the loop instruction and thus eliminate unnecessary access to the cache so as to reduce the power consumption of instruction fetching. Our experiments show that an average 16.7 % power saving can be achieved in instruction fetching without any performance degradation.

Keywords Instruction cache • Short loop • Branch folding • Low power

105.1 Introduction

With the popularity of portable terminal devices, the performance of embedded processors has been the subject of great development. Among the many techniques to improve the performance of embedded processors, the pipeline technique has played an important role. Although it has greatly improved the speed and throughput of embedded processors, branch and jump instruction reduces pipeline performance [1]. Therefore, an efficient mechanism to handle the branch and jump instruction forms a research focus in this regard [2].

Loop instructions take up a large proportion of the overall instructions. As presented in Table 105.1 [3], analysis of execution of the Powerstone benchmark suite shows that the branch instruction takes up 8.52 % of the overall instructions

W. Li (✉) • J. Xiao
Xi'an Microelectronic Technology Institute, 710054 Xi'an, China
e-mail: lw@stu.xjtu.edu.cn

Table 105.1 Branch and loop statistics using the Powerstone benchmark suite (from Yi et al. [3])

Benchmark	Total count	Branch		Loop		
		Branch count	Proportion of total (%)	Loop count	Proportion of branch (%)	Average size
adpcm	53,682	2,999	5.59	1,697	56.59	13.52
blit	24,220	2,009	8.29	2,002	99.65	12
crc	36,248	4,527	12.49	2,387	52.73	14.08
des	171,409	2,821	1.65	1,551	54.98	101
g3fax	1,165,904	167,835	14.40	124,859	74.39	8.89
jpeg	3,878,156	225,425	5.81	186,954	82.93	10.95
pocsag	51,169	5,844	11.42	3,257	55.73	16.65

while the loop branch instruction takes up 69.24 % of the total number of branch instructions [4]. Statistics show that within the 16 instructions the short loop instruction takes up the largest proportion of the overall instructions. The short loop indicates that the fetching instruction unit repeats fetching of the same instruction fragment. Therefore, a reduction in cache access can reduce dynamic power consumption in embedded processors.

Currently, methods for solving the loss of performance caused by branch instruction include loop unrolling [5], the branch target buffer [6], a small loop cache [7], and branch folding [8]. The general idea of loop unrolling is to replicate the code inside a loop body a number of times so as to improve the efficiency of instruction fetching, but this technique increases the code size and the cache miss as well, which may exert a negative effect on performance. In this sense, it is not suitable for embedded processors. As to the branch target buffer approach, it adds a branch target address buffer to store the branch target address and a branch predictor so as to predict whether the branch occurs or not. When the predictor indicates the branch will occur, the fetching instruction unit will pre-fetch the branch target instruction. The size of the branch target buffer and the accuracy of the predictor may affect the performance of processors. As to the small cache technique, it adds a small cache to store the replaced instructions, but this technique increases both hardware cost and power consumption. Branching folding is a technique where, on the prediction of most branches, the branch instruction is completely removed from the instruction stream presented to the execution pipeline. thus it can significantly improve the performance of branches and is easy to implement. Therefore, it has been widely used in embedded processors. Nevertheless, the disadvantage of this technique is also obvious, it can only record the branch target address. Although there is a loop instruction, the fetching instruction unit still has to access the cache. In any case, the energy efficiency showed no improvement, which means the technique is focused on performance improvement rather than power saving.

This paper presents a novel technique that adds a dynamic detecting unit to monitor both the short loop instructions and the short loop queue between the fetching unit and the decoding unit. In the course of detecting the unit short loop,

it turns on the short loop queue to buffer the instructions so as to reduce unnecessary access to the cache.

105.2 Principle of the Short Loop for Reduction of Power Consumption

The dynamic unrolling technique adds an instruction queue between the fetching unit and the decoding unit. The scheme is shown in Fig. 105.1. In the course of detecting the loop instruction, the loop is not only stored in the interstate registers, but also in the queue. When the program jumps to the address of the executed instruction, the fetch unit acquires the instruction for execution from the instruction queue instead of the instruction cache and disables the instruction cache to reduce the power consumption.

There are two different strategies: the direct buffer and the conditional buffer. The direct buffer stores the fetched instructions to the queue no matter whether there is a loop instruction. The conditional buffer stores the following instructions when the fetching unit detects the loop. As the first method does not need complex control, it is easy to implement; but when the pipeline doesn't execute the loop, this method adds extra power consumption resulting from the instruction queue. The second method demands that the dynamic detecting unit detects the loop. When detecting the loop, the detecting unit enables the queue to store the loop instructions. When not detecting the loop, this unit turns off the loop instructions. In consideration of the loop instruction proportion, this paper adopts the second method.

As shown in Fig. 105.2, the short loop queue controller includes four states. The queue sleeping state means the queue is in sleeping mode when no loop is detected

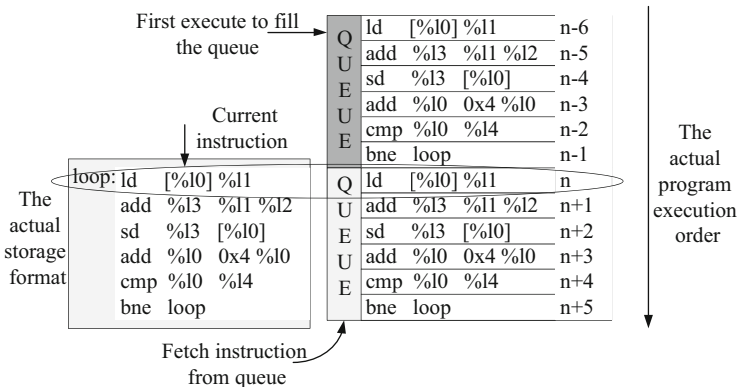
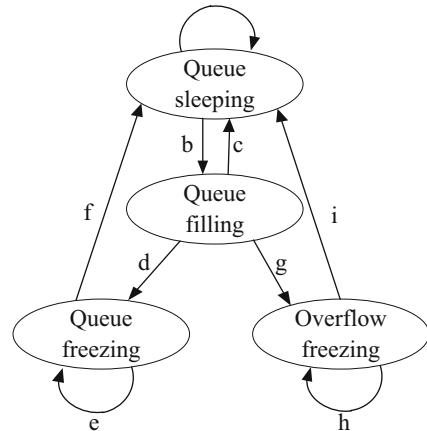


Fig. 105.1 Short loop dynamic unrolling

Fig. 105.2 State diagram of the short loop queue controller



by the detecting unit. When the loop is detected, the queue enters filling mode. In this mode, the queue stores the following instruction until it detects the branch instruction again. The queue then enters freezing mode, if the queue didn't overflow. Now, as the fetching instruction unit reads instructions from the queue instead of the cache, the instruction cache is disabled so that dynamic power consumption can be reduced. If the size of the loop is greater than the size of the queue, the queue overflows and accesses overflow freezing. In this mode, the overflow instruction is read from the cache while the rest of the instruction is read from the queue. In this way, the power consumption can be reduced to the greatest extent.

105.3 Design of the Short Loop Queue Based on the Dynamic Branch Folding Technique

The design of the short loop queue has three parts: the hit judgment, loop detecting, and the state controller. In the LEON3 processor, a conditional branch instruction must be in one loop. Conditional branch instruction can be used as the start indicator of the loop body. When detects the conditional branch from the decode unit, the controller controls the short loop queue enter to the filling instruction state until next conditional branch signal is detected. When the next branch target address is equivalent to the last branch target address stored in the register, the queue accesses the freezing state until the target address is out of range of the queue. Even though the proportion of the loop is smaller than the conditional proportion as shown in Table 105.1, the loop proportion still forms the major part of the branch. In this sense, this method can significantly reduce power consumption.

Additional hardware is demanded to implement the hit judgment, as shown in Fig. 105.3. Three registers are added: (1) the target_addr_register for storing the target address of the last branch; (2) the queue pointer register for storing the offset of the end address of the loop; and (3) the threshold for recoding the maxim offset allowed using the queue. The threshold can be a register or a constant.

The implementation is shown in Fig. 105.4. When the decode unit detects the conditional branch, which indicates a loop, the target_addr_register stores the PC as the queue start address. Then the queue stores the instructions fetched from the instruction cache and the queue pointer by self-adding always points to the bottom address of the queue. When the decode unit detects the conditional branch, the controller compares the PC and the target_addr_register. If the PC is out of range of the threshold, the controller generates a miss signal, which indicates there is no loop

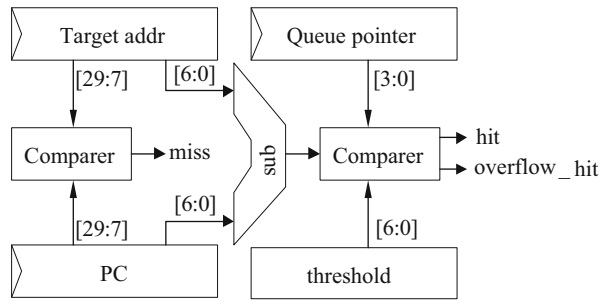


Fig. 105.3 Implementation of the hit judgment

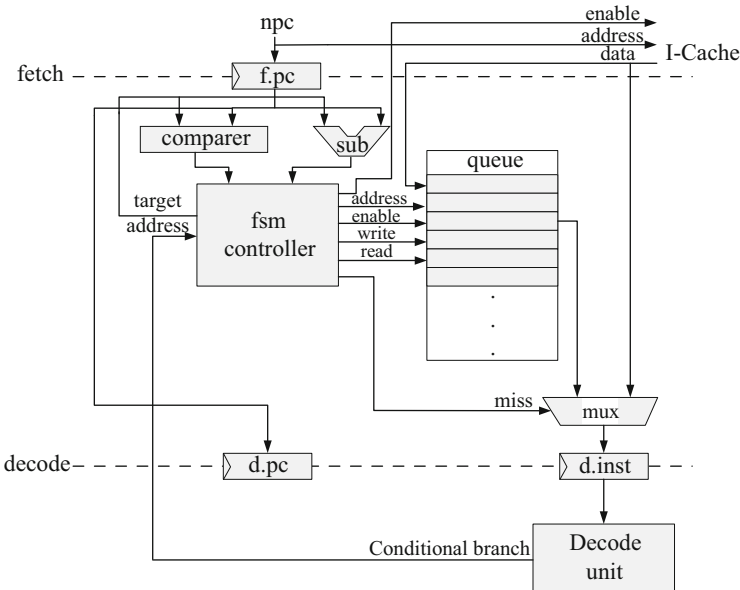


Fig. 105.4 Implementation of the short loop queue

or the loop is not a short loop. If the PC is within the range of the threshold, the controller gets the offset from the sub. Then if the offset is smaller than the value of the pointer register, the controller generates a hit signal. If the offset is greater than the value of the pointer register, the controller generates an overflow hit signal, which indicates there is only part of the loop in the queue; and the queue accesses the overflow freezing state.

105.4 Experiment and Analysis

The hardware platform uses the LEON3 processor synthesized using Synopsys DC in TSMC 90 nm. The instruction cache uses a four-way set associative cache. The cache size is 8 KB. Simulations were performed with the Powerstone benchmark suite to quantify the power saving of the loop queue technique.

Lee et al. [8] shows that about 81.2 % of conditional branch distances are 16 or less. Table 105.1 shows the average branch distance is mostly less than 16, therefore the size of the short loop queue is set to 16 and the threshold value is set to 128 in the power experiment.

As shown in Fig. 105.5, each test program shows different levels of power consumption reduction. The average power saving is about 17.6 %. The des test program shows a power saving of only 3 %, far below the average. On the basis of the statistical analysis (see Table 105.1), it was found that the average loop size in the des program was far greater than the size of the queue and only part of the power consumption of the loop was saved.

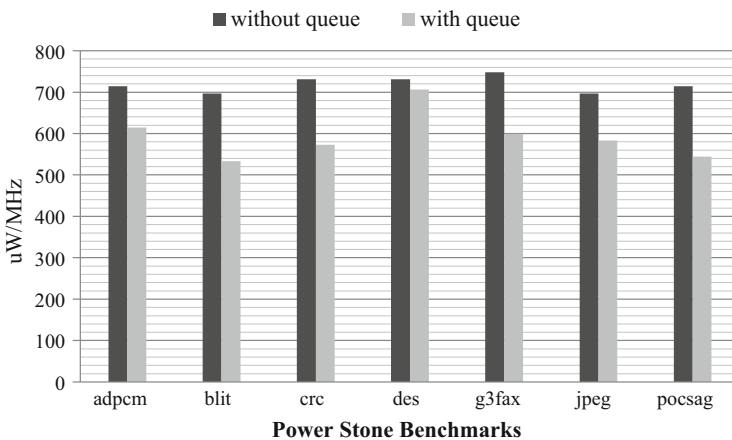


Fig. 105.5 A comparison of power consumption for the design without a short loop queue and the design with a short loop queue based on dynamic branch folding

Conclusions

This paper first analyzes the execution of the Powerstone benchmarks in embedded processors, and then presents and evaluates a design method for a short loop queue based on the dynamic branch folding technique by means of analysis of the execution of the Powerstone benchmarks. With the addition of the short loop queue between the fetch unit and the decode unit, it is obvious that this technique will reduce the power consumption of the fetching instruction. The experiments show power consumption can be reduced by ca. 17.6 %.

References

1. Emma PG, Davidson ES. Characterization of branch and data dependencies in programs for evaluating pipeline performance. *IEEE Trans Comput.* 1987;36(7):859–75.
2. Fan DR, Yang HB, Gao GR, Zhao RC. Evaluation and choice of various branch predictors for low-power embedded processor. *J Comput Sci Technol.* 2003;18(6):833–8.
3. Yi MJ, Yan XL, Ge HT, Xu HM. Instruction recycling based on low power branch folding. *J ZheJiang Univ.* 2010;44(4):632–8 (in Chinese).
4. Malik A, Moyer B, Cermak D. A low power unified cache architecture providing power and performance flexibility. In: *The International Symposium on Low Power Electronics and Design (ISLPED'00)*. Austin: IEEE; 2000. p. 241–3.
5. Davidson JW, Jinturkar S. Improving instruction-level parallelism by loop unrolling and dynamic memory disambiguation. In: *Proceedings of the 28th Annual International Symposium on Microarchitecture (MICRO'95)*. Ann Arbor: IEEE; 1995. p. 125–32.
6. Hennessy JL, Patterson DA. *Computer architecture: a quantitative approach*. 4th ed. San Francisco: Morgan Kaufmann Publishers; 2006. p. 138–41.
7. Bellas N, Hajj I, Polychronoulos C, Stamoulis G. Energy and performance improvements in microprocessor design using a loop cache. In: *Proceedings of the 1999 I.E. International Conference on Computer Design: VLSI in Computers and Processors (ICCD'99)*. Austin: IEEE; 1999. p. 378–83.
8. Lee LH, Scott J, Moyer B, Arends J. Low-Cost branch folding for embedded applications with small tight loops. In: *Proceedings of the 32th Annual International Symposium on Microarchitecture (MICRO'99)*. Haifa: IEEE; 1999. p. 103–11

Chapter 106

Chip Design of a Continuous-Time 5-MHz Low-Pass Sigma-Delta Modulator

Jhin-Fang Huang, Jiun-Yu Wen, and Wei-Chih Chen

Abstract A continuous-time low-pass sigma-delta modulator ($\Sigma\Delta\text{M}$) with a chain of integrators with weighted capacitive feedforward (CICFF) summation topology is fabricated by TSMC 0.18- μm CMOS process. The summation of feedforward signals is implemented by the weighted capacitors without the necessity of any additional active components. The quantizer uses a 1-bit comparator which may achieve high linearity easily. Under 1.8-V supply voltage, the measured results achieve a dynamic range of 52 dB over a 5-MHz signal bandwidth, a peak SNDR of 53.37 dB, an ENOB of 8.53 bits, an IM3 of -56 dB, and a power dissipation of 11.8 mW. With the pads included, the chip area is 0.35 (0.563×0.636) mm^2 .

Keywords Continuous time • Sigma-delta modulator • ADC • Low-pass filter • CICFF

106.1 Introduction

With the increasing development of wireless communication systems, there is a large demand of wireless communication for analog-to-digital converters (ADCs) which require signal bandwidth of several megahertz. Sigma-delta modulators are ideally suitable for such application. Compared to the discrete-time (DT) switched-capacitor circuit implementations, the continuous-time (CT) $\Sigma\Delta\text{M}$ s have the potentials of wider bandwidth and are also inherent anti-aliasing; however, it is difficult to implement the high-order passive filters by cascading practically because of the loading effect. Most of the loop filters of CT $\Sigma\Delta\text{M}$ s are built by active-RC and/or Gm-C integrator because the amplifiers inside the active integrators can provide gain, which may greatly reduce the input-referred noise; however, they suffer from

J.-F. Huang (✉) • W.-C. Chen
Department of Electronic Engineering, National Taiwan University of Science
and Technology, Taipei 10672, Taiwan
e-mail: jfhuang@mail.ntust.edu.tw

J.-Y. Wen
Television and Radio Administration Department, National Communications Commission,
Taipei 16072, Taiwan

the power consumption. Several literatures of $\Sigma\Delta$ Ms with passive loop filters are found [1–5]. Kim et al. finished a bandwidth of 4 MHz with high power consumption of 20.5 mW and a lower SNDR of 48.4 dB [1]. Although Song et al. made sound improvement of SNDR to 59.8 dB, it consumes more power of 22.3 mW and bigger chip area of 1.62 mm² [2]. On the basis of our previous studies [3–5], we continue to achieve a quadrature band-pass sigma-delta modulator [3], a 2-MHz low-pass sigma-delta modulator [4], and a 4-MHz low-pass modulator [5]. Under the required bandwidth, all of them have obtained sound performances; in addition, LTE has become a popular mobile communication system recently. It will be significant to integrate them together, and therefore a CT 5-MHz low-pass $\Sigma\Delta$ modulator is proposed to meet an LTE bandwidth of 5 MHz.

106.2 System Circuit Structure

106.2.1 $\Sigma\Delta$ Modulator Architecture

The chain of integrators with weighted feedforward (CIFF) summation is a traditional loop filter topology in the $\Sigma\Delta$ Ms shown in Fig. 106.1. In the CIFF topology, the output of each op amp has lower output swing than the chain of integrators with distributed feedback (CIFB) [1]. The CIFF topology is suitable for low-power application, but it needs additional current for the feedforward summation, which increases extra power consumption.

In order to reduce the active circuit by a capacitive feedforward summation structure as shown in Fig. 106.2, the last integrator’s output of loop filter in the CICFF topology has replaced the summation [2]. Therefore, no extra power in the feedforward branches is consumed. The CICFF topology is a great solution to obtain low-power application. This scheme proposes the third-order loop filter for the low-pass $\Sigma\Delta$ modulator.

The loop filter transfer function can transfer a polyphase quadrature band-pass loop filter from dc to the desired frequency, ω_c , by cross-coupling resistors [2]:

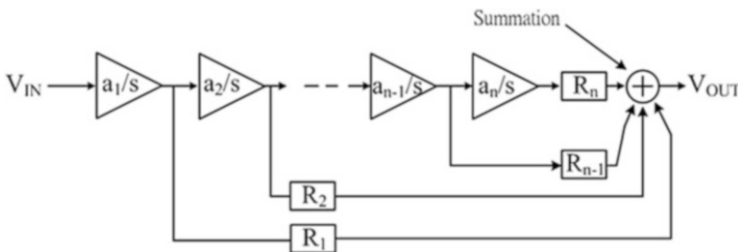


Fig. 106.1 Loop filter with CIFF topology

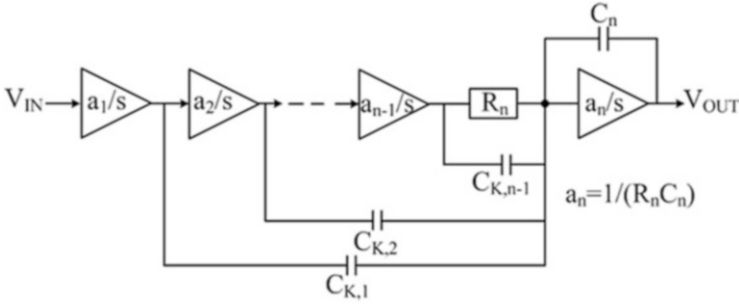


Fig. 106.2 Loop filter with CICFF topology

$$H_{BP}(j\omega) = H_{LP}(j\omega - j\omega_c). \tag{106.1}$$

All poles and zeros of the low-pass filter in the s -plane are transformed to center around the intermediate frequency (IF), ω_c . The i th complex integrator output is

$$V_{oi} = \frac{a_i}{s - j\omega_c} V_{oi-1}, \quad (i = 1, 2, \dots, n - 1) \tag{106.2}$$

where n is the order of the loop filter; therefore, all poles are moved around ω_c , but zeros are still located around dc. Finally, the output, V_{OUT} , can be defined as

$$V_{OUT} = \frac{a_n}{s - j\omega_c} y_{n-1} + \left(\frac{s}{s - j\omega_c} \right) \sum_{i=1}^{n-1} V_{oi} \frac{C_{K,i}}{C_U}. \tag{106.3}$$

Higher-order loop filter is considered of higher accuracy but increasing cost and more power consumption and circuit instability. In considerations of those factors, a third-order loop filter for the quadrature band-pass $\Sigma\Delta M$ is proposed in this paper. Figure 106.3 shows its simplified circuit from differential to single-ended schematic. The resistor, R_F , used in the loop filter shifts the three repeated zeros of the noise transfer function from real axis to complex plane and real axis. The noise floor is then suppressed in the $\Sigma\Delta$ modulator.

Based on Fig. 106.3, the related formula of the voltage gain transfer function is found from [3] as below:

$$\frac{V_{OUT}}{V_{IN}} = - \frac{s^2 \frac{C_{K,1}}{C_3} \frac{1}{R_1 C_1} + s \frac{C_{K,2}}{C_2} \frac{1}{R_3 C_3} \frac{1}{R_1 C_1} + \frac{1}{R_3 C_3} \frac{1}{R_2 C_2} \frac{1}{R_1 C_1}}{s^3 + s \frac{1}{R_3 C_3} \frac{1}{R_2 C_2} \frac{R_2}{R_F}}. \tag{106.4}$$

The coefficients of the transfer function are found from simulator, MATLAB toolbox, which is expressed as

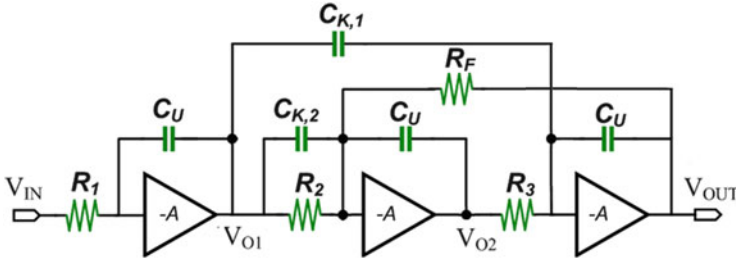


Fig. 106.3 Simplified single-ended schematic for loop filter topology

Table 106.1 Coefficients of the low-pass loop filter

Parameter	$\frac{1}{R_1 C_U}$	$\frac{1}{R_2 C_U}$	$\frac{1}{R_3 C_U}$	$\frac{C_{K,1}}{C_U}$	$\frac{C_{K,2}}{C_U}$	$\frac{R_2}{R_F}$
Coefficient	$0.75f_S$	$0.25f_S$	$0.25f_S$	0.95	1.38	0.02

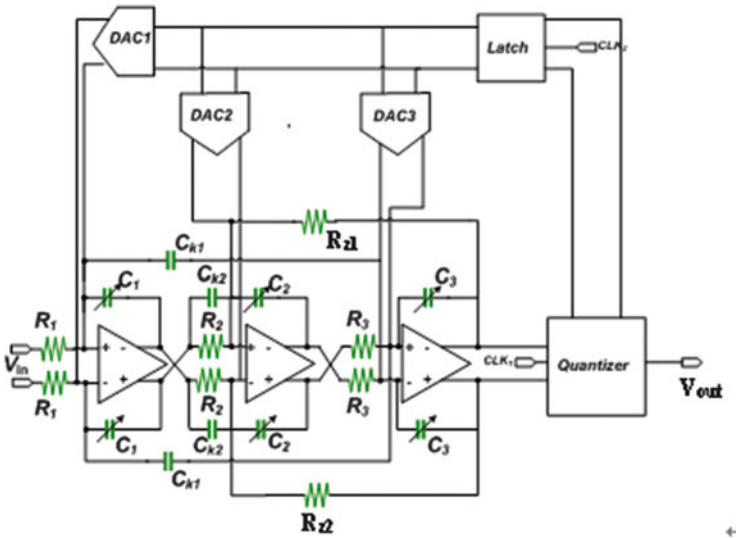


Fig. 106.4 Proposed CT low-pass $\Sigma\Delta$ modulator circuit

$$T(s) = \frac{0.67001s^2 + 0.23939s + 0.04446}{s^3 + 0.00658s} \tag{106.5}$$

The coefficients of the $\Sigma\Delta M$ in Eq. (106.4), the element values in the low-pass filter of Fig. 106.3, can be readily obtained, and they are listed in Table 106.1. The overall proposed third-order $\Sigma\Delta M$ with a tunable capacitor array for LTE application is shown in Fig. 106.4. As the modulator becomes more sensitive to instability because of cross couplings, it should add additional compensation cross-coupling resistors, RZ_1 and RZ_2 , as shown in Fig. 106.4 in the cross-coupling paths [3]. The

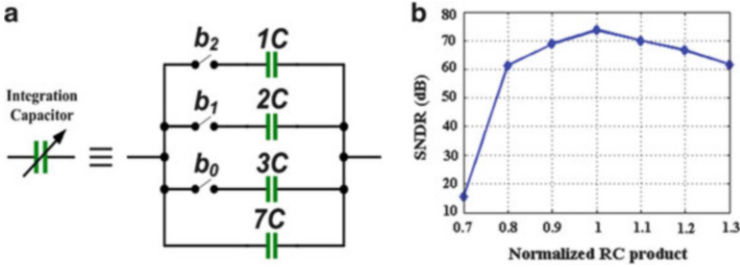


Fig. 106.5 (a) Switchable capacitor array and (b) its simulated SNDR values versus normalized RC product with a maximum SNDR as $RC = 1$

RZ_1 and RZ_2 are found by $RZ_1 = 1/\omega_c C_{K,1}$ and $RZ_2 = 1/\omega_c C_{K,2}$, respectively, and the element values are listed as $C_U = 1$ pF, $C_{K,1} = 0.95$ pF, $C_{K,2} = 1.38$ pF, $R_1 = 8.86$ k Ω , $R_2 = 25$ k Ω , $R_2 = 25$ k Ω , $R_F = 1,080$ k Ω , $R_B = 118$ k Ω , $RZ_1 = 24$ k Ω , and $RZ_2 = 85.5$ k Ω .

The signal bandwidth f_B is 5 MHz and the sampling rate is $f_S = 320$ MHz. The $\Sigma\Delta$ modulator is combined with CICFF low-pass filters, two 1-bit quantizers, and a current steering DAC circuit. The output signals of 1-bit flash ADC pass through the D-latch and DAC and then feedback into the loop filter, and the noise shaping is activated and performed in the circuit.

106.2.2 Tunable Capacitor Array

CMOS CT integrators are typically realized as their time constants RC or C/g_m circuits. CMOS processes usually do not control the values of R and C accurately; therefore, an automatic RC time constant tuned circuit is needed to ensure the $\Sigma\Delta$ stability and SNR performance over large RC time constant variations. To compensate this large RC product variation, capacitors are designed and implemented as capacitor arrays ($1C$, $2C$, $3C$) as shown in Fig. 106.5a. The array capacitors except $7C$ are “always-in-use” capacitors which equal the least significant bit (LSB). The 3-bit digital control codes are fed externally to choose the right capacitors. As the nominal value of the capacitor array is $7C$, the capacitor array is varied from $7C$ to $13C$ corresponding to 70–130 % variation. Figure 106.5b depicts the modulator SNDR versus the normalized RC product. Obviously, at normalized $RC = 1$, the SNDR is maximum.

106.2.3 Operational Amplifier Design

The op amp practically is one of the most important devices in analog $\Sigma\Delta$ modulator design. The primary requirement of an op amp is to have an open loop gain

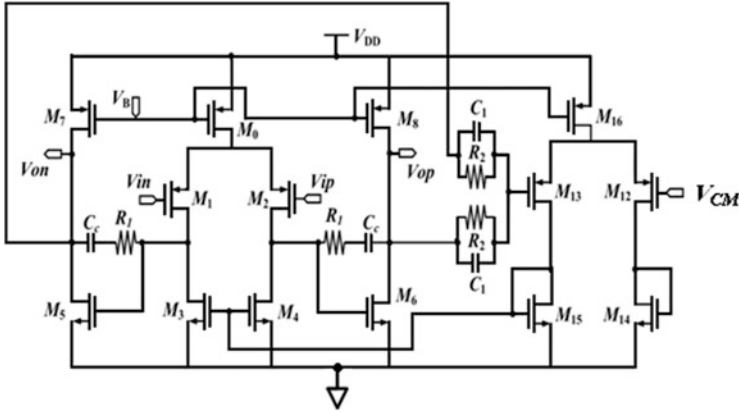


Fig. 106.6 CMOS two-stage op amp with common-mode feedback circuit

that is sufficiently large to implement the feedback function. One of the most popular CMOS op amps is a two-stage Miller amplifier. Figure 106.6 shows the proposed two-stage op amp circuit which consists of a differential input stage and a common-source output stage with a frequency compensation circuit of C_c in series of R_1 and a common-mode feedback (CMFB) circuit [3]. This choice is based on the low power demand and relaxing the stability requirements of the op amp. The resistor R_1 is optimized before layout so as to move the right-hand plane zero to the left-hand plane and place on the highest nondominant pole.

The required gain, bandwidth, and phase margin of the amplifier are tuned by simulation. Simulated results illustrate that the op amp achieves a unity GB of more than 350 MHz with a parallel load of 3 pF, a phase margin of 64° , and a dc gain of approximately 50 dB at 1.8-V supply voltage to ensure the stability of the circuit over the process and temperature corner cases. The CMFB circuit is superior of allowing rail-to-rail output swing; furthermore, it does not need any level shift or attenuation on the common-mode signal, unlike the differential pair CMFB circuits.

106.2.4 Dynamic Comparator Circuit and DAC Circuit

The dynamic comparator circuit with SR (set reset) latch is chosen because of its low power consumption [4]. Simulation verifies that the regeneration time is 1.5 ns, the offset voltage is less than 10 mV, and the power consumption is less than 30 W. The DAC is consisted of D-latch, switch driver, and current steering DAC cell. The circuit diagram of a single cell of DAC is found [4]. In order to reduce glitch of the input voltage, the V_{High} and V_{Low} operate at the 1 V and 0.2 V, respectively. Hence, it can increase DAC's linearity. An important block in a current steering DAC design is the switch driver composed of $M_9 \sim M_{14}$. The task of the switch driver is to latch the incoming DAC codes and to perform the final synchronization.

106.3 Measured Results

The proposed third CT $\Sigma\Delta$ is implemented in 0.18- μm CMOS process. The modulator samples signals at 320 MHz with 5-MHz bandwidth and operates with a 1.8-V voltage. The power consumption is 11.8 mW. Figure 106.7 shows the die microphotograph including the wire-bonding pads. The $\Sigma\Delta$ is essentially a mixed-signal system. In order to achieve high resolution and linearity, great caution should be taken in the layout design to reduce the effects of mismatch, parasitic, and digital noise coupling to analog blocks. The total chip area is 0.35 (0.563×0.636) mm^2 . The measured output stream of the $\Sigma\Delta$ is loaded into MATLAB and taken 16,384 points of FFT with Hanning window, and the results of output spectrum accompanying with the simulated results are almost the same as shown in Fig. 106.8a. The measured SNDR is 53.37 dB over a 5-MHz signal bandwidth. Figure 106.8b shows the simulation and measured IM3 to be -56 dB. The SNDR

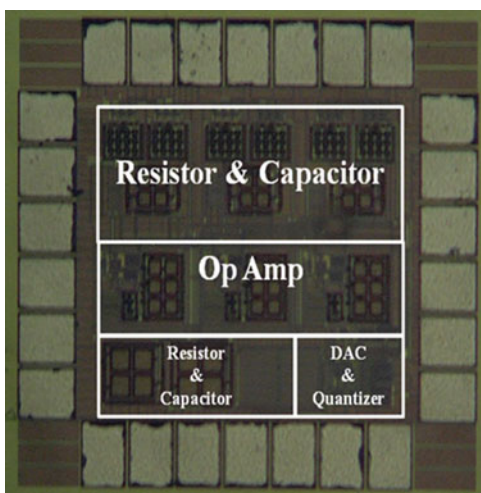


Fig. 106.7 Chip microphotograph of the proposed $\Sigma\Delta$ modulator with a chip area of $0.563 \times 0.636 \text{ mm}^2$

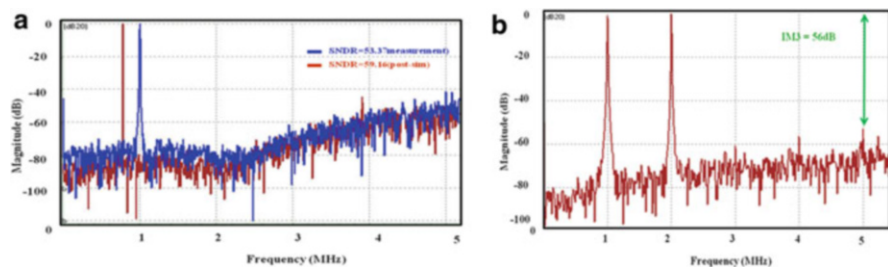


Fig. 106.8 (a) Output spectrum (input 1 MHz, 0.8VP-P) and (b) two-tone test (input 1 MHz, 2 MHz, 0.65 VP-P)

Fig. 106.9 SNDR with varying input levels

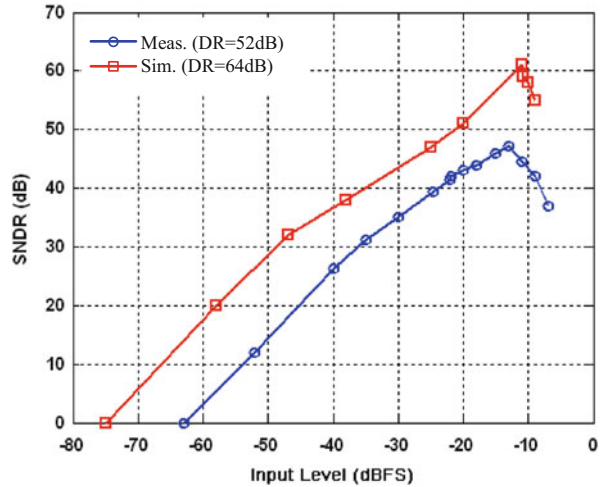


Table 106.2 Comparison with previously published papers

Ref.	Process (μm)	Power sup. (V)	Clock (MHz)	BW (MHz)	SNDR (dB)	ENOB (bit)	Power (mW)	FoM (pJ/conv.)	Chip area (mm ²)
[1]	0.25	1.8	125	4	48.4	7.75	20.5	11.9	0.2
[2]	0.18	1.8	100	1	59.8	9.6	22.3	19.6	1.62
[4]	0.18	1.8	128	2	63.3	10.2	9.52	2.02	0.836
[6]	0.13	2.5	3,500	100	53.1	8.5	650	8.8	4
[7]	0.18	1.8	800	10	68	11	160	3.9	2.5
This work	0.18	1.8	320	5	53.37	8.53	11.8	3	0.35

versus input signal level is plotted in Fig. 106.9, indicating that the measured dynamic range is 52 dB.

Table 106.2 shows the performances of this chip while compared with some recently reported ΣΔ modulator papers. The comparison with other reported ΣΔ modulators can be carried out by evaluating the figure of merit (FoM) [5]:

$$FoM = \frac{P}{2^B \times 2f_B}, \tag{106.6}$$

where P (mW) is the power consumption, B is number of bits, and f_B (MHz) is the bandwidth. The smaller the FoM value is, the better the overall performance will be. From this comparison table, it can be confirmed that the proposed modulator with low voltage operations can achieve the best FoM, the lowest power consumption, a wider bandwidth, and a lower power consumption.

Conclusion

A CT $\Sigma\Delta$ modulator with a 5-MHz low-pass filter is presented. The proposed hybrid CT $\Sigma\Delta$ modulator displays better performance when compared with some other active counterparts. In this paper, we extend our previous studies on CT 2 and 4-MHz low-pass $\Sigma\Delta$ modulator and quadrature band-pass $\Sigma\Delta$ modulator to 5-MHz low-pass $\Sigma\Delta$ modulator. In the course, the capacitive feedforward is adopted to reduce the hardware complexity and layout area. Measurement results have achieved the ENOB of 8.53 bits over a signal bandwidth of 5 MHz while consuming 11.8 mW from a 1.8-V supply voltage. The chip area is 0.35 mm², including the pads.

Acknowledgments The authors would like to appreciate the staff of CIC for their technical supports and greatly appreciate Professor Ron-Yi Liu for his valuable discussion.

References

1. Kim SB, et al. Continuous-time quadrature bandpass sigma-delta modulator for GPS/Galileo low-IF receiver, IEEE Int. workshop on radio-frequency integration technology (RFIT); 2007. pp 127–30.
2. Song T, Cao Z, Yan S. A 2.7-mW 2-MHz continuous-time delta sigma modulator with a hybrid active-passive loop filter [J]. IEEE J Solid State Circ. 2008;43(2):330–41.
3. Huang JF, et al. A CT sigma-delta modulator with a hybrid loop filter and capacitive feedforward. The 54th IEEE international midwest symposium on circuits and systems (MWSCAS); 2011. pp 1–4.
4. Huang JF, Chen KL, Liu RY. A high performance continuous-time sigma-delta modulator with a 2 MHz bandwidth hybrid loop filter for wireless healthcare applications, 2013 6th international conference on biomedical engineering and informatics (BMEI), IEEE; 2013. pp 411–5.
5. Huang JF, Lai WC, Huang KJ. Continuous-time quadrature bandpass sigma-delta modulator with capacitive feedforward summation technology for LTE application, International conference on control engineering and communication technology, (ICCECT 2013), IEEE; 2013. pp 6–9
6. Lu CY, et al. A sixth-order 200 MHz IF bandpass sigma-delta modulator with over 68 dB SNDR in 10 MHz bandwidth [J]. IEEE J Solid State Circ. 2010;45(6):1122–36.
7. Hart A, Voinigescu SP. A 1 GHz bandwidth low-pass $\Delta\Sigma$ ADC with 20–50 GHz adjustable sampling rate [J]. IEEE J Solid State Circ. 2009;44(5):1401–14.

Chapter 107

A Fine-Grained Power Gating Technique for Reducing the Power Consumption of Embedded Processor

Wei Li and Jianqing Xiao

Abstract In the deep submicron process, the power leakage has become the major part of power consumption in the embedded processor. This paper proposes a technique of fine-grained power gating by dynamically and timely turning on or turning off the power supply for functional components in advance. Full use of the structure of the pipeline may eliminate the delay caused by power gating. On the basis of analyzing and using the results of decode unit as the power gating signal, this technique can predict the execution of functional component in two cycles; thus the delay caused by power gating can be eliminated, while the power leakage of embedded processors can be reduced. Experiments show that the technique can reduce 48 % dynamic power consumption and 39 % leakage power consumption of LEON3 processor under the condition of no performance loss.

Keywords Low power • Power gating • Leakage power • Dynamic power

107.1 Introduction

The scaling down of gate geometries has resulted in a rapid growth of the gate leaking power. The leakage power has become the dominant part of the power consumption of embedded processors [1].

Prior reduction of the leakage power was focused on the circuit level including the low-threshold transistors [2], the multi-threshold circuit [3], the input vector optimization [4], the low-power clocking [5], and the power gating [6–8]. As to then-chip SRAMs (such as cache), designers propose the drowsy technique [9, 10]. These methods and techniques are widely adopted in the low-power design of embedded processors and significantly reduce the leakage power. In them, the power gating is very significant and easy for implementation because it is capable of eliminating the leakage completely by simple control. Some processor vendors

W. Li (✉) • J. Xiao
Xi'an Microelectronic Technology Institute, Xi'an 710054, China
e-mail: lw@stu.xjtu.edu.cn

supply the power gating processor supporting the sleep mode under OS control. When OS asserts the system is accessing a long idle state, it controls the processor's accession to the power gating so that the processor can save the power consumption. There are few methods considering the power gating of function component of processors when the processors are working. This paper shows a dynamic and timely power gating technique by adding PGC (power-gated controller) of processors. The PGC can detect the execution of function component by analyzing the result of the decode unit. It can dynamically switch the voltage supplies for different components.

107.2 Principle of Power Gating and Operand Isolation

There are two power architectures to turn off the power supply. The first is called header by switching VDD. The second is called footer by switching VSS. One or both architectures can be used in the design of power gating. Figure 107.1 shows how the footer works. When the controller detects the processor needs unit1 to work, it asserts the signal of "sleep1" and deserts the signal of "sleep2." The VSS of unit1 is connected to the actual GND. Unit1 can correct the work. The VSS of unit2 is switched to the virtual GND. Unit2 enters the sleep mode.

Figure 107.2 shows the power saving effect. At different times, the system needs unit1 or unit2 to work; thus the controller turns off and turns on different units to save both dynamic power and leakage power. In the 45 nm process, the leakage power consumption almost takes up one half of the total power consumption [11]. As a result, the power gating technique can reduce the dynamic and leakage power consumption as much as possible as shown in Fig. 107.2.

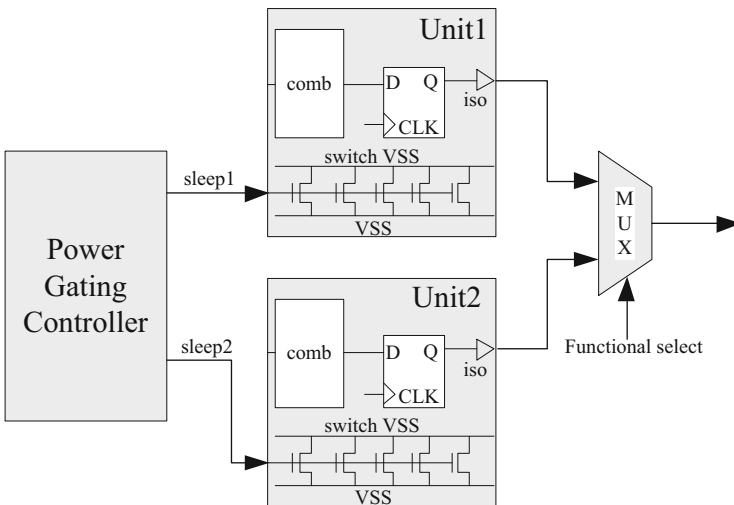


Fig. 107.1 Using footer for power gating

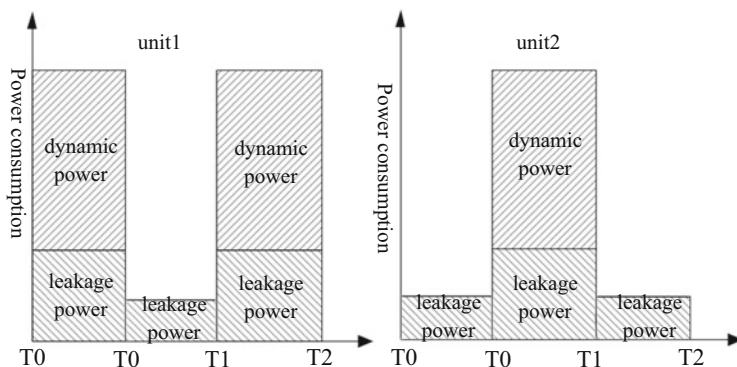


Fig. 107.2 Power saving with power gating

107.3 Fine-Grained Power Gating Design in Embedded Processors

As Fig. 107.3 shows, the IU (integer unit) includes ALU, multiplier, and divider in general design (such as LEON3). The operands are from the `ex_op1`, `ex_op2`, and Y register for all functional units. But only one unit has to be working at one moment, which means the remaining units waste the power at the same time. All kinds of instruction ratio in the power stone benchmarks are running in the LEON3, as Fig. 107.4 shows. Statistics show the multiply instruction and the division instruction take up only 0.3 % of total instructions, but the power consumption takes up the majority of IU power consumption because the multiplier occupies the major part of the size of all functional units, as shown in Fig. 107.5. The logic and shift instruction ratio is less than 6 and 8 %. The sum of add and sub instruction ratio is more than 25 %. The sum of others including the load, store, and etc. is more than 55 %. Considering the load/store instruction may use the adder to calculate the target address, the utilization of the adder may be higher; therefore, it is not necessary to gate the adder. In this paper, the ALU is divided into two parts. One is the adder to complete the sub, add, and calculate the target address; the other is ALU1 to complete the shift and logic. The implementation is shown in Fig. 107.6. When PGC detects the processor, it will use certain functional units, and the PGC asserts the corresponding sleep x signal to turn on the supply and asserts the rest sleep x signals to switch the rest unit to sleep mode. When the unit is in the sleep mode, the output signal is not driven. Thus each unit gated adds the isolation cell in the output of unit in order to ensure the connected unit to work correctly.

To illustrate the principle, this paper shows how the power gating states the scheme of multipliers in PGC, as Fig. 107.7 shows. When the multiplier result select is valid from the decoder, the PGC switches the multiplier from the sleep state into the wake-up state by the `sleep2` signal. When the power-up is finished, the multiplier is switched to working state which is called the wait-for-done state.

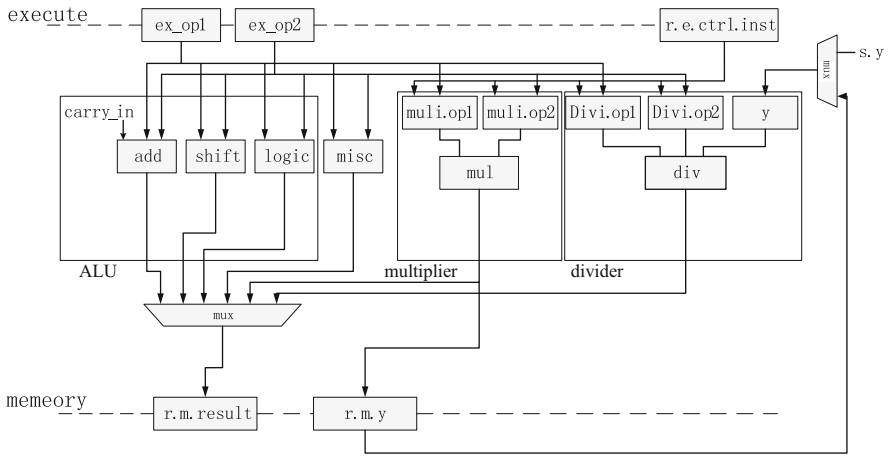


Fig. 107.3 Data path of the integer unit

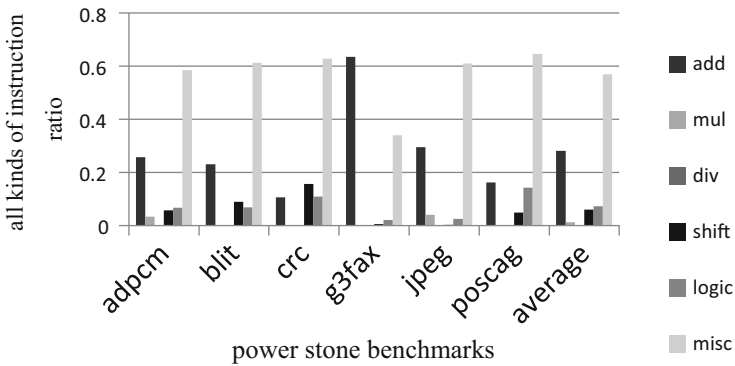


Fig. 107.4 All kinds of instruction ratio in power stone benchmarks

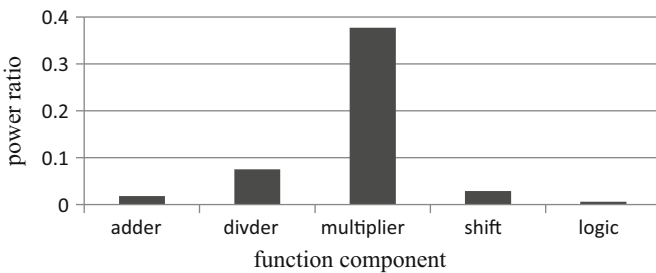


Fig. 107.5 Each function component power ratio

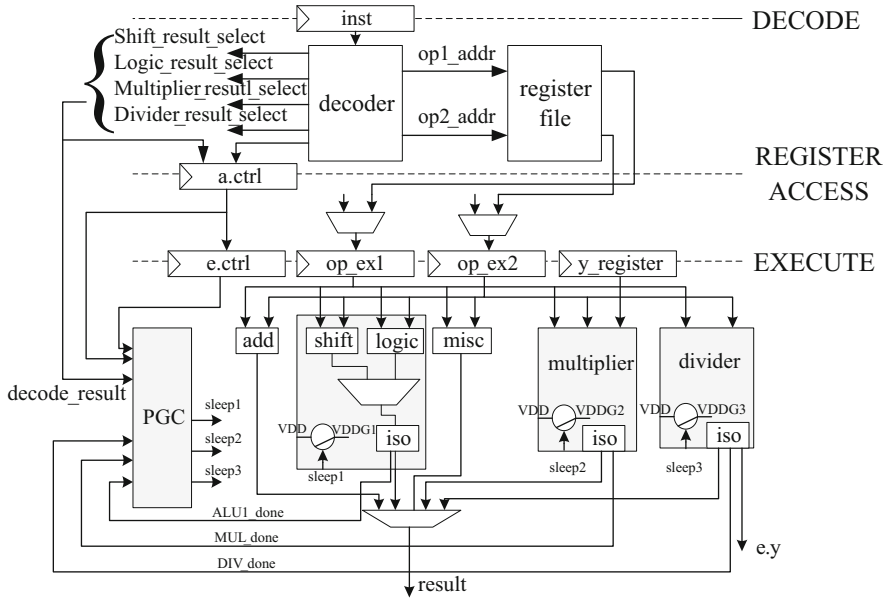
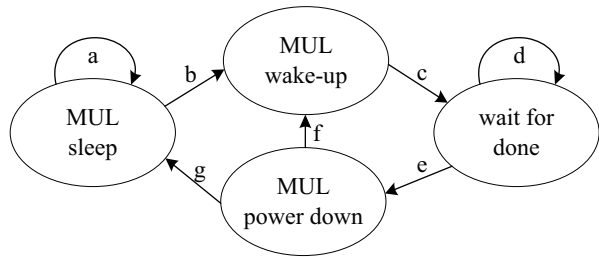


Fig. 107.6 Power gating for all functional components

Fig. 107.7 State scheme of multiplier in PGC



When the multiplier finishes the operation, the MUL done is asserted. If the select signal is not valid from the decoder and control registers, the multiplier accesses to the power-down state. If the multiplier result select signal is valid again, PGC cancels the power-down operation and switches the multiplier to the wake-up state; otherwise the multiplier is at the sleep state.

107.4 Experiment and Analysis

In order to quantify the power saving of the fine-grained power gating technique, the hardware platform uses the LEON3 processor on the basis of the architecture of SPARC V8. Cycle-based simulations are performed with the P benchmark suite. RTL codes are synthesized by the Synopsys DC-2010.03-SP1 under TSMC 90 nm

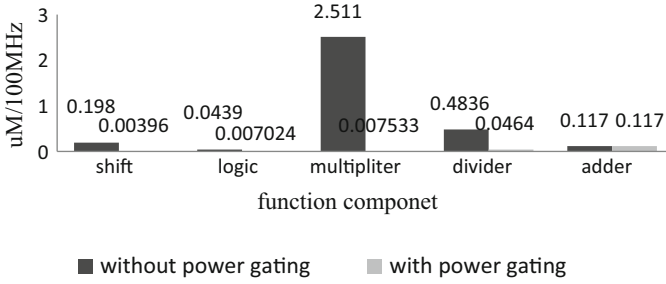


Fig. 107.8 Dynamic power comparison of component without power gating or with power gating

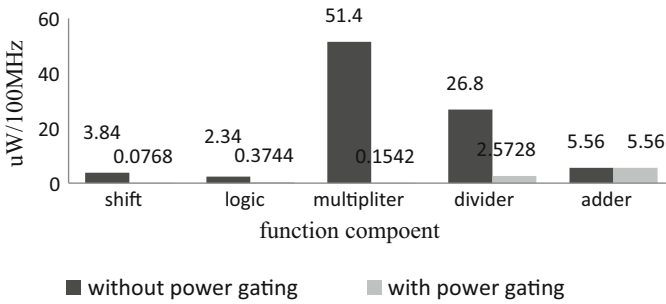


Fig. 107.9 Leakage power comparison of component without power gating or with power gating

process. Power analysis tools use the Synopsys PTPX-2010.06-SP3. The power manage control is described with UPF (unified power format).

As shown in Fig. 107.8, dynamic power consumption of each function component has been reduced at different degrees. The power saving of multiplier and divider is significant. The results of power saving are basically consistent with the statistical results except the divider. On the basis of analyzing the design of the divider, it has been found that the divider uses the multi-cycle (up to 32 cycles) design in order to improve the clock frequency of the processor. Even in this situation, the divider has a significant power saving. Similarly, the leakage power has been significantly reduced as shown in Fig. 107.9. While compared with the original design of LEON3 processor, the modified design with the fine-grained power gating technique can reduce 48 % dynamic power and 39 % static power.

Conclusion

This paper firstly analyzes the utilization and power consumption of each function component in the embedded processor. Based on the analysis, this paper shows a fine-grained power gating design method without extra cycle delay. On the basis of analyzing the pipeline of LEON3 processors, this paper

(continued)

(continued)

shows a design of PGC which controls whether or not each function component enters to the sleep mode based on the result of the decode unit instead of the execute unit as the power gating signal. In this way, the cycle delay caused by power gating can be eliminated. With comparison of the experiment results, it has been found that 48 % dynamic power and 39 % static power can be saved.

References

1. Hamzhaoglu F, Stan MR. Circuit-level techniques to control gate leakage for sub-100 nm CMOS. Proceedings of the 2002 international symposium on lower power electronics and design (ISLPED'02). IEEE; 2002. p. 60–63.
2. Markovic D, Wang CC, et al. Ultralow-power design in near-threshold region. Proc IEEE. 2010;98(2):237–52.
3. Kao J, Chandakasan A. Dual-threshold voltage techniques for low-power digital circuits. IEEE Trans VLSI Syst. 2000;35(7):1009–18.
4. Johnson M, Somasekhar D, Chiou D, Roy K. Leakage control with efficient use of transistor stacks in single threshold CMOS. IEEE Trans VLSI Syst. 2002;10(1):1–5.
5. Zhao PZ, Mcneely J, et al. Design of sequential elements for low power clocking system. IEEE Trans VLSI. 2011;19(5):914–8.
6. Powell M, Yang S, Falsafi B, et al. Gated-Vdd: a circuit technique to reduce leakage in deep-submicron cache memories. Proceedings of the 2000 international symposium on lower power electronics and design (ISLPED'00). IEEE; 2000. p. 90–95.
7. Sathanur A, Benini L, et al. Row-based power-gating: a novel sleep transistor insertion methodology for leakage power optimization in nanometer CMOS circuits. IEEE Trans VLSI. 2011;19(3):469–82.
8. Priyanka C, Natth PS. An approach for low power design of power gated finite state machines considering partitioning and state encoding together. J Low Power Electron. 2012;8(4):452–63.
9. Flautner K, Kim NS, Martin S, et al. Drowsy caches: simple techniques for reducing leakage power. Proceedings 29th annual international symposium on computer architecture (ISCA'02). IEEE; 2002. p. 148–57.
10. Fitzerald B, Lopez S, Sahuquillo J. Drowsy cache partitioning for reduced static and dynamic energy in the cache hierarchy. The 2013 international green computing conference (IGCC'13). IEEE; 2013. p. 1–6.
11. ITRS Organization. International technology roadmap for semiconductors 2008 update. Accessed from <http://public.itrs.net/>; 2008.

Chapter 108

Kinematic Simulation for Series-Parallel Combination Laser Machine Tool

Zhiqin Qian, Jiawen Wang, Lizong Lin, and Qun Cao

Abstract A laser cutting machine based on a three-degree-of-freedom (DOF) series-parallel structure is proposed in this paper, in which the composition is introduced and the DOF is solved. By analyzing the position, the constraint equation of the rods length is established, and then the kinematics inverse equation is obtained. Using the Solidworks and ADAMS software packages, a digital virtual prototype of a series-parallel combination laser cutting machine tool is created. The trajectory function of the moving platform is defined and a kinematic simulation carried out. By simulating the laser tooling point processing workpiece at a constant speed, the kinematic speed and acceleration curves of driving sliders is obtained. At the same time, the relationships between the speed input of the sliders and the speed output of the moving platform are obtained. All this work provides a theoretical basis for designing and processing the series-parallel machine tool.

Keywords Series-parallel machine • Three degree of freedom • ADAMS • Kinematic simulation

108.1 Introduction

Traditional two-dimensional laser cutting machines usually consist of a lathe bed and two axes in series [1]. Although this kind of layout features a large operation workspace, flexible range, independent movement of each axis, and simple motion control [2], it also has some inherent disadvantages. On the one hand, the force and thermal deformation are nonuniform [3]; on the other hand, the machine tool structure will bear not only tension and compression loads but also bending and torsion loads [4, 5]. In 2007, Xu et al. [6] published research on a parallel laser cutting machine, but cutting on this kind of machine has a smaller work space.

Because of the deficiency of laser cutting machines, which are composed of a simple serial structure or parallel structure, this paper presents a machine with a different structure that represents a series-parallel combination laser machine tool.

Z. Qian (✉) • J. Wang • L. Lin • Q. Cao
East China University of Science and Technology, Shanghai 200237, China
e-mail: qianzhiqin@ecust.edu.cn

The paper is organized as follows. Section 108.2 introduces the composition of the machine tool and solves the degrees of freedom (DOF) problem. In Sect. 108.3, where an analysis of the relationship between the laser head position and drive slider, the constraint equation of the rod lengths is formulated and an inverse kinematic equation is obtained. In Sect. 108.4, using the Solidworks and ADAMS software packages, a digitized virtual prototype is created. Section 108.5 concludes the paper.

108.2 Machine Tool Structure

This paper proposes a 2-DOF laser cutting machine tool, as shown in Fig. 108.1.

In this mechanism, a beam drives the ball screw with the help of the motor. Two sliders connected by a parallel structure are driven by gear and rack. The two servomotors move simultaneously to control the beam, and two ends of the two parallel bars are connected separately with sliders and the laser head through a revolution joint.

As for the disadvantages, the beam has large inertia during movement, and in a certain range of processing conditions, the parallel structure can be used to complete the processing, without causing the machine tools to vibrate under a high feed speed, and improve the processing efficiency. When the processing area is large, it can use the movements of the beam to assist in the parallel structure (parallel mechanism’s effective work area is small, can use the combined motion beam and parallel mechanism to complete the processing of large areas) and ensure that the machine will have a large processing range.

The machine has four mobile vises that serve as the drive vises, which is driven by the servomotor to move the guide bar and the laser head in x-y plane to do the processing work.

The laser head movement in the $x-y$ plane is controlled by the beam and two sliders. According to the DOF formula, the DOFs of the machine are as follows:

$$F = 3n - (2p_i + p_h), \tag{108.1}$$

where n is the number of parts, p_i the number of lower pair, p_h the number of higher pair, and F the degrees of freedom.

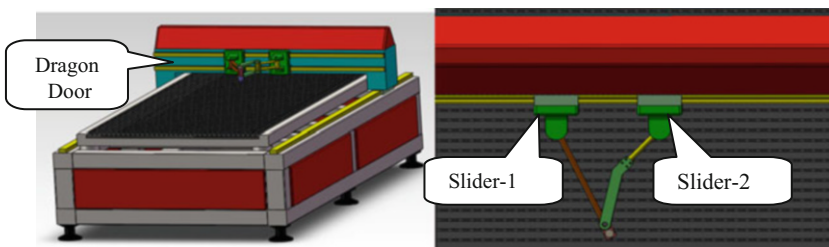


Fig. 108.1 Structure of machine tool

In this structure, $n = 5$, $p_i = 6$, and $p_h = 0$. From Eq. (108.1) it can be concluded that the mechanism has three DOFs.

108.3 Inverse Solution Analysis of Series-Parallel Machine Tool

To analyze the machine on the basis of kinematics, the model of the machine tool was simplified to that shown in Fig. 108.2.

A coordinate is built as shown in Fig. 108.2. First, the data coordinate system $O-XY$ is established with its origin in the middle of the base, and then the system $O'-X'Y'$, a moving coordinate system, with its origin on the laser head. Suppose the lengths of the two rods are L_1 and L_2 ; points B , C , and O in the benchmark system of the $O-XY$ coordinates are as follows: point $B(x_1, y_1)$, point $C(x_2, y_1)$, point $O'(x_0, y_0)$. First, the inverse equation of the parallel structure should be obtained when the machine is in as stationary state. Based on the rod length constraint, the mechanism's constraint equations are as follows:

$$\begin{cases} (x_0 - x_1)^2 + (y_0 - y_m)^2 = L_1^2, \\ (x_0 - x_2)^2 + (y_0 - y_m)^2 = L_2^2. \end{cases} \tag{108.2}$$

From Eq. (108.2) we know that

$$\begin{cases} x_0 = \frac{L_2^2 - L_1^2 + x_1^2 - x_2^2}{2(x_1 - x_2)}, \\ y_0 = y_m \pm \sqrt{L_1^2 - \left(\frac{L_2^2 - L_1^2}{2(x_1 - x_2)} - \frac{x_1 - x_2}{2}\right)^2}. \end{cases} \tag{108.3}$$

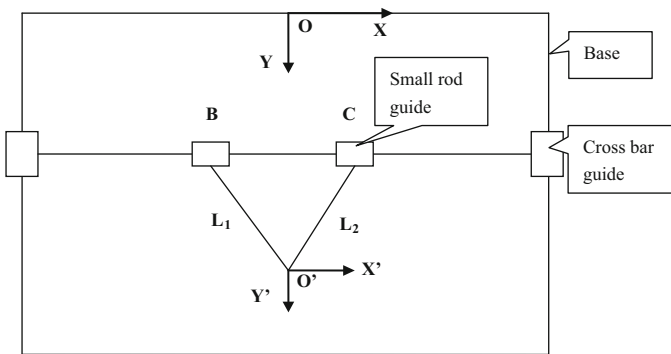


Fig. 108.2 Simplified structure of machine tool

Similarly, we know the inverse position:

$$\begin{cases} x_1 = x_0 \pm \sqrt{L_1^2 - (y_0 - y_m)^2}, \\ x_2 = x_0 \pm \sqrt{L_2^2 - (y_0 - y_m)^2}. \end{cases} \tag{108.4}$$

In Eqs. (108.3) and (108.4), the y_m is the location of the crossbar in the y -direction of the O - XY coordinate system, and the preceding equation for the crossbar is in a stationary state.

In the design, to ensure the parallel mechanism does not generate interference in the process of movement, we impose the following constraints:

$$(x_1 < x_0) \cap (x_2 > x_0) \tag{108.5}$$

Thus, after adding the travel constraints, the inverse kinematic equations of motion of Eq. (108.4) can be simplified as

$$\begin{cases} x_1 = x_0 - \sqrt{L_1^2 - (y_0 - y_m)^2}, \\ x_2 = x_0 + \sqrt{L_2^2 - (y_0 - y_m)^2}. \end{cases} \tag{108.6}$$

As Eq. (108.3) show, when $x_1 = x_2$, the kinematic equations of motion has an infinite solution, so the parallel mechanism is in an amorphous position. However, as shown by Eq. (108.5), the constraint conditions, the relation $x_1 > x_2$ was permanently established, so the parallel mechanism is not in an amorphous position, and the kinematic equation is a concise and explicit expression, and no motion coupling phenomenon arises.

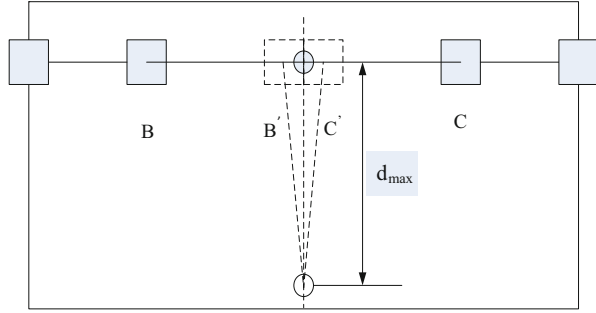
Based on the positive solutions of the machine tool, the Jacobi matrix of the parallel mechanism can be established as

$$J = \begin{bmatrix} -\frac{1}{2} - \frac{L_2^2 - L_1^2}{2(x_1 - x_2)^2} & -\frac{1}{2} - \frac{L_2^2 - L_1^2}{2(x_1 - x_2)^2} \\ y_m & y_m \end{bmatrix} \tag{108.7}$$

Similarly, we can calculate the inverse Jacobi matrix:

$$J^{-1} = \begin{bmatrix} 1 & \frac{y_0 - y_m}{\sqrt{L_1^2 - (y_0 - y_m)^2}} \\ 1 & -\frac{y_0 - y_m}{\sqrt{L_2^2 - (y_0 - y_m)^2}} \end{bmatrix} \tag{108.8}$$

Fig. 108.3 Range of parallel structure in y-direction



The determinant of the inverse Jacobi matrix $|J^{-1}|$ is

$$|J^{-1}| = - \frac{(y_0 - y_m) \left(\sqrt{L_1^2 - (y_0 - y_m)^2} + \sqrt{L_2^2 - (y_0 - y_m)^2} \right)}{\sqrt{L_1^2 - (y_0 - y_m)^2} \sqrt{L_2^2 - (y_0 - y_m)^2}} \quad (108.9)$$

Obviously,

$\sqrt{L_1^2 - (y_0 - y_m)^2}$ and $\sqrt{L_2^2 - (y_0 - y_m)^2}$ are set greater than zero, so that no dead points appear in the parallel mechanism. In addition, $y_0 - y_m \neq 0$. Therefore:

$$|J^{-1}| \neq 0 \quad \text{and} \quad |J^{-1}| \neq \infty \quad (108.10)$$

We can conclude that the series-parallel institution does not exist in singular form within the effective workspace and is a monotone domain.

However, the series-parallel structure has a limited movement range in the Y-direction. Figure 108.3 shows the maximum displacement of the Y-direction.

According to Fig. 108.3, when the crossbar is stationary, d_{\max} is reached if the two sliders are moved to the closest position. Suppose we need to set the laser head at $D_2(x_2, y_2)$, and $y_2 - y_1 > d_{\max}$; then we cannot allow the move to only rely on the parallel structure (we must move the crossbar for $D = y_2 - y_1 - d_{\max}$). At this point, B's and C's ordinate coordinates are changed to $y_2 - d_{\max}$.

108.4 Kinematic Simulation on Series-Parallel Structure Based on ADAMS

Because the parallel parts are complicated, the posture of the laser head and reverse solution of position obtained by calculation are only on a theoretical level. In addition, the laser machine will generate larger vibration when the processing curve curvature changes greatly, so the speed of laser machining is limited. As for materials of the same thickness and with changes in movement, generally, the speed

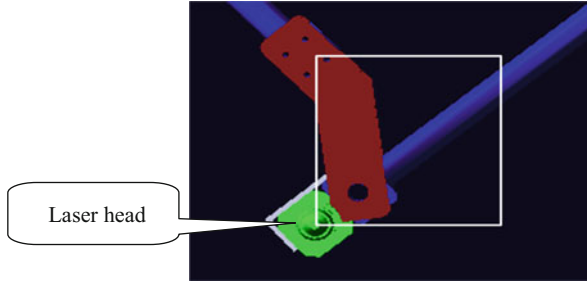


Fig. 108.4 Rectangular path

of the laser head is uniform. Therefore, when the laser head is working uniformly, three sliders need to be analyzed for their kinetic feature. Based on the kinetic trajectory of each slide, through the motion simulation can be drawn each slide's kinetic feature, which is of great significance in controlling the entire process.

First, the model of the machine is constructed using Solidworks (three-dimensional software). Then the model is imported into (Automatic Dynamic Analysis of Mechanical System) ADAMS. The proper constraint condition is added to the joints and add driving force on the sliders. Finally, the model must be initialized. Thus, a virtual digital model of a three-axis series-parallel laser cutting machine is established. After simulating the trajectory of the laser head as planned, the kinetic trajectory of each slider and laser cutting head can be mapped, together with the corresponding velocity and acceleration curves, in such a way that the change in their locations can be visualized.

Using the dynamic simulation software ADAMS, define the time function, imposing bidirectional excitation function on the laser head for cutting movement along a rectangular track.

The given rectangle parameters are 100×100 mm, as shown in Fig. 108.4:

The first 8 s are described as follows:

X :

$$\text{disp}(\text{time}) = \text{step}(\text{time}, 0, 0, 2, 200) + \text{step}(\text{time}, 2, 0, 4, 0) + \text{step}(\text{time}, 4, 0, 6, -200) \\ + \text{step}(\text{time}, 6, 0, 8, 0)$$

Y :

$$\text{disp}(\text{time}) = \text{step}(\text{time}, 0, 0, 2, 0) + \text{step}(\text{time}, 2, 0, 4, 200) + \text{step}(\text{time}, 4, 0, 6, 0) \\ + \text{step}(\text{time}, 6, 0, 8, -200)$$

The first 8 s are the time during which the laser head moves: at 0–2 and 4–6 s the laser head moves along the *X*-axis, while at 2–4 and 6–8 s, it moves along the *Y*-axis (Figs. 108.5, 108.6, 108.7, and 108.8).

We gained further curves illustrating the speed rate and the acceleration.

Comparing the speed and acceleration curves of the laser head with those of the two sliders, we find that the direction of the two sliders is the same at 0–2 and 4–6 s when the laser head is moving along the *X*-axis, as are the trend of speed rate and

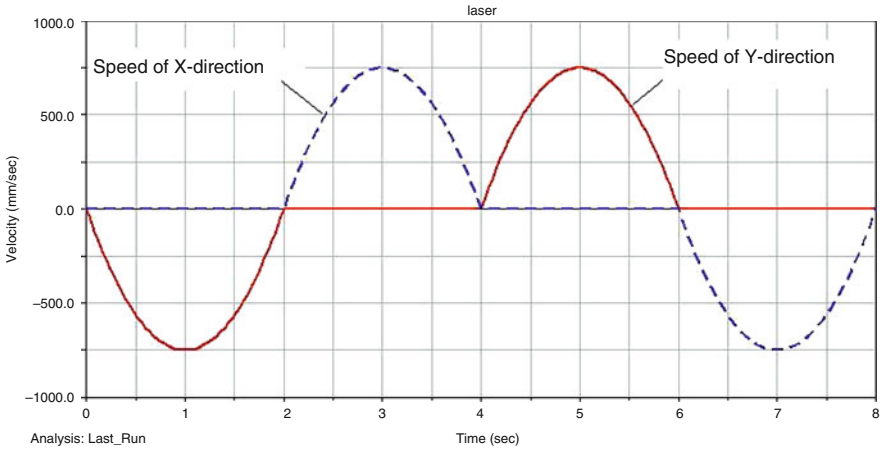


Fig. 108.5 Speed of laser head

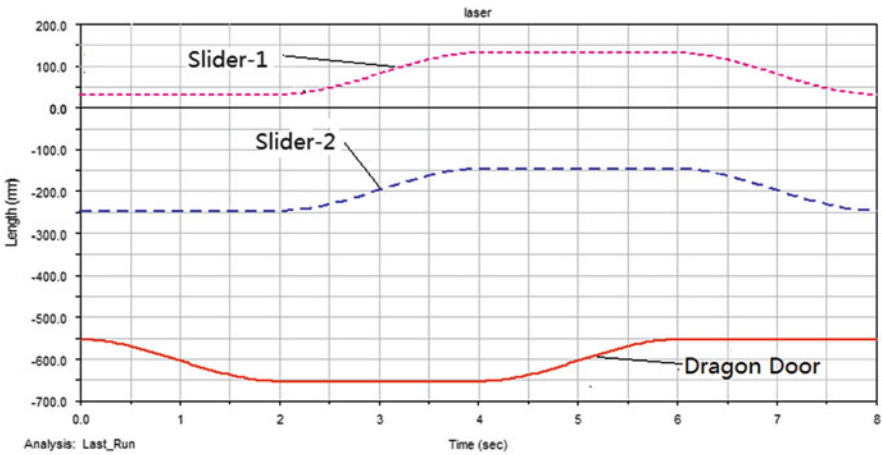


Fig. 108.6 Position curve of each component

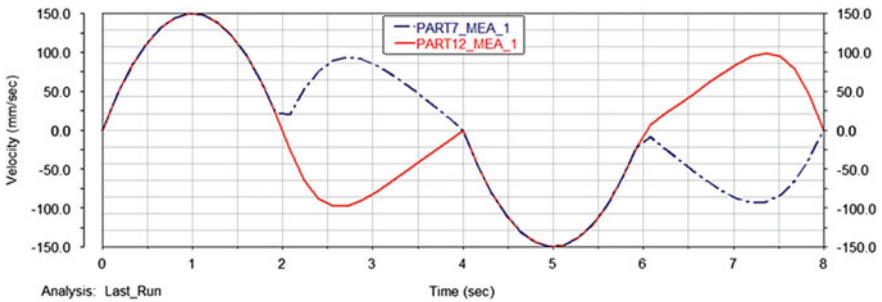


Fig. 108.7 Speed rate curve of two sliders

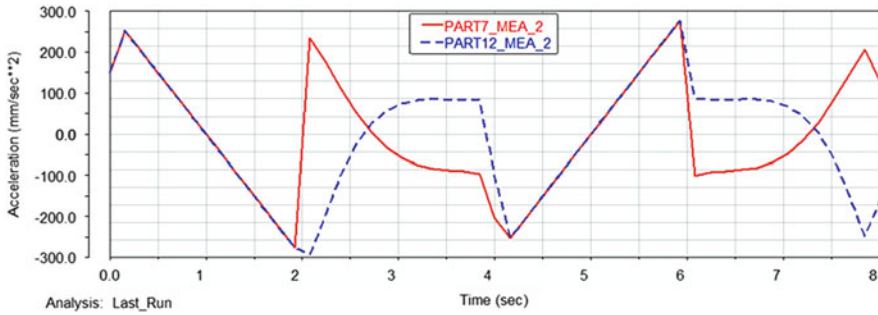


Fig. 108.8 Acceleration curve of two sliders

acceleration. In addition, the comparison of the two sliders shows the symmetry in direction and speed rate at 2–4 and 6–8 s when the laser head is moving along the Y-axis, but the accelerations show some differences.

Based on the comprehensive comparison of simulation results, we conclude that only when the laser head turns to an inverse direction does the motion of each slider show a sudden change in acceleration. Generally speaking, the kinetic characteristic curve in the whole process is smooth, which means the structure is stable, easy to control, and can fully satisfy the requirements of smooth operation.

Thus, we believe that the series-parallel structure satisfies the requirements not only of today’s laser cutting industry but also for tandem laser cutting, welding, and other processing machines.

Conclusion

This paper presents a new structure for a 2-DOF series-parallel combination laser cutting machine. As reflected by its inverse kinematics and motion simulation analysis, the paper arrived at the following conclusions. First, adding a parallel structure to the series structure makes the machine more compact and efficient. Second, the laser cutting head works uniformly and the sliders move smoothly, so that this new structure is suitable for laser machining.

References

1. Georgi MM, Aleksandr BL, Anton SG. Multifunction numerical control solution for hybrid mechanic and laser machine tool. *Procedia CIRP*. 2012;1:260–4.
2. Tang Z. Series design of large-scale NC machine tool. *J China Univ Min Technol*. 2007;17(2):272–6.
3. Jiang XW, Cheng XC. Method of humanity design for numerical control machine tool. *Energy Procedia*. 2012;17:650–4.

4. Sergej NG, Georgi MM. Scalable open cross-platform kernel of PCNC system for multi-axis machine tool. *Procedia CIRP*. 2012;1:238–43.
5. Skutella M. Algorithms and linear programming relaxations for scheduling unrelated parallel machines. In: *Experimental algorithms-12th international symposium, SEA 2013, Lecture Notes in Computer Science 7933*. p. 1–3.
6. Xu H, Wang X, Cai L. New laser cutting parallel engine bed working space studies. *Mach Des Manuf*. 2007;1(12):42–4.

Chapter 109

Implementation of a Fine-Grained Parallel Full Pipeline Schnorr–Euchner Sphere Decoder Algorithm Accelerator on Field-Programmable Gate Array

Shijie Li, Lei Guo, Yong Dou, and Jingfei Jiang

Abstract A new parallel full pipeline accelerator implemented on field-programmable gate array (FPGA) for the Schnorr–Euchner sphere decoding (SE–SD) algorithm is presented in this paper. We firstly transform the serial SE–SD algorithm into a parallel one. Afterwards, we use multiple processing elements (PEs) to deal with the workload (particularly for tree searching in the SE–SD algorithm) in parallel. Each separated SE–SD search workload is divided averagely. Each PE searches a sub-tree by using a multilevel pipeline to increase the data throughput, and the whole system obtains a batch of different input data chronologically. We select the number of PEs to distribute our system according to the hardware platform by using a distribution unit. We’ve successfully placed four PEs in an accelerator and eight accelerators in a single FPGA (XC6VLX240T). The system obtains remarkable benefit in changing the accelerate mode, including latency- and throughput-prior modes.

Keywords Multiple-input multiple-output (MIMO) • Schnorr–Euchner sphere decoding • Field-programmable gate array (FPGA) • Fine-grained • Full pipeline

109.1 Introduction

The multiple-input and multiple-output (MIMO) [1] technique has made a breakthrough as a smart antenna engineering in the field of wireless mobile communication. It can multiply the communication system capacity and the spectral efficiency without increasing bandwidth; moreover, it can be perceived as a key technology in the new generation of mobile communication systems.

S. Li • L. Guo (✉) • Y. Dou • J. Jiang
National laboratory for parallel and distributed processing,
National University of Defense Technology, 410073 Changsha, China
e-mail: 13739058625@163.com

SE–SD is most widely used in MIMO detection [2] because of its low complexity and excellent results; but when input data comes too big, its performance becomes poor, as its main problem [3]. Recently, several improvements have been introduced. Ronald Y et al. [4] proposed a method by incorporating a dynamic information storage-and-retrieval mechanism to avoid repetitive computation of previously processed results. Juanjo Noguera et al. [5] used high-level synthesis tools from AutoESL to make it possible to build a complex MIMO system. A one-node-per-cycle architecture on application-specific integrated circuits was introduced by Burg et al. [6]. A remarkable innovation made by this author is the modified sphere criterion based on the ℓ_1 -norm instead of the two-norm at an acceptable penalty of signal-to-noise ratio (SNR). Another sphere decoder based on the FSD algorithm was proposed by Wu [7] who introduced a four-nodes-per-cycle architecture and exploited parallelism through a pipelined task schedule scheme. Nevertheless, all of the aforementioned studies were focusing on a single fixed architecture. With the increase in FPGA resources, the present study develops a new algorithm that optimizes the use of FPGA to enhance performance and flexibility and to design an expanded architecture with the least cost.

A new parallel full pipeline accelerator implemented on FPGA for the SE–SD algorithm is proposed in this paper. This system can change the accelerate mode in the hardware layer to satisfy the requirements of latency and throughput. Compared with previous studies, our study extends the accelerator and improves its feasibility; and this study also exhibits acceptable performance on the FPGA platform.

109.2 SE–SD Algorithm

The basic idea of the SD algorithm can be described as below. Given an initial radius of the sphere C_0 , the search is performed in the sphere whose center of sphere is y and radius is C_0 . If no point belongs to $A_Q^{N_T}$ in this sphere, then the radius of the sphere is increased, and the searching continues in a new sphere; however, if a right point is found in the sphere, then the radius is reduced to $C = \|y - Hx\|$. Afterwards, the searching proceeds to the smaller sphere. The aforementioned process mentioned is repeated until a point that makes $C = \|y - Hx\|$ minimum is reached. Finally, the array is the result of the detection derived by the following equation:

$$\hat{x}_{SD} = \underset{x \in A_Q^{N_T}}{\operatorname{argmin}} \left\{ \|y - Hx\|^2 \leq C^2 \right\} \quad (109.1)$$

109.3 Fine-Grained Parallel Full Pipeline SE–SD Algorithm

A standard SE–SD algorithm is controlled by a while loop. After entering the while loop, the subsequent action should be decided, that is, whether to compare the first child, to compare the next sibling, or to backtrack. Data dependence occurs in the vertical dimension. Whenever a new decision is made, the historical data along the entire path change. By contrast, space for the exploiting parallelism is available in the horizontal dimension. The historical data among different paths are refreshed when the algorithm reaches the top layer. Thus, the data from the top layer can be divided, and the only associated data among different paths is the global weight of path w_g . When we search a smaller w_{pe} , we update w_g to a smaller one. We design a new parallel mode based on this idea. We use multiple PEs to search multiple paths in the second layer. When a certain PE obtains a local minimum w_{pe} , this PE compares its w_{pe} with the global weight w_g . If the w_{pe} is smaller, then w_g is updated and w_{pe} becomes the threshold in the path. Given that the root node has four children, we can assign four PEs to search the tree. As to each sub-tree, the algorithm runs in the same manner as when it is searching an entire tree (as shown in Fig. 109.1).

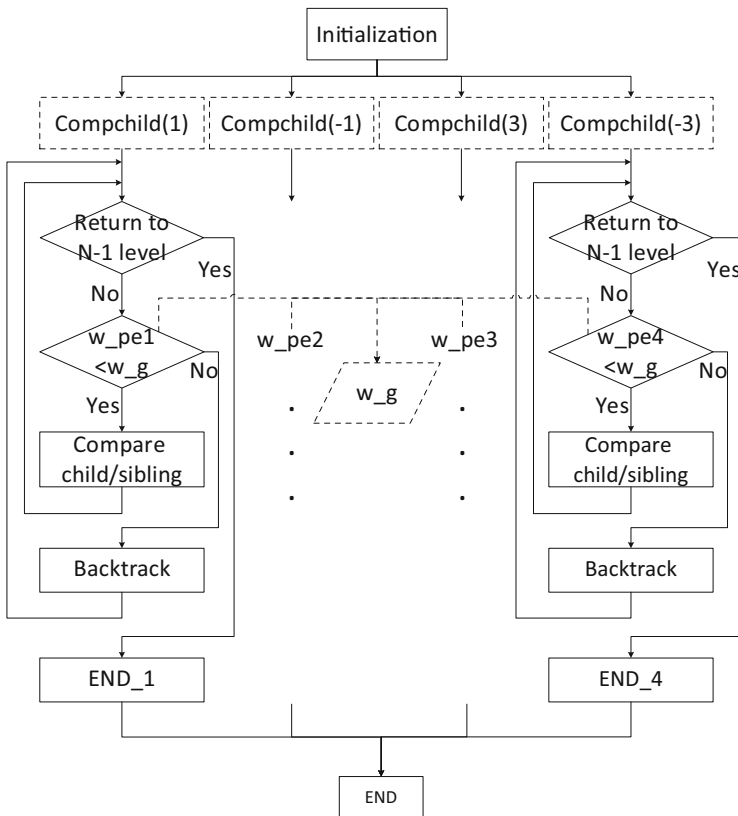


Fig. 109.1 Fine-grained parallel SE–SD algorithm

We can serve two accelerate modes, namely, latency- and throughput-prior accelerate modes. In the latency-prior mode, the accelerator finishes searching a single tree prior as early as possible. By contrast, the accelerator finishes searching as many multiple trees prior as possible in the throughput-prior mode. In this mode, the system configures the sources to a task-level parallel architecture and increases the number of searching tasks as much as possible.

109.4 SE–SD Algorithm Algorithm Accelerator

109.4.1 System Architecture

As shown in Fig. 109.2, an SE–SD algorithm accelerator includes two RAMs for recording input and output data and eight calculation unit (CALC) arrays. Users operate the accelerator by using two buttons, namely, reset and start.

The Distribute_unit is used to control CALCs, change the accelerate mode, or send data. CALCs are in charge of receiving data and calculating the signal point. Each CALC has four PEs.

Given that we have 4-PE and 16-PE latency-prior accelerate modes, one CALC can be formed into a group as a 4-PE parallel computing node.

109.4.2 Design and Implementation of CALC

The CALC module is in charge of calculating and determining the final path of a tree. Each CALC includes a prework module, four PE modules, and a folwork module.

The prework module is used to calculate initial data for a sub-tree because when data is rendered to a sub-tree, initial data have already been calculated once on the top layer.

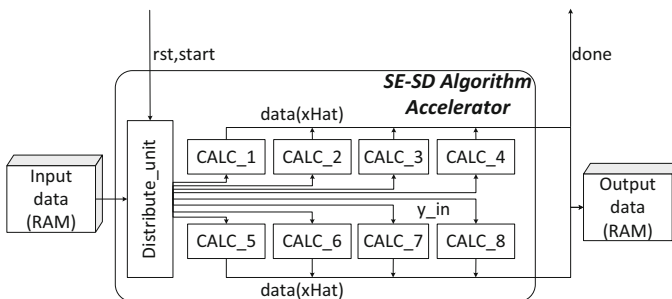


Fig. 109.2 System architecture

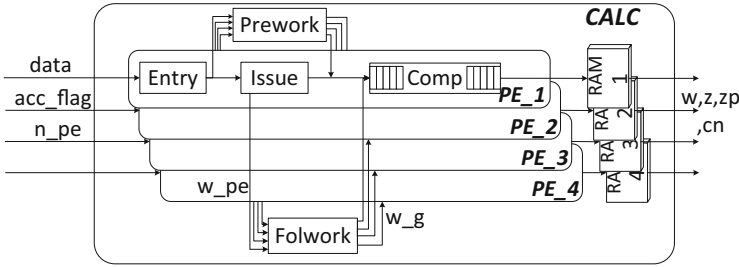


Fig. 109.3 CALC architecture

The folwork module is used to update w_g according to which of the four w_{pe} is the smallest. When data enter the issue module, the w_{pe} for each PE has already been compared with the w_g . Thus, the folwork module simply needs to compare the four w_{pe} , choose the smallest one, and update the w_g (Fig. 109.3).

109.5 FPGA Implementation Results

109.5.1 Experiment Environment

We implement our SE–SD accelerator on a Xilinx Virtex 6 FPGA (XC6VLX240T) and compare it with software running on a host PC with an Intel i7 3630 2.4 GHz CPU and 8 G main memory. The code of the SE–SD algorithm is written by Karen Su version 1.1 [8], and the software used is MATLAB R2012a.

109.5.2 Performance and Analysis of the Latency-Prior Accelerate Mode

We do not have a parallel SE–SD algorithm software version, and thus, we cannot run the code in parallel. We also do not have the condition to compare the throughput between the accelerator on FPGA and the software running on a PC with multiple datasets. Therefore, we compare the latency of the experiment results with a software platform.

Table 109.1 shows that in the random experiment, the latency of 4-PE is two times shorter than that of 1-PE, and the latency of 16-PE is four times shorter than that of 1-PE.

Considering that the trees we have searched have four forks in each level, we chose 4-PE (unfold 1 level) and 16-PE (unfold 2 levels) to perform the research.

We use four kinds of datasets marked by X-PE-Y ($X = 4, 16$; $Y = 1, 2, 3, 4$). For example, 4-PE-1 indicates that the dataset runs on a 4-PE platform and the final path

Table 109.1 Comparison of latency with software

Matlab (μ s)	1-PE (μ s)	4-PE (μ s)	16-PE (μ s)
19,840	65	35	16

Fig. 109.4 Length of search path when 4-PE-1

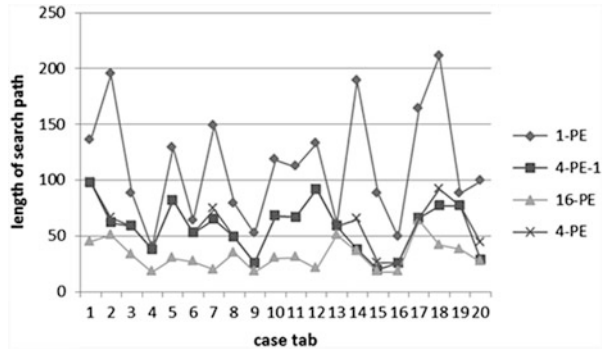
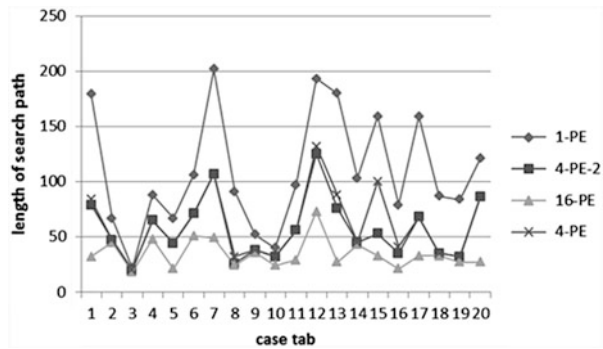


Fig. 109.5 Length of search path when 4-PE-2



appears in the first sub-tree. We select 20 examples for each kind of dataset, that is, 80 examples in total. The following figures were derived.

Comparing 1-PE and the other three groups of data in Figs. 109.4, 109.5, 109.6, and 109.7, the parallel technique exhibits an excellent result; however, the process is very time-consuming. By contrast, 1-PE enables us to derive the final result easily with almost the same time consumed as that when the parallel technique is used.

Meanwhile, 4-PE-N and 4-PE are almost the same. That is, when four PEs search in parallel, the latest sub-tree is simply the tree with the final path that comes out in the 1-PE mode in most cases. Therefore, if a final result is derived in a sub-tree, then it will spend most of the time searching and ensuring that it is really the best answer.

Comparing Figs. 109.4 and 109.7, the time consumed using 4-PE-N, 4-PE, or 16-PE is considerably less than that consumed using 1-PE when $N=4$. Moreover, the time consumed when using 4-PE-4 and 4-PE are almost the same. Thus, we can choose fewer number of PEs when we know that the final result will appear in the fourth path to save resources.

From the experiment results, the following conclusions can be derived.

Fig. 109.6 Length of search path when 4-PE-3

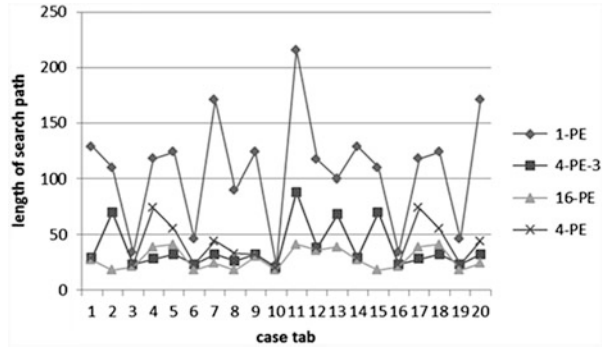
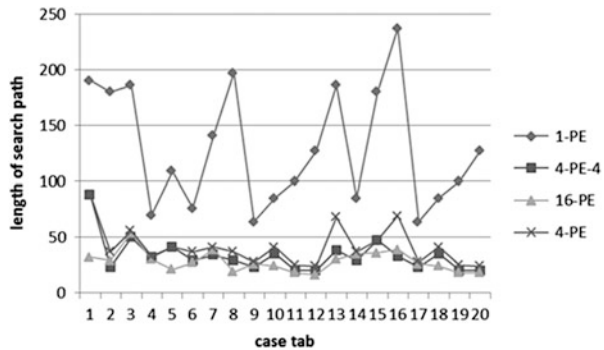


Fig. 109.7 Length of search path when 4-PE-4



- (a) Multiple PE architecture exhibits a more obvious effect when the final result appears in a later sub-tree. This result is attributed to the significant amount of time consumed in pruning waste sub-trees when a single PE is searching and the final result appears in a later sub-tree.
- (b) Search time with a single PE is random; however, when the number of PE is increased, search time will be more stable. This result is attributed to the final result appearing randomly in four sub-trees; thus, searching with a single PE is unnecessary. All paths need to be searched before finding the final result; therefore, the time cost is uncertain. However, when we search using N-PE, the possibilities of finding the final result for each PE are equal. We can set a global minimum w_g to prune waste sub-trees as early as possible.
- (c) N-PE architecture cannot run faster than 1-PE-N times, but less than N times not because of the overhead parallelism but because of the algorithm itself. The weight of the path is calculated as follows:

$$w_{i+1} = w_i + (py - Hr \times z_i)^2 \tag{109.2}$$

In this equation, z_i has four possible values (1, -1, 3, and -3). w grows slowest when z_i is 1; therefore, the algorithm tends to believe that the sub-tree with a value

Table 109.2 Comparison between related works and N-PEs

Reference	ASIC-I	SE-ac	FSD-ac		1-PE	4-PE	32-PE
SNR(dB)	20	20	20		3	3	3
Algorithm	SE-SD	SE-SD	FSD		SE-SD	SE-SD	SE-SD
Technology	ASIC	FPGA	FPGA	ASIC	FPGA	FPGA	FPGA
Max clock (MHz)	51	251	52	400	170	165	160
Throughput (Mps)	73	81.5	27.7	213.3	31	120	900

of 1 will possibly obtain the final result. Thus, whichever path the final result appears, searching the path with a value of 1 is always time-consuming.

109.5.3 Performance and Analysis of the Throughput-Prior Accelerate Mode

The SNR of our dataset is between 0 and 5 dB. We compare our accelerator with ASIC-I [6] which is a multi-cycle accelerator that uses a depth-first algorithm combined with a developed incomplete SE enumeration algorithm. The SE accelerator (SE-ac) [9] also uses FPGA; however, our system obtains a higher throughput. Wu et al. [7] uses the FSD algorithm (FSD-ac) compared with the SE-SD algorithm. Furthermore, backtracking is not involved in the FSD algorithm; thus, we always obtain a stable throughput when we build an accelerator on FPGA.

In the latency-prior mode, the throughput of 4-PE is twice that of 1-PE, and the throughput of 16-PE is four times that of 1-PE. However, when we choose the throughput-prior mode, the throughput of 4-PE is four times that of 1-PE. When we use full source on our FPGA, we can obtain 32 times the throughput of 1-PE. We use the following equation to show the throughput for each tree:

$$\theta = \frac{N_R \log_2 \#(\Omega)}{W} f_{\text{clk}} \text{ bps} \quad (109.3)$$

where W is the average number of visited nodes (including the backtrack nodes), and f_{clk} is the clock rate for 16-QAM, $\#(\Omega) = 16$.

Table 109.2 reveals that the throughput grows linearly as the number of PEs increases. Therefore, our system can adapt to numerous kinds of FPGA platforms. When an FPGA has additional hardware resources, we can further expand the size of the PE array.

Conclusion

In this paper, we present a new parallel full pipeline accelerator implemented on FPGA for the SE–SD algorithm. We select the number of PEs to distribute our system according to the hardware platform by using a distribution unit. We've successfully placed four PEs in an accelerator and eight accelerators in a single FPGA (XC6VLX240T). The system obtains remarkable performance in delay and throughput while compared with the state of art.

References

1. Paulraj A, Nabar R, Gore D. Introduction to space-time wireless communications. Cambridge, UK: Cambridge University Press; 2003. p. 178–97.
2. Bölcskei H, editor. Space-time wireless systems: from array processing to MIMO communications. Cambridge, UK: Cambridge University Press; 2006. p. 241–342.
3. Foschini GJ, Gans MJ. On limits of wireless communications in a fading environment when using multiple antennas. *Wireless Pers Comm*. 1998;6(3):311–35.
4. Chang RY, Lin SJ, Chung WH. Efficient implementation of the MIMO sphere detector: architecture and complexity analysis. *IEEE Trans Vehic Technol*. 2012;61(7):3289–94.
5. Noguera J, Neuendorffer S, Vissers K, et al. Wireless MIMO sphere detector implemented in FPGA. *Xcell J*. 2011;74:38–45.
6. Burg A, Borgmann M, Wenk M, et al. VLSI implementation of MIMO detection using the sphere decoding algorithm. *IEEE J Solid State Circ*. 2005;40(7):1566–77.
7. Wu B, Masera G. A novel VLSI architecture of fixed-complexity sphere decoder[C]//digital system design: Architectures, methods and tools (DSD), 2010 13th Euromicro conference on. IEEE; 2010. pp 737–44.
8. Su K. Efficient maximum likelihood detection for communication over multiple input multiple output channels. Cambridge: Department of Engineering, University of Cambridge; 2005.
9. Huang X, Liang C, Ma J. System architecture and implementation of MIMO sphere decoders on FPGA. *IEEE Trans Very Large Scale Integr Syst*. 2008;16(2):188–97.

Chapter 110

The Bandpass Sigma-Delta Modulator with Converter Chip Design for Positron Emission Tomography Front-End Application

Wen-Cheng Lai, Jhin-Fang Huang, Kun-Jie Huang, and Pi-Gi Yang

Abstract Positron emission tomography architectures have been traditionally dependent on zero-crossing discriminators, external voltage references, or fixed voltage references with restricted voltage steps. A continuous-time quadrature bandpass sigma-delta ($\Sigma\Delta$) modulator integration and CICFF topology are presented for positron emission tomography front-end application. The main advantage of the proposed modulator adopts the weighted capacitor technology to save a feedforward summation amplifier, hence reducing power consumption in TSMC 0.18- μm CMOS process.

Keywords Analog-to-digital converter • CICFF topology • Low-pass sigma-delta modulator

110.1 Introduction

Positron emission tomography (PET) front ends with filtering circuit architectures are popularly used to improve timing resolution. An analog front end with an integrating amplifier is presented [1]. Time-of-flight (TOF)-based PET architectures also require comparators [2] to detect threshold voltages. These threshold voltages have been set with off-chip references [2] or internally with constrained voltage steps [1]. However, as proposed [3], this DAC with slew-rate boosting technique has the drawback of high power consumption if the frequency increases, requiring enhanced driving capability of the class-AB output stage [4]. Sigma-delta modulation techniques and high accuracy analog/mixed signal are built in integrated circuit applications, as analog-to-digital converter (ADC), digital-to-analog converter (DAC), frequency synthesis, and power amplification. Moreover, sigma-

W.-C. Lai (✉) • J.-F. Huang • K.-J. Huang • P.-G. Yang
Department of Electrical Engineering, National Taiwan Univ of Science and Technology,
Taibei 10617, Taiwan
e-mail: d9902213@mail.ntust.edu.tw

delta modulators are widely used in receivers [5] because of their ability to provide high resolution with relatively low precision components and low power consumption. Continuous-time $\Sigma\Delta$ modulators (CTSDM) are ideally more suitable for wideband applications than discrete-time $\Sigma\Delta$ modulators (DTSDM) because the CTSDM is able to relax sampling frequency and is also inherent anti-aliasing; hence, there is no required additional anti-aliasing filter. The proposed quadrature bandpass sigma-delta modulator with 5-MHz signal bandwidth is applied in the baseband. With the considerations of power consumption, phase noise, and bandwidth, a continuous-time quadrature $\Sigma\Delta$ modulator consisting of a polyphase filter for operation in low-intermediate frequency (IF) receivers is proposed. The IF signals of in-phase and quadrature-phase (I/Q) channels perform the complex ADC and therefore decrease the flicker noise and DC offsets. The polyphase filter is executed by cross-coupling resistors to two low-pass integrated inputs and outputs for the analog I/Q paths and then shifts the filter signals from DC to IF [6]. The weighted capacitor fed through summation technology in this proposed modulator is able to save a summation amplifier and then to reduce the power dissipation.

110.2 The Proposed Loop Filter Structure

The CIFF is a traditional loop filter topology in the $\Sigma\Delta$ modulators. In the CIFF topology, the output of each op-amp has lower output swing than the chain of integrators with distributed feedback (CIFB) [6]. The CIFF topology suits for low-power application, but it requires additional current for the feedforward summation, which increases extra power consumption. In order to reduce the active circuit by a capacitive feedforward summation structure [7], the last integrator's output of loop filter in the CICFF topology has replaced the summation. Therefore, feedforward branches have no extra power to consume. The CICFF topology is a great solution to obtain low-power application. The schemes 3rd-order loop filter for the low-pass $\Sigma\Delta$ modulator. Since the modulator becomes more sensitive to instability because of cross couplings, it should add additional compensation cross-coupling resistors. Higher-order loop filter is considered for higher accuracy, while increasing cost, consuming more power, and causing circuit instability. With considerations of those factors, in this paper, a 3rd-order loop filter for the quadrature bandpass $\Sigma\Delta$ modulator is proposed. It is the simplified circuit from differential to single-ended schematic. The resistor used in the loop filter shifts the three repeated zeroes of the noise transfer function from real axis to complex plane and real axis. The noise floor is then suppressed in the $\Sigma\Delta$ modulator.

110.3 Continuous-Time Low-Pass $\Sigma\Delta$ Modulator

The overall proposed 3rd-order $\Sigma\Delta$ modulator with a tunable capacitor array for positron emission tomography front-end application. The signal bandwidth f_B is 5 MHz and the sample rate is $f_s = 200$ MHz. The $\Sigma\Delta$ modulator is combined with CICFF low-pass filters, two 3-bit flash ADCs, current steering DACs, and DWA circuit. The output signals of 3-bit flash ADC pass through the D-latch, DWA, and DAC and then feedback into the loop filter, and the noise shaping is activated and performed in the circuit. CMOS processes often do not have accurate control over R and C absolute values; therefore, an automatic RC time constant tuned circuit is needed to make sure of the $\Sigma\Delta$ modulator stability and SNR performance over large RC time constant variations. Hence, the capacitor (C_1 – C_3) is implemented as a capacitor array to compensate the RC product variation. The array capacitors are except the “always-in-use” capacitor which equals the least significant bit (LSB) capacitor, $7^\circ C$. This sizing method provides constant tuned steps with the bit codes of capacitors. The 3-bit digital control codes are fed externally. The nominal value of the capacitor is $10^\circ C$; hence, the capacitor array can be varied from 7 to 13 $^\circ C$ corresponding to 70–130 % variation.

110.3.1 Operational Transconductance Amplifier (OTA) Design

The load capacitance of each amplifier is almost the same due to appropriate design. The proposed OTA with active frequency compensation circuits is used. Simulation results verify that the amplifier achieves a unity gain bandwidth (GBW) over 400 MHz with a load capacitor of 3 pF, a low-frequency gain greater than 55 dB, and a phase margin of 63° .

110.3.2 Comparator and 3-Bit Flash ADC

The 8-level quantizer is made up of seven comparators. By the oversampling process, the quantizer has to operate at the speed required. Thence it must be implemented as a flash ADC [8]. The block diagram of the 3-bit flash ADC is used in the quantizer. It consists of seven differential comparators, a resistor ladder, and a thermometer to binary encoder. These comparators compare the input signal with reference voltages by a resistor ladder biased by the full-scale reference. The comparator outputs constitute a thermometer code, which is converted to binary by the encoder. Since flash architectures employ comparators, they are susceptible to metastability errors. In order to lower the probability of metastable states, the

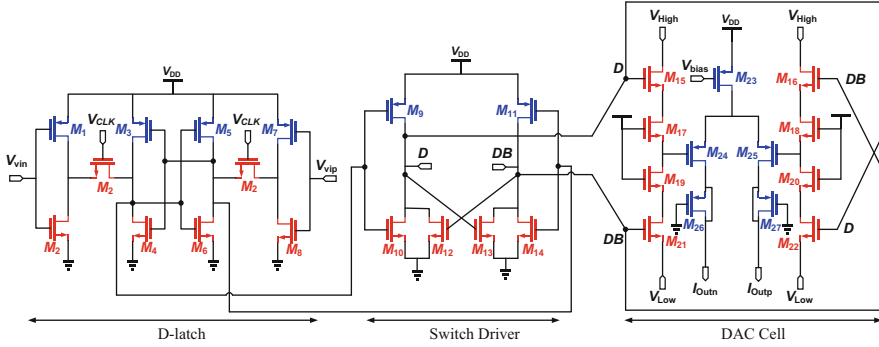


Fig. 110.1 Current steering DAC

thermometer to binary decoding can be pipelined so that potentially indeterminate outputs are allowed more regeneration time.

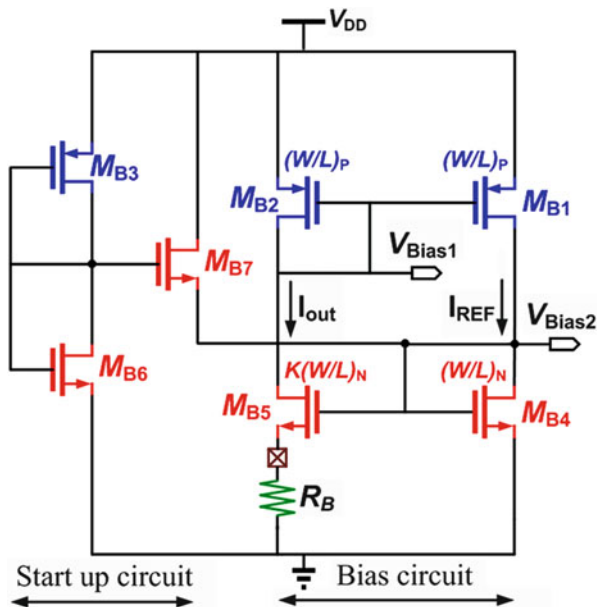
110.3.3 DAC Circuit

The DAC is consisted of D-latch, switch driver, and current steering DAC cell. The circuit diagram of a single cell of DAC is shown in Fig. 110.1. In order to reduce glitch of the input voltage, the V_{High} and V_{Low} operate at the 1 and 0.2 V, respectively. Hence, it can increase DAC’s linearity. An important block in a current steering DAC design is the switch driver composed of M_9 – M_{14} . The task of the switch driver is to latch the incoming DAC code and to perform final synchronization.

110.3.4 DWA Circuit

Good attenuation of DAC noise because of component mismatches can be provided by the data-weighted averaging algorithm, and DWA ideally can achieve a first-order DAC noise shaping [9]. The block diagram of the DWA logic input of the DWA logic is connected to the 3-bit quantizer output. The DWA logic converts the quantizer output code to the control signals, $S_i, i = 0, 1, \dots, 7$, for the element choice of the current steering DAC. A 3-bit adder and a 3-bit register produce two indexes. Then the two indexes are converted to two sets of 8-bit thermometer codes by two binary to thermometer decoders. If the carry signal of the adder sets to low, the output control signals are the mutual XOR of the two 8-bit thermometer codes. When the carry signal sets to high, the signals are the mutual XNOR of the two 8-bit codes.

Fig. 110.2 The bias circuit and start-up circuit



110.3.5 Bias Circuit and Start-Up Circuit

The bias circuit is used for amplifier and DAC circuit as shown in Fig. 110.2. The I_{out} is independent of the power supply which is expressed. Therefore the bias circuit requires a start-up circuit. When the gate voltage of M_{B4} and M_{B5} is zero, the M_{B7} is turned on to generate initial current. After M_{B5} and M_{B4} are turned on, the M_{B7} is turned off immediately. The M_{B7} is biased on M_{B3} and M_{B6} .

110.4 Measured Results

The CT low-pass SDM has carried out a 0.18- μm CMOS and the proposed prototype chip layout is shown in Fig. 110.3. The chip area is $1.32 \times 1.14 \text{ mm}^2$.

The additional transformer converts the single-ended analog signal of 1 MHz to a balanced different signal input. The measured output stream of the $\Sigma\Delta$ modulator with simulation is loaded into MATLAB with Hanning window. The measured peak SNDR is 57.68 dB over a 5-MHz signal bandwidth. The SNDR versus the input signal level is 56 dB of dynamic range (the simulation result is 64 dB). The measured performance is summarized in Table 110.1, and the performance of the $\Sigma\Delta$ modulator of this work is compared with that of other $\Sigma\Delta$ modulators in Table 110.2. Figure 110.4 shows the power breakdown of the presented design. From Fig. 110.4, the op-amps occupy most of the power [10–13].

Fig. 110.3 Chip microphotograph of proposed SDM

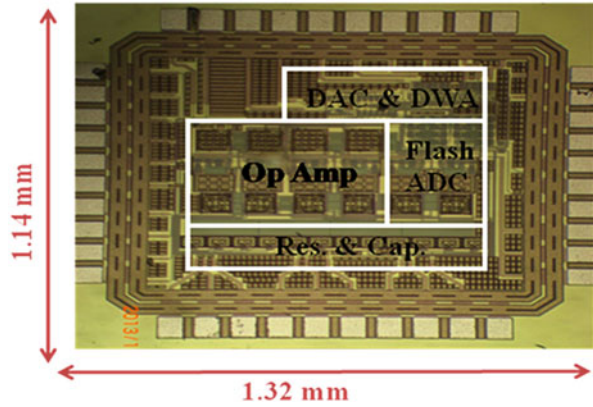


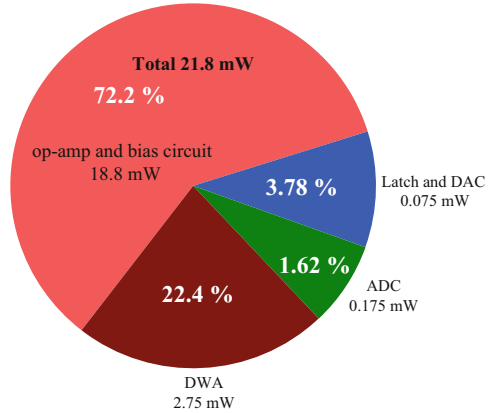
Table 110.1 Performance summary

Technology	0.18 μm
Power supply (V)	1.8
Clock frequency (MHz)	200
Input frequency (MHz)	1
Signal bandwidth (MHz)	5
Peak SNDR (dB)	57.68
ENOB (bit)	9.3
Dynamic range (dB)	56
Power (mW)	21.8
Chip area (mm^2)	1.32×1.14

Table 110.2 Performance comparison

Ref.					This work
Process (μm)	0.18	0.25	0.13	0.18	0.18
Power voltage (V)	1.8	1.8	2.5	1.8	1.8
Clock (MHz)	100	125	3,500	800	200
BW (MHz)	1	4	100	10	5
SNDR (dB)	59.8	48.4	53.1	68	57.68
ENOB (bit)	9.6	7.75	8.5	11	9.3
Power (mW)	22.3	20.5	650	160	21.8
FoM (pj/conv.)	19.6	11.9	8.8	3.9	3.45
Chip area (mm^2)	1.62	0.2	4	2.5	1.5

Fig. 110.4 Pie chart distribution of power consumption



Conclusion

In this paper, a CT low-pass $\Sigma\Delta$ modulator for positron emission tomography front-end application was presented. The proposed chip was designed in a 0.18- μm CMOS technology. The loop filter of $\Sigma\Delta$ modulator used the CICFF topology and saved a power of op-amp. Therefore the $\Sigma\Delta$ modulator is well suited for the low-power application than other paper comparisons. At 1.8-V supply voltage, the proposed $\Sigma\Delta$ modulator has a power consumption of 21.8 mW. It achieves a dynamic range of 52 dB and a peak SNDR 57.68 at 200 MHz of sampling frequency for PET applications.

References

1. Pratte JF, Junnarkar S, Deptuch G, Fried J, O'Connor P, Radeka V, Vaska P, Woody C, Schlyer D, Stoll S, Maramraju SH, Krishnamoorthy S, Lecomte R, Fontaine R. The RatCAP front-end ASIC. *IEEE Trans Nucl Sci.* 2008;55(5):2727–35.
2. Powolny F. Time-based readout of a silicon photomultiplier (SiPM) for time of flight positron emission tomography (TOF-PET). *IEEE Trans Nucl Sci.* 2011;58(3):597–604.
3. Knausz I, Bowman RJ. A low power, scalable, DAC architecture for liquid crystal display drivers. *IEEE J Solid-State Circ.* 2009;44(9):2402–10. *Trans Nucl Sci.* 2011;58(3):597–604
4. Bell M. An LCD column driver using a switch capacitor DAC. *IEEE J Solid-State Circ.* 2005;40(12):2756–65.
5. Shibata H, Schreier R, Yang W, Shaikh A. A DC-to-1 GHz tunable RF $\Delta\Sigma$ ADC achieving DR = 74 dB and BW = 150 MHz at $f_0 = 450$ MHz using 550 mW. *IEEE J Solid-State Circ.* 2012;47(12):2888–97.
6. Schreier R, Temes GC. *Understanding delta-sigma data converter.* Piscataway, NJ: IEEE Press; 2005. p. 100–25.
7. Kim SB, Joeres S, Wunderlich R, Heinen S. A 2.7 mW, 90.3 dB DR continuous-time quadrature bandpass sigma-delta modulator for GSM/EDGE low-IF receiver in 0.25 μm CMOS. *IEEE J Solid-State Circ.* 2009;44(3):891–900.

8. Lamarre L, Louerat M, Kaiser A. A simple 3.8 mW, 300 MHz, 4-bit flash analog-to-digital converter. Proceedings of the SPIE, microtechnologies for the new millennium 2005 VLSI circuits and systems II, Sevilla, Spain, vol. 5837, no. 51; 2005, p. 825–32.
9. Kuo TH, Chen KD, Yeng HR. A wideband CMOS sigma-delta modulator with incremental data weighted averaging. *IEEE J Solid-State Circ.* 2002;37:11–7.
10. Yang WL, Hsieh WH, Hung CC. A third-order continuous-time sigma-delta modulator for Bluetooth. In: Proceedings of IEEE international symposium on VLSI design, automation and test. 2009. p. 247–50.
11. Kim SB, et al. Continuous-time quadrature bandpass sigma-delta modulator for GPS/Galileo low-IF receiver. In: Proceedings of IEEE international workshop on radio-frequency integration technology. 2007. p. 127–30.
12. Hart A, Voinigescu SP. A 1 GHz bandwidth low-pass $\Delta\Sigma$ ADC with 20–50 GHz adjustable sampling rate. *IEEE J Solid-State Circ.* 2009;44:1401–14.
13. Lu CY, Siva-Rivas JF, Kode P, Siva-Martinez J, Hoyos S. A sixth-order 200 MHz IF bandpass sigma-delta modulator with over 68 dB SNDR in 10 MHz bandwidth. *IEEE J Solid-State Circ.* 2010;45(6):1122–36.

Chapter 111

Simulation Testing Apparatus and Method for Embedded System Based on Universal Serial Bus Host

Xin Li, Lingping Chen, Rentai Chen, and Shengwen Jiang

Abstract Nowadays, more and more embedded products are required to have capabilities of communicating with accessories or other devices through USB (Universal Serial Bus) as host. Different from USB device, the host occupies a unique position as the coordinating entity for the USB, and thus the mature methods used for USB device test do not work in USB host test. Especially, the USB host built in embedded system has special architecture and supports specified applications; thus normal USB devices in market cannot be used to test the USB host system. So how to verify the functionalities of USB host in embedded system or applications based on USB host is always a big challenge for developers. This paper presents a method to test USB host functionalities and even the entire system based on USB host. The core of the method is a configurable USB device simulator connected to PC (personal computer) and software on PC which can configure the simulator dynamically and extend functionality of the simulator. An apparatus based on the method has been developed and put to use in a real project.

Keywords USB host test • USB device simulator • USB class switch

111.1 Introduction

USB is a cable bus that supports data exchange between a host and a wide range of simultaneously accessible devices. There is only one host in any USB system and all data transfers are initiated by the host [1]. USB devices with similar functions are grouped into classes in order to share common features and even use the same device drivers [2].

New-generation embedded product has built-in USB host functionality to support USB accessories which work as USB device and follow different USB device class

X. Li (✉) • L. Chen • R. Chen • S. Jiang
Network and Information Management Center, Chengdu Normal University,
Chengdu 611130, China
e-mail: lixin_uestc@163.com

specifications such as HID (human interface devices), CDC (communication device class), MSD (mass storage device), etc. [3, 4]. Verification and validation of USB host functionality before the embedded product delivery is a major concern because there is always no accessory (USB device) for test. After the product is shipped, many third-party vendors will develop USB accessories for it, so the USB host system is requested to be ready for handling all usage scenarios based on the forecast.

Testing of USB host system (system means host and the device driver on top of it) is always a big challenge for developers. For USB device, developer can make use of commercial test tools as well as commercial operating system with mature USB drivers like Microsoft Windows[®] to do the test. However, this method does not work for testing embedded USB host system [5]. Purchasing an off-the-shelf USB host test equipment was considered, but searching result shows that it is absent in the market. Some USB protocol analyzers have the device simulation functionality, but they can only test the simple USB host usage scenarios such as device enumeration. They have no capability of testing the complex interaction between accessory and USB host [6].

To satisfy the USB host test requirement, a USB device simulator with capability of simulating various USB class devices has been developed. This simulator can dynamically load different USB device drivers and switch from one instance of driver to another, and thus this single apparatus can be used to test multiple USB functions on embedded USB host system. This simulator has a communication link like RS232 to PC. The software developed on PC can control the behavior of the simulator and extend the functionality of the simulator. This paper will describe the architecture of the method and the design of the simulator and give an example of testing a private application protocol based on USB host.

111.2 System Architecture and Design

111.2.1 System Structure

The system for testing USB host consists of USB device simulator and software running on PC. Figure 111.1 shows the setup method of the system.

The USB device simulator has two ports: one is the USB device port, which is used to connect with the target under test (USB host system) through USB cable, and the other is the RS232 port connected to PC.

Generally, USB host system supports various USB device classes. Class drivers are software components in host that are able to communicate with many USB devices of a particular class. The USB device simulator can act as different class devices. User console on PC can switch the simulator between the classes. For example, user console can send command *switch:hid* to make simulator act as an HID device and also can send command *switch:cdc* to switch simulator to CDC device. With this simulator, there is no need to prepare different devices for

Fig. 111.1 System physical structure

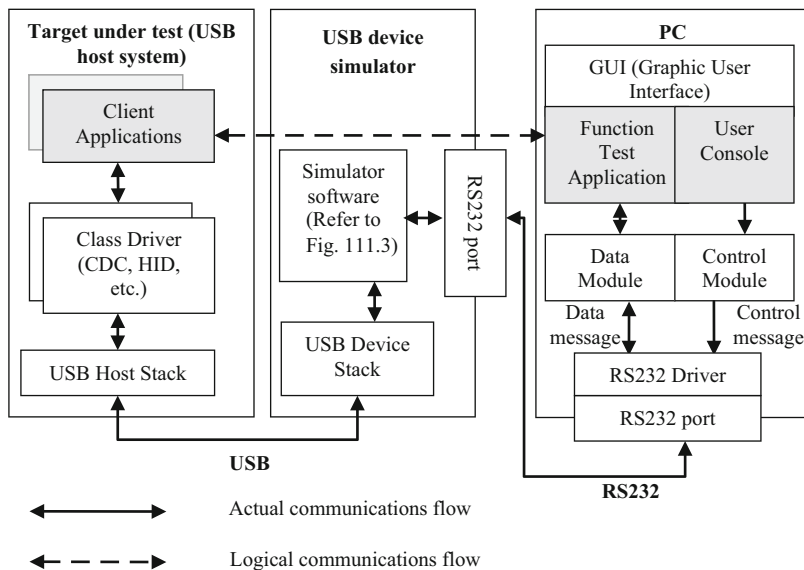
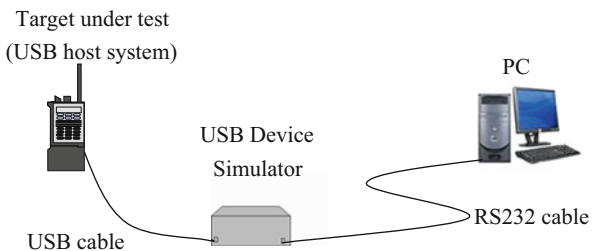


Fig. 111.2 System architecture

different USB class tests. This simulator has the capability of testing multiple USB host class drivers.

Upper-layer client applications based on USB host interoperate with different kinds of devices to form different features. This method can support client application test. To be more extendible and maintainable, testing components for client applications are not designed in USB device simulator but located on PC. As Fig. 111.2 shows, “Function Test Application” on PC is the component to test client applications on USB host. It focuses on the functionality of the corresponding client application regardless of transport layer. From logical view, Function Test Application interacts with Client Applications directly as the horizontal imaginary arrow shows. But from physical view, all the data between them pass through USB device simulator. Vertical arrows indicate the actual communication between PC and USB host system under test.

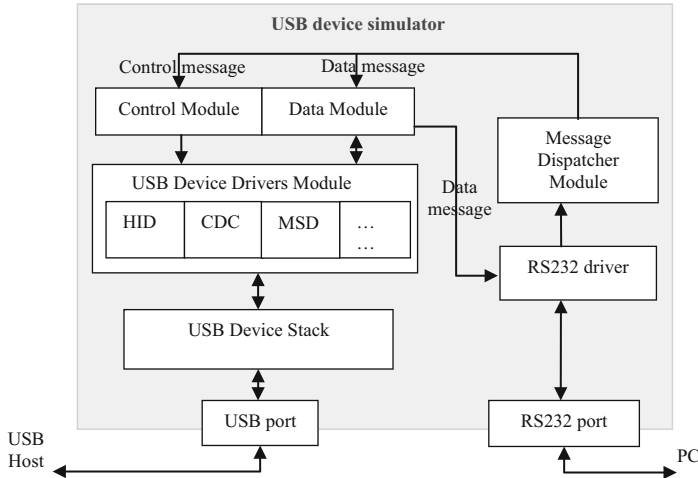


Fig. 111.3 USB device simulator

111.2.2 Design of USB Device Simulator

This section describes the structure and data flow inside the USB device simulator. As Fig. 111.3 shows, the USB device simulator includes six components: RS232 driver, Message Dispatcher Module, Control Module, Data Module, USB Device Drivers Module, and USB Device Stack [7].

There are two kinds of messages that can be sent from PC to USB device simulator: one is control message and the other is data message. Message Dispatcher Module parses all the messages from RS232 driver and routes them to proper module as Fig. 111.3 shows.

Control Module handles control messages coming from Message Dispatcher Module. Currently, only “switch class type” control message is supported. As Fig. 111.4 illustrates, this command will cause control module to load the new device driver from USB Device Drivers Module and then switch to the new class device. Control Module and control message can be extended to support more functions of configuration and control in the future.

USB Device Drivers Module provides multiple device drivers for different classes. Only the active driver instance functions at the same time. This module provides interfaces for Control Module to achieve the driver switching mechanism.

Each device driver in USB Device Driver Module has capabilities of sending or receiving data to or from USB port through USB Device Stack. USB Device Driver Module exposes consistent data send/receive interfaces to Data Module, in another word, no matter which driver functions, Data Module uses the same interfaces to send or receive data messages to or from USB device driver. USB device driver switch is transparent to Data Module.

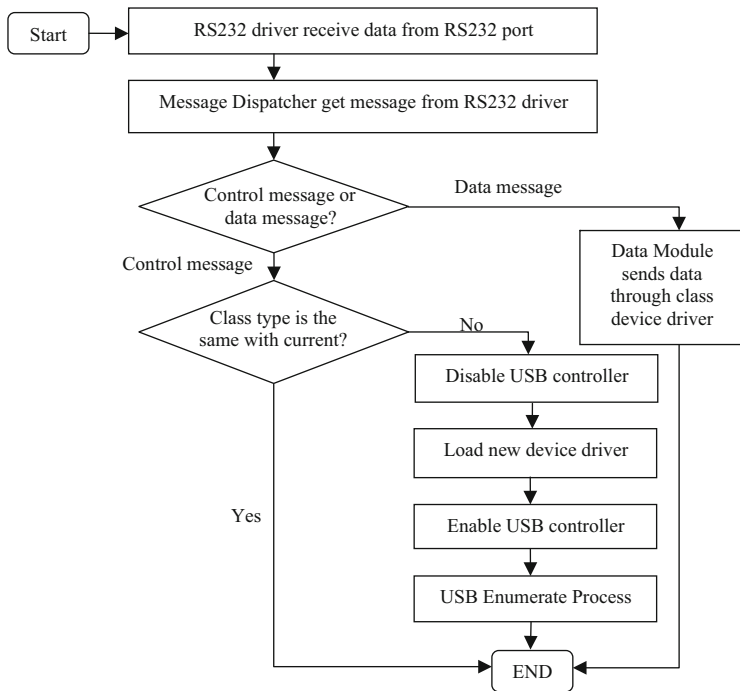


Fig. 111.4 USB device simulator data flow

Message Dispatcher Module routes data messages from RS232 driver to Data Module. Data Module picks the raw data from data message and sends it to USB Device Drivers Module. On the other hand, Data Module receives USB data from USB Device Drivers Module and packed the data into data message. The data message will be sent to PC through RS232.

111.2.3 Test Software Structure on PC

There are six components that comprise the software on PC as Fig. 111.2 has illustrated. GUI (graphic user interface) integrates services of lower-layer Function Test Application component and User Console to provide a unified and friendly interface for user. Function Test Application interacts with the USB host Client Applications logically. Data Module provides data send/receive interface for upper-layer Function Test Application. It packs data into data message and sends it to RS232 driver. And on the other hand, it forwards data from RS232 to the upper-layer Function Test Application. User Console provides interfaces for user to control and configure the USB device simulator, such as switch class driver. Control Module packs and sends control messages for User Console.

111.3 An Example: A Private Application Protocol on USB Host Test

As a practical example, we designed and developed a test platform to test a private application protocol on USB host.

Figure 111.5 shows how a USB control accessory communicates with the embedded product through a private application protocol. This private application protocol allows external control of the embedded product. Each entity running with this protocol can be designed and implemented separately regardless of other entities. It brings much convenience to the developer and some problems also, like how to test and validate functionalities on host when accessory is not available.

The control accessory works as a USB CDC device. The communication between accessory and embedded product follows USB CDC/ACM class specification.

Figure 111.6 shows how to use the USB device simulator instead of accessory when accessory is not available. It is flexible and easy to configure simulator as various accessories, and also the simulator provides more functions than real accessory, like dumping the test log and developing and maintaining the test cases on PC side. In this example, we configure the simulator as a USB CDC/ACM device.

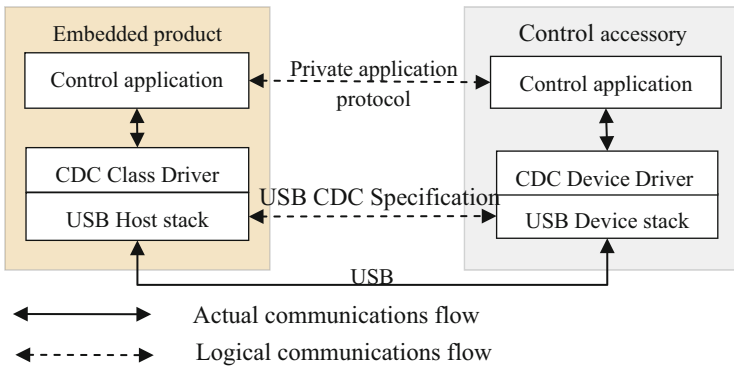


Fig. 111.5 Connection of embedded product and control accessory

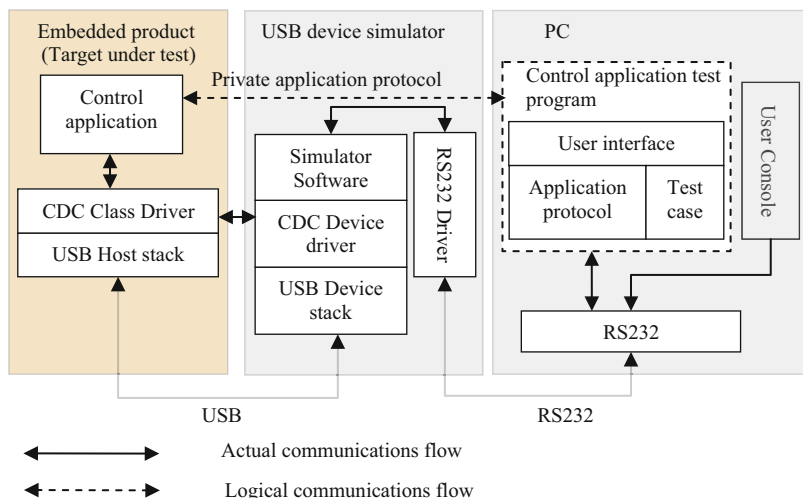


Fig. 111.6 Control application on USB host test platform

Conclusion and Future Work

With this method and apparatus, developers can get many benefits.

USB device simulator can work as various USB devices, so it is very useful for USB host system developers to test host functionality and different class drivers before accessories are available. In addition, test program to test client applications on USB host is built on PC which brings high flexibility and maintainability.

Besides that, accessory firmware developers can get benefit from this method. They can develop prototype based on this method before the hardware are ready and use it to validate the concept and requirement of the accessory. Unsuitable requirements can be discarded before design phase and incorrect design can be avoided before code phase. This method will reduce the risk and cost of accessory development.

Equipment to test USB host system is a shortage currently. Especially, it is difficult to test USB host behavior in error conditions. This apparatus not only has capabilities of testing functionalities of USB host system but also can be extended to simulate error conditions based on specified requirements.

With the increasing needs of market, embedded product is required to support more and more applications based on USB host system. The high flexibility and extendibility of the apparatus allow various test programs to be developed under the environment of PC to test different applications on USB host system.

References

1. USB Implementers Forum. Universal Serial Bus 3.1 Specification, Revision 1.0 [S/OL]. <http://www.usb.org>. Accessed 26 July 2013.
2. USB Implementers Forum. Universal Serial Bus Specification, Revision 2.0 [S/OL]. <http://www.usb.org>. Accessed 27 Apr 2000.
3. USB Implementers Forum. Universal Serial Bus Class Definitions for Communication Devices, Version 1.1 [S/OL]. <http://www.usb.org>. Accessed 19 Jan 1999.
4. USB Implementers Forum. Device Class Definition for Human Interface Devices, Version 1.11 [S/OL]. <http://www.usb.org>. Accessed 27 June 2001.
5. Tournemille J, Tamagno D. System and method for simulating universal serial bus smart card device connected to USB host [P]. US Patent: US6769622 B1. Accessed 3 Aug 2004.
6. Hu W, Zhang X, Li M, Zhang D, Liu H. Design of USB2.0 protocol analyzer based on FPGA [J]. *Comput Meas Contr.* 2008;9:047.
7. Ye C. Design and implementation of USB device stack [D]. Wuhan: The Huazhong University of Science and Technology; 2011 (In Chinese).

Chapter 112

Simple Simulation of Abandoned Farmland Based on Multiagent Modeling Approach

Xuehong Bai, Lihu Pan, Huimin Yan, and Heqing Huang

Abstract In recent years, the agent-based model (ABM) has been widely applied and popularized in land-use and land-cover change (LUCC). It expresses the spatiotemporal heterogeneities of a model with individuals and ultimately obtains the emergence of individuals' behaviors on a macroscopic scale. This paper takes Taipusi Banner in the Inner Mongolia farming-pastoral zone as the study area based on local questionnaire data. The model synthesizes climate factors, the Grain for Green policy, direct subsidies of grain, and socioeconomic factors and simulates household farmland use behaviors in the next 30 years based on the Repastj toolbox in the Java language and in Eclipse. This model precisely reflects the LUCC process and its corresponding factors' interactions, provides deep insight into the integration process of these factors, and gives advice to governments on how to make land-use and food-security policies long-lasting and reasonable.

Keywords Agent-based model • Artificial intelligence • Inner Mongolia farming-pastoral zone • Abandoned farmland • Climate

112.1 Introduction

Farmland use plays an irreplaceable role in the development of agriculture and national economy [1]. Few studies focus on the relationship of livelihoods and land use in China. Integrating households' livelihood to study changing trends in farmland and ways of adapting to those changes is a frontier area of research that can be explored to realize the sustainable development of ecologically fragile regions [2].

X. Bai (✉)

Institute of Geographic Sciences and Natural Resources Research, University of Chinese Academy of Sciences, 100049 Beijing, China
e-mail: baixh.12b@igsnr.ac.cn

L. Pan

School of Computer, Taiyuan University of Science and Technology, 030024 Taiyuan, China

H. Yan • H. Huang

Institute of Geographic Sciences and Natural Resources Research, 100101 Beijing, China

© Springer International Publishing Switzerland 2015

W.E. Wong (ed.), *Proceedings of the 4th International Conference on Computer Engineering and Networks*, Lecture Notes in Electrical Engineering 355,
DOI 10.1007/978-3-319-11104-9_112

979

A land system is a coupled system comprised of a human society and the natural environment. The Global Land Project asserts that we need to improve our understanding of how human activities influence the natural processes of the terrestrial biosphere [3]. However, traditional models, for example, System Dynamics, CLUE-S, Cellular Automata, and Markov chain, often ignore human activity. The agent-based model (ABM) can simulate individuals in complex systems from a bottom-up perspective. It defines behavior rules and interactive mechanisms of individuals and pays more attention to human influences. More and more applications and spreads have been adopted using ABM in the area of land-use and land-cover change (LUCC) [4]. In an early application of ABM in another country, Balmann developed a simulation of agricultural land change based on ABM in 1977. This simulation concerns the competitive relationships of farms under different policies [5]. In China, Chen [6] explored households' decision-making processes on different scales. Pan [7] studied different types of household land-use behaviors under natural-environment, government, and enterprise-subsidy mechanisms.

In recent years, farmers in the Inner Mongolia farming-pastoral zone have experienced land degradation, frequent drought, government subsidies, working in the city, among other things. Households' livelihood strategies and farmland use modes in this location change frequently. Farmers and related management institutions try new farmland uses, so an exhaustive study should be conducted to offer support for adaptive and sustainable farmland use.

112.2 Overview of Study Area

Taipusi Banner (Fig. 112.1) is located in the south of the Xilin Gol League. It is a fragile area in the north farming-pastoral zone. This banner is located in a fast-growing, high-yielding region, is part of a grain subsidy project, and falls within the Grain for Green project, so studying the effects of government policies can assist government in making improvements in policies. Recently, as the drought has intensified and the social economy developed, an increasing number of agricultural labors have gone to the big cities and more and more farmland has been abandoned. Because currently China's land system is one that gives responsibility to households, households' land-use decisions (especially for abandoned farmland) are directly related to farmland-use changes. The study of farmland-use changes necessarily entails understanding the households' farmland using behaviors.

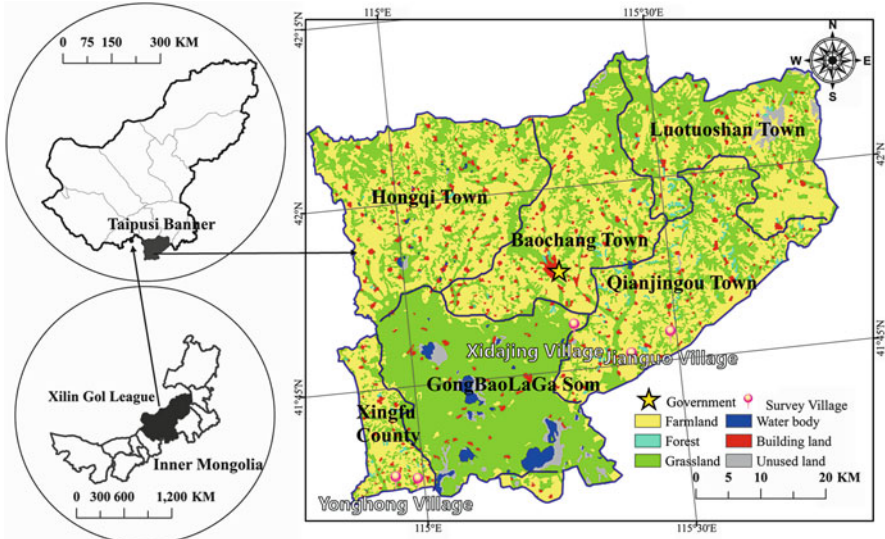


Fig. 112.1 Geographic location and land cover of Taipusi Banner (LUCC data in year 2000 are from the Data Center for Resources and Environmental Sciences, Chinese Academy of Sciences)

112.3 Research Data and Methods

This study uses questionnaire data gathered from households on the spot and statistical data on socioeconomic development. Questionnaire surveys can be used to obtain household information related to population and economic structure, means of livelihood, and farmland use.

Questionnaire surveys were carried out in July of 2011. Study villages' information is listed below (Table 112.1), and 161 households were interviewed. Questionnaires include three parts: (1) basic socioeconomic characteristics of households and their family members, for example, gender, age, job, and educational level; (2) farmland quality, current use and transfer, households' livelihoods' behaviors, sources of family income; (3) natural disasters and households' adaptive abilities.

In this paper, a statistical analysis technique is used to extract households' behavior rules based on questionnaire data. For ABM, the RepastJ toolbox and Java language are used to build a multiagent model platform for simulating households' farmland-use behaviors in a secondary development way.

Table 112.1 Basic information on villages surveyed in questionnaires

Village	Longitude (E)	Latitude (N)	Elevation (m)	Distance to center (km)	Number of questionnaires	Sample rate (%)
Jianguo	115°29'	41°47'	1,439	20	28	9
Jiuyingpan	115°24'	41°45'	1,421	15	36	12
Xidajing	115°18'	41°48'	1,446	10	19	13
Yonghong	114°57'	41°37'	1,418	50	40	17
Chongguang	114°59'	41°37'	1,390	45	39	17

112.4 Framework of Abandoned Farmland Model Based on ODD Protocol

Because theoretical research on ABM lags behind application research, Volker Grimm at the Leipzig-Halle Research Center in 2006 proposed the overview, design concepts, and details (ODD) protocol to describe a standard ABM [8]. He updated this protocol in 2010 [9]. This study describes ABM in abandoned farmland by households according to the ODD protocol (Table 112.2).

112.5 Main Model Components

112.5.1 Configuration of Running Environment

This study takes the RepastJ toolbox as the modeling tool and uses Java to construct an ABM platform in the Eclipse integrated development environment. Repast (Recursive Porous Agent Simulation Toolkit) is an agent modeling tool developed by Social Sciences Computing at the University of Chicago [10]. The initial running environment is land-use/land-cover data of a real geographical environment in the year 2010 with 100 m cell size. In the left panel of Fig. 112.2, the purple cells represent farmland, green cells represent grassland, red cells represent building land, blue cells represent water bodies, and white cells represent no data. In Fig. 112.2, middle, green cells represent planted farmland, pink cells represent abandoned farmland, and yellow cells represent rented farmland. In Fig. 112.2, right, in the parameter configuration window, some running parameters can be set initially by modelers.

Table 112.2 Structure of ABM of abandoned farmland in inner Mongolia based on ODD protocol

	Element of ODD protocol	Model description using ODD
Overview	1. Purpose	Simulating process and trend of farmland use in study area under the influence of socioeconomics, climate, and governmental policies in the next 30 years
	2. Entities, state variables, and scales	Entities: households and government; state variables: external–internal factors of households; scales: households—regional
	3. Process overview and scheduling	Decision making: farmland-use decisions, abandon or plant?; rule: profit maximization; model update: annually
Design concepts	4. Design concepts	Whether households abandon their farmland or not is related to the local environment, socioeconomic factors, and governmental policies. Households adjust their planting behaviors to adapt to changes based on profit maximization
Details	5. Initialization	Land cover of study area, internal factors of households in 2010
	6. Input data	Climatic factors, governmental policies (for related details see Table 112.3)
	7. Submodels	Agent-generating module, agent-classification module, and agent decision-making module

Table 112.3 Main input parameters of ABM and its initial value

Name	Meaning	Initial value	Source	Changing rule
averageLand	Farmland per person	0.39 hm ²	Questionnaire	Do not change
maxDeathAge	Life expectancy	65–100	Questionnaire	65–100
numAgents	Number of households	1,000	Statistical data	Do not change
numPerHousehold	Family size	5	Statistical data	3–8
everEarned	Income from migrant workers per person	11,000 yuan/year	Questionnaire	Increase by 1–10 %
subsidyGFG	Subsidy for green for grain	160 yuan/acre	Questionnaire	Do not change
subsidyFood	Food subsidy	30 yuan/acre	Questionnaire	Do not change

112.5.2 Behaviors and Properties of Agents

This model includes three types of agent. PersonAgent represents family members, householdAgent represent families, and governmentAgent represents a nation which is used to describe government policies.

The properties of PersonAgent include ID, age, gender, education, status (e.g., children, farmer, undergraduate, migrant workers, the elderly). The activities of personAgent include, for example, studying, producing, and going out for job.

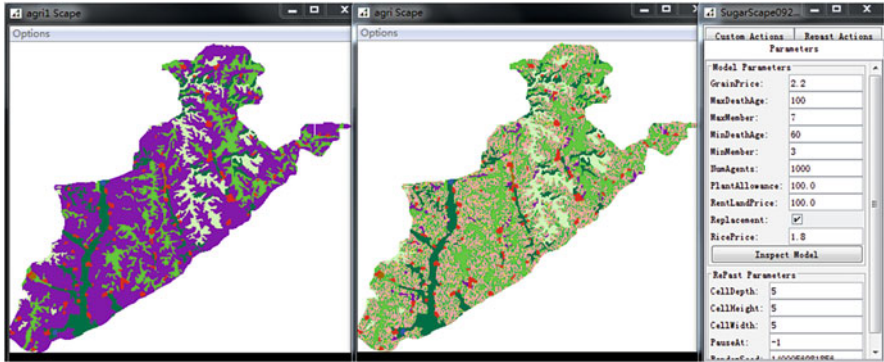


Fig. 112.2 Initial running interface (left), running interface at a specific time (middle), and parameter configuration window (right)

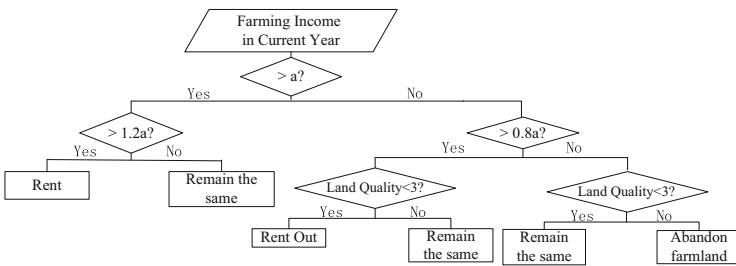


Fig. 112.3 Decision trees of household farmland-use behaviors

The properties of householdAgent include, for example, ID, family member, land, and family income. The activities of householdAgent include planting going out for job. The properties of governmentAgent include subsidy money and number of years of subsidies under the Grain for Green policy and food subsidies.

Based on questionnaires of people surveyed on the spot, this study obtains an average planting income for each household in 2010 of 1 yuan. Households adjust their planting decisions (rent, rent out, do not change, or abandon farmland) according to their planting income. The running rules of the model are displayed in a decision tree, as in Fig. 112.3.

112.6 Simulation Results

The model simulates changes in the number of current households that abandoned their farmland and population distribution of in the next 30 years. In this paper, the author analyzed five types of people: local workers, migrant workers, farmers, the elderly, and minors.

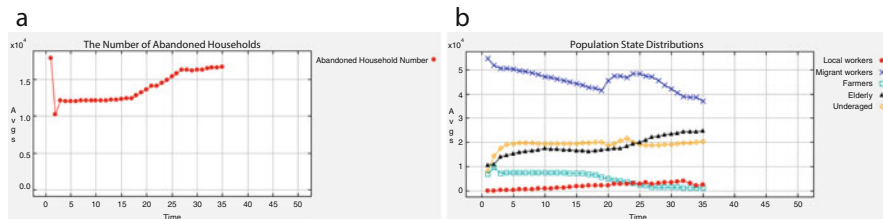


Fig. 112.4 Trends in number of abandoned households (a) and population distributions (b)

In Fig. 112.4, the x -axis represents the year, and the y -axis stands for the number of people. Figure 112.4a shows the number of households that abandoned their farmland remaining the same in the next 0–15 years. But in 15–26 years, the number of such households shows an increasing trend. Figure 112.4b shows that, in the next 0–15 years, the number of farmers will remain the same. But in 15–30 years, this number shows a decreasing trend. This changing pattern complements the trend of households abandoning their farmland. The number of migrant workers first shows a decrease and later an increase. The number of local workers does not obviously change, but there is a slightly increasing trend. The number of elderly people and minors shows a clear increasing trend.

On the basis of Fig. 112.4 we arrive at the conclusion that, under current conditions, a large proportion of farmland will be abandoned, and the composition of the population in the study area will be made up of elderly and young people.

The Grain for Green policy provided households with some financial support. This support caused some farmers to minimize their dependence on farmland and, to some extent, minimize the number of farmers. But the direct grain policy did not arouse the enthusiasm of households for planting farmland. This strategy needs to be adjusted; otherwise, more farmland will be abandoned in the future.

Conclusion and Discussion

The ABM represents a combination of a complex adaptive system and distributed artificial intelligence and has been applied and popularized in the area of LUCC. This paper adopts the ABM as the modelling method, simulates the process of changing land-use behaviors by households under current natural factors, socioeconomic factors, and national governmental policies and predicts changes in trends in decision making regarding farmland use by households in the next 30 years. The simulation results show that if the current situation continues, more farmland will be abandoned. The government’s Grain for Green policy has a negative impact on households’ willingness to plant, but the policy of direct subsidies for grain has not motivated households to plant. To change this severe situation with respect to farmland

(continued)

(continued)

use, households' awareness of the importance of planting needs to improve, and guidance is also needed on government policies.

The operating rules of this model are simple, for example, neglect state transfer mechanisms of households and family members and climate hazard factors. Households' decisions may have irregularities in this phenomenon, i.e., different households make the same decisions while the same households make different decisions. What's more, topographical factors, which may include spatial heterogeneities, are not included in this simulation. Last but not least, more multivariable and and multiscenario analyses will need to be conducted in the future.

Acknowledgments This work was supported by a special international cooperation program of the Ministry of Science and Technology (ID: 2013DFA91700) and the National Natural Science Foundation of China (41071344).

References

1. Cai Y, Fu Z, Dai E. Minimum per cultivated area regionally and farmland resources regulation. *J Geogr Sci.* 2002;57(2):0127–34 (in Chinese).
2. Munroe DK, van Berkel DB, Verburg PH, et al. Alternative trajectories of land abandonment: causes, consequences and research challenges. *Curr Opin Environ Sustain.* 2013;5(5):471–6.
3. IGBP Secretariat. *Global land project: science plan and implementation strategy.* Stockholm: IGBP Secretariat; 2005. p. 64.
4. Matthews RB, Gilbert NG, Roach A, et al. Agent-based land-use models: a review of applications. *Landsc Ecol.* 2007;22(10):1447–59.
5. Balmann A. Farm-based modelling of regional structural change: a cellular automata approach. *Eur Rev Agric Econ.* 1996;24(1):85–108.
6. Chen H, Wang T, Liang X. Building and simulation of households' land use based on multi-agent modeling. *J Geogr Sci.* 2009;64(12):1448–56 (in Chinese).
7. Pan L, Huang H. Application of artificial society model to study of land use change. *J Syst Simul.* 2010;22(8):1965–9 (in Chinese).
8. Grimm V, Berger U, Bastiansen F, et al. A standard protocol for describing individual-based and agent-based models. *Ecol Model.* 2006;198(1):115–26.
9. Grimm V, Berger U, DeAngelis DL, et al. The ODD protocol: a review and first update. *Ecol Model.* 2010;221(23):2760–8.
10. Repast CN. An extensible framework for agent simulation. *Univ Chicago Soc Sci Res.* 2003;36(1):1–18.

Chapter 113

Parallel Parity Scheme for Reliable Solid-State Disks

Jianbin Liu, Hui Xu, Hongshan Nie, Hongqi Yu, and Zhiwei Li

Abstract Recently, solid-state disks (SSDs) have been extensively applied in many fields. However, with increasing storage density in SSDs, a liability problem has emerged as a significant restriction. A parallel parity scheme is proposed in this paper. This scheme employs a mapping table based on a physical block address and a partial delayed parity update. Experimental results demonstrate the proposed scheme not only improves the reliability of SSDs, but also enhances their performance.

Keywords SSD • Reliability • Erasure code • Parity scheme

113.1 Introduction

With the development of solid-state disk technology, more and more people are choosing SSDs for storage memory. At present, three kinds of NAND Flash memory are used to build SSDs: SLC (single-level cell), MLC (multi-level cell), and TLC (triple-level cell). SLC flash memory has high performance and reliability, MLC flash memory has middling performance and reliability, while TLC flash memory has low performance and reliability. Manufactures prefer to use the denser MLC and TLC options rather than SLC in the commercial market. With the increasing capacity of SSDs, their reliability has become an increasingly serious problem.

Previous research on the reliability of SSDs has focused on error correct codes (ECC), which can ensure that fault tolerance is less than several bits in each page. Because of the structure of flash memory, the error rates of each bit are related to each other [1], so the traditional method of calculating the UPER (uncorrectable page error rate) is not accurate. When a bit is in error, the probability of error in adjacent bits is greatly increased. This has posed a great challenge for the ECC algorithm which only has limited error correction ability. In the face of low reliability flash memories such as MLC and TLC, SSDs need a more complex algorithm to ensure a certain reliability. In the case where a full page or full block has failed, even the most complex ECC algorithm is useless.

J. Liu (✉) • H. Xu • H. Nie • H. Yu • Z. Li
National University of Defense Technology, 410073 Changsha, China
e-mail: liujianbin08@163.com

113.2 Related Work

As the data concurrency model in SSDs is similar to that in RAID (redundant array of independent disks), erasure code technology from RAID began to be applied to intra-SSDs improving the reliability of such SSDs. Erasure codes are divided into RS (Reed–Solomon) codes, array codes, and LDPC (low-density parity-check codes). Five indexes: fault tolerance, storage efficiency, encoding, decoding, and updating have been widely introduced in the evaluation of erasure codes [2]. Generally, fault tolerance and storage efficiency are contradictory, namely, higher fault tolerance implies lower storage efficiency. As data cannot be updated in the original address in SSDs, those data as well as erasure codes should be updated elsewhere. Taking into account the relationship between original data and erasure, array codes and LDPC are not suitable for erasure codes in intra-SSDs.

In the design of SSDs, normally a multichannel parallel structure was put into use, which could resemble RAID-0. Thus, in order to enhance the reliability of SSDs, application of higher RAID levels including RAID-1, RAID-2, RAID-3, RAID-4, RAID-5, RAID-6, etc., was the next logical step to consider. Because of the characteristics of the “erase-before-write” feature of flash memory, data cannot be updated in-place. Applying RAID technology directly will lead to a great overhead, so a fine parity scheme and an efficient data updating method are desirable to give a positive answer.

Greenan et al. [3] proposed a RAID-4 SSD architecture which was normally accompanied with an NVRAM (non-volatile RAM) to hold the parity temporarily. It reduced the frequent parity updates for write requests and achieved the function of recovering data from a failed chip (die, block, page). On the basis of such a method, Soojun et al. [4] proposed a RAID-5 SSD architecture which improved the performance of SSDs. However, Soojun did not get rid of the burden (NVRAM), which manufacturers will not pay for.

In this paper, we propose a novel parallel parity scheme for flash memory SSDs in order to enhance reliability. The parity data can recover the original data from either a failed page or a failed block by exploiting the intra-SSD erasure code. Moreover, through establishing parity based on a physical block and using the partial delayed parity update, our method could solve the overhead problem caused by data updating.

113.3 Parallel Parity Architecture

113.3.1 Creating Parity

We consider a SSD with N channels as shown in Fig. 113.1. The SSD architecture stripe is the stripe of erasure codes, and the page in flash is the element of erasure codes. One SSD architecture stripe generally consists of N pages. In order to

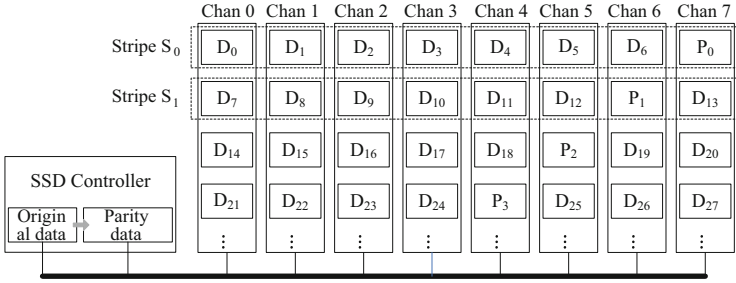


Fig. 113.1 SSD architecture with eight channels

guarantee fault tolerance more than 1, N channels at least contain one parity channel even if we use MDS (Maximum Distance Separable) codes, which can provide the highest space efficiency. So $N - 1$ channels are used for writing data, and the remaining one is used for writing parity data at the same time.

In the first step, if the SSD receives a request that the host needs to write data equaling K ($K \geq N - 1$) pages, the SSD controller writes $N - 1$ pages of data into channel registers. The SSD controller calculates a page of parity data through $N - 1$ pages of data which are then written into the remaining channel register. The next step is to write $N - 1$ pages of data and one page of parity data from the channel registers into flash memory. SSD repeats the above steps until K pages of data are written into flash memory.

There are N channels in a SSD and N pages in a stripe. The parity data are calculated with the XOR operation. The original data are denoted by $D = \{D_0, D_1, D_2, \dots, D_{k-1}\}$, while parity data are denoted by P . The mathematical formula for generating parity data is:

$$\begin{aligned}
 P_0 &= D_0 \oplus D_1 \oplus D_2 \oplus \dots \oplus D_{n-2}, \\
 P_1 &= D_{n-1} \oplus D_n \oplus D_{n+1} \oplus \dots \oplus D_{2n-3}, \\
 &\vdots
 \end{aligned}
 \tag{113.1}$$

where the sign \oplus denotes an *exclusive or* (XOR) function, which is simple to realize in the SSD controller, being only the equivalent of a bitwise sum.

If the original data are small data $D = \{D_0, D_1, \dots, D_{k-1}\}$ ($k < (n - 1)$), we adopt a partial delayed scheme to generate parity. In the same way, we dispose of the tail of the bulk data. The data to be written are:

$$P' = D_0 \oplus D_1 \oplus \dots \oplus D_{k-1}.
 \tag{113.2}$$

After the SSD controller writes D into the channel registers, temporary parity data can be calculated and written into the SSD cache. When another data item

$D' = \{D'_0, D'_1, D'_2, \dots\}$ is waiting to be written, we pieced D' and D into one. The parity data P' are updated to P'' :

$$P'' = P' \oplus D'_0 \oplus D'_1 \oplus \dots \oplus D'_{n-k-3}. \tag{113.3}$$

Finally, the complete stripe $D + D' + P''$ is generated. We adopt a delayed scheme to generate parity data if data are written twice in the same super block. According to the partial principle and flash management scheme, the partial delayed scheme is efficient in most cases.

113.3.2 Updating

Data cannot be overridden in SSDs, but the host doesn't know this due to the FTL (flash translation layer). So the problem of parity data updating caused by data updating does not exist in SSDs. If parity data is created based on a physical block address, the updating problem can be readily solved. On the basis of such an idea, a parity scheme based on a physical block address is proposed. FTL adopts a super-block mapping table. N blocks form a super block via a parity relationship. The mapping table for parity is built upon physical blocks and the mapping table of pages is built in a super block according to the order in the blocks. The mapping table is generated when blocks are allotted, and the mapping table is updated when Garbage Collection and Bad Block Management are part of the process.

In our algorithm, when a block containing many dirty pages is to be collected, dirty pages cannot be discarded, because the parity needs to be built between dirty pages and valid pages. The mapping table for parity is the tie that binds N blocks together. So the super block is the smallest garbage collection unit, valid pages are abstracted, and new parity data are generated. Afterwards, the mapping table for parity is updated (Fig. 113.2).

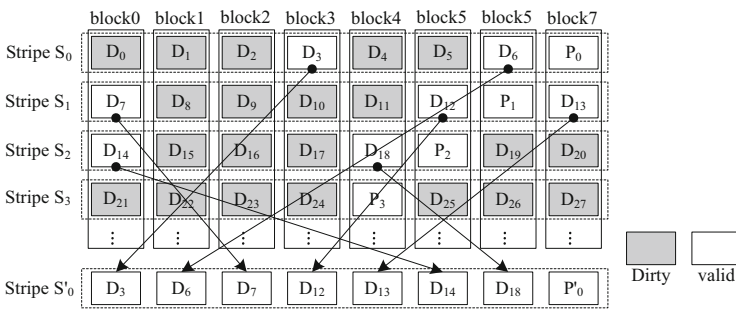


Fig. 113.2 Garbage collection

113.3.3 Recovery

When the SSD controller reads data from flash memory, a failure may occur due to bit roll-over, a page-level error, a block-level error, a die-level error, a chip-level error, or a channel-level error. When the error occurs, the steps shown in Fig. 113.3 are to be taken. If the error cannot be corrected by ECC, the algorithm we propose works. Parity data are generated through the formula:

$$P_0 = D_0 \oplus D_1 \oplus D_2 \oplus \dots \oplus D_{n-2}. \tag{113.4}$$

If the data D_i cannot be read as a result of a channel-level error, but it can be recovered from other data, then the recovery formula is:

$$D_1 = D_0 \oplus D_2 \oplus D_3 \oplus \dots \oplus D_{N-1} \oplus P_0. \tag{113.5}$$

The algorithm tolerates one channel-level failure in the worst case.

113.4 Experiments and Results

To evaluate the proposed scheme, we implemented an open-source SSD simulator (SSDsim), which was developed by Huazhong University of Science and Technology. SSDsim has accurate, modular, configurable characteristics. The platform

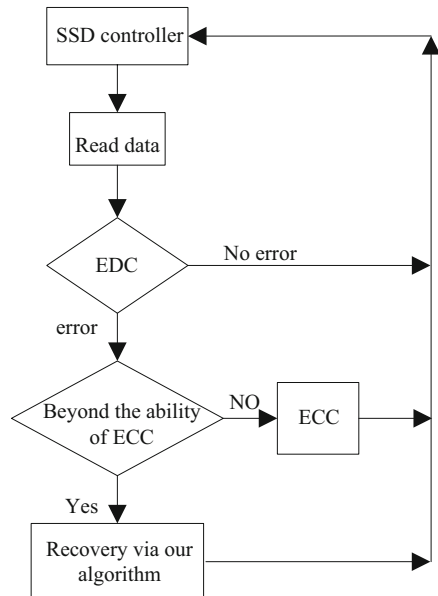


Fig. 113.3 The process of recovering from a failure

consists of eight channels and 32 chips. There are 4,096 blocks in a chip, 2,048 Bytes in a page. Grouping comparison was adopted. Methods can be divided into four groups: no parity scheme, RAID-5 scheme, the Qin scheme [5], and our scheme. We used two real disk I/O traces, pcNTFS and Financial. pcNTFS was collected on a desktop system through execution of several applications such as moving, web browsing, games, etc. Financial is an OLTP application trace [4]. We used two traces in three schemes to evaluate the proposed scheme.

113.4.1 Recovery Tests

In recovery mode, the worst situation occurs when one of N channels fails. When the host sends a request to read channel 1, the data consisting of all zeros are returned. In this way, we simulated one channel-level failure. The next step, the data recovery process, was shown in Fig. 113.3. Since the eight channels are equal, there is no harm in assuming that channel 1 had failed. The results of our experiments showed that the failed data can be recovered through the proposed scheme.

113.4.2 Read and Write Speed

We evaluated the performance penalty of the parity scheme in SSDs. Figure 113.4 shows the response time of both a read operation and a write operation in five modes with two traces. The no parity scheme is seen as the benchmark; the write response time of the RAID-5 scheme increased by 13.37 %, the Qin scheme by 14.04 %, and our scheme increased by 14.06 %.

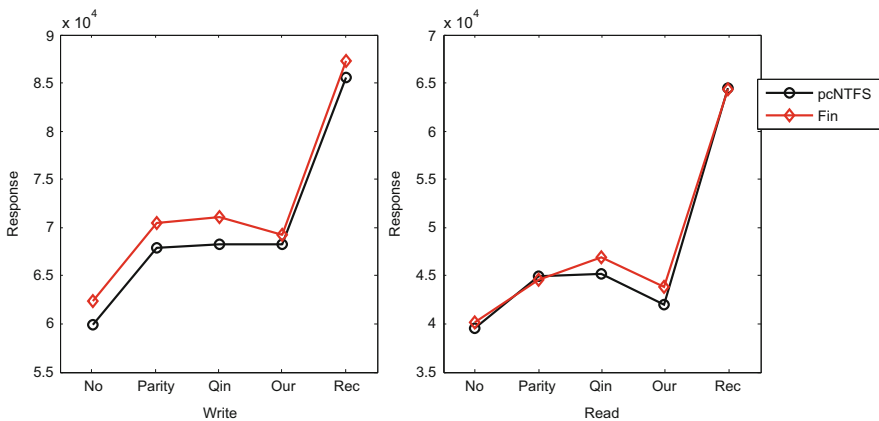


Fig. 113.4 Read and write response times

The read response time of the RAID-5 scheme increased by 13.51 %, the Qin scheme by 14.34 %, and our scheme increased by 6.12 %. The reason for the time increases is that the number of channels decreased; one of the channels was used to write parity data at all times. In the recovery mode of our scheme, the write response time increased by 43.03 %, and the read response time increased by 63.09 %. The incremental increase of the write response time is obviously less than that of the read response time. This result is related to the fact that the read process requires more basic operations in recovery mode.

In our scheme, the read operation was optimized. The SSD controller only reads the original data, and skips the parity data. The results demonstrated that in comparison with the no parity scheme, the read response time in our scheme increased slightly.

Conclusion

We achieved data reinforcement with limited resources. The algorithm can tolerate one channel-level failure as a worst condition. In the case of a failed chip, SSDs work properly. We solved the data updating problem through a mapping table based on a physical block address, and reduced the overhead of data updating. We reduced the SSDs WA (write amplification) coefficient, and improved their performance.

The inadequacy of the proposed algorithm is that we did not consider the variable reliability of flash memory. The reliability of flash memory will be reduced with an increased P/E circle, so a simplex fault tolerance may be a waste of resources during this initial time. To solve this problem, an algorithm with alterable fault tolerance would represent the next step.

References

1. Cai Y, Haratsch EF, Multu O, et al. Error patterns in MLC NAND flash memory: measurement, characterization, and analysis. In: Design, Automation & Test in Europe Conference & Exhibition (DATE), 2012. Los Alamitos: IEEE; 2012. p. 512–26.
2. Luo XH, Shu JW. Summary of research for erasure code in storage system. J Comput Res Dev. 2012;49(1):1–11 (in Chinese).
3. Greenan K, Kevin M. Building flexible, fault-tolerant flash-based storage system. In: The 5th Workshop on Hot Topics in Dependability (HotDep'09); 2009; Lisbon, Portugal.
4. Im S, Shin D. Delayed partial parity scheme for reliable and high-performance flash memory SSD. In: 2010 I.E. 26th Symposium on Mass Storage System and Technologies (MDDT). Washington, DC: IEEE; 2010. p. 1–6.
5. Qin Y, Feng D, Liu J, et al. A parity scheme to enhance reliability for SSDs. In: 2012 I.E. 7th International Conference on Networking, Architecture and Storage (NAS). Xiamen: IEEE; 2012. p. 293–7.

Chapter 114

Design of Tibetan Latin Transliteration System in Unicode

Xiaoying Chen, Jinyong Ai, and Xiaodan Guo

Abstract This paper presents the design and implementation of a new Tibetan Latin transliteration system based on small set. Based on an analysis of small-set characteristics and knowledge of Tibetan orthography, this paper shows a Latin transliteration algorithm based on Unicode encoding and explains the strategies of the algorithm.

Keywords Tibetan • Latin transliteration • Unicode • Consonant placeholder

114.1 Introduction

The use of Tibetan Latin transliteration in Tibetology studies promotes the use and spread of Tibetan documents. With the rapid development of information processing technology of Tibetan, more and more Tibetan Latin transliterations of various Tibetan documents are playing a primary role in terms of text recognition and other studies in the information processing technology of national languages while resolving compatibility issues with respect to different types of encoding in machine reading. However, most studies of Latin transliteration schemes are based on large set. For example, Chen developed a Latin transliteration algorithm based on large character set in the research and implementation of Tibetan transliteration [1]. Meanwhile, in the methods of Tibetan Latin transliteration, with all of the main Tibetan Latin transliteration methods established, Jiang also emphasized factors that need to be considered in a Latin transliteration algorithm and put forward a new Tibetan Latin transliteration algorithm [2]. However, the new algorithm represents an improvement in theory only rather than in implementation. In the standard model for Tibetan Latin transliteration of the international coding standard (2008), Qi put forward a new model that represented a method of converting long strings of

X. Chen (✉) • X. Guo

Information Engineering Institute, Tibet University for Nationalities, 712082 Xianyang, China
e-mail: ajycyt@126.com

J. Ai (✉)

Library, Tibet University for Nationalities, 712082 Xianyang, China
e-mail: 80508389@qq.com

Tibetan characters into Latin transliterations but failed to provide details about the algorithm [3]. At present, with more and more scholars preferring an input system based on small-set, most of electronic resources for Tibetan news and research are constructed using small sets. This paper describes some studies on a small-set encoding system and puts forward a Tibetan Latin transliteration system based on Microsoft Windows.

114.2 Structure and Encoding Characteristics of Modern Tibetan

114.2.1 Structure of Tibetan

Tibetan is a kind of alphabetical language with its characters coming from Sanskrit letters. Tibetan has 30 basic consonant characters and five vowel characters. Of these, each of the consonant characters can stand alone as a word, but the vowel characters must appear in words with the consonant characters. Tibetan word are separated by a syllabic sign, །, sentences are separated by a single vertical mark, །, and paragraphs are separated by a double vertical mark, །།. Every Tibetan syllable is composed of so-called basic character, superfix, subfix, prefix, suffix and tail suffix, and vowels; at the same time, the written language is read from left to right and top to bottom, with the sequence of prefix, basic character, suffix and tail suffix as the former's order with the sequence of superfix, basic character, subfix and vowel as the latter's order. Each Tibetan character is considered a widget. Every widget has its own construction and its position can be vacancy except for a basic character.

114.2.2 Encoding Characteristics of Tibetan

There are two methods of Tibetan information processing technology based on two different encoding systems. One is the national standard encoding system, which is a large set that shows Tibetan words as vertical combinations; the other is the international standard encoding system, which is a small set that shows Tibetan words as dynamic combinations. The large-set encoding system considers up-add characters and down-add characters as a whole. Such a processing method could lead to a large number of compatible character strings that add complexity to a system because the system needs to dynamically compose up-add characters, down-add characters, basic characters, and vowels into a Tibetan word. In addition, the large-set encoding system must the large character set encoding system must finish all of the pre-composing, which may make the system incompatible. Within all operating systems, the small-set encoding system processes all Tibetan words as alphabetic writings by considering all Tibetan characters such as vowels,

consonants, and additional characters as the basic encoding characters. Such a processing method highly conforms to all ISO evaluation processes and principles; at the same time, it is also currently the most popular international Tibetan encoding system.

114.3 System Structure

Figure 114.1 shows the structure of modern Tibetan Latin transliteration. Functionally, the whole system of modern Tibetan Latin transliteration integrates the management and maintenance of Tibetan structure knowledge base, Tibetan text preprocessing, and four modules of Latin transliteration. We can see each module's function and implementation.

114.3.1 Preprocessing of Tibetan Texts

While the other concerns the separation and reduction of affixed words aims at obtaining normalized Tibetan characters by processing the special parts of modern Tibetan, which consists of two parts. One part concerns the standardization of

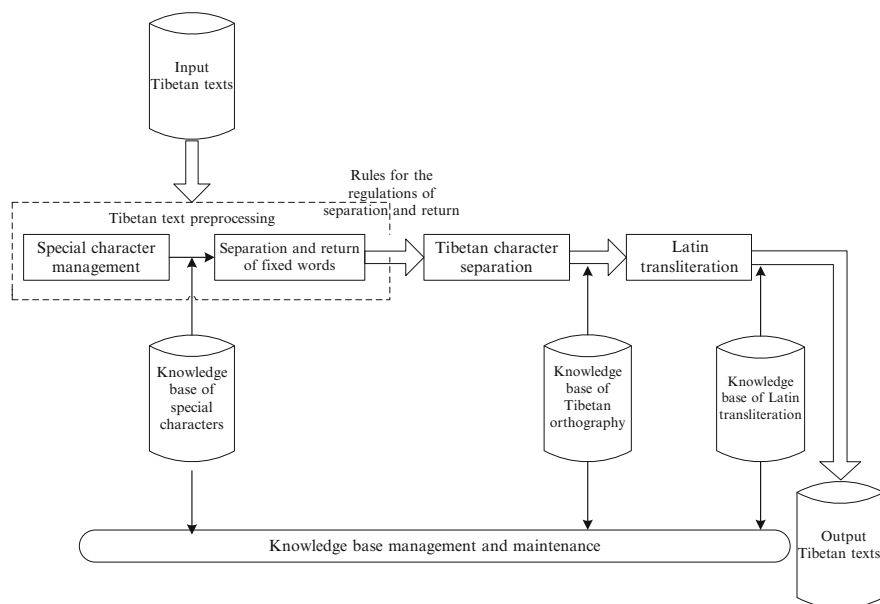


Fig. 114.1 Flowchart of Tibetan Latin transliteration

special Tibetan characters, while the other concerns the separation and reduction of affixed words.

114.3.1.1 Standardization Management of Special Tibetan Characters

In Tibetan texts, except for normalized Tibetan characters, there are some contraction of English vocabularies, short and simple words, numbers, and symbols that are different from Tibetan characters that will affect the processing, so some steps must be taken in terms of standardization before Latin transliteration. Those steps involve summerizing the types of nonnormative Tibetan characters, then establishing the transliteration rules and the corresponding knowledge base.

114.3.1.2 Separation and Return of Affixed Words

In classical Tibetan, separators appear between two words; in modern Tibetan, the separator has been omitted for the sake of convenience [4].

Certain case-auxiliary words, continuative words and end words may be affixed to suffix or basic character to compose a one-syllable word [5], although such structures do not conform to Tibetan orthography, they are considered correct in written form. Thus, it is necessary to do some separating on such occasions. The common ly affixed words in Tibetan texts include (1) the genitive auxiliary word “ེ”, (2) the continuative word “ལ”, (3) the separator word “ལ་”, (4) the end word “ེ”, and (5) the case-auxiliary words “ེ” and “ེ” [6]. The processing of these affixed words depends on the Tibetan character’s formation to design adaptive specifications. It highlights a correct rate of 99.3 % based on an analysis of experiments whose results are shown in Table 114.1.

114.3.1.3 Separation and Return of Affixed Words

In Table 114.1, we use the letter *S* to represent the dissociated form and the letter *SR* to represent the return form.

114.3.2 Management and Maintenance of Knowledge Base

The main function is to maintain and manage the normalization and management of three knowledge bases which are designed by Latin transliteration system. This means the improvement and maintainance of Tibetan orthography knowledge base, special symbol converting rules, and Latin transliteration knowledge base, thus making data calling and management effective.

Table 114.1 Results of separation and return of affixed words

Auxiliary word	Original form	English meaning	Dissociated form	Return form
འི	ངའི་ཕྱགས་བསམ།	My dream	ང་འི་ཕྱགས་བསམ།	
	ནམ་མཁའི་སྐར་མ།	Star	ནམ་མཁའི་སྐར་མ།	ནམ་མཁའི་སྐར་མ།
འང་	ང་ལ་འང་དགོས།	I want it too	ང་ལ་འང་དགོས།	
འམ	འགྲོ་འམ་ཐོང།	Walk or sit	འགྲོ་འམ་ཐོང།	
མོ	མེས་པ་དགའོ།	Happy	མེས་པ་དག་འོ།	མེས་པ་དགའ་འོ།མ།
འིས	ངས་བཤད།	I say	ང་ས་བཤད།	
ར	ཉན་པར།	Listen	ཉན་པ་ར།	

114.3.3 Separation of Tibetan Characters

114.3.3.1 Characters of Small-Set Encoding System

The small-set encoding system is designed for the encoding of basic Tibetan characters. In the course of the encoding process, different basic Tibetan characters will dynamically comprise a whole word horizontally or vertically [7]; however, the width of all the vertical basic character strings is equal to that of one character in the show process, and such a character width mainly depends on the first consonant of the vertical character string, with the first consonant known as an occupying consonant and its corresponding code known as an occupying consonant encode. Because other consonants of the vertical character string do not occupy any space, they are called nonoccupying consonant codes [8]. The vowel character is up or down in relation to the consonant character, so it does not occupy any space either. Because it is possible or impossible for each consonant to be an occupying consonant encode, each of them occupies or does not occupy two encoding standards. For example, in མ the consonant མ is an occupying consonant character, whose code is U+0F63; but in མམ, the consonant མ is not an occupying consonant character, and so the code is different. In Tibetan, all the pre-add, after-add, and final-add characters could occupying consonant characters, but the basic character and the vowel could not; in this sense, the separation of each Tibetan syllable could use such a character forming mechanism and locate one basic character from all the codes.

114.3.3.2 Separation of Tibetan Characters

The key to the separation of Tibetan characters is to find the basic character, which can be done using the character-formation rule of Tibetan syllables and the features of a small-set encoding system.

Define the letter C as an occupying consonant encoding set, the letter V as an occupying vowel encoding set, NC as a nonoccupying vowel encoding set, and the letter U as the down-add character set, which belongs to NC. At the same time, define a syllable's encoding string as $l1l2, \dots, ln(1 = <n \leq 7)$, the occupying encoding string as $C1C2, \dots, Cm(1 = <m \leq 4)$, and the nonoccupying encoding string as $NC0NC2, \dots, NCK(0 = <k \leq 2)$. In the nonoccupying encoding string, $k=0$ indicates that there is no occupying consonant in the syllable's encoding string. In the occupying vowel encoding string, $t=0$ indicates that there is no occupying vowel in the syllable's encoding string. As defined previously, associating with the features of a small-set encoding system and Tibetan orthography, the recognition algorithms are as follows:

Input the syllable encoding string $l1l2, \dots, ln$ using string-match methods to find the strings $C1C2, \dots, Cm, Vt$ and $NC0NC2, \dots, NCK$ in sets C, V, and NC. With the value of k , the position of the basic character and other parts' characters can be obtained:

1. When $k = 2$, the nonoccupying consonant encoding string of the syllable is $NC1NC2$. With the features of a small-set encoding system, this ensures that the combining characters contain the up-add character and the down-add character; then with the Tibetan output order, it ensures that the nonoccupying consonant $NC0NC2$ is the basic character *Ba*, and the down-add character is *Up*. Thus, the position of the basic character can be obtained.
2. When $k = 1$, the nonoccupying consonant encoding string of the syllable is $NC1$, and it is necessary to use Tibetan character formation to recognize whether $NC1$ is a basic character or a down-add character. First, determine whether or not $NC1$ belongs to set U. In Tibetan character display, as a down-add character, the code of the character ལ་ཅན་ལོ་ is different from that of the combining characters; meanwhile, in Tibetan orthography, another down-add character, ལ་, cannot be combined with an up-add character. As a result the judgement can only determine whether $NC1$ belongs to the suffix character set; if so, then NC will be the basic character *Ba*, or its occupying consonant must be the basic character *Ba* [9]. If it is different from the two aforementioned situations, it can also ensure that $NC1$ is the basic character *Ba*.
3. When $k = 0$, there is no nonoccupying consonant encoding string in the syllable, which means that there are no up-add or down-add characters in the Tibetan syllable. Thus, it is necessary to make sure the basic character's position based on the position of vowel character. When $h > 0$, the consonant character before the vowel is the basic character. When $t = 0$, it is necessary to use the width of the syllable to judge the basic character, specifically, in Tibetan orthography to analyze and obtain the basic character *Ba*.

After the basic character string *Ba* is determined, the positions of all the other characters' that belong to the combining characters when *Ba* belongs to NC set can be determined. If *Ba* belongs to the NC set, then the following occupying consonants are after-add and final-add characters. And the character that is closest to the consonant must be an up-add character; if a character is also in front of an up-add

character, then it must be a front-add character; in other circumstances, there are no up-add characters in Tibetan syllables; there are front-add characters in front of occupying consonants and after-add and final-add characters subsequently. Then, different character codes of the combining character can be obtained with the foregoing results.

114.3.4 Rules of Latin Transliteration

The Tibetan Latin transliteration system aims at converting Tibetan characters into Latin characters. Regarding the information processing technology of Tibetan, Latin transliteration is a very important tool in terms of the recognition and study of modern Tibetan. In this paper, each Tibetan syllable is a basic unit. All of them are taken to carry out Latin transliteration with its own structures so that the project of initial consonant and vowel transliteration of modern Tibetan can be realized. During transliteration, some key rules must be followed. Rule 1: read each part of the Tibetan syllable according to the method of spelling initial consonants and vowels; then take the transliteration with initial consonants and vowels from a Latin transliteration table. Rule 2: all marks are shown as small letters following Latin transliteration. Rule 3: a syllable without a vowel character must be considered as a syllable with an “a,” and the vowel “a” is located in front of vowels. Rule 4: if a syllable contains any vowel characters, translate the basic character ■ as “a,” and the whole syllable is deemed as zero initial.

Upon processing all parts of the combined characters according to the preceding rules, the following steps are followed to combine initial consonants and vowels with Tibetan syllabic structures, that is, in a single syllable, initial consonant = front-add character + basic character (without vowel), vowels = vowel + after-add character + final-add character. By contrasting the knowledge base of Tibetan Latin transliteration, corresponding Latin transliteration strings can be obtained with respect to each of the Tibetan initial consonants and vowels.

Conclusion

This paper focuses on a method of carrying out Tibetan Latin transliteration based on small-set encoding. In this paper, the rules of Latin transliteration depend on the combination rules of initial Tibetan consonants and vowels. The core of such rules is changing the contrast tables, the contrast table between initial Tibetan consonants and Latin transliteration the contrast tables of initial Tibetan consonants to Latin transliteration and Tibetan vowels to Latin transliteration. With these two reference tables, Tibetan Latin transliteration can be achieved. At the same time, such a method can be easily

(continued)

(continued)

adapted for use in other relevant fields, for example, in the study of International Phonetic Alphabet Transliterations of different Tibetan dialects, the different dialects' International Phonetic Alphabet can be automatically generated, and reliable results can be achieved by simply changing the initial consonant base; however, some Sanskrit or foreign new words have structures that are different from that of modern Tibetan syllables. In that case, it will be necessary in the future to create and adopt other adaptive processing methods.

Acknowledgments This project is subsidized by the special funds of the Tibet Autonomous Region the Tibetan special funds program as research on method of automatic phonetic marking on modern Tibetan syllable (13BY001) and the school project of the Tibet University for Nationalities (13myQ18).

References

1. Chen L. Research and implementation of Tibetan transliteration. *Comput Eng Des.* 2006;27(1):15–7.
2. Jiang D. The methods of Tibetan Latin transliteration: and the transliteration process for Tibetan in computer. *Minority Lang China.* 2006;1(1):45–53.
3. Qi K. The standard model for Tibetan Latin transliteration of the international coding standard. *J Northwest Univ Nationalities.* 2008;29(3):15–7.
4. Caidanxiarong. The introduction of Tibetan grammar. Xining: Qinghai Nationalities Publishing House; 1998. p. 35–40.
5. Guan B, Caikezhaxi K. Research on modern Tibetan syllables word automatically proofreading. *Comput Eng Appl.* 2012;48(29):151–6.
6. Caizhijie Z. Identification of abbreviated word in Tibetan word segmentation. *J Chin Inf Process.* 2009;23(1):35–43.
7. Zhaxiciren. The study of international standard encode set for Tibetan. *China Tibetology.* 1995; 2(2):127–43.
8. Huang X, Huang H. The division and determination of modern Tibetan syllables. *Comput Appl Softw.* 2012;29(9):62–5.
9. Zhou J. The tutorials of Tibetan spelling. Beijing: China Ethnic Publishing House; 1983. p. 80–90.

Chapter 115

Graphical User Interface Reliability Prediction Based on Architecture and Event Handler Interaction

Zhifang Yang, Sanxing Yang, Zhongxing Yu, Beibei Yin,
and Chenggang Bai

Abstract Graphical user interfaces (GUIs) are becoming increasingly important in software development because they are user friendly. Thus, a well-developed GUI is an important factor for software quality, while the reliability of GUIs is a relatively young research field. The existing software reliability assessment techniques are based on particular assumptions and preconditions that are not suitable for GUIs. Compared with traditional software, the profile of a GUI is quite complicated, and so event interactions and event states make GUI reliability very complex. This paper introduces a model of GUI reliability and discusses related issues encountered in the modeling process. Then a simple case is introduced based on the GUI reliability model.

Keywords GUI reliability models • GUI testing • Event interaction

115.1 Introduction

Graphical user interfaces (GUIs) are becoming increasingly important in software development because users can easily interact with software via a GUI. Thus, a well-developed GUI is an important factor in software quality [1].

There already exists a substantial body of meaningful work on GUI testing [2, 4, 5]. These works demonstrate how to improve the reliability of GUIs. Despite this, the reliability of GUIs is a relatively young research field. Belli [1] provided experimental insight and preliminary results and analyzed the existing software

Z. Yang (✉) • Z. Yu • B. Yin • C. Bai
School of Automation Science and Electrical Engineering, Beihang University,
100191 Beijing, China
e-mail: qwyzf@163.com

S. Yang
Zhengzhou Institute of Aeronautical Industry Management, 450000 Zhengzhou, China
e-mail: tristaryoung@gmail.com

reliability assessment techniques (SRATs) in GUIs. This work is important in GUI reliability, while more characteristic of GUI should be considered:

First, GUI test data are scarce, so the reliability assessment techniques will prove helpful. Second, a GUI profile is quite complex. Predicting the effect of a GUI testing profile is an important issue in GUI reliability assessment. Third, compared with traditional software, the failure of a GUI does not lend itself to quantitative description. Analyzing the effect of different kinds of failure on GUI reliability assessment is quite complicated. Finally, information about GUI architecture, components, windows, and their interactions can be used to guide the testing process and establish a reliable assessment of a GUI.

This paper describes an effective GUI reliability model, discusses the reliability of the model structure, and presents the issues encountered in the modeling process. The background is introduced in Sect. 2, the models for GUI reliability assessment are described in detail in Sect. 3, and the analysis, construction process, and a case study of the model are discussed in Sects. 4 and 5.

115.2 Background and Related Work

115.2.1 Related Work

Much meaningful work has already been carried out on GUIs. White et al. [2, 3] and Belli [4] demonstrated a complete interaction sequence between a user and a GUI application under testing. Memon et al. proposed a model of an event flow graph (EFG) and several approaches guiding GUI testing [5–7]. Yang et al. introduced an approach to GUI testing guided by a Bayesian model that quickly identifies more defects than previous methods [8]. Furthermore, Zhao introduced a new model of event handler based on EFG that develops a new GUI testing framework [9].

A GUI is an interface to a program that is composed of a certain number of windows and components. With the various components of a GUI, Memon proposed an EFG instead of all the event interactions in a GUI, and subsequently Zhao proposed the event handler (EH) and event handler interaction graph (HIG), defined as follows [9]:

$$\langle H, RHI \rangle . \quad (115.1)$$

In this model, H is the set of all vertices in the EFG, each vertex is one EH, and RHI is the set of edges indicating EH interaction.

115.2.2 Main Window, Modal Window, and Modeless Window

A main window is a parent window that is opened upon the GUI's startup. It launches a parent window that stays active on the user's screen until the GUI is closed. It is hidden behind modal windows while the modal windows are being used.

A modal window is any type of window that is a child (secondary window) to a parent window. It is commonly used when the author wants to maintain the user's focus on the information of the modal window when the user cannot interact with the other windows of the same process.

Like modal windows, modeless windows launch secondary windows that stay active on the user's screen until they are closed; they can be minimized or hidden behind other windows. A modeless window allows users to continue working with an application while the modeless window is still open.

115.3 Event-Handler-Based Windows Interaction Graph

In this paper, we utilize EFG for path searching and HIG interaction as the coverage criteria to obtain the GUI test case. Thus, we adopt the GUI profile and HIG interaction [9] and define the windows Interaction Graph based on Event Handler, which represents real test process:

$$\text{EHWIG} = \langle H, W, E \rangle, \quad (115.2)$$

where H is a set of EHs in the GUI, and each $h \in H$ represents an EH in the GUI, $H = \{h\}$; W is a set of windows in the GUI, and each $w \in W$ represents a type of window in the graph, $W = \{w\}$; and E is a set of edges in the GUI, and each $e \in E$ represents an edge in the graph, $E = \{e\}$.

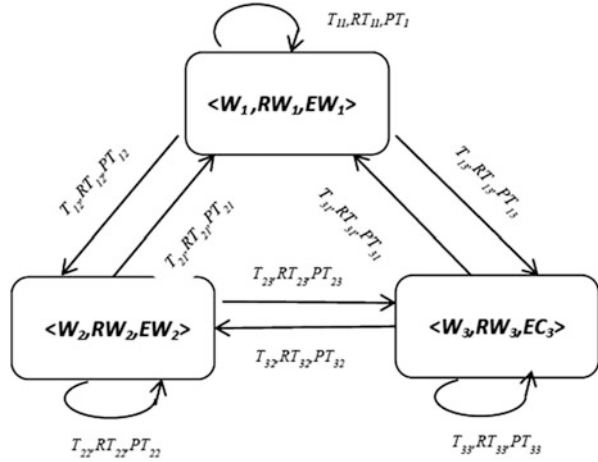
The node " w_i " is defined as $\langle W_i, RW_i, EW_i \rangle$. W_i is the i th type window in the graph, RW_i is the reliability of the EH-based i th type window in the graph, and EW_i is the average execution time of the i th type window in the graph. Note how many times the EH executes in the test process.

A directed edge e represents the execution path. As defined by $\langle T_{ij}, RT_{ij}, PT_{ij} \rangle$, T_{ij} is the transition from node n_i to n_j , RT_{ij} is the transition reliability, and PT_{ij} is the transition probability.

Now we define the EHWIG for GUI reliability assessment (Fig. 115.1).

We divide the input domain of the GUI into three equivalence classes belonging to three windows. It is given as follows:

Fig. 115.1 A real EH-based windows interaction graph for GUI reliability assessment



$$OP(\lambda) = \{ \langle W_i, P_{ij}, M_j \rangle, i = 1, 2, 3 \}, \tag{115.3}$$

where W_1 means that the EH belongs to the main window, W_2 means that the EH belongs to a modeless window, W_3 means that the EH belongs to a modal window, P_{ij} means that an input is selected from W_i with probability P_i in the j th state, and M_j means that the transition matrix from the j th state to the $j + 1$ th state. The [transition matrix](#) for this example is as follows:

$$P_{ij} = \begin{pmatrix} 0.9 & 0.075 & 0.025 \\ 0.15 & 0.8 & 0.05 \\ 0.25 & 0.25 & 0.5 \end{pmatrix}. \tag{115.4}$$

115.4 GUI Reliability Assessment Based on EHWIG

115.4.1 EHWIG Assessment Process

- Step 1. Divide the original test suite into three equivalence classes as three windows. It is given as previously: $OP(\lambda) = \{ \langle W_i, P_{ij}, M_j \rangle, i = 1, 2, 3 \}$.
- Step 2. The initialization parameter N , N means the test step, $n = 0$.
- Step 3. Initialize the failure detection rate parameter, $\theta^O = \{ \theta_1, \theta_2, \theta_3 \}$.
- Step 4. Construct the EHWIG and initializing parameters.
- Step 5. Record the results of testing, parameter learning, and data update according to the profile to select a number of test cases for testing.
- Step 6. Calculate the probability of execution of each window by estimating the frequency of execution of each window, and estimate the reliability of the windows (RW_i) and their average execution time (EW_i).

Step 7. Calculate the transition probability from one window to another for all functions (PT_{ij}), and estimate the transition reliability (RT_{ij}). For each function, calculate the execution time EW_i .

Step 8. $n = n + 1$; if $n < N$, return to Step 5; else, go to Step 10.

Step 9. Assess the reliability of the GUI according to Eq. (115.5):

$$R = \sum_{i=1}^k \sum_{j=1}^k RW_i * RT_{ij} * PT_{ij} * RW_j (EW_i + EW_j) / \sum_{i=1}^k kEW_i. \quad (115.5)$$

Step 10. Satisfy the test termination conditions and end the test.

115.4.2 Experimental Subject

In this paper, we use the open-source software *TerpPaint*, which is part of the *TerpOffice* series developed by Professor A.T. Memon and his students. It includes three windows, introduced in Sect. 2. In accordance with the function of this GUI, it is divided into five functions based on the nature of the GUI: File, Edit, View & image, Draw graph, and Filter & layer. The reliability model based on EHWIG relies on the five functions of *TerpPaint* introduced in Sect. 2. Obviously, each function shows different profiles involving three EH-based windows as introduced in Sect. 3 (Table 115.1).

115.5 Case Study

115.5.1 Reliability of Windows

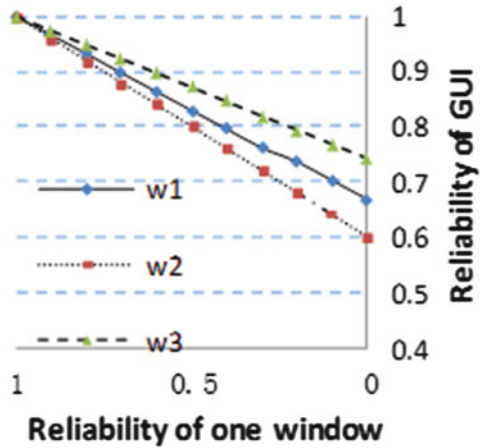
With the EHWIG assessment algorithm, we are able to investigate variations in the reliability of the windows. The graph in Fig. 115.2 shows the application reliability as a function of varying the reliability of one window, while the reliabilities of other windows are fixed at 1.0 for the sake of comparison.

Figure 115.2 shows that the reliability of three windows does not obviously vary with the variation (of one window at a time) because these windows are the core of the GUI and its profile is similar.

Table 115.1 Event-handler-based windows probabilities for five functions

EH-based windows	File	Edit	View & image	Draw graph	Filter & layer
W1	0.34	0.65	0.30	0.03	0.16
W2	0.20	0.08	0.06	0.94	0.23
W3	0.46	0.27	0.64	0.03	0.61

Fig. 115.2 Reliability of GUI as a function of windows



115.5.2 Reliability of Transition

The variation in the reliability of transitions (between different windows) is illustrated in Fig. 115.3. The reliability of a transition (one window at a time) fall within a range of 0 to 1, while the reliabilities of other components and transitions are fixed (equal to 1 for the sake of comparison).

Figure 115.3 shows that the transition reliabilities can significantly affect the reliability of the GUI; for example, the transition reliability $W_2 - W_2$ and $W_2 - W_3$ can significantly diminish the reliability of the GUI if there are mismatches or errors in the event interaction due to the nature of the GUI that GUI error usually found in event interaction.

115.5.3 Reliability of Five Functions

The change in the user considers GUI as a significant effect on the sensitivity of the GUI reliability because of different functions. Our model accounts for changes in five functions through the variations in the profile shown in Table 115.1.

As shown in Fig. 115.4, the sensitivity of GUI reliability to changes in the five functions varies with the usage profile. For example, the application reliability grows more sensitive to the reliability of the functions *View & image* and *Filter & layer*. *Draw graph* is considered a more important and foundational function of *TerpPaint* than the aforementioned functions because of its higher quality in terms of logic.

Fig. 115.3 Reliability of GUI and five functions

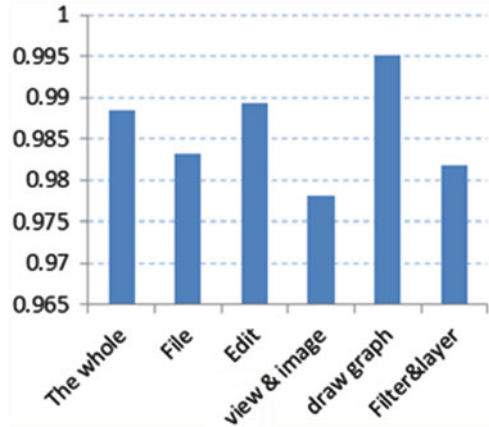
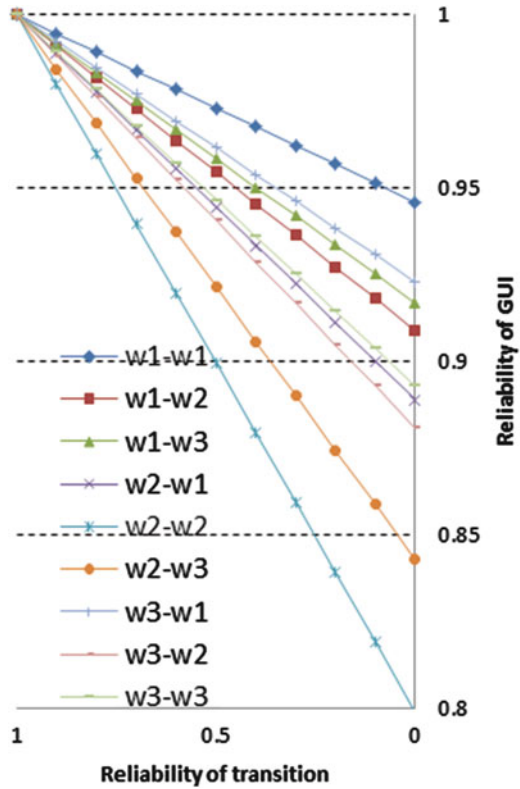


Fig. 115.4 Reliability of GUI as a function of transition (one at a time)



Conclusion

This paper describes an effective reliability model for GUIs and discusses the reliability model's structure as well as the issues encountered in the modeling process. As for the problem of a complex GUI architecture and information about the components, windows, and their interactions, we adopt a GUI reliability assessment based on EHWIG to guide the GUI reliability assessment process. Finally, a simple case study verifies the validity of the model during the GUI reliability assessment process. The model also reveals that GUI reliability changes significantly with different users having distinct purposes, which explains that GUI reliability is more complex than traditional software.

References

1. Belli F, Beyazit M, Guler N. Event-based GUI testing and reliability assessment techniques: an experimental insight and preliminary results. In: 2011 I.E. Fourth International Conference on Software Testing, Verification and Validation Workshops; IEEE Computer Society Press, Berlin, Germany; 2011. p. 212–21.
2. White L, Almezen H. Generating test cases for GUI responsibilities using complete interaction sequences. In: Proceedings of the 11th International Symposium on Software Reliability Engineering; IEEE Computer Society Press, San Jose, CA; 2000. p. 110–21.
3. White L, Almezen H, Alzeidi N. User-based testing of GUI sequences and their interactions. In: Proceedings of the 12th International Symposium on Software Reliability Engineering; IEEE Computer Society Press, Hong Kong; 2001. p. 54–63.
4. Belli F. Finite state testing and analysis of graphical user interfaces. In: Proceedings of the 12th International Symposium on Software Reliability Engineering; IEEE Computer Society, Hong Kong; 2001. p. 34–43.
5. Brooks PA, Memon AM. Automated GUI testing guided by usage profiles. In: Proceedings of the Twenty-Second IEEE/ACM International Conference on Automated Software Engineering; ACM, New York; 2007. p. 333–42.
6. Yuan X, Cohen MB, Memon AM. Towards dynamic adaptive automated test generation for graphical user interfaces. In: IEEE International Conference on Software Testing, Verification, and Validation Workshops; IEEE Computer Society Press, Washington; 2009. p. 263–66.
7. Yuan X, Cohen MB, Memon AM. GUI interaction testing: incorporating event context. *IEEE Trans Softw Eng.* 2011;37(4):559–74.
8. Yang ZF, Yu ZX, Bai CG. The approach of graphical user interface testing guided by bayesian model. In: Proceedings of the 2013 International Conference on Computer Engineering and Network. Lecture Notes in Electrical Engineering; Springer, Shanghai, China; 2013. p. 385–93.
9. Zhao L. GUI software testing based on event handlers. Beijing: Beihang University; 2010.

Chapter 116

An Energy-Efficient Dual-Level Cache Architecture for Chip Multiprocessors

Mian Lou, Longsheng Wu, Senmao Shi, and Pengwei Lu

Abstract As microprocessors begin to leverage multicore functionality, the power consumption incurred from tag comparison in a cache hierarchy of chip multiprocessors (CMPs) becomes greater. In this paper, a novel dual-level cache architecture is explored to reduce tag comparisons for mitigating power overhead. For one thing, a way-tagged L1 cache is adopted to access the L2 cache as a direct-mapping method during the write hits. Moreover, a combined multistep method is adopted to further reduce the L2 tag comparison with respect to both the cache hit and the miss predictions. With a simple predictor and the coherence status, a new prediction scheme for backward invalidation is proposed to compensate for the limitation of the two applied solutions in CMPs. Furthermore, a linear feedback shift register counter is exploited to replace traditional predictors to realize and optimize the proposed structure. Simulation results show that the proposed technique can reduce the total cache power consumption by an average of 49.7 % at the cost of acceptable performance degradation.

Keywords Multiprocessor • Cache • Power • Bloom filter • Linear feedback shift register

116.1 Introduction

The multilevel caches in chip multiprocessors (CMPs) are characterized by high switching power, especially due to the large amount of power consumed in tag-comparison operations [1]. In particular, the ever-growing usage and areas of application of the L2 cache may result in significant power consumption because of two factors. First, the L2 cache requires a high associativity to reduce conflict misses; second, the cache coherence for CMPs further increases the power consumed in tag comparisons.

M. Lou (✉) • L. Wu • S. Shi • P. Lu

Research Center of SoC, Xi'an Microelectronics Technology Institute, 710054 Xi'an, China
e-mail: citydremer@163.com; wls771@163.com; 515949659@qq.com; 623057652@qq.com

In this paper, with the combined use of two existing methods, we further propose a novel technique for designing a dual-level cache architecture, namely, L1 private cache and L2 shared cache. First, the technique can reduce the power consumption in an L1 tag comparison during backward invalidation. In addition, regarding the area overhead of the conventional predictors in L2 caches, we present an area-efficient structure. Accordingly, the proposed technique can be integrated with existing low-power cache design methods to further improve energy efficiency.

116.2 Related Work

116.2.1 Way-Tagged Cache

Many high-performance microprocessors employ a cache write-through policy to prevent the system from collapsing because of soft errors [2]; however, the write-through policy also incurs a large energy overhead because the data at all related levels of the cache hierarchy always remain consistent, and especially the lower cache is inclusive [3]. The basic idea of a way-tagged cache [4] is to maintain the way information of the L2 cache in the L1 cache during the read operations. This technique enables the L2 cache to directly locate the correct path during the write hits, which reduces power consumption significantly.

However, in an inclusive cache hierarchy, an evicted cache line in the lower cache needs to backward invalidate all the copies existing in the higher levels. It also requires all the L1 caches to execute tag comparisons, which results in a considerable amount of power.

116.2.2 Multistep Tag Comparison

To reduce tag comparisons within the L2 cache, the multistep tag comparison method [5] uses partial tag-enhanced counting Bloom filters (CBFs) to predict which L2 cache way owns the missing data from the L1 cache.

To estimate the liveness of the L2 cache line, a dynamic tracking method [5] associates one local 15-bit counter per cache line. If the counter is smaller than 1, the corresponding cache line is considered to be cold; nevertheless, the L2 cache is considerably larger than the L1 cache, so the area overhead incurred by associated counters will also have to be considered urgently.

116.3 Proposed Energy-Efficient Technique

116.3.1 Prediction for Backward Invalidation

Note that the way-tagged method is ineffective in backward invalidation because this kind of invalidation can only occur in cases of read-miss. Figure 116.1a shows the operation flow of our solution. First, an evicted cache line that is valid and inclusive could proceed to the next step; otherwise, it is unnecessary to carry out backward invalidation. Second, the inclusion implies that the higher-level caches must contain copies. To reduce tag comparisons within the L1 caches, a predictor with less hardware overhead is applied to select a potential local cache to compare in advance. Only when this initial selection fails do the remaining local caches have to be checked; otherwise, the coherence protocol (ESI in this paper) will be reused. The status “E” denotes that this data block is exclusive among the private caches. This means that the remaining comparisons can be avoided. The status “S” indicates that there are still other copies in local caches. Thus, the last step entails comparing the remaining local caches. If the status is “I,” then the predictor should be adjusted to improve the probability of correctness.

As the key component, the predictor can be operated as the flow in Fig. 116.1b. Each way of the L2 cache should be equipped with N counters, where each counter corresponds to one processor. First, it can be used to predict which L2 cache contains the miss data. If the prediction is correct, the counter corresponding to the initiator in that way should be increased. In contrast, the replace policy will select a method for updating. In this case, the operation will not only increase the counter of the initiator but also decrease each counter of the core that retains a copy of the replaced block. In addition, as mentioned previously, the misprediction also needs to decrease the selected counter while increasing all the counters corresponding to the actual copy owners.

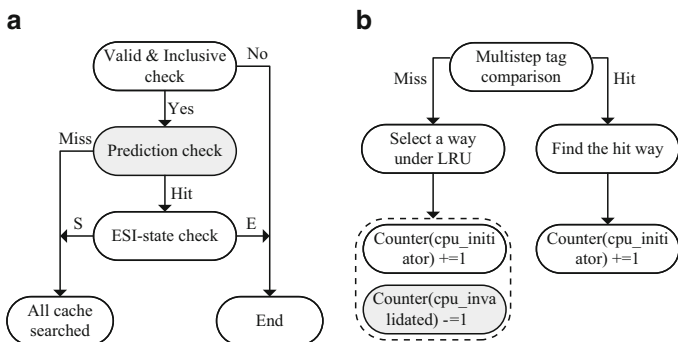


Fig. 116.1 Proposed prediction for backward invalidation (a) Backward invalidation flow (b) Prediction counter operation

116.3.2 Optimization for Multistep Tag Comparison

The multistep method [5] utilizes a counter-based prediction where each cache line has a 15-bit counter as depicted in Fig. 116.2. With this counter, the method can estimate the liveness of the cache line to reduce tag comparisons. Generally speaking, the preferred structure is a binary modulo-2n *n*-bit counter with a simplified design, whereas the speed and the area are conflicting qualities because of the carry propagation. On the other hand, with only one less state than a binary counter, a linear feedback shift register (LFSR) offers a speed–power–area-efficient solution, which could generate a nonbinary, pseudorandom counting sequence [6]. The generally used linear function of LFSR is XOR, that is, the tapped bits are XORed with the feedback loop before being shifted to the next position. Unfortunately, the initial state of this LFSR can be any value except zero, which is important in the multistep method.

This reversible “up/down” LFSR consists of a set of shift registers similar to the original LFSR, a 2-to-1 multiplexer per bit to select *up* or *down*, and twice as many XNOR gates as the unidirectional LFSR. Compared with an ordinary binary counter, the proposed bidirectional LFSR consumes fewer logic gates; in addition, a LFSR delay consists only of a flip-flop delay and an XNOR gate delay, namely, its delay is $O(1)$ and is independent of the counter size. In contrast, a binary counter has a delay of $O(n)$. Specifically, the counter in the multistep method requires no other values besides zero and one. Thus, these characteristics make the proposed LFSR a suitable counter choice.

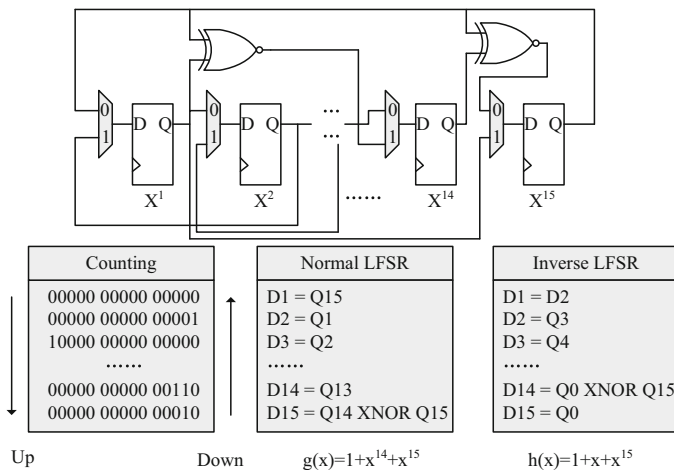


Fig. 116.2 Fifteen-bit maximum-length up/down LFSR

116.4 Implementation

This low-power technique can be implemented with three methods. First, the proposed technique associates the L1 cache with a way tag. When a miss datum returns from main memory, it must insert the L1 and L2 caches simultaneously to maintain the inclusion property. Thus, the L1 cache could receive accurate information about which way of the L2 cache has been inserted. With this indication of the associated way tag, a written request hit in a private cache can directly determine which way of the L2 cache should be written to keep the data consistent. This may lead to a significant energy reduction with no performance degradation.

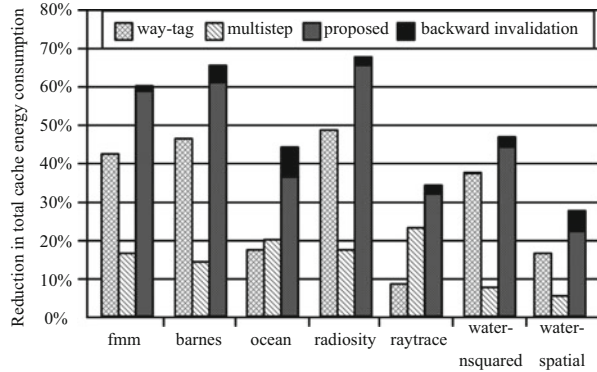
Second, assume that when either a read or a write miss occurs in a private cache, the technique adopts the multistep method to judge which way of the L2 cache might contain the data copy. This method uses two novel structures to realize this goal. The first step is designed to use each way-associated CBF to filter out cache ways that will for sure yield cache misses. From the remaining potential ways, the corresponding way-associated LFSR would further pick up the hot blocks rather than the cold ones to make a comparison in advance. If the prediction is successful, the energy consumption otherwise needed for comparison with the other tags can be conserved.

The last improvement is designed for backward invalidation when a read miss occurs in the L2 shared cache. In this case, the invalidated data must be broadcasted to the shared bus so that all private caches can check whether data copies exist. To decrease the unnecessary snoop power caused by the private caches, we also present a novel prediction method to divide the backward invalidation into three steps. The CPU_ID predictor first indicates which core might contain a copy. Then a scheduler checks this potential cache tag and the associated coherence status. If the status indicates that the data block has other owners, then tag comparisons with the remaining local caches are performed in the next cycle. Conversely, if the prediction is correct and the status is exclusive, then the other tag comparisons are skipped, which thereby saves energy.

116.5 Experimental Results

To estimate the benefit from this proposed architectural design, we utilize the Virtutech Simics multiprocessor simulator [7] and implement a quad-core system with a snoop-cache coherence protocol (i.e., ESI protocol). We choose a representative memory hierarchy having per-core 16 KB L1 instruction and data caches (256-entry, 4-way set-associative with a 16-byte line size) and a shared 1 MB L2 cache (1024-entry, 16-way with a 64-byte line size). The L1 data cache utilizes the write-through policy and the L2 cache is inclusive. This cache configuration will be used as a baseline system for comparison with the proposed technique.

Fig. 116.3 Reduction in total cache energy consumption



The experiment uses the application of the SPLASH-2 benchmark suite [8] to test the target system.

We use CACTI6.5 and 0.13 μm LSTP technology [9] to assess the power overhead of the cache hierarchy. Figure 116.3 shows the energy reduction with respect to the existing and proposed methods. The existing way-tagged method alone reduces the total cache power overhead by 9.2–49.5 %. Note that the energy reduction obtained by the diverse applications is not uniform because different applications have different write-hit rates. Simultaneously, another existing method (i.e., multistep tag comparison) reduces the power by 5.1–21.2 %, which was lower than the way-tagged method in most programs. This is because write operations are dominant in the L2 cache while read accesses in the L2 cache occur much less frequently. However, the programs *OCEAN* and *RAYTRACE* are exceptions because these programs have larger read miss rates than others. Finally, the proposed method significantly outperformed the existing ones. The average percentage reduction is up to 49.7 %. On one hand, the proposed solution with the combined use of two existing methods could reduce the tag comparisons incurred in both write-hit and read-miss; on the other hand, the solution could also decrease the tag comparisons incurred in backward invalidation. With respect to the performance overhead, the proposed solution does not yield cycle-level performance overhead compared to the multistep method. This is because the additional latencies introduced by the proposed method simply reuse the stall time of the pipeline.

The area overhead of the proposed technique mainly comes from three components: the way-tag arrays, Bloom filters, and counter-based predictors. The area overhead of each component can be calculated as follows. First, as depicted in Sect. 2.1, each L1 cache line has associated a 4-bit way-tag entry in addition to the existing 1-bit valid bit to denote which L2 cache way (16-way associative) can be accessed in an equivalent direct-mapping manner. As the crucial portion for reducing tag comparisons, the component is only approximately 1.04 % of the original baseline cache system. Second, the number of entries in the CBF is twice the number of tag entries per L2 cache way. In addition to the existing 3-bit counter and 1-bit zero indicator, each entry in the proposed Bloom filter also has an

Table 116.1 Delay and area of two implementations

Implementation	Area (μm^2)	Delay (ns)
Binary counter	1,322.27	1.1321
LSFR counter	762.13	0.3168

additional 4 bits (1-bit singleton and 3 partial tag bits). This section is approximately 2.28 % of the baseline system. Finally, the proposed method also requires an additional 15-bit counter for each L2 cache entry. Because this component is implemented with the register rather than the memory, we should evaluate its area overhead in another way, as follows.

We utilize *Design Compiler* in a commercial 0.13 μm fabrication technology to compare the implementations of the 15-bit counter per cache line. Table 116.1 shows the area and the delay for both the binary counter and the LFSR counter. It can be seen that the LFSR counter consumes 1.73 less area compared to the binary counter because the 15-bit binary counter consists of 15 flip-flops, 1 inverter, 14 XOR gates, and 91 AND gates. However, in addition to the same number of flip-flops, the LFSR counter just needs 15 2-to-1 multiplexers and 2 XNOR gates. In addition, the LFSR counter is 3.57 times faster than the binary counter during updates because the longest path of the LFSR counter only includes a multiplexer and an XNOR gate compared with 13 AND gates and 1 XOR gate of the binary counter. Consequently, the adopted LSFR counter could effectively reduce the area and delay of the traditional approach.

Conclusion

With the combined use of a way-tagged cache and a multistep tag comparison method, an energy-efficient, dual-level cache architecture is presented to significantly reduce cache power consumption in CMPs. Moreover, a novel approach is also proposed to reduce the number of tag comparisons in backward invalidation. To realize and optimize the proposed method, a LFSR counter with minimal delay and area is constructed to replace the traditional counter. Finally, experiments demonstrate that the proposed technique could significantly reduce the total cache power consumption in CMPs with an equivalent impact on the performance in comparison with the existing method.

References

1. Mathew S, Jagadeeswari DM. Task scheduling and memory partitioning for multiprocessor system-on-chip using low-power L2 cache architecture. *Int J Emerg Trends Eng Dev.* 2013;2(3):95–105.
2. Dai J, Wang L. An energy-efficient L2 cache architecture using way tag information under write-through policy. *IEEE Trans VLSI Syst.* 2013;21(1):102–12.
3. Park H, Yoo S, Lee S. A multistep tag comparison method for a low-power L2 cache. *IEEE Trans Comput Aided Des Integr Circuit Syst.* 2012;31(4):559–72.

4. Feliu J, Sahuquillo J, Petit S, et al. Understanding cache hierarchy contention in CMPs to improve job scheduling. In: IEEE 6th International Parallel and Distributed Processing Symposium; IEEE, Shanghai; 2012. p. 508–19.
5. Tian Y, Khan SM, Jimenez DA. Temporal-based multilevel correlating inclusive cache replacement. *ACM Trans Archit Code Optim.* 2013;10(4):33.1–24.
6. Chen KT, Wu PR, Lai BC. Reduce data coherence cost with an area efficient double layer counting bloom filter. In: 2012 Fifth International Symposium on Parallel Architectures, Algorithms and Programming; IEEE, Taipei; 2012. p. 7–12.
7. Tarkoma S, Rothenberg CE, Lagerspetz E. Theory and practice of bloom filters for distributed systems. *IEEE Commun Surv Tutor.* 2012;14(1):131–55.
8. Williams NB, Fensch C, Moore S. A communication characterisation of Splash-2 and Parsec. In: IEEE International Symposium on Workload Characterization; IEEE, Austin; 2009. p. 86–97.
9. Jouppi NP, Kahng AB, Muralimanohar N. CACTI with off-chip power-area-timing models. In: IEEE/ACM International Conference on Computer-Aided Design; IEEE, San Jose; 2012. p. 294–301.

Chapter 117

The Performance Optimization of Component-Based System

Daisen Wei, Xueqing Li, and Longye Tang

Abstract The performance of component-based software (CBS) has been a challenge of component technology as it can improve the flexibility of CBS. Optimizing the performance of CBS has been focused by academia and industry until now and is also the main content of this paper. First, one framework for supporting component-based development (CBD) was given to help analyze the main factors to affect the performance of CBS. And then, on the basis of this analysis, some corresponding methods such as instance cache and reflection optimization were proposed, respectively, to try to improve its performance. Finally, experiments showed that they had better time performance than the direct reflection method existed.

Keywords Component-based system • Performance • Reflection • Optimization • Caching

117.1 Introduction

Today's global markets are motivating software vendors to develop greater flexibility to better adapt to users' frequently changed requirements. The flexibility can be defined as an ability to adjust or change the current products or services and then provide new products or services. This can also be understood that such software products should have the ability to constantly evolve as required.

From 2000, component-based development (CBD) has continually promoted the developments of global software markets. CBD is implemented by reusing the predefined components. So, when users' requirements change, CBD can help improve the flexibility of developing and maintaining software products by replacing/updating components.

CBD, however, still faces some challenges such as the worse performance of CBS now. The main factors to affect the performance of CBS involved components and their assemblies. And in most cases, components exist in the form of outer

D. Wei • X. Li (✉) • L. Tang

College of Computer Science and Technology, Shandong University, 250101 Jinan, China
e-mail: xqli@sdu.edu.cn

© Springer International Publishing Switzerland 2015

W.E. Wong (ed.), *Proceedings of the 4th International Conference on Computer Engineering and Networks*, Lecture Notes in Electrical Engineering 355,
DOI 10.1007/978-3-319-11104-9_117

1019

entities such as .dll file and can be called reflection invoke. Obviously, calling outer components will spend more time than their direct call with the form of inner source code. So, how to improve the performance of CBS has been focused and pursued to be researched by academia and industry in recent years [1].

The performance problem, in some cases, resulted from the design phrase. Some design mistakes were defined as software antipatterns, and a corresponding approach had been proposed to automatically detect them [2]. A high-level model of Stochastic Petri nets, the stochastic well-formed nets (SWN), was used to assess the performance of components and their impacts on component-based architecture [3]. Some modeling and analysis tool, UML and interface automata and queuing network (QN), were used together to evaluate the performance of CBS at the architectural level [4].

Performance prediction is another technique used to help architects to promote the quality of software architectures in the design phrase. A reasoning framework was proposed to support this idea by mixing the measurement approach and model-based one [5]. The prediction model was improved, from the perspective of state modeling, by identifying and classifying state information related to CBS [6].

The main contributions of this paper are that (1) one service engine-based assembly framework was proposed to support CBD and the following researches and (2), under this framework, two approaches, component cache and dynamic method invoking, were proposed to improve the performance of CBS.

The remainder of this paper is organized as follows: In Sect. 117.2, a service engine-based composition framework was proposed and described in detail. In Sect. 117.3, some optimizing strategies were proposed to improve the time performance of CBS and then experiments were made to validate their effectiveness. And conclusions were given in final Sect. 117.4.

117.2 Service Engine-Based Component Assembly Framework

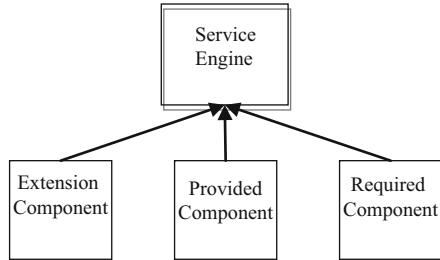
117.2.1 Service Engine

A service engine is a special type of class. It will be used as a glue template with the granularity of services to assembly components. In the case given in Sect. 117.3 below, a service engine was a .net class and an instance of it would be created and used to call/assembly components related to a business logic/process with certain input and output (Fig. 117.1).

The functions of a service engine are listed as follows:

1. A connector to assembly components. That is, users call each component via a service engine for their software product developments. Calling components is usually implemented by reflection invoke. Here, service engine decouples the business logic and components themselves. So, the use of it makes the

Fig. 117.1 The basic structure model of a service engine



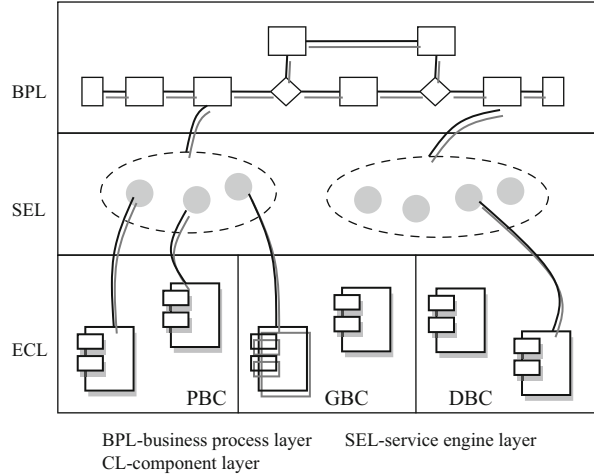
scheduling and maintenance of components more flexible. And meanwhile, the service engine defined in this paper also supports the pass by value and the nested component call.

2. Providing extension points. There are three types of extension points, AOP (aspect-oriented programming)-based ones and event-based ones and interface-based ones. The first ones can be used by the users to implement AOP-based configuration and connect their own computing logic. The second ones can allow the users to register some triggered events for components as required. And the third ones can help realize component interfaces and directly call the corresponding components developed by the users themselves.
3. Container of calling and monitoring the execution of components. A service engine can be regarded as a container that manages the whole lifecycle of components and maintains the contexts of calling them. That is, the instance of a component would be created and canceled in it.

Here, the creation of a service engine aims at increasing the transparency and flexibility of calling components. On the one hand, under this situation, the users call the needed components and do not have to know and grasp their implementations but the provided interfaces and their referenced locations. On the other hand, all components can be independently replaced or updated as business logic changes.

Note that for each component, a metadata file (MDF) must be created to record the necessary information such as the provided interfaces. It should also involve the attributes and services provided in the interfaces and the location of the corresponding .dll file of a component. This metadata file can be retrieved by the service engine to find component methods or attributes as required. For an MDF, it can be created together with the corresponding component, and at the same time, it must be updated simultaneously as the component changes. In this paper, an MDF is described as an XML file.

Fig. 117.2 The service engine-based framework for ERP component composition



117.2.2 Service Engine-Based Assembly Framework

According to the MDF of a component, this component can be called by using a service engine. Figure 117.2 illustrates the service engine-based framework for component scheduling and composition.

From Fig. 117.2, the framework consists of three logic layers, business process layer (BPL), service engine layer (SEL), and component layer (CL). And it implements a business process-driven component composition.

BPL is used to describe the business processes of enterprises and it is served by the low layers. SEL is to define and provide scheduling engines in terms of services. CL provides the predefined components which are classified into three ones, platform basic ones (PBC), general business ones (GBC), and domain business ones (DBC). PBC refers to the built-in components provided in the platform that usually implement the basic computing such as string, database, and file operations. GBC refers to domain-oriented components that can be reused in different products at the same domain. DBC includes those components which are extracted from a specific domain and usually reused in the family of a product with the distinguished domain business features.

Under this framework, components can be called and assembled according to the predefined business processes, and this call process involves four steps as follows:

1. Users call components via the APIs of a service engine. To implement it, the needed $\langle \text{component-id}, \text{parameters} \rangle$ must be passed directly to the service engine. Here, the component-id refers to the unique number of a component and the parameters the services provided in its interface.
2. After receiving $\langle \text{component-id}, \text{parameters} \rangle$, the service engine tries to find the newest version of the corresponding MDF and then retrieve the metadata entity

of the component. The metadata entity involves the information about the corresponding .DDL file and the interfaces and the services provided in them.

3. After finding the metadata entity of that component, the service engine executes component agent factory by reflection to create an instance of it.
4. After the step 3 runs successfully, the service engine can directly invoke the methods of this component.

In essence, a service engine as a middleware is to improve the flexibility of CBS and its maintenance. Under this framework, components can be independently updated or replaced as required. Using service engine to call components, however, may cause the performance degradation of CBS, and this also directly affects that of the related business processes.

117.3 Optimizing the Service Engine

117.3.1 *Analyzing the Performance Bottlenecks of CBS*

From the framework and the process of calling components given in Sect. 117.2.2, it can be seen that implementing a service engine, however, will result in the performance degradation because it changes the architecture of application system by inserting a layer between user's source code and the called components. Obviously, the implementation of the direct component call will have better performance than that of the indirect one.

Some bottlenecks to affect the performance of CBS can be analyzed and concluded from this framework, and three most important ones are listed as follows:

1. Find and load the DLL file in which components are included according to the component-id and the corresponding mapping file. This process involves the access to outer disk files, DDL file.
2. Service engine executes agent factory to create an instance for this component.
3. Retrieve this DLL file and then call the required methods by reflection. Currently, reflection is still a common method widely used for calling components.

One experiment had been made to analyze the time performance of the three subprocesses listed above. The experiment environments were (1) OS, windows 7 core 32, (2) one computer with CPU (Intel(R) Core (TM) i5-3320M, 2.60 GHz) and RAM 2 GB, and (3) one server run as a component library from which a component calculator was selected as the calling object. The calculator provided some basic arithmetic methods. For accurately getting the time spent by every period, the body of each method was set null. (4) Four time periods were selected

Table 117.1 Time spent by four operation processes, respectively, in four time periods

Operation	1,000 ms	10,000 ms	100,000 ms	1,000,000 ms
Load DLL file	4	46	435	4,387
Create an instance	<1	2	19	184
Method 1 (load+ create + direct call)	About 5	About 48	455	4,585
Method 2 (load+ create + reflection)	About 5.5	55	528	5,289

under the above environments, and they were 1,000/10,000/100,000/10,00,000 times, respectively. All experiment data were listed in Table 117.1.

The load DLL file spent much time. From Table 117.1 above, the time spent by it was about 82 % of the time spent by method 2, respectively, in four time periods (1,000/10,000/100,000/10,00,000).

This experiment was done only in a relatively simple environment. With the enlargement of component library, their impacts on the performance of CBS would be highlighted increasingly. So, how to improve their performance has been very necessary and important for CBS.

117.3.2 *Optimizing Strategies*

Strategy 1: DLL file and instance cache.

For the processes, load file and create instance, file and instance cache were adopted to improve the time performance of CBS. A caching strategy including two aspects was proposed as follows:

(A) To determine the appropriate granularity of a DLL file

The granularity is defined as the number of components included in a DLL file. And it shows the correlation among components, which can be used as a criterion to determine what components could be clustered together in a DDL file. In this paper, the correlation is defined as business process-driven/oriented clustering because business process can reflect the close relation among components.

Additionally, this strategy should be based on the good classification of components such as common ones and business ones. The common components usually involve the basic computing units at the programming or platform level. The business ones usually implement the domain-oriented business logic, so they have the obvious domain features. Research on these is outside the scope of this paper.

(B) Use frequency-based instance cache

Based on this strategy, the DLL file including all business-related components would be loaded only once and cached when a business process is implemented.

Table 117.2 Time spent, respectively, by three call methods

Methods	1,000 ms	10,000 ms	100,000 ms	1,000,000 ms
Direct call	About 0.1	About 0.2	1	14
Reflection	About 0.8	7	73	718
Emit-based dynamic call	About 0.2	About 0.5	2	24

The instance cache is to always cache the instances of the components which can be used frequently. Exactly, instance cache is implemented more difficultly than the DLL file cache because it must determine what instances of components should be cached and how the caching queue is maintained.

These involve the reuse frequency of components, which can be determined by referring to the scale of their reuse and the use frequency of the related business progresses. Some strategies for instance cache were proposed as follows:

- Multi-instance cache. That is, some components were instantiated and cached together when they were called for the first time. For example, when a business progress was implemented, the instances of all related components were created and cached. When the predefined conditions were stratified, all of them would be destroyed.
- Instance cache pool. For those highly concurrent instances, a cache pool can be created to cache them.

Note that the efficiency of the DLL and instance cache would be limited by the deployment environment such as the capacity of RAM.

Strategy 2: Optimizing the method of calling components.

From Table 117.1 above, it can be seen that the reflection invoking would spend more time to execute the call of components and their methods than the direct call. Reflection invoking usually consists of three operations, type comparison, retrieving members, and invoking members, all of which would affect the time performance of the process of component call.

Emit is one of the functions included in reflections. In contrast to reflection invoking, it can find the information on components and then call their methods in a dynamic environment. Experiment showed that its execution had better time performance than that of reflection invoking, and the related experiment data were given in Table 117.2. Three calling methods, direct call, reflection, and emit-based dynamic call, were compared from the perspective of the time spent, respectively, in four time periods (1,000/10,000/100,000/10,00,000).

Note that this experiment was made under the environment in which DLL file and the instances of components had been cached.

From Table 117.2, it can be obviously seen that the emit-based dynamic call method had better time performance than the general reflection. And the time spent

by it were about 4/15/35/30 times more than that by reflection, respectively, in four time periods. Additionally, the time spent by dynamic call was close to those spent by direct call, respectively, in four time periods.

Conclusion

Two strategies were proposed in this paper to improve the performance of CBS. One of them is to cache the DDL file and the instances of components. And the corresponding factors to affect its efficiency were analyzed in detail. The other is to optimize the ways to call components and their interface services by reflection emit. And the related experiments showed that these strategies were implemented well and had good time performance.

Of course, some limitations still existed. For example, one problem about caching was not avoided for the caching strategy. Whether the caching strategy is implemented successfully or not usually depends on two important factors, the capacity of RAM and an appropriate caching algorithm.

Our next work is to improve these from the perspective of optimizing the appropriate granularity of components and the related DLL file.

References

1. Koziolok H. Performance evaluation of component-based software systems: a survey. *Perform Eval.* 2010;67(8):634–58 (Special Issue on Software and Performance).
2. Parsons T. Automatic detection of performance design and deployment antipatterns in component based enterprise systems. A Ph.D. thesis, The University College Dublin of Ireland; 2007.
3. Salmi N, Ioualalen M. Towards efficient component performance analysis in component based architectures. *Lect Notes Bus Inform Process.* 2012;94:121–42.
4. Karimpour J, Isazadeh A, Izadkhah H. Early performance assessment in component-based software systems. *IET Software.* 2013;7(2):118–28.
5. Abdelaziz AA, Kadir WA, Osman A. Comparative analysis of software performance prediction approaches in context of component-based system. *Int J Comp Appl.* 2011;23(3):15–22.
6. Happe L, Buhnova B, Reussner R. Stateful component-based performance models. *Softw Syst Model.* 2013. doi:[10.1007/s10270-013-0336-6](https://doi.org/10.1007/s10270-013-0336-6). p. 1–25.

Chapter 118

Microblog Data Parallel Monitoring Algorithm on Compute Unified Device Architecture

Yunpeng Cao and Haifeng Wang

Abstract There is a large-scale information data in microblog systems to be processed in real time. Processing large-scale microblog data needs high-performance computing architectures and parallel algorithms. Graphic processing units are adaptable to process data-intensive computing tasks. Using parallel algorithm of GPUs is an effective method to deal with real-time microblog data. Dynamic thread configuration scheme was proposed to decompose the microblog data. The key optimization technique for accessing data on GPUs is solved. Finally, the experimental results show that the proposed parallel algorithm can achieve the average speedup ratio of about 15.3–17.9 and process more than 487 MB per second in practice.

Keywords CUDA • Microblog • String matching • Memory optimization

118.1 Introduction

Microblog system allows users to communicate with each other through real-time exchange of short messages and to form a novel social network based on users' relationships. The growing popularity of microblog system in recent years has attracted the attention of people and organizations that attempt to manipulate the message communication on the specific platform, such as rumors and advertisement information on microblog. To control the message communication on microblog, the sensitive information should be monitored in real time. This needs to process large-scale message data due to the fact that numerous users generate message data at anytime. And monitoring microblog message belongs to data-intensive tasks.

Y. Cao (✉)

College of Information, Linyi University, 276005 Linyi, Shandong, China
e-mail: lyucyp@163.com

H. Wang

Institute of LinYi, University of Shandong Provincial Key Laboratory of Network Based Intelligent Computing, 276005 Linyi, Shandong, China
e-mail: gadfly7@126.com

The GPU's (graphic processing unit) advantage is data-intensive computing, and it is suitable for parallel computing. Using GPUs to process data-intensive computing tasks in parallel is an effective method [1, 2]. CUDA (Compute Unified Device Architecture) is an architecture of software and hardware to process and manage GPU computing. Here to solve the problem of large-scale microblog message online monitoring, our goal is to put forward a detailed parallel algorithm based on CUDA and GPUs. There are several key techniques to be dealt with. These techniques involve how to map large-scale data to large thread set and how to optimize the data access on GPUs.

118.2 CUDA Parallel Processing

Monitoring microblog is a procedure to search and find sensitive information in microblog and take appropriate measurements. String matching technology is used in microblog monitoring. String matching is to search the appearance circumstances of substring P in character string W . W is called matched string, and P is called pattern string or characteristic string. In microblog monitoring the microblog is matched string W and the sensitive information is pattern string P . Classical matching algorithms are KMP, BM, Sunday, etc. [3–5].

118.2.1 CUDA Parallel Algorithm

(W, P) is called microblog-sensitive information couple composed of microblog W and sensitive information P . Processing (W, P) is to search P in W .

By combining any one of m microblogs $W_0, W_1, W_2, \dots, W_{m-1}$ and any one of n sensitive information $P_0, P_1, P_2, \dots, P_{n-1}$, $m \times n$ microblog-sensitive information couples $(W_0, P_0), (W_1, P_0), (W_2, P_0), \dots, (W_{m-1}, P_0), (W_0, P_1), (W_1, P_1), (W_2, P_1), \dots, (W_{m-1}, P_1), \dots, (W_i, P_j), \dots, (W_0, P_{n-1}), (W_1, P_{n-1}), (W_2, P_{n-1}), \dots, (W_{m-1}, P_{n-1})$ are produced. They can be regarded as elements of a $m \times n$ matrix which has m columns and n rows. (W_i, P_j) is the element at i th column and j th row, $0 \leq i \leq m-1, 0 \leq j \leq n-1$.

Suppose there are $s \times t$ blocks in a grid and $p \times q$ threads in a block, then the number of GPU threads is $u \times v$ where $u = p \times s, v = q \times t$. These threads are $T(0, 0), T(1, 0), T(2, 0), \dots, T(u-1, 0), T(0, 1), T(1, 1), T(2, 1), \dots, T(u-1, 1), \dots, T(i, j), \dots, T(0, v-1), T(1, v-1), T(2, v-1), \dots, T(u-1, v-1)$. They can also be regarded as a $u \times v$ matrix of u columns and v rows. The $m \times n$ microblog-sensitive information couple matrix can be divided into many $u \times v$ sub-matrixes, every GPU thread processes microblog-sensitive information couples at corresponding sub-matrix positions in turn, and this batch of microblog and sensitive information can be matched in balanced mode. The microblog-sensitive information couples processed by thread $T(i, j)$ are $(W_i, P_j), (W_{i+u}, P_j), (W_{i+2u}, P_j), \dots, (W_i, P_{j+v}), (W_{i+u},$

P_{j+v}), (W_{i+2u}, P_{j+v}) , ..., (W_i, P_{j+2v}) , (W_{i+u}, P_{j+2v}) , (W_{i+2u}, P_{j+2v}) , ..., ..., ... where $0 \leq i \leq u - 1$, $0 \leq j \leq v - 1$. One thread maps to many data (microblog-sensitive information couples) processed by itself.

The program matches all microblog and all sensitive information by two layers of loop. The corresponding algorithms are as follows:

Algorithm 1 Search all sensitive information in all microblog

MicroblogSuperVise(S[0..M-1], P[0..N-1])

1. If M(total amount of microblog) equals 0, go to 12
2. If N(total amount of sensitive information) equals 0, go to 12
3. Initialize iWB to 0
4. Initialize iWBBPS to 0
5. If iWB equals M(total amount of microblog), go to 11
6. Read in one microblog
7. add iWB by 1
8. add iWBBPS by 1
9. If iWBBPS(the number of microblog read in) equals microblog amount of one batch, then
 - Call WB_OneBatch to match this batch of microblog with all sensitive information
 - reset iWBBPS to 0
10. Go to 5
11. Call WB_OneBatch to match the left remnant microblog with all sensitive information
12. End

This algorithm uses any amount of microblog and sensitive information as input parameters, outputs the match results of all the microblog and sensitive information.

Algorithm 2 Search all sensitive information in a batch of microblog

WB_OneBatch(SBatch[0..iWBBPS-1], P[0..N-1])

This algorithm uses a batch of microblog and all sensitive information as input parameters and outputs the match results of this batch of microblog and all sensitive information.

1. If N(total amount of sensitive information) equals 0, go to 11
2. Initialize iMG to 0
3. Initialize iMGBPS to 0
4. If iMG equals N(total amount of sensitive information), go to 10
5. Read in one sensitive information
6. add iMG by 1
7. add iMGBPS by 1
8. If iMGBPS (number of sensitive information read in) equals sensitive information amount of one batch, then

- Call SearchOneBatch to match microblog with this batch of sensitive information
 Call BatchResult to process the result of SearchOneBatch
 Reset iMGBPS to 0
9. Go to 4
 10. Call SearchOneBatch to match microblog with the remnant sensitive information
 Call BatchResult to process the result of SearchOneBatch
 11. End

118.2.2 Key Technologies

There are two key technologies in parallel processing. One is storage optimization, the other is elastic thread resource configuration.

Microblog and sensitive information are accessed read-only, and the results of different microblog-sensitive information couples are stored in different addresses. Data storage way becomes an important element that influences performance [6–8]. According to present GPU's storage model, global memory is used to store microblog data. Sensitive information need less space and they can be stored into global memory, texture memory, or shared memory. Higher efficiency can be obtained by storing sensitive information into texture memory than global memory [9, 10].

Assign x the number of threads in every block, p the horizontal size of block, n the amount of processed sensitive information in every batch, z the storage saturation factor (the proportion of data transmitted at one batch to host memory or GPU memory), M_3 the space occupied by one microblog, y_1 the horizontal number of sub-matrix, and y_2 the vertical number of sub-matrix, and then the reasonable values of q , vertical size of block; m , the amount of processed microblog every batch; s , horizontal size of grid; t , vertical size of grid; u , horizontal size of sub-matrix; and v , the vertical size of sub-matrix, can be figured out automatically according to the following ideas:

1. Obtain the parameters of host and GPU; compute K, L .
2. Let x be integer times of 32 to utilize executive units efficiently; let p be 16 or integer times of 16 to increase the access efficiency of global memory and shared memory. $q = x/p$.
3. m should be as large as possible to decrease transmission times. But limited by M_1 , the total amount of host memory, and M_2 , the total amount of GPU memory, $m \leq z \times \min(M_1, M_2)/M_3$. According to experiments, z , the storage saturation factor, is more suitable to be 60 %. Usually M_3 is 280 bytes, and it is adjustable. The product of m and n should be integer times of L , so the match tasks can be

evenly assigned to every thread of GPU. After assigning the value of n , let m be the largest integer that satisfies conditions.

4. The grid dimension: $s = \text{int}((m+p-1)/p)/y_1$, $t = \text{int}((n+q-1)/q)/y_2$. The number of blocks should be at least two times of maximum active block amount of GPU, i.e., $st \geq 2K$.
5. $u = p \times s$, $v = q \times t$.

When running practically, the values of z , x , p , n , y_1 , y_2 can be adjusted to get the best thread resource scheduling scheme. The automatic configuration algorithm is as follows:

Algorithm 3 Thread resource configuration

ThreadResourceConfig(z , x , p , n , y_1 , y_2)

1. Get the total amount of host memory and GPU memory and store it to M_1 , M_2
2. Calculate the amount of active blocks per SM and store it to J
3. Get the amount of SM and store it to H
4. $K = H * J$
5. Select a value for x and p
6. $L = x * J * H$
7. $q = x / p$
8. $m = 1$
9. if $m > z * \min(M_1, M_2) / M_3$, go to 12
10. if $\text{mod}(m * n, L) = 0$, $m = m + 1$
11. go to 9
12. $m = m_1$
13. $S = \text{int}((m+p-1)/p)$, $T = \text{int}((n+q-1)/q)$
14. $s = S / y_1$, $t = T / y_2$
15. if $\text{mod}(S, y_1) = 0$ && $\text{mod}(T, y_2) = 0$ && $s * t \geq 2 * H * J$, go to 18
16. adjust y_1 , y_2
17. go to 5
18. $u = p * s$, $v = q * t$
19. return q , m , s , t , u , v

This algorithm automatically computes the thread resource scheduling parameters. So under various complicated circumstances, the program can run with reasonable configuration and get better performance.

118.3 Experiment

118.3.1 Experiment Environment

The computer configuration for the experiment is as follows: NVIDIA GeForce 9400GT (1 G video memory), CPU Intel Pentium Dual-Core E5300 at 2.60 GHz, memory 2 GB, HDD 500 GB, Windows XP Pro, and CUDA 5.0.

118.3.2 Comparison of Different Memory Optimization

The first traditional programming method was used to process the sample data, then GPU parallel processing method was used, and the sensitive information were put into global memory (GM), texture memory (TM), and shared memory(SM), respectively. The experiment result is shown in Fig. 118.1.

The experiment shows that by GPU's processing, the performance obtained by using shared memory is better than that obtained by using texture memory and the performance obtained by using texture memory is better than that obtained by using global memory.

118.3.3 Comparison of Different Data Size

Further analysis to the above experiment result shows, when processed by GPU + CUDA, for any one storage way, with the increase of data scale, the speedup ratio has an increasing trend. Because the bigger the data scale is, the more work intensive the GPU is, the proportion occupied by parallel processed part increases,

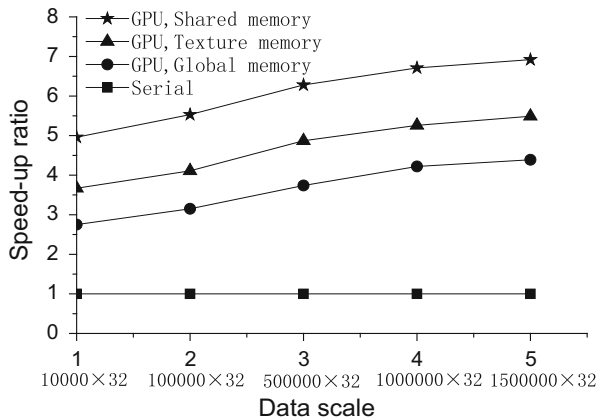
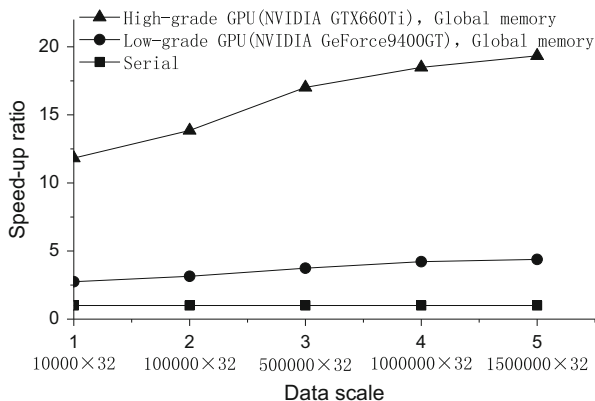


Fig. 118.1 Performance comparison of different storage schemes

Fig. 118.2 Performance comparison of GPUs of different grades



so the performance is improved to some extent. But when the data scale increases to a certain extent, the speedup ratio will be stable. If the data is too small, the saved time by parallel processing cannot compensate the data transmission overhead between host memory and GPU memory; it is possible that the acceleration performance is not obvious and even that the speedup ratio is less than one.

118.3.4 Performance of Different GPUs

Other configuration was unchanged, but the video card was changed to a more advanced one whose model is NVIDIA GTX660Ti. Process the sample data mentioned above and use global memory; the experiment result is shown in Fig. 118.2.

The experiment shows that if other condition is unchanged, an advanced GPU has obvious performance advantage.

Conclusion

To monitor the sensitive message in microblog, the proposed parallel algorithm can improve the computing performance, and the results indicate that the speedup performance and throughput can satisfy the requirement in practice. However, the size of loaded data on GPUs is a key performance factor. When the loaded data is too small, the computational power is not able to exert. So determining the threshold of loaded data size is very important. Here we used an experimental method to select the threshold value. In the future, finding such reasonable threshold value is our next work.

Acknowledgements This work is supported by the Shandong Province Natural Science Fund (No. ZR2013FL005) and Linyi Social Science Research Project (No. 2013SKL166).

References

1. Wang HF, Chen QK. Research summary of the key technologies in general-purpose computing of graphics processors. *Chin J Comp.* 2013;36(4):757–71 (In Chinese).
2. Wang HF, Chen QK. Power estimating model and analysis of general programming on GPU. *J Softw.* 2012;7(5):1164–70 (In Chinese).
3. Wang ZW, Ping LD, Lu MF. Research on efficient string matching algorithms. *Comp Eng Appl.* 2010;46(1):28–30 (In Chinese).
4. Boyer RS, Moore JS. A fast string searching algorithm. *Commun ACM.* 1977;20(10):762–72.
5. Sunday DM. A very fast substring search algorithm. *Commun ACM.* 1990;33(8):132–42.
6. Liu Y, Luo LP, Wang ZS, Huang DP, Huang JX, Jia LY. Research for Chinese word segmentation algorithm on GPU platform. *J Comput Inform Syst.* 2012;8(15):6515–22.
7. Hawick KA, Leist A, Playne DP. Parallel graph component labeling with GPUs and CUDA. *Parall Comput.* 2010;36(12):655–768.
8. Ferreira J, Lobo J, Dias J. Bayesian real-time perception algorithms on GPU. *Real-Time Image Process.* 2010;4(2):151–5.
9. Laan WJ, Jalba AC, Roerdink JB. Accelerating wavelet lifting on graphics hardware using CUDA. *IEEE Trans Parall Distr Syst.* 2011;22(1):132–46.
10. Brown JA, Capson DW. A framework for 3D model-based visual tracking using a GPU-accelerated particle filter. *IEEE Trans Vis Comp Graph.* 2012;18(1):68–80.

Chapter 119

Universal Central Control of Home Appliances as an Expanding Element of Smart Home Concepts

Jan Dvorak, Ondrej Berger, and Ondrej Krejcar

Abstract With the development of the electronic appliances has come an increase in the application of so-called smart home concepts. Nowadays, many standards and technologies exist that enable the control of home appliances. However, the common devices that support this via a controller on the basis of infrared transfer cannot be operated by Smart Home Systems. In a practical environment, the proposed solution is to replace the functioning of such controllers and enable users to operate the devices using a Web site application that is available, for example, through a smart phone. Part of the solution is an interface for the connection of the application to current smart home systems, as well as intelligent recognition and automatization of user actions with controllers. The result of the implementation is a functional prototype.

Keywords Smart home • Infrared • Remote control • Automation • Mobile • Multimedia

119.1 Introduction

Recent fast developments in the field of electronic appliances have been accompanied by the development of systems that contain elements of so-called smart homes [1], methods of cooperation with electronic devices performing the basic functions of a house. Originally, smart home technologies were developed for the control of energetically advanced systems, such as heating or lighting. However, the current level of electronic equipment enables the connection of almost any component into a smart home system. Moreover, this is not limited to switching on and off devices; it is also possible to carry out actions that would simplify the inhabitation of such an environment and save time on the basis of predefined or intelligent algorithms.

J. Dvorak • O. Berger • O. Krejcar (✉)
Center for Basic and Applied Research, Faculty of Informatics and Management,
University of Hradec Kralove, 50003 Hradec Kralove, Czech Republic
e-mail: jan.dvorak@uhk.cz; ondrej.berger@uhk.cz; ondrej.krejcar@uhk.cz

This is due to the instruments for monitoring user activity [2, 3]. With respect to smart buildings, recently the control and monitoring of their energy consumption has become a popular topic. This interest in energy consumption stems from the fact that, for example, up to 40 % of spending on energy is in commercial buildings, and this figure could be reduced by 70 % [4] using automated systems for controlling lighting. An example of an active operation in this field is research on the wireless control of lighting [5], technologies of smart transfer networks (smart grids [6]), or general usage of smart homes [7]. Current systems for smart homes usually contain a central controlling unit with attached end nodes—sensors or action members (using star or bus line topology). For the suppliers of the given solution, these nodes must support a specific standard communication protocol. The common representatives of such standards are, for example, C-Bus, which communicates using an Ethernet network, the international standard KNX [8], or a wireless system like ZigBee [9].

The purpose of the project described in this paper is to propose and implement hardware and software that will contribute to the centralized solution of home appliances that are operated using infrared controllers and do not support any of the standards for central controlling. The solution contains a Web site application that introduces a human–machine interface (HMI) and provides an application programming interface (API) for the integration of current smart home systems.

Moreover, the system continuously monitors the use of current controllers and on the basis of user activities suggests, for example, the unification of commonly consequential steps with mass actions (macros) or automatic implementation of regular actions. The result of this function should be to save time on and simplify everyday activities related to home appliances, which corresponds to the basic requirements of smart home technology users related to authors [3].

119.2 Problem Definition

The absence of a connection of most common multimedia appliances with a current smart home solution is a widespread problem in smart homes today. Some models support the HDMI consumer electronics control (CEC) standard [10] that enables the operation of interconnected appliances using HDMI cables. However, to adopt such a standard, it is necessary to connect to each device an individual module for the device's maintenance. This is not just technically but also financially a very demanding solution. On the other hand, traditional infrared (IR) remote controls are used by most multimedia home appliances. Moreover, the hardware for transmission and receiving is favorably priced. For example, one article is concerned with the processing of signals from IR controllers [11]. This article proposes a system of automatic switch-off of unused electric plugs and their repeated switch-on using IR signals.

Currently, few products on the market enable the functionality of centrally controlling appliances using IR signals. The Harmony product line from Logitech (<http://www.logitech.com>) contains a wide spectrum of universal remote controls,

Fig. 119.1 Commercial device enabling the central control of IR appliances



from which the Ultimate Hub, Smart Control, and Ultimate models take a Hub unit that provides similar functions as the proposed solution. For this solution, the company also offers applications for iOS and Android that are very well built and intuitive. Unfortunately, the Harmony product line is not an open standard (it does not allow for connections with other systems). This solution ranges in price from US\$100 to US\$350, depending on the specific model.

Moreover, the Open Source Universal Remote application is also worth mentioning in connection with open-source solutions. This application can be installed on any PC with an IR controller and enables the transmission of commands to appliances from any Web browser in a network, for example, even a smart phone. The disadvantage of this application is that it does not allow for recording signals of the current controller and, consequently, emulating them.

None of the aforementioned solutions has the ability to monitor user activities with the current controller and does not suggest the optimization of regular activities. The first two are shown in Fig. 119.1.

119.3 New Solution

This chapter introduces a proposed solution for controlling end devices in a new way that satisfies all needs mentioned in the previous chapter. Figure 119.2 illustrates the architecture of the whole system. It is important to notice the three basic communication directions:

- Through the Web application, users can operate end devices using an IR transmitter in the central point of the system.
- The central point captures commands that are sent from the original controller to the end devices.
- On the basis of the manual command, it is possible to duplicate the current controller and use it from the Web application.

The requirements for the central point include the ability to receive and transmit IR signals that are compatible with remote controls and communicate with other devices (e.g., Smart TV, amplifier, DVD recorder) using HTTP and a LAN home network.

Fig. 119.2 Devices present in system for central control of appliances

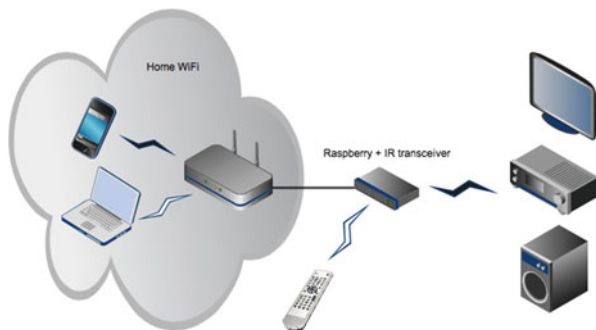
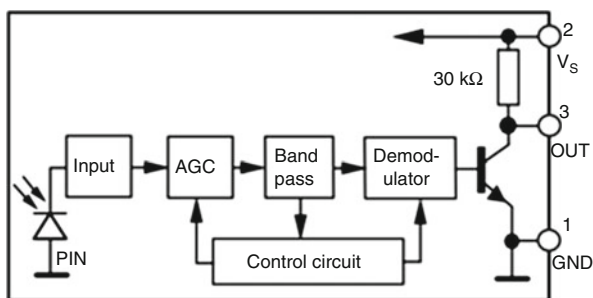


Fig. 119.3 The inner connection of the IR receiver TSoP 31238



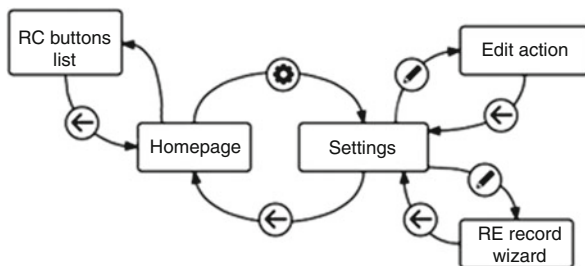
Most remote controls use IR transfer with coding on the 38 or 36 kHz frequency. Manchester, Pulse distance, or Pulse length coding is used for modulation. To decode these signals, it is possible to use a completed three-pin receiver that contains a demodulator and control circuit because of which the generated digital signal corresponds to the transmitted value. Compared with the simple IR photo-transistor, it is not necessary to manage the demodulation. The inner schema of the used receiver is shown in Fig. 119.3 [12].

The proposed transmission circuit contains two IR diodes and a switching transistor (in order not to overwork the data pin with too much current). Two of the used diodes, combined with wide-angle transmission, should cover all appliances in an average room.

The next task is to ensure the recognition of correct coding of digital signals that come from the receiving module, the subsequent transfer to a HEX representation of the pushed button, and the possibility of coding the value back and sending it through the IR transmitter. The linux infrared remote control (LIRC) library is used to uncover the coding [13]. It is composed of numerous basic subprograms:

- Irrecord: an interactive console application that enables “recording” of the current remote control; the final product is a configuration file, `liircd.conf`, which contains, for each operation, a description of the coding signal used and a mapping of individual HEX codes of symbols into their aliases;

Fig. 119.4 Diagram of transfers between individual pages of application



- Liircd—a system demon that acts on each defined end device with the connected IR transmitter; using the socket enables other applications to send the previously recorded IR commands;
- Irsend—associating console application that resends the entered saved command in the liircd socket;
- Irw—simple utility that reads the codes received from the socket and sends them to the standard output.

Before the actual implementation, a structured proposal of the user interface of the application was conducted. The frequency of the expected performance of individual tasks to be implemented was used for the distribution of the most important elements to the most reachable places. The most significant service of the application was the simulation of the push of the buttons for the recorded controllers. Therefore, the accomplishing of the mass actions was placed at the home page.

The special page for recording the controller operates on the basis of an interactive navigator with simple commands. It can retrieve data from users in the text format (as names for recorded buttons, showing the progress guide, or counting down the remaining time). Physically, the special page is an interface that in real time, using WebSockets communication technology, conveys the commands of the irrecord application to the user and immediately returns to user the obtained data. The structure of the application and possible paths between individual functions are shown in Fig. 119.4.

The unique function of the proposed solution is the detection of common actions. It is an implementation of an algorithm to search for repeated sequences in a recorded time row. Many papers cover this problem (e.g., [14, 15]). Most suggest using algorithms based on Markov chains or decision trees. However, with respect to Markov chains intended purpose for continuous data or even multidimensional data, decision trees are too complicated for the needs of this paper. The commonly used model of decision trees is used as part of a simpler algorithm that enables the recognition of samples in the recorded binary data that represent the button pushes of the controllers. The recorded time line is processed by the algorithm for the detection of clusters, and then each cluster and its metrics (e.g., average delay between individual commands) are recorded in the form of a sequence in the graphic database. This yields a system of sets of trees where each set represents a

Fig. 119.5 Finished prototype of central point



sequence of commands with identical first nodes. Therefore, each recorded sequence is connected to the current tree or a new tree is created. When the sequence is repeated, a counting mechanism is recorded only to database as incrementation.

From this continuously maintained database it is possible to simply obtain the sequences that are most commonly used and may be, for example, suggested to the user for creating macros.

119.4 Implementation of Solution

The compact computer Raspberry Pi, which functions on the ARM platform, is used to prototype the central point of the system (Fig. 119.5) [16]. This platform is sufficiently powerful to carry out all tasks and has better dimensions and more battery power than common x86 PC platforms. It is similar in size to those a credit card and costs around 25 euros. Moreover, it contains an integrated processor with 700 MHz frequency and 512 MB RAM. In comparison with simpler and cheaper devices, such as Arduino, it has a significant advantage in that it supports fully functioning operating systems on the basis of Linux, which allow to use of various software applications and technologies.

Conclusion

This paper proposes an open-source solution for centralized control of multimedia appliances that use an IR controller. The proposed solution can be used as a supplement to current smart home systems. Using the Web application, which is even accessible from smart phones, it is possible to record the commands of current controllers or emulate their functions using an individual approach, and on the basis of a user's long-term activity, it suggests the unification of frequent sequences of commands into macros. This functionality can save time for the user and increase one's comfort in working with multimedia appliances.

Acknowledgments This study was supported by the project “SP/2014/05—Smart Solutions for Ubiquitous Computing Environments” at the University of Hradec Kralove.

References

1. Ricquebourg V, et al. The smart home concept: our immediate future. In: E-Learning in Industrial Electronics, 2006 1ST IEEE International Conference on. Hammamet: IEEE; 2006. p. 23–8.
2. Naghiyev E, Gillott M, Wilson R. Three unobtrusive domestic occupancy measurement technologies under qualitative review. *Energy Build.* 2014;69(2):507–14.
3. Haines V et al. Probing user values in the home environment within a technology driven smart home project. *Pers Ubiquit Comput.* 2007;11(5):349–59.
4. Cheong KG, Kuinam JK. Implementation of a cost-effective home lighting control system on embedded Linux with OpenWrt. *Pers Ubiquit Comput.* 2014;18(3):535–42.
5. Benikovsky J, Brida P, Machaj J. Proposal of user adaptive modular localization system for ubiquitous positioning. *Lect Notes Comput Sci.* 2012;7197:391–400.
6. Melike EK. Wireless sensor networks for cost-efficient residential energy management in the smart grid. *IEEE Trans Smart Grid.* 2011;2:314–25.
7. Dhiren T, Al-Kuwari AMAH, Potdar V. Energy conservation in a smart home. In: 2011 Proceedings of the 5th IEEE International Conference on Digital Ecosystems and Technologies Conference (DEST). Daejeon: IEEE Publishing House; 2011. p. 241–6.
8. KNX Specification, “03_07_02 Datapoint Types v1.4 AS v20071214a. doc v1.4,” December 14, 2007.
9. Augustynek M, Penhaker M. Non invasive measurement and visualizations of blood pressure. *J Electron Electr Eng.* 2011;116(10):55–8.
10. Machacek Z, Slaby R, Vanus J, Hercik R, Koziorek J. Non-contact measurement system analysis for metallurgical slabs proportion parameters. *Elektronika ir Elektotechnika.* 2013;19(10):58–61.
11. Han J, Choi C-S, Lee I. More efficient home energy management system based on ZigBee communication and infrared remote controls. *IEEE Trans Consum Electron.* 2011;57(1):85–9.
12. Vishay Semiconductors. Datasheet: IR receiver modules for remote control systems [online]. 2014. <http://www.vishay.com/docs/82492/tsop312.pdf>. Accessed 2 Apr 2014.
13. Bartelmus C, et al. LIRC: Linux infrared remote control [online]. 2002. www.lirc.org.
14. Bodnarova A, Sobeslav V, Horalek J, Matyska J, Hatas M. Virtual laboratory. In: 2013 I.E. 11th International Conference on Emerging eLearning Technologies and Applications. Bayonne: IEEE Publishing House; 2013. p. 53–8.
15. Wan L, Liao J, Zhu X. A frequent pattern based framework for event detection in sensor network stream data. In: Third International Workshop on Knowledge Discovery from Sensor Data. New York: ACM; 2009. p. 87–96.
16. Behan M, Krejcar O. Modern smart device-based concept of sensoric networks. *EURASIP J Wirel Commun Netw.* 2013;2013(155):1–13.

Chapter 120

Lightweight Optimization of Android Permission Model

Peixin Que, Xiao Guo, and Zhen Wang

Abstract Permission management is the core security mechanism of the Android system framework, but the existing Android system doesn't provide security analysis and fine-grained management of its application permissions. In order to solve this problem, this paper proposes a lightweight permission management model which modifies and extends the existing Android application permission management mechanism so that it can analyze statically the permissions applied by the app and classify them by risk level upon installation; moreover, the users can dynamically revise the permissions as granted through the graphical user interface (GUI) upon installation. Experimental results show this model can achieve the basic functions of permission analysis and management and brings little cost to the system performance.

Keywords Android permission • Lightweight • Static analysis • Dynamic management

120.1 Introduction

Android is an open-source mobile operating system based on Linux. Its market share keeps rising ever since the release of the first version in 2007. It gave birth to a large amount of third-party apps and brought great convenience to people. At the same time, various kinds of malwares are available which steal the users' privacy and deduct fees. According to the "2013 Global Mobile Phone Security Report" as released by NetQin Mobile Inc., 134,790 malwares were verified during 2013, a growth of 106.6 % compared to 2012. 56.56 million mobile phones in total were affected in 2013, with a growth of 76.8 % compared to 2012 [1]. Most malwares are executed at background and possess certain permissions to use the phone resources; in this sense, a comprehensive permission management mechanism is of great significance.

P. Que (✉) • X. Guo • Z. Wang
Laboratory of Network Applications and New Technology,
Communication University of China, 100024 Beijing, China
e-mail: que5320xm@126.com

The existing Android permission mechanism doesn't provide security analysis and fine-grained management of permissions. In order to remedy this problem, this paper presents a lightweight permission management model which enables users to fully understand the risk when installing an app and dynamically grant or revoke certain permission applied by the app.

120.2 Analysis of Existing Permission Mechanism

The Android system has defined more than 130 application permissions to restrict the utilization of mobile phone resources. The android system uses a hierarchy to divide the application permissions into four levels: normal, dangerous, signature, and signatureOrSystem. The normal permissions can be utilized freely without risk to the system. The dangerous permissions must be stated and can be used only when the user grants it. It's the kind of permissions which this paper is focusing on. The signature system permissions demand the permission user to own the same signature with the existing one. Usually, two kinds of permissions are utilized by OEM and ODM manufactures.

If an app has to apply permissions of dangerous level, it must state the permissions in the `AndroidManifest.xml` file during development [2]; otherwise the system would throw out a security exception when the app tries to use the permission not stated. During an app's installation, "PackageInstaller" of the system would resolve the `AndroidManifest.xml` and list the permissions on the install-confirm interface. Although users are able to see all dangerous-level permissions applied by the app, they cannot exactly determine the potential risks; moreover, once the installation is allowed, it implies that the user agrees to grant all permission applied. There is no way to revoke the granted permissions except to uninstall. It's an all-or-none option. The existing mechanism forces users to accept all permissions and provides no dynamic management, which is definitely the defect why Android has long been criticized. To optimize the mechanism, it's necessary to modify the original Android system to improve its static analysis capabilities and append its dynamic managing functions.

120.3 Optimized Permission Mechanism

This chapter puts forward a lightweight permission model implemented by modifying the original permission framework. The modified framework is composed of static analysis and dynamic management with the static analysis displaying the applied permissions by risk level when an app is installed and jumping to the permission management GUI as soon as the accomplishment of installation. Every single permission can be modified on this management interface so that the users can also revoke or grant certain permissions in system settings anytime.

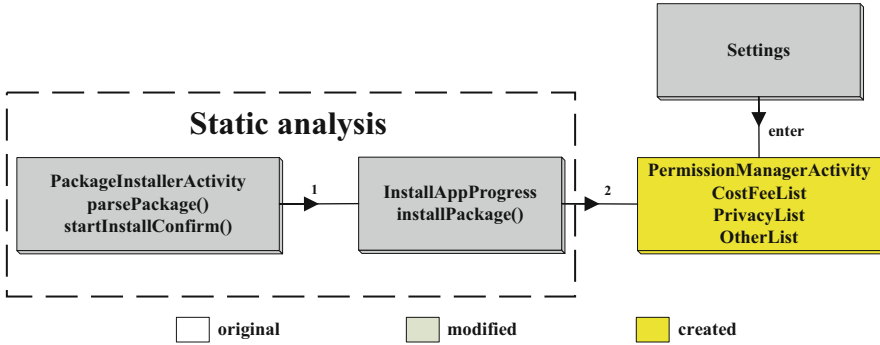


Fig. 120.1 Static analysis framework

120.3.1 Implementation of Static Analysis

The static analysis runs at install time so that the lightweight principles must be considered to avoid lengthy install time; thus, we resolve the AndroidManifest.xml file in apk package to get applied permissions and sort them into three groups according to the judging logic. Such three groups are fee-deduction related, privacy related, and other permissions. This makes the installation process much more clearer than the original system. Figure 120.1 shows the static analysis framework. As the original Android system only contains PackageInstallerActivity and InstallAppProgress, we have modified the two classes and created the PermissionManagerActivity as the GUI of permission management.

In Fig. 120.1, the apk installation process consists of two activities including the PackageInstallerActivity and the InstallAppProgress [3]. Firstly, the PackageInstallerActivity calls the parsePackage() method in PackageParser class to resolve profiles in apk package and obtain infos including package name, path, version number, applied permissions, etc. Then the system (unmodified) jumps to install-confirm interface, the startInstallConfirm() method lists all applied permissions, here we modify this method to make it a newly created method sortPermission(), the sortPermission() method uses a judging logic to classify the permissions into three groups as described above, and then the three kinds of permissions are separately displayed in three ListViews, called CostFeeList, PrivacyList, and OtherList, respectively. Then if the “install” button is pressed, the system would jump to the InstallAppProgress activity which carries out the real installation. We modify the installPackage() method in this activity by adding an Intent() method; then it jumps to PermissionManagerActivity and the GUI of dynamic permission management as soon as the accomplishment of installation. The GUI can set permission as allow, deny, or request with the implementation to be discussed below.

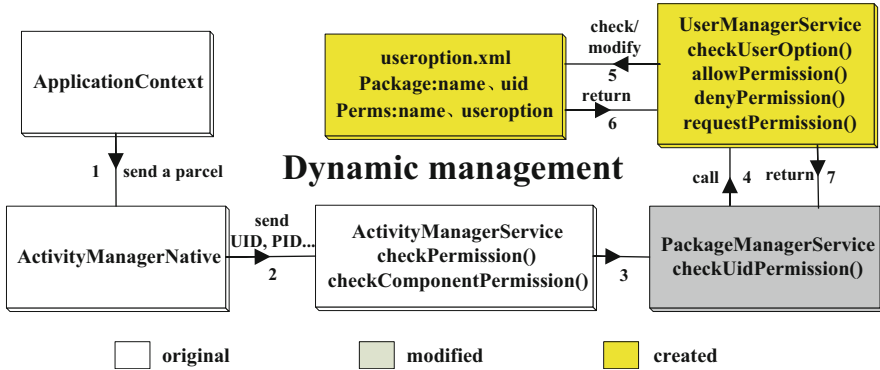


Fig. 120.2 Dynamic management framework

120.3.2 Implementation of Dynamic Management

As described above, the PermissionManagerActivity class is created as GUI for permission management, and it calls the newly created class UserManagerService which does the real work of permission management.

Figure 120.2 shows the process of dynamic permission checking and modification. As far as the checking is concerned, ApplicationContext class catches the raised intent and checks whether it needs permission [4]. If the permission is needed, the system will check the same if the calling intent owns that permission. The checking method is to send a parcel containing PID, UID (identify the application), and the specific permission name to the ActivityManagerNative class [5], which then resolves the parcel and sends the resolved parameters (PID, UID, and permission name) to checkPermission() method in ActivityManagerService class. The checkPermission() method is the only public entry point for the permission checking. This method then calls the checkComponentPermission(). It checks whether the calling intent belongs to the system or root level and returns PERMISSION_GRANTED directly if yes; otherwise it calls the checkUidPermission() in PackageManagerService class to see if the specific permission is contained in the app’s granted permissions [6]. The original checkUidPermission() method just judges whether a permission is contained in the app’s applied permissions because all applied permissions have been granted during the install time. Here we modify this method to let it check one step further users’ option recorded in UserOption.xml, which is newly created and can be checked or modified by the new class UserManagerService. The format of the xml file is shown in Fig. 120.3. The file contains multiple tags including the <package name>, <userId>, and <perms> with the contents in <perms> tag showing the app’s applied permissions’ name and the user’s policy. “0” represents allow, “1” represents deny, and “2” represents request.

```
<package name="com.example.testDemo" userId="10156">
<perms>
<item name="android.permission.ACCESS_NETWORK_STATE" useroption="0"/>
<item name="android.permission.INTERNET" useroption="1"/>
<item name="android.permission.CALL_PHONE" useroption="2"/>
</perms>
</package>
```

Fig. 120.3 Format of UserOption.xml

This file is generated when the system is initialized for the first time. We modify the writePackageLPr() method in the settings class so that the app's info is written into UserOption.xml whenever an apk package is installed.

The permission modification also works with this xml file. There are four permission-managing methods in UserManagerService, namely, the checkPermission(), the allowPermission(), the denyPermission(), and the requestPermission(). The checkPermission() method examines whether an app owns one specific permission by checking the value of <useroption> tag and then return it to PackageManagerService; the other three methods modify the user's permission policy by altering the value to 0, 1, or 2.

120.4 Experimental Verification

The model in this paper is modified based on Android 4.0 source code. The modified source code is compiled into system image according to official documents [7]. In order to ensure the universality of testing environment, we use the Android emulator contained in SDK as the platform with a test demo app utilized to examine the new features. To ease the presentation, we use "new system" to represent our modified system and original system for original Android system.

To facilitate the test, we use a self-written app testDemo. It applies six permissions including CALL_PHONE, READ_PHONE_STATE, SEND_SMS, INTERNET, ACCESS_COARSE_LOCATION, and WAKE_LOCK after importing the apk package into the new system. We click the package item and it turns to the new install-confirm interface as shown at the left side of Fig. 120.4. In order to examine the effects of permission management in the new system, we set the CALL_PHONE permission of testDemo as denied and requested in the permission management GUI; then we test the app's call function to observe the effects. When the system detects that the permission has been forbidden, it would throw out a security exception as in the middle of Fig. 120.4 and quit the application and ask for user's choice when the permission is set as "request" as showed at the right side of Fig. 120.4.

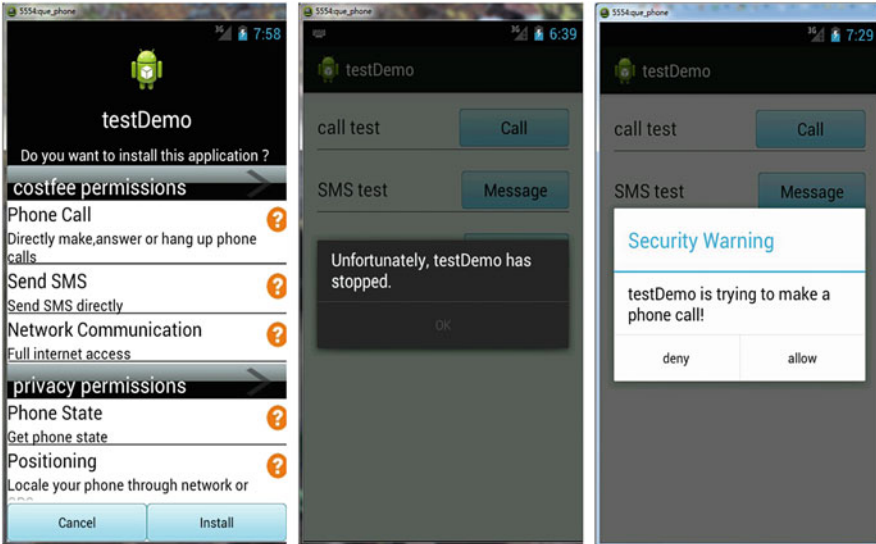


Fig. 120.4 New system features

To verify the lightweight feature of the new system, we use the CaffeineMark3.0 testing tool. CaffeineMark3.0 tests six aspects of JVM: Sieve item tests the prime numbers found by the classic sieve of Eratosthenes; Loop tests the use sorting and sequence generation so as to measure the compiler optimization of loops; Logic tests the speed, with which the virtual machine executes the decision-making instructions; String tests repeated string concatenations and searches for patterns in the concatenated strings; Float simulates a 3D rotation of objects around a point; Method test executes the recursive function calls to see how well VM handles the method calls; and the Total is the final score of the system. The results are shown in Fig. 120.5 with the data as the mean value of test results for five times.

As we can see in the above table, the Sieve, Logic, and String items of the new system are more or less lower than the original system; the Loop, Float, and Method items are close to the original system. The total score is 8,852, which is 3.2 % lower than 9,146 of the original Android system. The declined performance is mainly caused by the judging logic, processing module, and the reading and writing of xml file. Generally speaking, the new system has achieved new functions with small cost.

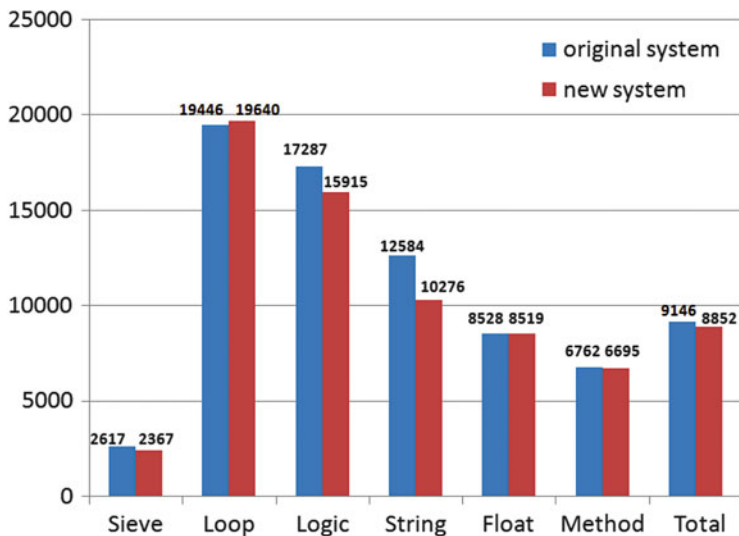


Fig. 120.5 Performance test

Conclusion

This paper has analyzed the weakness of existing Android permission mechanism and proposed a lightweight permission mechanism model which consists of static analysis and dynamic management. The modified system classifies the applied permissions into three groups. The system jumps to dynamic permission management GUI instantly after installation is done, and users are also able to grant or revoke certain permissions through the entrance in system settings. This model remedies the defects of the original Android system and does little harm to system performance.

When we have successfully incorporated this model in Android, a lot of work remains to be accomplished for fully exploiting the potential of the model. Firstly, the evaluation mechanism of malicious permission combination and intelligent protection engine should be imported in the core system; secondly, it's necessary to complete the handling mechanism of exception caused by permission missing; finally, the extra cost of system performance should be further reduced.

References

1. NetQin Mobile Inc. Global mobile phone security report, 2014. http://www.dqdaily.com/dqw/shms/2014-02/26/content_1894200.htm. 2013.
2. Google. Android reference: App Manifest. <http://developer.android.com/guide/topics/manifest/manifest-intro.html>. 2010.

3. Machigar O, et al. Semantically rich application-centric security in Android. *Security and Communication Networks*. 2012;5(6):658–73.
4. Felt A, et al. Android permissions demystified. *Proceedings of the 18th ACM conference on Computer and communications security*. ACM; 2011. p. 627–38.
5. Nauman M, Sohail K, XinWen Z. Apex: extending android permission model and enforcement with user-defined runtime constraints. *Proceedings of the 5th ACM Symposium on Information, Computer and Communications Security*. ACM; 2010. p. 328–32.
6. Kern M, Johannes S. Permission tracking in Android. *UBICOMM 2012, The sixth international conference on mobile ubiquitous computing, systems, services and technologies*. XPS; 2012.p. 148–55.
7. Google. Android Reference: initializing a build environment. <http://source.android.com/source/initializing.html>. 2010.

Chapter 121

Modeling of Virtual Electrical Experiment

Yinling Zhang, Deti Ji, and Renyou Zhang

Abstract Three types of models in virtual electrical experiment, circuit structural model, circuit computation model, and human-machine interaction model, are studied. The XML-based circuit structural model describes a circuit's structure by marking the composing components, which makes the model well formed and extensible. Computation model is constructed based on the circuit topology structure and electrical principles (KCL and KVL), and an algorithm of generating computation model is proposed. Interaction model is designed to describe the interaction information in the operation of the virtual experiment. The models are valuable in design and development of virtual electrical experiment.

Keywords Virtual experiment • Circuit • Modeling • Interaction

121.1 Introduction

Virtual experiment is turning into a frequently used teaching resource which improves the flexibility and quality of education effectively. During the past decades, different virtual experiments were developed to facilitate secondary or higher education. An optical simulation experiment was designed to overcome problems in the teaching of middle school physics optical experiments [1]. Maria Limniou integrated an interactive UV-visible spectrophotometer simulator to improve chemistry instrumentation teaching [2]. A virtual experiment for mechanism motion learning was developed by Shanghai Jiaotong University [3].

However, there is no general development pattern for virtual experiment, which leads to great duplicate efforts in the process of design and development. In this paper, we try to devise general model architecture to regulate the design pattern of virtual electrical experiment and then accelerate the implementation process.

Y. Zhang (✉) • R. Zhang
Academy of Armored Force, 233050 Bengbu, China
e-mail: frankxtu1@126.com

D. Ji
The Third High School of Bengbu, 233000 Bengbu, China

121.2 Models in Virtual Electrical Experiment

When doing the electrical experiment, the experimenter connects electronic components, operates virtual instrument, measures electrical quantity, and achieves the goal of exploring electrical principles. The procedure of a virtual experiment is shown in Fig. 121.1.

The simulation objects of the virtual experiment are circuit and the interaction between circuit and experimenter. Therefore, the models in electrical virtual experiment should include circuit structure model and interaction model. While another fundamental circuit model is the mathematical-physical model, hereinafter is referred to as computation model. The relationship of the three types of model is hierarchical, as shown in Fig. 121.2.

The computation model lies at the bottom of the hierarchical architecture. It is important but invisible in the system.

The structural model is located in the middle of the architecture. It connects the neighboring layers. It could be transformed into computation model, from which the values of voltage and current are calculated. The calculated result of computation model may affect the structural model in return, in case that some component is broken down.

The interaction model is on the top layer, which connects the system with its user.

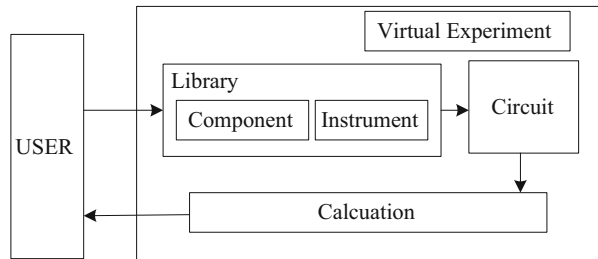


Fig. 121.1 Procedure of a virtual experiment

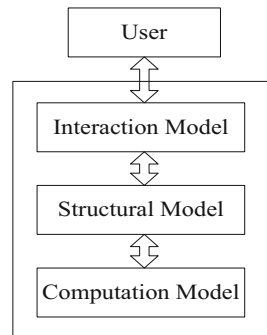


Fig. 121.2 Models in virtual experiment

121.3 Circuit Structural Model

The structure of circuit is the connection of electrical components, which is the foundation of circuit computation. The component of structural model maps one for one to each virtual component of the virtual system.

121.3.1 Components

In most electrical experiments of middle school, the components used are source, voltmeter, ammeter, bulb, switch, resistor, sliding rheostat, etc. Each kind of component or instrument has different pins or parameters, which comprise the main attributes of the component in circuit structural model.

Taking the circuit shown in Fig. 121.3 as an example, we can see that the circuit is composed of resistors, meters, etc.

121.3.2 XML-Based Structural Model

To meet the demands of virtual experiment on circuit structural model, we propose an approach to describe the circuit structure by marking the electrical components and instruments composing the circuit. The structural model adopts the thought of flexibility and extendibility [4]. It is encoded in XML language, which marks each component of the circuits. Figure 121.4 lists the attributes of common components and instruments.

The structural model of circuit in Fig. 121.3 is encoded as follows:

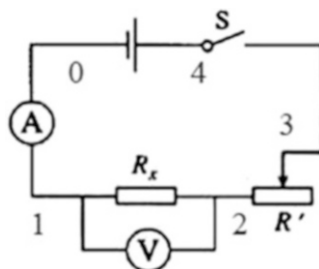


Fig. 121.3 Example circuit

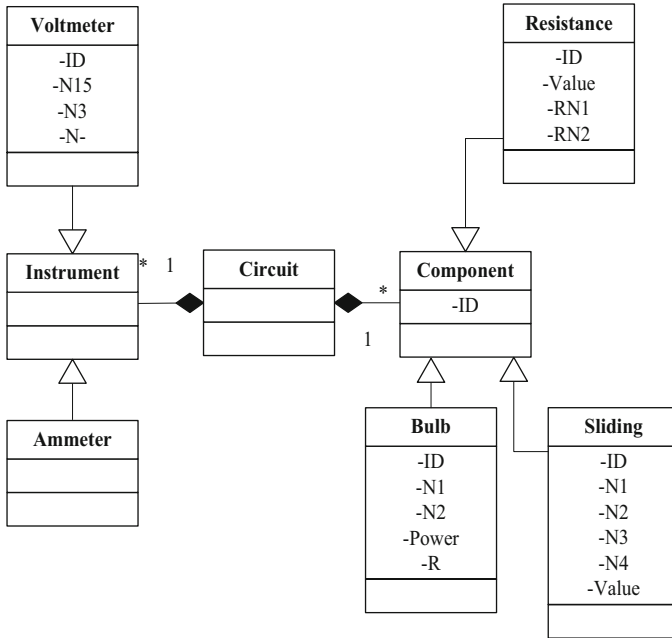


Fig. 121.4 Circuit structural model

```

<Circuit name="circuit1">
<Resistor id="Rx">
<value>rx</value>
<n1>1</n1>
<n2>2</n2>
</Resistor>
<Resistor id="R">
<value>1/g4</value>
<n1>2</n1>
<n2>3</n2>
</Resistor>
<Sliding id="R'">
<value>r'</value>
<n1>2</n1>
<n2>3</n2>
</ Sliding >
<Source id="SV">
<value>1.5</value>
<n1>0</n1>
<n2>4</n2>
</ Source >
<Ammeter id="AM">

```

```
<value>i</value>
<n1>0</n1>
<n2>4</n2>
</ Ammeter >
< Voltmeter id="SV">
<value>v</value>
<n1>0</n1>
<n2>4</n2>
</ Voltmeter >
</Circuit>
```

121.4 Computation Model

The computation model of a circuit is a set of mathematical formulae constructed on the principle of electricity, which computes electrical parameters of the circuit.

121.4.1 Kirchhoff's Laws

Kirchhoff's circuit laws are two equalities that deal with the current and potential difference (voltage) in the lumped element model of electrical circuits [5]. Both of the Kirchhoff's laws can be understood as corollaries of the Maxwell equations in the low-frequency limit. They are accurate for DC circuits and for AC circuits at frequencies where the wavelengths of electromagnetic radiation are very largely compared to the circuits.

121.4.2 Computation Process

We propose an algorithm to build the computation model based on KCL and KVL. The flow of the constructing algorithm is:

1. Determine whether the circuit is closed by checking the isolated node.
2. Close the node of the switches to get the topological structure of the circuit.
3. Construct the linear equation based on the topological structure.
4. Judge whether any component works beyond its rating range.
5. Calculate branch voltage and current according to the node potential and resistance values.

121.5 Interaction Model

121.5.1 Experiment Operation Flow

When users log in in the virtual experiment system, they select needed instruments and components, drag them into the experiment area, connect them by wires, and test the circuit by the meter's reading. The process of virtual experiment is the same as that of real experiment, which is dominated by experiment specification and electrical principle.

The virtual experiment is accomplished through the interaction between operator and virtual component, which represents the information transmission among virtual entities. The interaction model describes the entities and their interaction behaviors.

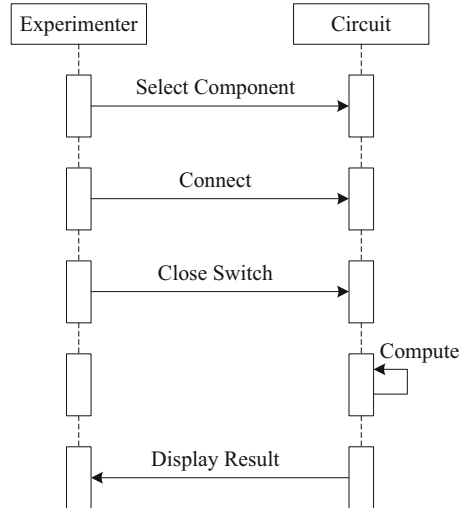
121.5.2 Entities

In virtual experiment, entities include experimenter, component, instrument, and signal. The entity of experimenter is the analog of real operator, whose attributes are name, student ID, and so on. The entity of component is the object of the experiment operation. In the interaction model, the attributes of component entity only include ID and its terminal numbers, but the electrical characteristic values are not necessary. The entity of the interaction model could be extracted from the structural model by removing the electrical characteristic attributes. The entity of signal is another important type of entity which is not included in the structural model of a circuit, because it is the result of the interaction between the operator and instrument. In direct current circuit, the signal may be a number, which represents a value of voltage or current. In alternating current circuit, it may be an AC signal.

121.5.3 Interaction Behavior

The interaction behavior includes [6]: selection of component, connection of the circuit, test of circuit using instrument (by closing the switch), computation of circuit, and displaying the computing result. All the behaviors are executed between the experimenter and the virtual experiment system.

Virtual experiment simulates the real experiment process, which permits the experimenter to operate freely. The experimenters may design an experiment, change the connection, and test value of any node, out of sequence. The interaction behavior process is shown in Fig. 121.5.

Fig. 121.5 Interaction behavior

Simulation and Conclusion

As a useful complementary of traditional experiment, virtual experiment is widely used in education. Because various experiments have different characteristics, it is impossible to unify the development modes of virtual experiment. The models studied in this paper provide virtual electrical experiment with a suitable design schema. A virtual experiment system has been implemented with the operating interface as shown in Fig. 121.6.

The readings listed in Table 121.1 are collected during the virtual experiment. When we repeat the same experiment with real circuit and instruments, we get highly consistent data with the readings measured in the virtual experiment. Some virtual values are more accurate than those of real experiment, because the real meters have reading errors. We conclude that as long as we construct correct computation model, the virtual experiment is validated. The circuit structural model and interaction model determine the effect of virtual experiment.

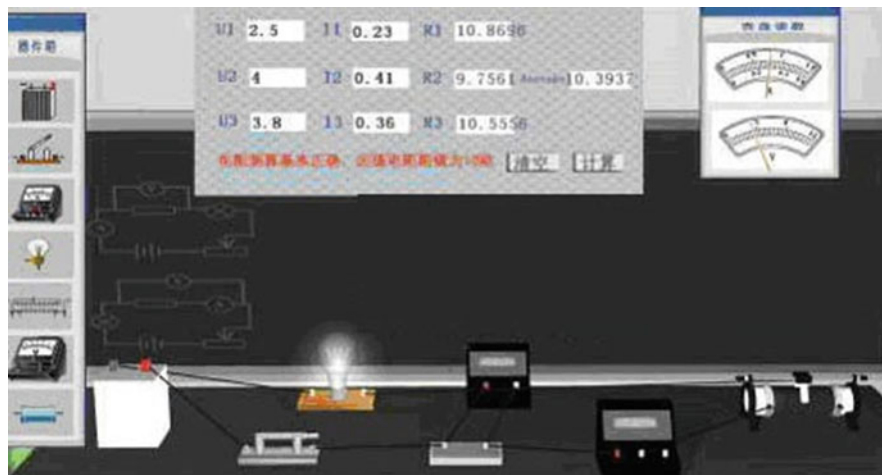


Fig. 121.6 Virtual experiment interface

Table 121.1 The simulation result

Variables	Values (V)	Variables	Values (A)
U1	2.5	I1	0.23
U2	4.0	I2	0.41
U3	3.8	I3	0.36

References

1. Ma X, Zhong S, Xu D, Zhang C. The design and implementation of middle school physics. In: Edutainment 2010. LNCS, Springer-Verlag Berlin Heidelberg, vol. 6249; 2010. p. 84–91
2. Limniou M, Papadopoulos N, Roberts D. An integrated lecture, virtual instrumentation lab approach to teaching UV-vis spectroscopy. *Educ Inf Technol.* 2007;12:229–44.
3. Fan X, Zhang X, Cheng H, et al. A virtual experiment platform for mechanism motion cognitive learning. In: *Virtual and mixed reality*, Springer-Verlag Berlin Heidelberg; 2011. p. 20–9
4. Jiufei T, Xingming O, Junqing Y. Research of virtual experiment based on Flex and XML. *Wuhan Univ J Nat Sci.* 2012;17:36–42.
5. Oldham KTS. The doctrine of description: Gustav Kirchhoff, classical physics, and the purpose of all science in 19th-century Germany. Ph.D. thesis. Berkeley; University of California: 2008. p. 52
6. Guotao H. Design and realization of virtual physics lab for junior high school. Wuhan: Central China Normal University; 2011 (in Chinese).

Chapter 122

Human Intervention Intelligent Flight Path Planning on Unexpected Threats

Peng Ren, Xiaoguang Gao, and Jun Chen

Abstract The technique of human intervention intelligent flight path planning on unexpected threats is proposed in this paper as a key technology to carry out manned and unmanned aerial vehicles cooperative combat. It makes full use of human brain to guide the solution procedures and combine artificial auxiliary decision with novel intelligence algorithm. Human's wisdom, experience, and synthetic judgments can make up for the lack of intelligence algorithm. A lot of simulation studies show that the online three-dimensional flight paths based on the improved technology can meet the requirements of the actual application with certain practicality.

Keywords Human intervention • Flight path planning • Unexpected threats

122.1 Introduction

In modern air battles, manned and unmanned aerial vehicles have respective advantages and are interdependent. They complement each other and divide labor and cooperation to achieve the more operational effectiveness. The manned and unmanned aerial vehicles cooperative combat is a revolutionary new combat method to make effective breaking through in terms of the integrated IADS (air defense system) and will be the main air combat pattern in the future [1–4]. Human-UAV (unmanned aerial vehicle)-coordinated operation fully utilizes human's wisdom, experience, and synthetic judgments and combines the special ability of UAV to carry out the mission of surveillance and precision strike in the most dangerous environment [5, 6]. With the dynamic development of the battlefield situation, the unexpected threats are inevitable. Because of huge three-dimensional flight path points, vast searching space, strong real-timeliness, and large conditions of constraint, the method of solution is extremely complex and difficult. It is difficult to guarantee the optimal solution by the traditional intelligent algorithms [7, 8].

P. Ren (✉) • X. Gao • J. Chen
Institute of Electronic Engineering, Northwestern Polytechnical University,
710072 Xi'an, China
e-mail: 2728428@qq.com; r122p@163.com

Human intervention intelligent flight path planning is proposed in this paper by combining the artificial auxiliary decision with the novel intelligence algorithm. In the most dangerous environment, it makes the best possible use of human brain to guide solution procedures of the flight path replanning on unexpected threat range. The novel intelligence algorithm originates from the evolutionary algorithm as a kind of niche adaptive pseudo parallel genetic algorithm. The method can replan the online three-dimensional flight paths when the starting and ending positions are set by human. A lot of simulation studies show that the online three-dimensional flight paths by this technology can meet the requirements of UAV low-altitude penetration and efficiently implement the threat avoidance, terrain avoidance, and terrain following.

122.2 Algorithm of Human Intervention Intelligent Flight Path Planning

With the low-altitude penetration especially under unknown unexpected threats, accurate mathematical model cannot be established. Generally, it is not effective and quick to obtain optimal solutions only relying on traditional intelligence algorithms. As human brain is a kind of superintelligence device with functions of striking self-learning, thinking, reasoning, judging, and memorizing, it can deal with many complicated environments very well. Therefore, under the conditions of current technological level, human intervention intelligent flight path planning is proposed in this paper to combine artificial auxiliary decision with novel intelligence algorithm.

122.2.1 Artificial Auxiliary Decision

With the separation of management and control function, the communication time delay including the delay of remote control commands and telemetry signals is available. The online path replanning may not be obtained so that UAV could not avoid new threats. In the course of combat, the target information obtained by UAV is transmitted to the manned aerial vehicles via data link; besides, the manned aerial vehicles have better battlefield situation awareness. Human has been endowed with special abilities of evaluating the air combat threat and the decision-making behavior. Human-UAV coordination has made full use of human's wisdom, experience, and synthetic judgments to help UAV path replanning and avoid threats. The flowchart of artificial auxiliary decision is shown in Fig. 122.1.

There are two situations:

UAV is beyond the unexpected threat coverage

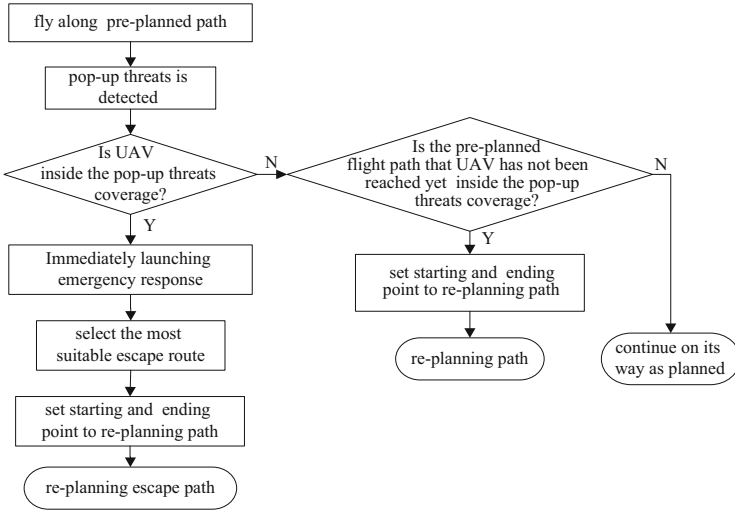


Fig. 122.1 Flowchart of artificial auxiliary decision

As the preplanned flight path that UAV has not been reached yet is inside the unexpected threat coverage, the human’s experience and synthetic judgments can be utilized to accurately determine the starting and ending point of replanning path by means of comprehensive assessment of the situation and threats with the novel intelligence algorithm thus applied to replan the path to avoid threats effectively and quickly. If the flight path points are too numerous, which demands more computing time, it is difficult to guarantee accessibility and timeliness only relying on novel intelligence algorithms. In order to avoid threats effectively, set few navigation points manually between the starting and ending points according to the actual situation and flight characteristics and then depart the path to calculate respectively. If the preplanned flight path is beyond the unexpected threat coverage, continue on its way as preplanned.

UAV is inside the unexpected threat coverage

Launch the emergent response immediately to escape routes as the scheduled angle interval in all directions, then select the most suitable escape route by comprehensive assessment of the situation and threats, then set the intersection of the selected escape route and the threat coverage region boundary as the starting point, and set the ending point on the preplanned path manually to replan the route between the new starting and ending point. In this way, utilize the human’s wisdom, experience, and synthetic judgments and the novel intelligence algorithm to guide UAV safely and reasonably within the unexpected threat coverage area.

122.2.2 Novel Intelligence Algorithm

The novel intelligence algorithm can be improved as below:

1. Divide the whole group into several subgroups to search multi-orientedly in the solution space so that both the depth and the extent of the search can be guaranteed. Every subgroup evolves different processors independently and synchronously. The diversity of population is maintained and the operation speed of the algorithm is enhanced.
2. Apply a kind of niche adaptive genetic mechanism in the subgroup. The individual in each generation can be divided into several categories, and the best individuals are selected from each category to form a new population.
3. The niche technique based on function sharing can effectively prevent premature, maintain the population diversity, and improve the search efficiency so that more optimal solutions can be achieved.

The novel intelligence algorithm takes the form:

1. Set evolution iteration counter, and generate m initial population $P(t)$.
2. Divide $P(t)$ into n subpopulations, every subpopulation has k individuals, $k = m/n$, where k is an integer. $P(t) = \{P_1(t), P_2(t), \dots, P_i(t), \dots, P_n(t)\}$.
3. Calculate f_{ij} ($i = 1, 2, \dots, n; j = 1, 2, \dots, k$) of $P_i(t)$ ($i = 1, 2, \dots, n$), in which f_{ij} denotes the fitness and $P_i(t)$ denotes the subpopulation.
4. Independent evolution based on niche adaptive:
 - (a) Set independent evolution iteration counter.
 - (b) $P_i(t)$ is sorted in a descending order according to the values of f_{ij} , keep previous q individuals, $q < k$.
 - (c) Make use of the improved operators of choice, adaptive crossover, and mutation to get new individuals $P'_i(t)$ ($i = 1, 2, \dots, n$).
 - (d) Niche evolution operation algorithm: q individuals are generated by step (b) and $P'_i(t)$ is generated by step (c) and together form a new population comprising $k + q$ individuals.
 - (e) Calculate the values of sharing degree about individual among group, S_{ij} ($i = 1, 2, \dots, n; j = 1, 2, \dots, k + q$) denotes the sharing degree. Adjust individuals according to S_{ij} , and new fitness f'_{ij} ($i = 1, 2, \dots, n; j = 1, 2, \dots, k + q$) of subpopulation can be obtained.
 f'_{ij} is calculated by the given expression:

$$f'_{ij} = f_{ij}/S_{ij} \quad (i = 1, 2, \dots, n; j = 1, 2, \dots, k) \quad (122.1)$$

S_{ij} is typically defined as

$$S_{ij} = \sum_{i=1}^{k-1} Sh[i, j] \quad (j = 1, 2, \dots, k; i \neq j) \quad (122.2)$$

where $Sh[i, j]$ refers to the sharing function and is often taken as

$$Sh[i, j] = \begin{cases} 1 - d_1[i, j]/\sigma_1 & d_1[i, j] < \sigma_1, \quad d_2[i, j] \geq \sigma_2 \\ 1 - d_2[i, j]/\sigma_2 & d_1[i, j] \geq \sigma_1, \quad d_2[i, j] < \sigma_2 \\ 1 - \frac{d_1[i, j] * d_2[i, j]}{\sigma_1 * \sigma_2} & d_1[i, j] < \sigma_1, \quad d_2[i, j] < \sigma_2 \\ 0 & d_1[i, j] \geq \sigma_1, \quad d_2[i, j] \geq \sigma_2 \end{cases} \quad (122.3)$$

where $d_1[i, j]$ is the Hamming distances between the i th and j th individual, $d_2[i, j]$ is the fitness distances between the i th and j th individual, and σ_1 and σ_2 are the individual maximum distance of genotype and phenotype, respectively.

- (f) $k + q$ individuals are sorted in a descending order according to the new values of f_{ij}^t , keep previous k individuals, and $P_i''(t)$ ($i = 1, 2, \dots, n$) is obtained.
 - (g) Niche judgment of terminal condition: if this condition is not met, independent evolution iteration counter should be updated, take the previous k individuals by step (f) as next subpopulation, and go to step (b), else exit niche evolution.
5. The island model in this algorithm is employed according to the information exchange between subgroups; thus $P_i(t + 1)$ ($i = 1, 2, \dots, n$) is obtained, in which $P_i(t + 1)$ denotes the next-generation population.
 6. Judgment of terminal condition: if this condition is not met, the evolution iteration counter should be updated and return to step (3); otherwise, give the optimized results and end the process.

Comparing evolutionary algorithms by calculation between the traditional ones and new algorithm, the results are shown in Table 122.1. It can be found that the novel intelligence algorithm can decrease the iteration number and gain optimal solution.

Table 122.1 Comparison results of performance of different evolutionary algorithms

Algorithm	Average convergence generations	Average convergence time/s	Note
Genetic algorithm			No solution
The niche adaptive Genetic algorithm	1,136	912	Optimal solution
The niche pseudo parallel genetic algorithm	725	556	Optimal solution
Novel intelligence algorithm	87	51.4	Optimal solution
	158	92.7	Suboptimal solution

122.3 Experimental and Simulation Results

In order to test and evaluate the performance of the proposed algorithm, a number of design and aircraft simulation tests have been carried out in the current work with details of the experimental and simulation results as described in the sections below.

122.3.1 Replanning Paths When UAV Is Beyond the Unexpected Threat Coverage

Figure 122.2 shows the replanning paths elevation chart by the novel intelligence algorithm and human intervention when UAV is beyond the unexpected threat coverage. Six known threats and effective distance $d_{Rmax} = 12,000$ m are represented by six same size hollow circles. One unexpected threat and effective distance $d_{tRmax} = 6,000$ m is represented by a red circle. From this figure, we can see that UAV could avoid threats and terrain along the preplanned paths I and II. When the unexpected threat is found and covers the preplanned path I that UAV should fly along, it is necessary to replan the path for UAV immediately. Now the human's wisdom and experience is adopted to set the starting and ending points of the replanning path. The starting point is on the preplanned path I that UAV has not been reached, and the ending point is on the preplanned path I or II that is beyond the unexpected threat coverage. Then replan the new section paths by the novel intelligence algorithm so that UAV could avoid threats and terrain along the new

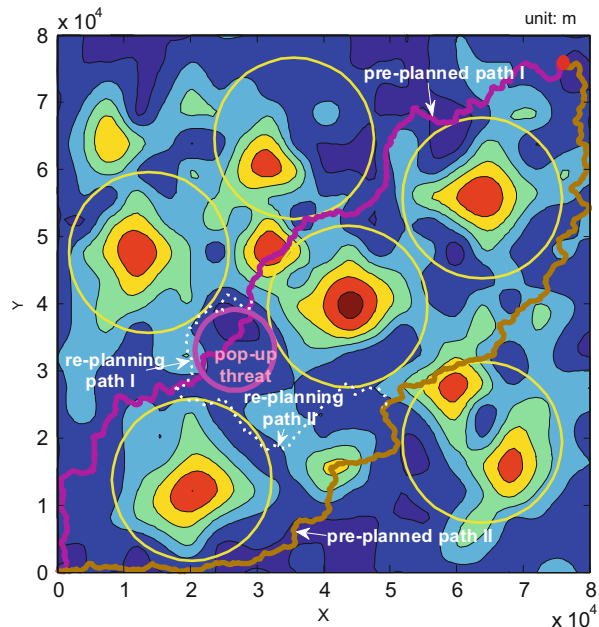


Fig. 122.2 Elevation chart of the replanned paths

section paths. The next step is to select one new suitable section path artificially according to the mission requirement of UAV and comprehensive situation assessment. If the unexpected threats are detected until later when the computing time for replanning path is not enough, set few navigation points manually between the starting and ending point, and then depart the replanning path to calculate, respectively, for avoiding threats effectively.

122.3.2 Replanning Paths When UAV Is Inside the Unexpected Threat Coverage

Figure 122.3 shows the elevation chart of escape paths when UAV is inside the unexpected threat coverage. The known and unexpected threats and preplanned paths are depicted the same as shown in Fig. 122.2. When the unexpected threat is detected and UAV is flying along preplanned path inside coverage areas of it, promptly launch emergency response program and imply five scheduled escape paths on the different directions by the dashed lines in Fig. 122.3, utilize human’s wisdom and experience to select a most suitable path for escaping according to comprehensive situation assessment, then put the intersection of threat coverage border and escape path as the starting point, and set the ending point artificial on the preplanned path I or II that is outside the threat coverage for the next replanning path, escape path is implied by the solid line. From this figure, we can see that UAV can avoid threats and terrain along two escape paths. Finally, UAV is guided on the

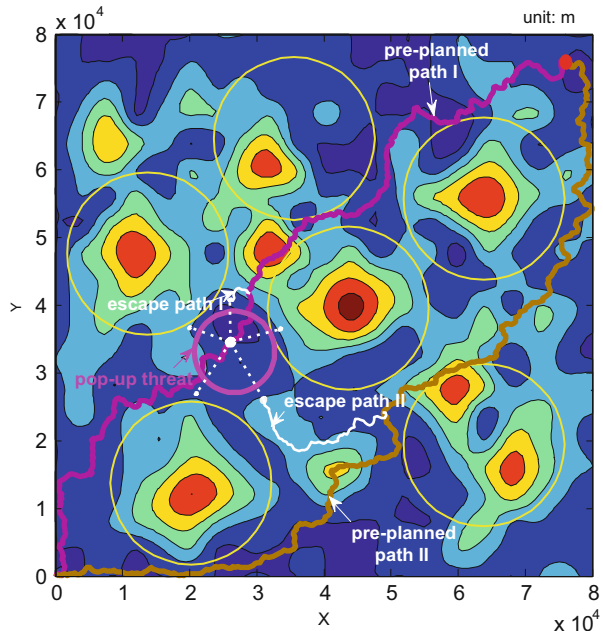


Fig. 122.3 Elevation chart of escape paths

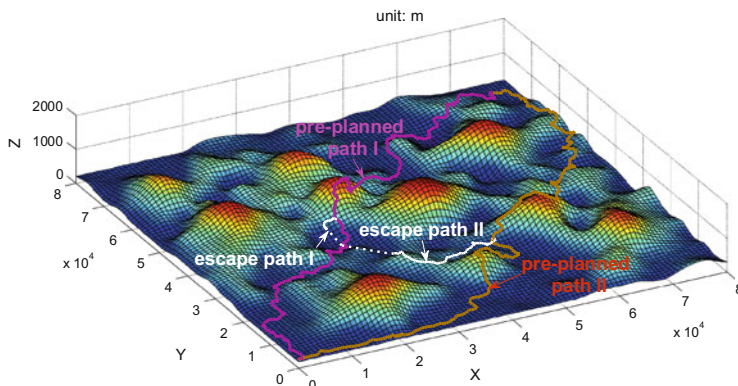


Fig. 122.4 Three-dimensional map of escape paths

preplanned paths. Figure 122.4 indicates the three-dimensional map of escape paths. They show that the replanning escape paths can meet the requirements of UAV low-altitude penetration and efficiently implement the threat avoidance, terrain avoidance, and terrain following.

Conclusion

In this paper, the algorithm of human intervention intelligent flight path planning is proposed to combine the artificial auxiliary decision with the novel intelligence algorithm. On the basis of lots of simulation studies, we can reach the following conclusions:

1. The novel intelligence algorithm based on evolutionary algorithm can decrease the iteration number and gain optimal solution within ideal time. When the threat and terrain information are known, set the starting and ending points artificially and then apply the novel intelligence algorithm to replan the flight paths that can meet the requirements of UAV low-altitude penetration.
2. Human's wisdom, experience, and synthetic judgments can make up for the lack of intelligence algorithm. It makes the best possible use of the human brain to guide the solution procedures of replanning flight path against the unexpected threats.

Finally, manned and unmanned aerial vehicles cooperative combat is a revolutionary new combat method and may be the main air combat pattern in the future. Human-UAV-coordinated operation could fully utilize human's wisdom, experience, and synthetic judgments to guide solution procedures of the flight path planning against unexpected threats. The simulation result shows that this method is feasible and effective. It is necessary to make the research in this regard more deeply and more widely.

Acknowledgments This work was sponsored by Nature Science Foundation of China (61305133).

References

1. Murray CC, Park W. Incorporating human factor considerations in unmanned aerial vehicle routing. *IEEE Syst Man Cybern Soc.* 2013;43(4):860–74.
2. Savla K, Temple T, Frazzoli E. Human-in-the-loop vehicle routing policies for dynamic environments. In: *Proceedings of the 47th IEEE conference on decision control, Cancun, Mexico.* 2008. p. 1145–50
3. Donald W. Manned/unmanned common architecture program (MCAP): a review. In: *Proceedings of the 22nd digital avionics systems conference, Indianapolis, United States.* 2003. p. 6.B.4/1–6.B.4/7
4. Valenti M, Schouwenaars T, Kuwata Y, et al. Implementation of a manned vehicle—UAV mission system. *AIAA-2004-5142.* 2004
5. Schouwenaars T, Valenti M, Feron E, et al. Linear programming and language processing for human/unmanned aerial vehicle team missions. *J Guid Contr Dyn.* 2006;29(2):303–13.
6. Ren P, Gao X-g. Operational effectiveness analyses of AH/UAV cooperative surveillance against mission. *Flight Dyn.* 2011;29(3):92–6 (in Chinese).
7. Fu X-w, Gao X-g. 3D flight path planning based on Bayesian optimization algorithm. *Acta Armamentarii.* 2007;28(11):1340–5 (in Chinese).
8. Shen Z-h, Zhao Y-k, Wang X-r. Niche pseudo-parallel genetic algorithms for path optimization of autonomous robot. *Mod Electron Tech.* 2005;206(15):85–7. 90 (in Chinese).

Part VI
Network Optimization

Chapter 123

Effectiveness Analysis of Communications Jamming to Battlefield Ad Hoc Network

Sijia Lou, Jun He, and Wei Song

Abstract Based on complex network theory, a scale-free network model is established to analyze the effectiveness of the battlefield ad hoc network (BAHN) in communication jamming conditions. Taking into consideration a BAHN's complex network characteristics, this paper combines its measurement and effectiveness. In analyzing the effectiveness of a BAHN, a quantitative analysis model is presented to connect the communication jamming equation with the concept of network node topology potential.

Keywords Battlefield ad hoc network • Complex network theory • Communications jamming • Node topology potential

123.1 Introduction

An ad hoc network is a kind of self-organizing wireless network based on a distributed protocol, so it has no central node. Such a network does not require a fixed communication infrastructure and has advantages in terms of setup, adaptability, invulnerability, node mobility, and system cost. Because of its high survivability and flexibility, ad hoc networks have been used in battlefield mobile communication environments by military forces [1].

Relying on the capabilities of routing reconstruction and connection recovery of ad hoc networks, communication jamming becomes difficult to achieve and its effectiveness of jamming is also difficult to analyze. Because the structure of an ad hoc network is similar to the that of the Internet, some people have even questioned the interference feasibility of communication jamming. An increasing number of people are looking for ways to carry out a cyber attack on high-tech communication networks, but the achievement is not satisfying. However, the emergence of complex networks provides new ideas and methods for topological evolution and dynamic analysis studies of ad hoc networks.

S. Lou (✉) • J. He • W. Song
Electronic Engineering Institute, 204 Room, 230037 Hefei, China
e-mail: lousijia99@sina.com

123.2 Battlefield Ad Hoc Network Model

123.2.1 *Finite Size of Barabási–Albert Scale-Free Network Model*

Complex network theory provides some basic models, for example, small-world networks, scale-free networks, and local-world evolving networks. While choosing a suitable model for studying BAHNs, the features of ad hoc networks should be fully taken into consideration. During BAHN communications, there will be few relay stations between two nodes; otherwise there would be command redundancy. Meanwhile, as with conventional communication, some relatively important nodes will also exist in ad hoc networks, and they will usually correspond to different command levels.

Based on the features of BAHN itself, though simplifying the discussion, a BAHN can be seen as a finite size Barabási–Albert (BA) scale-free network model. A BA scale-free network has characteristics of small-world and power-law networks, and, as Comellas' papers pointed out, models with small-world-network characteristics have been commonly used as communication network models [2], and models with power-law-network characteristics can reflect more the prominent role of some nodes in a network [3]. Meanwhile, the topology of the finite size of a BA scale-free network is often closer to the real battlefield, which is more suitable for military discussions [4].

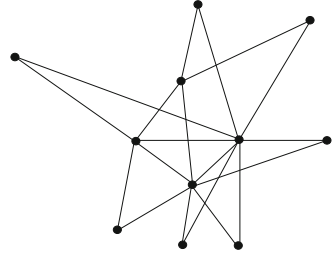
BA scale-free networks are characterized by an expansion of their size, and new nodes follow the so-called Matthew effect and will have a greater probability of connecting to nodes with a higher degree. The typical structure of a BA scale-free network algorithm is as follows [5]:

1. Growth: Starting from a network with m nodes, each time a new node is introduced, the existing m_0 nodes will connect to it, $m < m_0$.
2. Priority connection: A new node connects to an existing node i with a probability of p_i , the degree $\langle k_i \rangle$ of node i and the degree $\langle k_j \rangle$ of node j should satisfy the following relationship:

$$p_i = \frac{\langle k_i \rangle}{\sum_j \langle k_j \rangle}. \quad (123.1)$$

Figure 123.1 is an example of the finite size of a BA scale-free network with 11 nodes:

Fig. 123.1 Finite size of BA scale-free network



123.2.2 Basic Measurement Analysis

123.2.2.1 Average Path Length

The distance d_{ij} between two nodes i and j is defined as the number of edges on the shortest path between these nodes. The maximum distance between any two nodes in the network is called the *diameter*, denoted by D :

$$D = \max_{i,j} d_{ij}. \quad (123.2)$$

The average path length L of the network is defined as the average distance between two nodes:

$$L = \frac{1}{\frac{1}{2}N(N+1)} \sum_{i \geq j} d_{ij} \quad (123.3)$$

N is the total number of nodes. Studies have shown that, despite the huge number of nodes in many real complex networks, the average path length in the networks is alarming small.

123.2.2.2 Clustering Coefficient

If node i has k_i edges connected to other nodes, then the k_i nodes are called the *neighbors* of node i . Obviously, there will be at most $k_i(k_i - 1)/2$ edges between these k_i nodes. The clustering coefficient C_i is defined as the ratio between real existing edges E_i and possible edges, $k_i(k_i - 1)/2$:

$$C_i = 2E_i/k_i(k_i - 1). \quad (123.4)$$

The average of all nodes' clustering coefficients is called the whole network's clustering coefficient and is denoted by C :

$$C = \sum_1^N C_i \quad (123.5)$$

N is the total number of nodes. In particular, when $C = 0$, all nodes are isolated and there are no edges; when $C = 1$, the network is completely coupled and every two node has an edge.

123.2.2.3 Degree and Degree Distribution

The degree $\langle k_i \rangle$ of node i is defined as the number of other nodes connected to it. The value of a node's degree reflects its importance in the network. The greater the degree, the more force the node will have, and the effect of it in the network will be greater. The average of all nodes' degrees is called the *average degree* and is denoted by $\langle k \rangle$:

$$\langle k \rangle = \sum_1^N \langle k_i \rangle \quad (123.6)$$

N is the total number of nodes. The degree distribution denotes the probability distribution function of the degrees, and it reflects the probability that a random node's degree is k .

According to the preceding definition, it is not difficult to draw some useful conclusions. The smaller the average path length a BAHN has, the less time and fewer steps it will require during operation, which makes it more efficient. The larger the clustering coefficient of the BAHN, the better able it is to provide mutual support in combat. But once paralyzed, the network is very difficult to restore. The greater degree a BAHN has, the more uniform the importance distribution of nodes, that is to say, the network reflects a flatter technology in command and control mechanisms. The parameter values of these three important concepts are given in (Table 123.1):

Table 123.1 Some finite-size parameters of a BA scale-free network

Parameter	Value
Number of nodes, N	11
Average path length, L	2.18
Clustering coefficient, C	0.54
Degree, $\langle k \rangle$	4.27

123.3 Analysis of Communication Jamming in BAHNs

123.3.1 Communication Jamming Equation

In evaluating the effectiveness of communication jamming, a commonly used index is the *neutralizing coefficient*. Regarding the communicating nodes of an ad hoc network, the neutralizing coefficient can be defined as the ratio between the jamming power P_{rj} and the signal power P_{rt} of the receiving nodes' input when communication jamming is effective. With respect to digital communication, the standard of successful communication jamming is usually to achieve an error rate P_e of 0.2 [6]. The neutralizing coefficient is denoted by K_a :

$$K_a = \left. \frac{P_{rj}}{P_{rt}} \right|_{P_e=0.2} \tag{123.7}$$

Communication jamming in a BAHN often takes distributed disturbance methods, which are jammers using omnidirectional antennas. T , R , and J represent respectively the position of the communication transmitting node, communication receiving node, and communication jammer. R_t is the distance between the transmitting node and the receiving node, R_j is the distance between the jammer and the receiving node, and θ is the angle between R_j and R_t (Fig. 123.2).

The ratio between the jamming power and signal power obtained by communication receiving nodes should exceed the neutralizing coefficient K_a when communication jamming is effective. Using Fig. 123.2, a communication jamming equation can be established for a single jammer's interference in a single network node [7]:

$$\frac{P_{rj}}{P_{rt}} = \frac{P_j G_j q_{rj}(\theta) \gamma_j \varphi_j(R_j) B_{rj}}{P_t G_t q_{rt} \varphi_t(R_t)} \geq K_a \tag{123.8}$$

P_t and G_t respectively represent the power and gain of the transmitting node; P_j and G_j respectively represent the power and gain of the jammer; q_{rt} represents the gain of the receiving node in the direction of the transmitting node; $q_{rj}(\theta)$ represents the gain of the receiving node in the direction of the jammer, which is related to the

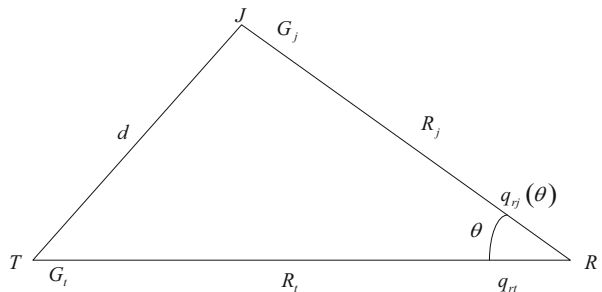


Fig. 123.2 Spatial relationship between transmitting nodes, receiving nodes, and jammers

angle θ ; γ_j represents the polarization loss (when $\gamma_j=0.5$, the polarization is circular); $\varphi_t(R_i)$ and $\varphi_j(R_j)$ represent respectively the transmission loss of the communication circuitry and the jamming circuitry; and B_{rj} represents the distance between the jammer's signal and the receiving node's signal.

While interfering the communication nodes in the network with N jammers, the receiving node achieves a jamming power that is the total power that the N jammers send to the node. For a special node i , the communication jamming equation is transformed into

$$\frac{\sum_{j=1}^N P_{rj}}{P_{rt}} \geq K_a (i = 1, 2, \dots, N). \quad (123.9)$$

123.3.2 Impact of Communication Jamming on BAHNs

As a soft-kill weapon, communication jamming cannot deliver a direct blow to the nodes of a BAHN, but it can provide effective support for the follow-up operations. As soon as interference in some network nodes is successfully implemented, the overall network operation will be affected. As a result, the network's interconnection capacity, restoring, and reorganization abilities and command and control capabilities will be greatly decreased.

Analysis of BAHNs under communication jamming should be based on the interference with each receiving node, and a general description should also reflect the situation of the entire network when disturbed. Thus, the first task must be to analyze closely the nodes in the network and then use the complex nature of the network itself to quantitatively analyze the whole network. The use of important concepts in complex networks, such as average path length, clustering coefficient, and degree, will better reflect the effect of communication jamming on BAHNs and facilitate one's understanding of the nature of the network itself and the significant issues in combat.

123.4 Effectiveness Analysis of Communication Jamming in BAHNs

123.4.1 Communication Node Topology Potential

The concept of node topology potential is based on data field theory in cognitive physics [8], where each node in a network topology has a certain potential. Node topology potential describes the potential values of a node in a network with the

effect on itself and its neighbor. A BAHN can be represented by, for example, how vulnerable it is to attack, the impact of invalidation on the other node, and the probability of recovery. Based on the parameters of complex networks and in particular the specific properties of BAHNs, a communication node's topology potential E_i is expressed as follows [9]:

$$E_i = \sum_{j=1}^N \left(\langle k_i \rangle \times e^{-\frac{d_{ij}}{C_i}} \right). \quad (123.10)$$

The sum of the potentials of all nodes in the network is equal to the overall potential E of the network:

$$E = \sum_1^N E_i (i = 1, 2, \dots, N). \quad (123.11)$$

When outside interference makes the communication node's potential E_i drop to Fibonacci number 0.618, the node is deemed disabled [10–13]; this critical point corresponds exactly to the neutralizing coefficient K_a , which just represents the invalidation of the nodes in the process of communication jamming. In addition, communication jamming of a BAHN can actually be regarded as a continuous process. The actual reaction occurs when a node is disturbed; each edge is not necessarily disconnected at the same time; E_i decreases continuously with increases in jamming power. When the interference condition does not satisfy the communication jamming equation, the amplitude of the reduction of the nodes' potential is relatively small. When the interference condition satisfies the communication jamming equation, the potential will be significantly reduced.

123.4.2 Effectiveness Analysis of BAHN Under Communication Jamming

When multiple nodes in a network are disturbed, the quality of the entire network will be affected. The communication jamming equation can be used to determine whether a node is currently in a disabled state. Based on the actual situation, if a node is disabled, it usually means the communication equipment has some trouble. The side who has been interfered will immediately repair the communication equipment or change its tactical application to complete the repair. When measuring a complex network, the clustering coefficient C is most closely related to the probability that the node will be repaired. Without considering the impact of other indicators, suppose the relationship between the probability of being repaired p_i and the clustering coefficient C is

$$p_i = e^{-K_i C_i}, \quad (123.12)$$

where K_i relates to the performance of the communication device itself [14].

Taking into account the communication jamming and node repair, the operational process of communication jamming in a BAHN can be deduced. If the potential of the whole network is reduced to 60 %, the network system can be regarded as having reached the tipping point [15]. Even if a small number of nodes do not become from the system, the entire complex network will have completely collapsed from the point of view of large-scale confrontation.

Conclusion

This paper used complex network theory to establish models that combine the effectiveness of BAHNs with their complex characteristics. Based on the proposed communication jamming equation and the concept of communication node topology potential, this paper analyzed quantitatively the effectiveness of a BAHN under conditions of communication jamming.

References

1. An H et al. Router arithmetic and agreement in ad hoc network. Beijing: Science Press; 2009. p. 9–10 (in Chinese).
2. Alderson DL. Catching the “Network Science” bug: insight and opportunity for the operations researcher. *Oper Res.* 2008;56(5):1047–65.
3. Albert R, Barabasi A-L. Statistical mechanics of complex networks. *Rev Mod Phys.* 2002;74(6):47–91.
4. Mueller S, Tsang RP, Ghosal D. Multipath routing in mobile ad hoc networks: issues and challenges. In: *The ACM SIGCOMM Conference on Communications Architectures*. London: London Press; 1994. p. 93–5.
5. Wang X, Li X, Chen G. Theory and application of complex network. Beijing: Tsinghua University Press; 2006. p. 10–2 (in Chinese).
6. Wang L, Wang M. Suppress area calculation of communications jamming. *EEI Trans.* 1998;1:52–4 (in Chinese).
7. Wang M, Zhong Z, Yi X, Yang J, Cai X. Elements of electronic countermeasures. Beijing: Military Sciences Press; 2013. p. 256–8 (in Chinese).
8. Li D et al. Incertitude artificial intelligence. Beijing: National Defence Industry Press; 2005. p. 64–9 (in Chinese).
9. Xiao L et al. Essentiality compositor and appraisal method to network nodes based on topology potential. *Wuhan Univ Trans.* 2008;33(4):77–9 (in Chinese).
10. Liu C et al. Study of modeling and simulation to consensus diffuse. Beijing: Nation Defense University Press; 2007. p. 66–8 (in Chinese).
11. Crosbie R, Zenor J. High level architecture module basic concepts. *Soc Comput Simul.* 2001;4:156–89.
12. Darilek R, Perry W. Measures of effectiveness for the information-age army. *Rand.* 2001;8:263–301.
13. Liu J. Consensus diffuse. Beijing: Tsinghua University Press; 2001. p. 100–2 (in Chinese).
14. Zhang M et al. Study of modeling and simulation method based on agent system. *Syst Simul Trans.* 2005;17(11):34–5 (in Chinese).
15. Hu X, Yang J, Si G, Zhang M. Simulation analysis and experimentation of martial complex system. Beijing: Nation Defense University Press; 2008. p. 277–8 (in Chinese).

Chapter 124

Research and Outlook on Wireless Channel Models

Yuqing Wang, Cuijie Du, Xiujuan Han, Yuxin Qin, and Hongqi Wang

Abstract With social progress and the rapid development of information technology, wireless communication has become an important means of communication. In this paper, several common and typical wireless channel models are reviewed and summarized. We analyze the characteristics of various channels so as to identify the channel models appropriate in different environments. Finally, comparison and suggestions are provided for the optimization of certain models and conclusions regarding the application of channel models is given.

Keywords Wireless communication • Channel model • Multipath fading • Path loss • UWB

124.1 Introduction

In recent years, communication between people has become more and more frequent. There is no doubt that wireless communication has emerged as one of the most popular and complicated ways to communicate. A wireless channel is the hub of a wireless communication system. It is also the medium by which transmitters and receivers are connected. There is a big difference between a cable channel and a wireless channel in that the latter is invisible while a cable channel usually means a transmission medium like a symmetrical cable, coaxial cable, optical cable, and so on; therefore, the signal propagation path in a cable channel is fixed and would not be easily affected by the surrounding environment. However, a variety of different interactions occur in wireless channels. Shadow fading and multipath delays produced by hills, trees, or walls may render a receiver incapable of distinguishing between different multipath components. Then the interference of

Y. Wang • C. Du (✉) • Y. Qin • H. Wang
School of Mechanical and Power Engineering of Henan Polytechnic University, 454000
Jiaozuo, Henan, China
e-mail: 158572832@qq.com

X. Han
College of Computer Science and Technology of Henan Polytechnic University, 454000
Jiaozuo, Henan, China

multipath signals with each other leads to the received signal strength is abated. As a result, the quality of the communication system is significantly degraded.

The development of a proper channel model has great significance for studying the characteristics of wireless communication systems and improving the quality of such systems. This paper is divided into four sections. In Sect. 2, we summarize the scope of the channel model, presenting related calculation formulas. In Sect. 3, a comparison is made of different channel models. In the last section, we draw conclusions. The aim here is to provide a reference for choosing a suitable channel model in different environments.

124.2 Typical Channel Models

Research on wireless communication was carried out in the nineteenth century. In 1895, Marconi succeeded in wirelessly transmitting a signal between an island in the UK and a tugboat [1]. Thus was born wireless communication in the modern sense. Nowadays, after much hard work over many years, a number of models have been established for the purpose of researching the characteristics of mobile channels in order to communicate in various environments. Those models have reached mature stages in our lifetimes. In what follows we review some typical wireless communication models.

124.2.1 Okumura's Model

The Okumura model is derived from measurements made by Okumura in 1968 [2]. Some empirical curves obtained using Okumura's model are among the most common models applied to predict signals. The frequency measured is from 150 to 1,920 MHz, even as high as 3,000 MHz. The distance between the base station and mobile station is 1–100 km. The transmitting and receiving antennae are 30–1,000 m tall [3]. The model can be separated into two sections as follows [4]:

1. The formula of Okumura's model in flat-terrain cities is

$$L_m = L_{bs} + A_m(f, d) - H_b(h_b, d) - H_m(h_m, f), \quad (124.1)$$

where L_{bs} is the path loss in free space.

2. The path loss of signal in irregular terrain and different environment is discussed as follows. On this basis, the median path loss value of irregular terrains and different places is obtained by adding the corresponding correction factor to Eq. (124.1):

$$L_m = L_{bs} + A_m(f, d) - H_b(h_b, d) - H_m(h_m, f) - k_s - k_h - k_A - k_{is}. \quad (124.2)$$

Okumura's model is based solely on test data, with no analysis available. The value which is out of the scope is produced by extrapolating curve. However, it supplies the most simple and precise solution to radio system path loss prediction for mature cellular and land mobile. Because of its practicability, Okumura's model has become the standard in land mobile radio system plans.

124.2.2 Hata Model and COST231

In Okumura's model, path loss is given by graph data. Hata then fits the path loss into an empirical formula, which is called the Hata model [5]. The frequency measured in the Hata model is from 150 to 1,920 MHz. Although Hata's model does not correct for errors of a specific path like Okumura's model, it is a very good approximation to Okumura's model when the transmission distance d is greater than 1 km. Hata's model is suitable for systems in widespread regions, but it does not reflect the propagation characteristics of a cellular system in smaller regions and at high frequencies, either. In addition, it does not reflect indoor propagation characteristics.

124.2.3 Jakes Model

To simulate a mobile channel, it is necessary to establish a random process on the basis of the attenuation produced by the multiple paths of the channel. This process possesses a specific envelope distribution density and a specific Doppler spectrum. The sum of series of sinusoidal signals is approximate to Rayleigh fading. The number of sinusoidal signals must be large so that probability density function of the envelope approximates that of a Rayleigh channel. In this way, the sine signal is weighted so that it can approximate the Doppler spectrum of the channel with enough accuracy. Based on the foundation, the Jakes model, developed by William Jakes at Bell Labs, was used to fit channels of wireless attenuation. The equation of channel transformation is as follows [6, 7]:

$$h(t) = E \sum_{i=1}^N C_i \exp[j(w_d t \cos \alpha_i + \varphi_i)], \quad (124.3)$$

where E is the fixed parameter, respecting the path loss power. In this model, we assume that the mobile station is moving and the frequency of the signal received changes with the movement, which is called the Doppler effect. The Doppler frequency shift is given by [8]

$$f_d = \frac{v}{\lambda} \cos \alpha = f_m \cos \alpha. \quad (124.4)$$

In the simulation of Jake's model, Jake used various forms to determine the amplitude attenuation of the low-frequency oscillator, doppler frequency shift and the phase angle of arrival wave. The attenuation wave involves a nonstationary process, which leads to some defects in simulating the real channel. In this sense, the improved Jakes model is commonly used in simulations. Some authors use MATLAB to obtain simulation curves by the improved Jakes model, and the conclusion is confirmed [9].

124.2.4 Clarke Model

Clarke established the Clarke model, which is suitable for the fading channels. Statistical properties of the field strength of a signal received by a mobile station are based on scattering [10]. In this model, we assume that there is a fixed transmitter with a vertical polarization antenna. Electromagnetic waves incident to the mobile station antenna consist of a set of plane waves. Those waves are in the carrier phase and have an incident angle and the same average amplitude. In the environment, there is no Line Of Sight (LOS), a path with no obstacles. Scattering components have the same attenuation upon being propagated a small-scale distance [3]. Clarke's model is commonly used in simulations. By the Jacobean [11], we obtain

$$p(r) = \begin{cases} \frac{r}{\sigma^2} \exp\left(-\frac{r^2}{2\sigma^2}\right), & 0 \leq r \leq \infty \\ 0 & r < 0 \end{cases}. \quad (124.5)$$

This produces a model of a simulated signal applied in the modulation path of orthogonal and in-phase. The frequency spectrum and the temporal statistical properties of a signal are very close to those of the measurement data. The Clarke model is suitable for environments with flat fading and without multipath delay; therefore, it is usually used to measure electromagnetic field statistical properties of signals received by a mobile station.

124.2.5 UWB Model

The Ultra Wideband (UWB) model appeared in 1960, but it was usually only used, for example, in the military or disaster relief or with positioning or ranging radar. In February 2002, it was approved for civil and commercial use for the first time. Then its market prospects attracted a lot of attention. The UWB model is used in data transmission and indoor voice communication, for example, in office buildings, shopping malls, factories, and hospitals. It modulates impulses directly. Impulses have a steep rise and fall time. This advantage causes the signal to have a bandwidth

in the gigahertz range, which solves the major issue that had plagued traditional antenna technology. It has become a research hotspot in indoor or short-distance wireless communication for its advantage of having a thick skin in fading, low transmission power, and low system complexity [12]. The methods used to measure UWB include frequency domain and time domain, but they can both be given by the channel impulse response:

$$h(t, \tau) = \sum_{n=1}^{N(t)} a_n(t) \delta(t - \tau_n(t)) e^{j\theta_n(t)}, \quad (124.6)$$

where $h(t, \tau)$ is the impulse response of the channel at time t , a_n is the amplitude of the n th path, τ_n is the arrival time of the n th path, θ_n is the phase for the n th path, and N is the number of paths. The distributions used to describe arrival times are the standard Poisson, modified two-state Poisson, and double Poisson.

The frequency domain autoregressive (AR) model is another approach to characterizing a UWB channel because the frequency response of a UWB channel at each point $H(f_n, x)$ can be modeled by an AR process. This model was initially introduced [13] for wideband systems and was used later for UWB channel models [14]. The process is given by the following equation:

$$H(f_n, x) - \sum_{i=1}^p b_i H(f_{n-1}, x) = V(f_n), \quad (124.7)$$

where $H(f_n, x)$ is the n th sample of the complex transfer function at location x , b_i is a complex model parameter, $V(f_n)$ is the complex white noise process, and p is the order of the model. The Z transform of the formula gives the following equation:

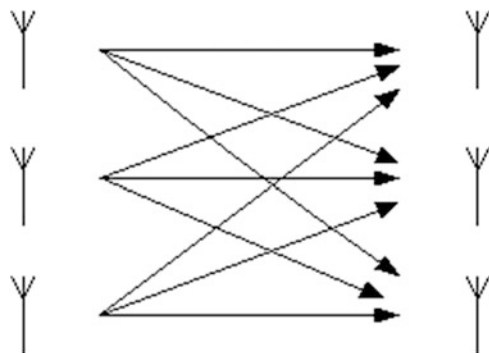
$$G(z) = \frac{1}{\prod_{i=1}^p (1 - p_i z^{-1})}. \quad (124.8)$$

Based on the frequency domain measurements, an AR model with two orders is reported to be sufficient for characterizing a UWB indoors at 4.3–5.6 GHz [15].

124.2.6 MIMO Model

With the strict requirements of wireless communication, traditional technology is unable to satisfy demand; therefore, more advanced technology emerged called multiple-input and multiple-output (MIMO) [16]. A MIMO model is an abstract mathematical model that describes a wireless communication system with multi-antenna. It transmits signals with multiple antennas in the transmitter and receives signals with multiple antennas in the receiver. Compared with a

Fig. 124.1 MIMO model



traditional simple-input and simple-output (SISO) model, in a MIMO model, the antenna array is used between the transmitter and receiver. A transmission subchannel is found in the transmission channel, which is called a MIMO channel [17]. We assume that the number of transmission antennas is N in the transmitter and the number of receiving antennas is M in the receiver; thus, the transmission path between them can be described by a matrix: H_{MN} . The arbitrary element h_{ij} represents a subchannel, which is also the transmission subchannel between the j th transmission antenna and the i th receiving antenna (Fig. 124.1).

In MIMO model, the relationship between the output and the input is given by [18]

$$y(t) = H(t) * s(t) + n(t), \quad (124.9)$$

where $s(t)$ is the transmission signal, $y(t)$ is the receiving signal, and $n(t)$ is the Additive white Gaussian Noise (AWNG). Although, a MIMO model could increase the system throughput widely and enlarges the transmission distance, it does not have to add the bandwidth at the same time or enhance the total transmission power. Because it uses multiple antennas, the number of antennas and the distance between antennas are important parameters. In particular, the latter is crucial for realizing the high-frequency spectrum efficiency of a MIMO model. If too many antennas are deployed, some issues will arise. Thus, the number of antennas should be equivalent. For example, if there are four antennas, we can set the distance between antennas to 10λ [19], where λ is the wavelength.

124.3 Comparison of Channel Models

The Okumura–Hata, Clarke, and Jakes models have traditional advantages, and the theories and technologies behind them are very mature. But with the rapid development of communications technology, UWB and MIMO models are attracting more and more attention. The UWB model could provide a simple system and -speed data transmission, even up to 1 Gbit/s. Experimental results show that UWB

signal can propagate in underground mine tunnels with a low rate of loss [20]. A RMS delay spread was found of approximately 11.8–29.7 ns for LOS and Non Line Of Sight (NLOS), respectively [21]. When compared to those of the conventional narrowband, these values are very small, which means that high data transmission rates can be achieved with UWB; therefore, UWB could be used in digital homes or office networks to achieve high-speed data transmission within short distances. Researchers at Bell LABS have devoted considerable effort to developing MIMO technology, which has the advantage of using multiple paths to provide higher data throughput, increase coverage, and improve reliability without taking up additional radio frequencies; in addition, it has resolved issues surrounding data transmission speed and coverage in radio technology.

Conclusions

Clearly, it is extremely important to establish accurate channel models for the design of a communication system, especially when wireless communication is used in confined environments with diffracting rough surfaces, such as mine coal. This paper presents six models. In fact, there are other models besides these six being used in real applications because of the many uncertain factors in wireless communication. We can easily draw some conclusions from this paper; for example, because of the different environments in which wireless communication can be deployed, results may differ, even if the same model is used. As for Okumura's model, there are corresponding correctional factors for cities, mountainous regions, and countries; therefore, there is no uniform standard for choosing a model because of environmental variations. Whatever the environment, the model will have disadvantages. The ideal situation is when we choose the model; our choice should be shaped by actual conditions, which will dictate the type of mobile device needed and the model parameter values. Only in this way can we enhance the validity of the experimental results.

In addition, different models have different formulas and path losses, which lead to differences in calculations and accuracy among the different models. In actual use, the real environment must be taken into consideration, including such factors as the location of obstacles and the range covered by the radio signal. In the laboratory, experiments should be carried out in combination with the environment and the channel properties. Then the information transmission of the wireless channel can be investigated effectively. In the future, UWB and MIMO technology will be better optimized and supported by increasingly mature technology for use in wireless communication devices. Of course, much work remains before this goal is achieved.

Acknowledgments This paper was supported by the National Natural Science Foundation (U1261115) and by the State Key Laboratory Cultivation Base for Gas Geology and Gas Control at the Henan Polytechnic University (WS2012A06).

References

1. Goldsmith A. *Wireless communication*. Beijing: Posts & Telecom Press; 2007. p. 24–5.
2. Okumura T, Ohmori E, Fukuda K. Field strength and its variability in VHF and UHF land mobile service. *Rev Electr Commun Lab*. 1968;16(9–10):825–73.
3. Rappaport TS. *Wireless communications: principles and practice*. 2nd ed. Brijing: Publishing House of Electronics Industry; 2009. p. 40–1.
4. Zhou L, Liu HP. Research on channel models of wireless communication system. *OME Inf*. 2010;27(4):26–30.
5. Hata M. Empirical formula for propagation loss in land mobile radio service. *IEEE Trans Veh Technol*. 1980;VT-29(3):317–25.
6. Zhang TD, Yuan GC. Simulation of an improved Jakes model. *Ship Electron Eng*. 2012;32(6):80–2.
7. Clarke RH. *A statistical theory of mobile-radio reception*. New York: Bell System; 1968. p. 957–9.
8. Li M, Sun EC, Zhang Y. Research on wireless channel models. *J China Acad Electr Inf Technol*. 2012;7(5):483–9.
9. Huang S, Yan YB, Li Y. Research and improvement of Jakes model. *J ChuXiong Normal Univ*. 2012;24(12):42–4.
10. Zhang M. Design and realization of Clarke model simulation system. *J Chongqing Technol Bus Univ*. 2005;8(23):63–7.
11. Rappaport TS, Seidel SY, Takamizawa K. Statistical channel impulse response model for factory and open plan building radio communication system design. *IEEE Trans Commun*. 1991;39(5):794–807.
12. Yu JG, Lu AH. Introduction to the UWB model. *J Xi'an Inst Ports Telecommun*. 2013;11(1):29–32.
13. Howard SJ, Pahlavan K. Autoregressive modeling of wide-band indoor radio propagation. *IEEE Trans Commun*. 1992;40(9):1540–52.
14. Turin W, Jana R, Ghassemzadeh SS, et al. Autogressive modeling of an indoor UWB radio channel. Baltimore,MD,USA In: 2002 I.E. Conference on Ultra Wideband System and Technologies; IEEE; 2002. p. 71–4.
15. Ghassemzadeh SS, Jana R, Rice CW, et al. A statical path loss model for in-home UWB channel. Baltimore,MD,USA In: 2002 I.E. Conference on Ultra Wideband System and Technologies; IEEE; 2002. p. 59–64.
16. Wu JT, Lin Y, Zhai JC. Review of MIMO model. *Mob Commun*. 2008;23(4):43–7.
17. Wang WS. Methods to model MIMO channel. *Commun Technol*. 2009;1(2):42–4.
18. Dai HY, Zhang XF, Li GH, et al. Modeling and simulation of MIMO system based on spatial channel model. *J China Acad Electr Inf Technol*. 2013;8(2):125–30.
19. Xiao ZR, Yu Z, Wu WL. Research progress of MIMO communication system. *J Chongqing Univ Posts Telecommun*. 2004;16(4):25–9.
20. Abdellah C, Paul F, Pierre MT. Characterization of the ultra-wideband channel in confined environments with diffracting rough surfaces. *Wirel Pers Commun*. 2010;62(1):859–77.
21. Taparugssanagorn A, Hama M, Iinatti J. Wideband and ultrawideband channel models in working machine environment. *Model Simul Eng*. 2012;11(55):1–10.

Chapter 125

Defending Against Whitewashing Attacks in Peer-to-Peer File-Sharing Networks

Weimin Luo, Jingbo Liu, Jiang Xiong, and Ling Wang

Abstract Nowadays, peer-to-peer (P2P) file-sharing networks have been widely applied because of the popularity of P2P software. Complete freedom not only allows for the development of P2P networks but also brings about security risks. Malicious nodes can escape the punishment of reputation mechanisms by performing some attacks such as a whitewashing attack. In this paper, we propose a novel reputation mechanism based on two kinds of reputation so as to resist a whitewashing attack. We analyze the reputation and the capacity of the node corresponding to two different behaviors. The relationship between the behavior, capacity, and reputation of the node is discussed. We give the calculation method of our reputation mechanism and run simulations. The results show that our reputation mechanism could defend against a whitewashing attack effectively.

Keywords P2P networks • Network security • Reputation mechanism • Whitewashing attack

125.1 Introduction

P2P softwares, such as BitTorrent, have been used extensively, and the scale of P2P networks is very large. The advantage of P2P networks, such as anonymity, open, and dynamics, allow nodes to exchange resources freely, which encourages the development of P2P networks but also brings about a variety of security risks to P2P networks. To identify and isolate malicious nodes, many reputation mechanisms have been proposed. Karl et al. [1] discuss and resolve some issues of trust management in P2P networks; nevertheless, when malicious nodes are identified by trust/reputation mechanisms, they can still rejoin networks with different identities by performing whitewashing attacks.

In this paper, we propose a novel reputation mechanism that is capable of effectively defending against whitewashing attacks. The rest of the paper is

W. Luo (✉) • J. Liu • J. Xiong • L. Wang
College of Computer Science and Engineering, Chongqing Three Gorges University, 404000
Chongqing, China
e-mail: weim_luo@163.com

organized as follows. Section 2 presents related works. Then we analyze the reputation and capacity of nodes in Sect. 3. Next we propose our mechanism and present the calculation method of the mechanism in Sect. 4. Simulations are run and an analysis of the results is provided in Sect. 5. Finally we give the conclusion of the paper.

125.2 Related Works

Muntasir et al. [2] provide a survey on the incentive mechanisms in P2P networks. They study free rider, whitewashing, and Sybil attacks and present the concept of such attacks and discuss how to defend against them. Michal et al. [3] study free rider and whitewasher attacks in P2P networks; however, the imposition of a penalty on all legitimate newcomers incurs a significant social loss. Pinninck et al. [4] propose a defense mechanism against whitewashing attacks. The key to their mechanism is that the transferred messages are evaluated by intermediate nodes and request messages from malicious nodes are blocked. Sohail et al. [5] study whitewashing attacks in mobile ad hoc networks. They propose a different trust mechanism based on the task completed. The new node joins the network and must complete a series of tasks. The attack cost is increased to prevent a whitewashing attack. Levine et al. [6] describe the process of a Sybil attack and point out that the trust mechanism may detect network attacks from many aspects, such as trusted certification, resource testing, and recurring costs and fees. Marti et al. [7] consider that all nodes are probably malicious, and this treatment could improve defense performance.

We find that most works focus on the trust/reputation of nodes that upload resources in transactions. Nodes that upload resources should be focused on by the trust mechanism [8], but ignoring the nodes that download resources reflects a lack of understanding of such nodes.

125.3 Two Kinds of Reputation

The node in P2P networks is the provider or consumer of resources, so it should have distinct reputation values according to different behaviors. We first define four concepts to facilitate the subsequent description. A node that uploads resources is called an upload node (UN). Whether or not a node is selected to be an UN is determined by its reputation value. Then the reputation is Upload Reputation (UR). A node that downloads resources is called a download node (DN). Whether or not a node is a DN is determined by its reputation value, and this reputation is the download reputation (DR).

125.3.1 Behavior and Reputation

In most P2P networks, the DN can freely and without limit download any resource from an UN and need not be chosen or evaluated by the UN. Thus, many studies only focus on URs, which is shortsighted.

Once a node uploads incorrect or malicious resources, the UR of the node will decrease. At the same time, if the node downloads and gives correct evaluations of the UN, then the node is a good DN and a bad UN. Other nodes will tend to choose the node to be a DN instead of an UN.

Once a node uploads good resources but gives bad evaluations to the UN after downloading, then the node is a bad DN and a good UN. It causes other nodes to choose the node to be an UN instead of a DN.

Two different scenarios indicate that the reputation of one node varies and is complicated. Whether one node is worth interaction or not, it is determined only by a single aspect will lead to an error.

125.3.2 Relationship Among Reputation, Behavior, and Capacity

A node's reputation should reflect the level of reputation and the behavior capacity. The behavior capacity can be divided into two types: download capacity and upload capacity. The download capacity determines the size of the resource the node can download from an UN in a single transaction. The upload capacity determines the size of the resource the node can upload to a DN in a single transaction.

The relationship among reputation, behavior, and capacity is complicated. We elucidate the relationship from the following three aspects:

1. Reputation can be influenced by behavior. A node should be responsible for its behavior. Good behavior leads to an increase in reputation and bad behavior leads to decrease in reputation. The value of a DR should be decreased if the node does not correctly evaluate the UN after the transaction. Accordingly, the value of an UR should be reduced if the node refuses to upload resources.
2. Reputation and capacity influence each other. When the DR of a node decreases, its download capacity should be reduced to prevent the node from giving a bad evaluation. When the UR of a node is reduced, the upload capacity should be reduced too.
3. The reputation and capacity of an upload or download influence each other. A change in the DR should affect both the download capacity and the upload capacity, as do changes in the UR. For simplicity, when a node's DR or UR changes, two kinds of capacity of the node will be affected.

125.4 Trust Mechanism Based on Two Kinds of Trust

Our reputation mechanism is based on two kinds of reputation, DR and UR, and takes the capacity into account. In our mechanism, the DN must evaluate the UN. At the same time, the UN also evaluates the DN, but this action will be performed automatically by the P2P system. The evaluation value is the value that DN i assigns to UN j after i has finished the number k transaction, which is defined as

$$E_{i \rightarrow j}^k = \begin{cases} 1 \\ -1 \end{cases}, \quad (125.1)$$

where 1 represents that DN is satisfied by the service of the UN and -1 represents that DN is not satisfied. Furthermore, the final evaluation should take into consideration both the resource size and the DR of the DN in order to avoid a rapid accumulation of UR. In this sense, the final evaluation value is calculated as follows:

$$E_{i \rightarrow j}^k = e^{-1/(S_{i \rightarrow j}^k \times R_i^k)} E_{i \rightarrow j}^k, \quad (125.2)$$

where $S_{i \rightarrow j}^k$ is the resource size in the number k transaction between DN i and UN j , R_i^k is the DR of DN i when the number k transaction occurs and $\lim_{S_{i \rightarrow j}^k \rightarrow +\infty, R_i^k \rightarrow +\infty} e^{-1/(S_{i \rightarrow j}^k \times R_i^k)} = 1$. This means that the final evaluation value is equivalent to the original one in order to avoid a rapid accumulation of UR by increasing the resource size or the DR of the DN.

The evaluation is given by the UN to the DN when the transaction is finished. Later it is revised by Eq. (125.2). When the final evaluation has been given, the related UR and DR will be calculated accordingly. The calculated value will be normalized and let UR and DR be in the range (0,1).

Different URs indicate different upload capacities, while the relationship between the DR and the download capacity is the same. We divide reputation and capacity into separate levels in Table 125.1.

Ipoque points out that the size of 81.49 % of files shared in P2P networks are less than 92 MB, and the size of 9 % of files shared are larger than 700 MB [8]. In our mechanism, the new node gets an initial UR of 0.25 and a DR of 0.5. The initial DR of 0.5 is enough to attract new users to acquire resources. The initial 0.25 UR is given so that new users can upload most resources. But the UR will decrease to a lower level rapidly when whitewashers upload malicious resources. The increase in the UR or DR will not cause them to exert an influence on each other. This indicates that the only way to increase the UR or DR is to finish related transactions; but when a decrease in the UR or DR reaches a lower level, the DR or UR will also decrease to a lower level.

Table 125.1 Relationship between reputation and capacity

UR or DR	Upload or download capacity (MB)
>0.75 and <1.00	>500
>0.50 and ≤0.75	>100 and ≤500
>0.25 and ≤0.50	>10 and ≤100
>0.10 and ≤0.25	>0 and ≤10
>0.00 and ≤0.10	0

Our mechanism does not punish nodes that only upload resources. However, a node will be punished when it only downloads resources. Its UR and DR will decrease to a lower level. Correspondingly, the capacity of the UR and DR will decrease. We introduce P to describe the trend of the behavior of a node and define T_k as the time consumed by the node for uploading resources at time k . T_k is calculated as

$$T_k = \begin{cases} e^{-1/(N_k \times S_k \times T_{\text{online}})} T_{\text{upload}}^k & N_k \neq 0, \\ 0 & N_k = 0, \end{cases} \tag{125.3}$$

where T_{upload}^k is the real time consumed by the node for uploading resources at time k , N_k indicates how many times the node uploads resources at time k , S_k is the resource size uploaded by the node at time k . Then P is calculated as

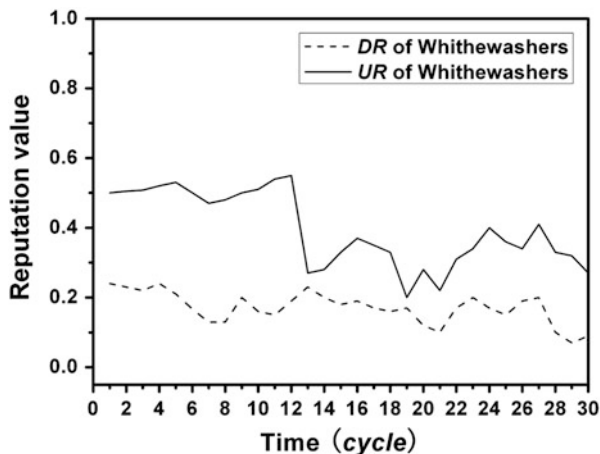
$$P = \frac{T_{k+1}}{\sum_{k=1}^n T_k/n}. \tag{125.4}$$

If P is less than 0.5 and stays at that value for at least three consecutive transactions, the mechanism will consider the possibility that the node is a whitewasher and let UR and DR of the node decrease to the next lowest level.

125.5 Simulations

We use *PeerSim* to implement and evaluate our mechanism. The network topology is obtained from *Brite*, including 1,000 peers, and satisfies a power law. There are 5,000 files distributed randomly to the normal nodes. In the simulations, the size range of 80 % of the files is (0,100], and the size range of the remaining files is (100,1,000]. In each cycle, each node downloads a random resource and issues an evaluation following the transaction. Twenty percent of the nodes are whitewashers in the network. Each experiment is run ten times, and the average of the results is taken as the final data.

Fig. 125.1 Change of DR and UR of whitewashers



125.5.1 Whitewashers Download Resources Only

Whitewashers do not attack other normal nodes and only download resources. Here whitewashers are similar to free riders. From Fig. 125.1 we see that the DR of the whitewashers increases initially and their UR does not change. Later, their UR begins to decrease because whitewashers do not upload files, and the DR also decreases to the lowest level. This means that whitewashers have been identified and could not download or upload resources any longer.

125.5.2 Whitewashers Perform Slander Attacks

Whitewashers usually perform slander attacks. They try to undermine the UR of normal nodes and destroy the effectiveness of the trust mechanism. As shown in Fig. 125.2, the UR of normal nodes is affected by a slander attack but does not decrease rapidly because the transaction evaluation given by the whitewashers is restricted by many factors; furthermore, the DR of whitewashers will decrease rapidly, as shown in Fig. 125.1, because they only perform slander attacks and do not upload resources.

125.5.3 Whitewashers Upload Malicious Programs

As the initial UR is low in our mechanism, whitewashers will accumulate their URs initially. We see in Fig. 125.3 that the UR increases at first when whitewashers upload normal resources; nevertheless, the UR decreases rapidly when they upload

Fig. 125.2 Change in UR of normal nodes

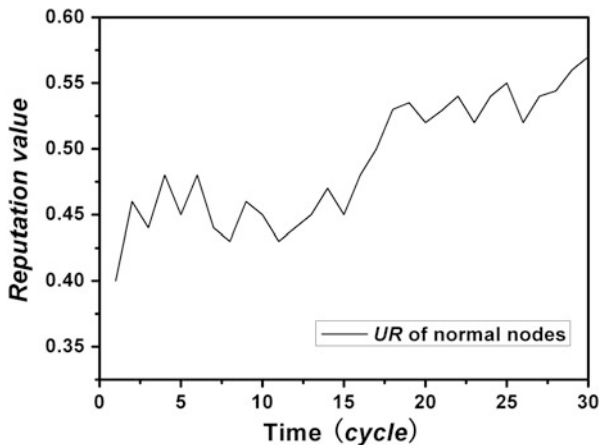
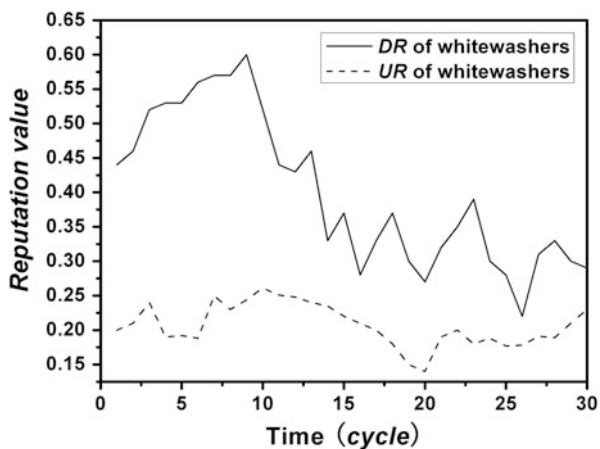


Fig. 125.3 Change of DR and UR of whitewashers



malicious resources for the bad evaluations given by other nodes. At the same time, the decrease in the UR results in a decrease in the DR.

Conclusion

In this paper, we propose a novel reputation mechanism based on two kinds of reputation with a consideration of the drawbacks of traditional reputation mechanisms in P2P networks. We discuss two kinds of node reputation along with the relationships among behavior, reputation, and capacity. The reputation mechanism is presented and the calculations given. Simulations are carried out, and the results show that our proposed mechanism can be applied to defend against whitewashing attacks.

References

1. Karl A, Zoran D. Managing trust in a peer-2-peer information system. In: Proceedings of the 10th International Conference on Information and Knowledge Management; ACM, Atlanta; 2001. p. 310–17.
2. Rahman MR. A Survey of incentive mechanisms in peer-to-peer systems, CS-2009-22. Waterloo: University of Waterloo; 2009.
3. Feldman M, Papadimitriou C, Chuang J, Stoica I. Free-riding and whitewashing in peer-to-peer systems. *Sel Areas Commun.* 2006;24(5):1010–9.
4. de Pinninck AP, Schorlemmer M, Sierra C, Cranefield S. A social-network defence against whitewashing. In: Proceedings of the 9th International Conference on Autonomous Agents and Multiagent Systems; ACM, Toronto; 2010. p. 1563–64.
5. Abbas S, Merabti M, Llewellyn-Jones D. Deterring whitewashing attacks in reputation based schemes for mobile ad hoc networks. In: Proceedings of the 2010 IFIP Wireless Days; IEEE, Venice; 2010. p. 1–6.
6. Levine BN, Shields C, Margolin NB. A survey of solutions to the Sybil attack, 2006-052. Amherst: University of Massachusetts Amherst; 2006.
7. Marti S, Garcia-Molina H. Identity crisis: anonymity vs reputation in P2P systems. In: Proceedings of the 3rd International Conference on Peer-to-Peer Computing; IEEE, Piscataway; 2003. p. 134–41.
8. Ipoque. P2P survey 2006. <http://www.ipoque.com/sites/default/files/mediafiles/documents/p2p-survey-2006.pdf>. 2007.

Chapter 126

A New Type of Metropolitan Area Network

Chuansheng Wu, Yunqiu Shi, and Shicheng Zhao

Abstract The novel network proposed in this paper includes two parts: an access network and a metropolitan area network, wherein the metropolitan area network has a network structure that is controlled in a centralized manner as in, for example, a star network or a ring network. Thus, two or more varieties of connection may exist between two devices that only have one address; therefore, the multiple connections between the two devices cannot be described using only the address. To accurately describe the connection relation between the subordinate network devices, a label is introduced to uniquely describe a subordinate network device; but, in comparison with the traditional multiprotocol label switching (MPLS) label, the allocation of a label is dominated by a metropolitan area network server while node switches and node servers both execute passively. This is different from the allocation of a MPLS label, a result obtained via the mutual negotiation of the switch and the server.

Keywords Metropolitan area network • Access network • Label • Switching nodes • Node server

126.1 Introduction

Today's network technicians seem to miss a basic theory: the root of the network packet loss phenomenon is not uniform velocity. Macroscopically, when the sending speed is high during one time period, it is certain to cause a jam during another time period; no upper limit can be given to the peak flow of the network as long as the network flow is not uniform and any arbitrary large bandwidth may be occupied in a short time. Using a light load plus Diff Serv technology, current network builders may deal with narrowband VoIP voice services because the voice does not occupy the main part of the total flow in a network. Once a jam occurs, the voice will take priority by sacrificing computer files; however, with high-bandwidth video communication, only a temporary improvement can be obtained by partial expansion. If the expansion is also carried out with respect to other nodes, the

C. Wu (✉) • Y. Shi • S. Zhao
University of Science and Technology, 110000 Liaoning, China
e-mail: gykwcs@163.com

nonuniformity of network flow will increase accordingly so that the effect of the originally expanded part will be reduced. If the expansion is carried uniformly across the network, the transmission quality will return to what it was before the expansion. In other words, the overall expansion will end up being ineffective [1].

126.2 Novel Network Device and Data Structure

126.2.1 Classification of Novel Network Device

1. Devices in may be divided into three main categories: a server, a switch, and a terminal (including, for example, various set-top boxes, code plates, and forms of storage) [2]. Generally, a novel network may be divided into a metropolitan area network (or state network and global network, for example) and an access network.
2. Devices in an access network may be divided into three main categories: a node server, an access switch, and a terminal (including, for example, various set-top boxes, code plates, and forms of storage for example). The node server is a node with a centralized control function in the access network and may control the access switch and the terminal. The node server may be directly connected to the access switch or the terminal [3].

The specific hardware structure of each access network device is shown in Fig. 126.1.

126.2.1.1 Node Server

As shown in Fig. 126.1, a node server mainly includes a network interface module, a switching engine module, a CPU module, and a disk array module.

Packets from the network interface module, the CPU module, and the disk array module all enter the switching engine module; the switching engine module checks the address table on the packets to obtain the orientation information of the packets;

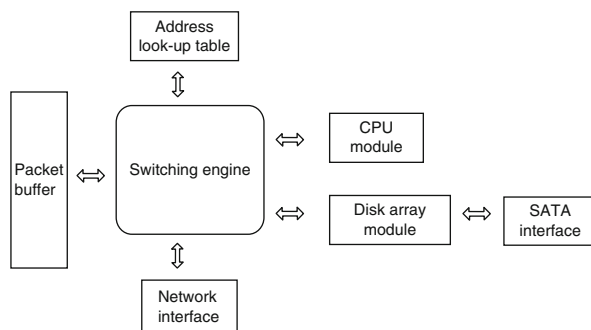


Fig. 126.1 Internal structural representation of node server in novel network

the packets are stored in a queue of the corresponding packet buffer based on the orientation information of the packets. If the queue of the packet buffer is full, the packets are discarded; the switching engine module polls all the packet buffer queues and forwards the queue if the following conditions are met: (1) the port of the sending buffer is not full and (2) the count of the packet counter in the queue is greater than 0. The disk array module mainly realizes the control on a hard disk, including, for example, operations of initialization, read, and write on the hard disk; the CPU module is mainly responsible for protocol processing with the access switch and the terminal, the configuration of the address table (including the downlink protocol packet address table, the uplink protocol packet address table, and the packet address table), and the configuration of the disk array module [4, 5].

126.2.1.2 Access Switch

The access switch may be divided into an access switch that performs flow control and an access switch that does not perform flow control, where the access switch that does not perform flow control mainly includes a network interface module, a switching engine module, and a CPU module. See the previously discussed node server for the specific processing of each module.

The structure of the access switch that performs the flow control is shown as follows:

As shown in Fig. 126.2, the access switch mainly includes a network interface module (the downlink network interface module and the uplink network interface module), a switching engine module, a CPU module, a packet checking module, a code rate control module, and a packet buffer.

The packets from the downlink network interface module (uplink data) enter the packet checking module; the packet checking module checks whether the destination address (DA), the source address (SA), the type, and the length of the packets meet

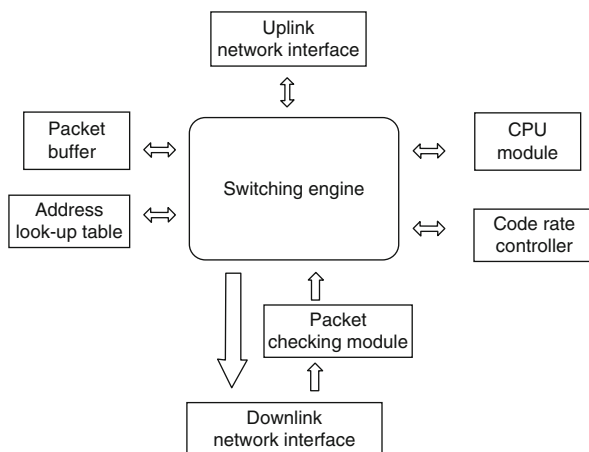


Fig. 126.2 Internal structural representation of an access switch

some requirement; if so, it allocates a corresponding stream identifier (stream-id) and inputs it into the switching engine module; otherwise, the packets are discarded.

126.2.1.3 Terminal

The terminal mainly includes a network interface module, a service processing module, and a CPU module; for example, a set-top box mainly includes a network interface module, a video and audio coding/decoding engine module, and a CPU module; a code plate mainly comprises a network interface module, a video and audio coding engine module, and a CPU module; and storage mainly comprises a network interface module, a CPU module, and a disk array module.

A device in a metropolitan area network may be mainly divided into two categories: a node server, a node switch, and a metropolitan area server [6], in which the node server is a node server in the access network, that is, the node server is in the access network and in the metropolitan area network. The metropolitan area server is a node with a centralized control function in the metropolitan area network and may control the node switch and node server. The metropolitan area server may be directly connected to the node switch or the node server. The metropolitan area server mainly includes a network interface module, a switching engine module, and a CPU module. The node server mainly includes a network interface module, a switching engine module, and a CPU module. See the previously discussed node server for the specific processing of the respective modules [7].

126.2.2 Definition of Novel Network Data Packet

126.2.2.1 Definition of Access Network Data Packet

As shown in Fig. 126.3, a novel network data packet mainly includes a DA, SA, reserved byte, protocol data unit (PDU), and cyclic redundancy check (CRC).

The DA consists of 8 bytes, where the first byte represents the packet type (e.g., protocol packet, multicast data packet, or unicast data packet). There are at most 256 possibilities, with the second to sixth bytes representing the metropolitan area network address and the seventh and eighth bytes representing the access network address.

8Byte	8Byte	2Byte	4Byte	
DA	SA	Reserved Byte	The detailed content of transmission	CRC

Fig. 126.3 Data structural representation of novel access network

The SA also consists of 8 bytes whose definition is the same as that of the DA. The reserved byte consists of 2 bytes.

The payload part has different lengths according to the different types of datagram. If it is a protocol packet, it has a length of 64 bytes; if it is an unicast or multicast data packet, it has a length of $32 + 1,024 = 1,056$ bytes; however, it is not limited to these two cases.

The CRC consists of 4 bytes, and the calculation method thereof conforms to the standard Ethernet CRC algorithm.

126.2.2.2 Definition of Metropolitan Area Network Data Packet

The topology of a metropolitan area network is a pattern type. There are two or more connections between two devices; that is, there may be more than two connections between a node switch and a node server, between a node switch and a node switch, and between a node switch and a node server; however, the metropolitan area network address of a metropolitan area network device is unique. To accurately describe the connection relation between metropolitan area network devices, a label is introduced in the embodiments of the so as to uniquely describe a metropolitan area network device.

As shown in Fig. 126.4, a data packet in a metropolitan area network mainly includes the following parts: the DA, the SA, the reserved byte (Reserved), the label, the payload (PDU), and the CRC, where regarding the label format, reference may be made to the following definition: a label consists of 32 bits, where the upper 16 bits are reserved and only the lower 16 bits used; the label lies between the reserved byte and the payload of a data packet.

126.3 Implementation of Novel Network

126.3.1 Implementation of Access Network

To simplify the design of the network, four types of data packet in the access network are defined: a downlink protocol packet (a protocol packet sent from a node server to an access switch or a terminal), and uplink protocol packet (a

8Byte	8Byte	2Byte	4Byte	4Byte	
DA	SA	Reserved Byte	Label	The detailed content of transmission	CRC

Fig. 126.4 Data structural representation of novel metropolitan area network

protocol packet that receives a reply from an access switch or a terminal to a node server), and unicast data packet, and multicast data packet.

Moreover, in an access network, with respect to these four types of data packet, the following four address lookup tables are configured for transmitting and orienting data packets or protocol packets according to the corresponding address lookup table after various types of data packet or protocol packet are received. Thus, the address lookup table may be divided into the following four table types:

1. Protocol packet address table: also referred to as the address table of a downlink protocol packet for transmitting and orienting a query packet or a service request protocol packet;
2. Reply packet address lookup table: also referred to as an address table of an uplink protocol packet for transmitting and orienting a reply packet;
3. Unicast data packet address table for transmitting and orienting an unicast data packet; and
4. Multicast data packet address table for transmitting and orienting a multicast data packet.

For example, an access network address consists of 16 bits, so the total number of access switches and terminals that can be accessed will be 65,536. Assume that the datagram type of the downlink protocol packet is “1000 0000” (binary system), i.e., 0×80 (hexadecimal system); then the datagram type of the uplink protocol packet will be “0000 1000” (binary system), i.e., 0×08 (hexadecimal system), the datagram type of the unicast data packet will be “0001 0000” (binary system), i.e., 0×10 (hexadecimal system), and the datagram type of the multicast data packet will be “0111 1000” (binary system), i.e., 0×78 (hexadecimal system); by combining like terms, an address table with a length of 8 bits may be mapped to an address table with a length of 2 bits.

126.3.2 Implementation of Metropolitan Area Network

To simplify the design of the network, there are a total of four types of packet in a metropolitan area network: a metropolitan area query label packet (a protocol packet containing a label sent by a metropolitan area server to a node switch and a node server), a metropolitan area reply label packet (a protocol packet containing a label sent by a node switch and a node server to a metropolitan area server), an unicast label data packet (formed by a node server by adding a label to an unicast or multicast data packet), and a multicast label data packet (formed by a node server by adding a label to an unicast or multicast data packet).

The address of a metropolitan area network has a total length of 40 bits, which are divided into three layers here—8 bits, 16 bits, and 16 bits—which are defined in turn as a state network, a wide area network, and a metropolitan area network. Data transmission between terminals in the same metropolitan area network and in the same access network is controlled by a node server of the access network.

Conclusion

IP Internet tries to absorb the instantaneous flow by employing a memory, which causes the increase of transmission delay. The storage capacity is limited, but the burst flow has no upper limit; therefore, by employing the memory method, it can only improve the packet loss of the current device, and the burst flow absorbed at the current node will put much pressure on the next node. Video stream flow is ceaseless, and the storage mode of the switch intensifies the accumulation of the burst flow to a weak node, thus network packet loss is inevitable. At preset, device manufacturers recommend ultra-wideband access networks of tens or even hundreds of Megabit to each household. However, even if optical fiber enters each household, it is difficult to exhibit a video communication service with good QoS to the consumers. In spite of what complex QoS measures are taken, the transmission quality of IP Internet can only be "improved", and no quality of network transmission can be "guaranteed". This system can improve the above shortcomings.

References

1. Han S, Jiang K, Zeng H. Security issues of current home-based Wlans. Lecture Notes in Information Technology—Proceedings of the 2012 2nd International Conference on Future Computers in Education (ICFCE 2012); Zeng Fort Hays State University, Hays; 2012. p. 63–88.
2. Salih ALJY, Despins C, Affes S. Ultra-wideband fast acquisition system for positioning in an underground mining environment. In: Proceedings of the Symposium on Signal Processing for Communication of ICC. Trans Tech Publications Ltd 2008; 2008. p. 26–33.
3. Lin S-Y, Tsai H-F. Evolutionary algorithm for constrained reader network planning. *Int Sci Acad Eng Technol.* 2013;10:68–73.
4. Wang F, Sun S, Liu J, Li L. Multi-channel cooperative spectrum sensing based on information theoretic criterion. In: Proceedings of the 2012 I.E. 14th International Conference on Communication Technology; 2012. p. 230–45.
5. Jia Z, Ding A, Zhang Y, Guo H. A digital voice transmission system based on visible light communication. In: Proceedings of the 2013 5th IEEE International Conference on Broadband Network & Multimedia Technology, Springer Verlag; 2013. p. 230–45.
6. Bonenfant P, Rodriguez-Moral A. Generic framing procedure (GFP): the catalyst for efficient data over transport network. *IEEE Commun Mag.* Springer Verlag 2012;111–223.
7. Cavendish D, et al. New transport services for next-generation SONET/SDH systems. *IEEE Commun Mag.* 2012;216–234.

Chapter 127

Improved Hierarchical Routing Scheme Based on Game Theory in Wireless Sensor Networks

Wan Qiang Han, Hai Bin Wu, and Zhi Jia Lu

Abstract In this paper, we propose an improved hierarchical routing scheme based on game theory, in which the sensor network is divided into two layers for a hierarchical architecture, routing within and between clusters. Within the clusters, a cluster head (CH) is selected by the game theory and one-hop communication is used from general nodes to the CH; between clusters, a data package is forwarded by the shortest-path algorithm to the base station. The most important features of the proposed scheme include its adaptability, efficiency, and reliability. The simulation results prove that this scheme can effectively prolong the life of a network and offer well-balanced network performance.

Keywords Wireless sensor networks • Game theory • Cluster head • Routing scheme

127.1 Introduction

Wireless sensor networks (WSNs) include a large number of micro low-cost sensor nodes with low power and multiple functions that possess such capabilities as information gathering, data processing, and wireless communication [1]. Because they are constrained by objective conditions, sensor nodes are very limited in power; therefore, the power control for WSNs is a hotspot of research. Although many routing protocols have been developed based on a reduction in node energy consumption, the problem of balancing network energy consumption is given less consideration in those schemes, and thus data traffic often concentrates on paths

W.Q. Han (✉) • H.B. Wu • Z.J. Lu
Institute of Physics and Electrical and Information Engineering, Shijiazhuang University,
050035 Shijiazhuang, China
e-mail: han.wq@163.com

with the minimum energy consumption. Those paths would be “hot regions” in which the energy is consumed very fast and the nodes frequently sending and receiving information in those regions consume energy relatively fast. Whenever those nodes exhaust their energy, the network becomes separated and the lifetime of the network diminishes significantly.

The cluster-based routing protocol is the current hot area of research in routing protocols because of its many advantages: the topological structure of the network is easy to manage, no complex routing table needs to be maintained, and the scalability is better suited for large-scale networks. An early cluster-based routing protocol, the low energy adaptive clustering hierarchy (LEACH) protocol [2], effectively reduced network power consumption and extended the network lifetime without taking into account the residual energy of nodes.

The proposed scheme features such important characteristics as a trust mechanism that ensures the information transmission reliability and protocol security, an ability to maintain energy efficiency as high as possible, and an ability to achieve load balancing and a well-balanced network performance between contradictory requirements.

Many hierarchical routing protocols have been developed to improve the energy and routing efficiency of networks. The hybrid energy-efficient distributed (HEED) protocol [3] generates cluster heads (CHs) based on a distributed algorithm, drives up the rate of clustering, and creates well-distributed CHs.

Xu and Zhang [4] proposed an improved algorithm based on LEACH, considering the premise of node energy and the optimum number of CH and selecting cluster nodes to balance the energy depletion of each node by limiting the number of nodes in each cluster.

Chen et al. [5] proposed an improved LEACH algorithm based on a heterogeneous energy of nodes for the same initial energy and multiple hop data transmissions among CHs. It establishes a new threshold that introduces the current and average energy of a node to CH election probability so as to ensure that these nodes with higher residual energy will have a greater probability of becoming CHs than one with a low residual energy.

Xie et al. [6] presented a localized game-theoretical clustering algorithm (LGCA) in which each node selfishly plays a localized clustering game only with its neighbors within a communication radius. Moreover, exactly one node can successfully bid for a position of the cluster head in one district, thereby achieving an optimal payoff.

Zheng et al. [7] analyzed routing in WSNs based on a Bayesian game. A Harsanyi transformation is introduced to form a static game of complete but imperfect information.

Tian et al. [8] proposed a routing protocol based on game theory to solve the cooperation problem. They analyzed the performance of node selfishness and its effects on network efficiency and summarized the typical application of game theory in terms of data packet forwarding and the cluster routing protocol of WSN routing mechanisms.

Xu et al. [9] proposed a density-based, energy-efficient, game-theoretic routing algorithm (DEGRA) that, as a clustering algorithm, adopts game theory and establishes a utility function based on a node's density, residual energy, and average energy consumption of its neighboring nodes. In the algorithm, CHs are iteratively selected. They also design intracluster and multihop intercluster routing algorithms.

Wang et al. [10] introduced a hierarchical routing mechanism, Trustworthy Energy-Efficient Routing algorithm (TEER), based on trust with energy efficiency. Most of the schemes related to Derun et al. and Zhanyang et al. did not consider the hostile action of nodes, although a trust mechanism is introduced in TEER, but the energy consumption at the CHs increased because of one-hop communication between the CHs and the base station.

127.2 Network Operating Description

Network operations are divided into two stages. The first stage is clustering formation, in which the nodes are deployed in a relatively stable topological region to form a network that is a stable net with no node motion. The node joins in a cluster according to its placement, for example, temperature and humidity monitors on buildings or on the cropland. The sensors are deployed according to their respective placements, and each sensor node has its own ID and location information and u value. Once a node joins a cluster, it will no longer join the other clusters. Since they are identical initially, nodes that lie closer to the sink in the cluster will be CHs in the first round. The CHs in each subsequent round will be determined by the last round of CHs. The method is as follows: after performing a task, the CH from the last round sends a poll to the cluster members, in which the trust value R_i of each node is included, and all the receivers answer a message (with its own ID, u value and geographic location), on the basis of which the current CH will identify the node with the maximum u value and send confirmation to this node along with basic information about family members. After receiving confirmation, that node becomes the new head of the cluster and sends the time slot table to cluster members. Then the operation enters the next stage, the communication stage. At this point, a two-level hierarchy is used. Communication within a cluster is carried out using the time division multiple access method, in which cluster members send a data package to the CH in turns in a one-hop manner. Cluster members regularly sleep/wake to reduce idle time. The data package is fused and compressed by the CH in each cycle, and the package is then forwarded in a multihop manner to the sink node, so that the information can be transferred between CHs to reach the sink node. Because the least communication cost path can be considered as a shortest path, the path setup problem becomes a shortest path problem, and Dijkstra's algorithm is the optimal method for solving the problem [11].

127.3 General Routing Scheme

An improved routing scheme, called game-theoretic active energy saved routing (GTAER), is discussed here, in which a trust mechanism is introduced and nodes communicate with each other wirelessly. The goal of the scheme is to detect, collect, process information in a cooperative manner in the given geographical location, and then send it to a sink node.

127.3.1 Routing Scheme Within Cluster

1. The network model is built based on game theory: we consider players (sensor nodes) to be in set $S = \{s_1, s_2, \dots, s_n\}$, and all the nodes are intelligent enough that they can weigh gains and losses in terms of energy efficiency with respect to their own and global aims. Let $v = \{v_1, v_2, \dots, v_n\}$ be the set of node strategies, i.e., if node i chooses to be a CH, then $v_i = 1$; otherwise, $v_i = 0$. A node's payoff function u is expressed as

$$u_i = \alpha \frac{E_r}{E_m} \cdot R_i - \beta \frac{\sum P_{\text{pathloss}}}{n_i P_{\text{max}}}, \quad (127.1)$$

- where α and β denote weight factors, $\alpha + \beta = 1$, E_r and E_m denote respectively the node's residual energy and initial energy, R_i denotes the current trust level. The trust level is confirmed by the CH, and the initial trust level of each node is 1. We consider that the node is malicious if it does not send messages. If the CH did not receive messages from one node, then the trust level of that node will be 0.5. If that node does not transfer the package in three continuous cycles, then the trust level R_i between the nodes will be 0, and the normal nodes' R_i will stay at 1. $-\sum P_{\text{pathloss}}/n_i P_{\text{max}}$ denotes the node's average path loss to its neighbors.
2. Each node establishes an information set of the neighboring nodes (including an ID, u value, and geographical location) and broadcasts its own u value.
 3. The node that receives the broadcast will compare the u value with its own and add the node whose u value is greater than its own to the information set.
 4. If a node's neighbor's set is still empty, this node will declare itself to be a CH and broadcast the declaration message to all its neighbors. If a general node receives more than one declaration message, it will choose the node with the highest u value in the set to be its own CH. If more than one CH has the same u value, it will choose one randomly to be its own cluster and send the message belonging to it to that CH.
 5. If a network node receives a message belong to a node that is in a set of neighboring nodes but has not received any declaration message. This suggests

that the node is beyond the range of any existing CH and will delete the information and return to Step 4.

6. As all the nodes make their decisions, a cluster-based routing protocol is established and data transmission starts.

The balance of this scheme is different from traditional a Nash equilibrium. First, the game in this routing program is a multistage action game in an extended game. Throughout the process, the game goes on in stages in an orderly fashion, and all participants know the actions of the other related participants in the given stage before choosing their strategies. Second, all participants select actions based on the historical actions and related information of all other related participants. Meanwhile, the combination of multistage game strategies in each stage is a Nash equilibrium, and the final strategy combination is an equilibrium of a perfect subgame [12].

127.3.2 Routing Scheme Between Clusters

CHs send packets through short-distance and multihop links to a sink node. Based on Dijkstra’s algorithm, we establish a multihop route from the source CH to the sink node, with each link established based on real-time dynamic adjustment.

To estimate the real-time fitness of the communication link, we define the dynamic value of each link as l :

$$l_{ij} = \lambda \cdot \frac{E_j}{E_m} \cdot \left(1 - \frac{d_{ij}}{D_m} \right) + \eta \cdot \frac{L_j}{L_m}, \tag{127.2}$$

where d_{ij} denotes the distance between CH i and CH j , E_j is the current residual energy of node j , L_j is the queue length of node j , E_m is the initial energy, D_m is the largest coverage, L_m is the maximum queue length. d_{ij} is estimated by RSSI (Frii transmission formula) [13], and the queue length L is defined as a flow of buffer degrees, often as a threshold to detect network congestion. If the data input rate exceeds the output ratio, then the routing packets will cause congestion and the queue length L will increase. According to this condition, we can determine whether the packet overflow. λ and η are two control parameters used to estimate the real-time link, whose range is $[0,1]$. In the scheme, the value of node j is E_j/E_M , with a dynamic adjustment so that system can adapt to the current network according to real-time network monitoring. The parameter η is an impact factor used to estimate the degree of packet congestion. To avoid the negative impact of packet loss, the degree of congestion depends entirely on the dynamic value l ; here we set η to 1.

The concrete steps are as follows:

1. First, each CH node estimates the dynamic value of the local link according to the distribution of values.

2. d_{ij} , E_j , and L_j of CH j are reasonably estimated using a real-time method.
3. λ and η of CH j are intended to be E_j/E_M and 1.
4. The source CH finds the least costly path to the sink node using Dijkstra's algorithm as follows:
 - (a) The source CH node specifies the starting link weight as zero.
 - (b) The current CH node chooses a link with minimum weight to the neighbor node and adds the weight to the previous node.
 - (c) The selected CH node starts to search recursively for a link with the minimum weight to the next CH.
 - (d) Repeat Step (b) till the sink node is reached.
 - (e) Finally, the path from the source CH node to the sink node with minimum consumption is established.

127.4 Simulation Analysis

All parameters are set up as follows: 200 identical nodes are deployed uniformly in an area of $200 \times 200 \text{ m}^2$ with a base station $100 \times 100 \text{ m}$ in area, as shown in Fig. 127.1. We assume the network clustering to be fixed at a rate of 10 %, with only one CH in a cluster. We consider a node dead when its energy declines to below 0.0001 J. The data fusion rate is assumed to be 1, and α and β are confirmed to 0.7 and 0.3, respectively (Table 127.1).

We compare the proposed GTAER algorithm with the TEER protocol [10] and LEACH [2] (Figs. 127.2 and 127.3), with the results showing only that the LEACH protocol and TEER node death begins to appear in rounds 851 and 516, respectively, while in the GTAER scheme it does not appear until round 1,144, and additionally

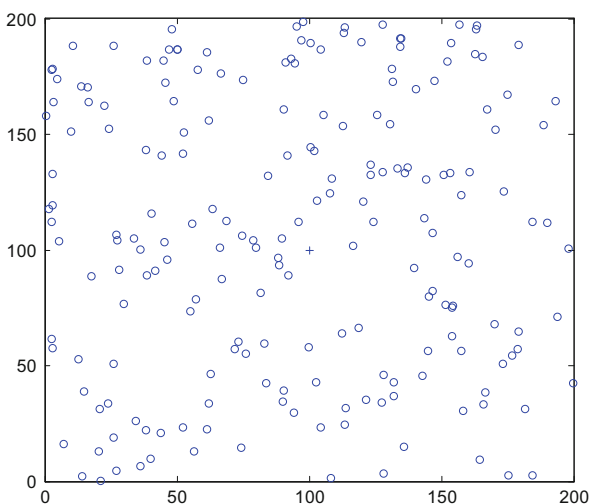


Fig. 127.1 Network node distribution

Table 127.1 Simulation parameters setting

Data packet length (bit)	4,000
Broadcast length (bit)	40
Initial energy (J)	1.0
Communication distance (m)	20
Sending and receiving circuit loss (nJ/bit)	50
Data fusion consumption (nJ/bit)	5
Amplifier parameters at a short distance (pJ/bit/m ⁴)	0.0013
Amplifier parameters at a long distance (pJ/bit/m ²)	10
α	0.7
β	0.3

Fig. 127.2 Network node death comparison

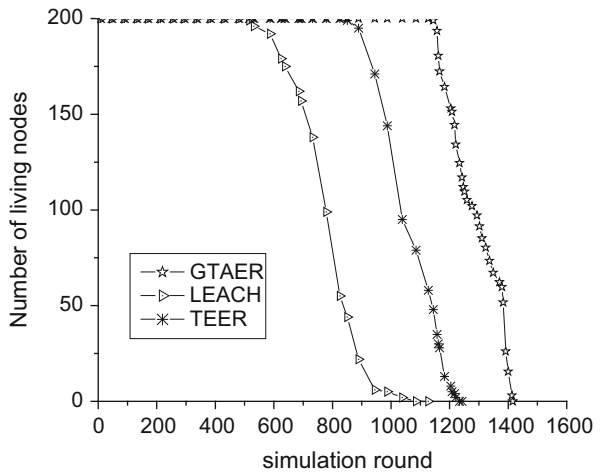
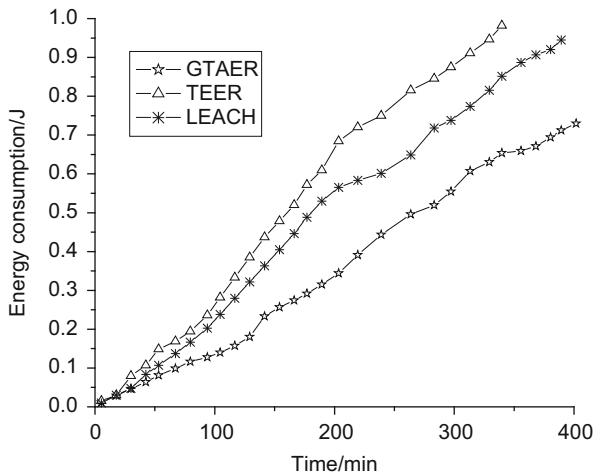


Fig. 127.3 Energy consumption comparison among CH nodes



in GTAER the network life cycle is better than that of the first two protocols. Because the multihop style and the optimal path algorithm are used in routing between clusters, the energy consumption of CH nodes is significantly lower than in the first two protocols.

Conclusion

An improved scheme (GTAER) is proposed in this paper that possesses many features, such as adaptability, efficiency, and reliability. Simulations show that the algorithm can effectively extend the network life cycle and reduce the rate at which CH nodes die. Future work will address the issue of clustering heterogeneous sensor networks.

Acknowledgments This work is supported by Grant Z2013025 of the High School Scientific Research Project of Hebei Province, Grant 13220344 of the Science and Technology Support project of Hebei Province, and Grant XJPT002 of Shijiazhuang University.

References

1. Jiang C, Xiang M. *Wireless sensor networks: routing protocol and data management*. Beijing: People's Posts and Telecommunications Press; 2013. p. 2–13.
2. Heinzelman WB, et al. An application-specific protocol architecture for wireless microsensor networks. *IEEE Trans Wirel Commun*. 2002;1(4):660–70.
3. Younis O, Fahmy S. HEED: a hybrid energy efficient distributed clustering approach for Ad Hoc sensor networks. *IEEE Trans Mobile Comput*. 2004;3(4):366–79.
4. Xu L, Zhang J. Improved LEACH cluster head multi-hops algorithm in wireless sensor networks. In: 2010 9th International Symposium on Distributed Computing and Applications to Business, Engineering and Science, DCABES. Hong Kong: IEEE; 2010. p. 263–7.
5. Chen G, et al. An improved LEACH algorithm based on heterogeneous energy of nodes in wireless sensor networks. In: 2012 International Conference on CMCSN. Taiyuan: IEEE; 2012. p. 101–4.
6. Xie D, et al. An efficient clustering protocol for wireless sensor networks based on localized game theoretical approach. *Int J Distrib Sens Netw*. 2013;2013:1–11. Article ID 476313.
7. Zheng G, Liu S, Qi X. Clustering routing algorithm of wireless sensor networks based on Bayesian game. *J Syst Eng Electron*. 2012;1:154.
8. Tian D, et al. Application of game theory in wireless sensor network routing mechanism. *J Hunan Univ Technol*. 2012;26(1):55–60.
9. Xu Z, et al. A density-based energy-efficient routing algorithm in wireless sensor networks using game theory. *Int J Futur Gener Commun Netw*. 2012;5(4):99–112.
10. Wang J, Chen Z, Deng X. A trustworthy energy-efficient routing algorithm based on game-theory for WSN. In: *Proceeding of the Wireless Mobile and Computing (CCWMC 2009)*, IET International Communication Conference on Wireless Mobile and Computing. Shanghai: Shanghai University; 2012. p. 192–6.

11. Boukerche A, et al. A wireless actor and sensor networks QoS-aware routing protocol for the emergency preparedness class of applications. In: Proceedings of the 2006 31st IEEE Conference on Local Computer Networks (LCN); 2006. p. 832–9.
12. Drew F, Jean T. Game theory. Beijing: China Renmin University Press; 2010. p. 120–39.
13. Blumenthal J, Reichenbach F, Timmermann D. Minimal transmission power vs. signal strength as distance estimation for localization in wireless sensor networks. In: SECON'06. Reston: IEEE; 2006. p. 761–6.

Chapter 128

An Item-Based Collaborative Filtering Framework Based on Preferences of Global Users

Chengchao Li, Pengpeng Zhao, Jian Wu, Jiumei Mao, and Zhiming Cui

Abstract Nowadays, Internet services and products are increasingly abundant, and efficient and reliable recommender systems become increasingly important and have been widely accepted by users. Item-based collaborative filtering (CF) is one of the most popular techniques for determining recommendations. A common problem of traditional item-based CF approaches is that they only consider ratings of co-rated users when computing item similarities, which are likely to ignore relationships between items and result in unreliable relationships between different items. To improve the quality of recommendation, this paper proposes a new scheme of similarity measurement between items, computing the similarity based on the preference distribution of global users. In this paper, a data model for denoting the relationships among items and an SKL-based item similarities computing approach are proposed. Finally, experimental results show that the proposed approach can make better recommendation results compared with classical item-based CF approaches.

Keywords Collaborative filtering • Item similarity • Preference distribution • Global user

128.1 Introduction

Efficient and reliable recommender systems become increasingly important as average users are exposed to growing amounts of Internet services [1]. Personalized recommendation approaches have gained great momentum both in the commercial and research areas. One of the most widely used recommendation techniques is collaborative filtering [2], which leverages the user-item preference patterns derived from a large amount of historic data to make the recommendation. Depending on whether the preference information is derived from observing the similarity of users rating the same items or the similarity of items rated by different

C. Li • P. Zhao (✉) • J. Wu • J. Mao • Z. Cui

School of Computer Science and Technology, Soochow University, Suzhou 215006, China
e-mail: szlichengchao@gmail.com; szcolinzhao@gmail.com

users, a user-based and an item-based CF approach can be distinguished [3]. In addition, some researchers present empirical evidence that item-based algorithms can provide better computational performance than traditional user-based collaborative methods [4–6]. Item-based collaborative filtering builds off-line an item-item similarity matrix for prediction. Since it uses a precomputed model, it will recommend items quickly.

One critical step in the item-based collaborative filtering algorithm is to compute the similarity between items and then uses them to identify the most similar items. The quality of similarity measurement has a great influence on the performance of recommendation. Traditional item-based CF approaches only consider ratings of co-rated users, which are likely to ignore relationships between items and result in unreliable relationships between different items [5], due to the lack of user preference information on items, that is, the ratings from users are sparse. If no user rates on two items at the same time, traditional IBCF approaches couldn't measure the similarity between the two items and would only set similarity value to zero. In fact, the items are more likely to be relevant. Also, the ratings in the co-rated users may not be representative of the true level of similarity between two items, which leads to inappropriate weights in the recommendation model. It can be seen as a viewpoint of local users that only considering the behavior of co-rated users to measure the relationships between items. On contrary to the flexible relationship between users, similarities between items are relatively static. The perspective of global users, that is, from the viewpoint of global users' overall rating on items, can better reflect the relationship between the items.

Based on what is mentioned above, this paper proposes a new pattern of similarity measurement between items, computing the similarity from the ratings of global users. For each item, users who have rated will be divided according to their various preferences on this item into three subsets, namely, "no interest," "low interest," and "high interest." Next, compute the similarity between items based on the probability distribution of users' preferences. It can better reflect the underlying relationships between items when considering overall users, as the item relations remain static.

128.2 Related Work

Item-based algorithms represent items in the user-rating space R , i.e., an item is a vector whose dimensions are the ratings given by the m users. As a consequence, item i corresponds to the i th column of R , and the relationships among items are expressed by means of the similarities among the related vectors [4, 5]. The basic idea in similarity computation between two items i and j is to first work on the users who have rated both of these items and then to apply a similarity computation technique to determine the similarity [6, 7]. Commonly deployed methods are the cosine-based similarity metric, adjusted cosine similarity, and the Pearson correlation coefficient [8].

Many improvement attempts have been proposed to make better recommendation performance. Jin and Mobasher used semantic similarity to enhance item-based collaborative filtering [9]. Their algorithm achieved better results than standard item-based CF algorithms. Further attempts to improve the performance of item-based CF have focused on enriching the information in user-item matrix. Gao and Wu incorporated personalized contextual information in item-based collaborative filtering [10]. Gao et al. incorporated the weight of a user-rank into the computation of item similarities [11]. The technique improves accuracy of predictions. Latha and Nadarajan calculated probability-based relevance score, and rating predictions are made based on the model built on the scores [12]. But these approaches tend to require extensive computational effort or include the incorporation of additional knowledge about items that must be drawn from an external knowledge source.

128.3 Proposed Approach

Our approach would like to eliminate extra calculation that inflates the computational complexity and also avoid the need for addition of potentially expensive external knowledge resources. Different from the relationship between the users, similarities between items are relatively static. Instead of only considering the rating behaviors of co-rated users in classical item-based algorithms, we compute similarities between items according to the preference distribution of global users. Figure 128.1 illustrates this process. We propose a data model for denoting the relationship among items and present an SKL-based approach for computing item similarities.

128.3.1 Data Model

On the basis of initial user-item rating matrix, we get user preference distribution for items. For each item, users will be divided according to their various preferences on this item into three subsets: (1) users who have no interest in the item

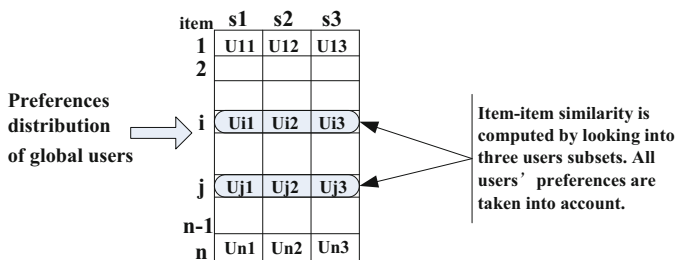


Fig. 128.1 Proposed framework for similarity computation for item-based CF

Table 128.1 UPDM

	No interest	Low interest	High interest
I_1	N_{11}	N_{12}	N_{13}
I_2	N_{21}	N_{22}	N_{23}
...
I_n	N_{n1}	N_{n2}	N_{n3}

Table 128.2 UPDPM

	No interest	Low interest	High interest
I_1	P_{11}	P_{12}	P_{13}
I_2	P_{21}	P_{22}	P_{23}
...
I_n	P_{n1}	P_{n2}	P_{n3}

(no interest), (2) users who have low interest in the item (low interest), and (3) users who have high interest in the item (high interest). If users' preferences are shown in the form of ratings, we mark off users' interests according to different rating values. In addition, as users' rating scales are different, we can transform different scales into the same level. After counting up the number of users for corresponding category, we get the user preference distribution matrix (UPDM). UPDM in Table 128.1 is an $n \times 3$ user preference distribution matrix, which records the number of users in three subsets for each item. n denotes the cardinality of the set of items. In our approach, I_m denotes item m , and u indicates user u .

Furthermore, by measuring the distribution of user preferences in three categories in terms of probability distribution, we get the user preference distribution probability matrix (UPDPM). UPDPM in Table 128.2 is a probability matrix that records the probability distribution of users for each item according to the number of users in each category. It can be computed with the formula

$$UPDPM(I_i, j) = \frac{UPDM(I_i, j)}{\sum_{j=1}^3 UPDM(I_i, j)} = \frac{N_{ij}}{\sum_{j=1}^3 N_{ij}}, \quad P_{ij} = UPDPM(I_i, j) \quad (128.1)$$

For each item, the sum of probability values of three categories will be 1. Formally,

$$\sum_j UPDPM(I_i, j) = \sum_j \frac{UPDM(I_i, j)}{\sum_{j=1}^3 UPDM(I_i, j)} = \sum_j \frac{N_{ij}}{\sum_{j=1}^3 N_{ij}}. \quad \text{There is}$$

Here for each item I_i , $\sum_{j=1}^3 N_{ij}$ is a constant, which indicates the number of all users of corresponding

row. Given $c = \sum_{j=1}^3 N_{ij}$, then $\sum_j UPDPM(I_i, j) = \frac{1}{c} \times \sum_j N_{ij} = \frac{1}{c} \times c = 1$.

128.3.2 Item Similarity Computation and Analysis

According to the analysis in Sect. 128.3.1, we can consider each item as a discrete random variable. Then UPDPM is a probability distribution matrix which is composed of n random variables. According to the information theory, Kullback–Leibler divergence [13] is the asymmetry difference measurement between two probability distributions, which can be used to compute the similarity between two probability distributions. For items I_m and I_n , KL divergence between them can be defined as:

$$D_{\text{KL}}(P_{I_m} \parallel P_{I_n}) = \sum_{j=1}^3 P_{I_m}(j) \ln \frac{P_{I_m}(j)}{P_{I_n}(j)}, \quad P_{I_m}(j) = P_{mj} \quad (128.2)$$

KL divergences are asymmetric, while the relationships between items are mutually static to each other. Therefore, we define the symmetry KL (SKL) divergence between items as follows:

$$\text{SKL}(P_{I_m}, P_{I_n}) = \frac{1}{2}(D_{\text{KL}}(P_{I_m} \parallel P_{I_n}) + D_{\text{KL}}(P_{I_n} \parallel P_{I_m})) \quad (128.3)$$

Finally, the similarity of items I_m and I_n can be computed as

$$\text{sim}(I_m, I_n) = \exp(-\text{SKL}(P_{I_m}, P_{I_n})) \quad (128.4)$$

Actually, for all items, users' ratings are sparse, namely, the number of "no interest" subset is large. The proposed approach can effectively solve the problem through the abovementioned similarity measurement model. As item similarities are obtained by using the SKL divergence, the largest ratio of probability values between two items in groups by "interest" has the largest contribution to the value SKL. Since the number of "no interest" of each item is large, the ratio between "no interest" terms is small, so impact on item similarities is mainly embodied in "low interest" and "high interest" columns:

(1) In principle, if two items have larger ratios between "low interest" and "high interest," from the overview of users' overall rating, the two items should be less similar and the value $\text{sim}(I_m, I_n)$ also should be smaller.

(2) According to our approach, the larger the ratio of two items' probability distribution, the greater the value of SKL, the smaller the similarity.

We can know that results in situations (1) and (2) are consistent, and our approach is in conformity with the actual analysis. Theoretical analysis verifies the validity of our approach.

128.4 Experimental Study

In this section, we examine experimentally the performance of the proposed approach. The experiments are repeated 100 times and the average results are reported in the corresponding parts.

128.4.1 Experimental Setup

We used the MovieLens [14] dataset to evaluate our approach. The dataset consists of 100,000 ratings from 943 users on 1,682 movies, which is randomly split into training and test set according to a preset ratio r . The estimation metric used in this paper is mean absolute error (MAE). Since it is used to measure the closeness of predicted ratings to the true ratings, lower MAE corresponds to higher prediction accuracy. As described in Sect. 128.3, our approach computes the similarity between items based on the preference distribution of global users, which is called item-based global user preference similarity (IBGUP). We examine experimentally the effect of different rating divisions for each “interest” category.

In this way, many sub-methods can be derived from IBGUP. Here we take two instances IBGUP-1 and IBGUP-2, for example, the rating divisions of which are shown in Table 128.3. IBGUP-1 approach considers 0 ratings as “no interest,” while IBGUP-2 computes similarity without using 0 ratings and considers 1–2 ratings as “no interest.” We designate the classical approaches described above as item-based Pearson similarity (IBPS) and item-based adjusted cosine similarity (IBAC) and adopt them as baselines for the comparative analysis presented in this paper.

128.4.2 Two Instances of Global User Preference Framework

As is mentioned above, IBGUP has many sub-methods. Now we compare those methods in detail. Here we only show the comparison result between IBGUP-1, IBGUP-2, and traditional methods. The results are shown in Fig. 128.2.

To determine the sensitivity of density of the dataset, we carried out an experiment where the value of ratio r varied from 0.5 to 0.9 in an increment of 0.1. We

Table 128.3 Rating divisions of two instances of IBGUP

	IBGUP-1	IBGUP-2
No interest	0	1–2
Low interest	1–3	3
High interest	4–5	4–5

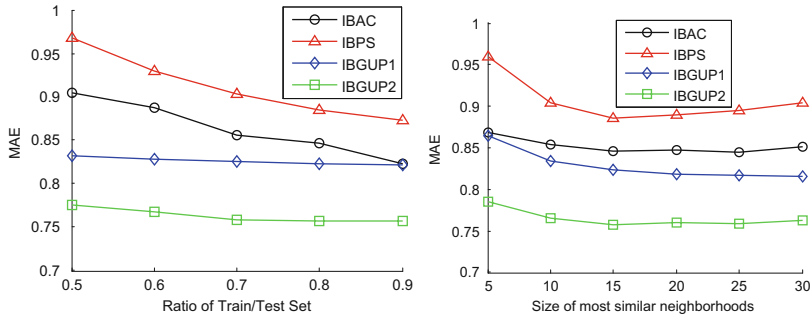


Fig. 128.2 Results of two instances of IBGUP

observed that the quality of prediction increased as r increased. The size of the most similar neighbors also has a significant impact on the prediction performance. To estimate the sensitivity of this parameter, we performed an experiment where we varied the number of the most similar neighbors with $r = 0.8$. We choose the items with top k similarity values to the current test item as its k most similar neighbors. It can be observed that these approaches show different types of sensitivity on this parameter. IBPS method improves as we increase the neighbor size from 5 to 15, after that the increase diminishes. Other two approaches improve as we increase the neighbor size from 5 to 25, after that the rate of increase diminishes and the curve tends to be flat. In Fig. 128.2, the advantages of the proposed approach over IBPS and IBAC methods are obvious.

In Fig. 128.2, IBGUP-1 outperforms IBGUP-2 with the same r and k . It demonstrates that 0 ratings also contribute to item similarity computation within our framework. Even though IBGUP-2 does not consider 0 ratings, it is still superior to IBAC and IBPS. As a whole, our similarity computation framework is superior to classic approaches.

Conclusion

In this paper we presented a new similarity computation model for traditional item-based CF algorithms. Different from the relationship between the users, similarities between items are relatively static. Instead of only considering the rating behaviors of co-rated users in classical item-based algorithms, we compute similarities between items according to the preference distribution of global users. Experimental results show that our approach can produce higher-quality recommendations than traditional methods.

Acknowledgments This work is partially supported by NSFC (Nos. 61003054 and 61170020), College of Natural Science Research Project of Jiangsu Province (No. 10KJB520018), Science and Technology Support Program of Suzhou (No. SG201257), Science and Technology Support Program of Jiangsu Province (No. BE2012075), and Open Fund of Jiangsu Province Software

Engineering R&D Center (SX201205). This work is also partially supported by the Natural Science Foundation of China under grant Nos. 61003054 and 61170020, Jiangsu Province Colleges and Universities of Natural Science Research Project under grant Nos. 10KJB520018 and 13KJB520021, Jiangsu Province Science and Technology Support Program under grant No. BE2012075, and Suzhou City Science and Technology Support Program under grant No. SG201257.

References

1. Bergamaschi S, Guerra F, Leiba B. Guest editors' introduction: information overload. *IEEE Internet Comput.* 2010;14(6):10–3.
2. Park DH, Kim HK, Choi IY, et al. A literature review and classification of recommender systems research. *Expert Syst Appl.* 2012;39(11):10059–72.
3. Shi Y, Larson M, Hanjalic A. Exploiting user similarity based on rated-item pools for improved user-based collaborative filtering. In: *Proceedings of the third ACM conference on recommender systems.* ACM; 2009. p. 125–32.
4. Sarwar B, Karypis G, Konstan J, et al. Item-based collaborative filtering recommendation algorithms. In: *Proceedings of the 10th international conference on World Wide Web.* ACM; 2001. p. 285–95.
5. Lü L, Medo M, Yeung CH, et al. Recommender systems. *Phys Rep.* 2012;519(1):1–49.
6. Shapira B. *Recommender systems handbook.* Berlin: Springer; 2011. p. 24–32.
7. Deshpande M, Karypis G. Item-based top-n recommendation algorithms. *ACM Trans Inform Syst.* 2004;22(1):143–77.
8. Hameed MA, Jadaan OA, Ramachandram S. Collaborative filtering based recommendation system: a survey. *Int J Comput Sci Eng.* 2012;4(5):859–76.
9. Jin X, Mobasher B. Using semantic similarity to enhance item-based collaborative filtering. In: *Proceedings of the 2nd IASTED international conference on information and knowledge sharing.* Acta Press; 2003. p. 1–6.
10. Gao M, Wu Z. Incorporating personalized contextual information in item-based collaborative filtering recommendation. *J Software.* 2010;5(7):729–36.
11. Gao M, Wu Z, Jiang F. UserRank for item-based collaborative filtering recommendation. *Inform Process Lett.* 2011;111(9):440–6.
12. Latha R, Nadarajan R. *User relevance for item-based collaborative filtering. Computer information systems and industrial management.* Berlin: Springer; 2013. p. 337–47.
13. Jiang B, Pei J, Tao Y, Lin X. Clustering uncertain data based on probability distribution similarity. *IEEE Trans Knowl Data Eng.* 2011;25(4):1.
14. Jung JJ. Attribute selection-based recommendation framework for short-head user group: an empirical study by MovieLens and IMDB. *Expert Syst Appl.* 2012;39(4):4049–54.

Chapter 129

Disassortativity of Class Collaboration Networks

Dong Yan, Keyong Wang, and Maolin Yang

Abstract In the software engineering, the class diagrams in the Unified Modeling Language show the collaboration relationship among classes to describe the structure of a system; nevertheless, how do the classes tend to collaborate with each other? This paper chooses the prevalent Java Development Kits to study the connectivity tendency of actual Java class collaboration networks based on the assortativity method. The collaboration between actual Java classes is analyzed and illustrated by statistics and charts. The empirical analysis finds that the out- and in-degrees of these networks display the anticorrelation and the weak disassortativity. The collaboration relationship between classes can be classified as strong and weak collaborations according to their assortativity coefficients, which is a highly statistically significant distinction.

Keywords Complex networks • Class collaborations • Assortativity

129.1 Introduction

Complex systems are often modeled as networks to analyze the mixing patterns, feedback mechanisms, flow of information, and interdependency of individual entities which make up such systems. It has been shown that the topological analysis of directed networks is more nuanced because of greater number of mixing patterns arising among such networks. A more detailed characterization concerns the exploration of connectivity correlations [1, 2] as called assortativity by Newman [3]. Assortativity is defined to quantify the tendency in networks where individual nodes are connected with other similar nodes [3].

The structure of a software system described by class diagrams can form a large collaboration network. In 2003, Myers studied the collaboration networks associated with six different open-source C/C++ software systems and found the anticorrelation between a large in-degree and a large out-degree and the positive

D. Yan • K. Wang (✉) • M. Yang
College of Mechanical Engineering, Shanghai University of Engineering Science,
Shanghai 201620, China
e-mail: yd_email@aliyun.com

assortative mixing among out-degrees [4]. Subelj et al. also found that some software networks may reveal dichotomous degree mixing that is assortative in the out-degrees and disassortative in the in-degrees [5]; however, the module collaboration graphs of Firefox, Blender, VLC, MySQL, OpenSSH, and SQLite exhibit disassortative mixing, i.e., high-degree nodes tend to connect to low-degree nodes and vice versa [6]. The class collaboration networks of some open-source software such as “Azureus,” “Thunderbird,” and “LibreOffice,” etc., are investigated to be very weak disassortative by degree [7, 8]. Similarly, the online collaborative design community “OpenIDEO” is actually disassortative [9]; however, the Twitter reciprocal reply networks with respect to happiness [10] exhibit positive assortativity.

In this paper, the classical Java Development Kits (JDK) from JDK 1.1.6 to JDK 1.3.0 are chosen to study the assortative characteristics of directed Java class collaboration networks (JCCN) based on the assortativity method proposed by Pastor-Satorras et al. [1]. In Sect. 129.2, the directed Java class collaborations are illustrated by class diagrams. In Sect. 129.3, the degree correlations and disassortativity of Java class collaboration relationships are investigated. In Sect. 129.4, the collaboration relationships between individual Java classes are analyzed and discussed based on the disassortativity law. In Section “Conclusion”, the conclusions are made.

129.2 Class Collaborations Based on Class Diagrams

In the software engineering, a class diagram in the Unified Modeling Language (UML) is a type of static structure diagram that describes the structure of a system by showing the system’s classes, attributes, operations (or methods), and relationship among objects, as shown in Fig. 129.1. Thus, the class diagrams of a Java software system with source codes can be abstracted as a complex network by the import relationship among classes according to the UML. Generally speaking, the import relationship between Java classes is unidirectional for the purpose of low coupling. For example, in Fig. 129.1, the class “java.util.Observable” imports “java.lang.NullPointerException,” while “java.lang.NullPointerException” does not import “java.util.Observable.” But the bidirectional import relationship also appears casually, for instance, the interface “java.util.Observer” and the class “java.util.Observable” are imported with each other; therefore, this paper aims at studying the characteristics of import relationships among Java classes based on the assortativity method [2].

129.3 Degree Correlations and Disassortativity

Correlations between out-degrees and in-degrees of classes can reveal whether a class importing a large number of other classes tends to be imported largely by others or otherwise. Figure 129.2 shows the inverse relationship between in-degrees

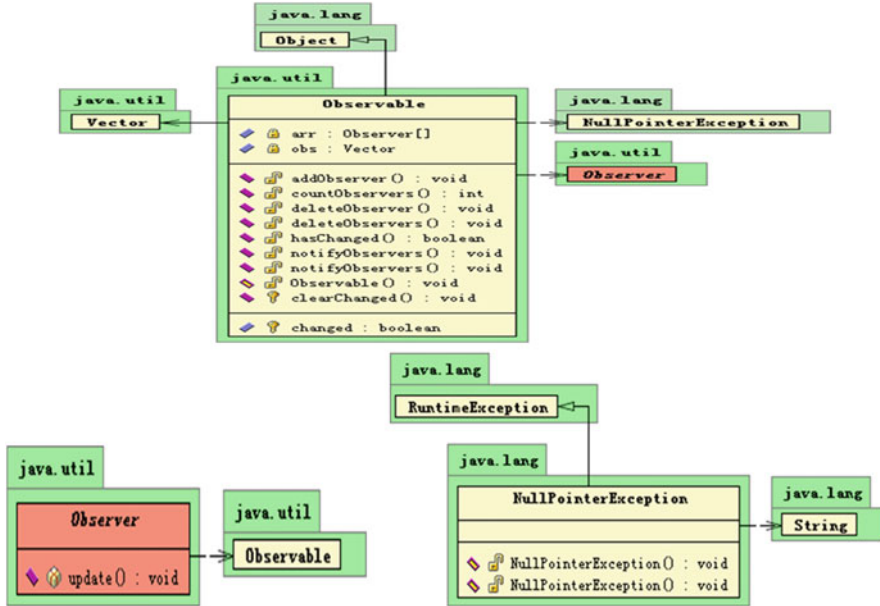
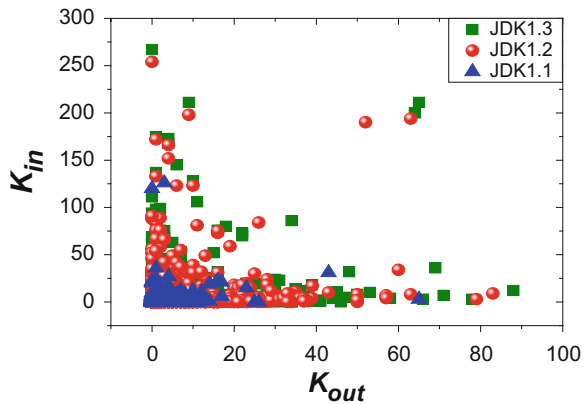


Fig. 129.1 Three class diagrams on classes `java.util.Observer`, `java.lang.NullPointerException`, and `java.util.Observable` of JDK1.1.6

Fig. 129.2 Scatter plot of the number of incoming links vs. the number of outgoing links, for every node in the JCCN of the JDKs from 1.1 to 1.3



and out-degrees, where each node in the graph represents a pair of out-degree and in-degree of each Java class, which is denoted by (k_{out}, k_{in}) . It is visually apparent that classes with large out-degree generally have small in-degree and vice versa, called as anticorrelation of large in- and out-degrees by Myers [4], i.e., “disassortativity” [2, 3].

The assortativity degree indicates the tendency that high-degree nodes in a network tend to attach with high-degree ones, while the disassortativity is on the contrary [2]. They can be measured by monotonicity between the average nearest neighbor degrees and degrees of all nodes.

Supposing that class i imports k_i^{out} other classes in the JCCN, the tendency that class i imports a class j with in-degree k_j^{in} can be quantified by the average in-degree of its neighbors, i.e.,

$$k_{nn,i}^{\text{outin}} = \frac{1}{k_i^{\text{out}}} \sum a_{ij} k_j^{\text{in}} \quad (129.1)$$

where if node i points to node j by a directed link, $a_{ij} = 1$; otherwise, $a_{ij} = 0$. On the contrary,

$$k_{nn,i}^{\text{inout}} = \frac{1}{k_i^{\text{in}}} \sum a_{ji} k_j^{\text{out}} \quad (129.2)$$

In the scope of the whole network, the tendency that classes with out-degree k_{out} imports classes with in-degree k_{in} can be quantified by the average nearest neighbor in-degree k_{nn}^{in} of nodes with out-degree k_{out} , i.e.,

$$k_{nn}^{\text{in}}(k_{\text{out}}) = \frac{1}{N_{k_{\text{out}}, i, k_i^{\text{out}}=k_{\text{out}}}} \sum k_{nn,i}^{\text{inout}} \quad (129.3)$$

Conversely, the tendency that classes with in-degree k_{in} are imported by classes with out-degree k_{out} is quantified by the average nearest neighbor out-degree k_{nn}^{out} of nodes with in-degree k_{in} , written as

$$k_{nn}^{\text{out}}(k_{\text{in}}) = \frac{1}{N_{k_{\text{in}}, i, k_i^{\text{in}}=k_{\text{in}}}} \sum k_{nn,i}^{\text{outin}} \quad (129.4)$$

In Fig. 129.3a, b, $k_{nn,i}^{\text{outin}}$ and $k_{nn,i}^{\text{inout}}$ tend to be inversely proportional to k_i^{out} and k_i^{in} on double linear scales. Thus, nodes with a high out-degree (or in-degree) tend to make the import relationship with that of a small in-degree (or out-degree); that's the disassortativity phenomenon of class collaboration. The phenomenon can be further verified in plots (c) and (d) of Fig. 129.3, where the slopes of linear fits as exponents are, respectively, -0.004 and -0.054 . Plot (c) on linear-logarithmic scales reveals the approximately random feature and the disassortativity of importing behaviors, while plot (d) on double logarithm scales indicates the preferential bias and the disassortativity of the behaviors that classes are imported [11].

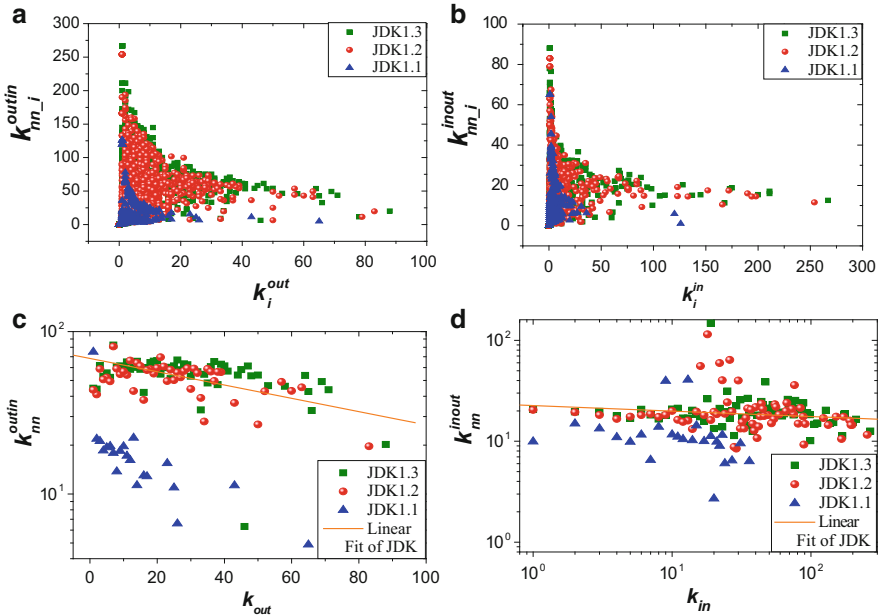


Fig. 129.3 Degree disassortativity of the actual JCCN plot (a, b) shows the local disassortativity of each class and its neighbors, while (c, d) displays the global one of classes with a certain out-degree (or in-degree) value and their neighbors

129.4 Class Collaborations Based on Assortativity

The assortativity between classes can be applied to evaluate their collaborations in the phases of definition and design for a developed system, although the strength of each relationship may be uncertain. As to a couple of interactive classes i and j , if that i imports j is considered as the forward collaboration from i to j , then that i is imported by j is called as the reverse collaboration.

129.4.1 Forward Collaboration

The forward collaboration from i to j , such as “java. util. Observable → java. util. Observer” in Fig. 129.1, is the probability that i tends to import j in the JCCN, characterized by a forward assortativity coefficient. According to Eq. (129.1), the forward assortativity coefficient $k_{nn,ij}^{out}$ is defined as the ratio of in-degree $k_{in,j}$ of j imported by i to the out-degree $k_{out,i}$ of i , written as

$$k_{nn,ij}^{out} = \frac{a_{ij} \times k_{in,j}}{k_{out,i}} \tag{129.5}$$

129.4.2 Reverse Collaboration

The reverse collaboration between classes i and j , such as “java. util. Observer \rightarrow java. util. Observable,” is the probability that j tends to import its neighbor i in the JCCN, characterized by a reverse assortativity coefficient. It is the ratio of in-degree $k_{in,i}$ of i imported by j to the out-degree $k_{out,j}$ of j , denoted as

$$k_{nn,ji}^{outin} = \frac{a_{ji}k_{in,i}}{k_{out,j}}. \quad (129.6)$$

129.4.3 Analysis of Class Collaborations

In Fig. 129.4, the class collaborations of the actual JDK networks are characterized and ranked. The assortativity coefficients of all class collaborations are ranked in plot (a), where the ratios between strong and weak assortativity coefficients are shown in Table 129.1. Plot (b) shows the assortativity coefficients of unidirectional or bidirectional collaborations between classes on log–log scales, where all coefficients are added. 1. According to the strong-weak boundary of assortativity coefficients, plot (b) is divided into four zones. All pairs of classes in zone A hold a bidirectional strong collaboration, and those in zone B hold the forward weak and reverse strong collaborations. But all pairs of classes in zone C and those in D are contrary to A and B, respectively. The percentages of class collaborations in the four zones for the JDKs are shown in Table 129.2. In the JCCN, a few class collaborations are bidirectional, while most are unidirectional. When an information system is developed, the alternatives in the prompt box can be ranked according to the assortativity coefficients of class collaborations rather than the order of the English alphabet.

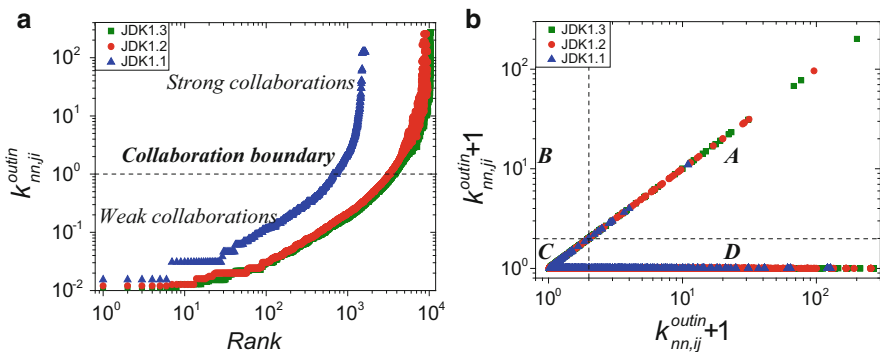


Fig. 129.4 Assortativity coefficients of the JCCN are ranked and characterized to show the collaboration tendency between classes

Table 129.1 The ratios between strong and weak assortativity coefficients

	JDK1.1 (%)	JDK1.2 (%)	JDK1.3 (%)
Percentages of weak collaborations	44.5	37.1	36.6
Percentages of strong collaborations	55.5	62.9	63.4

Table 129.2 The percentages of assortativity coefficients in the four different division zones of Fig. 129.4b

	A (%)	B (%)	C (%)	D (%)
JDK1.1	0.8	0	44.5	54.7
JDK1.2	0.7	0	37.1	62.2
JDK1.3	0.6	0	36.6	62.8

Conclusion

In this paper, JCCN is examined to investigate the mixing patterns of code reuse by means of the import statement. The in-degrees of JCCN exhibit anticorrelation and disassortativity with preferential behaviors, while the out-degrees show that with random behaviors. It is a little different from the assortativity of some software networks.

The disassortative correlations between out- and in-degrees conduce that the source codes of basic and excellent classes tend to be reused largely. The collaborations between classes may be weak or strong, which can be measured by the assortativity coefficients. Thus, the assortativity method can be applied to the class rank in the “prompt box” of development tools for the intelligentized purpose.

Acknowledgments This work is supported by the National Natural Science Foundation of China (Grant No. 51205220) and the Scientific Research Foundation of Shanghai University of Engineering Science (Grant No. E1-0501-14-0106).

References

1. Pastor-Satorras R, Vázquez A, et al. Dynamical and correlation properties of the Internet. *Phys Rev Lett.* 2001;87(25):258701-1-4.
2. Barrat A, Barthélemy M, et al. Modeling the evolution of weighted networks. *Phys Rev E.* 2004;70(6):066149-1. 12.
3. Newman MEJ. Assortative mixing in networks. *Phys Rev Lett.* 2002;89(20):208701-1-4.
4. Myers CR. Software systems as complex networks: structure, function, and evolvability of software collaboration graphs. *Phys Rev E.* 2003;68(4):046116-1-15.
5. Subelj L, Zitnik S, et al. Node mixing and group structure of complex software networks. *Adv Complex Syst.* 2014;15(1):53-79.
6. Bhattacharya P, Iliofotou M. Graph-based analysis and prediction for software evolution. In: *Proceedings of the 34th international conference on software engineering.* Piscataway: IEEE Press; 2012. p. 419-29.

7. Pan WF, Li B, et al. Multi-granularity evolution analysis of software using complex network theory. *J Syst Sci Complex*. 2011;24(6):1068–82.
8. Zanetti MS, Sarigöl E, et al. A quantitative study of social organisation in open source software communities; 2013. arXiv:1208.4289.
9. Fuge M, Tee K, et al. Network analysis of collaborative design networks: a case study of OpenIDEO. *J Comput Inf Sci Eng*. 2014;14(2):021009-1–8.
10. Bliss CA, Kloumann IM, et al. Twitter reciprocal reply networks exhibit assortativity with respect to happiness. *J Comput Sci*. 2012;3(5):388–97.
11. Barabási AL, Albert R, et al. Mean-field theory for scale-free networks. *Physica A*. 1999;272(1–2):173–87.

Chapter 130

Online Social Networks Based on Complex Network Theory and Simulation Analysis

Xin Jin, Jianyu Li, and Lei Zhang

Abstract The complex network is a diagram with many complicated topology structures and also a network contributed by the intricate relationship between a huge number of nodes. In order to allow people to better understand and explain the complexities of the real world, more researches on practical network under the guidance of researches on the general nature of the network have been carried out, which have become very challenging and prospective. From the perspective of data mining, the analysis of complex networks regards disciplines interested by users as nodes in the network. In this paper, we study the network degree distribution of nodes, the average path length, the clustering coefficient, the community modularity, and the largest faction through the network only to find that the network is a scale-free network with small-world effect. On the basis of sampling and analysis on millions of level data excavated from the social groups, the study reveals the hierarchy of online social networks and the relations and tightness among individual nodes.

Keywords Complex network • Degree distribution • Clustering coefficient • Average path length

130.1 Introduction

The network is a node-contained system with node interaction and is also a figure to describe a phenomenon or relation that is formed by individual (nodes) and node interaction (edge) abstractly [1]. Research on relationship between the microscopic nature such as values of nodes in the network, the edge weight, and the macroscopic properties such as geometric properties, efficiency, and stability [2] of the complex network [3] is the core of the study.

X. Jin (✉) • L. Zhang
School of Computer Science, Communication University of China, 100024 Beijing, China
e-mail: jinxin0923@cuc.edu.cn

J. Li
Engineering Research Center of Digital Audio and Video, Communication University of China, Beijing 100024, China

Many complex systems in real life can be solved through complex network modeling, such as the series of real networks: the Internet, the personal networks, the protein interaction networks, and the citation networks, all of which can be represented by a structure diagram of the network. Then, the nodes represent various entities which constitute the network, while the connection between nodes represents an association between the entities.

In recent years, based on the study on complex networks, the following characteristics are founded in natural networks and artificial networks, such as small world [4], scale free [5, 6], cluster [7], and community [8], which provide good ideas and solutions [9] to our in-depth network studies.

130.2 Data Sources

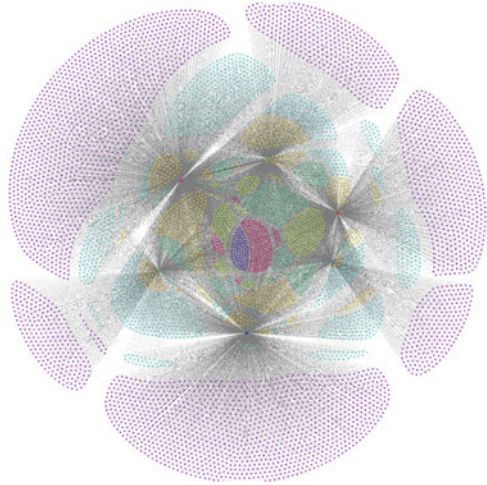
The network can be divided into undirected, directed, and weighted network among complex network systems. The study in this regard is to find the specific relationship among nodes of interest. According to the characteristics of the millions of level data from the forum named StackOverflow and as demanded by the research, the network will be regarded as undirected network and its structure includes 7,059 nodes/interest and 13,825 edges. The relationship among the information categories of the disciplines interested by all users is defined as follows: (1) Each category of interest disciplines is a node in the network; (2) we suggest that there is one-side connection in two or more disciplines one is interested in. Usually, when a certain connection exists between two points, it will form a side. If not, there will be no side formed. The two points connected by one side are considered to be adjacent in the network. We focus on the relationship of edge between nodes. Usually, the network structure not demonstrated by the specific location and the specific form of nodes shall be called the network topology. The network model generated by 7,059 interest discipline nodes is shown in Fig. 130.1.

130.3 Network Research and Simulation Analysis

In order to realize the statistical analysis on the network, this study introduces two important parameters to achieve the purpose of capturing the small-world effect of the network. The two parameters refer to the clustering coefficient and the average shortest path [10].

In order to find the close relationship and the degree of similarity from several interest disciplines, the network expressed by $G(V, E)$, V is a collection of nodes of interest disciplines, and E is a set of edges between the connected nodes. Among them, $V = \{v\}$, $E = \{\xi_{ij}\}$, $\xi_{ij} = (v_i, v_j)$, $i, j = \{1, 2, \dots, N_c\}$, v_i , and v_j are the nodes of interest disciplines; ξ_{ij} is the edge between the connected v_i and v_j . If the edge is

Fig. 130.1 Network model diagram



present, its value is 1; otherwise, it is 0. N_c is the total number of information of interest disciplines.

130.3.1 Average Clustering Coefficient

Firstly, as far as the clustering coefficient is concerned, it refers to the probability of the two nodes linked to it which are also connected to other nodes. If d_i is the degree of node i , among the subnets constituted by d_i adjacent nodes that contain node i , the ratio of $|S_i|$ which is the actual existence of the number of edges and the total number of edges $d_i(d_i - 1)/2$, in which all d_i nodes are connected completely, is the clustering coefficient of node i that can be expressed by C_i [11]:

$$C_i = \frac{2|S_i|}{d_i(d_i - 1)} \quad (130.1)$$

S_i represents a set of the actual existence of edges [12] among d_i nodes. In geometry, the clustering coefficient C_i of node i indicates the ratio of the number of triangle which contains the node i . N_c is the total number of information of interest disciplines. Then, the clustering coefficient of the entire network is equal to the average of clustering coefficient of all nodes:

$$C = \frac{1}{N_c} \sum_{i=1}^{N_c} C_i \quad (130.2)$$

Fig. 130.2 Relationship between average clustering coefficient of the network with network size

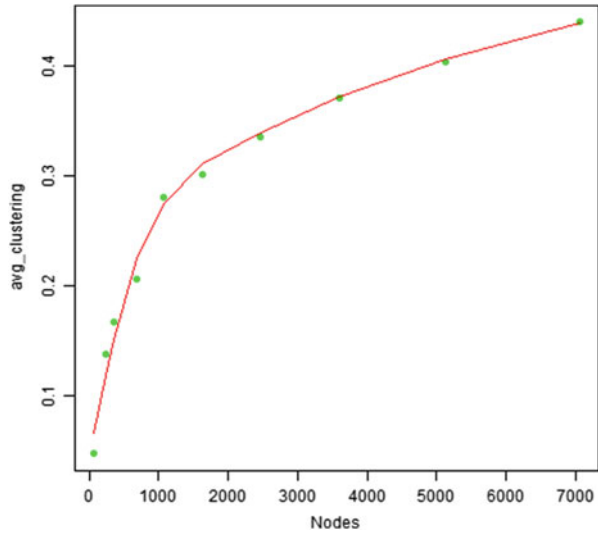


Figure 130.2 shows the average clustering coefficient of information network of interest disciplines on online forum site varies with the size of networks. In Fig. 130.2, the horizontal axis represents the size of the network and the vertical axis represents the size of clustering coefficient in the network model. The network size is from 63 to 7,059. As seen from the simulation results, the clustering coefficient of the network model does not obviously depend on the network model but basically stay in the vicinity, $C=0.5$. Thus, the network model has a high clustering coefficient.

130.3.2 The Average Shortest Path

Assume the shortest path from a given node i to the target node j is d_{ij} , N_c is the total number of information of interest disciplines, and the average shortest path from node i to all other nodes in the network is [13]:

$$d_i = \frac{1}{N_c} \sum_{j=1}^{N_c} d_{ij} \quad (130.3)$$

In this sense, the average shortest path of the entire information network of interest disciplines is $d = (1/2N_c) \sum_{i=1}^{N_c} d_i$.

Calculate with the above-said method. The average shortest path is $d = 2.44$ and the clustering coefficient is $C = 0.44$.

If the average path length (APL) of the network is proportional to the logarithm of the network, the network is called a small-world network [14]. The figure shows

Table 130.1 Relationship between APL and network size

Nodes	63	230	3,52	681	1,069	1,624	2,461	3,592	5,131	7,059
APL	2.94	2.65	2.65	2.68	2.61	2.57	2.57	2.51	2.47	2.44
C_i	0.05	0.17	0.17	0.21	0.21	0.30	0.34	0.37	0.40	0.44

the relationship between the APL of the information network APL and the network size. In the table, the horizontal axis represents the size of the network and the vertical axis represents the APL of the network model.

As shown in Table 130.1, when the network size increases, there will be the phenomenon of “hold together” and “bridge” among the parts of interest disciplines to improve the clustering coefficient of the network. Some key disciplines often play the role as a “bridge” among the clusters in the various sectors and as a bridge between clusters to be the “shortcut” of interest swap which has reduced the APL of the network. Thus, a shorter APL owned by the network model fully proves that the network has small-world effect.

130.3.3 Network Diameter

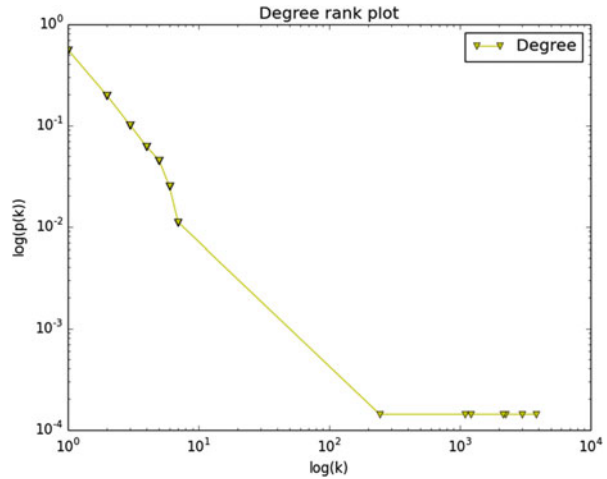
The network diameter is defined as the maximum value of the shortest path length between any two nodes in the network [15] and also the minimum number of edges connecting any two nodes in the network. The indicators measure the social network from an overall perspective of the network and the connectivity is of great value.

Researches show that the existence of lots of redundant connections makes the network diameter less than $3(d < 3)$ in spite of the variety of information disciplines, which means that only three steps are demanded between two nodes. This high clustering and short average path of the network have confirmed that it has small-world effect.

130.3.4 Degree Distribution

The degree is to describe the basic properties of the network diagram. As to the undirected network diagrams, the degree of node i represents the number of edges connected to it. But as to the directed network diagrams, the node i is divided into two part, the in-degrees and the out-degrees. The in-degrees refer to the number of edges which regards the node i as the end and the out-degrees refer to the number of edges which regards the node i as the start. The size of degree of nodes represents the importance of the nodes. The arithmetic average of all the degree of nodes in the network is the average of the network, which can be denoted by $\langle k \rangle$. The distribution of nodes in the network is described by the distribution function $p(k)$ which

Fig. 130.3 Degree distribution of interest disciplinary network



indicates the probability distribution that the degree is k as randomly selecting a node [16]. Figure 130.3 is the degree distribution of nodes generated by 7,059 nodes of interest disciplines.

As shown in Fig. 130.3, the degree distribution follows the power-law distributions $p(k) \sim k^{-r}$ with slow declination and continues to increase with the degree, which is almost horizontal without many changes. As described in the scale-free networks, the degree of most nodes is small, but big nodes also exist. As the power-law distributions are not on the characteristic scale, the network which obeys the power-law distributions is also known as scale-free network, namely, the network of interest disciplines that has scale-free properties.

130.3.5 Relationship with the Value of Degree and Clustering Coefficient

The relationship is shown in Fig. 130.4; the dotted line is -1 . While $C(k)$ and k are obviously not satisfied with the power-law, the relationship between them is still featured. Generally, the power-law relationship between $C(k)$ and k indicates the presence of a clear hierarchy among networks, namely, small groups of nodes in a hierarchical way to organize the large groups of nodes with the scale-free structure unchanged. Thus, Fig. 130.4 shows that the network topology exhibits some degree of hierarchy [17].

As shown in Fig. 130.4, the characteristics of hierarchical network topology indicate the basic disciplines mastered by network users. In addition, in Fig. 130.5, major supporting disciplines can be analyzed from all the interest disciplines, such as Java and JavaScript as the best tool of dynamic pages to reflect the breadth and

Fig. 130.4 Relationship graph between clustering coefficient and values of degree

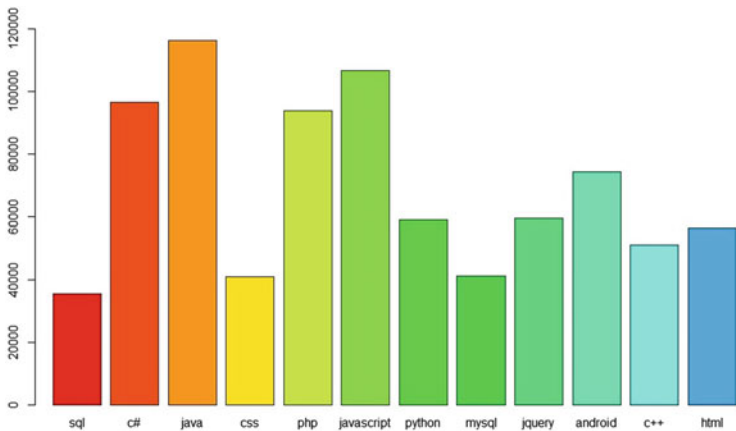
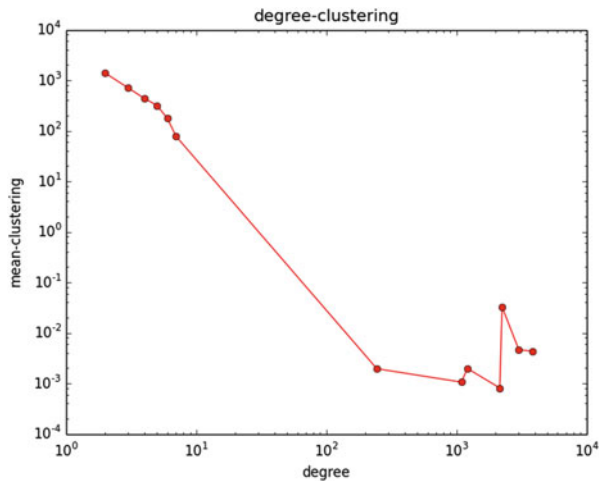


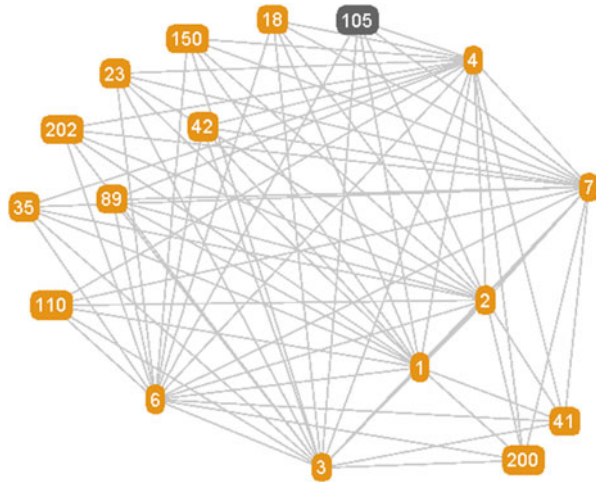
Fig. 130.5 Frequency histogram

portability of scope of the language discipline, the compactness and the easiness of learning.

130.3.6 *k*-clique Community

Typically, a community consists of interconnected complete subgraphs, which are called the cliques. *k*-clique indicates the figure containing *k* nodes [18]. *K*-1 public nodes in two *k*-cliques can be called two adjacent *k*-cliques. If one *k*-clique can reach another *k*-clique through several adjacent *k*-cliques, the two *k*-cliques are deemed as connected; thus, the *k*-clique community in the network can be

Fig. 130.6 7-clique community of network (mode 1, SQL Server; node 2, SQL; node 3, C#; node 4, WPF; node 6, .NET; node 7, Java; node 18, SQL UPDATE; node 42, SSIS; node 23, casting; node 35, VMware; node 41, error handling; node 89, Azure; node 105, regex; node 110, smalldatetime; node 150, hibernate; node 200, iPhone; node 202, SQLite)



considered as the set of adjacent k -cliques. The “overlap” phenomenon of k -clique in complex networks refers to some nodes as nodes in many k -cliques; but the k -clique communities are not adjacent, which indicates that the nodes are the “overlap” parts of different k -cliques without $k-1$ public nodes.

Based on the above analysis, the k -cliques are some complete subgraphs and the network is connected by complete subgraph correctly separated from the network by k -clique discovery algorithm which elaborated the relations among different disciplines and the similarity among disciplines interested in. Figure 130.6 below describes the size of the network of 7,059 nodes as the largest k -clique. 7-clique complete subgraph is detected by the k -clique algorithm.

As analyzed by k -clique algorithm, 7-clique graph includes a total number of 17 nodes, 81 edges, and 11 subgraphs. In the complete subgraph combined by the SQL Server, SQL, C#, WPF, .NET, and Java, the height of the first two nodes is deemed as the database-level language with the height of the last four nodes as programming languages. SQL, as a structured query language, can be used for programming design and technical standard of query. SQL Server is a specific program implemented with standard SQL structure. The interlinked points are available both in the implementation on technical specifications and procedures for programming; C# and Java, both object-oriented languages, can be compiled into a cross platform and cross language codes, which can only run in a controlled environment. The drawing advantage from Java and C# has similar grammar. Java emphasizes more on the object oriented and focuses on standardization and perfectness, while C# emphasizes more on practicality and ease of use; C# and .NET platform are released by Microsoft. Compared with .NET, C# is a strongly typed and object-oriented language which adopts simple syntax to express more, while .NET platform is the “NET PLAN” cornerstone of Microsoft. WPF and .NET are also introduced by Microsoft. WPF, as a graphical interface processing of Microsoft, belongs to a part of .NET Framework.

Thus, it can be learned that close connections exist among the disciplines interested in. As a result, while learning and studying a language, we need to link it to more disciplines related.

In summary, the degree distribution of information network of interest disciplines follows the power-law distribution with high clustering and short APL [19]. The information network model in nature reflects the hierarchy of interest, the connectivity and relations among interest disciplines [20].

Conclusion

This study has designed and implemented the data acquisition and analysis system in the online academic exchange forum and finally analyzed the large data of massive information of interest disciplines. With the introduction of the theory of complex networks, the study focuses on analyzing the network topology, the degree distribution, the clustering coefficient, and the APL of information networks of interest disciplines through the collations of millions of magnitude data. According to the method of network generation proposed in the study, there's a complex network among interest disciplines. On the basis of analysis of the simulation visualization, the study not only figures out that information network of interest disciplines is a small-world effect, scale-free, short-path, and high clustering network but also explores the linkages and tightness between interest disciplines in the network.

Acknowledgments The authors would like to appreciate Prof. Li for his helpful suggestions and comments. This work has been supported by the Project of Case-Based Teaching Construction for Professional Degree of Postgraduate Courses in Communication University of China.

References

1. Jin X, Wang Y. Research on social network structure and public opinions dissemination of micro-blog based on complex network analysis. *J Netw.* 2013;8(7):1543–50.
2. Criado R, García del Amo A, Hernández-Bermejo B, Romance M. New results on computable efficiency and its stability for complex networks. *J Comput Appl Math.* 2006;192(1):59–74.
3. Li X, Chen G, Li CG. Stability and bifurcation of disease spreading in complex networks. *Int J Syst Sci.* 2004;35(9):527–36.
4. Watts DJ, Strogatz SH. Collective dynamics of small-world networks. *Nature.* 1998;393(6684):440–2.
5. Barabási AL, Albert R. Emergence of scaling in random networks. *Science.* 1999;286(5439):509–12.
6. Albert R, Barabási AL, Jeong H. Error and attack tolerance of complex networks. *Nature.* 2000;406(6794):378–82.
7. Adamic LA, Huberman BA. Power-Law distribution of the World Wide Web. *Science.* 2000;287(5461):2115.
8. Duch J, Arenas A. Community detection in complex networks using extremal optimization. *Phys Rev E.* 2005;72(2):027104.

9. Wang XF, Chen GR. Complex networks: small-world, scale-free and beyond. *IEEE Circuits Syst Mag.* 2003;3(1):6–20.
10. Han Y, Li J-Y, Huang X-L, Qi Y-J. The complex networks of the parts word in Chinese structure. *J Harbin Eng Univ.* 2006;27(1):123 (In Chinese).
11. Saramäki J, Kivela M, Onnela J-P, Kaski K, Kertész J. Generalizations of the clustering coefficient to weighted complex networks. *Phys Rev E.* 2007;75(2):027105.
12. Wang D, Jin X-Z. On weighted scale-free network model with tunable clustering and congestion. *Acta Phys Sin.* 2012;61(022):537–45 (In Chinese).
13. Ebel H, Mielsch L-I, Bornholdt S. Scale-free topology of e-mail networks. *Phys Rev E.* 2002;66(3):035103.
14. Newman MEJ. The structure and function of complex networks. *SIAM Rev.* 2003;45(2):167–256.
15. Jackson MO. Average distance, diameter, and clustering in social networks with homophily. *Internet and network economics.* Berlin: Springer; 2008. p. 4–11.
16. He M-F, Hai-Xuan X, Sun Q. Opinion evolution on a scale-free network with leaders. *Int J Mod Phys C.* 2004;15(07):947–53.
17. Hai-Bo H, Wang K, Ling X, Wang X-F. Analysis of online social networks based on complex network theory. *Complex Syst Complexity Sci.* 2008;5(2):1214.
18. Soundarajan S, Hopcroft JE. Use of local group information to identify communities in networks. *Netw Protoc.* 2012;1:34.
19. Jin-Hu L, Xing-Huo Y, Chen G-R, Cheng D-Z. Characterizing the synchronizability of small-world dynamical networks. *IEEE Trans Circuits Syst Regul Pap.* 2004;51(4):787–96.
20. Leskovec J, Lang KJ, Dasgupta A, Mahoney MW. Statistical properties of community structure in large social and information networks. In: *Proceedings of the 17th international conference on World Wide Web.* Beijing: ACM; 2008. p. 695–704.

Chapter 131

Analysis of Network Accessibility

Shujian Zhang and Ying Zhang

Abstract To characterize the unblockability degree of one network, the authors explored the concept of network accessibility and proposed one approach for calculating the network accessibility index. The proposed approach considers network characteristics to help overcome the shortcomings of previous approaches to the calculation of accessibility measures. The proposed accessibility index can reflect the accessibility level of networks and has many potential uses. The index can serve as a guide in the design of transit networks and in the allocation of network flow.

Keywords Network • Accessibility index • K shortest paths

131.1 Introduction

With the expansion of human social networking comes the need of human beings for a better understanding of the behavior of various artificial and natural networks [1, 2]. Network flow always encounters impedance and can even be clogged for a number of reasons. As congestion gives rise to the need for real-time rerouting, networks should have the capacity to provide alternative paths. In this paper, an effective index called the network accessibility index (NAI) is proposed for the characterization of this aforementioned feature.

Network accessibility has a wide range of applications [3, 4], including the selection of commercial and factory locations as well as automobile routes and the planning of a transportation system. Accessibility can be calculated through several methods. Many scholars have studied the problem of accessibility in the past decades [5–8]. The term accessibility is often used in a number of scientific fields such as transport planning, urban planning, public policy, and geography and plays an important role in policy making. However, it is difficult to find an operational and theoretically sound concept of accessibility [9]. Gould [10] states, “accessibility . . . is a slippery notion . . .” Although there is no universally acknowledged definition of accessibility, various indicators with different theoretical

S. Zhang (✉) • Y. Zhang
Huzhou Vocational and Technical College, Huzhou 313000, China
e-mail: zsjsouth@163.com

backgrounds and complexities have been proposed and implemented in empirical investigations.

Although there are so many accessibility measures, there is no best one for accessibility because accessibility is a combination of different elements. Researchers have proposed several criteria to evaluate the usefulness and limitations of accessibility measures for different study purposes [11]. Our criteria are:

1. Reasonability, a network accessibility measure should ideally take into account the properties of the network, such as the distribution of the nodes and the paths. An accessibility measure should firstly be sensitive to changes in the networks, such as the changes of the topological structure of the network. As an improvement in the network, the accessibility should increase.
2. Feasibility, this is the ease with which the measure can be used in practice, for example, the complexity of calculating the measure.
3. Interpretability, the measure is not complex and easy to interpret.
4. Usability, the measure can be used in practice, for example, in evaluating the impacts of transportation network improvement on solving congestion problem.

131.2 Network Structure and Symbols

The network is described with graph $G = \{V, E, W\}$ (shown in Fig. 131.1), which comprises three parts: a non-null node set $V = \{1, 2, \dots, n\}$, the number of nodes is n ($|V| = n$), one arc set $E_{v \times v}$ ($|E| = m$), and the set of cost (weight) functions W . Each arc $e_{ij} = (i, j) \in E$ in the graph is endowed with a cost W_{ij} . The value of the cost is nonnegative.

A path is an alternating sequence of limited nodes and arcs. A path from source node s to destination node d can be expressed as $r(s = i, e_{ij}, j, e_{jk}, k, \dots, n = d)$. Circles are not allowed in the path. The total cost of the path $r(s, d)$ is the sum of the costs of the arcs through which the path passes. This cost is denoted by l_r :

$$l_r = \sum_{(i,j) \in r} w_{ij} \tag{131.1}$$

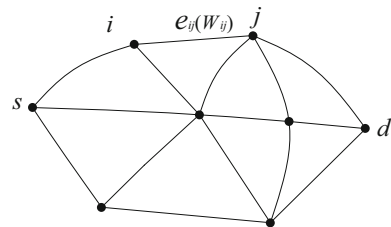


Fig. 131.1 Example of a network

131.3 Measuring Network Accessibility

In this study, node-to-node accessibility is defined as the ability of networks to guarantee an efficient network flow from the source node to the destination node despite changes in network states.

In networks, network flow toward the target destination is expected to be achieved using the least cost (e.g., least time or shortest distance) and the least network delays. For instance, when traveling, people always tend to choose the shortest path requiring the least time. Network states often change, resulting in clogging of the preselected path from one point to another. In case of such blockage, other paths (K shortest paths) must be selected. A network with a high level of accessibility should be able to provide more alternative paths such that it can more easily avoid blockage. In Fig. 131.2a, b, the costs of the shortest paths from the source node s to the destination node d are the same. However, in Fig. 131.2a, when the arc so is blocked, it becomes inaccessible from the source node s to the destination node d . In Fig. 131.2b, when the arc so is blocked, node d can still be reached from node s . Thus, network accessibility can be calculated based on the shortest paths.

The degree of the node is an important feature of networks. A node with a higher degree indicates that more paths are necessary to reach the node. Hence, the accessibility of the node is also higher.

In this case, node-to-node accessibility is defined as the ease with which one node can be reached from another node considering possible network congestion. The node-to-node accessibility index can be interpreted as a measure of the level of ease with regard to reaching the destination node from the source node. This index can quantify the ability to avoid network congestion when the preselected path is blocked.

Thus, the node-to-node accessibility index can be calculated by the following equation:

$$\text{NAI}_{ij} = \frac{G(d_i, d_j)}{F(W_e(t))} \quad (131.2)$$

where NAI_{ij} is the node-to-node accessibility index from node i to node j ; $G(d_i, d_j)$ is the function of the degree of the nodes; d_i and d_j are the degrees of nodes i and j , respectively; $F(W_e(t))$ is the function of the costs of the arcs of the K shortest paths; and $W_e(t)$ is the cost of the arc e at time t .

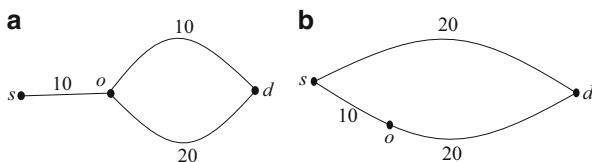


Fig. 131.2 Examples of network accessibility

For simplicity without loss of generality, $G(d_i, d_j)$ is defined as the product of d_i and d_j , i.e., $G(d_i, d_j) = d_i \times d_j$. The calculation for $F(W_e(t))$ is described as follows.

As shown in Fig. 131.2, among the K shortest paths between two nodes, disjoint paths (i.e., paths with no identical arcs) contribute more to accessibility than paths with identical arcs, as the latter hinders accessibility when any one of the identical arcs is clogged. This problem does not exist in disjoint paths. Considering that a penalty value is imposed on paths with identical arcs, a penalty function is defined as follows:

$$f = \begin{cases} n \\ 1 \end{cases} \tag{131.3}$$

where n is the number of repetitions of identical arcs. If the clogging possibility of identical arcs is relatively large, then the penalty should be greater. The penalty function can be defined as

$$f = e^n \tag{131.4}$$

Thus, $F(W_e(t))$ can be calculated using the following formula:

$$F(W_e(t)) = \sum_{u=1}^K \left(\sum_{e \in r_u} W_e(t) \cdot f \right) \tag{131.5}$$

where $\sum_{u=1}^K \left(\sum_{e \in r_u} W_e(t) \cdot f \right)$ is the summation of the costs of the K shortest paths imposed with the penalty value.

In calculating $F(W_e(t))$, an algorithm for the K shortest paths is first used to obtain the K shortest paths from node i to node j . The K shortest paths are then stored in the set $R_{s,d}^K = (r_1, r_2, \dots, r_k)$, where r_1 is the first shortest path, r_2 is the second shortest, and r_k is the K th shortest path. Next, the costs of the K shortest paths are calculated sequentially. The detailed steps are described below.

Step 1: Using the K shortest path algorithm [12], the costs of the path starting from the first shortest path r_1 are calculated. The arcs of the path are added to the set S_{arc} .

Step 2: Then, the sum of the costs of the second shortest path imposed with a penalty value is determined. The number of repetitions of arcs with the first shortest path is calculated by comparing the arcs of the second shortest path with those in the set S_{arc} . The costs of arcs identical to those of the first path are multiplied by n , which is the number of repetitions. Finally, all costs of the arcs with penalty value are summed up.

The arcs of the second shortest path are added to the set S_{arc} . If one arc is already in the set, then the number of repetitions of the arc is added with one and marked.

Step 3: The costs of the $K - 2$ shortest paths are calculated sequentially according to Step 2.

Step 4: $F(W_e(t))$ is calculated according to Formula (131.5).

Then, NAI_{ij} can be calculated through the following formula:

$$\text{NAI}_{ij} = \frac{G(d_i, d_j)}{F(W_e(t))} = \frac{d_i \times d_j}{\sum_{u=1}^K \left(\sum_{e \in r_u} E(W_e(t)) \cdot f \right)} \quad (131.6)$$

where NAI_{ij} is proportional to the degree of the nodes and inversely proportional to the sum of the costs of the K shortest paths.

131.4 Experimental Study

Three small-scale networks with different topological structures are constructed. The three networks have the same scale (the number of network nodes $n = 62$, the number of network arcs $m = 103$), and the costs of their arcs are identical. Figure 131.3a is a regular network whose node degree is subject to the delta distribution. Figure 131.3b is a stochastic network whose node degree is subject to the Poisson distribution. Figure 131.3c is a scale-free network whose node degree is subject to the power-law distribution. The costs of each arc are shown in Table 131.1.

This proposed accessibility measure is implemented in a computer program developed with C# in the VS.NET development environment under the support of GIS software ArcGIS. The previous five shortest paths are used to calculate the NAIs based on these equations above. We can get the results: $\text{NAI}_{\text{reg}} = 3.6 \times 10^{-3}$, $\text{NAI}_{\text{sto}} = 3.2 \times 10^{-3}$, and $\text{NAI}_{\text{free}} = 8.3 \times 10^{-3}$. The difference between NAI_{reg} and NAI_{sto} is not distinct. However, the scale-free network accessibility NAI_{free} increases distinctly because the scale-free network has a small-world property, whose average path length is relatively shorter. The shortest paths passing through nodes with high degree are relatively greater in number; thus, the betweenness of the nodes is high. The example highlights the differences in the levels of accessibility of networks with different topological structures.

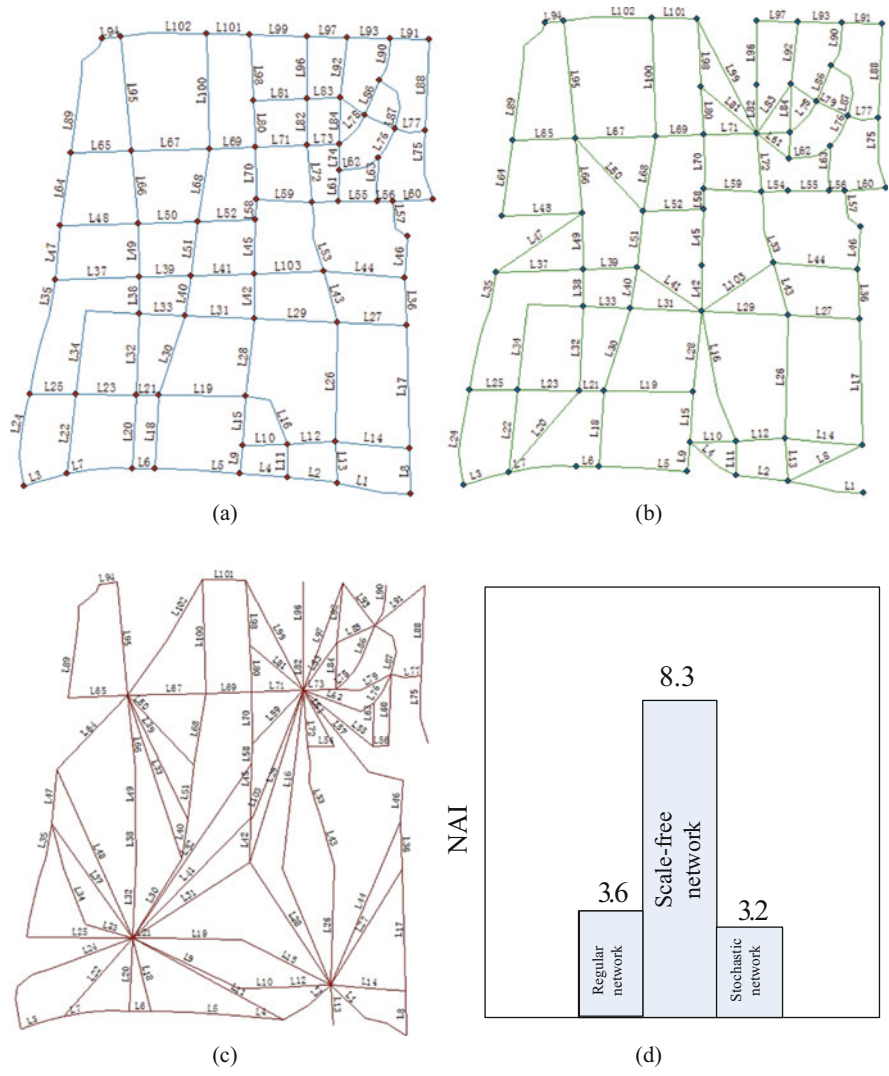


Fig. 13.1.3 Examples of NAIs with different topological structures (a) Regular network (b) Stochastic network (c) Scale-free network (d) Comparison chart of NAIs

Table 131.1 Costs of each arc

Arc	Costs	Arc	Costs	Arc	Costs	Arc	Costs	Arc	Costs	Arc	Costs	Arc	Costs	Arc	Costs
L1	85	L16	82	L31	78	L46	47	L61	36	L76	38	L91	44		
L2	57	L17	60	L32	93	L47	62	L62	48	L77	35	L92	69		
L3	51	L18	84	L33	52	L48	89	L63	50	L78	45	L93	49		
L4	54	L19	99	L34	157	L49	62	L64	84	L79	38	L94	20		
L5	97	L20	84	L35	82	L50	67	L65	68	L80	53	L95	132		
L6	24	L21	26	L36	55	L51	63	L66	83	L81	61	L96	71		
L7	75	L22	92	L37	95	L52	66	L67	89	L82	53	L97	45		
L8	52	L23	68	L38	41	L53	81	L68	84	L83	38	L98	75		
L9	32	L24	108	L39	59	L54	30	L69	52	L84	53	L99	66		
L10	51	L25	52	L40	46	L55	45	L70	60	L85	33	L100	132		
L11	38	L26	137	L41	72	L56	17	L71	58	L86	43	L101	49		
L12	54	L27	78	L42	51	L57	47	L72	64	L87	68	L102	98		
L13	47	L28	90	L43	61	L58	22	L73	37	L88	104	L103	78		
L14	85	L29	95	L44	93	L59	63	L74	29	L89	142				
L15	56	L30	96	L45	62	L60	45	L75	80	L90	50				

Conclusion

In conclusion, calculating the accessibility of networks is important for many reasons. From the network evaluation perspective, network accessibility succinctly reflects the connection quality of the transit network system and can be used to evaluate the ability to provide alternative paths between any two nodes in a network, that is, the ability to avoid blockage in networks. Accessibility can also be used to evaluate the efficiency of a transit network. Networks with a high level of accessibility indicate that the destination node can be easily reached from the source node. From the network flow allocation perspective, to reach the destination more efficiently, source locations are always settled in nodes with a high level of accessibility, such as the location of a commercial center. When the real states of networks change, the NAI assesses the impact of the changes in the network to guide the allocation of network flow in case of emergency. Take the transportation network as an example. When danger takes place in one location, the network needs to transfer people from a dangerous place to a safe place. The path with a high level of accessibility must be selected, and nodes with low levels of accessibility are avoided.

References

1. Zhanikeev M, Tanaka Y. Modelling network performance of end hosts. *IEICE Trans Inf Syst.* 2012;95(7):1872–81.
2. Zhipeng Y, Tadashi D. Survivability analysis for a wireless ad hoc network based on semimarkov model. *IEICE Trans Inf Syst.* 2012;95(12):2844–51.
3. Chen SP, Christophe C, et al. A spatio-temporal modelling approach for the study of the connectivity and accessibility of the Guangzhou metropolitan network. *J Transp Geogr.* 2014;36(3):12–23.
4. Simone C, Andrea DM. Accessibility and complex network analysis of the U.S. commuting system. *Cities.* 2013;30(2):4–17.
5. Páez A, Scott DM, et al. Measuring accessibility: positive and normative implementations of various accessibility indicators. *J Transp Geogr.* 2012;25(11):141–53.
6. Lubamba K, Paul J, et al. Multimodal accessibility modeling from coarse transportation networks in Africa. *Int J Geogr Inf Sci.* 2013;27(5):1005–22.
7. Miller HJ, Wu YH. GIS software for measuring space-time accessibility in transportation planning and analysis. *GeoInformatica.* 2000;4(2):141–59.
8. Matisziw TC, Grubestic TH. Evaluating locational accessibility to the US air transportation system. *Trans Res A Policy Pract.* 2010;44(9):710–22.
9. Geurs KT, Wee B. Accessibility evaluation of land-use and transport strategies: review and research directions. *J Transp Geogr.* 2004;12(2):127–40.
10. Gould P. Spatial diffusion. Association of American Geographers Resource paper no. 4. Washington, DC: Commission on College Geography; 1969.
11. Baradaran S, Ramjerdi F. Performance of accessibility measures in Europe. *J Transp Stat.* 2001;4(2/3):31–48.
12. Yen JY. Finding the K shortest loopless paths in a network. *Manag Sci.* 1971;17(11):712–6.

Chapter 132

Mobile Botnet Propagation Modeling in Wi-Fi Networks

Na Li, Yanhui Du, and Guangxuan Chen

Abstract Wi-Fi wireless networks have become a popular method of Internet connectivity, but the penetration of malware and viruses will be an increasing threat to the fundamental security of open Wi-Fi networks. Current security solutions for smartphones and mobile devices are very limited in preventing those attacks. In this paper, we study the feature of malicious software spreading in Wi-Fi networks, the specific characteristics of smart mobile devices' mobility, the traits of the human online behaviors, and the view of the cloud security; a novel worm propagation model is proposed. This model can help defenders develop defense strategies or make prevention policy to block the propagation of the malware Wi-Fi wireless networks. At last, a simulation scenario has been conducted to determine how a malware might spread under different conditions.

Keywords Wi-Fi networks • Mobile botnets • Propagation modeling

132.1 Introduction

By December 2013, the number of netizens, who used mobile phones to access the Internet in China, has reached 500 M, which is an increase of 19.1 % compared to a year earlier [1]. Among all of the netizens, the mobile Internet users rose to 81 % from 74.5 %, and the number grew steadily. With the rapid popularization of smartphones and smart mobile devices, lower service fees, and increasing coverage of Wi-Fi, smart mobile devices have become the main impetus of the mobile network development. Comparing to matured security defenses in PC, the security solutions for smart mobile devices are limited and different.

Propagation modeling has a long history. It is widely applied in botnet propagation analysis in traditional network. Propagation modeling can also mimic the self-replication and spread of viruses and malware in smart mobile devices. For

N. Li (✉) • Y. Du
People's Public Security University of China, Beijing 100038, China
e-mail: n_li@163.com

G. Chen
Zhejiang Police College, Hangzhou 310053, China

example, SIP [2] is a SIR-based model for the spread of malware between wireless-enabled devices. Yan et al. [3] presented a mobile botnet propagation model by counting the average number of infected devices in Bluetooth radio range. Later, blend Bluetooth and other propagation ways have been introduced, such as Bluetooth and SMS [4] and SEIR-based Bluetooth and SMS/MMS [5].

Wi-Fi networks became more popular than Bluetooth networks now. But there has been very little research on propagation modeling in Wi-Fi networks. Szongott et al. [6] and Wang et al. [7] analyzed the threat of epidemic mobile malware in Wi-Fi networks, but it was just a prototype and did not consider human behaviors. Hu et al. [8] develop an epidemiological model that simulates the spread of a contagion between Wi-Fi routers, but it was not Wi-Fi networks. So it is necessary to study the security of Wi-Fi networks.

132.2 Wi-Fi Malware Propagation Model Requirements

Mobile botnet propagation modeling in Wi-Fi networks is different from PC-based botnet propagation modeling. Some more aspects are considered, such as human behaviors, limited Wi-Fi transmission range, and devices' density and velocity. In this section, we will introduce those requirements in detail.

132.2.1 Probability of Transmission Time

Assume that t is a smart mobile device entering the transmission range of Wi-Fi hot spot which is a circle of radius R , traveling along AB and exiting the transmission range at B . The distance $l(\theta)$ of the mobile device inside the Wi-Fi transmission range is $l(\theta) = 2R \cos \theta$. Hence, the time that the device spends in Wi-Fi is $t_{\text{link}} = (2R \cos \theta)/v$. We define the cumulative distribution function (CDF) of the link lifetime t_{link} as

$$F_{\text{link}}(t) = P\{t_{\text{link}} \leq t\} = 1 - P\left\{|\cos \theta| > \frac{vt}{2R}\right\} \quad (132.1)$$

Now,

$$F_{\text{link}}(t) = 1 - P\left\{|\cos \theta| > \frac{vt}{2R}\right\} \quad (132.2)$$

$$= 1 - \int_{v=0}^{2R/t} \int_{-\cos^{-1}(vt/2R)}^{\cos^{-1}(vt/2R)} f(v, \theta) v d\theta \quad (132.3)$$

From the differential equation with respect to t , we can see that the probability of the distribution shifts towards the increasing velocity.

132.2.2 Infection Rate

The infection rate caused by one infected Wi-Fi hot spot is proportional to contact rate, probability of transmission time, density of mobile devices, and Wi-Fi transmission range. It is inversely proportional to the velocity of mobile devices and the radius R . So if the device is moving too fast or the link time is too short, there is not enough time to spread the malware. For high-density mobile devices, the infection rate will be higher. The infection rate at time t of the network is given by

$$\beta(t) = \beta_i \frac{I(t)}{N} \quad (132.4)$$

where $I(t)$ is the number of infected devices at time t and N is the total number of devices in the Wi-Fi network.

132.2.3 Incorporating Human Behaviors

Yang et al. [9] analyzed the traffic generated by smartphones in Beijing, China. They found that the end users go online with a regular pattern. For instance, between 9:00 and 23:00, there are more online users than between 2:00 and 6:00. The switching on and off of Wi-Fi is an important attribute of our model. We assume standard deviation $\sigma = t_{\text{spread}}/3$. A mean μ corresponds to 24 h of every day. The windowed distribution is given in

$$f(t|\lambda, \sigma) = \frac{1}{(\sigma)\sqrt{2\pi}} e^{\frac{-(t-\lambda)^2}{2(\sigma)^2}} \quad (132.5)$$

132.3 Wi-Fi Malware Propagation Model

In this section, we focus on introducing the mobile botnet propagation modeling in Wi-Fi networks. This model is also called the SEIDCOOC model.

132.3.1 SEIDCOOC Model

Figure 132.1 shows the compartments and transitions of the SEIDCOOC model. The mobile botnet propagation modeling in Wi-Fi networks has eight different states, which include susceptible (S), exposed (E), infected (I), offline (O), contained (C), death (D), cloud security (Cl), and exposed-offline (Eo). So we call this model as the SEIDCOOC model. When smart mobile devices are offline, the malware cannot infect those devices. Our assumption is that the end users switch their devices on and off at a rate τ_1 and τ_2 every day. We found that many end users often have Wi-Fi turned on in their devices; they may become exposed to the malware. The exposed devices also may be online or offline at a rate ν_1 and ν_2 . Susceptible devices switch on Wi-Fi and may suffer a man-in-the-middle attack. They may get a malware and become exposed to the malware at a rate $\beta(t)$, or they may become infected at a rate μ . The infected devices may return to susceptible state by updating or reinstalling at rate α . Those infected devices are likely entering into cloud security at a ι rate, thus becoming the susceptible devices at a rate ω . Once smart mobile devices are infected, they may be contained by the botmasters, but as soon as they reenter the network, they can be infectious at ϵ_1 and ϵ_2 rate, respectively. All susceptible, infected, and contained devices may become death and quit network for some other reason. The terms of this model are explained as shown in Table 132.1.

132.3.2 Dynamical System Equation

In this paper, we have outlined the properties and patterns of malware propagation via smart mobile devices in Wi-Fi networks. In this section, a function differential equations model which describes this transmission pattern is investigated. In this equation, $\beta(t)$ denotes the infection rate which we discussed in Sect. 132.2.2 and τ_1 and τ_2 denote the susceptible devices offline and online rate. The traits of the human online behaviors are investigated in Sect. 132.2.3. In the next section, we will evaluate the accuracy of the SEIDCOOC model and whether it characterizes well the propagation process of malware in Wi-Fi network.

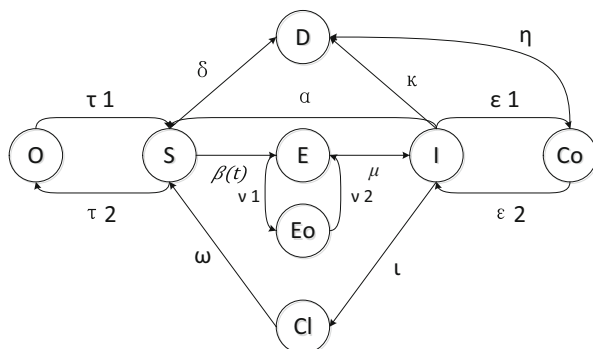


Fig. 132.1 The SEIDCOOC model

Table 132.1 The parameters and description for the SEIDCOOC model

Parameters	Description
Susceptible (S)	The vulnerable smart mobile devices
Exposed (E)	The devices are exposed to malware
Infected (I)	The infected devices can spread malware
Offline (O)	The offline susceptible devices
Contained (C)	The devices are contained by botmasters
Death (D)	The devices have death and quit network
Cloud security (Cl)	The devices in cloud security
Exposed-offline (Eo)	The exposed devices which are offline
$\beta(t)$	The infection rate at time t
μ	The ratio of the exposed via the number of infection
α	The recovery rate
ω	The ratio of the number of devices in cloud security via the number of susceptible
ι	The immunity rate, which refers to the ratio of the infected devices become protected by cloud security
τ_1, τ_2	The susceptible devices offline and online rate
$\varepsilon_1, \varepsilon_2$	The infected devices become contained devices rate and the contained devices become infected devices rate
ν_1, ν_2	The exposed devices offline and online rate
δ, κ, η	The death rate, which refers to the ratio of the number of susceptible/infected/contained via the number of death

Based on Sect. 132.3.1 assumptions and description of parameters, the differential equations describing the dynamical system of the SEIDCOOC model are listed as follows:

$$\left\{ \begin{array}{l}
 \frac{dS(t)}{dt} = \alpha I(t) + \tau_1 O(t) + \omega Cl(t) - (\beta(t) + \delta + \tau_2)S(t) \\
 \frac{dE(t)}{dt} = \beta(t)S(t) + \nu_2 Eo(t) - (\mu + \nu_1)E(t) \\
 \frac{dI(t)}{dt} = \mu E(t) + \varepsilon_2 Co(t) - (\alpha + \iota + \varepsilon_1)I(t) \\
 \frac{dD(t)}{dt} = \delta S(t) + \kappa I(t) + \eta Co(t) \\
 \frac{dCo(t)}{dt} = \varepsilon_1 I(t) - (\varepsilon_2 + \eta)Co(t) \\
 \frac{dO(t)}{dt} = \tau_2 S(t) - \tau_1 O(t) \\
 \frac{dEo(t)}{dt} = \nu_1 E(t) - \nu_2 Eo(t) \\
 \frac{dCl(t)}{dt} = \iota I(t) - \omega Cl(t) \\
 N(t) = S(t) + E(t) + I(t) + D(t) + O(t) + Eo(t) + Co(t) + Cl(t)
 \end{array} \right. \tag{132.6}$$

132.4 Simulation Experiments

We implemented the research of the SEIDCOOC model in Matlab R2013b. The total number of the smart mobile devices under consideration is 1,220, so $N=1,220$. The data released in 2013 by the Beijing Statistics Bureau reveal that the population of permanent residents in Beijing totaled 21.148 million. The population density is 1,289 per km^2 [10]. The national ministry of industry and information reveals that mobile phone penetration rate is as high as 90.8 % in February 2014 [11]. So the density of phones per m^2 is 1.172×10^{-6} . The average speed of motor vehicles is 7.3 m/s [12]. The average walking speed of a 170-cm-high adult man is 0.9193 m/s. So we give an average speed of 2.3 m/s for the phones. The number initially susceptible is set at 990.

Figure 132.2 shows how quickly the same population of devices in Wi-Fi network become infected for the four different Wi-Fi transmission ranges of 15, 45, 75, or 100 m. As expected, the transmission range makes a difference to the spread of malware. For example, in a range of 100 m, the population that becomes infected is more than a 15-m range. So if the transmission range is increased, the number infected is also increased.

Figure 132.3 depicts eight different states of devices as a function of propagation time derived from the SEIDCOOC model. The number of susceptible smart mobile devices is steadily declining; the number of death smart mobile devices is gradually increasing. But the number of infected devices and offline devices reaches the peak and then declines. We can see that those curves are consistent and characterize well the propagation process of malware in Wi-Fi network.

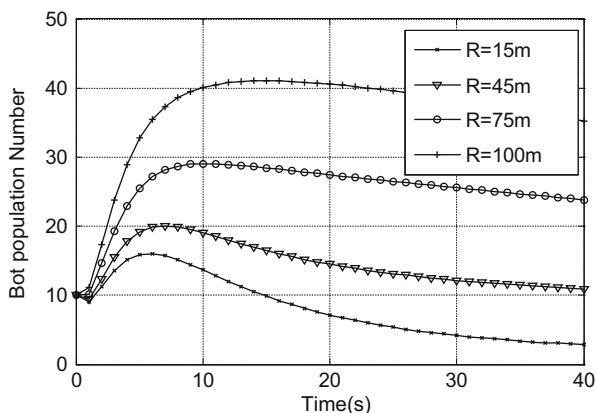


Fig. 132.2 The effect of Wi-Fi transmission range on the number infected over time

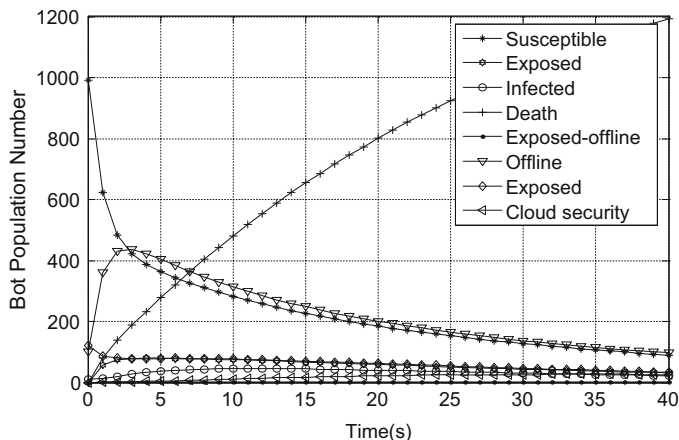


Fig. 132.3 Numerical solution of the SEIDCOOC model

Conclusion

Smart mobile devices are becoming part of people's life; the great convenience of wireless connectivity makes the smart mobile devices the first major Internet terminal. Especially when Wi-Fi appeared, many users use app to connect to the Internet. This paper is based on the classical theory of epidemic models. We proposed the SEIDCOOC model and considered the impact of mobility patterns, Wi-Fi radio range, the density of the mobile devices, the human behavior, etc. The SEIDCOOC model simulates truly the spread of mobile botnets in Wi-Fi networks. Using this model, we can put forward more targeted botnet detection and defensive measures to defend malware.

References

1. CNNIC. The 33th statistical report on internet development in China. Beijing: CNNIC; 2014.
2. Rhodes CJ, Nekovee M. The opportunistic transmission of wireless worms between mobile devices. *Phys A*. 2008;387(27):6837–44.
3. Yan G, Eidenbenz S. Modeling propagation dynamics of bluetooth worms. In: *Distributed computing systems*. Washington, DC: IEEE Computer Society; 2007. p. 42.
4. Gao C, Liu J. Modeling and predicting the dynamics of mobile virus spread affected by human behavior. In: *World of wireless, mobile and multimedia networks (WoWMoM)*. Washington, DC: IEEE Computer Society; 2011. p. 1–9.
5. Ramachandran K, Sikdar B. Modeling malware propagation in networks of smart cell phones with spatial dynamics. *INFOCOM*. Washington, DC: IEEE Computer Society; 2007. p. 2516–20.
6. Szongott C, Henne B, Smith M. Evaluating the threat of epidemic mobile malware. In: *Wireless and mobile computing, networking and communications (WiMob)*. Washington, DC: IEEE Computer Society; 2012. p. 443–50.

7. Wang C, Bai X, Ma J. Malicious code modeling and analysis in WiFi-based MANETs. In: *Wireless communications, networking and mobile computing*. Washington, DC: IEEE Computer Society; 2008. p. 1–4.
8. Hao H, Myers S, Colizza V, Vespignani A. WiFi networks and malware epidemiology. *Proc Natl Acad Sci*. 2009;06(5):1318–23.
9. Yang J, Zhang S, Zhang X, Liu J, Cheng G. Characterizing smartphone traffic with MapReduce. In: *Wireless personal multimedia communications (WPMC)*. Washington, DC: IEEE Computer Society; 2013. p. 1–5.
10. Beijing Statistics Bureau. The Beijing national economic and social development statistical bulletin in 2013. 2014. http://www.bjstats.gov.cn/sjtd/jjxs/201402/t20140213_267718.htm. (Cited 2014, May).
11. The National Ministry of Industry and Information. The main targets finished state of telecommunication industry in February 2014. 2014. <http://www.miit.gov.cn/n11293472/n11293832/n11294132/n12858447/15938146.html>. (Cited 2014, May).
12. Municipal Transportation Commission. Beijing traffic index. 2014. <http://www.bjjtw.gov.cn>. (Cited 2014, May).

Chapter 133

Dynamic Evaluation of Suppliers for Industrial Value Chain Value-Added Service Platform

Hua Pan and Linfu Sun

Abstract In order to meet the requirement of evaluating suppliers flexibly in collaboration platform of industrial value chain, this paper establishes a mathematical model for the dynamic evaluation of suppliers and proposes a dynamic evaluation scheme of suppliers for collaboration platform. Based on the XML configurability, the proposed scheme may realize the configurability of dynamic evaluation by establishing an algorithm library of dynamic evaluation. The feasibility and effectiveness of this scheme are verified via its application on the collaboration platform of industrial value chain.

Keywords Industrial value chain • Value-added service • Supplier evaluation • Dynamic evaluation system

133.1 Introduction

The value-added service platform of industrial value chain is a third-party public service platform based on SaaS (software as a service), which may realize the business collaboration of enterprise value-added services in the industrial chain, satisfy the requirements of multiple unions of enterprise clusters, and provide services to the chair enterprises in multiple clusters. Thus, how to make an objective and accurate assessment of suppliers is the problem demanding a prompt solution in the whole value-added service platform of industrial value chain.

The current foreign and domestic researches of supplier assessment have gained a series of rather mature theories, and scholars abroad like Johnson, who considered cost (C), time (T), quality (Q), and service (S) [1] to be important influential factors in the analysis of suppliers, have carried out a great quantity of studies deeply and extensively. Based on FCM, the dynamic evaluation method of enterprise supply chain performance [2] and the stability of supply chain under dynamic conditions

H. Pan (✉) • L. Sun

CAD Center of Southwest Jiao Tong University, Chengdu, Sichuan 610031, China

e-mail: linqpanhua@126.com

[3] were also studied. Based on rough set, the gray system of sustainable supplier selection [4] and an effective method for the evaluation of suppliers based on the selection of support vector machine [5] were proposed. Nevertheless, the abovesaid works analyzed the evaluation system and methodology only from the perspective of supplier assessment; thus, it may not work when adopted in the value-added service platform of industrial value chain which provides supplier assessment for multiple enterprise clusters.

Based on the above analysis and various customization technologies [6–9] for the collaboration platform of industrial chain, this paper explores a dynamic supplier assessment technology on the value-added service platform of industrial value chain and proposes a strategy of dynamic supplier assessment, which may realize the customizability of dynamic supplier assessment and satisfy the supplier's assessments by different chair enterprises on the platform.

133.2 Requirements of Dynamic Supplier Assessment for Service Platform of Industrial Value Chain

With the manufacturing industries as the leaders, the value-added service platform of industrial value chain attracts business-related upstream and downstream enterprises as well as management institutions to form a dynamic union of enterprises. In order to make it convenient for relevant staff to gain knowledge in terms of the situation and make decisions, the platform establishes a warehouse to automatically extract and analyze relevant data from such systems as PT, YONGYOU, sales system, and parts system and finally present the quality information statistics visually to customers by means of graphics. This dynamic union consists of some manufacturing industry as the leader and relevant enterprises (like suppliers, dealers, and servers) on the industrial value chain as the members, which always develop their business around their leader. We show the specific service platform architecture of industrial value chain in Fig. 133.1.

The requirements of dynamic supplier assessment on the service platform of industrial value chain mainly reflect dynamic customization of the supplier assessments by chair enterprises on the platform. In order to meet the needs of different chair enterprises to dynamically assess their corresponding collaborative enterprises, the customizability mainly focuses on three fundamental points:

1. As the enterprises in different unions have different businesses, the evaluation indexes of the supplier may vary.
2. Even though enterprises in different unions have the same evaluation indexes, their weights may vary, for example, the service is more sensitive to response time in auto after-sales service.
3. Different enterprises in different unions require different contents and forms to display the evaluation results, such as histogram and pie chart.

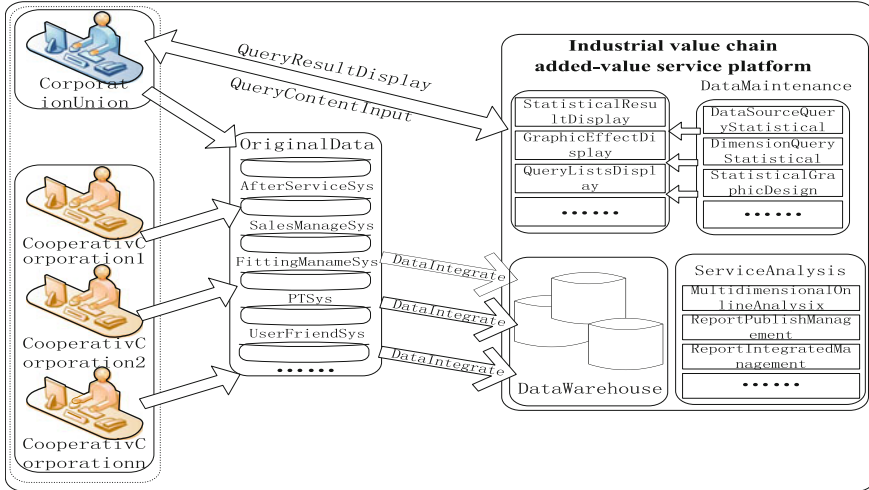


Fig. 133.1 Service platform architecture of industrial value chain

133.3 Dynamic Supplier Assessment Model on the Value-Added Service Platform of Industrial Value Chain

133.3.1 Dynamic Supplier Assessment on the Service Platform of Industrial Value Chain

In order to satisfy various requirements of dynamic supplier assessment by different unions and establish mathematical model of dynamic assessment to realize customizability of the assessment system, we now formalize the involved assessment index library and unions on the value-added service platform of industrial value chain as below.

Definition 1 In the circumstance of the value-added service platform of industrial chain for multiple unions, an enterprise union U_i is denoted as a four-tuple $U_i = (E_{U_i}, T_{U_i}, R(T_{U_i}), E \rightarrow R(T_{U_i}))$, where:

$E_{U_i} = \{E_1, E_2, \dots, E_n\}$ denotes the enterprises in the union, and n is the number of enterprises.

$T_{U_i} = \{T_{U_i1}, T_{U_i2}, \dots, T_{U_in}\}$ denotes the set of collaboration types between enterprises in a union, involving dealers, servers, and suppliers.

$R(T_{U_i})$ denotes the partitioning of enterprises into areas according to the collaboration type; thus, there exists a mapping relation $T_{U_i} \rightarrow A_i$ for any area A_i .

$E \rightarrow R(T_{U_i})$ denotes the set of collaboration in union U_i .

In order to meet varied business needs, we design a dynamic system of assessment indexes consisting of quantitative index and qualitative index. We obtain the value of quantitative index through dynamic configuration of the business database,

while the qualitative index is obtained by means of expert’s scoring; as a result, the objectivity and science of supplier assessment is guaranteed.

Definition 2 The index library is denoted as $P = \{P_1, P_2, \dots, P_n\}$. As different suppliers correspond to different assessment indexes, any index is represented as $P_j = \{P_{\text{nub}}, P_{\text{name}}, P_{\text{weight}}, P(R)\}$, where:

P_{nub} denotes the index number.

P_{name} denotes the index name.

P_{weight} denotes the index weight (as different unions have different requirements on index weights, we could adopt different algorithms to compute weights by establishing a dynamic algorithm library for unions as choice).

$P(R)$ denotes the supplier index associated with areas.

Definition 3 The assessment system is denoted as $S_k = \{S_{\text{nub}}, S_{\text{name}}, S_{\text{goal}}, S(P_k)\}$, where:

S_{nub} denotes the assessment system number.

S_{name} denotes the assessment system name.

S_{goal} denotes the assessment system objective.

$S(P_k)$ denotes the assessment system associated with assessment indexes.

Taking Definitions 1–3 into account, we can derive the model of dynamic supplier assessment as below (Fig. 133.2).

133.3.2 Model Load Based on Identification and Business Driving

In the enforcement of the dynamic assessment model, we adopt the model load strategy based on the identification and the business driving to guarantee that only valid objects that are business related and have been authenticated could visit and execute the service nodes. The specific model driving algorithm is as follows:

Algorithm: A Loading Algorithm for Assessment Model

Input: enterprise union E_{U_i} , enterprise identifier E_{iID}

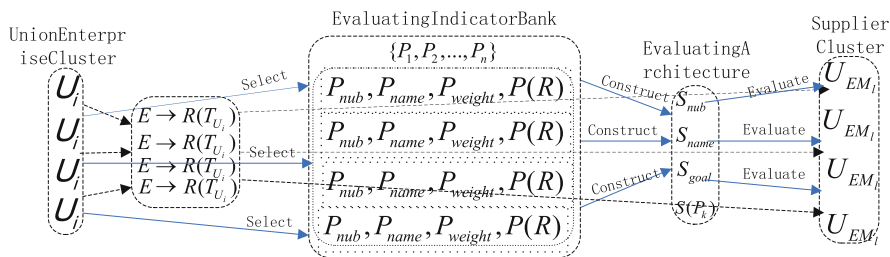


Fig. 133.2 Dynamic supplier evaluation model

```

Output: model execution result
BEGIN
Step 1: union  $E_{U_i}$  user login platform;
Step 2: if  $E_{iTD} == \text{"true"}$ , go to the Step 3; else login message false;
Step 3: select  $E \rightarrow R(T_{U_i})$  where Tid=Rid;
Step 4: get enterprise alliance list of  $E_{U_i}$ ;
Step 5: select model driven permissions where  $E_{iTD} = \text{RoleID}$ ;
Step 6: act the evaluation model;
Step 7: select evaluation index  $P_{name}$ ;
Step 8: set the weight  $P_{weight}$ , constitute evaluation system  $S_{name}$ ;
Step 9: get Rulex to evaluate suppliers;
Step 10: select show form of evaluation results for the user to view.
END
    
```

133.4 Dynamic Supplier Assessment Solution on the Value-Added Service Platform of Industrial Value Chain

In order to satisfy the need of dynamic supplier assessment on the value-added service platform of industrial chain, we propose a solution to the dynamic assessment of suppliers on the platform, as shown in Fig. 133.3.

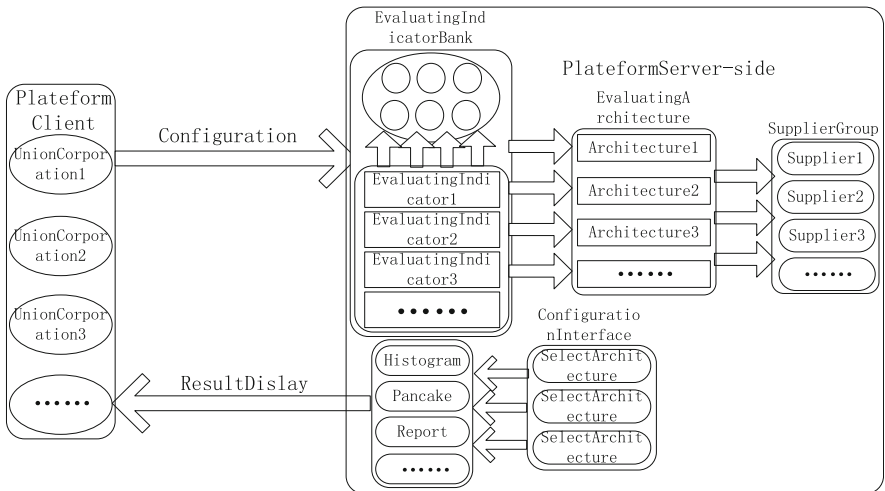


Fig. 133.3 Dynamic supplier assessment solution on the value-added service platform

This solution mainly discusses the index system of dynamic supplier assessment, dynamic supplier assessment algorithm, and display of supplier assessment results. The solution mainly focuses on three fundamental points: (1) establishment of the assessment indexes, namely, establishment of a basic assessment index library to generate the index weights and choose a specific algorithm from the above library; (2) establishment of assessment system, namely, to generate the assessment system via the assessment indexes; and (3) the supplier assessment, namely, to dynamically evaluate different suppliers via different assessment systems and display the assessment results in different forms.

133.5 Application and Validation

Each enterprise union can dynamically configure the supplier assessment according to its business and can modify and update the existing configuration in real time. This paper chooses from the value-added service platform of industrial chain enterprise union A to evaluate its suppliers. The specific progress is as below.

133.5.1 Assessment Index

Enterprise union A can configure the assessment indexes dynamically, namely, dynamically adding, deleting, or editing the assessment indexes. The specific interface is shown in Figs. 133.4 and 133.5.

IndicatorName	Indicator	IndicatorDescription	ViewData	Abscissa	Ordinate	Series	Operation
SupplyTimelyDate	W03	Evaluating whether timely delivery is guaranteed	QView	date	date	cyname	/ Edit
ProductFailureDate	W04	Evaluating the potential failures of products	QView	date	sum	cyname	/ Edit
ProductScrapDate	W05	Evaluating the product scrap during usage	QView	date	date	cyname	/ Edit

Fig. 133.4 Supplier evaluation indicator

CreateEvaluationIndicator

IndicatorName	Indicator	IndicatorDescription	ViewData	Abscissa	Ordinate	Series	Operation
SupplyTimelyDate	W03	Evaluating whether timely delivery is guaranteed	select * from IntSellData where ID=1 or ID=2	<input type="radio"/> cyname <input checked="" type="radio"/> date <input type="radio"/> sum	<input type="radio"/> cyname <input checked="" type="radio"/> date <input type="radio"/> sum	<input checked="" type="radio"/> cyname <input type="radio"/> date <input type="radio"/> sum	+ Update + Cancel
ProductFailureDate	W04	Evaluating the potential failures of products	QView	date	sum	cyname	/ Edit

Fig. 133.5 Edit of the evaluation indicator

133.5.2 Assessment System

According to different collaboration types, the enterprise union A can configure different assessment systems and edit each specific assessment system. The interface of supplier assessment system is shown in Fig. 133.6.

Click the “supplier assessment system” button to see the details, and then you can set the weights by clicking the “Edit” button. The specific interface is shown in Fig. 133.7.

133.5.3 Assessment Results

Finally, the enterprise union A displays the assessment results of its suppliers in graphics, where the graphical format and the display fields can be configured dynamically as needed. The specific assessment interface is shown in Fig. 133.8.

Architecture	ArchitectureName	EvaluatingGoal	EvaluatingIndicator	Operation
1001	SupplierEvaluateArchitecture	Q View	SupplyTimelyRate,ProductFailureRate,Pr.....	Edit
1002	AgentEvaluateArchitecture	Q View	SalesMarketShare,ReconciliationRate	Edit

≡ Delete

Fig. 133.6 Supplier evaluation architecture

IndicatorName	Indicator	IndicatorDescription	ViewData	Weight	Operation
TimelySupplyingGoodsRate	103	Evaluating whether timely delivery is guaranteed.	Q View	<input type="text" value="20.0000"/>	<input type="button" value="↑ Update"/> <input type="button" value="↓ Reset"/>
ProductFailureRate	104	Evaluating the Potential failures of products	Q View	60.0000	<input type="button" value="/ Edit"/>
ProductScrapRate	105	Evaluating the product scrap during usage	Q View	0.0000	<input type="button" value="/ Edit"/>

Fig. 133.7 Setting of weights of the evaluation indicator

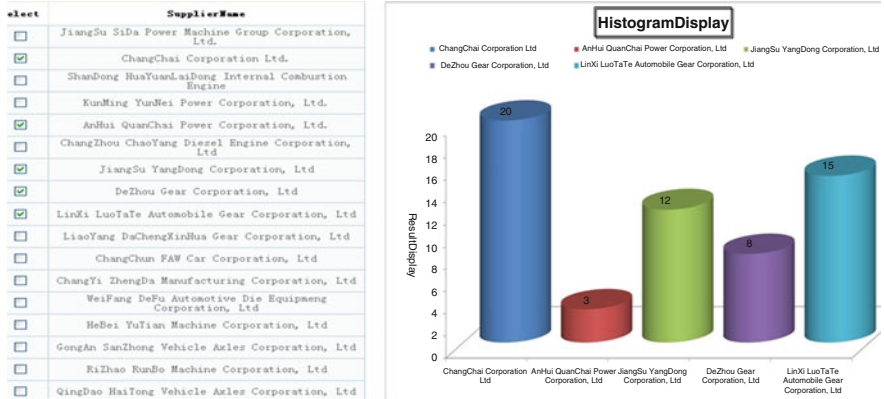


Fig. 133.8 Evaluation of results

Conclusion

The dynamic supplier assessment model as proposed has been applied to the value-added service platform of industrial value chain to allow each enterprise union to configure the assessment indexes dynamically and associate the abovesaid indexes with its own business data according to its own supplier assessment criteria. Meanwhile, we have designed a dynamic assessment algorithm library to allow unions to choose so as to satisfy different requirements of index weights by different unions. As to the future work, continuous perfection of the assessment algorithm library will be performed to better evaluate the suppliers while the security technology will be taken into account during the assessment progress.

Acknowledgements The national science and technology support program (2012BAH20F01); collaboration and information support Key Laboratory of Sichuan Province manufacturing industry chain (201302).

References

1. Wu J. Study on supplier evaluation and selection based on fuzzy integral. Harbin: Harbin University of Science and Engineering; 2008 [in Chinese].
2. Chen Y, Hu C, Peng J. Dynamic valuation method study of enterprise supply chain performance based on FCM. Appl Res Comput. 2011;28(1):185–8 [in Chinese].
3. Zhang W, Lin J. The stability of supply chain under dynamic conditions analysis. Comput Integr Manuf Syst. 2006;12(1):123–6 [in Chinese].

4. Bai C, Sarkis J. Integrating sustainability into supplier selection with grey system and rough set methodologies. *Int J Prod Econ.* 2010;24(1):252–64.
5. Tang X-L. Study on selection of logistics supplier based on support vector machine. In: 2009 International conference on machine learning and cybernetics. Baoding: IEEE Xplore; 2009. p. 1231–5.
6. Pan H, Sun L, Liu S. Research on the personality customizable dynamic form technology for SaaS platform. *Appl Res Comput.* 2013;30(10):3026–9 [in Chinese].
7. Thomas K, Thao N, Linh L. A software as a service with multi-tenancy support for an electronic contract management application. In: 2008 I.E. International conference on services computing, Hawaii; 2008. p. 79–186.
8. Zhang K, Zhang X, Sun W. A policy-driven approach for software-as-services customization. In: Proceedings of the 9th IEEE international conference on E-commerce technology (CEC) and the 4th IEEE international conference on enterprise computing (EEE), Tokyo, Japan; 2007. p. 123–30.
9. Cao J, Li M, Zhang S. Service process configuration based on multi-agent negotiation. *Chinese J Comput.* 2006;29(7):1116–24 [in Chinese].

Chapter 134

Energy-Saving Mechanisms for Delay- and Disruption-Tolerant Networks

Yankun Feng and Xiangyu Bai

Abstract In recent years, a lot of studies have been devoted to make communications possible between the nodes in the disconnected network scenarios, such as delay-/disruption-tolerant network (DTN). However, many DTN scenarios rely on mobile devices with restricted energy capacity which would directly affect the lifetime and performance of the network composed by these devices. So we pay attention to the energy-saving mechanisms of DTN in this paper and introduce the architecture, theoretical basis, evaluation metrics, classification, and challenges of the energy-saving mechanism. Next, the main energy-saving mechanisms are compared; the research on the energy management for DTN is summarized and analyzed in this paper, and the open issues for future research are also pointed out to motivate new research and development in the energy management field of DTN.

Keywords Delay-/disruption-tolerant network (DTN) • Energy-saving mechanism • Sleep scheduling • Social-aware • Social attribute of device

134.1 Introduction

DTN was formally proposed by Kevin [1] in 2003 and characterized by data transmission between nodes with huge delay and intermittent end-to-end connection. As the network technology continues to evolve, DTN has gradually been interpreted as delay- and disruption-tolerant networks. As the network topology changes and the network partitioning occurs frequently, the end-to-end communication path between the source node and destination node is maintained difficultly. DTN breaking through the restriction of sending and receiving nodes must maintain the end-to-end connection in the traditional network communications process, which results in the TCP/IP protocols not able to continue to work normally in DTN, and the use of “Story-Carry-Forward” [1, 2], a new data transfer mode, has solved the disconnected problem. In the data transfer process, the message (Bundle)

Y. Feng • X. Bai (✉)
School of Computer Science, School of Software Engineering,
Inner Mongolia University, Hohhot 010021, China
e-mail: bxxy@imu.edu.cn

[1] forwards from one node to the next node for storage and then forwards to the subsequent node opportunistically. This approach isolates the delay, enabling the communication between the nodes with intermittent connection.

In recent years, the key issue that focused on DTN has become a hot spot in academia and industry, and the technology of DTN has provided a strong support and protection in the message interaction of the military war, space communications, emergency rescue, environmental monitoring, remote communications, and many other fields with huge delay even intermittently interrupted. The DakNet project in rural India, Wizzy project of South Africa, and SNC project of Finland nomadic [2] are typical in this application. It is good for economic and social benefits.

Most or even all terminal nodes of DTN are mobile and portable devices with low-cost and short-range wireless communication capabilities. These devices often use battery with limited energy capacity rather than continuous power supply to provide energy. So the energy of the terminal device is very limited, which makes DTN to have the obvious characteristic of energy confinement and become a prominent problem and impacts the network availability seriously. Energy efficiency optimization will help improve the performance of DTN. However, traditional energy-saving mechanisms are designed based on the well-connected networks and do not apply to DTN. Therefore, the energy management mechanism for DTN is very necessary.

We research the main energy-saving mechanisms and introduce the theoretical basis, classification, and challenges of the energy-saving mechanism in this paper. The rest of the contents of this paper are organized as follows: in Sect. 134.2, we make a comprehensive investigation of existing wireless network energy-saving mechanisms. We compare those protocols' performance in Sect. 134.3. We make a summary and provide some future research point and possible direction for our work in Section "Conclusion".

134.2 Energy-Saving Mechanisms

Considering the energy confinement problem of the wireless network terminal devices, researchers have proposed many energy-saving mechanisms for various network architectures [3–5], like ad hoc network/mobile ad hoc network (MANET), pocket switched networks (PSN), wireless sensor networks (WSN), vehicular network [6], and delay-tolerant network (DTN) presented in this section.

134.2.1 *Energy-Saving Mechanisms of Ad Hoc Network*

A power-aware multi-access protocol (PAMAS) [7] has been provided by several researchers for ad hoc networks. A separate low-power radio signaling was used by PAMAS to wake up the device for data communications. In the PAMAS, the

researchers used the total bytes transmitted number B_t and the total received bytes number B_r to measure the energy savings. If energy conservation was used, the received bytes number would tend to be smaller; the percentage of energy saved would be

$$P_{\text{Percentage of Power Saved}} = 1 - \frac{B_t + 0.5 \times B_r^c}{B_t + 0.5 \times B_r} \quad (134.1)$$

A technology [8] based on the RFID tag to wake up the devices in the wireless ad hoc networks used a simple circuit based on RFID tag technology to generate a wake-up signal to activate the devices' powered battery remotely. The energy management mechanism always ensured that energy saving is more than zero. The mechanism could adjust to different node characteristics and queue the requests of service. The mechanism used L different states of a node device, the energy consumption of each state P_i , the delay overhead W_i , the state transition energy cost P_i^t , and the minimum time that the node was kept in sleep state Z_i (to save energy). They required that $P_1 < P_2 < \dots < P_L$ and $W_1 > W_2 > \dots > W_{L-1}$. The minimum time Z_i derived from Eq. (134.2) is

$$Z_i = \max \left\{ \begin{array}{l} 0, \\ \frac{W_i \times (P_i^t - P_{i+1}) + W_{i+1} \times (P_{i+1} - P_{i+1}^t)}{(P_{i+1} - P_i)} \end{array} \right\} \quad (134.2)$$

The quorum concept was used in quorum-based protocols [9]. In these protocols, an energy-saving node just needed to transmit $O(1/n)$ beacons (n is the all beacon intervals). A traffic-aware energy-saving mechanism was proposed in the study [10] for IEEE 802.11 multi-hop ad hoc networks. Their sleep-awake patterns were determined by the mobile stations relying on a quorum approach. Generally, the quorum cycle length determined the energy consumption ratio. In this mechanism, they used the network utilization as an index to determine how to adjust to the grid size.

134.2.2 Energy-Saving Mechanisms of Pocket Switched Networks

The nodes' mobility pattern in the pocket switch network (PSN) shows strong social property. The cooperative duty cycling (CDC) [11] solves the energy-efficient discovery and contact issues in PSN. The CDC significantly reduces energy consumption and achieves comparable data delivery performance in the meantime. Both the simulation results and theoretical analysis indicate those performances.

134.2.3 Energy-Saving Mechanisms of Wireless Sensor Networks

An iterative geometric programming (IGP) [12] united the routing and sleep scheduling into consideration, yielding a near optimal sleep and routing scheduling mechanism to prolong the lifetime of WSN.

After node i woke up, the RF circuits of node i would be initialized immediately. They assumed that the initialization of the node RF circuits took the node E_{rf} amount of energy and T_{rf} time. If a node wanted to deliver packets, firstly, it would take a period of time to listen to the channel to see whether there were packets being transmitted by its neighbors. They defined the total time $T_{\text{rf}} + T_{\text{lis}}$ from which the node woke up to the time it goes to sleep again. T_{slp} was defined as the sleep time of a node. If the receiver node was exactly in the sleep mode, the source node would retransmit the Request To Send (RTS) preamble after a period of time T_{sav} in an energy-saving mode. They assumed that the energy consumption to transmit all preambles and packets was a constant energy level p_{tx} . And a receiver took the power of p_{rx} to receive any packet. In the same way, they assumed that all the packet lengths were the same and denoted the data packet duration by T_{data} and assumed the same length T_{pre} to denote RTS, CTS, and ACK packets. T_{det}^j requires

$$T_{\text{det}}^i \geq \max_{j \in \mathcal{N}_i} (2T_{\text{rf}} + 3T_{\text{pre}} + T_{\text{sav}}^j) \quad (134.3)$$

The mean value of energy consumption used by the packet transmission between node i and node j is shown as

$$\begin{aligned} \bar{E}_{\text{tx}}^{ij} = & (E_{\text{rf}} + p_{\text{rx}}T_{\text{det}}) - E_{\text{rf}} + (E_{\text{rf}} + (p_{\text{tx}} + p_{\text{rx}})T_{\text{pre}}) \\ & \times \left(\frac{T_{\text{slp}}^j/2 - (2T_{\text{pre}} + T_{\text{sav}} + T_{\text{rf}} + 2T_{\text{pre}})}{T_{\text{rf}} + 2T_{\text{pre}} + T_{\text{sav}}} + 2 \right) \\ & + p_{\text{tx}}T_{\text{data}} + p_{\text{rx}}T_{\text{pre}} \end{aligned} \quad (134.4)$$

A novel approach [13] uses a distributed adaptive signal processing framework to reduce the energy consumption in sensor networks. The simulation results indicate that the mechanism is an efficient algorithm.

134.2.4 Energy-Saving Mechanisms of Vehicular Network

DSRC-AA [6] is a MAC layer sleep scheduling protocol based on IEEE 802.11 and designs the energy-saving module of intelligent transportation system for the vehicle networks. The mechanism is based on the regional characteristics of a moving vehicle that is a cluster and uses different strategies, such as assigning

different sleep schedules for the vehicles inside the group or assigning different sleep schedules for the vehicles with different communication latencies produced by different moving speeds. ATIM is the Announcement Traffic Indication Message.

$P_{X \rightarrow Y}^{\text{new}}$ and $P_{X \rightarrow Y}^{\text{old}}$ denote the receiving power of the current and last beacon frames from node Y . Every station X keeps a relative mobility metric M for its neighbor node Y , which is expressed as

$$M_X^{\text{rel}}(Y) = 10 \log_{10} \frac{P_{X \rightarrow Y}^{\text{new}}}{P_{X \rightarrow Y}^{\text{old}}} \quad (134.5)$$

134.2.5 Energy-Saving Mechanisms of Delay-Tolerant Network

According to traffic load and node density to determine the sleep schedule, the CAPM [14] proposed an asynchronous clock-based sleep scheduling protocol. Some research work have contributed to the increase of the dynamic self-adaptability of the sleep scheduling mechanism. Compared with the missed probability of the contact opportunities between nodes with the probe frequency for neighbor nodes, the STAR [15] and the AEB [16] get that the optimal detection frequency is the function of the incidence of contact which varies with time and propose the adaptively adjusted algorithm of intervals. Some researchers have presented an energy-efficient hardware and software architecture named throwboxes [17].

A message-driven-based algorithm [18] add-on to the existing routing protocols was proposed to improve energy efficiency in delay-tolerant network. The existing routing protocols are some simple protocols such as two-hop routing and epidemic routing.

134.3 Classification and Comparison

First, we should know that the mobile node itself not only sends and receives data but also needs to participate in the process of forwarding data between other nodes. And almost every delay-tolerant network node will experience idle mode, sleep mode, transmit mode, and receive mode in the course of their work. The node would consume energy in every mode, shown in Table 134.1.

Table 134.1 Power usage of a lucent IEEE 802.11 Wavelan PC Card

Mode	Transmit	Receive	Idle	Sleep
Power (W)	1.3272	0.9670	0.8437	0.0664

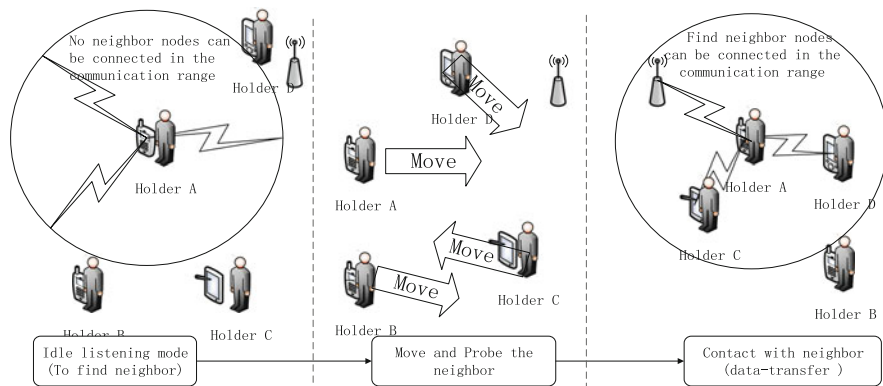


Fig. 134.1 State transition of the device

The idle mode, receive mode, and transmit mode can be collectively referred to as wake-up mode. Figure 134.1 shows the state transition process of the device from idle mode to transmit mode. Generally, the duration between the contacts of nodes in sparsely connected network are an order of a magnitude larger than contact durations [19], which shows that most of the lifetime of the nodes was consumed in the idle mode state. Therefore, we should try to minimize the idle mode time (e.g., when the idle mode time is unimportant, we can turn the node to sleep mode) while not affecting the network performance. Related experimental researches [20, 21] indicate that the energy consumption of listening to the neighbor nodes in idle mode and the energy consumption in a receiving mode is almost the same.

Above 95 % of the total energy of the devices is consumed in the idle mode by searching for their neighbors [17], instead of by infrequent data transfers. So this indicates that most of the device life is in the idle mode. In the idle mode, it is necessary to research distributed and effective energy-saving mechanisms for DTN to decrease energy consumption.

134.3.1 Classification According to Wake-Up Method

In this paper, we mainly divided the existing energy-saving mechanisms into two types: on-time wake-up mechanisms and on-demand wake-up mechanisms.

134.3.1.1 On-Demand Wake-Up Mechanisms

The principle of the on-demand wake-up mechanism is that nodes should be awakened just when it has to receive a packet from a neighboring node. So this idea minimizes the energy consumption of nodes and makes on-demand wake-up

mechanisms particularly suitable for energy confinement network scenarios which have a very low duty cycle, such as surveillance of machine failures, fire detection, and, more generally, all event-driven scenarios. In these scenarios, nodes spend most of their lifetime in the idle mode and only to perceive the environment. Nodes will transit their state from one mode to the other mode whenever an event is detected. The on-demand wake-up mechanisms are drawn a bead on reducing the energy consumption of the nodes in the idle mode state, at the same time ensuring a limited latency for transitioning in the receive mode and transfer mode.

One of the main problems associated with on-demand wake-up mechanisms is how to inform the node in the sleep mode that some other nodes are willing to communicate with it. Generally, the implementation of such mechanisms typically depends on two different channels: a wake-up channel for waking nodes when needed and a data channel for the normal data communication. The principle is that a node should wake up only when it has packet to transmit or other nodes want to communicate with it. For on-demand wake up mechanisms, mobile nodes are also allocated with two radio modules: a high-power radio module and a low-power radio module. The high-power radio module is used to transmit data. The low-power radio module is used to wake up its high-power radio to be ready to transmit data. Such mechanisms in PAMAS [7] and a RFID tag [8] are realized.

The additional cost for the wake-up ratio is the drawback of the on-demand wake-up mechanisms. And the other main problem coming up with on-demand wake-up mechanisms is that if the node in the sleep mode does not want to communicate with the node that wakes it up, the wake-up process is meaningless.

134.3.1.2 On-Time Wake-Up Mechanisms

On-time wake-up mechanisms require that the nodes should be on the same state in the period when they want to communicate with each other.

On-time wake-up mechanisms can be further divided into synchronous wake-up mechanisms and asynchronous wake-up mechanisms. Figure 134.2 shows the condition for communication between nodes in synchronous wake-up mechanisms and asynchronous wake-up mechanisms.

Synchronous Wake-Up Mechanisms

Synchronous wake-up mechanisms are also called scheduled wake-up mechanisms [16] or scheduled rendezvous schemes [5]. Synchronous wake-up mechanisms require all neighboring nodes to wake up at the same time to ensure that neighboring nodes can be in the same mode. Typically, nodes wake up periodically at synchronized intervals to examine for potential communications. If there are no communications, they would return to sleep mode until the next rendezvous time. This guarantees that when a node wakes up, all its neighbors are awake as well, as

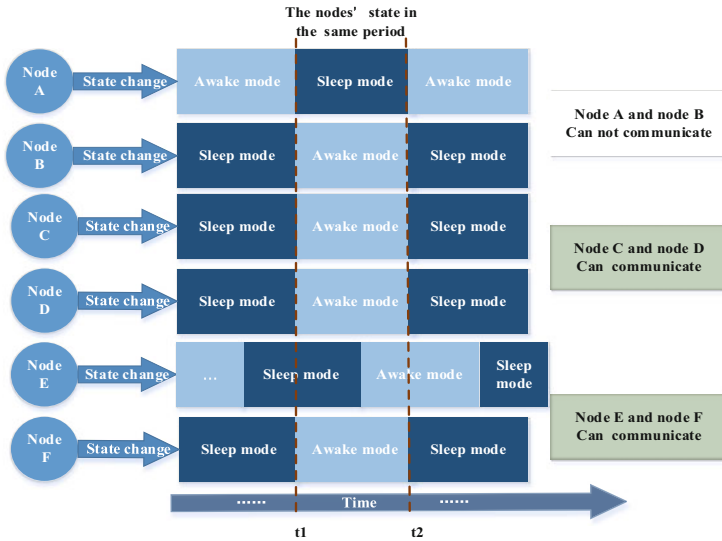


Fig. 134.2 The communication between nodes can or cannot happen

node C and node D in Fig. 134.2. This allows nodes to send broadcast messages to all their neighbors.

IEEE 802.11 PSM [22] is the best-known synchronous energy-saving mechanism; however, it is initially designed for single-hop networks. The devices, with the synchronous clock, turn on or off their radio periodically.

In synchronous wake-up mechanisms, the normally default fact is that all nodes use the global clock to maintain clock synchronization. So the synchronous wake-up mechanisms that are not fit in the global clock are impractical or impossible scenarios.

Asynchronous Wake-Up Mechanisms

The synchronized clock is not required by asynchronous wake-up mechanisms. Asynchronous wake-up mechanisms are appropriate in those scenarios without the global clock. In the asynchronous wake-up mechanism, each node wakes up independently of the others to guarantee neighbor nodes as always having overlapped active periods within a specified number of cycles. As node E and node F in Fig. 134.2, the awakening periods of these neighbors have overlapped.

Nodes wake up at scheduled time intervals to connect with each other in asynchronous wake-up mechanisms that provide the overlap of awakening intervals between neighboring nodes [9, 11]. Quorum-based protocols [9] are the earliest works about the asynchronous wake-up mechanisms.

Dual power management module and the global synchronization clock are often difficult to achieve, and asynchronous sleep scheduling mechanism is often used in DTN.

134.3.2 Classification According to Adaptability

The performance trade-off between network performance and energy efficiency almost exists in all energy-saving mechanisms. If the sleep schedule can be adaptively used by every node depending on the individual performance, it would improve the performance further. According to the wake-up mechanism, we can divide the ability of automatic adaptation into adaptive and nonadaptive.

Those nonadaptive wake-up mechanisms use the sleep schedule rigidly and fixedly, not flexibly. Therefore, their energy-saving effect is not very good. The traditional IEEE 802.11 power-saving mode requires nodes to wake up at fixed intervals that cannot adjust to the characteristics of the node and network, such as traffic. It is a typical nonadaptive wake-up mechanism.

The performance comparison of some mechanisms is shown in Fig. 134.3, which we learn from the existing experimental work. Figure 134.3 shows the relationship between mobility, packet rate, and energy consumption.

A group of energy-saving mechanisms are provided in the adaptive sleep scheduling mechanisms that can adapt well to the characteristic changes of the network and nodes. Table 134.2 shows the comparison of some energy-saving mechanisms.

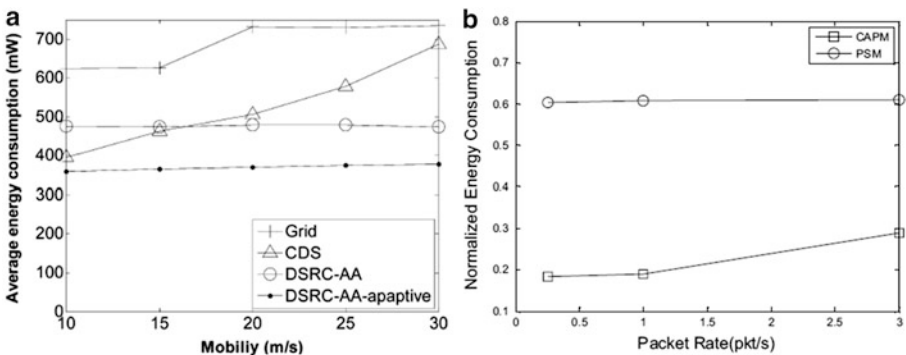


Fig. 134.3 (a) Grid, CDS, and DSRC-AA [6]. (b) CAPM [14] and PSM [22]

Table 134.2 The energy consumption of different mechanisms

Protocol or mechanism	Year	Application scenarios	Adaptivity	Remarks
PAMAS [7]	1998	Ad hoc networks	Nonadaptive	Simulations contain 10–20 nodes performing over ad hoc networks
CAPM [14]	2007	DTN	Nonadaptive	The CAPM is compared to the case without sleeping
STAR [15]	2007	DTN	Adaptive	Compared with a constant contact probing interval scheme
AEB [16]	2009	DTN	Adaptive	The AEB is optimized for using distribution of contact durations
IGP [12]	2010	WSN	Nonadaptive	Fixed sleep scheduling with optimal routing and based on social network
DSRC-AA [6]	2011	Vehicular networks	Adaptive	Compared with the existing AQPS protocols in vehicular networks. Based on social network
CDC [11]	2012	PSN	Nonadaptive	Local synchronous. Based on social network

Conclusion

Infrastructure networks do not provide service connectivity in those rural and remote areas. If the cellular networks do not consider the trade-off of cost and benefit, it could be used in alternative. Nowadays, technology innovation has brought new development opportunities for network, such that more and more intelligent terminal devices can use the wireless network interface and wireless technology to build self-organizing techniques. DTN could be a feasible solution to improve the level of communication technology in remote and backward areas.

DTN is a frontier hot area of future wireless network technology research, and the wireless terminal devices with the characteristics of mobility, portability, and intelligence will be widely used in the future wireless network. The energy restriction problem of the terminal devices will be a core issue. In this paper, we made a brief analysis of the DTN basic characteristics and the challenges which the energy mechanism design faced. On this basis, we carried out a comprehensive analysis and discussion on the obtained main results of the energy-saving mechanism (sleep scheduling mechanism) of DTN at home and abroad in recent years from three aspects: the wake-up mechanism, dynamic adaptability, and sleep scheduling based on social networks.

We will continue to study and analyze the social network characteristics of terminal devices, according to its holder's social network properties, and design and implement more efficient sleep scheduling mechanisms based on the social network properties to achieve better energy-saving efficiency of the device.

Acknowledgements This work was supported by the National Natural Science Foundation of China (61062004, 61162006, and 61362011) and Application Development Foundation of Inner Mongolia (20100509).

References

1. Kevin F. A delay-tolerant network architecture for challenged internets. In: Proceedings of the 2003 conference on applications, technologies, architectures, and protocols for computer communications. ACM; 2003. p. 27–34.
2. Yongping X, Limin S, Jianwei N, et al. Opportunistic networks. *J Software*. 2009;20(1):124–37.
3. Jones CE, Sivalingam KM, Agrawal P, et al. A survey of energy efficient network protocols for wireless networks. *Wireless Networks*. 2001;7(4):343–58.
4. Karl H. An overview of energy-efficiency techniques for mobile communication systems. Telecommunication Networks Group, Technical University Berlin, Berlin, Germany. Technical report TKN-03-017; 2003.
5. Anastasi G, Conti M, Di Francesco M, et al. Energy conservation in wireless sensor networks: a survey. *Ad Hoc Networks*. 2009;7(3):537–68.
6. Wu SH, Chen CM, Chen MS. An asymmetric and asynchronous energy conservation protocol for vehicular networks. *IEEE Trans Mobile Comput*. 2010;9(1):98–111.
7. Singh S, Raghavendra CS. PAMAS—power aware multi-access protocol with signalling for ad hoc networks. *ACM SIGCOMM Comput Commun Rev*. 1998;28(3):5–26.
8. Chiasserini CF, Rao RR. A distributed power management policy for wireless ad hoc networks. In: *Wireless communications and networking conference, WCNC 2000*, vol. 3. IEEE; 2000. p. 1209–13.
9. Tseng YC, Hsu CS, Hsieh TY. Power-saving protocols for IEEE 802.11-based multi-hop ad hoc networks. *Comput Networks*. 2003;43(3):317–37.
10. Chen YS, Tsai MK, Chiang LS, et al. Adaptive traffic-aware power-saving protocol for IEEE 802.11 ad hoc networks. In: *2011 I.E. 17th international conference on parallel and distributed systems (ICPADS)*. IEEE; 2011. p. 866–71.
11. Yang S, Yeo CK, Lee BS. CDC: an energy-efficient contact discovery scheme for pocket switched networks. In: *2012 21st International conference on computer communications and networks (ICCCN)*. IEEE; 2012. p. 1–7.
12. Liu F, Tsui CY, Zhang YJ. Joint routing and sleep scheduling for lifetime maximization of wireless sensor networks. *IEEE Trans Wireless Commun*. 2010;9(7):2258–67.
13. Chou J, Petrovic D, Ramachandran K. A distributed and adaptive signal processing approach to reducing energy consumption in sensor networks. In: *Twenty-second annual joint conference of the IEEE computer and communications, INFOCOM 2003*, vol. 2. IEEE Societies, IEEE; 2003. p. 1054–62.
14. Xi Y, Chuah M, Chang K. Performance evaluation of a power management scheme for disruption tolerant network. *Mobile Networks Appl*. 2007;12(5):370–80.
15. Wang W, Srinivasan V, Motani M. Adaptive contact probing mechanisms for delay tolerant applications. In: *Proceedings of the 13th annual ACM international conference on mobile computing and networking (MobiCom 2007)*. ACM; 2007. p. 230–41.
16. Choi BJ, Shen X. Adaptive exponential beacon period protocol for energy-saving in delay tolerant networks. In: *IEEE international conference on communications, ICC'09*. IEEE; 2009. p. 1–6.
17. Banerjee N, Corner MD, Levine BN. An energy-efficient architecture for DTN throwboxes. In: *26th IEEE international conference on computer communications, INFOCOM 2007*. IEEE; 2007. p. 776–84.

18. Manam VK, Gurav G, Murthy C. Performance modeling of message-driven based energy-efficient routing in delay-tolerant networks with individual node selfishness. In: 2013 Fifth international conference on communication systems and networks (COMSNETS). IEEE; 2013. p. 1–6.
19. Feeney LM, Nilsson M. Investigating the energy consumption of a wireless network interface in an ad hoc networking environment. In: Twentieth annual joint conference of the IEEE computer and communications societies, INFOCOM 2001. Proceedings IEEE, vol. 3. IEEE; 2001. p. 1548–57.
20. Keränen A, Ott J. Increasing reality for dtn protocol simulations. Helsinki University of Technology. Technical report; 2007.
21. Stemm M. Measuring and reducing energy consumption of network interfaces in hand-held devices. *IEICE Trans Commun.* 1997;80(8):1125–31.
22. IEEE 802.11: Wireless LAN Medium Access Control (MAC) and Physical Layer (PHY) specifications (2007 revision). IEEE; June 2007.

Chapter 135

Improved Sensor-MAC Protocol for Wireless Sensor Networks

Jian Di and Zhijun Ma

Abstract In wireless sensor networks, S-MAC (Sensor-MAC) protocol based on competition cannot make the nodes to adjust the active time according to the dynamic changes of the traffic load; besides, the idle listening of the nodes also brings about the energy consumption problem. In this paper, an improved method for the S-MAC protocol is proposed to solve such problems while in combination with the L-MAC (Low-MAC) protocol. Simulation results show that the proposed method can improve the node active time adaptable to the dynamic changes of traffic load and greatly reduce the energy consumption brought by idle listening as well.

Keywords Wireless sensor networks • S-MAC • Energy consumption • L-MAC

135.1 Introduction

Wireless sensor network, a wireless network with a large number of stationary or moving sensors, is configured by self-organization and multi-hop. The wireless sensors cooperatively perceive, acquire process, and transmit information of the perceived objects within the network covering a geographic area and ultimately send information to the network owner [1]. The size of sensor node is small. Generally speaking, the sensors usually rely on energy-limited battery; therefore, how to reduce the power consumption has become the current challenge.

As to the wireless network, as a result of a single shared channel, how to allocate the channel directly affects the performance of the network implementation; besides, it also puts forward new requirements to MAC layer protocols. According to the characteristics of wireless sensor network (WSN), Ye and Heidemann put forward a kind of MAC layer protocol based on competition, named S-MAC (Sensor-MAC) protocol in 2003. The core idea of S-MAC is the introduction of periodic wake/sleep mechanism so as to reduce the energy consumption caused by idle listening. The realization of the S-MAC protocol is simple because it does not

J. Di • Z. Ma (✉)

School of Control and Computer Engineering, North China Electric Power University,
Baoding 071000, China

e-mail: mzjgunner@163.com

© Springer International Publishing Switzerland 2015

W.E. Wong (ed.), *Proceedings of the 4th International Conference on Computer Engineering and Networks*, Lecture Notes in Electrical Engineering 355,

DOI 10.1007/978-3-319-11104-9_135

1177

require strict clock synchronization and can reduce the energy consumption effectively; therefore, the S-MAC protocol is used in the field of environmental monitoring and medical management. However, as the sleep time of each node is fixed, S-MAC protocol cannot adapt to changes in network load, which will also cause the node idle listening and increase the energy loss in the network.

L-MAC protocol introduces the dynamic duty cycle adjustment mechanism based on the S-MAC protocol [2]. It adjusts the duty cycle dynamically through the network traffic prediction. Whenever the network traffic increases, each cycle in S-MAC will be divided into several short cycles to improve the duty cycle and accommodate the increased traffic.

135.2 S-MAC Protocol Mechanism

S-MAC is a kind of a MAC protocol based on competition [3]. The core idea of the S-MAC is the introduction of periodic wake/sleep mechanism so as to reduce the energy consumption caused by idle listening. Each node wakes up after a period of sleep and listens to the channel to detect whether there are data sent by other nodes. Then the nodes will transfer the wireless transceiver to a low power state and open a corresponding timer when they are sleeping and wake up automatically when time is up. The S-MAC protocol primarily introduces the virtual cluster mechanism and periodic wake/sleep mechanism.

135.2.1 Virtual Cluster Mechanism

1. Firstly, the node listens at least one synchronous cycle time. If no sleep schedule is listening during this time, the node will randomly select a sleep schedule as their sleep schedule and broadcast its schedule to its neighboring nodes via SYNC frame.
2. When the node receives a sleep schedule of neighbor before choosing or announcing its sleep schedule, the sleep schedule of neighbor will be set as its own sleep schedule.
3. When the node receives a sleep schedule of neighbor after choosing or announcing its sleep schedule, if the node has no neighbors, it will discard the current sleep schedule and use the newly received sleep schedule; if the node has any neighbor, it will be awoken according to different sleep scheduling tables in turn.

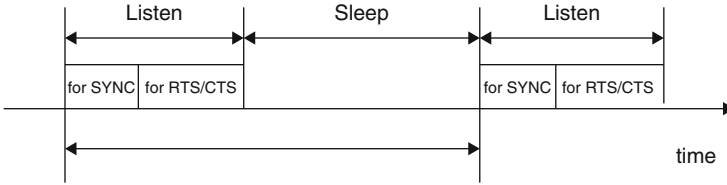


Fig. 135.1 The periodic wake/sleep mechanism of S-MAC protocol

135.2.2 Periodic Wake/Sleep Mechanism

The time will be divided into multiple frames in S-MAC protocol. Each frame consists of two parts: active state and dormant state. In the active state, the node communicates with its neighboring nodes to receive or transmit data. The active state is usually fixed at 300 ms. In the dormant state, the node will shut down its receiver and transmitter to reduce energy loss. If there is data to be processed at this time, they will be cached until the node is active [3]. Through periodic activity/sleep mechanism, S-MAC protocol greatly reduces the energy loss caused by idle listening. The cycle of S-MAC protocol is shown in Fig. 135.1.

The S-MAC protocol features the forming planar topology that can make the neighboring nodes to communicate with each other. As the synchronization nodes form a virtual cluster without communication conflict, it is easy to adapt to changes in topology.

135.3 L-MAC Protocol Mechanism

The L-MAC protocol introduces a dynamic duty cycle adjustment mechanism based on the S-MAC protocol. It predicts changes in network traffic based on the number of packets in the queue. When the network traffic is heavy, the original cycle will be divided into several shorter cycles. The synchronization frame only occurs at the beginning of the long cycle rather than the short cycle.

Set the number of the short period of N_i ; each short cycle time is as follows:

$$T_{\text{short}} = (T_{\text{RTS/CTS}} + T_{\text{sleep}}) / N_i \tag{135.1}$$

N_i can be obtained by the number of packet queue in node i . When the number of packets in the queue of node i is 0, take $N_i = 1$; L-MAC has the same wake/sleep cycle as S-MAC at this time. The value of N_i is determined at the beginning of each long cycle. At the same time, increase one byte in RTS/CTS packet to represent N_i . The neighboring nodes within one hop can adjust their schedule based on the value of N_i after receiving RTS or CTS. The cycle of S-MAC protocol is shown in Fig. 135.2.

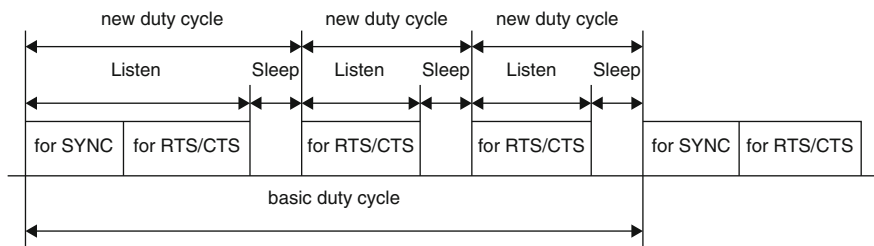


Fig. 135.2 Periodic wake/sleep mechanism of the S-MAC protocol

135.4 Existing Problems of S-MAC and L-MAC

S-MAC protocol uses the periodic wake/sleep mechanism with active time usually fixed; but the network traffic is always changing. Thus, the length of active time of the protocol cannot adjust changes in the network traffic dynamically, and it can also cause energy loss. When the node is in the dormant state, if an event is detected, it has to wait until the communication module converts to the active state to send data [4]. When an intermediate node of the network transmits data, the next hop node may be in the dormant state, and it also has to wait until the next hop node has converted to the active state. The delay of node dormancy increases with the number of hops.

L-MAC protocol has the same performance with S-MAC in the constant traffic load, but in case of changing load, especially in the condition of large and burst traffic, it can save more energy than the S-MAC protocol while keeping reasonable throughput and shorter delay characteristics. The L-MAC protocol divides a cycle into several short cycles, extending the active time of node in a cycle to adapt to the change of network traffic. However, as the node can only transmit limited data in a short cycle because the time of short cycle is shorter, the delay characteristics of the protocol have to be further improved.

135.5 Improved Design of the S-MAC Protocol

The main problem of the S-MAC protocol is not adapted to the changes in the network load. How to make the S-MAC adapt to changes in the network load to achieve energy saving more effectively? We can consider existence and occurrence of external things in combination with the protocol and improve the protocol based on the idea of central limit theorem. The central limit theorem is defined as below.

If $\xi_1, \xi_2, \xi_3, \dots$ is a list of independent and identically distributes random variables and $E\xi_k = a, D\xi_k = \sigma^2 (\sigma > 0), k = 1, 2, \dots$, we can know the formula as below:

$$\lim_{n \rightarrow \infty} P \left(\frac{\sum_{k=1}^n \xi_k - na}{\sigma \sqrt{n}} < x \right) = \frac{1}{\sqrt{2\pi}} \int_{-\infty}^x e^{-\frac{t^2}{2}} dt \quad (135.2)$$

The theorem shows that if a random phenomenon is caused by many random factors, each factor has no significant role in the overall changes. We can infer that the description of the random variables of random phenomenon is approximately subject to normal distribution. Thus, we can conclude that in nature and production, some phenomena are affected by many independent random factors. If the impact of each factor is very small, the overall impact can be seen as subject to normal distribution, so changes of things can be seen as subject to normal distribution. The network traffic is also subject to normal distribution.

As discussed above, the S-MAC protocol can be improved as below: set the threshold of M and L , $M > L$. The number of tasks in the queue represents network traffic. When the network traffic is between L and M , we use the same cycle as S-MAC. When the node withstands continuous load less than L , the sleep time of node will be expanded to two times of the S-MAC protocol's sleep time to reduce the idle listening time so as to achieve the purpose of energy saving. When the node withstands continuous load higher than M , the sleep time of the node will be reduced to 1/2 of the S-MAC protocol's sleep time. This can reduce sleep time of node and network delay and increase the network throughput. L and M should be selected according to the normal distribution of network traffic. The probability of network traffic between L and M should be 80 % (Fig. 135.3).

The improved protocol also notes the following: (1) when the node updates its length of sleep time, it does not add a new frame format, but continues to use the existing SYNC frame, in which only a new field is added to represent the multiple relationship between the new sleep time length and normal sleep time length. (2) Each node sends or forwards SYNC frames to adjust the length of sleep time in the neighbor discovery process.

135.6 Performance Evaluation

In this paper, the simulation software used is NS2 (Network Simulator, version 2), which is an object-oriented network emulator developed by UC Berkeley. NS2 simulation software uses script as the input to describe the network topology, the

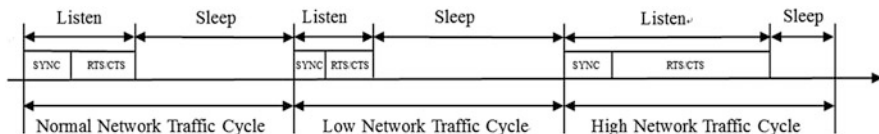


Fig. 135.3 Periodic wake/sleep mechanism of improved S-MAC protocol

Table 135.1 Parameters of the simulation scenario

Channel	Channel/wireless channel
propType	Propagation/TwoRayGround
llType	LL
adhocRouting	DSR
ifqType	Queue/DropTail/PriQueue
ifqLen	50
energyModel	EnergyModel
txPower	0.3442 W
rxPower	0.3682 W
idlePower	0.3442 W
sleepPower	$5.0e-5$
transitionPower	0.386 W
transitionTime	0.0005
initialEnergy	1000 J
simulation time	1000 s

network protocol, the network load, and some control parameters [5]. The output of NS2 is a series of data, such as the number of packets sent by each data source and delays of each network node.

The simulation topological structure is a linear topological structure consisting of six nodes. The first node is the source node and last node is the sink node. The distance of every two nodes in topology is 200 m with a transmission range of nodes of 250 m. The node can communicate with one hop node around so that we can ensure that the data can only be transferred to one hop node. Table 135.1 describes the parameters of the simulation scenario.

In the simulation, the improved S-MAC protocol is called ES-MAC. The data flow used in experiment is CBR, and data packet length of CBR stream is fixed; conversely, the larger the packet interval value represents, the network traffic decreases. In Fig. 135.4, we can see that the ES-MAC protocol saves more energy than S-MAC and L-MAC when the network traffic is small. When the network traffic is small, the L-MAC protocol has the same cycle with the S-MAC protocol; however, ES-MAC protocol can increase the sleep time of nodes and save energy as a result. When the network traffic is ordinary, ES-MAC is not necessary to adjust the duty cycle; therefore, it has the same duty cycle with S-MAC and L-MAC. Thus, the energy consumption of the three protocols is the same. When network traffic is large, ES-MAC protocol reduces the sleep time of nodes and extends the active time of nodes; therefore, it has more energy consumption than S-MAC. However, as the L-MAC protocol divides the cycle into more short cycles, it has longer active time than ES-MAC with more energy consumption than that of ES-MAC.

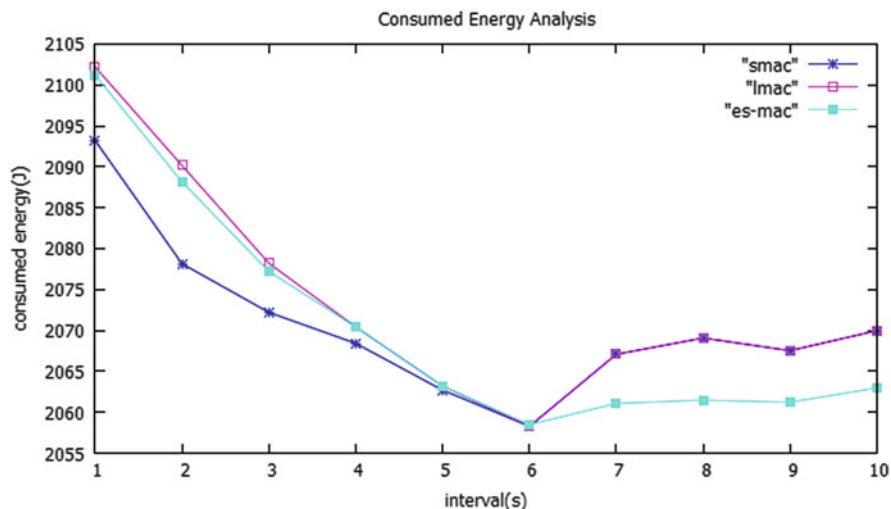


Fig. 135.4 Comparison of the consumed energy between ES-MAC (square) with L-MAC (cross) and S-MAC (asterisk)

Conclusion

In this paper, we propose a new protocol to improve S-MAC protocol for wireless sensor networks based on the network traffic condition so that the nodes can adjust the sleep time dynamically. In the simulation, in comparison with the energy consumption of ES-MAC, S-MAC, and L-MAC, we see that ES-MAC can save more energy than the other two protocols as far as the node is concerned and extend the life cycle of the nodes. In this sense, ES-MAC is more suitable for the sensor networks with sparse data.

References

1. Li X. Wireless sensor network technology. Beijing: Beijing Institute of Technology Press; 2007. p. 185–8, 241–56 [in Chinese].
2. Li X. Energy conservation for wireless sensor networks based on S-MAC protocol. Kunming: Kunming University of Science; 2013 [in Chinese].
3. Yoo D-S, Park S-S, et al. Dynamic S-MAC protocol for wireless sensor networks based on network traffic states. In: 14th Asia-Pacific conference on communications. Tokyo: IEEE; 2008. p. 1–5.
4. Yadav R, Varma S, Malaviya N. A survey of MAC protocols for wireless sensor networks. UbiCC J. 2009;4(3):827–33.
5. Huang H, Feng H. NS network simulation and protocol emulation. Beijing: Posts & Telecommunications Press; 2010. p. 205–10 [in Chinese].

Chapter 136

An Approach of Analyzing Transmission Capacity of Multi-hop Wireless Sensor Networks

Shaoqing Wang, Kai Cui, and Ning Zhou

Abstract Transmission capacity is a key issue in the research of network information theory. This paper proposes a new approach for analyzing transmission capacity (TC) of multi-hop wireless sensor networks (WSN). The multi-hop transmission capacity (MTC) is defined as the product of the spectrum efficiency multiplied by expected forward distance per hop (EFD). According to the stochastic geometry model of nodes located in WSN and the routing strategy of the nearest forward progress, we derive expressions of the spectrum efficiency and the EFD. The numerical results of MTC are given, and comparisons between MTC and single hop capacity are also made. It is shown that TC heavily depends on the contention density and transmission probability, and there are optimal contention density and optimal transmission probability for multi-hop capacity.

Keywords Wireless sensor networks • Multi-hop transmission capacity • Spectrum efficiency • Stochastic geometry • Expected forward distance

136.1 Introduction

Wireless network capacity is a hot topic in wireless communication research in recent years. Being different from channel capacity, the network capacity is to design the system from the view of an overall network capacity, which is called as the network information theory. However, due to the limitation of both wireless transmission effects and interference from other users, the network capacity is difficult to handle [1]. Gupta discussed the concept of transport capacity, proposed to study the scaling limit of the achievable rate, and obtained a scaling law of $O(\lambda^{1/2})$, where λ is defined as the density of transmitting nodes [2]. Under the same model, strategies achieving the same capacity scaling laws have been given [3, 4]. Information theoretic scaling laws have been established in a more general context [5–7].

S. Wang (✉) • K. Cui • N. Zhou
The Electronic System Engineering Company of China, Beijing 100000, China
e-mail: 429086198@qq.com

Although scaling laws have provided insight on the wireless sensor networks (WSN), a finer view of throughput limits is needed for understanding how different technologies affect the performance of WSN. In order to provide more insights on protocol design, the transmission capacity is discussed [8–10]. Stochastic geometry is used to characterize interference and outage in order to determine TC. However, the concept of transmission capacity defined is not sufficient for evaluating TC of multi-hop networks, since it is inherently a metric of single hop capacity [11, 12].

An approach for analyzing MTC of WSN is proposed in the paper. The MTC is expressed as the product of the spectrum efficiency per unit area multiplied by EFD per hop. The expression of EFD is deduced. Then, the spectrum efficiency per unit area is deduced by integrating the media access control (MAC) protocol and the effects of the realistic physical layer characteristics. Finally, the expression of MTC is derived and the impacts of key designing parameters on MTC are discussed through simulation.

136.2 System Model and Assumptions

Considering a multi-hop WSN with N nodes uniformly distributed in a circular area of radius R centered at the origin o as shown in Fig. 136.1, the positions of the nodes can be modeled by a two-dimensional Poisson point process (PPP). So, the probability that there are k nodes in a region with area of S is given by

$$P[k \text{ in } S] = \frac{e^{-\lambda S} (\lambda S)^k}{k!} \quad (136.1)$$

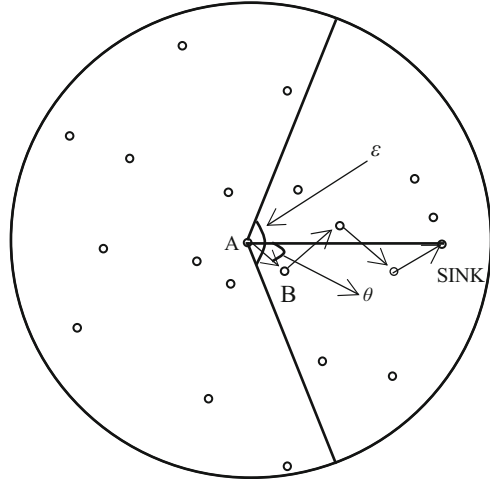
where λ , equal to $N/\pi R^2$, is the average number of nodes per unit area.

Throughout this paper, the NFP routing strategy is considered as packet forwarding, which means that each node in a multi-hop route always relays the packets to its nearest node in the direction to the SINK node. Figure 136.1 shows the case where a transmitter A is located at the origin and intermediate nodes are selected according to NFP route strategy within a sector of angle ε toward the direction of the destination as the next hop. In this case, a route can be seen as a deviation from the straight line between A and SINK. Let θ denote the angle that each hop deviates with the straight line. θ is a random variable, which is uniformly distributed in the interval $[0, \varepsilon/2)$.

In the WSN, the distance from a node to its nearest relaying node, denoted by r_0 , is a random variable and can be described by its probability density function as follows.

For the case of node A transmitting packets to SINK in a multi-hop network, the complementary cumulative distribution function (CDF) of r_0 is the probability that there are no nodes closer than r_0 within the sector of angle ε and can be expressed as

Fig. 136.1 NFP routing forwarding strategy



$$\bar{F}_{R_0}(r_0) = \exp(-\lambda \epsilon r_0^2 / 2) \quad (0 < r_0 \leq R) \tag{136.2}$$

So, the PDF of r_0 is written as

$$f_{R_0}(r_0) = -\frac{d\bar{F}_{R_0}}{dr_0} = \lambda \epsilon r_0 \exp(-\lambda \epsilon r_0^2 / 2) \quad (0 < r_0 \leq R) \tag{136.3}$$

Then, we have

$$E[r_0] = \int_0^R r_0 f_{R_0}(r_0) dr_0 \approx \left(\frac{\pi}{2\lambda \epsilon}\right)^{1/2} \tag{136.4}$$

where $E[\]$ is the expected operator. By projecting each hop onto the straight line between A and SINK and assuming that r_0 is independent of θ , the expected forward distance (EFD) per hop can be expressed as

$$r_e = E[r_0]E[\cos \theta] = \frac{\sqrt{2\pi} \sin(\epsilon/2)}{\sqrt{\lambda \epsilon \epsilon}} \tag{136.5}$$

Supposing that the system is slotted, each node transmits packets with fixed length in the slots with the probability of p and the fixed power level P_t , and the slot duration is sufficiently large so as to allow carrier synchronization. We consider a pair of nodes, the transmitter A and receiver B, located apart from a distance $E[r_0]$ as mentioned in Eq. (136.4). So, within a slot, all the packets transmitted by other transmitters become interferences for the pair, and the interferers are randomly distributed as a PPP with parameter λp , known as contention density, over the circular area. Assuming that wireless channel is a narrowband Rayleigh fading channel, the PDF of the received power from the desired transmitter A is

$$F_{P_0}(P_0) = \frac{1}{E[P_0]} \exp\left(-\frac{P_0}{E[P_0]}\right) \quad (0 < P_0 < \infty) \tag{136.6}$$

where α is the path loss exponent and the expected received power $E[P_0]$ can be written as

$$E[P_0] = P_t(E[r_0])^{-\alpha} \tag{136.7}$$

Similarly, considering that Friis formula can only be applied in the far-field region, the average total interfering power I received by the receiver B in a slot can be expressed as

$$I = E\left[\sum_{i=1}^j P_t \min[1, r_i^{-\alpha}]\right] \quad (i = 1, 2 \dots j) \tag{136.8}$$

where $j = \lambda p \pi R^2$ is the number of interfering nodes and r_i represents the distance from the i th interfering node to the receiver B. Because all the interferers are randomly distributed as a PPP with parameter λp over the circular area, the distance r_i is uniformly distributed over the circular area and the PDF of r_i is

$$f_{r_i}(r_i) = \begin{cases} 2r_i/R^2 & r_i \leq R \\ 0 & r_i > R \end{cases} \quad (i = 1, 2 \dots j) \tag{136.9}$$

Combining Eqs. (136.8) and (136.9), we have

$$\begin{aligned} I &= E\left[\sum_{i=1}^j P_t \min[1, r_i^{-\alpha}]\right] \\ &= \lambda p \pi R^2 P_t \int_0^R \min[1, r_i^{-\alpha}] f_{r_i}(r_i) dr_i = 2\pi \lambda p P_t \left(\frac{1}{2} + \frac{R^{2-\alpha} - 1}{2 - \alpha}\right) \end{aligned} \tag{136.10}$$

If the number of nodes in WSN is very large, the total interfering power I can be modeled as Gaussian noise. So, the signal-to-interference-and-noise ratio (SINR) can be expressed as

$$\gamma = \frac{E[P_0]}{N_0 + I} \tag{136.11}$$

where N_0 is the average power of noise. Assuming that the system is interference limited, we have

$$\gamma = \frac{E[P_0]}{I} \tag{136.12}$$

Substituting expressions (136.7) and (136.10) into Eq. (136.12), one can rewrite Eq. (136.12) as

$$\gamma = \frac{P_t(E[r_0])^{-\alpha}}{2\pi\lambda p P_t\left(\frac{1}{2} + \frac{R^{2-\alpha}-1}{2-\alpha}\right)} = \frac{(2-\alpha)(E[r_0])^{-\alpha}}{\pi\lambda p(2R^{2-\alpha}-\alpha)} \quad (136.13)$$

136.3 Multi-hop Transmission Capacity

Firstly, defining the spectrum efficiency, denoted by F_e , as the effective symbol rate all transmissions per unit area, we have

$$F_e = \lambda p(1 - \text{PER})\eta R_s = \lambda p(1 - \text{PER})\eta \log_2(1 + \gamma) \quad (136.14)$$

where R_s is the channel symbol rate, η is coding rate, and PER is the packet error rate of the A–B link. For the BCH coding considered in this paper, PER can be expressed as

$$\text{PER} = 1 - \sum_{i=0}^t \binom{n}{i} (\text{BER})^i (1 - \text{BER})^{n-i} \quad (136.15)$$

where n is the packet length in bit, t is the number of error correcting, and BER is the bit error rate of the A–B link. For BPSK modulation scheme and Rayleigh block fading channel [13], we have

$$\text{BER} = \frac{1}{2} \sqrt{1 - \frac{\gamma}{1 + \gamma}} \quad (136.16)$$

Combining Eqs. (136.13)–(136.16), we have

$$F_e = \lambda p(1 - \text{PER})\eta \log_2\left(1 + \frac{(2-\alpha)(E[r_0])^{-\alpha}}{\pi\lambda p(2R^{2-\alpha}-\alpha)}\right) \quad (136.17)$$

Substituting expression (136.4) into Eq. (136.17), one can rewrite Eq. (136.17) as

$$F_e = \lambda p(1 - \text{PER})\eta \log_2\left(1 + \frac{(2-\alpha)\left(\frac{\pi}{2\lambda\epsilon}\right)^{-\alpha/2}}{\pi\lambda p(2R^{2-\alpha}-\alpha)}\right) \quad (136.18)$$

Then, multi-hop transmission capacity (MTC) can be defined as the product of the spectrum efficiency multiplied by EFD per hop. So, the expression of MTC can be written as

$$C_m = F_e r_e \quad (136.19)$$

Substituting expressions (136.5) and (136.18) into Eq. (136.19), we have

$$C_m = \sqrt{\lambda} \times \frac{\sqrt{2\pi p \eta} \sin(\varepsilon/2)}{\sqrt{\varepsilon \varepsilon}} (1 - \text{PER}) \log_2 \left(1 + \frac{(2 - \alpha)(\pi/2\varepsilon)^{-\alpha/2} \lambda^{\alpha/2-1}}{\pi p (2R^{2-\alpha} - \alpha)} \right) \quad (136.20)$$

For the purpose of comparison, single hop transmission capacity (STC) can be obtained by

$$C_s = F_e = \lambda p \eta (1 - \text{PER}) \log_2(1 + \gamma) \quad (136.21)$$

It should be noticed that the STC in this paper is different from the traditional STC which was defined as the symbol rate per unit area, subject to a constraint on outage probability δ , and the redundant symbols used for channel coding are also included in the STC, hence described as

$$C = \lambda p (1 - \delta) \log_2(1 + T) \quad (136.22)$$

where T is an SINR threshold and $\delta = P(\gamma < T)$ is also the packet error rate. In other words, the effect of coding rate η on the single transmission is not considered. So the STC described in Eq. (136.21) in this paper is more accurate than the traditional STC.

136.4 Numerical Results and Analysis

Numerical results of MTC and STC are presented and discussed in this section. Some important parameters we take in our work are given:

$$\lambda = 0.1, n = 128 \text{ [bit]}, t = 10, \eta = 1/2, R = 200 \text{ [m]}, \alpha = 3, \varepsilon = \pi/2.$$

In Figs. 136.2 and 136.3, the impact of contention density λp on MTC and STC is illustrated respectively. It is shown that TC depends on the contention density, and there is optimal contention density for MTC and STC, respectively.

The impacts of transmission probability on MTC and STC for different angle limitation ε are shown in Figs. 136.4 and 136.5.

We can observe that there are different optimal transmitting probabilities in which MTC and STC are maximized respectively. Moreover, it is easy to observe that the optimal transmitting probability decreases as the angle ε decreases. This can be explained as follows: given the nodes density λ in an ad hoc network, expected forward distance per hop increases as the angle limitation ε decreases, which results in the decrease of expired received power P_0 and SINR, so the STC and MTC are reduced too.

Fig. 136.2 MTC versus contention density

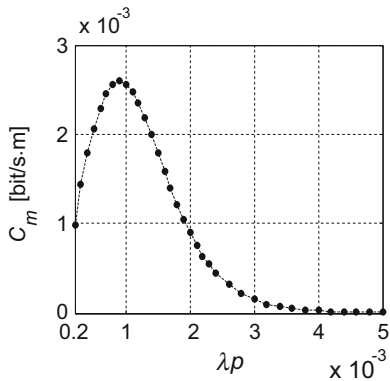


Fig. 136.3 STC versus contention density

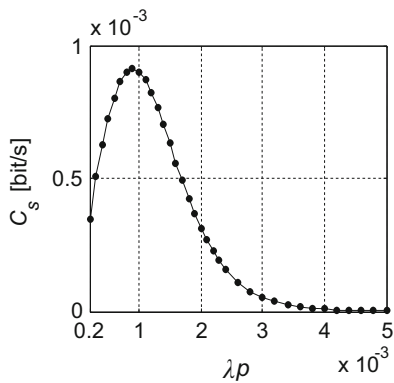


Fig. 136.4 MTC versus transmission probability for different angle limitation

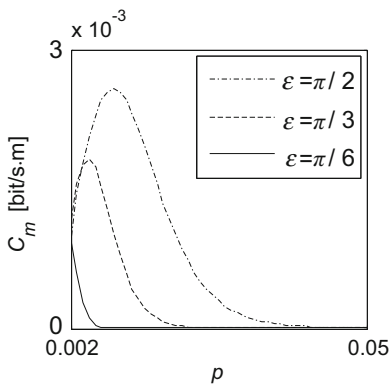
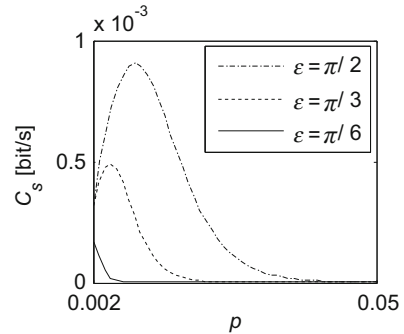


Fig. 136.5 STC versus transmission probability for different angle limitation



Conclusion

A novel approach for evaluating MTC of WSN is presented in this paper. We derive the expression of MTC. It is shown that the transmission capacity is greatly influenced by the contention density and transmission probability, and there are optimal contention density and optimal transmission probability for MTC.

Acknowledgments The research was supported by the National Science and Technology Major Project under Grant No. 2012ZX03006003. At last, the authors wish to thank the reviewers for their very helpful comments.

References

1. Andrews JG, Jindal N, et al. Rethinking information theory for mobile ad hoc networks. *IEEE Commun Mag.* 2008;46(12):94–101.
2. Gupta P, Kumar P. The capacity of wireless networks. *IEEE Trans Inf Theory.* 2000;46(2):388–404.
3. Franceschetti M, Dousse O, et al. Closing the gap in the capacity of wireless networks via percolation theory. *IEEE Trans Inf Theory.* 2007;53(3):1009–18.
4. Kulkarni SR, Viswanath P. A deterministic approach to throughput scaling in wireless networks. *IEEE Trans Inf Theory.* 2004;50(11):1041–9.
5. Aeron S, Saligrama V. Wireless ad hoc networks: strategies and scaling laws for the fixed SNR regime. *IEEE Trans Inf Theory.* 2007;53(6):2044–59.
6. Xie L, Kumar PR. A network information theory for wireless communication: scaling laws and optimal operation. *IEEE Trans Inf Theory.* 2004;50:748–67.
7. Franceschetti M, Migliore M, Minero P. The capacity of wireless networks: information-theoretic and physical limits. *IEEE Trans Inf Theory* 2005;55(8):1212–26.
8. Weber S, Yang X, et al. Transmission capacity of wireless ad hoc networks with outage constraints. *IEEE Trans Inf Theory.* 2005;51(12):4091–102.
9. Weber S, Andrews JG, Jindal N. The effect of fading, channel inversion, and threshold scheduling on ad hoc networks. *IEEE Trans Inf Theory.* 2007;53(11):4127–49.

10. Hasan A, Andrews JG. The guard zone in wireless ad hoc networks. *IEEE Trans Wireless Commun.* 2007;6(3):897–906.
11. Hunter A, Andrews JG, Weber S. The transmission capacity of ad hoc networks with spatial diversity. *IEEE Trans Wireless Commun.* 2008;7(12):5058–71.
12. Weber S, Andrews JG, et al. Transmission capacity of wireless ad hoc networks with successive interference cancellation. *IEEE Trans Inf Theory.* 2007;53(8):2799–814.
13. Rappaport TS. *Wireless communications principles and practice.* 4th ed. Upper Saddle River: Prentice-Hall; 2008.

Chapter 137

A Rapid Payload-Based Approach for Social Network Traffic Identification

Yanping Li and Yabin Xu

Abstract With the fast development of social network, social network traffic is witnessing a significant increase, which makes it hard for the common net management software and traffic identification device to identify and manage social network traffic. In this paper, three dominant social network traffics were taken as research objects; and an effective approach to identifying social network traffics was proposed by deeply analyzing the payload characteristics. Furthermore, MapReduce was used to accelerate the identification. The experimental results showed this approach could provide rapid and accurate identification of social approach traffic.

Keywords Payload characteristics • Social network • Traffic identification • MapReduce

137.1 Introduction

A social networking service is a platform to build social networks or social relations among people who, for example, share interests, activities, backgrounds, or real-life connections. According to a report of China Internet Network Information Center (CNNIC), social network applications in China are increasing rapidly. By the end of June 2013, China microblog users had exceeded 331 million, increasing by 22.16 million since the end of 2012, while the proportion of microblog users in netizens had reached 56.0 %, increasing by 1.3 % [1]. To sum up, the emerging trend in social network has brought the soar of social network traffic.

Currently, traditional network management software and traffic identification device are unable to identify various kinds of social network traffic. However, it is necessary for network operation and maintenance departments to know almost everything about network traffic to avoid congestion and allocate bandwidth effectively as well as support in-depth analysis of the social network's influence and

Y. Li (✉) • Y. Xu

Beijing Key Laboratory of Internet Culture and Digital Dissemination Research, School of Computer, Beijing Information Science & Technology University, 100101 Beijing, China
e-mail: liyanning@bistu.edu.cn; lyphynhc@126.com

public opinion. Therefore, researching and analyzing social network traffic play a vital role in network management and public opinion analysis.

Although there are enormous researches about the identification of P2P network traffic, the attention on social network is few. One of them introduces an approach for traffic identification-based machine learning, but it fails to meet the need for traffic real-time identification [2]. Another approach focuses on traffic identification and analysis to social network sites at the expense of causing serious delay in data transmission [3]. Overall, the effective approach for rapid identification of social network traffic is still lacking.

137.2 The Basic Idea

With TCP/IP network architecture, different applications rely on different application layer protocols, which have unique datagram characteristics. These characteristics are actually some specific strings or bit sequences. The payload-based identification approach focuses on finding these specific sequences, which serve the clue to classifying different social network traffics. For example, this kind of approach can be used to distinguish the network traffic generated from Tencent QQ, Renren, and Sina Weibo by matching the respective characteristic strings in network data.

However, the above approach would lead to a large delay, which is not able to meet the need of real-time online identification. Meanwhile, with the fast development of cloud computing and cloud storage, it is completely possible to use cloud platform to speed up the identification of social network traffic. Thus, in this paper, Hadoop MapReduce, an open-source cloud computing platform, was used to parallel the above process. As a result, a real-time, rapid identification of social network traffic could be achieved.

137.3 The Identification and Characteristic Extraction of Social Network Traffic

In today's China, Tencent QQ, Renren, and Sina Weibo play the main role in social network application. Thus, in this paper, these three applications were used as examples, whose data packages were captured (by Wireshark) and analyzed.

137.3.1 The Identification of Social Network Traffic Characteristics

By visiting renren.com, relevant data packages could be parsed by Wireshark, and the information in them could be obtained manually. It was found that the sequence $0 \times 72 0 \times 65 0 \times 6e 0 \times 72 0 \times 65 0 \times 6e 0 \times 2e 0 \times 63 0 \times 6f 0 \times 6d$ always appeared in the packages which began with $0 \times 48 0 \times 54 0 \times 54$ or $0 \times 47 0 \times 45 0 \times 54$. Thus these characteristics could be used to identify social network traffic from Renren.

Sina Weibo is another widely used social network site. The data packages from it contained the sequence $0 \times 77 0 \times 65 0 \times 69 0 \times 62 0 \times 6f 0 \times 03 0 \times 63 0 \times 6f 0 \times 6d$, and their headers were $0 \times 21 0 \times f0, 0 \times 00 0 \times 00$, which were clues to identify social network traffic from Sina Weibo.

Tencent QQ is a very popular social network application. It has its own protocol—OICQ [4]. The analysis for it showed the data part of packages started with 0×02 or 0×07 and ended with 0×03 . In all those datagrams which were not encrypted, the data part of their IP datagrams always started with 0×07 . The data packages from it contained the sequence $0 \times 71 0 \times 71 0 \times 03 0 \times 63 0 \times 6f 0 \times 6d$. Thus these characteristics could be used to identify social network traffic from Tencent QQ.

137.3.2 The Extraction of Social Network Traffic Characteristics

The feature library is an important part to traffic identification, as it provides the characteristic string to identify traffic [5]. The feature library would also do necessary changes with the update of social network applications. Table 137.1 shows the characteristic strings for Renren, Sina Weibo, and Tencent QQ [6] (the comma in Table 137.1 is used to split different characteristic strings).

137.4 The Identification of Social Network Traffic

137.4.1 The Basic Approach of Payload Characteristic Matching

Characteristic string matching algorithms play a vital role in the payload characteristic identification approach. In order to guarantee the accuracy and efficiency of traffic identification, exact string matching algorithms are widely used in payload-based approaches. Exact string matching algorithms could be categorized as

Table 137.1 Feature library

Type	Renren	Sina Weibo	Tencent QQ
Characteristic strings	0 × 72 0 × 65 0 × 6e	0 × 77 0 × 65 0 × 69 0 × 62 0 × 6f 0 × 03 0 × 63 0 × 6f 0 × 6d,	0 × 71 0 × 71 0 × 03 0 × 63 0 × 6f 0 × 6d,
	0 × 72 0 × 65 0 × 6e	0 × 21 0 × f0,	0 × 02, 0 × 07
	0 × 2e 0 × 63 0 × 6f	0 × 00 0 × 00	0 × 03
	0 × 6d,		
	0 × 48 0 × 54 0 × 54,		
	0 × 47 0 × 45 0 × 54		

single-pattern matching algorithms and multiple-pattern matching algorithms according to different matching approaches. Algorithms which match a single pattern once are called single-pattern matching algorithms, while others that match multiple patterns at the same time are called multiple-pattern matching algorithms. Typical single-pattern matching algorithms include KMP, BM (Boyer-Moore), and so on. Typical multiple-pattern matching algorithms include AC (Aho-Corasick) and WM (Wu-Manber) [7].

During the process of matching pattern strings, targeted strings are hardly related to each other, which means it is easy to parallel multiple-pattern matching algorithms with Hadoop MapReduce. The AC string pattern algorithm is a kind of dictionary-matching algorithm that locates elements of a finite set of strings (the “dictionary”) within an input text. The complexity of it is $O(m + n)$ (m and n are the lengths of the patterns and searched text). By contrast the WM algorithm has lower complexity— $O(Bn/m)$ ($B \leq m$)—as it applies the bad-character rule and has less memory consumption. Thus, in this paper, the combination of WM algorithm and Hadoop MapReduce was chosen to identify the payload characteristics.

137.4.2 Data Structure

The core concept of WM algorithm relies on three tables: a SHIFT table, a HASH table, and a PREFIX table [8]. The relationship of the three tables is shown in Fig. 137.1. (We assume there are three patterns. They are “abcde,” “bcade,” and “adcbbe.” “hash ()” means the hash process.)

The SHIFT table is similar to the regular shift table in the Boyer-Moore-type algorithm, which is comprised of the first m characters of each pattern (m is the

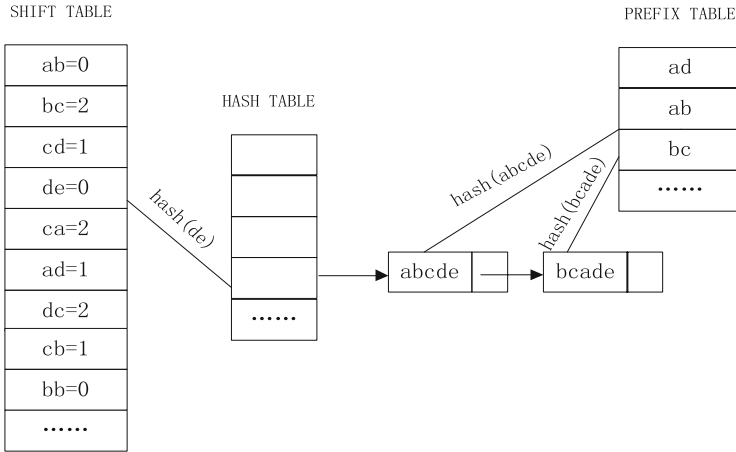


Fig. 137.1 The relationship of the three tables

length of the shortest pattern). We consider the characters in blocks of size B , and we assume B as 2 in this paper. Each string of size B is mapped to an integer used as index to the SHIFT table. Let $X = x_1 \dots x_B$ be the B characters in the text we are scanning, and assume X is mapped into the i th entry of the SHIFT table. Then, if X does not appear as a substring in any pattern, we store in $\text{SHIFT}[i]$ the number of $m - B + 1$; if X appears in some patterns and X ends at position q in pattern P_j and X does not end at any position greater than q in any other pattern, we store $m - q$ in $\text{SHIFT}[i]$.

The HASH table stores the map between block B and patterns. Only blocks whose responding value in the SHIFT table is 0 are stored in the HASH table. $\text{HASH}[i]$, the i th entry of the HASH table, contains a pointer of a list of patterns whose last B characters hash into i , and the value of $\text{SHIFT}[i]$ is 0.

The PREFIX table stores the first B characters of all patterns, in which B could be 2 or 3. Then we find a SHIFT value of 0, and we go to the HASH table to determine if there is a match. The HASH table contains not only the list of all patterns with certain suffixes but also their prefixes. In this way, it makes it efficient to filter patterns whose suffix is the same but whose prefix is different.

137.4.3 The Algorithm of Payload Characteristic Matching

The workflow of the WM algorithm is shown in Fig. 137.2.

1. Compute a hash value h based on the current B characters from the text.
2. Check the value of $\text{SHIFT}[h]$: if $\text{SHIFT}[h] > 0$, shift $\text{SHIFT}[h]$ bits and go to 1; otherwise, go to 3.

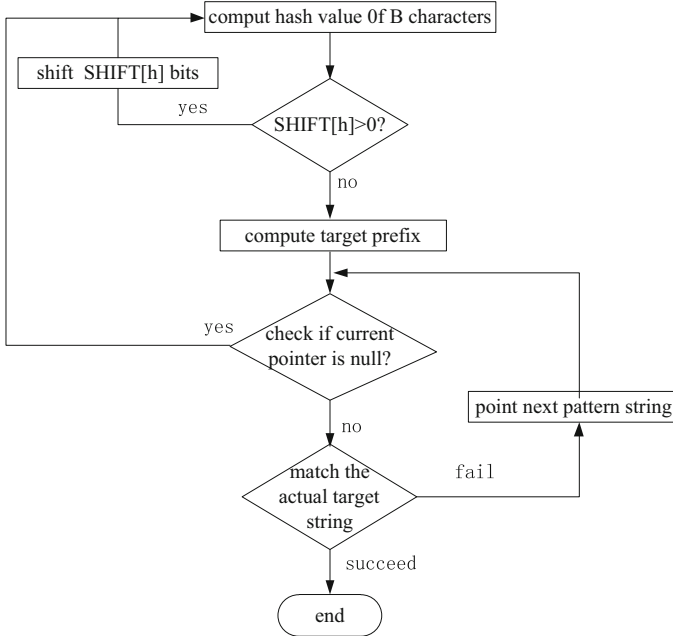


Fig. 137.2 Workflow of the WM algorithm

3. Compute the hash value of the prefix of the text, which could be called target prefix.
4. For each pattern string p ($HASH[h] < p < HASH[h + 1]$), check if $PREFIX[p] =$ target prefix.
5. If they are equal, match the actual patterns against the text 1 by 1 until the matched pattern is found; otherwise, go to 1 and start processing the next B characters.

137.5 The Identification of Social Network Traffic Based on MapReduce

An iteration of WM algorithm maps a MapReduce computing process. In this process, the dataset contained n data object that would be divided into p pieces of data fragments (the size of every piece of data fragment is n/p) and assigned to p map process. Finally, the overall results would be generated by reduce process.

Figure 137.3 shows the basic idea of using MapReduce to identify social network traffic.

The working process of the above model is as follows: When traffic data is put into cloud computing platform, the system puts it into cache and divides it into data fragments. Then, the JobTracker, the job assignment server in Hadoop cluster,

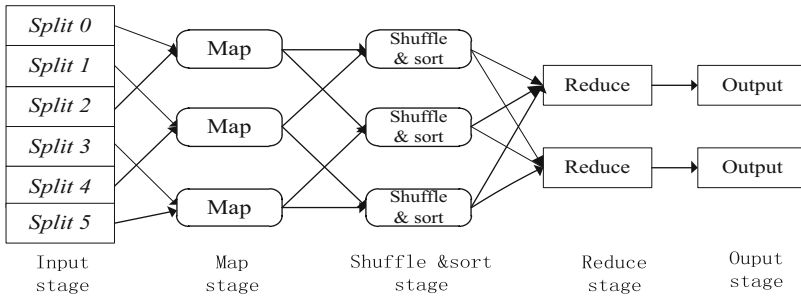


Fig. 137.3 The model of traffic identification based on MapReduce

assigns data fragments to TaskTrackers. The TaskTrackers would do the map process at first. In the map process, WM algorithm is used to do pattern string matching. In the MapReduce process, all data is kept in $\langle \text{key}, \text{value} \rangle$ form. Traffic data is transferred into the form of $\langle \text{number}, \text{packet} \rangle$ as input of every map process. Then each map process uses WM algorithm to match pattern strings, each successful match maps an output line, which is also displayed in the form of $\langle \text{number}, \text{type-package} \rangle$ (type means which kind of network traffic the package belongs).

The output data of the map process is actually the input data of the reduce process. The reduce process would classify the packages by types. The output of reduce process is a list of sorted $\langle \text{key}, \text{value-list} \rangle$, in which key means the number of the specific type of value-list and value-list means all the packages belonging to this type of network traffic. In this way, the number of different types of social network packages could be counted.

137.6 The Experimental Conditions and Analysis of the Results

137.6.1 The Experimental Conditions

In this paper, the experimental platform was Hadoop V0.20.2, an open-source cloud computing platform. In the experiment, 11 nodes were used in which 1 node was used as NameNode and JobTracker, while the remaining 10 nodes were used as DataNode and TaskTracker. Each node was equipped with a 2.6 GHz*2 CPU, 16 GB memory, 80 GB hard drive, and an onboard dual gigabit network controller. Figure 137.4 shows the structure of this experimental platform.

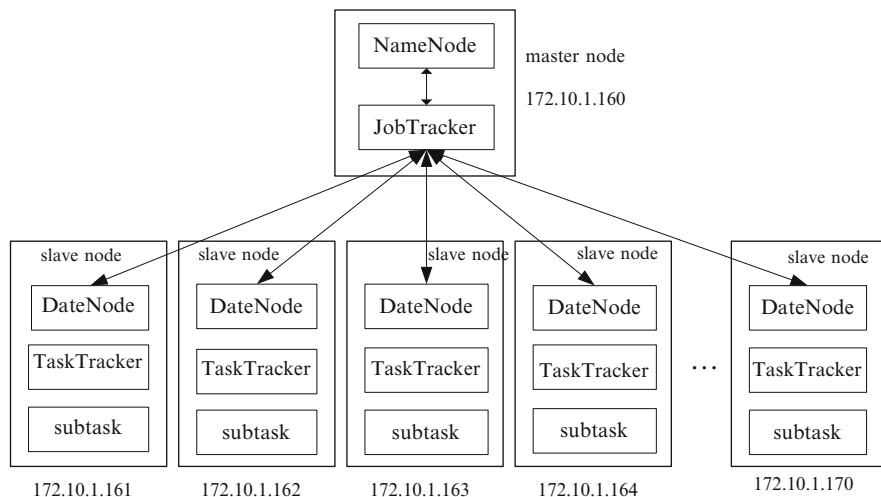


Fig. 137.4 The structure of experimental platform

137.6.2 The Experimental Data

In this paper, the dataset required for the experiment was 4.03 GB, with 15 data blocks and a total of 6,054,443 packets. It consists of two parts. The first part was collected from Beijing Information Science and Technology University campus network at 15:00 on September 5, 2013. The size of the data collected was 3.2 GB, which was divided into 10 blocks with a total of 4,532,685 packets; the second part was from Datatang, which was a dataset of online social networks (WOSN 2008). The dataset was 0.83 GB, which was divided into 5 blocks, with a total of 1,521,758 packets.

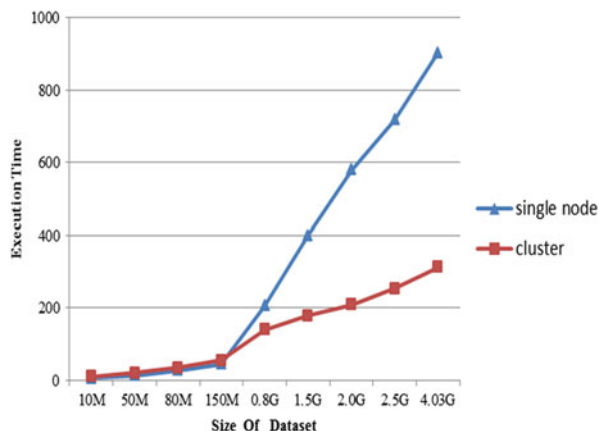
137.6.3 Analysis of the Experimental Results

This experiment showed the comparison of results in single node and cluster by giving the execution time, recognition accuracy, and traffic proportion, respectively. The method given in this paper can be used to identify any kinds of data traffic. But in this paper, only three kinds of social network traffic were extracted and studied.

137.6.3.1 Time Efficiency Experiment

In this experiment, the execution times in single node and cluster were measured under different amounts of data. According to the result, compared with single

Fig. 137.5 The comparison of execution time under different sizes of dataset



node, cluster showed lower execution time and higher identification accuracy. Figure 137.5 shows the comparison of execution time in cluster with 10 DataNodes and single node under different sizes of dataset.

The datasets with sizes of 10M, 50M, 80M, 150M, 0.8G, 1.5G, 2.0G, 2.5G, and 4.03G were selected in the above experiments. Figure 137.5 shows the execution times for a single node were 16, 32, 48, 55, 221, 423, 575, 724, and 913 s, respectively, and the execution times required for the cluster were 24, 43, 54, 60, 139, 179, 208, 256, and 303 s, respectively. According to the result, compared with single node, cluster could execute the matching process more efficiently.

Figure 137.5 shows that when the size of dataset was about 100M, the execution times on single node and cluster were nearly the same. When the size of the dataset was relatively small, single node actually appeared to be more efficient. By contrast, the bigger the dataset was, the more efficient the cluster was compared with single node. The reason for that was when processing data on cluster, the system would take time to divide the dataset and distribute data fragments, which would not change during the increase of the dataset. Thus, when the dataset was getting bigger, cluster had more obvious advantage compared with single node in processing tasks.

137.6.3.2 The Accuracy and the Proportion of Network Traffic

The recognition accuracy and the proportions of different social network traffics were also obtained in this experiment. The results of the experiment showed that the recognition accuracy was up to 92.4 % in both different environments, which demonstrated that the effectiveness of the algorithm was the same in different environments. However when it came to encrypted traffic, the method of payload characteristic identification was not valid enough. Moreover, each kind of network traffic usually includes more than one characteristic string. Thus it would likely misjudge when identifying encrypted traffic.

Fig. 137.6 The proportions of three network traffics in different methods (% of 6,054,443 packets)

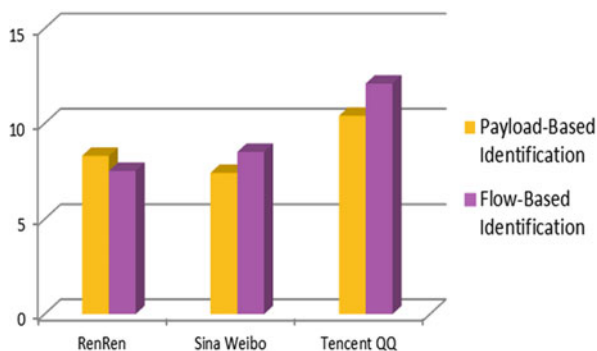


Figure 137.6 shows the result of the second experiment.

The result in Fig. 137.6 shows the proportions of social network traffic from Renren, Sina Weibo, and Tencent QQ in the campus network. Although the result is not typical enough, it reveals the popularity of the different types of social network applications among users.

Conclusion

This paper describes the analysis and extraction of payload characteristic strings in network traffic from Renren, Sina Weibo, and Tencent QQ. WM algorithm was used as the basic algorithm for social network traffic identification, and the open-source cloud computing platform Hadoop MapReduce served as the parallel platform to accelerate the identification. The result showed that the payload-based method could identify social network traffic with high accuracy, but also revealed its drawback of failing to identify encrypted traffic. In the next step, the combination of payload-based approach and flow characteristics approach will be used to identify social network traffic.

Acknowledgments This work is supported by the Foundation of Beijing Educational Committee (No. KM201211232012), Project of Construction of Innovative Teams and Teacher Career Development for Universities and Colleges Under Beijing Municipality (IDHT20130519), and Key Laboratory of Internet Culture and Digital Dissemination Research (ICDD201309).

References

1. CNNIC. China internet development statistics report [R]. The 32nd China internet development statistics report; 2013.
2. Callado A, Kelner J, Sadok D, et al. Better network traffic identification through the independent combination of techniques. *J Netw Comput Appl.* 2010;33(4):433–46.

3. Mislove A, Marcon M, Gummadi KP, et al. Measurement and analysis of online social networks [C]. In: Proceedings of the 7th ACM SIGCOMM conference on internet measurement. New York: ACM Press; 2007. p. 29–42.
4. Jiao XJ, Zhong C, et al. Identifying the P2P flow based on traffic and payload characteristics. *Comput Eng Sci*. 2010;32(8):25–7.
5. Lu G, Zhang HL, Ye L. P2P traffic identification. *J Softw*. 2011;22(6):1281–98.
6. Liu XB, Yang JH, Xie G, et al. Automated mining of packet signatures for traffic identification at application layer with a priori algorithm. *J Commun*. 2009;29(12):51–9.
7. Li WN, E YP, Ge JG. Multi-pattern matching algorithms and hardware based implementation. *J Softw*. 2006;17(12):2403–15.
8. Liu WG, Hu YG. An improved multipattern matching algorithm based on WM algorithm. *J Cent South Univ Sci Technol*. 2011;42(12):3765–71.

Chapter 138

Performance Prediction of WSNs' Mobile Nodes Based on GM-Markov Method

Xiaohui Cheng, Jinzhou He, and Qiliang Liang

Abstract In a variety of applications in wireless sensor networks, sensor nodes generally consist of stationary nodes and mobile nodes; the irregularity in the process of moving has led to the characteristics of nonlinearity and stochastic volatility in the performance change of mobile nodes, which thus easily impairs the performance index of data transmission between sensor nodes and thereby affects the performance of the entire network. In order to solve this problem, firstly, the objective weight decision model is adopted to calculate the comprehensive performance values of mobile nodes; then the grey GM(1,1) model is adopted to predict the comprehensive performance values of mobile terminal nodes, and finally, through the combination of the grey GM(1,1) model and Markov state transition matrix, the prediction is implemented again. In order to obtain the data samples of network performance index, the node mobility experimental verification scheme based on OPNET has been designed with the comparative analysis showing that the GM-Markov method can predict the performance of mobile nodes accurately under the condition of a small sample and poor information.

Keywords Wireless sensor network • Mobile node • Performance prediction • Grey theory • Markov chain

138.1 Introduction

The performance of mobile nodes of wireless sensor networks (WSNs) highlights the characteristics of nonlinearity and stochastic volatility, which will cause some unknown effects on the application service of the entire network. As to this problem, it is very important for network management and planning to make predictions scientifically and reasonably of the performance change of the mobile nodes at some point in the future.

The current prediction methods that have been widely used include: the support vector regression prediction [1], the time-series analysis prediction [2], the variable

X. Cheng (✉) • J. He • Q. Liang
College of Information Science and Engineering, Guilin University of Technology,
Guilin 541000, China
e-mail: Aaron_HJZ@126.com

weight combination prediction [3], the neural network and Markov prediction [4], etc. Some models require a large number of data samples, some require a certain statistical regularity among data, and some are too computationally intensive with insufficient information and less intuitive results.

In this paper, the network performance comprehensive value calculation method is adapted to obtain the network performance comprehensive values of mobile nodes at different moments [5, 6]. Because of the characteristic that many information cannot be determined in the mobile node performance prediction of WSN, the grey GM(1,1) model is adopted to predict the comprehensive performance values of mobile terminal nodes and combined with Markov state transition matrix, and then the GM-Markov prediction method is further adopted for prediction again. The analysis shows that the error of the prediction model established by the GM-Markov method is smaller and the data of mobile node performance is accurate, which thus proves the model is correct and the applicability of the GM-Markov model in the short-term prediction of mobile nodes.

138.2 Network Performance Prediction Theory of Mobile Nodes

138.2.1 The Grey Prediction Theory

The main principle of the grey system theory is to obtain valuable information from the current small amount of known information, and then to predict new information. The performance of mobile nodes is consistent with such a rule that it is practical to use the grey GM(1,1) model to discover the inherent regularity from the disorganized data and predict the performance change at some point in the future [7].

The GM(1,1) model is a single sequence of first-order linear dynamic model, which is conducting an accumulation processing to the original data and using differential equations to implement an approximate fitting.

The grey prediction model of $x^{(1)}$ is:

$$\hat{x}^{(1)}(k+1) = \left(x^{(0)}(1) - \frac{b}{a}\right)e^{-ak} + \frac{b}{a} \quad (k = 1, 2, \dots, n-1) \quad (138.1)$$

The grey prediction model of $x^{(0)}$ is:

$$\hat{x}^{(0)}(k+1) = \hat{x}^{(1)}(k+1) - \hat{x}^{(1)}(k) \quad (k = 1, 2, \dots, n-1) \quad (138.2)$$

138.2.2 Markov Prediction Theory

Those stochastic processes feature no aftereffects and have discrete time and states [8]. The Markov chain method is usually adopted for modeling; but the performance of WSN mobile nodes has exactly this non-aftereffect.

Markov basic equation:

$$a_i(t + 1) = \sum_{j=1}^r a_j(t)p_{ij} \tag{138.3}$$

Introduction of the state probability vector and the state probability transition matrix:

$$a(t) = [a_1(t), a_2(t), \dots, a_r(t)]$$

$$P = \begin{bmatrix} p_{11} & p_{12} & \dots & p_{1r} \\ p_{21} & p_{22} & \dots & p_{2r} \\ \dots & \dots & \dots & \dots \\ p_{r1} & p_{r2} & \dots & p_{rr} \end{bmatrix}$$

Thus the Markov chain basic equation can be written as:

$$a(t) = a(t - 1)P \tag{138.4}$$

138.3 GM-Markov Prediction Model

At the moment of making predictions of the performance of WSNs' mobile nodes, as to the advantage of GM-Markov, the rambling performance data of a few current known WSNs' mobile nodes can be fitted through the grey prediction method, and the inherent regularity can be found, which may compensate the requirements of non-aftereffect and stationary process of the Markov prediction method. Meanwhile, the Markov prediction method compensates the prediction accuracy of random volatile data sequence of the grey prediction method. The steps for establishing the GM-Markov prediction model are shown as below:

- Step 1: Do 1-AGO generation for the raw performance data of mobile nodes.
- Step 2: Use the least square fitting to determine the data matrix B, Y .
- Step 3: Obtain the development coefficient $-a$ of the model and grey action b .
- Step 4: Establish the grey GM(1,1) model and calculate the residual.
- Step 5: Divide the transition state interval, and determine the state interval of the original data at each time to determine the state value according to the relative error value.
- Step 6: Calculate the state transition matrix.
- Step 7: Calculate the final performance prediction value.

Step 8: Test the precision. Calculate the residual, relative error, a posteriori error ratio, and small error probability so as to test the precision according to the prediction precision inspection level table.

138.4 Network Performance Prediction and Result Analysis of Mobile Nodes

According to the principle of selection of the performance evaluation indicators, three measurement indicators are selected: delay, throughput, and data dropped. By means of the Opnet simulation software, the influencing factors of dynamic nodes are simulated in the network by changing the node trajectory in the simulation experiment. The mobile node path is set as a hexagonal route, and the simulation time is set to 25 min. The original network performance comprehensive values of mobile nodes could be obtained by the method [5, 6], as shown in Fig. 138.1.

138.4.1 Performance Prediction of Mobile Nodes

1. The GM(1,1) prediction model of the mobile nodes' network performance.

From 540 to 885 s, the performance samples are selected after the network achieved stability, from which 24 samples are selected as the raw data for GM(1,1) modeling, and the network performance of mobile terminal nodes from 900 to 1,005 s are predicted. Here sampling the prediction sample values every 15 s from 900 to 1,005 s, 8 time points are selected. According to the GM(1,1)

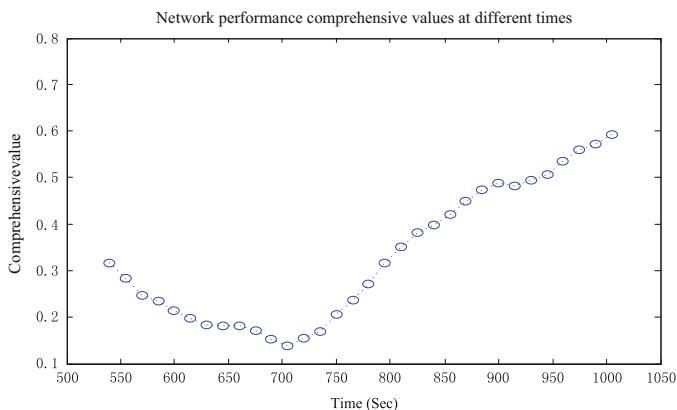


Fig. 138.1 Original network performance comprehensive values of mobile nodes

model, conduct an accumulation to the original data $X^{(0)}$ to obtain the sequence $X^{(1)}$ with the equation of prediction model as:

$$\hat{x}(k + 1) = 2.5682e^{0.0512k} - 2.252 \tag{138.5}$$

2. The division of transition state interval of the network performance value.

Assuming that the initial vector is v_0 at some point, then the state vector becomes $v_0 p^{(k)}$ after k step transition; supposing that the performance value of a mobile node which is about to predict is in the state of E_i , and it is in line i after transition, if $\max(p_{ij}) = p_{ik}$, then consider the network performance values of mobile nodes' transfer from the \otimes_i state to the \otimes_k state the next moment.

According to raw data of network performance from 540 to 885 s, the transition state interval is divided into six states:

$$\begin{aligned} \otimes_1 &= (-0.65, -0.45], & \otimes_2 &= (-0.45, -0.25] \\ \otimes_3 &= (-0.25, -0.05], & \otimes_4 &= (-0.05, 0.15] \\ \otimes_5 &= (0.15, 0.35], & \otimes_6 &= (0.35, 0.55] \end{aligned}$$

The state transition matrix P is:

$$P = \begin{bmatrix} 2/3 & 1/3 & 0 & 0 & 0 & 0 \\ 1/2 & 0 & 1/2 & 0 & 0 & 0 \\ 0 & 1/5 & 2/5 & 2/5 & 0 & 0 \\ 0 & 0 & 1/4 & 5/8 & 0 & 1/8 \\ 0 & 0 & 0 & 1/2 & 1/2 & 0 \\ 0 & 0 & 0 & 0 & 1/3 & 2/3 \end{bmatrix}$$

From the table we can see that the network performance integrated value of the 885th second is in state 4 with the initial vector $v_0 = (0 \ 0 \ 0 \ 1 \ 0 \ 0)$, then predict the network performance value of the next sampling point—the 900th second.

3. Calculation of the GM-Markov model prediction value.

According to the initial matrix and state transition matrix, the state of the next sampling point can be calculated, which is a matrix consisting of probabilities of each state and denoting that the matrix of the 900th second is $P(1)$:

$$P(1) = v_0 * P = \left[0 \ 0 \ \frac{1}{4} \ \frac{5}{8} \ 0 \ \frac{1}{8} \right] \tag{138.6}$$

When calculating the final prediction value, two states that have the highest probabilities are selected, while the median in each state prediction interval is taken as the final prediction value.

The state is 4 in the 900th second; the calculation method of the prediction interval is:

$$x^{(0)}(25) = \frac{\hat{x}^{(0)}(25)}{1 - \Delta(25)} \tag{138.7}$$

The relative residual value $\Delta(k)$ is the value of state 4, which is corresponding to $(-0.05, 0.15]$, so $x^{(0)}(25) \in (0.4177, 0.516)$; the same is true of other states, and finally calculate the network performance prediction of the 900th second as 0.49. The real value of 900th second of the network simulation experiment is 0.4873, which is within the prediction interval; thus the GM-Markov prediction model of mobile terminal nodes of network performance has certain feasibility.

After the prediction of network performance in the 900th second, the network performance of the 915th second is predicted by means of $v_0 * P^2$, and the prediction value obtained is 0.448. Similarly, the final prediction value of each sampling point can be calculated.

The results of the two prediction methods are shown in Fig. 138.2.

138.4.2 Model Precision Testing and Comparative Analysis

1. Precision testing and analysis of the Grey GM(1,1) model.

From Tables 138.1 and 138.2, among these 8 sampling points, the relative error precision level is 1 “good,” 5 “qualified,” 1 “barely qualified,” and 1 “unqualified.” A few sampling points’ prediction grades are not qualified, and the average relative error is 0.037; therefore, it is necessary to improve the precision level.

2. Precision testing and analysis of the GM-Markov model.

When the GM-Markov model is used, among these 8 sampling points, the relative error precision level is: 3 “good,” 4 “qualified,” 1 “barely qualified,” and

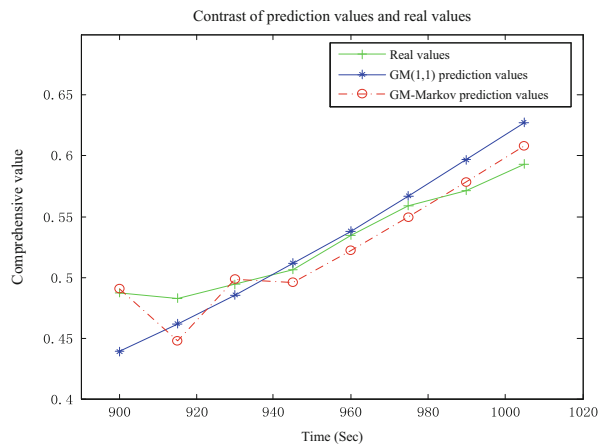


Fig. 138.2 Contrast of prediction values and real values of two prediction models

Table 138.1 Error comparison of the future eight moments

GM relative error	GM average relative error	GM-Markov relative error	GM-Markov average relative error
0.1001	0.037	0.008	0.023
0.043		0.072	
0.017		0.008	
0.009		0.021	
0.007		0.023	
0.014		0.016	
0.043		0.0098	
0.058		0.026	

Table 138.2 Judgment standard of prediction precision authentication level

Precision level	Relative error q	Standard deviation ratio C	Small error probability P
Good	$q < 0.01$	$C < 0.35$	$P > 0.95$
Qualified	$q < 0.05$	$0.35 \leq C < 0.5$	$0.8 < P \leq 0.95$
Barely qualified	$q < 0.1$	$0.5 \leq C < 0.65$	$0.7 < P \leq 0.8$
Unqualified	$q > 0.1$	$0.65 \leq C < 0.8$	$0.6 < P \leq 0.7$

0 “unqualified.” The overall average error is 0.023. While compared with the average relative error of the GM(1,1) model, the error rate is reduced by 38 %.

It can be seen from Table 138.2 that among the selected 8 sample points, the precision level rate of the GM(1,1) model—good, qualified, barely qualified, and unqualified—is of 12.5 %, 62.5 %, 12.5 %, and 12.5 %, respectively. The GM-Markov model is 37.5, 50, 12.5, and 0 %. It can be seen that the GM-Markov model has increased the “good” level probability of precision three times, and there is no “unqualified” condition. Thus the overall prediction effect has been better than that of the GM(1,1) model.

Conclusion

This paper has applied the grey GM-Markov prediction model to the prediction of network performance of mobile nodes. On the basis of analyzing factors which affect the network performance, the prediction model is established and compared with the grey GM(1,1) prediction model. The results show that the error is smaller based on the grey GM-Markov prediction model and the network performance data is more accurate. Meanwhile, the applicability of the grey GM-Markov prediction model in predicting short-term network performance is verified. In practical applications, this method can be used to predict the performance of the whole network or a network node accurately, which enables a more scientific management and planning of a network and provides a basis for scientific prediction of network performance of WSNs in a complex environment.

Acknowledgments As the research of the thesis is sponsored by the National Natural Science Foundation of China (No: 61262075) and major scientific research project of Guangxi higher education (No: 201201ZD012), we would like to extend our sincere gratitude to them.

References

1. Zou CZ. Node data prediction based on SVR in wireless sensor network. *J Comput Appl.* 2010;30(1):127–30 (In Chinese).
2. Shao XQ, Ma XM. Modeling and simulation of chaotic time series prediction. *Comput Simul.* 2011;28(5):228–31 (In Chinese).
3. Jiang LY, Wang L, Xi JH. Study on variable weight combined forecasting method of wear trend for aero engine. *Comput Eng Appl.* 2011;47(28):228–31 (In Chinese).
4. Gao R, Tang L. Application research of data prediction in wireless sensor network based on neural network. *Comput Sci.* 2012;39(5):44–7 (In Chinese).
5. Cheng XH, Liang QL, He JQ. Research on objective weight determine method of ZigBee network performance index. *Appl Res Comput.* 2013;30(10):3068–70 (In Chinese).
6. Cheng XH, Liang QL, He JQ. A method for comprehensive evaluation on WSNs performance. *Transducer Microsyst Technol.* 2013;32(8):26–31 (In Chinese).
7. Wei HL, Li XB, Shen Y, Zhang H. The research on dynamic power management of wireless sensor networks based on grey model. *Chin J Sens Actuators.* 2011;24(1):140–4 (In Chinese).
8. Shi Z, Zhu Q. Performance analysis and optimization based on Markov process for heterogeneous wireless networks. *J Electron Inf Technol.* 2012;34(9):2224–8 (In Chinese).

Chapter 139

Virtual Network Mapping Algorithm Based on Bi-level Programming Research

Mingchun Zheng, Xinxin Ren, Xiao Li, Panpan Zhang, and Xuan Liu

Abstract The network virtualization is considered as a feasible way to solve the problem of Internet ossification, and the construction of a virtual network is the key problem in the network virtualization technology. In this chapter, the construction of a virtual network is to solve the network optimization design problem, which means that virtual network providers decide to choose nodes and links of the substrate network according to the needs of users and their optimization goal to extend a virtual network. This network design will be represented as a bi-level programming model: the upper is a virtual network system optimization model and the lower is Wardrop user equilibrium model which is satisfied with user's selfish behavior. Bi-level programming model integrates the virtual node mapping and the link mapping to a unified progress, and ultimately to reach the global optimum system. Simulation results show that this model obtains better virtual request acceptance rate and network revenue.

Keywords Network virtualization • Bi-level programming • Wardrop user equilibrium

139.1 Introduction

The core idea of the network virtualization [1] is using virtual technology to divide the existing network service providers into two separate roles [2]: the infrastructure provider (InP) and the service provider (SP). InPs deploy and manage the resources of substrate network (SN), operate and maintain substrate infrastructure. SPs lease resources from one or more InPs to establish a virtual network (VN) and customize protocols. SPs provide end-to-end service for VN users by the implementation of a programming for the distribution network resources. The virtual network mapping problem (VNMP) [3, 4], as the key technology to realize the network virtualization, is a progress that maps the VN with virtual nodes and virtual links to SN. The virtual nodes are mapped to physical nodes of the SN while the virtual links are

M. Zheng (✉) • X. Ren • X. Li • P. Zhang • X. Liu
College of Management Science and Engineering, Shandong Normal University,
Shandong 250014, China
e-mail: lightday_1988@163.com

mapped to physical links of the SN in accordance with the constraints of resource requirements.

The static resource allocation algorithm which is simple has less deployment expenses, but it is limited to a special circumstance; therefore, there is no superiority for ensuring resource equilibrium between virtual networks in the static resource allocation algorithm [5–7].

The dynamic resource allocation algorithm [8–10] requires the networks to reassign the mapped resources based on the load of nodes and links in order to optimize the usage of resources of the substrate network. The periodic remapping mechanism [11] can keep all requests of virtual network at an optimal state all the time; however, it will lead to excessive remapping of virtual nodes and links and increase the overhead of network as well.

The existing VN mapping algorithms start from the perspective of the SN so as to maximize the benefits of the SN which allocates physical resources correspondingly according to the requests of virtual network resources. In the life cycle of the VN, the resource allocation does not change. These resource allocation algorithms for SPs lack adaptability, especially as to dynamically changing of the resource requirements of the VN. The virtual network may reapply to the SN resource only after expiry of the current allocation of resources. This not only reduces the income of the SN, but effectively guarantees the QoS of VN [12].

This chapter considers the selection problem of SN resource from the perspective of the VN, and takes the virtual network as a leader in the mapping problem. Research on resource allocation problem under a network virtualization environment is based on the bi-level programming. By studying the network virtualization architecture, the Wardrop equilibrium model in transportation network is applied to the communication network. Thereby we get the flow distribution methods in virtual network.

139.2 Related Work

139.2.1 *Bi-level Programming Model*

As the huge system of decision-making problems has to consider a variety of influence factors, and their decision objectives involve the profits of various roles, these goals and profits in many cases are connected with each other with mutual conflict; therefore it is necessary to adopt a bi-level decision method. The bi-level programming considers the decision objectives of the two decision-making levels and the interaction between decision objectives of two decision-making levels synthetically. The model is shown in the following formula:

The upper-level model:

$$\min_x Z(x, y)$$

subject to

$$G(x, y) \leq 0 \text{ (constrain of the leader)}$$

where $y = y(x)$ is the solution of the following problem.

The lower-level model:

$$\min z(x, y)$$

subject to

$$g(x, y) \leq 0 \text{ (constrain of the follower)}$$

The superior decision-makers influence the inferior decision-makers by decision variable x , and interact with the inferior decision-makers; the lower-level decision variable y is a function of the decision variable x , i.e., $y = y(x)$. This function is generally called the reflection function.

139.2.2 Evaluation Index

The main objective of virtual network mapping is to make full use of limited resources of substrate network, provide service for more virtual network requests, thus improving the operating revenue of substrate network. We will firstly define the revenue function and cost of virtual network mapping, and then give a formal description of the evaluation index.

At time t , the revenue that the substrate network accepts a virtual network can be defined as below:

$$R(G_v, t) = \alpha \sum_{n_v \in N_v} P(n_v) + (1 - \alpha) \sum_{l_v \in L_v} B(l_v) \tag{139.1}$$

where $P(n_v)$ is the computing power-required value of virtual node n_v . $B(l_v)$ represents the bandwidth capacity-required value of virtual link l_v . Parameters α and $1 - \alpha$ can be used to adjust relative weight of the computing resources and bandwidth resources. As to the virtual network mapping problem, the revenue generally refers to such a concept that the acceptance of the virtual network requests obtaining the economic benefit for InPs.

At time t , the cost that the substrate network accepts a virtual network can be defined as the total resources which is allocated to the virtual network by substrate network.

$$C(G_v, t) = \alpha \sum_{n_v \in N_v} P(n_v) + (1 - \alpha) \sum_{l_v \in L_v} \sum_{l_s \in L_s} B(f_{l_s}^{l_v}, l_v) \tag{139.2}$$

where $f_{l_s}^{l_v} \in \{0, 1\}$, when substrate links allocate bandwidth resources to virtual links $f_{l_s}^{l_v} = 1$; otherwise, $f_{l_s}^{l_v} = 0$. $B(f_{l_s}^{l_v}, l_v)$ is the value of bandwidth that l_s assigned to l_v . The meaning of parameter α and $1 - \alpha$ is consistent with Eq. (139.1).

The InPs need efficient virtual network mapping algorithm to maximize their operating revenue. The long-time average operating revenue of substrate network can be described as follows:

$$\lim_{T \rightarrow \infty} \frac{\sum_{t=0}^T R(G_v, t)}{T} \tag{139.3}$$

Under the same condition of substrate resources, an efficient virtual network mapping algorithm should be able to accept more virtual network requests. The acceptance rate of virtual network can be defined as:

$$\lim_{T \rightarrow \infty} \frac{\sum_{t=0}^T V_s}{\sum_{t=0}^T V} \tag{139.4}$$

where $\sum_{t=0}^T V_s$ is the number of virtual networks which is successfully mapped from time $t = 0$ to T . $\sum_{t=0}^T V$ is the total number of virtual network requests from time $t = 0$ to T .

The long-time average revenue-to-cost rate of virtual network can reflect the utilization rate of substrate network to some extent. It can be defined as

$$\lim_{T \rightarrow \infty} \frac{\sum_{t=0}^T R(G_v, t)}{\sum_{t=0}^T C(G_v, t)} \tag{139.5}$$

139.3 Virtual Network Mapping Model Based on Bi-level Programming

The network virtualization has realized the diversity of the Internet architecture. It abstracts and isolates the physical resources of infrastructure composed by multiple virtual networks to provide service for users; therefore, multiple heterogeneous

networks from different service providers are to coexist in network virtualization environments and share physical resources of the substrate network. We can consider the virtual network mapping problem as a leader-follower [13] problem. The substrate network is the leader and the virtual net is the follower. This relationship can be described by bi-level programming model [14], which can analyze two different and contradictory goals in the progress of decision-making simultaneously. The equilibrium point indeed is the optimal solution of the above bi-level programming problem, which is the interaction of two seemingly contradictory requirements. The benefit of using the bi-level programming to solve the problem of virtual network mapping is that the SPs in constructing virtual network take the behavior of users' choice into account. We assume that there is one leader and one follower in this bi-level decision system. Let x and y be the decision vector of the leader and the follower, respectively. We also assume that the objective functions of the leader and follower are $Z(x_a)$ and $z(x_a)$, respectively.

We assume that the leader firstly chooses a control vector x and the follower subsequently determines their control vector y .

The leader can only influence (rather than dictate) the reactions of the follower through their own decision variables. The upper model of bi-level programming describes the decision of SP on costs with its goal maximizing the comprehensive efficiency of the virtual network. We usually use the shortest total travel time or generalize the minimal travel cost to measure this system model. We assume the demand of O-D is fixed; the objective function that the upper-level model should consider is to minimize the total cost:

$$\min Z = \sum_a x_a t_a(x_a) \tag{139.6}$$

where x_a is the resource on the road a and t_a is cost (or impedance) on the road a .

The follower has full authority to decide how to optimize their objective function in view of the decisions of the leader. We select the optimal assignment model of user equilibrium for description

$$\min z = \sum_a \int_0^{x_a} t_a(\omega) d\omega \tag{139.7}$$

subject to

$$\sum_k f_k^{rs} = q_{rs} \quad \forall r, s \tag{139.8}$$

$$f_k^{rs} \geq 0 \quad \forall k, r, s \tag{139.9}$$

$$x_a = \sum_{rs} \sum_k f_k^{rs} \delta_{a,k}^{rs} \quad \forall a \tag{139.10}$$

where f_k^{rs} is the resource of the road k in O-D for $r-s$,
 $\delta_{a,k}^{rs}$ is $\{1, \text{if the road } a \text{ on a path } k \text{ of } r-s; \text{ else } 0\}$,
 q_{rs} is the demand for resources of $r-s$.

Equation (139.8) makes all path resources of each O-D be equal to the demand of corresponding O-D. The relationship between road traffic and link traffic is described as Eq. (139.10).

139.4 Algorithm of Bi-level Programming

Generally speaking, the bi-level programming problem is an NP-hard problem. As there is no polynomial algorithm, it is very complex to solve the bi-level programming problem; and in most cases, we only find local optimal solution rather than global optimal solution. As a result, this chapter uses the bi-level iterative algorithm based on the particle swarm optimization (PSO-BLIA) [15] to solve the model.

Step 1: initialization: initialize the parameters of PSO. Generate initial solution of the lower model randomly (need to satisfy the constraint conditions). Initialize the particles' position X_i and speed V_i randomly, $i \in [1, m]$; m is the population size (the number of particles). Set the i th particle of P_i to the current position of this particle and P_g is set to the optimum particle position of the initial population.

Step 2: as to all particles in particle swarm, perform the following operations:

1. Update position and speed according to Eqs. (139.11) and (139.12).
2. (Solve the lower-level model) Put the position of the particle i (X_i , the solution of the upper-level model) into the lower-level model. Use traditional methods to solve the lower-level model and get the optimal solution y_i^* of this model.
3. Put X_i and y_i^* into the objective function of the upper-level model; and calculate the fitness of particle $F(X_i, y_i^*)$, $i \in [1, m]$.
4. If the fitness of particle i is better than that of P_i , P_i will update for X_i which is the current position of this particle. The lower-level model of the optimal solution yP_i corresponding to P_i is updated to y_i^* .

Step 3: determine whether the convergence criteria are satisfied; if yes, turn to step 5; otherwise, turn to step 4.

Step 4: according to Eq. (139.11) to update P_g , use traditional methods to solve the lower-level model and get the optimal solution yP_g which is corresponding to P_g .

Step 5: output the optimal solution of bi-level programming model P_g and yP_g , and calculate the value of objective function of the upper- and lower-level model. End of the algorithm.

In the progress of each iteration, the entire population of all the particles is updated according to the following two equations [16]:

$$V_i^{k+1} = \omega V_i^k + c_1 r_1 (P_i^k - X_i^k) + c_2 r_2 (P_g^k - X_i^k) \quad (139.11)$$

$$X_i^{k+1} = X_i^k + V_i^{k+1} \quad (139.12)$$

where P_i is the current optimum position that the i th particle finds itself (individual optimal). P_g is the optimal solution of the whole particle swarm that can be found currently. r_1 and r_2 are random numbers between 0 and 1; c_1 and c_2 are called learning factors, usually $c_1 = c_2 = 2$; ω is a weighting coefficient and takes a value between 0.1 and 0.9.

In this algorithm, if a particle finds that the current optimal position is a local optimal point, the particle swarm can't search again within the solution space; thus the algorithm falls into a local optimum. We can increase a random disturbance of P_g to improve the convergence of this algorithm and the global search ability.

η is a random variable that obeys the standard normal distribution, namely $\eta \sim N(0, 1)$, then

$$P_g = P_g \times (1 + \eta) \quad (139.13)$$

139.5 Experimental Analysis

In order to verify the effectiveness of the PSO-BLIA, we implement this algorithm in the Visual Studio 6.0 platform with C++. In this chapter, the main evaluation index of Sect. 2.2 is given to evaluate the performance of the mapping algorithm, and compare it with the mapping algorithm of BACA.

139.5.1 Experiment Settings

The substrate network topology is set for 100 nodes and 500 links. The CPU resources and bandwidth resources of substrate network obey uniform distribution of 50–100. Assume that the arrival process of the virtual network requests obeying the Poisson process with time units of 100 and the intensity of 5. Survival time for each virtual network obeys exponential distribution with the parameter of 400. Request the virtual nodes of each virtual network, shall be subject to the uniform distribution of 2–10, and each pair of virtual nodes be connected by the probability of 0.5. The CPU resources and bandwidth resources of virtual network obey uniform distribution of 0–50.

139.5.2 Simulation Results and Comparisons

Figures 139.1 and 139.2 show the experimental result comparison charts, respectively. The charts include two parts: the acceptance rate of virtual network request and the average revenue of the substrate network.

As can be seen from Fig. 139.1, since the physical resources are rich at beginning, the request rates of PSO-BLIA and BACA are 1.0 basically. With the gradual consumption of resources, PSO-BLIA takes the nodes' load and links' load to balance at the same time as the goal, avoids the resource bottleneck of substrate network, and provides a more balanced substrate network so as to improve the success rate of establishing virtual network; however, the reason why the acceptance rate in the late reduces gradually lies on its easiness of causing the emergence of network resource bottleneck upon removal of the intermediate node resources consumption of BACA. Because the PSO-BLIA and BACA with dynamic arrival and departure of virtual networks request reaching a steady-state process, both the requests of acceptance rates are stable.

Figure 139.2 shows that the average revenue of InPs of PSO-BLIA is higher than that of BACA. We get information from Fig. 139.1 that the requests of acceptance rates of PSO-BLIA are higher than those of BACA. It shows that successful mapping of virtual network requests in the same period is more than that of BACA, which makes the average revenue of InPs of PSO-BLIA higher than that of BACA

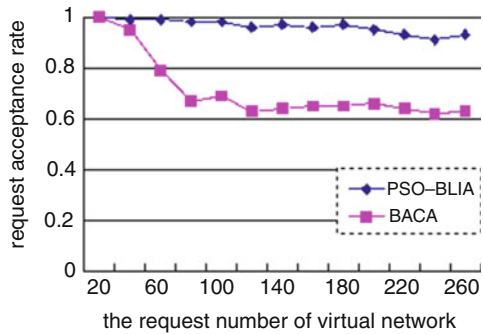


Fig. 139.1 The request acceptance rate of virtual network

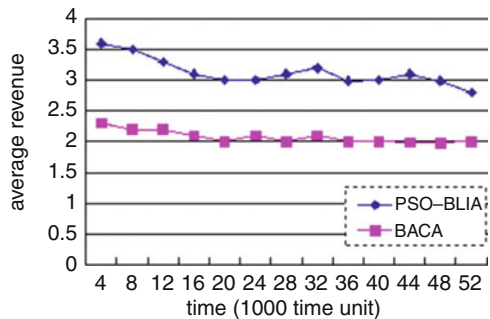


Fig. 139.2 The average revenue of substrate network

Conclusion

In this chapter, as to the problem of allocating on-demand physical resources effectively in the network virtualization environment, we propose a mapping method based on the bi-level programming. Researches have been carried out in terms of the optimization of virtual network structure and mapping algorithm simultaneously while contacting the relationship between nodes and links comprehensively and increasing their correlation. As the upper level optimizes the structure of virtual network through system optimal model, the entire bi-level programming model solves the virtual network mapping problem. This chapter uses the PSO algorithm to solve the bi-level programming with good results achieved.

References

1. Feamster N, Gao L, Rexford J. How to lease the Internet in your spare time. *ACM SIGCOMM Comput Commun Rev.* 2007;37(1):61–4.
2. Chen J, Gao Z. Optimum strategy in railway fares based on bi-level programming model. *J North Jiaotong Univ (Soc Sci Ed).* 2003;2(3):38–41.
3. Chowdhury NMMK, Boutaba R. A survey of network virtualization. *Comput Netw.* 2010;54(5):862–76.
4. Haider A, Potte R, Nakao A. Challenges in resource allocation in network virtualization. In: *Proceedings of the 20th ITC Specialist Seminar.* 2009;18:20.
5. Trinh T, Esaki H, Aswakul C. Quality of service using careful overbooking for optimal virtual network resource allocation. In: *Proceedings of IEEE ECTI Conference, Fort Worth, TX;* 2011. p. 296–9.
6. Muhammad I, Zhuang W. A distributed multi-service resource allocation algorithm in heterogeneous wireless access medium. *IEEE J Sel Areas Commun.* 2012;30(2):425–32.
7. Lischka J, Karl H. A virtual network mapping algorithm based on subgraph isomorphism detection. In: *Proceedings of the 1st ACM SIGCOMM workshop on virtualized infrastructure systems and architectures;* 2009. p. 81–8.
8. Zhu Y, Ammar M. Algorithms for assigning substrate network resources to virtual network components. In: *Proceeding of the IEEE INFOCOM, Barcelona;* 2006. p. 1–12.
9. He J, Zhang SR, Li Y. Davinci: dynamically adaptive virtual networks for a customized internet. In: *Proceedings of the ACM CoNEXT conference, Madrid;* 2008. p. 15.
10. Motiwala M, Elmore M, Feamster N, Wempala S. Path splicing. In: *Proceedings of the ACM SIGCOMM 2008 conference on data communication;* 2008. p. 27–38.
11. Butt NF, Chowdhury M, Boutaba R. Topology-awareness and reoptimization mechanism for virtual network embedding. In: *Proceedings of the 9th IFIP networking conference, Chennai;* 2010. p. 27–39.
12. Jawwad S, Monica B. QoSMap: QoS aware mapping of virtual networks for resiliency and efficiency. In: *Proceedings of the IEEE GLOBECOM workshop, Washington, DC;* 2007. p. 1–6.

13. Wang ZK, Huang T. A hierarchical virtual resource management architecture for network virtualization. In: The 6th international conference on wireless communications networking and mobile computing; 2010. p. 1–4.
14. Gao ZY. Bi-level programming models, approaches and applications in urban transportation network design. *Probl J Transp Syst Eng Inf Technol.* 2004;2:35–6 (in Chinese).
15. Zhao ZG, Gu X, Li TS. Solving the bi-level programming model by particle swarm optimization algorithm. *Syst Eng Theory Pract.* 2007;8:92–8 (in Chinese).
16. Kennedy J, Eberhart RC. Particle swarm optimization. In: Proceedings of the IEEE international conference on neural networks, IV Piscataway, NJ: IEEE Service Center; 1995. p. 1942–8.

Chapter 140

Kalman Filter-Based Bandwidth and Round Trip Time Estimation for Concurrent Multipath Transfer Performance Optimization in SCTP

Wen Li, Wenbo Wang, Xiaojun Jing, and Wen Liu

Abstract Concurrent multipath transfer (CMT) makes use of the multihoming feature of the Stream Control Transmission Protocol (SCTP) to transmit data over multiple end-to-end paths in a multihomed SCTP association. As the disparity of multipath, it is facing a great challenge to solve the disorder of the received data packets. To lighten the reordering degree and then to improve the throughput performance, we need to estimate the real-time paths' bandwidth and Round Trip Time (RTT) as exactly as possible. The Kalman filter can estimate the current system state and predict the future states correctly by iterative method. In this chapter, we utilize the extended vector Kalman filter to estimate the available bandwidth and RTT of each path simultaneously. Furthermore, we propose a predictive data allocation algorithm for CMT in SCTP. The simulation results show that the data allocation algorithm based on the estimations of each path's bandwidth and RTT can improve the system total throughput by lessening the data packet disordering.

Keywords Concurrent multipath transfer • Stream Control Transmission Protocol • Extended vector Kalman filter • Round Trip Time (RTT) • Throughput

W. Li (✉)

School of Information and Communication Engineering, Beijing University of Posts and Telecommunications, 100876 Beijing, China

Institute of China Electronics System Engineering Company, 100000 Beijing, China
e-mail: 13811226834@139.com

W. Wang • X. Jing

School of Information and Communication Engineering, Beijing University of Posts and Telecommunications, 100876 Beijing, China

W. Liu

Institute of China Electronics System Engineering Company, 100000 Beijing, China

© Springer International Publishing Switzerland 2015

W.E. Wong (ed.), *Proceedings of the 4th International Conference on Computer Engineering and Networks*, Lecture Notes in Electrical Engineering 355,

DOI 10.1007/978-3-319-11104-9_140

140.1 Introduction

In the recent decade, advancements in wireless communications have reached unprecedented heights. The demand of higher transmitting rates continues growing, which stimulates the researchers to find new ways to meet this need. Multihoming incorporating multiple network interfaces into a single device is thought as an efficient solution to improve the system performance. The Stream Control Transmission Protocol (SCTP) [1] is the first transport protocol supporting multihoming, which only uses one path to transmit data and regards the other paths as backup ones providing redundancy. To make use of the multihoming feature fully, some modified SCTPs have been proposed, which can improve the performance of network system. The concurrent multipath transfer (CMT) extension of SCTP [2, 3] can increase the network throughput by concurrent transferring data packets through all available paths within an association. The concurrent transferring paths may have differences with bandwidth, Round Trip Time, and packet loss rate, which can result in packet disordering and then block the receiver buffer.

It is necessary to correctly describe each path's characteristics for improving the network's performance. Kashihara [4] proposed an algorithm to select the best path according to the estimation on RTT and bandwidth of each path. Fracchia [5] proposed the wireless SCTP extension, which uses the low-pass filter to estimate the bandwidth and RTT and then utilizes the estimations to select paths. Westwood SCTP [6] estimated the bandwidth by the smoothing ARMA filter and then introduced a congestion control method to lessen the disordering. Forward Prediction Scheduling (FPS) [7, 8] could select the appropriate path to send each packet by the correct estimations of arrival times for all available paths. Zhang utilized Kalman filter to estimate packet transmitting delay [9] and available bandwidth [10] of each path separately and then proposed a corresponding predictive data allocation algorithm for CMT in SCTP.

The changing conditions of multiple paths are often different and change dynamically which are the most important factors causing the disordering and performance degrading. To estimate each path's performance parameters in the exact and within the acceptable period is primary and key problem to improve the performance. Although the aforementioned methods have improved the system performance in different degrees, they can't reflect the diversity of the multiple paths exactly and can't keep up with the changing speed of these paths. The results introduced by Zhang [9, 10] have made a bit progress to resolve it, but these algorithms took bandwidth and RTT into account separately, which can't adequately make use of the mutual effects between bandwidth and RTT.

To address the above-mentioned challenges and basing on the results [9, 10], we utilize the extended vector Kalman filter to estimate each path's bandwidth and RTT simultaneously, and then propose a predictive data allocation algorithm. The rest of this chapter is organized as follows. Section 140.2 describes the extended vector Kalman filter. Section 140.3 describes how to use the extended vector Kalman filter to estimate bandwidth and RTT at the same time. Section 140.4

proposes a predictive data allocation algorithm by the estimation of bandwidth and RTT. Section 140.5 presents the simulation results and the chapter is concluded in Sect. 140.6 at last.

140.2 Extended Vector Kalman Filter

The Kalman filter is an efficient discrete time linear filter which can not only estimate and correct the current system states, but also forecast the future states based on the newest state. In practice it is often faced with a state equation and an observation equation which is nonlinear. So the linear Kalman filter then is no longer valid. The extended Kalman filter is invented to deal with these nonlinear problems. In extended Kalman filter, instead of linear Kalman filter models

$$\mathbf{s}[n] = \mathbf{A}\mathbf{s}[n-1] + \mathbf{B}\mathbf{u}[n]; \quad \mathbf{x}[n] = \mathbf{H}[n]\mathbf{s}[n] + \mathbf{w}[n] \quad (140.1)$$

We would have

$$\mathbf{s}[n] = \mathbf{a}(\mathbf{s}[n-1]) + \mathbf{B}\mathbf{u}[n]; \quad \mathbf{x}[n] = \mathbf{h}(\mathbf{s}[n]) + \mathbf{w}[n] \quad (140.2)$$

where \mathbf{a} is a p -dimensional function and \mathbf{h} is an M -dimensional function. The dimensions of the remaining matrices and vectors are the same as before. Now $\mathbf{a}(\mathbf{s}[n-1])$ represents the true physical model for the evolution of the state, while $\mathbf{u}[n]$ accounts for the modeling errors, unforeseen inputs, etc. Likewise, $\mathbf{h}(\mathbf{s}[n])$ represents the transformation from the state variables to the ideal observations (without noise). For this case the MMSE estimator is intractable. The only hope is an approximate solution based on linearizing \mathbf{a} and \mathbf{h} , much the same as was done for nonlinear LS. The result of this linearization and the subsequent application of linear Kalman filter result in the extended Kalman filter. Proceeding with the derivation, we linearize $\mathbf{a}(\mathbf{s}[n-1])$ about the estimate of $\mathbf{s}[n-1]$ or about $\hat{\mathbf{s}}[n-1|n-1]$. Likewise, we linearize $\mathbf{h}(\mathbf{s}[n])$ about the estimate of $\mathbf{s}[n]$ based on the previous data $\hat{\mathbf{s}}[n|n-1]$ that we will need the linearized observation equation to determine $\hat{\mathbf{s}}[n|n]$. The extended vector Kalman filter is described in detail as follows:

Prediction:

$$\hat{\mathbf{s}}[n|n-1] = \mathbf{a}(\hat{\mathbf{s}}[n-1|n-1]) \quad (140.3)$$

Minimum Prediction MSE Matrix ($p \times p$):

$$\mathbf{M}[n|n-1] = \mathbf{A}[n-1]\mathbf{M}[n-1|n-1]\mathbf{A}^T[n-1] + \mathbf{B}\mathbf{Q}\mathbf{B}^T \quad (140.4)$$

Kalman Gain Matrix ($p \times M$):

$$\mathbf{K}[n] = \mathbf{M}[n|n-1]\mathbf{H}^T[n](\mathbf{C}[n] + \mathbf{H}[n]\mathbf{M}[n|n-1]\mathbf{H}^T[n])^{-1} \quad (140.5)$$

Correction:

$$\hat{\mathbf{s}}[n|n] = \hat{\mathbf{s}}[n|n-1] + \mathbf{K}[n](\mathbf{x}(n) - \mathbf{h}(\hat{\mathbf{s}}[n|n-1])) \quad (140.6)$$

Minimum MSE Matrix ($p \times p$):

$$\mathbf{M}[n|n] = (\mathbf{I} - \mathbf{K}[n]\mathbf{H}[n])\mathbf{M}[n|n-1] \quad (140.7)$$

where

$$\mathbf{A}[n-1] = \left. \frac{\partial \mathbf{a}}{\partial \mathbf{s}[n-1]} \right|_{\mathbf{s}[n-1] = \hat{\mathbf{s}}[n-1|n-1]}; \quad \mathbf{H}[n] = \left. \frac{\partial \mathbf{h}}{\partial \mathbf{s}[n]} \right|_{\mathbf{s}[n] = \hat{\mathbf{s}}[n|n-1]}$$

140.3 Bandwidth and RTT Estimation by Using Extended Vector Kalman Filter

Now, we estimate bandwidth and RTT simultaneously by using extended vector Kalman filter. And the estimated results are used to select the appropriate path for the predictive data allocation algorithm for CMT in SCTP.

To estimate each path's bandwidth and RTT at the same time, we firstly construct the quality factor of the i -th path as

$$q_i[n] = \left(1 + \frac{b_i[n]}{rtt_i[n]} \right)^{(1-\sqrt{p_i})} \quad (140.8)$$

where $q_i[n]$ denotes the i -th path quality factor at time n , which can be observed and measured online; $b_i[n]$ is the i -th path bandwidth at time n ; $rtt_i[n]$ represents the i -th path RTT at time n ; and p_i is the packet loss rate of the i -th path. For simplification, all the p_i of paths are equal and constant. From Eq. (140.8), we can see that the larger $b_i[n]$ is, the better the $q_i[n]$, and the larger $rtt_i[n]$ and p_i are, the worse the $q_i[n]$ is. So the quality factor can depict the real state of the path and make a connection between bandwidth and RTT.

Secondly, we establish the state model and measurement model as

$$\mathbf{s}_i[n] = \mathbf{s}_i[n-1] + \mathbf{u}_i[n]; \quad x_i[n] = \mathbf{h}_i(\mathbf{s}_i[n]) + w_i[n] \quad (140.9)$$

where $\mathbf{s}_i[n] = \begin{bmatrix} b_i[n] \\ rtt_i[n] \end{bmatrix}$; $\mathbf{h}_i(\mathbf{s}_i[n]) = \left(1 + \frac{b_i[n]}{rtt_i[n]} \right)^{(1-\sqrt{p_i})}$

So

$$\mathbf{A}[n-1] = 1 \quad (140.10)$$

$$\mathbf{H}[n] = \left[\frac{(1-\sqrt{\rho})}{\hat{rt}_i[n|n-1]} \left(1 + \frac{\hat{b}_i[n|n-1]}{\hat{rt}_i[n|n-1]} \right)^{-\sqrt{\rho}} - \frac{(1-\sqrt{\rho})\hat{b}_i[n|n-1]}{\hat{rt}_i^2[n|n-1]} \left(1 + \frac{\hat{b}_i[n|n-1]}{\hat{rt}_i[n|n-1]} \right)^{-\sqrt{\rho}} \right] \quad (140.11)$$

As a result, the progress of the union estimation of the bandwidth and RTT for CMT in the SCTP follows as:

Prediction:

$$\hat{\mathbf{s}}_i[n|n-1] = \hat{\mathbf{s}}_i[n-1|n-1] \quad (140.12)$$

Minimum Prediction MSE Matrix:

$$\mathbf{M}_i[n|n-1] = \mathbf{M}_i[n-1|n-1] + \begin{bmatrix} \delta_b^2 & 0 \\ 0 & \delta_t^2 \end{bmatrix} \quad (140.13)$$

Kalman Gain Matrix:

$$\mathbf{K}_i[n] = \frac{\mathbf{M}_i[n|n-1]\mathbf{H}_i^T[n]}{\delta_w^2 + \mathbf{H}_i[n]\mathbf{M}_i[n|n-1]\mathbf{H}_i^T[n]} \quad (140.14)$$

Correction:

$$\hat{\mathbf{s}}_i[n|n] = \hat{\mathbf{s}}_i[n|n-1] + \mathbf{K}_i[n](x_i(n) - \mathbf{h}_i(\hat{\mathbf{s}}_i[n|n-1])) \quad (140.15)$$

Minimum MSE Matrix:

$$\mathbf{M}_i[n|n] = (\mathbf{I} - \mathbf{K}_i[n]\mathbf{H}_i[n])\mathbf{M}_i[n|n-1] \quad (140.16)$$

where δ_b^2 , δ_t^2 are the process noise covariance and δ_w^2 is the measurement noise. They are independent. δ_b^2 and δ_t^2 denote the system model's accuracy, and δ_w^2 affects the measuring accuracy. In the following simulations, δ_b^2 and δ_t^2 are both set to 0.001, and δ_w^2 is set to 1.

140.4 Data Allocation Algorithm for CMT

Based on the above estimation of bandwidth and RTT of each path in CMT-SCTP, we can calculate a new data packet's coming time for each path i as follows:

$$T_i = \max((D + O_i)/\hat{b}_i[n], \hat{rtt}_i[n]) \quad (140.17)$$

where D denotes the data packet size and O_i is all of the outstanding chunks of path i . $\hat{b}_i[n]$ and $\hat{rtt}_i[n]$ are the predictive bandwidth estimation and RTT estimation at the time of this computation, respectively. Then, this data packet will be distributed by the path with the smallest T_i . Making reference to the flow allocation algorithm [10], we propose the data allocation algorithm as follows:

Data Allocation Algorithm for CMT in SCTP

For each data packet to be transferred

for all path i **do**

 compute T_i using Equation (17)

 sort all paths with T_i ascending

end for

pick path j whose value T_j is smallest for transition

while (the size of CWND \leq Outstanding chunks) **for** path j **do**

 replace path j by the next path $j + 1$

end while

transfer the data packet through path j

In addition, the predictive arrive time T_i denotes the transferring time from the transmitter to receiver for the current data packet and the effects of bandwidth and RTT at the same time are taken into account, which results in a more correct estimation of the multiple paths' state. High bandwidth $\hat{b}_i[n]$ and small RTT $\hat{rtt}_i[n]$ bring a faster data delivering and faster feedback. The proposed data allocation algorithm will send the data packet through the quickest path according to the estimations of the bandwidth and RTTs.

140.5 Simulations and Results

To compare the performance of our algorithm and algorithm [10], we adopt the same simulation scenarios [10] and use NS-2 to evaluate the performance of both algorithms.

140.5.1 Simulation Scenarios

Figure 140.1 is a client–server topology used in our simulations, in which there are two terminals A and B. The terminal A represents the multihomed client with two 802.11b wireless interfaces and the terminal B is the multihomed server with two

Fig. 140.1 Simulation topology

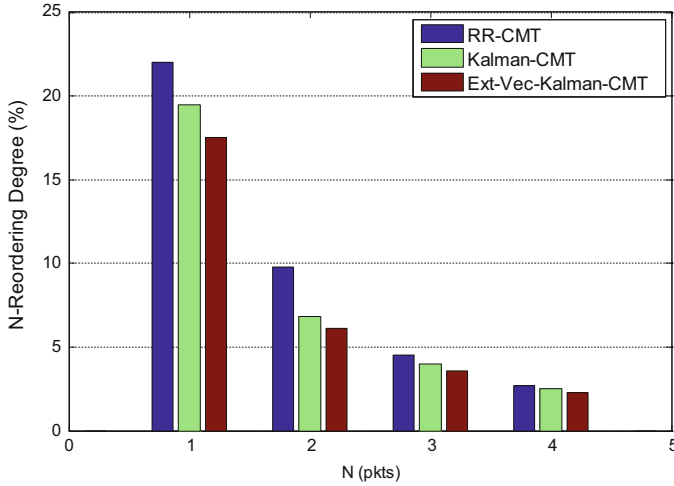
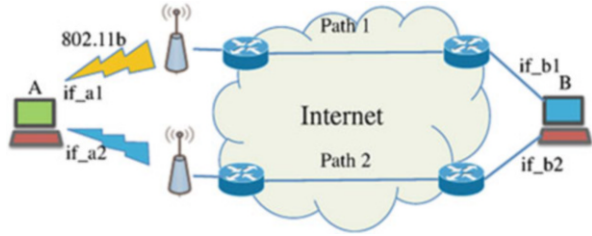


Fig. 140.2 Comparison of reordering degree (packet loss rate of Path 1 is set to 1 %; packet loss rate of Path 2 is 8 %)

wired interfaces. In our simulations, the two 802.11b wireless interfaces can avoid interferences by assigning two different channels for each other. Otherwise, we assume there is no loss in the wired links, and the frame loss rate of the first wireless link is fixed to 1 % and the others of the second wireless link vary from 1 to 10 %.

For simplification, we regard the original CMT extension as RR-CMT that adopts the Round-Robin flow allocation algorithm and regard the CMT approach based on Kalman filter presented by Zhang [10] as Kalman-CMT. Similarly, our proposed algorithm based on the extended vector Kalman filter is denoted as Ext-Vec-Kalman-CMT in the simulations.

140.5.2 Simulation Results

Figure 140.2 compares the reordering degree of the above three algorithms assuming the packet loss rate of Path 2 is fixed to 8 %. In Fig. 140.2, the histograms are the

percentage values of the reordering degree. The x -axis value n is ranging from 1 to 4. When one packet i is n -reordered, it means that the sequence numbers of all the packets received before i are always greater than i 's. It is easy to see that n -reordering degree reflects the reordering degree of the receiver. In this chapter, the n -reordering degree is represented as the ratio between the number of n -reordered packets and the total received packets. In this figure, the reordering degree of our proposal, Ext-Vec-Kalman-CMT, is lower than the original RR-CMT and Kalman-CMT [10]. For instance, 1-reordering degree reduces from 22 % for RR-CMT and 19.5 % for Kalman-CMT to about 17.5 %. So, it is easy to see that our algorithm can improve the network performance by reducing the reordering degree.

Figure 140.3 makes a comparison of system throughput performance between the three methods. In our simulation, we make Path 2 packet loss rate vary from 1 to 10 % which can efficiently validate our proposal under different conditions. To obtain the sufficient confidence of our results, we make thousands of simulations and calculate the mean value of those results for every point in Fig. 140.3. Both curves decrease with the increasing of the packet loss rate and our proposed algorithm outperforms RR-CMT and Kalman-CMT in all the Path 2 packet loss rate regions. From the figure, we can also see that the advantage between our method (Ext-Vec-Kalman-CMT) and RR-CMT will become larger when the packet loss rate ascends, which is the same as the comparison between Kalman-CMT and RR-CMT. Moreover, our method outperforms and obtains performance gain about 150 kbps than Kalman-CMT.

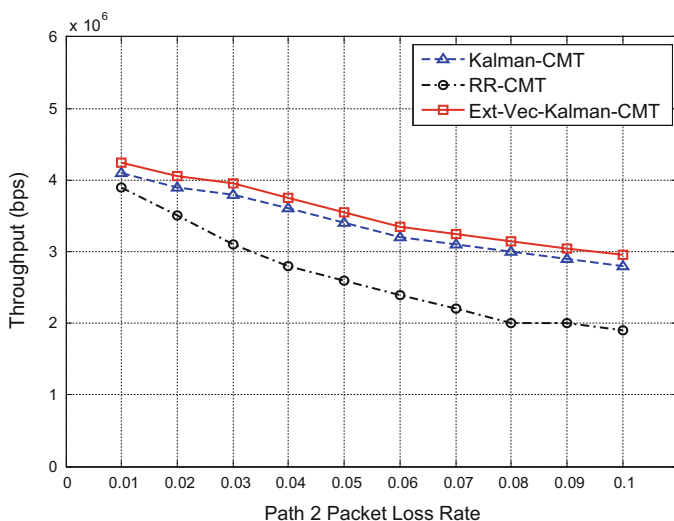


Fig. 140.3 Throughput comparison with the changing Path 2 packet loss rate

Conclusion

In our chapter, we propose the predictive algorithm on bandwidth and RTT based on extended vector Kalman filter and then present a data allocation algorithm for CMT in SCTP. All the researches are based on the study of Zhang. Our proposal takes the relationship between bandwidth and RTT of multiple paths into account and estimates the two factors simultaneously, which can make a prediction for the state of multipath as exactly as possible and can improve the throughput performance for CMT in SCTP further. The simulation results show that our proposal outperforms RR-CMT and Kalman-CMT.

In our proposal, the correctness of the online observation and calculation of the quality factor in Eq. (140.8) makes a great influence on the method's performance, so we will find and optimize the more appropriate method to deal with it in our future work.

References

1. RFC 2960. Stream Control Transmission Protocol [S]; 2000.
2. Iyengar JR, Shah KC, et al. Concurrent multipath transfer using SCTP multihoming. *SPECTS*. 2004;23(5):1230–8.
3. Iyengar JR, Amer P, Stewart R. Concurrent multipath transfer using SCTP multihoming over independent end-to-end paths. *IEEE/ACM Trans Netw*. 2006;14(5):951–64.
4. Kashiwara S, Nishiyama T, et al. Path selection using active measurement in multihomed wireless networks. In: *The proceedings of IEEE conference of SAINT, Tokyo; 2004*. p. 273–6.
5. Fracchia R, Casetti C, et al. WiSE: best-path selection in wireless multihoming environments. *IEEE Trans Mob Comput*. 2007;6(10):1130–41.
6. Casetti C, Gaiotto W. Westwood SCTP: load balancing over multipaths using bandwidth-aware source scheduling. In: *The proceedings of 60th IEEE conference of vehicular technology, Los Angeles, CA. 2004*;4:3025–9.
7. Mirani F, Boukhatem N, et al. A data-scheduling mechanism for multi-homed mobile terminals with disparate link latencies. In: *The proceedings of 71st IEEE conference of vehicular technology, Taipei, Taiwan; 2010*. p. 1–5.
8. Mirani FH, Zhang X, et al. Cross-layer FPS: a SCTP-based cross-layer data scheduling approach. In: *The proceedings of consumer communications and networking conference, Las Vegas, NV; 2011*. p. 192–7.
9. Zhang X, Nguyen TMT. Concurrent multipath transfer performance optimization using Kalman filter based predictive delay estimation in wireless networks. In: *The proceedings of global information infrastructure symposium, Da Nang; 2011*. p. 1–5.
10. Zhang X, Nguyen TMT, et al. Kalman filter based bandwidth estimation and predictive flow allocation for concurrent multipath transfer in wireless networks. In: *The proceedings of the 3rd IEEE international conference on network infrastructure and digital content, Beijing; 2012*. p. 305–9.

Chapter 141

Common-Knowledge and Cooperation Management I

Takashi Matsuhisa

Abstract Recently there are many issues of moral hazards and adverse selection presented in each and every contract, in which we have a self-interest and information that the other party does not possess. There is still a need for more information on how we handle a party to a contract with more information than us. This paper re-examines the issue in the framework of a principal-agent model under uncertainty based on **S5n**-knowledge. It highlights epistemic conditions for a possible resolution of the moral hazard between buyer and suppliers. We show that if the buyer and suppliers commonly know each agent's belief on the others' efforts, then all effort levels such that the expected marginal costs actually coincide for them can be characterised as the critical points of the refunded proportional rate function. This implies our recommendation that, for removing out such moral hazard in the buyer-supplier cooperation, the buyer and suppliers should commonly know their beliefs on the others' effort levels.

Keywords Belief • Communication • Effort level • Moral hazard • Principal-agent model under uncertainty

141.1 Introduction

Recently there are many issues of moral hazard and adverse selection presented in each and every contract, in which we have a self-interest and information that the other party does not possess. Even though this is a fertile research area, there is still a need for more information on how we handle a party to a contract with more information than us. One of the epitomes is the Global Financial Crisis, which still perplexes bankers and shareholders alike: Shareholders have been had problems

T. Matsuhisa (✉)

Department of Natural Sciences, Ibaraki National College of Technology,
Nakane 866, Hitachinaka-shi, Ibaraki 312-8508, Japan

Mathematical Research Institute of BUSAIKU-BUHI Foundation, Tokiwa-cho 1-4-13,
Mito-shi, Ibaraki 310-0033, Japan

Institute of Applied Mathematical Research, KarRC, RAS, Pushkinskya Str. 11,
Petrozavodsk 185910, Russia

e-mail: mathisa@ge.ibaraki-ct.ac.jp; takashimatsuhisa.mri.bsbs@gmail.com

© Springer International Publishing Switzerland 2015

W.E. Wong (ed.), *Proceedings of the 4th International Conference on Computer Engineering and Networks*, Lecture Notes in Electrical Engineering 355,

DOI 10.1007/978-3-319-11104-9_141

1235

with how they can handle their agents (managers); on the other hand insurers and bankers have been struggling to make products that will reduce the impact of moral hazard. Such issues are also the bottlenecks in buyer-supplier cooperation, and so the buyer-supplier management is another epitome.

The moral hazard can arise when there are many agents that affect gross returns and their individual actions are not observed by each other. The first formal analysis of the principal-agent relationship and the phenomena of moral hazard was made by Arrow [1]. The principal-agent model with many-sided moral hazard was investigated by Holmstrom [2]. He formulated the issue as a partnership model whether there exist any sharing rules that both balances the budget and under which an efficient action is a Nash equilibrium. Further, Holmstrom [2] and Williams and Radner [3], respectively, analysed the conditions for existing the sharing rule under which some actions profile satisfies the first-order conditions for an equilibrium.

In the game theoretical framework, Aumann [4] introduced the formal notion of common-knowledge in the partition information structure and showed that if all agents commonly know their posterior, then all the posteriors must be equal to each other. Further, Krasucki [5] extended the theorem in the framework of the communication model introduced by Parikh and Krasucki [6]. He showed that after long-run communication among agents, all the limiting values of revisions of posteriors must coincide.

Recently, Matsuhisa [7] and Matsuhisa and Jiang [8] adopted a new approach to the many sided moral hazard from the epistemic model point of view as above. They analysed the moral hazard as the disagreement on expected marginal costs between the principal and agents in an extended model of principal and agents under uncertainty. A necessity condition for that the moral hazard will not be appeared was given; that is, under some technical assumptions, the principal and agent model under uncertainty disappears the moral hazard if the principal and agents could share fully information on their expected marginal costs in the following two cases: first they commonly know the marginal expected costs [7] and secondly they communicate the costs as long run [8]. However, in these papers they assume the existence of decision function consistent to certain artificial assumptions, and it has not been guaranteed.

This paper aims to remedy the defect. We re-examine a buyer-supplier cooperation with moral hazard as a problem of the principal-agent relationship. We present an extended principal-agent model under uncertainty, and we highlight hidden conditions for a possible resolution of the moral hazard between the buyer and the suppliers. For removing out such moral hazard in the buyer-supplier cooperation, our recommendation is that the buyer and suppliers should commonly know their beliefs on the others' effort.

To investigate in detail we shall extend the principal-agent model with incomplete information, where the principal is the buyer and the agents are the suppliers. Now we assume each agent as well as the principal, k , has his/her private information structure induced from a *partition* relation associated with the multi-modal logic **S5n**. Let us consider the situation that the principal and the agents interact each other from sharing information about the others' effort levels. We shall show:

Theorem 1. *Under the above situations, all effort levels such that the expected marginal costs actually coincide for buyer and suppliers can be characterised as the critical points of the refunded proportional rate function. Consequently, if the refunded proportional rate is constant then all marginal costs have to coincide with each other; i.e., there is no moral hazard.*

The paper is organised as follows: Sect. 141.2 reviews the moral hazard in the classical principal-agent model, Sect. 141.3 recalls the formal model of common-knowledge, and presents the principal-agent model under uncertainty and Sect. 141.4 states the theorem formally with sketch of the proof. Finally we conclude remarks.

141.2 Moral Hazard

Let's start to consider a firm consisting of the principal P and n agents $\{1, 2, \dots, k, \dots, n\}$ ($n \geq 1$) following Sect. 2 in Matsuhisa [7]. The principal makes a profit by selling the productions made by the agents. She makes a contract with each agent k that the total amount of all profits is refunded to each agent k in proportion to the agent's contribution to the firm.

Let e_k denote the measuring managerial effort for k 's productive activities, called k 's *effort level* or simply k 's *effort*, with $e_k \in \mathbb{R}_+$. Let $I_k(x_k)$ denote a real-valued continuously differentiable function on \mathbb{R}_+ , interpreted as the profit obtained by selling the productions made by the agent k with his effort e_k and with the cost $c(e_k)$. Let I_P be the total amount of all the profits: $I_P(x) = I_P(x_1, x_2, \dots, x_k, \dots, x_n) = \sum_{k=1}^n I_k(x_k)$.

The principal P cannot observe these efforts e_k , and he/she shall view it as a random variable \mathbf{e}_k on a probability space (Ω, μ) ; i.e., \mathbf{e}_k is a μ -measurable function from Ω to \mathbb{R}_+ . We introduce the *ex-post* expectation:

$$\text{Exp}[I_P(e)] := \sum_{\xi \in \Omega} I_P(\mathbf{e}(\xi))\mu(\xi) \quad \text{and} \quad \text{Exp}[I_k(e_k)] := \sum_{\xi \in \Omega} I_k(\mathbf{e}_k(\xi))\mu(\xi).$$

The optimal plan for the principal then solves the following problem:

$$\text{Max}_{e=(e_1, e_2, \dots, e_k, \dots, e_n)} \text{Exp}[I_P(e)] - \sum_{k=1}^n \text{Exp}[c(e_k)].$$

By $W_k(e_k)$ we denote the total amount of the refund to agent k : $W_k(e_k) = r_k I_P(e)$, with $\sum_{k=1}^n r_k = 1, 0 \leq r_k \leq 1$, where r_k denotes the proportional rate representing k 's contribution to the firm.

The optimal plan for each agent also solves the problem: For every $k = 1, 2, \dots, n$,

$$\text{Max}_{e_k} \text{Exp}[W_k(e_k)] - \text{Exp}[c(e_k)] \quad \text{subject to} \quad \sum_{k=1}^n r_k = 1, 0 \leq r_k \leq 1.$$

We assume that r_k is constant; i.e., it is independent of e_k .

We can observe the necessity conditions for critical points which are given as follows: For each agent $k = 1, 2, \dots, n$, we obtain

$$\frac{\partial}{\partial e_k} \text{Exp}[I_k(e_k)] - \text{Exp}[c'(e_k)] = 0 \quad \text{and} \quad r_k \frac{\partial}{\partial e_k} \text{Exp}[I_k(e_k)] - \text{Exp}[c'(e_k)] = 0$$

in contradiction to $0 \not\cong r_k \cong 1$ because $c'(e_k) = \frac{\partial}{\partial e_k} \text{Exp}[I_k(e_k)] = r_k \frac{\partial}{\partial e_k} \text{Exp}[I_k(e_k)]$.

This contradictory situation is called a **moral hazard** in the principal-agent model; i.e., there is no equilibrium effort level as a solution of the contract design problem.

141.3 The Model

Let N be a set of finitely many agents and let k denote an agent and P the principal. Let \bar{N} denote $N \cup \{P\} = \{P, 1, 2, \dots, k, \dots, n\}$ consisting of the principal P and the agents $N = \{1, 2, \dots, k, \dots, n\}$ in a firm. A state-space Ω is a non-empty set, whose members are called *states*, and each subset of Ω is called an *event*. We denote by 2^Ω the field of all subsets of it. An event E is said to occur at a state ω if $\omega \in E$.

141.3.1 Information and Knowledge

A *partition information* structure is a tuple $\langle \Omega, (\Pi_i)_{i \in \bar{N}} \rangle$ consisting of $\Pi_i: \Omega \rightarrow 2^\Omega$ with the three postulates as below: for each $i \in \bar{N}$ and for any $\omega \in \Omega$,

Ref $\omega \in \Pi_i(\omega)$; **Trn** $\xi \in \Pi_i(\omega)$ implies $\Pi_i(\xi) \subseteq \Pi_i(\omega)$;

Sym If $\xi \in \Pi_i(\omega)$ then $\omega \in \Pi_i(\xi)$.

The set $\Pi_i(\omega)$ is interpreted as the set of all the states of nature that i knows to be possible at ω , or as the set of the states that i cannot distinguish from ω , and it is called i 's *information set* at ω . It is noted that the structure coincides with the Kripke semantics for the multi-modal logic **S5n**.

We can now introduce the formal model of knowledge as follows:

Definition 1. By *S5n-knowledge structure* we mean a tuple $\langle \Omega, (\Pi_i)_{i \in \bar{N}}, (K_i)_{i \in \bar{N}} \rangle$ that consists of a partition information structure $\langle \Omega, (\Pi_i)_{i \in \bar{N}} \rangle$ and a class of i 's knowledge operator $K_i: 2^\Omega \rightarrow 2^\Omega$ defined by $K_i E = \{ \omega \in \Omega \mid \Pi_i(\omega) \subseteq E \}$.

We will interpret $K_i E$ as the set of states for which i knows E to be possible. The properties of i 's knowledge operator are recorded as below: For every E, F of 2^Ω ,

- N** $K_i \Omega = \Omega$; **K** $K_i(E \cap F) = K_i E \cap K_i F$; **T** $K_i E \subseteq E$;
4 $K_i E \subseteq K_i(K_i E)$; **5** $\Omega \setminus K_i E \subseteq K_i(\Omega \setminus K_i E)$.

According to these properties we can say the structure $\langle \Omega, (K_i)_{i \in \bar{N}} \rangle$ is a model for the multi-modal logic **S5n**.

141.3.2 Common-Knowledge

Let S be a non-empty subset in \bar{N} . The *mutual knowledge operator* among a coalition S is the operator $K_S: 2^\Omega \rightarrow 2^\Omega$ defined by the intersection of all individual knowledge, $K_S F = \bigcap_{i \in S} K_i F$, whose interpretation is that every member in S knows E .

Definition 2. The *common-knowledge operator* among S is the operator $K_C^S: 2^\Omega \rightarrow 2^\Omega$ defined by $K_C^S F = \bigcap_{n \in \mathbb{N}} (K_S)^n F$.

We interpret $K_C^S E$ as the event that ‘every agent in S knows E ’ and ‘every agent in S knows that “every agent in S knows E ”,’ and ‘every agent in S knows that “everyone knows that “every agent in S knows E ”,”’. That is, all members in S *commonly know* (or E is a *common-knowledge* among S) at $\omega \in \Omega$ if $\omega \in K_C^S E$.

141.3.3 Principal-Agent Model Under Uncertainty

Let notations and assumptions be the same as in the above section. We shall introduce the extended principal-agent model with additional conditions as below. These play an essential role to resolve the moral hazard problem.

Definition 3. By a *principal-agent model under uncertainty* we mean structure

$$\mathcal{M} = \langle \bar{N}, (I_k)_{k \in \bar{N}}, (\mathbf{e}_k)_{k \in N}, (r_k)_{k \in N}, \Omega, \mu, (\Pi_k)_{k \in N}, (c_k)_{k \in N} \rangle$$

in which

1. $\bar{N} = P, 1, 2, \dots, k, \dots, n$ where P is the principal and each k is an agent;
2. $\mathbf{e}_k: \Omega \rightarrow \mathbb{R}$ is a random variable with $\mathbf{e}_k(\omega)$ a real variable indicating agent k 's effort level;

3. $I_k(x_k)$ is an agent k 's profit function with $I_k(e_k)$ the profit by his/her effort e_k , which is sufficiently many differentiable on \mathbb{R}_+ with $I_k' \geq 0$;
4. $I_P(x) = I_P(x_1, x_2, \dots, x_n) = \sum_{k=1}^n I_k(x_k)$ is the profit function of the firm (the total amount of all the agents' profits);
5. (Ω, μ) is a probability space;
6. r_k is a proportional rate function in the contract, which is sufficiently many differentiable and weakly increasing on \mathbb{R}_+ with $0 < r_k \leq 1$ for $k = 1, 2, \dots, n$;
7. $(\Pi_k)_{k \in \bar{N}}$ is a partition information structure satisfying the three postulates **Ref**, **Trn** and **Sym**;
8. c_k is the cost function for agent k , which is sufficiently many differentiable on \mathbb{R}_+ with $I_k' \geq 0$ with c_k interpreted as the cost of k for effort level e_k .

For each profile of efforts $e = (e_1, e_2, \dots, e_k, \dots, e_n) \in \mathbb{R}^n$ let us denote by $[e_k(\omega)]$ the event of k 's effort $[e_k] = \xi \in \Omega | \mathbf{e}_k(\xi) = e_k$ and by $[e]$ the event of total efforts $[e] = \bigcap_{k \in N} [e_k]$. For any non-empty subset S of \bar{N} , we will denote $[e_S] = \bigcap_{k \in S} [e_k]$, and $[e_{-k}] = \bigcap_{l \in N \setminus \{k\}} [e_l]$.

141.3.4 Bayesian Approach

According to this we have to assume that each agent k knows his/her own effort e_k but k cannot know the others' effort e_k , and also the principal P cannot know efforts for any agents. The former assumption can be formulated as

KE $[e_k] \subseteq K_k([e_k])$ for each effort e_k .

The later assumption means that the principal cannot have the exact knowledge on the agents' effort levels e and also each agent cannot have the exact knowledge on the others' effort e_{-k} .

141.3.5 Belief and Conjecture

Following the interpretations we have to introduce the notion of *belief on the others' effort level*: By the principal P 's *belief* on the agents' efforts e we mean a probability $q_P(e)$ of e , and by an agent k 's *belief* on the other agents' effort e_{-k} we mean a probability $q_k(e_{-k})$ of e_{-k} . The *conjecture* $\mathbf{q}_P(e; \omega)$ of the principal P for the agents' effort $e_k \in \mathbb{R}$ ($k \in N$) is defined by $\mathbf{q}_P(e; \omega) = \mu([e] | \Pi_P(\omega))$, and the *conjecture* $\mathbf{q}_k(e_{-k}; \omega)$ of agent k for the other agents' effort $e_{-k} \in \mathbb{R}$ is $\mathbf{q}_k(e_{-k}; \omega) = \mu([e_{-k}] | \Pi_k(\omega))$. By the event of P 's belief on the agents' efforts e we mean

$[q_P(e)] := \{\xi \in \Omega \mid \mathbf{q}_P(e; \omega) = q_P(e)\}$, and by the event of k 's belief on the other agents' efforts e_{-k} $[q_k(e_{-k})] := \{\xi \in \Omega \mid \mathbf{q}_k(e_{-k}; \omega) = q_k(e_{-k})\}$.

141.3.6 Interim Expectation

By the *interim expectation* (or simply *expectation*) of I_P we mean

$$\text{Exp}[I_P(\mathbf{e}) \mid \Pi_P](\omega) = \sum_{\xi \in [e]} I_P(\mathbf{e}_1(\xi), \mathbf{e}_2(\xi), \dots, \mathbf{e}_n(\xi)) \mu(\xi \mid \Pi_P(\omega)) = I_P(e) \mathbf{q}_P(e; \omega)$$

and by the *interim expectation* (or simply *expectation*) of I_k we mean

$$\text{Exp}[I_k(e_k) \mid \Pi_k](\omega) := I_k(e_k) \mathbf{q}_k(e_{-k}; \omega) = \sum_{\xi \in [e_{-k}]} I_k(e_k(\xi)) \mu(\xi \mid \Pi_k(\omega))$$

and the interim expectation of agent k 's income W_k is

$$\begin{aligned} \text{Exp}[W_k(e_k) \mid \Pi_k](\omega) &:= r_k(e_k) \text{Exp}[I_P(e_k, \mathbf{e}_{-k}) \mid \Pi_k(\omega)] \\ &= \sum_{e_{-k} \in E_k} r_k(e_k) I_P(e_k, e_{-k}) \mathbf{q}_k(e_{-k}; \omega). \end{aligned}$$

141.3.7 Contract Design Problem

We investigate the maximisation problems as for the optimal plans for the principal and agents: to find out the effort levels $e = (e_1, e_2, \dots, e_k, \dots, e_n) \in \mathbb{R}^n$ such that,

subject to $\sum_{k=1}^n r_k = 1, 0 < r_k \leq 1$,

PE $\text{Max}_{e=(e_k)_{k=1,2,\dots,n}} \text{Exp}[I_P(e) \mid \Pi_P(\omega)] - \sum_{k=1}^n \text{Exp}[c_k(e_k)];$

AE $\text{Max}_{e_k} \text{Exp}[W_k(e_k) \mid \Pi_k(\omega)] - \text{Exp}[c_k(e_k)].$

Example 1. Let us consider the principal-agent model under uncertainty as follows: There are the principal P and two agents 1, 2, who have the below information partition:

- $\Omega = \{\omega_1, \omega_2, \omega_3, \omega_4\}$ with the equal probability μ ; i.e., $\mu(\omega) = \frac{1}{4}$;
- $(\Pi_i)_{i=P,1,2}$: $\Pi_P = \{\Omega\}$, $\Pi_1 = \{\{\omega_1, \omega_2\}, \{\omega_3, \omega_4\}\}$, $\Pi_2 = \{\{\omega_1, \omega_3\}, \{\omega_2, \omega_4\}\}$;
- $\mathbf{e}_i : \Omega \rightarrow \mathbb{R}$ with $\mathbf{e}_i(\omega)$ a real variable is defined as Table 141.1; i.e.,

Table 141.1 Types of variables

e_*	y_h	y_l
x_h	ω_1	ω_2
x_l	ω_3	ω_4

$$e_1(\omega) = \text{for } \omega = \omega_i (i = 1, 2), e_1(\omega) = x_1 \text{ for } \omega = \omega_i (i = 3, 4) \text{ with } x_h \geq x_l,$$

$$e_2(\omega) = y_h \text{ for } \omega = \omega_i (i = 1, 3), e_2(\omega) = y_l \text{ for } \omega = \omega_i (i = 2, 4) \text{ with } y_h \geq y_l.$$

This means that agent 1’s effort at ω_1, ω_2 is higher than the effort at ω_3, ω_4 , and agent 2’s effort at ω_1, ω_3 is higher than the effort at ω_2, ω_4 .

- $I_1(x)$ and $I_2(y)$ are profit functions and $I_P(x, y) = I_1(x_1) + I_2(x_2)$ is the total amount of the profits.

In this situation we obtain that $E[W_1|\Pi_1](\omega) = r_1(x_h)I_P(x_h, y_j) (\omega = \omega_1, \omega_2, j = h, l), E[W_1|\Pi_1](\omega) = r_1(x_l)I_P(x_l, y_j) (\omega = \omega_3, \omega_4, j = h, l), E[W_2|\Pi_2](\omega) = r_2(y_h)I_P(x_i, y_h) (\omega = \omega_1, \omega_3, i = h, l), E[W_2|\Pi_2](\omega) = r_2(y_l)I_P(x_i, y_l) (\omega = \omega_2, \omega_4, i = h, l)$ and $E[I_P|\Pi_P](\omega) = \frac{1}{4} \sum_{i,j=h,l} (I_1(x_i) + I_2(y_j))$. Then we can observe that there are no

moral hazard if $r_1(e) = r_2(e) \equiv \frac{1}{2}$; hence any effort level can be a solution of the above contract problem **PE** and **AE**.

141.4 Main Theorem and Proof

We can now restate Theorem 1 as follows:

Theorem 2. *In the principal-agent model under uncertainty with **KE**, assume that the principal P and each agent k have beliefs q_P, q_k on the others’ effort, respectively, and assume that all the agents commonly know the principal’s belief q_P at some state. If all agents commonly know the principal’s belief q_P then every effort level $e_k (k \in N)$ as solutions of the contract design problem **PE**, **AE** must be a critical point of r_k for every $k \in N$; i.e.: $r'_k(e_k) = 0$ if $K_C^N ([q_P]) \neq \emptyset$. In this case the proportional rate r_k is determined by the principal belief: $r_k(e_k) = q_P(e_k)$.*

Example 2. Theorem 2 gives an explanation of the resolution of moral hazard of Example 1: In fact, since $K_C^{1,2}([q_P(e(\omega)); \omega]) = \Omega$, we can see that $[q_P(e(\omega)); \omega]$ is a common-knowledge everywhere among agents 1 and 2, and further, r_1 and r_2 are the constants with $r_1(e_1(\omega)) = q_P(e_1(\omega); \omega) = \frac{1}{2}, r_2(e_2(\omega)) = q_P(e_2(\omega); \omega) = \frac{1}{2}$. Hence the resolution of moral hazard in Example 1 can be described by Theorem 2.

141.4.1 Critical Points Condition

Partially differentiating the expressions in the parentheses of the problems **PE** and **AE** with respect to e_k yields the necessity condition for critical points for every $k \in N$: From **PE** we have

$$\text{Exp}[I'_k(e_k)|\Pi_P(\omega)] = I'_k(e_k)\mathbf{q}_P(e; \omega) = c'_k(e_k); \quad (141.1)$$

and from **AE** the condition is also that, subject to $0 < r_k < 1$ and $\sum_{k \in N} r_k = 1$,

$$r'_k(e_k)\text{Exp}[I_k(e_k)|\Pi_k(\omega)] + r_k(e_k)\text{Exp}[I'_k(e_k)|\Pi_k(\omega)] = c'_k(e_k). \quad (141.2)$$

The below proposition plays another central role to prove Theorem 2:

Proposition 1 (Decomposition Theorem). *Under the same situations in Theorem 2, we obtain that for every $k \in N$, $q_P(e) = q_k(e_{-k})q_P(e_k)$ for any $e = (e_k)_{k \in N} \in \mathbb{R}^n$.*

141.4.2 Proof of Theorem 2

Notations and assumptions are the same in Proposition 1. On viewing Eqs. (141.1) and (141.2), the former part of Theorem 2 follows from Proposition 1. Especially, if r_k is a constant function, then $r'_k = 0$, and so the latter part also follows immediately.

141.5 Concluding Remarks

This paper advocates a new approach to treat a moral hazard problem in principal-agent model by focusing on the beliefs of effort levels. Highlighting the structure of sharing private information on their beliefs about effort levels for principal and agents helps us to make progress in ‘problematic’ classical principal-agent models. In particular, common-knowledge on the conjectures on their effort levels play crucial role in removing out the moral hazard in the classical principal-agent model. In fact, for removing out the moral hazard in the buyer-supplier cooperation management we will recommend that by making common-knowledge on the efforts, they (the buyer and suppliers) should share fully information on only their conjectures on the others’ effort levels but not expected marginal costs.

Acknowledgements I was partially supported by JSPS Grants-in-Aid for Scientific Research (C) No. 23540175 and by BUSAIKU-BUHI Foundation for Scientific Research.

References

1. Arrow KJ. Uncertainty and welfare economics of medical care. *Am Econ Rev.* 1963;53:941–73.
2. Holmstrom B. Moral hazard in teams. *Bell J Econ.* 1982;13:324–40.
3. Williams S, Radner R. Efficiency in partnerships when the joint output is uncertain. Discussion Paper No.: 76; Kellogg School of Management, Northwestern University; 1989. <http://kellogg.northwestern.edu/research/math/papers/760.pdf>.
4. Aumann RJ. Agreeing to disagree. *Ann. Stat.* 1976;4:1236–39.
5. Krasucki P. Protocol forcing consensus. *J. Econ. Theor.* 1993;70:266–72.
6. Parikh R, Krasucki P. Communication, consensus, and knowledge. *J. Econ. Theory* 1990;52:178–89.
7. Matsuhisa T. Moral hazard resolved by common-knowledge in principal-agent model. *Int. J. Intell. Inf. Database Syst.* 2012;6(3):220–29.
8. Matsuhisa T, Jiang D.-Y. Moral hazard resolved in communication network. *World J. Social Sci.* 2011;1(3):100–15.

Chapter 142

Detection of Topic Communities in Social Networks Based on Tri-LDA Model

Wei Ou, Zhanfu Xie, Xiping Jia, and Binbin Xie

Abstract Social networks, in particular microblogs, have gained huge popularity in recent years. The detection of topic communities in social networks carries high value in commercial promotion, public opinion monitoring, etc. There are some existing algorithms that can detect topic communities very well. In this chapter we propose a new approach by using probabilistic generative topic model LDA (Latent Dirichlet Allocation): we add a modification to LDA to get Tri-LDA model, to process the data of friendship between users in a social network for detection of topic communities. The experiment result shows that the topic communities found by Tri-LDA are basically consistent with the realistic topic communities that are hand-labeled by the authors in the test data set.

Keywords LDA • Topic community discovery • Social networks

142.1 Introduction

The most widely used probabilistic topic model in the field of text mining is pLSI (probabilistic Latent Semantic Indexing) proposed by Hoffman [1] and LDA (Latent Dirichlet Allocation) proposed by Blei [2]. pLSI is a generative model that can be used to discover the mixture weights of topics of documents in a training data set; however, it is limited by the fact that it cannot properly infer the topic mixture weights of unseen documents. Based on the principle of pLSI, Blei proposed LDA that addressed this issue. LDA is a fully generative model that patterns each document m as a distribution $\vec{\theta}_m$ over all topics K and each topic k as a distribution $\vec{\varphi}_k$ over all words in the vocabulary V . LDA first draws $\vec{\theta}_m$ and $\vec{\varphi}_k$ from Dirichlet distributions, then samples a topic for each word position in each document m in the corpus according to $\vec{\theta}_m$, and finally emits relative words from the topic-word distribution $\vec{\varphi}_k$.

W. Ou (✉) • Z. Xie • X. Jia • B. Xie
School of Computer Science and Technology, Guangdong Polytechnic Normal University,
510665 Guangzhou, China
e-mail: studyouwei@gmail.com

LDA has been widely applied to text mining, digital image processing, etc. Usually the current applications of LDA are always “content-based” that process the content of text or pixels in images. To our best knowledge, LDA has not been used to handle social network structure data (in the context of this chapter “social network structure data” means data of friendship or relation between users in a social network; in the following sections “network structure data” and “friendship data” are used interchangeably) to detect the underlying topic communities in a social network. In this chapter, we attempt such a new application by adding a slight modification to LDA.

In the following sections, we first specify the incapability of LDA in handling social networks’ friendship data, and then we introduce our model—Tri-LDA to address it. Lastly we test the effectiveness of our method through an experiment.

142.2 Tri-LDA Model

Figure 142.1 (left) displays the Bayesian network of LDA [2]. By borrowing the generation process of documents in the LDA model specified by Blei [1] and Heinrich [3], we interpret LDA’s generation of the friendship data in a social network with N users (each user has arbitrary N_u friends) and K topic communities as follows:

- i. Sampling topic probability mixture $\vec{\theta}_u$ for each user u from the Dirichlet distribution with a prior of \vec{a} , where $\vec{\theta}_u = \{\theta_{u,k}\}_{k=1}^K$ represents the degree to which u likes about each topic k . At the meantime, sampling a distribution $\vec{\varphi}_k$ for each topic k over all the users from the Dirichlet distribution with a prior of $\vec{\beta}$, where $\vec{\varphi}_k = \{\varphi_{k,u}\}_{u=1}^U$ represents the possibility of each user being added by others as a friend in topic k .
- ii. For the n^{th} position in user u ’s friend list that has N_u positions for potential friends: firstly, sampling a topic z_a ($a = [u, n]$) for the n^{th} friend from $\vec{\theta}_u$ (this represents that user u will add a new friend who is active in this very topic for this friend position) and secondly, sampling a friend f_a according to
$$p(f_a | \vec{\varphi}_{z_a}, z_a) = \varphi_{z_a, f_a}.$$
- iii. Repeat step 2 till all friends of all users are generated.

However, it can be easily found that $\vec{\theta}_u$ and $\vec{\varphi}_k$ are correlated, instead of being independent of each other: for an arbitrary topic k , the more a user likes about it, the more likely this user could be added by other users who also like the topic k to their friend lists. Or, namely, the higher the probability $\theta_{u,k}$, the higher $\varphi_{k,u}$ is.

We solve this correlation problem by adding a new parameter that is directly proportional to $\vec{\theta}_u : \vec{\pi}_u^{(k)}$ that represents the degree to which u accept other users from

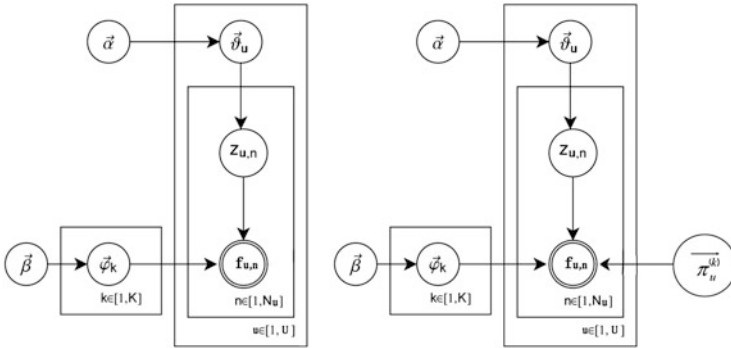


Fig. 142.1 Bayesian networks of LDA (left) and Tri-LDA (right)

the same social network in topic k as his or her friends. In the meantime, we give $\vec{\varphi}_k$ a new meaning to make the generation process more natural: the activeness of each user in topic k . The possibility of an arbitrary user u adding another user who is active in topic z_a to the n^{th} position in his or her friend list as friend f_a is determined by the joint distribution of $\vec{\varphi}_{z_a}$ and $\vec{\pi}_u^{(z_a)}$, which is expressed by the following equation:

$$p\left(f_a \mid \vec{\varphi}_{z_a}, z_a, \vec{\pi}_u^{(z_a)}\right) = \varphi_{z_a, f_a} \pi_{u, f_a}^{(z_a)} \tag{142.1}$$

By adding this slight modification, we get the modified LDA model—Tri-LDA. Figure 142.1 (right) displays the Bayesian network structure of Tri-LDA. In this chapter we simplify $\vec{\pi}_u^{(k)}$ as: $\pi_{u_1, u_2}^k = \begin{cases} 0 & \text{if } u_1 = u_2 \\ \theta_{u_2, k} & \text{if } u_1 \neq u_2 \end{cases}$

That means, firstly, no user would add himself or herself to his or her friend list and, secondly, the degree to which user u_1 accepts another user u_2 as a friend in topic k equals to $\theta_{u_2, k}$, the degree to which user u_2 likes about topic k . Therefore based on the simplification, we can get the following equation:

$$p\left(f_a \mid \vec{\varphi}_{z_a}, z_a, \vec{\pi}_u^{(z_a)}\right) = \varphi_{z_a, f_a} \theta_{f_a, z_a} \tag{142.2}$$

There are two methods that are commonly used to infer latent parameters for high-dimensional probabilistic models like LDA: EM (Expectation Maximization) and Gibbs sampling. In this chapter, for Tri-LDA, we choose Gibbs sampling to infer $\vec{\theta}$, the matrix that represents the degree to which each user likes about each topic in a social network.

Gibbs sampling is a simple implementation of the Monte Carlo algorithm, which is usually used to infer the latent parameters of high-dimensional probabilistic topic

models [4]. Gibbs sampling starts from a randomly sampled initial state, then continuously transits to new states based on the current state to build up a Markov chain. After a certain number of transitions, the Markov chain would become stable. The stable state of the Markov chain can be regarded as an approximated observation of the query distribution. In this chapter we run Gibbs sampling methods on the social network to get an approximated observation of $\vec{\theta}$: the topic indices \vec{z} from which users add their friends to his or her friend list. We specify the implementation of Gibbs sampling on a social network as the following steps:

- i. Randomly allocate a topic k for every friend in every user's friend list.
- ii. In an arbitrary user u 's friend list, choose the n^{th} friend position, indexing it with i . Remove the topic k that previously allocated on f_i , and then resample a new topic for it based on the following two known conditions: all the friends of all users \vec{f} and all the topics of all friends in all users' friend lists except for the topic of f_i : z_i .
- iii. Repeat step ii through all friends in user u 's friend list.
- iv. Repeat step iii through all users in the social network.

In step 2, the posterior probability $p\left(\vec{z}_i | \vec{z}_{-i}, \vec{f}\right)$ needs to be computed. According to Tri-LDA stated above, we can get the following equation:

$$p\left(\vec{f}, \vec{z} | \vec{\theta}, \vec{\varphi}, \vec{\pi}\right) = \prod_{u=1}^U \prod_{k=1}^K \theta_{u,k}^{n_u^{(k)} + n_{u'}^{(k)}} \prod_{k=1}^K \prod_{u=1}^U \varphi_{k,u}^{n_{u'}^{(k)}} \tag{142.3}$$

where n_u^k denotes the number of friends who are allocated with topic k in the friend list of user u and $n_{u'}^k$ denotes in the friend lists of other users the number of times that user u is allocated with topic k . Then, we get the following equation:

$$p\left(\vec{f}, \vec{z} | \vec{a}, \vec{\beta}, \vec{\pi}\right) = \prod_{k=1}^K \frac{\Delta\left(\vec{n}_{u'} + \vec{\beta}\right)}{\Delta\left(\vec{\beta}\right)} \prod_{u=1}^U \frac{\Delta\left(\vec{n}_u + \vec{a} + \vec{n}_{u'}\right)}{\Delta\left(\vec{a}\right)} \tag{142.4}$$

where $\vec{n}_{u'} = \left\{n_{u'}^{(k)}\right\}_{k=1}^K$, $\vec{n}_u = \left\{n_u^{(k)}\right\}_{k=1}^K$. Assume the i^{th} friend in u 's friend list is user u_o , and then we get the following posterior distribution $p\left(\vec{z}_i | \vec{z}_{-i}, \vec{f}\right)$:

$$\begin{aligned}
 p\left(z_i = k \mid \vec{z}_{-i}, \vec{f}\right) &\propto \frac{p\left(\vec{f} \mid \vec{z}\right) p\left(\vec{z}\right)}{p\left(\vec{f}_{-i} \mid \vec{z}_{-i}\right) p\left(\vec{z}_{-i}\right)} \\
 &\propto \frac{n_{u_o, -i}^{(k)} + \beta_{u_o}}{U} * \left(a_k + n_{u, -i}^{(k)} + n_{u'}^{(k)}\right) * \left(a_k + n_{u_o}^{(k)} + n_{u_o, -i}^{(k)}\right) \\
 &\quad \sum_{u=1} n_{u', -i}^{(k)} + \beta_u
 \end{aligned} \tag{142.5}$$

where $n_{u_o, -i}^{(k)}$ denotes the number of times that user u_o is allocated with topic k excluding i in all other users' friend lists and $n_{u, -i}^{(k)}$ denotes the number of friends who are allocated with topic k in the friend list of user u excluding i . After running Gibbs sampling on the social network, we get all the topic indices from which all friends of all users are sampled that can be regarded as an approximated observation of $\vec{\theta}$. With the approximated observation, we can compute the expectation of the Dirichlet distribution and use it as an estimator for the desirable $\theta_{u,k}$, the degree to which a user u likes about topic k (Table 142.1).

$$\theta_{u,k} = \frac{n_u^{(k)} + a_k + n_{u'}^{(k)}}{\sum_{k=1}^K n_u^{(k)} + a_k + n_{u'}^{(k)}} \tag{142.6}$$

142.3 Experiment

We collect a data set that includes the connections between 2,315 Sina Weibo users. The friends of each user are limited to be the users in this data set. By reviewing the data set, we find that around 70% of nodes (or users) are richly connected with each other, and around 10% of nodes are relatively isolated. We randomly choose 2,179 of them as the training data set and the remaining as test data set. By manually checking the posts and tags those users posted on the site, we find there are 17 different topics involved in the data set: information technology, business, finance, military, charity, food, education, car, travel, photography, everyday life information, show business, politics, sports, literature, painting, and religion. Based on the contents of each user's post page, we score the degrees to which each user is interested in those topics. By using the scores, we represent each user's interest by a vector with 17 elements: \vec{h}_u . Then the similarity of interests between two users u_1, u_2 can be expressed as:

$$\text{Sim}_{u_1, u_2} = \frac{|\vec{h}_{u_1} \cdot \vec{h}_{u_2}|}{|\vec{h}_{u_1}| |\vec{h}_{u_2}|} \quad (142.7)$$

In this experiment, we first run Gibbs sampling based on the Tri-LDA model to discover the underlying topic communities. We measure the effectiveness of Tri-LDA by computing the fittingness of the outputted result to the actual topic communities manually labeled by us. We also run k -medoid clustering algorithm on the texts and tags posted by the users and see users of each cluster in the output as a topic community [5]. To test the generalization property of Tri-LDA, we compare the predictive perplexity of Tri-LDA with that of k -medoid clustering mentioned above.

In the training process of LDA, we set the prior parameter of a in the range [0.1, 1.5] with an incremental step of 0.1, the prior parameter of β in the range [1.0, 10.0] with an incremental step of 0.1, and the topic number K in the range [5, 20] with an incremental step of 1. We run Gibbs sampling with all the possible parameter combinations and select the one whose output has the best fittingness value. After the learning process, the desirable topic probability mixture $\theta_{u,k}$ for every user u , which represented the degree to which user u likes about a topic k , is outputted. We set a threshold value 0.25 for $\theta_{u,k}$: if $\theta_{u,k} \geq 0.25$, then we conclude that u is interested in topic k . Denoting T_k as the set of users in the k^{th} topic community, then $T_k = \{u | \theta_{u,k} \geq 0.25\}$.

In the real-world social networks, users from the same topic community always have relatively high interest similarities. To measure the credibility of the learning result, we use the interest similarity equation stated above to compute the interest similarity between each two users in a topic community obtained by Tri-LDA and take its averaged value to measure the fittingness of the learning result to the real-world situation. We express the fittingness of the learning result as the following equation:

Table 142.1 Pseudocode of Gibbs sampling algorithm for Tri-LDA

Initialization
for all users $u \in [1, U]$ in the social network do
 for all friend positions $n \in [1, N_u]$ in user u 's friend list do
 randomly allocate n with a topic $k \in [1, K]$

Building a Markov Chain
while not convergent do
 for all users $u \in [1, U]$ in the social network do
 for all friend positions in user u 's friend list do
 resample n with a new topic k according to equation (142.5)

Parameter estimation
for every user u in the social network do
 compute $\vec{\theta}_u$ according to equation (142.6)

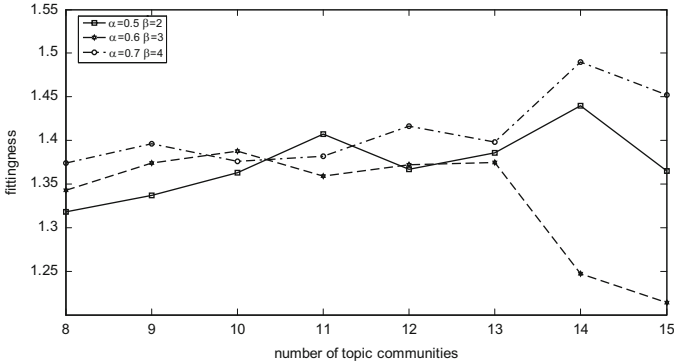


Fig. 142.2 Fittingness of the Tri-LDA model

$$f = \frac{\sum_{k=1}^K \text{avg}(\text{Sim}_k)}{K} \tag{142.8}$$

where $\text{avg}(\text{Sim}_k)$ denotes the average interest similarity between every two users in a topic community. In the experiment we find that when $a = 0.7, \beta = 8, k = 14$, the topic communities outputted by the algorithm have the best fittingness value. Figure 142.2 displays the fittingness value of the learning results under some of the parameter settings in this experiment. The result shows that the average fittingness f under different parameter settings in this experiment is around 0.70, which indicates the learning results can basically reflect the actual interest similarities between users in the selected social network.

We denote the degree to which a user d in the test data set likes about topic k as $\theta_{d,k}$, then

$$\theta_{d,k} = \frac{n_d^{(k)}}{N_d} \tag{142.9}$$

where $n_d^{(k)}$ is the number of friends who belong to topic community k in d 's friend list and N_d is the total number of friends in d 's friend list. Use the learning result to predict the interest of users in the test set, and express the predictive perplexity of the predication with the following equation:

$$\text{perplexity} = \frac{\sum_{d=1}^D H(d)}{D} \tag{142.10}$$

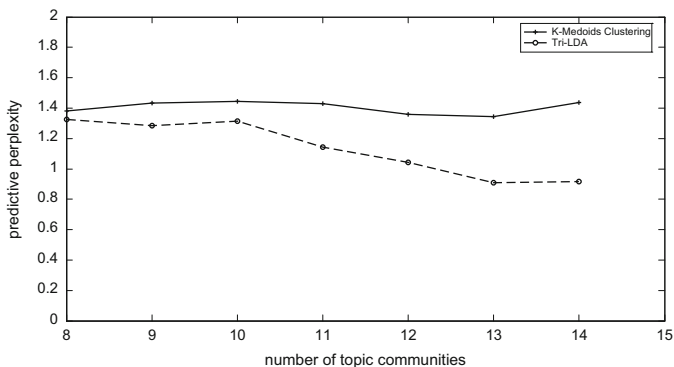


Fig. 142.3 Comparison of predictive perplexity between Tri-LDA and k -medoid clustering

where $H(d) = -\sum_{k=1}^K \theta_{d,k} \log \theta_{d,k}$ and D is the total number of users in the test data

set. A relatively lower predictive perplexity always suggests better generalization property. We compare Tri-LDA's predictive perplexity, when $a=0.7$, $\beta=8$, $k=8, 9, 10, 11, 12, 13, 14$, with the predictive perplexity of k -medoid clustering with the medoid number as 8, 9, 10, 11, 12, 13, 14, respectively. Figure 142.3 displays the comparison between the predictive perplexity of Tri-LDA and k -medoid clustering in this experiment. The result indicates that Tri-LDAs have a lower predictive perplexity than k -medoid clustering; therefore Tri-LDA has a better generalization performance that can be used to predict the interests of unseen users than k -medoid clustering in this experiment.

Conclusion and Future Work

We propose a modified LDA model—Tri-LDA—to detect topic communities in social networks by processing network structure data. The experiment result shows that the learning result is consistent with the realistic topic communities hand-labeled by us in the test data set. Also the experiment result shows that Tri-LDA has a decent generalization performance in predicting the interests of unknown users. In the future we plan to add some further modification to Tri-LDA to allow it to process the combined data of network structure and communications between users to detect the underlying topic communities in a social network.

References

1. Hofmann T. Probabilistic latent semantic analysis. In: Proceedings of the 15th conference on uncertainty in artificial intelligence. Stockholm: Morgan Kaufmann; 1999. p. 289–96.
2. Blei DM, Ng A. Latent Dirichlet allocation. *J Mach Learn Res.* 2003;3:993–1022.
3. Heinrich G. Parameter estimation for text analysis[DB/OL]. 2005. faculty.cs.byu.edu
4. LianWen Z. Introduction to Bayesian networks [M]. Beijing: Science Press; 2006 (In Chinese).
5. Li X. Tag-based social interest discovery. In: Proceeding WWW '08 Proceedings of the 17th international conference on World Wide Web. US: ACM; 2008. p. 675–84.

Chapter 143

Communications and Quality Aspects of Smart Grid Network Design

Vladimir Sobeslav and Josef Horalek

Abstract This chapter presents the global perspective of communication infrastructure and its specific use and the application approaches and specificities of Smart Grid network features. It presents a general view of Smart Grid domain qualities. It further specifies the distribution flows from the perspective of application and use of Smart Grid technologies and their adaptation to individual regions on the basis of their global analysis in respect to the dependency of electricity distribution, energy resources, and alternative and standard energy accessibility. This chapter shows the implementation analysis of the Smart Grid networks by the most prominent producer and distributor of electric power in the Czech Republic.

Keywords Energy management • Power distribution lines • Power grids • Smart Grids • Current supplies • Power system reliability substation automation

143.1 Introduction

The Smart Grid has become a popular and modern issue recently. Thanks to its dynamic development, Smart Grid offers various topical perspectives. At first, Smart Grid is subject to energy-communicational perspective considering the large variety of the communication norms used in energetics. They not only include the family of IEC 60870, IEC 61850, or IEC 61968/61970 standards [1, 2].

Principles and structure of the Smart Grid network communication offer another perspective of their use as the main component of the intelligent control and management of energy networks. Although this perspective may appear elemental and fully solved, the reality is different; due to frequent focus on local issues, such as the communication of alternative electrical energy sources with the SCADA systems, the possibility of Smart Grid implementation is significantly influenced by requirements of the network infrastructure and requirements of individual communication elements in Smart Grid networks. This point of view is accentuated [3, 4]

V. Sobeslav (✉) • J. Horalek
Computer Networks and Operating System Laboratories, Faculty of Informatics
and Management, University of Hradec Kralove, Rokitanskeho 62,
Hradec Kralove 500 03, Czech Republic
e-mail: vladimir.sobeslav@gmail.com

© Springer International Publishing Switzerland 2015
W.E. Wong (ed.), *Proceedings of the 4th International Conference on Computer
Engineering and Networks*, Lecture Notes in Electrical Engineering 355,
DOI 10.1007/978-3-319-11104-9_143

1255

where the authors are focusing on the analysis of quality and meaning of the information transferred, which is highly symptomatic of Smart Grid networks. More technical Smart Grid perspectives are provided [5], where the authors correlate the connection between the IEC 61850 protocol and the communication of ISO/OSI network model with the application of packet analyzer. The question yet to be resolved concerns the Smart Grid network particularities and their components and general architecture; according to the implementation of Smart Grid networks such as intelligent remote data collection from electrometers or remote optimization of electricity consumption units that use the Smart Grid metering, these issues are insightfully treated; however, it only focuses on the provision of electricity and its way from the source to the distributor. For example, this perspective is offered. It can be used generally for understanding the requirements of Smart Grid networks if we ignore the photovoltaic system specificities [6]. Similarly, the authors solely considered the use and optimization of Smart Grid networks in the field of wind power plants [7]. The authors provided a groundbreaking and comprehensive treatment of implementation and optimization of Smart Grid networks [8].

Furthermore, the project [9] cannot be omitted although it predominantly deals with the practical implementation of Smart Grid networks and their reliability. It introduces reliability and measurement calculations. This project is also connected [10], which deals with the error detection of Smart Grid network.

This chapter is a result of the analysis of the implementations and use of Smart Grid networks at a Czech location selected by the most prominent producers and distributors of electric power; therefore, this chapter constitutes a different perspective from other researches in the field. This analysis scrutinizes not only the horizontal perspective of Smart Grid implementation but also the vertical perspective, in other words, the perspective from distributor to individual customers of various types. The present local specification is influenced by the regional activity of the company; nevertheless, their generalization enables to realize similar solutions in the whole of Europe, where the citizen stratification differs from the case of the Czech Republic.

143.2 Smart Grid Concept of Power Distribution

This analysis presents similar understanding and approaches toward the Smart Grid issues as treated [11]. Similarly [12], this chapter specifies the approach to the migration of the IT technologies to the Smart Grids and further accentuates a classical perspective via the ISO/OSI model in the process of implementing the network elements into Smart Grid networks; however, the Smart Grid implementation and its possibilities, uses, and optimizations are influenced by its geographical locations and classical distribution network topology. The requirements of both the Smart Grid network implementation and its individual organizational networks, as involved in this analysis, are greatly influenced by the current situation in the

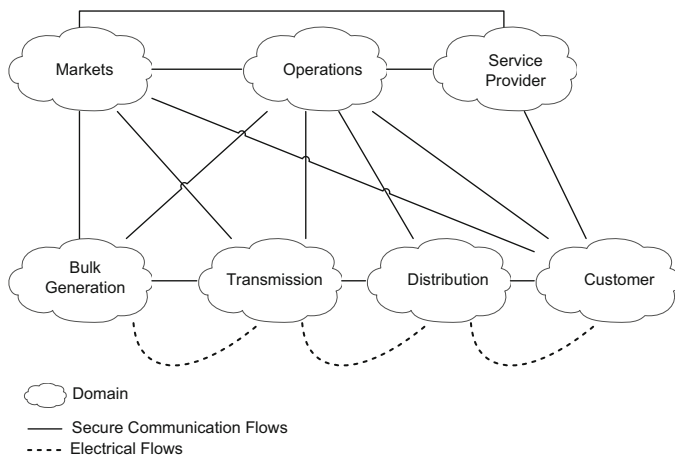


Fig. 143.1 Smart Grid domains

Czech Republic, where the conditions in similar geographical settings of distribution networks are similar to those in Western Europe.

Figure 143.1 depicts the domains affected by the changes related to the implementation of the Smart Grid concept. It is a large field (territory), but this work deals with the distribution of electric energy and its control. The significance and complexity of the specification of individual requests for Smart Grid concept in the field of electric energy distribution and its control shall be highlighted in comparison with the state-of-the-art condition.

143.3 Secure Smart Grid Distribution Flows

The Smart Grid concept is primarily to optimize the operation of the distribution system and the consumption control at individual consumer level. The optimization of the local sources and their use during the control of self-contained regions of distribution network are also important. The Smart Grid distribution enables the island operation and its control, limits the number of blackouts, and minimizes the blackout impact by automated interference in network configuration (self-healing). Besides, efforts are made to increase the resistance of the energy system, increase the operation efficiency, provide detailed information to the customer concerning his consumption, balance the peak load of the network, and decrease the influence of unpredictable sources on the network stability. The electric energy distributors require a high level of automation of the controlling processes and systems, close cooperation with the central control systems (Dispatching Control System), temporary autonomous operation during blackouts between the region and central systems (data island), and high security of solution. Because of their complexity and high investment, Smart Grid regions evolve gradually with great differences in

terms of the regional sizes, source possibilities, population density, consumption, and balance. On the basis of these main differences, it is necessary to define the type of regions, which can cover the whole distribution system with respect to regional distribution characteristics. The following section briefly outlines various types of regions in respect of Smart Grids: the region of high population density, which is a small-scale utilization with high population density; the region of scattered population density, which consists of a number of medium-sized large cities and smaller communities; the industrial region, which features a highly developed energy-intensive industry; and the region of low population density, which lacks regional resources and features problematic development for many reasons.

Communicative infrastructure is a crucial element of the whole network. Without the complex of corresponding communication, it means to create the required vertical and horizontal connections, and Smart Grid concept cannot be realized. It shall be established based on the existence of the communication connection with the backbone communication system of distribution at the abovementioned structure level. The distribution switching station of 110 kV/hV system should be designed with regard to its sufficient flexibility and usual solutions used within its distribution system. This point is the place which ensures the connections of all partial subsystems of individual layers according to their requirements. Inconsistent development requires integration or coexistence of other kinds of solutions different from the required vertical connections at a lower level (e.g., application of GSM/GPRS communication in controlling systems of switching points in the network). This kind of communication is solved centrally; there is a direct vertical connection between the given point and the central level. This solution rather complicates the potential use for local control of such constructed switching points. A typical division of communication infrastructure into individual network segments is depicted in Fig. 143.2. The backbone network also provides the connection to the SCADA system. The MAN SG (Metropolitan Area Network Smart Grid)

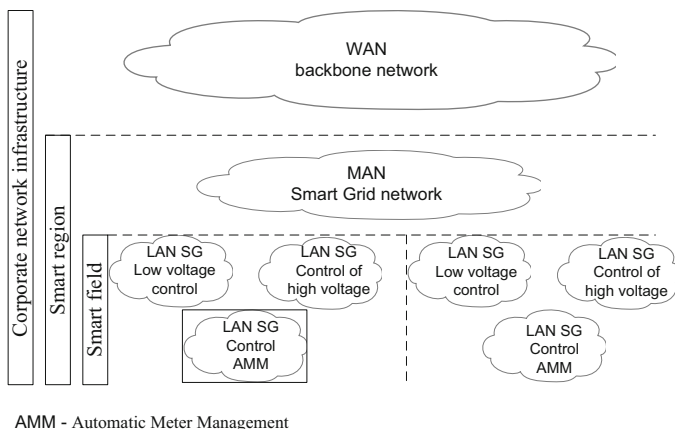


Fig. 143.2 Segments of the communications infrastructure

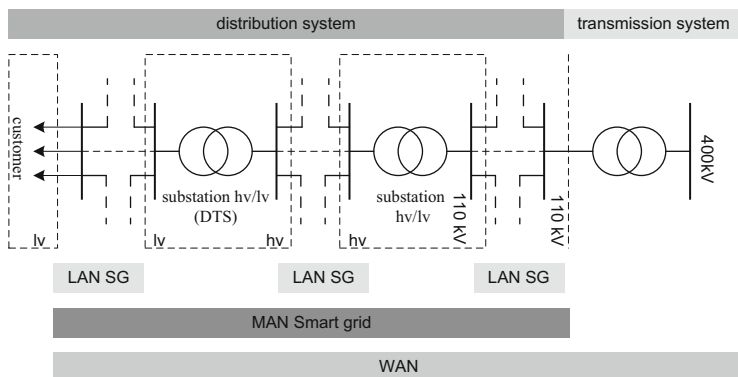


Fig. 143.3 Relationship between IT network and distribution system

network is also connected to the backbone network; MAN SG provides connection between individual LAN SGs (Local Area Network Smart Grid), which represents individual local networks of Smart Grid architecture. The MAN SG is typically spreading at the level of one smart region, which connects individual LAN SG local networks at the smart field level.

Regarding the requirements for communication infrastructure, we may define the following levels and fields that are or can be components of communication infrastructure within Smart Grid concept.

The vertical connection between technology controlling systems and central level is applied both to the MAN SG level and LAN SG level. These connections are mostly realized in case of 110 kV or hv objects; their fundamental application is essential in regions which can be controlled (DTS), but mostly not yet controlled nowadays. If lv objects are controlled, lv increases in each given hv field.

In case of the horizontal connection for protection function adaptation (e.g., between neighboring hv substations), it is necessary to realize the data networks to enable fast and reliable communication, which can be achieved by using simple technology (without complicated processing of transmitted data) with minimum intermediate elements (Fig. 143.3).

143.4 Requirements for the Smart Grid Network Elements

On the basis of executed analysis, the generally valid requirements on this type of networks may be specified. The Smart Grid implementation in the Czech environment is influenced by the way of construction, operation, and control of distribution network. The task of SG is to ensure the function and distribution of electric energy in the hv network part and adjacent lv network in the following extent: automation of hv network including hv objects part of transformation of hv/lv (DTS), substation hv DTS, and automation of lv network in hv/lv objects of transformation (DTS),

substation I_v DTS and isolation and secure boxes, possibly in bifurcation boxes of the I_v network. This basic set of distribution network requires a corresponding communication technology type. Each unit of the energy system will be remotely controlled and monitored and define a basic set of requirements on permeability, latency, and reliability.

The permeability describes the speed of transmitted data from the source device to the target device. It takes a message sent from the source device to the target device. Reliability is affected by electronic or magnetic interferences or meteorological conditions. The goal of efficient Smart Grid network element architecture is to have maximum permeability, low latency, and high reliability. Figure 143.4 shows basic organization of physical communication infrastructure in Smart Grid region.

Protection network and command network are organized into a circuit for communication redundancy in case of switch blackouts. This network transmits commands and GOOSE communications. Access network for Smart Grid region connection to backbone is MAN and WAN network, through which it is connected to the central systems. Rather than physical communication infrastructure, we

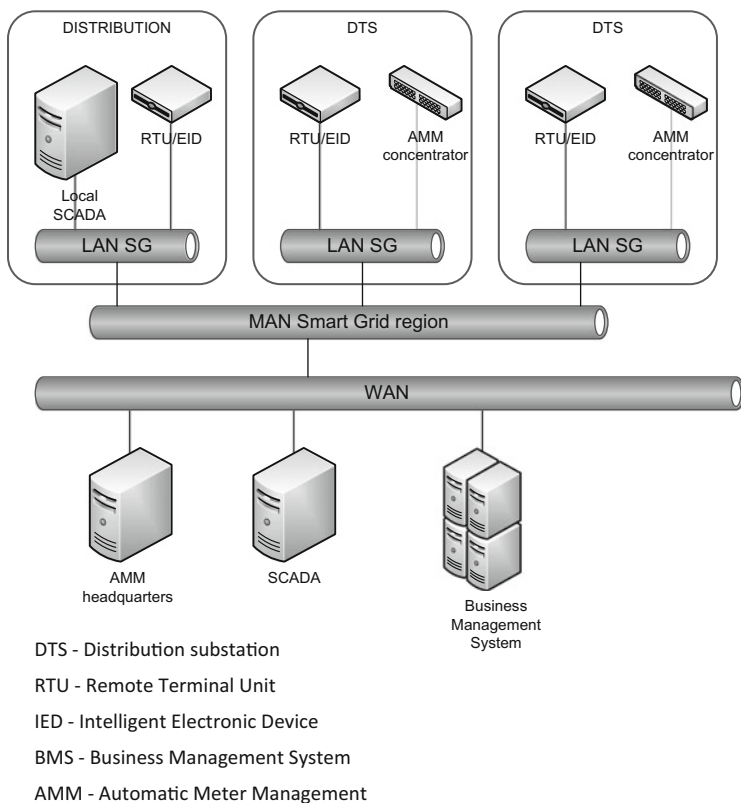


Fig. 143.4 Basic scheme of the communication infrastructure

recommend the implementation of virtual LAN networks according to IEEE 802.1Q standard. Individual networks will be used for separating individual communication types. The separation of individual communication types is substantial to ensure qualitative parameters of service (QoS) for individual communication types and logical separation of individual operation types for security reasons. Basic VLAN networks are used for security, respectively, GOOSE communication on horizontal level between IED and various DTS devices. Considering the fact that the network is also used for control commands and GOOSE communication, high reliability and low latency technologies such as optical lines, BPL, and WiMAX are recommended. The design of the Smart Grid network should also contain primary and backup communication lines by preferably using different technologies. The optical fibers fulfill the challenging demands of network safety, throughput, and other qualities of services criteria. The utilization of BPL and WiMAX technologies is rather inappropriate because of their security and transmission stability mechanism. The Ethernet and its industry sub-versions is the fundamental protocol, which is implemented at higher network communication layers. The access network to the Smart Grid central system and the backbone of the region are MAN and WAN networks. This kind of network technology efficiently transfers a large amount of data over long distances including the control commands and priority settings (higher latency tolerance). The communication parameters and the Quality of Service (QoS) mechanisms are very important to the design of Smart Grid networks.

Conclusion

In order to meet the elemental aims of Smart Grid, effective communication with network elements on the consuming side must be ensured. The absence of standards for interoperability between data concentrator AMM and RTU units cannot provide the desired outcome, i.e., management of appliances via smart electrometers; therefore, the chapter provides a different perspective. Unlike similar analyses, it accentuates not only the horizontal perspective of Smart Grid implementation but predominantly the vertical perspective, i.e., from the distributor to various individual customers. The present regional specification is influenced by the local operation of producers, although the generalized results can be realized all over Europe, where the citizen distribution is the same as that in the Czech Republic. This work and the contribution has been supported by project “SP/2014/05—Smart Solutions for Ubiquitous Computing Environments” from the University of Hradec Kralove.

References

1. Wu J, Zhang P, Yu J. IEC 61968 standard-based distribution systems integration solutions and application research. In: 2nd International conference on energy, environment and sustainable development, vol 614–615, issue 2. Jilin: EESD 2012; 2012. p. 785–91.
2. Horalek J, Sobeslav V. Remote control in power substation automation. In: Recent researches in circuits, systems, communications and computers. 1. Puerto De La Cruz: WSEAS; 2011. p. 110–7.
3. Li W, Liu J, Tian W. Study on classification of information to realize grid intelligent. In: Environment and sustainable development, vol 614–615, issue 3, Jilin: EESD 2012; 2012. p. 1706–9.
4. Krejcar O, Frischer R. Real time voltage and current phase shift analyzer for power saving applications. *Sensors*. 2012;12(8):11391–405.
5. Changhun L, Myungoh P, Jiyoung I, Inwhhee JI. Design and implementation of packet analyzer for IEC 61850 communication networks in Smart Grid. *Computer Applications for Communication, Networking, and Digital Contents Communications in Computer and Information Science*. 2013;350(12):33–40.
6. Sechilariu M, Wang BC, Locment F. Building integrated photovoltaic system with energy storage and Smart Grid communication. *IEEE Trans Industr Electron*. 2013;60(4):1607–18.
7. Chen Y, Xu Z, Ostergaard J. Islanding control architecture in future smart grid with both demand and wind turbine control. *Electric Power Syst Res*. 2013;95(6):214–24.
8. Khan RH, Khan JY. A comprehensive review of the application characteristics and traffic requirements of a smart grid communications network. *Computer Networks*. 2012;57(5):1–21.
9. Gudzius S, Gecys S, Markevicius LA, Miliune R, Morkvenas A. The model of Smart Grid reliability evaluation. *Electron Electr Eng*. 2011;116(10):25–8.
10. Gudzius S, Markevicius LA, Morkvenas A. Characteristics of fault detection system for Smart Grid distribution network. *Electron Electr Eng*. 2011;112(6):123–6.
11. Cepa L, Kocur Z, Muller Z. Migration of the IT technologies to the Smart Grids. *Electron Electr Eng*. 2012;123(7):123–30.
12. NIST Smart Grid Homepage. NIST Smart Grid [online]. The National Institute of Standards and Technology (NIST) is an agency of the U.S. Department of Commerce, 24. 8. 2010, 29. 3. 2012. <http://www.nist.gov/smartgrid/>. Accessed 16 April 2012.

Chapter 144

An Adaptive Greedy Geographical Routing Protocol for Mobile Multihop Wireless Network

Feng Liu, Jianli Li, Gong Qin, and Fanhua Kong

Abstract In this chapter, we analyze the performance deficiency of traditional routing protocol based on the actual geographical setting and propose a novel adaptive greedy geographical routing protocol. Through analyzing two factors affecting network mobility—the moving speed and the pause time of nodes—the protocol adjusts the beacon sending cycle and selects the better next hop to achieve the goals of reducing overload and increasing the delivery success ratio. Simulation results show that the protocol can acquire better effects compared to GPSR (greedy perimeter stateless routing).

Keywords Ad hoc • Greedy forwarding • Adaptive • Geographical position • Routing protocol

144.1 Introduction

In the numerous attractive research fields of the mobile ad hoc network (MANET), the route problem is still one of the most basic and challenging problems [1, 2]. With the development of the locating device and algorithm, the greedy routing protocol based on geographical location information has attracted the attention of scholars. In this kind of protocol, the moving node gets the information such as position and address of the neighbor nodes through periodically sending beacon group and builds the information database of the neighbor node, and then every intermediate node uses the greedy strategy to choose the most suitable neighbor node to send the group till to the goal node. The existing greedy strategies include GPSR (greedy perimeter stateless routing) [3], NC (Nearest Closer) [4], DIR (Directional Routing) [5], and so on. But now most of the greedy routing protocols based on geographical locative information have some common disadvantages including:

F. Liu (✉) • J. Li • G. Qin • F. Kong
Department of Electronic Information, Hubei Three Gorges Polytechnic,
443002 Yichang, Hubei, China
e-mail: leocandylvjojo@gmail.com

© Springer International Publishing Switzerland 2015
W.E. Wong (ed.), *Proceedings of the 4th International Conference on Computer Engineering and Networks*, Lecture Notes in Electrical Engineering 355,
DOI 10.1007/978-3-319-11104-9_144

1263

1. High node density. The number of nodes which distribute randomly in certain areas is so large that the chance appearing the phenomenon of void and communication temporary blindness is very small, which has covered some reliable problems based on geographical information routing protocol and appearing occasionally in certain problems.
2. Slow node speed. In MANET, the mobility of node is one of the main characteristics. In the process of low speed or even stop, the network has a higher success rate of packet delivery [3, 6]; at the same time the phenomenon of communication temporary blindness will appear rarely. On the contrary, the node in high speed will hardly ensure the success of the retransmission.
3. Long stay time. In most models, the pause time plays an important role that reflects the mobility of node. The network node in stationary state obviously has better performance [3]. The longer stay time means that there are more nodes in stationary state, but this phenomenon does not conform to the mobility and actual situation of the MANET network.

In this chapter, we present an adaptive mobile ad hoc greedy geographical routing protocol which uses adaptive beacon exchange algorithm and automatically chooses the sending beacon cycle mainly based on the stay time of the node itself. The method makes the node in the transmission path able to maintain a relatively accurate neighbor list which reflects the location and speed information of neighbor nodes, which provides the real-time information for the greedy forwarding algorithm and reduces the protocol overload. The greedy forwarding strategies adaptively choose the next hop according to the rate of neighbor node preserved in the neighbor list that leads to higher success rates of retransmission.

144.2 Greedy Routing Protocols Based on Geographical Locative Information

The greedy routing protocol based on geographical locative information mainly consists of beacon exchange protocol and greedy forwarding algorithm. In this chapter, we will introduce and compare adaptive greedy perimeter stateless routing (AGPSR) with the GPSR protocol.

144.2.1 The Beaconing Protocol

Every node periodically sends a beacon to the broadcast MAC address, just including its identifier (e.g., IP address) and position information. To avoid synchronization of neighbors' beacons, the GPSR protocol jitters each beacon's transmission by 50 % of the interval B between beacons, so that the mean inter-beacon transmission interval is B , uniformly distributed in $[0.5B, 1.5B]$.

Upon not receiving a neighbor's beacon or effective data packet among the neighbor list after the time interval T , the forwarding node in GPSR assumes that the neighbor node has failed or stayed away from the wireless transmission distance, and deletes all the information of the node from the neighbor list. The 802.11 MAC layer also gives direct indications of link-level retransmission failures to neighbors. With the movement of the neighbor node, the position information of the neighbor will be out of date; the accuracy of the neighbor set will decrease since the new neighbor node will come into the area of wireless transmission. Because of that, to maintain the accuracy of the information of the neighbor list, the GPSR protocol should choose a suitable beacon interval B which is influenced by the mobility rate, the stay time of network node, and the distance of wireless transmission.

144.2.2 Greedy Forwarding Algorithm

Under GPSR, packets are marked by source node with their destinations' locations. As a result, a forwarding node can make a locally optimal, greedy choice in choosing a packet's next hop. Specifically, if a node knows the positions of all the neighbor nodes, the locally optimal choice of the next hop is the neighbor geographically closest to the packet's destination. Forwarding in this regime follows successively closer geographic hops, until the destination is reached.

144.3 Problem Descriptions and Improvement of the GPSR Protocol

144.3.1 The Density of Network Nodes

As described in Sect. 144.1, the performance of the GPSR protocol will be quite different for high or low node density. In the simulation environment, there is one node per 9,000 m² on average [3]. A radio range is nearly 200,000 m². As a result, there is an average of approximately 20 neighbors within range of the average node in these networks. At a high level of connectivity, and a high number of neighbor nodes, the packet delivery success rate is more than 99 % on average.

In a real-world scenario, however, the high density of network configuration is rarely achievable. For example, Figs. 144.1 and 144.2 show the packet delivery ratio of GPSR for 40 network nodes with identical traffic sources in the 1,000 by 1,000 m scenario. The density of network nodes is 1/25,000 at this time, i.e., there are only 8 neighbor nodes on average around every node. As is shown in the figures, the desired performance cannot be achieved with high node speed and longer pause time.

Fig. 144.1 The influence of the stay time on the success rate of packet delivery node

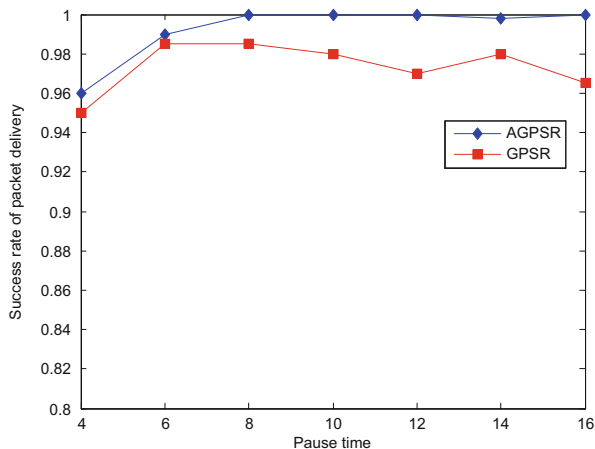
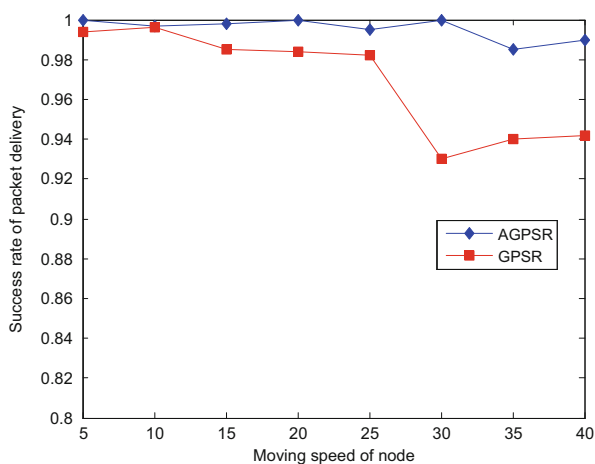


Fig. 144.2 The influence of the moving speed on the success rate of packet delivery



144.3.2 The Pause Time of Node

The pause time that reflects the degree of mobility plays an important role in the success rate of packet delivery in the GPSR protocol. From Fig. 144.1, one can see that the network mobility decreases with the increase of the pause time in the early time, which causes the high success rate of packet delivery. However, it will only rise to a certain point before the performance degrades significantly. The reason is that the density of network node is very low, which leads to more void areas in the network. In the case, the network topology is almost in stationary state at this time. There are not enough moving nodes to fill the void, which makes the forwarding rate decrease. A proposed self-healing on-demand geographic path routing protocol adjusts the beacon sending frequency based on the distance parameter s and works well [7]. In addition, the grid's location service (GLS) [8] combined with

geographic forwarding allows the construction of ad hoc mobile networks that scale to a larger number of nodes. Every mobile node periodically updates the position of a small set of nodes within its positional service area, which prevents all neighbors to send beacons. Considering the nodes may not only move around but also enter and leave the network, the chapter presented a solution to the presence detection problem [9]. It uses a Bloom filter-based beaconing mechanism to aggregate and distribute information about the presence of network nodes.

In the chapter, an adaptive beacon sending mechanism that adjusts beacon interval based on the pause time of node is proposed. An optimal pause time P_{optimal} for GPSR can be obtained by achieving the best performance for packet delivery; consequently we set the beacon transmission interval B_{new} by the following formulation:

$$B_{\text{new}} = (P/P_{\text{optimal}})B \quad (144.1)$$

where P is the expected pause time for an individual node and B is the original beacon interval in GPSR.

Therefore, it is shown that the current network topology is unstable when the current pause time P is less than the optimal pause time P_{optimal} in GPSR, which suggests that the new beacon interval B_{new} should be shortened based on B . Based on Eq. (144.1), our mechanism increases the beacon sending frequency, which maintains the neighbor node's position information in real time; when P is larger than P_{optimal} , we can see that the ad hoc network is in the relatively stable period. In this case, the beacon sending frequency is decreased; subsequently the whole network load is reduced.

144.3.3 The Movement of Node

There is no doubt that the moving speed of node is an important indicator to measure the network mobility. With the increase of the movement rate, the position information of the neighbor nodes cannot be updated, which leads to the decrease in the success rate of packet delivery in the GPSR protocol. Figure 144.2 shows that the movement of node plays an important role in the success rate of packet delivery. It can be seen that the transmit success rate will decrease as the speed of movement increases.

The greedy forwarding strategy in GPSR has the advantages of high efficiency and easy to operate by selecting the next hop whose geographical position is closest to the destination. However, the node that has the shortest distance to the destination is the one that has the longest distance to itself. Based on the characteristics of the wireless network communication, the further the transmit distance is, the more serious the distortions of the signal are, and the higher the packet losing rate is. The authors proposed a forwarding strategy: the neighbor node that is closest to itself is

selected to be the next hop node so that we can decrease the temporary communication blindness in the ad hoc network [4]. The disadvantage of the approach is that the energy consumption and the delay on packet transmission will be a more serious problem as the increase in the hop counts. The DIR selects the neighbor as the next hop, whose direction is closest to the direction of the destination among all neighbor nodes [5]. However the DIR may create a routing loop in the worst case. The chapter proposed an on-demand protocol for searching for a multipath QoS route from a source host to a destination host in a MANET, where a multipath is a network with a source and a sink satisfying certain bandwidth requirement [10]. A distributed, randomized algorithm is proposed, where nodes make local decisions on whether to sleep or to join a forwarding backbone as a coordinator [11]. Each node bases its decision on an estimate of how many of its neighbors will benefit from it being awake and the amount of energy available to it.

To maintain the success rate of packet delivery, we present an AGPSR protocol based on the moving speed of nodes, which combines adaptive beacon exchange mechanism. Our proposed protocol has obvious advantages on reducing the communication temporary blindness and the network communication load. The detailed descriptions of AGPSR are listed in Algorithm 1. Note that the field of every beacon packet includes the position information of the current node and also the current speed value. The forwarding node usually chooses the neighbor of smallest speed in the neighbor set that is closer to the destination node than itself within the transmission. In particular, when multiple nodes in the neighbor set are in the quiescent state (i.e., the speed value is zero), the node that has the shortest distance to the destination node will be selected as the next hop.

Algorithm 1

```

Find_NextHop()
for each Neighbor Node(Location, Speed) ∈ N(self) do
  N=Find (N(self)) // Find the neighbor set that is closer to destination node
than itself
end for
Speedbest = N[0].Speed;
Dbest=Distance(N[0].Location , Destination. Location);
// Calculate the distance between itself and the destination node
for each n(Location, Speed) ∈ N do
  D=Distance (n. Location , Destination. Location);
  if (n.Speed <= Speedbest)
    if(n.Speed = Speedbest=0)
      if(D< Dbest) Dbest = D; nbest = n ;
    end if
  end if
  else Speedbest = Speed ; nbest = n ;
end if
end for
return nbest

```

144.4 The Simulation and Analysis

In this section, we evaluate the performance of the AGPSR protocol via simulations by the OPNET Modeler as a tool of network simulation. In order to illustrate the merits on the success rate of the average packet delivery and network load in MANET, we compared AGPSR with the GPSR protocol. In our scenario, 40 nodes with 802.11 MAC Wave LAN radios are randomly distributed in a $1,000\text{ m} \times 1,000\text{ m}$ area. All nodes move according to the random waypoint model, with a maximum velocity of 20 m/s. The source node randomly chooses the destination node: the size of the generated package is a constant 2,048 bit, 2 packages per second; the number of CBR is 16; the range of wireless transmission is 250 m. The sending cycle B of the stable beacon in the GPSR protocol is 3 s, and each simulation lasts for 15 min of simulated time.

144.4.1 The Success Rate of Packet Delivery

Figure 144.1 shows the pause time changed from 4 to 16 s; the moving speed of every node randomly gets the values between 0 and 20 m/s. We can see that the success rate of packet delivery is the highest when the pause time is about 8 s in the GPSR protocol, so P_{optimal} is set to 8 s and B_{new} equals to 3 (pause time/8). Based on the above calculated value, we can get the success rate of packet delivery on different pause times in AGPSR. Obviously, with the change of the pause time, AGPSR has higher success rate of packet delivery and better stability than GPSR except the extremely short pause time.

Figure 144.2 shows the success rate of packet delivery for the changing node's moving speed when the pause time is fixed at 8 s. With the increase of the move speed, the success rate in GPSR shows a trend of gradual decrease, but our AGPSR keeps better stability and higher success rate.

144.4.2 The Network Load

Figures 144.3 and 144.4 show the average network load under the condition of the same parameters in Figs. 144.1 and 144.2. Because of using the adaptive beacon sending mechanism, our mechanism decreases the beacon amount that is repeatedly sent for the big pause time, and the greedy forward algorithm based on the move speed of nodes maintains the high success rate of packet delivery and reduces the amount of retransmission; hence, the network load in AGPSR under the condition of all the parameters is still lower than GPSR.

Fig. 144.3 The influence of the stay time on average load

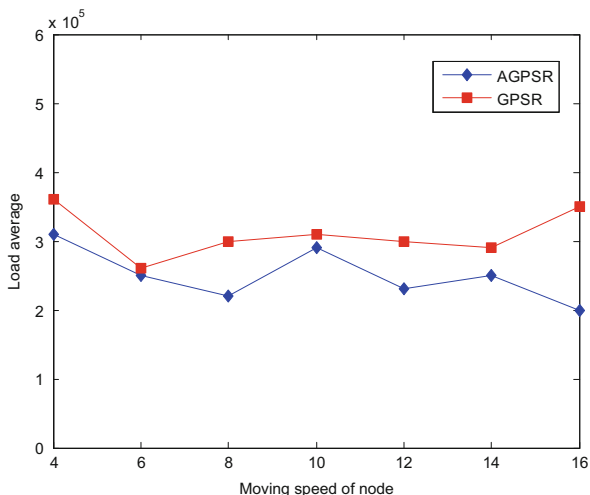
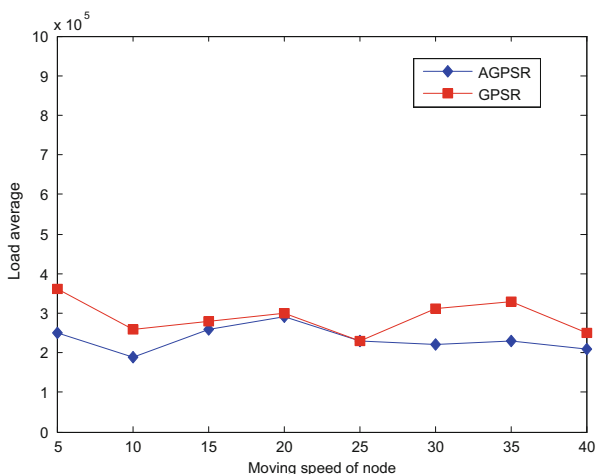


Fig. 144.4 The influence of the moving speed on average load



Conclusion

In this chapter, we present an adaptive geographical routing protocol AGPSR which improves the performance of the traditional GPSR based on position information in the MANET. In AGPSR, the selection of the next hop to transmit is not completely according to the greedy standard that has the shortest distance to the destination node, but takes the influence that move

(continued)

(continued)

speed of nodes on the network performs into consideration. The different beacon sending cycles for different pause times of nodes saved communication amount and decreased the whole load of the network. But the simulation shows the small improvement of this protocol on the hop count and the delay of the network; further improvement of the performance will be one of the subsequent research works.

References

1. Rahman AHA, Zukarnain ZA. Performance comparison of AODV, DSDV and I-DSDV routing protocols in mobile ad hoc networks. *Eur J Sci Res.* 2009;31(4):566–76.
2. Taneja S, Kush A. A survey of routing protocols in mobile ad hoc networks. *Int J Innov Manage Technol.* 2010;1(3):279–85. ISSN: 2010-0248.
3. Karp B, Kung HT. GPSR: greedy perimeter stateless routing for wireless networks. In: *Proceedings of the 6th annual international conference on mobile computing and networking.* Boston: ACM; 2000. p. 243–54.
4. Stojmenovic I, Lin X. Power-aware localized routing in wireless networks. *IEEE Trans Parallel Distrib Syst.* 2001;12(11):1122–33.
5. Kranakis E, Singh H, Urrutia J. Compass routing on geometric networks. In: *Proceedings of the 11th Canadian conference on computational geometry.* Ottawa: ACM; 1999. p. 1–4.
6. Ssu KF, Yang CH, Chou CH, et al. Improving routing distance for geographic multicast with Fermat points in mobile ad hoc networks. *Comput Netw.* 2009;53(15):2663–73.
7. Giruka VC, Singhal MA. Self-healing on-demand geographic path routing protocol for mobile ad-hoc networks. *Ad Hoc Netw.* 2007;5(7):1113–28.
8. Li JY, Jannotti J, Douglas SJ, et al. A scalable location service for geographic ad hoc routing. In: *Proceedings of the 6th ACM international conference on mobile computing and networking.* Boston: ACM; 2000. p. 380–91.
9. Tran TMC, Scheuermann B, Mauve M. Lightweight detection of node presence in MANETs. *Ad Hoc Netw.* 2009;7(7):1386–99.
10. Liao WH, Wang SL, Shen JP. A multi-path QoS routing protocol in a wireless mobile ad hoc network. *Telecommun Syst.* 2002;19(3):329–47.
11. Chen B, Jamieson K, Balakrishnan H, Morris R. Span: an energy-efficient coordination algorithm for topology maintenance in ad hoc wireless networks. *Wireless Netw.* 2002;8(5):481–94.

Chapter 145

A Coverage-Enhancing Algorithm Based on Local Virtual Force Equilibrium for Wireless Sensor Networks

Yujian Wang and Kaiguo Qian

Abstract To improve the coverage performance of nodes randomly deployed in a wireless sensor network, this paper proposes a local stress force–balanced method that enhances the coverage performance of mobile nodes. With this algorithm, the sensor nodes move to where the node stress virtual force by neighboring nodes in the local area (node two times the radius of perception) are in equilibrium to enhance coverage performance. A simulation experiment shows that the proposed algorithm quickly improves the coverage performance to more than 98 %. The algorithm is rapidly and efficiently deployed.

Keywords Wireless sensor network (WSN) • Stress balance • Node movement • Coverage performance

145.1 Introduction

Wireless sensor networks (WSNs) [1] are self-organizing network systems that are widely used in environmental monitoring, medical care, urban traffic management, warehouse management, and military reconnaissance and has emerged as a hot research field. The features of WSNs [2] include limited node energy, a nonuniform distribution of large-scale node networks, node mobility, and dynamic network topology. It is important for node deployment in wireless sensor network, which affects the cost of building a network, topology control, the design of routing protocols, and network coverage, and so forth. The deployment of randomly sown sensor nodes [3] is usually adopted in large-scale inaccessible wireless sensor network applications, in which it is hard to place sensor nodes in the desired location. Node coverage overlap or sparse distribution inevitably occur to form

Y. Wang

School of Information and Technology, Kunming University, 650214 Kunming, China

K. Qian (✉)

Department of Physics Science and Technology, Kunming University,

650031 Kunming, China

e-mail: qiankaiguo@qq.com

© Springer International Publishing Switzerland 2015

W.E. Wong (ed.), *Proceedings of the 4th International Conference on Computer Engineering and Networks*, Lecture Notes in Electrical Engineering 355,

DOI 10.1007/978-3-319-11104-9_145

1273

covered blind areas. To remedy this weakness, more sensor nodes are needed to satisfy coverage performance requirements, which will increase costs. In recent years, mobile sensor nodes have been designed [4, 5] for use in sensor network deployment. Using node mobility, nodes can be controlled in such a way that they move to the optimum location after random deployment to enhance coverage performance. The key technology involves controlling the mobile sensor node to set it at the ideal position so that the sensor nodes are uniformly distributed in the task area.

The mechanism of a virtual force-oriented control algorithm is introduced for controlling sensor network nodes moving to idea position [6]. This algorithm builds a virtual force model that takes into consideration the priority deployment location of the task area to node, interactions between sensor nodes and obstacle factors to node to control node movement to improve network coverage performance. Recent studies [7, 8] have appeared on a virtual force-oriented algorithm in mobile sensor networks that easily introduce node collisions for similarly oriented virtual force algorithms with no clear node moving targets in the process of movement. At the same time in the iteration process, to calculate the virtual force, temporary global information network coverage must be obtainable at any time, resulting in a high communication cost. A divide-and-conquer deployment strategy has been proposed [9] to realize complete coverage of subareas so as to cover an entire area by dividing the task into several subareas, every subarea selects part of nodes to constitute minimum cover sets. Based on an analysis of the distribution of sensor network nodes and research on the virtual force algorithm, it is found that, as long as the size of the virtual force model is reasonable, a consideration of the simple force balance between nodes can yield excellent coverage performance. The algorithm calculates the virtual force of a node within a range of 2 perception radii to control a mobile node. The simulation results show that in 20 iterative rounds the algorithm can gain more than 98 % coverage.

145.2 System Model and Problem Description

The following network node models are used to analyze the new algorithm performance.

145.2.1 Network Model

1. All nodes in the network are isomorphic, with the same perception, communication, and mobility. All nodes can acquire their geographic location information at any time.

2. The effect of obstacles in the monitoring area are not considered. Sensor nodes randomly deployed can obtain their own node serial number ID and their own location coordinates.
3. Assume that sensor nodes' perception radius is r and the communication radius is R . This meets the requirement for complete coverage of the region; at the same time, nodes can communicate with each other, so as to meet $R = 2r$.

145.2.2 Problem Description

A mutual acting force is introduced between the sensor nodes to control node movement to the ideal position using their mobility after random deployment to complete the coverage task for the whole area.

1. Number of nodes.

The number of sensor nodes needed to cover an area is calculated according to the honeycomb grid coverage, which uses n nodes of effective coverage for each sensor node to cover a task area $M \times N$. The minimum coverage node number is calculated by Eq. (145.1), which is used to determine the initial number of sensor networks:

$$n = \frac{2 \times M \times N}{3\sqrt{3}\pi r^2}. \quad (145.1)$$

2. Coverage ratio.

The coverage ratio is defined as the union sets of all sensor nodes comparing to the task area, calculated using Eq. (145.2):

$$d_{\text{coverage}} = \frac{\bigcup_{i=1}^N \text{cover area}(s_i)}{M \times N}. \quad (145.2)$$

3. Convergence time.

Convergence time is defined as the iteration rounds needed for the algorithm to meet the performance requirements. The shorter the convergence time, which means a faster sensor network deployment, the more applicable the algorithm is for practical applications.

145.3 Coverage-Enhancing Algorithm

The coverage-enhancing algorithm based on force equilibrium builds a stress force model according to the node location distribution and the distance between nodes. The stress force behaves nodes attraction and repulsion depending on whether the

distance is greater than the equilibrium distance. Nodes move under the action of attraction and repulsion. They stop when the attraction and the repulsion are in balance, then they update their own positions so as to establish random nodes that are redeployed after seeding. The force model is limited within the scope of the 2 times sensor radius in order to avoid having the node move long distances, that is, the node in the local area.

145.3.1 Stress Virtual Force Model

We set the sensing radius of the sensor nodes to r and the communication radius to R . Guarantee a complete coverage of the wireless sensor network to the nodes can communicate with each other, it sets R to $2r$. The general distribution of a local area after the random deployment of sensor nodes is shown in Fig. 145.1.

Nodes S2, S3, S4, and S5 are distributed around node S1. The distance d_{12} between S1 and S2 is small, which is less than the coverage radius r of sensor nodes, so the overlapping area of the two nodes is larger. The distance d_{15} between nodes S5 and S1 is equal to $\sqrt{3}r$, which is the balance distance. The distance d_{13} between nodes S1 and S3 is equal to two times the sensor node coverage radius; there is only one intersection point between each node, no overlapping coverage, which means the effective coverage area between the two nodes is the largest. But it is difficult to determine the position of the third node, S4. If the distance d_{14} from S4 to S1 is greater than R and d_{34} is greater than the distance R , then the area will be covered in holes. It can be proved that three sensor nodes constitute regular triangle coverage with the length of one side for satisfying $d_0 = \sqrt{3}r$, which achieves the best performance. In the analysis stress model for S1, which moved in the direction of the left S2, near S3 direction. S5 is not affected by nodes S4 and S5. S5 is located in the optimal location and set the balance of the force. Based on the node stress

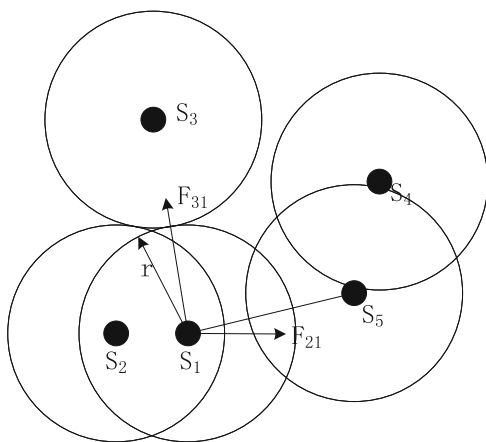


Fig. 145.1 Local node distribution

virtual force analysis for the local optimum coverage performance, a mechanical model of the node is shown by Eq. (145.3):

$$F(s_i, s_j) = \begin{cases} \frac{Km_i m_j}{d(i, j)^\alpha}, & \text{if } \text{disk}(s_i, s_j) \leq 2r, \\ 0, & \text{otherwise.} \end{cases} \quad (145.3)$$

In the preceding equation, with the condition $2r \geq d(i, j) \geq d_0$, $K = 1$, F is the attractive force, and the nodes move close to each other under the action of gravity. As shown in Fig. 145.1, node S1 moves in the direction of S3. With the condition $K = -1$, F is the repulsion force. The nodes move away from each other under the acting force. Figure 145.1 shows that nodes S1 and S2 move far away from each other. When F is zero, the nodes stop moving. In the next simulation experiment, the parameters Eq. (145.3) are set as follows: $m_i = 1$, $m_j = 1$, $\alpha = 1$, $d_0 = \sqrt{3}r$. In the local area of s_i , the sum of all the repulsive forces of s_i stress forces from its neighboring nodes is calculated using Eq. (145.4):

$$F = \sum_{j=1, j \neq i}^N F(s_i, q_j). \quad (145.4)$$

145.3.2 Node Location Update

According to Eq. (145.4) for node s_i reaction force, node s_i moves with step is set to 10 m. The location update relations are shown as Eq. (145.5) in each round:

$$\begin{cases} x'_i = x_i + F_{ix}/F_i * \text{step}, \\ y'_i = y_i + F_{iy}/F_i * \text{step}. \end{cases} \quad (145.5)$$

When a node is removed from the outside edge of a region to a task, it defines its location directly with respect to the border of $r/2$.

145.4 Simulation Experiment

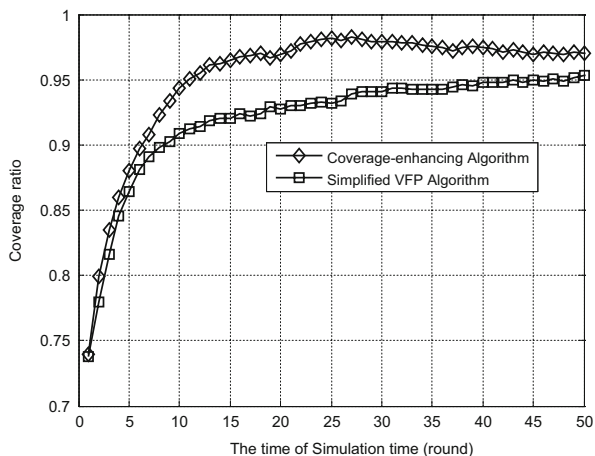
In MATLAB R2012a, a $1,000 \times 1,000$ task area, the algorithm is run with the sensor's perception radius r set to 90. The iteration time is set to 50 rounds. Based on Eq. (145.4), the number of deployed sensor nodes is determined to be 60.

1. Coverage ratio enhancement experiment

A coverage ratio comparison for the virtual force positioning (VFP) algorithm and coverage-enhancing algorithm is shown in Fig. 145.2.

It can be seen from the graph that the coverage ratio for the coverage-enhancing algorithm has increased from approximately 76 % at the initial deployment to

Fig. 145.2 Coverage rate



around 98 % through the iteration of 20 rounds. After 20 rounds, the coverage ratio remained steady at around 98 %, floating up and down by no more than 0.5 %. The coverage ratio of the VFP algorithm is lower than 95 %, which shows that the algorithm is an efficient, fast, wireless sensor network coverage-enhancement algorithm.

2. Mobile trajectory of sensor node

We set the simulation time to 20 rounds and 50 rounds and map the nodes' mobile trajectory diagram as shown in Figs. 145.3 and 145.4.

The red dots represent the initial deployment location of the sensor nodes, the blue lines represent the node movement trajectory, and the terminal represents the location of the nodes at the end of the simulation. Combining the coverage change curve and the two nodes' movement trajectories, it can be found that the coverage ratio reaches 98.18 % with 20 round after nodes random deployment. At this point, all nodes almost move to the location of the force balance. In the time about next 30 rounds, the nodes perform minor swings back and forth at the force balance point, and the coverage ratio almost does not change.

Conclusion

Set covering deployment is the basic technology that affects the design of routing protocols, network topology control, and management technology for wireless sensor networks. With the force balance algorithm, nodes move to locations under the control of stress forces from their neighbors. The nodes do not move when they arrive at the location of the node force equilibrium; accordingly, the nodes are relatively evenly distributed throughout the task

(continued)

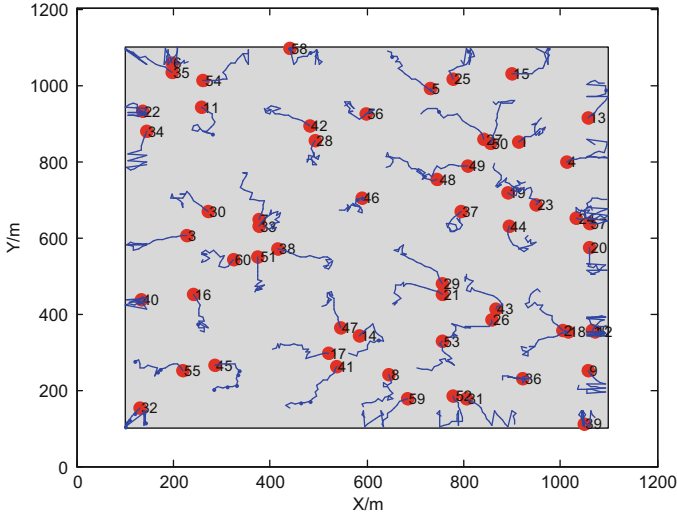


Fig. 145.3 $t = 20$, node movement trajectory

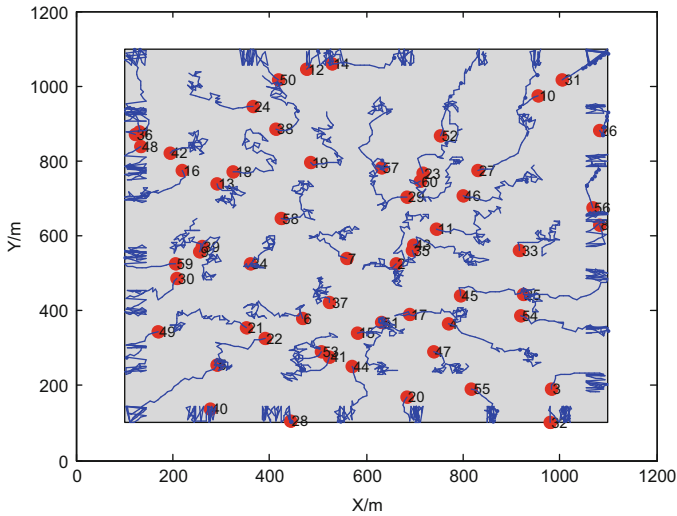


Fig. 145.4 $t = 50$, node movement trajectory

(continued)

area, and the coverage ratio improves to more than 98 % to meet the requirements of coverage performance. Experiments show that the new algorithm represents a kind of fast efficient deployment method to improve network coverage algorithm.

Acknowledgments This research was supported by the Foundation of Kun Ming University (XJL12004), China. The authors thank the anonymous reviewers whose comments have helped to significantly improve the quality of the article.

References

1. Akyildiz LF, Su WL, Sankarasubramaniam Y, Cayirci E. A survey on sensor networks. *IEEE Commun Mag.* 2002;40(8):102–14.
2. Ren FY, Huang HN, Huang HN, Lin C. Wireless sensor networks. *J Softw.* 2003;14(7):1282–91 (in Chinese).
3. Poduri S, Patten S, Krishnamachari B. A unifying framework for tunable topology control in sensor networks. Technical report, CRES-05-004. University of Southern California; 2005. p. 1–15.
4. Wang B, Lim HB, Ma D. A survey of movement strategies for improving network coverage in wireless sensor networks. *Comput Commun.* 2009;32(13):1427–36.
5. Liu B, Brass P, Dousse O, et al. Mobility improves coverage of sensor networks. In: *Proceedings of the 6th ACM International Symposium on Mobile Ad Hoc Networking and Computing*. Urbana-Champaign: ACM; 2005. p. 300–8.
6. Zou Y, Chakrabarty K. Sensor deployment and target localization based on virtual forces. In: *Proceedings of the IEEE INFOCOM*. San Francisco: IEEE; 2003. p. 1293–1303.
7. Aitsaadi N, Achir N, Boussetta K. Potential field approach to ensure connectivity and differentiated detection in WSN deployment. In: *IEEE international Conference on Communication*. Paris: IEEE Press; 2009. p. 1–6.
8. Tan I, Yu C, Yang M. Self-deployment algorithm of mobile sensor network based on uniform density cluster. In: *WiCOM 2010*. Chengdu: IEEE Press; 2010. p. 1–4.
9. Khedr AM, Osamy W. Mobility-assisted minimum connected cover in a wireless sensor network. *J Parallel Distrib Comput.* 2012;72:827–83.

Chapter 146

Network Node Importance Measurement Method Based on Vulnerability Analysis

Yahui Li, Hongwa Yang, and Kai Xie

Abstract As to select the important nodes from network, the key problems are to determine the basis and quantitative standard of evaluating node importance. This chapter proposes the measurement method of network node importance from the aspect of vulnerability, including topological structure vulnerability evaluation standard based on degree distribution, betweenness centrality, round-robin betweenness centrality, and extension degree distribution; and application vulnerability evaluation standard based on maximum load link and information value. The experiment results show that the measure standard of network node importance based on extension degree distribution not only reflects the value of the node itself, but comprehensively considers indirect effect of node to network; it can well describe the differences among nodes in a network, and time complexity of the algorithm is smaller.

Keywords Topological structure vulnerability • Application vulnerability • Node importance • Measurement method

146.1 Introduction

In real life, many systems can be described by the way of network, such as the Internet, telecommunication network, financial network, airport network [1], interpersonal network [2], sensor network, and command network. Based on the type,

Y. Li (✉)

Science and Technology on Communication Information Security Control Laboratory,
314000 Jiaxing, China

Northern Electronic Instrument Institute, 100191 Beijing, China

e-mail: eeihui@163.com

H. Yang

Science and Technology on Communication Information Security Control Laboratory,
314000 Jiaxing, China

K. Xie

Northern Electronic Instrument Institute, 100191 Beijing, China

e-mail: Xiekai8@126.com

© Springer International Publishing Switzerland 2015

W.E. Wong (ed.), *Proceedings of the 4th International Conference on Computer Engineering and Networks*, Lecture Notes in Electrical Engineering 355,

DOI 10.1007/978-3-319-11104-9_146

network can be divided into regular network, random network, fully connected network, small-world network [3], complex network [4], etc.

With continuous deepening of network research, the research of which nodes play important roles in network function operation has caused wide attention of scholars both at home and abroad, and proposed many evaluation methods of node importance combined with different actual backgrounds. All of them are based on differences among nodes to explore the importance of network node from some aspects, such as the status of node itself in interpersonal network, control ability of node to information transmission on the Internet, and the flow of node processing information in traffic network, etc.

For selecting an important goal node from network, the key problem is to determine the basis and quantitative standard of evaluating node importance c_i from the aspect of vulnerability. Generally, the node with greater effects to surrounding nodes can be regarded as having more value. The node importance c_i can be expressed as:

$$c_i = (1 + \alpha)L_i \quad (146.1)$$

in which L_i is the load of node i , namely, the intrinsic value of the node, and α is redundant capacity of the node and the value is more than 0. Generally, the node with the maximum value distribution c_i is most important to the security of network, and related to network topological structure and the capacity of node itself.

Vulnerability is defined as a method to measure system vulnerabilities, which are the points of causing system loss. From the aspect of topological structure vulnerability and application vulnerability, this chapter extracts general characteristics of different networks in order to provide measurement methods of network node importance. The topological structure vulnerability focuses on analyzing the importance of node in network structure, namely, the influence to network when the node is destroyed; the application vulnerability focuses on analyzing the fragility of network during business operation, which is closely related to the network type and requires specific analysis accordingly, for example, processing goal number overload problem of sensor network information integration center.

146.2 Analyzing Network Node Importance Based on Topological Structure Vulnerability

Network topological structure vulnerability analysis is equal to removing a node from network (i.e., removing all edges connected to the node at the same time); thus it may cause some paths among nodes being interrupted. The network will be regarded as being robust to the destruction of nodes if most of nodes of the network are still connected after removing a small amount. The network will be regarded as

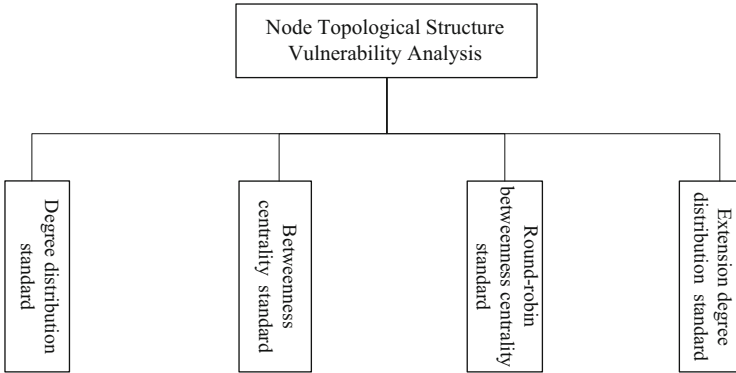


Fig. 146.1 System diagram of node topological structure vulnerability analysis

having a high vulnerability to sabotage if the connectivity of network is greatly affected after the sabotage of a small amount of nodes.

In the aspect of topological structure vulnerability analysis, this chapter gives consideration to computation complexity of algorithm itself as well as the influence of nodes in topological view, and proposes the following standard to measure and sequence it, as shown in Fig. 146.1.

1. Based on degree distribution standard

It can obtain important nodes of network with fastest speed if assuming that node value is directly related to node degree value and sequence the nodes of network in accordance with descending order of degree value.

In the network, the degree of node means the number of edge connected to the node. The degree k_i of node i is defined as follows:

$$k_i = \sum_{j=1}^N e_{ij} \tag{146.2}$$

If the edges in network have directions, such as the edge of sensor network from source node to receiving node, the degree of nodes will be divided into out-degree and in-degree. The out-degree of node means edge number from this node to other nodes; the in-degree of node means edge number from other nodes to this node.

2. Based on betweenness centrality standard

Betweenness centrality includes node betweenness centrality and edge betweenness centrality; it is a global variable and reflects the effect and influence of a node or an edge. The node betweenness centrality means the number ratio of all shortest paths in network passing through the node, where there is very strong interdependency between node betweenness centrality and degree. The betweenness centrality distribution is quite different for different type networks;

generally, the betweenness centrality will be higher if the edge connected with node is more, and similarly, the node importance will be higher.

$$l_i = \sum_{j=1}^N \sum_{k=j+1}^N \frac{\text{num}(d_{jk}^i)}{\text{num}(d_{jk})} \quad (146.3)$$

in which $\text{num}(d_{jk})$ is the number of shortest paths between node j and node k and $\text{num}(d_{jk}^i)$ is the number of shortest paths passing through the node i between node j and node k .

3. Based on round-robin betweenness centrality standard

In order to reflect the dynamic characteristics of network, the network structure will change accordingly along with the state change of each node. The feature of network degree distribution being extremely uneven determines that some key nodes have un-negligible influence to network structure, such as core node. Therefore, various features of target network will always have varying degrees of damage after destroying the node with maximum betweenness centrality value. In order to capture and describe the detail, we need to carry out round-robin mode of “compute betweenness centrality—simulate destruction—compute betweenness centrality,” to remove the node with maximum betweenness value in current network in turn.

4. Based on extension degree distribution standard

In addition to consider node degree (i.e., the first-layer neighbor of node), the influence of node should also be extended to the influence of neighbors of node neighbor (the second-layer neighbor of the node), if necessary, to the third-layer neighbors. The sum of degree of the node itself and degree of surrounding first-layer neighbor node is called extension degree of the node. Its sequence is in accordance with extension degree value of nodes in the network and higher of extension degree value of node higher of node value. This method gives consideration to balance between evaluation accuracy and computation complexity. The design idea is simple and practical, and also it overcomes the weakness of using node degree only which does not accurately express node value in network. For example, the degree value of one node is very high, but the nodes connected to it are not important, then, this node will be not important actually, and the extension degree of node is smaller; on the other hand, the node will be very important in reality if its degree value is not too high, but most of nodes connected to it are very important, and the extension degree of node is also high; thus, it is consistent with the performance of node importance in the real world.

If we only calculate the second-layer neighbor of the node, the extension degree k'_i of node i is defined as follows:

$$k'_i = k_i + \sum_{j \in N \& j \neq i} e_{ij} \cdot k_j \tag{146.4}$$

146.3 Analyzing Network Node Importance Based on Application Vulnerability

Aiming at fully connected network, random network, small-world network, etc. it is difficult to determine the important nodes of network through topological structure vulnerability analysis. Therefore, we should combine application vulnerability analysis with business characteristics of network and use it to determine the important nodes of network when analyzing them.

In the aspect of application vulnerability analysis, this chapter gives consideration to network flow, information, and structure, and proposes the following standard to measure and sequence the value of node in network, as shown in Fig. 146.2.

1. Based on maximum load link standard

Combined with the characteristics of practical application of network, this chapter takes into account the nodes that directly are connected with maximum load link into destruction objects. Here, load L of a link e is defined as a positive correlation function between link degree and bidirectional network flow passing through this link. Generally, the link load of topological meaning is measured by link betweenness centrality $C_B(e)$. It is obvious that the computation of $C_B(e)$ needs to use global information of network topology [5], and it is unrealistic in huge network.

Combined with local network topology and flow information, link load $L(e)$ is expressed as follows:

$$L(e) = L_{\text{Topological}} \cdot L_{\text{Traffic}} = k_u \cdot k_w \frac{\sum T_e}{\sum_{u \in V'} \sum T_u} \tag{146.5}$$

in which $\sum T_e$ is the number of the transmitted data packet through this link, $\sum_{u \in V'} \sum T_u$ is the number of the generated data packet, V' is the local topology

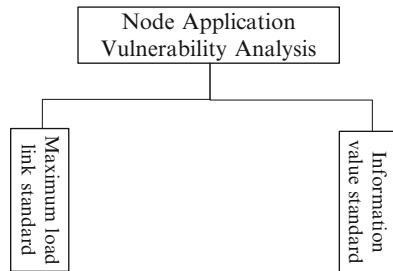


Fig. 146.2 System diagram of node application vulnerability analysis

range known as current nodes, and k_u and k_w mean the degree of nodes at two ends of link.

$k_u \cdot k_w$ is expressed as degree k_e of link. Holme [6], etc. have proved that in k_u , k_w , $k_u + k_w$, $\min(k_u, k_w)$, and $\max(k_u, k_w)$ have several kinds of link degree-related definition, and the actual simulation result of the first kind has the highest interdependency about link betweenness centrality.

2. Based on information value standard

Generally, one node runs many different services, such as command service, information processing service, etc. The same service among different nodes is transmitted through special links, thus forming the information network of this service. The information resource value (information value) of the same service in different nodes or different services in the same node is different, and the information value of node service reflects the relative importance of this node in information network of this service. Therefore, the computation method of service information value should be based on this principle: the higher the value of service information of a node is, the more important this node is in service information network. The evaluation indicators of various types of services are different, for example, the command service indicators are command guide groups, guide information density, etc. while the major indicators of information processing service are information processing accuracy, handling delay, and so on. Therefore, the service importance evaluation is dynamic, multivariable, and with certain subjectivity, and has no general rule.

If we set the parameter indicator vector of information value of service s_j as \vec{V}_j , the computation formula of information value SIV_{ij} of s_j on node h_i will be as follows:

$$SIV_{ij} = \vec{w}_j \cdot \vec{v}_{ij} \tag{146.6}$$

in which \vec{w}_j is the weighted vector of information value parameter vector \vec{V}_j of service s_j and \vec{v}_{ij} is the quantitative evaluation of service s_j on node h_i based on \vec{V}_j . The quantitative method of various information value indicators will be given according to the expert experience.

The information value of a node depends on service information value and number running on this node. If S_i is the service set provided by node H_i , the information value HIV_i of H_i will be as follows:

$$HIV_i = \sum_{s_j \in S_i} (\omega_j \cdot SIV_{ij}) \tag{146.7}$$

in which SIV_{ij} represents the information value of service s_j on h_i and ω_j is the weight of service s_j in all service types. The higher the information value of a node is, the more important the information provided by this node is.

146.4 Evaluation Case Analysis of Network Node Importance

Choosing an interpersonal social relation network as the research object, as shown in Fig. 146.3, we evaluate and sequence node importance of interpersonal social relation network, respectively, by degree distribution, betweenness centrality, round-robin betweenness centrality, and extension degree distribution standards. The evaluation results of top 12 important nodes are shown in Table 146.1.

We can find from Table 146.1 that it can't perfectly distinguish important nodes of network only by node degrees, for example, the nodes 8, 11, 20, and 38 have the same degree 3; however, their roles in network are obviously different due to the effect of degree differences among neighbor nodes connected with them.

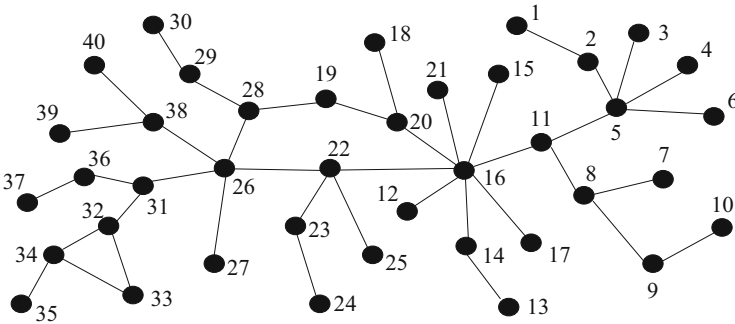


Fig. 146.3 Interpersonal social relation network structure [7]

Table 146.1 Evaluation results of node importance (top 12)

Importance	Degree distribution		Betweenness centrality		Round-robin betweenness centrality		Extension degree distribution	
	Node	Value	Node	Value	Node	Value	Node	Value
1	16	8	16	0.660	16	0.371	16	24
2	5	5	26	0.537	26	0.215	22	20
3	26	5	22	0.518	11	0.191	26	19
4	22	4	11	0.453	31	0.131	11	19
5	8	3	31	0.314	5	0.125	20	14
6	11	3	5	0.280	22	0.109	5	13
7	20	3	8	0.191	8	0.084	28	13
8	28	3	32	0.189	32	0.075	28	12
9	31	3	28	0.178	38	0.075	32	11
10	32	3	20	0.159	28	0.069	14	11
11	34	3	38	0.146	20	0.056	38	10
12	38	3	19	0.108	14	0.052	8	9

The experimental results show that the measurement method of network node importance based on extension degree can describe the differences among nodes in network in more detail.

Different evaluation standard explores the same problem from different aspects, so the standard may not be good or bad, and each standard has its own advantages and disadvantages, for example, node degree distribution standard focuses on local influence and the algorithm is simple, but it can't reflect the overall role of nodes in network; the evaluation results of node betweenness centrality standard are more accurate, more in line with objective fact, but the algorithm time is long and complexity is high; node extension degree standard starts with local feature of network, not only fully reflects the influence of the node itself, but also comprehensively considers indirect influence of neighbors to the node itself. In interpersonal network, channel sales network, infectious disease network, and many other actual networks, as well as under the situation of obtaining the non-global information of network and a huge network scale [8], its algorithm complexity is smaller, but the result is not very accurate, so it needs to be extended to the third-layer neighbors and further.

Conclusion

The importance of nodes in network reflects the performance influence magnitude to network under possible fault conditions. The chapter carries out qualitative analysis and quantitative evaluation to node importance from the two aspects, topological structure vulnerability and application vulnerability, and gives comparative analysis to the evaluation standards. In most of the actual networks, such as the Internet, WWW, email network, and interpersonal network, the network scale is huge and topological structure is complex, so it is very important to find a kind of evaluation standard which is simple, with small computation complexity as well as effective to evaluate network node importance, such as improving extension degree distribution evaluation algorithm.

References

1. Guimera R, Amaral LAN. Modeling the world-wide airport network. *Eur Phys J B*. 2004;38(2):381–5.
2. Newman MEJ. The structure and function of complex networks. *SIAM Rev*. 2003;45(2):167–256.
3. Watts DJ, Strogatz SH. Collective dynamics of small-world networks. *Nature*. 1998;393(6684):440–2.
4. Barabási A, Albert R. Topology of evolving networks: local events and universality. *Phys Rev Lett*. 2000;85(24):5234–7.
5. Yong C, Aiuqn H, Tianyou C, et al. Evaluation method of link importance in communication network. *Electron J*. 2003;31(4):573–5 (In Chinese).

6. Holme P, Kim BJ, Yoon CN, et al. Attack vulnerability of complex networks. *Phys Rev E*. 2002;65(5):056109.
7. Klodahl AS. Social networks and the spread of infectious diseases: the AIDS example. *Soc Sci Med*. 1985;21(11):1203–16.
8. Junliang Z. Reliability research of complex network. Dalian: Dalian University of Technology; 2006 (In Chinese).

Chapter 147

Modeling for Information Transmission of Consumer Products Quality and Safety Based on the Social Network

Yingcheng Xu, Xiaohong Gao, Ming Lei, Huali Cai, and Yong Su

Abstract This chapter considers the web information of consumer products quality and safety as research object. As to the transmission characteristics of social network, we established an information transmission model without the government's intervention based on the social network to analyze the relationship of parameters in terms of the information transmission by means of simulation. The results show that the proposed model is more effective and feasible.

Keywords Web information • Consumer products quality safety • Information transmission model • Social network

147.1 Introduction

In recent years, incidents in respect of the consumer product's quality and safety often occur in rapid succession in our country, such as Kumho Tires, Da Vinci furniture, faucet lead beyond the standard, poison uniforms event, and so on; these events directly affect national economy and people's livelihood. They are not only the top priority of consumer attention but also the focus of public opinion and governments. With the development of web 2.0, especially the appearance of emerging social media which users are greatly involved in such as WeChat, blogs, wikis, Weibo, BBS, social networks, and content community. The modes of information transmission are more and more diversified and complicated. Web has gradually become an important platform for the information release of product quality safety, evolution, and monitoring of public opinions. Sarafidis carried on further researches on network public transmission in network community and

Y. Xu • X. Gao • H. Cai (✉) • Y. Su
Quality Management Branch, China National Institute of Standardization,
100191 Beijing, China
e-mail: springblue410@126.com

M. Lei
Quality and Technical Review Center, 710048 Xi'an, China
e-mail: kathy-lei@163.com

© Springer International Publishing Switzerland 2015
W.E. Wong (ed.), *Proceedings of the 4th International Conference on Computer Engineering and Networks*, Lecture Notes in Electrical Engineering 355,
DOI 10.1007/978-3-319-11104-9_147

1291

furthermore proposed scientific warnings and effective intervention strategies [1]. Isham et al. proposed the correlation functions of degree based on the rumor spreading model and analyzed the influence of network topology on rumor spreading by numerical calculation [2]. Becker et al. proposed a generic framework which utilized clustering method to identify relevant events of social media [3]. Zhang et al. discussed the information dissemination model on online social network [4]. Xie et al. carried out some simulation researches on two competition topics of dissemination based on complex network [5]. Wang et al. carried out relevant researches on evolution of public opinions of the microblog based on complex network theory [6]. Jalili analyzed the formation of social power and public opinions based on complex network as well as carried out simulation experiment in terms of small-world and scale-free network [7]. Zhang et al. studied the relationship between the tie-strength and information propagation on online social networks [8]. Although numerous researches have been carried out, the results are still far from satisfaction. Firstly, the depth and the mode of web information dissemination need to be further analyzed; secondly, the information dissemination rule in terms of main channels, structure, path, and evolutionary cycles should be investigated as well. On the basis of previous researches, this chapter attempts to build an information transmission model of product quality and safety incidents based on social network with contributions made primarily from the following two aspects, namely, the proposal of a life-cycle model and the media influence factors including the characteristics of product quality and safety information and the establishment of an information transmission model of product quality and safety with the social network.

147.2 Information Transmission Mode Based on the Social Network

The essence of newly developed social network is online social network service. Different from the organization way based on content, online social network consists of users. Participating users join in network, release personal information and any content, and connect with anyone related to them. As a kind of online service platform, it strives to build and react to social network made up of human relations. Online social network is made up of users and connections. Imagine there are n members in a social network, of which the i th member is A_i ($i = 1, \dots, n$), the relation of A_i and A_j is r_{ij} , then online social network can be represented as a form of matrix $E = (r_{ij})_{n \times n}$.

Users often join online social network by means of registration. The connections among users can be acquaintance in real world or known based on virtual world. According to the difference of website services, connections can be bidirectional or unidirectional. Online social network has big advantages in terms of information sharing and seizing social relationship. Early online social network can be dated to

the network formatted by e-mail sending-receiving among e-mail users. Current online social networks like social network and blog have become the most influenced network media forms.

$$E = \begin{bmatrix} r_{11} & r_{12} & \cdots & r_{1n} \\ r_{21} & r_{22} & \cdots & r_{2n} \\ \cdots & & & \cdots \\ r_{n1} & r_{n2} & \cdots & r_{nn} \end{bmatrix}$$

This section primarily studies information transmission in social network. Essentially, human behavior modes can be summarized based on the following two kinds:

1. Push mode (information-diffusing): When node A in the network possesses information and has transmission will, node A will transmit the information to another node B actively. Similarly, node A transmits information to a node and node set one by one or at the same time. Information transmission acts as radial pattern at this moment.
2. Pull mode (information-seeking): When node A in the network possesses information and another node B is interested in the information, node B will emit the curiosity signal when it knows node A possesses the information. After that, node A transmits information to node B and the whole information transmission process competes. Similarly, this kind of information transmission chain is formed among many nodes. Now the network becomes a complex information transmission network.

147.3 Information Transmission Model of Consumer Products Quality and Safety

In the SIR model, when the susceptible (S) crowd touches infective (I) crowd, they always turn into infective (I) state passively and won't exit whether they accept to become infective (I) subjectively. This is discrepant with the information transmission model based on social network which we are studying; therefore, we propose another model on the basis of SIR model.

Our study model continuously maintains two characteristics of SIR transmission model. Individual transmission process is divided into multiple statuses and infected person is immune ultimately. In order to describe the transmission process, we divide the individual statuses into four statuses such as the susceptibly infected status, the non-informed and may be told (S , suspected); the infection status, the informed (I); the involved in transmission (D , disseminating) status, the informed but not transmitted (including stopping transmission status); and R (resistant) status. The status of the node in the network continuously changes along with individual decision. Status transition of node is shown in Fig. 147.1.

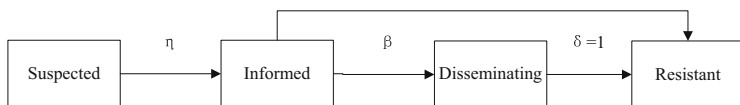


Fig. 147.1 Status transition of node

We need attention in the model. Status D is a child status of status I . Actually we can see status I as an intermediate status. Upon the node’s arrival at status I , it immediately chooses to be transmitted to status D or not transmitted to status R . At the moment of t , the number of nodes in status S is 0. We introduce status I in order to conveniently compute the number of insiders in the model. When counting actually, status I , status D , and status R will be computed repeatedly, which needs $S(t) + D(t) + R(t) = 1$.

As shown in Fig. 147.1, see from status D at the moment of t . The node loses interest in information with probability δ after the transmission’s completion. The status turns into the stopping transmission status R . When the node is in the susceptible infection status S , D will have two kinds of changes while touching the transmission node. One change is interested in information and reading information (inform will), and the node will be transmitted from status S into status I . The other change is not interested in information and reading information (no inform will). The node doesn’t change status and maintain at status S . When the nodes read information and become informed (status I), a part of those will produce transmission aspiration after becoming insiders and then will be D . The other parts of the nodes that don’t produce transmission will become immune nodes and stop transmission.

In reality, the number of individual directional contracted people is equal and closed to obey the Poisson distribution; therefore, the network to be discussed is homogenous network. Imagine the average degree of network is k , according to status transition of node in Fig. 147.1; at the moment of t , we can get the formula as follows:

$$\begin{cases} dS/dt = -\alpha S(t)D(t) \\ dI/dt = \eta\alpha S(t)D(t) \\ dD/dt = \beta\alpha S(t)D(t) - \delta D(t) \\ dR/dt = (1 - \beta)\eta\alpha S(t)D(t) + \delta D(t) \end{cases} \quad (147.1)$$

where $I(t) = D(t) + R(t)$, $S(t) + D(t) + R(t) = 1$.

Parameters in the model are explained as:

1. Relative contract proportion α : The proportion of friends who can accept information appointed by disseminators in all friends. The proportion is influenced by the disseminator’s subjective will and network-provided functions. In social network and blog, the functions of sharing and forwarding are usually facing all friends with the contract proportion reaching 1.

2. Inform will η : The probability of the individual who receives disseminator's information scans the information. After receiving the information, the individual will make a rough estimation of information content by scanning title. The event attributes title contains (severity of the event, potential impact on users made by event), which will be an important gist for individual estimation. By estimating the earnings (inform) and cost (time cost) of scanning the information, the individual will make a decision whether they've known each other deeply. Therefore, the inform rate will be functioned by both relative contract proportion and inform will.
3. Inform rate λ : The proportion of informed friends in all friends when the information disseminators transmit information to friends. The proportion is decided by the number of friends selected by such disseminators and the subjective will of scanning the information. In this model, the inform rate λ is the product of relative contract proportion α and inform will η ; thus $\lambda = \alpha * \eta$. In social network and blog, $\alpha = 1$, so $\lambda = \eta$.
4. Transmission will β : The probability of insiders transmitting the scanned web information of consumer quality and safety to friends. As an insider, the individual will make a decision whether or not to transmit information to friends. The decision is influenced by the user's character and behavior on the one side. On the other side, it is influenced by the earnings (such as satisfaction of the drawing attention) and the time cost acquired by transmitting the information.
5. Proportion of losing interest δ : The probability of disseminator losing interest in or forgetting the transmitted information. After transmitting information of consumer product's quality and safety, the individual may believe the information unworthy and thus lose interest in or forget the information.

Taking $\alpha = 1$ into differential Eq. (147.1), we get Eq. (147.2):

$$\begin{cases} dS/dt = -S(t)D(t) \\ dI/dt = \eta S(t)D(t) \\ dD/dt = \beta S(t)D(t) - \delta D(t) \\ dR/dt = (1 - \beta)\eta S(t)D(t) + \delta D(t) \end{cases} \quad (147.2)$$

where $I(t) = D(t) + R(t)$, $S(t) + D(t) + R(t) = 1$.

147.4 Experiment Study

Simulating the above-described model and imagining there are 100 nodes as SIR model assumption, there are three sickened and infective nodes, 96 non-sickened and infective nodes, and one lifelong immune node at the moment of $t = 1$; thus $S(t) = 0.96$, $I(t) = 0.04$, $D(t) = 0.03$, and $R(t) = 0.01$. Setting up parameters $\eta = 0.8$, $\beta = 0.5$, $\delta = 0.1$, and numerical simulation of 50 steps (in the simulation process compute $D(t)$ and $R(t)$ firstly, and then compute $S(t)$ and $I(t)$), we get the currency of $S(t)$, $I(t)$, $D(t)$, and $R(t)$ as shown in Fig. 147.2:

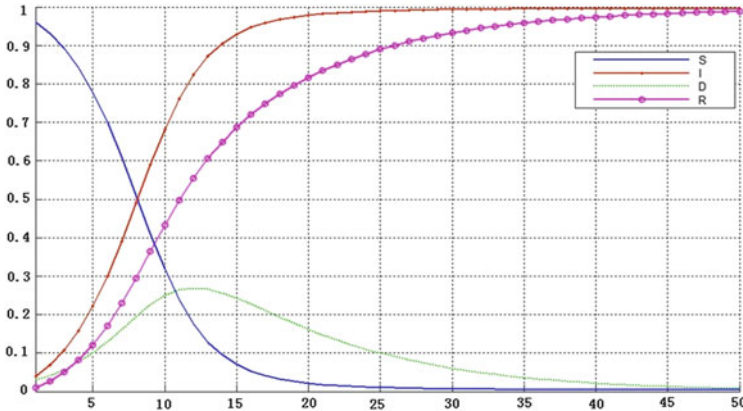


Fig. 147.2 Changing currency

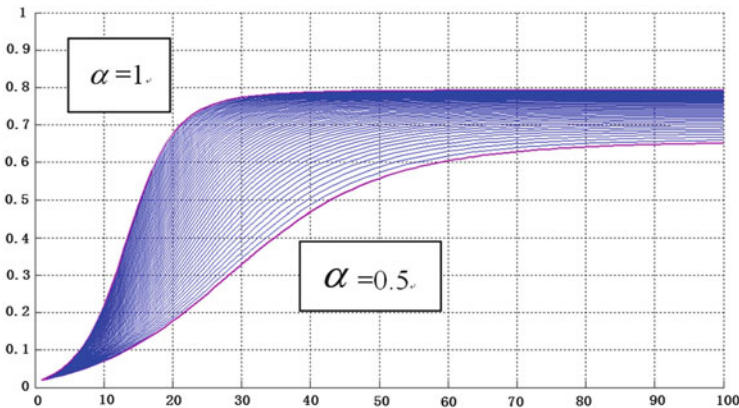


Fig. 147.3 $I(t)$ changes with α

As can be seen from Fig. 147.2, $S(t)$ decreases and $R(t)$ increases when the time t increases as similar as SIR model. The newly added node number $D(t)$ will increase and then decrease as the time increases. $S(t)$ increases as time increases, but tends to a value less than 1 finally. This indicates that all the nodes in the network can't become insiders even if the whole transmission process finishes, which is different from all the nodes that will be infected in SIR model. This is because we add parameter of inform will η . Susceptible nodes will choose to be informed or not informed according to their own inform will when contracting information; nevertheless, in the SIR model, they passively become infective.

On the basis of simple analysis to the model, we know that the inform proportion is the proportion of information-informed persons in all the persons. At the moment of t , the inform proportion in the network can be indicated by $I(t)/(S(t) + I(t) + R(t))$. In the above model, the inform proportion is $I(t)$, which is an increasing process and tends to a specific value when time increases. Figure 147.3 shows that the bigger the

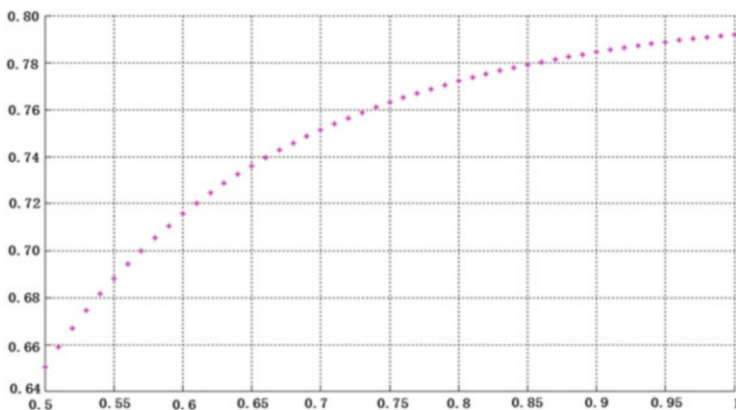


Fig. 147.4 I_0 changes with α

α is, the faster the inform proportion will become maximum. Figure 147.4 shows the ultimate value of $I(t)$, $I_0 = \lim_{t \rightarrow \infty} I(t)$ changes as α changes, and the bigger α is, the bigger the ultimate value of $I(t)$ is.

Conclusion

In this study, we propose an information transmission model without the government's intervention as to the event information characteristics of consumer product's quality and safety. The research on the transmission rule of product's quality and safety based on social network has provided decision support for the monitoring and management of web information of consumer product's quality and safety.

Acknowledgements This research is supported by the National Natural Science Foundation of China (Grant Nos. 71301152, 71271013 and 71301011), National Social Science Foundation of China (Grant No. 11AZD096), National Key Technology R&D Program of the Ministry of Science and Technology (Grant Nos. 2013BAK04B02 and 2013BAK04B04), Quality Inspection Project (Grant No. 201410309), and China Postdoctoral Science Foundation (Grants Nos. 2013T60091 and 2012M520008).

References

1. Sarafidis Y. What have you done for me lately-release of information and strategic manipulation of memories. *Econ J.* 2007;117(3):307–26.
2. Isham V, Harder S, Nekovee M. Stochastic epidemics and rumors on finite random networks. *Physica A.* 2010;389:561–76.
3. Becker H, Naaman M, Gravano L. Learning similarity metrics for event identification in social media. In: *Proceedings of the third ACM international conference on Web search and data mining*, New York, USA, DBLP, 2010. p. 291–300.

4. Zhang YC, Liu Y, Zhang HF, et al. The research of information dissemination model on online social network. *Acta Phys Sin.* 2011;60(5):60–6.
5. Xie MS, Jia Z. Simulating the spreading of two competing public opinion information on complex network. *Appl Math.* 2012;3:1074–8.
6. Wang R, Jin YS, Li F. A review of microblogging marketing based on the complex network theory. In: 2011 International conference in electrics, communication and automatic control proceedings. New York: Springer; 2012. p. 1053–60.
7. Jalili M. Social power and opinion formation in complex networks. *Phys A Stat Mech Appl.* 2013;392(4):959–66.
8. Zhang H, Wang D, Wang L, Bi Z, Chen Y. A semantics-based method for clustering of Chinese web search results. *Enterp Inf Syst.* 2014;8(1):147–65.

Chapter 148

A Multi-classifier-Based Multi-agent Model for Wi-Fi Positioning System

Shiping Zhu, Kewen Sun, and Yuanfeng Du

Abstract Fingerprint-based Wi-Fi localization systems have become attractive for researchers in indoor location-based services. Due to the fluctuant characteristics of received signal strength (RSS) and the lack of the research on environmental factors affecting the signal propagation, the accuracy of the previous systems heavily relies on environmental conditions. In this chapter, we propose a novel multi-agent fusion algorithm which combines multiple classifiers. Unlike previous multi-classifier combination rule, the proposed approach considers the relativity among classifiers according to co-decision matrix. Experimental results show that the multi-classifier approach outperforms single classifier in the test environment with the average accuracy and standard deviations greatly improved in the test environment.

Keywords Wi-Fi localization • Multi-agent fusion algorithm • Co-decision matrix • Multi-classifier

148.1 Introduction

In recent years, the rapid development of mobile smart phone technologies has made indoor location-based service (LBS) more available, such as indoor localization, navigation, and location-based security; nevertheless, owing to the complicacy of the indoor environment, GPS (global positioning system) can't provide reliable and precise positioning services in indoor environment. WLAN (wireless local area networks)-based indoor positioning system has been extensively studied with a lot of solutions proposed in the past two decades [1], and most of the researches have focused on received signal strength indication (RSSI) method. Compared with time-of-arrival (TOA) and angle-of-arrival (AOA) [2] algorithms, RSS can be easily received by a Wi-Fi-integrated mobile device.

S. Zhu • K. Sun (✉)

School of Computer and Information Engineering, Hefei University of Technology,
230009 Anhui, China

e-mail: kewen.sun@hfut.edu.cn

Y. Du

School of Electronic and Information Engineering, Beihang University, 100000 Beijing, China

© Springer International Publishing Switzerland 2015

1299

W.E. Wong (ed.), *Proceedings of the 4th International Conference on Computer Engineering and Networks*, Lecture Notes in Electrical Engineering 355,

DOI 10.1007/978-3-319-11104-9_148

According to the published results and literature surveys [3, 4], RSS (fingerprint) methods outperform other techniques in indoor positioning scenarios. Fingerprint wireless positioning method [5] is performed on two phases: off-line phase and online phase. In off-line phase, RSSs are received at various positions of the target place and stored in a database called radio map. In online phase, RSS measured by a WLAN-enabled device is used to estimate a location by means of a variety of techniques, such as k -NN [4], Gaussian distribution [6], Bayesian [7], and PPMCC [8].

In this work, we propose a multi-classifier approach for Wi-Fi-based positioning system, and introduce a multi-agent model [9] for multiple classifier fusion. In order to demonstrate the effectiveness of multi-classifier, we have evaluated the proposed system in the test environment by adopting three classifiers such as k -NN, Gaussian distribution, and PPMCC.

There are few studies related to the multi-classifier method for Wi-Fi-based indoor localization. One introduced a fuzzy rule-based multi-classification system by using standard methodologies for component classifier generation such as bagging and random subspace along with fuzzy logic to deal with the huge uncertain characteristics of Wi-Fi signal [10]; another combined the Bayesian combination rule and the majority vote for multi-classifier, assuming that the classifiers are independent between each other [11]. In our work, we introduce a multi-agent combination approach, which can provide higher positioning accuracy in our experiment; it considers the correlation of each classifier, while the Bayesian rule is not taken into account.

The remainder of this chapter is organized as follows. In Sect. 148.2, we introduce a multi-classifier approach for the Wi-Fi-based positioning systems. In Sect. 148.3, the effectiveness of the proposed system is demonstrated by experiments. This chapter summarizes our work and suggests further research in section “Conclusion”.

148.2 Proposed Method

The algorithm of the proposed system can be illustrated in Fig. 148.1. In the off-line phase, the RSSs from all APs (access points) to each RP (reference point) are collected in the test environment as learning data. The learning data can be divided into two parts, the classifier training set $U1$ and the fusion training set $U2$.

The classifier training set $U1$ is used to construct the fingerprint database. Assume that there are m APs, denoted by AP_1, AP_2, \dots, AP_m , and n RPs, denoted by RP_1, RP_2, \dots, RP_n . Each fingerprint is composed of a pair of data containing MAC address of an AP and its signal strength, and each RP consists of multiple pairs of data, such as $\{\langle MAC_1, RSS_1 \rangle, \langle MAC_2, RSS_2 \rangle, \langle MAC_3, RSS_3 \rangle, \dots\}$. After collecting the fingerprint, sort the RSSs for each RP and cluster the RPs at the same order of RSSs from detectable APs [12]. This cluster not only reduces the computational overhead from Youssef’s research [13], but also reduces the sparsity

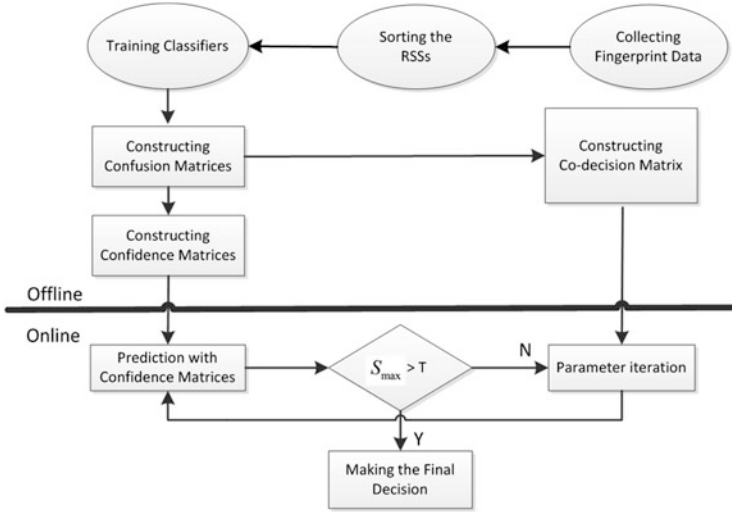


Fig. 148.1 Architecture of proposed indoor positioning system

of the confusion matrices, confidence matrices, and co-decision matrices which will be used in the rest of this chapter.

The fusion training set U_2 is used to construct the confusion matrix C . In the positioning system, if there are M possible locations, the confusion matrix C contains $K M \times M$ matrices $C^{(k)}$ ($k = 1, 2, \dots, K$) and the element of $c_{ij}^{(k)}$ represents the number of the samples collected in location i , which is assigned to location j by the classifier k .

Obviously, the total number of samples collected in location i can be expressed as a row sum $\sum_{i=1}^M c_{ij}^{(k)}$, and the total number of samples assigned to location j can be expressed as a column sum $\sum_{i=1}^M c_{ij}^{(k)}$. Then, the confidence matrix B can be calculated by the confusion matrices C according to Bayes' theorem, which can be written as below:

$$b_{ki}(x) = P(E(x) = i | e_k(x) = j_k) = \frac{c_{ij_k}^{(k)}}{\sum_{i=1}^M c_{ij_k}^{(k)}} \quad (148.1)$$

The element of $b_{ki}(x)$ represents the probability that the fingerprint x is assigned to location j_k by the classifier k ; as to any unknown fingerprint x , the row sum of confidence matrix $B(x)$ is equal to 1, namely,

$$\sum_{i=1}^M b_{ki}(x) = 1 \quad k = 1, 2, \dots, K \quad (148.2)$$

The co-decision matrix D shows the decision correlation made by the two

classifiers. That is, $D = [d_{j_1, j_1, i, k_1, k_2}]_{M \times M \times M \times K \times K}$, where the element of $d_{j_1, j_1, i, k_1, k_2}$ can be defined as below:

$$d_{j_1, j_1, i, k_1, k_2} = P(E = i | e_{k_1} = j_{k_1}, e_{k_2} = j_{k_2}) \tag{148.3}$$

The classifier k_1 assigns fingerprint x to j_{k_1} , the classifier k_2 assigns fingerprint x to j_{k_2} , and the fingerprints x belonging to i are the conditions, under which $d_{j_1, j_1, i, k_1, k_2}$ demonstrates the probability.

$$\begin{aligned} d_{j_1, j_1, i, k_1, k_2} &= \frac{A_3}{\sqrt{A_1 A_2}} \\ A_1 &= |\{x | E(x) = i, e_{k_1} = j_{k_1}, \forall x \in U_2\}| \\ A_2 &= |\{x | E(x) = i, e_{k_2} = j_{k_2}, \forall x \in U_2\}| \\ A_3 &= |\{x | E(x) = i, e_{k_1} = j_{k_1}, e_{k_2} = j_{k_2}, \forall x \in U_2\}| \end{aligned} \tag{148.4}$$

In (148.4), A_1 is the number that the location i is assigned to location j_{k_1} by classifier k_1 . A_2 is the number that the location i is assigned to location j_{k_2} by classifier k_2 . A_3 is the number that the location i is assigned to location j_{k_1} by classifier k_1 and also assigned to location j_{k_2} by classifier k_2 .

In online phase, as to the unknown fingerprint x , the final result can be obtained by the following methods:

- (a) Calculate the confidence matrix $B(x)$.
- (b) Define the decision matrix $Z = [z_{ki}]_{K \times M}$, in which the element of z_{ki} is the probability that classifier K assigns fingerprint x to the location i . The row sum of Z is equal to 1, and the diagonal elements denote the probability that the classifiers assign fingerprint x to the correct location. Initially, assume $Z(x) = B(x)$.
- (c) The matrix S is the final belief value, which can be expressed as below:

$$S = \left[\frac{1}{K} \sum_{k=1}^K z_{ki} \right]_{1 \times M}, i = 1, 2, \dots, M, \text{ and } l \text{ is the location with maximum belief value } S_{\max}.$$
- (d) If $S_{\max} > T$, go to (h); otherwise, go to (e). T is a certain threshold.
- (e) Change the decision matrix Z according to the correlation between classifiers, which can be expressed as below:

$$z_{ki} = z_{ki} + \frac{1}{K} \sum_{k_1=1, k_1 \neq k}^K d_{j, j_1, i, k, k_1} \cdot \sqrt{z_{ki} \cdot z_{k_1, i}} \tag{148.5}$$

$\frac{1}{K}$ is used to adjust the increment within the proper range, does not oscillate, and can converge quickly.

- (f) Normalize each row of matrix Z , still making it to 1.
- (g) Recalculate S_{\max} and l , and go to (d).
- (h) Let l be the final location for the multi-classifier.

148.3 Experimentation

148.3.1 Experimental Setup

The experiment is carried out on the 12th floor in the Tian Chuang Technology Building at Zhongguancun in Beijing, where the dimension of the space is 55×10 m. Referring to Fig. 148.2, there are 4 APs and 25 RPs (19 in the corridor, 6 in the room). The distance between every two neighboring RPs is 3 m. In order to collect data, we used the SAMSUNG I9100 mobile phone with Android 2.3.5 platform, and adopted the API provided by the platform. For each RP, 120 samples of the fingerprints are collected from each AP. 60 samples are used in the training set $U1$, 30 samples are used in the fusion training set $U2$ and 30 samples are used in the testing set $U3$.

To analyze the effectiveness of multi-classifier, we use three classifiers, k -NN (with $k = 1$), Gaussian distribution, and PPMCC to build multi-classifier, and the performance comparison of multi-classifier with these three classifiers, as shown in Table 148.1. When calculating the maximum belief value S_{\max} , set T equal to 0.6.

148.3.2 Experimental Results

It is clear to observe that the multi-classifier outperforms the conventional single classifier with the positioning accuracy, which is shown in Fig. 148.3. The average positioning accuracy of the multi-classifier is 1.55 m, while the average positioning

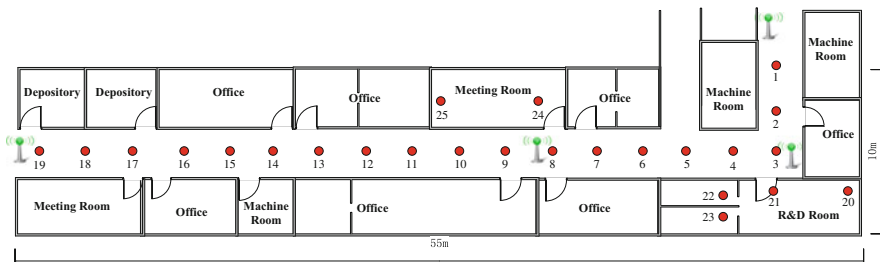


Fig. 148.2 Layout of the floor and positions of the 25 reference points

Table 148.1 Average positioning accuracy results for different classifiers

Classifiers	Average (m)	Std. dec (m)	67th Percentile	95th Percentile
k -NN	1.87	3.79	1.5	9
GAUSS	1.78	3.84	0	9
PPMCC	3.16	4.59	3	11.24
Multi-classifier	1.55	3.77	0	8.5

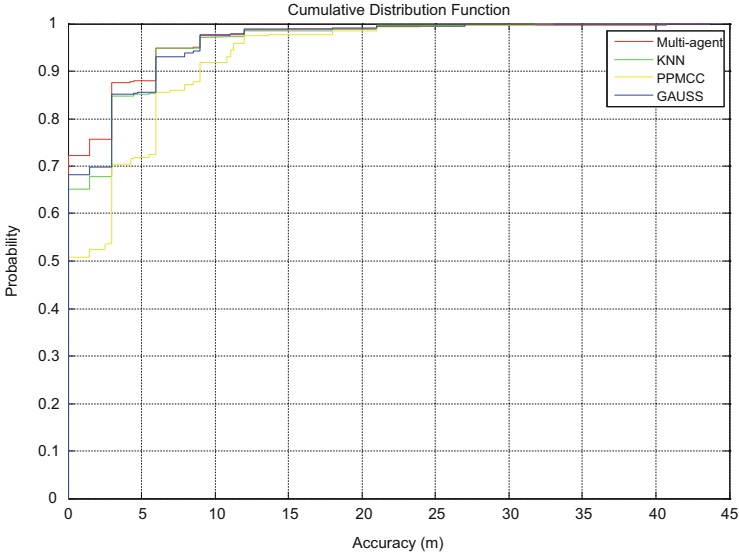


Fig. 148.3 Cumulative distribution function with all positions

accuracy values of k -NN, Gaussian distribution, and PPMCC are 1.87, 1.78, and 3.16 m, respectively.

Table 148.1 illustrates the average positioning accuracy results for different classifiers. The standard deviation of the positioning accuracy of multi-classifier is 3.77 m, while the standard deviations of the positioning accuracy for k -NN, Gaussian distribution, and PPMCC are 3.79, 3.84, and 4.59 m, respectively.

By analyzing the results, we conclude that multi-classifier can improve the accuracy in localization, which can be considered as a promising approach in Wi-Fi-based positioning systems.

Conclusion

In this chapter, the multi-classifier-based multi-agent model is proposed in Wi-Fi-based positioning system. The experimental results have proved that the localization performance of the proposed approach outperforms the existing k -NN, Gaussian distribution, and PPMCC in terms of the positioning accuracy and standard deviations.

In our current work, only three classifiers have been used. In further research, we will propose more efficient classifier fusion approach to reduce the complexity overhead by the multiple numbers of classifiers, and more classifiers will be adopted for the multi-classifier fusion in the near future.

References

1. Deak G, Curran K, Condell J. A survey of active and passive indoor localisation systems. *Comput Commun.* 2012;35(16):1939–54.
2. Borenovic M, Neskovic A. Comparative analysis of RSSI, SNR and noise level parameters applicability for WLAN positioning purposes. In: *Proceedings of the IEEE EUROCON 2009*; 2009. p. 1895–900.
3. Farivar R, Wiczer D, Gutierrez A, Campbell RH. A statistical study on the impact of wireless signals' behavior on location estimation accuracy in 802.11 fingerprinting systems. Washington, DC: IEEE Computer Society; 2009. p. 1, 8, 23–9.
4. Liu H, Darabi H, Banerjee P, Liu J. Survey of wireless indoor positioning techniques and systems. *IEEE Trans Syst Man Cybernet C Appl Rev.* 2007;37(6):1067–80.
5. Fang S-H, Lin T-N, Lee K-C. A novel algorithm for multipath fingerprinting in indoor WLAN environments. *IEEE Trans Wireless Commun.* 2008;7(9):3579–88.
6. Youssef MA. HORUS: a WLAN-based indoor location determination system. College Park: University of Maryland; 2004.
7. Madigan D, Elnahrawy E, Martin R. Bayesian indoor positioning systems. In: *Proceedings of INFOCOM.* IEEE Computer Society: Washington, DC; 2005. p. 1217–27.
8. Tsui AW, Chuang Y-H, Chu H-H. Unsupervised learning for solving RSS hardware variance problem in WiFi localization. *Mobile Netw Appl.* 2009;14(5):677–91.
9. Kou Z-B, Zhang C-S. Multi-agent based classifier combination. *Chinese J Comput.* 2003;26(2):174–9 (in Chinese).
10. Trawinski K, Alonso JM, Hernández N. A multiclassifier approach for topology-based WiFi indoor localization. *Soft Comput.* 2013;17(10):1817–31.
11. Shin J, Jung, SH, Yoon, G, Han, D. A multi-classifier approach for WiFi-based positioning system. *Electrical engineering and applied computing. Lecture notes in electrical engineering, LNEE*, vol. 90; 2011. p. 135–47.
12. Chen L-H, Wu EH-K, Jin M-H, Chen G-H. Homogeneous features utilization to address the device heterogeneity problem in fingerprint localization. *IEEE Sensors J.* 2014;14(4):998–1005.
13. Youssef M, Agrawala A, Shankar A. WLAN location determination via clustering and probability distributions. In: *Proceedings of the first IEEE international conference on pervasive computing and communications.* Washington, DC: IEEE Computer Society; 2003. p. 143–50.